



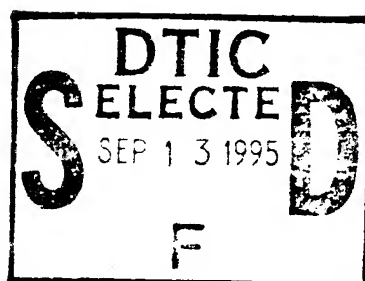
COMMISSION OF THE
EUROPEAN COMMUNITIES

EUROPEAN
MATERIALS
RESEARCH
SOCIETY

SYMPOSIA PROCEEDINGS 46

Amorphous Insulating Thin Films II

R.A.B. Devine
W.L. Warren
J. Kanicki
M. Matsumara
editors



DISTRIBUTION STATEMENT N

Approved for public release
Distribution Unlimited

€-MRS

AMORPHOUS INSULATING
THIN FILMS II

Accession For		
NTIS	CRA&I	<input checked="" type="checkbox"/>
DTIC	TAB	<input type="checkbox"/>
Unannounced		<input type="checkbox"/>
Justification		
By <i>form 50</i>		
Distribution /		
Availability Codes		
Dist	Avail and/or Special	
<i>A-1</i>		

1/10/81

19950912 040

EUROPEAN MATERIALS RESEARCH SOCIETY SYMPOSIA PROCEEDINGS

- Volume 1: Ceramic Materials Research (ed. R.J. Brook)
- Volume 2: Photon, Beam and Plasma Assisted Processing (eds. I.W. Boyd and E.F. Krimmel)
- Volume 3: Deep Implants (eds. G.G. Bentini, A. Golanski and S. Kalbitzer)
- Volume 4: Metastable Alloys: Preparation and Properties (eds. K. Samwer, M. von Allmen, J. Bøttinger and B. Stritzker)
- Volume 5: Superconducting and Low-Temperature Particle Detectors (eds. G. Waysand and G. Chardin)
- Volumes 6A, 6B: High T_c Superconductors (eds. P.F. Bongers, C. Schlenker and B. Stritzker)
- Volume 7: Solid State Ionics (eds. M. Balkanski and C. Julien)
- Volume 8: Rare-Earth Permanent Magnets (ed. I.R. Harris)
- Volume 9: Defects in Silicon (eds. C.A.J. Ammerlaan, A. Chantre and P. Wagner)
- Volume 10A, 10B: Silicon Molecular Beam Epitaxy (eds. E. Kasper and E.H.C. Parker)
- Volume 11: Acoustic, Thermal Wave and Optical Characterization of Materials (eds. G.M. Crean, M. Locatelli and J. McGilp)
- Volume 12: Beam Processing and Laser Chemistry (eds. I.W. Boyd and E. Rimini)
- Volume 13: Interfaces in Biomaterials Sciences (eds. D. Muster and G. Hastings)
- Volume 14A, 14B: High T_c Superconductor Materials (eds. H.-U. Habermeier, E. Kaldis and J. Schoenes)
- Volume 15: Metal Matrix Composites (eds. G. Chadwick and L. Froyen)
- Volume 16: Magnetic Thin Films, Multilayers and Superlattices (eds. A. Fert, G. Güntherodt, B. Heinrich, E.E. Marinero and M. Maurer)
- Volume 17: Metallurgical Coatings and Materials Surface Modifications (eds. H. Hintermann and J. Spitz)
- Volume 18: Surface Processing and Laser Assisted Chemistry (eds. I.W. Boyd, E. Fogarassy and M. Stuke)
- Volume 19: Materials for Optoelectronic Devices, OEICs and Photonics (eds. H. Schlöterer, M. Quillec, P.D. Greene and M. Bertolotti)
- Volume 20: SiC, Natural and Synthetic Diamond and Related Materials (eds. A.A. Gippius, R. Helbig and J.P.F. Sellschop)
- Volume 21: Analytical Techniques for the Characterization of Compound Semiconductors (eds. G. Bastard and H. Oppolzer)
- Volume 22: Micronic Integrated Sensors (ed. J.L. Robert)
- Volume 23: High Energy and High Dose Ion Implantation (eds. S.U. Campisano, J. Gyulai, P.L.F. Hemment and J.A. Kilner)
- Volume 24: Laser Surface Processing and Characterization (ed. I.W. Boyd)
- Volume 25: Nuclear Methods in Semiconductor Physics (eds. G. Langouche, J.C. Soares and J.P. Stoquert)
- Volume 26: Clays and Hydrosilicate Gels in Nuclear Fields (ed. A. Meunier)
- Volume 27: Chemistry of Cements for Nuclear Applications (eds. P. Barret and F.P. Glasser)
- Volume 28: Nuclear Materials for Fission Reactors (eds. H. Matzke and G. Schumacher)
- Volume 29: Modifications Induced by Irradiation in Glasses (ed. P. Mazzoldi)
- Volume 30: Polyconjugated Materials (ed. G. Zerbi)
- Volume 31: SiGe Based Technologies (eds. E. Kaspar, Y. Shiraki and T.P. Pearsall)
- Volume 32: Materials Surface Processing (eds. M. Stuke, E.E. Marinero and I. Nishiyama)
- Volume 33: Chemistry for Electronic Materials (eds. Y. Pauleau, G. Wahl, K.F. Jensen and T. Hirai)
- Volume 34: Semiconductor Materials Analysis and Fabrication Process Control (eds. G. Crean, R. Stuck and J. Woollam)
- Volume 35: Synthetic Materials for Non-Linear Optics and Electronics (eds. C. Taliani, Z.V. Vardeny and Y. Maruyama)
- Volume 36: CdTe and Related Cd Rich Alloys (eds. R. Triboulet, W.R. Wilcox and O. Oda)
- Volume 37: Single Chamber Processing (eds. Y.I. Nissim and A. Katz)
- Volume 38: High T_c Superconductors (eds. J. Dumas, H.W. Neumüller, H.F. Braun, V.P. Seminozhenko and Yu.D. Tretyakov)
- Volume 39: Materials under Extreme Conditions and Nanophase Materials (eds. G. Kostorz, I. Gorynin, V. Trevilov, H.-D. Kunze, B. Günther, B. Skorokhod and V. Troitsky)
- Volume 40: Semiconductor Materials for Optoelectronics and LTMBE Materials (eds. J.P. Hirtz, C. Whitehouse, H.P. Meier, H.J. von Bardeleben and M.O. Manasreh)
- Volume 41: Stimulated Deposition Processes and Materials Aspects of Ion Beam Synthesis (eds. H. Freller, J.M. Martínez-Duart, Y. Pauleau, J. Dieleman, P.L.F. Hemment and J.A. Kilner)
- Volume 42: Integrated Processing for Micro- and Optoelectronics (eds. Y.I. Nissim, A. Katz and G.W. Rubloff)
- Volume 43: Light Emission from Silicon (eds. L.T. Canham, W. Lang and J.C. Vial)
- Volume 44: Advances in Solidification Processes (eds. H. Fredriksson, H. Jones and G. Lesoult)
- Volume 45: Molecular Electronics (eds. Ch. Ziegler, W. Göpel, and G. Zerbi)
- Volume 46: Amorphous Insulating Thin Films II (eds. R.A.B. Devine, W.L. Warren, J. Kanicki and M. Matsumara)
- Volume 47: Photon-Assisted Processing of Surfaces and Thin Films (eds. J. Dieleman, U.K.P. Biermann and P. Hess)
- Volume 48: Photorefractive Materials (eds. G. Roosen, F. Agulló-López and O. Schirmer)
- Volume 49: Organic Materials for Electronics (eds. J.L. Brédas, W.R. Salaneck and G. Wegner)
- Volume 50: High Temperature Electronics (eds. K. Fricke and V. Krozer)
- Volume 51: Porous Silicon and Related Materials (eds. R. Hérino and W. Lang)

AMORPHOUS INSULATING THIN FILMS II

PROCEEDINGS OF SYMPOSIUM A ON
AMORPHOUS INSULATING THIN FILMS II
OF THE 1994 E-MRS SPRING CONFERENCE

STRASBOURG, FRANCE, MAY 24–27, 1994

Edited by

R.A.B. DEVINE
CNS/CNET, Meylan, France

W.L. WARREN
Sandia National Laboratories, Albuquerque, NM, USA

J. KANICKI
University of Michigan, Ann Arbor, MI, USA

M. MATSUMARA
Tokyo Institute of Technology, Tokyo, Japan



1995

ELSEVIER

Amsterdam – Lausanne – New York – Oxford – Shannon – Tokyo

DTIC QUALITY INSPECTED

Published by:
North-Holland
Elsevier Science B.V.
Sara Burgerhartstraat 25
P.O. Box 211
1000 AE Amsterdam
The Netherlands

ISBN: 0 444 82161 9

Reprinted from:
JOURNAL OF NON-CRYSTALLINE SOLIDS 187 (1-3)

The manuscripts for the Proceedings were received by the Publisher:
January – February 1995

© 1995 ELSEVIER SCIENCE B.V. All rights reserved.

No part of this publication may be reproduced, stored in a retrieval system, or transmitted, in any form or by any means, electronic, mechanical, photocopying, recording or otherwise, without the prior written permission of the copyright owner, Elsevier Science B.V. Copyright & Permissions Department, P.O. Box 521, 1000 AM Amsterdam, The Netherlands.

Special regulations for readers in the U.S.A. - This publication has been registered with the Copyright Clearance Center Inc. (CCC), 222 Rosewood Drive, Danvers, MA 01923. Information can be obtained from the CCC about conditions under which photocopies of parts of this publication may be made in the U.S.A. All other copyright questions, including photocopying outside of the U.S.A., should be referred to the copyright owner, Elsevier Science B.V., unless otherwise specified.

No responsibility is assumed by the Publisher for any injury and/or damage to persons or property as a matter of products liability, negligence or otherwise, or from any use or operation of any methods, products, instructions or ideas contained in the material herein.

Printed on acid-free paper.

Printed in The Netherlands



ELSEVIER

Journal of Non-Crystalline Solids 187 (1995) vii

JOURNAL OF
NON-CRYSTALLINE SOLIDS

Preface

The contents of this volume of the Journal of Non-Crystalline Solids contains a large fraction of the papers presented at the symposium 'Amorphous Insulating Thin Films II' which took place in Strasbourg, France from 24 to 27 May 1994. The symposium was organized under the auspices of the European Materials Research Society and was a follow-up to one organized in the USA during the Fall 1992 meeting of the Materials Research Society in Boston. 113 participants were registered for the Strasbourg meeting representing more than 20 different countries from around the world. Presentations at the symposium were divided between oral and poster sessions, and for the first time we introduced the concept of an extended panel session entitled 'Microscopic Characterization of the Si/SiO₂ Interface' during which invited speakers were asked to present different characterization methods. This session was well attended and the organizers would like to sincerely acknowledge the efforts made by Tatsumi Mizutani who set up and steered the session and J.-J. Benattar, W.M. Lau, A. Ishitani, B. Drevillon and A. Crossley who kindly accepted to 'defend their causes'.

Of the 112 papers scheduled for presentation either in the poster or as oral format, 73 originated from University laboratories, 28 from national research laboratories and 11 from industrial laboratories. If these statistics can be generalized, they give a good insight into the trends in materials research and indicate that, increasingly, it is being performed in the academic environment rather than in the industrial sector. Finally, we would like to thank all of the participants who made the effort to come to Strasbourg and who made the symposium the success that it was.

Rod Devine
Bill Warren
Jerzy Kanicki
Masakiyo Matsumura

Sponsors

This Conference was held under the auspices of
The Council of Europe
The European Parliament

It is our pleasure to acknowledge with gratitude the financial assistance provided by

Banque Populaire	(France)
Centre de Recherches Nucléaires	(France)
Centre National de la Recherche Scientifique	(France)
Elsevier Science B.V.	(The Netherlands)
Magasins Printemps, Strasbourg	(France)
Ville de Strasbourg	(France)
Office du Tourisme, Strasbourg	(France)
The Commission of European Communities	
The Council of Europe	
The European Parliament	

and particularly with respect to

Symposium A:

L'Air Liquide	(France)
CCE-Euroconferences	
Centre National d'Etudes de Telecommunications (CNET)	(France)
IBM Corporation	(USA)
NEC Corporation	(USA)
US Army European Research Office	(London, UK)



ELSEVIER

Journal of Non-Crystalline Solids 187 (1995) ix–xiv

JOURNAL OF
NON-CRYSTALLINE SOLIDS

Contents

<i>Preface</i>	vii
<i>Sponsors</i>	viii
<i>Contents</i>	ix

Section 1. General

Dielectrics in microelectronics – problems and perspectives P. Balk	1
--	---

Section 2. Silicon dioxide, oxidation and unusual structures

Buried oxides: where we have been and where we are going J.-L. Leray	10
RTP – temperature monitoring by means of oxidation J.-P. Zöllner, V. Cimalla and J. Pezoldt	23
Low-temperature voltage enhanced UV-assisted oxidation of silicon A. Dolique and A.H. Reader	29
Rapid thermal annealing of SiO ₂ for VLSI applications A. Paskaleva, E. Atanassova and G. Beshkov	35
A synchrotron Si2p and As3d core level study of the As-terminated Si(0 0 1) surface oxidation C. Poncey, F. Rochet, G. Dufour, H. Roulet, W.N. Rodrigues, M. Sauvage-Simkin, J.C. Boulliard, F. Sirotti and G. Panaccione	40
Oxidation of amorphous and crystalline silicon A. Szekeres and P. Danesh	45

Section 3. Silicon dioxide, deposition

Fluorinated interlayer dielectric films in ULSI multilevel interconnections T. Homma	49
Deposition of ultra-thin oxide dielectrics for MOSFETs by a combination of low-temperature plasma-as- sisted oxidation, and intermediate and high-temperature rapid thermal processing G. Lucovsky, V. Misra, S.V. Hattangady, T. Yasuda and J.J. Wortman	60
New substances for atomic-layer deposition of silicon dioxide S. Morishita, W. Gasser, K. Usami and M. Matsumura	66
Dual-mode radio frequency/microwave plasma deposition of amorphous silicon oxide thin films R. Etemadi, C. Godet, M. Kildemo, J.E. Bourée, R. Brenot and B. Drévillon	70
Hydrogen incorporation in silicon oxide films deposited by ArF laser-induced chemical vapor deposition E.G. Parada, P. González, J. Serra, B. León, M. Pérez-Amor, M.F. da Silva, H. Wolters and J.C. Soares	75

Effects of plasma treatment on the properties of room-temperature liquid-phase deposited (LPD) oxide films	
C.-F. Yeh and S.-S. Lin	81
Oxygen-rich phase segregation in PECVD a-SiO _x :H semi-insulators	
G. Suchaneck, O. Steinke, B. Alhallani and K. Schade	86
Section 4. Silicon dioxide, structure, defects and characterization	
IR study of short-range and local order in SiO ₂ and SiO _x films	
I.P. Lisovskii, V.G. Litovchenko, V.B. Lozinskii, S.I. Frolov, H. Flietner, W. Fussel and E.G. Schmidt	91
Comparison of experimental and calculated TO and LO oxygen vibrational modes in thin SiO ₂ films	
C. Martinet and R.A.B. Devine	96
Structural damage and defects created in SiO ₂ films by Ar ion implantation	
B. Garrido, J. Samitier, S. Bota, C. Domínguez, J. Montserrat and J.R. Morante	101
Boron diffusion in SiO ₂ based dielectric thin layers	
S. Nédélec, D. Mathiot, M. Gauneau and A. Straboni	106
Formation of visible photoluminescence bands in Si ⁺ -implanted silica glasses and thermal oxide films on crystalline Si	
T. Shimizu-Iwayama, K. Fujita, M. Akai, S. Nakao and K. Saitoh	112
Parameters controlling the generation of natural intrinsic EX defects in thermal SiO ₂ on Si	
A. Stesmans and F. Scheerlinck	119
Wavelength resolved thermally stimulated luminescence of SiO ₂ films	
M. Martini, F. Meinardi, E. Rosetta, G. Spinolo and A. Vedda	124
A novel ellipsometric set up for high precision thin films measurements	
J. Monin, H. Sahsah and O. Brevet-Philibert	129
Section 5. Silicon dioxide, defects and degradation	
Effects of iron contamination in silicon on thin oxide breakdown and reliability characteristics	
W.B. Henley, L. Jastrzebski and N.F. Haddad	134
Instability of charged defects in electrically stressed metal-tunnel oxide-silicon diodes	
P. Lundgren, M.O. Andersson, K.R. Farmer and O. Engström	140
Influence of FN electron injections in dry and dry/wet/dry gate oxides: relation with failure	
E. Ciantar, P. Boivin, M. Burle, C. Niel, J.M. Moragues, B. Sagnes, R. Jerisian and J. Oualid	144
Investigation on the interfacial reaction of SiO ₂ /Ti _{0.1} W _{0.9} system	
H.-H. Park, S. Nahm, K.-S. Suh, J.-L. Lee, K.-I. Cho, K.-S. Kim, S.-C. Park, J.-S. Lee and Y.-H. Lee	149
Influence of WSi ₂ polysilicide gate process on integrity and reliability of gate and tunnel oxides	
J.M. Moragues, B. Sagnes, R. Jerisian, J. Oualid, E. Ciantar, J.L. Liotard and P. Merenda	156
Modeling and simulation of homogeneous degradation for N-channel MOSFETS	
I. Limbourg, L. Hardy, M. Jourdain, R. Bouchakour and J.J. Charlot	160
Section 6. Silicon dioxide, charge trapping	
Interface traps induced by hole trapping in metal-oxide semiconductor devices	
Y. Roh, L. Trombetta and D.J. DiMaria	165
Comparison of X-ray-induced electron and hole trapping in various materials (YSZ, SIMOX, thermal SiO ₂)	
P. Paillet, P. Gonon, C. Schwebel and J.-L. Leray	170
Influence of the oxide charge build-up during Fowler-Nordheim stress on the current-voltage characteristics of metal-oxide-semiconductor capacitors	
S. Elrhbari and M. Jourdain	175

Comparison of the generated oxide charge by injection of electrons for both polarities A. Meinertzhagen, G. Yard, C. Petit, M. Jourdain, A. El-Hdiy, G. Salace and G. Reimbold	181
Field mechanism of defect generation at Si-SiO ₂ interface under hot electron injection I.P. Lisovskii, G.P. Romanova and E.G. Schmidt	186
Comparison of rapid ramp voltage and tunnelling injection stress experiments for the characterization of thin MOS gate oxides O. Brière, P. Cottin and A. Straboni	190
Leakage current reduction due to hot carrier effects in n-channel polycrystalline silicon thin film transistors G. Tallarida, A. Pecora, G. Fortunato, F. Plais, P. Legagneux, T. Kretz and D. Pribat	195

Section 7. Si/SiO₂ interface, characterization and electrical properties

Enhanced MOS 1/f noise due to near-interfacial oxygen deficiency D.M. Fleetwood, W.L. Warren, M.R. Shaneyfelt, R.A.B. Devine and J.H. Scofield	199
The microscopic nature of donor-type Si-SiO ₂ interface states K.G. Duijff, J.M.M. de Nijs, E. v.d. Drift, V.V. Afanas'ev, E.H.A. Granneman and P. Balk	206
Three-level charge pumping study of radiation-induced defects at Si-SiO ₂ interface in submicrometer MOS transistors J.-L. Autran, B. Balland and D. Babot	211
The no-thermal activation of the defect generation mechanism in a MOS structure A. El-Hdiy, G. Salace, A. Meinertzhagen, M. Jourdain, C. Petit and A. Aassime	216
A study comparing measurements of roughness of silicon and SiO ₂ surfaces and interfaces using scanning probe microscopy and neutron reflectivity A. Crossley, C.J. Sofield, J.P. Goff, A.C.I. Lake, M.T. Hutchings and A. Menelle	221
Characterization of ion-implanted silicon-insulator interfaces by reflected optical second harmonic generation I.V. Kravetsky, L.L. Kulyuk, A.V. Micu, V.I. Tsytanu and I.S. Vieru	227

Section 8. Hydrogen in MOS structures and oxides

Dissociation of H ₂ at silicon dangling orbitals in a-SiO ₂ : a quantum mechanical treatment of nuclear motion A.H. Edwards	232
Atomic hydrogen-induced degradation of thin SiO ₂ gate oxides E. Cartier, D.A. Buchanan, J.H. Stathis and D.J. DiMaria	244
The role of hydrogen in the action of fluorine in Si/SiO ₂ structures V.V. Afanas'ev, J.M.M. de Nijs and P. Balk	248
Hydrogen-annealing induced positive charge in buried oxides: correspondence between ESR and C-V results K. Vanheusden, A. Stesmans and V.V. Afanas'ev	253
Chemical reactions of hydrogenous species in the Si/SiO ₂ system E.H. Poindexter	257
Measurement and analysis of hydrogen depth profiles in MOS-structures by using the ¹⁵ N nuclear reaction method J. Krauser, F. Wulf and D. Bräunig	264
Electrical properties of hydrogen-rich Si/SiO ₂ structures P. Danesh and A. Szekeres	270
Surface potential dependence of interface state passivation in metal-tunnel oxide-silicon diodes M.O. Andersson, A. Lundgren and P. Lundgren	273

Section 9. Nitrides, structure and defects

Structural and bonding properties of amorphous silicon nitride films S. Hasegawa, T. Inokuma and Y. Kurata	278
A comparative study on structural and electronic properties of PECVD a-SiO _x with a-SiN _x K. Maeda, N. Sakamoto and I. Umezu	287
The effect of hydrogen and temperature on the optical gaps of silicon nitride and comparative stoichiometry studies on SiN thin films J. Petalas, S. Logothetidis, S. Bouladakis and A. Markwitz	291
Nature of the Si and N dangling bonds in silicon nitride J. Robertson, W.L. Warren and J. Kanicki.	297
Morphology of LPCVD Si ₃ N ₄ films after high temperature treatment and HF etching G. Beshkov, V. Lazarova and D.B. Dimitrov	301
Hydrogen content of amorphous PECVD SiN _x :H films by infrared spectroscopy and hydrogen forward scattering results G. Morello	308
Bias stress studies of a-SiN:H/a-Si:H MIS structures from quasistatic capacitance measurements J. Reynaud, J.P. Kleider and D. Mencaraglia	313
Selective thermal – as opposed to non-selective plasma – nitridation of Si-Ge related materials examined by in situ photoemission techniques D. Aubel, M. Diani, L. Kubler, J.L. Bischoff and D. Bolmont	319

Section 10. Silicon nitride, deposition

Influence of gas residence time on the deposition of nitrogen-rich amorphous silicon nitride D.T. Murley, R.A.G. Gibson, B. Dunnett, A. Goodyear and I.D. French.	324
Influence of the deposition parameters on the bonding and optical properties of SiN _x ECR films S. Garcia, J.M. Martin, I. Martil, M. Fernandez, E. Iborra and G. Gonzalez-Diaz	329
Room-temperature deposition of SiN _x using ECR-PECVD for III/V semiconductor microelectronics in lift-off technique A. Wiersch, C. Heedt, S. Schneiders, R. Tilders, F. Buchali, W. Keubart, W. Prost and F.J. Tegude	334
Control of bonded-hydrogen in plasma-deposited silicon nitrides: Combined plasma-assisted deposition and rapid thermal annealing for the formation of device-quality nitride layers for applications in multilayer dielectrics Z. Lu, S.S. He, Y. Ma and G. Lucovsky	340
Plasma-enhanced silicon nitride deposition for thin film transistor applications L.J. Quinn, S.J.N. Mitchell, B.M. Armstrong and H.S. Gamble	347
Deposition of amorphous silicon nitride thin films by CO ₂ laser-induced chemical vapour deposition J. Serra, T. Szörényi, D. Fernández, P. González, E. García, J. Pou, B. León and M. Pérez-Amor	353

Section 11. ONO and nitrided oxides

Structural and electrical properties of thin SiO ₂ layers grown by RTP in a mixture of N ₂ O and O ₂ A.J. Bauer and E.P. Burte	361
Damage induced by carrier injection in 8 nm thick oxides and nitrided oxides A. Bravaix, D. Vuillaume, V. Thirion, D. Dorval and A. Straboni	365
Characterization of thin nitrided oxide layers using high spatial resolution transmission electron energy loss spectrometry C. Bernardi and C. d'Anterrosches.	369

A comparison of Si-SiO ₂ interface trap properties in thin-film transistors with thermal and plasma nitrided oxides	
J.-L. Autran, C. Plossu, F. Seigneur, B. Balland and A. Straboni	374
Structural and optical properties of nitrided silicon oxide layers rapid thermally grown in a pure N ₂ O ambient	
E. Hartmannsgruber, U. Rossow, A. Hoyer and P. Lange	380

Section 12. Silicon oxynitride and other dielectrics

Structural identification of point defects in amorphous silicon oxynitrides	
Y. Cros and J. Krautwurm	385
Silicon oxynitride study by the tetrahedron model and by spectroscopic ellipsometry	
A. Sassella, P. Lucarno, A. Borghesi, F. Corni, S. Rojas and L. Zanotti	395
Effect of process parameters on the properties of electron cyclotron resonance plasma deposited silicon-oxynitride	
P.V. Bulkin, P.L. Swart and B.M. Lacquet	403
Electrical properties of Au/Bn/InP MIS diodes	
O. Baehr, M. Barrada, A. Bath, B. Lepley, P. Thévenin and J. Schoonman	409
Surface plasmon-induced luminescence: a probe to study electrical aging and dielectric breakdown in polymer-like thin films	
A. Foulani, C. Laurent and P. Canet	415
Structure rearrangement and electrochromic properties of amorphous tungsten trioxide films	
I.V. Shiyankovskaya	420

Section 13. High ϵ materials and ferroelectrics

Low pressure chemical vapour deposition of tantalum pentoxide thin layers	
E.P. Burte and N. Rausch	425
Investigation of the film growth of a new titanium precursor for MOCVD	
F.-R. Lang, E.C. Plappert, K.-H. Dahmen, R. Hauert, P. Nebiker and M. Döbeli	430
Low temperature deposition of gallium phosphate amorphous dielectric thin films by aerosol CVD	
F. Tourtin, S. Daviero, A. Ibanez, A. Haidoux, C. Avinens and E. Philippot	435
Fabrication, characterization and electro-optic performances of proton-implanted waveguides in LiNbO ₃	
A. Boudrioua, P. Moretti and J.C. Loulergue	443
Photo-assisted switching and trapping in BaTiO ₃ and Pb(Zr, Ti)O ₃ ferroelectrics	
W.L. Warren and D. Dimos	448
Optical properties of sol-gel derived ferroelectric films	
M. Bertolotti, S. Mura, E. Pennella, F. Senesi, C. Sibilia, A. Montenero, G. Gnappi and S. Pigoni . . .	453

Section 14. Optical applications

Chemical interaction in ion-implanted amorphous SiO ₂ and application to formation and modification of nanosize colloid particles	
H. Hosono	457
Light-assisted deposition of silicon-based dielectrics for optical interconnection in optoelectronics	
A. Sayah and Y.I. Nissim	473
PECVD a-SiN _x :H films for dielectric insulation in buried ridge structure Fabry-Perot and distributed feedback laser devices	
R. Audino, F. Cannistraci, G. Morello and P. Valenti	477
Properties and applications of electron cyclotron plasma deposited SiO _x N _y films with graded refractive index profiles	
P.V. Bulkin, P.L. Swart and B.M. Lacquet	484

Light-modulated carrier injection across the interface between transparent conducting oxide (n^+ -SnO ₂) and semi-insulating amorphous silicon-carbide R. Vincenzoni, M.C. Rossi, G. Leo and F. Galluzzi	489
Thermo-optic mode extinction modulation in polymeric waveguide structures F.R. Akkari, K.H. Cazzini and W. Blau	494
Author index	499
Subject index	505



ELSEVIER

Journal of Non-Crystalline Solids 187 (1995) 1–9

JOURNAL OF
NON-CRYSTALLINE SOLIDS

Section 1. General

Dielectrics in microelectronics – problems and perspectives

P. Balk*

DIMES, Delft University of Technology, P.O. Box 5053, 2600 GB Delft, The Netherlands

Abstract

This review is focussed on the most demanding application of dielectrics in microelectronics, namely that in field effect technology. It is shown that the requirements of this technology can only be met in silicon devices; the developments over the past 30 years indicate that there is no reliable replacement for Si–SiO₂ in the gate system. However, for DRAM capacitors the use of alternative dielectrics with higher dielectric constant and of ferroelectrics turns out to be unavoidable but also manageable. The limitations of other semiconductor systems with regards to dielectrics are briefly reviewed.

1. Introduction

Dielectrics fulfill a number of essential functions in the fabrication and operation of semiconductor devices and integrated circuits. The chemical characteristics of these materials are generally decisive when employing them as masks in classical diffusion processes or to define areas of localized growth and when using them as capping layers to prevent loss of material when thermally activating implants. Critical applications are certainly those where a particular dielectric is selected because of its effect on the electrical characteristics of devices and circuits. Typical examples are the application as an insulator between conductors or as a material to passivate the surface of the semiconductor. Particularly demanding are functions as capacitor dielectric or as gate dielectric in the insulated gate field effect device technology. For the gate applica-

tion the stability of device threshold and transconductance is the prime requirement. On the other hand, the capacitor application demands high storage capacity at very low charge leakage.

For most semiconductors these requirements, particularly for field effect device and capacitor application, are hard to fulfill. A favorable situation in silicon technology, which is related to the properties of thermally grown SiO₂, is the exception rather than the rule. By the same token, this feature of the Si–SiO₂ system is the reason for its dominance in the field of microelectronics. A discussion of the requirements of device applications and their fulfillment in Si technology using SiO₂ and, when necessary, also alternative dielectrics will therefore constitute the main theme of this review.

2. Requirements on dielectrics in field effect technology

It is essential for the design and operation of metal-oxide-silicon field effect transistor (MOS-FET) circuits to have devices with controlled

* Corresponding author. Tel: +31-15 78 4963. Telefax: +31-15 62 2163.

characteristics. In practice this means a well-defined threshold and transconductance obtained by having a minimum amount of charge trapped in the gate dielectric and a minimum density of traps at the semiconductor–dielectric interface. Moreover, these characteristics should not change with time. Injection of carriers into the dielectric will lead to charge capture and generation of new bulk and interface traps, and thus to changes in the device characteristics. This implies that the barrier against injection of carriers into the insulator should be high, which is generally the case for high band gap dielectrics. Moreover, the efficiency for generating bulk and interface states should be as low as possible [1, 2].

In dynamic random access memories (DRAMs) the basic cell consists of a MOSFET in series with a capacitor. In the two logical states of the cell the capacitor is either charged or free of charge. Since the capacitor does not have a channel like the MOSFET, the electrical properties of the interface are not critical. In fact, metal electrodes may be inserted between semiconductor and dielectric. However, the memory only functions if at least a minimum amount of charge is stored, which defines a lower limit of the capacitance of the device [3]. In the ultra large scale integration (ULSI) technology this can be realized by extending the capacitor area in the third dimension (employing trenches, stacked folded layers or structured surfaces) or by using high dielectric constant materials. In addition, to limit the number of refresh operations, there is a minimum acceptable amount of charge loss by leakage (10^{-7} – 10^{-8} A cm⁻²).

In contrast to the DRAM technology, where the information is lost when the supply voltage is switched off, non-volatile memories maintain the information independent of such interruptions. In this case the cell consists of one single field effect transistor with two logical states corresponding to two threshold values. One of these threshold values is that for the charge-free gate insulator system, the second is that for the charged gate insulator system.

Two different approaches are being used for charge storage. In the first the charge is stored in the dielectric itself, which therefore should have a large trapping state density. The dielectric mostly used for storage is Si₃N₄, with a very thin barrier of SiO₂ on the channel side to improve the interfacial

properties and increase the storage time. In the second approach an electrically floating poly-Si electrode is used for storage; it is insulated from the channel and the control gate by SiO₂ films. Charging and discharging take place by means of tunnel injection of carriers or by hot carrier injection. It should be noted that these are the very processes which one tries to avoid in the operation of standard MOSFETs since they lead to permanent changes in the device characteristics. Such degeneration phenomena limit the number of feasible charge-discharge operations to around 10⁵ for floating gate structures (FLOTOX: floating gate tunnel oxide memory), to over 10⁷ for storage in a nitride film with an additional SiO₂ layer on the gate electrode side to improve charge retention (SONOS: poly-Si gate/oxide/nitride/oxide/semiconductor memory) [4].

3. Dielectrics in the classical MOSFET technology

It has been known for many years that SiO₂ obtained by thermal oxidation of Si in an O₂ or H₂O atmosphere is a nearly ideal insulator and exhibits an excellent ‘fit’ to the semiconductor substrate. The Si–SiO₂ system provides high temperature diffusion masking, constitutes a passivated semiconductor surface and, above all, is the basis of the MOSFET technology. Since its inception in the early sixties this technology has developed rapidly. Originally the interest was mainly focussed on the macroscopic material properties of the insulator. The question of the atomic structure of electrically active defects in Si–SiO₂ became a major topic in the seventies. At the present time most of these developments are textbook material [5, 6].

The most striking features of the Si–SiO₂ system are the following: high temperature annealing in neutral ambients after oxidation suffices to lower the oxide charge to less than 10¹¹ electron charges per cm². A low temperature post-metallization anneal in the presence of an Al gate electrode reduces the density of interface states below 10¹⁰ cm⁻². The combination of these annealing steps produces a well-defined threshold voltage and a high transconductance in MOSFETs. These features are both essential for the operation of integrated circuits.

The main reliability problems related to the gate dielectric in early MOSFETs were low field breakdown and electrical shorts, caused by extended defects in the film or by contaminants, particularly Na^+ ions. Na^+ ions also affect the threshold voltage. The introduction of clean processing and the insertion of a barrier layer on the gate side of the oxide effectively solved these problems. Low phosphorus concentration phosphosilicate glass (PSG), chemically vapor deposited (CVD) Si_3N_4 and CVD Al_2O_3 were proposed as barrier or trapping layers of Na^+ . By keeping a SiO_2 layer adjacent to the silicon the favorable properties of the Si-SiO₂ interface were preserved in the gate structure. Only the SiO_2 -PSG combination has been extensively used. Interestingly, SiO_2 - Al_2O_3 has also been considered as a gate dielectric for enhancement n-channel MOSFETs because of the tendency of Al_2O_3 to charge up negatively due to its affinity for electrons [7]. Because of its technical interest the physics and technology of the Si-SiO₂ system dominated the programs of the different scientific conferences in the field of semiconductor-insulator technology.

Two of these have been held regularly for many years: the Semiconductor Interface Specialists Conference (SISC, in the USA, mostly annually since 1965); the Insulator Films on Semiconductors Conference (INFOS, in Europe, biennially since 1979). The published proceedings of the latter conference present an excellent overview of the development of the field over the past 15 years.

4. Newer developments

The development of the MOSFET technology to higher densities and smaller dimensions in the seventies and eighties had major consequences for the gate dielectric. Because of the higher fields in devices of reduced dimensions the problem of carrier heating, injection across the semiconductor-dielectric barrier and trapping in the dielectric became acute. This made the use of PSG, Si_3N_4 and Al_2O_3 with their high trap densities [7] problematic, so that gradually only single films of SiO_2 were employed. Consequently, attention shifted to the trapping behavior and the corresponding point defects of thermally grown SiO_2 . Even though the

defect densities in this dielectric (typically 10^{11} - 10^{12} cm^{-2}) are lower by a few orders of magnitude (typically 10^{11} - 10^{12} cm^{-2}) their control became of considerable importance.

Electrically active defects in SiO_2 may be introduced by foreign atoms, like Si dopants [8], but in most cases their concentrations are negligible. The so-called water-related defects [9] (Si-OH groups or H_2O dissolved in the SiO_2 network) are difficult to avoid and may be present in concentrations of 10^{11} - 10^{12} cm^{-2} . They strongly affect the characteristics of the device when charge is injected. Electrically active intrinsic defects are known to occur in connection with oxygen deficiency [10] or strain in the oxide [11]. To this category also belongs the dangling bond ('trivalent silicon') interface state at the Si-SiO₂ interface [12].

Quantitatively more important than the defects which are present in the as-prepared MOS structure are those generated by injected carriers or by energetic radiation. The condition for the generation of these defects, which appear as bulk and as interface states, is the capture of the carriers by bulk defects [13]. Also, the presence of water-related defects and hydrogen transport appear to be conditions for the generation of interface states [14]. Since these states cause considerable changes in the characteristics of MOSFETs it is important to prevent them by minimizing the density of injected carriers and the fraction of these carriers that will interact with the oxide to form new defects.

5. Optimizing the Si-SiO₂ system

Notwithstanding attempts to reduce the exposure to high temperatures by using CVD-SiO₂ as a gate insulator, it appears that in order to match the quality of thermally grown SiO_2 films high temperature annealing is required. Thus, thermal oxidation remains the preferred method for preparing this gate insulator. However, considerable efforts have been made to maximize the level of control of the film properties and to move the limits of application of SiO_2 by reducing its sensitivity to carrier injection. In line with the development of the MOSFET technology to small dimensions this work focussed on SiO_2 films thinner than 10 nm.

In this thickness range the rate of generation of interface states and the density of injected charge necessary to cause breakdown of the film for a given average field in the oxide decrease with film thickness [15]. By itself, fabrication of functioning n- and p-channel MOSFET devices with gate oxides as thin as 3.5 nm does not appear to present special problems [16,17]. The requirement of a maximum tolerable leakage current puts the lower limit of SiO₂ thickness for a corresponding DRAM technology near 4 nm [18]. However, thickness and uniformity of the films in this thickness range are strongly dependent on the details of the growth technology. Developments in recent years were concerned with the following three aspects of film growth: preparation of the silicon surface for growth; minimizing the level of contamination; improving the properties of the Si–SiO₂ system by means of small concentrations of additives.

The goal of the substrate preparation technique is the removal of a thin (a few nm) layer of silicon by wet chemical oxidation and etching of the resulting oxide film in order to remove surface damage, particulate matter and contaminants, particularly metals. These factors, as well as rough surfaces, lead to films with reduced breakdown strength [19, 20]. Exposure to HF vapor or to an aqueous solution of HF as the final step in surface preparation will result in a hydrogen-terminated Si surface, which by heating in neutral ambients is turned into an extremely reactive ‘naked’ Si surface. In the presence of hydrocarbons this will lead to the formation of SiC, which affects the quality of the subsequently grown oxide [21].

Covering the substrate by a wet chemically prepared oxide film provides a well-defined starting point for the subsequent thermal oxidation and consequently for the growth of a film of uniform thickness and optimum properties.

High demands are being put on the purity of chemicals and gases used in this process. From the point of view of control the use of a closed system for surface preparation, oxidation and poly-silicon gate deposition, i.e. for the preparation of a sealed gate system, looks very attractive [19]. However, definite proof of the advantages of this cluster tool approach still has to be produced.

The region in the SiO₂ film close to the Si substrate, where the oxide network joins the crystalline semiconductors, is the site of strain and defects. It may be expected that incorporation of impurities in the Si–O ring structure may lead to strain relief and chemical saturation of the oxide structure. With this goal in mind the effect of addition of small amounts of nitrogen and fluorine on the oxide has been extensively studied in recent years.

Nitrogen-doped oxides are prepared by oxidation in N₂O/O₂, annealing in N₂O [22], annealing in NH₃ and O₂ [23], or N-implantation in the poly-Si gate followed by annealing [24]. Such low-N-doped oxides improve the resistance of the gate system to hot carrier degradation of the MOSFET characteristics and extend the number of write-erase cycles in FLOTOX memory devices [25]. Moreover, the outdiffusion of B from the poly-Si gate is markedly suppressed. N-doped oxides also slow down the diffusion of H, which plays a role in the hot carrier induced generation of interface states [14].

Whereas N-incorporation most likely takes place in the Si–O ring structure, providing additional flexibility to the network, the role of F is probably to chemically stabilize broken-up ring structures. Implantation into the poly-Si gate appears to be a practical way of introducing the F dopant into the oxide for thin oxide MOS-structures [26, 27]. Again charge trapping and the generation of interface states are suppressed. Only very low concentrations (approximately 10¹³ cm⁻²) are necessary to reach these goals [28].

6. Insulators in other semiconductor technologies

Suitable materials for masking, capping, surface passivation and interconnection isolation have been found for most semiconductor technologies. However, for the most critical application, that of gate dielectric, this is not the case.

We first consider oxides obtained by thermal oxidation of the semiconductor. The thermally grown oxide of Ge has a tendency to be oxygen-deficient; this is also the case at the interface. Consequently, the Ge–Ge–oxide system has a large density of interface states and exhibits pronounced

carrier capture in the insulator [29]. When attempting to prepare a semiconductor insulator system on SiGe alloy, one is confronted with the same problems as encountered in Ge-technology. In the thermal oxidation process Ge tends to be rejected [29]. A study of Ge-implanted SiO_2 shows that Ge, if incorporated into the oxide, traps one electron per Ge-atom [30]. Oxidation of III-V or II-VI semiconductors presents basically the same problems as that of SiGe: one of the components is preferentially consumed or incompletely oxidized, with attendant electrically active oxide defects and high concentrations of interface states.

CVD insulator films (like SiO_2) in combination with annealing treatments have led in some cases to acceptable interface state densities but not to low bulk trapping levels. In recent years the idea of using an epitaxially grown wider gap semiconductor layer has been borrowed from HEMT (high electron mobility transistor) technology. This layer should be sufficiently thick to prevent tunneling of carriers. A conventional large gap insulator could be added on but the electrical stability of these configurations remains to be proven [31].

7. Features of the ideal semiconductor-insulator system

Next, we will attempt to define the characteristics of the ideal insulator for field effect gate and storage capacitor application. For the gate insulator the density of traps in the bulk of the material and at its interface with the semiconductor should be as low as possible. To reduce carrier injection the material should have a wide band gap. The requirement of low defect density would be ideally fulfilled in crystalline materials. To obtain also a perfect interface the insulator should be grown epitaxially on the substrate. In practice, it turns out that such an insulator-semiconductor combination is very rare occurrence. The results on the one system which has been studied fairly extensively, CaF_2 grown with 0.6% mismatch on (100) Si, have not been encouraging [32].

An alternative would be the growth of a vitreous insulator on the semiconductor. Vitreous materials are covalently bonded and exhibit considerable

flexibility in their structure. For this reason they should be able to provide a low defect density interface. A prime example of this case is the Si-SiO₂ system. SiO₂ is a vitreous material which shows nearly perfect short range order determined by chemically saturated SiO₄ building blocks. Their flexible structure allows the formation of Si-O rings of different sizes [33, 34] which provides a good fit and minimizes the strain near the Si-SiO₂ interface. This explains why in the absence of hydrogen passivation defect densities as low as a few times 10^{11} cm^{-2} are obtained [35].

Covalent bonding as required for vitreous materials generally occurs between non-metals which do not differ too much in electronegativity. These conditions and that of a sufficient band gap are met by the elements on the upper right-hand side of the periodic table. In addition to SiO₂, typical vitreous materials are Si₃N₄ (which has a rather high electrically active defect density) and the chalcogenides like As₂S₃ (which has a relatively narrow band gap). Consideration of the vitreous insulators thus does not leave us with many additional choices. These considerations indicate that for MISFET gate applications an optimized SiO₂ film still provides the best option for control and reliability. For capacitor dielectrics the defect structure of the interface is of lesser importance. The prime requirements are high dielectric constant and low leakage, i.e. sufficiently large band gap. Since these two features generally do not go together, one will have to compromise on band gap. This compromise turns out to be unproblematic, since a high dielectric constant allows the use of reduced fields in the insulator. It turns out that oxides present a favorable compromise [36]. It should be pointed out that in using polycrystalline materials conduction along grain boundaries may present a problem and will require special attention. However, in contrast to the application for the gate system the use of alternative dielectrics for capacitors appears feasible and worth further consideration.

8. Alternative dielectrics for capacitors

Notwithstanding the use of trenches, stacked layers and structured surfaces Mbit DRAMs

constitute the end of the road for SiO_2 capacitor dielectrics. Locally reduced oxidation rates at concave and convex surfaces cause defects and reduced breakdown fields and thus constitute a reliability problem. CVD will alleviate this problem. One approach is the use of the so-called ONO (oxide–nitride–oxide) system, where a CVD Si_3N_4 film is deposited on a thin thermally grown SiO_2 film and finally covered by a thin SiO_2 layer obtained by thermal oxidation of the nitride [37]. Electron capture in the nitride will automatically reduce the injecting field and counteract current leakage through weak spots in the SiO_2 barrier. Although the dielectric constant of Si_3N_4 has nearly twice the value of that of SiO_2 (7 versus 3.9) the gain in storage capacity for such sandwich structures is rather modest because of the effect of the SiO_2 films.

As expected, more benefit of a Si_3N_4 dielectric is derived by controlling the thickness of the native oxide to very small values in a HF vapor phase cleaning step before depositing the nitride and by avoiding oxidation of the nitride. In this case an equivalent SiO_2 thickness of 4 nm, with acceptable levels of a leakage current and large time to breakdown, have been claimed, making this approach suitable for the 64 Mbit DRAM technology [38]. Apparently, the effect of the lower nitride band gap compared to that of SiO_2 (5.1 versus 8.9 eV) is offset by the larger dielectric constant.

For 64 Mbit DRAMs and beyond three dielectrics with considerably larger dielectric constants have been proposed: Y_2O_3 , TiO_2 and Ta_2O_5 . The first two oxides are used in polycrystalline form and are combined with a thin SiO_2 film, which reduces the effect of the larger dielectric constant.

The Y_2O_3 films were prepared by thermal oxidation in O_2 of sputtered Y. Since Y has a very high affinity to oxygen its oxide is very stable. Combined with a 4 nm SiO_2 film thermally grown on the substrate a dielectric constant was deduced of approximately 20, without SiO_2 film of approximately 12. In both cases a very low leakage current and a breakdown strength of about 4 MV cm^{-1} were measured for the Y_2O_3 [39, 40].

The data on TiO_2 [41, 42] were obtained on reactively sputtered films. Heating after deposition to above 700°C produces the rutile phase with a dielectric constant above 100. At the same time

the morphology of the films is roughened. This annealing process, particularly when carried out in Ar/O_2 , strongly lowers the conductivity of the TiO_2 , reducing the leakage current below that for equivalent thickness SiO_2 films. Charge transport and breakdown appear to be determined by the grain boundaries.

The third dielectric, Ta_2O_5 , has been rather thoroughly studied [36] because of its extensive use in classical capacitor technology. A dielectric constant in the range of 20–50 has been reported, depending on the method of preparation. The optical band gap is only 4.2 eV, which suggests that conduction through the films will be bulk limited.

First studies on Ta_2O_5 for DRAM capacitor application were performed on material obtained by thermal oxidation of Ta films. The lowest conductivity was measured on films prepared from amorphous metal layers, keeping the oxidation temperature below 600°C , which is the crystallization temperature of the oxide. The leakage currents obtained in these films appear to meet the requirements for storage application [43].

In recent years impressive improvements were obtained using low pressure CVD (from $\text{Ta}(\text{OC}_2\text{H}_5)_5$ and O_2) at relatively low temperatures (450°C), followed by an anneal in O_2 at 800°C [44–46]. Important features of the overall preparation process are the nitridation of the Si substrate in NH_3 , producing approximately 1.5 nm of Si_3N_4 , and the deposition of a TiN top electrode by sputtering. The nitride films prevent interaction of the Ta_2O_5 with the silicon. This approach allows production of capacitors of 2.5 nm equivalent SiO_2 thickness, suitable for 256 Mbit DRAMs. Substituting the nitrided Si bottom electrode by the refractory metal W makes it possible to reduce the equivalent SiO_2 thickness of the dielectric to 1.6 nm, required for 1 Gbit memories. A leakage current of $10^{-8} \text{ A cm}^{-2}$ for a 1.5 V supply voltage could be realized [47]. The Ta_2O_5 capacitor technology, which is the only one which has been studied at realistic geometries, is certainly the most promising of those discussed in this section. This capacitor technology for 256 Mbit and 1 Gbit DRAMs includes the use of structured surfaces, so that here the limits of the Ta_2O_5 technology have been reached.

9. Ferroelectrics

Because of these limits, at the end of the eighties the search for materials with a very high dielectric constant was started. Such high dielectric constants are known to occur in ferroelectrics. Well-known representatives of this group of materials are $\text{PbZr}_x\text{Ti}_{1-x}\text{O}_3$ (PZT), $\text{Ba}_x\text{Sr}_{1-x}\text{TiO}_3$ (BST), $\text{Bi}_4\text{Ti}_3\text{O}_{12}$ and BaMgF_4 . In addition, these materials exhibit a spontaneous polarization which can be reversed by application of a sufficiently large electric field. When switching the material back and forth between these two polarizations by changing the direction of the field the polarization shows hysteresis. The difference between the polarization at maximum applied field and the remanent polarization at zero applied field represents a charge storage capacitance per unit area. This capacitance corresponds to an equivalent dielectric constant, with values in the range of 100-1000.

Ferroelectric films are polycrystalline. Their properties depend strongly on details of the preparation procedure, characteristics of the electrodes and film thickness. Most materials are deposited by sputtering or by spin coating the substrate with a solution of organometallic compounds followed by a heat treatment.

Most attention for DRAM application was given to the high dielectric constant material $\text{Ba}_x\text{Sr}_{1-x}\text{TiO}_3$ (BST) with $x = 0.5-0.75$ [48-50], using Pt electrodes, sometimes provided with a Ta or a TiN barrier to prevent diffusion of Si into the ferroelectric, which lowers its dielectric constant, possibly by formation of SiO_2 . BST exhibits a negligible frequency dependence of the dielectric constant. As an example of the type of results which have been obtained, for a film with $x = 0.75$ an equivalent SiO_2 thickness as low as 0.47 nm with a dielectric constant of 250 and a leakage current less than $1 \times 10^{-7} \text{ A cm}^{-2}$ for a supply voltage of 2.5 V has been realized [50]. The studies so far were aimed at 256 Mbit DRAMs, where the required storage capacity can be obtained using a planar cell structure. For Gbit memories structured surfaces will be necessary and thus the development of appropriate CVD methods.

Given the possibility to electrically switch the remanent polarization of ferroelectric films, their

use in non-volatile memory devices offers itself immediately. The simplest application is that in capacitor structures in a ferroelectric RAM (FERAM) technology, which is under active study [51].

These memories combine non-volatility with fast read and write characteristics, a very large number of write cycles, high device density and low operating voltage. Using a ferroelectric film as the gate insulator of a MOSFET would produce a single device non-volatile memory cell (FEFET-device). However, this would require us to solve the problem of the interaction of the ferroelectric with the silicon substrate.

Finally, the use of ferroelectrics may also allow us to make memories available to other semiconductor technologies. In a recent study the incorporation of FERAMs in the GaAs junction FET technology was explored [52].

10. Conclusions

In the mid-nineties the role of dielectrics in microelectronics is as important as ever, so that continued research towards understanding and control of these materials remains essential for the progress of the field. Our review leads to the following conclusions.

(1) SiO_2 is keeping its place as a gate insulator because of its excellent characteristics also for thicknesses well below 10 nm.

(2) Essential for the position of SiO_2 is the control realized in surface preparation, the avoidance of contaminants and the use of low level doping with N and F.

(3) Because the requirements of a minimum amount of stored charge cannot be satisfied with SiO_2 , notwithstanding the use of three-dimensional structures, the use of higher dielectric constant materials like Ta_2O_5 is unavoidable in the Mbit DRAM capacitor technology.

(4) For Gbit DRAMs ferroelectric high dielectric constant capacitor insulators offer further possibilities to extend the technology. Deposition on structured surfaces and charge leakage will have to be studied. The use of ferroelectrics as gate materials in non-volatile FETs presents technological

problems. Non-volatile FERAM devices look like a better option.

(5) An insulated gate field effect technology based on other semiconductors (SiGe, II-V, II-VI) still appears very difficult. A combination with wider band gap materials (like GaAlAs on GaAs) may present a compromise. Combination of FERAMs with GaAs junction FET technology may be a further option.

References

- [1] E. Takeda, in: *Insulating Films on Semiconductors 1989*, ed. F. Koch and A. Spitzer (North-Holland, Amsterdam, 1989) p. 535.
- [2] W. Weber, M. Brox, A.v. Schwerin and R. Thewes, in: *Insulating Films on Semiconductors 1993*, ed. P. Balk and J.M.M. de Nijs (Elsevier, Amsterdam, 1993) p. 253.
- [3] A.F. Tasch Jr. and L.H. Parker, *Proc. IEEE* 77 (1989) 374.
- [4] H.E. Maes, J. Witters and G. Groeseneken, in: *Proc. ESSDERC 1987*, Bologna, Italy, p. 743.
- [5] E.H. Nicollian and J.R. Brews, *MOS Physics and Technology* (Wiley, New York, 1982).
- [6] P. Balk, ed., *The Si-SiO₂ System* (Elsevier, Amsterdam, 1988).
- [7] P. Balk, in: *Solid State Devices*, 1973, *Inst. of Phys. Conf. Ser. No. 19* (Institute of Physics, Bristol, 1973) p. 51.
- [8] M. Offenberger, P.J. Grunthaner, D.D. Krut and P. Balk, in: *The Physics and Technology of Amorphous SiO₂*, ed. R.A.B. Devine (Plenum, New York, 1988) p. 223.
- [9] F.J. Feigl, D.R. Young, D.J. DiMaria, S. Lai and J. Calise, *J. Appl. Phys.* 52 (1981) 5665.
- [10] M. Aslam, P. Balk and D.R. Young, *Solid State Electron.* 27 (1984) 709.
- [11] K. Kasama, F. Toyokawa, M. Tsukiji, M. Sakamoto and K. Kobayashi, *IEEE Trans. Nucl. Sci.* NS-27 (1986) 1210.
- [12] G.J. Gerardi, E.H. Poindexter, P.J. Caplan and N.M. Johnson, *Appl. Phys. Lett.* 49 (1986) 348.
- [13] L. Do Thanh, M. Aslam and P. Balk, *Solid State Electron.* 29 (1986) 829.
- [14] E. Cartier, D.A. Buchanan and G.J. Dunn, *Appl. Phys. Lett.* 64 (1994) 901.
- [15] D.J. DiMaria, D. Arnold and E. Cartier, *Appl. Phys. Lett.* 61 (1992) 2329.
- [16] G.A. Sai-Halasz et al., *IEDM 1987, Digest of Technical Papers*, p. 397.
- [17] Y. Taur et al., *IEEE Electron Dev. Lett.* 14 (1993) 304.
- [18] M. Hirose, M. Hiroshima, Y. Yasaka, M. Takakura and S. Miyazaki, in: *Insulating Films on Semiconductors 1993*, ed. P. Balk and J.M.M. de Nijs (Elsevier, Amsterdam, 1993) p. 3.
- [19] E.H.A. Granneman, in: *Insulating Films on Semiconductors 1993*, ed. P. Balk and J.M.M. de Nijs (Elsevier, Amsterdam, 1993) p. 11.
- [20] S. Verhaverbeke, M. Meuris, M. Schaekers, L. Hasperlagh, P. Mertens, M.M. Heyns, R. De Blank and A. Philipossian, in: *1992 Symp. on VLSI Technology, Digest of Technical Papers*, p. 23.
- [21] S.I. Raider, in: *Insulating Films on Semiconductors 1993*, ed. P. Balk and J.M.M. de Nijs (Elsevier, Amsterdam, 1993) p. 29.
- [22] Y. Okada, P.J. Tobin, P. Rushbrook and W.L. Dettart, *IEEE Trans. ED* 41 (1994) 191.
- [23] C.G. Sodini and K.S. Krisch, in: *IEDM 1992, Digest of Technical Papers*, p. 617.
- [24] T. Kuroi, T. Yamaguchi, M. Shirata, Y. Okumura, Y. Kawasaki, M. Inuishi and T. Tsubouchi, in: *IEDM 1993, Digest of Technical Papers*, p. 325.
- [25] K. Sharma, R. Moazzami, P. Tobin, Y. Okada, S.K. Cheng and J. Yeargain, in: *IEDM 1992, Digest of Technical Papers*, p. 461.
- [26] T.P. Ma, *J. Vac. Sci. Technol. A* 10 (1992) 705.
- [27] V.V. Afanes'ev, J.M.M. de Nijs and P. Balk, in: *Proc. ESSDERC 1993*, p. 415.
- [28] V.V. Afanes'ev, M. Depas, J.M.M. de Nijs and P. Balk, in: *Insulating Films on Semiconductors 1993*, ed. P. Balk and J.M.M. de Nijs (Elsevier, Amsterdam, 1993) p. 93.
- [29] S.C. Jain and P. Balk, *Thin Solid Films* 223 (1993) 348.
- [30] J.M.M. de Nijs and P. Balk, in: *Insulating Films on Semiconductors 1993*, ed. P. Balk and J.M.M. de Nijs (Elsevier, Amsterdam, 1993) p. 123.
- [31] J.G. Swanson, in: *Insulating Films on Semiconductors 1993*, ed. P. Balk and J.M.M. de Nijs (Elsevier, Amsterdam, 1993) p. 111.
- [32] R.W. Fathauer and L.J. Schowalter, *Appl. Phys. Lett.* 45 (1984) 519.
- [33] W.H. Zachariasen, *J. Am. Chem. Soc.* 54 (1932) 3841.
- [34] A.G. Revesz, *J. Non-Crys. Solids* 11 (1973) 309.
- [35] K.L. Brower, *Phys. Rev. B* 42 (1990) 3444.
- [36] P. Balk, *J. Electron. Matter* 4 (1975) 635.
- [37] W. Hönlein and H. Reisinger, in: *Insulating Films on Semiconductors 1989*, ed. F. Koch and A. Spitzer (North-Holland, Amsterdam, 1989) p. 178.
- [38] M. Nakano, N. Shinmura, K. Iguchi, T. Watanabe and K. Sakiyama, in: *1992 Symp. on VLSI Technology, Digest of Technical Papers*, p. 16.
- [39] M. Gurvitch, L. Manchanda and J.M. Gibson, *Appl. Phys. Lett.* 51 (1987) 919.
- [40] L. Manchanda and M. Gurvitch, *IEEE Electron Dev. Lett.* 9 (1988) 180.
- [41] A. Spitzer, H. Reisinger, J. Willer, W. Hönlein, H. Cerva and G. Zorn, in: *Insulating Films on Semiconductors 1991*, ed. W. Eccleston and M. Uren (Adam Hilger, Bristol, 1991) p. 187.
- [42] T. Nakayama, *J. Electrochem. Soc.* 141 (1994) 237.
- [43] G.S. Oehrlein, *J. Appl. Phys.* 59 (1986) 1587.
- [44] S. Kamiyama, T. Saeki, H. Mori and Y. Numasawa, in: *IEDM 1991, Digest of Technical Papers*, p. 827.
- [45] P. Fazan, V.K. Mathews, N. Sandler, G.Q. Lo and D.L. Kwong, in: *IEDM 1992, Digest of Technical Papers*, p. 263.

- [46] K.W. Kwon, S.O. Park, C.S. Kang, Y.N. Kim, S.T. Ahn and M.Y. Lee, in: IEDM 1993, Digest of Technical Papers, p. 53.
- [47] S. Kamiyana, H. Suzuki, H. Watanabe, A. Sakai, M. Ushida, T. Tatsumi, T. Tanigawa, N. Kasai and A. Ishitani, in: IEDM 1993, Digest of Technical Papers, p. 49.
- [48] K. Koyama, T. Sakuma, S. Yamamichi, H. Watanabe, H. Aoki, S. Okya, Y. Miyasaka and T. Kikkawa, in: IEDM 1991, Digest of Technical Papers, p. 823.
- [49] E. Fujii, Y. Uemoto, S. Hayashi, T. Nasu, Y. Shimada, A. Matsuda, M. Kibe, M. Azuma, T. Otsuki, G. Kano, M. Scott, L.D. McMillan and C.A. Paz de Arango, in: IEDM 1992, Digest of Technical Papers, p. 267.
- [50] T. Eimri et al., IEDM 1993, Digest of Technical Papers, p. 631.
- [51] P.K. Larsen, R. Cuppens and G.A.C.M. Spierings, *Ferroelectrics* 128 (1992) 265.
- [52] S.K. Dey and R. Zuleeg, *Ferroelectrics* 112B (1990) 309.



ELSEVIER

Journal of Non-Crystalline Solids 187 (1995) 10–22

JOURNAL OF
NON-CRYSTALLINE SOLIDS

Section 2. Silicon dioxide, oxidation and unusual structures

Buried oxides: where we have been and where we are going

Jean-Luc Leray*

CEA, Centre d'Etudes de Bruyères-Le-Châtel, B.P. 12, 91680 Bruyères-Le-Châtel, France

Abstract

Buried oxides in semiconductors (so-called BOX) demonstrate a large flexibility of applications, not only in the domain of pure electronic circuits, but also in new areas such as integrated optoelectronics, micromachining and sensors. This is mainly due to the variety of dielectric properties that can play electrical as well as mechanical roles and can act as a buffer layer. Compound structures containing a buried insulator or buried oxide are most of the time identified as silicon-on-insulator (SOI), or more generally semiconductor-on-insulator instead of BOX. This paper briefly covers the roots of the concepts, and classifies and depicts the techniques used to investigate SOI as well as their main applications over the past 60 years.

1. Introduction

Semiconductor on insulator is conceptually the most natural way to make field-effect controlled transistors. It is interesting to note that the early pioneering works of field-effect transistors actually concerned semiconductor-on-insulator thin films [1,2]. These patents described the control of the value of a thin-film resistor through a spacer insulator which at the moment was proposed to be mica. Heil [2] in the UK (1935) proposed that the conductivity of a thin 'gap semiconductor' could be modulated by an external field and Shockley demonstrated the device by using silicon and quartz in 1948 [3]. Since the 1960s, everyday life is now affected by bulk silicon. However, the use of silicon-

on-insulator progressed during the last 30 years, new techniques emerged and gave birth to industrial thin films actually used in specific applications, such as satellites.

2. Why silicon-on-insulator?

The motivations for semiconductors on insulators have evolved since the 1930s and will continue to evolve. Interest in silicon-on-insulator mostly comes from the ability to isolate electrically transistors from one another, as well as the selectivity of etching between the silicon and the silicon dioxide. A last interest comes from the ease of bonding silicon or silicon oxide surfaces by use of Si-H and Si-OH bond condensation. These new advantages can be of great interest and importance for micro-machine and sensor technology.

* Corresponding author. Tel: +33-1 69 26 47 90. Telefax: +33-1 69 26 60 17.

2.1. Full isolation

Radiation resistance was historically the main advantage. Radiation encountered in space consists mainly of isolated cosmic rays that are ions or protons, or in electrons trapped in Van Allen Belts. Ground level radiations are basically the product of fusion or fission nuclear reactions (weapons and reactors), and consist of gamma rays and neutrons. Any of these particles causes ionization, which creates electron–hole pairs in and around junction areas. These carriers are swept by potential gradients caused by applied voltages or doping gradients or diffuse towards PN junctions. As a result, the collected photocurrents can cause upsets in circuit nodes. These effects are proportional to junction areas. Another harmful effect comes from the minority carrier leakage paths that can flow between adjacent transistors and temporarily link them. In the early 1960s, the complementary metal-oxide-semiconductor (CMOS) was reliably processed and improvements in transistor density caused transistor interactions to increase. These leakage paths tied parasitic bipolar transistors of two types (NPN and PNP) and caused the latch phenomenon. The effect is mostly encountered when the radiation flux is delivered in short or very short times, i.e., from the high-energy photons caused by nuclear weapons (10 ns to 10 ms), or when the device is struck by cosmic rays, a frequent scenario on satellites (the electric shock duration is shorter than the picosecond).

By using silicon-on-insulator, most of the PN junctions were converted into dielectric isolation and bulk leakage paths were automatically avoided. Moreover, lateral etching of the surrounding silicon outside the transistors allows the full isolation and cuts off surface leakage paths. Therefore, a substantial gain is obtained since transistors can be made simpler and closer to each other and, most of all, any latch between transistors is inherently prevented. This specific radiation resistance is called radiation ‘hardness’ and the action of converting a given structure and process into such improved devices is called ‘hardening’. Fig. 1 illustrates the basic ability of any transistor structure being converted into silicon on insulator [4]. Again, the silicon-on-insulator structure takes advantage of

smaller active volumes and smaller areas exposed to the incoming fluxes, as suggested by Fig. 2. It can be shown [4] that improvements resulting from the SOI structures are:

- assurance from transistor and circuit latch-up;
- reduction of the leakage photocurrents by two or three orders of magnitudes;
- reduction of the transistors cross sections by one or two orders of magnitudes against a given particle flux.

2.1.1. High-temperature performance

Another advantage of full isolation and reduction of junction area is clearly seen in the field of high temperature: automotive under-the-hood or anti-lock braking systems, deep earth drilling and dwells logging, geothermal reservoirs, aircraft or spacecraft equipment require functioning at 250 °C. In thin film Si, source-drain junction areas are much smaller than those in Si MOSFETS. In addition, the total volume of Si in SOI devices is also very small. These two considerations show that the diffusion current can be reduced by orders of magnitudes and therefore also the leakage current across the junction, especially at high temperature, as it was first pointed out in Ref. [5]. This was clearly demonstrated in 1989 [6] when a 16-kbit memory (SRAM) withstood temperatures of 300 °C, with leakage current 2 or 3 orders of magnitudes lower than the bulk silicon CMOS counterpart. High-temperature testing up to 400 °C was successfully performed [7] and even to 425 °C with ultrathin silicon thickness of 23.5 nm [8]. These two references show correct transfer characteristics up to 400 °C and fully operable characteristics for circuits up to 250 °C, whereas standard bulk devices fail above 150 °C. Such experiments suggested that limitations in the range 300–400 °C would not come from the silicon but from the aluminum. Other well-established metallization techniques such as tungsten would have to be implemented in the CMOS process. Thus, it is clearly advantageous to use well matured and up-to-date silicon-on-insulator technologies in these domains of temperatures, instead of costly and not assured SiC or C technologies.

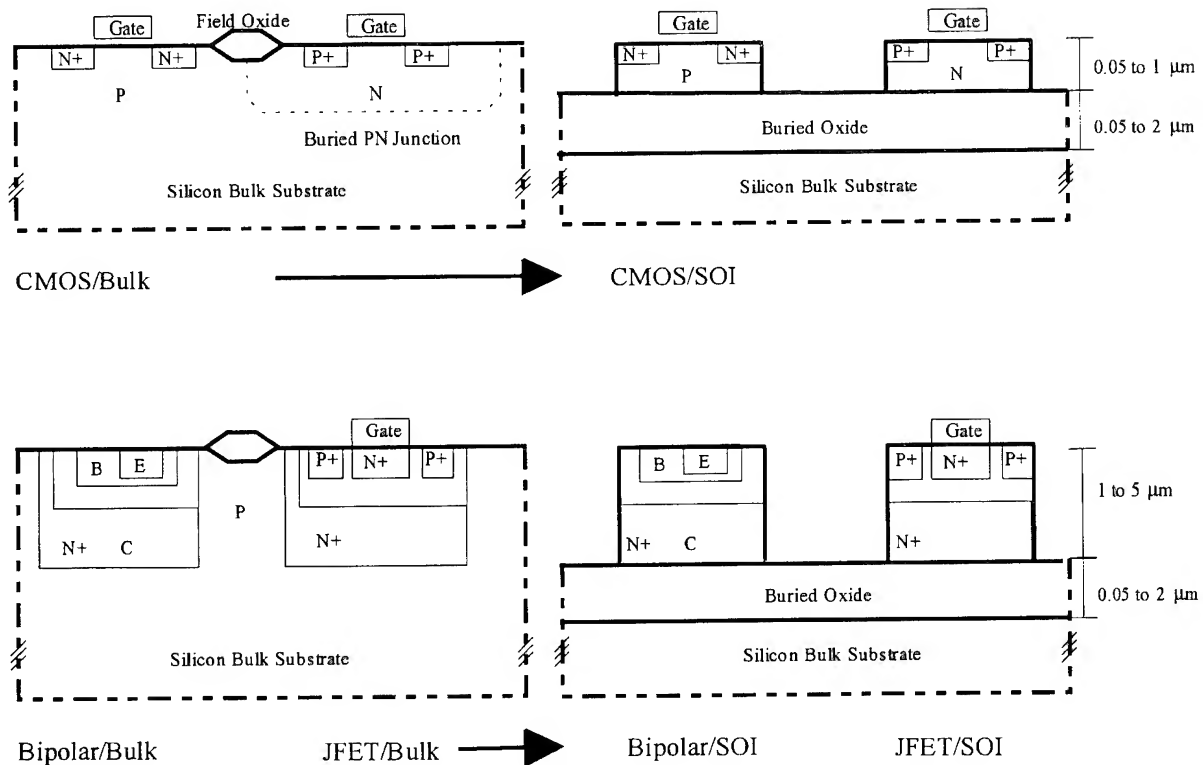


Fig. 1. Examples of silicon-on-insulator structures made on thin buried oxide.

2.2. Dielectric advantages

Advantage of isolation by lateral and buried oxide results not only from preventing cross-coupling of transistors by leakage currents, but also in reducing cross-coupling by capacitances. When replacing the junction isolation of transistors by buried or lateral silicon dioxide, parasitic capacitances decrease junction firstly because of favorable dielectric constant ratio ($\epsilon_{\text{Si}} = 11.9/\epsilon_{\text{SiO}_2} = 3.9$), and operating speed is expected to increase by a ratio depending on transistor size and circuit layout. In the 1980s, this enhancement factor has been asserted to ranging from 30% to 50% for transistors of gate length of 1–2 μm [9, p. 196; 10–12]. For 0.5 μm transistors, the increase of speed has been measured to be a factor of two, and this factor is thought to increase even for deeper submicronic technology and low power supplies of 2.5, 1.5 V and below [13].

Other advantages of dielectric insulation result from the reduced losses in the microwave frequency domain. In silicon technologies, dielectric losses in isolation junctions are one of the reasons that reduce silicon integrated microwave circuits above a few hundred Megahertz. For the same reasons, surface inductors or transmission lines are precluded in silicon wafers, as opposite to gallium arsenide substrate where such losses do not exist. SOI can be a way to overcome this drawback, and in the 1970s, Gigahertz applications were demonstrated in silicon-on-sapphire (SOS) technologies, and in the late 1980s in silicon-on-silicon dioxide (6.2 GHz prescaler) with 50% improvement over the silicon counterpart [14]. In the 1990s, MOS/SOI transistors demonstrated power gain of 9 dB at 10 GHz and initiated the possibility to integrate CMOS digital command of microwave transistors operating in the L and X bands [15]. This technique used special high resistivity silicon

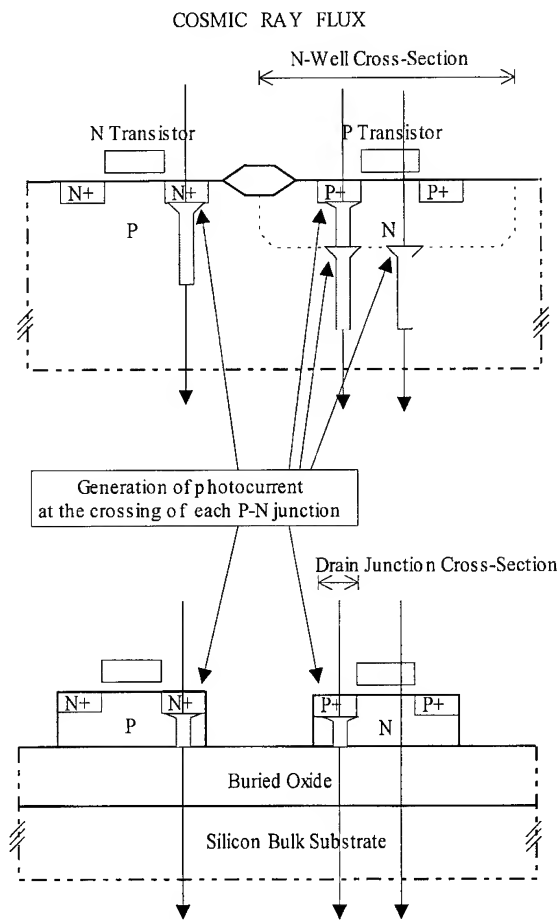


Fig. 2. SOI technologies assets: smaller ionizing track and smaller cross-section against the cosmic ions flux.

substrate of $4 \times 10^4 \Omega \text{ cm}$ obtained by multiple-refining float-zone (FZ) to minimize silicon losses. Applications are clearly seen at least for cellular low-cost telephone networks.

2.3. Scaling down and consequences

Beyond this state of the art, perspective in term of buried oxides may take into account the general trends in silicon technology. As lateral scaling continues in VLSI, vertical dimensions should be reduced, thus demanding source and drain junction depths less than $0.1 \mu\text{m}$. Thanks to the buried oxide

underlayer, thin silicon-on-insulator devices do not have such vertical junctions, and hence, do not pose such problems. This advantage and its consequences can be described as follows.

2.3.1. Junction barriers

Although supply voltage scales down, two non-scaleable parameters constitute obstacles. These are the non-scaleable threshold voltage and the increase of junction capacitance as the reverse bias voltage drops (the latter causing loss in speed improvements). Large improvements come from BOX isolation and very thin SOI layers: (1) the sharp potential barriers of the Si/insulator band discontinuity; and (2) the low dielectric constant of SiO_2 compared to Si, giving much less parasitic capacitance at equal oxide or junction depleted thicknesses. The basic device parameters and speed are less sensitive to the reduction of the supply voltage as compared to bulk CMOS [16].

2.3.2. Silicon electric breakdown

The linewidth scaling down goes faster than the voltage scaling down. Therefore, the electric fields in the semiconductor increases. Silicon voltage breakdown or other phenomena associated with carrier multiplication must be avoided by careful electric field control and doping profile design. Some analyses prove that very thin films on insulators are superior in this field-and-doping optimization, by exploiting the deep depletion mode, unique feature of silicon-on-insulator technology. Anyway, an increase in the electric field displaces the distribution of electron and hole kinetic energies in the very hot electron region of the electron volt, thus increasing the proportion of electrons able to cross the insulator barrier. Refs. [17] and [18] reported the ability of certain kinds of BOX to trap injected electrons from silicon to oxide. However, a substrate electric field of 1 MV cm^{-1} has been used for that purpose, far exceeding the actual fields that never exceed 100 kV cm^{-1} in the BOX for the moment. That is why no specific reliability issues have been recognized in SIMOX technology for the moment [4,19]. But in the near future, technologies of $0.2 \mu\text{m}$ and below will appear and hot electron energy will reach $1\text{--}1.5 \text{ eV}$ [20], thus gaining more probability to be injected into the BOX and be

trapped. This is another strong reason to measure and control the electron trap density in advanced SOI technology.

2.3.3. Junction reliability

As junctions become steeper, electromigration and stress migration become more stringent [21]. In this respect, very thin silicon on insulator minimizes junction area, which become perimetral instead of surfacic. It has been noted that electromigration in this special case pile up to the underlying insulator and produce no device consequence as drain-channel short circuit [9]. This is also a cause of interest for very thin SOI devices. The maximum required thickness is of the order of 100–200 nm in this case.

2.3.4. Doping fluctuations

Another very serious problem in giga-scale integration of transistors with 0.1 μm or smaller sizes is the fluctuation of impurity atoms in PN-junctions [21]. This number falls in the range of 10^2 – 10^3 , thus causing fluctuations in the electrical characteristics. Therefore, the threshold voltage fluctuates and circuit failure could arise from leakage current coming from the wide statistics due to the enormous number of transistors. In this respect, basic equations relating the threshold voltage to doping and silicon and oxides thicknesses show that in very thin films of silicon on insulator, the threshold voltage is not defined by film junction but the doping ratios of the source and the gate. In this type of unique SOI structure, this specific cause of threshold voltage fluctuation due to channel doping vanishes. For this application, silicon thicknesses of less than 50 nm are required and there is a close relationship between the method of synthesizing the silicon film and the buried insulator. To date, only the separation by implantation of oxygen technique (SIMOX, see below) process can provide surface roughness uniformity although the bond and etch-back (BESOI) is making rapid progress.

2.4. Buried optics

Integration of optical and electronic components including signal treatment for integrated optoelec-

tronics requires optical waveguiding. In this matter, the high refractive index contrast between Si ($n = 3.5$) and SiO_2 ($n = 1.5$) can be fully exploited. The most simple structure consisting of guided wave in silicon (photon energy below band gap) and SOI structure is well suited, the BOX acting as a spacer plane between the active silicon guide and the mechanical silicon substrate. A minimum thickness of the BOX oxide ($\lambda/2$ to $\lambda/3$) is required to minimize losses due to evanescent coupling of light through the oxide into the silicon substrate. The minimum thickness of the silicon waveguide is determined by the coupling conditions at the exit plane of the guide [22], and is of the order of λ . Variant structures have been discussed in Ref. [23] along with the possibility of electro-optic light modulator based on the Mach–Zehnder principle and using the dependence of the silicon refractive index on the electron carrier density. This carrier density is in turn determined by the current flowing in the PN junction. Another optical modulator based on a Fabry–Perot resonant cavity has been described [24] and also uses a diode phase modulator placed inside the cavity. For this application, the Si/ SiO_2 buried interface acts as a cavity mirror and the BOX thickness is chosen equal to 0.2 μm to optimize the reflectance at $\lambda = 1.3 \mu\text{m}$.

Optical waveguiding at a wavelength of $\lambda = 1.3 \mu\text{m}$ has been observed in SOI wafers (SIMOX). Applications concern technology compatible with electronic device processing and aims at targets such as silicon-based optoelectronic integration or wide bandwidth on-chip optical network by imitation of GaAs/GaAlAs or InGaAsP/InP. Applications for SiO_2/Si take advantage of the excellent interface uniformity, and the natural oxide thicknesses of 0.4 μm provide single mode waveguiding propagation at $\lambda = 1.3 \mu\text{m}$. Under these conditions, the first mode attenuation was 4.67 db cm^{-1} , making this structure attractive for further applications [25].

2.5. Micromachining

Since the beginning of the 1990s, the field of micromachining is in full expansion. This field is based on the application of microelectronic etching and epitaxy techniques to mechanical or mixed

mechanical/electrical microstructures. Applications concern actuators and sensors (mostly motors and accelerometers, although pressure gauges, pumps, magnetometers, chemical sensors are also considered [26]). The dual aspect of buried oxides and silicon-on-insulator layers can be efficiently exploited due to:

- the high etching selectivity between silicon and silicon dioxide (e.g., 500:1 for SIMOX in KOH)

- the monocrystalline structure of most of the SOI layers, allowing specific electric properties compared to polycrystalline silicon, and specific etching profiles (especially in wet etching).

3. The semiconductor-on-insulator family

The silicon-on-insulator, or more generally the semiconductor-on-insulator family can be described by the way the synthesis occurs. A classification can be proposed as follows.

3.1. Silicon deposition on an insulator (e.g., TFT or ELO)

This is the most natural. Silicon can be deposited on top of a pre-existing insulator. In the 1940s, the first evidence of field effect was produced by Shockley and Pearson [3] in 1948. Evaporated Ge (P-type) or Si (N) or Cu_2O of thickness in the range 20–50 μm was modulated by a metal plate underneath. An insulated plate of fused quartz (70 μm) was used both as mechanical holder, substrate for deposition and gate insulator. Conductivity modulation was ‘as high’ as 11% and at its best with Cu_2O and 3 kV voltage. Theory included the concept of interface state density, which was calculated to be $5 \times 10^{13} \text{ cm}^{-2} \text{ eV}^{-1}$.

In the 1960s, this technique gave birth to the hydrogenated amorphous silicon on glass with buried gate on quartz or glass. In this structure (thin film transistor or TFT), the gate is first deposited on the substrate insulator. Then, the gate insulator and finally the active semiconductor are deposited. The structure is therefore pictorially the reverse of a normal transistor. The semiconductor is amorphous, giving mostly poor electrical performance but this technique allows large manufactur-

ing of large areas at low cost and is still used for large panels or arrays of transistors for flat panel display, for example [27].

The epitaxial lateral overgrowth (ELO) was discovered in the 1970s to overcome the aforementioned problems with amorphous semiconductors and, thus, allow monocrystal growth over the insulator. In this monoepitaxial technique, silicon is deposited after patterning etched windows in the insulator, and the epitaxy proceeds both vertically and laterally from the seeding windows. Seeds coming from the etched pits meet together to form continuous films [28,9]. However, limitations originate from the seeding rates in the horizontal and vertical directions, which impose to build films as thick as 10 μm to cover insulator films with seed windows patterns as close as 20 μm .

3.2. Crystalline silicon deposition on crystalline bulk insulator (e.g., SOS)

In the case of α -quartz, a phase transition at 573°C prevented high-temperature treatments, thus precluding any MOS-compatible process. For this reason, silicon epitaxy must be made on amorphous SiO_2 with polycrystalline or amorphous films as a result.

In the early 1960s, due to progress in monocrystalline sapphire, slicing, polishing and surface preparation (prefiring in hydrogen), crystalline silicon-on-sapphire (Al_2O_3) was successfully realized at RCA Labs and reported in 1964 by Manasevits and Simpson [29]. A variant was the use of Spinel $\text{Al}_2\text{O}_3\text{--MgO}$. The first transistor on sapphire resulted from the works of Heiman (1966) [30] and consisted in P-type MOS transistors that were connected in and arrays of 16 transistors. These techniques were labeled as complementary MOS on sapphire or spinel (CMOS/SOS), and this process was sufficiently mature to allow the first commercial offer by Inselek Company in 1971. A thorough review showing both materials and circuits accomplishments can be found in Ref. [31]. The 1970s marked the triumph of the heteroepitaxy technique. Union Carbide and Kyocera became the main wafer suppliers, thereby, realizing SOS for radiation hardened circuits. Advanced applications were aiming to take advantage of low capacitance,

high voltage, and simpler processes: the first micro-processor was made by Toshiba and Hewlett Packard proposed SOS for pocket calculators. In Europe, works were undertaken for high-voltage applications and for wrist-watch low power circuits. The silicon quality remained the primary issue.

3.3. First and second epitaxy of dielectric and semiconductor

Another principle is to deposit epitaxially the buried insulator on the mechanical monocrystalline silicon substrate, then in a second epitaxy, add the active layer. In a review made in the 1980s, Golecki [28] cites the following materials on which epitaxial silicon films have been grown: BeO (1966), α -SiO₂ (quartz), α -SiC (1963), CaF₂ (1963), yttria-stabilized zirconia YSZ or (Y₂O₃)_m-(ZrO₂)_{1-m} with $m \cong 0.3$ (so-called silicon-on-zirconia SOZ, 1983). Several others attempts were also reported: silicon on chrysoberyl (BeO-Al₂O₃) [32], ThO₂, ZrSiO₄, LaAlO₃ [28], NaCl [33].

In case of CaF₂, early attempts aimed to deposit monocrystalline silicon on this insulator, tried to take advantage of the little mismatch between the two cubic crystals. Interest has been recently revisited with the intent of coupling III–V and II–VI devices to silicon technology and to build stacked silicon devices [34]. Reverse epitaxy of semiconductors (or metals) was found to be much more difficult than epitaxy of dielectrics on semiconductors. This is attributed to the large difference of surface energies which prevents smooth layer-by-layer growth. For instance, in the case of CaF₂/Si(111), it has been shown that Fermi level was pinned at the silicon valence-band maximum [34] and that surface charge was as high as 10^{13} cm^{-2} . This was attributed to the reduction of the Ca²⁺ interface ion to Ca⁺ by silicon and the removal of a fluorine layer.

3.4. Superconductor on buried insulator

It can be noted that monocrystalline YSZ is also a material of choice for deposition of superconducting monocrystalline YBaCuO. Recently, the feasibility of this superconductor on a buried oxide

structure has been demonstrated [35]. In this configuration, YSZ acts as a buffer layer and is itself deposited over silicon. This kind of bolometers could prove superior performance to HgCdTe photodetectors in the $\lambda = 10\text{--}20 \mu\text{m}$ wavelength range, the most important issue being not to expose it to very low cryogenic temperatures. This technique associates both wafer bonding of Si₃N₄ and Si, and pulsed laser ablation to deposit at 775°C successively 70–80 nm of YSZ and 50–70 nm of YBaCuO on the silicon dice to form 50 $\mu\text{m} \times 50 \mu\text{m}$ squares.

3.5. Deposition leading to amorphous or polycrystalline silicon and subsequent recrystallization (ZMR)

In 1963, Maserjian used a scanned electron beam for melting a small zone of polycrystalline germanium crystal deposited on a supporting dielectric [36]. This technique was revisited 11 years later after, due to the apparition of laser to fabricate device-quality silicon film area through zone melting recrystallization (ZMR) [37].

Beyond numerous demonstrations of ZMR of silicon on SiO₂ or Si₃N₄ (a review can be found in [9, pp. 13–35]), other demonstrations have been made, such as silicon-on-diamond (SOD), where the buried oxide is replaced by polycrystalline CVD-deposited diamond acting as an insulator. In the case described in Ref. [8], the deposition of silicon takes place on a very thin barrier/adhesion SiO₂ layer of 30 nm, and as a result the silicon film has to be recrystallized by ZMR. Transistors have been made with modest performance up to now due to surface defects affecting carrier transport mobility: roughness, graphitization due to high temperature melting process, etc.

An interesting concept was developed by Greve et al. [38] in the domain of magnetic memories, by taking profit of the possibility to fabricate semiconductor devices on foreign devices. Advantages were numerous, as access time was limited by the rate at which bubbles can be moved past the magnetoresistive detector. Integration of MOS transistors and circuits would have increase sensitivity by comparison of off-chip sensitive amplifier, and would have allowed parallel outputs to increase byte flux. NMOS transistor was realized by

recrystallization of polysilicon layer deposited on a 1 μm sputtered SiO_2 or plasma or LPCVD Si_3N_4 . However, the bubble memory market did not reveal its promise, being disregarded by magnetic disk storage. This attempt remained isolated, but well illustrated the interest and flexibility of the SOI concept.

3.6. Oxygen introduction under the silicon surface (e.g., SIMOX, FIPOS, GAA)

Buried oxide can be made by oxygen introduction underneath the surface, with condition of preserving the crystallinity in a sufficiently thick surface layer. The following three methods have been used.

3.6.1. Synthesis of BOX by oxygen implantation in silicon (SIMOX)

This requires direct implantation of oxygen (end of the 1970s [39]) followed by ultra high temperature anneal (SIMOX, beginning of the 1980s). The top silicon and the buried oxide thicknesses are respectively determined by the ion energy (giving the implantation peak and range in silicon), and by the oxygen fluence. They can be varied to some extent [40]. It was shown in the late 1970s that the parameters giving the best results require high doses ($1.5\text{--}1.8 \times 10^{18}$ ions cm^{-2}) of oxygen ions implanted at 200 keV [41]. In 1985, the SOI team in Grenoble [42] noticed that very abrupt interfaces and high quality of silicon were determined by high temperature treatments (500–600°C during implantation, and 6 h post implantation anneal at 1300°C in argon + 1% oxygen ambient) [43]. In the late 1980s, other implant conditions were found and excellent ultra-thin BOX (between 47 and 90 nm) and SOI layers were also obtained by 120 and 80 keV O^+ implants [40]. Variants were proposed in order to implant nitrogen (SIMNI), or even carbon. Nitrogen implants gained successes and oscillators were made in 1983 [44]; however carbon implants encountered problems due to graphitization, apparently unsolved up to now.

3.6.2. Oxidation of microchannels made by selective anodic dissolution of silicon (FIPOS)

Another interesting method was to oxidize selectively silicon through microchannels or pipes which

have been elaborated by means of anodic etching (invented 1981 [45]). This technique has been reviewed in Ref. [11] and updates can be found in Ref. [46].

3.6.3. Localized thermal buried oxidation of silicon (gate all around)

Recently, other technique of localized oxidation underneath the transistor channel has been described as the 'gate all around' SOI or GAA [47–49]. Fabrication is straightforward in principle. SIMOX substrate is used as a starting material and, by means of a single supplementary mask, the buried oxide is etched underneath a defined silicon island. Then the silicon bridge can be thermally oxidized and a polysilicon gate is deposited all around the bridging channel. This method takes advantage of the etching selectivity between the silicon and the BOX and is much easier than the vertical surrounding gate transistor (SGT) which has been proposed for 64/256 Mbit DRAMS [50]. Device assets are the better control of the transistor giving higher transconductance and the absence of contribution of the buried oxide back-gate effects. To date, N, P and logic gates have been made with good radiation resistance [51].

3.7. Insulators bonding (BESOI)

This method does not employ additive atomic construction of new layers, but the surface adhesion of two partner wafers. Layers are prepared apart and can be as various as Si, SiO_2 , Si_3N_4 , SiC, etc., each in its best conditions of preparation, and brought together in a second time. However, one of the two bonded slices must be thinned after so as to meet the thickness needed by the SOI concepts and architecture. In the 1980s, more and more successes were gained at bonding preoxidized wafers.

Bonding occurs by construction of hydrogen bond at silanol group $\text{Si-OH} \dots \text{HO-Si}$ (weak bonding) or covalent siloxane Si-O-Si bonds. Bonding was not achieved without externally applied forces until 1985 [52]. Surfaces must present very small microroughness (less than 10 nm), must be cleaned to avoid contaminants (metallic particles, alkali ions, etc.) and are generally prepared (hydrophilization in $\text{NH}_4\text{OH} + \text{H}_2\text{O}_2 + \text{H}_2\text{O}$ and

rinsing in desionized water, for instance [53]). Current processes differ according to the bonding temperature, ambient and subsequent treatments [54]. Below 130°C, fragile hydrogen bond dominates. The interface energy (and also the adhesion force) is approximately insensitive to annealing temperature between 200°C and 800°C for hydrophilic surfaces, due to the predominant silanol condensation allowing transformation of hydrogen bonds into siloxane bonds. This bond formation is accompanied by elastic deformation of the wafers [54]. For hydrophobic surfaces, bonding becomes efficient only beyond 600°C [55]. Beyond 800°C, Si–O–Si formation is supported by plastic flow of the oxide. These properties allow a variety of applications, especially in the low-temperature domain, but most of the problems come from the formation of voids or from the incorporation of particles or contaminating adsorbates.

SiC on SiO₂ on Si (3C–SiC) has been obtained by wafer bonding: advantages of SiC-based devices are obtained for applications operating in high temperature, high power conditions due to its higher band gap, higher avalanche voltage and thermal conductivity over silicon. In Ref. [56], SiC is epitaxially deposited on Si (4 in) and the SiC layer is then oxidized. Then the bonding and thinning take place. Problems arise from the fact that the SiC was polycrystalline but the SiC/SiO₂ was clean and continuous. However, SiC wafers are limited to 2 in in diameter.

SOI and diamond properties have been investigated using wafer bonding [57]. The authors try to solve the problem of transistor self-heating due to the poor conductivity of SiO₂ by using deposited polycrystalline diamond, the thermal conductivity of which is tenfold larger. The temperature increase measured with test diodes is 3 to 4 time less with this 'silicon on diamond' structure.

Gallium arsenide has also been bonded to silicon by CVD-depositing a thin phosphosilicate glass (PSG) layer at 400°C on the surface of a polished wafer [58]. Bonding occurs at 300–600°C under an applied voltage of 10–30 V across the 1–3 µm oxide layer. Content of phosphorous in PSG is adjusted to match the combined thermal expansion of GaAs and Si. GaAs is then etched back. This method aims to circumvent the inconvenience of the direct epi-

taxy of GaAs on silicon, which is possible but leads to strained interface. InP has also been bonded to Si by using a similar deposited SiO₂ bonding layer. After etch-back and etching a stress-relief grid in InP, heterostructure InGaAs/InAlAs is deposited by molecular beam epitaxy (MBE) and a standard fabrication of HEMT took place [59]. Beyond the III–V, Ge has also been bonded to Si, and Si to fused quartz using a buffer SiO₂ layer [59].

4. Background and perspective

4.1. The 1980s and the 1990s

Fig. 3 shows the progresses of current technologies, with a criterion of performance which is defined as 'circuit complexity'. Other criteria do exist, notably for sensors and actuators, micromachining, radiation hardness, temperature resistance, and three-dimensional integration. However, assessments in these domains are not easy to make.

This roadmap clearly reveals promises and accomplishment of materials and the evolution caused by emerging new ones and progressed. At the end of the 1960s, SOS dominated the market due to well-established positions settled in the late 1970s, but SIMOX emerged due to the excellent physical and electrical properties of this material and to the availability of industrial implanters [43].

Zone melting recrystallization was rediscovered after the historical Patent of 1963. E-beam as a heating source was replaced by a scanned laser beam and advanced applications were aimed toward three dimensions.

Oxygen implantation techniques met the quality grade and improved industrial applications in systems and, thus, found a market. Two companies provided the world niche market in these applications. Early wafer-bonding developed rapidly. These 1980s are really the cradle of silicon on silicon dioxide [4] and are the scene for the full debate between SIMOX and wafer-bonding.

SIMOX flourishes for advanced applications, especially in the very thin silicon film domain (30–50 nm) because of the better material quality and flexibility. Material improved drastically, as indicated by the thin silicon film defect density,

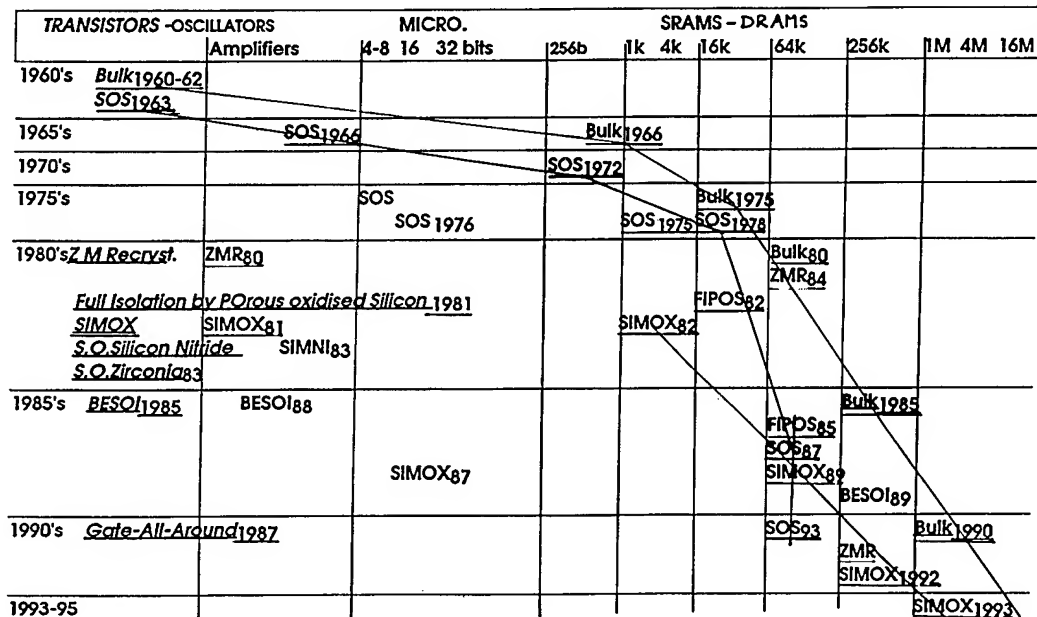


Fig. 3. The main SOI technologies learning curves expressed with the number of transistor per chip as an indicator of the maturity.

which improved at a constant rate of one decade per year since 1985 (10^9 defects cm^{-2} , mostly threading dislocations) to 1992 (10^2 defects cm^{-2} , pairs of dislocation half-loops [60], narrow or pyramid stacking faults pinned on residual precipitates [61]). This defectivity has become comparable to bulk silicon [16].

However, SOS with many more defects and only applications in CMOS radiation-hardened circuits is still flourishing because of its well-established niche markets such as components for satellites. This situation is consolidated by the high degree of skill of the production lines and the full completion with reliability standards requirements.

Wafer bonding is rapidly developing, allowing large diameter wafers providing the fact that the thinning technique and the interface roughness can be overcome. Wafer supplier companies appear in the market. In the domain of micromachining and sensors, wafer bonding offers the unique ability to make hollow or sealed cavities [62], with or without added diaphragms. Applications concern pressure transducers, microvalves, liquid shear-stress

sensors, resonant load cells and accelerometers [63].

4.2. Perspectives, applications and requirements

These unique versatility allows applications of buried oxides in many innovative domains:

- mixed-mode analogue digital circuits based on bipolar, junction field-effect (JFET), CMOS transistors merged on the same chip;

- 'smart-power circuits', i.e., associating medium voltage transistors and integrated CMOS drivers;

- high-temperature circuits due to the reduced junction areas in SOI compared to junction-isolated CMOS;

- sensors, actuators, micromachining due to the ease of epitaxy and the etching selectivity between Si and SiO_2 .

Fig. 4 depicts the various silicon-on-insulator materials by using dimensional classification in terms of buried oxide and silicon film thicknesses (adapted and completed from Ref. [64]). This representation precises the domains of application of

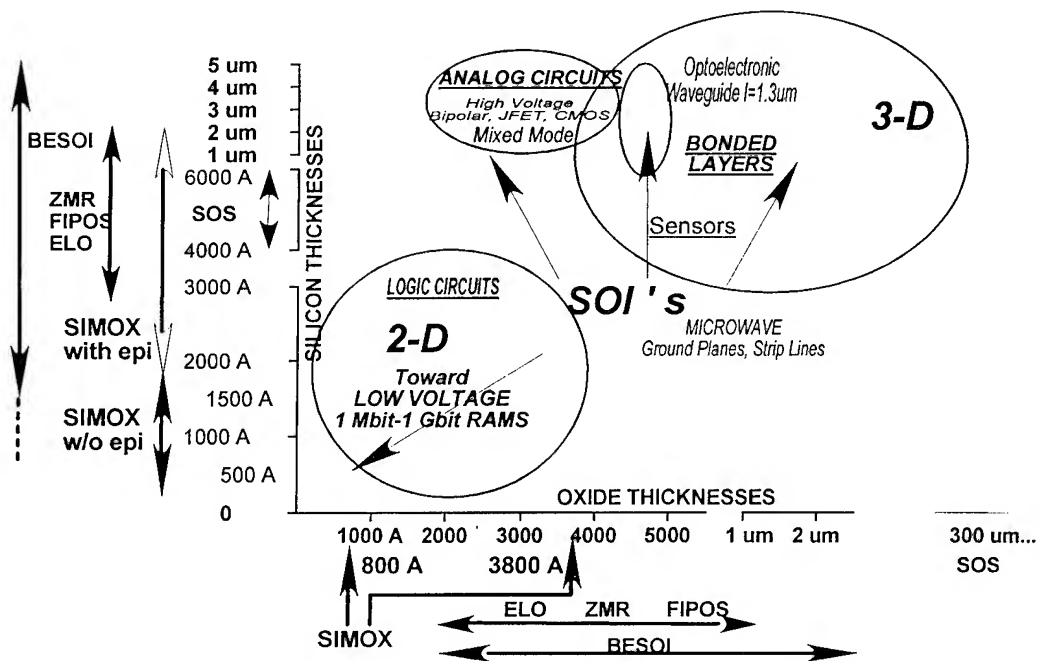


Fig. 4. Mapping of the SOI technologies with buried oxide thicknesses and silicon film in the X and Y axis. The mapping allows one to clarify which structure is the best suited for a given application.

the various techniques (SOS, SIMOX, BESOI, etc.). Trends emerge which shows that there is no unique answer to the question of the future of BOX and SOI [65].

5. Conclusions

Beyond the mainstream trend of microelectronics toward deep submicron technologies, other integration techniques are currently emerging. Most of them use the buried insulator concept, either for process simplification, electrical insulation or as active layer contributing to the transistor field-effect. Leading categories include integrated micromachining and sensors. Mixed optical devices on silicon wafers could be attainable. Generalized multilevel wafer bonding might be the successor of the current technology of the multi-chip modules (MCM). Technologies are primarily the result of the starting material. Buried insulators could open the gateway of the realm of the something-on-something.

The author would thank Dr Roderick A.B. Devine for his strong encouragements to write this paper, and Dr William L. Warren for the strong improvements concerning the English expression of this text.

References

- [1] J.E. Lilienfeld, US patent 1,745,175 (filed in 1926, issued in 1930).
- [2] Oskar Heil, German patent 439,457 (March 2, 1934).
- [3] W. Shockley and G.L. Pearson, Phys. Rev. 74 (1948) 232.
- [4] J.L. Leray, in: Proc. 1st European SOI workshop, Meylan, France, 1988; Microelectron. Eng. 8 (3&4) (1988) 187.
- [5] W.A. Krull and J.C. Lee, in: Proc. 1988 IEEE SOS/SOI Workshop, IEEE (1988) 69.
- [6] D.P. Vu, M.J. Boden, W.R. Henderson, N.K. Cheong, P.M. Zavracky, D.A. Adams and M.M. Austin, in: Proc. 1989 IEEE SOI conf., IEEE catalog no. 89CH2796-1 (1989) 165.
- [7] R.R. Grzybowski and S.M. Tyson, in: Proc. 1993 SOI Conf., ISBN 0-7803-1346-1/93 (1993) 176.
- [8] P.C. Karulkar, in: Proc. 1993 SOI Conf., ISBN 0-7803-1346-1/93 (1993) 136.

- [9] J.-P. Colinge, *Silicon-On-Insulator Technology: Material to VLSI* (Kluwer Academic, Boston, 1991).
- [10] A.J. Auberton-Hervé, M. Bruel, C. Jaussaud, J. Margail, W. d'Hespel, J.F. Péré, A. Vitez and A. Tissot, in: *Proc. VLSI Symposium*, San Diego, CA (1988).
- [11] S. Tsao, *IEEE Circuits Device Mag.* 3 (6) (1987) 3.
- [12] L.K. Wang, in: *Proc. 1986 Symp. on VLSI Technology* (1986) 359.
- [13] S.R. Wilson, B.-Y. Hwang, J. Foerstner, T. Wetteroth, M. Racanelli, J. Tsao and M. Huang, in: *Silicon-On-Insulator Technology and Devices*, *Proc. 6th Int. Symp. on Silicon-On-Insulator Technology and Devices*, ed. S. Cristoloveanu (The Electrochemical Society, Pennington, NJ, 1994) p. 413.
- [14] A. Kamgar, S.J. Hillenius, H.I. Cong, R.L. Field and J.C. Sturm, *Techn. Dig. IEDM* (the IEEE, 1989) 829.
- [15] M.H. Hanes, A.K. Argawal, T.W. O'Keeffe, H.M. Hobgood, J.R. Szedon, T.J. Smith, R.R. Siergiej, P.G. McMullin, H.C. Nathanson, M.C. Driver and R.N. Thomas, *IEEE Electron Devices Lett.* 14 (5) (1993) 219; *IEDM Tech. Digest* (1991) 687.
- [16] B. Davari, H.J. Hovel and G.G. Shahidi, in: *Proc. 1993 IEEE SOI Conference*, ISBN 0-7803-1346-1 (1993) 4.
- [17] T. Ouisse, S. Cristoloveanu and G. Borel, *IEEE Electron Device Lett.* 12 (6) (1991) 312.
- [18] P. Paillet, P. Gonon, C. Schwebel and J.L. Leray, *these Proceedings*, p. 170.
- [19] L. Cohn, H.H. Hosak, R. Cherne and P. Fechner, in: *Proc. 1993 SOI Conference*, ISBN 0-7803-1348-8 (1993) 158.
- [20] C. Brisset, *thèse de Doctorat*, Université d'Orsay Paris 11 (1994) (unpublished).
- [21] Y. Takeishi, K. Natori and S. Iwabuchi, in: *Proc. 20th Int. Conf. on the Physics of the Semiconductors*, Thessaloniki, Greece, Aug. 6–10 (1990).
- [22] R. Watts, A.L. Robinson and R.A. Soref, in: *Proc. 1991 IEEE SOI Conference*, ISBN 0-7803-0184-6/91 (1991).
- [23] D.G. Hall, *Mater. Res. Soc. Symp. Proc.* 298 (1993) 367.
- [24] X. Xiao, J.C. Sturm, P.V. Schwartz and K.K. Goel, in: *Proc. IEEE SOI Conference*, ISBN 0-87942-573-3 (1990) 171.
- [25] N.M. Kassim, T.M. Benson, D.E. Davies and A. McManus, in: *INFOS'91 Conf. Proc.* (Institute of Physics, Bristol, 1992) p. 319.
- [26] P.W. Barth, *Sensors Actuators A21-A23* (1990) 919.
- [27] H.C. Tuan, in: *Material Research Society Proceedings*, Vol. 33, ed. H.W. Lam and M.J. Thompson (North-Holland, Amsterdam, 1984) p. 247.
- [28] I. Golecki, in: *Material Research Society Proceedings*, Vol. 33, ed. H.W. Lam and M.J. Thompson (North-Holland, Amsterdam, 1984) p. 3.
- [29] H.M. Manasevit and W.I. Simpson, *J. Appl. Phys.* 35 (1964) 1349.
- [30] F.P. Heiman, *IEEE-ED* 13 (12) (1966) 855.
- [31] T. Sato, J. Iwamura, H. Tango and K. Doi, in: *CMOS/SOS VLSI Technology*, *Material Research Society Proceedings*, Vol. 33, ed. H.W. Lam and M.J. Thompson (North-Holland, Amsterdam, 1984) p. 3.
- [32] H.M. Manasevit and D.H. Forbes, *J. Appl. Phys.* 37 (1966) 734.
- [33] G. Shimoka and S.C. Chang, *J. Vac. Sci. Technol.* 6 (1972) 235.
- [34] F.J. Himpsel, U.O. Karlsson, F.R. McFeely, J.F. Morar, D. Rieger, A. Taleb-Ibrahimi and J.A. Yarmoff, *Mater. Sci. Eng. B1* (1988) p. 25.
- [35] C.A. Bang, J.P. Rice, M.I. Flik, D.A. Rudman and M.A. Schmidt, *J. Microelectron. Syst.* 2 (4) (1993) 160.
- [36] J. Maserjian, *Solid-State Electron.* 6 (1963) 477.
- [37] G.L. Hutchins and R.A. Laff, *IBM Techn. Disclos. Bull.* 16 (10) (1974) p. 3488.
- [38] D.W. Greve, M.H. Kryder and P.H.L. Rasky, in: *Proc. Mater. Res. Soc. Symp.* 53 (1986) 375.
- [39] K. Izumi, M. Doken and H. Ariyoshi, *Electron. Lett.* 14 (1978) 593.
- [40] F. Namavar, E. Cortesi, B. Buchanan and P. Sioshansi, in: *Proc. 1989 SOI Conf.*, IEEE catalog number 89CH2796-1 (1989) p. 117.
- [41] P.L.F. Hemment, *Proc. Mater. Res. Soc.* 33, ed. H.W. Lam and M.J. Thompson (North-Holland, Amsterdam, 1984) p. 41.
- [42] J. Stoemenos, C. Jaussaud, M. Bruel and J. Margail, *J. Cryst. Growth* 73 (1985) p. 546.
- [43] M. Bruel, J. Margail, C. Jaussaud, A.J. Auberton-Hervé and J. Stoemenos, *Microelectron. Eng.* 8 (1988) 149.
- [44] G. Zimmer and H. Vogt, *IEEE Trans. Electron Devices* 30 (1983) 1515.
- [45] K. Imai, *Solid-State Electron.* 24 (1981) p. 59.
- [46] J.M. Keen, presented at *European Material Research Symp. 1994 Spring Meeting*, May 24–27, 1994, Strasbourg, France.
- [47] J.P. Colinge, *IEEE Trans. Electron Devices* 34 (4) (1987) 845.
- [48] J.P. Colinge, M.H. Gao, A. Romano-Rodriguez, H. Maes and C. Claes, in: *Proc. 1990 IEEE IEDM* (1990) 595.
- [49] R.K. Lawrence, J.P. Colinge and H.L. Hughes, in: *Proc. 1990 IEEE SOI Conf.*, ISBN 0-7803-0184-6/91 (1990) p. 80.
- [50] K. Sunouchi, H. Takato, N. Okabe, T. Yamada, T. Ozaki, S. Inoue, K. Hashimoto, K. Hieda, A. Nitayama, F. Horiguchi and F. Masuoka, in: *Proc. 1989 IEEE IEDM* (1989) 23.
- [51] P. Francis C. Michel, D. Flandre and J.P. Colinge, *IEEE Trans. Nucl. Sci.* 41 (2) (1994) 402.
- [52] J.B. Lasky, S.R. Stiffer, F.R. White and J.R. Abernathey, *IEDM Tech. Digest* (1985) p. 684.
- [53] M. Mishima, T. Yasui, T. Mizuniwa, M. Abe and T. Ohmi, *IEEE Trans. Semiconductor Manufac.* 2 (3) (1989) 69.
- [54] W.P. Maszara, G. Goetz, A. Caviglia and J.B. McKittrick, *J. Appl. Phys.* 64 (1988) 4943.
- [55] Q.Y. Tong, G. Cha, R. Gafiteanu and U. Gösele, *IEEE J. Microelectromech. Syst.* 3 (1994) 29.
- [56] Q.Y. Tong, U. Gösele, C. Yuan and A.J. Steckle, in: *Proc. 1993 IEEE SOI Conf.*, ISBN 0-7803-1348-8 (1993) 60.
- [57] A. Söderbäck, B. Edholm, J. Olsson, S. Tiensuu and E. Johansson, in: *Proc. 1993 IEEE SOI Conf.*, ISBN 0-7803-1348 (1993) 58.
- [58] Q.A. Huang, S.J. Lu and Q.Y. Tong, in: *Proc. 1989 SOI Conf.*, IEEE Catalog number 89CH2796-1 (1989) p. 62.

- [59] G.G. Goetz and A.M. Fathimulla, in: Proc. 1989 SOI Conf., IEEE Catalog number 89CH2796-1 (1989) p. 125; A. Fathimulla, H. Hier and J. Abrahams, in: Proc. GaAs and Related Compounds Conf., Atlanta, GA, 1988.
- [60] J.M. Lamure, B. Biasse, C. Jaussaud, A.M. Papon, J.F. Michaud, F. Gusella, C. Pudda, A.M. Cartier, A. Soubie and J. Margail, in: Proc. 1990 IEEE SOI Conf., ISBN 0-87942-573-3 (1990) 45.
- [61] D. Venables, S.J. Krause, J.C. Park, J.D. Lee and P. Roitman, in: Proc. 1993 IEEE SOI Conf., ISBN 0-7803-1346-1/93 (1993) 48.
- [62] L. Parameswaran, V.M. McNeil, M.A. Huff and M.A. Schmidt, in: Tech. Dig. Transducers'93, 7th Int. Conf. Solid-State Sensors and Actuators, Yokohama, Japan, 1993 p. 274.
- [63] M.A. Huff, A.D. Nikolich and M.A. Schmidt, *J. Microelectromech. Syst.* 2 (1993) 74.
- [64] A.J. Auberton-Hervé in: Proc. 1993 SOI Conf., ISBN 0-7803-1346-1 (1993) 8.
- [65] G.W. Cullen, M.T. Duffy and A.C. Ipri, in: Proc. 6th Int. Symp. on Silicon-On-Insulator Technology and Devices, ed. S. Cristoloveanu (The Electrochemical Society, Pennington, NJ, 1994) p. 5.



ELSEVIER

Journal of Non-Crystalline Solids 187 (1995) 23–28

JOURNAL OF
NON-CRYSTALLINE SOLIDS

RTP – temperature monitoring by means of oxidation

Jens-Peter Zöllner*, Volker Cimalla, Jörg Pezoldt

TU Ilmenau, Institut für Festkörperelektronik, PSF 327, 98684 Ilmenau, Germany

Abstract

In rapid thermal processing (RTP), an accurate temperature distribution adjusting is necessary for manufacturing of homogeneous thin layers and junctions. A common practice is to evaluate RTP systems in this direction by ellipsometric measurements of oxide thickness grown on silicon wafer. The oxide thickness is a function of the temperature distribution during the complete rapid thermal oxidation process including heating and cooling. The goal of this work is to judge the effect of the heating up period on oxide growth. The influence of different heating cycles (different ramp rates and process temperatures) on the oxide thickness distribution is investigated.

1. Introduction

Rapid thermal processes (RTP) are characterized by the advantage to carry out high-temperature processes in the range of some seconds up to few minutes. This is the basis for the manufacturing of ultra-thin layers and small structures used in sub-micron devices [1]. For manufacturing of layers with constant thickness homogeneous temperatures across the whole wafer are a fundamental prerequisite.

For temperature measurement and adjustment, thermocouple wafer are normally used. This method allows only the temperature determination at few points of the wafer. For temperature mapping, ion implanted test wafers are annealed or bare wafers are oxidized. With modulated optical reflectance and sheet resistance measurements, respec-

tively, the modification of the implanted wafer is determined, which corresponds to the annealing temperature. For oxidized wafers the measured oxide thickness distribution yields the two-dimensional temperature profile. This method is suitable for processing temperatures $> 900^{\circ}\text{C}$ [2].

The calculation of the temperature from the oxide thickness is carried out by using a kinetic growth model. The initial oxide growth under dry environment, typical for gate oxide manufacturing with rapid thermal oxidation (RTO), has an enhanced growth rate described by different models [3,4]. Recently, Messaoud et al. [5] compared the experimental growth kinetics of ultra-thin oxide films with the parallel oxidation model [3] for RTO and found an excellent agreement. This parallel oxidation model was applied in this work, too. Because the oxide thickness depends on the temperature-time behaviour of the complete oxidation process, especially during the periods of maximum temperature, for short processes, the heating up and cooling down phase must be taken into

* Corresponding author. Tel: +49-3677 69 1673. Telefax: +49-3677 69 3132.

account. In [2,6,7] was shown, that temperature inhomogeneities occur in scalar controlled RTP-equipments. Temperature overshooting was found to occur near the wafer edge due to steep ramping up.

The aim of this work is to investigate this effect in RTO, and to determine consequences for temperature mapping with oxidation, which are also valid for implant monitoring.

2. Experimental procedure

The oxidation processes were carried out with 100 mm-diameter Czochralski silicon wafers that were phosphorus doped ($1\text{--}50\ \Omega\ \text{cm}$) with (100) surface orientation. Prior to the oxidation, the wafers were cleaned using the RCA process [8] with additional dip in dilute HF. The cleaning sequence consisted of solutions of $\text{H}_2\text{O}\text{--}\text{H}_2\text{O}_2\text{--}\text{NH}_4\text{OH}$ (mixture of 6:1:1 by volume, 85°C , 10 min) and $\text{H}_2\text{O}\text{--}\text{H}_2\text{O}_2\text{--}\text{HCl}$ (6:1:1, 85°C , 10 min) with 5 min DI water rinse after each process finally followed by a dip in 1:50 by volume $\text{HF}:\text{H}_2\text{O}$ and a DI water rinse of 12 min duration. The wafers were dried by a N_2 gas flow.

The loading of the RTO reactor took place under an inert gas flow (argon, 2 l/min). After 20 s

the chamber was pumped out under a reduced argon flow (10 sccm) for 60 s and then under an oxygen flow (15 sccm) for the same time. After the reactor was filled under oxygen flow of 3 l/min, the O_2 gas flow rate was set to 250 ml/min for the normal pressure oxidation process. The complete thermal cycle is illustrated schematically in Fig. 1. All processes were started with a 60 s preheating period of 400°C to obtain a defined initial condition in the chamber because of the memory effect due to slow cooling down of the quartz glass window from the previous process. With different ramp rates (50°C/s , 100°C/s and 200°C/s) the wafers were heated for oxidation at temperatures of 1050°C , 1100°C and 1150°C and times of 10 s, 30 s and 60 s, respectively. 30 s after the heat source was switched off, the gas flow was changed from oxygen to argon.

The used RTP system consists of a cylindrical cooled wall chamber with a rotation symmetrical lamp heating made of three concentric lamp rings [7]. The process temperature was monitored with three thermopiles with a time responds of 25 ms and controlled in scalar closed-loop mode with fixed relative lamp power setting (inner lamp ring 100%, middle 64% and peripheric 43%).

The oxide thickness distribution was determined with a PLASMOS SD 2300 ellipsometer (light

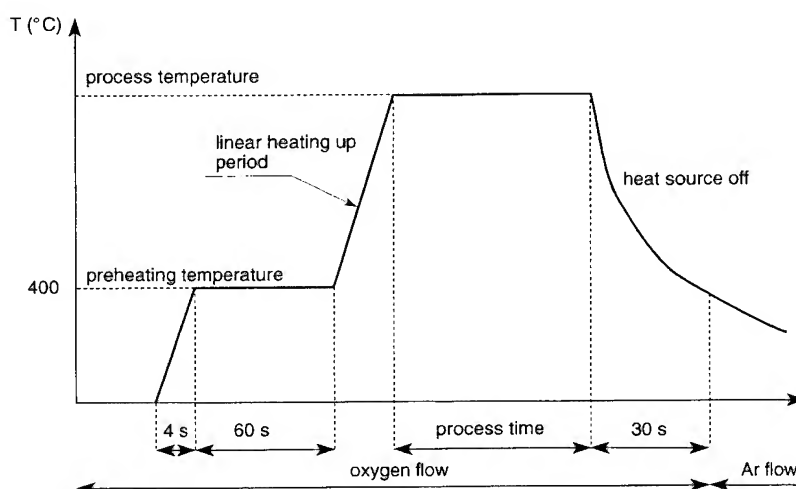


Fig. 1. Scheme of the entire thermal cycle of the RTO process.

wavelength 632.6 nm, incident angle 70°, fixed refractive index mode with $n = 1.465$ for the thermal oxide).

3. Oxide thickness calculation

The oxidation model developed by Han and Helms [3] was used for theoretical thickness determination of oxides produced by RTO. The model based on the assumption of two parallel non-interacting processes, which respond to the fundamental linear-parabolic law [9]. The total oxidation rate can be expressed as

$$\frac{dd_{\text{ox}}}{dt} = \frac{B_1}{2d_{\text{ox}} + A_1} + \frac{B_2}{2d_{\text{ox}} + A_2}, \quad (1)$$

where d_{ox} is the oxide thickness, t the time and A and B growth constants for the mechanisms 1 and 2, respectively. For calculation of oxide growth on (100) silicon the expressions for the parabolic rate constants are

$$B_1 = 1.0833 \times 10^8 \exp\left(-\frac{2.2 \text{ eV}}{kT}\right) \frac{\text{nm}^2}{\text{s}} \quad (2a)$$

and

$$B_2 = 4.333 \times 10^6 \exp\left(-\frac{1.6 \text{ eV}}{kT}\right) \frac{\text{nm}^2}{\text{s}} \quad (2b)$$

and for the linear rate constants

$$\frac{B_1}{A_1} = \infty \quad (2c)$$

and

$$\frac{B_2}{A_2} = 4.333 \cdot 10^4 \exp\left(-\frac{1.9 \text{ eV}}{kT}\right) \frac{\text{nm}}{\text{s}} \quad (2d)$$

were applied. Because of the short processing time during RTO, the complete heating cycle must be taken into account in oxide growth calculations. According to recently published results of Mes-saoud et al. [5], the initial oxide film thickness is necessary to simulate the kinetic growth in RTO. The initial oxide thickness measured before loading the chamber was 0.5 nm.

4. Results

The measured radial oxide thickness distributions in relative units, to the average thickness in the wafer centre, are shown in Fig. 2 for a oxidation temperature 1150°C. With increasing process time,

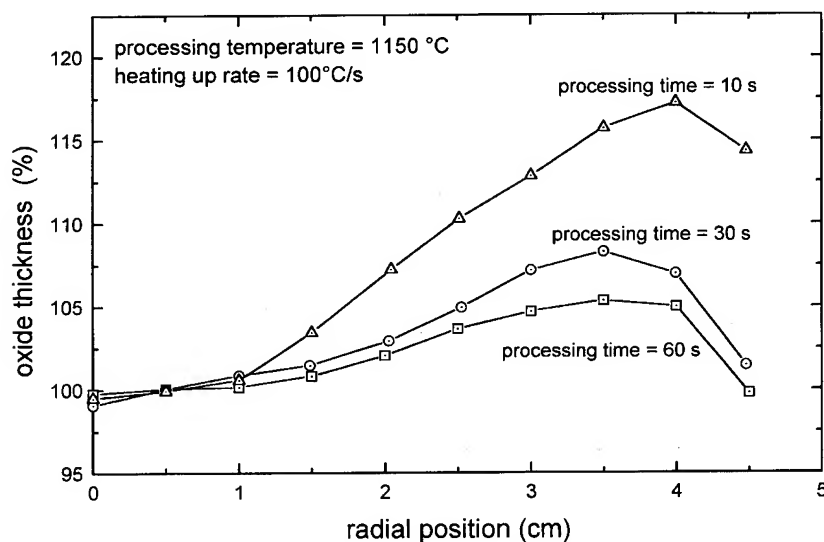


Fig. 2. Radial relative oxide thickness distribution for different oxidation times. Lines are drawn as guides for the eye.

the relative oxide thickness near the wafer edge (mainly at $r > 3$ cm) is reduced. The corresponding temperature behaviours in situ measured at the radial position $r = 0$ cm and $r = 4$ cm show the temperature overshooting near the wafer edge. The

occurring temperature difference is represented in Fig. 3. It is clearly seen, that the temperature overshooting appears during heating up and at the beginning of the essential oxidation period (plateau region). Because the overshooting has relaxed in

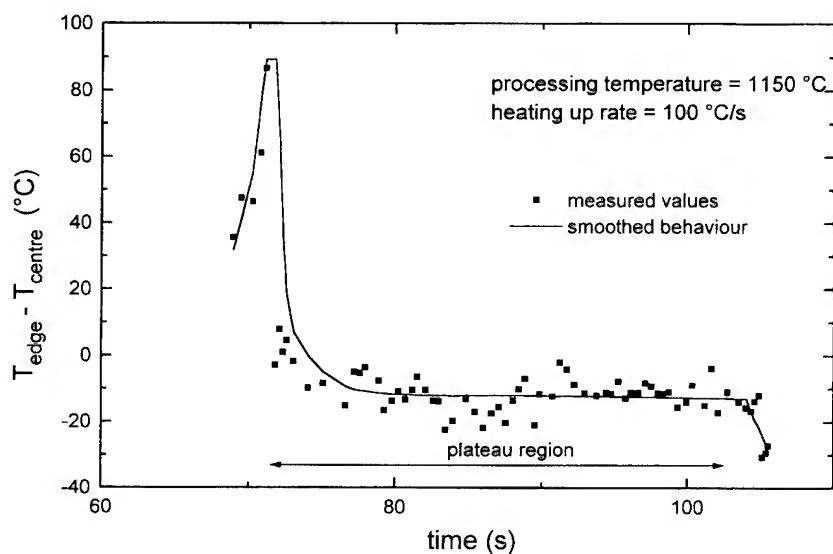


Fig. 3. Measured temperature difference between the wafer edge ($r = 4$ cm) and the centre ($r = 0$ cm) for an oxidation process of 30 s and 1150°C.

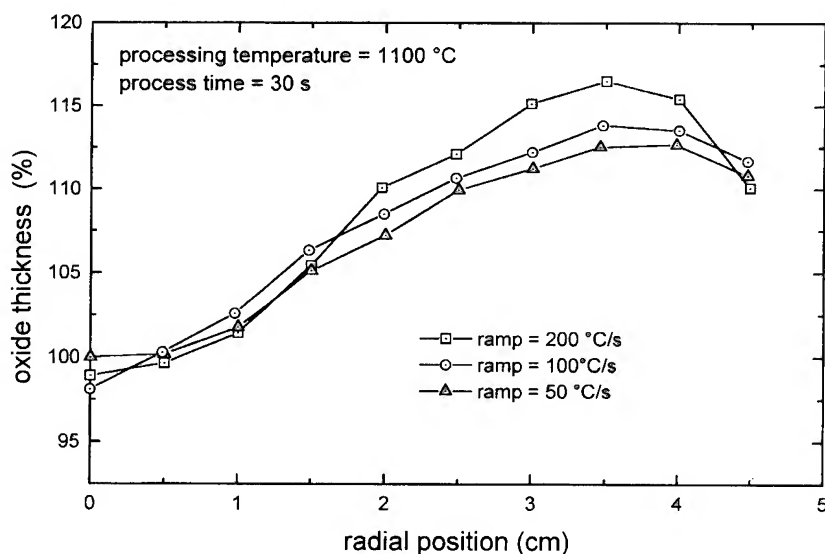


Fig. 4. Radial relative oxide thickness distribution for an oxidation process of 1100°C with several heating velocities. Lines are drawn as guides for the eye.

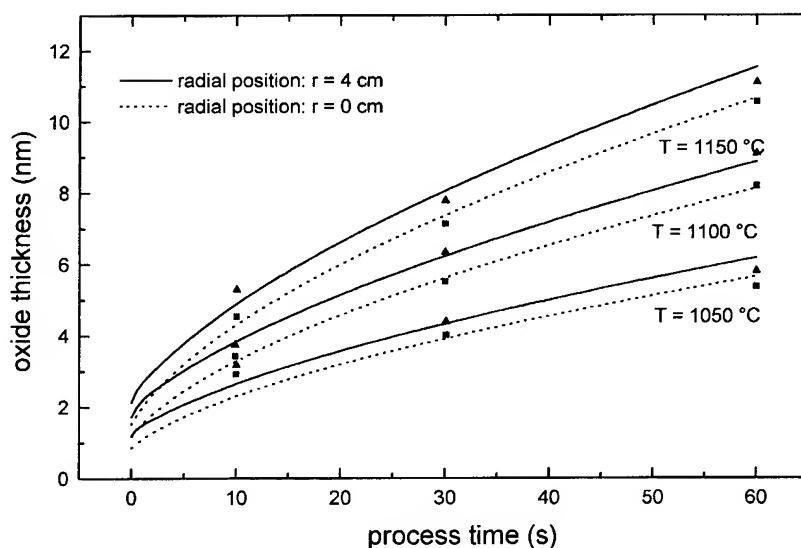


Fig. 5. Calculated oxide thickness as function of the oxidation time for ideal temperature behaviour with a ramp of 100°C/s at the wafer centre (dotted line, without overshooting) and near the wafer edge (full line, with overshooting) in comparison with experimental results. For the wafer center a 10°C lower process temperature was assumed.

approximately 5 s after reaching the plateau region, its influence on the oxide thickness is reduced with increasing process time. Steeper heating ramp rates lead to greater overshooting and consequently to larger thickness inhomogeneities (Fig. 4).

The oxide thickness as function of time was calculated for 3 different process temperatures with and without including of the overshooting by means of the parallel oxidation model (Fig. 5). For the wafer centre the growth was calculated using the ideal temperature behaviour according to Fig. 1. Due to the irradiation deficiency of the applied lamp heater in the wafer centre (see Fig. 3) a 10°C lower process temperature was utilized. The oxide growth near the edge was simulated for the ideal temperature profile superimposed with the overshooting difference. The results are in good agreement with the experimental datas.

The reverse procedure is used when monitoring the oxidation temperature from the measured oxide thickness, the corresponding temperature must be determined by iteratively solving the oxidation equation. The accuracy depends on the quality of the oxidation model and for short processes from the local temperature behaviour including the overshoot effect. Disregarding this dynamic temper-

ature effect, overestimates the temperature at the wafer periphery. The deviations are for instance for a process temperature of $T = 1150^{\circ}\text{C}$: 11°C at a 10 s-process, 2.4°C at a 60 s-process, for a 1050°C -process: 8.3°C at a 10 s-process, and 1.4°C at a 60 s-process. The influence of overshooting is quite intensive for short process times.

5. Conclusion

Because the oxide thickness is a function of the whole temperature cycle, dynamic temperature inhomogeneities must be taken into account in oxidation temperature monitoring for RTP. The temperature overshooting leads to an overestimation of the oxidation temperature near the wafer edge for short processes. For process times > 60 s the influence of dynamic effects can be neglected.

References

- [1] R. Singh, J. Appl. Phys. 63 (1988) R59.
- [2] R. Kakoschke, E. Bußmann and H. Föll, Appl. Phys. A50 (1990) 141.

- [3] C.J. Han and C.R. Helms, *J. Electrochem. Soc.* 134 (1987) 1297.
- [4] H.Z. Massoud and J.D. Plummer, *J. Appl. Phys.* 62 (1987) 3416.
- [5] A.Y. Messaoud, E. Scheid, G. Sarraeyrouse, A. Claverie and A. Martinez, *Jpn. J. Appl. Phys.* 32 (1993) 5805.
- [6] R. Kakoschke, E. Bussmann and H. Föll, *Appl. Phys.* A52 (1990) 52.
- [7] G. Leitz, J. Pezoldt, I. Patzschke, J.-P. Zöllner and G. Eichhorn, *Mater. Res. Soc. Symp. Proc.* 303 (1993) 171.
- [8] W. Kern and D.A. Puotinen, *RCA Rev.* 31 (1970) 187.
- [9] B.E. Deal and A.S. Grove, *J. Appl. Phys.* 36 (1965) 3770.



ELSEVIER

Journal of Non-Crystalline Solids 187 (1995) 29–34

JOURNAL OF
NON-CRYSTALLINE SOLIDS

Low-temperature voltage enhanced UV-assisted oxidation of silicon

A. Dolique^a, A.H. Reader^{b,*}^a Philips Research Laboratories, Prof. Holstlaan 4, 5600 JA Eindhoven, The Netherlands^b Centre Commun CNET: ST Microeln., 850 rue Jean Monnet, BP16, 38921 Crolles, France

Abstract

The use of ultra-violet (UV) irradiation as a way to assist the thermal oxidation of silicon in a dry O₂ ambient has been previously studied. A new low temperature (~650°C) oxidation method is presented here which uses the basic UV assisted process in addition to a voltage, applied to the silicon wafer, and reduced processing pressure. This combination results in a greatly improved oxidation rate. The applied voltage has several purposes: firstly it helps to remove the build-up of negative charge at the Si-SiO₂ interface which occurs by the diffusion of negative oxygen ions (O⁻) through the growing oxide. The second purpose of the voltage is to improve the kinetics of the O⁻ supply and diffusion to the interface. A reduced processing pressure allows effective electrical breakdown of the oxidizing ambient to occur, thus concentrating the voltage drop in the system across the growing oxide. Results of experiments to optimize the oxidation rate are described.

1. Introduction

The oxidation of silicon is a process of paramount importance in integrated circuit technology. Indeed, silicon dioxide has many properties that are exploited in this field such as passivation of Si surfaces and insulation. A general trend has appeared in the past few years to reduce the temperature of integrated circuit processing. High temperatures induce an unavoidable excessive diffusion of dopants in silicon. In order to limit dopants diffusion during processing the temperature should be decreased to about 700°C. However, oxidation is

also a phenomenon governed by diffusion and therefore also follows an exponential type relationship with the reciprocal temperature. Hence at low temperatures the oxide's growth rate is very low if normal thermal oxidation is used.

In the oxidation process, oxide growth initially follows a linear relationship with time (t) up to t_0 :

$$d_{ox} = \alpha t$$

for oxide thicknesses (d_{ox}) below the 10 nm order of magnitude. After this initial period ($t > t_0$), oxidation becomes limited by diffusion through the oxide and the relationship becomes the characteristic parabolic (diffusion) dependence on time:

$$d_{ox} = [\beta^2(t - t_0) + d_0^2]^{0.5}.$$

* Corresponding author. Telefax: +33 76 08 98 25.

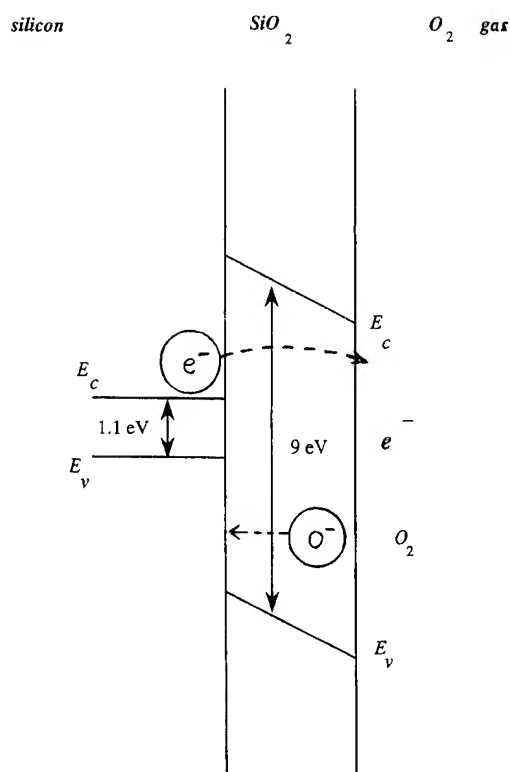


Fig. 1. Energy band diagram of the band gaps in Si (1.1 eV) and SiO_2 (9 eV) showing the energy barrier for electrons at the Si-SiO₂ interface. Electron tunnelling through the barrier is also indicated.

Models of this relationship have been presented for thermal oxidation by Deal and Grove [1] (reviewed by Blanc [2]) and for plasma oxidation by Taylor et al. [3].

According to Wolters and Zegers-van Duinhoven [4], the mechanism for the growth of silicon dioxide in the parabolic oxidation regime is governed by the diffusion of oxygen (O^-) ions through the SiO_2 . Fig. 1 shows the basic principle of this mechanism: An equilibrium is set between, on the one hand, oxygen species (O^-) hopping from one vacancy site to another and electrons tunnelling through the energy barrier at the Si-SiO₂ interface, attempting to returning to the free surface. As a result of the high improbability of the tunnel effect, particularly as the barrier widens (i.e. as the oxide thickens), the electron-removal rate from the interface is a very low. Thus an important limitation on

the diffusion process is the negative charge that builds up at the Si-SiO₂ interface which leads to the creation of an electric field over the oxide, opposing oxygen ion diffusion in the material. If this limitation can be overcome, the growth rate should improve.

Recently, an ultra-violet (UV) assisted oxidation process [5] has been described that allows relatively thick oxide growth at low temperatures. This process involves the creation of O_3 and results in an enhanced oxidation rate. Oxidation is still ultimately limited by the build-up of charge at the Si-SiO₂ interface, although in this case, increased electron promotion over the Si-SiO₂ tunnelling barrier by energetic photons reduces the charge build-up, improving the O^- diffusion kinetics and thus increasing the growth rate.

This paper describes the supplementary idea of using a voltage, applied to the Si wafer, as a way to overcome this limitation of electron tunnelling. By applying a positive voltage to the wafer, electrons can be removed through the substrate and thus electrons generated at the Si-SiO₂ interface no longer have to tunnel through the oxide. For this to occur, conduction through the oxidation ambient is necessary so that a large voltage drop forms across the growing oxide. As conduction through the ambient depends strongly upon the pressure, experiments will be described which investigate the influence of the oxygen pressure during processing on the oxidation rate.

2. Experimental

A cross-sectional schematic of the stainless-steel reactor cell is displayed in Fig. 2. Silicon wafers were placed on the heating plate (also the anode) below a nickel-steel grid (cathode), directly below a UV lamp. The UV lamp used was a Philips high pressure mercury lamp: HOK-4, having two main radiations at wavelengths of 185 and 254 nm in the ratio 1:10. The UV lamp to grid distance is ~ 5.0 cm. The external electrical circuit includes a voltage supply, a voltmeter to control the voltage across the cell (V_c) and an ammeter to measure the resulting current in the circuit. Provided that electrical breakdown of the ambient occurs during

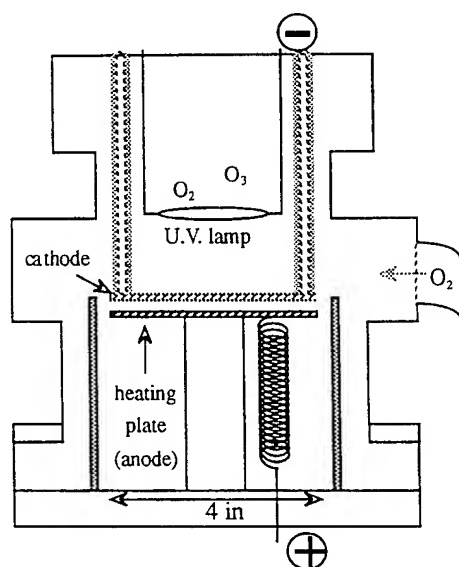


Fig. 2. Cross-sectional schematic of the reactor cell. The Si wafer to be oxidized is placed on the heating plate (anode), below the nickel-steel grid (cathode).

oxidation, it was possible to infer the voltage drop across the oxide by reference to the value of voltage measured on the voltmeter and assuming no other resistances in the equivalent circuit inside the cell.

It should be pointed out here that caution was exercised to ensure the efficiency of electron removal from the substrate. It was found necessary to remove (by buffered HF cleaning) any undesired oxide that was present on the back side of the wafer. The presence of such an oxide leads to less voltage being available across the growing oxide on the wafer's front side.

Silicon epi-wafers were used in this study: substrates were n-type (Sb-doped) (100) oriented ($525 \pm 25 \mu\text{m}$ thick; $0.008 \leq \rho \leq 0.020 \Omega \text{ cm}$) and the epi-layer was $10\text{--}12 \mu\text{m}$ thick (epi-doping $\sim 6 \times 10^{16} \text{ cm}^{-3}$). The wafer's surface area is 78 cm^2 . The experiments were carried out at the same temperature (650°C) and time (6 h) using dry pure oxygen at various pressures. After having pumped the air out of the cell (to a vacuum of about 10 Pa), pure oxygen was introduced. After switching on the lamp, the cell was heated to 650°C and the bias (V_s) was applied after the temperature had

stabilized (positive potential on the heating plate). After oxidations, oxide thicknesses were determined either by C–V measurements (when the oxidized area produced was sufficiently large) or by optical methods.

3. Results

The resulting oxide thicknesses after oxidation as a function of the oxygen pressure in the cell are displayed in Fig. 3. As expected, a clear dependence of oxide thickness upon the oxygen pressure was found. The largest growth rate recorded was for an initial oxygen pressure of about 5000 Pa. At low pressures (below about 1000 Pa), the oxygen atom concentration in the cell is not high enough to supply sufficient O^- ions for high oxidation rates. However, electrical breakdown through the gas was easy to obtain and therefore the oxide thicknesses were relatively homogeneous over wafers. At high pressures (above about 8000 Pa), electrical breakdown was not attainable for a bias (V_s) under about 600 V and therefore low growth rates were obtained.

In Fig. 3, the effect of changing the voltage in the cell is also shown. For pressures around 6000 Pa, the

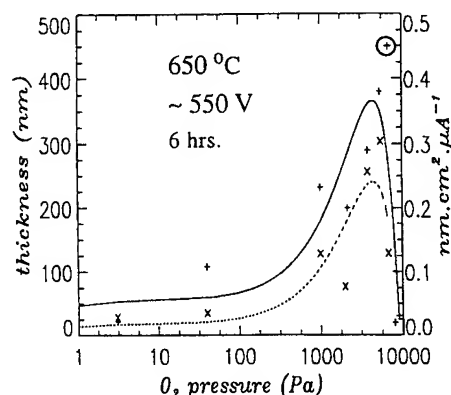


Fig. 3. Oxide thickness (left-hand axis) resulting from the different oxygen pressures used at the temperature and voltage stated: the continuous curve is a fit to the experimental data (+). The circled data point was obtained with a voltage of 700 V. Additional data points (x) obtained at other voltages are displayed as oxide thicknesses normalized by the current density (right-hand axis) and have been fitted with the dashed curve.

voltage was increased to 700 V (encircled point) to determine what thicknesses could be achieved at pressures corresponding to the largest growth rates. As can be seen, thicker oxides were indeed formed. Furthermore, more current flowed in the external circuit. However, when these thicknesses are normalized with the respect to the (initial) current that flowed and the resulting oxidized area, i.e. normalized by the current density (a factor of $[I_c/A]^{-1}$), it can be seen (right hand axis in Fig. 3) that the curve has the same shape as the original plot. This relationship indicates that it is only the pressure that really accounts for the variation in electrical breakdown of the ambient.

Table 1 summarizes the main results achieved: for each sample, the pressure p (in Pa), the voltage across the cell (V_c), the initial current (I_c) in the external circuit, the oxide thickness (d_{ox}), and oxidized area are given. Only the initial current is given in this table, as in fact, the current decreases continuously during an oxidation experiment, except at one point as described below. The efficiency, η , of the process will be discussed later.

Experiments to follow the evolution of oxide thickness with time at a specific constant oxidation condition (pressure 3000 Pa, temperature 650°C and applied bias 600 V) were also carried out. From these experiments, the constants of the growth-rate equations for the linear and parabolic regimes were determined to be $\alpha = 0.15 \text{ nm s}^{-1}$ and $\beta = 4.5 \text{ nm s}^{-1/2}$. These values represent increases by factors of 200 and 50 for α and β , respectively, from values for the UV oxidation process. Further, the linear regime appears to have increased in terms of

oxide thickness: for the UV process, the parabolic growth regime begins at an oxide thickness of about 10 nm whereas for this process, this regime starts from around 60 nm. The start of the parabolic growth regime was marked by a sudden current drop, the origin of which will be discussed later.

4. Discussion

In this section, discussion will be limited to the results obtained for pressures between 500 and 5500 Pa (in Fig. 3) where the enhancement process becomes really effective and a substantial increase in oxide thickness is achieved. The effects of the applied voltage will now be discussed.

First of all, applying a bias leads to an electrical breakdown in the ambient of the cell, insuring that most of the voltage drop is concentrated across the growing oxide. This ensures that the electrons released at the Si-SiO₂ interface by O⁻ ions will be removed to the metal anode and extracted to the external circuit. However, as electrical breakdown is typically a local phenomenon, the homogeneity of oxide growth is poor.

The second effect of applying a voltage across the growing oxide is to enhance the flow of O⁻ ions through the oxide during the diffusion phase of the oxidation process. According to Fick's first law for diffusion, the O⁻ ion flux is increased by an additional drift diffusion term (due to the electric field across the oxide and proportional to the field strength). In addition, in the early stages of the oxidation, the applied voltage increases the concentration of O⁻ ions at the surface of the very thin SiO₂ layer. This results in an enhanced growth rate in the linear oxidation regime as well. Hence, in both regimes of the oxidation process, the voltage improves the growth rate when compared to normal thermal oxidation.

Not only does the voltage increase the growth rate constants α and β but it also causes the linear oxide growth region to be greater. Indeed, as explained by Taylor et al. [3], parabolic growth starts when the charge at the surface of the oxide becomes too small to supply the oxidation with O⁻ ions at the same rate. This causes the charge to suddenly

Table 1
Summary of the most significant results obtained

P (Pa)	V_c (V)	I_c (μA)	d_{ox} (nm)	A (cm^2)	η (%)
6.5	450	200	30.1	6	5
40	470	2200	107.3	0.71	0.5
800	430	2200	160	3.5	3
1000	450	2850	232	1.57	1.5
2150	510	1010	200	0.39	1
3800	575	2000	290	1.77	4
5350	730	3300	380	2.4	3.5
6800	730	4000	450	1.15	2

spread all over the oxide, resulting in a current drop, as was observed. In this study, the applied voltage increases the charge concentration on top of the oxide, which prolongs the supply of charge for the linear regime, thus causing the diffusion controlled regime to start later (at large thicknesses).

Concomitantly with the voltage effects described above, the UV lamp has three major effects as well. The first of them is to produce ozone (with $\lambda = 185$ nm photons). Chemically more reactive than the oxygen molecule, ozone is decomposed into oxygen and the excited 1D state of the O atom (with $\lambda = 254$ nm photons) – see Chao et al. [6].

Second, with this particular experimental set-up, a large percentage of UV light reaches the wafer's surface. (With a lamp to wafer distance of ~ 5.5 cm and a pressure of ~ 1000 Pa, an absorption of $\sim 2\%$ of the 185 nm radiation will occur in the oxidizing ambient according to Robinson [7]; for a 5000 Pa pressure, the absorption is $\sim 10\%$. The 254 nm radiation is mainly absorbed by ozone which was assumed to be at sufficiently low concentration in the cell to have a negligible absorption effect.) Shining UV radiation directly on the wafer has the additional effect of breaking Si–Si bonds, at the Si–SiO₂ interface (creating electron–hole pairs) as suggested by Schafer and Lyon [8] and confirmed by Young and Tiller [9, 10]. This latter effect enhances the oxidation rate as the diffusing O[−] ions can now bond to these modified Si atoms relatively easily. This effect is especially strong during the early stages of oxidation when according to Blanc [3] the density of oxygen species would otherwise be considerably higher than that of broken Si–Si bond.

The third role of the UV radiation is to help conduction through the oxidizing ambient by photo-generating electrons from the nickel–steel grid cathode. This latter effect combined with a homogeneous illumination (which was not present in this cell) may be considered as a first step on the way to a homogeneously thick oxide.

The efficiency, η , of the process was evaluated by comparing the experimental thickness to the corresponding value that would have been reached if the total charge collected at the anode (computed by numerical integration of the current) was due to

electrons released by diffused O[−] ions. Indeed, knowing the total number of electrons that reached the anode gives the maximum theoretical number of SiO₂ molecules that could be formed. When the oxidized area is known, the maximum theoretical value can be inferred for the oxide thickness (from the SiO₂ density). Obviously the efficiency η (displayed as a percentage) in Table 1 indicates that not every electron really contributes to the oxidation: 100% efficiency would mean that every electron that passes through the cell ionises an oxygen atom and then is released by the ion when it reacts to form SiO₂ at the Si–SiO₂ interface.

5. Conclusions

The application of a voltage to a Si wafer during oxidation has been shown to lead to a significant enhancement in the oxidation rate of Si. Thicknesses of an order of magnitude large than those achievable with UV-assisted oxidation at similar temperatures have been obtained. Furthermore, the constants of the growth-rate equations are considerably larger than those for the UV-assisted process and the linear growth regime has been increased in terms of oxide thickness. Nevertheless, further work is required to improve the homogeneity of the oxide produced by this technique which is particularly poor due to the inherent instability of electrical breakdowns in gases at high electric fields. A compromise remains to be found between high growth rates and better homogeneity.

The authors would like to thank members of the Advanced Semiconductor Material Science group of Philips Research Laboratories in Eindhoven who supported this work.

References

- [1] B.E. Deal and A.S. Grove, *J. Appl. Phys.* 36 (1965) 3770.
- [2] J. Blanc, *Appl. Phys. Lett.* 33 (1978) 424.
- [3] S. Taylor, W. Eccleston and K.J. Barlow, *J. Appl. Phys.* 64 (1988) 11.
- [4] D.R. Wolters and A.T.A. Zegers-van Duinoven, *J. Electrochem. Soc.* 139 (1992) 241.
- [5] V. Craciun, A.H. Reader, W. Kersten and I.W. Boyd, *J. Appl. Phys.* 75 (1994) 1972.

- [6] S.C. Chao, R. Pichai and Y.H. Lee, J. Electrochem. Soc. 136 (1989) 2751.
- [7] N. Robinson, Solar Radiation (Elsevier, New York, 1966) ch. 3.
- [8] S.A. Schafer and S.A. Lyon, J. Vac. Sci. Technol. 19 (1981) 494.
- [9] E.M. Young and W.A. Tiller, Appl. Phys. Lett. 42 (1983) 63.
- [10] E.M. Young and W.A. Tiller, Appl. Phys. Lett. 50 (1987) 46.



ELSEVIER

Journal of Non-Crystalline Solids 187 (1995) 35–39

JOURNAL OF
NON-CRYSTALLINE SOLIDS

Rapid thermal annealing of SiO₂ for VLSI applications[☆]

A. Paskaleva*, E. Atanassova, G. Beshkov

*Institute of Solid State Physics, Bulgarian Academy of Sciences, 72 Tzarigradsko Chaussee blvd.,
1784 Sofia, Bulgaria*

Abstract

The influence of the rapid thermal annealing (RTA) in vacuum on the properties of thermally grown SiO₂ has been investigated by means of high field Fowler–Nordheim tunneling injection. The results indicate that the RTA process anneals the original electron traps existing in as-grown oxides while also introducing positive charge manifested as electron traps. The dependence of these charges on the annealing temperature (1073–1473 K) is a strong function of the technological history of the samples.

1. Introduction

The increasing demands of the IC performance have imposed the necessity of new technological approaches. This has provoked the development of so-called rapid thermal processes which appear to be very beneficial and convenient for application in the advanced technology devices with submicron dimensions [1]. Much attention has been focused on the post-oxidation rapid thermal annealing (RTA) of SiO₂ layers, as a possibility for improving the quality and the reliability of SiO₂ films. There is evidence, however, that the annealing behavior strongly depends on both the process parameters and the technological history of the samples. As a result, in some cases, RTA could improve, as well as worsen the quality of Si–SiO₂ system. Regardless of the intensive investigations of the RTA influence on the properties of Si–SiO₂ based devices, the processes which lead to the introduction of defects

in some cases of RTA are not well clarified. The origin of these defects as well as their relation to the chemical ambient and to the temperature of annealing are not also elucidated [2,3]. Because of this, albeit the evident merits of RTA technique in comparison with classical thermal treatments, its use has not yet obtained wide application.

The purpose of this paper is to investigate the influence of RTA in vacuum at temperatures $T_a = 1073$, 1273 and 1473 K on the properties of Si–SiO₂ structures with two oxide thicknesses $d = 11$ and 39 nm obtained at different oxidation conditions, i.e. with different technological history before the RTA. The effect of the temperature at which the RTA was performed in vacuum as well as the quality of the initial Si–SiO₂ structures were studied using the Fowler–Nordheim (FN) electron injection technique on MOS capacitors.

2. Experimental procedure

All the samples were MOS capacitors on p-type (100) Si (15–17 Ω cm). After the conventional

[☆] This work was partly supported by the Bulgarian Ministry of Science and Education in the frame of Project Φ73.

* Corresponding author. Tel: + 359-2 74 311, ext. 448. Telefax: + 359-2 757 032. E-mail: elenada@bgearn.bitnet.

chemical cleaning for MOSLSIs, part of the wafers were oxidized in dry oxygen at 1273 K (with N_2 annealing at the same temperature) to $d = 11$ nm. The rest of the wafers were oxidized at the same temperature in dry oxygen with 4% HCl (without high temperature annealing in N_2) to $d = 39$ nm. The samples from both groups were submitted to RTA in vacuum for 60 s at the three mentioned temperatures. Annealing was performed in a commercial resistance type heater at vacuum 5×10^{-5} Torr. MOS capacitors were defined by evaporation of Al (gate area $1.96 \times 10^{-3} \text{ cm}^2$). To study only the effect of RTA the wafers received no post-metalization annealing. The ramp rate of I – V measurements was 0.15 V/s and the gate was always biased negatively. For both I – V and I – t dependencies the current was measured using a Philips PM 6509 leakage current meter with an accuracy of 1×10^{-11} A.

3. Results and discussion

The experimental results show that the FN tunneling is the dominant conduction mechanism in the oxides investigated before as well as after annealing, i.e. the current J flowing through the oxide is $J = AE^2 \exp(-B/E)$. The constants A and B are functions of both the barrier height Φ_b at the Al– SiO_2 interface and of the effective electron mass m^* . E is the cathode electric field. $B = (8\pi/3h)(2m^*)^{1/2} \Phi_b^{3/2}$ ($m^* = 0.42m_0$, m_0 is the free electron mass). Table 1 presents the value of B deduced from the I – V curves for all cases investigated. It is seen that the effect of the RTA is different for the two oxides and the following peculiarities could be observed.

Case i. $d = 11$ nm. No reduction of Φ_b at 1073 K was observed. Higher annealing temperature results in lowering of the barrier and therefore increased conductivity. This reduction implies the generation of positive charge near the injecting interface. The oxide annealed at 1473 K, however, showed qualitatively different behavior indicating in fact a change of film conductivity mechanism after annealing. The I – V curves in this case are best fitted by the Richardson–Dushman equation which is representative for

Table 1

Values of the constant B ($\times 10^8$ V/cm) derived from experimental I – V curves

d (nm)	As-grown oxide	RTA		
		800 °C	1000 °C	1200 °C
11	2.42	2.41	2.18	—
39	2.25	2.00	2.15	2.23

RTA, rapid thermal annealing.

the Schottky emission. So, the calculated value of the relative dielectric constant ϵ from the slope J versus \sqrt{E} is 4.25, i.e. this value is slightly higher than the well known value of 3.9 typical of perfect SiO_2 . Based on these results we conclude that Schottky emission occurs in the 11 nm oxides after 1473 K RTA. According to Tromp et al. [3] when thin oxide layers are annealed at $T_a \geq 1373$ K in vacuum, SiO_2 decomposition occurs and the oxide is removed. The process is highly non-uniform and it leads to defect generation in the oxide including formation of SiO_x ($1 \leq x < 2$). Based on these results we assume that the presence of these non-stoichiometric oxides may be responsible for the higher value of ϵ at 1473 K. In addition, the 11 nm oxides after annealing at 1473 K exhibit extremely large leakage current even at low electric fields (3–5 MV/cm). These large currents observed are an additional support of the suggestion that in this case the oxide is strongly defected. At such high temperatures the anneal in vacuum most likely produces some sort of structural defects (like regions of non-stoichiometric oxide due to the decomposition of SiO_2) with high density and the current flows through them.

Case ii. $d = 39$ nm. The annealing at 1473 K (Table 1) does not alter the Φ_b of 39 nm oxide at all. With decreasing the T_a the barrier height also decreases and the lowest temperature (1073 K) affected it stronger. The calculated reduction of the barrier is $\Delta\Phi_b = 0.25$ eV. In this way, our data clearly show an increase of hole trapping with decreasing T_a for $d = 39$ nm, i.e. RTA at lower annealing temperature seems to favor the generation of positive charge.

Let us now trace the I - t characteristics when a constant electric field (7–11 MV/cm) is applied. For all samples the current decreases monotonically with time to a saturation level, J_s . As is seen (Fig. 1), the I - t curves for $d = 39$ nm after annealing lie above this for the as-grown sample. The higher the temperature the shorter the decay region is and the higher J_s . Generally, the current decay may be due to the presence of electron trapping near the injecting electrode. This results in a reduction of the external field $E_c = E_a - (qN \cdot \bar{x}/\epsilon)$, where N is the bulk density of the trapped charge and \bar{x} is the distance of the charge centroid from the non-injecting interface. Following the procedure described in [4] we have calculated the product $N_f = N\bar{x}$ from the experimental I - t curves (Table 2). The reduction ΔN_f of the traps after annealing is a function of T_a and d . ΔN_f increases with increasing T_a for $d = 39$ nm and the highest reduction $\Delta N_f = 1 \times 10^{12} \text{ cm}^{-2}$ is obtained after annealing at 1473 K. The reduction of electron traps after annealing of the 11 nm oxides is also observed but the effect in this case is weaker ($\Delta N_f = (1.5 - 3) \times 10^{11} \text{ cm}^{-2}$). These oxides, however, exhibit different rapid thermal characteristics – the dependence on the temperature is reverse, ΔN_f decreases with increasing the temperature. Generally, the reduction of the electron traps after RTA is observed from many authors [1,5]. Probably this reduction

Table 2

Values of the effective trap density $N_f = N\bar{x}$ ($\times 10^{12} \text{ cm}^{-2}$) for the samples investigated before and after rapid thermal annealing

d (nm)	As-grown oxide	RTA		
		800°C	1000°C	1200°C
11	1.4	1.1	1.27	—
39	1.4	1.1	0.85	0.4

is due to the annealing of the originally existing traps in the initial oxides. The hydrogen containing species are most likely responsible for the observed electron traps [6]. Their concentration in the as-grown oxides is probably significant especially for the 39 nm oxides which were not subjected to the post-oxidation N_2 annealing. As it is seen from our results the effect of the RTA on the Si-SiO₂ system depends in very complicated way on the quality and on the parameters of the initial oxide and its interface with the Si.

Although the dependence of Φ_b on T_a is different for the two oxides investigated, there exists very interesting correlation between the reduction $\Delta\Phi_b$ and the annealed traps ΔN_f (Fig. 2). As it is seen ΔN_f ($\Delta\Phi_b$) is a decreasing function for both oxides, and the greater the reduction of the barrier height (i.e. the greater the induced positive charge), the smaller the reduction of the electron traps. We assume that the most possible candidate for the positive oxide trapped charge is the trivalent silicon ($\equiv \text{Si}^\cdot$) (in all forms – as interface states as well as oxide charge) which is obtained, most likely, after breaking of Si-H and Si-OH groups. The $\equiv \text{Si}^\cdot$ acts as a hole trap and induces positive charge. Subsequent injected electrons are captured at this site. So, such a capture can compensate a part of the hole centers $\text{O}_3 \equiv \text{Si}^+ - \text{Si} \equiv \text{O}_3$ [7–9]. The experimental results indicate that RTA in vacuum is effective in reducing the density of native electron traps presented in the initial oxides and at the same time RTA leads to the formation of an additional positive charge which subsequently acts as electron traps. This seems to be the reason that the greatest reduction of the electron traps is observed for the samples which do not show a change of Φ_b (i.e.

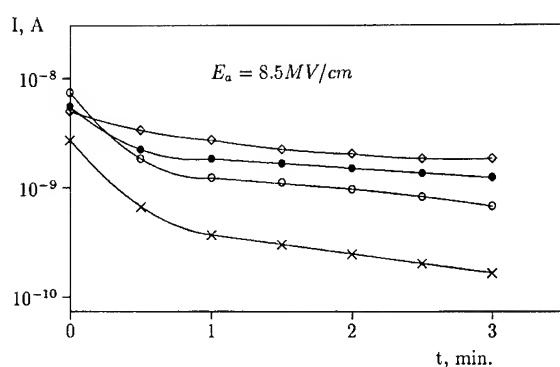


Fig. 1. I - t characteristics for $d = 39$ nm oxides before (x) and after RTA treatment: \circ , 1073 K; \bullet , 1273 K; \diamond , 1473 K. Lines are drawn as guides for the eye.

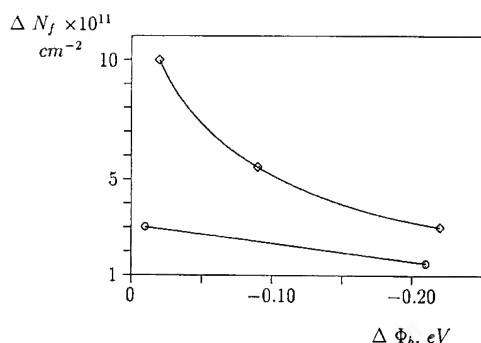


Fig. 2. ΔN_f versus $\Delta\Phi_b$ for the two oxides investigated: ○, 11 nm; ◇, 39 nm. Lines are drawn as guides for the eye.

a generation of positive charge, RTA 1073 K for 11 nm and 1473 K for 39 nm oxides, Table 1), and conversely the smallest is the reduction of electron traps for samples exhibiting the greatest reduction of Φ_b . This correlation was observed for both oxides although it is stronger for the thicker one. These data exclude the possibility that the decrease of the electron traps is due to the charge compensation and is not a real annealing of traps. In the case of compensation the greatest reduction ΔN_f of traps should be observed for the samples performing greatest positive charge generation (i.e. greatest $\Delta\Phi_b$). It is known that, when breaking the hydrogen containing group, hydrogen species are dissociated and they drift easily through the oxide. From the slope ΔN_f versus $1/T_a$ we have extracted the activation energy 0.4 eV for the traps annealing in the case of $d = 39$ nm. This value is very close to that which is usually reported for the hydrogen transport in the SiO_2 [10]. This provides further support for the conclusion for a key role of the hydrogen in the RTA process. The results indicate also that more hole traps are created in the 11 nm oxides with increasing T_a , which is in accordance with the data of the others [5]. One possibility for the increased hole trapping is the oxygen deficiency model [11]. Within this model high temperature annealing in an inert ambient causes a deficiency of oxygen in SiO_2 . Hole traps are believed to result from the missing oxygen atoms which locally disrupt the normal Si–O bonds. It is surprising, however, that 39 nm oxides show reverse tendency – the

hole traps decrease with increasing T_a . Recently Devine et al. [12] have detected also the presence of oxygen-vacancy centers and oxygen-vacancy related complexes but in the thick oxide and after long time high temperature annealing. These defects result from the diffusion of O from the SiO_2 network into the Si. In fact, the physical origin of hole traps generation during RTA is not yet known. Although some questions about RTA effects have been answered, there are still unresolved problems. For example, at higher temperatures, the hydrogen or water outdiffusion is possible, which increases the interface state density. However, until now, it has not been conclusively shown which of the several processes, e.g. hydrogen generation, diffusion or recombination dominate the annealing at the conditions of RTA. In addition, which type of interface states formed during the RTA (acceptor or donor) will be dominant depends on the initial oxide quality. All this could lead to a specific for a given oxide dependence of the hole traps generation on T_a which we actually observe. However, it is clear that the origin of the traps cannot be determined by these experiments alone and other experiments including analytical ones must be performed to correlate the results.

4. Conclusion

As a result from this investigation, some important conclusions can be done. Rapid thermal annealing in vacuum leads to generation of positive charge which results in lowering of the barrier height. This reduction depends on the annealing temperature as well as on the technological history of the samples. The results reveal that the RTA has different effect on the hole trapping depending on the quality of the initial oxide and on its interface with Si. RTA at higher annealing temperature seems to favor the generation of hole traps in more perfect oxides (with post-oxidation conventional N_2 annealing). Conversely higher temperature results in decreasing of hole traps for defected oxides (i.e. as-grown, non-annealed oxides). We believe that the dependence of the RTA behavior on the properties of the initial oxides is an unique characteristic of the RTA process.

Besides the positive charge formation after RTA an annealing of the original electron traps in the SiO_2 was also observed. The obtained activation energy of the annealing process provides supporting evidence for the important role of hydrogen transport in the process of RTA in vacuum.

Our experiments also confirm the observed from other authors dramatic deterioration of the properties of the thin Si-SiO_2 structures after RTA at 1473 K, which most likely is due to the high temperature decomposition of the SiO_2 .

References

- [1] H. Fukuda, T. Arakawa and S. Ohno, *IEEE Trans. Electr. Dev.* 39 (1992) 137.
- [2] J.Z. Xie, H. Kauget and S.P. Murarka, *J. Vac. Sci. Technol.* B7 (1989) 141.
- [3] R. Tromp, G.W. Rubloff, P. Balk, F.K. LeGoues and E.J. van Loenen, *Phys. Rev. Lett.* 55 (1985) 2332.
- [4] A. Paskaleva and E. Atanassova, *Semicond. Sci. Technol.* 8 (1993) 1566.
- [5] S.K. Lee, D.L. Kwong and N.S. Alvi, *J. Appl. Phys.* 60 (1986) 3360.
- [6] A. Hartstein and D.R. Young, *Appl. Phys. Lett.* 38 (1981) 631.
- [7] S.K. Lai, *J. Appl. Phys.* 54 (1983) 2540.
- [8] P.M. Lenahan and V. Dressendorfer, *J. Appl. Phys.* 55 (1984) 3495.
- [9] W.L. Warren, *J. Electrochem. Soc.* 139 (1992) 880.
- [10] R.A.B. Devine, *J. Appl. Phys.* 58 (1985) 716.
- [11] P. Balk, M. Aslam and D.R. Young, *Solid State Electron.* 27 (1984) 709.
- [12] R.A.B. Devine, D. Mathiot, W.L. Warren, D.M. Fleetwood and B. Aspar, *Appl. Phys. Lett.* 63 (1993) 2926.



ELSEVIER

Journal of Non-Crystalline Solids 187 (1995) 40–44

JOURNAL OF
NON-CRYSTALLINE SOLIDS

A synchrotron Si2p and As3d core level study of the As-terminated Si(001) surface oxidation

C. Poncey^{a,*}, F. Rochet^a, G. Dufour^a, H. Roulet^a, W.N. Rodrigues^b, M. Sauvage-Simkin^c, J.C. Boulliard^c, F. Sirotti^d, G. Panaccione^d

^a Laboratoire de Chimie Physique (URA 176), Université Pierre et Marie Curie, 11 rue Pierre et Marie Curie, 75231 Paris cédex 05, France

^b Departamento de Física, ICEx-UFMG CP702, 30.161-970 Belo Horizonte MG, Brazil

^c Laboratoire de Minéralogie Cristallographie (URA 09), Université Pierre et Marie Curie, 4 place Jussieu, 75252 Paris cédex 05, France

^d LURE, Centre Universitaire Paris-Sud, 91405 Orsay cédex, France

Abstract

The resistance of the As-terminated Si(001) surface to oxidation in O₂ is the subject of this study. Photoemission spectra of As3d and Si2p core levels excited with synchrotron radiation reveals that spectral changes are evident, simultaneously for As and Si, only from $\sim 10^{12}$ L (Langmuir) on, in stark contrast with a previous report indicating a saturation coverage in the 400–2000 L range. Oxidation proceeds slowly, as dimerized As remain intact ($\sim 24\%$) up to exposures of $\sim 10^{13}$ L. In the oxidized areas, the four Si oxidation states (indicative of subsurface oxidation) and three As oxidation states *plus* metallic arsenic show up. This suggests a reduction of the arsenic oxide by silicon. Arsenic losses are also observed, probably via sublimation of As₄O₆ molecules.

1. Introduction

The exposure of the Si(001)- 2×1 surface to an As₄ beam leads to the adsorption ('on-top' or 'displacive', according to experimental conditions [1–2]) of arsenic atoms on the Si surface and to As dimerization (Fig. 1), to give also a 2×1 reconstruction. As a result the Si dangling-bond states characteristic of the clean surface are removed and replaced by an As lone-pair state well below the Fermi level (Si is 3s²3p², while As is 4s²4p³). Because of the low electronic density of surface states

close to the Fermi level, the dissociation of the O₂ molecule on the As/Si(001)- 2×1 surface, which is a limiting step for oxygen chemisorption, is made difficult. The surface is thus passivated. Another remarkable feature of As/Si(001)- 2×1 is that it consists in a well-ordered surface with symmetric As dimers and elimination of missing dimer defects characteristic of the Si(001)- 2×1 surface [3].

The present work on the oxidation of the Si(001)- 2×1 surface overlaid by one monolayer of arsenic atoms is a synchrotron radiation X-ray photoemission spectroscopy (XPS) study ($h\nu = 135 - 165$ eV) of the evolution of Si2p and As3d core levels with increasing oxygen exposure. Being sensitive to the first layers, thanks to the

* Corresponding author. Tel: +33-1 44 27 66 21. Telefax: +33-1 44 27 62 26. E-mail: poncey@ccr.jussieu.fr.

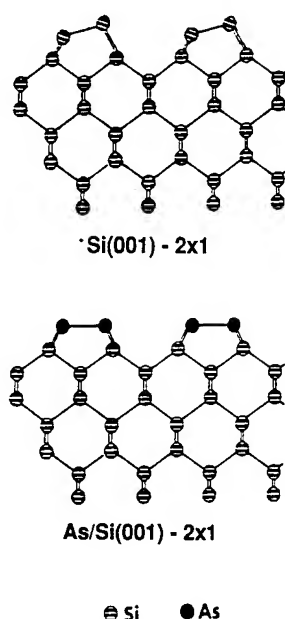


Fig. 1. Schematic atomic models of the Si(001)-2 \times 1 and As/Si(001)-2 \times 1 surfaces.

synchrotron radiation tunability, and to the nearest neighbour bonding this method provides accurate information on both the different chemical configurations of As and Si atoms and their relative distribution.

2. Experimental procedure

The As-terminated Si(001) surfaces were prepared in an ultra-high vacuum (UHV) molecular beam epitaxy (MBE) chamber, equipped with a low energy electron diffraction (LEED) apparatus. Si substrates, previously cleaned by flash-annealing cycles, were kept at 350°C or 500°C (two samples have been prepared, but no difference either in the As resulting coverage or in the resistance to oxidation was observed) and exposed to an As₄ flux under a pressure of about 10⁻⁶ Torr. After As deposition, the As/Si(001) samples were transferred, under UHV conditions, to the photoemission analysis chamber, set on beamline SU7 at the SUPER-ACO storage ring (LURE). Room temperature exposures to high-purity O₂ were carried out

directly in the analysis chamber for low pressures (2 \times 10⁻⁶–2 \times 10⁻⁵ Torr) and in a dedicated oxidation cell isolated by a valve from the analysis chamber for high pressures (4.5 \times 10⁻¹–525 Torr).

Photoelectron energy distribution curves were measured with monochromatic synchrotron radiation excitation and a partially angle-integrating electrostatic electron energy analyzer.

2.1. Data treatment

For quantitative analysis, we subtracted an extrinsic, secondary electron background plus an intrinsic, energy loss background [4], and the low spin-orbit component was removed systematically for the Si2p core levels. To fit the Si2p_{3/2} spectra (Fig. 2), each chemical state, that is, bulk Si (denoted Si⁰), silicon bonded to As (denoted Si(As)), and the four silicon oxidation states (spaced by ~0.9 eV), conventionally denoted Si¹⁺, Si²⁺, Si³⁺ and Si⁴⁺ (SiO₂), is represented by a Gaussian convoluted by a Lorentzian of 0.1 eV full-width at half-maximum (FWHM), accounting for lifetime broadening. In the fitting procedure of the As3d spectra (Fig. 3), each chemical state of arsenic, that is, As dimers (denoted As^{dim}), As metal (As^{met}), and the three attested oxidation states (spaced by 1.2–1.3 eV), attributed to As with one, two and three oxygen atom first neighbours and denoted As(I), As(II), As(III), is represented as well by a convolution of a Gaussian by a Lorentzian of 0.16 eV FWHM. To facilitate the identification of the As oxidation states, the As3d_{3/2} can also be stripped off: this was done on the most heavily oxidized spectrum (Fig. 4).

3. Results and discussion

3.1. The clean As/Si(001) surface

The Si2p_{3/2} core-level (Fig. 2) is fitted by two components, the surface component Si(As) at +0.4 eV and the bulk line. A weak structure needs to be introduced at ~+1 eV to take into account the curve asymmetry. It has to be attributed to energy losses rather than to contamination (Si¹⁺ of Si-OH is found at the same binding energy) since it

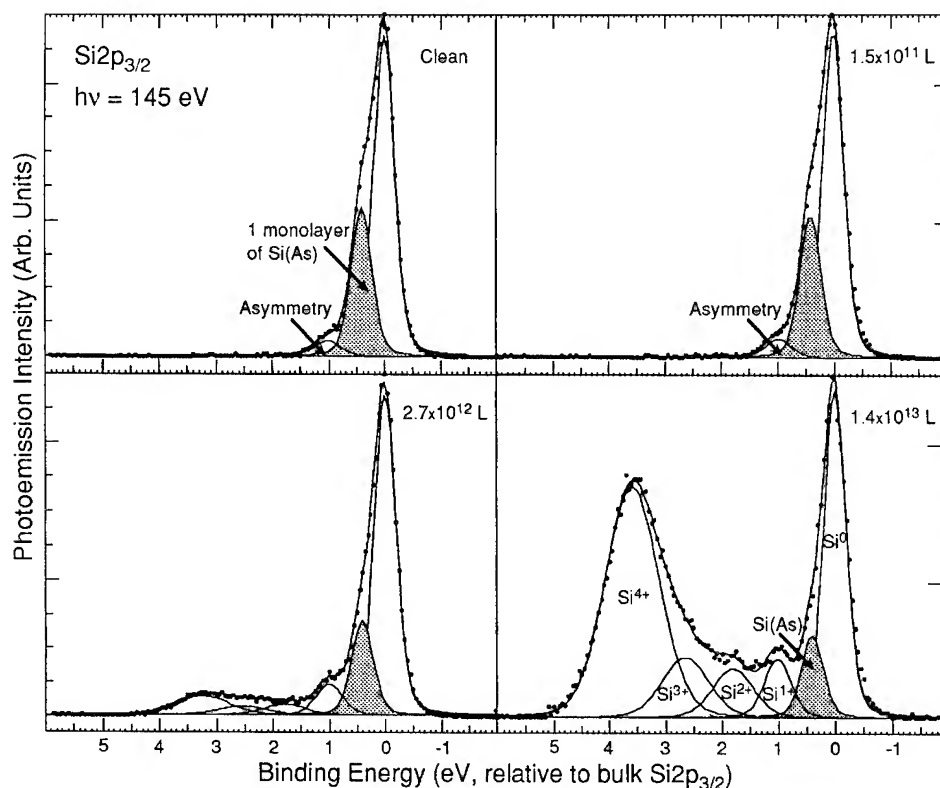


Fig. 2. Spectral decomposition of $\text{Si}2p_{3/2}$ core-levels ($h\nu = 145 \text{ eV}$) for indicated O_2 exposures. For the spin-orbit deconvolution, we used a splitting of 0.6 eV and a branching ratio $2p_{1/2} : 2p_{3/2}$ of 0.5 (the statistical value). The raw $\text{Si}^0 : \text{Si(As)} : \text{Si}^{1+} : \text{Si}^{2+} : \text{Si}^{3+} : \text{Si}^{4+}$ ratio is 31:7:7:8:9:38 at $\sim 10^{13} \text{ L}$, with Gaussian FWHM (in eV) of 0.40, 0.40, 0.50, 0.80, 0.92 and 1.08, respectively.

does not evolve under O_2 adsorption up to $\sim 10^{11} \text{ L}$ ($1 \text{ L} = 10^{-6} \text{ Torr s}$). The surface-to-bulk ratio (32:68 at $h\nu = 145 \text{ eV}$, 30:70 at $h\nu = 135 \text{ eV}$) corresponds to a monolayer ($6.8 \times 10^{14} \text{ atoms/cm}^2$) of silicon bonded to arsenic, by comparison with template surfaces $\text{Si}(001)\text{-}2 \times 1$ and NH_3 -exposed $\text{Si}(001)$ [5]. Since the $\text{As}3d$ spectrum (Fig. 3) presents a single chemical state, the fixation of only one monolayer of As is confirmed.

3.2. The O_2 -exposed $\text{As/Si}(001)$ surface

Our study points to the following five important observations.

(i) A strong resistance to oxidation. For O_2 exposures below 10^{12} L , the $\text{Si}2p$ and $\text{As}3d$ spectra (Figs. 2 and 3) show no appreciable change with respect to the clean surface, either in shape or in

binding energy position. An exposure as high as $2.7 \times 10^{12} \text{ L}$ (under 525 Torr) is necessary to initiate the oxygen bonding to As (and Si). Contrary to our findings, Zhong and co-workers [6] using Auger electron spectroscopy (induced by an electron gun) have found that oxygen adsorbs on such a surface, already after 20 L with a saturation coverage of 0.5 monolayer in the 400–2000 L range. The disagreement with Zhong's group results may arise from an electron initiated dissociation of the O_2 molecules which readily react with the As–As dimers.

(ii) A slow process. The simultaneous observation at the largest exposure ($\sim 10^{13} \text{ L}$) of Si(As) and As^{dim} components, in the $\text{Si}2p$ (in grey in Fig. 2) and $\text{As}3d$ spectra, respectively, bears evidence that a fraction of the As–As dimers remains unaffected. The As^{dim} relative intensity gives directly the

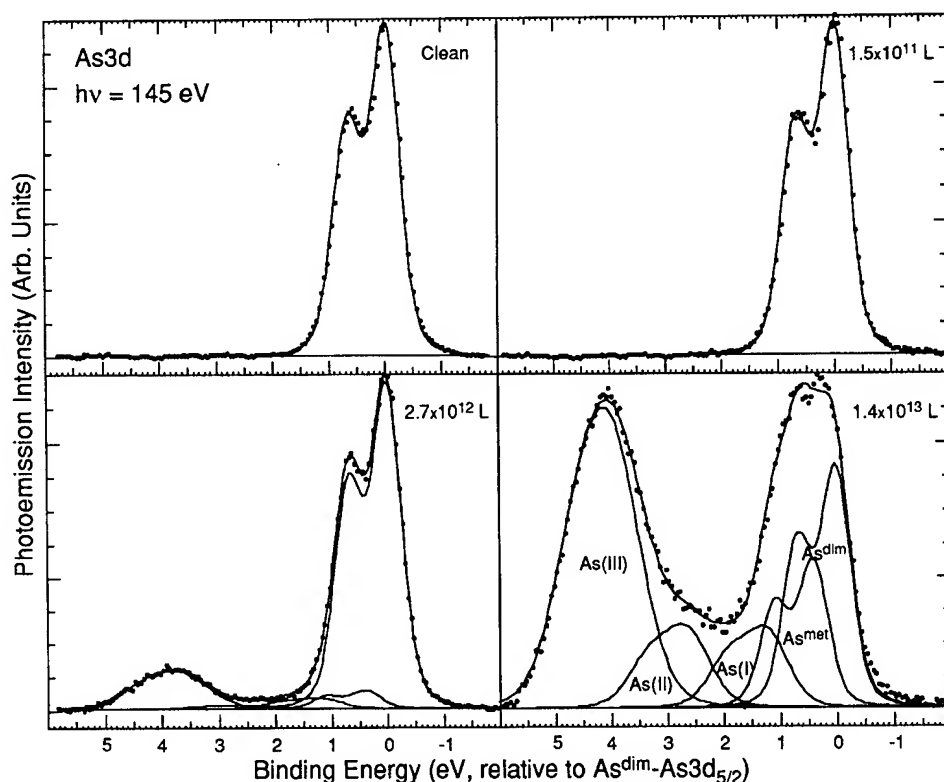


Fig. 3. Spectral decomposition of As3d core-levels ($h\nu = 145$ eV) for indicated O_2 exposures. For the spin-orbit deconvolution, we used a splitting of 0.69 eV and a branching ratio $3d_{3/2}:3d_{5/2}$ of 0.69 (3% greater than the statistical value). The raw As^{dim} , As^{met} , $As(I)$, $As(II)$, $As(III)$ ratio is 24:15:10:10:41 at $\sim 10^{13}$ L, with Gaussian FWHM (in eV) of 0.52, 0.52, 0.75, 0.81 and 1.05, respectively.

fraction of the surface remained unspoiled, $\sim 80\%$ at 2.7×10^{12} L and as large as $\sim 24\%$ at 1.4×10^{13} L.

(iii) The oxidation process is not limited to the surface. At 2.7×10^{12} L, corresponding to an oxygen coverage below the equivalent (001) monolayer, essentially As(III) develops and at the same time the four oxidation states of Si show up (Si^{1+} and Si^{4+} are the most intense). Thus, not only are As–As dimer bonds attacked, but oxygen is inserted in the As and Si backbonds, leading to a stage of local subsurface oxidation.

(iv) The formation of As metal. Along with arsenic oxidation states, a component at $\sim +0.4$ eV shows up (see Figs. 3 and 4). For the As^{dim} line it causes an apparent change in the $3d_{3/2,5/2}$ spin-orbit ratio, already visible at 2.7×10^{12} L and

1.4×10^{13} L, it is responsible for the apparent lack of resolution of the non-oxidized As3d peak. This component, clearly distinguishable from the first oxidation state As(I) at $+1.2$ eV, is attributed to As metal and may be explained by the reaction of As(III) oxide with silicon. Indeed the reaction $As_4O_6 + 3Si \rightarrow 4As + 3SiO_2$ is exothermic ($\Delta H \approx -98$ kcal/mol [7]).

(v) As losses with time. After proper normalization of the As3d spectra, peak area measurement and comparison with spectral area of the clean surface, we have noticed As losses under UHV conditions for the 1.4×10^{13} L exposed surface. These losses affect essentially the As(III) chemical state, probably via the sublimation of As_4O_6 molecules.

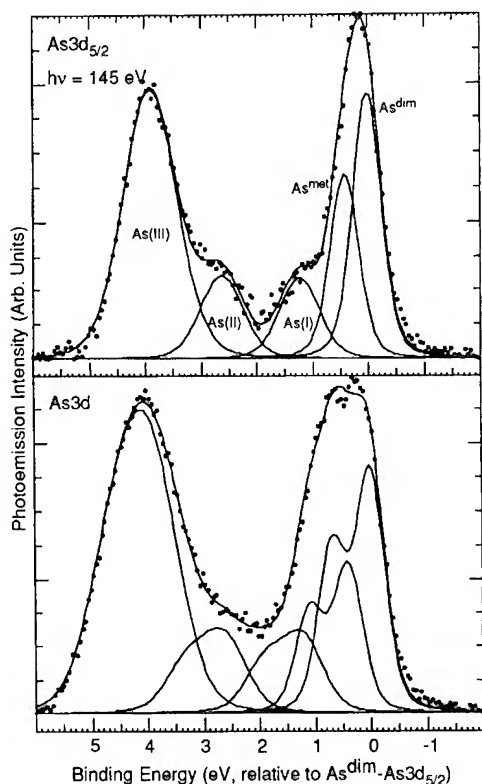


Fig. 4. $\text{As}3d_{5/2}$ and $\text{As}3d$ spectra (1.4×10^{13} L exposure). The decomposed $\text{As}3d_{5/2}$ spectrum clearly shows up the different chemical states for the As atoms and facilitates the determination of their binding energy position.

4. Conclusion

This study of the oxidation of the As-terminated $\text{Si}(001)$ surface by synchrotron radiation induced photoemission of the $\text{Si}2p$ and $\text{As}3d$ core levels

confirms the passivating effect of an As layer on silicon and shows that such a surface presents a much stronger resistance to O_2 oxidation than previously reported (the onset of oxidation is in the 10^{12} L range). We have evidenced that $\text{As}/\text{Si}(001)$ oxidation is spatially inhomogeneous (a fraction of the As dimers remains intact up to 10^{13} L exposure); it is not limited to the As surface either since in-depth Si oxidation is observed. A reduction of the As oxide (As(III)) can be seen, probably by reaction with silicon atoms, leading to the formation of As metal. As losses, probably via the sublimation of As_4O_6 molecules, are also detected.

As the clean Si surface can be easily restored to its pristine state in removing the arsenic layer by thermal desorption at moderate temperature ($\sim 800^\circ\text{C}$ [2]), capping the surface with As provides a very convenient and efficient method to protect silicon wafers from oxygen contamination.

W.N.R. was supported by a FAPEMIG grant.

References

- [1] R.D. Bringans, D.K. Biegelsen and L.-E. Swartz, *Phys. Rev. B* 44 (1991) 3054.
- [2] R.M. Tromp, A.W. Denier van der Gon and M.C. Reuter, *Phys. Rev. Lett.* 68 (1992) 2313.
- [3] R.S. Becker, T. Klitsner and J.S. Vickers, *J. Microsc.* 152 (1988) 157.
- [4] F.J. Himpsel, F.R. McFeely, A. Taleb-Ibrahimi, J.A. Yarmoff and G. Hollinger, *Phys. Rev. B* 38 (1988) 6084.
- [5] G. Dufour, F. Rochet, H. Roulet and F. Sirotti, *Surf. Sci.* 304 (1994) 33; F. Rochet, C. Poncey, G. Dufour, H. Roulet, W.N. Rodrigues and M. Sauvage-Simkin, unpublished.
- [6] Z.T. Zhong, D.W. Wang, Y. Fan and C.F. Li, *J. Vac. Sci. Technol. B* 7 (1989) 1084.
- [7] C.D. Hodgman, ed., *Handbook of Chemistry and Physics* (CRC, Cleveland, OH, 1961).



ELSEVIER

Journal of Non-Crystalline Solids 187 (1995) 45–48

JOURNAL OF
NON-CRYSTALLINE SOLIDS

Oxidation of amorphous and crystalline silicon

A. Szekeres*, P. Danesh

Institute of Solid State Physics, Bulgarian Academy of Sciences, 72 Tzarigradsko Chaussee, Sofia 1784, Bulgaria

Abstract

The oxidation of c-Si and a-Si:H in dry O_2 and in H_2O steam at temperatures ranging from 800 to 1060°C is studied. It is shown that the oxide grows on a-Si:H film linearly with time, while its growth on c-Si obeys the linear-parabolic law. The nature and magnitude of the oxide stress depend on the oxidizing material and the oxidation conditions. It is suggested that the observed oxide stress behavior is related to the different types of hydrogenous species and to the difference in the structure of the oxidizing material.

1. Introduction

While the oxidation kinetics of crystalline silicon (c-Si) in dry oxygen has been well investigated, there is still some uncertainty in the literature concerning the stress behavior and its influence on the oxidation kinetics when the Si wafers are oxidized in different kinds of oxidation ambient. The stress in the oxide is created by density differences between SiO_2 and Si substrate. Therefore, it can be expected that oxidation of porous amorphous Si (a-Si) films would lead to a decrease of the oxide stress in the prepared Si- SiO_2 structures.

This paper presents a brief report on the comparative study of c-Si and a-Si:H oxidation kinetics emphasizing the role of oxide stress.

2. Experimental procedures

Cz-Si wafers with (111) orientation and 6–9 Ω cm resistivity were used as substrates. Two types of samples, c-Si wafers (denoted as SiE) and hydrogenated a-Si (a-Si:H) layers deposited onto c-Si substrates (denoted as SiA) were oxidized in separate runs at temperatures ranging from 800 to 1060°C at atmospheric pressure in dry O_2 (< 3 ppm H_2O content) and in H_2O steam. Based on the observation that the out-diffusion of hydrogen from the a-Si:H layer starts in molecular form at sufficiently low temperatures $\sim 350^\circ\text{C}$ [1] it is expected that during a-Si:H oxidation hydrogen is released to some extent from the a-Si:H volume and contaminates the pure oxygen ambient. Entering into the oxidizing environment hydrogens would affect the oxidation process of crystalline silicon. In order to check this suggestion the SiA samples were placed on a quartz boat together with bare c-Si substrates in the close vicinity to

* Corresponding author. Telefax: +359-2 757 032.

each other and then they were simultaneously oxidized in dry oxygen. In this case a-Si:H layers served as a hydrogen source in dry O₂ ambient. Here the oxidized c-Si substrates are denoted as SiC samples.

Deposition of a-Si:H layers (30–40 nm) onto Si substrates was carried out in a PECVD system at a temperature of 270°C using a gas mixture of 10% silane in hydrogen. The plasma was excited by a rf generator operating at frequency of 13.56 MHz, at a power density of 48 mW cm⁻² and at a gas pressure of 133 Pa. These deposition conditions ensured approximately 10% of hydrogen incorporation in the a-Si:H layer.

Ellipsometric measurements at room temperature were used for determination of total oxide stress in SiO₂ films. The latter was deduced from the refractive index values using a first-order compressibility relationship [2]. The thickness of the oxides and their refractive index were determined by using an LEF 3M-1 ellipsometer at fixed wavelength of 632.8 nm and at light incidence angles ranging from 60° to 75°. The accuracy of the polarizer, analyzer and incidence angles is within ± 0.01°. To avoid the influence of the backside oxide on the stress in the frontside oxide [3] the former was etched away before each measurement. The intrinsic oxide stress was obtained by subtraction of the thermal component from the total stress [4].

The oxide stress is determined with an accuracy of about 1×10^9 dyn cm⁻². In the case of a-Si:H

oxidation the calculation of stress from the refractive index values is correct only for oxide thicknesses larger than 30 nm [5].

3. Results and discussion

The kinetics of oxide growth on c-Si (SiE and SiC samples) at 850°C and 1060°C can be well described for the thickness range used by a linear-parabolic equations [6], in which the constants' value depends on the oxidation conditions. Oxides formed from a-Si:H (SiA samples), however, do not follow the linear-parabolic law of growth. In this case the oxide grows linearly with time until it reaches the a-Si/c-Si interface. If the oxidation process continues the substrate starts oxidizing and the dependence obtained obeys the linear-parabolic law. All results obtained by the approximation of the experimental kinetics curves are given in Table 1, where L_0 is the integration constant related to the initial oxide thickness, K_L and K_P are the linear and parabolic rate constants, respectively. A smaller value of K_L for SiA samples is an indication of a slower oxidation of a-Si:H than of c-Si. However, the increase of the oxidation rate in steam is much higher for a-Si:H than for c-Si. (see the ratio of K_L steam/ K_L dry) For illustration Fig. 1 shows the kinetics of oxide growth in dry O₂ at 850°C and 1060°C for samples SiE, SiA and SiC.

Table 1
Experimental conditions and growth kinetics constants of amorphous and crystalline silicon oxidation

Type of samples	Temperature (°C)	Oxidation ambient	L_0 (nm)	K_L (nm/min)	K_P (nm ² /min)
SiE	850	Dry O ₂	1.46	0.50	26.00
SiC	850	Dry O ₂ ^a	2.17	0.62	18.00
SiA	850	Dry O ₂	9.8	0.16	—
SiE	850	Steam	0.00	2.56	1073.27
SiA	850	Steam	7.0	2.23	—
SiA ^b	850	Steam	6.72	2.60	1073.26
SiE	1060	Dry O ₂	4.20	4.78	282.00
SiC	1060	Dry O ₂ ^a	4.70	5.14	270.00
SiA	1060	Dry O ₂	12.00	2.30	—
SiA ^b	1060	Dry O ₂	10.50	5.7	201.00

^a Oxygen ambient is contaminated with hydrogen.

^b The c-Si substrate is oxidized after the consumption of the whole a-Si:H film.

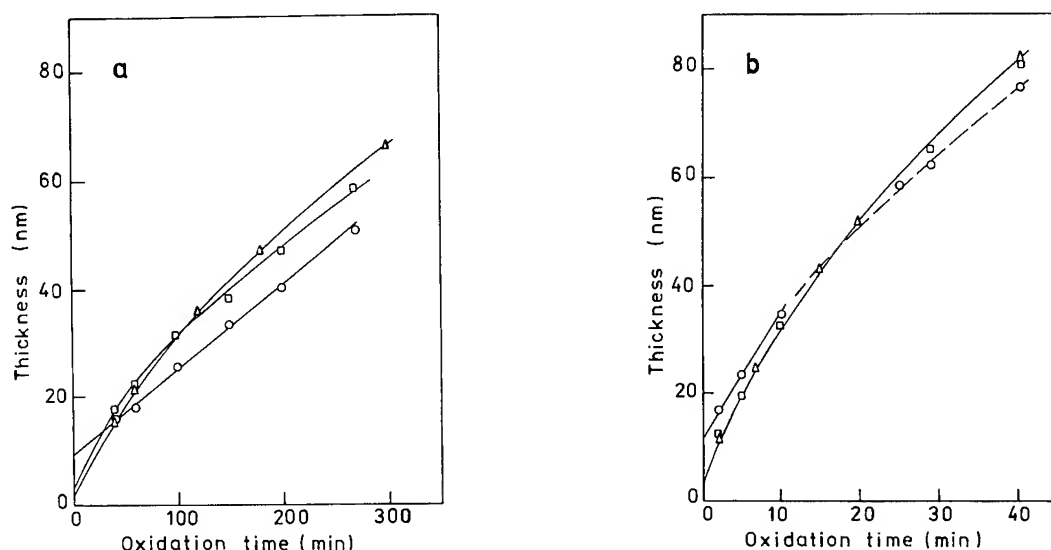


Fig. 1. SiO₂ film thickness dependence on oxidation time at 850°C (a) and 1060°C (b) for oxidation of c-Si in dry oxygen (Δ), in dry oxygen contaminated with hydrogen (□), as well as for oxidation of a-Si:H in dry oxygen (○). The dashed line shows the oxidation of c-Si substrate after the consumption of the a-Si:H film. The solid lines are as guides for the eye.

The oxidation of a-Si:H is accompanied by a short crystallization process. The Raman spectroscopy measurements have shown that the crystallization proceeds during the first few minutes and that both the volume fraction of crystallinity and the microcrystallite size do not change with prolonged thermal treatment. This is demonstrated in Fig. 2 where the volume fraction of crystallinity versus time for a-Si layer annealed in N₂ at 850°C is shown.

The intrinsic stress in the oxides grown on c-Si is always compressive. The oxidation in steam causes the smallest stress, while contamination of O₂ ambient with hydrogen leads to a higher level of stress than that characteristic of dry oxidation. At low temperatures the oxidized a-Si:H films are compressively stressed and the level of stress is smaller than that for dry oxidation of c-Si. With increasing the temperature above 900°C the oxide stress becomes tensile. The results are summarized in Fig. 3 where the intrinsic oxide stress in dependence on oxidation temperature are given for 50–60 nm thick oxides. The compressive and tensile stresses are plotted with negative and positive signs, respectively.

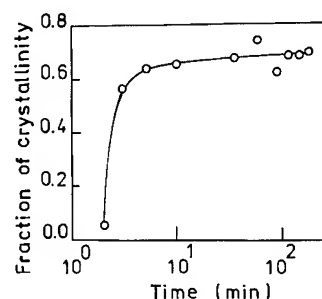


Fig. 2. Dependence of the volume fraction of crystallinity on annealing time for a-Si:H layer annealed in N₂ at 850°C. The lines are drawn as guides for the eye.

In the case of steam oxidation the opening up of the SiO₂ network by formation of SiOH groups leads to a strong increase of the oxidation rate and the oxides grow in a relatively stress-free condition. However, for dry oxidation of c-Si the addition of a small amount of hydrogen to the oxidizing ambient leads to considerably higher stresses and a change of the oxidation rate. Obviously, the formation of SiOH groups does not dominate here but rather hydrogen diffuses into the growing oxide and creates additional strain in it. In the linear

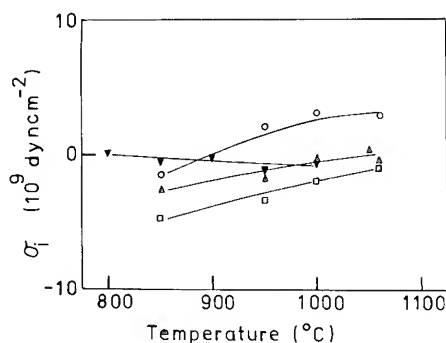


Fig. 3. Dependence of the intrinsic stress on oxidation temperature in 50–60 nm thick oxides grown on c-Si in dry oxygen (Δ), in dry oxygen contaminated with hydrogen (\square) and in H_2O steam (\blacktriangledown), as well as grown on a-Si:H in dry oxygen (\circ). The lines are drawn as guides for the eye.

regime the oxidation rate is limited by the chemical reaction between the free silicon atom and oxygen, and any stress in the oxide will facilitate the disruption of Si–Si bonds and accelerate the process. But in the thicker oxides, where the oxidation process is diffusion-controlled, the higher the stress the lower the oxygen diffusivity and lower the oxidation rate. This is well manifested in case of SiC samples, where larger values of L_0 and K_L and smaller value of K_p predict higher oxide stress, as it is observed. More complicated is the case of a-Si:H oxidation. The existence only of a linear regime in the oxide growth suggests that the oxidation process is controlled by the reaction between the oxidant and the free Si atoms. There is no correlation between the rate constants and the oxide stress. The oxidizing film should contain a large amount of remaining

hydrogen which would behave similarly as in SiC samples. But this is not observed and the different oxidation and stress behavior is rather due to the difference in the structure of the oxidizing material.

4. Conclusions

It has been established that oxidation of c-Si and a-Si:H can be characterized by linear-parabolic and linear dependence on oxidation time, respectively. The oxidation rates and the process-induced stress depend on the oxidizing material and the oxidation conditions. The results obtained suggest that hydrogen and hydroxyl groups have a completely different influence on the stress magnitude, as the former increased and the latter decreased the stress. The effect of Si structure is more complex and ambiguous.

This work was supported by the Bulgarian Ministry of Science and Education under Contract No. F-95.

References

- [1] W. Beyer and H. Wagner, *J. Appl. Phys.* 53 (1982) 8745.
- [2] R. Bruckner, *J. Non-Cryst. Solids* 5 (1970) 123, 177.
- [3] S. Alexandrova, A. Szekeres and K. Christova, *Philos. Mag. Lett.* 58 (1988) 33.
- [4] E. Kobeda and E.A. Irene, *J. Vac. Sci. Technol.* B5 (1987) 15; *J. Vac. Sci. Technol.* 6 (1988) 574, and references therein.
- [5] A. Szekeres, K. Christova and P. Danesh, *Philos. Mag.* B68 (1993) 29.
- [6] B.E. Deal and A.S. Grove, *J. Appl. Phys.* 36 (1965) 3770.



ELSEVIER

Journal of Non-Crystalline Solids 187 (1995) 49–59

JOURNAL OF
NON-CRYSTALLINE SOLIDS

Section 3. Silicon dioxide, deposition

Fluorinated interlayer dielectric films in ULSI multilevel interconnections

Tetsuya Homma*

ULSI Device Development Laboratories, NEC Corporation, 1120 Shimokuzawa, Sagami-hara, Kanagawa 229, Japan

Abstract

Fluorinated interlayer dielectric films for ultra large scale integrated circuit (ULSI) multilevel interconnections are investigated. The interlayer dielectric film properties and their formation techniques have to meet three requirements such as: (1) a high planarization capability, (2) a low dielectric constant and (3) a low deposition temperature. To satisfy the three requirements, the technologies such as (i) a fluorinated spin-on-glass (SOG) film by fluorotrialkoxysilane vapor treatment (FAST-SOG), (ii) a fluorinated SiO_2 (SiOF) film by room temperature chemical vapor deposition (RTCVD-SiOF) using fluorotrialkoxysilane (FTAS) and pure water as gas sources, (iii) a room temperature liquid phase deposition (LPD) SiO_2 film, and (iv) fluorinated polyimide siloxane (F-PSI) films are desirable. The RTCVD, FAST and LPD techniques have shown the possibility to reduce the film formation temperature to room temperature by catalytic reactions. The dielectric constant for SiO_2 films can be reduced to 3.7 at 1 MHz by using the RTCVD and LPD techniques. The dielectric constant of 2.7 at 1 MHz can be achieved for the F-PSI films, and is lower than those for conventional polyimide films (3.2–3.5) and SiO_2 films (3.9–4.2). Although the FAST-SOG, RTCVD-SiOF and F-PSI films cannot achieve full planarization, the LPD technique can achieve both global and local planarization because this technique has high capability for selective SiO_2 film deposition. The fluorinated films have other good properties such as low residual stress, low residual OH contents and low moisture absorption, which can enlarge the fabrication margins of multilevel interconnections. These other properties are also very effective for improving the ULSI devices performance.

1. Introduction

Multilevel interconnections are essential to realize ultra large scale integrated circuits (ULSIs) such as dynamic random access memories (DRAMs), microprocessors (MPUs) and application specific integrated circuits (ASICs). The SiO_2 films have been investigated and mainly utilized as the inter-

layer dielectric films. Many interlayer dielectric film formation and planarization techniques such as chemical vapor deposition (CVD) [1–3], spin coating of SOG and polyimide [4,5], and biased sputtering [6] have been investigated. However, these conventional techniques cannot be implemented for the future interlayer dielectric film formation, because the film properties and their formation techniques cannot simultaneously satisfy the three requirements such as a high surface planarization capability, a low dielectric constant and a low deposition temperature. Therefore, new dielectric film

* Corresponding author. Tel: +81-427 71 0669. Telefax: +81-427 71 0938. E-mail: tetsu-h@lsi.tmg.nec.co.jp.

formation techniques will be desired, especially for quarter-micron multilevel interconnections. The author has proposed four desirable techniques to satisfy at least one of the three requirements. They are: (i) a fluorinated spin-on-glass films by fluoroalkoxysilane vapor treatment (FAST-SOG) [7], (ii) a fluorinated SiO_2 films by room temperature chemical vapor deposition (RTCVD-SiOF) using fluorotrialkoxysilane (FTAS) and pure water as gas sources [8,9], (iii) a room temperature liquid phase deposition (LPD) SiO_2 films [10,11], and (iv) a fluorinated polyimide siloxane (F-PSI) films.

The purpose of this paper is to compare the fluorinated dielectric films with each other, and to clarify the vision of what the future interlayer dielectric films in the ULSI multilevel interconnections should be. The fluorinated film properties for the interlayer dielectric application will be described, then the pros and cons of each technique will be explained. The fluorinated film properties will also be compared with non-fluorinated films such as an atmospheric pressure chemical vapor deposition (APCVD) SiO_2 film formed using tetraethoxysilane (TEOS) and ozone (O_3) as gas sources, and conventional polyimide siloxane (PSI) film [12].

2. Experimental procedure

2.1. Film formation processes

2.1.1. Inorganic films

FAST-SOG film [7]. In this work, a silanol-based solution is used for the SOG films formation. Fluorotriethoxysilane [$\text{FSi}(\text{OC}_2\text{H}_5)_3$] (FTES) monomer solution was used for fluoroalkoxysilane vapor treatment (FAST) process. The FAST process sequence for SOG films was: (i) spin coating the SOG solution on silicon (Si) substrates at a spin speed of 4000 rpm for 20 s, followed by (ii) hot plate baking at 100°C for 60 s, then (iii) exposing the SOG films to FTES vapor at 25°C for 120 min in a chamber at 760 Torr, finally (iv) annealing at 300°C for 60 min in nitrogen (N_2) atmosphere. The hot plate baked SOG and FAST-SOG films thicknesses were 0.24 and 0.25 μm , respectively.

RTCVD-SiOF film [8]. The SiOF film's deposition was carried out with a low pressure chemical vapor deposition (LPCVD) system. Gas flow rates for FTES and pure water, with nitrogen as the carrier gas, were 100 and 75 sccm, respectively. Bubbling temperatures for FTES and pure water were set at 50°C . Total gas pressure in the chamber was 5 Torr. The deposition rate was 10 nm/min.

LPD-SiO₂ film [10]. A hydrofluosilicic acid (H_2SiF_6) solution saturated with SiO_2 was used for the LPD-SiO₂ films deposition. In order to make the saturated H_2SiF_6 solution supersaturated, a boric acid (H_3BO_3) aqueous solution with the concentration of 0.1 mol/l was used. The LPD-SiO₂ films were deposited on Si substrates at 35°C . The deposition rate was 0.3 nm/min.

TEOS-O₃ SiO₂ film (non-fluorinated) [8]. As a comparison, TEOS-O₃ SiO₂ films were formed under atmospheric pressure at the substrate temperature of 350°C . Bubbling temperature for TEOS was set at 50°C . Gas flow rate of nitrogen for TEOS bubbling was 1 SLM, and ozone concentration was 3%. The films deposition rate was 70 nm/min.

2.1.2. Organic films

F-PSI films. Two types of polyamic acid solutions to form the F-PSI films were prepared. One is for the films (F-PSI1), using 4,4'-(hexafluoroisopropylidene)bis(phthalic anhydride) (6FDA) as a dianhydride monomer. The other is for the films (F-PSI2), using 2,2-bis{4-(4'-aminophenoxy)phenyl}-hexafluoropropane (BDAF) as a part of diamine monomers. The polyamic acid solution for F-PSI1 films was prepared by the reactions among 6FDA, paraphenylenediamine (PPDA) and p-aminophenyltrimethoxysilane (APTMS). The solution for F-PSI2 films was also prepared by the reactions among BDAF, benzophenonetetracarboxylic dianhydride (BTDA) and APTMS. A solution for conventional PSI films (PSI) was also prepared by the reactions among benzophenonetetracarboxylic dianhydride (BTDA), oxydianiline (ODA) and APTMS [12]. Dimethylacetamide was employed as the solvent. The typical solid contents in the solutions for F-PSI1, F-PSI2 and conventional PSI films formation were 28.5, 28.1 and 30 wt%, respectively. The films were formed by spin coating the solutions, followed by two step

prebaking at 100°C for 1 min on a hot plate and 250°C for 30 min in an oven with N₂ atmosphere. The films were postbaked at 400°C for 60 min in a furnace with N₂ atmosphere.

2.2. Application to interlayer dielectric films

The application capability of the fluorinated films for the interlayer dielectrics was investigated. To clarify the gap filling and/or surface planarization capabilities, the films were formed on 1 μm thick aluminum (Al), or 0.7 μm thick tungsten (W) wirings with 0.1 μm thick titanium tungsten (TiW) underlayers. For the FAST-SOG film, the interlayer dielectric films planarization process is as follows. The Al wirings were covered with a 0.3 μm thick SiO₂ film formed by a plasma enhanced chemical vapor deposition (PECVD) technique. The double-layered FAST-SOG films were formed without any intermediate annealing, where the FAST process time was fixed for 60 min. Next, the samples were post-annealed at 300°C for 60 min, followed by the formation of another 0.3 μm thick PECVD-SiO₂ film. For the LPD-SiO₂ film, the selective deposition technique was applied to W wirings for gap filling. The W patterns with photoresist masks, which were formed on a thermal CVD-SiO₂ film, were used for this experiment. The thermal CVD-SiO₂ films were formed at 400°C under atmospheric pressure using silane and oxygen as source gases. The processes for other films formation are the same as those mentioned in Section 2.1. (film formation processes). The gap filling and/or surface planarization characteristics were observed by a scanning electron microscopy (SEM). Local and global planarization degrees (PD) were evaluated from the SEM pictures, using the following formula:

$$\text{PD (local)} = (1 - t_{s1}/t_0) \times 100 (\%), \quad (1)$$

$$\text{PD (global)} = (1 - t_{s2}/t_0) \times 100 (\%), \quad (2)$$

where t_0 is wirings step height, t_{s1} is dielectric films step height at narrow gaps, and t_{s2} is dielectric films step height between wirings and field regions.

2.3. Other properties of films

Chemical, physical, thermal and electrical properties of the fluorinated films were investigated, and their interrelationships were examined. Fluorine atomic concentrations and their uniformities across the films were analyzed by secondary ion mass spectroscopy (SIMS). The films refractive index, thickness, and Fourier transform infrared (FTIR) spectra were measured by using Auto EL IV (Rudolph Research), Nano Spec/AFT Model 200 (Nanometrics), and Model QS-100 (Bio-Rad), respectively. The films density was calculated from the films weight and volume, where the films weight was measured by using an electrical microbalance. The thermal stress variations in a heating cycle for the fluorinated SiO₂ films formed on 500 μm thick 4 in Si substrates were measured by using an in situ wafer displacement measurement system, FIS-1000 (Shinku-riko Inc.). The temperature was increased from 25°C at a rate of 19.8°C/min, stayed at the maximum temperature for 30 min, and then decreased back to 25°C at the same rate. Residual stress values for the films formed on 4 in (100)-oriented Si substrates were calculated from the residual wafer warpage [13]. Etching rate of the films was measured by using 1:30 buffered hydrofluoric (HF) acid aqueous solution. Leakage current densities were measured by applying a negative voltage to the Al electrodes of an Al/fluorinated films/p-Si structure, where the Al electrode area is 1 mm². The dielectric breakdown strength was determined by the electric field at the leakage current density of 1 μA/cm². The films dielectric constant was calculated from the maximum capacitance values in the capacitance–voltage ($C-V$) characteristics measured at 1 MHz, using the same structure samples as those used for the leakage current measurements.

3. Results and discussion

3.1. Application to interlayer dielectric films

Figs. 1(a)–(c) show SEM cross-sectional views of the FAST-SOG, 0.8 μm thick RTCVD-SiOF and 0.8 μm thick LPD-SiO₂ films formed on the

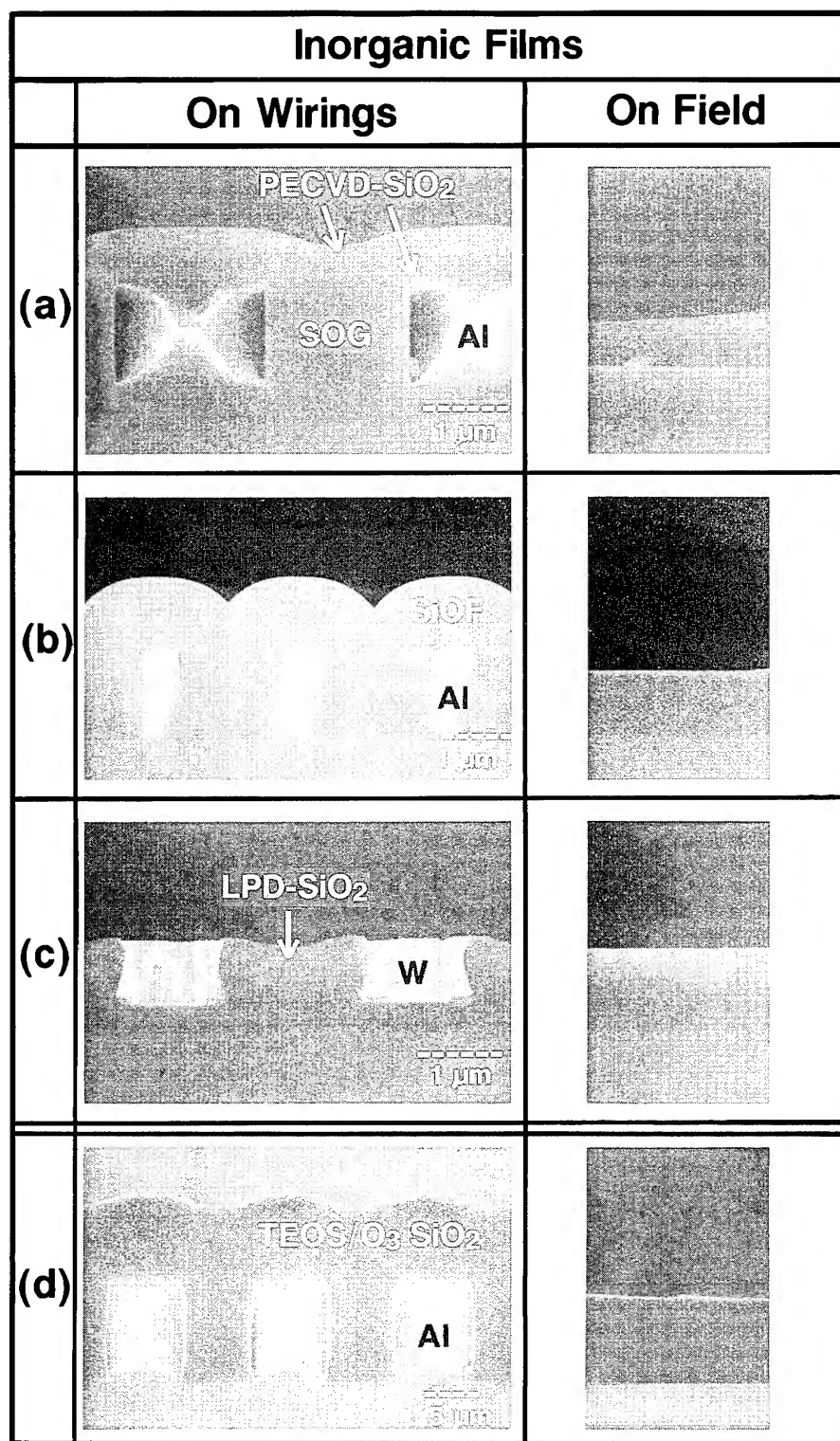


Fig. 1(a)–(d).

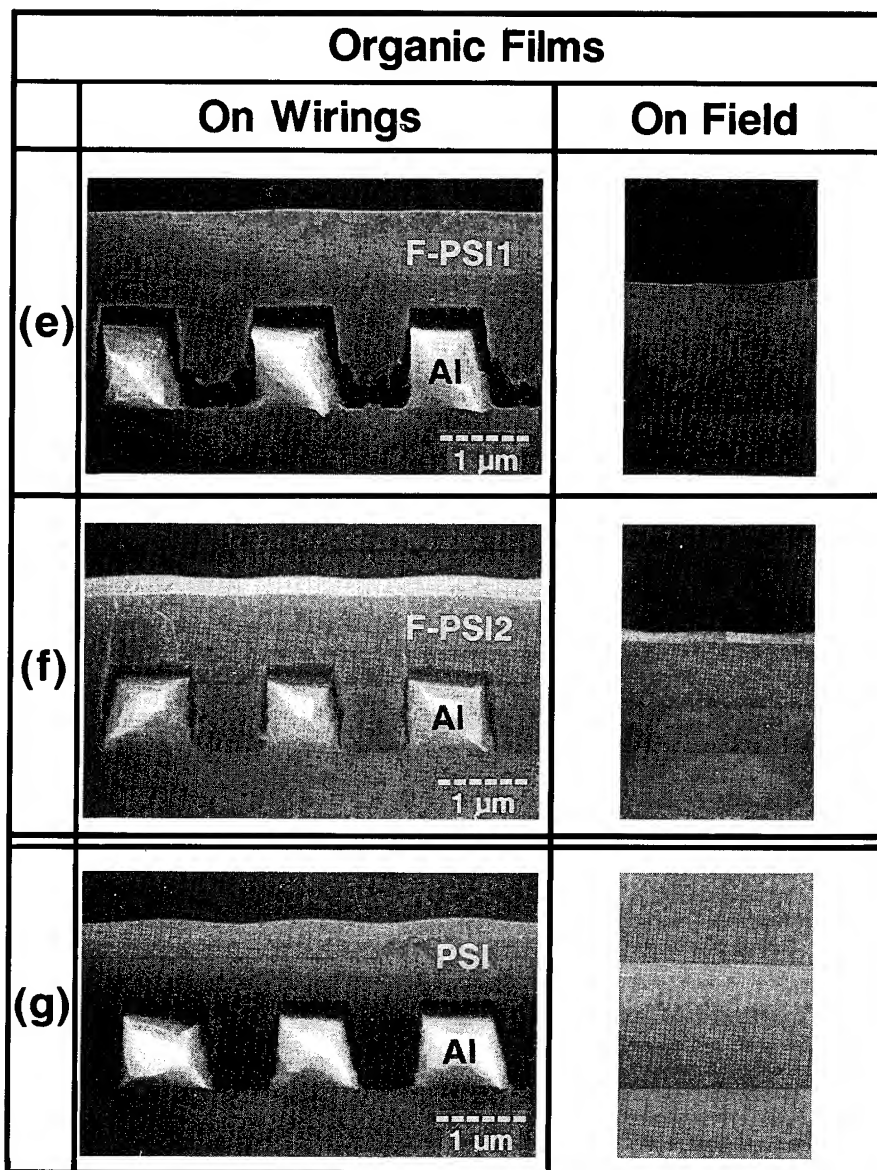


Fig. 1. SEM cross-sectional views of the inorganic and organic films formed on the substrates' surfaces with Al or W wirings, where (a), (b), (c), (d), (e), (f) and (g) are for the FAST-SOG, RTCVD-SiOF, LPD-SiO₂, TEOS-O₃ SiO₂, F-PSI1, F-PSI2 and conventional PSI films, respectively. The FAST-SOG film is sandwiched between the PECVD-SiO₂ films and the LPD-SiO₂ film is selectively deposited between the W wirings.

substrates surfaces with Al or W wirings, respectively. The 0.8 μm thick TEOS-O₃ SiO₂ film formed on the substrate surface with Al wirings is shown in Fig. 1(d), as comparison. Figs. 1(e) and (f)

show the F-PSI1 and F-PSI2 films formed on the substrates surfaces with Al wirings, respectively, as compared to the conventional PSI film which is shown in Fig. 1(g). The films thicknesses on the Al

Table 1
Summary of the three criteria for the interlayer dielectric films

Property	Inorganic films				Organic films		
	FAST-SOG	RTCVD-SiOF	LPD-SiO ₂	TEOS-O ₃ SiO ₂	F-PSI1	F-PSI2	PSI
Formation temperature (°C)	25	25	35	~400	400	400	400
Dielectric constant at 1 MHz	—	3.7	3.7~3.9	4.3	2.7	2.8	3.2
Planarization degree ^a (%)							
global	13	0	90	0	30	42	54
local	81	33	90	87	96	92	92

^a Planarization degree (PD) = $(1 - t_s/t_0) \times 100$ (%), where t_0 : wiring height, t_s : step height at the dielectric films' surface.

wirings are 1 μm . No crack or void is observed for any of the films. However, peeling from underlayer PECVD-SiO₂ film is observed for the F-PSI1 film. This problem is due to thermal decomposition of the F-PSI2 film.

Table 1 summarizes film formation temperatures, dielectric constant and degree of planarization, which are the three major criteria for the interlayer dielectric films. For the inorganic films, the FAST, RTCVD and LPD techniques can reduce the films formation temperature to 25–35°C, due to the catalytic reactions by fluorine [14]. The dielectric constant at the frequency of 1 MHz can be reduced to ~3.8 by fluorination of SiO₂ films. For the organic films, the dielectric constant at 1 MHz can be reduced from 3.2 to 2.7–2.8 by fluorination of the PSI films. These reductions of dielectric constant is due to polarization reduction by fluorine atoms. For the degrees of global planarization, the selective LPD-SiO₂ film shows the highest values of 90%. With the RTCVD-SiOF and TEOS-O₃ SiO₂ films, it is almost impossible to achieve the global planarization. For local planarization, the organic films have higher capability than inorganic films, except for the LPD-SiO₂ films. This is because the thick organic films can be formed by spin-coating techniques. Since these fluorinated interlayer dielectric films and their formation techniques can satisfy at least one of the three requirements mentioned previously, these techniques are very desirable for the interlayer dielectric films formation.

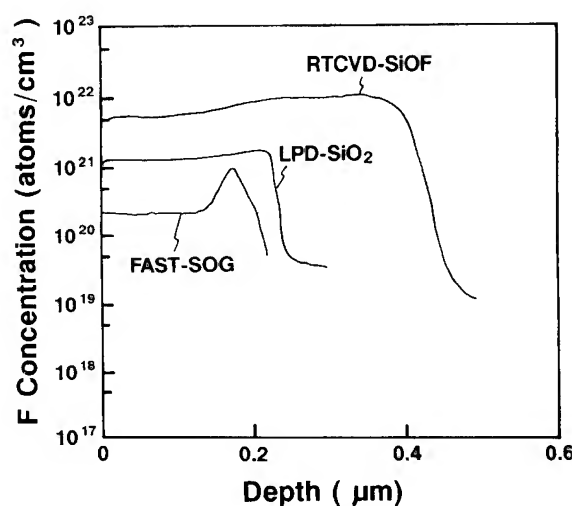


Fig. 2. SIMS depth profiles of fluorine atoms for the FAST-SOG, RTCVD-SiOF and LPD-SiO₂ films.

3.2. Other properties of films

3.2.1. Inorganic films

Fig. 2 shows SIMS depth profiles of fluorine atoms for the FAST-SOG, RTCVD-SiOF and LPD-SiO₂ films. For the RTCVD-SiOF and LPD-SiO₂ films, fluorine atoms are uniformly distributed across the films with the concentrations of about 5.3×10^{21} and 1.4×10^{21} atoms/cm³, respectively. For the FAST-SOG film, fluorine atoms are piled up near the interface between the Si substrate surface and the film. This is due to the out diffusion

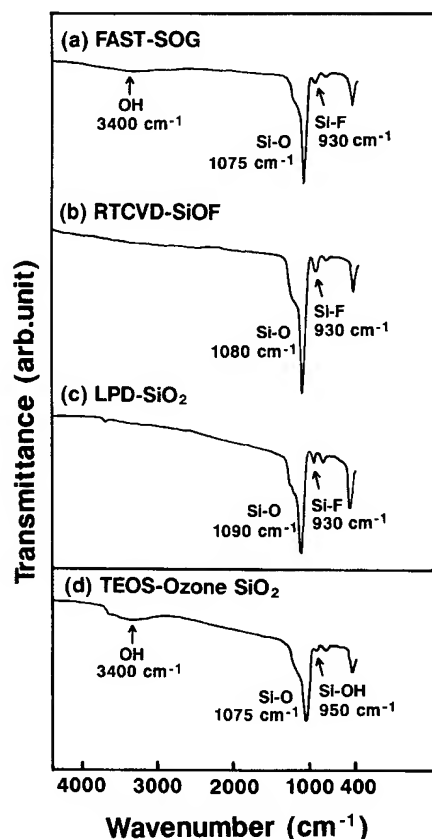


Fig. 3. FTIR spectra for (a) FAST-SOG, (b) RTCVD-SiOF and (c) LPD-SiO₂ films, as compared with that for (d) TEOS-O₃ SiO₂ film.

of fluorine or FTES from the FAST-SOG films during the annealing at 300°C. The fluorine concentration near the films surface is about 2.2×10^{20} atoms/cm³.

Fig. 3 shows FTIR spectra for the FAST-SOG, RTCVD-SiOF and LPD-SiO₂ films, as compared with that for the TEOS-O₃ SiO₂ film. For the FAST-SOG film, three absorption peaks corresponding to Si-F and Si-O bonds, and OH group are observed at the wave numbers of 930, 1075 and 3400 cm⁻¹, respectively. The Si-O bond absorption peak position is the same as that of the TEOS-O₃ SiO₂ film. The absorption peak intensity of the OH group is weaker than that of the TEOS-O₃ SiO₂ film. For the RTCVD-SiOF film, two absorption peaks corresponding to Si-F and Si-O bonds

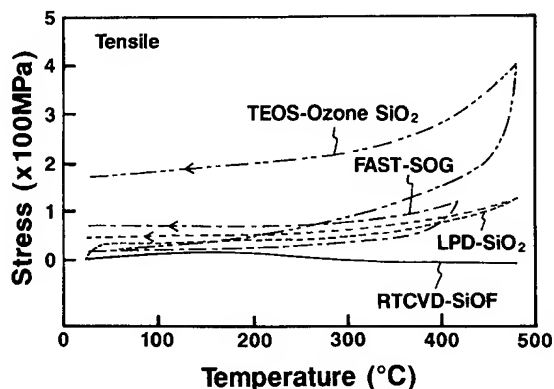


Fig. 4. Stress variations during a heating cycle for the FAST-SOG, RTCVD-SiOF and LPD-SiO₂ films, as compared with the TEOS-O₃ SiO₂ film.

are observed at the wave numbers of 930 and 1080 cm⁻¹, respectively. The absorption peak position of the Si-O bond for the RTCVD-SiOF film is higher than those for the FAST-SOG (1075 cm⁻¹) and TEOS-O₃ SiO₂ (1075 cm⁻¹) films. The absorption peak corresponding to OH group is not observed in the RTCVD-SiOF film spectrum. The spectrum for the LPD-SiO₂ film also has two absorption peaks corresponding to Si-F and Si-O bonds at the wave numbers of 930 and 1090 cm⁻¹, respectively. The absorption peak position of the Si-O bond for the LPD-SiO₂ film is higher than those for the FAST-SOG, RTCVD-SiOF and TEOS-O₃ SiO₂ films. No absorption peak of OH group is observed in the spectrum of the LPD-SiO₂ film. The shift of the Si-O bond absorption peak position to the high wave numbers indicates tightly bonded Si-O networks. Therefore, the Si-O bond quality for the fluorinated films, even for the FAST-SOG films, is higher than that for the TEOS-O₃ SiO₂ film. This high quality of Si-O bond is due to the fluorine atoms which have higher electronegativity (4.0) than oxygen atoms (3.5).

Fig. 4 shows stress variations during a heating cycle for the FAST-SOG, RTCVD-SiOF and LPD-SiO₂ films, as compared with the TEOS-O₃ SiO₂ film. The stress variations and residual stress during the heating cycle for the fluorinated films are lower than those for the TEOS-O₃ SiO₂ film. The generated tensile stress during the heating

Table 2

Other properties of the fluorinated inorganic films, as compared to the TEOS-O₃ SiO₂ film

Property	Inorganic films			
	FAST-SOG	RTCVD-SiOF	LPD-SiO ₂	TEOS-O ₃ SiO ₂
Refractive index	1.398	1.400	1.433	1.451
Density (g/cm ³)	2.20	2.20	2.19	2.11
Etching rate (1:30 BHF) (nm/min)	> 500	200	83	120
Residual tensile stress (MPa)	74	50	20	200
Moisture absorption ^a (wt %)	2.0	—	—	—
Leakage current density ^b (pA/cm ²)	2250	190	38	88
Dielectric breakdown strength ^c (MV/cm)	—	2.0	6.3	2.7

^a After 30 days in pure water at 23°C.^b At 5 V for 1 μm thick films.^c At 1 μA/cm².

cycle for the fluorinated films is lower than 120 MPa at maximum temperatures, and is at least 70% lower than that for the TEOS-O₃ SiO₂ film. The residual stress values after conducting the heating cycle for the fluorinated films are lower than 75 MPa, and are at least 40% lower than that for the TEOS-O₃ SiO₂ film. These low stress variations and low residual stress values are due to small amount of residual OH group. The fluorine contained in the films is also effective for the stress relaxation [15].

Table 2 summarizes other properties of the fluorinated inorganic films, compared to the TEOS-O₃ SiO₂ film. Refractive indexes for the fluorinated inorganic films are lower than that for the TEOS-O₃ SiO₂ film, due to fluorine atoms [16]. The densities of the fluorinated inorganic films are very close to each other, and higher than that of the TEOS-O₃ SiO₂ film. This high film density is due to tightly bonded Si–O networks, and to containing fluorine atoms which are heavier than oxygen atoms. Etching rates for the FAST-SOG and RTCVD-SiOF films are higher than that for the TEOS-O₃ SiO₂ film. This difference is because the fluorine atoms contained in the fluorinated films will dissolve into the etching solution and sub-

sequently increase the HF concentration. For the LPD-SiO₂ film, the etching rate is lower than that for the TEOS-O₃ SiO₂ film. This is due to tightly bonded Si–O networks as mentioned in the FTIR spectrum analysis results. Residual stress values for the fluorinated inorganic films are lower than that for the TEOS-O₃ SiO₂ film. Especially for the LPD-SiO₂ film, the residual stress value is by one order of magnitude lower than that for the TEOS-O₃ SiO₂ film. The low stress values for the fluorinated inorganic films are due to lower deposition temperature and lower deposition rate, compared to the TEOS-O₃ SiO₂ film. It is also considered that the fluorine atoms in the films will relax the stress [15]. Leakage current densities for the FAST-SOG, RTCVD-SiOF and LPD-SiO₂ films are about 2500%, 200% and 43% of that for the TEOS-O₃ SiO₂ film, respectively. Dielectric breakdown strength for the LPD-SiO₂ film is much higher than that for the TEOS-O₃ SiO₂ film. Although the dielectric breakdown strength for the RTCVD-SiOF film is lower than that for the TEOS-O₃ SiO₂ film, the value is sufficient for the interlayer dielectric film application. These results indicate that other properties of the fluorinated inorganic films, even for the FAST-SOG film, are

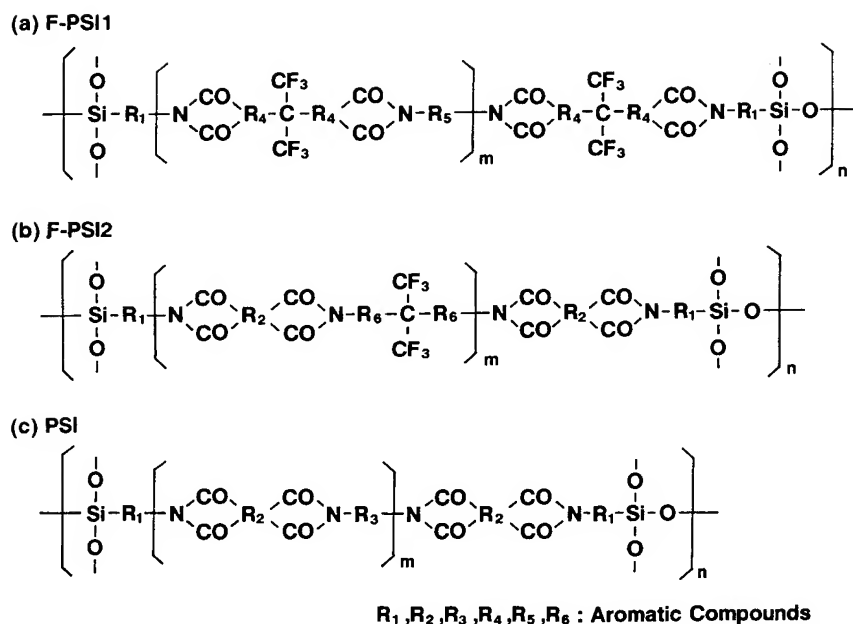


Fig. 5. Illustrations of the chemical structures of oligomers for (a) F-PSI1, (b) F-PSI2 and (c) conventional PSI films.

sufficiently good for the interlayer dielectric film application.

3.2.2. Organic films

Figs. 5(a)–(c) show illustrations of the speculated chemical structures for the oligomers of F-PSI1, F-PSI2 and conventional PSI films, respectively. The Si–O bonds of oligomers end group are arranged in a way to make the polymerization reactions three-dimensional, and to promote the adhesion to inorganic films such as silicon oxide and silicon nitride films. F-PSI1 and F-PSI2 films have hexafluoro-propane segments in their chemical structures. Figs. 6(a)–(c) show FTIR spectra for the F-PSI1, F-PSI2 and conventional PSI films, respectively. The absorption peaks corresponding to carbonyl bonds ($C=O$) of imide structures are observed at the wave numbers of 1725 and 1775 cm^{-1} in the FTIR spectra for the F-PSI1, F-PSI2 and conventional PSI films. The absorption peak corresponding to silicon oxide (Si–O) bonds is also observed at the wave number of 1080 cm^{-1} in the spectra for all the films. For the

F-PSI1 and F-PSI2 films, the absorption peak corresponding to fluorocarbon (C–F) bonds is observed at the wave number around 1160 cm^{-1} . These results indicate that the F-PSI1 and F-PSI2 films contain fluorocarbon segments, as illustrated in Fig. 5.

The amounts of moisture absorption for the F-PSI1, F-PSI2 and conventional PSI films were 0.3, 0.6 and 2.3 wt%, respectively, indicating that the moisture absorption for the F-PSI films are lower than that for the conventional PSI film. This low moisture absorption is due to hydrophobic properties of C–F bonds contained in the F-PSI films. The residual tensile stress values for the F-PSI1, F-PSI2 and conventional PSI films were 44, 17 and 35 MPa, respectively. These values are sufficiently low for the interlayer dielectric film application. The leakage current densities at 5 V for the 1 μm thick F-PSI1, F-PSI2 and conventional PSI films were 6, 5 and 13 pA/cm^2 , respectively, and are over one order of magnitude lower than those for inorganic fluorinated films. The leakage current densities for the F-PSI1 and F-PSI2 films are lower

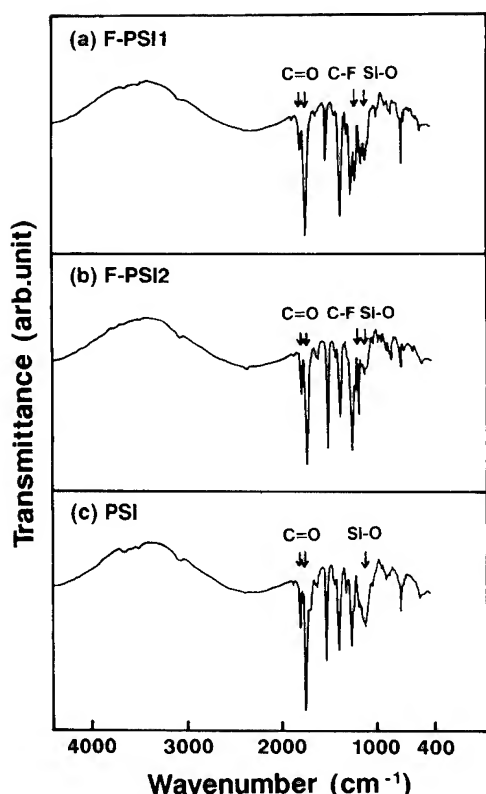


Fig. 6. FTIR spectra for (a) F-PSI1 and (b) F-PSI2 films, as compared to (c) conventional PSI film.

than that for the conventional PSI films, and are sufficiently low for the interlayer dielectric films application. Since the leakage current increments for the polyimide films are generally explained as being due to hydrolysis of the imide structure, this low leakage current increments for the F-PSI films are due to low moisture absorption. Dielectric breakdown strength for the F-PSI1, F-PSI2 and conventional PSI films were 2.8, 4.8, 3.0 MV/cm, respectively. These values are high enough for the interlayer dielectric films application. The chemical, physical and electrical properties of the F-PSI films are more useful for the interlayer dielectric films, as compared with the conventional PSI film.

4. Conclusions

Fluorinated interlayer dielectric films for ULSI multilevel interconnections have been investigated.

The four fluorinated dielectric films such as (i) FAST-SOG, (ii) RTCVD-SiOF, (iii) LPD-SiO₂, and (iv) F-PSI films can satisfy at least one of the three requirements such as (1) a high planarization capability, (2) a low dielectric constant and (3) a low deposition temperature. The FAST, RTCVD and LPD techniques can reduce the SiO₂ films formation temperatures to around room temperature through the catalytic behavior of fluorine. The dielectric constants for the SiO₂ and polyimide films can be reduced by fluorination. The fluorinated films have other properties such as a low residual stress, low residual OH contents and low moisture absorption which can enlarge the multilevel interconnections fabrication margins and subsequently improve the manufacturing yield. These other properties are also very effective for improving the ULSI devices performance. At the present time, the selective LPD technique is the best way to form the interlayer dielectric films, because this technique can achieve the three requirements simultaneously. The fluorinated interlayer dielectric films are useful for the future quarter-micron ULSI multilevel interconnections and their fabrication.

The author would like to thank Dr M. Kamoshida, Dr M. Ogawa, Dr M. Kikuchi, Dr A. Ishitani, Dr Y. Murao and Dr D. T. C. Huo for their useful advice and encouragement. He also would like to thank Mr A. Kubo for the TEOS-O₃ SiO₂ films' deposition. He would like to express appreciation to Mr Y. Kutsuzawa, Mr K. Kunimune, Mr K. Tsuji and Mr S. Konotsune of Chisso Corporation for material preparation. He also appreciates Mr R. Yamaguchi, Mr K. Mihirogi, Mr H. Machida and Mr Y. Takamatsu of Tri Chemical Laboratory, Incorporated, for material preparation.

References

- [1] K. Fujino, Y. Nishimoto, N. Tokumasu and K. Maeda, *J. Electrochem. Soc.* 137 (1990) 2883.
- [2] F. Fracassi, R. d'Agostino and P. Favia, *J. Electrochem. Soc.* 139 (1992) 2636.
- [3] M. Hatanaka, Y. Mizushima, O. Hataishi and Y. Furumura, in *Proc. Int. VLSI Multilevel Interconnection Conf. Proc.*, Santa Clara, CA, June 1991, p. 435.

- [4] P.L. Pai, A. Chetty, R. Roat, N. Cox and C. Ting, *J. Electrochem. Soc.* 134 (1987) 2829.
- [5] L.B. Rothman, *J. Electrochem. Soc.* 130 (1983) 1131.
- [6] Y. Hazuki and T. Moriya, in: *Proc. Int. VLSI Multilevel Interconnection Conference Proceedings*, Santa Clara, CA, June 1986, p. 121.
- [7] T. Homma and Y. Murao, *J. Electrochem. Soc.* 140 (1993) 2046.
- [8] T. Homma, R. Yamaguchi and Y. Murao, *J. Electrochem. Soc.* 140 (1993) 687.
- [9] T. Homma, R. Yamaguchi and Y. Murao, *J. Electrochem. Soc.* 140 (1993) 3599.
- [10] T. Homma, T. Katoh, Y. Yamada and Y. Murao, *J. Electrochem. Soc.* 140 (1993) 2410.
- [11] T. Homma and Y. Murao, *Thin Solid Films* 249 (1994) 15.
- [12] T. Homma, K. Kutsuzawa, K. Kunimune and Y. Murao, *Thin Solid Films* 235 (1993) 80.
- [13] W. A. Brantley, *J. Appl. Phys.* 44 (1973) 534.
- [14] E. M. Rabinovich and D. L. Wood, *Mater. Res. Soc. Symp. Proc.* 73 (1986) 251.
- [15] D. Kouvatsos, J. G. Huang, V. Saikunar, P. J. Macfarlane, R. J. Jaccodine and F. A. Stevie, *J. Electrochem. Soc.* 139 (1992) 2322.
- [16] S. Shibata, T. Kitagawa and M. Horiguchi, *J. Non-Cryst. Solids* 100 (1988) 269.



ELSEVIER

Journal of Non-Crystalline Solids 187 (1995) 60–65

JOURNAL OF
NON-CRYSTALLINE SOLIDS

Deposition of ultra-thin oxide dielectrics for MOSFETs by a combination of low-temperature plasma-assisted oxidation, and intermediate and high-temperature rapid thermal processing

G. Lucovsky*, V. Misra, S.V. Hattangady, T. Yasuda, J.J. Wortman

Departments of Physics, Materials Science and Engineering, and Electrical and Computer Engineering, North Carolina State University, Raleigh, NC 27695-8202, USA

Abstract

In order to match shrinking lateral dimensions in ULSI devices, there will be a need to reduce equivalent oxide thicknesses for gate dielectrics to at least 5–6 nm, and perhaps to as thin as ~ 3 nm. This reduction will have to be accomplished with low thermal budget, and more-than-likely low temperature processing as well. In this paper the important processing steps required for formation of ultra-thin gate oxides by thin film deposition as contrasted with conventional thermal oxidation, or the emerging technique of rapid thermal oxidation (RTO), are identified. Several different low thermal budget/low-temperature processing alternatives are identified in which interface formation, bulk oxide deposition, and structural and chemical relaxation are performed separately and controlled independently.

1. Introduction

As device dimensions shrink into the deep sub-micron regime, $< 0.25 \mu\text{m}$, there will be a need to reduce the equivalent oxide thickness of gate dielectrics for field effect transistors (FETs) to at least 5–6 nm and even less. In some instances this may mandate the use of deposited rather than thermally grown oxides, simply because the processing tem-

peratures and/or thermal budgets required for the thermally grown or rapid thermal oxidation (RTO) oxides are too high to prevent diffusion and spreading of junction boundaries within devices. Devices with deposited oxides will be required to have performance and reliability equivalent to those employing conventional furnace-grown or RTO oxides. This paper discusses processing studies that have lead to the evolution of a three-step approach to gate dielectric formation in which interface formation, bulk oxide deposition, and chemical and/or structural relaxation are separately and independently optimized and controlled.

* Corresponding author. Tel: +1-919 515 3301. Telefax: +1-919 515 7331.

2. Processing steps for gate dielectrics

2.1. Pre-deposition surface processing and passivation

Pre-deposition treatment of the Si surface that will be in contact with the gate oxide is crucial to obtaining device-quality performance and reliability. This has been separated into two steps: (i) an ex situ hot RCA clean, followed by a rinse in dilute HF; and (ii) an in situ plasma assisted surface/cleaning passivation step, where two different in situ passivation approaches have been investigated [1, 2]. To evaluate these, one has to characterize the surface of the Si(100) wafer after the RCA clean and HF rinse, upon insertion of the Si(100) substrate into a UHV-compatible processing system. This has been accomplished in several different multi-chamber systems which provide on-line Auger electron spectroscopy (AES) for chemical characterization, and either back-view low energy electron diffraction (LEED) or reflection high energy electron diffraction (RHEED). Upon initial examination, the ex situ processed Si(100) H-terminated surfaces have a 1×1 symmetry, and show residual C-atom and O-atom contamination with ~ 2 – 10 at.% surface coverages. Exposure to plasma-generated H (i) removed residual C to below the level of AES detection ($\sim 5 \times 10^{14} \text{ cm}^{-2}$) after 2 min, but (ii) did not remove residual O for exposure times as long as 5 min [2]. Studies of Si–SiO₂ interfaces (with oxides formed by the remote plasma-deposition process described below) by high resolution transmission electron microscopy (HRTEM-lattice imaging) indicated considerable surface roughening after the H-treatment with facet formation in the (111) directions. Electrical studies of capacitors indicated poor performance, the details of which will be discussed in the next section.

This H-treatment was replaced by a pre-deposition oxidation process [1], which when combined with either (i) low temperature (300°C) plasma-assisted deposition (remote PECVD) or (ii) rapid thermal chemical vapor deposition (RTCVD) yields much improved electrical performance [2]. The source gas for the oxidation step was O₂, and the source gases for the PECVD [2] and RTCVD

[3] oxide depositions were N₂O and SiH₄. The oxidation step (i) removes residual C-atom contamination to a level of $\sim 10^{12} \text{ cm}^{-2}$ (SIMS), (ii) promotes formation of a low defect density Si–SiO₂ interface ($D_{it} \sim 1$ – $3 \times 10^{10} \text{ cm}^{-2} \text{ eV}^{-1}$) that can withstand processing temperatures to at least 900°C, (ii) forms ~ 0.5 – 0.6 nm of SiO₂ which serves as a platform for the oxide depositions, and (iv) prevents uncontrollable incorporation of N-atoms at the Si–SiO₂ interface during oxide deposition from N₂O, thereby preventing increases in D_{it} . A similar process has been used with other remote PECVD dielectrics: silicon oxynitride alloys [4] and SiO₂/Si₃N₄ composites [5]; however, in these cases the gate dielectric structure requires a rapid thermal annealing (RTA) step at 900°C for 30 s to have properties similar to those quoted above for the oxide dielectrics. A further refinement of the oxidation step has replaced the O₂ source gas with N₂O and in this increased the bonded N-content at the Si–SiO₂ interface, improving both properties and reliability [6].

2.2. Oxide deposition

This was accomplished in two ways; (i) by remote PECVD at 300°C [2], and (ii) by RTCVD at 800°C [3]. Equivalent remote PECVD processes have been performed in three different multi-chamber systems. The Si-source gas silane (SiH₄) was injected downstream from the plasma, and the O-source gas nitrous oxide (N₂O) was pre-mixed with He and injected through the plasma generation region. The plasma was powered by a 13.56 MHz RF source. Deposition rates varied from 2.5 to 10 nm/min with no significant differences in film properties or device performance. The RTCVD depositions were performed in an ultra-clean system with the same two source gases, SiH₄ and N₂O, and at a temperature of 800°C [3]. The deposition rate was 6 nm/min. Both processes yield stoichiometric oxide films with equivalent performance in MOS and FET devices.

2.3. Fabrication of MOS and FET devices

MOS and FET devices were fabricated using different combinations of plasma- and rapid thermal

processing [7–9]: (i) all devices incorporating remote PECVD oxides employed the plasma-assisted oxidation pre-deposition process [9]; whereas (ii) devices incorporating RTCVD oxides used four different pre-deposition steps: (a) ex situ RCA cleans with, and without a final rinse in dilute HF, (b) the in situ plasma oxidation process described above, and (c) a pre-deposition rapid thermal oxidation (RTO) [7–9]. For the devices employing the remote PECVD oxides, the maximum processing temperature was determined by the nature of the gate electrode: (i) 400°C for Al electrodes used in MOS capacitor studies, and (ii) 900°C for phosphorus doped (POCl₃ process) polycrystalline Si gate electrodes. For devices employing RTCVD oxides, the maximum temperature was (i) 800°C, the temperature of the oxide deposition for devices with Al electrodes, (b) 900°C for devices with doped polycrystalline Si electrodes, but not using a pre-deposition RTO, and (c) 1000°C for devices with doped polycrystalline electrodes that also utilized a pre-deposition RTO.

3. Properties of MOS capacitors and FETs

The properties of MOS capacitors and FETs with deposited oxides are discussed, with comparisons between different processing techniques for FETs are shown in Figs. 1–3. To converge toward the identification of the essential elements of a

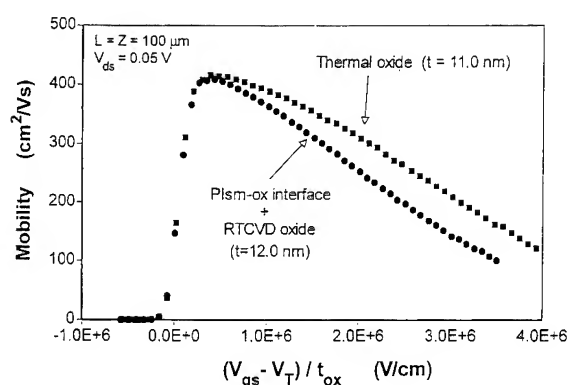


Fig. 1. Channel mobility versus effective Si surface field in the channel region.

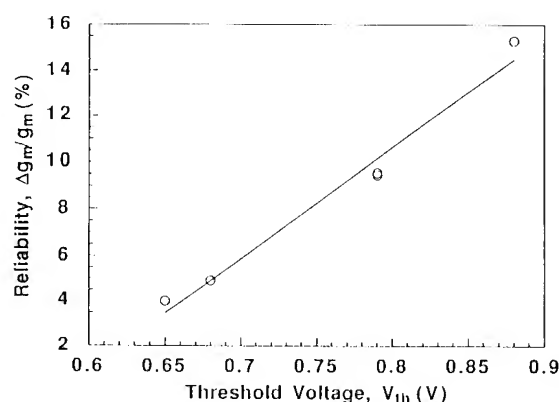


Fig. 2. Normalized stress-induced decreases in g_m versus ΔV_{th} . The line is drawn as a guide for the eye.

generic processing sequence for optimizing the electrical performance of FET devices with deposited oxides, we compared the properties of pairs of devices processed in different ways:

(a) MOS capacitors with Al contacts and remote PECVD oxides, with H and O plasma cleans (300°C processing with 400°C PMA). This comparison establishes the superiority of the plasma oxidation process to the plasma-H clean. The combination of a pre-deposition plasma-assisted oxidation and a remote PECVD oxide deposition provides separate control of interface formation, and oxide deposition, and this results in superior electrical properties to the combination of a plasma-H clean and remote PECVD deposition wherein the interface formation takes place during film deposition by a subcutaneous oxidation process. For example, D_{it} values decreased from $8 \pm 5 \times 10^{10}$ to $1.5 \pm 2 \times 10^{10} \text{ cm}^{-2} \text{ eV}^{-1}$, and breakdown fields increased from 5–8 to 9–11 MV cm⁻¹, when the plasma oxidation step replaced the plasma H passivation/cleaning process [3,9].

(b) MOS capacitors with P-doped polycrystalline Si electrodes (900°C) with oxides formed by remote PECVD (300°C) and RTCVD (800°C). This comparison establishes an equivalence between remote PECVD oxides (300°C) and RTCVD oxides (800°C) with doped polycrystalline Si electrodes (900°C). The conclusion drawn from this comparison is that the annealing at 900°C for the

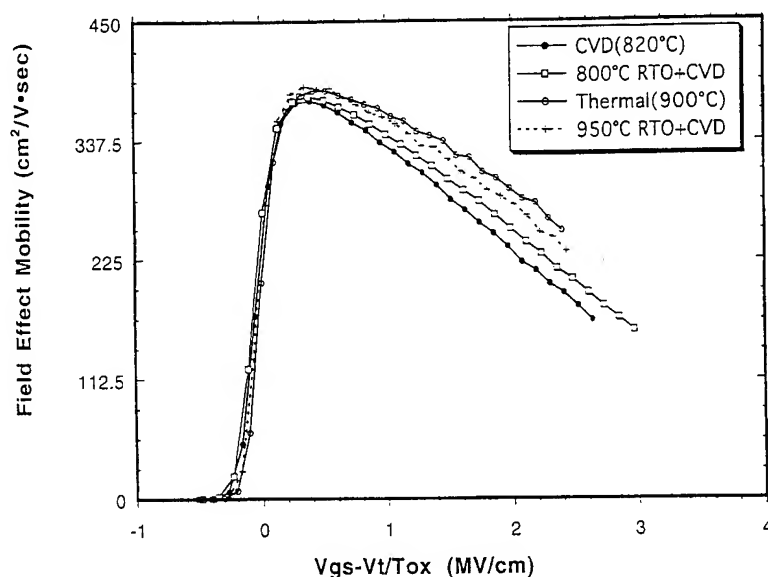


Fig. 3. Channel mobility versus effective Si surface field in the channel region.

30 min duration of the POCl_3 doping process is sufficient to render the two types of oxides indistinguishable to the extent that fixed oxide charge (Q_f), and interfacial defects (D_{it}) are effectively the same; i.e., $Q_f < 10^{11} \text{ cm}^{-2}$ and $D_{it} \sim 10^{10} \text{ cm}^{-2} \text{ eV}^{-1}$ [9].

(c) MOS capacitors with Al contacts and RTCVD (800°C) oxides, for different pre-deposition processing [7]. These comparisons for MOS capacitors establish that separate control of interface formation and film deposition via the integration of a plasma-assisted oxidation and RTCVD oxide deposition leads to better electrical properties than for RTCVD deposition following an RCA clean with or without a rinse in dilute HF, where interface formation is not independently controlled by an in situ process. For example, values of D_{it} for the RCA cleaned samples were about 2–4 times higher than for the plasma-assisted oxidation, and the values of the threshold voltage for the RCA-clean interfaces yielded fixed charge levels $> 10^{11} \text{ cm}^{-2}$, whereas the values of Q_f for the plasma-oxidized interfaces were $< 10^{11} \text{ cm}^{-2}$.

(d) FETs with doped polycrystalline Si gate electrodes (900°C) and RTCVD oxides (800°C), for different pre-deposition processing, and including mid-process RTAs [8,10]. These comparisons for

FETs reinforce the conclusion drawn in (c), and combined with Fig. 1 indicate a difference in performance with respect to FETs with thermally-grown oxides, namely in the rate at which the channel mobility falls off with the electrical field at the Si surface of the channel region.

(e) FETs with doped polycrystalline Si gate electrodes (900°C) and RTCVD oxides for different pre- and post-deposition processing, including 900 – 1000°C pre-deposition RTOs, and post-deposition RTAs in an oxygen ambient. These comparisons for FETs demonstrate that a process sequence which provides separate control for interface formation through the pre-deposition RTO step, and for oxide quality through the RTCVD deposition yields electrical performance that is essentially the same as obtained for thermally grown oxides. This includes the decreased rate at which channel mobility falls off with the electrical field at the Si surface of the channel region (see Fig. 3). Additional experiments have shown that the similar performance is obtained if the pre-deposition RTO is eliminated, but a post-deposition RTA in oxygen (effectively a post-deposition RTO) is inserted at the end of the RTCVD oxide deposition process.

4. Process optimization

The combination of experimental results discussed above establishes that three processing steps are essential for the fabrication of FETs with deposited oxides in order for their electrical properties to be equivalent to those of state of the art FETs with thermally grown oxides. These are: (i) an oxide deposition that yields a stoichiometric oxide; (ii) separate and distinct processes for Si–SiO₂ interface formation and oxide deposition; (iii) creation of the Si–SiO₂ at elevated temperatures, $\sim 1000^\circ\text{C}$. The properties of the remote PECVD and RTCVD oxides are essentially the same if both are subjected to a 900°C anneal during the gate electrode doping process; however, it is not possible to perform plasma-assisted depositions and rapid thermal processes (RTP) in the same chamber due to the fact that plasma-assisted deposition occurs not only on the film substrate, but also on chamber walls and fixtures, including the optical access windows required for RTP processing. This favors RTCVD oxide deposition over remote PECVD oxide deposition. However, if it becomes necessary to use oxynitride alloys, nitrified oxides and/or oxide–nitride–oxide sandwiches (ONO structures), then remote PECVD deposition must be considered as a process alternative in light of the high-quality oxynitride and ONO dielectrics that have been formed by the combination of (i) a plasma-assisted oxidations (300°C); (ii) remote PECVD film depositions (300°C); and (iii) a 30 s, 900°C RTAs [4,5].

The low-temperature (300°C) pre-deposition plasma-assisted oxidation, and the pre-deposition and post-deposition RTOs provide independent process control over Si–SiO₂ interface formation, however, they are not equivalent in promoting the same rate of fall-off of the channel mobility with the field at the Si surface of the channel region. The inclusion of interface formation at elevated temperatures, $\sim 1000^\circ\text{C}$, appears to be the only way to achieve Si–SiO₂ interfacial properties similar to those obtained during the high/temperature growth or annealing of thermal oxides. Note that an optimized process consisting of a RTCVD oxide deposition, and pre- or post-deposition RTO requires a lower budget than is required for a conven-

tional thermal oxide, or an RTO process by itself. However, if in addition to thermal budget constraints there are constraints on maximum temperatures, then the combination of (i) a plasma-assisted oxidation at 300°C with an RTCVD deposition (800°C), or (ii) a plasma-assisted oxidation at 300°C , a remote PECVD oxide deposition at 300°C and a post-deposition RTA at a temperature between 800°C and 900°C become attractive process alternatives. As discussed above, these two options will produce FETs with slightly reduced drive currents at the maximum operating gate voltages due to higher rate of channel mobility fall-off with the electric field at the Si surface of the channel region.

Finally, an additional set of comparisons based on reliability criteria is needed. The experimental data in Fig. 2 present an interesting dimension for at least one aspect of FET reliability [11]. They demonstrate that a reliability parameter, $-\Delta g_m/g_m$ (g_m is the peak value of the transconductance), is proportional to a quality parameter, ΔV_{th} , the shift of the threshold voltage relative to a reference device made with a conventional thermal oxide. Note that an important contribution to these shifts in the value of V_{th} is fixed oxide charge in the immediate vicinity of the Si–SiO₂ interface, and that the generation of additional fixed charge can contribute to degradation in channel transport is manifested in the reliability factor $-\Delta g_m/g_m$. A possible interpretation is that an interfacial region that contains a higher concentration of bonding defects that contribute to the fixed charge that contributes to the shifts in V_{th} is more susceptible to stress-induced generation of additional charged defect sites and/or interface traps that reduce g_m . We are currently studying controlled N-atom incorporation at Si–SiO₂ interfaces in a new two-step process that also combines separate control of interface formation and oxide deposition [6]. Preliminary experiments suggest that this link between reliability and quality may be more widespread than is generally anticipated. This suggests that an alternative process sequence that substitutes a pre-deposition 300°C plasma-assisted oxidation using N₂O and a pre- or post-deposition RTA at 1000°C , combined with an 800°C RTCVD oxide may have provided increased reliability

through controlled incorporation of N-atoms at the Si–SiO₂ interface.

This research is supported by ONR, the NSF, SEMATECH and the SRC.

References

- [1] S.S. Kim and G. Lucovsky, *J. Vac. Sci. Technol.* A8 (1990) 2039.
- [2] T. Yasuda, Y. Ma, S. Habermehl and G. Lucovsky, *Appl. Phys. Lett.* 60 (1992) 434.
- [3] X.-L. Xu, R.T. Kuehn, J.J. Wortman and M.C. Ozturk, *Appl. Phys. Lett.* 60 (1992) 3063.
- [4] Y. Ma, T. Yasuda, S. Habermehl and G. Lucovsky, *J. Vac. Sci. Technol.* B11 (1993) 1533.
- [5] Y. Ma and G. Lucovsky, *J. Vac. Sci. Technol.* B12 (1994) 2504.
- [6] D.R. Lee and G. Lucovsky, unpublished.
- [7] G. Lucovsky, S.V. Hattangady, C. Silvestre, J.R. Hauser and J.J. Wortman, *Mater. Res. Soc. Symp. Proc.* 303 (1993) 339.
- [8] V. Misra, S. Hattangady, X.-L. Xu, M.J. Watkins, B. Hornung, G. Lucovsky, J.J. Wortman, U. Emmerichs, C. Meyer, K. Leo and H. Kurz, *Microelectron. Eng.* 25 (1994) 209.
- [9] G. Lucovsky, Yi Ma, T. Yasuda, C. Silvestre and J.R. Hauser, *Jpn. J. Appl. Phys.* 31 (1992) 4387.
- [10] V. Misra, S.V. Hattangady, T. Yasuda, X.-L. Xu, B. Hornung, G. Lucovsky and J.J. Wortmann, *J. Vac. Sci. Technol.* A12 (1994) 1371.
- [11] G. Lucovsky, J.J. Wortmann, T. Yasuda, X.-L. Xu, V. Misra, S.V. Hattangady, Yi Ma and B. Hornung, *J. Vac. Sci. Technol.* B12 (1994) 2839.



ELSEVIER

Journal of Non-Crystalline Solids 187 (1995) 66–69

JOURNAL OF
NON-CRYSTALLINE SOLIDS

New substances for atomic-layer deposition of silicon dioxide

S. Morishita, W. Gasser, K. Usami, M. Matsumura*

Department of Physical Electronics, Faculty of Engineering, Tokyo Institute of Technology, 2-12-2 O-okayama, meguro-ku, Tokyo 152, Japan

Abstract

Based on the first result of the layer-by-layer deposition of silicon dioxide films by a cyclic exposure of water and tetra isocyanate silane, $\text{Si}(\text{NCO})_4$, new isocyanate compounds preferable to $\text{Si}(\text{NCO})_4$ have been proposed for ideal layer-by-layer deposition characteristics. Preliminary results are also presented for one of the substances.

1. Introduction

The aim of this paper is to find an atomic-layer chemical-vapor deposition (AL-CVD) technology for the deposition of silicon dioxide (SiO_2) films. Although the SiO_2 film is amorphous and therefore its monolayer thickness cannot be defined precisely, quasi monolayer-controlled deposition of SiO_2 is still very attractive for various applications, due to good uniformity and accuracy in the deposited film thickness, i.e., due to the inherent properties of the layer-by-layer process [1].

AL-CVD of the SiO_2 film has been successfully demonstrated by alternative exposure of tetra isocyanate silane [TICS: $\text{Si}(\text{NCO})_4$] and water vapor [2]. On TICS, only very few reports are published every year, although its properties have been well known for a long time [3] and it is commercially available now. SiO_2 can be formed by mixing TICS and water even at room temperature [4]. This reaction is due to the strong dipole moments

in the source molecules such as $\equiv \text{Si}-\text{N}^--\text{C}^+=\text{O}$ and $\text{H}^+-\text{O}^--\text{H}^+$, resulting in alternating replacements of an $\text{N}-\text{C}=\text{O}$ group in $\equiv \text{Si}-\text{N}-\text{C}=\text{O}$ to an $\text{O}-\text{H}$ group, and of an H atom in $\equiv \text{Si}-\text{O}-\text{H}$ to an $\text{Si}-\text{N}-\text{C}=\text{O}$ group. Based on the elemental kinetics at the surface, we have succeeded in the first SiO_2 AL-CVD [2]. The deposition rate was, however, saturated at about 0.17 nm/cycle for a suitable set of AL-CVD parameters, i.e., less than the calculated approximate thickness, 0.36 nm, of an SiO_2 monolayer (ML). This paper discusses better substances towards the ideal deposition rate of 1 ML/cycle.

2. Isocyanate compounds for ideal deposition characteristics

A big and complex three-dimensional form of TICS molecules is the predominant origin of the non-ideal deposition rate. Their chemisorption on the surface is hindered before the whole OH groups covering the surface react with them. Thus, we propose here a series of isocyanate compounds, $\text{X}_n\text{Si}(\text{NCO})_{(4-n)}$, where X is hydrogen atom,

* Corresponding author. Tel: +81-3 5734 2559. Telefax: +81-3 5734 2559. E-mail: matsumura@pe.titech.ac.jp.

Table 1
Physical properties of several silicon compounds

	<i>M</i> (g/mol)	<i>G</i> (g/cm ³)	<i>G</i> / <i>M</i> (mol/cm ³)	BP (°C)	MP (°C)
Si(NCO) ₄	196	1.442	0.007357	186	26
CH ₃ Si(NCO) ₃	169.2	1.267	0.007488	164	2.7
(CH ₃) ₂ Si(NCO) ₂	142.2	1.076	0.007566	138	– 31
(CH ₃) ₃ SiNCO	115.1	0.867	0.007532	90	– 49
CH ₃) ₄ Si	88.2	0.646	0.007324	26	—
C ₂ H ₅ OSi(NCO) ₃	197	1.300	0.006989	178	Not known
n-C ₄ H ₉ Si(NCO) ₃	211	1.141	0.005408	215	Supercooling

halogen atom, alkyl group or alkoxy group, and *n* is 1, 2, or 3, respectively. The molecular weight, *M*, specific gravity, *G*, boiling temperature and melting temperature are tabulated in Table 1 for several compounds. The distance between molecules, which is inversely proportional to the third root of *G*/*M*, decreases with increasing *n* from zero. The long spacing especially for *n* = 3 and 4 is attributed to the rapid decrease in the boiling temperature or the melting temperature, i.e., to the reduced intermolecular force. Thus we concluded that a molecule becomes small with increasing *n*. The size of molecules depends also on the kind of non-cyanate groups as seen in Table 1. Therefore, the smallest isocyanate compound molecule, the best substance for the SiO₂ AL-CVD, is mono isocyanate silane, H₃SiNCO. There are other big advantages in this substance, that its SiH bonds can be easily oxidized and that it is gaseous under room temperature conditions.

Superior AL-CVD kinetics of alternative exposure of H₃SiNCO and ozone can be visualized in Fig. 1. In the first phase, the OH-covered surface is exposed to H₃SiNCO. H₃SiNCO can react with an OH-covered surface as TICS, since it has an NCO group, resulting in the chemisorption of SiH₃ groups as shown schematically in (a). The SiH₃ group has a smaller size than the Si(NCO)_{*n*} group, and its bond is straight and not bent as in the case of the NCO group. Thus the stereoscopic problem can be solved, and a higher surface covering density is expected, resulting in the ideal 1 ML chemisorption. Since the dipole moment in an Si–H bond is very small, the surface loses its chemical reactivity

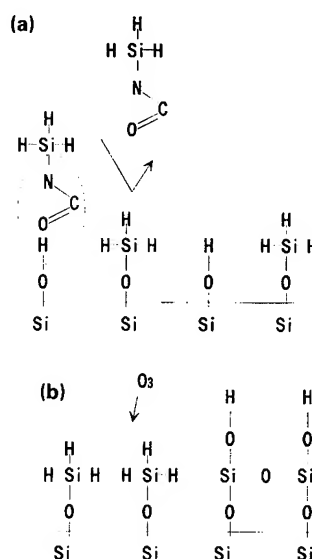


Fig. 1. Schematic kinetics of the SiO₂ AL-CVD using H₃SiNCO and ozone: (a) chemisorption of SiH₃ group by H₃SiNCO exposure; (b) oxidation for forming the Si–O–Si bond and OH-terminated surface by ozone exposure.

to H₃SiNCO after 1 ML chemisorption of the SiH₃ group. Exposure to ozone in the second phase leads to formation of both Si–O–Si bonds between adjacent Si atoms and OH groups at the surface as shown schematically in (b). These modifications can be achieved completely and quickly by the effects of small size and chemical reactivity of H atoms. Then the cycle repeats itself with the ideal 1 ML/cycle deposition rate.

3. Experimental

Unfortunately, H_3SiNCO is not commercially available yet. Thus we have investigated an alternative substance, i.e., mono methoxysilane tri isocyanate, $\text{CH}_3\text{OSi}(\text{NCO})_3$.

The AL-CVD system is schematically shown in Fig. 2. A counterpart of $\text{CH}_3\text{OSi}(\text{NCO})_3$ was 31% hydrogen peroxide in water, instead of pure water in the TICS experiments. Pure nitrogen was used as a carrier gas that causes alternately a bubbling in the pure $\text{CH}_3\text{OSi}(\text{NCO})_3$ and hydrogen peroxide vessels, respectively, and brings these vapors to the reaction chamber. As the total system was under room temperature conditions, the partial pressures of source materials were given by their saturated vapor pressures. There was a third gas line for an optional exposure to oxygen with or without 5% ozone, and also a fourth line for the nitrogen cleaning. Total pressure in the chamber was kept at 400 Torr. In order to achieve AL-CVD, we had to evacuate completely all source molecules remaining in the chamber after each exposure to one of the two source materials before the exposure to the other source material. For complete evacuation, we used a serial combination of a mechanical booster pump and a rotary pump, leading to a vacuum quality of about 10 m Torr within 10 s evacuation, together with insertion of three additional cleaning phases with nitrogen after each exposure. This reduced effectively the deposition rate of the film to a value that could not be decreased with further improved evacuation.

4. Results and discussion

The deposition rate is shown in Fig. 3 by a solid curve together with results (sharp curve) of TICS experiments. Although the number of data is not sufficient, it is clear that a better deposition rate is obtained by using the new combination.

Auger electron spectroscopy (AES) signals arising from N atoms (around 370 eV) were below the resolution limit of the spectrometer. In contrast to the TICS experiments, however, a signal relating with C atoms was observable at around 270 eV, revealing that the methoxyl group was not removed

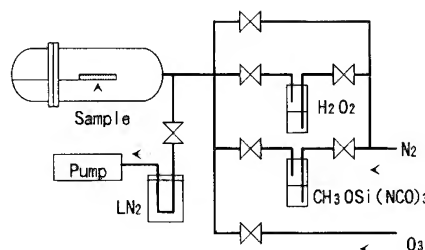


Fig. 2. The schematic SiO_2 AL-CVD system.

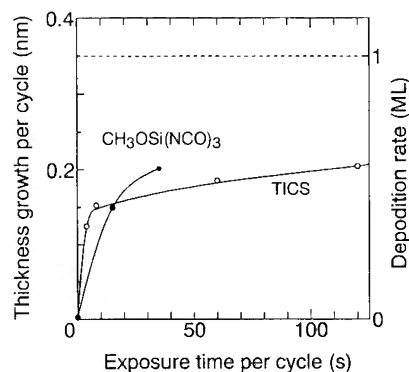


Fig. 3. Deposition rate as a function of the Si-source exposure time: sharp curve, TICS and water exposure; solid curve, $\text{CH}_3\text{OSi}(\text{NCO})_3$ and peroxide exposure. The curves are drawn as a guide for the eye.

completely from the film. The composition ratio of Si : O : C was about 1 : 1.7 : 0.15, thus the film was Si-rich. The C content could be decreased to one-third by insertion of an ozone exposure phase in each cycle. An X-ray photoelectron spectroscopy (XPS) measurement indicated that the film was also Si-rich that is, the ratio of the Si^{4+} , Si^{3+} , Si^{2+} and Si^{1+} bondings was about 44.2 : 19.6 : 32.3 : 3.9, respectively.

Infrared absorption spectra are given in Fig. 4 for three different films deposited by a cycle consisting of exposure of (a) $\text{CH}_3\text{OSi}(\text{NCO})_3$ and hydrogen peroxide, (b) $\text{CH}_3\text{OSi}(\text{NCO})_3$, ozone and hydrogen peroxide, and (c) TICS and water for reference purposes. For all films, the central Si–O stretching mode appeared clearly at 1070 cm^{-1} , and the Si–O rocking mode at 800 cm^{-1} , respectively, very close to their reported values [5]. Thus the film had a lot of Si–O bonds. Typical

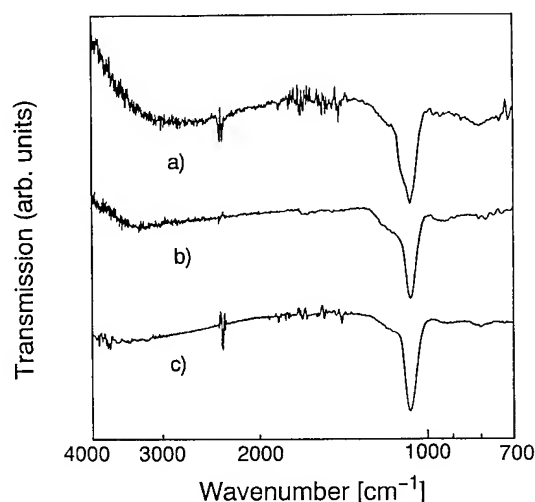


Fig. 4. Infrared absorption spectrum of the films deposited by: (a) cyclic exposure of $\text{CH}_3\text{OSi}(\text{NCO})_3$ and peroxide; (b) cyclic exposure of $\text{CH}_3\text{OSi}(\text{NCO})_3$, ozone and peroxide; (c) cyclic exposure of TICS and water.

absorption lines for the N–H stretching mode at 3400 cm^{-1} were not found in the films (a) and (b), in agreement with the AES results, but were seen a little in the film (c). Strong absorptions around 2350 cm^{-1} were caused by the Si–H group or the NCO group. For the film (c), the Si–H group has been confirmed to be the predominant origin of these absorptions. For the films (a) and (b), since N atoms could not be detected in their AES spectrum, and since these absorptions did not disappear after some days (Si–NCO can react quickly with water vapor in the air), it is preferable to assign also the absorptions to Si–H bonds. The absorption line at 930 cm^{-1} was attributed to Si–OH bonds. In the film (c), due to the oxidation of the Si–H bonds by O_3 , the absorption line at 2350 cm^{-1} was small and the absorption at 930 cm^{-1} was large, in comparison to those in the film (a). The oxidation process plays a very important role for new substances. The

C–H rocking mode absorption at 1000 cm^{-1} was not observable. Si–C bond absorption should be visible at 780 cm^{-1} , but perhaps was hidden by the strong Si–O absorption. The shift of this absorption line to around 800 cm^{-1} from the typical value (810 cm^{-1}) in the films (a) and (b), however, can be attributed to the Si–C bonds. Finally it should be noted that small spikes from 1400 to 1900 cm^{-1} arise mainly from CO_2 absorptions.

5. Conclusion

Isocyanate compounds $\text{X}_n\text{Si}(\text{NCO})_{4-n}$ were proposed as more desirable source molecules than TICS for ideal AL-CVD of silicon dioxide, where X is hydrogen, halogen, alkyl or alkoxy, respectively, and $n = 1, 2$, or 3 . By $\text{CH}_3\text{OSi}(\text{NCO})_3$, one of the proposed substances, an improvement of the deposition rate, towards ideal 1 ML/cycle , could be obtained, and deposited film properties were evaluated. It was found that oxidation should be done satisfactorily. Thus, H_3SiNCO is the most preferable among the proposed substances because it is the smallest in size and oxidized easily.

The authors would like to express their thanks to Showa-Denko for preparation of $\text{Si}(\text{NCO})_4$ and $\text{CH}_3\text{OSi}(\text{NCO})_3$.

References

- [1] T. Suntola and M.J. Antson, US patent no. 4,058,430 (1977).
- [2] W. Gasser, Y. Uchida and M. Matsumura, *Thin Solid Films* 250 (1994) 219.
- [3] G.S. Forbes and H.H. Anderson, *J. Am. Chem. Soc.* 62 (1940) 761.
- [4] O. Sugiura, H. Taniguchi, W. Gasser and M. Matsumura, in: *Extended Abstracts of Int. Conf. on Solid State Devices and Materials* (1993) p. 513.
- [5] W. Bensch and W. Bergholz, *Semicond. Sci. Technol.* 5 (1990) 421.



ELSEVIER

Journal of Non-Crystalline Solids 187 (1995) 70–74

JOURNAL OF
NON-CRYSTALLINE SOLIDS

Dual-mode radio frequency/microwave plasma deposition of amorphous silicon oxide thin films

R. Etemadi*, C. Godet, M. Kildemo, J.E. Bourée, R. Brenot, B. Drévilon

Laboratoire de Physique des Interfaces et des Couches Minces (UPR 0258 CNRS), Ecole Polytechnique, 91128 Palaiseau cédex, France

Abstract

A new dual-plasma (surface wave-coupled microwave and capacitively-coupled radio frequency) plasma enhanced chemical vapor deposition reactor for high growth rate deposition of amorphous insulating alloys has been developed. A high degree of flexibility for thin film material synthesis is expected, because the energy of the ion bombardment can be controlled independently of the microwave plasma chemistry. In situ spectroscopic ellipsometry is used for the optimization of the dual-mode plasma deposition of hydrogenated silicon oxides $a\text{-SiO}_x\text{:H}$ (with $0 \leq x \leq 2$) providing monitoring of the index of refraction and deposition rate. A new procedure for the real-time calculation of both parameters is reported. The growth rate of nearly stoichiometric oxides increases as a function of the oxygen flow rate with a maximum value of 33 Å s^{-1} using a 315 W microwave power.

1. Introduction

For large area thin film deposition and surface treatment by plasma enhanced chemical vapor deposition (PECVD) techniques, different plasma frequencies are available and the actual choice is dictated by the type of substrate and the material to be grown [1]. The influence of the plasma frequency on the electron energy distribution function (EEDF) has been modelled only for a few rare gases [2]. The EEDF determines the production of primary species (radicals, ions and excited species), which may then react with other gas phase species or recombine on the walls. The plasma frequency also has a major influence on the energy of positive

ion bombardment which is of the order of a few eV for microwave (MW) and ECR plasmas but reaches tens of eV at the smaller electrode in radio frequency (RF) plasmas. We expect that a single-vessel multi-plasma system can combine the advantages of different plasma frequencies at a manageable level of complexity.

In this paper, we describe a dual-frequency (RF at 13.56 MHz and MW at 2.45 GHz) plasma reactor with coupling of the microwave power from a waveguide to a quartz tube. The substrate is located at the end of the tube in the MW post-discharge region. In contrast to some dual mode MW/RF reactors where the substrate is simultaneously exposed to MW and RF plasmas [3], in our case the two plasmas are localized at different places. We will show that the MW and RF plasmas are not strictly independent and they do interact

* Corresponding author. Tel: +33-1 69 33 36 83. Telefax: +33-1 69 33 30 06.

in the MW post-discharge region, close to the substrate location, providing a complex system with many experimental parameters. To investigate the interaction of the RF and MW plasmas during the growth, in situ diagnostics have been implemented for the characterization of the gas phase using optical emission spectroscopy (OES), and the film surface using UV-visible spectroscopic ellipsometry (SE). Some characteristic properties of the dual-plasma using helium–argon gas mixtures have been reported in previous studies [4,5]. In this study, a low substrate temperature (70°C) was chosen for the deposition of a-SiO_x:H thin films as functional coatings on polymers which are unable to sustain temperatures above 100°C [6].

2. Experimental

The dual-plasma system has been discussed in detail elsewhere [4,7]. In summary, helium, argon and oxygen are injected at the extremity of a quartz tube. Microwave power is fed to the discharge via an impedance matching network and a field applicator. In the small quartz tube, surface-wave propagation takes place in the direction of the bell-shaped termination of the quartz tube. Silane is injected in the MW post-discharge, close to the substrate. The RF plasma is located downstream from the tube between the 200 cm² RF-polarized substrate holder and the grounded surfaces (reactor walls and the plane of the silane injector grid).

Optical characterizations of the amorphous films have been performed in situ with a UV-visible phase-modulated ellipsometer (Instruments S.A) and ex situ using conventional IR transmission, IR Fourier transform phase modulated ellipsometry (FTPME) [8], and energy-dispersive X-ray analysis (EDX) [9].

3. Results and discussions

3.1. Growth monitoring by ellipsometry

By simulating the (Ψ , Δ) ellipsometric real-time trajectory with a fixed refractive index model at 3.8 eV, a homogeneous growth model provides the deposition rate (R_d) and the complex refractive index of the film (Fig. 1). This trajectory is

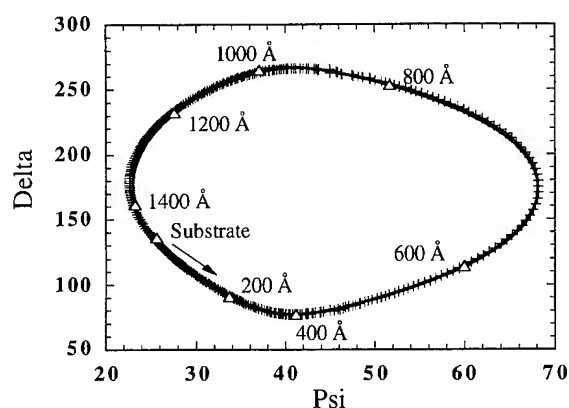


Fig. 1. Kinetic trajectory at 3.8 eV of silicon dioxide film deposition (+ + +, experiment; —, and model)

a closed loop, making a half tour for a thickness of approximately $\lambda/4$ and returning towards the initial values of (Ψ , Δ) at approximately $\lambda/2$. The procedure described above to calculate R_d and the refractive index, normally performed off-line (after data acquisition) can be replaced by a real-time inversion procedure giving rapid access to the physical properties.

An on-line system performing inversion of the ellipsometric equations in real time [10] has been developed. From a single set of measurements (Ψ , Δ) at a chosen wavelength we extract two physical properties (refractive index and thickness or deposition rate) in the case of a transparent film or a film with known absorption. Specifically, we use a method developed by Charlot and Maruani [11] for the inversion of the standard equation describing the optical structure and measurement with respect to the refractive index of the film n and its corresponding thickness (Fig. 2). The discrepancies at the beginning of the deposition could be due to noise in the measurement of the first point and possibly to the influence of a thin film of higher void fraction on the silicon of film surface. The measured thickness is interactively used to stop the film growth. Thickness and refractive index are also deduced from the spectroscopic measurement and modelling of the experimental pseudo-dielectric function, assuming a harmonic oscillator behavior [12]. The results are coherent with the on-line method.

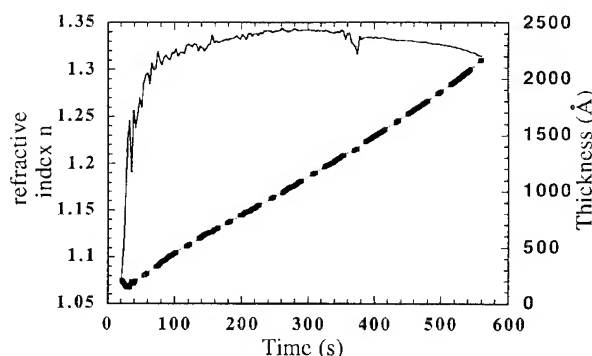


Fig. 2. Refractive index n (continuous line) and thickness of the silicon dioxide film as a function of time.

Since in the case of transparent films, the kinetic trajectory passes through the (Ψ, Δ) of the substrate for thicknesses approaching $\lambda/2$ (Fig. 1), one cannot at a chosen wavelength extract optical properties with a direct procedure at this thickness. The development of a multiwavelength detection system for real time applications has the potential to overcome this problem [12].

3.2 Film properties

Using a constant MW power of 315 W at 80 mTorr and a He–Ar mixture (300–125 sccm), the influence of the oxygen flow rate and the RF power on the deposition rate and optical properties of a-SiO_x:H films has been investigated. For a-SiO_x:H deposition, a variable flow rate of O₂ up to 60 sccm is injected with the helium–argon mixture (300–125 sccm) into the MW discharge. Since oxygen and argon have similar ionization potentials and EEDF [2], the MW plasma characteristics are expected to remain relatively unaffected by the O₂ flow rate. The silane flow rate is held constant at 6.5 sccm and the oxygen to silane ratio R is varied from 0.08 to 2.3. The radial homogeneity of the oxide deposition rate is rather good. The thickness (measured using step-profiler) is greatest at the center and typically 15% lower at 7 cm from the center.

With the MW plasma only, a sharp increase of the deposition rate as a function of R has been measured (Fig. 3(a)), from 1.3 Å s⁻¹ at $R = 0.08$ up to 5 Å s⁻¹ at $R = 2.3$. Although the influence of

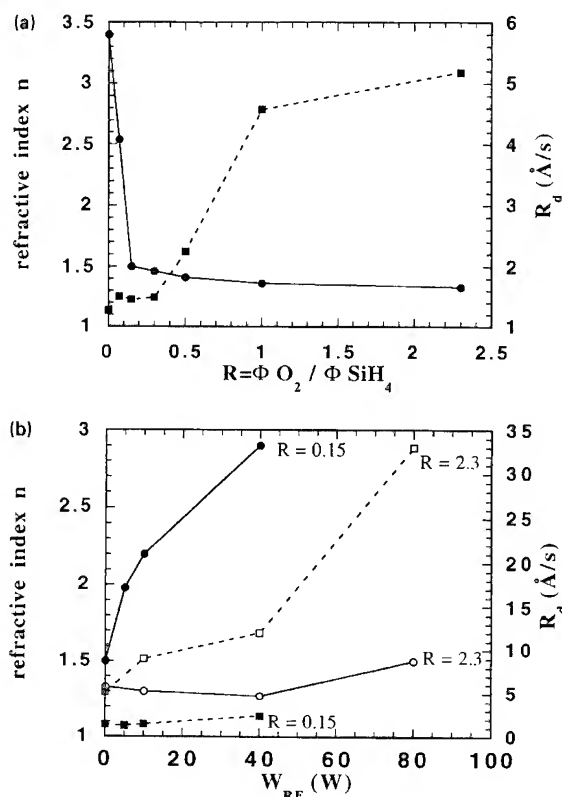
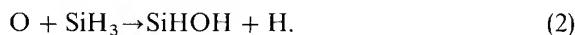


Fig. 3. Refractive index (continuous line) and deposition rate (dashed line) at a constant 6.5 sccm silane flow rate as a function of (a) the oxygen to silane ratio (R) without RF power, (b) the RF power. Lines are drawn as guides for the eye.

excited He (He*) species on the silane decomposition cannot be completely ruled out, this may reveal a Penning reaction of He* with O₂ and a dissociative reaction of oxygen radicals with silane molecules, following some of the reactions which may produce silyl and silanol radicals [13]:



It is observed that the relative effect of adding a 40 W RF plasma to the MW (315 W) plasma is an increase of the growth rate by a factor of 2, independent of R . In the oxygen depleted regime ($R = 0.15$) the stoichiometry changes from $x \cong 2$ to lower (Si-rich) values, which causes an increase of the refractive index, while in the oxygen excess regime

($R = 2.3$) the stoichiometry is unaffected (Figs. 3(a) and (b)). The main effect of the RF plasma seems to be the enhancement of the electronic dissociation of SiH_4 to produce SiH_3 radicals which are transformed to silanol radicals through reaction (2).

The influence on the deposition rate of the contribution of the RF and MW plasmas is more an interactive effect than an adding effect ($R_{d, \text{RF+MW}} > R_{d, \text{RF}} + R_{d, \text{MW}}$). This behaviour reveals the beneficial effects of the dual-plasma mode in the case of insulating thin film deposition. In this high growth rate regime, R_d saturates as a function of the O_2 flow rate. As the full incorporation of injected silane would correspond to a 65 \AA s^{-1} deposition rate, this indicates a depletion of silane and a high sticking coefficient of the silicon-related deposition precursors on the growing $\text{a-SiO}_x\text{:H}$ ($x \approx 2$) surface. The high growth rate ($R_d \approx 33 \text{ \AA s}^{-1}$) obtained for silicon oxide films in our reactor compares favorably to other dual-plasma systems [3,14] which have demonstrated growth rates of $2 \leq R_d \leq 20 \text{ \AA s}^{-1}$, and to an RF plasma reactor [15] with R_d reaching 15 \AA s^{-1} .

Analysis of IR spectra from either ellipsometric or transmission measurements reveals a decrease of the stretching frequency ν of the Si–O bonds as the RF power is increased (Fig. 4). The shift to lower frequency can be attributed to the densification of the film (revealed by the increase of n), induced by positive ion bombardment of the film surface [15].

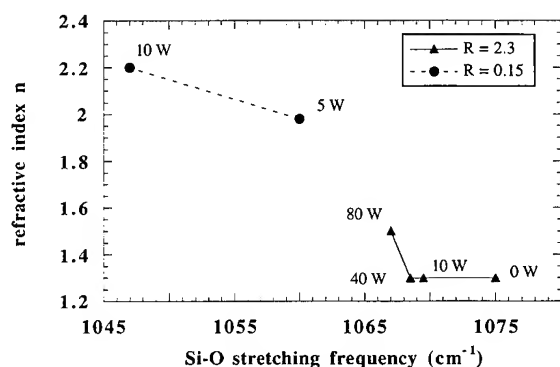


Fig. 4. Refractive index as a function of the (Si–O) stretching frequency for different RF power (continuous line $R = 2.3$ and dashed lines $R = 0.15$). Lines are drawn as guides for the eye.

The position of the stretching frequencies are invariant for the same R , even if the O_2 and SiH_4 flow rates are increased by a factor 2 (at constant R).

It is also interesting to note that $\nu_{R=0.15} < \nu_{R=2.3}$. For $R = 0.15$, the presence of Si–Si bonding groups induces a low frequency shift of the Si–O stretching mode [16] in these silicon suboxide films (SiO_x , $x < 2$), which are rich in Si–Si and Si–H bonds. In these conditions, at a high RF power density, it is possible to obtain silicon-rich material with $x < 1$. In contrast, for $R = 2.3$, the resulting oxygen-rich films show SiOH bonding between 3300 and 3700 cm^{-1} , but no Si–Si or Si–H bonds. Complementary stoichiometry measurements by energy dispersive X-ray analysis at low electron voltage (3.6 keV) confirm the high oxygen contents in these films $[\text{O}]/[\text{Si}] \approx 2.3$. This quantitative analysis of $[\text{O}]/[\text{Si}]$ ratio has been performed by taking into account this ratio measured from the spectrum of silica obtained under similar analysis conditions.

4. Summary and conclusion

A dual-plasma reactor (surface wave-coupled MW and capacitively-coupled RF) with in situ monitoring by ellipsometry has been developed for the deposition of insulating thin films. He–Ar– O_2 mixtures have been used for the microwave plasma, while silane is injected in the MW post-discharge. Both plasmas are not strictly independent because interesting interactive effects are observed in the $\text{a-SiO}_x\text{:H}$ deposition rate.

The growth rate of $\text{a-SiO}_x\text{:H}$ increases as a function of the oxygen flow rate and the power injected to the plasma from 1.3 \AA s^{-1} with the single-RF plasma and low oxygen flow up to 33 \AA s^{-1} using the double-mode plasma and sufficient oxygen to obtain stoichiometric material. From our results, we deduce: (1) a strong dissociation of silane by oxygen-related species produced in the MW plasma; (2) a high sticking coefficient of the silicon-related deposition precursors; (3) and enhanced dissociation of silane when the RF plasma is added to the MW plasma. From these preliminary results, it can be inferred that this reactor is well adapted for the deposition of insulating thin

films. Future studies will aim at increasing the MW and RF power, porosity characterization, and electronic properties assessment.

The authors are grateful to J. Perrin for valuable suggestions and discussions concerning plasma physics. They would like to thank J. Huc, J.Y. Parey, G. Rose, J.-C. Rostaing and F. Coeuret for helpful discussions and technical assistance. This project has been granted by the Ministry for Research.

References

- [1] M. Moisan, C. Barbeau, R. Claude, C.M. Ferreira, J. Margot, J. Paraszczak, A.B. Sá, G. Sauvé and M.R. Wertheimer, *J. Vac. Sci. Technol.* B9 (1991) 8.
- [2] C.M. Ferreira, L.L. Alves, M. Pinheiro and A.B. Sá, *IEEE Trans. Plasma Science* 19 (1991) 229.
- [3] J.M. Klemberg-Sapieha, O.M. Küttel, L. Martinu and M.R. Wertheimer, *Thin Solid Films* 193&194 (1990) 965.
- [4] R. Etemadi, O. Leroy, B. Drévillon and C. Godet, *Mater. Res. Soc. Symp. Proc.*, San Francisco, Apr. 1994, p. 109.
- [5] R. Etemadi, C. Godet, O. Leroy, P. Morin and B. Drévillon, in: *Proc 12th Photovoltaic Solar Energy Conferences*, Amsterdam, Apr. 1994, p. 342.
- [6] J.C. Rostaing, F. Coeuret, B. Drévillon, R. Etemadi, C. Godet, J. Huc, J.Y. Parey and V.A. Yakovlev, *Thin Solid Films* 236 (1993) 58.
- [7] R. Etemadi et al., submitted to *J. Vac. Sci. Technol. A*.
- [8] A. Canillas, E. Pascual and B. Drévillon, *Rev. Sci. Instrum.* 64 (1993) 2153.
- [9] J.C. Russ, *Fundamentals of Energy-dispersive X-ray Analysis* (Butterworths, Boston, MA, 1984).
- [10] I. Fan Wu, J.B. Dottellis and M. Dagenais, *J. Vac. Sci. Technol. A* 11 (1993) 2398.
- [11] D. Charlot and A. Maruani, *Appl. Opt.* 24 (20) (Oct 1985) p. 3368.
- [12] B. Drévillon, *Prog. Cryst. Growth Charact. Mater* 27 (1993) 1.
- [13] M.J. Kushner, *J. Appl. Phys.* 74 (1993) 6538.
- [14] K.A. Buckle, K. Pastor, C. Constantine and D. Johnson, *J. Vac. Sci. Technol. B* 10 (1992) 1133.
- [15] C. Charles, G. Giroult-Matlakowski, R.W. Boswell, A. Goulet, G. Turban and C. Cardinaud, *J. Vac. Sci. Technol. A* 11 (1993) 2954.
- [16] G. Lucovsky, D.V. Tsu, S.S. Kim, R.J. Markunas and G.G. Fountain, *Appl. Surf. Sci.* 39 (1989) 33.



ELSEVIER

Journal of Non-Crystalline Solids 187 (1995) 75–80

JOURNAL OF
NON-CRYSTALLINE SOLIDS

Hydrogen incorporation in silicon oxide films deposited by ArF laser-induced chemical vapor deposition

E.G. Parada^{a,*}, P. González^a, J. Serra^a, B. León^a, M. Pérez-Amor^a, M.F. da Silva^b,
H. Wolters^c, J.C. Soares^c

^a Departamento de Física Aplicada, Universidade de Vigo, Lagoas-Marcosende 9, 36280 Vigo (Galicia), Spain

^b Departamento de Física, ICEN/INETI, 2685 Sacavém, Portugal

^c Centro de Física Nuclear da Universidade de Lisboa, Av. Prof. Gama Pinto 2, 1699 Lisbon, Portugal

Abstract

An evaluation of the hydrogen content present in silicon oxide thin films obtained from a gas mixture of N_2O and SiH_4 by ArF excimer laser-induced chemical vapor deposition in a parallel configuration reactor is presented. By tuning the oxidant–monosilane ratio, a complete set of films ranging from hydrogen-rich silicon suboxides to silicon dioxide were deposited. To evaluate the bonded hydrogen in the matrix and the total quantity of hydrogen atoms, the films were respectively analyzed by Fourier-transform infrared (FTIR) spectroscopy and elastic recoil detection analysis (ERDA). Additional analyses by ellipsometry and Rutherford backscattering spectrometry (RBS) were performed. As the silane quantity in the gas mixture increases, the RBS measurements reveal a continuously decreasing film stoichiometry towards suboxides. Simultaneously, a dramatical increase in the quantity of Si–H bonds is observed in the FTIR spectra, but an unexpected decrease in the total number of hydrogen atoms is detected by ERDA. The total hydrogen content correlates with the film growth rate, while the Si–H bond incorporation correlates with the SiH_4 content in the gas mixture.

1. Introduction

The use of UV chemical vapor deposition (UVCVD) methods to obtain dielectric films for microelectronic device technology is growing due to the need for finding low-temperature deposition processes [1,2]. Among these techniques, the ArF excimer laser-induced CVD in a parallel configuration geometry has evoked interest for its high de-

position rates over large areas with no radiation damage and easy control over film properties [3–6].

In spite of silica films by ArF laser CVD using N_2O and SiH_4 gas mixture being a well-studied process, the chemical reaction paths induced by UV photons and the subsequent incorporation of photofragments in the films are not well understood yet. Among the main parameters determining the deposition process and the resulting film properties, the gas mixture composition and the total gas pressure are the more important ones. As described elsewhere [7], films with different

* Corresponding author. Tel: +34-86 812 216. Telefax: +34-86 812 201. E-mail: egparada@seinv.cesga.es.

compositions and densities can be obtained by appropriate control of the oxidant-monosilane ratio.

Due to the use of silicon hydrides as precursors, some of the H atoms contained in the precursor gases are incorporated in the film in different chemical paths, particularly when deposition is performed at low temperatures ($< 300^{\circ}\text{C}$). The H incorporation in the film has an important influence in chemical and electrical film properties and in the film stability. For this reason, good control over the chemically bonded hydrogen as well as the total quantity of H atoms in the film is necessary. In this contribution, a study of the evolution of the H incorporated in the film as a function of the oxidant-monosilane ratio is presented.

2. Experimental

An extensive set of silicon oxide films were obtained by irradiation of a N_2O , SiH_4 gas mixture diluted in Ar (purging gas) inside a reaction chamber which has been described previously [8]. The oxidant-monosilane flow ratio was changed from 2.5 to 100 by varying the silane flow rate, keeping the N_2O and the Ar flow rates constant at 40 and 60 sccm, respectively. The total pressure in the reactor was kept constant at 40 Torr by an exhaust control valve. Photons were supplied by a Questek 2460 ArF excimer laser ($\lambda = 193\text{ nm}$). The rectangular beam is focussed and enters into the reactor parallel to the substrate through a Suprasil window. The substrate is placed horizontally on a temperature-controlled holder. All experiments were performed at a fixed laser pulse energy in the chamber of 40 mJ at 10 Hz (energy density = 200 mJ cm^{-2}) and on (100) silicon samples at 250°C . This serves to deposit well-adhering and scratch-resistant films for a useful range of gas flow rates and total pressure in the chamber [2].

The refractive index, n , and thickness of the films were measured by single-wavelength ($\lambda = 632.8\text{ nm}$) ellipsometry. Information about the resonant bonds in the film in the infrared region was obtained by transmission Fourier-transform spectroscopy (FTIR). The bonded H is detected by infrared spectroscopy as Si-H ($2100\text{--}2260\text{ cm}^{-1}$ and 880 cm^{-1} bands), Si-OH and H_2O

($3300\text{--}3700\text{ cm}^{-1}$ and 940 cm^{-1} vibrations [9–12]. Film stoichiometries were determined by Rutherford backscattering spectrometry (RBS). Elastic recoil detection analysis (ERDA) was used to quantify the hydrogen content of the films.

3. Results

The presence of a broad range of Si-H and Si-OH groups detected by FTIR is shown in Fig. 1. Special attention was paid to the Si-H stretching mode because this band is not overlapped by the presence of any other vibration mode. A very clear evolution of the Si-H modes is observed when oxidant-monosilane ratios are increased. Simultaneously, the Si-O bending band emerges indicating that full-oxidized films have been obtained. Furthermore, the presence of hydroxyl groups (Si-OH and absorbed water) incorporated into the film during the ageing in atmospheric humidity, was observed in the bands located at 3350 and 940 cm^{-1} (Fig. 1). The evolution of the Si-OH and the Si-H bonds with the $[\text{N}_2\text{O}] / [\text{SiH}_4]$ ratio is shown in Fig. 2. The decrease in the Si-H stretching area correlates with an increase in the silanol groups, reaching both the saturated values for ratios ≥ 20 .

The stoichiometry and the hydrogen content in the film was obtained using RBS and ERDA techniques, respectively. No carbon or nitrogen was detected in the films. These contaminants, although usually quite relevant for low-temperature processes and when using N_2O as oxygen donor, do not reach the level of sensitivity of the techniques used. The H content as determined by ERDA versus the precursor gases ratio is plotted in Fig. 3. As observed, the higher the $\text{N}_2\text{O}/\text{SiH}_4$ flow rate ratio, the greater the H content in the film. Opposite tendencies are observed in Fig. 4, where the quantity of Si-H bonds and H content are plotted as a function of deposition growth rate. The Si-H bond concentration was calculated from the FTIR data and the film thickness [13, 14].

In addition, ellipsometry and RBS analyses were performed to get a more complete knowledge of the film. From the ellipsometric and infrared characterization of the layers, the evolution of refractive

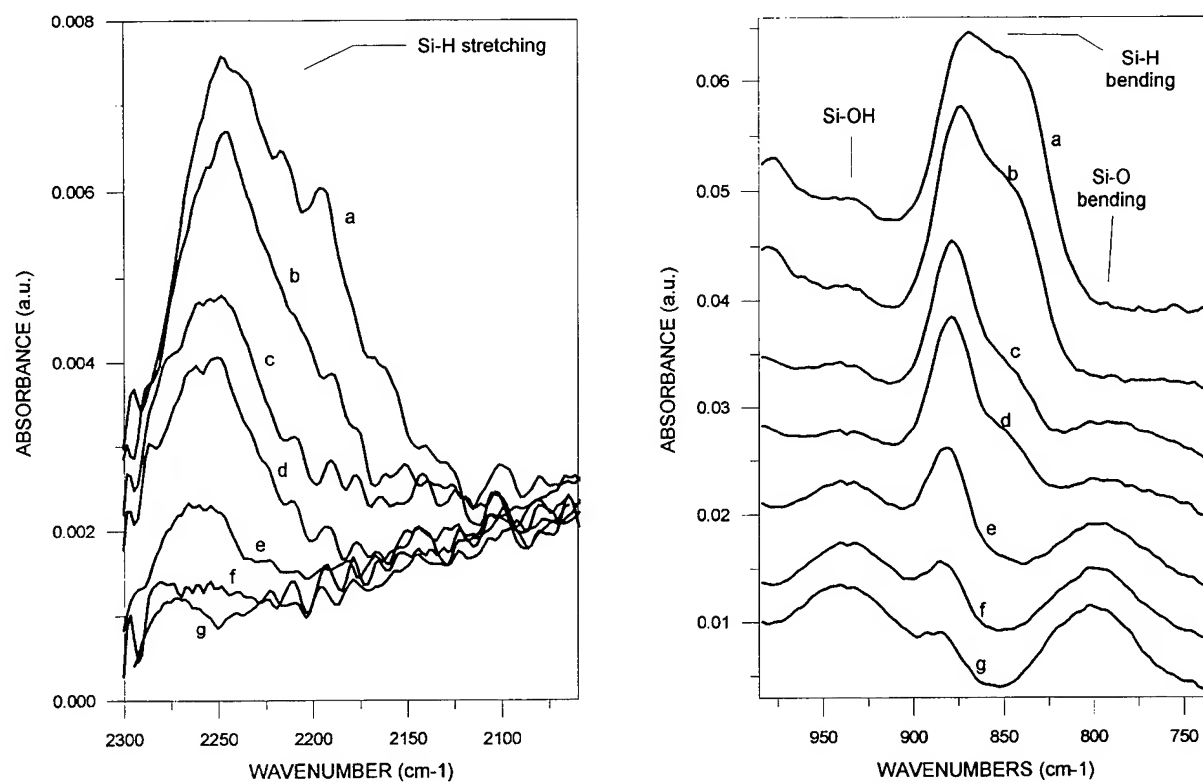


Fig. 1. Partial infrared spectra of samples deposited at different $[\text{N}_2\text{O}] / [\text{SiH}_4]$ ratios: (a) 2.5, (b) 5, (c) 10, (d) 15, (e) 20, (f) 50, (g) 100.

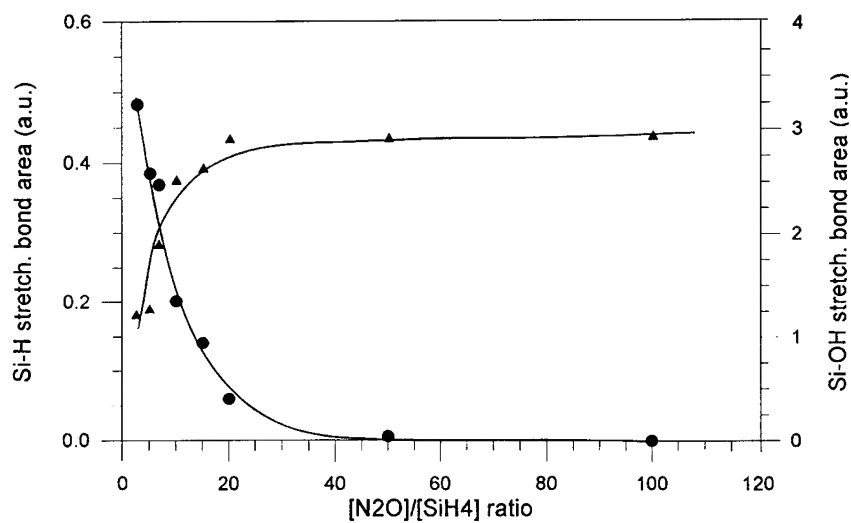


Fig. 2. IR peak area evolution of the bands assigned to the Si-H stretching (●) and Si-OH (▲) vibrations with the $[\text{N}_2\text{O}] / [\text{SiH}_4]$ ratio.

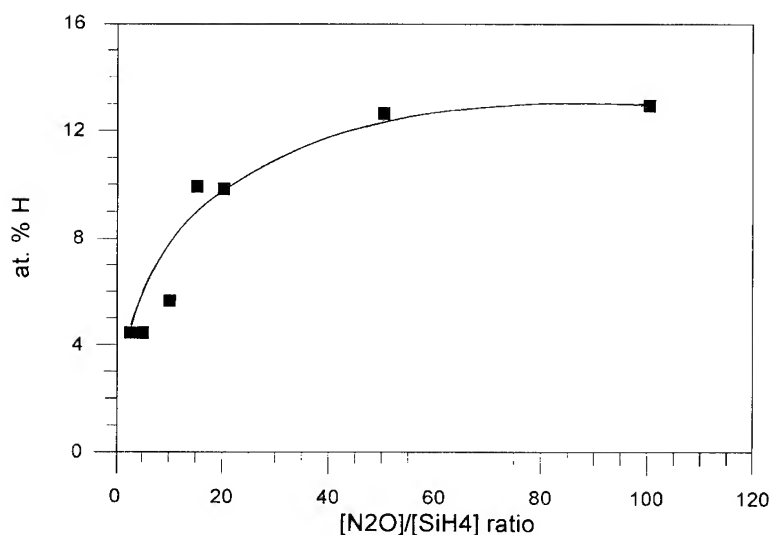


Fig. 3. Hydrogen content of samples determined by ERDA as a function of precursor gases concentration.

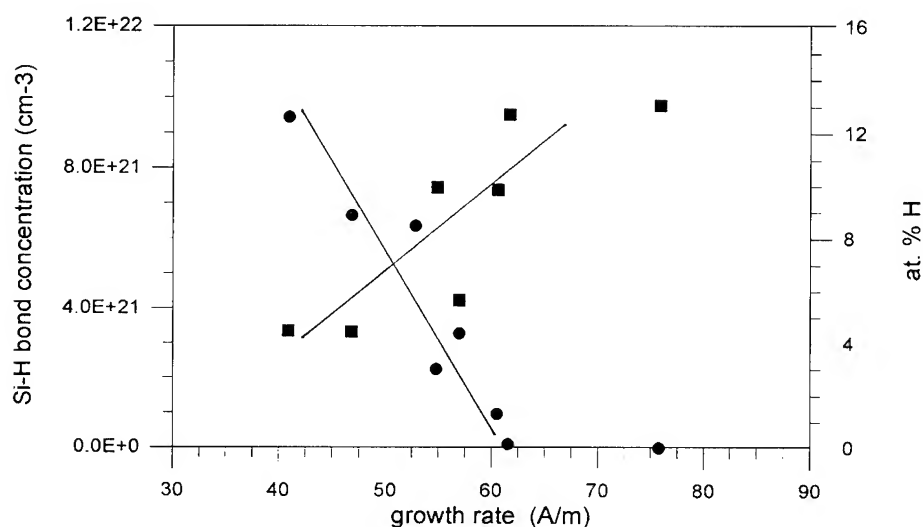


Fig. 4. Concentration of Si-H bonds (●) determined by FTIR and hydrogen content (■) measured by ERDA versus film growth rate.

indices, film stoichiometry and main spectral features as a function of flow rate ratios were analyzed. For low N_2O/SiH_4 flow rate ratios the deposited films exhibit refractive index values higher than those of thermally oxidized films ($n = 1.46$), decreasing towards saturation values around 1.45 as the ratios become higher. This evolution is also in agreement with the stoichiometric values observed

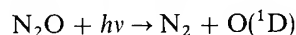
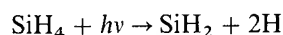
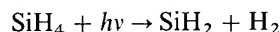
by RBS. As the oxidant quantity in the gas mixture increases, the deposited material changes from suboxide ($SiO_{1.4}$) to stoichiometric silica (SiO_2). Moreover, the FTIR data confirm this behavior. The band assigned to the Si-O-Si stretching bond mode [15, 16] quickly shifts from 1043 cm^{-1} to a saturation value of 1070 cm^{-1} , commonly assigned to the stoichiometric low-temperature

deposited silica films, as the $\text{N}_2\text{O}/\text{SiH}_4$ flow rate ratio increases. Simultaneously, a decrease is observed in the width at half-maximum (FWHM) for this mode, from 90 to 68 cm^{-1} in the saturation region. As the oxidant presence increases, the film is quickly oxidized, getting a smaller range of non-stoichiometric Si–O groups. The films reach the stoichiometric properties for SiO_2 layers for a relatively low $\text{N}_2\text{O}/\text{SiH}_4$ flow rate ratio in comparison with other low-temperature methods. Similar behaviors were already observed and analyzed in a previous work [7].

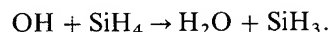
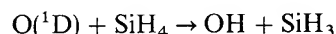
4. Discussion

These effects are based upon the fact that chemical reactions induced by ArF laser photons in the gas phase generate a long set of products such as SiO_xH_y , H_2 and H_2O that can be incorporated into the film.

Precursor gases, nitrous oxide ($\sigma = 1.04 \times 10^{-19} \text{ cm}^2$ per molecule [7]) and silane ($\sigma = 1.2 \times 10^{-21} \text{ cm}^2$ per molecule for single-photon absorption [17] and $\sigma = 6 \times 10^{-44} \text{ cm}^4$ per molecule for two-photon absorption [18]) are photodissociated, resulting in many species and radicals, such as



and the subsequent chemical reactions, for instance:



Therefore, the products of the reactions in the gas phase are controlled by the nitrous oxide–silane ratio. For this reason, the higher the silane partial pressure, the higher the bonded Si–H quantity in the silicon oxide matrix (Figs. 1 and 2). Moreover, from the region 2000–2260 cm^{-1} in the infrared spectra, additional information about the local environment of the Si–H group in the silicon oxide matrix is obtained. Four distinct subbands located

at 2000, 2100, 2195, and 2260 cm^{-1} can be assigned to $\text{HSi-Si}_{3-n}\text{O}_n$ ($n = 0 - 3$) local environment respectively [10]. For high silane ratios, there is the contribution of two subbands centered at 2260 and 2195 cm^{-1} (Fig. 1), which correspond with a tetrahedral environment for the Si of HSi-O_3 and HSi-SiO_2 , respectively. As the silane is reduced in the gas mixture, both peaks decrease under the FTIR detection level, which means that the layers are being gradually more oxidized, showing that the matrix evolves towards SiO_2 .

On the other hand, from Figs. 4 and 2, it is quite clear that while the hydrogen content correlates with the deposition rate, the Si–H bond incorporation does it with the SiH_4 content in the gas mixture. As the $\text{N}_2\text{O}/\text{SiH}_4$ flow rate ratio is increased, higher growth rates are achieved because the nitrous oxide molecules exhibit a greater UV photon absorption cross-section than silane. When these photoproduct species reach the substrate surface at relatively low temperatures, they do not have enough time to avoid the creation of voids and/or μ -voids containing, mainly, H_2 and H_2O , which is in agreement with the increase in H atoms observed by ERDA (Fig. 4) and the increase of silanol groups observed by FTIR (Fig. 2). It should be noted that molecular hydrogen is not detectable by infrared spectroscopy.

5. Conclusions

The incorporation of hydrogen in silicon oxide films deposited by ArF laser-CVD using N_2O and SiH_4 as precursor gases was analyzed. Two opposite tendencies were found for the Si–H bond quantity and the total H content in the film when the oxidant–monosilane ratio was varied. A correlation between the film growth rate and the precursor gases ratio explains these effects by the generation of voids and/or μ -voids containing, mainly, H_2 and H_2O in the film.

The authors wish to thank J. Pou and D. Fernández for their collaboration in the experimental work and Rodrigo V. Mateus for helping with ERDA analyses. This work was supported under CICYT project MAT 92'0373.

References

- [1] I.W. Boyd and R.B. Jackman, eds., *Photochemical Processing of Electronic Materials* (Academic Press, London, 1992).
- [2] P. González, D. Fernández, J. Pou, E. García, J. Serra, B. León and M. Pérez-Amor, *Thin Solid Films* 218 (1992) 170.
- [3] P.K. Boyer, W.H. Ritchie and G. J. Collins, *J. Electrochem. Soc.* 129 (1982) 2155.
- [4] E.W. Sabin, *Proc. Electrochem. Soc.* 86 (1986) 284.
- [5] A. Tate, K. Jinguri, T. Yamada and N. Takato, *Appl. Phys.* A38 (1985) 221.
- [6] T. Szörényi, P. González, D. Fernández, J. Pou, B. León and M. Pérez-Amor, *Thin Solid Films* 193&194 (1990) 619.
- [7] P. González, D. Fernández, J. Pou, E. García, J. Serra, B. León, M. Pérez-Amor and T. Szörényi, *Appl. Phys.* A57 (1993) 180.
- [8] T. Szörényi, P. González, D. Fernández, J. Pou, B. León and M. Pérez-Amor, *Appl. Surf. Sci.* 46 (1990) 206.
- [9] G. Lucovsky, J. Yang, S.S. Chao, J.E. Tyler and W. Czubyti, *Phys. Rev.* B28 (1983) 3225.
- [10] D.V. Tsu, G. Lucovsky and B.N. Davidson, *Phys. Rev.* B40 (1989) 1795.
- [11] W.A. Pliskin, *J. Vac. Sci. Technol.* 14 (1977) 1064.
- [12] W.A. Pliskin and W.A. Lehman, *J. Electrochem. Soc.* 112 (1965) 1013.
- [13] A.C. Adams, F.B. Alexander, C.D. Capio and T.E. Smith, *J. Electrochem. Soc.* 128 (1981) 1545.
- [14] K.H. Beckmann and N.J. Harrick, *J. Electrochem. Soc. Solid State Sci.* 118 (1971).
- [15] G. Lucovsky, M.J. Manitini, J.K. Srivastava and E.A. Irene, *J. Vac. Sci. Technol.* B5 (1987) 530.
- [16] W.A. Pliskin, *Thin Solid Films* 2 (1968) 1.
- [17] J.H. Clark and R.G. Anderson, *Appl. Phys. Lett.* 32 (1978) 46.
- [18] C. Fuchs, E. Boch, E. Fogarassy, B. Aka and P. Siffert, *Laser and Particle-beam Chemical Processing for Microelectronics* (Materials Research Society, Pittsburgh, PA, 1988) p. 361.



ELSEVIER

Journal of Non-Crystalline Solids 187 (1995) 81–85

JOURNAL OF
NON-CRYSTALLINE SOLIDS

Effects of plasma treatment on the properties of room-temperature liquid-phase deposited (LPD) oxide films

Ching-Fa Yeh*, Shyue-Shyh Lin

Department of Electronics Engineering and Institute of Electronics, National Chiao-Tung University, Hsinchu, Taiwan

Abstract

Effects of plasma treatment including H_2 or O_2 on the properties of LPD oxide were investigated. After plasma treatment, the physicochemical characteristics of LPD oxide films were greatly improved. No matter whether with H_2 or O_2 plasma treatment, the LPD oxide film exhibited higher refractive index and lower P-etch rate than as-deposited films. The electrical characteristics were also improved. This indicates that plasma treatment can effectively passivate the vacancies in LPD oxide. It was also found that the treatment using O_2 source was better than using H_2 . This was the same as for the case of thermal annealing. Because the plasma treated LPD oxide exhibited superior results to the thermally annealed one and the temperature in plasma treatment was much lower than that in thermal annealing, plasma treatment is more suitable for improving the characteristics of LPD oxide films.

1. Introduction

In recent years, much attention has been paid to liquid-phase deposited (LPD) silicon dioxide [1–6] for its extremely low-temperature processing and simple apparatus. The electrical properties of LPD oxide are better than those of chemical vapor deposited (CVD) oxide [3], but still worse than those of thermal oxide. In order to further enlarge the application of LPD oxide film to VLSI fabrication, much higher quality of LPD oxide and a better interface have to be achieved.

To improve the quality of the CVD oxide film, thermal annealing has usually been adopted [7–10]. In the previous study by Yoshitomi et al.

[11], LPD oxide films after O_2 thermal annealing showed much improved characteristics. However, the annealing temperature had to be 600°C , which was so high that the merit of low-temperature LPD oxide would be lost. In this study, we have tried to use plasma treatment, which is low-temperature process, to improve the properties of LPD oxide.

2. Experimental

Experimental apparatus and basic equilibrium equations for LPD oxide deposition have been described in detail in our previous study [4]. Thus, we only give a brief description of the LPD process in this study.

The immersing solution was prepared with 75 g of silica added to 1.4 l of H_2SiF_6 solution at 23°C . After stirring and filtering out undissolved silica,

* Corresponding author. Tel: +886-35712 121, ext. 3288
Telefax: +886-35711 992.

a solution saturated with silica was obtained. Then, the saturated solution was diluted to a concentration of 3.8 mol/l. In order to make a supersaturated state in the solution, a boric acid solution (0.1 mol/l) was added. When a Si substrate was immersed into the supersaturated solution, a deposition of oxide film started rapidly. All the samples were prepared at 30°C, while the film thickness was mainly controlled by immersion time.

The n-type (100) substrates with 4–7 Ω cm were used. After deposition, the samples were subject to H₂ or O₂ plasma treatment at 300°C for one hour. Plasma treatment was performed in a commercial 13.5 MHz parallel-plate plasma reactor with power density of 0.7 W/cm². A gas mixture of H₂/N₂ (60 sccm/60 sccm) at 0.25 torr was used in the H₂ plasma treatment and O₂ gas (150 sccm) at 0.25 torr was used in the O₂ plasma treatment. For comparison, some samples were treated by thermal annealing at 600°C in O₂ ambient.

The film thickness and refractive index were measured ellipsometrically. The P-etch rate was examined using the solution (48% HF:70% HNO₃:H₂O = 3:2:60 in volume) at room temperature. The chemical composition was analyzed by Auger electron spectroscopy (AES). The electrical characteristics of the LPD oxide film, such as leakage current, breakdown field and interface state density were evaluated with metal oxide semiconductor (MOS) capacitors. The area of the Al gate electrode was 0.126 mm².

3. Results and discussion

3.1. Physical/chemical effect

To understand the effects of plasma treatment on the physical/chemical properties of the films, we investigated the refractive index and P-etch rate first. The results for LPD oxide films with and without plasma treatment are summarized in Table 1. The results of the sample with 600°C O₂ thermal annealing are also shown for comparison. At first, we found that the refractive index of the LPD oxide after plasma treatment increased nearly to the value of thermal oxide. As reported in other studies, the oxide film with a lower refractive index

Table 1

Summary of refractive index and P-etch rate of LPD oxide films with plasma treatment and thermal annealing

LPD oxide films	Refractive index, <i>n</i>	P-etch rate (Å/s)
As-deposited	1.43	20
H ₂ plasma	1.45	9.2
O ₂ plasma	1.456	7.5
600°C O ₂ annealing	1.432	7.6

had a less dense structure [12] and contained fluorine [13]. So, from the change of refractive index, we concluded that the LPD oxide structure was denser after plasma treatment. This conclusion was consistent with the results of the P-etch rate test, which indicated that the P-etch rate of LPD oxide decreased after plasma treatment. The denser the LPD oxide structure becomes, the lower the value of the P-etch rate. The reason why LPD oxide became denser after plasma treatment may also be due to the release of fluorine contained in the film. This fluorine-release effect could also increase the refractive index of LPD oxide [13]. Studies concerning the mechanism of release for Si–F bonds are still in progress.

Comparing the difference between O₂ and H₂ plasma treatment in Table 1, we find that the refractive index of LPD oxide after O₂ plasma treatment had a higher value of refractive index and lower value of P-etch rate than those after H₂ plasma treatment. This was consistent with the results of thermal annealing [11]. To investigate this phenomena, the atomic composition for the LPD oxide with O₂ or H₂ plasma treatment was studied. Figs. 1(a)–(c) showed the result for as-deposited LPD oxide and LPD oxide after O₂ or H₂ plasma treatment, respectively. The AES depth profile indicated that O/Si ratio in the LPD oxide with O₂ plasma treatment was larger than that with H₂ plasma treatment. These results imply that the O₂ plasma diffused O₂ molecules into the film and filled the oxygen vacancies [14]. As a result the film became much denser in structure. Because the oxygen molecules were more suitable to fill the oxygen vacancies, the effect of the O₂ plasma treatment

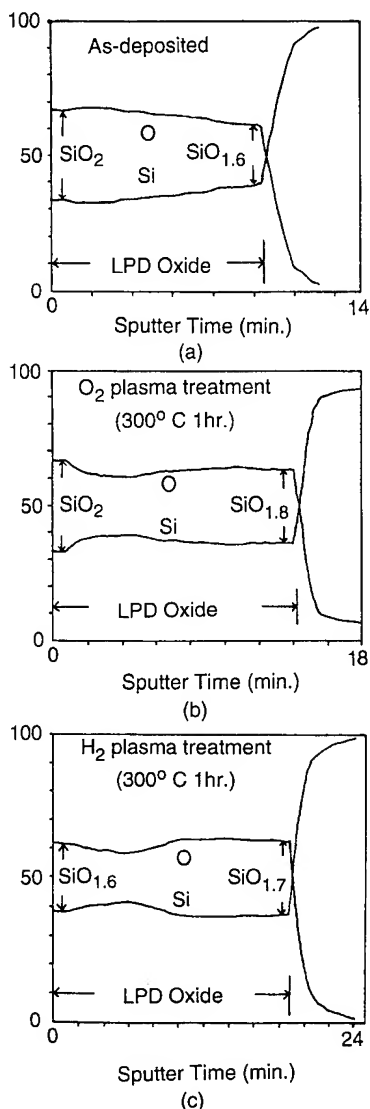


Fig. 1. AES depth profiles for the LPD oxide (a) as-deposited, (b) with O_2 plasma treatment, and (c) with H_2 plasma treatment.

was better than that of H_2 plasma treatment on improving the properties of LPD oxide.

As shown in Table 1, the effect of plasma treatment appears to be better than that of the thermal annealing for the refractive index and the P-etch rate. It implies that plasma treatment is a good procedure for replacing thermal annealing to improve the properties of LPD oxide.

3.2. Electrical effects

To further check the effect of plasma treatment on the properties of LPD oxide, the electrical characteristics of LPD oxide including I - V and interface-state were investigated. The typical I - V characteristics of LPD oxide films before and after plasma treatment for 1 h are shown in Fig. 2. The characteristics of the sample with O_2 thermal annealing are also shown for comparison. The plasma-treated samples showed a lower leakage current at low electric field (< 3 MV/cm) and a higher breakdown field than as-deposited and thermal annealed samples. In particular, the sample with the O_2 plasma showed a much higher breakdown field than that with H_2 plasma. This phenomenon was suspected to be due to less oxygen vacancies in the structure of O_2 plasma-treated LPD oxide. That is, the LPD oxide with O_2 plasma treatment had a denser structure and better atomic composition, and as a result exhibited better electrical characteristics. In comparison with O_2 thermal annealing (600°C), the results also reveal that the O_2 plasma treatment could effectively passivate the defects in LPD oxide film at low temperature. The histogram of breakdown field for the samples including as-deposited, O_2 annealed, H_2 plasma

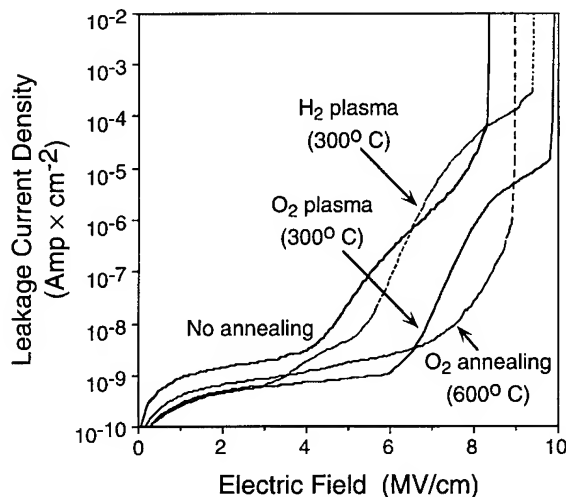


Fig. 2. J - E characteristics for the samples with and without plasma treatment and the sample with O_2 thermal annealing at 600°C .

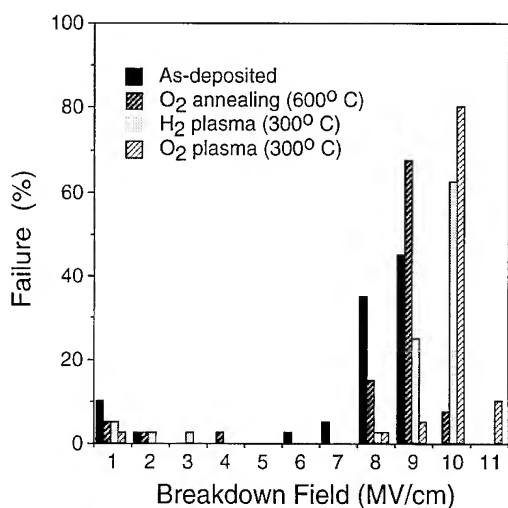


Fig. 3. Breakdown field histogram for the LPD oxide with or without plasma treatment and the sample with O₂ thermal annealing at 600°C.

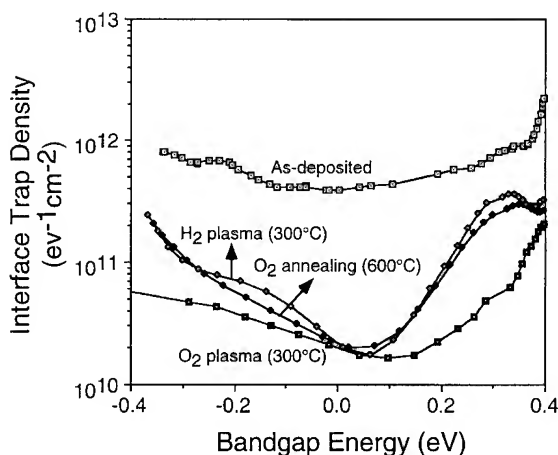


Fig. 4. Interface state density distribution for the samples with and without plasma treatment and the sample with O₂ thermal annealing at 600°C. Lines are drawn as guides for the eye.

and O₂ plasma are shown in Fig. 3. We find that the O₂ plasma-treated LPD oxide has a better distribution at high breakdown field than others.

To investigate the interface characteristics of LPD oxide after plasma treatment, the interface trap densities (D_{it}) for the samples after O₂ or H₂ plasma treatment were calculated by the Terman method [15]. As shown in Fig. 4, the interface trap

density was about $5 \times 10^{11} \text{ eV}^{-1} \text{ cm}^{-2}$ for as-deposited samples, while it was as low as $2 \times 10^{10} \text{ eV}^{-1} \text{ cm}^{-2}$ for O₂ plasma treated samples. The improvement of D_{it} at midgap was almost the same for the samples with O₂ or H₂ plasma treatment, and it is suspected that H or O could passivate the interface traps at midgap [16]. In addition, the reduction of D_{it} at the band edge by O₂ plasma treatment was more obvious than that by H₂ plasma treatment. The interface traps near the band edge were attributed to be oxygen vacancies and weak Si–O bonds [17], so in O₂ plasma treatment oxygen might diffuse into the films and reduce D_{it} near the band edge.

4. Summary

The physicochemical characteristics of LPD oxide films after plasma treatment exhibit great improvement. They have higher refractive index and lower P-etch rates because they have denser structures and less fluorine. The electrical characteristics also exhibited much improvement: there is a lower leakage current and higher breakdown field due to the passivation effect. The plasma treatment using O₂ was more effective than using H₂. The plasma treatment also appeared superior to thermal annealing. Thus we conclude that plasma treatment is a more suitable method for improving the characteristics of LPD oxide films.

This work was supported by the National Science Council, Taiwan, under contract number NSC-83-0404-E-009-121.

References

- [1] N. Nagayama, H. Honda and H. Kawahara, J. Electrochem. Soc. 135 (1988) 2013.
- [2] T. Goda, H. Nagayama, A. Hishinuma and H. Kawahara, Mater. Res. Sym. Proc. 105 (1988) 283.
- [3] C.F. Yeh, S.S. Lin, C.L. Chern and Y.C. Yang, IEEE Electron Device Lett. EDL-14 (1993) 403.
- [4] C.F. Yeh, S.S. Lin, T.Z. Yang, C.L. Chern and Y.C. Yang, IEEE Trans. Electron Devices ED-41 (1994) 173.
- [5] T. Horiuchi, K. Kanba, T. Homma, Y. Murao and K. Okumura, IEEE Trans. Electron Devices ED-40 (1993) 1455.

- [6] T. Homma, T. Katoh, Y. Yamada and Y. Murao, *J. Electrochem. Soc.* 140 (1993) 2410.
- [7] J. Lee, I.C. Chen and C. Hu, *IEEE Electron Device Lett.* EDL-7 (1986) 506.
- [8] B.K. Ip, K.C. Kao and D.J. Thomson, *Solid State Electron.* 33 (1990) 123.
- [9] M. Shyang-Chyong Luo and C.T. Sah, *Proc. Int. VLSI-TSA Conf.* (1987).
- [10] C.T. Sah, *Solid State Electron.* 33 (1990) 147.
- [11] S. Yoshitomi, S. Tomioka and N. Haneji, *Proc. 1992 Int. Electron Devices and Materials Symp.* (1992) p. 22.
- [12] W.A. Pliskin, *J. Vac. Sci. Technol.* 14 (1977) 1064.
- [13] J.W. Fleming and D.L. Wood, *Appl. Opt.* 22 (1983) 3102.
- [14] J. Perriere, B. Pelloie, E. Fogarassy and A. Slaoui, *Appl. Surf. Sci.* 29 (1987) 433.
- [15] E.H. Nicollian and J.R. Brews, *MOS (Metal Oxide Semiconductor) Physics and Technology* (Wiley, New York, 1982).
- [16] T. Sakurai and T. Sugano, *J. Appl. Phys.* 52 (1981) 2889.
- [17] H. Fukuda, M. Yasuda and T. Iwabuchi, *J. Appl. Phys.* 72 (1992) 1906.



ELSEVIER

Journal of Non-Crystalline Solids 187 (1995) 86–90

JOURNAL OF
NON-CRYSTALLINE SOLIDS

Oxygen-rich phase segregation in PECVD a-SiO_x:H semi-insulators

G. Suchaneck*, O. Steinke, B. Alhallani, K. Schade

Dresden University of Technology, Institute of Semiconductor Technology and Microsystems, Mommsenstr. 13, D-01062 Dresden, Germany

Abstract

Photosensitive, low H content ($C_H = 4\text{--}6$ at.%) a-SiO_x:H, $x \ll 1$, semi-insulating films were deposited by means of the admixture of small amounts of oxygen during plasma enhanced chemical vapour deposition (PECVD) to the monosilane process gas. Oxygen incorporation into the films was favoured by a rotating two-pole magnetic field (0–27 mT) and by increasing the power-source frequency from 1.2 to 13.56 MHz. Film characterization was performed measuring UV/VIS/IR transmission, photo- and dark conductivities and determining the gap state distribution by the constant photocurrent method (CPM). IR-analysis included also the previously neglected formation of dihydride configurations. Three Si–O–Si stretching vibrations at 980, 1030 and 1080 cm^{−1} assigned to different oxydation states were found. Thus, the reported shift of the Si–O stretching vibration frequency with increasing oxygen concentration is caused by a changing distribution of bonding configurations with a different oxidation state. Evidence for the formation of a clustered O-rich phase was found in films with an oxygen content as low as 0.4 at.%. The deposition rate dependence of the defect state density was consistent with a model of surface reactions including a two-step dangling bond termination via an intermediate Si–O–Si state whose first step of Si–O–Si formation is rate determining and whose second step is the recombination of two Si–O–Si configurations releasing O₂ and leaving two Si–Si bonds. The distribution of oxygen induced defect states was calculated from measured CPM data.

1. Introduction

Amorphous silicon insulators with a small oxygen content a-SiO_x:H, $x \ll 1$, are a suitable material for a variety of thin film applications including pn-junction passivation layers, non-volatile memory devices, X-ray sensors, vidicons and xerographic copying drums. The incorporation of small

amounts of oxygen into glow discharge a-Si:H films improves the charge acceptance of xerographic drums [1]. A remarkable enhancement of the photoconductivity was observed in sputtered a-Si:H films doped with a slight amount of oxygen due to an electron mobility enhancement and a reduced Si dangling bond density [2].

A great deal of work has been done on IR-transmission analysis of the oxygen bonding environment in plasma enhanced chemical vapour deposition (PECVD) deposited a-SiO_x:H films [3–13]. Up to now IR-transmission analysis was

* Corresponding author. Tel: +49-351 463 4420. Telefax: +49-351 463 7721. E-mail: kottwitz@ehmgwl.et.tu-dresden.de.

restricted to the situation in which the hydrogen is incorporated in the monohydride configuration [3,5,12], although evidence of dihydride bonding is found from analyzing data in Ref. [3,5].

The nature of localized states in a-SiO_x:H was investigated in [14]. It was found that the incorporation of oxygen increases the density of charged dangling bonds in comparison to a-Si:H.

This work deals with low hydrogen content a-SiO_x:H films deposited by PECVD varying the strength of rotating magnetic fields (0–27 mT) and the rf frequency (1, 2; 13.56 MHz).

2. Experimental procedure

Magnetically enhanced glow discharge deposition was performed in a capacitively coupled diode type reactor which consists of two electrodes (area – 109 cm², electrode gap – 2.5 cm) inside a cylindrical quartz glass tube. The silane gas was injected by means of a gas shower through the rf electrode. Two- and four-pole magnetic fields rotating with a frequency of 2.7 Hz in parallel with the substrate surface were generated by electromagnets positioned outside the glass tube.

Semi-insulating a-SiO_x:H film was deposited at 250°C, 40–50 Pa, 4 W (1.2 MHz) or 2 W (13.56 MHz). The admixture of small amounts of oxygen (50–500 ppm) was realized using hydrogen as a diluent.

The thickness, refractive index and optical gap of films deposited on Corning 7059 glass substrates were determined from optical transmission measurements. Electrical properties were measured using coplanar aluminium electrodes. Absorption spectra for lower photon energies (down to 0.5 eV) were derived from dc constant photocurrent measurements (CPM). The absorption coefficient at 1.2 eV was used to estimate the defect density n_D cm⁻³ = $3 \times 10^{16} \alpha_{1.2 \text{ eV}} \text{ cm}^{-1}$ [15]. The absorption spectra were deconvoluted following [16] to extract the density of states (DOS). Stability against illumination was investigated by determining the light soaked gap state densities using CPM [17].

IR-spectra of films deposited on silicon substrates were deconvoluted using software developed previously for the analysis of the C–H stretch

Table 1
Frequencies of the Si–H and Si–O stretching modes

Si–O modes		Si–H modes	
Frequency (cm ⁻¹)	Bond configuration	Frequency (cm ⁻¹)	Bond configuration
0.980	H–Si–O	1995	SiH (a-Si:H)
1.030	O ₂ Si ₂ –O–Si ₂ O ₂	2070	SiH ₂ (a-Si:H)
1.080	Si–O (a-SiO ₂)	2090	HSi ₃ O
		2150	H ₂ Si ₂ O
		2190	HSi ₂ O ₂
		2220	H ₂ SiO ₂
		2250	HSiO ₃

modes of a-Si_{1-x}C_x:H films [18]. Fit parameters (number of peaks, peak position, peak half maximum full width) as well as those known in literature were used. A nearly constant hydrogen content in the films of about 6 at.% was estimated using the 630 cm⁻¹ absorption. Local stretching vibrations of a configuration in which oxygen and hydrogen atoms are bound to the same silicon atom are summarized in Table 1.

3. Results and discussion

The deposition temperature and growth rate dependence of the defect density in a-SiO_x:H films differs from the one proposed for a-Si:H. In the latter case, based on the balance between rates of microscopic dangling bond creation and saturation reactions on the steady-state growing surface [19]:

$$n_s = C_1 \exp\left(\frac{E_1}{kT}\right) + \frac{C_2}{R} \exp\left(\frac{E_2}{kT}\right),$$

where n_s is the defect density per unit area, $C_1 = 10^7 \text{ cm}^{-2}$, $C_2 = 1.042 \times 10^{10} \text{ cm}^{-1} \text{ s}^{-1}$, $E_1 = 0.3 \text{ eV}$, $E_2 = 0.9 \text{ eV}$ and R is the growth rate in cm/s. For a-SiO_x:H we add an additional term

$$C_3 \cdot R \cdot \exp(-E_3/kT),$$

where $E_3 = 0.45 \text{ eV}$ and C_3 rises with oxygen admixture as well as with increasing magnetic field strength or rf-frequency, e.g., with increasing plasma excitation. The deposition rate dependence of the additional term is consistent with a two-step

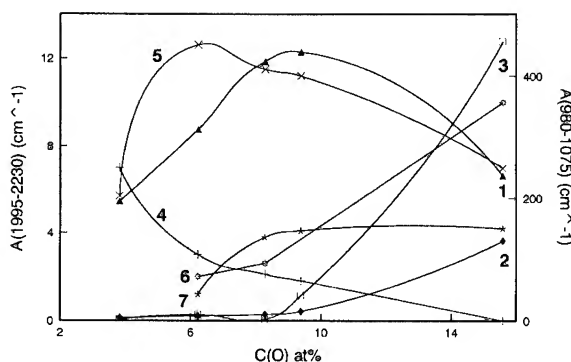


Fig. 1. Integral absorption strengths versus oxygen content: 1, 980 cm^{-1} ; 2, 1030 cm^{-1} ; 3, 1080 cm^{-1} ; 4, 1995 cm^{-1} ; 5, 2080 cm^{-1} ; 6, 2150 cm^{-1} ; 7, 2230 cm^{-1} . Lines are drawn as guides for the eye.

surface recombination process whose first step is rate determining. In the first step, an intermediate Si–O–Si state is formed. Then, the Si–O–Si configuration migrates on the growing surface. The second step is the recombination of two Si–O–Si configurations releasing O_2 and leaving two Si–Si bonds. A similar process for Si–H–Si was proposed in Ref. [20].

Fig. 1 shows the integral absorption strength of oxygen and hydrogen related peaks as a function of oxygen content. The three obtained Si–O–Si stretching modes (the first one with a peak position at 980 cm^{-1} and a FWHM value of 140 cm^{-1} , the second one around 1030 cm^{-1} and a FWHM value of about 40 cm^{-1} and a last one at 1070–1080 cm^{-1} whose FWHM value is about 80 cm^{-1}) reproduce the broad shifting from 980 to 1080 cm^{-1} found in the literature [4–8]. The threshold for the detection of the 1030 cm^{-1} vibration was as low as 0.4 at.% oxygen. The out of phase mode at 1150 cm^{-1} in which the silicon and oxygen sublattices of SiO_2 clusters move against each other was detected in samples with an oxygen content exceeding 10 at.%. Correlations of the oxygen content with the absorption strength of other oxygen related IR peaks were similar with results in Ref. [3] with the exception of a weaker dependence of the absorption at 780 cm^{-1} on oxygen content.

To estimate the total oxygen content, the shift of the frequency of the IR vibration ω_i (Fig. 2) as well

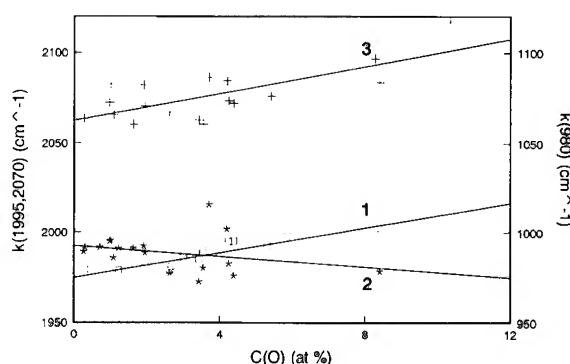


Fig. 2. Dependence of IR peak maximum wave number on oxygen content: 1, 980 cm^{-1} ; 2, 1995 cm^{-1} ; 3, 2080 cm^{-1} . Lines are drawn as guides for the eye.

as changes of the refractive index n , assumed to be frequency independent, and the effective charge of the bond e_s^* were taken into account. The number density of IR active bonds is given by [21]

$$N = \left(\frac{2c\epsilon_0 n \omega_i m}{\pi e_s^{*2}} \right) \int \frac{\alpha(\omega) d\omega}{\omega},$$

where c is the speed of light, m the reduced mass and α the absorption coefficient. With increasing oxygen content n decreases while the frequency of oxygen related IR modes increase due to the induction effect [22], e.g., the modification in the electron distribution about the silicon atoms caused by the increasing electronegativity of the nearest neighbour atoms. On the other side, the decrease of the stretching frequency of silicon–hydrogen bonds at 1995 cm^{-1} (Fig. 2) and of the Si–Si TO-phonon (not shown) is caused by lower force constants in films with more weak bonds as expected from broader band tails (Fig. 4). To quantify the induction effect more precisely, effective bond charges were calculated from known calibration constants [23]:

$$C = \frac{2c\epsilon_0 n \omega_i m}{\pi e_s^{*2}},$$

and correlated with the bond orbital radii [24]:

$$R_\sigma = R_\sigma^A - R_\sigma^B,$$

a quantum mechanical measure of bond charge transfer from a cation A to an anion B (Fig. 3).

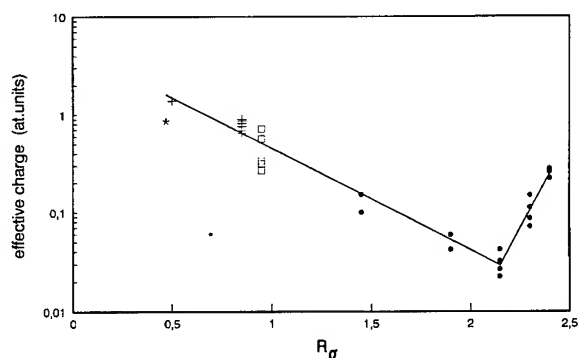


Fig. 3. Calculated effective bonds charges correlated with bond-orbital electronegativity. The Line drawn as is a guide for the eye.

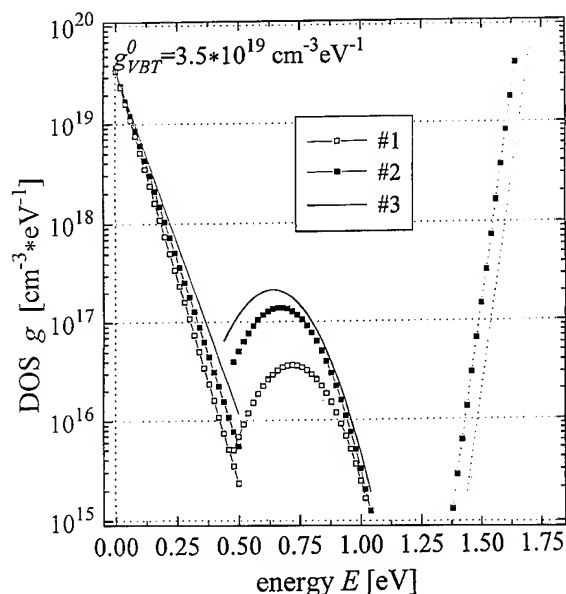


Fig. 4. Density of states of a-SiO_x:H films in dependence on oxygen content: 1, 0.7 at.%; 2, 5.5 at.%; 3, 10.8 at.%.

The observed minimum on Fig. 3 coincides with the change of the sign of the Pauling electronegativity difference. Because of the satisfactory description of the bond behaviour by a single bond in a cavity of a surrounding material whose polarizability is characterized by n^2 and taking into account the small changes of $n\pi_i$ with increasing oxygen content, the same calibration constant was used for

all oxydation states. Published values of C (980 cm⁻¹) scatter within a factor of 3 [3,9]. In this work the oxygen content was estimated using a value of $C = 1 \times 10^{19}$ cm⁻².

Local atomic arrangements of Si, O and H in a-SiO_x:H have been studied by IR-transmission for an oxygen concentration of 0.9–12.7 and 30 at.% in a-SiO_x:H films containing 10–15 at.% hydrogen [3]. Contrary to our results, up to 12.7 at.% oxygen, only bonding environments containing one oxygen atom were found. Additional IR features associated with a bonding arrangement in which the silicon atom has more than one oxygen neighbour were observed at 30 at.% oxygen.

Fig. 4 shows the deconvoluted DOS. The increase of the calculated Urbach tail slopes and the nearly constant defect peak half-widths of about 0.135 eV are in good agreement with data in [8,14]. Contrary to previous work, the defect formation energy decreases with increasing oxygen content.

4. Conclusions

(1) A clustered O-rich phase was detected by IR absorption in a-SiO_x:H films with an oxygen content as low as 0.4 at.% deposited by magnetic field enhanced PECVD. The threshold of the formation of H-Si-O_x, $x = 2, 3$, bonding configurations was obtained at an oxygen content of 2.8 at.%.

(2) The previously reported shift of the Si-O stretching vibration frequency from 980 to 1080 cm⁻¹ with increasing oxygen concentration is caused by a changing distribution of bonding configurations with a different oxydation state. Regardless of the oxydation state, the same calibration constant can be used for IR absorption oxygen content determination.

(3) Both the increasing number of weak bonds characterized by broader band tails and the decreasing dangling bond formation energy are responsible for the increase of the dangling bond density in a-SiO_x:H films.

The help of J. Schmal performing DOS calculations is greatly appreciated by the authors. This work was supported by the German Bundesministerium für Forschung und Technologie.

References

- [1] K. Wakita, Y. Nakayama and T. Kawamura, *Photogr. Sci. Eng.* 26 (1982) 183.
- [2] K. Jiranapakul and J. Shirafuji, *Jpn. J. Appl. Phys.* 26 (1987) 517.
- [3] G. Lucovsky, J. Yang, S.S. Chao, J.E. Tyler and W. Czubytyj, *Phys. Rev. B* 28 (1983) 3225.
- [4] P.G. Pai, S.S. Chao, Y. Takagi and G. Lucovsky, *J. Vac. Sci. Technol. A* 4 (1986) 689.
- [5] D. Della Sala and G. Fortunato, *J. Electrochem. Soc.* 137 (1990) 2550.
- [6] J.C. Knights, R.A. Street and G. Lucovsky, *J. Non-Cryst. Solids* 35&36 (1980) 279.
- [7] M. Nakamura, Y. Mochizuki and K. Usami, *J. Electrochem. Soc.* 132 (1985) 482.
- [8] B.G. Yacobi, R.W. Collins, G. Moddel, P. Viktorovitch and W. Paul, *Phys. Rev. B* 24 (1981) 5907.
- [9] E.C. Freeman and W. Paul, *Phys. Rev. B* 18 (1978) 4288.
- [10] T. Shimidzu, M. Kumeda, I. Watanabe and K. Kamono, *J. Non-Cryst. Solids* 35&36 (1980) 303.
- [11] W.A. Pliskin, *J. Vac. Sci. Technol.* 14 (1977) 1064.
- [12] G. Lucovsky, Z. Jing and J.L. Whitten, *J. Non-Cryst. Solids* 137&138 (1991) 119.
- [13] M.A. Paesler, D.A. Anderson, E.C. Freeman, G. Moddel and W. Paul, *Phys. Rev. Lett.* 21 (1978) 1492.
- [14] T. Shimizu, H. Kidoh, A. Morimoto and M. Kumeda, *Jpn. J. Appl. Phys.* 28 (1989) 586.
- [15] R. Zedlitz, M. Heintze and G.H. Bauer, *Mater. Res. Symp. Proc.* 258 (1992) 147.
- [16] J. Schmal, R. Kirsch, M. Albert, F. Stahr and R. Bindemann, *J. Non-Cryst. Solids* 164&166 (1993) 415.
- [17] G. Suchaneck, B. Alhallani, O. Steinke, F. Wirbeleit and K. Schade, in: *Proc. 11th Int. Symp. on Plasma Chemistry, Loughborough, Symp. Proc., Vol. 3* (1993) 787.
- [18] G. Suchaneck, M. Albert, W. Beyer, H. Stötzl and K. Schade, *J. Non-Cryst. Solids* 137&138 (1991) 701.
- [19] G. Ganguly and A. Matsuda, *J. Non-Cryst. Solids* 164&166 (1993) 31.
- [20] T. Kamei, G. Ganguly, N. Hata and A. Matsuda, *J. Non-Cryst. Solids* 164&166 (1993) 43.
- [21] M.H. Brodsky, M. Cardona and J.J. Cuomo, *Phys. Rev. B* 16 (1977) 3556.
- [22] G. Lucovsky, *Solid State Commun.* 29 (1979) 571.
- [23] G. Suchaneck, unpublished.
- [24] J.R. Chelikowsky and J.C. Phillips, *Phys. Rev. B* 17 (1978) 2453.



ELSEVIER

Journal of Non-Crystalline Solids 187 (1995) 91–95

JOURNAL OF
NON-CRYSTALLINE SOLIDS

Section 4. Silicon dioxide, structure, defects and characterization

IR study of short-range and local order in SiO_2 and SiO_x films

Igor P. Lisovskii^{a,*}, Vladimir G. Litovchenko^a, Vladimir B. Lozinskii^a, Sergey I. Frolov^a,
Hans Flietner^b, Walter Fussel^b, Elena G. Schmidt^a

^a *Institute of Semiconductor Physics of the Ukrainian Academy of Sciences, Prospekt Nauki 45, Kiev 252650, Ukraine*

^b *Hahn-Meitner Institute, Berlin D12489, Germany*

Abstract

The structure of vitreous SiO_2 and SiO_x films has been studied using IR-spectroscopy, gravimetry and computer modeling. Deconvolution of the silicon–oxygen stretching band into Gaussian profiles is carried out, the main parameters of elementary vibrational bands are determined and the corresponding Si–O–Si bond angles are calculated. Comparison of these data with oxide density and with the results of computer simulation of the silica structure in the context of the random bonding model enables definite conclusions on the nature of the fundamental structural composition of SiO_2 and SiO_x films to be made.

1. Introduction

The structure of vitreous silica is characterized by both short-range and local order. In the case of SiO_2 , SiO_4 tetrahedra form interconnecting rings of certain configurations [1]. The structure of SiO_x is often represented as a mixture of $\text{Si}-\text{O}_y-\text{Si}_{4-y}$ complexes ($0 \leq y \leq 4$) [2]. Such structural components (certain types of rings or molecular complexes) have to possess different parameters (mainly Si–O–Si bond angle values) and should be characterized by a certain range of oxygen vibrational frequencies [3]. Using deconvolution of the IR-absorption spectral curve into elementary profiles and analyzing their positions and intensities, one can

determine the kind and the contribution of structural components and estimate the structural arrangement of the constituent atoms. In the present paper such an approach was used for the analysis of SiO_2 and SiO_x film structures.

2. Experimental procedure

SiO_2 films were thermally grown at 900 or 1000°C in dry oxygen on p-type silicon substrates. Oxide thickness varied within the range $4 \leq d_0 \leq 30$ nm. SiO_x films (130–950 nm thick) of various compositions ($0.2 < x < 1$) were deposited on the Si substrates using standard chemical vapour deposition (CVD) technology. The value of x was determined using Rutherford backscattering technique.

The transmission infra-red spectra of the films were measured over the wave number range

* Corresponding author. Tel: +7-44 265 3852. Telefax: +7-44 265 8342. E-mail: mickle@semicond.kiev.ua.

$950 < \nu < 1300 \text{ cm}^{-1}$, where the main absorption band of SiO_2 and SiO_x is located. The analysis of the shape of the absorption band was carried out by the method of computer deconvolution of the absorbance curves into Gaussian profiles [3]. The position of the maximum, W , full width, H , at half-maximum and the areas, S , were determined for every elementary band. Mean values of W were used for calculation of the mean values of Si–O–Si bond angles (θ), which correspond to every elementary vibrational band [3,4]:

$$W \approx (2\pi c)^{-1} \left[\frac{2}{m} \left(\alpha \sin^2 \frac{\theta}{2} + \beta \cos^2 \frac{\theta}{2} \right) \right]^{1/2}, \quad (1)$$

where m is the mass of oxygen atom, and α and β are central and non-central force constants (610 and 100 N m^{-1} , respectively [3,4]). On the other hand, we have calculated the distribution function for the oxygen bond angles in different types of SiO_2 clusters consisting of a mixture of six- and threefold, six- and fourfold, six- and fivefold rings of SiO_4 tetrahedra. Every cluster contained about 150 atoms. The energy minimization was carried out on the basis of a semiempirical technique [5].

In the case of SiO_2 films the weight of the both side oxidized substrates and the substrates after subsequent removal of the oxide by etching was obtained with an accuracy of $2 \times 10^{-5} \text{ g}$ using an analytical balance. The difference between these values divided by $2d_0$ gave us the oxide density, ρ . The measurement of the oxide film thickness was performed by laser ellipsometry (632.8 nm) under several angles of beam incidence (45° , 60° and 70°);

the random error did not exceed 2%. The accuracy of ρ determination was within the range $\sim 3\text{--}10\%$.

3. Results

Fig. 1 shows the results of deconvolution of the main absorption band of ultrathin SiO_2 film. The parameters of both elementary bands (Table 1) correlates rather well with those obtained in earlier works [3,6,7]. According to Eq. (1) the profiles may be caused by stretching transverse vibrations of the bridging oxygen atoms with most probable Si–O–Si angles of $\sim 131^\circ$ and $\sim 143^\circ$.

In the inset of Fig. 1 the comparison between IR and gravimetry data is shown. It is important to note that properties of ultrathin oxide films strongly depend on oxide thickness [8–10]. For our samples

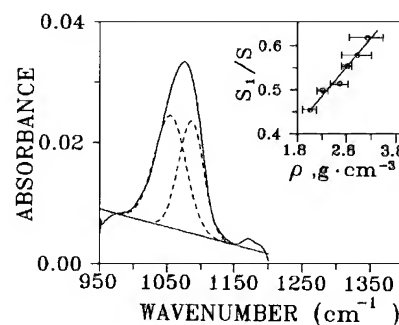


Fig. 1. Deconvolution of Si–O band into Gaussian profiles for SiO_2 film 7 nm thick. The inset shows the correlation between the contribution of the elementary band 1 and the oxide density.

Table 1
Parameters of the elementary bands

Band	Maximum position (cm^{-1})	Full width at half maximum (cm^{-1})	Si–O–Si angle	Dominant structural component
<i>SiO₂ films</i>				
1	1054 ± 4	57 ± 3	$131 \pm 1^\circ$	fourfold SiO_4 rings
2	1090 ± 5	43 ± 3	$143 \pm 1^\circ$	four- and sixfold SiO_4 rings
<i>SiO_x films</i>				
X ₁	1000 ± 10	56 ± 5	$118 \pm 2^\circ$	Si–O–Si ₃ complex
X ₂	1038 ± 3	47 ± 7	$127 \pm 1^\circ$	Si–O ₂ –Si ₂ complex
X ₃	1066 ± 5	55 ± 5	$136 \pm 2^\circ$	Si–O ₃ –Si complex
X ₄	1092 ± 7	63 ± 1	$145 \pm 3^\circ$	Si–O ₄ tetrahedron

the oxide density varied from $\sim 2.1 \text{ g cm}^{-3}$ ($d_0 \approx 14 \text{ nm}$) up to $\sim 3.2 \text{ g cm}^{-3}$ ($d_0 \approx 4 \text{ nm}$). The shape of the absorbance curve changed with oxide thickness also, which was connected with the change in the relationship among the contribution of elementary bands. It is seen from Fig. 1 that specific area of the first profile Si/S (where S is the whole band area) is proportional to oxide density value.

Fig. 2 shows the distribution of Si–O–Si bond angles obtained as the result of computer simulation. It is seen that if the oxygen atom is a member of five- and/or sixfold rings of SiO_4 tetrahedra its bond angle varies in a rather narrow range ($135^\circ < \theta < 155^\circ$) and has the most probable value $\sim 144^\circ$. If oxygen is incorporated into three- and fourfold rings its angle distribution becomes broad and shifts to smaller angles: in these cases the contribution of $\theta < 135^\circ$ is rather high.

In contrast to SiO_2 films the main absorption band of SiO_x films is deconvoluted into four funda-

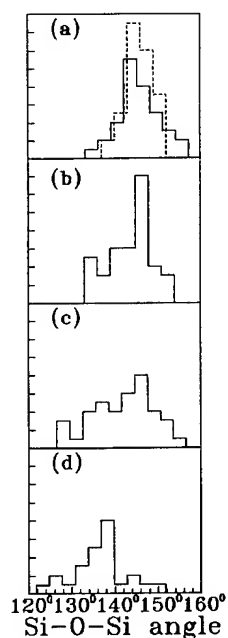


Fig. 2. Distribution of Si–O–Si bond angles for different cases of oxygen atom arrangement in the SiO_2 network: oxygen is a member of only sixfold rings (a) and is simultaneously incorporated into five- and sixfold (b). Six- and fourfold (c). Six- and threefold (d) rings. The dashed line in (a) represents θ distribution for α -quartz [3].

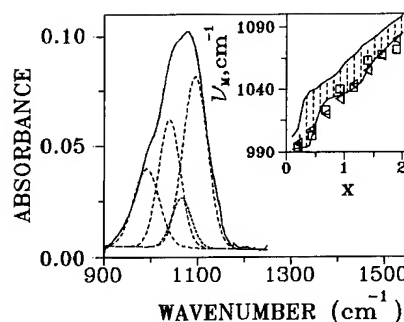


Fig. 3. Deconvolution of Si–O band into Gaussian profiles for SiO_x film with $x \approx 0.28$. The film was annealed in dry N_2 at 900°C during 1 h. In the inset the dependence of the main absorption band maximum position on x value is shown. The dashed area represents the results of calculation, experimental data shown as squares [13] and triangles [14].

mental elementary bands (Fig. 3). The profiles were present in the spectra of both initial oxide films and those after heat treatment (900°C , 1 h). Parameters of the elementary bands and corresponding values of Si–O–Si bond angles calculated according to Eq. (1) are represented in Table 1. Relative intensities of profiles varied with x and due to annealing.

4. Discussion

Recently [3], we have assumed that the elementary vibrational bands ~ 1055 and $\sim 1090 \text{ cm}^{-1}$ are connected with the motion of bridging oxygen atoms which are members of fourfold and sixfold SiO_4 rings correspondingly. The results obtained in the present work bring an additional information to this model. Computer simulation of SiO_2 structure shows that only three- and fourfold rings possess the bridging angles less than 135° . Thus, the oxygen atoms incorporated in such rings can provide the vibrational frequencies which correspond to the elementary band 1. At the same time fourfold rings cannot provide the existence of the bond angles smaller than $\sim 125^\circ$, such angles are present only in the case of threefold rings. This may evidence the fact that the SiO_2 network contains some threefold rings along with fourfold rings. Such a conclusion is in agreement with Raman scattering data [11].

The contribution of the first elementary band correlates rather well with the oxide density and, in particular, is maximum when ρ reaches its maximum value ($\sim 3.2 \text{ g cm}^{-3}$). Such large value is characteristic for coesite ($2.9\text{--}3.0 \text{ g cm}^{-3}$). The main structural component of coesite is a fourfold SiO_4 ring. Hence, summarizing the above-mentioned points and taking into account that the amount of threefold rings in silica lattice is rather small [11] one can conclude that the first elementary band ($\sim 1055 \text{ cm}^{-1}$) is mainly connected with vibrations of the oxygen atoms incorporated into fourfold SiO_4 rings.

The second elementary band ($\sim 1090 \text{ cm}^{-1}$) corresponds to vibrations of the oxygen atoms with bridging angles close to $\sim 144^\circ$. Such angles are present in four-, five- and sixfold SiO_4 rings (see Fig. 2). The availability of fivefold rings is assumed in the structure of such artificial SiO_2 polymorph like keatite, but sixfold ring is the main structural component of various SiO_2 polymorphs [1, 12]. Therefore, we assume that in the case of vitreous silica, sixfold rings are also more probable and thus the second elementary band is connected with the vibrations of the oxygen atoms incorporated into four- and sixfold SiO_4 rings.

Results of deconvolution of the main absorption band of SiO_x films have shown that in contrast to SiO_2 these oxides contain peculiar structural components. The random bonding model (RBM) of the SiO_x structure [2] suggests that these films consist of clusters $\text{Si-O}_y\text{-Si}_{4-y}$ ($0 \leq y \leq 4$). Four of them ($1 \leq y \leq 4$) are IR active. Deconvolution of the SiO_x absorption band revealed the existence of four elementary contributions. Hence, one may suppose that certain types of $\text{Si-O}_y\text{-Si}_{4-y}$ complexes correlate with definite elementary bands. If this is the case, then in the context of RBM statistics the areas of the elementary bands must relate to the probabilities of the oxygen bridges existing with the bond angle θ . This value is determined by [13]

$$P = yP_y/2x, \quad (2)$$

where P_y is the probability of the cluster existing [13]:

$$P_y = \frac{4!}{y!(4-y)!} (x/2)^y (1-x/2)^{4-y}, \quad (3)$$

Modeling of the absorption band as a sum of four Gaussian profiles has been carried out. The ranges of variations in elementary band parameters W_i and H_i were chosen using our experimental data (see Table 1); the intensities of each Gaussian profile for fixed value of x were taken as $I_i = P/H_i$, where P was determined by Eqs. (2) and (3), and y corresponded to the number of the elementary band i . Using Monte-Carlo method the range of possible variations of the absorption band maximum position, ν_M , was calculated for each value of x within the range $0 < x < 2$. The inset in Fig. 3 shows the results of calculation and the known data [13,14] determined experimentally for the SiO_x films. Good agreement enables us to infer that the elementary bands X_1 , X_2 , X_3 and X_4 are connected with molecular complexes $\text{Si-O}_y\text{-Si}_{4-y}$ with $y = 1, 2, 3$ and 4 , respectively.

5. Conclusions

The silicon–oxygen stretching band may be represented as a sum of stable vibrational elementary bands with parameters depending on the characteristics of short-range and local order. Oxygen bond angles and correspondingly vibrational frequencies are distributed not chaotically but possess the most probable values which are rather unambiguously connected with the kinds of SiO_4 tetrahedra rings (in the case of SiO_2) or with the types of molecular $\text{Si-O}_y\text{-Si}_{4-y}$ complexes (in the case of SiO_x with $x < 2$). Hence, analyzing the elementary band position and intensities one can determine the type of structural component and its contribution to the silica lattice.

References

- [1] F.J. Grunthaner and P.J. Grunthaner, Mater. Sci. Rep. 1 (1986) 65.
- [2] H.R. Philipp, J. Phys. Chem. Solids 32 (1971) 1935.
- [3] I.P. Lisovskii, V. G. Litovchenko, V. B. Lozinskii and G. I. Steblovsky, Thin Solid Films 21 (1992) 164.
- [4] A. Lehmann, L. Schumann and K. Hubner, Phys. Status Solidi B117 (1983) 689.
- [5] J.G. Vinter, A. Davis and M. R. Saunders, J. Comput.-Aided Molec. Des. 1 (1987) 31.

- [6] I.W. Boyd, Appl. Phys. Lett. 51 (1987) 418.
- [7] B. Garrido, J. Samitier, J.R. Morante, L. Fonseca and F. Campabadal, Appl. Surf. Sci. 56–58 (1992) 861.
- [8] I. W. Boyd and J. B. Wilson, Appl. Phys. Lett. 50 (1987) 1037.
- [9] A. Kalnitsky, S. R. Tay, J. P. Ellul, S. Chongsawangvirod, J. W. Andrews and E.A. Irene, J. Electrochem. Soc. 137 (1990) 234.
- [10] I.P. Lisovskii, V.G. Litovchenko and V.V. Khatko, Microelectron. Eng. 22 (1993) 39.
- [11] F.L. Galeener, Solid State Commun. 44 (1982) 1037.
- [12] A.G. Revesz, Phys. Status Solidi A57 (1980) 235.
- [13] A. Lehmann, L. Schumann and K. Hubner, Phys. Status Solidi A121 (1984) 505.
- [14] A.L. Shabalov, M.S. Feldman and M.Z. Bashirov. Izv. Akad. Nauk Az. SSR, Ser. Fiz. -Tekh. Mat. Nauk. 3 (1986) 78.



ELSEVIER

Journal of Non-Crystalline Solids 187 (1995) 96–100

JOURNAL OF
NON-CRYSTALLINE SOLIDS

Comparison of experimental and calculated TO and LO oxygen vibrational modes in thin SiO₂ films

C. Martinet*, R.A.B. Devine

CNET-CNS, France-Telecom, BP 98, 38243 Meylan cédex, France

Abstract

The oxide growth temperature and oxide film thickness dependence of the longitudinal and transverse vibrational mode frequencies for the oxygen-related asymmetric stretch in SiO₂ have been measured. By comparison with calculations, a significant film thickness dependence of the transverse mode frequency is found due entirely to geometrical effects. The longitudinal mode is insensitive to the thickness, at least in the range 5–400 nm. The oxide growth temperature dependence is consistent with oxides produced at 800°C being 1.6–2% denser than those produced at 1050°C. Absorption frequency variations observed for film thicknesses less than 20 nm cannot be explained entirely in terms of geometrical effects and are tentatively attributed to densification or bridging bond angle reduction in the oxide close to the interface with the substrate.

1. Introduction

Trends in silicon-based microelectronics technology suggest that if we simply scale down future devices, then metal-oxide-semiconductor (MOS) field-effect transistors which have gate lengths of $\sim 0.25 \mu\text{m}$ will require gate oxides $\leq 5 \text{ nm}$ thick. Such thin oxides will pose several problems. For example, can one manufacture, in a rigidly controlled fashion, oxide/Si interfaces which have a roughness which is a minor fraction of the oxide thickness? What are the physical characteristics of such oxides as compared to their thicker counterparts and how are they modified by the interfacial

strain resulting from the lattice mismatch between the Si and the SiO₂? A reply to the latter question requires a reliable method of characterizing such oxides and this, in itself, is not a negligible problem given the thickness of the oxide and the consequently small sample volumes with which one must deal. The most promising technique to characterize thin oxides would appear to be infra-red absorption spectroscopy either using the technique directly or coupled with attenuated total reflection [1].

In the present work we have carried out a detailed study of the infra-red absorption spectrum of SiO₂ films grown thermally on Si. We have concentrated on the vibrational peak associated with the asymmetric stretching motion of the bridging O moving in the plane of the adjacent Si's. We have studied not only the transverse optic mode (TO)

* Corresponding author. Tel: +33 76 76 44 15. Telefax: +33 76 90 34 43. E-mail: devine@cns.cnet.fr.

(nominally at an energy corresponding to $\sim 1090 \text{ cm}^{-1}$) but also the longitudinal mode (LO) at $\sim 1258 \text{ cm}^{-1}$. In the data and calculations presented in the following, we study the frequency shift of the TO and LO modes as a function of growth temperature of the oxide and, particularly, as a function of the oxide thickness. Comparing calculations and experiment we demonstrate the effects arising from purely geometrical optics considerations and thus extract those variations resulting from physical changes in the thin films. The role of interfacial stress is elucidated.

2. Experimental and results

A range of thermal oxides were grown using standard clean room procedures and a dry oxygen atmosphere. Substrates were typically single face polished Si (100) p type (either Czochralski or float zone). The thickest oxide obtained (400 nm) was grown at 1050°C while other oxides ($\sim 45 \text{ nm}$) were grown at 800°C . For thicker oxides at the lower temperature, growth time was prohibitive. In general, to obtain infra-red absorption data as a function of oxide thickness, samples were thinned in a buffered HF acid solution (commercial 'ENERLEC BE 7:1', solution of $\text{NH}_4\text{F}/\text{HF}/\text{H}_2\text{O}$). However, a series of oxides in the thickness range 5–25 nm was grown directly using fixed temperature (900°C) and varying the growth time by diluting the dry oxygen in N_2 . Following oxidation, the rear face (unpolished) oxide was removed in a solution of HF in ethanol; this had the advantage of leaving the Si surface H terminated and free of the native oxide. Film thickness measurements were made using single wavelength ($\lambda = 632.8 \text{ nm}$) ellipsometry or using spectroscopic ellipsometry.

Fourier transform infra-red (FTIR) spectroscopy measurements were carried out using a Bruker IFS 66 spectrometer at room temperature. The resolution was set to 4 cm^{-1} and multiple scans were performed. Repetition of the experiment several times enabled us to check the reproducibility of the measurement and the accuracy of the determination of the absorption peak position. The TO mode was studied using a normal incidence beam while the LO mode required off-normal incidence and

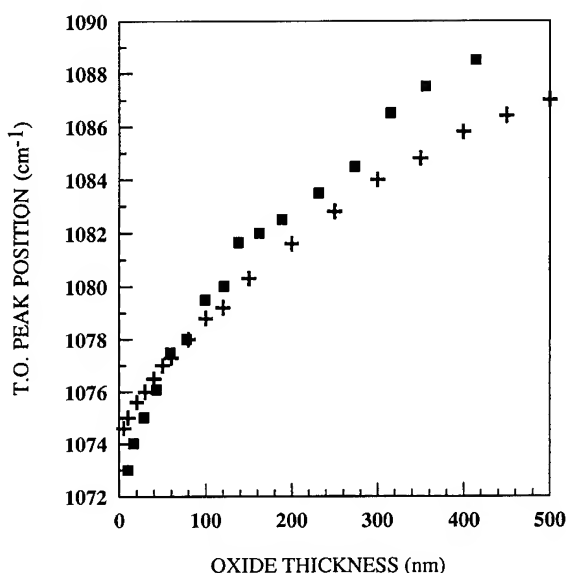


Fig. 1. Measured (■) and calculated (+) variation of the position of the O asymmetric stretch related TO vibrational mode as a function of film thickness in SiO_2 grown on Si substrates. The oxide growth temperature was 1050°C .

p polarization (electric field parallel to the incidence plane). The angle yielding the most intense LO peak was found to be between 65° and 70° to the normal. In both TO and LO mode studies, background reference samples were used. These were obtained from the oxidized wafer after stripping the oxide from both faces using the HF acid/ethanol etch solution designed to leave the Si surface native oxide free and hydrogen terminated.

In Fig. 1 we show the results of measurements of the position of the TO absorption peak as a function of oxide thickness for a nominally 400 nm thick film (1050°C growth temperature) subsequently etched back. Fig. 2(a) shows similar data for a series of samples obtained at different oxidation temperatures. For the 800°C oxidized samples the starting thickness was $\sim 45 \text{ nm}$ while the 900°C samples were grown to the thickness indicated by varying the growth time/ O_2 partial pressure. Note that one set of data is for samples grown initially to 45 nm at 800°C in dry oxygen, then annealed in N_2 at 1000°C for 30 min. All samples show a monotonic reduction in the frequency of the

TO absorption peak position as a function of oxide thickness. In Fig. 2(b) we include data on the variation of the LO mode peak position as a function of oxide thickness; one observes here that the peak positions show essentially no variation as a function of film thickness (except for the thinnest oxide studied, $\sim (3\text{--}4\text{ nm})$).

3. Discussion

In the central and non-central force approximation the absorption frequencies (ω) of the LO and TO modes are given by [2]

$$\omega_{\text{TO}} = \left[\frac{2}{m_0} \left(\alpha \sin^2 \frac{\theta}{2} + \beta \cos^2 \frac{\theta}{2} \right) \right]^{1/2}, \quad (1)$$

$$\omega_{\text{LO}} = \left[\frac{2}{m_0} \left(\alpha \sin^2 \frac{\theta}{2} + \beta \cos^2 \frac{\theta}{2} + \gamma^{\text{ss}} \right) \right]^{1/2}, \quad (2)$$

where m_0 is the mass of the oxygen atom and θ is the Si–O–Si bridging bond angle between adjacent SiO_4 tetrahedra. α and β are the central and non-central force constants; it is generally assumed that $\alpha \approx 6\beta$. γ^{ss} is a Coulomb force constant defined as [2]

$$\gamma^{\text{ss}} = \frac{(Z_{\text{OS}}^{\text{T}})^2}{\epsilon_{\infty} \epsilon_0 (2m + M)} \rho, \quad (3)$$

where M is the atomic of Si and ρ is the density of the SiO_2 . Z_{OS}^{T} is the transverse electric charge related to the oxygen stretching motion. ϵ_{∞} is the static electronic dielectric constant. Eqs. (1) and (2) are very similar so that we would expect that any thickness-dependent variation (for example, in θ) should manifest itself in the positions of both the

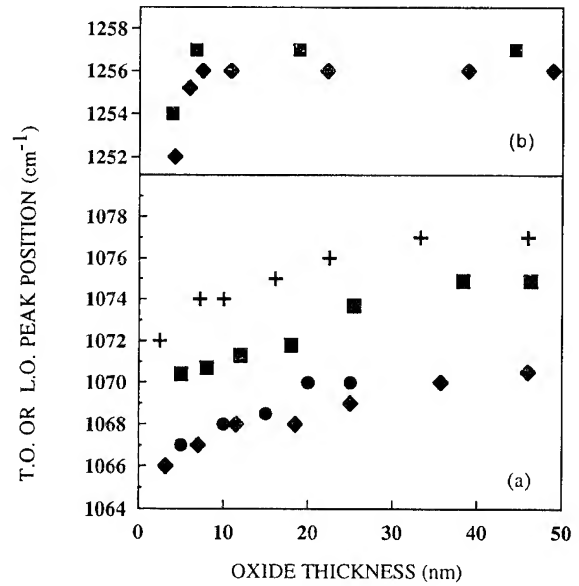


Fig. 2. Infra-red absorption peak positions in cm^{-1} for TO and LO modes in SiO_2 as a function of film thickness and oxide growth temperature: \blacklozenge , 800°C ; \blacksquare , 1050°C ; $+$, $800^\circ\text{C} + 1000^\circ\text{C}$ anneal; \bullet , 900°C .

more in detail the possible geometrical optics reasons for effective peak shifts.

We consider the cases of TO and LO modes using a classic approach for the multiple reflection of beams incident on a thin film of SiO_2 on an Si substrate [3]. We treat first the case of the TO mode, then the LO mode. The index of the SiO_2 is assumed complex ($n_{\text{SiO}_2} = n - ik$) while that of the Si is real (n_{Si}). It is then straightforward to calculate the transmission coefficients.

TO mode

$$T = \frac{\tau_1^2 \tau_2^2 n_{\text{Si}}}{e^{\frac{4\pi}{\lambda} dk} + \rho_1^2 \rho_2^2 e^{-\frac{4\pi}{\lambda} dk} + 2\rho_1 \rho_2 \cos\left(\phi_1 + \phi_2 - \frac{4\pi}{\lambda} dn\right)}, \quad (4)$$

LO and TO peaks. In Figs. 2(a) and (b) we see that thickness-dependent variations in the TO peak position are not similarly observed for the LO peak. The only difference, the γ^{ss} parameter given by Eq. (3), has no reason as far as we can see to show film thickness dependence. One must therefore ex-

where

$$\rho_1 e^{i\phi_1} = \frac{(1-n) - ik}{(1+n) - ik}; \quad \rho_2 e^{i\phi_2} = \frac{(n-n_{\text{Si}}) - ik}{(n+n_{\text{Si}}) - ik},$$

$$\tau_1 e^{i\kappa_1} = \frac{2}{(n-ik) + 1}; \quad \tau_2 e^{i\kappa_2} = \frac{2(n-ik)}{(n-ik) + n_{\text{Si}}}.$$

LO mode

We use a similar approach to that for the TO mode expect that we must now allow for an angle of incidence θ_1 and consider the reflection and transmission coefficients for the p polarized wave.

Then

$$T_p = \frac{\tau_{p_1}^2 \tau_{p_2}^2 n_{Si} \cos \theta_3}{\cos \theta_1 (e^v + \rho_{p_1}^2 \rho_{p_2}^2 e^{-v} + 2 \rho_{p_1} \rho_{p_2} \cos u)}, \quad (5)$$

$$v = \frac{4\pi}{\lambda} d(k\alpha + \beta n),$$

$$u = \phi_1 + \phi_2 - \frac{4\pi}{\lambda} d(n\alpha - k\beta),$$

with

$$\tau_{p_1} e^{iK_1} = \frac{2 \cos \theta_1}{n \cos \theta_1 + \cos \theta_2};$$

$$\tau_{p_2} e^{iK_2} = \frac{2 n \cos \theta_2}{n_{Si} \cos \theta_2 + n \cos \theta_3}$$

and

$$\rho_{p_1} e^{i\phi_1} = \frac{-n \cos \theta_1 + \cos \theta_2}{n \cos \theta_1 + \cos \theta_2};$$

$$\rho_{p_2} e^{i\phi_2} = \frac{-n_{Si} \cos \theta_2 + n \cos \theta_3}{n_{Si} \cos \theta_2 + n \cos \theta_3}.$$

We have assumed $\sin \theta_1 = (n - ik) \sin \theta_2 = n_{Si} \sin \theta_3$ and $\cos \theta_2 = \alpha - i\beta$ with α and β real.

We note that Eqs. (4) and (5) contain the oxide thickness, d , so that variation of the transmission with d is expected. Using the tabulated [4] frequency dependence of n and k together with values of n_{Si} we have calculated the position of the maximum of the absorbance, A , assuming $A = \log(1/T)$ as a function of oxide film thickness. The results are shown in Figs. 1 and 3. We observe that the peak position of the LO mode is essentially film thickness independent and equal to 1250 cm^{-1} . The LO peak position difference between experiment and simulation can be explained by the fact that in the region of weak infra-red absorption (about $8 \mu\text{m}$, e.g. 1250 cm^{-1}), the index values are inaccurate [4]. The position of the maximum of the absorbance of the TO mode is thickness-dependent as observed

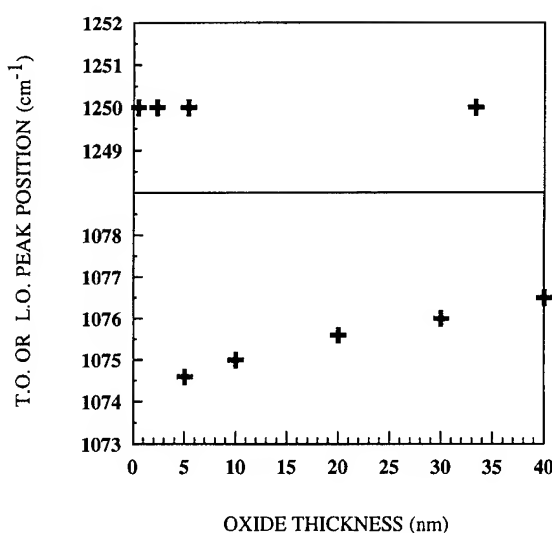


Fig. 3. Simulated behaviour of the TO and LO mode peak positions as a function of oxide film thickness. The variations are due entirely to geometrical effects.

experimentally in Fig. 1. This conclusion then accounts for our observations concerning apparent peak shifts as a function of oxide film thickness. The theoretical and experimental data presented in Fig. 1 suggest that, for oxide film thicknesses $\leq 300 \text{ nm}$, the thickness-dependent shift of the TO mode frequency is well anticipated by Eq. (4).

If we examine the calculations presented in Fig. 3 for the TO mode and the experimental data for the 1050°C grown oxide shown in Fig. 2(a), we see that for thicknesses $\leq 20 \text{ nm}$ the experimental peak position shifts more rapidly to smaller wave numbers than anticipated. This more rapid variation appears for all of the oxides studied independent of their growth temperature. From Fig. 2(a) the 'excess' shift is estimated to be about -5 cm^{-1} for a 5 nm thick oxide. Although the data are limited for the LO mode (Fig. 2(b)) it would also appear that, for the thinnest oxide studied, there is a shift of the peak to lower wave numbers $\sim 3 \text{ cm}^{-1}$. It is possible that these shifts may be related to physical rather than 'geometrical' phenomena.

Shifts in the peak position of the infra-red absorption may be related to physical variation of the internal structure of the SiO_2 network. From data on plastically densified SiO_2 it has been found [5]

that the TO mode frequency shift, $d\omega$, with density is

$$\frac{d\omega}{d\rho} = -93 \text{ cm}^2 \text{ g}^{-1}. \quad (6)$$

Inspecting the data shown in Fig. 2(a), we can estimate that for the 800°C grown oxide the absorption peak is shifted by $\sim -5 \text{ cm}^{-1}$ with respect to the 1050°C grown oxide. From Eq. (6) we would estimate, then, that the 800°C oxide has a density $\sim 2.5\%$ larger than that of the 1050°C grown oxide. The refractive indices for these two oxides were 1.463 (1050°C) and 1.470 (800°C). Nothing that the refractive index also varies with density [6] and assuming [5] $dn/d\rho = 0.20 \text{ g}^{-1} \text{ cm}^3$ we would deduce from this measurement that the 800°C grown oxide was 1.6% more dense than the 1050°C grown oxide. The densification hypothesis can be further confirmed if we compare ratios of $[\omega_{\text{LO}}^2 - \omega_{\text{TO}}^2]$. From Eqs. (1) and (2) we see that this difference is equal to $2\gamma^{\text{SS}}/m_0$ which, from Eq. (3) is proportional to the density. Comparing values for oxides grown at 1050°C and 800°C we conclude that the 800°C oxide is $\sim 2.1\%$ denser than the oxide grown at 1050°C.

At the present time we have insufficient measurements on the TO and LO mode behaviour for very thin oxides. The TO mode data shown in Fig. 2(a) suggest that the very thin oxides ($< 5 \text{ nm}$) are again denser than the thicker oxides by $\sim 2.5\%$ and the difference increases with decreasing thickness. Unfortunately, refractive index measurements on such thin oxides are too inaccurate for us to independently confirm this trend. Similar trends are, however, suggested in recent [1] ATR measurements of film thicknesses in the range 0.5–3 nm.

4. Conclusions

The present experiments underline the importance of taking account of purely geometrical effects

when analyzing variations in infra-red absorption peak positions in SiO_2 films. We find that consideration of the effects of multiple reflections satisfactorily accounts for peak shifts observed in samples in the thickness range $20 \text{ nm} \leq d \leq 300 \text{ nm}$. Oxide growth temperature induced infra-red peak shifts for LO and TO modes are consistent with density variations determined by refractive index measurements reinforcing the hypothesis that lower growth temperatures result in densification of the oxide film. Trends in the shift of the TO mode peak position for oxide thicknesses $< 20 \text{ nm}$ suggest that for a given growth temperature the film may be even denser close to the Si/SiO₂ interface. This hypothesis is supported by recent ATR measurements [6] on the behaviour of the LO mode as a function of decreasing oxide thickness which also show a shift to lower wavenumber. More experiments are clearly needed to provide detailed insight into the structure of the films very close to the substrate/oxide interface.

C.M. is grateful to France Télécom and the MESR for financial support.

References

- [1] T. Yamazaki, S. Miyazaki, C.H. Bjorkman, M. Fukuda and M. Hirose, *Mater. Res. Soc. Symp. Proc.* 318 (1994) 419.
- [2] A. Lehmann, L. Schumann and K. Hübner, *Phys. Status Solidi (b)* 117 (1983) 689.
- [3] O.S. Heavens, *Optical Properties of Thin Solid Films* (Butterworth, New York, 1955) p. 46.
- [4] H.R. Philipp, in: *Handbook of Optical Constants of Solids*, ed. E.D. Palik (Academic Press, New York, 1985) p. 760.
- [5] R.A.B. Devine, *Trans. Mater. Res. Soc. Jpn.* 8 (1992) 165.
- [6] R. Brückner, *J. Non-Cryst. Solids* 5 (1970) 123.



ELSEVIER

Journal of Non-Crystalline Solids 187 (1995) 101–105

JOURNAL OF
NON-CRYSTALLINE SOLIDS

Structural damage and defects created in SiO₂ films by Ar ion implantation

B. Garrido^{a,*}, J. Samitier^a, S. Bota^a, C. Domínguez^b, J. Montserrat^b, J.R. Morante^a

^a LCMM, Departament de Física Aplicada i Electrònica, Universitat de Barcelona, Diagonal 645-647, E-08028, Barcelona, Spain

^b Centro Nacional de Microelectrónica, CNM-CSIC, Campus UAB, E-08193, Bellaterra, Spain

Abstract

The structural damage produced by Ar ion implantation into SiO₂ layers has been analyzed with the help of different characterization techniques. By using infrared absorption spectroscopy, compaction, bond distortion and structural disorder have been investigated. The results suggest that the dominant effect of the ion implantation is creation of structural damage consisting of point defects such as broken bonds and vacancies. The number of absorbing Si–O bonds have been calculated from the dielectric function dispersion analysis which gives a saturation for doses of the order of 10¹⁴ cm⁻². This saturation is reached after 15.5% of Si–O bond breaking. The infrared results are also discussed together with the results obtained by electroluminescence measurements performed in electrolyte-SiO₂-Si systems. Further, X-ray photoelectron spectroscopy measurements of Si 2p core level binding energy have allowed the damaged oxide to be modelled as if it were composed of suboxide-like species.

1. Introduction

The effects of radiation on SiO₂-Si structures have been studied for many years and with focus on different purposes. In particular, ion implantation in SiO₂ is of great interest on account of its technological applications in microelectronics as well as its interest in the field of basic research in amorphous materials.

In principle, defects created as a consequence of ion implantation in SiO₂ are expected to be similar to the ones produced by other radiation sources: strained Si–O–Si units and dispersion of

intertetrahedral angles which are connected, respectively, with densification and disorder. However, distinction must be made between ion implantation and other radiation sources, that is nuclear collisions with target atoms emerge here as the main source of damage. Thus, damage will consist of vacancies, interstitials, dangling bonds and some other modifications of the local atomic arrangement. In this framework, we report experimental observations of structural damage in thermal SiO₂ films grown on silicon substrates and irradiated with different doses of 130 KeV Ar ions. By using infrared absorption spectroscopy we investigate modifications of the structure, for instance densification, bond distortion and the density of defects such as broken bonds and non-bridging oxygens. The infrared results are compared and

* Corresponding author. Tel: +34-3 402 1147. Telefax: +34-3 402 1148. E-mail: blas@irisys.fae.ub.es.

discussed together with the results of the application of an electroluminescence technique based in charge injection processes in electrolyte-SiO₂-Si systems. Furthermore, XPS measurements are also reported to obtain a better understanding of the local structure of the silicon centred tetrahedra.

2. Samples and experiment

The substrates used were $\langle 100 \rangle$ n-type silicon wafers with $\rho = 3\text{--}5 \Omega \text{cm}$. 2500 Å thick oxide layers were grown by wet oxidation at 950°C. In different samples we have performed Ar ion implantations with doses ranging from 3.2×10^{12} to $3.2 \times 10^{16} \text{cm}^{-2}$, two doses in every decade (Table 1). The energy of the ions, 130 KeV, was chosen so that the maximum of the Ar implanted distribution stays in the middle of the layer and the damaged thickness comprises most of the layer (this was previously calculated by TRIM simulation). The implantation was performed by using an Eaton Nova 4206 equipment; cooling and low beam currents were used to avoid heating. Film thicknesses were measured by optical interferometry with a Nanospec AFT 200 of Nanometrics.

For the Fourier transform infrared spectroscopy (FTIR) experiments, the SiO₂ film on the back side of the substrate was etched-off in order to prevent infrared absorption by the unimplanted film. Both reflection and transmission operation modes were used in a Bomem DA3 spectrometer. Infrared spectra were measured for all the samples in the mid-IR range ($4000\text{--}400 \text{cm}^{-1}$) at a resolution of 2cm^{-1} . Raw spectra were appropriately compared with respect to a bare silicon spectrum. XPS analysis of Si 2p core level was performed with a Perkin Elmer PHI 5500 after etching the layers to half thickness in order to obtain results from bulk analysis as surface deviations are expected.

The electroluminescence (EL) measurements were performed with an alternative technique which is based on the use of an electrolyte-oxide-semiconductor system (EOS system) to carry out a controlled injection and heating of electrons in SiO₂ films depending on the applied electric field. This technique enabled us to perform defect

Table 1

Implantation dose and the values for the position, linewidth and area of the TO₃ band for the layers studied

Dose (cm^{-2})	Position (cm^{-1})	Width (cm^{-1})	Area (a.u.)
0	1082.0	76.0	23.35
3.2×10^{12}	1080.0	77.5	22.55
1.0×10^{13}	1077.5	82.5	22.43
3.2×10^{13}	1069.5	92.5	21.91
1.0×10^{14}	1056.0	107.0	20.67
3.2×10^{14}	1047.0	109.0	20.04
3.2×10^{15}	1044.0	108.5	20.23
1.0×10^{16}	1043.0	109.5	20.42
3.2×10^{16}	1042.5	110.5	19.90

characterization without the need to deposit any metal or polycrystalline silicon contact.

3. Results and discussion

3.1. Densification

We have observed that for all the samples the thicknesses diminish by up to 1.5% after the high dose implantation (of the order of 10^{16}cm^{-2}). With respect to this, some authors have reported that ion implantation into silica causes local densification of the structure, the same as is found after X-ray or neutron irradiation [1]. This is obviously a consequence of the diminution of the Si-O-Si mean angle, as density is closely related with Si-Si distance. Densification by Si-O-Si angle reduction seems to have a limited value of 6% [2] and after irradiation with neutron or X-rays a 4% densification has been reported [2]. This seems to be the same situation after ion implantation since none of the samples were outside this range. Moreover, the absence of infrared bands arising from Si-OH and water means that the samples are not expected porous and contamination from moisture is negligible, which is also in favour of densification [1–4].

3.2. Infrared results

The absence of impurity bands leads us to focus our infrared work in studying the evolution of the TO

modes. The TO_3 bond stretching band is by far the most intense band and it has been extensively connected with the mean Si–O–Si intertetrahedral angle and with the width of this angle distribution [5,6]. The values for the position, FWHM and area of the TO_3 bands are shown in Table 1. The characteristic behaviour of the silica stretching band is briefly summarized as (i) a shift to lower frequencies, (ii) a broadening and (iii) a decrease of the intensity and area. These experimental results show that shifts are as large as 40 cm^{-1} and the FWHM increase is about 35 cm^{-1} . Fig. 1 displays the evolution of the band maximum and the linewidth with dose. All the parameters of the band have in common a saturation after doses of the order of 10^{14} cm^{-2} (1 Ar atom each 5600 Si atoms). This dose corresponds to a nuclear deposited energy density of $4.7 \times 10^{23} \text{ eV/cm}^3$, which is very similar to the value reported by Hiraiwa and coworkers [7] for saturation of etching rate measurements after B, P and As low energy implantations. It is very interesting to note that this deposited energy in saturation is only slightly higher than the Si–O bond energy density, which is 3.8 eV/bond or $3.4 \times 10^{23} \text{ eV/cm}^3$.

The values for the shifts and broadenings of the TO_3 bands are far larger than those deduced from considering only distortion mechanisms and dispersion of intertetrahedral angles. From the central force model one important fact is that stressed oxides present a TO_3 band which is shifted towards lower wave numbers. The maximum frequency of the TO_3 band and mean Si–O–Si angle are connected by $\kappa_{\text{max}} = \kappa_0 \sin \theta/2$ where $\kappa_0 = 1134 \text{ cm}^{-1}$. This model also connects the linewidth with the angular dispersion and density with mean angle [5,6].

As was presented before, densification in our samples after high dose implantation was about 1.5% and hence, from the central force model we expect not more than a 7 cm^{-1} shift of the maximum of the TO_3 band to lower wave numbers (1082 cm^{-1} is the value for the non-implanted reference oxide), which corresponds to an increment of stress of $\Delta\epsilon = -2.0 \times 10^9 \text{ dyn/cm}^2$ and a diminution of the Si–O–Si mean angle of 2.2° (from its reference value of 144°). Likewise, the maximum increase on the FWHM of the TO_3 band expected

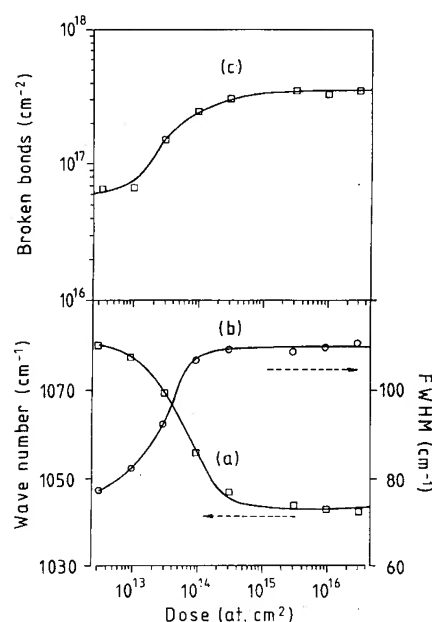


Fig. 1. Evolution with implantation dose of (a) peak position, (b) linewidth and (c) the number of broken bonds. The axis on the right is for curve c. Saturation is always present for doses higher than 10^{14} cm^{-2} . The lines are drawn as guides for the eye.

from the dispersion mechanism is about 10 cm^{-1} (reference value $\text{FWHM} = 76 \text{ cm}^{-1}$) which means that the maximum width achieved by the bond angle distribution is $\Delta\theta = 29^\circ$ (reference value $\Delta\theta = 26^\circ$). These are the maximum expected shift and deformation values of stretching band after the implantation process, if only distorted tetrahedral units are considered.

It must be emphasized that the values obtained for the shift and broadening of the TO_3 band, 40 and 35 cm^{-1} , respectively, are clearly higher than those expected from considering only deformation of the basic bond units. This situation leads to suggest that, at high doses, the dominant mechanism of structural modification is the damage originated by broken bonds and displaced atoms. So, it is the presence of these point defects which are connected with alteration of the environment of the silicon atom that is mainly responsible for the modification of the vibrational spectra [4]. For instance, the Si–O bond stretching mode is positioned at around 1080 cm^{-1} when the structure is

undamaged and when oxygen is non-bridging two tetrahedra as a consequence of one broken bond, the value is close to 950 cm^{-1} [8]. Such a low frequency component is expected to cause the whole band to shift markedly towards lower wave numbers. Moreover, even the absorption frequency of bridging oxygens in a damaged environment is known to decrease systematically depending upon the number of non-bridging oxygens located in the neighbourhood and on the electronegativity of the atoms surrounding the bond [8,9].

3.3. Concentration of absorbing Si–O bonds

The number of absorbing Si–O bonds may be calculated using Smakula's relationship between the concentration, N , and the dielectric function of the layers. By integrating $\omega\Delta\epsilon$ over the absorption band of interest one obtains the well-known sum rule:

$$N = \frac{2\mu}{\pi e_s^2} \int_{\text{band}} \omega \text{Im}(\Delta\epsilon) d\omega \equiv B \int_{\text{band}} \omega \text{Im}(\Delta\epsilon) d\omega. \quad (1)$$

For the frequency dependence of the dielectric function, a suitable model for amorphous materials was chosen [10]. Dispersion analysis was performed by fitting both the transmission and reflection infrared spectra of the samples with probe functions T and R , whose dependence with dielectric function is given by the Fresnel equations for layered systems [11]. The proportionality factor B was evaluated from the unimplanted reference oxide and results in $B = 9.89 \times 10^{16} \text{ cm}^{-1}$. It must be said that we have assumed that factor B is constant regardless the implantation dose. This is expected since oscillator strength depends firstly on the Si–O bond itself and the modification of the Si–O environment is expected to be a secondary effect [1]. As a result of the calculations, the number of broken bonds obtained, N_R , is also plotted in Fig. 1 as a function of the implantation dose, where a saturating law is also observed. The maximum number of broken bonds reached in saturation is 15.5% of the total initial number. All of these results point out that although increasing irradiation above the threshold for saturation, no further net damage is produced. Somehow, the equilibrium reached is

dynamical and that means damage is produced at the same rate that interstitial–vacancy pairs recombine and atomic bonds are restored.

3.4. The electroluminescence measurements

The electroluminescence (EL) measurements were performed with a technique based on the use of an electrolyte-oxide-semiconductor system (EOS system) [12]. Regarding the implanted samples, their EL spectrum contains three bands located at 1.9, 2.7 and 4.3 eV which are related with specific kinds of defects of the oxide. The 1.9 eV band is currently assigned to Si–OH [13]. The implantation produces modifications on the intensity of this band but it is difficult to assign such a big increase to only Si–OH groups. However, a similar SiO^- defect could be created by electron trapping at non-bridging oxygen hole centres (NBOH) so it is possible to attribute the rise of this band to this centre which increases with bond breaking. The 2.7 eV EL band is related with an oxygen vacancy defect [13] and its evolution with dose is found to be similar that for the density of broken bonds. The 4.3 band is connected with defects at interface [12,13] and its evolution with dose is minimal.

3.5. XPS measurements and the environment of the silicon atom

XPS analysis of damaged oxides is complex since the Si 2p core level spectra have different components arising from chemical shifts and broadenings which are a direct consequence of the different environments that silicon atoms can have. In damaged oxides, broken bonds and oxygen vacancies mean that silicon oxidation number could be less than 4 (Si^{+1} , Si^{+2} , Si^{+3}). This situation is similar to, but not the same as, the determination of suboxide concentration near oxide–silicon interface [14]. When the oxide becomes damaged, the band shifts to lower binding energies and broadens (Fig. 2). This is certainly to be regarded as an effect of the alteration of silicon environment and therefore an increase of the components with lower oxidation numbers. Saturation is also observed after similar doses to the ones reported above for infrared results, so locally there exists a similar

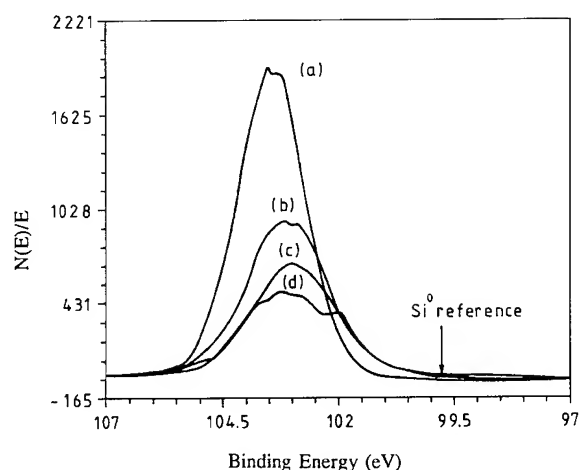


Fig. 2. XPS spectra for (a) reference unimplanted samples, (b) $3.2 \times 10^{13} \text{ cm}^{-3}$, (c) $3.2 \times 10^{14} \text{ cm}^{-3}$ and (d) $3.2 \times 10^{16} \text{ cm}^{-3}$. The vertical arrow is the reference position for silicon Si^0 .

Table 2

Values for the shifts and linewidths of the components obtained from the fitting of the Si 2p XPS peak

	Si^{+1}	Si^{+2}	Si^{+3}	Si^{+4}
Shift	1.00	1.95	2.95	3.86
Linewidth	0.70	0.95	1.10	1.30

trend as that for the structural behaviour commented before [15]. We have fitted the experimental XPS spectra by allowing chemical shifts and linewidths of the components to vary and the results (Table 2) are in accordance with the values reported in literature for SiO_x compounds [14].

4. Conclusions

The degree of compaction and disorder of the SiO_2 structure after implantation are not able to explain the large shifts and broadenings of IR bands. Alternatively, the dominant effect of the implantation is to create structural damage, that is

point defects such as broken bonds and vacancies. From IR results we have obtained a saturation behaviour after doses of the order of 10^{14} cm^{-2} which corresponds to 15.5% of bond breaking. The EL results prove that there is an increase of the density of vacancies and non-bridging oxygens with the implantation dose. Moreover, XPS analysis has shown that there are different local environments for silicons which evolve in the same way as the IR spectra. Chemical shifts and linewidths for the XPS spectra components are similar to the quoted results for SiO_x compounds.

The authors acknowledge A. Baraban and P.P. Koronov for the electroluminescence measurements.

References

- [1] M.C. Busch, A. Slaoui, P. Siffert, E. Dooryhee and M. Toulemonde, *J. Appl. Phys.* 71 (1992) 2596.
- [2] F. Liebau, in: *The Physics and Technology of Amorphous SiO_2* , ed. R.A.B. Devine (Wiley, New York, 1988).
- [3] P. Mazzoldi, A. Carnera, F. Caccavale, M.L. Favaro, A. Boscolo-Boscoletto, G. Granozzi, R. Bertoncello and G. Battaglin, *J. Appl. Phys.* 70 (1991) 3528.
- [4] C. Domínguez, B. Garrido, J. Montserrat, J.R. Morante and J. Samitier, *Nuclear Instr. Meth. B80&81* (1993) 1367.
- [5] G. Lucovsky, M.J. Manitini, J.K. Srivastava and E.A. Irene, *J. Vac. Sci. Technol.* B5 (1987) 530.
- [6] J.T. Fitch, C.H. Bjorkman, G. Lucovsky, F.H. Pollak and X. Yin, *J. Vac. Sci. Technol.* B7 (1989) 775.
- [7] A. Hiraiwa, H. Usui and K. Yagi, *Appl. Phys. Lett.* 54 (1989) 1106.
- [8] T. Furukawa, K.E. Fox and W.B. White, *J. Chem. Phys.* 75 (1981) 3226.
- [9] G. Lucovsky, *Solid State Commun.* 29 (1979) 571.
- [10] M.L. Naiman, C.T. Kirk, B.L. Emerson, J.B. Taitel and S. Senturia, *J. Appl. Phys.* 58 (1985) 779.
- [11] B. Harbecke, *Appl. Phys.* B39 (1986) 165.
- [12] A.P. Baraban, P.P. Koronov, S.A. Bota and J.R. Morante, *Mater. Res. Soc. Symp. Proc.* 298 (1993) 253.
- [13] J.H. Stathis and M.A. Kastner, *Phys. Rev.* B35 (1987) 2972.
- [14] P.J. Grunthaner, M.H. Hecht, F.J. Grunthaner and N.M. Johnson, *J. Appl. Phys.* 61 (1987) 630.
- [15] B. Garrido, J. Samitier, J.R. Morante, J. Montserrat and C. Domínguez, *Phys. Rev. B*, in press.



ELSEVIER

Journal of Non-Crystalline Solids 187 (1995) 106–111

JOURNAL OF
NON-CRYSTALLINE SOLIDS

Boron diffusion in SiO₂ based dielectric thin layers

S. Nédélec^{a, b, *}, D. Mathiot^a, M. Gauneau^c, A. Straboni^a^a CNET-CNS (France Telecom), 28, Chemin du vieux chêne, BP 98, 38243 Meylan cédex, France^b SGS-Thomson, 850, rue Jean Monnet, BP 16, 38921 Crolles cédex, France^c CNET-LAB (France Telecom), route de Trégastel, BP 20, 22301 Lannion cédex, France

Abstract

Boron diffusivity has been quantified in pure and plasma nitrided thin oxide films. For this study, p + polysilicon metal-oxide-semiconductor (MOS) structures with pure or nitrided oxide gates have been used. Boron diffusivity has been determined by fitting in the substrate the experimental boron profile with a calculated one. The diffusivity in pure oxide has been obtained in the 900–1200°C temperature range, and the influence of nitridation has been quantified. As expected, a lower diffusivity in nitrided oxide has been obtained. This decrease is found to be mainly due to a lower pre-exponential term in the Arrhenius law. A linear decrease of the activation energy with the nitrogen content has been observed and an explanation has been given for this behaviour.

1. Introduction

In ultralarge-scale integration technology, the trend toward smaller device dimensions and higher integration density implies that very thin gate oxides are required in complementary metal-oxide-semiconductor (CMOS) devices. Such dielectrics should have a good chemical stability, a low interface state density, and constitute a good diffusion barrier for impurities. In CMOS devices in which the p + polysilicon gate electrode is highly doped with boron, this diffusion may be indeed responsible of the oxide deterioration through the forma-

tion of interface states or fixed negative charges in the oxide. The thinner the oxide, more severe can be the degradation [1]. As the thickness of the oxide tends to decrease well below 10 nm, it is important to be able to predict how much the boron will diffuse in the gate oxide during the process steps, and thus to know the boron diffusivity in the oxide layer. So the boron diffusivity has been studied over a large temperature range in pure oxide annealed in an inert ambient.

To prevent any boron diffusion coming from the polysilicon gate during the high temperature steps, the nitridation of the oxide appears to be efficient [2,3]. In this work, this fact has been confirmed by studying plasma nitrided oxides, and the efficiency of this barrier of diffusion has been quantified.

* Corresponding author. Tel: +33 76 76 40 00. Telefax: +33 76 90 34 43. E-mail: nedelec@cns.cnet.fr.

2. Experimental procedure

2.1. Sample preparation and analysis

2.1.1. Sample preparation

N- and p-type (100) Si substrates were oxidized in dry O_2 around 900°C–950°C for various durations of time to grow oxide films in the 5–16 nm range. Both plasma nitrided and non-nitrided dielectrics were formed from the thermally grown oxide: the plasma nitridation was performed at 950°C in an ammonia plasma at a power of 600 W with a gas pressure of 3×10^{-2} Torr for times ranging from 1 to 6 h. A description of the nitridation apparatus and conditions can be found in Ref. [2]. A 380 nm thick polysilicon layer was then deposited on each oxide film at 620°C and boron implanted with a few 10^{15} cm^{-2} dose and energy in the range 25–40 keV. The samples were encapsulated by a 40 nm thick CVD oxide layer to prevent from any outward diffusion of boron, and then annealed in dry N_2 in the 900°C–1200°C temperature range for a long duration, i.e., from 3 h to 4 days, depending on the oxide thickness and the annealing temperature.

2.1.2. Nitrogen profile analysis

Auger depth profiles have been realized on plasma nitrided 16 nm thick oxide films in order to obtain the nitrogen content.

The raw Auger profiles do not give the actual film composition because of certain physical limitations like the broadening of the profiles due to surface roughening and the escape depth of the Auger electron. So the raw Auger profiles have to be deconvoluted to take these effects into account [2]. Through the deconvoluted Auger profiles, the nitrogen content in oxides, plasma nitrided for 10 min, 1, 3, and 6 h, has been obtained: the major part of nitrogen is concentrated at the surface oxide for a few nanometers and just a few Å of nitrogen at the Si/SiO₂ interface. The bulk oxide remains essentially nitrogen free. Typical nitrogen profiles at the surface of the oxide layer are shown in Fig. 1. In this figure, the nitrogen atomic density has been derived from the relative concentration (given by Auger analysis) by considering a total density of 4.5×10^{22} sites per cm^3 on the O sub-network.

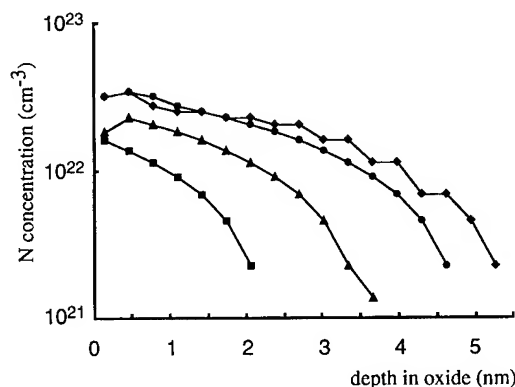


Fig. 1. Nitrogen content at the surface of an oxide plasma nitrided during: ■, 10 min; ▲, 1 h; ●, 3 h; ◆, 6 h.

From this figure, it is deduced that the nitrided oxide can be roughly approximated as a bilayer structure: a superficial nitrogen rich layer over the remaining pure oxide. The average nitrogen concentration $[N]$ and the thickness X of the superficial nitrogen rich layer are estimated from Fig. 1 for the four nitridation times.

2.1.3. Boron profile analysis

Due to the extremely low thickness of the oxide film, it is not possible to characterize accurately the boron profile in the thin oxide layer. For this reason, as will be discussed shortly, the boron diffusivity has been extracted from the boron profile in the substrate. This substrate profile has been measured by secondary ion mass spectroscopy (SIMS) and spreading resistance profiling (SRP). Good agreement has been found between the two techniques.

2.2. Modelling

Boron diffusion is simulated through the structure (polysilicon–oxide–substrate) using the TITAN process simulator [4].

The polysilicon layer acts as a constant source diffusion of boron: the concentration of boron in polysilicon is constant because the boron diffusion in polysilicon is rapid (assuring a flat profile after a very short time), and the amount of boron penetrating into the oxide and the substrate is small

compared to the total implantation dose into the polysilicon. Boron diffuses through the pure or plasma-nitrided oxide film with an unknown diffusivity, and, as the samples have been annealed for a long duration, can penetrate into the Si substrate for each oxide thickness. The boron concentration is rather low in the substrate and the diffusivity of boron in silicon is the intrinsic diffusivity which is already well known. So the boron profile in the substrate depends only on its effective diffusivity in the oxide. This diffusivity can be obtained by fitting in the substrate the experimental profile and the simulated one.

The value of the segregation coefficient at the Si/SiO₂ and Poly/SiO₂ interfaces is not unambiguously determined. At the Si/SiO₂ interface, Charitat and Martinez [5] obtained an average segregation coefficient equal to 0.6, nearly independent of the temperature in neutral ambient, whereas Antoniadis et al. [6], by investigating the segregation during the oxide growth, found a segregation coefficient dependent on the temperature, with values between 0.13 at 900°C and 0.86 at 1200°C. Since the experimental conditions in the present work are similar to the ones used by Charitat and Martinez, the boron segregation coefficient has been chosen to be $m_{\text{Si/SiO}_2} = 0.6$ for both Si/SiO₂ and Poly/SiO₂ interfaces.

With this approach the pure oxide film has been studied first by considering that the boron diffusivity D^{ox} is constant for a given annealed temperature. Once the boron diffusivity in pure oxide was determined, it was possible to get, in the same way, the diffusivity of boron in the plasma-nitrided oxide. This oxide can be indeed considered, as mentioned above, as the superposition of the nitrogen rich layer in which the boron diffusivity is D^{nit} and the pure oxide layer with the boron diffusivity D^{ox} , just determined.

Under these conditions good fits were always obtained between the simulated and experimental profiles from both SIMS and SRP data on 0.5 to 1 μm in the substrate. In Fig. 2, the quality of the fits is illustrated: for a sample with a pure 5 nm thick oxide and annealed at 930°C for 48 h, the SIMS profile and the calculated profile are perfectly adjusted by using $m_{\text{Si/SiO}_2} = 0.6$ and $D^{\text{ox}} = 10^{-18} \text{ cm}^2 \text{ s}^{-1}$. By changing the segregation

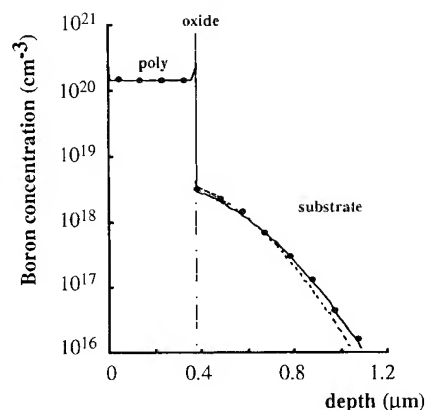


Fig. 2. Comparison between SIMS (●) and simulated profiles (5 nm thick pure oxide, annealed 48 h at 930°C): full line: $m_{\text{Si/SiO}_2} = 0.6$; dashed line: $m_{\text{Si/SiO}_2} = 0.17$.

coefficient according to the expression given by Antoniadis et al. [6], i.e. at 930°C $m_{\text{Si/SiO}_2} = 0.17$, the quality of the adjustment is poorer in the substrate, whereas the new value we got for D^{ox} ($= 6 \times 10^{-19} \text{ cm}^2 \text{ s}^{-1}$) is about the same. This result confirms the choice for the segregation coefficient.

3. Results

3.1. In pure oxides

By fitting experimental and simulated profiles obtained on samples whose oxide is 5, 8 or 11 nm thick, boron diffusivity has been obtained in pure oxide over a large (900°C–1200°C) temperature range.

Values of the diffusivity have been obtained in the 1000°C–1200°C temperature range through the 11 nm thick oxide. To extend the temperature range to lower temperatures thinner oxide films were used. It has been first verified that the diffusivity of boron is independent of the oxide film thickness: it has been found that the extracted diffusivities in some 5 nm thick oxides and 11 nm ones differ by at most a factor of two. This factor actually corresponds to experimental scattering: this same factor between the diffusivities has also been extracted from SIMS data obtained on the same sample.

Hence, examination of 5 and 8 nm thick oxide films, allowed the temperature range to be extended to 900°C–1000°C.

All the extracted diffusivities can be fitted on a single Arrhenius law:

$$D^{\text{ox}} = D_0^{\text{ox}} \exp(-Q^{\text{ox}}/kT)$$

with $Q^{\text{ox}} = 3.2$ eV and $D_0^{\text{ox}} = 2 \times 10^{-5} \text{ cm}^2 \text{ s}^{-1}$ represented by the graph (a) in Fig. 3. As the oxide thickness has no systematic influence on the diffusivity, the 5, 8 or 11 nm thick oxides have not been distinguished in this figure.

The results are in good agreement with the ones given in literature for the temperature range 1000°C–1200°C, particularly with the ones obtained by Wong and Lai [7]. The use of a wider temperature range in this study enables the determination of the activation energy with a better accuracy.

3.2. In plasma nitrided oxides

Once the boron diffusivity in a pure oxide is known, adjustments are made for each of the plasma nitrided films described as a bilayer (nitro-

gen rich layer with thickness X -pure oxide layer). Next the boron diffusivity D^{nit} in the nitrogen rich layer as a function of its average nitrogen concentration $[N]$ has been obtained for several temperatures. As shown in Fig. 3, by reporting these diffusivities as a function of the inverse of the temperature, the expected variation has been obtained for a given temperature, the more nitrided the oxide, the lower the diffusivity, confirming that the oxide nitridation acts as a barrier of diffusion for boron. But this efficiency tends to decrease with the annealing temperature and is even expected to disappear around 850°C as evidenced by the extrapolation shown by dashed lines in Fig. 3. This important fact will have to be verified in future work.

For each average nitrogen concentration, the diffusivity values are fitted to an Arrhenius law, to extract the activation energy Q^{nit} , and the pre-exponential term D_0^{nit} . When the nitrogen concentration increases both terms decrease. The difference $-(Q^{\text{nit}} - Q^{\text{ox}})$ and $-\ln(D_0^{\text{nit}}/D_0^{\text{ox}})$ are expressed as a function of the nitrogen concentration (cf. Figs. 4(a) and (b)) and a linear decrease of the activation energy Q^{nit} and an exponential decrease of the pre-exponential term D_0^{nit} with the nitrogen content have been observed. Using this method the following relation between diffusivity and the average nitrogen concentration has been obtained:

$$D^{\text{nit}} = D_0^{\text{nit}} \exp(-Q^{\text{nit}}/kT),$$

$$Q^{\text{nit}} = Q^{\text{ox}} - \lambda_Q[N] \text{ with } \lambda_Q = 1.06 \times 10^{-22} \text{ eV cm}^3;$$

$$D_0^{\text{nit}} = D_0^{\text{ox}} \exp(-\lambda_S[N]) \text{ with } \lambda_S = 1.06 \times 10^{-21} \text{ cm}^3.$$

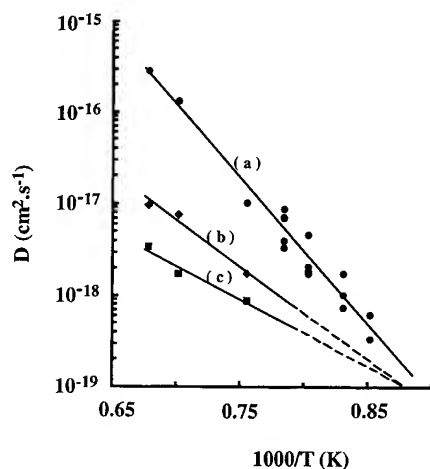


Fig. 3. Boron diffusivity in (a) pure oxide, (b) oxide nitrided for 1 h: average $[N] = 1.4 \times 10^{22} \text{ cm}^{-3}$, (c) oxide nitrided for 3 h: average $[N] = 2 \times 10^{22} \text{ cm}^{-3}$.

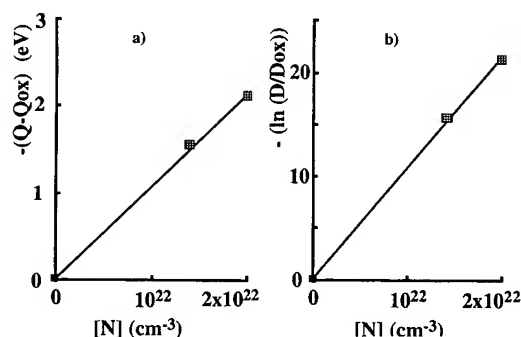


Fig. 4. Influence of N content on (a) the activation energy, and (b) the pre-exponential factor of boron diffusivity.

The exponential decrease of D_0^{nit} can, thus, be interpreted as a linear decrease of the diffusion entropy with $[N]$.

In order to improve the evaluation of λ_Q and λ_S , the actual local nitrogen content has been taken into account after deconvoluting the Auger profiles in the whole layer (outer surface and Si/SiO₂ interface). Next, Fick's equation is solved for the (oxide–substrate) structure with a boron diffusivity dependent on the local nitrogen concentration:

$$\frac{\partial[B]}{\partial t} = \frac{\partial}{\partial x} \left(D^{\text{nit}}([N]) \frac{\partial[B]}{\partial x} \right).$$

By fitting this calculated profile with the experimental one, values of λ_Q and λ_S are obtained with standard deviations of less than 2% of the average value:

$$\lambda_Q = 1.05 \times 10^{-22} \text{ eV cm}^3 \quad \lambda_S = 9.60 \times 10^{-22} \text{ cm}^3.$$

4. Discussion

In this section a simple model is proposed to qualitatively explain the linear decrease of the activation energy with the nitrogen concentration.

The rather high activation energy in the pure oxide suggests that boron does not diffuse via an interstitial mechanism. Furthermore, the stable configuration of the boron atom is a substitutional site on the Si sub-network. So boron can diffuse through the oxide if its bonds with first neighbours are broken, i.e. B–O bonds in pure oxide and both B–O and B–N bonds in nitrided oxides. Nitrogen atoms are assumed to be randomly distributed on the O sub-network. For this reason, in SiO₂, the activation energy Q^{ox} is a function of the energy bond strength B–O, whereas, in SiO_{2-x}N_x, Q^{nit} is a function of both B–O and B–N bond strengths. It is assumed that in the first order, Q^{nit} varies roughly as the average bond strength between B and its neighbours:

$$Q^{\text{nit}} = k(x Q_{\text{BN}} + (1-x) Q_{\text{BO}}),$$

where Q_{BO} and Q_{BN} are the bonding energies of B–O and B–N, respectively.

The coefficient of proportionality k is considered first: in pure oxide, $x = 0$ and $Q^{\text{ox}} = k Q_{\text{BO}}$. Using

the relation $x = [N]/4.5 \times 10^{22}$, Q^{nit} is expressed as a function of nitrogen concentration $[N]$:

$$Q^{\text{nit}} = Q^{\text{ox}} - \lambda[N] \quad \text{with} \quad \lambda = \frac{Q^{\text{ox}}}{Q_{\text{BO}}} \left(\frac{Q_{\text{BO}} - Q_{\text{BN}}}{4.5 \times 10^{22}} \right).$$

The exact values of Q_{BO} and Q_{BN} are not experimentally determined but all existing thermodynamical data favour that Q_{BO} is greater than Q_{BN} . In the diatomic molecules, the bond strengths are 8.4 eV for B–O and 4 eV for B–N, whereas, the formation enthalpies are 6.5 eV per B atom in B₂O₃ and 2.6 eV for BN. So $Q_{\text{BO}} - Q_{\text{BN}}$ is positive, supporting the linear decrease of Q^{nit} with the nitrogen concentration.

The value of λ has been obtained by using bond strengths B–O and B–N in diatomic molecules as $\lambda = 3.8 \times 10^{-23} \text{ eV cm}^3$; from the formation enthalpies $\lambda = 4.3 \times 10^{-23} \text{ eV cm}^3$. Both these theoretical values compare reasonably well with the experimental one, supporting the simple model that there is a correlation between Q^{nit} and the average bond strength in nitrided oxide. This correlation explains the linear decrease of the activation energy with nitrogen concentration.

5. Conclusions

By using p+ polysilicon MOS structures, annealing for long duration allows boron to diffuse through the thin oxide into the substrate. By fitting the boron experimental profile with the calculated one, boron diffusivity in the oxide has been obtained for each structure annealed at a given temperature. In order to get the boron diffusivity for a large range of temperatures, structures with various oxide thicknesses have been studied. All diffusivities have been fitted to a single Arrhenius law.

Boron diffusion in plasma nitrided oxide has been quantified at temperatures above 1000°C. As expected lower diffusivities have been observed in nitrided oxides as compared to pure ones, and this is primarily due to a lower value of the pre-exponential term. But the efficiency of the nitrided oxide as a barrier of diffusion for boron has to be better determined at lower temperatures particularly around 800°C–850°C. Finally, an explanation has been given for the observed linear decrease

of the activation energy with the nitrogen content: in the nitrated oxides, the diffusion activation energy is correlated with the average bond strength between B and its neighbours O and N.

References

- [1] B. Piot, K. Barla, B. Garcin and A. Straboni, *Microelectron. Eng.* 15 (1991) 475.
- [2] K. Barla, D. Nicolas, R. Pantel, B. Vuillermoz, A. Straboni and Y. Caritini, *J. Appl. Phys.* 68 (1990) 3635.
- [3] P. Debenest, K. Barla, A. Straboni and B. Vuillermoz, *Appl. Surf. Sci.* 36 (1989) 196.
- [4] A. Gérodolle, C. Corbex, A. Poncet, T. Pedron and S. Martin, in: *Software Tools for Process, Device and Circuit Modelling*, ed. W. Crans (Boole, Dublin, 1989) p. 56.
- [5] G. Charitat and A. Martinez, *J. Appl. Phys.* 55 (1984) 2869.
- [6] D.A. Antoniadis, A.G. Gonzales and R.W. Dutton, *J. Electrochem. Soc.* 124 (1978) 813.
- [7] C.Y. Wong and F.S. Lai, *Appl. Phys. Lett.* 48 (1986) 1658.



ELSEVIER

Journal of Non-Crystalline Solids 187 (1995) 112–118

JOURNAL OF
NON-CRYSTALLINE SOLIDS

Formation of visible photoluminescence bands in Si⁺-implanted silica glasses and thermal oxide films on crystalline Si

Tsutomu Shimizu-Iwayama^{a,*}, Katsunori Fujita^a, Mitsuru Akai^a, Setsuo Nakao^b,
Kazuo Saitoh^b

^a Department of Materials Science, Aichi University of Education, Igaya-cho, Kariya-shi, Aichi 448, Japan

^b National Industrial Research Institute of Nagoya, Hirate-cho, Kita-ku, Nagoya 462, Japan

Abstract

Photoluminescence in Si⁺-implanted silica glasses and thermal oxide films has been studied, as-implanted and subsequent to annealing. Si ions were implanted at room temperature or liquid nitrogen temperature to a fluence of $\sim 10^{17}$ ions/cm². Two visible luminescence bands were found in both silica glasses and thermal oxide films: one peaked around 2.0 eV, observed in as-implanted specimens and annealed completely at about 600°C; the other peaked around 1.7 eV, observed only after heating specimens to about 1100°C, the temperature at which Si segregates from SiO_x. In addition, a periodic interference pattern in the luminescence spectra was observed only in ion implanted thermal oxide films. It was found that the peak energy of the luminescence band around 2.0 eV depends on the fluences of the implanted Si ions and implantation temperatures, but that of the luminescence band around 1.7 eV does not. It was also found that the 2.0 eV band anneals in parallel to the oxygen vacancy (E') centers, and that the Raman lines due to Si–Si bonds grow and the interference patterns in optical absorption spectrum are induced by annealing Si⁺-implanted specimens at higher temperature. Based on these studies, the 2.0 eV band is ascribed to electron–hole recombination in Si-rich SiO₂ and the 1.7 eV band to electron–hole recombination in the interface between the Si nanocrystal and the SiO₂ formed by segregation of crystalline Si from SiO_x.

1. Introduction

Ion implantation has been extensively employed to modify the surface layers of materials and to synthesize the new phases having novel properties.

The ion implantation technique has the advantage that given numbers of ions can be placed in a controlled depth distribution and it is extensively used for microelectric applications. Many studies of ion implantation on insulating materials have also been carried out for the purpose of modifying the optical properties [1–7]. Recently, it has been found that implantation of ions into some insulating glasses gives rise to non-linear optical properties, due to metallic colloid formation [8–10].

* Corresponding author. Tel: +81-566 36 3111, ext. 554.
Telefax: +81-566 36 4337. E-mail: tiwayama@auecc.aichi-edu.ac.jp.

Si-related materials such as SiO_2 are widely used in the microelectronics industry throughout silicon and other semiconductor based technologies as gate oxides in metal-oxide semiconductor field effect transistors and as electrical insulation. Recently, much attention has also been paid to porous Si [11,12] and Si ultrafine particles [13–16] as a light source in the visible range. Electroluminescent (EL) devices of porous Si have also been made by a number of research groups [17,18]. Although many models of the light emission from these nanostructures have been proposed, the mechanism is still controversial.

The present authors [19–21] have found that implantation of Si ions into silica glass yields characteristic luminescence bands near 2.0 eV, similar to those of porous Si and Si ultrafine particles, suggesting that Si nanoparticles are formed in the glass phase. The Si nanocrystals in SiO_2 has advantages over porous Si and Si ultrafine particles as a luminescence source, since the particles are embedded and shielded from the atmosphere. Two types of luminescence bands have been found, one in the specimen as implanted and the other after annealing at 1100°C, at which SiO_x becomes unstable. The luminescence observed after annealing at 1100°C is of particular interest, since the segregation of Si from SiO_x should result in formation of Si nanocrystals. Because of possible use of Si nanocrystals in oxides as a higher photon energy luminescence source, it is of interest to examine carefully the photoluminescence properties of Si^+ -implanted silica glass and thermal oxide films.

The purpose of this paper is to report detailed studies of photoluminescence from Si^+ -implanted silica glass and thermal oxide films. By employing the studies of electron spin resonance (ESR), Raman scattering and optical absorption, we show that the luminescence band observed around 2.0 eV in as-implanted specimen arises from defects in Si-rich SiO_2 and the luminescence band observed around 1.7 eV after high-temperature annealing arises from the interface between the Si nanocrystal and the SiO_2 formed by segregation of crystalline Si from SiO_x . The mechanism of the emission of the luminescence and the similarities and the differences of the luminescence in silica glasses and thermal oxide films are discussed.

2. Experimental procedure

Synthetic silica glasses (Suprasil W), and oxidized boron doped p-type Si wafers with a resistance of 0.01–0.02 Ωcm were used in the present experiments. The orientation of the Si wafers was (100). Thermal oxide films were obtained through oxidation of the wafers at 1050°C for 10 h in 60% H_2 and 40% O_2 ambient. The oxide thickness was about 1.75 μm . Si ions with an energy of 1 MeV were implanted into specimens placed in vacuum to fluences of $(1\text{--}4) \times 10^{17}$ ions/ cm^2 . Implantation of 150 keV Si ions was also used for Raman measurements, for which a higher density of implantation was needed. The temperature of the substrates during ion implantation was kept at room or liquid nitrogen temperature. Heat treatments of the implanted specimens were carried out in a vacuum using an electric oven.

Photoluminescence and Raman spectra of the Si^+ -implanted specimens before and after annealing were measured at room temperature using a conventional method. An Ar-ion laser (488 nm, 2.54 eV) was used as an excitation source and the luminescence and scattered light were detected by a cooled photomultiplier tube, employing the photon counting technique. ESR spectra were also measured at room temperature using an X-band spectrometer with a modulation frequency of 100 kHz and a low microwave power of 5 μW . Optical absorption spectra were measured at room temperature with a conventional dual-beam spectrophotometer.

3. Results

Implantation of Si ions into silica glass produces an optical absorption spectrum increasing from about 1.0 eV towards the ultraviolet. Annealing below 1100°C does not change the spectrum appreciably, but annealing at 1100°C produces a periodic pattern with a constant interval, as shown in Fig. 1. It is clear that the substantial change in the structure of implanted Si is induced by annealing at 1100°C, the temperature at which the SiO_x phase becomes unstable. In order to confirm the segregation of Si nanocrystals after annealing, we examined the

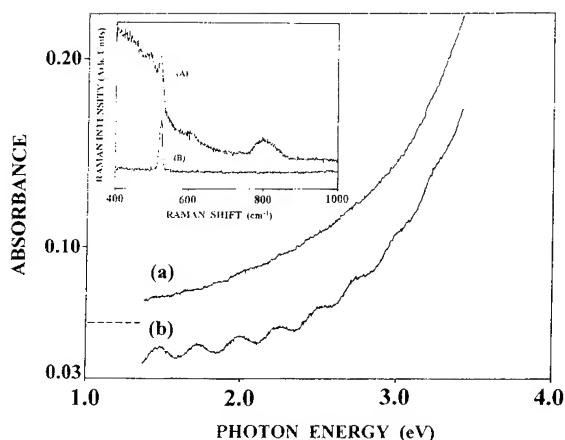


Fig. 1. Optical absorption spectra of 1 MeV Si^+ -implanted silica glass with a fluency of 2×10^{17} ions/ cm^2 at room temperature, (a) without annealing and (b) after annealing at 1100°C for 960 min. Curve (a) is shifted vertically to the position of the horizontal dashed line. The insets show Raman spectra of (A) 150 keV Si^+ -implanted silica glass with a fluency of 6×10^{17} ions/ cm^2 at room temperature, after annealing at 1100°C for 240 min and that of (B) unimplanted crystalline Si wafer.

Raman spectrum. The Raman spectra of unimplanted specimens exhibit a broad peak at 800 cm^{-1} , attributed to the Si–O–Si symmetric stretching vibration mode [7,22]. We could not observe any change in Raman spectrum of the specimen implanted at 1 MeV after annealing at 1100°C . We observed, however, a growth of the Si–Si Raman line around 520 cm^{-1} in a specimen implanted with 150 keV Si ions to higher fluency after annealing at 1100°C , as shown in Fig. 1. It is noted that no luminescence was observed in this specimen.

Photoluminescence spectra of the specimens implanted at room temperature and liquid nitrogen temperature to several fluencies were obtained before heat treatments. The results are shown in Figs. 2 and 3. A broad luminescence band around 2.0 eV is observed. The peak energy shifts to lower energy with increasing fluency of Si ions and to higher energy as implantation temperature decreases. Moreover, a periodic pattern with a constant interval is observed only in the thermal oxide specimens.

The luminescence spectrum observed after annealing at 1100°C was completely different from

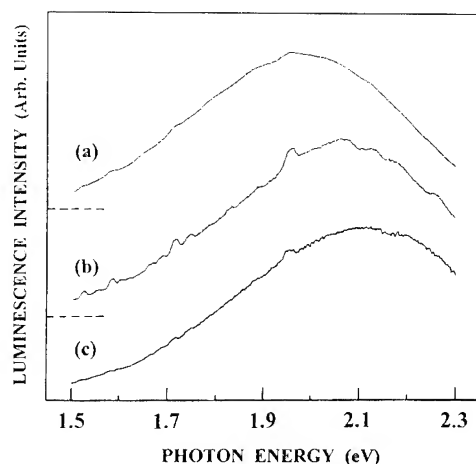


Fig. 2. Photoluminescence spectra of 1 MeV Si^+ -implanted silica glass (a) with a fluency of 2×10^{17} ions/ cm^2 at room temperature, and a fluency of 1×10^{17} ions/ cm^2 (b) at room temperature and (c) at liquid nitrogen temperature, without annealing. The zero lines of curve (a) and (b) are shifted vertically to the position of the horizontal dashed line.

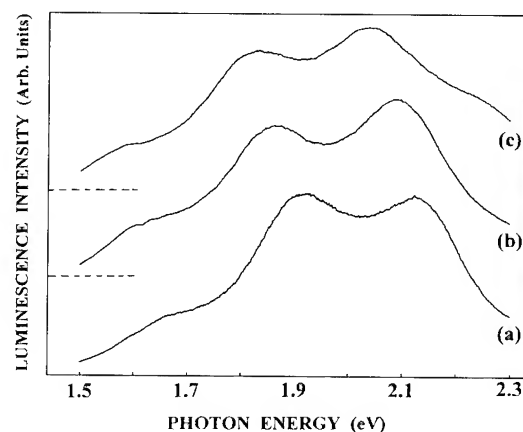


Fig. 3. Photoluminescence spectra of 1 MeV Si^+ -implanted thermal oxide films on crystalline Si with fluencies of (a) 1×10^{17} , (b) 2×10^{17} and (c) 4×10^{17} ions/ cm^2 at room temperature, without annealing. The zero lines of curve (b) and (c) are shifted vertically to the position of the horizontal dashed line.

that shown in Figs. 2 and 3, reflecting the change in the morphology of implanted Si. The spectra of the luminescence induced after annealing at 1100°C are shown in Fig. 4. It is clear in the figure, that an additional peak is observed on the low-energy side

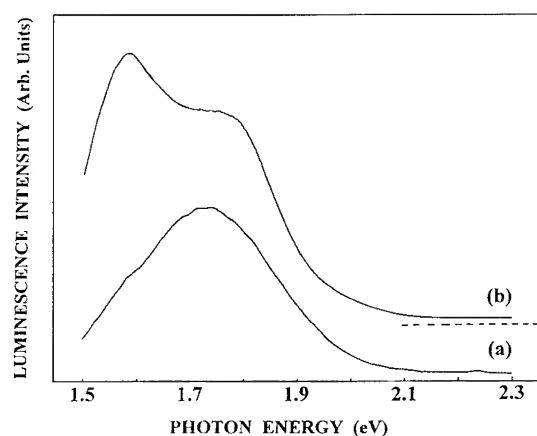


Fig. 4. Photoluminescence spectra of 1 MeV Si^+ -implanted (a) silica glass and (b) thermal oxide film with fluences of 2×10^{17} ions/ cm^2 at room temperature, after subsequent annealing at 1100°C for 90 min. The zero line of curve (b) is shifted vertically to the position of the horizontal dashed line.

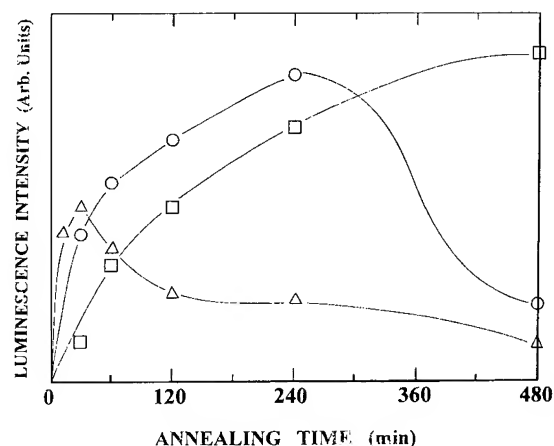


Fig. 5. Changes of the photoluminescence intensity as a function of annealing time at 1100°C . 1 MeV Si^+ was implanted into silica glass with fluences of (circle) 2×10^{17} and (triangle) 4×10^{17} ions/ cm^2 at room temperature, and with fluence of (square) 2×10^{17} ions/ cm^2 at liquid nitrogen temperature.

of the spectrum for the Si implanted thermal oxide specimen. Moreover, the luminescence intensity of the film is much stronger than that of silica glass. A similar luminescence band is also observed in specimens implanted with Si ions to other fluences at room and at liquid nitrogen temperatures and annealed at 1100°C . We also found that the shapes of these curves are almost the same and independent of annealing time, only the intensities depend on annealing time.

In order to make clear the origins of the photoemission, we examined the growth and annealing of these two bands carefully. Though the results are not shown, we found that the 2.0 eV luminescence band starts to decrease around 300°C and disappears after annealing at 600°C for 30 min, in parallel to the intensity of the E' center line of the ESR spectrum.

The results for the evolution and annealing of the 1.7 eV luminescence band during annealing at 1100°C are shown in Fig. 5. Evidently the luminescence intensity grows and then decreases for all specimens studied: the growth and reduction occur faster in the specimens implanted at room temperature and furthermore in those implanted to higher fluences. A peak shift of the 1.7 eV band was not observed during annealing at 1100°C .

A significant difference is observed between the property of luminescence centers exhibiting the 2.0 eV band, formed in as-implanted specimens and the 1.7 eV band, formed after annealing at 1100°C . The peak energy of the luminescence band depends on fluences and implantation temperatures in the former, but not in the latter. Moreover, the latter does not show any peak shift during growth and annealing. Since the former anneals along with the E' centers, they are probably associated with the defects. The latter, which is formed above the decomposition temperature of SiO_x , may be ascribed to crystalline Si precipitates.

4. Discussion

In this paper we found two luminescence bands around 2.0 and 1.7 eV: the 2.0 eV band is produced in specimens in which implanted Si is in the form of SiO_x or amorphous Si, while the 1.7 eV band arises from the specimens in which implanted Si forms most probably as a crystalline Si phase. Both of these luminescence bands were not observed in silica glass and thermal oxide film implanted with other ions, such as Ar, B and Al ions, and hence are related to implanted Si ions.

The 2.0 eV luminescence band is evidently related to defects since it is annihilated along with the E' centers. The result indicates that the luminescence center is either an oxygen deficiency center or oxygen interstitials stabilized by the SiO_x phase in SiO₂. It appears that electron-hole pairs are produced in the SiO_x phase by photo excitation and emission is induced at the defect sites in the SiO_x phase. Since the value of *x* in SiO_x depends on fluences and implantation temperatures, the peak energy of the luminescence band decreases as the Si segregation becomes dominant. Thus we consider that Si excess defects formed near SiO_x are responsible for the luminescence.

The periodic patterns with a constant interval which appeared in the photoluminescence spectra of ion implanted thermal oxide films, as shown in Fig. 3, originate from the interference of the reflected light at the surface and the interface. The interval of the interference pattern due to multiple reflections is interpreted by using the following equation [23]:

$$2nd = (1/\lambda_2 - 1/\lambda_1)^{-1},$$

where *n* is the refractive index, *d* is the thickness of the film, and λ_1 and λ_2 ($\lambda_1 > \lambda_2$) are the maximum peak wavelengths appearing in the spectra. Using the value of *d* = 1.75 μm (thickness of the thermal oxide film), we obtain *n* = 1.58. This value *n* is little larger than that of SiO₂ (*n* = 1.46). Since part of implanted Si ions form SiO_x (*x* < 2) [24,25], the average value of the refractive index in implanted layer differs from that of SiO₂.

Before discussing the origin of the luminescence band that appears around 1.7 eV after annealing at 1100°C, we emphasize that the Si phase is separated from SiO_x in this temperature range [26]. The appearance of a periodic pattern in the optical absorption spectra after annealing at 1100°C can be ascribed to precipitation of Si. The large difference of refractive indices between SiO₂ and Si and the preferential precipitation of Si near the end of the Si⁺ implantation range will produce the interference pattern, the interval of which depends on implantation energy but not on the annealing time. Using the equation above, we obtain the value of 1.5 μm for the depth of the precipitated Si rich layer from the surface. This depth agrees well with the

peak value of the range of 1 MeV Si in SiO₂ obtained by TRIM calculation [27]. Thus we can conclude that the Si precipitates develop around the depth of 1.5 μm after annealing at 1100°C. The precipitation of Si by annealing at 1100°C is further evidenced by the growth of the Raman line around 520 cm⁻¹ attributed to the crystalline Si. Thus it is most likely that the 1.7 eV luminescence band is formed as a result of crystalline Si precipitation and hence of formation of Si nanoparticles.

Now, we discuss on the presumption that the 1.7 eV luminescence band is due to crystalline Si nanoparticles formed by segregation of Si from SiO_x. As seen from Fig. 5, the growth rate of the luminescence is faster for specimens implanted with higher fluence, and also for specimens implanted at room temperature than those at low temperature, if the fluence is the same. The growth rate of the size of the Si particles is expected to increase as the fluence increases and the temperature of implantation increases. Thus the dependence of the initial growth rate on the implantation energy and temperature, as shown in Fig. 5, is consistent with the presumption that the 1.7 eV luminescence band is due to crystalline Si nanoparticles. According to Fig. 5, prolonged annealing reduces the intensity of luminescence. The reduction is faster for the specimens for which the growth is faster. Therefore it appears that the intensity of the luminescence depends on the size of the nanoparticles; strong emission is observed when the Si particles have an appropriate size. According to Okada et al. [28], the intensity of the Raman line increases abruptly as the size of the particle increases; practically no Raman line is observed when the size of the Si particle in the specimen is below 8 nm. Thus the absence of the Si-Si Raman line in the specimen in which the 1.7 eV luminescence band is observed and its presence in the densely implanted specimens, in which no 1.7 eV luminescence is observed, is in accordance with the presumption on that there is a critical size at which the luminescence is enhanced. Although the intensity of the luminescence appears to be governed by the size, the peak energy does not. Therefore the 1.7 eV luminescence, if it is emitted by Si nanoparticles, it is not due to recombination of electron-hole pairs confined quantum mechanically.

Based on the arguments above, we propose that the 1.7 eV emission is due to defect sites at the interface between crystalline Si nanoparticles and SiO_2 . The size dependence of the luminescence intensity can be explained as follows. If the size is too small, the incident photons (2.54 eV) cannot induce the band-to-band transition whose energy increases from the Si band-to-band transition energy due to quantum confinement. According to the theoretical calculation by Takagahara et al. [29], the radius of the Si particle corresponding to this energy is 1.5 nm. There are a few possible reasons why the emission yield decreases as the size increases. Firstly the band-to-band transition energy of the confined system should be larger than the emission energy. The theoretical calculation indicates that the radius corresponding to this energy is 2 nm. Secondly as the size increases the interface-to-volume ratio decreases. Thirdly the probability of the energy transfer to the interface will decrease, particularly if the nanocrystals include imperfection. In any case we expect that the nanocrystals of a radius of 1.5–2 nm induces the emission at the highest efficiency, excited with an Ar-ion laser (2.54 eV). Though the origin of the low-energy band observed only in thermal oxide films is not yet clear in the present experiments, it probably arises from the interference as previously discussed.

5. Conclusions

We showed that the implantation of Si ions into silica glasses and thermal oxide films produces characteristic bands near 2.0 eV. The one that is observed in as-implanted specimens can be attributed to the excess Si defects formed in the SiO_x environment. The one that is observed after annealing at 1100°C can be attributed to the defects in the interface between the SiO_2 and the Si nanocrystals formed by precipitation from SiO_x . The present experimental results indicate that the emission near 2.0 eV arises from a variety of defects in Si-excess SiO_2 or by slight oxidation of Si. The present experimental results suggest strongly that electron-hole pairs produced in the nanocrystals dissipate the energy more likely at the surface of

nanocrystals rather than emitting photons within the nanocrystals. Luminescence from thermal oxide films may therefore be applicable to the Si-based optical devices in a similar way to that from porous Si.

The authors would like to express their gratitude to Professor Noriaki Itoh, Nagoya University, for valuable discussions.

References

- [1] A. Perez, Nucl. Instrum. Methods B1 (1984) 612.
- [2] A.H. van Ommen, J. Appl. Phys. 56 (1984) 2790.
- [3] S. Noda, H. Doi, T. Hioki, J. Kawamoto and O. Kamigaito, J. Mater. Sci. 22 (1987) 4267.
- [4] P.D. Townsend, Rep. Prog. Phys. 50 (1987) 501.
- [5] R.H. Magruder III, R.A. Weeks, R.A. Zuhr and G. Whichard, J. Non-Cryst. Solids. 129 (1991) 46.
- [6] H. Hosono, Y. Suzuki, Y. Abe, K. Oyoshi and S. Tanaka, J. Non-Cryst. Solids, 142 (1992) 287.
- [7] T. Shimizu-Iwayama, T. Niimi, S. Nakao and K. Saitoh, Jpn. J. Appl. Phys. 32 (1993) L1451.
- [8] K. Becker, L. Yang, R.F. Haglund Jr, R.H. Magruder, R.A. Weeks and R.A. Zuhr, Nucl. Instrum. Methods B59 & 60 (1991) 1304.
- [9] H. Hosono, Y. Abe, Y.L. Lee, T. Tokizaki and A. Nakamura, Appl. Phys. Lett. 61 (1992) 2747.
- [10] Y. Takeda, T. Hioki, T. Motohiro and S. Noda, Appl. Phys. Lett. 63 (1993) 3420.
- [11] L.T. Canham, Appl. Phys. Lett. 57 (1990) 1046.
- [12] V. Lehmann and U. Gösele, Appl. Phys. Lett. 58 (1991) 856.
- [13] D.J. DiMaria, J.R. Kirtley, E.J. Pakulis, D.W. Dong, T.S. Kuan, F.L. Pesavento, T.N. Theis and J.A. Cutro, J. Appl. Phys. 56 (1984) 401.
- [14] S. Furukawa and T. Miyasato, Jpn. J. Appl. Phys. 27 (1988) L2207.
- [15] H. Takagi, H. Ogawa, Y. Yamazaki, A. Ishizaki and T. Nakagiri, Appl. Phys. Lett. 56 (1990) 2379.
- [16] H. Morisaki, F.W. Ping, H. Ono and K. Yazawa, J. Appl. Phys. 70 (1991) 1869.
- [17] A. Richter, P. Steiner, F. Kozlowski and W. Lang, IEEE Electron Device Lett. EDL-12 (1991) 691.
- [18] N. Koshida and H. Koyama, Appl. Phys. Lett. 60 (1992) 347.
- [19] T. Shimizu-Iwayama, M. Ohshima, T. Niimi, S. Nakao, K. Saitoh, T. Fujita and N. Itoh, J. Phys.: Condens. Matter. 5 (1993) L375.
- [20] T. Shimizu-Iwayama, K. Fujita, S. Nakao, K. Saitoh, T. Fujita and N. Itoh, J. Appl. Phys., 75 (1994) 7779.
- [21] T. Fujita, M. Fukui, S. Okada, T. Shimizu-Iwayama, T. Hioki and N. Itoh, Nucl. Instrum. Methods B91 (1994) 418.
- [22] B.G. Varshal, V.N. Denisof, B.N. Marvin, G.A. Pavlova, V.B. Padobedov and K.E. Sterin, Opt. Spektrosk. 47 (1979) 344.

- [23] M. Born and E. Wolf, Principles of Optics (Pergamon, New York, 1974).
- [24] K.F. Heidemann, Radiat. Eff. 61 (1982) 235.
- [25] T. Shimizu, N. Itoh and N. Matsunami, J. Appl. Phys. 64 (1988) 3663.
- [26] T. Matsushita, T. Aoki, T. Ohtsu, H. Yamoto, H. Hayashi, M. Okayama and Y. Kawana, Jpn. J. Appl. Phys. Suppl. 15 (1976) 35.
- [27] J.F. Ziegler, J.P. Biersack and U. Littmark, The Stopping and Range of Ions in Solids, Vol. 1 (Pergamon, New York, 1985).
- [28] T. Okada, T. Iwaki, K. Yamamoto, H. Kasahara and K. Abe, Solid State Commun. 49 (1984) 809.
- [29] T. Takagahara and K. Takeda, Phys. Rev. B46 (1992) 15 578.



ELSEVIER

Journal of Non-Crystalline Solids 187 (1995) 119–123

JOURNAL OF
NON-CRYSTALLINE SOLIDS

Parameters controlling the generation of natural intrinsic EX defects in thermal SiO₂ on Si

A. Stesmans*, F. Scheerlinck

Department of Physics, Katholieke Universiteit Leuven, 3001 Leuven, Belgium

Abstract

A K-band electron spin resonance study of the appearance of the natural intrinsic EX center in dry and wet thermal (001) and (111)Si/SiO₂ is presented. In order to isolate the key parameter(s) responsible for EX generation, the oxidation growth conditions, together with substrate characteristics, are systematically varied over broad ranges, revealing that the grown oxide thickness is the sole physical quantity determining the areal defect density. SiO₂ etchback experiments in combination with accurate stylus profilometry are used to determine the spatial location and volume concentration of the EX defects. The center's thermochemical properties are investigated through alternated isochronal anneals in vacuum and H₂ ambient. The EX generation is interpreted in terms of O enrichment in combination with the aspect of gradual structural relaxation of the SiO₂ layer.

1. Introduction

Since impurity contamination has ceased to be a major concern with present preparation techniques for thin (~ 100 Å) thermal SiO₂, attention is mainly focused on intrinsic (not impurity-related) imperfections such as the natural P_b interface defect [1] in as-grown Si/SiO₂ and various radiation-induced defects in a-SiO₂ [2].

Stesmans [3] has recently reported the ESR observation of a 'new' intrinsic defect in as-grown thermal SiO₂ on (111)Si. This so-called EX center displays a remarkably isotropic three-peak ESR spectrum comprising a Voigt-like central line at

$g = 2.00246 \pm 0.00003$ of $\Delta B_{pp} \approx 1$ G, amid a ²⁹Si hyperfine doublet of 16.1 G splitting.

In order to elucidate the mechanism(s) of EX generation during thermal oxidation of Si, it is necessary to find out where and under what circumstances the center is produced in the Si/SiO₂ structure. This is achieved through systematically varying the SiO₂ growth conditions such as oxidation temperature (T_{ox}), time (t_{ox}), and oxygen pressure (p_{O_2}), and the water content of the oxidizing ambient, in combination with ESR diagnosis.

2. Experimental procedures

Thin Si slices measuring 2×9 mm² for ESR analysis were oxidized and exhaustively dehydrogenated

* Corresponding author. Tel: +32-16 327 179. Telefax: +32-16 327 987. E-mail: andre.stesmans@fys.kuleuven.ac.be.

(vacuum annealed) in a conventional furnace [4] after a prethermal substrate cleaning. The SiO_2 thickness was measured using stylus profilometry on patterned oxides [5]. ESR experiments were carried out in adiabatic slow passage mode at 4.3 K in a K-band (~ 20.2 GHz) spectrometer [6]. Areal spin densities N_A^{EX} were determined relative to a c-Si:P marker sample ($[P] = 1.7 \times 10^{18} \text{ cm}^{-3}$).

3. Experimental results

A first set of systematic variations included the substrate room temperature resistivity (~ 10 – $1000 \Omega \text{ cm}$), the surface orientation [(111) or (001)], and the precleaning method (RCA procedure and an HF-based treatment [4]), neither of which leads to an essentially different EX generation behavior, although HF-precleaned surfaces (the focus of this work) are more prone to defect production during thermal oxidation.

An important observation was that, when accounting for the difference in oxidation rate between (001) and (111) surfaces, almost identical EX densities are introduced for both surface orientations. On samples postoxidation vacuum annealed at 790°C for ~ 1 h, a maximum of $(1.2 \pm 0.1) \times 10^{12} \text{ cm}^{-2}$ is observed in the N_A^{EX} versus d_{ox} profile for $T_{\text{ox}} = 800^\circ\text{C}$ [3]. This suggested the importance of the oxide thickness d_{ox} , prompting us to combine ESR diagnosis and stylus profilometry on various sets of samples grown under broadly varying conditions, i.e., $T_{\text{ox}} = 700$ – 930°C , $t_{\text{ox}} \approx 15$ min–24 h, $p_{\text{O}_2} \approx 0.4$ – 1.1 atm, while both wet (2.4% H_2O) and dry O_2 ambients were used. The results are summarized in the N_A^{EX} versus d_{ox} plot in Fig. 1: all the data points assemble around a single growth curve, whatever the substrate characteristics or oxidation temperature. This striking observation strongly suggests that N_A^{EX} is solely set by the oxide thickness. It needs to be remarked that low p_{O_2} and wet growth affect somewhat the maximum N_A^{EX} value (within a factor of 2), without however altering the generally observed defect generation behavior: from $d_{\text{ox}} \approx 100 \text{ \AA}$ onwards the EX centers become detectable, N_A^{EX} rising steeply with growing d_{ox} and peaking at $\sim 1.2 \times 10^{12} \text{ cm}^{-2}$ for $d_{\text{ox}} \approx 125 \text{ \AA}$,

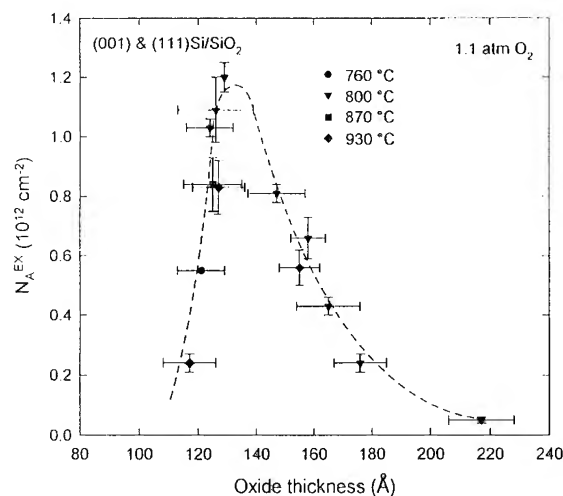


Fig. 1. Areal spin density profile of the EX center, measured at 4.3 K, as a function of measured d_{ox} for both (001) and (111)Si/SiO₂ structures grown at various T_{ox} in the range 760–930°C in 1.1 atm O₂, after subsequent dehydrogenation at 790°C. The dashed line is a guide to the eye.

whereupon a slower decline towards zero is observed for larger d_{ox} . (For $d_{\text{ox}} \approx 215 \text{ \AA}$, $N_A^{\text{EX}} \approx 5 \times 10^{10} \text{ cm}^{-2}$; for $d_{\text{ox}} \approx 600 \text{ \AA}$ the center can only be observed in oxidized Si powders, where the oxide-to-Si-substrate ratio is much enhanced.)

Next, the location of the EX defects in the Si/SiO₂ structure is addressed. It was previously [3] argued that the Si bulk and the Si/SiO₂ interface are excluded as possible EX locations, leaving only the a-SiO₂ layer as the possibility. Controlled SiO₂ etchback experiments were initiated on three (111) Si/SiO₂ samples grown in 1.1 atm dry O₂ at 800°C for 103, 221, and 255 min, respectively, and dehydrogenated at 790°C . The initial EX densities amounted to $(0.64 \pm 0.06) \times 10^{12} \text{ cm}^{-2}$, $(0.43 \pm 0.05) \times 10^{12} \text{ cm}^{-2}$, and $(0.05 \pm 0.01) \times 10^{12} \text{ cm}^{-2}$, respectively. Sequential SiO₂ etchback alternated with diagnostic ESR observations resulted in the EX volume density profiles shown in Fig. 2.

A first noticeable feature concerns the large ($> 10^{18} \text{ cm}^{-3}$) local defect concentrations. Second, it is observed that, even for wet oxides, the largest local spin densities occur near the free SiO₂ surface, while the volume concentration drops steadily in the oxide to become undetectable beyond about

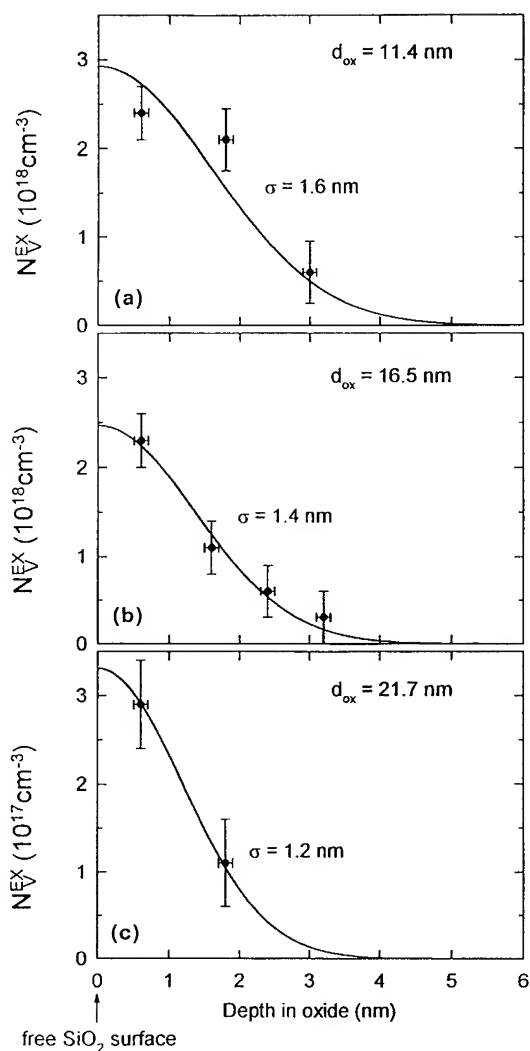


Fig. 2. Variation of the local volume density of the EX centers with depth in the SiO₂ layer for three (111)Si/SiO₂ structures grown at 800°C in 110 kPa dry O₂, obtained by crude derivation of the 4.3 K ESR areal density etchback profiles. The solid lines are fits to the data of hemi-Gaussian curves centered at the air/SiO₂ interface.

40 Å deep – closely identical for all three samples. The solid lines in Fig. 2 represent fits to the data of Gaussian functions centered at the air/SiO₂ interface, whose associated standard deviations σ provide a measure for the EX distribution width. The σ 's are found to be nearly identical: $\sigma \approx 16$, 14, and

12 Å in Figs. 2(a)–(c), respectively, indicating that EX remains a top ~ 40 Å phenomenon.

Finally, the thermochemical properties of the EX defect are considered. Starting from the observation that a postoxidation degassing treatment in vacuum (pressure $p < 3 \times 10^{-5}$ Pa) at $\sim 790^\circ\text{C}$ enhances N_A^{EX} significantly, isochronal annealing experiments were carried out on a ~ 115 Å thick Si-oxide grown at 800°C (containing $\sim 0.23 \times 10^{12}$ EX/cm² after full dehydrogenation at 790°C) to study the influence of the degassing temperature T_{dh} . After a hydrogen treatment in 1.1 atm 99.9999% pure H₂ for ~ 20 min at 360°C, which completely obliterated the EX ESR signal, a series of vacuum anneals was applied at various T_{dh} for a fixed time $t_{\text{dh}} \approx 1$ h (i.e., isochronal) where, after each anneal, N_A^{EX} was measured and reset to zero by an H₂ anneal as specified above. The normalized EX depassivation data (filled circles) in Fig. 3 show that H release from inactivated EX entities (depicted as HEX) in detectable amounts starts at $T_{\text{dh}} \geq 400^\circ\text{C}$, but full

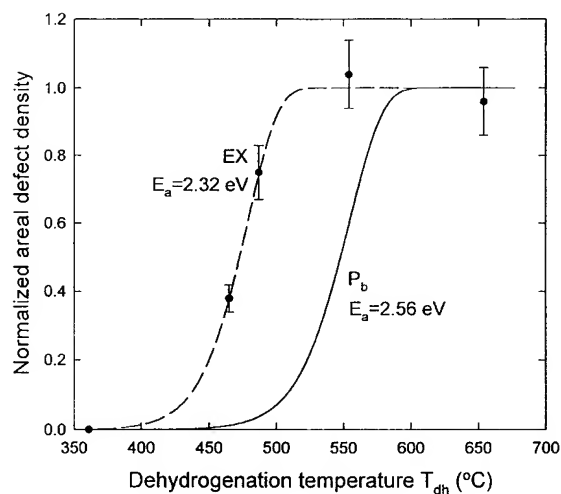


Fig. 3. Normalized areal EX concentration N_A^{EX} (filled circles), measured at 4.3 K in (111)Si/SiO₂ grown at 800°C for 105 min, versus dehydrogenation temperature. Following the initial full passivation of the EX defects in 100 kPa H₂ at 360°C (~ 20 min), each point represents N_A^{EX} after annealing in vacuum at the corresponding temperature for ≈ 1 h. The vertical error bars represent a standard 10% error in N_A^{EX} . The dashed line is a fit as explained in the text, while the full curve represents the theoretical P_b behavior.

dehydrogenation is only attained at $T_{\text{dh}} \gtrsim 500^\circ\text{C}$. The EX depassivation data may be compared to the P_b behavior, depicted by the full curve in Fig. 3, which represents the theoretical P_b depassivation, assuming linear kinetics [7]:

$$N_A^{P_b}/N_A^{P_b^*} = 1 - \exp[-k_{d0}t \exp(-E_d/kT_{\text{dh}})]. \quad (1)$$

$N_A^{P_b^*}$ is the maximum areal P_b density, $k_d = k_{d0} \exp(-E_d/kT_{\text{dh}})$ is the linear rate constant for depassivation; E_d , k , and t represent the activation energy, Boltzmann's constant, and anneal time, respectively. Brower [7] found an activation energy $E_d = 2.56 \pm 0.06$ eV for the P_b -degassing process. A similar analysis for the EX center, depicted in Fig. 3 by the dashed line, leads to an activation energy for EX depassivation of ~ 0.25 eV lower. While a full H_2 interaction kinetics scheme for EX, like the one unveiled for P_b [8], has still to be established, comparison of the P_b and EX behavior, however, indicates that the EX thermochemical properties are also dominated by the interaction with hydrogen. As an important corollary, these results additionally show that EX, like P_b and unlike postoxidation damage-induced defects, is an (inherently) network-stabilized natural defect.

4. Discussion

EX incorporation appears to be inextricably connected with the thermal SiO_2 formation process. The following key observations are important as to unveil the origin of the EX center: (1) The defects are invariably located in the top 40 Å of the oxide. (2) Their density is solely set by the grown oxide thickness. (3) N_A^{EX} gradually disappears when the oxide grows thicker. (4) The EX defect is thermally stable up to at least 930°C , unlike radiation-induced defects [2]. It may further be useful to remark that the EX defect is generated in a region which may be expected to be supersaturated with oxygen, nearby the SiO_2/O_2 ambient border. As EX is an intrinsic defect, it may thus concern an excess-oxygen center rather than a Si-based defect, in agreement with ^{29}Si hf data [6].

A conceivable explanation for the gradual disappearance of EX with growing d_{ox} is that thin thermal oxides ($d_{\text{ox}} \leq 200$ Å) may not yet have reached the superb structural quality of their thicker counterparts. It suggests that the thermal oxide, when thickening, undergoes some kind of rearrangement – possibly what has been termed a pseudo-polymorphic transformation [9] – into what may be called a high-quality oxide. Also, with the oxide growing thicker, the structural transformation extends ever upwards towards the free oxide surface, eventually, above a substantial thickness (> 600 Å), the upper oxide part having been included. Finally, if we admit that the high-quality, structurally relaxed a- SiO_2 is more inert to continuous surface modification in ambient O_2 , we may understand the observed EX incorporation. It is thus needed to incorporate an aspect of structural adaptation of the oxide layer effectuating in different degrees with growing oxide thickness. The interpretation that the upper part of the thermal oxide can only fully transform into standard a- SiO_2 beyond a certain oxide thickness, is not unreasonable, as the Si/ SiO_2 mismatch-induced compressive stress in the SiO_2 layer may only gradually fade away as the oxide thickens.

5. Conclusions

The natural intrinsic EX center in thermal Si/ SiO_2 has been observed by ESR within the T_{ox} window from 700 up to 930°C , enclosing the T_{ox} range favored in current Si processing technology. It appears that the sole physical parameter setting the defect density – at least what concerns those in the ESR-active state – is the grown oxide thickness, whatever T_{ox} : a universal N_A^{EX} versus d_{ox} curve with a maximum of $\sim 1.2 \times 10^{12} \text{ cm}^{-2}$ for $d_{\text{ox}} \approx 125$ Å was observed. SiO_2 etchback experiments show that the EX defects invariably reside in the top ~ 40 Å of the oxide layer, independent of their areal density, and with the largest local volume densities occurring near the free SiO_2 interface. These generation specifics unveil EX as an intrinsic threat to Si/ SiO_2 -based devices.

The defect's thermochemical properties are dominated by the interaction with hydrogen.

Passivation in molecular hydrogen starts at $\sim 225^\circ\text{C}$, while, when fully passivated, dehydrogenation in vacuum only sets in at $\sim 400^\circ\text{C}$, full degassing being achieved after ~ 1 h above $\sim 500^\circ\text{C}$. Analysis of the passivation data in terms of linear kinetics results in an activation energy of (2.37 ± 0.02) eV, about $1/4$ eV lower than for the P_b center.

Likely it concerns an O-rich defect, thermally stable up to high temperatures (900°C), the generation kinetics of which are governed by the O abundance at the SiO_2/O_2 border, in interplay with structural relaxation effects of the oxide, effective at different levels depending on the grown oxide thickness.

References

- [1] See, for example, E.H. Poindexter, P.J. Caplan, B.E. Deal and R.R. Razouk, *J. Appl. Phys.* 52 (1981) 879.
- [2] D.L. Griscom, *Rev. Solid State Sci.* 4 (1990) 565.
- [3] A. Stesmans, *Phys. Rev.* B45 (1992) 9501.
- [4] A. Stesmans, *Phys. Rev.* B48 (1993) 2418.
- [5] K. Vanheusden and A. Stesmans, *J. Appl. Phys.* 69 (1991) 6656.
- [6] A. Stesmans and F. Scheerlinck, *Phys. Rev.* B50 (1994) 5204.
- [7] K.L. Brower, *Phys. Rev.* B42 (1990) 3444.
- [8] K.L. Brower and S.M. Myers, *Appl. Phys. Lett.* 57 (1990) 162.
- [9] A.G. Revesz, B.J. Mrstik and H.L. Hughes, in: *Proc. Symp. on the Physics and Technology of Amorphous SiO_2* , ed. R.A.B. Devine (Plenum, New York, 1987) p. 297.



ELSEVIER

Journal of Non-Crystalline Solids 187 (1995) 124–128

JOURNAL OF
NON-CRYSTALLINE SOLIDS

Wavelength resolved thermally stimulated luminescence of SiO_2 films

M. Martini, F. Meinardi, E. Rosetta, G. Spinolo, A. Vedda*

Dipartimento di Fisica, Università di Milano, Via Celoria 16, I-20133 Milan, Italy

Abstract

A wavelength resolved thermally stimulated luminescence (TSL) study has been carried out for the first time on X-irradiated chemical vapor deposition SiO_2 films deposited on a silicon substrate, from room temperature, to 400°C . Upon irradiation, the TSL glow curve features a prominent structure at a maximum temperature, T_{max} , of approximately 62°C (heating rate = 1°C/s); the analysis of the emission wavelength shows a peak at 457 nm (2.71 eV). The shape of the TSL peak is complex, and cannot be described in the frame of classical first- or second-order kinetics. Moreover, T_{max} has a strong and monotonic shift to higher temperatures after partial pre-heating treatments while the spectral emission is not modified: a similar phenomenon has already been observed in bulk fused silica of various types, different from crystalline quartz which does not present any shift of T_{max} as a function of pre-heating. These results suggest that the TSL peak is characterized by a distribution of trap parameters: specifically, a continuous distribution of trap energy or of the frequency factor can be taken into account. Considerations on the characteristics of the trap parameter distribution are made.

1. Introduction

Although thermally stimulated luminescence (TSL) above room temperature has been widely used in the study of defects in quartz and silica, very few papers have dealt with TSL in the other amorphous form, i.e. thin films that are extensively used in the electronic industry [1–3].

The principal drawbacks in studying the TSL of thin films have been the small amount of sample and the limited information gained due to the lack

of knowledge of the emitting wavelength. Both these disadvantages are overcome by the measurement of TSL using newly designed high sensitivity spectrometers that give three-dimensional information, i.e. the intensity of TSL as a function of both temperature and emission wavelength [4].

By means of such a spectrometer we have analyzed the TSL of CVD SiO_2 films; the results obtained on the wavelength distribution of the TSL emission are discussed in comparison with the spectral emission of bulk SiO_2 .

Moreover, a thorough analysis of the principal ‘ 62°C ’ glow peak, using partial heating and the ‘initial rise’ method, leads us to consider the presence of a distribution of trap parameters.

*Corresponding author. Tel: +39-2 239 2352. Telefax: +39-2 239 2414. E-mail: vedda@mi.infn.it.

2. Experimental results

This TSL study has been undertaken on 3 μm thick films of amorphous SiO_2 purchased from MEMC SpA, Novara (Italy): they were obtained by chemical vapor deposition (CVD) at 900°C on silicon wafers and cut for the measurements into a square shape of 1 cm^2 area.

TSL measurements were performed from room temperature to 400°C with a linear heating rate of 1°C/s by means of two different apparatuses: in the first the total emitted light was detected as a function of temperature by the technique of photon counting using an EMI 9635 QB photomultiplier tube with quantum efficiency peaking at 380 nm. The second consisted of a high sensitivity spectrometer measuring the TSL intensity as a function of both temperature and emission wavelength: the detector is a double stage Microchannel plate followed by a 512 diode array; the dispersive element is a 140 lines/mm holographic grating, the detection range being 200–800 nm.

Irradiations have been done at room temperature using a Machlett OEG 50 X-ray tube operating at 40 kV.

Fig. 1 (curve a) shows the TSL glow curve of a CVD sample irradiated with an X-ray dose of approximately 10^3 Gy: a strong peak at 62°C is evident. The shape of this peak appears to be complex. In fact, the TSL emission is asymmetrically extended to high temperatures contrary to the expectations both for the cases of first- and second-order kinetics [5]. Moreover, the peak maximum temperature, T_m , is shifted to higher temperature as a function of partial cleaning treatments: this is indicated by curves b and c of the same figure, which show measurements obtained after irradiation and partial heating, to 51°C and 94°C, respectively (T_{stop}), before the recording of the glow curve. The T_m shift is approximately linear as a function of pre-heating temperature, as evidenced by the inset of the figure.

This phenomenon suggests that the trap responsible for this TSL peak is characterized by a distribution of trap parameters, i.e. of the thermal energy, E , or possibly of the frequency factor, ν [6]. In order to evaluate whether indeed a distribution of trap depths is present, a simple and preliminary

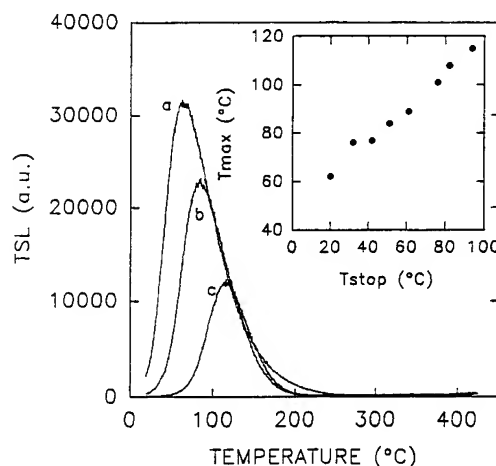


Fig. 1. TSL glow curves of a 3 μm CVD SiO_2 sample after an X-ray dose of 10^3 Gy. The heating rate was 1°C/s. Curve a, as irradiated; curves b and c, after a pre-heating treatment of 51°C and 94°C, respectively. The inset shows the shift of the peak maximum temperature as a function of pre-heating treatments.

analysis of the peak shape has been performed, based on the initial rise method. In Fig. 2 we show an enlargement of the 20–100°C range of the TSL glow curves obtained after different T_{stop} temperatures. Here, a semilog plot has been chosen to evidence the fact that the portions of the curves reported here follow an exponential behavior, which allows us to determine the trap energy using the initial rise method. The results of the exponential fitting are shown in Fig. 3, where the trap depths obtained are presented as a function of T_{stop} . The spread of the data has to be ascribed to different sources of errors such as the measurement of the sample temperature and background subtraction. However, the values appear to be independent of T_{stop} , and a mean energy has been calculated: $E_m = 0.81 \text{ eV} \pm 0.06 \text{ eV}$. It is to be noted that for $T_{\text{stop}} = 84^\circ\text{C}$, an appreciable lowering of the energy is in fact observed ($E = 0.68 \text{ eV}$); at the present time no specific conclusions can be drawn about this. The significance and the limits of validity of this method will be discussed in the next section.

The results of wavelength resolved TSL measurements are presented in Fig. 4 with a three-dimensional plot and in Fig. 5 as a contour plot. The '62°C' peak is characterized by a single emission

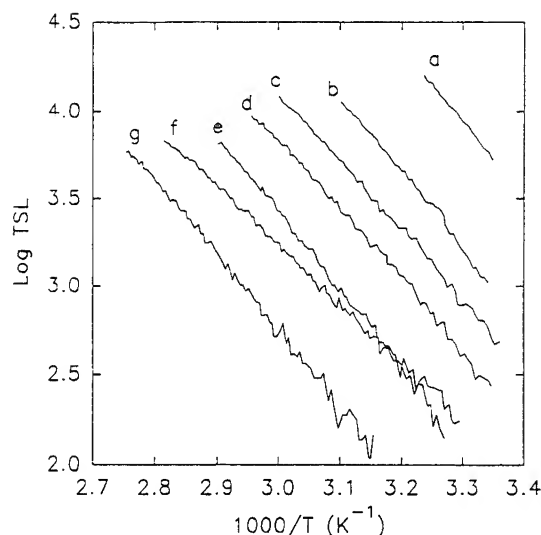


Fig. 2. TSL intensity versus $1/T$ of various glow curves of CVD SiO_2 measured after partial heating treatments. The different T_{stop} temperatures are (a) 20°C; (b) 32°C; (c) 51°C; (d) 61°C; (e) 76°C; (f) 84°C; (g) 94°C. The temperature scale is enlarged in order to show only the portions of the glow peak that manifest an exponential behavior. The X-irradiation was 10^3 Gy; heating rate = 1°C/s .

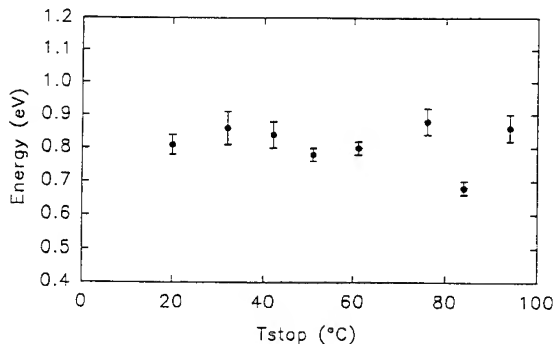


Fig. 3. Thermal energy of the '62°C' TSL peak of CVD SiO_2 film as a function of partial pre-heating treatment. The values are calculated with the initial rise method.

centered at 2.71 eV (457 nm), with a halfwidth of 0.45 eV. Measurements performed as a function of pre-heating at 50°C and 100°C, respectively, are presented in Fig. 5 (curves b and c): they show that the emission energy is not influenced by this treatment.

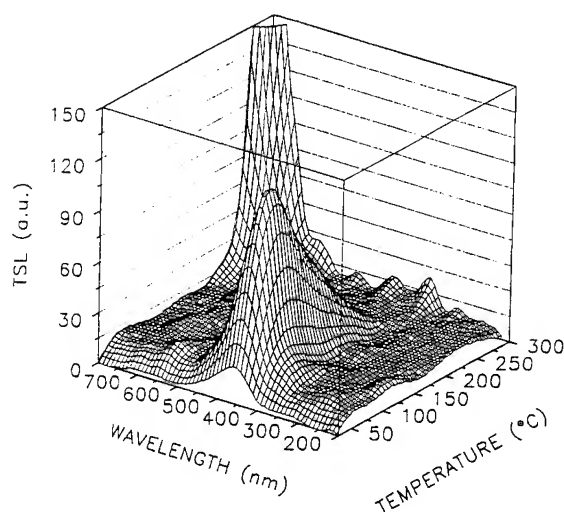


Fig. 4. Three-dimensional plot of a wavelength resolved TSL measurement performed on a CVD SiO_2 sample irradiated with an X-ray dose of 10^3 Gy; Heating rate = 1°C/s .

3. Discussion

This study has demonstrated that the TSL features of CVD films present characteristic properties that can be ascribed to the amorphous nature of the material. As already suggested [6], some similarities with the glow peak of crystalline quartz are found, but the detrapping–recombination phenomena appear to be specific of the amorphous form.

In the following, two main aspects will be discussed: one concerns the emission spectrum; the second relates to the observed detrapping phenomena.

Only one emission energy at 2.71 eV has been detected for the broad TSL glow peak under study. Interestingly a similar emission, denoted as the γ band, has already been found in photoluminescence and phosphorescence studies of amorphous bulk SiO_2 and neutron irradiated crystalline quartz [7–9].

The defect responsible for the emission appears to be of intrinsic origin. Specifically, two models have been proposed up to now, both related to oxygen deficiency: the neutral oxygen vacancy, a bond between two silicon atoms [7], and the twofold coordinated silicon [10]. In this context,

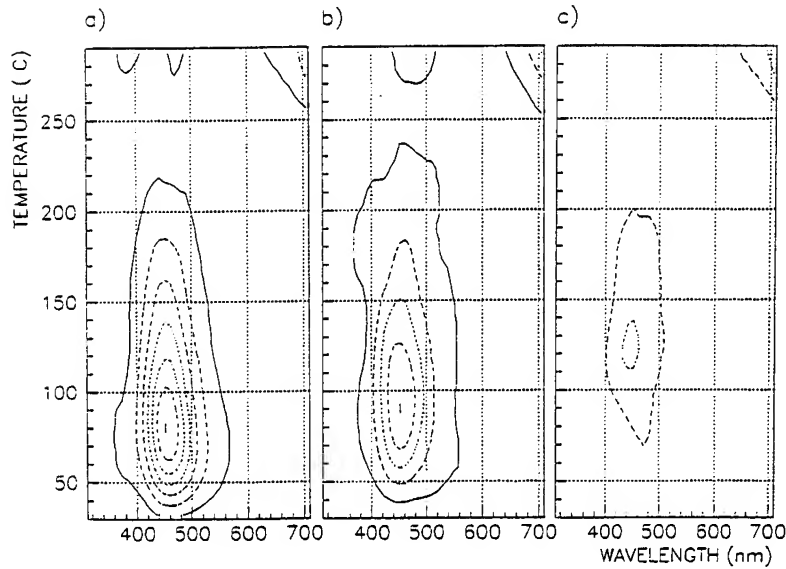


Fig. 5. Contour plots of wavelength resolved TSL measurements performed on a CVD SiO₂ sample irradiated with an X-ray dose of 10³ Gy; curve a, as irradiated; curve b, after a partial heating at 50°C; curve c, after a partial heating at 100°C. Heating rate = 1°C/s.

this conclusion is in agreement with the fact that up to now different experimental evidence has been obtained that oxygen deficient defects are commonly present in the structure of thin SiO₂ films [11].

Let us consider now the complex detrapping phenomena observed. As illustrated in Fig. 1, the TSL peak detected at 62°C has a broad and asymmetric shape and manifests a strong shift of the maximum temperature upon pre-heating treatments. From the analysis of the thermoluminescent processes, a simple relation can be derived between the maximum temperature of a peak and the trap parameters:

$$\beta E/kT_m^2 = s \exp(-E/kT_m), \quad (1)$$

where β is the heating rate, k is the Boltzmann's constant, E is the trap depth and s is the frequency factor; s can be expressed as $\nu\chi \exp(S/k)$, where ν is the thermal vibration frequency, χ is the transmission coefficient of the trap and $\exp(S/k)$ is an entropy factor. The variation of T_m upon heating treatments suggests that the TSL peak observed is characterized by a distribution of lifetimes τ_i defined as

$$\tau_i = (1/s_i) \exp(E_i/kT). \quad (2)$$

Such a lifetime distribution can in principle reflect the existence of both a distribution of energy trap depths or of frequency factors. Actually, in a study of the TSL properties of Ge-silica optical fibers doped with Nd the existence of a continuous distribution of trap depths has already been suggested [12].

We have made an effort in order to evaluate the existence of a continuous distribution of trap depths by using the initial rise method on measurements performed with different pre-heating temperatures; the results obtained do not show any evident increase of E as a function of the T_{stop} temperature. The spread of the data does not allow us to exclude the existence of a narrow distribution, but in this case its width should probably be lower than 0.1 eV.

Alternatively, a distribution of frequency factors can be proposed. In this respect, the operating mechanism could be tunnel recombination of electrons from traps to emitting centers specifically giving rise to a distribution of transmission coefficients χ of the trap, as already suggested in the case of the TSL of different materials [13,14]. Further experimental work, and a more thorough numerical analysis of the TSL glow curve, is needed

in order to verify whether this particular recombination process is in fact responsible for the observed phenomenology.

References

- [1] J.P. Mitchell, IEEE Trans. Nucl. Sci. 15 (1968) 154.
- [2] T.W. Hickmott, J. Appl. Phys. 43 (1972) 2339.
- [3] T.W. Hickmott, J. Appl. Phys. 45 (1974) 1060.
- [4] P.D. Townsend and Y. Kirsh, Contemp. Phys. 30 (1989) 337.
- [5] S.W.S. Mc Keever, Thermoluminescence of Solids, Cambridge Solid State Science Series (Cambridge University, Cambridge, 1985).
- [6] M. Martini, G. Spinolo, A. Vedda and C. Arena, Solid State Commun 91 (1994) 751.
- [7] R. Tohmon, H. Mizuno, Y. Ohki, K. Sasagane, K. Nagasawa and Y. Hama, Phys. Rev. B39 (1989) 1337.
- [8] J.H. Stathis and M.A. Kastner, Phys. Rev. B35 (1987) 2972.
- [9] M. Guzzi, G. Lucchini, M. Martini, F. Pio, A. Vedda and E. Grilli, Solid State Commun. 75 (1990) 75.
- [10] L.N. Skuja, A.N. Streletsky and A.B. Pakovich, Solid State Commun. 50 (1984) 1069.
- [11] S.T. Pantelides, ed., The Physics of SiO₂ and its Interfaces (Pergamon, New York, 1978).
- [12] Y. Kirsh, J.E. Townsend and P.D. Townsend, Phys. Status Solidi A114 (1989) 739.
- [13] P. Avouris and T.N. Morgan, J. Chem. Phys. 74 (1981) 4347.
- [14] R. Visocekas, T. Ceva, C. Marti, F. Lefaucheux and M.C. Robert, Phys. Status Solidi A35 (1976) 315.



ELSEVIER

Journal of Non-Crystalline Solids 187 (1995) 129–133

JOURNAL OF
NON-CRYSTALLINE SOLIDS

A novel ellipsometric set up for high precision thin films measurements

J. Monin*, H. Sahsah, O. Brevet-Philibert

LRCCI, Université Jean Monnet, 23 rue du Dr P. Michelon, 42023 Saint-Etienne cédex 2, France

Abstract

In this paper, an ellipsometric method well suited for optical property measurements of a single layer, or even, a multi-layers surface film over layed on a substrate is described. This method allows a high precision on the ellipsometric angles Ψ and Δ , especially when the angle of incidence, φ_i , is fixed near the principal angle of incidence, φ_p . This ellipsometer is very easy to build and implement. It only requires classical polarimetric and electronic components. Moreover, it is achromatic and easy to automate. Measurement of a very thin SiO_2 layer on Si is presented.

1. Introduction

Nowadays, computing algorithms allow the determination of the thicknesses and the optical constants of thin films on a thick substrate using the ellipsometric angles Ψ and Δ measured for several incidence angles φ_i . These iterative methods only lead to an accurate convergence (of the computer search process) if

(1) the measurements of Ψ and Δ are very precise (the thinner the deposited film, the higher the accuracy must be);

(2) the angle of incidence and the light wavelength are choosen in such a way the measurements of the ellipsometric angles are highly dependent on the presence of the very thin deposited films (e.g. 20 Å).

There are of course various sources of errors in ellipsometric measurements: mechanical and optical components are often not perfect. Among

them, the retardation plates or optical compensators (Babinet-soleil, Bravais) are rarely accurately calibrated [1]. Furthermore, their properties are altered by the multiple reflections phenomena inside the transparent anisotropic plate, especially if the light is more coherent.

All ellipsometric methods need very precise adjustments of the azimuth angle of the polarizer, analyzer, retarders and eventually phase modulators, respectively, with respect to the plane of incidence. If not, severe systematic errors appear in the ellipsometric measurements. We have perfected several methods [2,3] allowing reliable and methodical (systematic) alignments. They involve a polarization modulation in conjunction with a synchronous electronic detection.

The presence of a very thin film deposited on a substrate only modify the values of the ellipsometric angles (Ψ , Δ) associated to the substrate, in the vicinity of its principal incidence φ_p .

We have conceived a novel ellipsometric method especially suited to achieve measurements (both

* Corresponding author. Tel: +33 77 42 15 36. Telefax: +33 77 42 18 22.

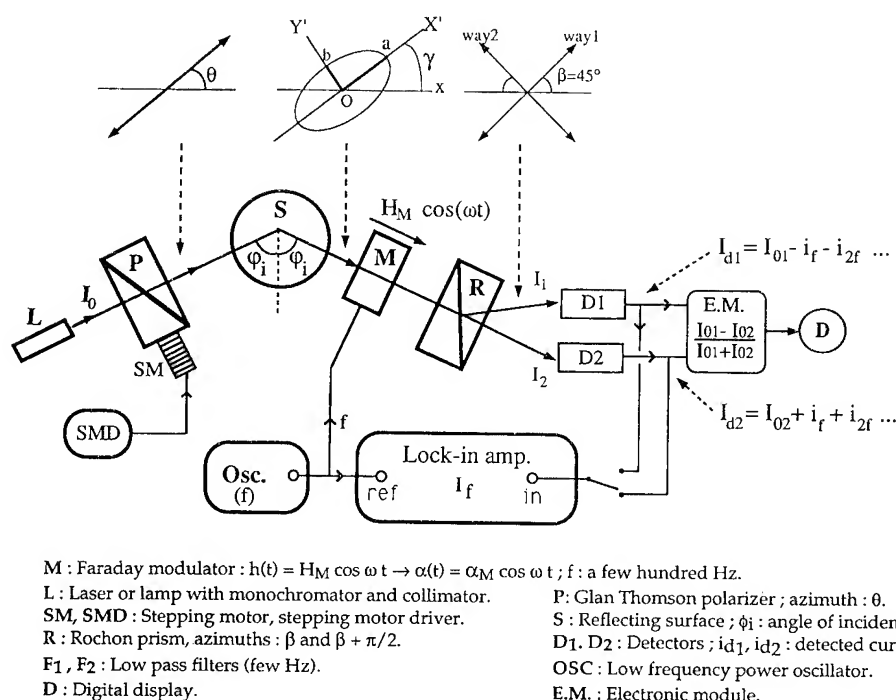


Fig. 1. The experimental set-up.

thicknesses and optical constants) of very thin films on a semiconductor or metallic substrate. It makes use of a Faraday modulation of the light reflected by the surface. For such a case, the measured values of the ellipsometric angles Ψ and Δ are independent of the amplitude of the Faraday modulation.

It will be shown that our ellipsometric set-up performs maximum sensitivity and precision when it works near the principal angle of incidence when the reflected light vibration is an elliptical, near circular, one.

2. Experimental set-up

The experimental set-up is represented in Fig. 1.

3. Calculations

The plane wave of a monochromatic light wave is emitted by the source L (Fig. 1). Its polarization

direction makes an angle θ with the plane of incidence. The wave, reflected by the surface S, is generally elliptical and is characterized by its ellipsometric angles Ψ and Δ according to the relation $r_p/r_s = \tan \Psi e^{j\Delta}$ (r_p and r_s are the reflection coefficients, parallel and perpendicular to the plane of incidence, respectively).

OX' and OY' are the axes of the reflected elliptical wave (their half axes are a and b). $\gamma = \widehat{OX, OX'}$ is the ellipse inclination with respect to the plane of incidence. We can easily demonstrate:

$$\tan 2\gamma = \frac{2 \tan \Psi \tan \theta \cos \Delta}{\tan^2 \Psi - \tan^2 \theta}. \quad (1)$$

The reflected wave passes through the Faraday modulator M and is being rotated according to $\alpha(t) = \alpha_M \cos \omega t$. Then the modulated light wave passes through a two way analyzer (Rochon prism) whose azimuths W_1 and W_2 make the angles β and $\beta + \pi/2$ with the plane of incidence, respectively. Consequently, the directions W_1 and W_2 make an angle $(\beta - \gamma)$ with OX' and OY' axes, respectively.

After some calculus, using the Jones matrix method, we obtain the light intensities I_1 , and I_2 received by the two photodetectors D_1 and D_2 :

$$I_1 = a^2 \cos^2(\alpha + x) + b^2 \sin^2(\alpha + x),$$

$$I_2 = a^2 \sin^2(\alpha + x) + b^2 \cos^2(\alpha + x),$$

with $x = \beta - \gamma$ and $\alpha = \alpha_M \cos \omega t$.

Introducing Bessel's functions of the first kind, J_0 ($2\alpha_M$), J_1 ($2\alpha_M$) ..., I_1 and I_2 can be expressed by the Fourier series:

$$I_1 = \left[\frac{1}{2}(a^2 + b^2) + \frac{1}{2}(a^2 - b^2) J_0(2\alpha_M) \cos 2x \right] - [(a^2 - b^2) J_1(2\alpha_M) \sin 2x] \cos \omega t + \dots$$

Then

$$I_1 = I_{01} - I_f \cos \omega t + \dots \quad (2)$$

Also

$$I_2 = \left[\frac{1}{2}(a^2 + b^2) - \frac{1}{2}(a^2 - b^2) J_0(2\alpha_M) \cos 2x \right] + [(a^2 - b^2) J_1(2\alpha_M) \sin 2x] \cos \omega t + \dots$$

Then

$$I_2 = I_{02} + I_f \cos \omega t + \dots$$

With

$I_f = (a^2 - b^2) J_1(2\alpha_M) \sin 2x$, being the amplitude of the component for the modulation frequency f in the two channels 1 and 2, which must be calibrated (see Section 5)

4. Measurement of the ellipsometric angles, Ψ and Δ

4.1. Measurement of Ψ , sensitivity and accuracy

Method (see Fig. 1). The azimuth of the Rochon prism (way 1) is fixed to $\beta = 45^\circ$. The polarizer azimuth θ is adjusted until the amplitude of the fundamental term I_f vanishes, $I_f = 0$ and $\theta = \theta_0$; Then we get $\sin 2x = \sin 2(\beta - \gamma) = 0$ and so $\gamma = \beta = 45^\circ$ or $\gamma = \beta + \pi/2 = 135^\circ$, hence $\tan 2\gamma = \pm \infty$. According to Eq. (1), we have necessary $\theta = \theta_0 = \Psi$.

Sensitivity. The sensitivity of this measurement is

$$S_\theta = |\Delta I_f / \Delta \theta| = |\Delta I_f / \Delta \gamma| |\Delta \gamma / \Delta \theta|$$

$$\text{near } x = \beta - \gamma = 0.$$

From Eqs. (2) and (1), after some tedious calculus, we get

$$S_\theta = \left| \frac{\Delta I_f}{\Delta \gamma} \right| \left| \frac{\Delta \gamma}{\Delta \theta} \right| \approx 2 I_0 J_1(2\alpha_M) |r_s|^2 \tan \Psi |\cos \Delta| \left[1 - \left(\frac{2 \tan \Psi \tan \theta \sin \Delta}{\tan^2 \Psi + \tan^2 \theta} \right)^2 \right]^{-1/2}.$$

One can demonstrate that (given Ψ and Δ) S_θ is maximum for $\theta = \Psi$ (and consequently $\gamma = 45^\circ$ or $\gamma = 135^\circ$). This maximum is $(S_\theta)_{\max} \approx 2 I_0 |r_s|^2 J_1(2\alpha_M) \tan \Psi$. It is independent of Δ . This means that the sensitivity $(S_\theta)_{\max}$ is independant of the reflected light form (linear, elliptical or circular).

A sensitivity better than 0.001° on Ψ measurement is always obtained (in visible spectrum and in the case of specular surfaces).

Accuracy. The accuracy on Ψ depends also on many other points of the ellipsometric device. For example:

- (1) accuracy calibration of the azimuthal scales of the polarizer and analyzer,
- (2) accuracy on the angle of incidence ϕ_i ,
- (3) Faraday modulator showing no residual birefringence and no stray magnetic field radiation,
- (4) accuracy on the ellipsometric azimuthal alignments, i.e. on the plane of incidence location.

For this last point, we have perfected an original method, very easy to implement, allowing to locate the plane of incidence with a high precision, better than 0.005° [3].

With our ellipsometric device, after cancelling the various possible inaccuracies previously pointed out, we may estimate the accuracy on Ψ measurement at about 0.01° . This is limited by the stepping motor resolution (0.005°) in the half-step mode.

4.2. Measurement of Δ -accuracy

The value of Δ is obtained using the ratio of dc components I_{01} and I_{02} obtained after filtering the detected signals, and the function $J_0(2\alpha_M)$. According to Eq. (2) we can write (when $x = 0$)

$$I_{01} = \frac{1}{2}(a^2 + b^2) + \frac{1}{2}(a^2 - b^2) J_0(2\alpha_M),$$

$$I_{02} = \frac{1}{2}(a^2 + b^2) - \frac{1}{2}(a^2 - b^2) J_0(2\alpha_M).$$

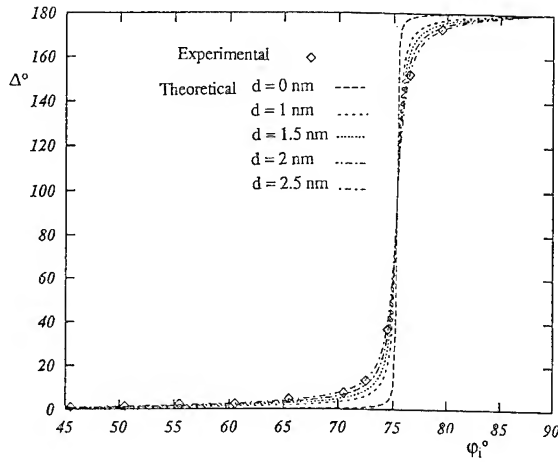


Fig. 2. Measurements of the ellipsometric angle Δ in degrees on a commercial Si wafer at some angles of incidence φ_i ($\lambda = 670$ nm) and theoretical curves for $d = 10$ – 15 – 20 – 25 Å.

Let $\varepsilon = \arctan b/a$ be the ellipticity angle, and $e = b/a$ the ellipticity, ε may be related to Ψ , Δ , θ [4] (choosing $0 \leq \Delta \leq \pi$):

$$\sin 2\varepsilon = \frac{2 \tan \theta \tan \Psi \sin \Delta}{\tan^2 \Psi + \tan^2 \theta}.$$

And so, for $\theta = \Psi$, $\sin 2\varepsilon = \sin \Delta$ and $\cos 2\varepsilon = \pm \cos \Delta$.

Furthermore relations (2) allow us to write

$$M = \frac{I_{01} - I_{02}}{I_{01} + I_{02}} = \frac{1 - e^2}{1 + e^2} J_0(2\alpha_M) \\ = J_0(2\alpha_M) \cos \Delta \approx (1 - \alpha_M^2) \cos \Delta \quad (\alpha_M \approx 1^\circ).$$

The measured value M is equal to $\cos \Delta$ with a relative systematic error α_M^2 ($\alpha_M^2 \approx 3 \times 10^{-4}$ with our ellipsometric set-up). Then, the relative systematic error on $\sin \Delta$ is $\alpha_M^2 / \tan^2 \Delta$ (≈ 0 when φ_i is fixed in the vicinity of φ_p).

5. Calibration

When the zero frequency term of the light transmitted by the ways 1 and 2 are equal the measured value M must be zero. To carry out the calibration of the EM (see Fig. 2) we proceed so: θ is adjusted at 0° or 90° , β staying fixed at 45° , I_{01} and I_{02} should

be equal and $M = 0$. If it is not the case, the electronic module (EM) is adjusted (amplifications and offset voltages) to have exactly $M = 0$.

6. Some measurements

As an illustration of our method, we have made measurements on a single layer surface film of SiO_2 overlaid on a Si substrate (commercial Si Wafer). We have operated at a wavelength $\lambda = 670$ nm and at an angle of incidence $\varphi_i = 74.5^\circ$, in the vicinity of the principal angle of incidence of the Si substrate, $\varphi_p \approx 75^\circ$.

Our aim is to determine the optical constants n_1 , (of the film), n_2 and k_2 (of the substrate) and the thickness d of the SiO_2 film with the measurements of Ψ and Δ at one angle of incidence φ_i , by using an iterative method described elsewhere [5].

Using international notations, one may write

$$\rho = \tan \Psi e^{j\Delta} \\ = \frac{r_p}{r_s} = \frac{r_{01p} + r_{12p} e^{-2j\delta}}{1 + r_{01p} r_{12p} e^{-2j\delta}} \frac{1 + r_{01s} r_{12s} e^{-2j\delta}}{r_{01s} + r_{12s} e^{-2j\delta}} \\ \text{with } \delta = \frac{2\pi d n_1 \cos \varphi_1}{\lambda}.$$

Introducing $\eta = e^{-2j\delta}$ in the expression of ρ gives

$A\eta^2 + B\eta + C = 0$ and then:

$$\eta = \frac{(-B \pm \sqrt{B^2 - 4AC})}{2A},$$

A , B and C depending on n_1 , n_2 , k_2 , φ_i , Ψ and Δ . Assuming $|\eta| = 1$ and by iterating, we obtain

Measurements: $\varphi_i = 74.5^\circ$, $\Psi = 2.178^\circ$, $\Delta = 36.25^\circ$.

Determinations: $n_1 = 1.456$, $n_2 = 3.816$, $k_2 = 0.014$, $d \approx 25$ Å, $|\eta| - 1 \approx 10^{-6}$.

Moreover, Fig. 2 shows the experimental curve $\Delta = f(\varphi_i)$ at $\lambda = 670$ nm for different angles of incidence. This curve fits well the theoretical one corresponding to $d = 25$ Å.

7. Conclusions

We have described a novel ellipsometric set-up using a Faraday modulation. It is very easy to implement and calibrate.

It allows high precision ellipsometric angles measurement. It is well suited to make measurements on very thin films overlayed on a substrate, at any light wavelength (UV, Vis or IR) available.

References

- [1] D.A. Holmes, *J. Opt. Soc. Am.* 54 (1964) 1115.
- [2] J. Monin, these de doctorat d'état, Université de Paris VI (1972).
- [3] J. Monin, H. Sahseh, A. Sibli and O. Brevet-Philibert, *Appl. Opt.* 33 (1994) 1213.
- [4] R.M.A. Azzam and N.M. Bashara, *Ellipsometry and Polarized Light* (North-Holland, Amsterdam, 1977).
- [5] S.S. So and R. Vedam, *J. Opt. Soc. Am.* 62 (1971) 16.



ELSEVIER

Journal of Non-Crystalline Solids 187 (1995) 134–139

JOURNAL OF
NON-CRYSTALLINE SOLIDS

Section 5. Silicon dioxide, defects and degradation

Effects of iron contamination in silicon on thin oxide breakdown and reliability characteristics

Worth B. Henley^{a,*}, Lubek Jastrzebski^a, Nadim F. Haddad^b

^aCenter for Microelectronics Research, University of South Florida, 4202 E. Fowler Avenue, Tampa, FL 33620, USA

^bIBM Corporation, Manassas, VA, USA.

Abstract

Effects of iron contamination on the breakdown and reliability characteristics of thin silicon gate oxides are discussed. Gate oxide integrity is measured for thermal oxides of 8, 10, 13 and 20 nm grown on silicon wafers intentionally contaminated with 10^{10} – 10^{14} cm⁻³ of iron. Iron concentration in silicon is measured using surface photovoltage (SPV) minority carrier lifetime analysis. The density of gate oxide weak spots as a function of iron concentration for the various oxide thicknesses is reported. For 10 nm oxides, iron concentration cannot exceed 8×10^{10} cm⁻³ without severe degradation in oxide quality. The threshold contamination level for 20 nm oxides is 200 times higher.

1. Introduction

Silicon based technologies have dominated integrated circuit (IC) fabrication because of the ability to grow ultra-thin, ultra-high quality oxide layers on the silicon surface. Atomic level purity and physical uniformity are required in such films to prevent oxide weak spots and resulting premature electrical breakdown. Unintentional low-level chemical contaminants cause defects which reduce oxide quality. Foremost among oxide defect generators are transition metal impurities introduced into the silicon through contaminated chemicals or 'dirty' processing equipment. Metallic contamination is often introduced through the wafer surface.

Due to high diffusivity, metallic surface contamination becomes distributed throughout the wafer after even animal thermal processing [1]. Iron is the most common metallic contaminant owing to the prevalence of stainless steel used in semiconductor process equipment such as ion implanters, gas supply lines, plasma equipment, diffusion furnaces, and physical deposition tooling [2,3]. A recent survey of starting Czochralski silicon substrates showed background iron contamination in the range of 5×10^9 to 1×10^{12} cm⁻³ within the starting material [1,4].

The effect of heavy metal impurities on silicon electrical properties depends on the form the impurity takes in the silicon crystal matrix [5]. Metallic impurities which remain dissolved within the silicon matrix create efficient mid-band gap recombination centers and lead to increased diffused junction leakage. Heavy metal impurities may also

* Corresponding author. Tel: +1-813 974 2096. Telefax: +1-813 974 3610. E-mail: henley@felix.and.usf.edu.

agglomerate and form distinct, separate phase, high conductivity, metal-silicide precipitates. Heavy metal precipitates which occur within the device fabrication region are extremely detrimental to IC yield. The ratio between the amount of precipitated heavy metals and the amount of dissolved, interstitial heavy metals is characteristic for each type of heavy metal and the process conditions [6,7].

For advanced VLSI process technologies, the most critical yield limiting aspect of heavy metal contamination is the detrimental effect of heavy metal silicide precipitates on thin gate oxide dielectric breakdown [8]. The problem is exacerbated as technology scaling reduces feature size and film thickness such that the precipitate defects are more pronounced in effect. Previous studies which have investigated the effects of iron impurity contamination on silicon devices have shown that iron precipitates primarily as a rod-like FeSi_2 phase [9]. These precipitates were shown to occur at or near the silicon surface or Si-SiO₂ interface [10] and can reduce the breakdown voltage of thin SiO₂ layers. Most of these experiments were performed at very high levels of iron contamination, e.g. $[\text{Fe}] = 10^{14}$ to 10^{15} cm^{-3} , which is much above the range required for state-of-the-art micron and sub-micron fabrication technologies. Contamina-

tion levels relevant for typical process conditions today are in the range of 10^9 to $10^{13} \text{ atoms/cm}^3$.

2. Experimental procedure

The experimental effort consisted of MOSDOT fabrication on clean wafers and on wafers intentionally contaminated with iron. High quality $2 \Omega \text{ cm}$, $\langle 100 \rangle$, 3" p-type float zone wafers were used for the experimentation. Float zone wafers were chosen to eliminate any unwanted internal gettering uncertainties. During several of the experimental runs, equivalent Czochralski process wafers were included for comparison to the float zone wafer results. Following a SC1/HF/SC2 clean sequence [11], specific wafers were intentionally contaminated with iron by spin applying a 1 to 40 ppm aqueous FeCl_3 solution onto the wafer before the oxidation [12]. This surface iron contamination was driven into the wafer bulk by an in situ preoxidation anneal in N_2 at the oxidation temperature for 25 min before the oxygen flow began. Prior to the study, significant effort was expended to isolate all second-order effects concerning oxide processing, especially background ionic and metallic contamination. This effort resulted in a furnace background iron contamination level of

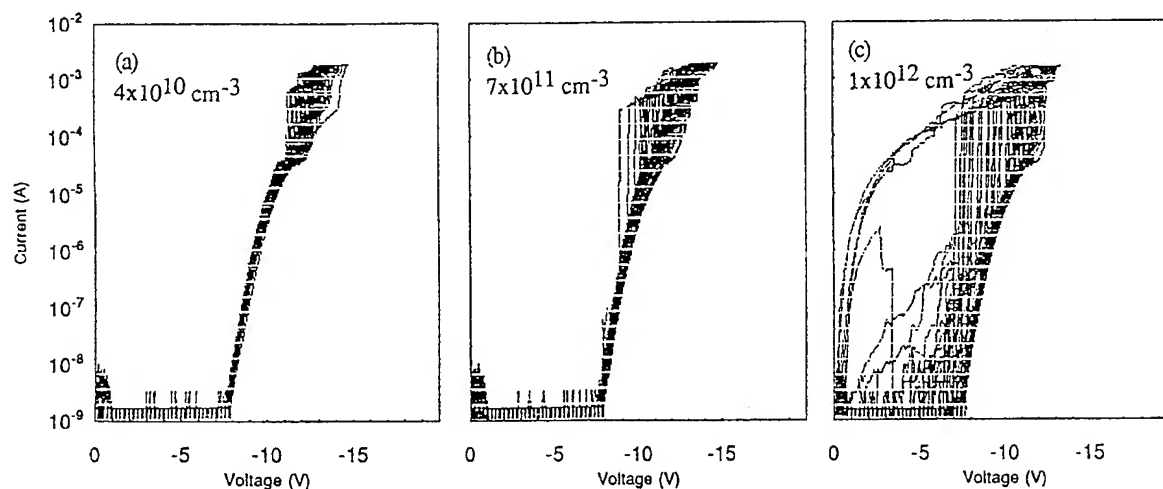


Fig. 1. Ramp voltage I - V curves for 8 nm oxide grown on silicon wafers with iron concentration of: (a) $4 \times 10^{10} \text{ cm}^{-3}$, (b) $7 \times 10^{11} \text{ cm}^{-3}$, (c) $1 \times 10^{12} \text{ cm}^{-3}$.

1 to 4×10^{10} atoms/cm³. Thermal oxides of 8, 10, 13, 16, and 20 nm were grown at 850°C in dry O₂. Oxide thickness uniformity was verified by wafer mapping to be within 3% across the wafer area. Aluminium electrodes and backside contact were formed by thermal evaporation to define the MOSDOT capacitors. The wafers were annealed for 20 min at 450°C in a 5% H₂/95% N₂ forming gas ambient.

Iron concentration was measured on all samples after oxidation via diffusion length analysis. Diffusion length was measured using a surface photovoltage (SPV) procedure [13]. The iron concentration analysis procedure using diffusion length measurements is outlined in Fig. 1 and discussed in detail by Zoth and Bergholz [1]. The SPV iron determination method provides an iron detection limit of $\sim 1 \times 10^{10}$ cm⁻³. In all cases, the iron concentration was determined *after* the oxide processing. The controlled contamination procedure yielded iron concentrations in the range of 5×10^{11} to 5×10^{14} cm⁻³. Iron concentration uniformity was typically 5% across the wafer.

Oxide breakdown was determined by applying a ramp voltage stress in accumulation mode of 1 MV/cm/s until a current of 0.02 A/cm² was exceeded. At this current level, significant deviation from Fowler–Nordheim tunneling had occurred. Time dependent dielectric breakdown (TDDB) stress testing was performed by applying constant electric field (typically 10 MV/cm) and monitoring the leakage current through the capacitor. Approximately 250 MOSDOTs were used for the ramp voltage I–V testing and 100 MOSCOTs on each wafer were used for the TDDB testing. All testing was performed at 22°C.

3. Results

3.1. MOSDOT current–voltage test results

The detrimental effects of low-level iron contamination on gate oxide quality is clearly shown by the ramp voltage oxide breakdown testing. Current–voltage, *I*–*V*, traces for clean and iron contaminated MOSDOT wafer samples are shown in Figs. 1(a)–(c). The traces represent the *I*–*V* test re-

sults from 137 individual MOSDOT test structures on each of three separate 8 nm oxide test wafers. The clean sample (Fig. 1(a), [Fe] = 4×10^{10} cm⁻³) is typical of a good reference quality oxide. No low field breakdowns are apparent; the distribution of *I*–*V* curves is tightly grouped, and the average breakdown field approximately 13 MV/cm. Fig. 1(b) shows the moderately contaminated ([Fe] = 7×10^{11} cm⁻³) 8 nm oxide sample. Comparison to the clean sample shows some low field breakdowns occur, and there is greater dispersion at the catastrophic breakdown point. The [Fe] = 4×10^{11} cm⁻³ contaminated sample (Fig. 1(c)) shows a much larger distribution of the *I*–*V* characteristics. It is obvious a distinct reduction in oxide quality occurs as a result of the iron contamination.

The breakdown *I*–*V* characteristics shown in Fig. 1 indicate that two distinct breakdown phenomenon are present. The clean samples are very typical of reported ramp voltage breakdown test results [14,15]. Uniformity in the *I*–*V* curves suggests that the underlying mechanism responsible for the ultimate current at breakdown is uniformly distributed across the wafer surface and a well controlled material parameter. The iron contaminated samples (Figs. 1(b) and 1(c)) have numerous MOSDOTs in which the catastrophic current–voltage breakdown point is reduced compared to the clean reference sample. We propose these breakdowns are triggered by iron precipitates which occur at or near the Si–SiO₂ interface. The conductive precipitates enhance the local field in the vicinity of the precipitate (the ‘lightning-rod’ effect), thus enhancing current injection at a lower applied voltage. Dispersion in precipitated size and aerial density across the surface of the wafer result in the dispersion of breakdown *I*–*V* characteristics. The average breakdown field for each of the oxide thickness as a function of iron concentration is shown in Fig. 2.

Using ramp voltage test data, defect density calculations were made on the clean and iron contaminated oxides. Failure was defined as a MOSDOT capacitor which exhibited breakdown at an electric field lower than 8 MV/cm. Results of this analysis for the oxide samples are shown in Fig. 3, where defect density is plotted as a function of iron

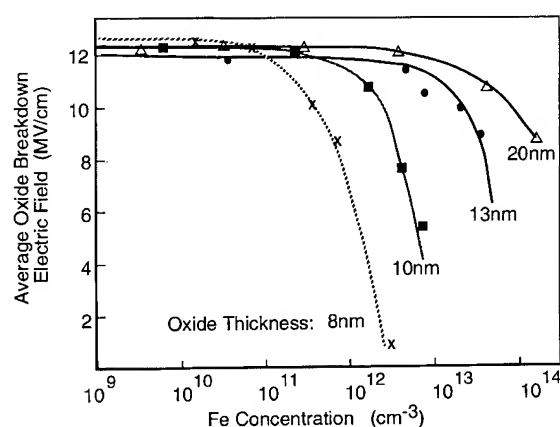


Fig. 2. Average oxide breakdown electric field as a function of iron concentration for the various oxide thicknesses.

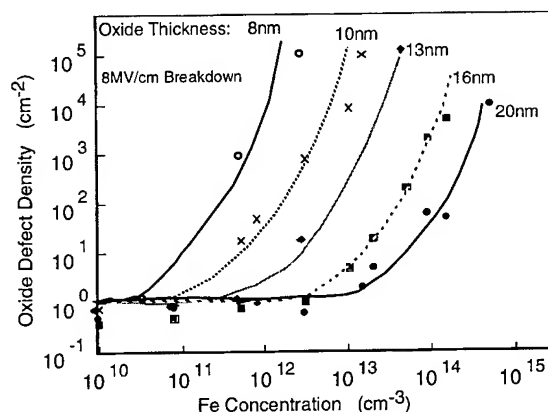


Fig. 3. Oxide defect density versus iron contamination for the various oxide thicknesses evaluated. A defect is defined as breakdown occurring at less than 8 MV/cm during ramp voltage I - V test.

concentration for the oxide thicknesses evaluated. The evidence of a critical iron contamination threshold for each oxide thickness is clearly shown in this figure. As would be expected, the iron contamination threshold which degrades oxide quality decreases as the oxide thickness is reduced.

3.2 Oxide failure mechanism related to iron contamination

To investigate the effects of iron contamination on thin oxide dielectric properties, a modeling and

experimental effort was undertaken. For the electrical modeling of thin oxide structures, PISCES [16] computer simulation models were developed which represented conductive defects at the Si-SiO₂ interface. The defect was modeled as a conductive region which penetrated into the oxide at the lower electrode. Reflecting boundary conditions were placed on the sidewall regions. Various defect heights, bias conditions, and oxide thicknesses were modeled.

The oxide electric field is increased near the region of the conductive defect. Fig. 4 represents cross-sections of the electric field through the oxide layer at various points along the x (position) axis. The cross-section taken at the defect edge shows the field at the defect corner to be significantly higher than that of the bulk, unperturbed, oxide regions. The increase in maximum electric field present in the oxide layer (at the defect corner) as a function of various size conductive defects is shown in Fig. 5. The simulation indicates enhancement in field magnitude due to the conductive region is far higher than can be accounted for by oxide thinning alone.

The electrostatic modeling analysis predicts that the localized electric field will increase linearly with defect size according to

$$E_{\max}^{\text{loc}} = \frac{V}{t_{\text{ox}}} (1 + \alpha d),$$

where d is defect size (cm), V is voltage, α is constant equal to $7 \times 10^6 \text{ cm}^{-1}$, t_{ox} is oxide thickness (cm). This result is in general agreement with the work of Honda [9], where thin oxide breakdown voltage in the presence of iron precipitates was approximately 2.5 times lower than that predicted by oxide thinning considerations.

To extend this electrostatic modeling work to oxide breakdown analysis, we begin with the previous work of Lee et al. [17]. Our electrostatic field analysis was applied to this breakdown modeling which relates time to breakdown to electric field by

$$t_{\text{BD}} = \tau_0 \exp(G/E) = \tau_0 \exp(Gt_{\text{eff}}/V),$$

where $G = 320 \text{ MV/cm}$, $\tau_0 = 1 \times 10^{-11} \text{ s}$, E is electric field, V is applied voltage, and t_{eff} is the 'effective' oxide thickness at the breakdown site. Note,

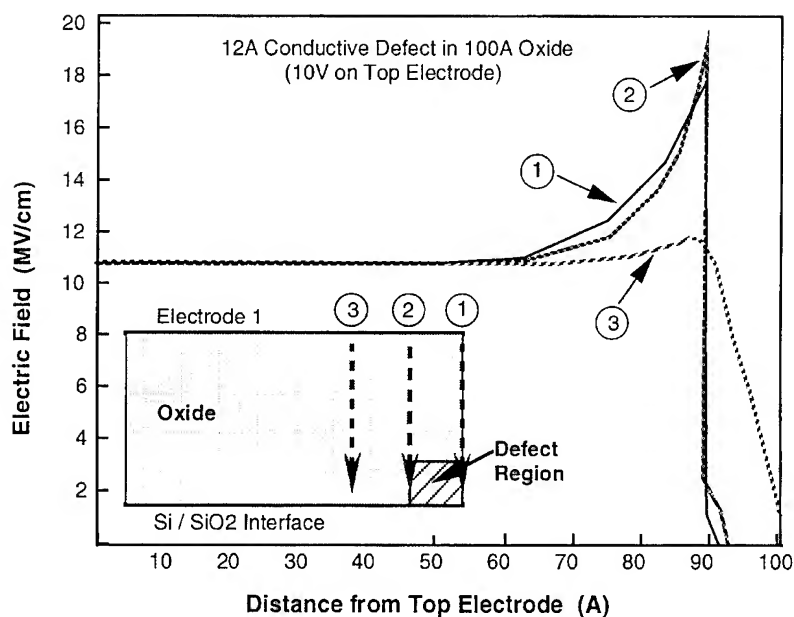


Fig. 4. Electrostatic analysis simulation model. This plot illustrates the oxide electric field distribution through the oxide in the presence of a conductive defect. Paths begin at $x = 0$ (surface) and proceed through the oxide to the Si-SiO₂ interface.

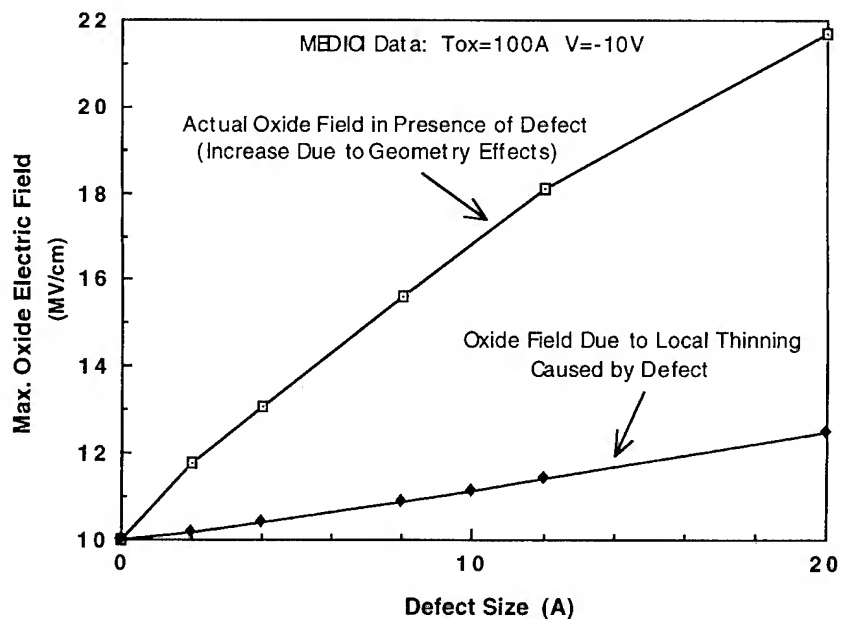


Fig. 5. Electrostatic analysis simulation results. The maximum oxide electric field is due to the presence of conductive defect region at Si-SiO₂ interface. The enhancement of oxide electric field magnitude is greater than can be attributed to oxide thinning alone.

t_{eff} does not necessarily equal t_{ox} due to localized thinning or defects structure.

Our analysis builds on this work by modifying the t_{eff} term to account not only for oxide thinning in the region of the precipitate, but also the enhancement in electric field due to the 'lightning-rod' effect. Using this model, the effective oxide thickness and precipitate defect size may be estimated by

$$t_{\text{eff}} = \frac{t_{\text{ox}}}{(1 + \alpha d)} \quad \text{or} \quad d = \frac{1}{\alpha} \left(\frac{t_{\text{ox}}}{t_{\text{eff}}} - 1 \right).$$

Note the definition of t_{eff} now accounts for field enhancement due to the geometrical singularity effect of the conductive precipitate.

Using this analysis for ramp voltage breakdown testing, the breakdown voltage V_{BD} for oxides with heavy metal precipitates may be expressed as [18]

$$\tau_0 = 10^{-11} = \frac{V_{\text{BD}}^2}{GRt_{\text{eff}}} \exp \left(\frac{-Gt_{\text{eff}}}{V_{\text{BD}}} \right)$$

where R is the voltage ramp rate and t_{eff} includes the α factor to account for the electrostatic geometrical singularity effect of the conductive precipitate.

4. Conclusions

The susceptibility of thin silicon oxides to low-level iron contamination has been evaluated by comparing the oxide breakdown and reliability characteristics of oxides grown on clean wafers to oxides grown on wafers intentionally contaminated with iron. Experimental results show the dramatic lowering of gate oxide integrity (GOI) and reliability in the presence of iron contamination. As expected, thinner oxide films require more stringent contamination control specifications. The data in-

dicates that a reduction of oxide thickness from 20 to 10 nm, corresponding to a transition from 1.0 to 0.5 μm technology, requires a reduction in iron contamination level by two orders of magnitude (from 10^{13} to 10^{11} cm^{-3}).

This work was supported by the SRC/Sematech Center of Excellence (SCOE) program and the IBM Corporation.

References

- [1] G. Zoth and W. Bergholz, *J. Appl. Phys.* 67 (1990) 6764.
- [2] K. Honda et al., in: *Microscopy of Semiconductor Materials Conference* (1987) p. 463.
- [3] Y. Niki, S. Nadahara and M. Watanabe, in: *International Conference on Science and Technology of Defect Control in Semiconductors*, Yokohama, Japan (1989).
- [4] L. Jastrzebski, W. Henley and C. Neuse, *Solid State Technol.* 35 (12 Dec. 1992) 27.
- [5] A. Ohsawa et al., *Semiconductor Silicon 90-7* (1990) 601.
- [6] K. Hiramoto et al., *Jpn. J. Appl. Phys.* 28 (1989) L2109.
- [7] K. Honda, A. Ohsawa and N. Toyokura, *Appl. Phys. Lett.* 46 (1985) 582.
- [8] L. Jastrzebski, *Semiconductor Silicon PV90-7* (1990) 614.
- [9] K. Honda, A. Ohsawa and N. Toyokura, *Appl. Phys. Lett.* 46 (1985) 582.
- [10] R. Takizawa, T. Nakanishi and A. Ohsawa *J. Appl. Phys.* 62 (1987) 4933.
- [11] W. Kern and D.A. Puotinen, *RCA Rev.* 31 (1970) 187.
- [12] M. Hourai et al., *Jpn. J. Appl. Phys.* 27 (1988) L2361.
- [13] J. Lagowski, et al., *Semiconductor Sci. Technol.* 7 (1992) A185.
- [15] R. Falster, *J. Appl. Phys.* 66 (1989) 3355.
- [16] M.R. Pinto, *Pisces II-B*. 1985, Stanford University.
- [17] J.C. Lee, J.C. Chen and C. Hu, *IEEE Trans. Elect. Dev.* 35 (1988) 2268.
- [18] S. Holland et al., *IEEE Elect. Dev. Lett* EDL-5 (1984) 302.



ELSEVIER

Journal of Non-Crystalline Solids 187 (1995) 140–143

JOURNAL OF
NON-CRYSTALLINE SOLIDS

Instability of charged defects in electrically stressed metal-tunnel oxide–silicon diodes

Per Lundgren^{a,*}, Mats O. Andersson^a, K.R. Farmer^b, Olof Engström^a

^a Department of Solid State Electronics, Chalmers University of Technology, S-412 96 Göteborg, Sweden

^b Department of Physics, New Jersey Institute of Technology, University Heights, Newark, NJ 07102, USA

Abstract

The results of a study of the stability of electrical stress-induced positive charge in aluminum gate metal-tunnel oxide–silicon diodes exposed to various temperature and bias treatments are presented. It is found that the electrical stress-induced charge relaxes over time, being neutralized in a manner that is dependent both on the ambient temperature and on the mean oxide field, suggesting that the stress-induced oxide charge can communicate with free carriers via activated tunneling.

1. Introduction

The relevance of studying ultra-thin oxides (2.0–4.0 nm) on silicon is validated partly by the continuous scaling of conventional metal-oxide–silicon (MOS) based device technologies, and partly by the fact that the metal-tunnel oxide–silicon (MTOS) diode can be utilized in other device structures such as electrically alterable read only memories, MOS tunnel emitter transistors and solar cells. Surprisingly, the MTOS device is potentially less sensitive to electrical stress than thicker oxide devices when comparing stress at similar oxide electric fields. This has been reported repeatedly [1–3], and can be attributed to the fact that the harmful impact of tunneling

electrons may be more closely related to the applied voltage than to the oxide electric field for thin enough oxides.

This investigation concerns the stability of electrical stress-induced positive charge in the oxide. We have previously studied the mechanism for positive charge build-up during electrical stress of MTOS diodes and reported striking similarities to effects seen in conventional MOS structures. Applying a negative bias to the (aluminum or poly-Si) gate of 2.0–3.5 nm oxide devices will lead to the appearance of positive charge in the oxide if the voltage is greater than a threshold of ~ -3 V [4–8]. The similarities persist when we examine the effects of temperature and bias on the relaxation of this stress-induced charge. We believe that it is fruitful to consider these results in context with conventional MOS studies to gain further insights into the physical mechanisms behind device degradation and breakdown.

* Corresponding author. Tel: +46-31 772 1882. Telefax: +46-31 772 3622. E-mail: per@ic.chalmers.se.

2. Experimental procedure

2.1. Device characteristics

The samples in this study are aluminum gate MTOS devices formed on a $\sim 50 \Omega \text{ cm}$, p-type, $\langle 100 \rangle$ oriented silicon substrate. The tunnel oxides were grown at low temperature (750°C) in dry oxygen to a thicknesses of $\sim 2.3 \text{ nm}$ as estimated using a capacitance method described by Ricco et al. [9]. Using a method suggested by Maserjian [10] to measure the oxide capacitance resulted in an oxide thickness value of $\sim 2.1 \text{ nm}$. All of the devices were initially subjected to a 15 min post-metallization anneal at 350°C in a 10%- H_2/Ar atmosphere to improve the oxide quality [7,11–13].

2.2. Measurement methods

The change in tunnel current during electrical stress can be taken as a measure of the change in the net amount of charge in the oxide. This can be seen from the following experiment.

At intervals during electrical stressing of a 2.3 nm device at 100 K, the bias is turned off and capacitance–voltage ($C-V$) characteristics are measured at 100 kHz. As the stress time increases, the $C-V$ curve shifts towards more negative voltages while the tunnel current gradually increases. Assuming that positive charge centers appear in the oxide as a result of the stress, each center will induce a local enhancement of the electron tunnel current. The total increase in current with time will thus be proportional to the number of point charge centers created, provided that, on average, each charge center gives rise to the same local current enhancement.

Fig. 1 shows the amount of net positive charge needed to give rise to the observed fractional change in current, N_{OXI} , plotted versus the amount of charge in the oxide calculated from the $C-V$ shift, $N_{\text{OXC-V}}$. The effect of a single positive point charge in the oxide on the tunnel current of an MTOS device has been calculated on the basis of previous work by Schmidlin [14] and Andersson et al. [15]. The calculation is virtually identical to the one described in Ref. [15], with only a change of

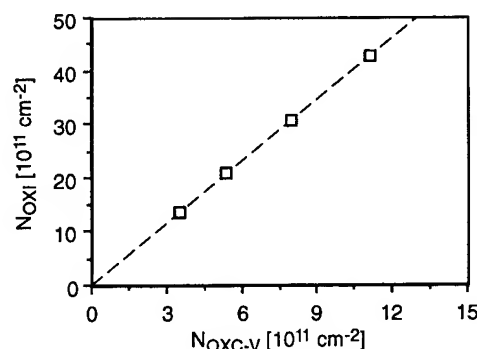


Fig. 1. Point charge density calculated from current increase versus charge density calculated from $C-V$ shift. The dashed line is a guide to the eye.

sign for the potential contribution from the point charge, since that paper treats only negative charge centers. The effective mass for the tunneling electrons in the oxide has been set to 0.3 times the free electrons mass, which is a reported value [10,13,16] as well as what we find to yield the best theoretical fit to measured current–voltage characteristics. Successful descriptions of charging phenomena in thin oxides have previously been achieved with Schmidlin's model in work by Maserjian and Zamari [17]. In our case the charge has been assumed to appear near the center of the oxide. In Fig. 1 the two measures are clearly very well correlated in the sense that they are proportional to each other. Thus, plotting the change in current during relaxation, $|\Delta I_{\text{R}}|$, normalized to the current change induced by prior electrical stress $|\Delta I_{\text{S}}|$ can be expected to yield the same measure of the relaxation as plotting the shift in $C-V$ characteristics $|\Delta V_{\text{R}}|$ normalized to $|\Delta V_{\text{S}}|$.

3. Results

3.1. Relaxation temperature dependence

The effect of temperature on the relaxation was studied using current versus time ($I-t$) measurements and subjecting different devices to different relaxation temperatures for the same duration. Devices were stressed at 150 K, -3.4 V , and the relaxation time was 1000 s. Zero bias was applied during the relaxation. In Fig. 2 the

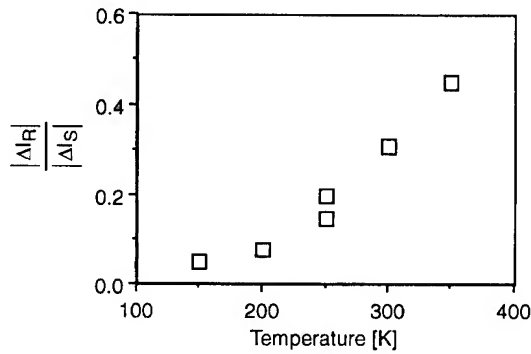


Fig. 2. The change in current during relaxation normalized to the current increase during prior stress versus relaxation temperature. Zero bias was applied during the relaxation.

fractional recovery is plotted versus relaxation temperature. The fractional recovery is taken as the mean of four consecutive relaxations; after 1000, 3000, 10 000 and 30 000 s of stress (the relaxation is roughly the same in all four cases). Clearly, the relaxation effect is enhanced for elevated temperatures. Each data point is for one device.

3.2. Relaxation electric field dependence

The same kind of measurements as described in the previous section were carried out with different relaxation biases at 300 K. In this case a clear effect of the oxide electric field can be seen. This is presented in Fig. 3, in which the fractional recovery (again taken as the mean of four consecutive 1000 s relaxations; after 1000, 3000, 10,000 and 30,000 s of stress) is plotted versus the mean oxide field strength. The voltage drop over the oxide has been derived from an experimental $C-V$ curve taken at 10 kHz, using the Berglund technique [18]. For the bias point of +2 V, the voltage distribution over the device is not known, hence the large error bar for this point.

3.3. Relaxation dynamics

To look at the relaxation dynamics we measure the capacitance transient at an applied gate bias of -1.1 V at the same temperature as the initial stress. The small observed increase in capacitance is approximately proportional to the voltage shift of

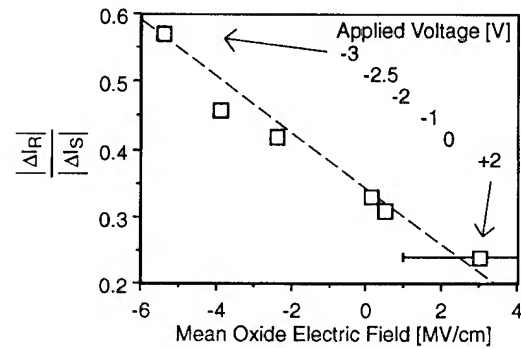


Fig. 3. The change in current during relaxation normalized to the current increase during prior stress versus mean oxide electric field during relaxation. The relaxation took place at room temperature. The dashed line is a guide to the eye.

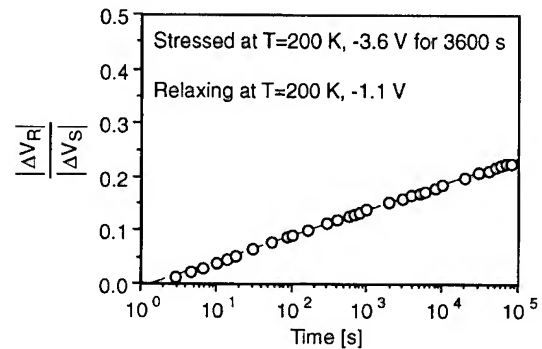


Fig. 4. The shift in $C-V$ characteristic during relaxation normalized to the initial stress-induced shift versus relaxation time. The dashed line is a guide to the eye.

the $C-V$ characteristic, which in turn is proportional to the change in oxide charge concentration. In Fig. 4 we plot the shift of the $C-V$ characteristic during relaxation normalized to the initial stress-induced shift. The curve is sublinear with relaxation time. We note that similar slow relaxation dynamics has been reported for charge in thicker oxides [19,20].

4. Discussion

In principle, the disappearance of positive charge in the tunnel oxide agrees very well with the suggested hole detrapping that is reported for

thicker oxides [19,21,22]. A logarithmic time dependence for the charge center depopulation has been proposed to result from tunnel emission from trap centers that are evenly distributed throughout the oxide [20,23]. The observed temperature dependence suggests some kind of thermal activation of the process.

The fact that the relaxation increases for higher temperature and higher electric field has an important implication; if electrical stressing leads to the formation of hole traps, fewer of these will be detected as positively charged at elevated fields and temperature as compared to lower field and temperature. Hence, the stress-induced oxide damage at increased bias and temperature levels will be underestimated when monitoring the positive charge content of the oxide during stress.

5. Conclusion

In summary we see that the positive charging effect in an MTOS device is equally well monitored by consecutive $C-V$ measurements or by a continuous $I-t$ measurement. The net positive charge that appears in the oxide during stressing at least partially disappears when removing the stress bias. This relaxation effect depends on both temperature and applied voltage. The effect of electrical stress at higher negative biases or elevated temperatures will thus be underestimated as compared to low-temperature, low-bias stress when only monitoring the amount of positive charge in the oxide, since the concurrent relaxation process will be enhanced at higher bias and temperature.

References

- [1] K.F. Schuegraf and C. Hu, in: Proc. IEEE Int. Rel. Phys. Symp. 1993 (Atlanta, 1993) p. 7
- [2] M. Depas, B. Vermeire, P.W. Mertens, M. Meuris and M.M. Heyns, in: Proc. 1994 VLSI Symposium, Honolulu, 1994.
- [3] N.K. Patel and A. Toriumi, Appl. Phys. Lett. 64 (1994) 1809.
- [4] K.R. Farmer, M.O. Andersson and O. Engström, Appl. Phys. Lett. 58 (1991) 2666.
- [5] K.R. Farmer, M.O. Andersson and O. Engström, Appl. Phys. Lett. 60 (1992) 730.
- [6] K.R. Farmer, P. Lundgren, M.O. Andersson and O. Engström, in: Amorphous Insulating Thin Films, ed. J. Kanicki et al., Mater. Res. Soc. Proc. Fall 1992 (Materials Research Society, Pittsburgh, PA, 1992) p. 229.
- [7] M.O. Andersson, P. Lundgren, O. Engström and K.R. Farmer, in: Proc. INFOS'93, ed. P. Balk (Elsevier, Amsterdam, 1993) p. 2350.
- [8] D.A. Buchanan, private communication.
- [9] B. Ricco, P. Olivo, T.N. Nguyen, T.S. Kaun and G. Ferriani, IEEE Trans. El. Dev. 35 (1988) 432.
- [10] J. Maserjian, in: The Physics and Chemistry of SiO_2 and the Si- SiO_2 Interface, ed. C. Helms and B.E. Deal (Plenum, New York, 1988) p. 497.
- [11] P.V. Dressendorfer, S.K. Lai, R.C. Barker and T.P. Ma, Appl. Phys. Lett. 36 (1980) 850.
- [12] P. Lundgren, M.O. Andersson and K.R. Farmer, J. Appl. Phys. 74 (1993) 4780.
- [13] M. Depas, R.L. van Meirhaeghe, W.H. Laflere and F. Cardon, Solid-State Electron. 37 (1994) 433.
- [14] F.W. Schmidlin, J. Appl. Phys. 37 (1966) 2823.
- [15] M.O. Andersson, K.R. Farmer and O. Engström, J. Appl. Phys. 71 (1992) 1846.
- [16] M. Hirose, M. Hiroshima, T. Yasaka, M. Takakura and S. Miyazaki, in: Proc. INFOS'93, ed. P. Balk (Elsevier, Amsterdam, 1993) p. 3.
- [17] J. Maserjian and N. Zamani, J. Vac. Sci. Technol. 20 (1982) 743.
- [18] C.N. Berglund, IEEE Trans. El. Dev. 13 (1966) 701.
- [19] M.V. Fischetti, R. Gastaldi, F. Maggioni and A. Modelli, J. Appl. Phys. 53 (1982) 3136.
- [20] K. Yamabe, Y. Miura, J. Appl. Phys. 51 (1980) 6258.
- [21] A.V. Schwerin, M.M. Heyns and W. Weber, J. Appl. Phys. 67 (1990) 7595.
- [22] M. Bourcier, B.S. Doyle, J.C. Marchetaux, J.C. Soret and A. Boudou, IEEE Trans. El. Dev. 37 (1990) 708.
- [23] H. Köster Jr. and M. Schmidt, Mater. Sci. Forum 38–41 (1989) 1331.



ELSEVIER

Journal of Non-Crystalline Solids 187 (1995) 144–148

JOURNAL OF
NON-CRYSTALLINE SOLIDS

Influence of FN electron injections in dry and dry/wet/dry gate oxides: relation with failure

Eric Ciantar^{a,*}, Philippe Boivin^a, Michel Burle^a, Christophe Niel^a, J. Michel Moragues^b, Bruno Sagnes^b, Robert Jerisian^b, Jean Oualid^b

^a SGS-Thomson Microelectronics, 13790 Rousset, France

^b Laboratoire des Matériaux et Composants Semiconducteurs, ENSPM, 13397 Marseille cedex 20, France

Abstract

The resistances of dry and dry/wet/dry gate oxides to Fowler–Nordheim injections are compared. Two types of test MOS capacitors were used in order to verify whether a simplified process can lead to reliable results. A dry/wet/dry oxide exhibits higher injected charge to intrinsic breakdown and smaller density of net effective trapped charge than a dry oxide does. The interface state generation rates are identical for both oxides. The improvement is attributed to higher electron trapping in dry/wet/dry oxide.

1. Introduction

In transistors used for non-volatile memories, the gate (or tunnel) oxide must keep its integrity after strong cumulated electron injections. One of the proposed solutions consists in using dry/wet/dry (DWD) rather than standard dry (D) gate oxides. Reliability problems of non-volatile memories mainly come from oxide defects and from charges created by electron injection either in the bulk oxide or at the interface Si/SiO₂. The oxide immunity to Fowler–Nordheim (FN) electron injection can be measured by the densities of trapped charges and created interface states. Another way of

qualifying the thin oxides consists in determining the distributions of breakdown field, E_{bd} , or of the charge injected before breakdown, Q_{bd} , from which it is possible to define the oxide defectivity. In this contribution, we compare the intrinsic charge injected before breakdown determined by the exponential ramp current stress (ERCS) method with the bulk charge and the interface states created by FN electron injections in D and DWD gate oxides.

2. Experiment

Two types of test MOS capacitors on P-type silicon substrates ($\rho \approx 2 \Omega \text{ cm}$) with dry or dry/wet/dry oxide were used. The PC capacitors were realized with the same process steps as those used for EEPROM memories. They have an area of

* Corresponding author. Tel: +33 42 25 88 00. Teleax: +33 42 53 22 88.

$A = 0.1 \text{ mm}^2$ delimited by an N^+ diffused ring and a simple polysilicon gate. The TC capacitors were realized on test wafers using a simplified process. They have different areas (between 0.063 and 6.3 mm^2), delimited by a field oxide (LOCOS). In order to reduce the series resistance effect [1] a layer of WSi_2 silicide was deposited by LPCVD on the polysilicon gate.

Various methods have been proposed to determine the oxide defectivity using accelerating tests performed on MOS capacitors at constant high gate voltage, constant current or with a linear ramp voltage stress (LRVS) method. In this work, we used essentially the ERCS method, which consists in applying an exponential ramp current and measuring the injected charge Q_{bd} before breakdown. The ERCS method has been shown to provide the best sensitivity in the shortest time [2]. This method is particularly well adapted to tunnel oxides. We think that the ERCS method also gives useful information concerning the quality of gate oxides ($100\text{--}400 \text{ \AA}$). The Q_{bd} distribution is generally constituted of two parts.

(i) The failures observed for low Q_{bd} values are called extrinsic breakdowns, characterized by the oxide defectivity usually defined by Ref. [3]: $D(Q_{bd}) = -\ln(1 - P(Q_{bd})) / A$, where $P(Q_{bd})$ is the cumulated probability for capacitors to fail for Q_{inj} less than Q_{bd} . In order to define the defectivity of the studied gate oxides, we chose $Q_{bd} = 10^{-3} \text{ C/cm}^2$, a value low enough to be related to the product yield [4].

(ii) Breakdowns obtained for the highest values of Q_{bd} are called intrinsic. We defined the intrinsic breakdown by $P(Q_{bd}) = 0.9$.

Extrinsic and intrinsic breakdowns as well revealed by the Gumbel diagram, which gives the variation of $\ln(-\ln(1 - P))$ versus $\log(Q_{bd})$. Evidently, the gate oxide must have the lowest defectivity and the highest intrinsic Q_{bd} value.

The quasi-static capacitance method was used in order to determine the charges trapped in the bulk of the gate oxides and the generated interface states after different constant current FN injections applied during the same time (10 s). In Fig. 1, the normalized $C_{qs}/C_{ox} = f(V_g)$ characteristics of D and DWD PC capacitors are plotted before and after stress ($Q_{inj} = 1.1 \text{ C/cm}^2$). They were measured

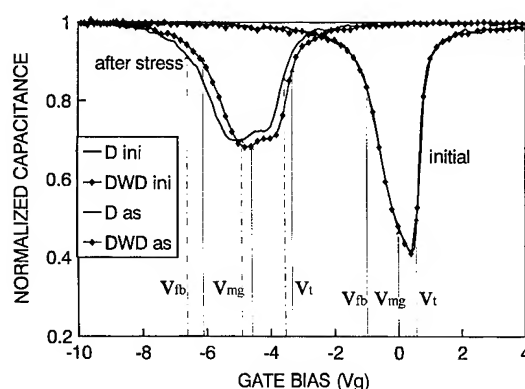


Fig. 1. $C_{qs} - V_g$ characteristics before and after stress (1.1 C/cm^2) of D (full line) and DWD (diamond) oxide of PC capacitors. Arrows show the different voltages V_{fb} , V_{mg} , V_t before and after stress.

at 60°C in order to increase the ramp rate (0.1 V/s). Before stress, both normalized characteristics (D and D/W/D) are practically identical. After stress, the characteristics shift to negative voltage, which indicates a creation of net effective positive charges for both gate oxides. The minimum of the quasi-static capacitance is increased after stress by nearly the same amount for both oxides, which indicates that the densities of generated interface states are quite similar after an identical stress. By assuming that the interface states are amphoteric (acceptor-like above mid-gap, donor-like below mid-gap), the density N_{ox} of net effective trapped charges as well as the mean densities N_{ss}^A and N_{ss}^D of acceptor and donor interface states are given by, respectively, the mid-gap, threshold, flat-band voltage shifts, in the case of P-type MOS capacitors.

The leakage current of the junction N^+ ring/substrate due to the generation of minority carriers by the interface states is maximum when the interface under the gate is depleted. There is no surface generation of minority carriers when the interface is strongly accumulated or inverted. So, the difference between the leakage currents measured when the interface is depleted and strongly inverted is proportional to the density of interface states located near the mid-gap. The difference between the leakage currents measured when the interface is strongly inverted or accumulated depends on the minority carrier lifetime in the substrate [5].

3. Experimental results

In Fig. 2, we compare the probability distributions relative to TC capacitors having D and D/W/D gate oxides and two different areas. The gate is negatively biased so that the interface is strongly accumulated and the voltage is entirely applied to the gate oxide. More than 100 capacitors having the same area and the same oxide were tested. In the inset of Fig. 2 we show that the defectivity in the extrinsic region increase when the area of MOS capacitors decreases. This observation can be justified by more important density of

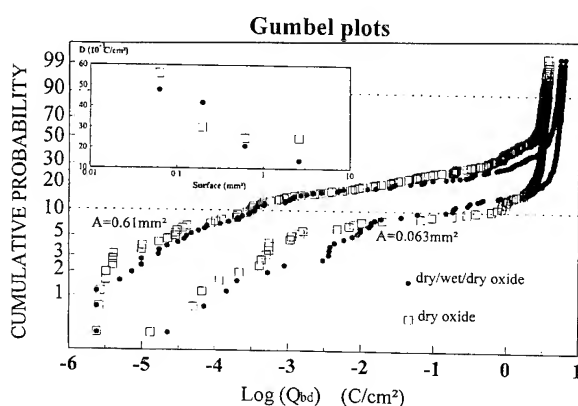


Fig. 2. Distribution of Q_{bd} obtained by the ERCS method of D (open square) and DWD (filled circle) oxides for two TC capacitor areas ($A = 0.61 \text{ mm}^2$ and $A = 0.063 \text{ mm}^2$). In the inset the defectivity $D (10^{-3} \text{ C/cm}^2)$ versus the surface is plotted for the two oxide types.

Table 1
Principal characteristics and results of the studied capacitors

	TC capacitors		PC capacitors	
	D Polysilicon + WSi_2 silicide	DWD	D Polysilicon	DWD
t_{ox} (nm)	27.0	28.0	33.5	32.3
N_a (cm^{-3})	6×10^{15}	6×10^{15}	3×10^{16}	3.2×10^{16}
Q_{bd} , at $P = 0.9$	3.2	5.1	4.3	5.8
$D(Q_{bd} = 10^{-3} \text{ C/cm}^2)$	48	45	30	15
$N_{ox} (10^{10} \text{ cm}^{-2})$ at $Q_{inj} = 0.1 \text{ C/cm}^2$	255 ± 5	240 ± 5	230 ± 5	218 ± 5
$N_{ss} (10^{10} \text{ cm}^{-2})$ at $Q_{inj} = 0.1 \text{ C/cm}^2$	375 ± 25	320 ± 20	23 ± 3	22 ± 2

defects near the edges of TC capacitors which are delimited by a field oxide. It is well known that the bird's beak could be a sink of defects and contamination. Intrinsic breakdown is slightly higher for DWD than D gate oxide when both oxides present nearly the same defectivities. This latter observation was also verified on PC capacitors. In Table 1, which sums up the results obtained with D and DWD gate oxides, it can be noted that the intrinsic breakdown is slightly higher and the defectivity (given for the same: $A = 0.1 \text{ mm}^2$) is smaller for the MOS capacitors which have been made using the complete process. These observations can be justified also to the different periphery of the two types of capacitors.

The net effective charge trapped in the gate oxide after negative FN electron injections is positive and varies like $\log(Q_{inj}/Q_0)$ for both types of capacitors, as shown in Fig. 3, and as found by Wolters and Verwey [6]. The generation rate is nearly identical for both oxides. It is slightly higher for PC than for TC capacitors. The density of effective trapped charges, N_{ox} , is slightly higher for D than DWD gate oxides for the two types of capacitors. It can be observed that it is not possible to measure the oxide trapped charge density for TC capacitors after an electron injection higher than 10^{-1} C/cm^2 , due to the very high density of generated interface states. In this condition, the $C_{qs} - V_g$ characteristic is nearly flat after stress.

The increase in generated interface states with the fluence is different for TC and PC capacitors, as shown in Fig. 4. The density of interface states

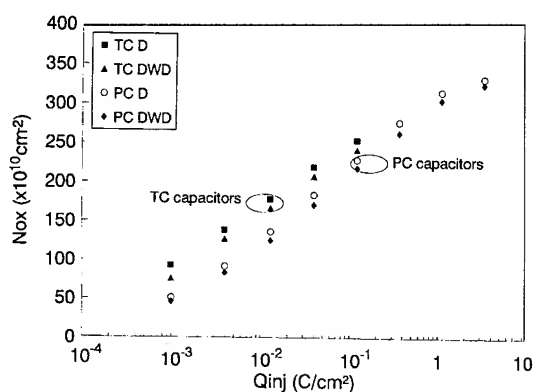


Fig. 3. Evolution of net effective trapped charges after successive 10 s negative FN injections for each type of capacitor and gate oxide.

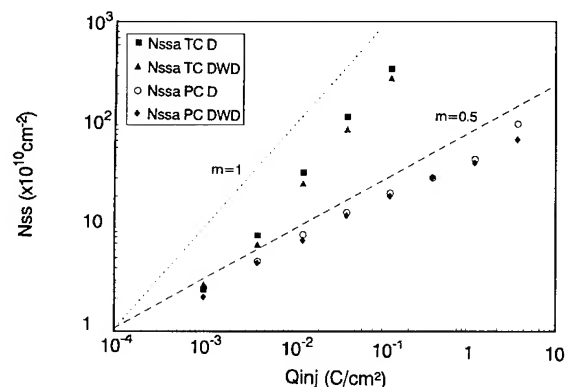


Fig. 4. Evolution of acceptor-like interface state densities during injection on TC and PC capacitors for D and DWD oxides.

N_{ss} varies as Q_{inj}^m , with $m \approx 1$ for TC capacitors and $m \approx 0.5$ for PC capacitors. N_{ss} is much higher in TC capacitors than in PC capacitors particularly after strong FN injection. The empirical law $N_{ss} \approx Q_{inj}^{0.5}$ is verified by previous results given by DiMaria et al. in particular [7]. The quasi-linear variation of N_{ss} with Q_{inj} is associated with the process of WSi_2 deposition, as is demonstrated in another communication [8]. N_{ss} is also slightly higher for D than for DWD gate oxide in TC capacitors, however strong the injected charge may be. For PC capacitors, the densities N_{ss} are quasi-identical.

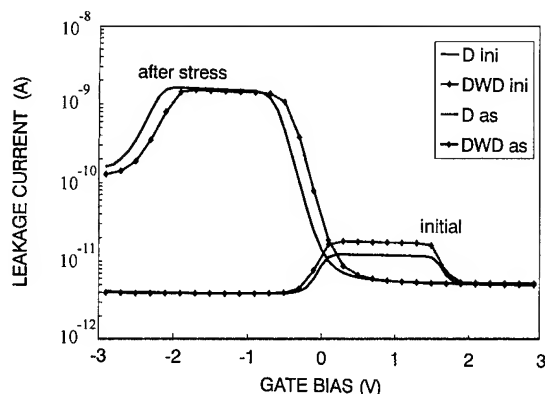


Fig. 5. Leakage current versus gate bias (gate controlled diode characteristics) before and after stress ($Q_{inj} = 0.32 \text{ C/cm}^2$) of D (full line) and DWD (diamond) oxides of PC capacitors.

In Fig. 5, we give the variation of the leakage current with the gate bias (gate controlled diode characteristics) determined on PC capacitors with D and DWD gate oxide, before and after stress. These characteristics were obtained at 60°C and with a reverse bias $V_R = 1 \text{ V}$ applied to the N^+ ring. The substrate is grounded. Before stress, the leakage current is identical for D and for DWD capacitors if the interface is strongly inverted or accumulated, which indicates that the type of oxidation has no influence on the minority carrier lifetime in the substrate. The interfacial current observed when the interface is depleted is weaker for D than for DWD capacitors. In consequence, the initial density of interface states is slightly higher in DWD capacitors. After stress, the hump is shifted to negative voltage, indicating a net generation of positive charges. For the same fluence, the shift is more significant for D than for DWD capacitors, as observed on the $C_{qs} - V_g$ characteristics given in Fig. 1, in accordance with the higher density of net effective trapped charges in D capacitors (Fig. 3). The maximum leakage currents are quasi-identical for both types of capacitors, which confirms that the interface states are generated at the same rate in PC capacitors with D or DWD gate oxides (Fig. 4). If the interface is strongly inverted, the leakage current is identical to the initial current indicating that an FN injection has no influence on the minority carrier lifetime in the substrate.

The different characterizations have shown that the charges injected before intrinsic breakdown measured with the ERCS method are higher for DWD than for D gate oxides. On the other hand, the interface states are generated at the same rate in both oxides for PC capacitors. This latter observation could indicate that the densities of positive charges trapped near the interface may be identical after a same stress applied to D or DWD gate oxide. Indeed, it seems well admitted that the creation of anomalous positive charges (or slow states) and the generation of interface states by FN injection are correlated [9]. So, the difference between the densities of net effective trapped charges in the two oxides could be attributed to a higher electron trapping in DWD oxide [10]. This hypothesis can be justified by the decrease in the gate current during a constant voltage FN injection, the decrease being more important for DWD than for D oxide. The mean electric field applied for a same constant current FN injection is, at every moment, higher for D than for DWD capacitors, which explains why the charge to intrinsic breakdown is smaller [6]. So, it is confirmed that the process involving DWD oxide seems to improve the reliability of oxides for non-volatile memories. It would be important to define the optimized conditions for the realization of DWD oxides in order to increase the immunity to FN electron injections.

4. Conclusions

All the results given in this contribution confirm that DWD oxides possess a better integrity to

electron injections than D oxides and, consequently, they present a better potential for non-volatile memories, even if the initial density of interface states is slightly higher. The test capacitors made with the simplified process give reliable results concerning the ability to qualify different oxide processes even if the polysilicide step which is used involves a higher generation of interface states.

References

- [1] F. Pio, L. Ravazzi and C. Riva, in: *Proc. European Symp. on Reliability of Electron Devices Failure Physics and Analysis (ESREF)* (1992) p. 105.
- [2] P. Cappelletti, P. Chezzi, F. Pio and C. Riva, in: *Proc. IEEE Int. Conf. on Microelectronic Test Structure (ICMTS)*, Vol. 4 (1991) p. 81.
- [3] C.M. Osburn and D.W. Ormond, *J. Electrochem. Soc.* 119 (1972) 591.
- [4] E. Ciantar, P. Boivin, M. Burle and J. Oualid, accepted oral presentation at the *European Symp. on Reliability of Electron Devices Failure Physics and Analysis (ESREF '94)*.
- [5] J. Oualid, J. Dugas, R. Jerisian, A. Bouassis, D. Labrunye and J.M. Mirabel, *J. Phys III* 1 (1991) 369.
- [6] D.R. Wolters and J.F. Verwey, *Instabilities in Silicon devices*, ed. G. Barbottin and A. Vapaille (North-Holland, Amsterdam, 1986) p. 315.
- [7] D.J. DiMaria, E. Cartier and D. Arnold, *J. Appl. Phys.* 73 (1993) 3367.
- [8] J.M. Moragues, B. Sagnes, R. Jerisian, J. Oualid, E. Ciantar, J.L. Liotard and P. Merenda, these proceedings, p. 156.
- [9] M.V. Fischetti, *J. Appl. Phys.* 57 (1985) 2860.
- [10] F.J. Feigl, D.R. Young, D.H. Dimaria, S.H. Lai and J.A. Calisse, *J. Appl. Phys.* 52 (1981) 5665.



ELSEVIER

Journal of Non-Crystalline Solids 187 (1995) 149–155

JOURNAL OF
NON-CRYSTALLINE SOLIDS

Investigation on the interfacial reaction of $\text{SiO}_2/\text{Ti}_{0.1}\text{W}_{0.9}$ system

Hyung-Ho Park^{a,*}, Sahn Nahm^a, Kyung-Soo Suh^a, Jong-Lam Lee^a, Kyoung-Ik Cho^a,
Kyung-Soo Kim^a, Sin-Chong Park^a, Jae-Sung Lee^b, Yong-Hyun Lee^b

^a*Semiconductor Technology Division, Electronics and Telecommunications Research Institute, Yousung PO Box 106,
Taejeon 305–600, South Korea*

^b*Department of Electronic Engineering, Kyungbook National University, Taegu, South Korea*

Abstract

The thermal behavior of antifusing device characteristic with $\text{SiO}_2/\text{Ti}_{0.1}\text{W}_{0.9}$ system was investigated. Amelioration and destruction of device properties were found after annealing at 400°C and 600°C, respectively. Through in situ heat treatment at 400°C, it was revealed that metallic tungsten was formed at the interface due to decomposition of WO_3 . Annealing above 600°C induces decomposition of SiO_2 and results in failure of the antifusing device characteristic.

1. Introduction

Metal/dielectric/metal structure is the most probable candidate for an antifuse structure of field programmable gate arrays. This antifuse structure should have low programming voltage and leakage current in application to very large integrated devices. For this reason, application of silicon oxide, silicon nitride, amorphous silicon, silicon oxynitride, and a bilayer of silicon oxide/silicon nitride to intermediate dielectric layer have been widely studied [1,2].

Deposition of the dielectrics are usually performed by sputtering technique, because this technique has several advantages such as good adhesion and thickness uniformity over large planar

area [3]. Furthermore, low temperature deposition is preferable for avoiding the interaction with substrate material during the deposition. But for obtaining an improved device characteristic, annealing after the low temperature deposition must be done for recovery of the characteristic of deposited material and amelioration of the interfacial state.

In this study, X-ray photoelectron spectroscopy (XPS) was used to investigate the interfacial reaction between SiO_2 and $\text{Ti}_{0.1}\text{W}_{0.9}$ system by preparing ultrathin SiO_2 layer to analyze the interface without modifying the sample. To avoid the microcontamination during the annealing, heat treatment under ultra high vacuum (UHV) was applied within thermally stable temperature range of the dielectric. In metal/dielectric/metal system, atmospheric impurity is not permissible by the relatively thicker upper metal layer, although normal annealing treatment was used inside inert gas atmosphere. Furthermore, the failure of device characteristic due to the annealing process at high temperature

* Corresponding author. Tel: +82-42 860 6200. Telefax: +82-42 860 5645. E-mail: hhpark@cadvax.etri.re.kr.

has been determined and explained from the interaction between dielectric and metal.

2. Experimental procedures

Three kinds of samples were prepared. To analyze the effect of post-anneal to IV characteristics, layers of $\text{Ti}_{0.1}\text{W}_{0.9}$ (500 nm thick) and SiO_2 (14 nm) thick were deposited successively on a chemically cleaned 5–35 Ω cm (100) silicon wafer at room temperature by sputtering technique. Further the samples were annealed for 1 h at 400°C and 600°C under nitrogen atmosphere, respectively. Aluminum was used as an electrode.

SiO_2 (3 nm)/ $\text{Ti}_{0.1}\text{W}_{0.9}$ (500 nm) system was prepared for in situ heat treatment under UHV ($< 1 \times 10^{-9}$ torr) of XPS. The thickness of SiO_2 film was measured by transmission electron microscopy (TEM) analysis with Philips CM20T/STEM. The operating voltage was 200 kV. A specially designed heatable stub was used for in situ annealing from 25°C to 700°C. The sample was heated for 1 h and cooled down to room temperature for XPS analysis. The 4 nm thick layer of SiO_2 was deposited on the chemically cleaned silicon substrate in order to monitor the thermal stability of SiO_2 under UHV.

The XPS experiments were performed on a V.G. Scientific ESCALAB 200R spectrometer using Mg $k\alpha$ (1253.6 eV) radiation operating at 300 W. The angle resolved technique was used for non-destructive depth profile analysis. Narrow scan spectra of all regions of interest were recorded in order to quantify the surface composition and identify the elemental bonding states with pass energy of 20 eV and take-off angles of 10°, 50°, and 90°, respectively.

3. Results

Fig. 1 represents IV characteristics of antifuses with $\text{SiO}_2/\text{Ti}_{0.1}\text{W}_{0.9}$ system as a function of anneal temperature. The amelioration of antifusing characteristic due to heat treatment was observed. 11.5 V of yield voltage was obtained before anneal

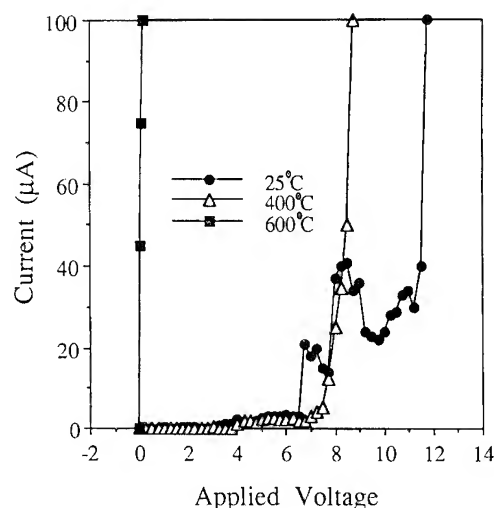


Fig. 1. IV characteristics of antifuses with SiO_2 (14 nm)/ $\text{Ti}_{0.1}\text{W}_{0.9}$ system as a function of anneal temperatures. Lines are drawn as guides for the eye.

but 9.8 V was obtained after annealing at 400°C. But with annealing above 600°C, the failure of antifusing device characteristic due to the destruction of dielectric film was observed.

Fig. 2 shows a cross-sectional TEM image of as-deposited SiO_2 (3 nm)/ $\text{Ti}_{0.1}\text{W}_{0.9}$ system. About 13 nm thick gold layer was deposited to distinguish the SiO_2 layer from epoxy, which was used for the cross-sectional TEM specimen preparation. The SiO_2 layer was continuous and uniform. The interface was sharply defined and smooth.

Narrow scan spectra of W, Ti, Si, and O with 10° to take-off angle are given in Fig. 3. The W 4f spectrum can be resolved into W1 (W in W–Ti), W2 (W–O in WO_2), and W3 (W–O in WO_3). The binding energy of 30.6 eV for W1 4f7 was observed for metallic W. This implies that no chemical shift is present when tungsten binds to titanium. The Ti 2p spectrum can be resolved into three peak components as Ti1 (Ti in Ti–W), Ti2 (Ti–O in Ti_2O_3 and/or Ti_3O_5), and Ti3 (Ti–O in TiO_2). The presence of the TiO component cannot be considered because Ti2p3 shows the binding energy of 454.6 eV in TiO [4]. The binding energy of 103.5 eV for Si1 2p peak implies complete oxidation of silicon. Oxygen presents O1 (O in O–Ti/W) and O2 (O in SiO_2) bonding states. Peak attributions,

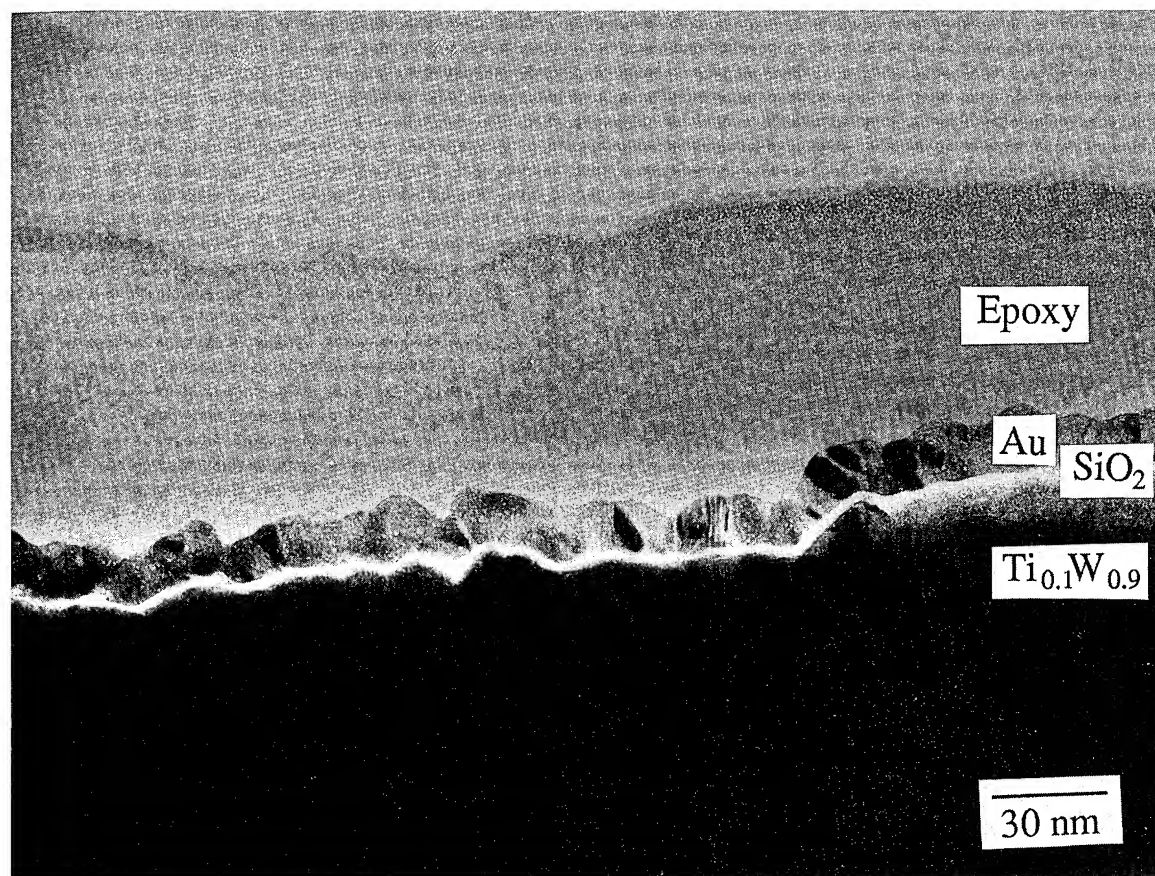


Fig. 2. Cross-sectional TEM image of as-deposited SiO_2 (3 nm)/ $\text{Ti}_{0.1}\text{W}_{0.9}$ system.

binding energy, full width at half maximum, and percent of each peak area are listed in Table 1.

The variation of chemical contributions of W and Ti with take-off angle are presented in Fig. 4. In this configuration, as the angle increase, contribution of the surface bonding state to the observed peak intensity decreases. The distribution of bondings can be determined from comparison of the slope changes of various bonding contributions with take-off angle. For tungsten and titanium, it was revealed that metallic form was found under the oxidized state. This implies that tungsten and titanium were partially oxidized at the interface before the anneal.

Fig. 5 shows W 4f (a), Ti 2p (b), Si 2p (c), and O 1s (d) photoelectron spectra obtained at 10° take-off

angle after in situ annealing treatment. Fig. 6 shows the changes observed in bond distribution for each element. After annealing at 400°C , decrease of WO_3 , sharp increase of metallic W, and slight increases of WO_2 and Ti_2O_3 (Ti_3O_5) were observed. The sharp increase of metallic W and Ti, sharp decrease of WO_3 , and slight decrease of WO_2 and TiO_2 were found at 500°C . Above 600°C , Si 3s 2p peaked at 99 eV of binding energy appears due to the decomposition of SiO_2 . Further the appearance of metallic silicon induces partial formation of silicon carbide. After the deposition, the sample was exposed to air for transferring to UHV chamber, monolayer of carbon was always physisorbed on the top of the sample. This carbon does not reduce SiO_2 but reacts with Si and forms SiC at 600°C

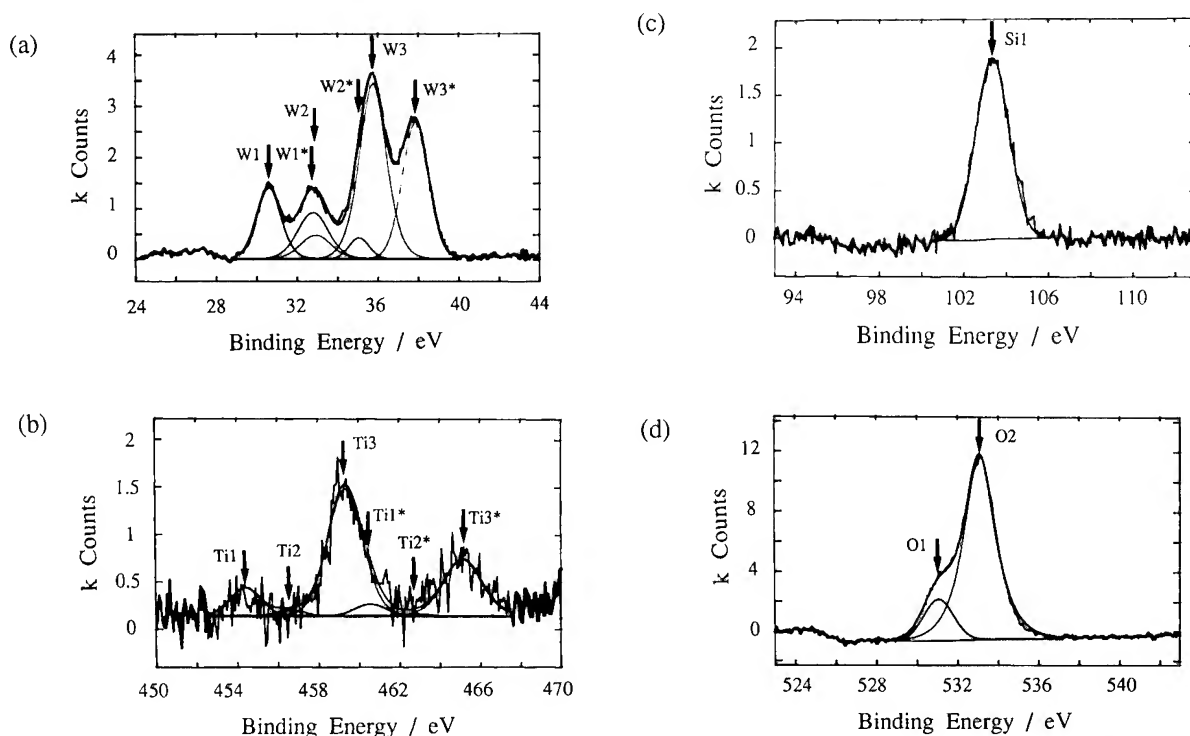
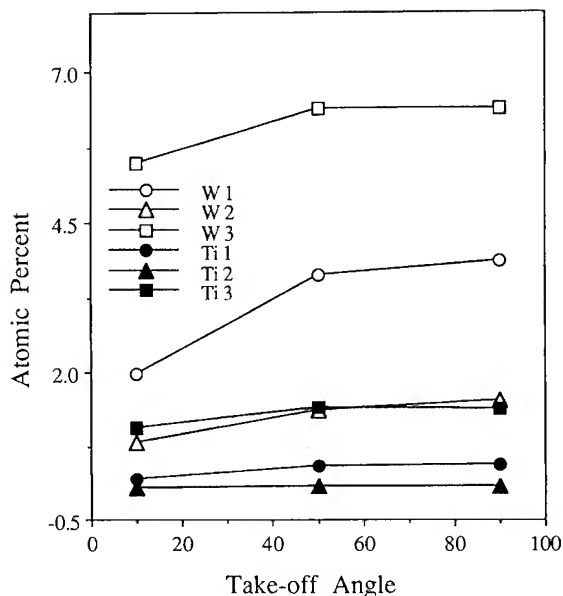


Fig. 3. Deconvolutions of narrow scan spectra for SiO_2 (3 nm)/ $\text{Ti}_{0.1}\text{W}_{0.9}$ system with 20 eV of pass energy and 10° of take-off angle: W 4f (a), Ti 2p (b), Si 2p (c), and O 1s (d) (W1 (W–Ti), W2 (WO_2), W3 (WO_3), Ti1 (Ti–W), Ti2 (Ti_2O_3 and/or Ti_3O_5), Ti3 (TiO_2), Si1 (SiO_2), O1 (Ti/W oxides), and O2 (SiO_2); W, Ti, W*, Ti* correspond W 4f7, Ti 2p3, W 4f5, and Ti 2p1, respectively).

Table 1
Decompositions of W 4f, Ti 2p, Si 2p, and O 1s core level distributions

	Peak attribution	Peak binding energy (eV)	FWHM (eV)	% of area
W 4f7	W1 (TiW)	30.6	1.42	33
	W2 (WO_2)	32.8	1.61	19
	W3 (WO_3)	35.7	1.48	48
Ti 2p	Ti1 (TiW)	453.9	1.88	18
	Ti2 (Ti_2O_3 , Ti_3O_5)	456.0	1.84	10
	Ti3 (TiO_2)	459.1	2.02	72
Si 2p	Si1 (SiO_2)	103.5	1.92	100
O 1s	O1 (O–Ti, W)	531.7	1.90	29
	O2 (SiO_2)	533.5	1.89	71

Fig. 4. Take-off angle dependencies of observed bonding species (W1 (W–Ti), W2 (WO_2), W3 (WO_3), Ti1 (Ti–W), Ti2 (Ti_2O_3 and/or Ti_3O_5) and Ti3 (TiO_2)). Lines are drawn as guides for the eye.



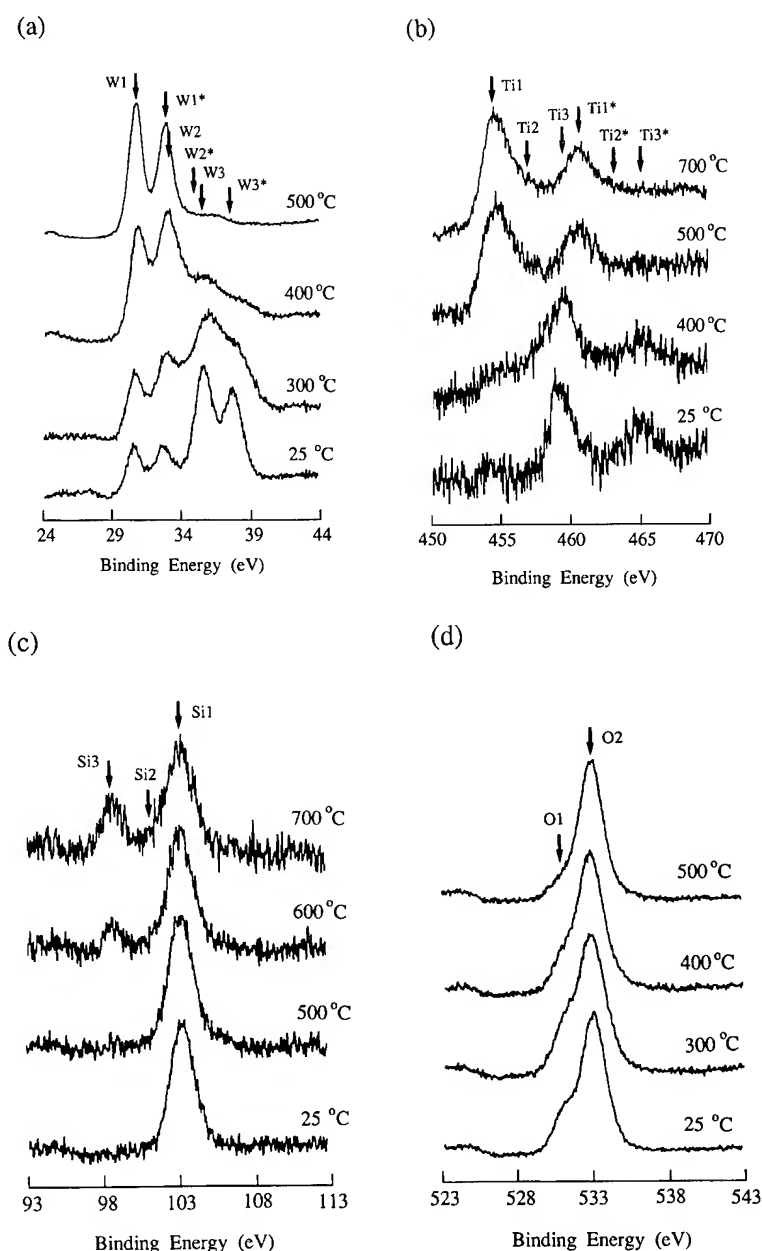


Fig. 5. Changes of W 4f (a), Ti 2p (b), Si 2p (c), and O 1s (d) photoelectron spectra as a function of in situ anneal temperature with 10° of take-off angle (W1 (W–Ti), W2 (WO_2), W3 (WO_3), Ti1 (Ti–W), Ti2 (Ti_2O_3 and/or Ti_3O_5), Ti3 (TiO_2), Si1 (SiO_2), Si2 (SiC), Si3 (Ti/W silicides), O1 (Ti/W oxides), and O2 (SiO_2); W, Ti, W*, Ti* correspond W 4f7, Ti 2p3, W 4f5, and Ti 2p1, respectively).

under UHV condition [5]. The increases of metallic W, Ti, and Si, and decrease of SiO_2 observed at above 600°C , but the other compositions were almost constant.

Fig. 7 shows composition changes of bonding species in SiO_2 (4 nm)/Si system as a function of in situ annealing temperature. Composition of oxygen slightly decreases but maintains almost constant

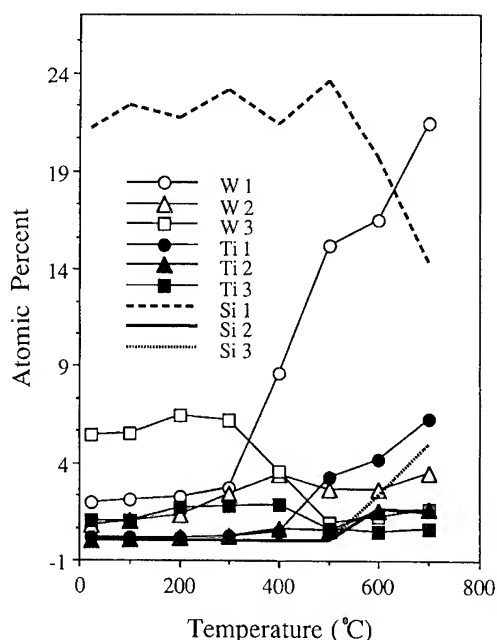


Fig. 6. Changes of bond distribution for SiO_2 (3 nm)/ $\text{Ti}_{0.1}\text{W}_{0.9}$ system as a function of in situ anneal temperature with 10° of take-off angle (W1 (W–Ti), W2 (WO_2), W3 (WO_3), Ti1 (Ti–W), Ti2 (Ti_2O_3 and/or Ti_3O_5), Ti3 (TiO_2), Si1 (SiO_2), Si2 (SiC), and Si3 (Ti/W silicides); W, Ti, W*, Ti* correspond W 4f7, Ti 2p3, W 4f5, and Ti 2p1, respectively). Lines are drawn as guides for the eye.

above 400°C . Formation of SiC was not observed because SiO_2 does not decompose.

4. Discussion

Slight increases for all of bonding species were observed after annealing to 200°C . This is due to liberation of the physisorbed or chemisorbed oxygen on the surface. This relative increase was maintained at 300°C but the decomposition of WO_3 began. The amelioration of antifusing device characteristic was observed after annealing at 400°C . Annealing at this temperature, WO_3 decomposes and mainly forms metallic tungsten. This controlled interface improves the device characteristic. The slightly increased TiO_2 and WO_2 due to the decomposition of WO_3 , also decompose at 500°C . This results in the formation of elemental titanium. The increase of elemental states for Ti, W induces the decomposition of SiO_2 . Above 600°C , sharp

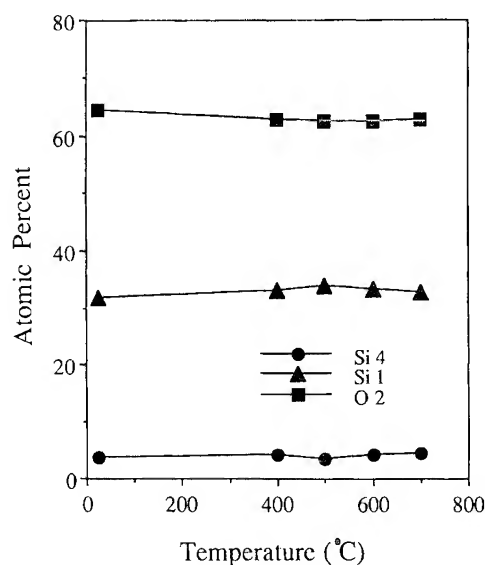


Fig. 7. Composition change of bonding species in SiO_2 (4 nm)/Si system as a function of in situ anneal temperature (Si1 (SiO_2), Si4 (Si substrate), and O2 (SiO_2)). Lines are drawn as guide for the eye.

decrease of SiO_2 and sharp increase of metallic states were observed. Other bonding states remained almost constant. Through angle resolved analysis, this metallic silicon was revealed to be found mainly under the SiO_2 . The silicon may bind with titanium and form Ti-silicide because titanium silicide is easily formed by annealing above 500°C . Further negative heat of formation for titanium silicide is two or three times larger than that of tungsten silicide [6]. By XPS analysis, we cannot distinguish elemental silicon from Si in silicide, because they have almost the same binding energy of about 99 eV. Antifusing device characteristic of metal/dielectric/metal structure may be destroyed due to the connection between the upper and lower metal layers by silicide channel after annealing at above 600°C .

5. Conclusions

With in situ anneal of SiO_2 (3 nm) / $\text{Ti}_{0.1}\text{W}_{0.9}$ system at 300°C under UHV condition, decomposition of WO_3 was found. At 400°C , decrease of WO_3 , sharp increase of metallic W, and slight increases of WO_2 and Ti_2O_3 (Ti_3O_5) were observed.

The reduction and oxidation behaviors induce the controlled interface resulted in the amelioration of antifusing device characteristic. At 600°C, the formation of metallic silicon due to the decomposition of SiO₂ results in the failure of antifusing device characteristic.

References

- [1] D.K.Y. Liu, K.L. Chen, H. Tigelaar, J. Paterson and S.O. Chen, *IEEE Electron Device Lett.* 12 (4) (1991) 151.
- [2] K.L. Chen, D.K.Y. Liu, G. Misium, W.M. Gosney, S.J. Wang, J. Camp and H. Tigelaar, *IEEE Electronics Device Lett.* 13(1) (1992) 53.
- [3] L.I. Maissel and R. Glang, eds., *Handbook of Thin Film Technology* (McGraw-Hill, New York, 1983) ch. 7.
- [4] C.D. Wagner, W.M. Riggs, L.E. Davis, J.F. Moulder and G.E. Muilenberg, eds., *Handbook of X-ray Photoelectron Spectroscopy* (Perkin-Elmer, New York, 1979) p. 68.
- [5] H.H. Park, K.H. Kwon, B.H. Kwon, S.M. Lee, S.H. Jhung, J.W. Lee, S.G. Kim, O.J. Kwon, B.W. Kim and Y.K. Sung, in: *Proc. 2nd Int. Conf. on VLSI and CAD*, Seoul, 22–25 October (1991) p. 123.
- [6] Einspruch, ed., *VLSI Electronics: Microstructure Science* (Academic Press, New York, 1983) ch. 6.



Influence of WSi_2 polysilicide gate process on integrity and reliability of gate and tunnel oxides

J.M. Moragues^{a,*}, B. Sagnes^a, R. Jerisian^a, J. Oualid^a, E. Ciantar^b, J.L. Liotard^b,
P. Merenda^b

^a *Laboratoire des Matériaux et Composants Semiconducteurs (LMCS), ENSPM Domaine Universitaire de Saint-Jérôme,
13397 Marseille cédex 20, France*

^b *SGS-Thomson Microelectronics, 13790 Rousset, France*

Abstract

The deposition of polysilicide layers can contribute to the generation of defects in gate or tunnel oxides which can have a detrimental influence on the reliability of non-volatile memories. Two processes of WSi_2 deposition were studied. The charge and the interface state densities created by Fowler–Nordheim electron injections in the gate oxide, the charge before intrinsic breakdown and the programming window degradation after erase/write cycles of EEPROM were compared. The three types of tests are well correlated.

1. Introduction

The use of a polysilicide layer over the polysilicon gate is being generalized to reduce the transistor gate resistivity and, thus, the access resistance to each point of a non-volatile memory. At the same time, present integrated circuits need very thin gate and tunnel oxides which must keep their integrity after strong cumulated electron injections. So, it is important to study the influence of the silicide deposition process on the oxide defectivity and on the gate oxide resistance to Fowler–Nordheim electron injections.

In this work, the degradation of gate oxides in metal-oxide-semiconductor (MOS) capacitors after

Fowler–Nordheim electron injections is studied by using the method of quasi-static capacitance voltage ($C_{\text{QS}} - V_{\text{G}}$), gate-controlled diode (GCD) and exponential ramp current stress (ERCS) on MOS test capacitors. The results are compared with the programming window degradation of electrical erasable programmable read-only memory (EEPROM) devices. It is assumed that the results obtained on MOS capacitors can be used to predict the behavior of MOS transistors during stressing. Thus, it is very important to understand the degradation mechanisms which occur in the capacitors.

We compare the influence on gate and tunnel oxides and on Si/SiO_2 interfaces of two processes used for the LPCVD deposition of a WSi_2 polysilicide layer.

The devices and experimental methods used throughout this study will be presented and

* Corresponding author. Tel. +33 91 28 80 76. Telefax: +33 91 28 88 13.

described first. Then, the experimental results concerning the effects of Fowler–Nordheim electron injections in gate oxides of MOS capacitors and the change before breakdown are compared for both processes. The programming window degradation after erase/write cycles of the EEPROM circuits which used the two processes of WSi_2 deposition are presented.

2. Devices

Two types of p-type MOS capacitors (S and DCS) were realized with the same process as the one used for EEPROM memories. The capacitor area is 0.1 mm^2 . A N^+ ring, which is used for the GCD characterization, is implanted. The oxide was grown in dry oxygen at 950°C and its thickness was planned to be 27 nm at the end of the process. The WSi_2 layer ($t \approx 250 \text{ nm}$) was deposited by LPCVD on the polysilicon gate ($t \approx 180 \text{ nm}$) at 430°C during 55 s using SiH_2Cl_2 , WF_6 and Ar gases for DCS capacitors and at 280°C during 300 s using SiH_4 , WF_6 and Ar gases for S capacitors by Genus Sonnyvale Application Laboratory, USA. After the usual passivation, the process concludes with annealing at 420°C in forming gas ($\text{H}_2 + \text{H}_2$).

We analyzed the two types of capacitors by SIMS. The main difference is a fluorine concentration in the gate oxide ten times higher with the S process than with the DCS one.

3. Experiments

In order to determine the kinetics of trapped charges and generated interface states, we applied successive negative Fowler–Nordheim injections of 10 s each at different constant currents. The densities of effective trapped charges and of acceptor-like and donor-like interface states (N_{ox} , N_{ss}^{A} and N_{ss}^{D} , respectively) were deduced from the threshold, mid-gap and flat-band voltage shifts measured on quasi-static $C_{\text{QS}} - V_{\text{G}}$ characteristics plotted before and just after each stress at 60°C [1]:

(i) the net effective trapped charge density, N_{ox} , is deduced from the mid-gap voltage shift, ΔV_{MG} , by the relation

$$N_{\text{ox}} = -\frac{C'_{\text{ox}}}{q} \Delta V_{\text{MG}}, \quad (1)$$

(ii) the generated acceptor-like interface state density, N_{ss}^{A} , located in the upper-half band gap of silicon, is given by

$$N_{\text{ss}}^{\text{A}} = \frac{C'_{\text{ox}}}{q} [\Delta V_{\text{T}} - \Delta V_{\text{MG}}], \quad (2)$$

while (iii) the donor-like interface state density, N_{ss}^{D} , located in the lower-half band gap, is calculated by

$$N_{\text{ss}}^{\text{D}} = \frac{C'_{\text{ox}}}{q} [\Delta V_{\text{MG}} - \Delta V_{\text{FB}}]. \quad (3)$$

To obtain a GCD characteristic, the capacitor must have a N^+ ring around it. The leakage current of the junction N^+ ring/substrate, due to the generation of minority carriers by the interface states, is maximum when the interface under the gate is depleted. There is no surface generation of minority carriers when the interface is strongly accumulated or inverted. So, the difference between the leakage currents, measured when the interface is depleted and when it is strongly inverted, is proportional to the density of interface states located near the mid-gap.

The ERCS method used to determine the oxide quality has several advantages:

- (a) it is a time-saving accelerated test (less than 10 s for each capacitor test),
- (b) it explores a large Q_{BD} range (more than 6 orders of magnitude),
- (c) it is of particular interest in the determination of early fails,
- (d) the oxide breakdown is clearly revealed.

The initial current density is 10^{-5} A/cm^2 and the ramp rate used is 0.1 decade/s. Gate voltage readings are performed just at the end of each step. The breakdown is reached when the voltage abruptly shuts down ($V_i < 0.8V_{i-1}$). The results can be plotted on an histogram giving the probability for a capacitor to fail within $[Q_{\text{BD}} - 0.5, Q_{\text{BD}} + 0.5]$.

Erase/write cycling performances were extracted for S and DCS technologies. Parameters for pulse shape definition were set up in accordance with the signal applied on the memory array.

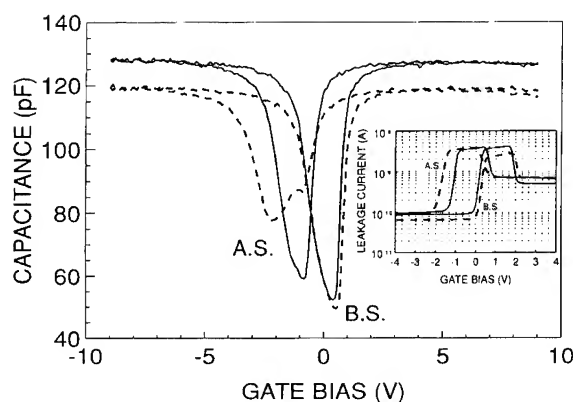


Fig. 1. Quasi-static capacitance and gate controlled diode characteristics before (b.s.) and after (a.s.) stress ($Q_{inj} = 0.04 \text{ C/cm}^2$) of S (grey line) and DCS (black line) capacitors ($A = 0.1 \text{ mm}^2$) at $T = 60^\circ\text{C}$.

4. Discussion

The oxide capacitances, measured on S and DCS capacitors (Fig. 1), indicate that the effective gate oxide thickness is higher in S than in DCS capacitors (28.5 and 27 nm, respectively). Nearly the same difference was observed between S and DCS tunnel oxides (10.5 and 9.2 nm, respectively). This difference may be associated with the fluorine concentration measured by SIMS, which is stronger in S than in DCS capacitors: $5 \times 10^{19} \text{ at/cm}^3$ and $5 \times 10^{18} \text{ at/cm}^3$ respectively.

Before stress, $C_{QS} - V_G$ and GCD characteristics (Fig. 1) indicate a higher negative charge density in S than in DCS capacitors, shown by a larger shift towards positive gate bias. This could also be associated with the higher fluorine concentration in the gate oxide of S capacitors. A higher interface state density appears in DCS capacitors, as shown by the two characteristics.

After an identical stress ($Q_{inj} = 0.04 \text{ C/cm}^2$), the $C_{QS} - V_G$ and GCD characteristics clearly reveal a more important generation of positive charges and interface states in S than in DCS capacitors. These observations are fully confirmed in Figs. 2 and 3 which give the variations of N_{ox} , N_{ss}^A and N_{ss}^D with the density of injected charges, Q_{inj} , during the stress.

These results are in complete contradiction with those obtained when fluorine is introduced in the gate oxide by ionic implantation and for a simplified aluminium gate technology [2,3]. Our results

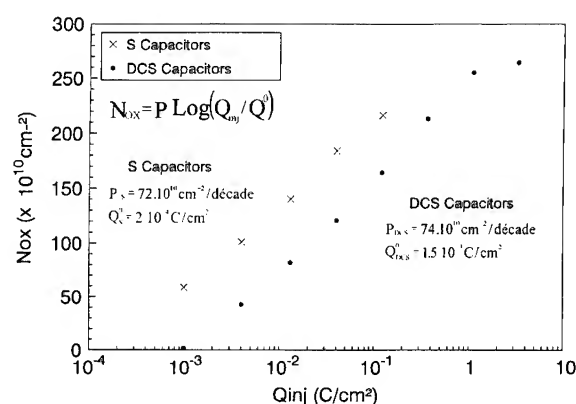


Fig. 2. Evolution of the effective positive charge density, N_{ox} , after successive 10 s Fowler-Nordheim electron injections at different constant currents.

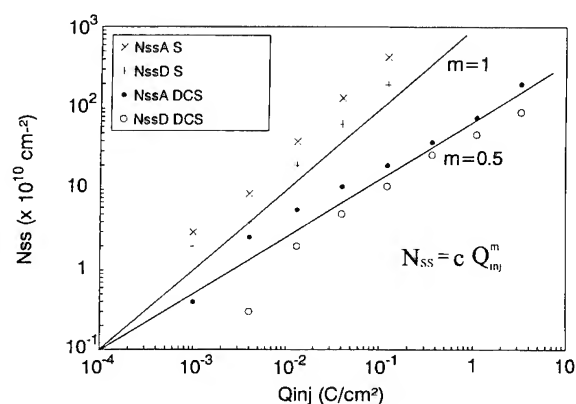


Fig. 3. Evolution of acceptor-like, N_{ss}^A , and donor-like, N_{ss}^D , interface state densities after the same injections than as 2.

can be justified if it is assumed that the diffusion of hydrogen, during the WSi_2 deposition and the following process steps (particularly the last annealing in forming gas), is enhanced by fluorine. In this condition, it can be admitted that more positive charges associated to hydrogen and more related interface states were created by electron injections in S capacitors. The lower relaxation rate observed on S capacitors after stress under positive gate bias can justify this hypothesis.

Moreover, it can be noticed in Fig. 3, that for both types of capacitors, N_{ss}^A is slightly higher than N_{ss}^D , as usual. The generation rate of interface states varies like Q_{inj}^m with $m \approx 1$ for S capacitors and

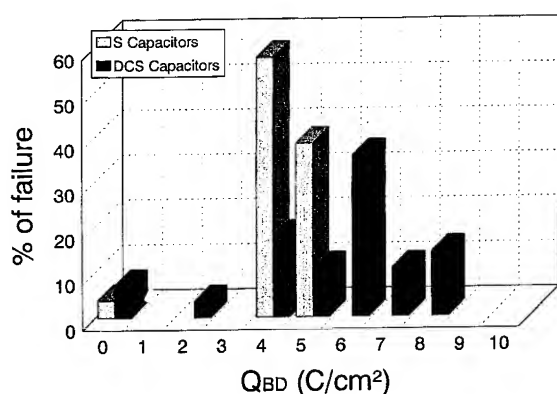
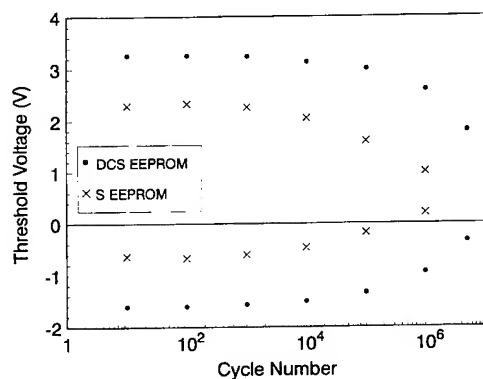
Fig. 4. Q_{BD} histogram for S and DCS capacitors.

Fig. 5. Erase/write cycles of EEPROM devices: S process (x), DCS process (dots).

$m \approx 0.5$ for DCS capacitors. The law $N_{ss} \propto Q_{inj}^{0.5}$ was also observed for MOS capacitors with a simple polysilicon gate and two types of gate oxide (dry and dry/wet/dry) [4].

All these observations can be correlated with those obtained by the ERCS method. The histogram (Fig. 4) shows that the charge breakdown (Q_{BD}) is lower for S capacitors (4–5 C/cm²) than for DCS capacitors (≈ 6 C/cm²). This may be justified by a higher density of electron traps associated with fluorine and by a higher density of hydrogen in S capacitors [5].

Fig. 5 gives the comparison of the degradation with the number of erase/write cycles of the programming window measure on EEPROM devices made by means of the two technologies. An impor-

Table 1

Principal characteristics and results of each studied capacitors

	S capacitors	DCS capacitors
t_{ox} (nm)	28.5	27
N_a (cm ⁻³)	4.4×10^{16}	4.15×10^{16}
Q_{BD} (C/cm ²)	4–5	6
N_{ox} (10^{10} cm ⁻²)	215 ± 5	165 ± 2
$(Q_{inj} = 0.1 \text{ C/cm}^2)$		
N_{ss}^A (10^{10} cm ⁻²)	425 ± 3	20 ± 2
$(Q_{inj} = 0.1 \text{ C/cm}^2)$		
N_{ss}^D (10^{10} cm ⁻²)	195 ± 3	10 ± 2
$(Q_{inj} = 0.1 \text{ C/cm}^2)$		

tant degradation is observed for the S process memories and can also be correlated with the previous results.

The principal results obtained on S and DCS capacitors are resumed in Table 1.

All these characterizations indicate that the use of the DCS process for the WSi₂ layer deposition leads to the improvement of the integrity and fiability of gate and tunnel oxides in MOS capacitors and non-volatile memories.

5. Conclusion

All the results obtained for this study show that the DCS process for the WSi₂ polysilicide gate deposition gives a better oxide integrity to electron injections even if the initial density of interface states is slightly higher. We have also obtained a good correlation between the results obtained for MOS capacitors and for non-volatile memories.

References

- [1] J.M. Moragues, E. Ciantar, R. Jérísian, B. Sagnes and J. Oualid, to be published in J. Appl. Phys.
- [2] V.V. Afanas'ev, M. Depas, J.M.M. de Nijs and P. Balk, Microelectronic Eng. 22 (1993) 93.
- [3] A. Balasinski, M.H. Tsai, L. Vishnubhotla, T.P. Ma, H.H. Tseng and P.J. Tobin: Microelectron. Eng. 22 (1993) 97.
- [4] E. Ciantar, P. Boivin, M. Burle, C. Niel, J.M. Moragues, B. Sagnes, R. Jérísian and J. Oualid, these Proceedings, p. 144.
- [5] D.R. Wolters and J.F. Vervet, in: Instabilities in Silicon Devices, ed. G. Barbotin and A. Vapaille (North-Holland, Amsterdam, 1986) p. 315.



ELSEVIER

Journal of Non-Crystalline Solids 187 (1995) 160–164

JOURNAL OF
NON-CRYSTALLINE SOLIDS

Modeling and simulation of homogeneous degradation for N-channel MOSFETS

I. Limbourg^{a,*}, L. Hardy^a, M. Jourdain^a, R. Bouchakour^b, J.J. Charlot^b

^a *Laboratoire d' Applications de la Microélectronique, Faculté des Sciences de Reims, Moulin de la Housse, 51062 Reims cédex, France*

^b *Laboratoire de Modélisation, Simulation et Caractérisation des Dispositifs, Telecom-Paris, 46 rue Barrault, 75013 Paris, France*

Abstract

In this work, the effects of the degradation generated by homogeneous hot-electron injection in a one-dimensional model of current–voltage characteristics for short-channel MOSFETs are introduced. A distributed charge model, implemented in the SABER simulator is used. Simulation results obtained for n-MOS transistors demonstrate good agreement with the experimental data for interface state density inferior to $3 \times 10^{11} \text{ cm}^{-2} \text{ eV}^{-1}$. The samples are degraded by homogeneous electron photoinjection and the interface trap density is performed by the pumping charge method.

1. Introduction

As short-channel MOS transistors are extensively used in integrated circuits and systems and as the density of VLSI chips increases with shrinking design rules, long-term reliability of MOS circuits becomes a more important issue. The hot-carrier-induced degradation of MOS transistor characteristics is one of the primary mechanisms affecting the long-term reliability of MOS VLSI circuits. In short-channel MOSFETs, it is well known [1–6] that generation of defects at the Si–SiO₂ interface and oxide charge trapping can be caused by hot-carrier injection. Taking into account the degradation in device simulations is a necessity for accurate

prediction of the long-term reliability characteristics. But the more powerful approach used to reach this goal is the development of two- or three-dimensional device simulation programs which, however, are very time consuming. The latter requirement leads to interest in developing a one-dimensional pseudoanalytical short-channel MOSFET model.

The purpose of this paper is to compare experimental and simulated current–voltage (I – V) characteristics of n-MOS transistors uniformly degraded over the entire channel region. In our model the channel is divided into cells; in each of them, the charge neutrality condition is applied. The model describes the device characteristics in all of the operating regimes without introducing discontinuities in the drain current with respect to bias voltages. The accuracy of the model is demonstrated with a complete characterization.

* Corresponding author. Tel: +33 26 05 32 61. Telefax: +33 26 05 31 06.

2. Experimental

2.1. Samples

Devices used in this investigation were fabricated on $\langle 100 \rangle$ p-type silicon substrate in a conventional n-well CMOS technology. The transistors have a channel width of $50 \mu\text{m}$, an effective channel length L_{eff} of $1.5 \mu\text{m}$ and a gate thermal oxide thickness of 40 nm .

2.2. Homogeneous degradation

To realize hot electron (HE) degradation and control current flow through the oxide layer independently from the applied field, optically induced HE injection was performed from Si substrate. This method was used for the first time by Ning et al. [7]. The substrate is biased in inversion; the photoelectrons created in the substrate by a monochromatic light are accelerated towards the Si–SiO₂ interface by the space charge region electric field. A small fraction of them gain enough energy to be injected into the gate oxide, biased positively [8]. The injected oxide charge density (N_{inj}) is deduced from the gate current.

2.3. Charge pumping measurements

The average density of generated interface traps \overline{D}_{it} has been extracted from charge pumping (CP) measurements [9,10]. \overline{D}_{it} is deduced from the charge pumping current I_{cp} which is given by [11]: $I_{\text{cp}} = q^2 \overline{D}_{\text{it}} \Delta\psi_s f A$, where $\Delta\psi_s$ is the surface potential swept during charge pumping, A is the channel area, f is the signal frequency and q the elementary charge.

2.4. Results

Figs. 1 and 2 show the I_{cp} curves for three different injected charges N_{inj} . From Fig. 1, we deduce the densities \overline{D}_{it} which are given in Table 1. The plateaus show good homogeneity of the interface trap density along the channel. From the normalized curves $I_{\text{cp}}/I_{\text{cp,max}}$ (Fig. 2) we deduce: first,

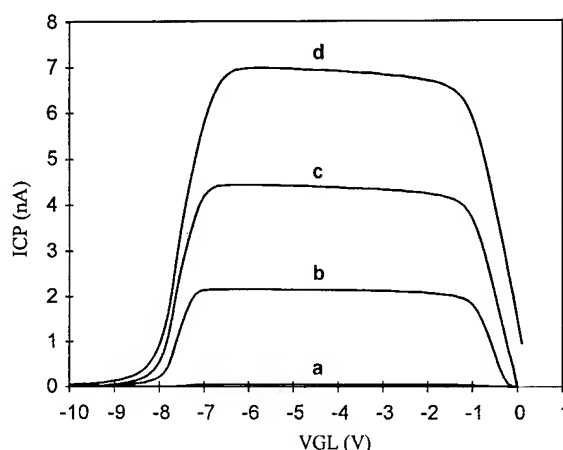


Fig. 1. Charge pumping current I_{cp} as a function of the low-level gate pulse V_{GL} for different injected charges N_{inj} (see Table 1). The stress conditions of the transistor were $V_{\text{GS}} = 24 \text{ V}$ and $V_{\text{BS}} = -15 \text{ V}$.

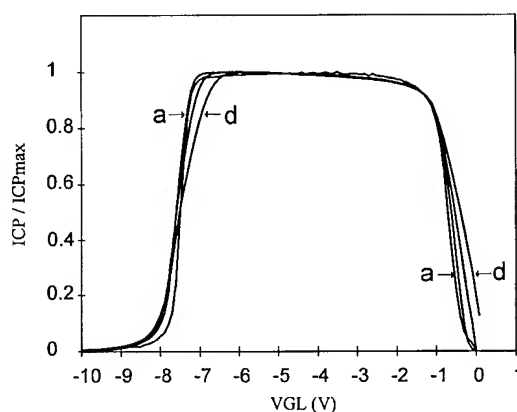


Fig. 2. Normalized charge pumping current $I_{\text{cp}}/I_{\text{cp,max}}$ as a function of the low-level gate pulse V_{GL} for different injected charges N_{inj} (see Table 1). The stress conditions are the same as in Fig. 1.

Table 1

Injected charge densities and average densities of interface traps for three successive degradations

Curve	$N_{\text{inj}} (\text{cm}^{-2})$	$\overline{D}_{\text{it}} (\text{cm}^{-2} \text{ eV}^{-1})$
a	0	2.6×10^9
b	2×10^{19}	1.35×10^{11}
c	3×10^{19}	2.78×10^{11}
d	3.75×10^{19}	4.37×10^{11}

the flat band voltage V_{FB} , which is given by the right trailing edge [12], increases with the degradation, indicating an increase of acceptor-type interface traps with degradation, and second, because there is no noticeable shift of the curves with the degradation, we conclude that the oxide trapped charge density (N_{ot}) is very small and we have therefore neglected it in the simulation.

3. The DCM model of the MOS transistor

3.1. Description

With the distributed charge model (DCM) [13,14], we can simulate the electrical characteristics of the MOS transistor. It is a charge sheet model [15] based on the charge neutrality condition. The channel is divided into several cells, like in Wang's model [16]. The charge is zero in each cell (Fig. 3) and we can write: $Q_{gi} + Q_{bi} + Q_{ci} + Q_{oti} + Q_{iti} = 0$, where Q_{gi} is the gate charge, Q_{bi} the bulk charge, Q_{ci} the inversion channel charge, Q_{oti} the oxide-trapped charge and Q_{iti} the interface-trapped charge in the cell i . Thus, we can calculate, in every cell, the surface potential and then deduce the other electrical quantities along the channel. We use a number of 10 cells which is a good compromise between time consuming and accuracy.

3.2. Modeling of the degradation effects

A very important effect of the buildup of interface traps is mobility degradation. Initial works [17,18] suggested that reductions in mobility were due to increased lattice and Coulomb scattering by charged interface traps and that the average surface mobility was proportional to $1/\overline{D_{it}}$. We have used for the mobility μ at low voltage, the empirical relationship of Galloway et al. [19]: $\mu = \mu_0 / (1 + \theta \Delta \overline{D_{it}})$, where $\Delta \overline{D_{it}} = \overline{D_{it}} - \overline{D_{it0}}$, and $\overline{D_{it0}}$ and μ_0 , respectively, the average density of interface traps and the mobility at low voltage before degradation, and θ is a mobility degradation parameter optimized by simulation.

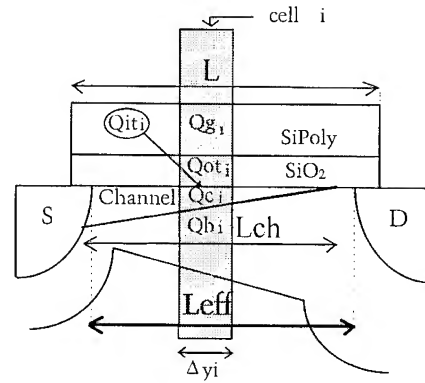


Fig. 3. Schematic of the distributed charge model (DCM) of the transistor along the channel, with the different charges in a cell i .

If we consider that the generated interface traps are acceptor type, the flat-band potential V_{FB} is given by

$$V_{FB} = V_{t0} - 2\psi_B - \gamma \sqrt{2\psi_B} + \overline{D_{it}} \frac{(E_g/2 - q\psi_B)}{C_{ox}},$$

where γ is the body factor, V_{t0} the initial threshold voltage (before degradation), ψ_B the Fermi-potential, C_{ox} the oxide capacitance per area and E_g the band-gap energy.

In inversion, the interface-trapped charge in a cell i , is

$$Q_{iti} = -q \overline{D_{it}} \frac{(\psi_{Si} - V_i)}{C_{ox}}$$

with ψ_{Si} the surface potential and V_i the potential in the channel in a cell i , so we can write

$$\psi_{Si} = V_{GS} - V_{FB}$$

$$- \gamma \sqrt{\psi_{Si} + U_{th} \exp\left(\frac{\psi_{Si} - 2\psi_B - V_i}{U_{th}}\right)} - U_{th} - q \overline{D_{it}} \frac{\psi_{Si} - V_i}{C_{ox}},$$

with U_{th} the thermodynamic potential and V_{GS} the gate voltage.

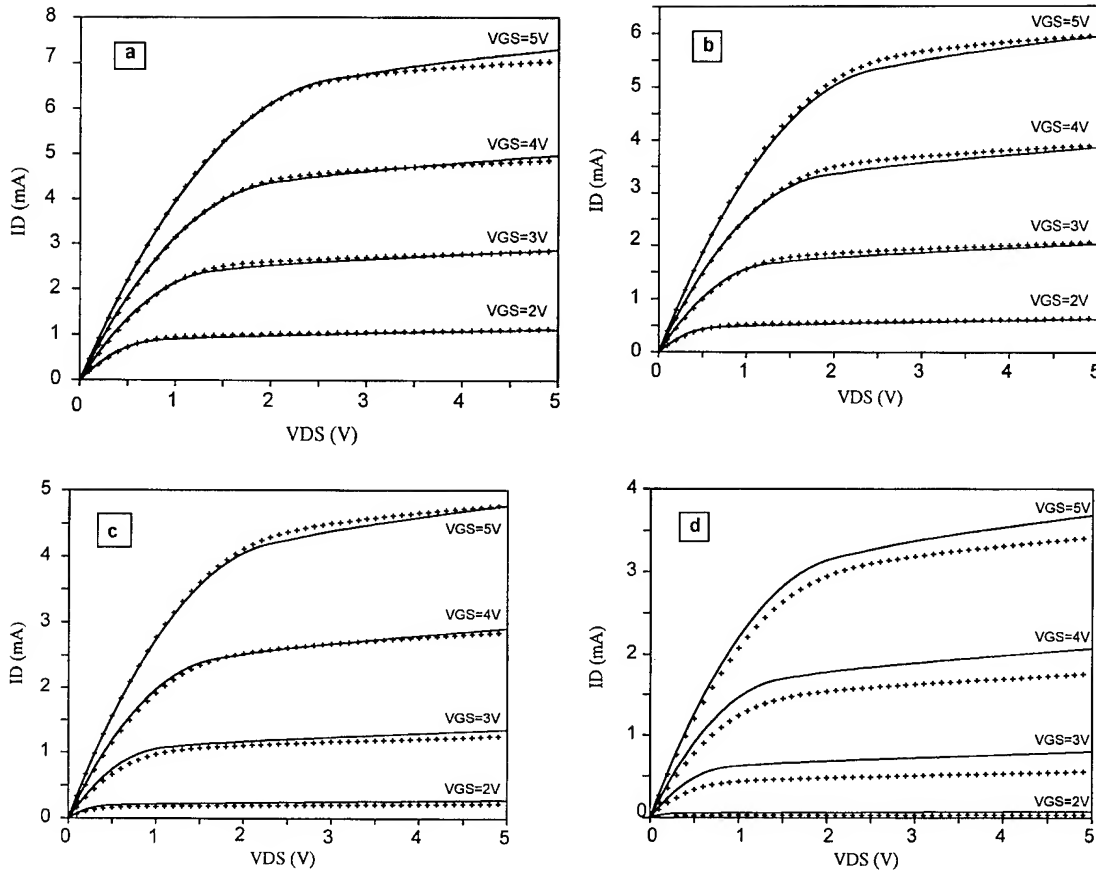


Fig. 4. I_D - V_{DS} characteristics for different gate voltages V_{GS} for the (a) non-degraded transistor (see sample a in Table 1). Crosses are experimental points while lines are simulation curves; (b) degraded transistor ($\bar{D}_{it} = 1.35 \times 10^{11} \text{ cm}^{-2} \text{ eV}^{-1}$; see sample b in Table 1). Crosses are experimental points while lines are simulation curves; (c) degraded transistor ($\bar{D}_{it} = 2.78 \times 10^{11} \text{ cm}^{-2} \text{ eV}^{-1}$; see sample c in Table 1). Crosses are experimental points while lines are simulation curves; (d) degraded transistor ($\bar{D}_{it} = 4.37 \times 10^{11} \text{ cm}^{-2} \text{ eV}^{-1}$; see sample d in Table 1). Crosses are experimental points while lines are simulation curves.

4. Simulation results

The DCM model has been implemented in the simulator SABER. The parameters of the non-degraded transistor have been extracted by the characterisation software IC-CAP coupled with the simulator SABER, by using the I - V measurements performed with an HP4145B semiconductor-parameter analyzer.

Figs. 4 and 5 show the experimental and simulated curves for three different injected charges given in Table 1. Fig. 4(a) corresponds to a non-degraded sample. For the degraded samples

(Figs. 4(b)–(d)), we observe that the degradation is correctly modeled for \bar{D}_{it} less than about $3 \times 10^{11} \text{ cm}^{-2} \text{ eV}^{-1}$. This can be seen also in I_D - V_G curves of the Fig. 5.

5. Conclusions

In this paper, an accurate one-dimensional device model has been presented for the simulation of short-channel nMOS transistors with homogeneous hot-carrier degradation. This model was validated for interface trap density less than

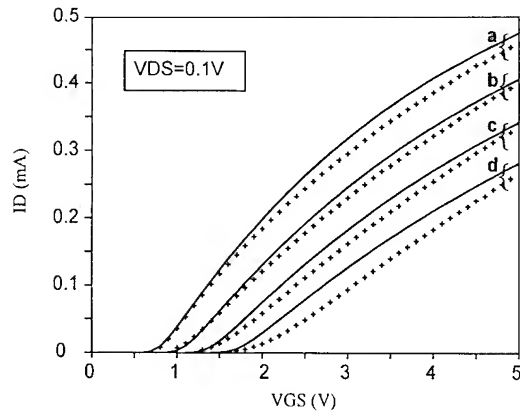


Fig. 5. I_D - V_{GS} characteristics for a drain voltage $V_{DS} = 0.1$ V before (a) and after (b–d) hot electron degradation (see Table 1). Crosses are experimental points while lines are simulation curves.

$3 \times 10^{11} \text{ cm}^{-2} \text{ eV}^{-1}$. For strong degradation there is a weak disagreement and this perhaps can be corrected if we take into account the buildup of the oxide trapped charge density.

This model is based on physical model and do not necessitate empirical parameters. Beside previous works, our model allows to simulate all the electrical quantities along the channel (surface potential, electric fields, electric charges, etc.).

Another advantage of this model is to allow the study of inhomogeneous degradation in introducing in cells near the drain, the oxide damage by using a realistic density distribution.

References

- [1] P. Heremans, R. Bellens, G. Groeseneken and H.E. Maes, *IEEE Trans. Electron. Dev.* 35 (1988) 2194.
- [2] B. Doyle, M. Bourcier, J.C. Marchetaux and A. Boudou, *IEEE Trans. Electron. Dev.* 37 (1990) 744.
- [3] F.C. Hsu and S. Tam, *IEEE Electron Dev. Lett.* EDL5 (1984) 50.
- [4] S. Sun and J. Plummer, *IEEE Trans. Electron. Dev.* 27 (1980) 1497.
- [5] D.J. Di Maria and J.W. Stasiak, *J. Appl. Phys.* 65 (1989) 2342.
- [6] M.M. Heyns, D. Krishna Rao and R.F. De Keersmaecker, *Proc. Infos* (1989) 327.
- [7] T.H. Ning, C.M. Osburn and H.N. Yu, *J. Appl. Phys.* 48 (1977) 286.
- [8] R.E. Cottrell, R.R. Trautman and T.H. Ning, *IEEE Trans. Electron. Dev.* 26 (1979) 520.
- [9] J.S. Brugler and G.A. Jaspers, *IEEE Trans. Electron. Dev.* 16 (1969) 297.
- [10] G. Groeseneken, H.E. Maes, N. Beltran and R.F. Dekeersmaecker, *IEEE Trans. Electron. Dev.* 31 (1984) 42.
- [11] E. Takeda and S. Suzuki, *IEEE Electron Dev. Lett.* 4 (1983) 111.
- [12] P. Heremans, J. Witters, G. Groeseneken and H.E. Maes, *IEEE Trans. Electron. Dev.* 36 (1989) 1318.
- [13] J.J. Charlot, note technique, Ecole Nationale Supérieure des Télécommunications, Paris D83002 (1983).
- [14] J.J. Charlot and S. Toutain, *IEE Proc.* 133 (1986).
- [15] J.R. Brews, *Solid State Electron.* 21 (1978) 345.
- [16] N.N. Wang, *IEEE Trans. Electron. Dev.* 28 (1981).
- [17] A.G. Stanley, *IEEE Trans. Nucl. Sci.* 6 (1967) 266.
- [18] E.T. Gaw and W.G. Oldham, *IEEE Trans. Nucl. Sci.* 6 (1974) 124.
- [19] K.F. Galloway, M. Gaitan and T.J. Russel, *IEEE Trans. Nucl. Sci.* 31 (1984) 1497.



ELSEVIER

Journal of Non-Crystalline Solids 187 (1995) 165–169

JOURNAL OF
NON-CRYSTALLINE SOLIDS

Section 6. Silicon dioxide, charge trapping

Interface traps induced by hole trapping in metal-oxide semiconductor devices

Y. Roh^a, L. Trombetta^{a,*}, D.J. DiMaria^b^a *Electrical Engineering Department, University of Houston, Houston, TX 77204-4793, USA*^b *IBM TJ Watson Research Center, Yorktown Heights, NY 10598, USA*

Abstract

Interface traps near the Si–SiO₂ interface induced by hole trapping *alone* are reported. It is found that interface traps are generated directly due to the presence of trapped holes in metal-oxide-semiconductor devices, and that the loss of trapped holes due to annihilation by electron injection is accompanied by a reduction of interface traps. This observation is distinct from previous reports of a ‘conversion’ of trapped holes to interface traps or a process of interface trap generation in which the presence of trapped holes is required in an intermediate step. It is shown that the origin of these interface traps is not the P_b center, nor a recombination center in general; thus the phenomenon may help to explain the discrepancy between the density of electrically measured interface traps and P_b center densities measured using electron paramagnetic resonance.

1. Introduction

Interface traps at the Si–SiO₂ interface in metal-oxide semiconductor (MOS) devices have been extensively investigated for improving device reliability. For example, mobility degradation and threshold voltage shifts are known to be caused by electron trapping at the Si–SiO₂ interface. Further, it has been recently suggested that interface-trap creation by hot electrons and by trapped holes during device operation will eventually lead to destructive breakdown of the SiO₂ [1]. Consequently, understanding and control of these defects have been at the core of research among semiconductor

interface specialists, and represent a critical step in the fabrication of integrated circuits.

Interface traps play a central role in the degradation and breakdown of the Si–SiO₂ interface. They are generated during electrical stress by both hot electron-related mechanisms [1] and by trapped hole-related mechanisms [2,3]. During Fowler–Nordheim tunnel (FNT) injection, for example, electrons with energy greater than about 2 eV above the SiO₂ conduction band edge cause the release of hydrogen at the anodic interface. The hydrogen then diffuses to the cathodic interface where it is believed to depassivate ≡Si–H bonds, leaving dangling-bond defects. This process takes place at the Si–SiO₂ interface if electrons are injected from the Si substrate. However, substantial hydrogen release is observed only after a threshold electron injection fluence of approximately 0.001 C/cm².

* Corresponding author. Tel: +1-713 743 4424. Telefax: +1-713 743 4444. E-mail: ltrombetta@uh.edu.

The trapped hole is also known to create interface traps *indirectly*. Specifically, it can serve as a cracking site for hydrogen, thereby generating H^+ , which will drift to the Si–SiO₂ interface under positive gate bias and depassivate $\equiv Si-H$ bonds after capturing an electron at the interface [3]. It has also been shown that annihilation of trapped holes via recombination with electrons introduced using photoinjection at low electric fields generates interface traps in Al-gate MOS capacitors [2]. The mechanism of trap generation is believed to involve the release and/or dissociation of hydrogen by energy released in the recombination event; the hydrogen then forms interface traps via a depassivation process.

In many cases following hot carrier or radiation damage processes, the energy distribution of interface traps (D_{it}) in the Si band gap shows a peak at 0.8 eV above the valence band edge. This peak is frequently observed when D_{it} is obtained from capacitance–voltage measurements, and is often regarded as being due to the P_b center, or more generally, to a dangling bond defect. In FNT and hole annihilation experiments described above, electrically measured interface trap spectra show such a peak. However, it is not always true that electrically measured interface defects can be assigned to P_b centers. Several cases involving hot electron damage have been reported in which interface states have been observed electrically but epr experiments do not show P_b -like signals [4,5].

In this work, we report interface traps near the Si–SiO₂ interface induced by hole trapping *directly*. We find that interface traps are generated due only to the presence of trapped holes in MOS devices, and that the loss of trapped holes by annihilation with injected electrons is accompanied by a reduction of interface traps.

2. Experimental details

Polycrystalline-silicon (poly-Si) gate MOSCs and MOSFETs were used in this work. The gate oxides for MOSCs were grown on n-type (100) 0.1 Ω cm Si wafers at 1000°C, resulting in an oxide thickness of 675 Å and with a gate area of 1×10^{-3} – 1×10^{-2} cm². Details of the fabrication process have been discussed in a previous publica-

tion [6]. Data on MOSFETs were obtained on n-channel devices with an oxide thickness of 245 Å. Hole trapping was performed using avalanche hole injection (AHI) and FNT injection for MOSCs and MOSFETs, respectively. The average current density for AHI was 1.9×10^{-8} A/cm² with various injection fluences. Holes previously trapped in the oxide were annihilated using either FNT injection or substrate hot electron injection (SHE) to explore the consequences of removing trapped holes. High frequency (HF) and quasi-static (QS) capacitance–voltage (C–V) techniques were used to measure D_{it} in MOSCs. Charge pumping (CP) and HF C–V techniques were used to measure the densities of trapped holes and interface states in MOSFETs [6]. The possibility that lateral nonuniformities (LNU) were responsible for experimental artifacts mimicking interface traps was investigated using a procedure described by Brews and Lopez [7]. Finally, possible contributions to D_{it} from anomalous positive charge (APC) were investigated.

3. Results

Hole trapping and interface trap generation in MOSCs are illustrated in Fig. 1. In Fig. 1(a), the C–V curves are shifted in the direction of negative voltage after AHI (thick, unbroken lines), indicating that hole trapping has occurred. In addition, interface traps are induced by AHI as is clear from the QS C–V curve and from the corresponding D_{it} spectrum in Fig. 1(b). Annihilation of trapped holes using FNT electron injection from the gate electrode to a fluence of 8×10^{-4} C/cm² results not only in a shift of the C–V curves in the direction of positive voltage (dashed lines), but also in recovery of the QS C–V curve to nearly its original shape. The corresponding D_{it} spectrum shows that most interface traps have been removed.

The fluence used for FNT electron injection in Fig. 1 was not sufficient to initiate interface trap creation by hydrogen, but was enough for both impact ionization [1] and electron–hole recombination [2]. Fig. 1(a) indicates only a partial annihilation to a steady-state density of trapped holes due to the competing effects of electron–hole recombination and impact ionization.

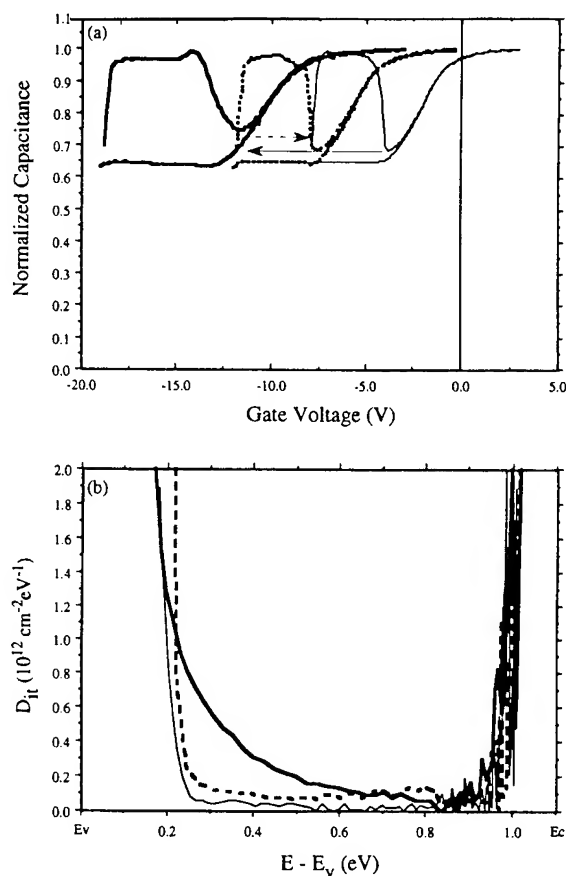


Fig. 1. (a) Reversible interface traps induced by hole trapping in MOSCs: (a) HF/QS C–V curves before (solid line) and after (thick solid line) AHI to a trapped hole fluence of $3 \times 10^{-5} \text{ C/cm}^2$. Trapped holes are annihilated using FNT electron injection from the gate electrode to an injection fluence of $8 \times 10^{-4} \text{ C/cm}^2$ (thick broken line). (b) D_{it} derived from Fig. 1(a).

Generation of trapped holes and interface traps during 11 MV/cm FNT electron injection on n channel MOSFETs is shown in Fig. 2. The generation of interface traps (open circles) tracks that of trapped holes (open inverted triangles); both charge species were monitored using C–V techniques, as indicated on the figure by (C–V). In agreement with the results of Fig. 1, interface states disappear after total annihilation of the trapped hole distribution using SHE injection (solid circles). Most interestingly, interface traps generated at fluences less than 0.01 C/cm^2 are detected in substantially fewer numbers using CP techniques

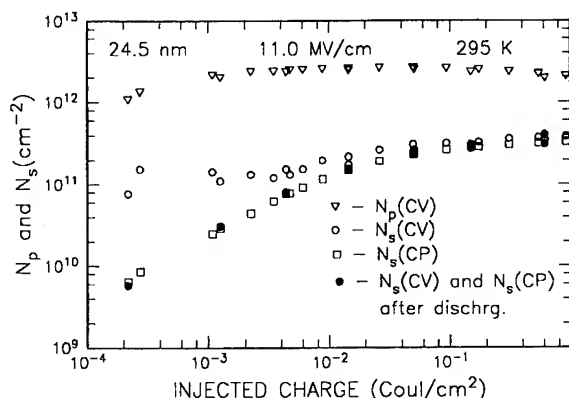


Fig. 2. Number of interface states N_s and trapped positive charge N_p generated during high field stress (11 MV/cm) as a function of injected electron fluence determined using C–V and CP techniques. The curves labeled 'dischrg.' correspond to the number of interface states remaining after total annihilation of the trapped holes using SHE at low field (1.5 MV/cm) and fluence ($1 \times 10^{-6} \text{ C/cm}^2$).

(open squares). Charge pumping is sensitive to the capture cross section of interface traps and, in fact, measures recombination currents at the defect center. On the other hand, C–V techniques are dependent only on the charge states of the defect. The discrepancy in the number of interface traps detected using these techniques thus suggests that the hole induced interface trap is not a recombination center. At fluences beyond 0.01 C/cm^2 , however, CP and C–V measurements detect equal densities of interface traps. In this fluence range, interface trap creation is dominated by hydrogen diffusion; at least some component of traps generated by this mechanism is evidently due to the P_{bo} center [4], which is a recombination center and therefore detectable by CP techniques. Note also that following hole annihilation, C–V and CP techniques detect the same density of interface traps at all injection fluences.

4. Discussion

4.1. Nature of interface traps induced by hole trapping

An important result of the present work is that interface traps induced by hole trapping, as

illustrated in Fig. 1, are not due to P_b centers. Spectral features of the defects observed here are decidedly different from the doubly peaked structure of the P_b center as observed on as-grown samples [8]. The spectra observed in Fig. 1 are also clearly different from the ubiquitous 0.8 eV peak observed following FNT injection and radiation damage; this peak, as we have suggested, may or may not be related to the P_b center. Additionally, although interface trap peaks in Al gate MOSCs have been reported to develop over time after AHI has stopped [9], we observe no such development in the present spectra. We have, however, observed the 0.8 eV peak following substrate FNT injection in our samples, demonstrating that the failure to develop a peak is not sample dependent.

The discrepancy in the measured density of interface traps observed by CP and by C–V (see Fig. 2) is quite interesting, and demonstrates that the hole induced interface traps observed here are not recombination centers, or else that their interaction with the substrate is too slow to be detected using CP. This assertion is supported by recent work by Stathis and DiMaria monitoring interface trap generation in MOSFETs during hot electron injection using spin-dependent recombination (SDR) [4], which is also sensitive to recombination currents at the defect site. In that work, hot electron injection at fluences less than 0.001 C/cm^2 resulted in interface traps which were observed using C–V techniques but not using SDR. Hot electron injection generates holes via impact ionization; the holes are subsequently trapped at the Si–SiO₂ interface and, we suggest, induce defect states having the energy distribution seen in Fig. 1. In Ref. [4] an SDR signal was observed, however, for fluences larger than 0.001 C/cm^2 . In this fluence range, interface trap generation is dominated by depassivation of Si–H bonds by hydrogen, resulting in interface traps which were identified as the P_{bo} variation of the P_b center.

We note that similar effects have been observed following radiation damage [10]. In these studies, near-interface oxide traps (referred to as ‘border traps’) were detected using current–voltage techniques but not using CP. In addition, changes in oxide charge were observed to correlate with

changes in interface trap density in a manner consistent with our observations. It is thus reasonable to suggest that defects observed here are similar in nature to those observed in the radiation work, and may be properly categorized as border traps.

It is well known that lateral non-uniformities in the density of trapped charge (LNU) can mimic the presence of interface traps. To explore this as a possible cause of apparent interface traps in our samples, we examined our HF C–V data using a method suggested by Brews and Lopez [7]. In this method, the surface potential, ϕ , is plotted as a function of substrate depletion depth, w , for the MOS capacitor before and after AHI. Because the depletion depth is uniquely determined by the substrate dopant distribution which is invariant, changes in w as a function of ϕ following AHI suggest the presence of lateral nonuniformities. Application of this test to our samples reveals little difference in the $\phi - w$ curves, suggesting very little contribution to interface trap spectra from LNU. In addition, comparison of charge densities detected using C–V and current-sensing techniques have been made on MOSFETs. These comparisons show similar results, again suggesting that lateral nonuniformities are not present in substantial quantities.

We also investigated a possible contribution to D_{it} from APC by the monitoring flatband voltage (V_{fb}) of injected MOS capacitors as a function of time under an applied bias of alternating sign; this test for APC is described in Ref. [9]. We find no evidence of APC generation in our samples following AHI.

4.2. Interface-trap generation mechanisms

Trapped holes have been reported to play a role in interface trap generation either by serving as a cracking site or via electron–hole recombination. The result of the former process is predicted to be a dangling bond defect which may be related to the P_b center, but at least is expected to be a recombination center. Ref. [4] shows that electron–hole recombination does not produce an SDR signal and is thus not a recombination center, but other work has shown that the process results in the 0.8 eV peak [2]. Finally, the disappearance of interface traps on removal of trapped holes is not

consistent with either the hydrogen cracking or electron–hole recombination mechanisms. Thus we are led to conclude that a different mechanism leads to the interface trap spectra observed in Fig. 1. We suggest instead that interface traps are created as a direct result of the presence of trapped holes, and are removed along with them. We do not know the microscopic identify of such interface traps at present.

5. Conclusions

We report interface traps near the Si–SiO₂ interface induced by hole trapping alone. We find that interface traps are generated directly due to the presence of trapped holes in MOS devices, and that the loss of trapped holes due to annihilation by electron injection is accompanied by a reduction of interface traps. We do not believe the origin of these interface traps to be P_b centers. More generally, we find that these traps are not recombination centers; thus the phenomenon may help to explain the discrepancy between the density of electrically measured interface traps and P_b center densities measured using EPR. The underlying mechanism(s) for the current observations are still unknown, but

there has been further understanding of interface trap generation mechanisms in terms of hot carriers involved in electrical stressing.

References

- [1] D.J. DiMaria, E. Cartier and D. Arnold, *J. Appl. Phys.* 73 (1993) 3367.
- [2] S.K. Lai, *J. Appl. Phys.* 54 (1983) 2540.
- [3] D.L. Griscom, D.B. Brown and N.S. Saks, in: *The Physics and Chemistry of SiO₂ and the Si/SiO₂ Interface*, ed. C.R. Helms and B.E. Deal (Plenum, New York, 1988) p. 287 and references therein.
- [4] J.H. Stathis and D.J. DiMaria, *Appl. Phys. Lett.* 61 (1992) 2887.
- [5] L.P. Trombetta, D.J. DiMaria, G.J. Gerardi and E. Tierney, *J. Appl. Phys.* 64 (1988) 2434.
- [6] D.J. DiMaria and J.W. Stasiak, *J. Appl. Phys.* 65 (1989) 2342.
- [7] J.R. Brews and A.D. Lopez, *Solid State Electron.* 16 (1973) 1267.
- [8] E.H. Poindexter, G.J. Gerardi, M.E. Rueckel, P.J. Caplan, N.M. Johnson and D.K. Biegelsen, *J. Appl. Phys.* 56 (1984) 2844.
- [9] L.P. Trombetta, F.J. Feigl and R.J. Zeto, *J. Appl. Phys.* 69 (1991) 2512.
- [10] D.M. Fleetwood, M.R. Shaneyfelt, L.C. Riewe, P.S. Winokur and R.A. Reber Jr., *IEEE Trans. Nucl. Sci.* NS-40 (1993) 1323; D.M. Fleetwood, M.R. Shaneyfelt and J.R. Schwank, *Appl. Phys. Lett.* 64 (1994) 1965.



ELSEVIER

Journal of Non-Crystalline Solids 187 (1995) 170–174

JOURNAL OF
NON-CRYSTALLINE SOLIDS

Comparison of X-ray-induced electron and hole trapping in various materials (YSZ, SIMOX, thermal SiO₂)

P. Paillet^{a,*}, P. Gonon^a, C. Schwebel^b, J.-L. Leray^a

^a CEA, Centre d'Etudes de Bruyères-Le-Châtel, BP 12, 91680 Bruyères-Le-Châtel, France

^b Institut d'Electronique Fondamentale, CNRS UA 022, Université Paris-Sud, 91405, Orsay cédex, France

Abstract

Charge trapping after X-ray irradiation has been studied in various materials, such as thermally grown SiO₂, ion-implanted SiO₂ (SIMOX process), and yttria stabilized zirconia (YSZ). The charge trapping characteristics are investigated by studying both the dose and applied field dependences. The results show a significant difference between X-ray radiation response of YSZ and SiO₂-based materials. Both hole and electron trapping occur in YSZ in a nearly symmetrical manner, even after a low dose irradiation. In SiO₂-based samples, hole trapping is dominant, although electron trapping is observed in SIMOX materials irradiated at high dose.

1. Introduction

Silicon on insulator (SOI) technology is being actively developed for fabricating rad-hard integrated circuits and is considered for future deep submicron technologies. A lot of processes were successively developed, and various insulators have been used, such as Al₂O₃ substrate (SOS, silicon on sapphire), YSZ substrate (SOZ, silicon on zirconia) [1, 2], and more recently SiO₂-based buried layers (wafer bonding, oxygen implantation in Si for SIMOX). Since the thin active silicon layer (200 nm) is isolated by means of either a buried oxide layer or an insulating substrate, SOI devices have an improved transient radiation and single-

event upset sensitivity. But the presence of many insulating layers (such as buried oxide or substrate, field oxide, etc.) leads to additional problems due to ionizing radiation-induced charge trapping in these surrounding oxides (back-channel or lateral leakage paths). These charge trapping phenomena clearly depend on the nature of each insulating layer, as well as on its fabrication process. The use of materials with higher dielectric constant could lead to lower radiation-induced voltage shifts. This type of material could also be useful in the scope of the future development of deep submicron technologies: as the process dimensions scale down, electric fields inside the semiconductor increase. Silicon voltage breakdown or other phenomena associated with carrier multiplication must be avoided, and high dielectric constant materials could provide a means to reduce the electric field, or to confine the field lines to the silicon film.

* Corresponding author. Tel: +33-1 69 26 46 46. Telefax: +33-1 69 26 60 17.

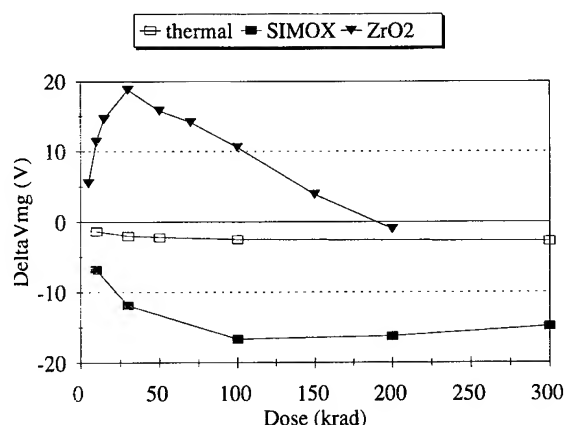


Fig. 1. Measured mid-gap voltage shift as a function of X-ray dose. The irradiation bias was -1 MV cm^{-1} : \square , thermal oxide; \blacksquare , SIMOX; \blacktriangledown , YSZ. The lines are drawn as guides for the eye.

2. Samples and method

Two different types of insulator have been studied, SiO_2 -based layers (thermal oxide and ion-implanted oxide) and yttria stabilized zirconia (YSZ). The thermal oxide samples used in this experiment were obtained by first oxidizing $8\text{--}15 \text{ } \Omega \text{ cm}$ (1 0 0) CZ wafers in dry O_2 at 1050°C to a thickness of 430 nm . The ion-implanted oxide samples were obtained from the standard SIMOX process (Separation by IMplantation of OXygen), implantation of O^+ ions, $1.8 \times 10^{18} \text{ cm}^{-2}$, 200 keV , with a thickness of 400 nm . The superficial Si film (20 nm) was subsequently etched off in XeF_2 gas. The so-called 'YSZ' material, yttria stabilized zirconia, was made by ionic sputtering of $[(\text{ZrO}_2)_{0.77}(\text{Y}_2\text{O}_3)_{0.23}]$, onto a Si substrate in three steps. First a thin SiO_2 layer ($< 200 \text{ nm}$) was grown on the Si substrate. Then a first sputtering was done at 700°C , and finally a last sputtering was done at a temperature of 900°C , to a thickness of 700 nm . The aim of the first two steps is to build a buffer layer, in order to avoid incorporation of Si into the YSZ layer. The resulting YSZ layer has the composition $[(\text{ZrO}_2)_{0.8}(\text{Y}_2\text{O}_3)_{0.2}]$, which is very close to the starting material. MOS capacitors were formed by evaporating Al dots onto the oxides. The samples were then irradiated using 10 keV X-rays (Aracor 4100 system, tungsten target) or 48 keV

X-rays. To study the radiation-induced charge trapping characteristics, standard high frequency capacitance–voltage measurements (C–V, 1 MHz) [3] were carried out to determine the radiation-induced mid-gap voltage shift from which the oxide trapped charge can be deduced [4]. In the following, we present the results obtained as a function of both total irradiation dose and electric field applied during irradiation.

3. Results

3.1. Irradiation dose dependence

In Fig. 1, we present the results of mid-gap voltage shift (ΔV_{mg}) versus dose obtained with a negative applied field (-1 MV cm^{-1}). In the case of SiO_2 -based samples (both SIMOX and thermal dry oxide), ΔV_{mg} is negative, showing net positive charge trapping. For thermal dry oxide, very few holes are trapped at the SiO_2/Si interface. SIMOX samples show a minimum in the mid-gap voltage shift, which is associated with the appearance of negative trapped charge [5,7] along with positive trapped charge. On the other hand, YSZ samples exhibit positive ΔV_{mg} , indicating that there is strong electron trapping in this material.

3.2. Applied field dependence

In Fig. 2, we present the low dose (10 krad (SiO_2)) mid-gap voltage shift versus electric field applied during irradiation, for the different samples. For SiO_2 -based samples, ΔV_{mg} is negative whatever the sign of the applied bias, indicating global positive trapped charge. Hole trapping is therefore dominant in this low dose regime [6]. On the other hand, in YSZ samples charge trapping clearly depends much on the electric field applied during irradiation, in a nearly symmetrical manner. For positive applied field, this material exhibits positive charge buildup, whereas for negative applied field, Fig. 2 shows evidence of electron trapping even in this low dose regime.

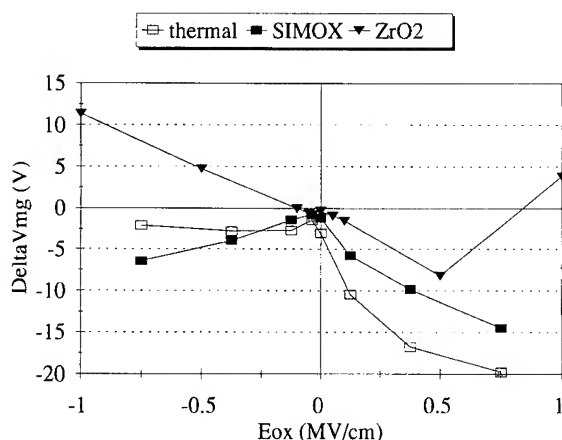


Fig. 2. Measured mid-gap voltage shift as a function of the electric field applied during irradiation (10 krad (SiO_2)): \square , thermal oxide; \blacksquare , SIMOX; \blacktriangledown , YSZ. The lines are drawn as guides for the eye.

4. Interpretation and discussion

The data of Fig. 1 are obtained with a negative applied field during irradiation. In this case, the fraction of radiation-generated carriers that escape initial recombination are separated by the electric field. Holes are drifted toward the gate, and electrons are swept to the oxide/Si interface. In the case of SiO_2 -based samples, ΔV_{mg} is negative in the whole range of dose, indicating that a net positive charge is trapped. Thermal oxide is usually assumed to have a hole trap distribution located very close to the SiO_2/Si interface and no or very low electron trap density. Data for our samples are consistent with this assumption: very little negative shift is observed under negative bias, since holes are driven away from the hole trap distribution. Electrons moving toward the interface are not trapped. We note that electron trapping has also been shown to occur in thermal oxide, using the thermally stimulated current technique [8]. But in this material, the negative charge contribution is too low to be detected by a voltage shift measurement. On the other hand, SIMOX samples are believed to exhibit a uniform hole trap density throughout the oxide, since even under this bias condition, a net positive amount of trapped charge occurs which is shown here to saturate after 100 krad. This saturation

is in fact a combination between space-charge effect (i.e., the so-called 'field collapse' effect) and negative charge trapping at higher dose, as shown elsewhere [6,7,9]. The difference in location of hole trap distribution in the two SiO_2 -based oxides can be seen in Fig. 2. The field dependence of net hole trapping shows that thermal oxide exhibits charge trapping only for positive applied fields. In SIMOX however, charge trapping occurs whatever the sign of the electric field, consistent with the assumption of uniform hole trap density [9]. Thus for SiO_2 -based samples, net positive charge trapping is measured by the C-V method. Only SIMOX oxide shows evidence of electron trapping after irradiation, because the amount of negative charge in this material is large enough to reduce the net total charge.

In the case of YSZ samples, Fig. 1 shows that ΔV_{mg} is now positive. Thus, since the negative field drives electrons toward the YSZ/Si interface, the negative charge is trapped in the vicinity of this interface. At higher dose, a decrease in this negative charge is then observed. It is probably due to the fact that electron traps are filled while hole trapping still takes place, thus reducing the net trapped charge. The dose dependence of YSZ samples is more detailed in Fig. 3, where the voltage shift (ΔV_{mg}) versus dose is displayed for different applied electric fields. It is clearly seen that depending on the sign of the applied bias, this material exhibits positive or negative net trapped charge, in a nearly symmetrical manner. This symmetry in applied

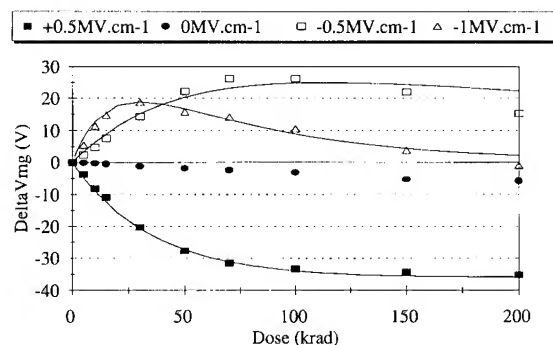


Fig. 3. Measured mid-gap voltage shift as a function of X-ray dose in YSZ samples. The lines are results of a model fit. See text for details.

field is highlighted also in Fig. 4, showing field dependence for different doses. For negative fields, electron trapping increases with dose. As dose increases (from ~ 100 krad on), hole trapping also occurs for high negative fields, reducing the net amount of trapped charge. For positive fields, hole trapping increases with dose, for fields up to 0.5 MV cm^{-1} . For high positive field (1 MV cm^{-1}), charge trapping appears negligible in the whole dose range. This behavior could be interpreted by electron tunneling from the substrate at this high positive field, then counterbalancing the positive charge buildup. The YSZ material thus exhibits both hole and electron trapping.

In an attempt to evaluate the characteristic parameters of these traps, a simple model is used [7]. It is assumed that each charge trapping takes place at the interface, and thus the voltage shift can be written as

$$\Delta V_t = \pm \frac{qt_{\text{ox}}}{\epsilon} N_T [1 - \exp\{-\sigma g_0 Y(E) D t_{\text{ox}}\}], \quad (1)$$

with $+$ for electron shift and $-$ for hole shift, and where q is the electrical charge, N_T the trap surface density projected at the interface, t_{ox} the oxide thickness, ϵ the dielectric constant, g_0 the number of electron-hole pairs generated per unit dose, σ the capture cross-section, $Y(E)$ the probability of escaping initial recombination (so-called 'yield function' for electron-hole pairs production), D the dose and E the local field (approximated as bias field for large biases).

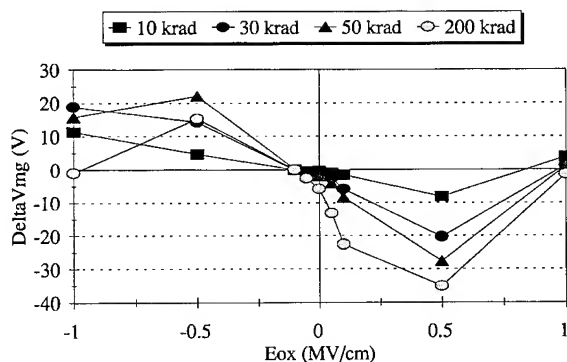


Fig. 4. Measured mid-gap voltage shift as a function of the electric field applied during irradiation in YSZ samples. The lines are drawn as guides for the eye.

From Eq. (1), we can extract two physical parameters, the equivalent trap density at the interface, N_T , and the capture cross-section, σ , both for hole and electron traps. For the sake of comparison, the capture cross-section is in fact determined as the product $\sigma Y(E)$, since the yield function $Y(E)$ may differ for SiO_2 and YSZ samples. The result of a fit using Eq. (1) is shown by the solid curves in Fig. 3 for YSZ samples. Very good agreement is found with experimental data. For positive fields, only hole trapping is taken into account, whereas for negative fields a combination of both trapped species is used to account for the reduction in net negative charge at high dose. A comparison of equivalent trap densities at the interface and products $\sigma Y(E)$ for YSZ and SiO_2 -based samples is shown in Table 1. The equivalent densities of hole and electron traps are identical in YSZ samples, reflecting the near-symmetrical behavior observed. Moreover, these trap densities are close to SIMOX. Thermal oxide has a larger hole trap density, since in this case holes are trapped very close to the interface, where the effect is maximum. Capture cross-sections also are of the same order of magnitude. This material is in fact a three-layer structure, with a very thin SiO_2 layer (less than 2 nm), a thin low temperature formed YSZ layer and a thick high temperature YSZ layer. The total thickness of YSZ is 700 nm. It seems very likely that charge trapping could in fact occur at the interfaces between each layer of the structure, as is the case for Si/ONO structures for example. The more distant of these three interfaces, (YSZ LT/YSZ HT), is located at a distance of around 20 nm from the Si substrate. Since the total YSZ thickness is 700 nm, the inter-layer interfaces are in fact very close to the true

Table 1

	Standard thermal	Standard SIMOX	YSZ
<i>Hole traps</i>			
$N_T (\text{cm}^{-2})$	7.2×10^{12}	4.9×10^{12}	5.7×10^{12}
$Y(E) (\text{cm}^2)$	4.6×10^{-14}	3.8×10^{-14}	1.6×10^{-14}
<i>Electron traps</i>			
$N_T (\text{cm}^{-2})$	—	1.1×10^{12}	5.7×10^{12}
$Y(E) (\text{cm}^2)$	—	2.0×10^{-14}	3.8×10^{-14}

Si-bulk/insulator interface. Thus, charge trapping is well interpreted by the exponential model of Eq. (1).

5. Conclusion

The results presented here show that the X-ray radiation response of YSZ is significantly different from SiO₂-based materials. The latter show dominant hole trapping, although electron trapping is directly observed in SIMOX oxide. On the other hand, both hole and electron trapping occur in YSZ even after a low dose irradiation. Moreover, this charge trapping appears to be nearly symmetrical with applied field. Further studies are needed to investigate the nature of the generated traps, but the model could be generalized to investigate other insulators such as Ta₂O₅/Si, Si₃N₄/Si or Si/ONO structures.

References

- [1] E. Dupont-Nivet, A. Umbert, J.L. Leray, L.M. Mercandalli, B. Dessertene, D. Dieumegard and J. Siejka, in: *Proc. Electrochemical Society Meeting*, Atlanta, GA, 1988.
- [2] I. Golecki, H.M. Manasevit, L.A. Moudy, J.J. Yang and J.E. McE, *Appl. Phys. Lett.* 42 (1983) 501.
- [3] S.M. Sze, *Physics of Semiconductor Devices* (Wiley, New York, 1981) ch. 7.
- [4] P.J. McWhorter, P.S. Winokur and R.A. Pastorek, *IEEE Trans. Nucl. Sci.* NS-35 (1988) 1154.
- [5] O. Flament et al., *IEEE Trans. Nucl. Sci.* NS-39 (1992) 2132.
- [6] D. Hervé, J.L. Leray and R.A.B. Devine, *J. Appl. Phys.* 72 (1992) 3634.
- [7] P. Paillet, D. Hervé and J.L. Leray, in: *RADECS European Conf. Proc.*, Saint-Malo, IEEE no. 93-TH0616-3, 1993, p. 140.
- [8] D.M. Fleetwood, S.L. Miller, R.A. Reber Jr., P.J. McWhorter, P.S. Winokur, M.R. Shaneyfelt and J.R. Schwank, *IEEE Trans. Nucl. Sci.* NS-39 (1992) 2192.
- [9] D. Hervé, P. Paillet and J.L. Leray, in: *RADECS European Conf. Proc.*, Saint-Malo, IEEE no. 93-TH0616-3, 1993, p. 154.



ELSEVIER

Journal of Non-Crystalline Solids 187 (1995) 175–180

JOURNAL OF
NON-CRYSTALLINE SOLIDS

Influence of the oxide charge build-up during Fowler–Nordheim stress on the current–voltage characteristics of metal-oxide-semiconductor capacitors

Simon Elrhbari, Marc Jourdain*

Laboratoire d'Applications de la Microélectronique, Université de Reims, Moulin de la Housse, 51062 Reims cedex, France

Abstract

A study of the influence of the oxide charge build-up during Fowler–Nordheim is presented, emphasizing the current–voltage characteristics. In some cases, a diminution of the slope of current–voltage characteristics was observed. It is shown that the slope variation is due to a change of the cathode field which is basically related on the location of the oxide charge. The proximity of this oxide charge (positive or negative) to substrate-Si/SiO₂ or gate/SiO₂ interfaces modifies the shape of the tunneling barrier. From a qualitative analysis of the voltage shifts of current–voltage and capacitance–voltage characteristics, the origins of the oxide charge have been discussed and the degradation of the oxide is found to be consistent with both mechanisms of trap creation and/or impact ionization.

1. Introduction

Fowler–Nordheim current is the mechanism used in the programming and erasing of memory cells in electrically erasable-programmable read-only memories (EEPROM). This mechanism leads to a creation of charges in the bulk oxide and interface traps which significantly affect metal-oxide-semiconductor (MOS) device performance [1]. In order to consider the mechanism of the oxide charge generation, it is important to obtain information on the distribution of trapped charges in the oxide. Useful techniques to extract the densities of charges in oxide, interface traps at the

substrate-Si/SiO₂ interface and other physical parameters, are based on a combination of capacitance–voltage ($C-V$) and current–voltage ($I-V$) characteristics. The fast interface states have no effect on the $I-V$ characteristics in MOS capacitors but do affect $C-V$ characteristics. The current is dependent only on the cathode region field strength. This latter characteristic of $I-V$, sensing only the effect of bulk trapped charge, allows a separate determination of both the bulk charge centroid and the total amount of trapped charge.

However, the common practice of extracting the location and the magnitude of these charges, from the positive or negative voltage shifts of the $I-V$ characteristics must be used with caution, because it usually assumes a triangular barrier for tunneling electrons, i.e. parallel voltage shifts. Depending on

* Corresponding author. Tel: +33 26 05 33 32. Telefax: +33 26 05 31 06.

the location of the trapped charge, the assumption may or may not be true.

The purpose of this paper is to investigate the influence of the oxide charge build-up during Fowler–Nordheim stress on the I – V characteristics which are analyzed not only in the low current density region where the voltage shifts are measured to extract the location and the magnitude of the oxide charge, but in the whole Fowler–Nordheim region.

2. Experiments

2.1. Sample characteristics and data processing

The P-MOS capacitors were fabricated on boron doped Si <100> substrate ($N_A \approx 2.5$ – $3.3 \times 10^{15} \text{ cm}^{-3}$). The gate has an area of $5.44 \times 10^{-4} \text{ cm}^2$ and the oxide thickness is deduced from the capacitance measurement. All the samples were supplied by the Laboratoire d'Electronique, de Technologie et d'Instrumentation (LETI) (Grenoble France). Main sample characteristics are listed Table 1.

2.2. Electrical measurements

Our experimental method is the following: C – V and I – V curves of non-stressed samples were measured first to test the electrical quality of the devices (we make certain that the I – V measurements do not stress the sample). Then, a constant high electric field stress (HEFS) was applied during a predetermined time and C – V and I – V curves were recorded thereafter. The HEFS is performed by Fowler–Nordheim tunneling (FNT) injection of electrons from the gate. The magnitude of the injected charge density, N_{inj} , is obtained by current

integration over the stress time. This procedure was repeated until the breakdown of the sample.

The I – V characteristics were obtained in the two injection modes, i.e. injection with a positively or negatively biased gate (V_g^+ or V_g^- modes, respectively). To obtain the I – V characteristic, the sample must be illuminated continuously, in a white light to prevent a deep depletion by supplying enough minority carriers through photo-generation. The present investigations are limited in the regions where the oxide current is dominated by the tunneling Fowler–Nordheim regime.

3. Experimental results

Figs. 1 and 2 show the I – V characteristics for the two samples where the curves 1 are measured before stress and curves 2, after stress. Figures a and b show the I – V characteristics measured, respectively, for V_g^+ and V_g^- modes. We observe a decrease in the slope of the I – V curves, except for the Al-gate sample in V_g^- mode, and an increase of the current, except for the Poly-Si-gate sample in V_g^+ mode.

For both samples, the positive charge is located near the substrate-Si/SiO₂ interface. In order to separate the influence of negative charge from the positive charge on the I – V curves, we neutralize the positive charge by sweeping the bias in V_g^+ mode (in FNT region) a couple of times without stressing, hence, injection of few electrons is made through the substrate-Si/SiO₂ interface. In this case, the C – V curves shift towards their non-stressed position which shows that the positive charge has been neutralized, but the number of interface traps created remains unchanged [2]. In Fig. 3(a), we plot some I – V curves (measured in V_g^+ mode before and after HEFS in V_g^- mode) of the Al-gate

Table 1
Sample characteristics

Sample	Substrate doping density, N_A (cm^{-3})	Oxidation conditions	e_{ox} (nm)	Post anneal	Gate
LIR04	2.65×10^{15}	900°C–O ₂ + 5% HCl	29.4	Ar 1050°C	Al
LIR19	3.30×10^{15}	900°C–wet O ₂ + 6% HCl	42.5	Ar 1050°C	Si-Poly

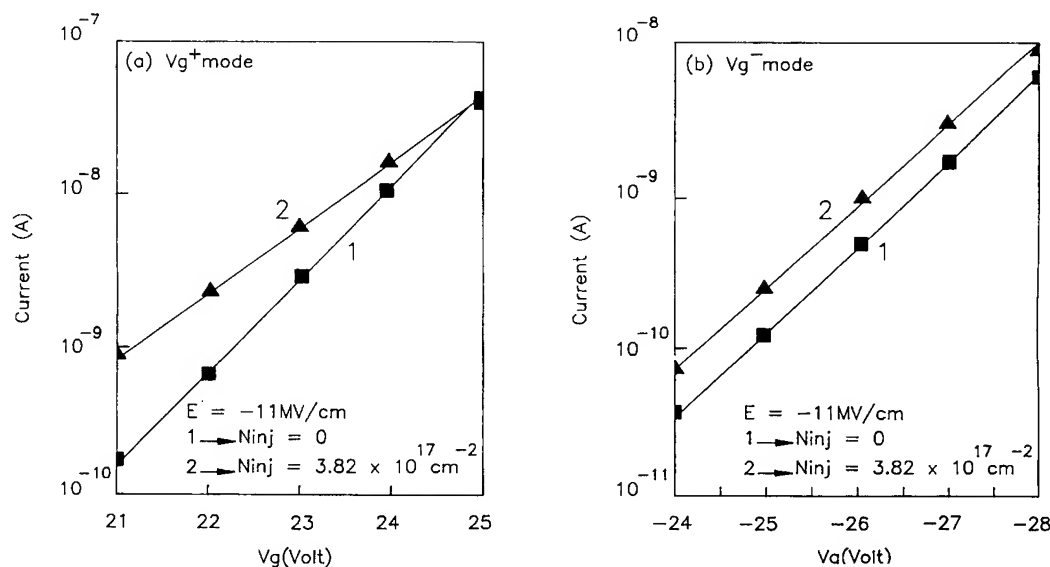


Fig. 1. I - V characteristics for Al-gate sample before and after high electric field stress of -11 MV/cm, measured in the Fowler-Nordheim region in the case of both (a) V_g^+ and (b) V_g^- modes. The curve 1 is measured before stress and curve 2, after stress (N_{inj} is the value of the charge density injected during HEFS). The lines are drawn as guides for the eye.

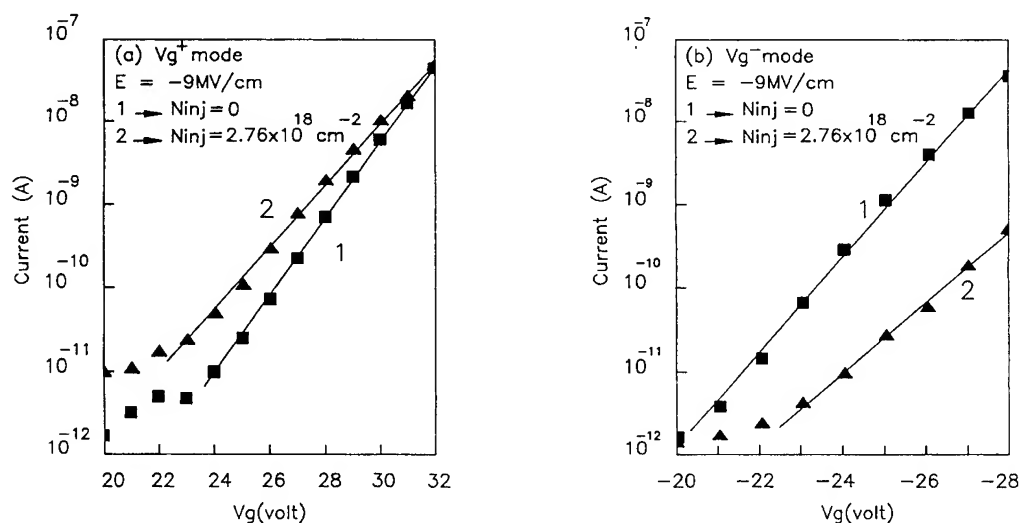


Fig. 2. I - V characteristics for Poly-Si-gate sample before and after high electric field stress of -9 MV/cm, measured in the Fowler-Nordheim region in the case of both (a) V_g^+ and (b) V_g^- modes. The curve 1 is measured before stress and curve 2, after stress (N_{inj} is the value of the charge density injected during HEFS).

sample (we obtain the same evolution of the I - V curves in V_g^+ mode for the poly-Si-gate sample). The curve 1 corresponds to a non-stressed sample and the curves 2 and 3 to the same stressed sample

for two different injection densities. After curve 2 of Fig. 3(a) was taken, we again neutralized the positive charge and subsequently stressed the same sample at $2.45 \times 10^{17} \text{ cm}^{-2}$ (curve 3). The

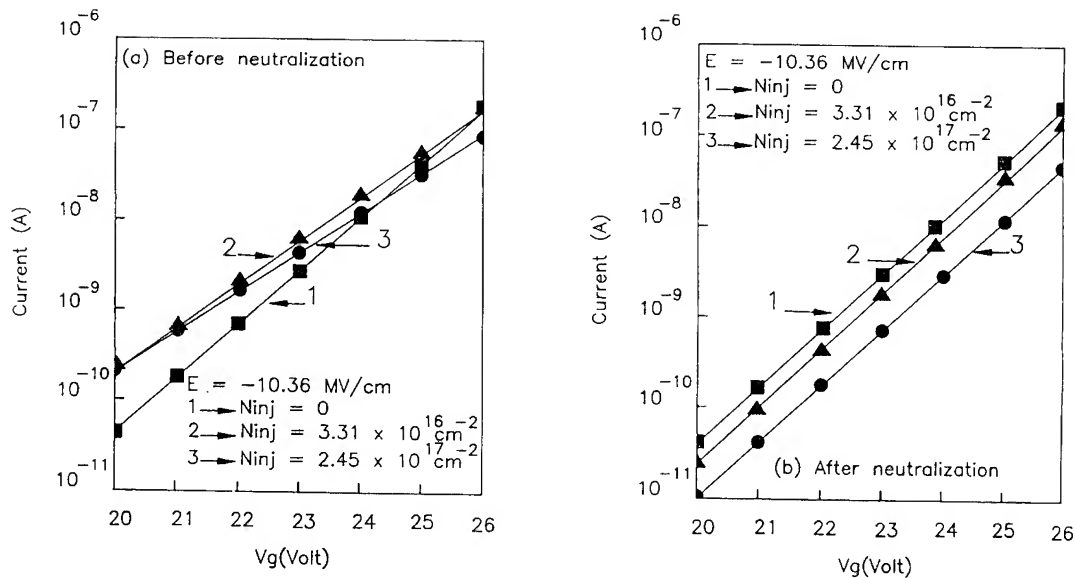


Fig. 3. Evolution of I - V characteristics before neutralization (a) and after neutralization (b) of the positive charge for: curve 1 – Sample non-stressed; curve 2 – Sample stressed at ($E = -10.36$ MV/cm; $N_{inj} = 3.31 \times 10^{16} \text{ cm}^{-2}$); curve 3 – Sample stressed at ($E = -10.36$ MV/cm; $N_{inj} = 2.45 \times 10^{17} \text{ cm}^{-2}$).

recombination of electrons with positive charge does not simply result in the return to the unstressed conditions. We notice (Fig. 3(b)) on the I - V characteristics, that the slopes also take back their original value and that a turn around effect is observed. The new parallel shifts increase with the injected charge density, and they indicate a negative charge. It can be seen that these variations of the slopes of I - V curves are related to the proximity of the charge (positive or negative) to substrate-Si/SiO₂ or gate/SiO₂ interface. The modified shape of the tunneling barrier due to the oxide charge and its related I - V curve is sketched on the Fig. 4.

The oxide charge being sensed very close to Substrate-Si/SiO₂ interface, by the I - V curve in V_g^+ mode, is positive for both samples and it is consistent with the shifts of C - V curves. However, we have shown elsewhere [3] that for the Al-gate sample, the situation is more complex at the substrate-Si/SiO₂ interface, when HEFS is made in V_g^+ stress mode, i.e. negative charge is sensed by the I - V curves in V_g^+ mode, very close to the substrate-Si/SiO₂ interface, whereas positive

charge is sensed by the negative flatband voltage shifts. The I - V and C - V behavior is interpreted consistently if the positive charge is located between the negative charge and the substrate-Si/SiO₂ interface. The shifts are parallel for the Al-gate sample from I - V curves measured in V_g^- mode. In this case, we think that the charge centroid \bar{X} is greater than tunneling distance X_t and that the oxide charge is located beyond 25 Å from the Al/SiO₂ interface. For the poly-Si-gate sample, the negative charge is located very close to the poly-Si/SiO₂ interface, the centroid is located between the tunneling distance and the poly-Si/SiO₂ interface.

4. Discussion

It has been suggested [4,5] that two mechanisms could produce the generation of a positive charge at both interfaces; these are the phenomena of trap creation and band-gap ionization. Trap creation is produced by any electron with energy greater than 2 eV and for injected charge density superior to

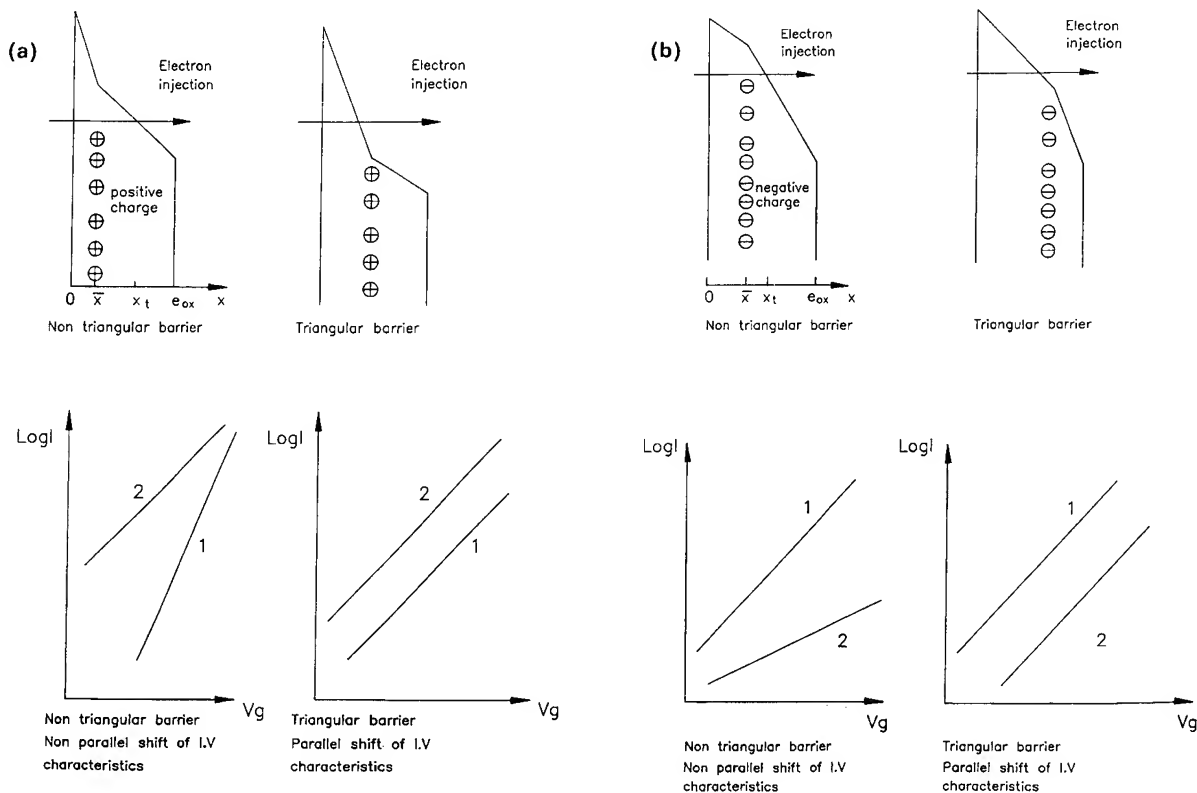


Fig. 4. (a) Effect of positive charges on I - V characteristics depending on its location: case of triangular barrier and non-triangular barrier. (b) Effect of negative charges on I - V characteristics depending on its location: case of triangular barrier and non-triangular barrier

10^{-4} – 10^{-3} C/cm²; the energy of 2 eV is sufficient to release hydrogen from defect sites near the anode interface. Impact ionization occurs for energy exceeding 9 eV and for fluences greater than 10^{-6} C/cm². This being the case, holes are then produced in the oxide bulk closer to the anode interface and subsequently move to the cathode interface where some are trapped. Some of the injected electrons from the cathode recombine with these trapped holes producing interface states and traps near the cathode. For these authors, trap creation and impact ionization can occur simultaneously under certain conditions, particularly at high electric fields. Furthermore, it has been shown that similar interfacial defect generation can also occur near the anode for both mechanisms [6].

We can conclude that the shifts of I - V characteristics after HEFS for our samples can be well explained by the both mechanisms of trap creation and/or impact ionization, but in this paper, we have not attempted to separate both mechanisms. The field stresses have values greater than 9 MV/cm and injected charge density $> 10^{15}$ cm⁻²; impact ionization could occur at all fluences. We have shown in Ref. [7] that in our Al-gate samples, one could interpret the generation of positive charge in SiO₂ by impact ionization at fluences of 10^{15} – 10^{18} electrons per cm² and high-fields superior to 7 MV/cm. This threshold field of 7 MV/cm is required to accelerate electrons to energies high enough to cause electron-hole pair generation by impact ionization under high-field stress. Trombetta et al. [8] suggest that positive charge near the

substrate-Si/SiO₂ interface exists in at least two fundamentally different forms. These forms are referred to as the trapped hole and the anomalous positive charge (APC) center or 'slow states'. We used the same procedure described in Ref. [8] to verify if the positive charge can be interpreted as APC or trapped holes: APC center can be reversibly charged or discharged by application of a dc gate bias (4.5 MV/cm) of appropriate sign for an extended period of time (minute to hours). With a 4.5 MV/cm field, only a portion of the positive charge has disappeared on the stressed Al-gate sample, certainly by tunneling of holes to the substrate-Si. If we begin again the same procedure several times, no variation of the positive charge is observed. In our case, the positive charge cannot be reversibly charged and discharged by application of a moderate bias of alternating sign. As mentioned earlier, the positive charge has been neutralized by a series of sweeping bias in V_g^+ mode in FNT region (the involved fields are between 6 and 8 MV/cm), during a short time, therefore the injected charge remains very small. These results indicate that the generated positive charge on the Al-gate sample cannot be interpreted as anomalous positive charge or slow states but rather results from impact ionization and the subsequent trapping of the generated holes. For the poly-Si-gate sample, the fluence level ($2.76 \times 10^{18} \text{ cm}^{-2}$) is enough to cause significant trap creation. DiMaria et al. [9] attribute the generation of a negative charge by the mechanism of trap creation described elsewhere. The mobile species created by trap creation can move to the cathode interface where it

produces a distribution of electron traps in the oxide near the interface.

5. Conclusion

We have shown that oxide charge build-up during HEFS have an influence on the slopes of I - V characteristics. The non-parallel voltage shifts of I - V characteristics obtained in some cases are explained by the shape of tunneling barrier, triangular or not, according as the tunneling distance is smaller or not than the centroid of charge. The evolutions of the I - V characteristics are consistent with two mechanisms of trap creation and/or impact ionization.

References

- [1] I.C. Chen, S. Holland and C. Hu, *IEEE Electron. Dev. Lett.* 7 (1986) 164.
- [2] A. Meinertzhagen, S. Elrhbari and M. Jourdain, *Appl. Phys. Lett.* 60 (1992) 2222.
- [3] S. Elrhbari, M. Jourdain and A. Meinertzhagen, *J. Appl. Phys.* 76 (1994) 1013.
- [4] D.J. DiMaria, D. Arnold and E. Cartier, *Appl. Phys. Lett.* 60 (1992) 2118.
- [5] D.J. DiMaria and J.W. Stasiak, *J. Appl. Phys.* 65 (1989) 2342.
- [6] D.A. Buchanan and D.J. DiMaria, *J. Appl. Phys.* 67 (1990) 7439.
- [7] S. Elrhbari, M. Jourdain, A. Meinertzhagen, A. EL Hdiy and C. Petit, *J. Phys. III (Paris)* 4 (1994) 1045.
- [8] L.P. Trombetta, F.J. Feigl and R.J. Zeto, *J. Appl. Phys.* 69 (1991) 2512.
- [9] D.J. DiMaria, E. Cartier and D. Arnold, *J. Appl. Phys.* 73 (1993) 3367.



ELSEVIER

Journal of Non-Crystalline Solids 187 (1995) 181–185

JOURNAL OF
NON-CRYSTALLINE SOLIDS

Comparison of the generated oxide charge by injection of electrons for both polarities

A. Meinertzhagen^{a,*}, G. Yard^a, C. Petit^a, M. Jourdain^a, A. El-Hdiy^b, G. Salace^b,
G. Reimbold^c

^a *Laboratoire d' Applications de la Microélectronique and ^b Laboratoire d' Analyse des Solides, Surfaces et Interfaces, U.F.R. Sciences, Moulin de la Housse, BP 347, 51062 Reims cédex, France*

^c *CEA-LETI, Avenue des Martyrs, 38041 Grenoble, France*

Abstract

Fowler–Nordheim tunneling injections were performed, from the gate, or from the substrate, in P-type metal oxide semiconductor capacitors with polysilicon gates in both wet and dry oxides. When the injection was from the gate, trapped holes, as well as negative and anomalous positive charges were created and it was possible to determine their amplitude and their centroid. When the injection was from the substrate, only negative and anomalous positive charges were created, but the determination of the centroids was not always possible since the positive charge appears to be located at both interfaces.

1. Introduction

Many studies exist on the charge generated by the avalanche injection of minority carriers into the oxide of N or PMOS capacitors. Studies also exist on Fowler–Nordheim (FN) tunneling injections made from the substrate into the oxide of NMOS capacitors, but less attention has been paid to FN injections made from the gate or from the substrate into PMOS capacitors. It is known that the damage performed by these injections consists of generated positive and/or negative charge together with interface states at the Si–SiO₂ interface. The positive oxide charge can be a combination of trapped

holes and anomalous positive charge (APC) [1–11]. In the present paper, we describe the oxide charge distribution which results from FN electron injections from both electrodes into PMOS capacitors. Active edge (N⁺) has been implanted in Si substrate to facilitate the formation of the inversion layer and to allow the realization of FN injection from the substrate into the PMOS capacitors. To find the localization of the positive and negative charges in SiO₂, and to differentiate between bulk and interface trapped charges, C–V and I–V measurements must be performed. It is from the shift of these characteristics, relative to the initial curves, that this information can be obtained. Nonetheless, the trapped holes are discharged irreversibly by an appropriate gate bias, whereas APC is charged or discharged reversibly. So the accuracy of any method, which uses I–V or C–V shifts after stress,

* Corresponding author. Tel: +33 26 05 32 61. Telefax: +33 26 05 31 06.

becomes questionable. It is our opinion that before extracting informations from these shifts, it is important to establish: (a) whether the positive charge is made up of trapped holes or APC or a mixture of both; (b) if such charges do exist, which gate bias can charge or discharge them; (c) what are the time constants of the charge and discharge.

2. Samples

The PMOS samples studied contained two different types of oxide: one was wet ($850^{\circ}\text{C} + \text{H}_2\text{O}$) and the other was dry ($950^{\circ}\text{C} + \text{HCl}$). Their thickness is 22 nm and their gate was in polysilicon. All the samples were supplied by the Laboratoire d'Electronique, de Technologie et d'Instrumentation (LETI), Grenoble, France. Constant bias FN injections were performed under an oxide field of approximatively $\pm 10 \text{ MV cm}^{-1}$.

3. Results

It is well known that the generated oxide charge has an effect on the gate current at constant gate bias level. In studying this effect, one obtains an overall view of the nature of the trapped charge. For dry oxides when the injections are made from the gate, the increase of the current at low fluence and its decrease at high fluence, as seen in Fig. 1, show the creation of a positive charge followed by the buildup of negative charge, but when, on the other hand, the injection was made from the substrate, the buildup of the negative charge started at a lower fluence, and no positive charge was detected. On the other hand, for the wet oxide, when the injections were made from the gate, the buildup of the negative charge started at a lower fluence than for the dry oxides, as seen in Fig. 2, and the negative charge is detected at the same fluence for both injections.

In this paper, ΔV_{FN}^- and ΔV_{FN}^+ stand, respectively, for the shift of the I - V curves with negative and positive gate bias. From the measurement of these two values, it is possible to calculate the magnitude and the centroid of the oxide charge [12]. ΔV_{mg} stands for the shift of the C - V curves, when the

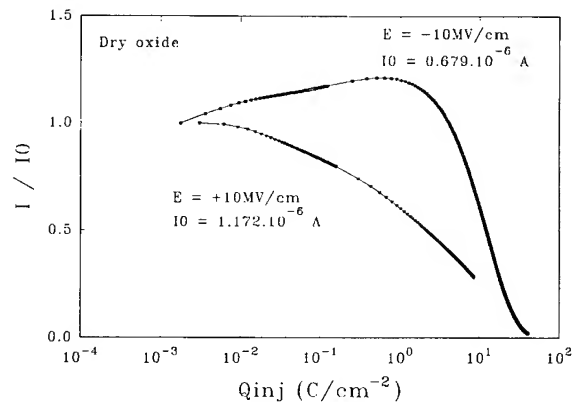


Fig. 1. Typical gate current variation with the charge fluence at constant gate bias level for a dry oxide. E is the average electric field in the oxide which corresponds to a gate bias of $\pm 22 \text{ V}$.

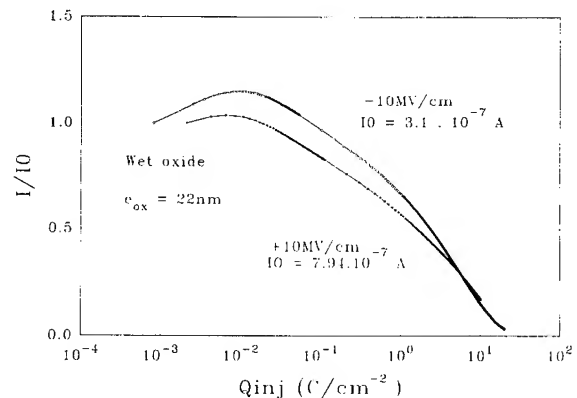


Fig. 2. Typical gate current variation with the charge fluence at constant gate bias level for a wet oxide. E is the average electric field in the oxide which corresponds to a gate bias of $\pm 22 \text{ V}$.

Fermi level is at midgap position; it can give the same information as ΔV_{FN}^+ provided that the surface states above midgap are acceptor while those below midgap are donor, and that both are equal in number. In what now follows, Q represents the magnitude of an oxide charge and \bar{x} its centroid from the substrate. The trapped hole charge, the APC and the negative charge will be marked by indices one, two and three, respectively.

3.1. FN injection from the gate

In the dry and wet oxides, after stress, ΔV_{mg} shows the presence of a positive charge in the oxide

Table 1

Magnitude and centroid of different oxide charges measured after different injected charges for a negative stress ($E = -10 \text{ MV cm}^{-1}$), Q_2 being the magnitude of the APC which can be charged and discharged by a gate bias of $\pm 12 \text{ V}$

	Injected charge density (C cm^{-2})	Positive charge centroid (\AA) ($\bar{x}_1 = \bar{x}_2$)	Negative charge centroid (\AA) (\bar{x}_3)	Trapped holes (C cm^{-2}) (Q_1)	Anomalous positive charge (C cm^{-2}) (Q_2)	Negative charge (C cm^{-2}) (Q_3)
Dry oxide	0.016	25	—	2.44×10^{-7}	3.64×10^{-8}	0
	0.16	22	57	3.62×10^{-7}	1.51×10^{-7}	5.88×10^{-8}
	1.6	23	59	7.15×10^{-7}	1.81×10^{-7}	2.13×10^{-7}
	8	27	60	7.63×10^{-7}	2.4×10^{-7}	4×10^{-7}
Wet oxide	0.016	16	140	1.9×10^{-7}	6.8×10^{-8}	5.7×10^{-8}
	0.16	18	99	3.36×10^{-7}	1.85×10^{-7}	1.66×10^{-7}
	1.6	17	97	4.3×10^{-7}	3.6×10^{-7}	3.8×10^{-7}

bulk. The effects on this charge of a positive or a negative gate bias have been studied (Fig. 3). In doing this, we had to make certain that no further damage occurred, by putting the sample into the FN regime, and therefore, the variation of the gate bias was limited to $-13 \text{ V} < V_{\text{gate}} < +13 \text{ V}$:

(a) A negative gate bias applied after stress had no effect, which made possible the measure of ΔV_{FN}^- at that point.

(b) On the other hand, a positive gate bias applied following stress annihilated this positive charge, and made the measurement of ΔV_{FN}^+ unreliable. When the positive charge was annihilated, ΔV_{mg} showed the presence of negative charges. Now if a negative gate bias was applied, a small part of the positive charge reappeared, which made impossible the measurement of ΔV_{FN}^- at that point. But this showed that the positive charge consisted of trapped holes and APC.

(c) In order to assess the influence of the charge and the discharge on ΔV_{mg} and ΔV_{FN}^- , it is important to know if, and how, they depend on the bias level. It was observed that the amounts of APC that could be charged or discharged increased with the gate bias level and that these varied linearly with $\ln(t)$ [3,7]. The slope was independent of the magnitude of the gate bias and 50% of the APC was charged or discharged in less than 50 s. The trapped holes decay varied with the magnitude of the gate bias, and is faster at 12 V than the APC decay.

It was then possible to determine a procedure to obtain the maximum possible information regarding the oxide charge:

(1) The measurement after stress of ΔV_{mg} and ΔV_{FN}^- gave two relations between the Q_i and \bar{x}_i .

(2) The positive charge was annihilated (in applying 12 V on the gate, this value was chosen to minimize the experimental time). At this stage, only ΔV_{mg} was measured which gave a third relation between Q_3 and \bar{x}_3 .

(3) The APC was recharged by applying -12 V on the gate. Then the measurement of ΔV_{mg} and ΔV_{FN}^- gave two more relations.

One equation is missing to resolve the problem. The best course at this point is to assume that the APC centroid is the same as that of the trapped holes. The results for the dry and wet oxides are given in Table 1.

3.2. FN injection from the substrate

Fig. 4 shows that a positive stress had created a negative charge and an APC. It is seen in Fig. 4 that the positive charge after stress was small and that the application of a negative gate bias increased it, which ruled out the possibility of measuring ΔV_{FN}^- just after stress without changing the charge. This result is understandable as the stress field was positive and therefore discharged the APC that it had created. A negative bias would recharge it. But a part of this charge was discharged

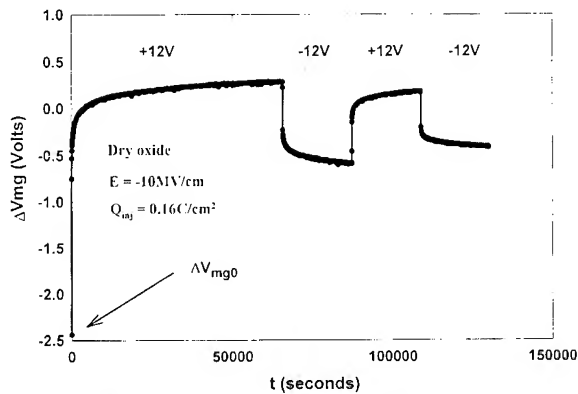


Fig. 3. Effect on the generated oxide charge, by FN injection from the gate, of a positive or negative gate bias (± 12 V). $E = -10$ MV cm $^{-1}$ is the average oxide field applied on the sample during the stress. ΔV_{mgo} is the ΔV_{mg} value just after stress. The oxide is dry.

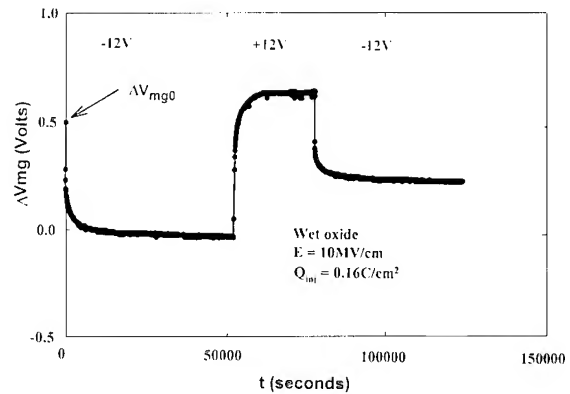


Fig. 4. Effect on the generated oxide charge, by FN injection from the substrate, of a positive or a negative gate bias (± 12 V). $E = +10$ MV cm $^{-1}$ is the average oxide field applied on the sample during the stress. ΔV_{mgo} is the ΔV_{mg} value just after stress. The oxide is wet.

irreversibly by a positive gate bias. We observed, like other researchers [1, 11], that the magnitude of the APC always decays slightly with time when an alternative gate bias is applied. But, here, this phenomenon was much more important than usual during the first decay. For us Q_1 and \bar{x}_1 characterize the positive charge which disappears irreversibly during the first decay and it was assumed that $\bar{x}_1 = \bar{x}_2$. The results for the wet oxide are given in Table 2.

In the dry oxide, the negative charge is zero when the fluence is 0.016 C cm $^{-2}$, so the APC centroid can be extracted from the measurements without any supposition \bar{x}_1 was found to be equal to 76 Å and \bar{x}_2 to 97 Å which is quite surprising for an APC which can be charged and discharged by a small gate bias.

For a fluence of 0.16 C cm $^{-2}$, a negative charge was observed. It was not possible to resolve the equations in Q and \bar{x} by simply supposing, as we have done until now, the existence of one negative and two positive charges. To explain these results satisfactorily, it is necessary to suppose the existence of a third positive charge situated near the anode. Then the surprising value of 97 Å for an APC centroid would be explained as it would be the centroid of one positive charge situated near the gate and one positive charge near the substrate.

The effect of this third positive charge could not be visible in the wet oxide because of the higher negative charge.

Table 2

Magnitude and centroid of different oxide charges measured after different injected charges for a positive stress ($E = +10$ MV cm $^{-1}$), Q_2 being the magnitude of the APC which can be charged and discharged by a gate bias of ± 12 V

	Injected charge density (C cm $^{-2}$)	Positive charge centroid (Å) ($\bar{x}_1 = \bar{x}_2$)	Negative charge centroid (Å) (\bar{x}_3)	Anomalous positive charge (C cm $^{-2}$)		Negative charge (C cm $^{-2}$) (Q_3)
				(Q_1)	(Q_2)	
Wet oxide	0.016	15	144	1.2×10^{-8}	3.25×10^{-8}	4.81×10^{-8}
	0.16	30	101	3.41×10^{-8}	7×10^{-8}	1.9×10^{-7}
	1.6	58	149	5.43×10^{-8}	2.89×10^{-7}	5.27×10^{-7}

4. Conclusion

We have investigated Fowler–Nordheim tunneling injection from the gate or from the substrate in PMOS capacitors in both wet and dry oxides. We have established a new procedure to perform accurately the measurements of the magnitude and of the centroid of the different charges generated during FN injection.

We have demonstrated the asymmetry of the degradation for both injection polarities. Both injections create a positive and a negative charge. When the injection is made from the gate, for both oxides, the created positive charge consists of trapped holes and APC situated near the Si–SiO₂ interface. When the injection is made from the substrate the positive charge, situated near the Si–SiO₂ interface, consists only of APC for both oxides.

Besides for the dry oxide, when the injection is from the substrate, to explain the results satisfactorily, it is necessary to suppose the existence of an additional positive charge near the poly–Si gate.

The magnitude and the centroid of the negative charge do not depend on the injecting electrode but

on the type of oxide. In the wet oxide, its magnitude is twice larger and its centroid further away from the substrate than in the dry oxide.

References

- [1] F.J. Feigl, D.R. Young, D.J. DiMaria, S. Lai and J. Calise, *J. Appl. Phys.* 52 (1981) 5665.
- [2] S.K. Lai and D.R. Young, *J. Appl. Phys.* 52 (1981) 6231.
- [3] M.V. Fischetti, R. Gastaldi, F. Maggioni and A. Modelli, *J. Appl. Phys.* 53 (1982) 3136.
- [4] S.K. Lai, *J. Appl. Phys.* 54 (1983) 2540.
- [5] M.V. Fischetti, *J. Appl. Phys.* 57 (1985) 2860.
- [6] S.T. Chang and S.A. Lyon, *Appl. Phys. Lett.* 48 (1986) 136.
- [7] V. Lakshmana and A.S. Vengurlekar, *J. Phys.* 63 (1988) 4548.
- [8] L.P. Trombetta, F.J. Feigl and R.J. Zeto, *J. Appl. Phys.* 69 (1991) 2512.
- [9] D.A. Buchanan and D.J. DiMaria, *J. Appl. Phys.* 67 (1990) 7439.
- [10] D.A. Buchanan, *Appl. Phys. Lett.* 60 (1992) 216.
- [11] Y. Roh, L. Trombetta and J. Stathis, *Microelectron. Eng.* 22 (1993) 227.
- [12] G. Barbottin and A. Vapaille, *Instabilities in Silicon Devices* (North-Holland, Amsterdam, 1986).



ELSEVIER

Journal of Non-Crystalline Solids 187 (1995) 186–189

JOURNAL OF
NON-CRYSTALLINE SOLIDS

Field mechanism of defect generation at Si–SiO₂ interface under hot electron injection

Igor P. Lisovskii*, Galina P. Romanova, Elena G. Schmidt

Institute of Semiconductor Physics Academy of Sciences. Prospekt Nauki 45, Kiev, 252650, Ukraine

Abstract

Using C – V , photoinjection and SIMS techniques the processes of interfacial defect creation and changes in hydrogen containing complexes due to electron injection and field treatment of MOS structures were compared. It is shown that interfacial defects are formed with the participation of hydrogen whose release is initiated by the action of the field.

1. Introduction

Processes of generation of electrically active defects at the Si–SiO₂ interface are field dependent, which makes it possible to assume that corresponding reactions should involve hot charge carriers. However, our recent results [1] have shown that creation of interfacial defects in MOS structures with the negative charge distributed in the oxide could occur in the absence of injected electron current. Application of a positive voltage to the gate electrode proves to be quite sufficient. The resulting defect concentration reaches almost the same value as in the corresponding experiments with injection. This fact leads us to search for a common defect formation mechanism associated with the direct action of the electric field.

2. Experimental procedure

MOS structures with thermally grown wet oxide ($d = 240$ nm) and semitransparent NiCr gate electrodes were studied. To create the negative charge distributed within the oxide, all samples were illuminated for a short time by a mercury tube. The injection level was kept constant by variation of the gate voltage and amounted to 1×10^{-7} A cm⁻². Then some of the samples were subjected to electron injection (UV-illumination with a constant positive bias, the value of gate voltage U_G varied within 17–343 V range from sample to sample). Other MOS-structures were subjected to field treatment (applying the voltage U_G to the structure in darkness).

High-frequency C – V and photocurrent–voltage characteristics were measured. From the latter, the negative charge captured by traps in the oxide bulk (Q_{ot}) was determined. The surface state density at midgap (N_t) was figured out from the slope of the

* Corresponding author. Tel: +7-44 265 3852. Telefax: +7-44 265 8342. E-mail: mickle@semicond.kiev.ua.

C–V curves, surface states spectra $N_t(U_s)$ were also calculated. The density of the positive charge captured near the Si–SiO₂ interface (Q_{it}) was estimated from the shift in the current–voltage characteristics and the flat band variation, accounting for the charge accumulated in the fast surface states. The depth distribution of the secondary ions (SCI) Si⁺, SiO⁺, SiH⁺ and SiOH⁺ was measured using the SIMS technique. The primary beam consisted of single charge Ar⁺ ions (25 $\mu\text{A cm}^{-2}$, 2 kV). To analyze the results, we normalized the yield values of all the SCI with respect to that of Si⁺ (N).

3. Results

The first step of the electron injection into the oxide of MOS structures resulted in the creation of a negative charge, pretty uniformly distributed over the SiO₂ layer, with its density $0.7\text{--}2.1 \times 10^{12} \text{ cm}^{-2}$. Density of the fast states also increased within the whole Si-gap with respect to the initial structure (Fig. 1, curve 0) up to the value of $N_t^* \approx 2\text{--}5 \times 10^{11} \text{ eV}^{-1} \text{ cm}^{-2}$ at the midgap (Fig. 1, curve 1'). Almost no positive charge was observed to be created in the oxide close to the Si–SiO₂ interface. These results are in agreement with the known data [2, 3].

Subsequent continuous electron injection or field treatment of such MOS systems resulted in the following effects: a positive charge was built up at the Si–SiO₂ interface; the density of the fast surface states significantly increased.

Fig. 1 shows the changes in surface state spectra after prolonged photoinjection (curve 1) or field treatment (curve 2). It is seen that surface state density increases remarkably within the whole gap, and the peak of N_t occurs near the midgap. These changes are almost the same both in the case of injection and field treatment.

Fig. 2 demonstrates the kinetic curves $Q_{it}(t)$ and $\Delta N_t(t)$ (where the value of $\Delta N_t(t)$ was determined at the midgap as $N_t - N_t^*$) for the samples subjected to electron injection or to field treatment (the gate voltage was the same ($U_G = 24 \text{ V}$) for both samples). It is seen that the efficiency of N_t and Q_{it} creation was approximately the same in the case of both electron injection and field treatment.

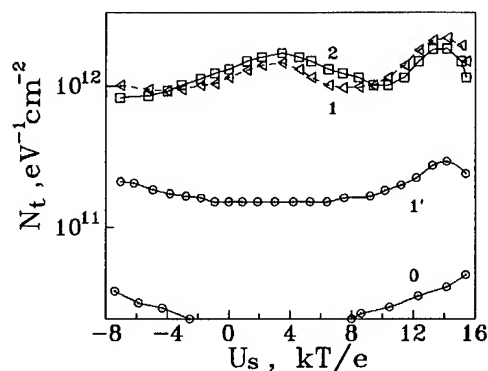


Fig. 1. Spectra of fast surface states for initial (0), preliminary UV-irradiated (1'), subjected to electron injection (1) and field treated (2) MOS structures. Lines are drawn as guides for the eye.

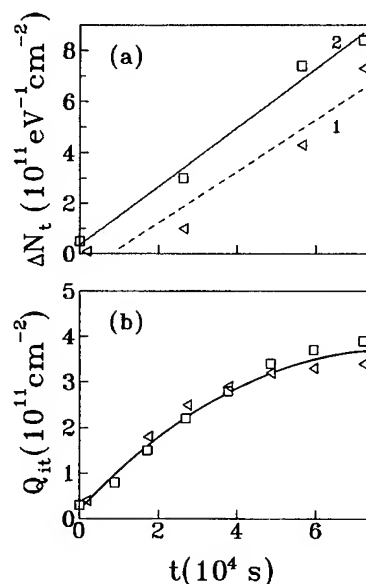


Fig. 2. Kinetic curves of ΔN_t (a) and Q_{it} (b) for the case of electron injection (triangles) or field treatment (squares). The structures were initially UV illuminated at 296 K ($\Delta V_{FB} = 16 \text{ V}$). Lines are drawn as guides for the eye.

The SiOH⁺ profiles are shown in Fig. 3. The main features of these results may be described as follows. In the initial structures, the distribution of SiOH complexes (curve 0) is characterized by a curve rising to the outer interface, with its shape

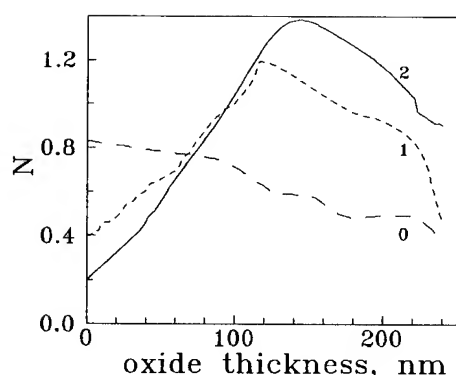


Fig. 3. The profiles for $\text{SiOH}^+/\text{Si}^+$. The curves 0, 1 and 2 correspond to the initial sample, the structure subjected to electron injection and the sample subjected to field treatment ($U_G = 24$ V), respectively.

being in qualitative agreement with the known IR-spectroscopy data [4]. For the structures, subjected to electron injection or to field treatment (curves 1 and 2, respectively) the distribution changes drastically: the yield of SiOH^+ substantially decreases near the outer interface, while an increase is observed near the internal interface. As a result, in these structures the distribution of $\text{SiOH}^+/\text{Si}^+$ is described by a non-monotonic curve.

Field treatment of the initial (non-illuminated) structures or those illuminated at $U_G = 0$ (with a small negative oxide charge in SiO_2) did not cause any change in both the charge and surface state density. No changes in the parameters N_i and Q_{it} were observed after electron injection or after field treatment of MOS systems at 80 K.

4. Discussion

The processes responsible for the creation of positively charged defects near the Si– SiO_2 interface (so-called ‘anomalous positive charge’ – APC) and those underlying generation of the fast surface states (FSS), which are initiated by various kinds of electron injection have been studied rather thoroughly by now. It was also pointed out that the defect mentioned emerged only after a negative charge had been built into the oxide of MOS structures [3, 5, 6]. In our case, formation of APC and

FSS as well as redistribution of hydrogen-containing components may take place even in the absence of the electron injection into the oxide but as a result of the field treatment itself. However, even in this case the effects considered occurred only in those structures where a negative charge had been created by preliminary UV-illumination.

The experiments have also shown that the efficiency of N_i and Q_{it} creation was approximately the same in the case of both electron injection and field treatment (when injection current is absent) depending only on the U_G value. Moreover, in both cases the same redistribution of SiOH complexes within the oxide took place. Thus, one can conclude that processes observed are field induced ones.

The influence of the negative charge in the presence of a positive bias on the distribution of the electric field strength E within the oxide have been studied earlier [5, 7]. It was shown that the magnitude of the electric field strength depends on the oxide thickness and its maximum is localized at the metal– SiO_2 interface. Hence, the outer interface of the oxide is the region where the probability of field stimulated processes is at its maximum.

Data on redistribution of SiOH complexes obtained from the SIMS measurements are of special interest. Their distribution changes greatly and most significantly: hydrogen-containing complexes are shifted from the outer interface towards the inner one (Fig. 3, curves 1, 2). It is obvious that such a redistribution may result only from SiOH decomposition in the outer part of oxide, hydrogen migration to the Si– SiO_2 interface and its interaction with the SiO_2 lattice there.

The results obtained can be interpreted in the framework of the following consideration. Electron injection into the oxide of MOS structures (first step of UV illumination) results in a creation of the negative oxide charge. If its density is high enough, the following application of positive bias (under illumination or in darkness) leads to the appearance of a region with high electric strength in the oxide layer near the gate electrode. Here the field decomposition of SiOH complexes takes place accompanied by proton release and its drift to the Si– SiO_2 interface. Reaction of protons with Si–O–Si bonds results in a generation of interfacial

defects (positively charged traps and fast surface states).

The threshold value of the electric field strength, which is necessary to provide the reaction of proton release was estimated to amount to $\approx 1.3 \text{ MV cm}^{-1}$ [7]. Therefore, this value can be regarded as the limit – at lower fields SiOH decomposition becomes impossible. It is interesting that the estimated threshold value for electric field strength during the defect-creation process induced by hot electron injection has given approximately the same value of $E \sim 1.5 \text{ MV cm}^{-1}$ [8, 9]. Such a correlation may suggest additional evidence for the model proposed in the present work.

At the same time, the treatment of initial (nonilluminated) MOS structures with bias providing a field strength exceeding $E \approx 1.3 \text{ MV cm}^{-1}$, did not give rise to generation of defects. Thus one may suppose that application of high fields is an essential rather than a sufficient condition for the defect-creation reaction. Most likely, preliminary injection of electrons was necessary not only for oxide charging but also for some structural changes in the oxide network; for example, such changes may lead to the formation of quasidefect sites which later can be easily transformed into stable defects under certain conditions. This assumption may apply both to metal–SiO₂ (creation of weakened bonds in SiO–H) and to Si–SiO₂ interfaces. The latter case occurs more frequently as was already discussed in our earlier papers [3, 10]. In particular, in the model of multistage reaction of surface state creation [10], along with participation of hydrogen, the process of interface Si–SiO₂ activation by hot electrons was introduced. Active sites created due to such processes interact with hydrogen and give rise to stable electrically active centers.

5. Conclusions

The processes of interfacial defect formation in MOS structures under electron injection are very similar to those under field treatment if the negative oxide charge was previously introduced into the oxide. In both cases, a redistribution of SiOH complexes within the SiO₂ layer also takes place which is an evidence for hydrogen migration towards the Si–SiO₂ interface and its interaction there with Si–O bonds. Interfacial defect generation is a multistage process. The stage of hydrogen release is field assisted. Electron injection results in an oxide region with high electric field strength and, very likely, leads to activation of the SiO₂–Si interface.

References

- [1] V.G. Litovchenko and I.P. Lisovskii, *J. Phys.* 49 (1988) 137.
- [2] K. Saminadayar and J.C. Pfister, *Phys. Status Solidi (A)* 36 (1976) 679.
- [3] I.P. Lisovskii, V.G. Litovchenko and R.O. Litvinov, *Phys. Status Solidi (A)* 53 (1979) 253.
- [4] K.H. Beckmann and N.J. Harrick, *J. Electrochem. Soc.* 118 (1971) 614.
- [5] M.V. Fischetti, *J. Appl. Phys.* 57 (1985) 2860.
- [6] Z.A. Weinberg, D.R. Young, D.J. DiMaria and G.W. Rubloff, *J. Appl. Phys.* 50 (1979) 5757.
- [7] I.P. Lisovskii, V.G. Litovchenko, G.P. Romanova, P.I. Didenko and E.G. Schmidt, *Phys. Status Solidi (A)* 142 (1994) 107.
- [8] D.J. DiMaria, *Appl. Phys. Lett.* 51 (1987) 655.
- [9] M.M. Heyns, D. Krishna Rao and R.F. De Keersmaecker, *Appl. Surf. Sci.* 39 (1989) 327.
- [10] V.G. Litovchenko, I.P. Lisovskii and R.O. Litvinov, *Appl. Surf. Sci.* 6 (1980) 15.



ELSEVIER

Journal of Non-Crystalline Solids 187 (1995) 190–194

JOURNAL OF
NON-CRYSTALLINE SOLIDS

Comparison of rapid ramp voltage and tunnelling injection stress experiments for the characterization of thin MOS gate oxides

O. Brière^{a,*}, P. Cottin^b, A. Straboni^c

^a *Matra MHS S.A., La Chantrerie, Route de Gachet, CP 3008, 44087 Nantes cedex 03, France*

^b *CNET, France Telecom, Chemin du Vieux Chêne, 38243 Meylan cedex, France*

^c *Laboratoire LPM, Université de Poitiers, 40 Avenue du Recteur Pineau, 86022 Poitiers cedex, France*

Abstract

Ramp voltage, V_{bd} , and current injection stress, Q_{bd} , experiments were used to compare CMOS capacitors samples. The respective advantages and drawbacks of V_{bd} and Q_{bd} measurements are shown using samples of different quality levels. A Q_{bd} method is presented, combining a very short current ramping followed by a constant current stress which presents the advantages of good sensitivity to determine as-born and early failures as well as to describe the intrinsic distribution.

1. Introduction

As the physical dimensions of CMOS devices are reduced, the gate dielectric thickness decreases leading to an increase of the oxide field. The Fowler–Nordheim current, due to the tunnelling electrons through the barrier, increases exponentially with the oxide field. Degradation due to this mechanism may become preponderant for the next CMOS generations using ultra thin films.

Furthermore, Fowler–Nordheim injection stress experiments are increasingly used to evaluate the reliability of MOS structures in both research laboratories and in industry. For a long time, ramp-voltage experiments (V_{bd}) [1–4] were used to measure breakdown distributions from low field to intrinsic 10 MV/cm fields. Tunnelling experiments (Q_{bd}) [4–7] are now more widely used

because they reveal a better sensitivity to qualify MOS structures. Different methods have been compared using constant current stress (CCS) or exponential ramp current stress (ERCS). However, no direct comparison between V_{bd} and Q_{bd} measurements on the same structures is available in the literature. The purpose of this work is to perform both stress experiments on adjacent structures, and critically compare the respective advantages and drawbacks of V_{bd} and Q_{bd} measurements.

2. Experimental procedure

The MOS capacitors used in this work were prepared on 100 mm differently doped N- or P-well silicon substrates with $\langle 100 \rangle$ orientation. After a two-level flow-chart, including LOCOS and gate definition, or after a complete CMOS dual-gate technology, 8–12 nm gate oxides were grown in a conventional furnace in dry oxygen at

* Corresponding author. Present address: CNET DFC/TMS, France Telecom, Chemin du Vieux Chêne, 38243 Meylan cedex, France. Tel: +33 76 76 44 01. Telefax: +33 76 76 42 99. E-mail: briere@cns.cnet.fr.

atmospheric pressure and 925°C. The thickness of the dielectric films was measured by ellipsometry and cross checked by high-frequency capacitance–voltage measurement.

All measurements were carried out using a Keithley automatic prober. In order to reduce the measurement time, we have designed a special mask where all MOS capacitors are grouped in the same die localized in an N or a P well. Then, this arrangement allows us to test four capacitors in parallel. All the structures are biased (+ or –) by independent sources with the common being connected to the well (N or P). The V_{bd} and current stress experiments are monitored by a VAX 6410 and the RS1 / ZOSR software was used for statistical exploitation.

The number of capacitors tested was in a range from more than 100 to several hundreds for each sample. One sample can be anywhere from one to 24 wafers.

In our work, we have used both types of breakdown measurement to test and compare each set of samples. Half of the capacitors in a die were tested using rapid-ramp voltage and the others using current injection stress. We used the Weibull and the histogram representations to draw the statistical distribution of each sample.

3. Results and discussion

3.1. Methodology

The rapid ramp voltage, V_{bd} , measurement consists in applying a voltage ramp and measuring the breakdown voltage which is defined as the value at which the current density exceeds 0.01 A/cm². Capacitors are in accumulation. We have chosen 20 MV/cm s for the slope of the ramp, in order to reduce measurement time, while retaining a good sensitivity of the V_{bd} measurement.

Our Q_{bd} measurement consists of the injection of a constant current density, with a previous current ramping from the thousandth of this nominal density to the nominal density in 11 (Fig. 1). The time-dependent dielectric breakdown is defined as the time when the applied voltage decreases more

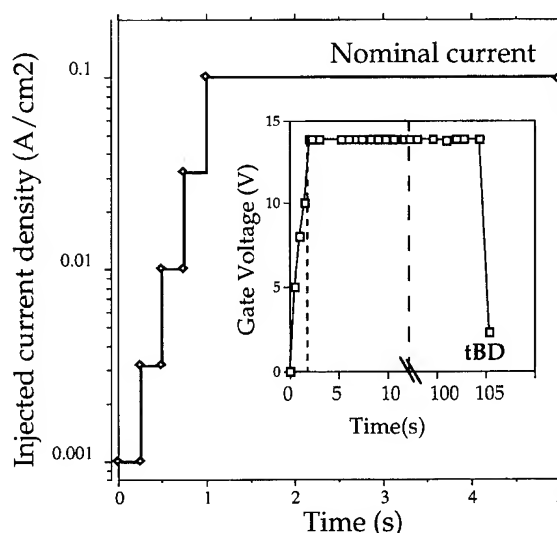


Fig. 1. Q_{bd} measurement for 8 nm capacitors.

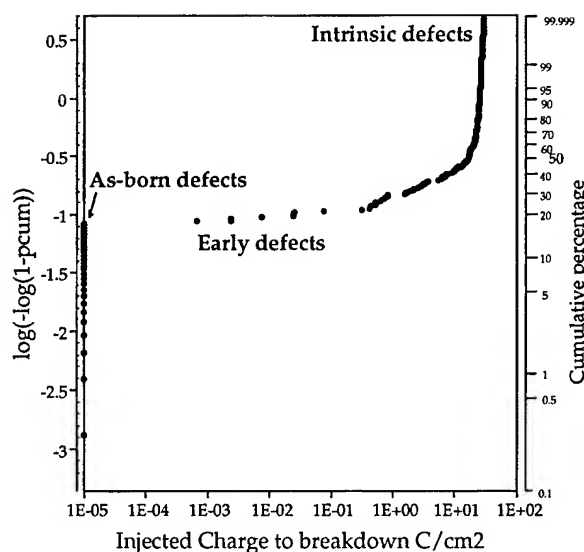


Fig. 2. Weibull representation of Q_{bd} .

than 20% between two steps of measurement. Capacitors are again in accumulation.

Fig. 2 shows the cumulative failure as a function of Q_{bd} measured on N⁺MOS structures on P-well substrates, with a 12 nm oxide, following injection from the gate at 200 mA/cm². The area of the capacitors tested is 0.006 cm².

Three populations can be clearly distinguished.

(1) As-born defects corresponding to the capacitors which were not able to reach the Fowler–Nordheim regime ($Q_{bd} = 1 \times 10^{-5} \text{ C/cm}^2$).

(2) Early failures corresponding to breakdown that occurs at low fluences, failing during the ramping current ($Q_{bd} < 0.1 \text{ C/cm}^2$).

(3) Near-intrinsic or intrinsic failures corresponding to breakdown during constant current stress, with fluences ranging from 0.1 up to 20 C/cm^2 for the oxide thickness used here.

Note that this intrinsic distribution is very sharp with a good resolution; this is due to the constant current stress. For our Q_{bd} method the charge resolution is determined by the time step which is short (500 ms) and constant. On the other hand, for the ERCS method the charge resolution is lower, because the current is quite high in the last steps.

These results show that our Q_{bd} method that combines a very short current ramping followed by a constant current stress, presents the advantages of a good sensitivity, to determine as-born and early failures as well as describe the intrinsic distribution.

Fig. 3 shows the charge corresponding to 50% of breakdown, for different gate oxide thicknesses, as a function of the injected current density.

We observe that the $Q_{bd50\%}$ decreases slowly with injected current density. However, we chose

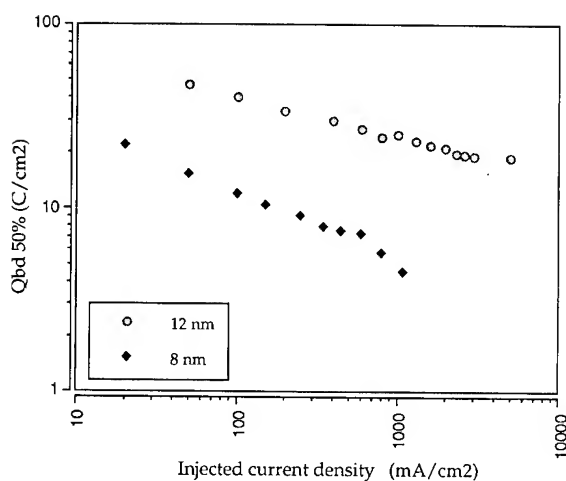


Fig. 3. Intrinsic charge to breakdown as a function of the injected current density.

our nominal current densities in the relatively low current regions ($j = 200 \text{ mA/cm}^2$ for 120 Å , $j = 100 \text{ mA/cm}^2$ for 80 Å) in order to keep a good sensitivity. As a matter of fact, if the used current density is too high, the number of breakdown events during the ramping stage becomes higher, with a loss of sensitivity.

3.2. Comparison between V_{bd} and Q_{bd} measurements in the case of 'intrinsic' samples

Fig. 4 shows the Weibull representations, corresponding to two slightly different samples, for both measurements. The samples are different in the sense that the active area was etched and cleaned before the gate oxide growth. The area of the capacitors tested is 0.006 cm^2 ; the oxide thickness is 12 nm .

As evidenced, by V_{bd} , both samples show excellent behaviour, there are no as-born and early failures, so the V_{bd} statistical distributions are very close to 10 MV/cm . Hence, using such a method, it is not possible to differentiate between the samples.

On the other hand, for the same structures, the Q_{bd} experiment shows marked contrast between the samples; it magnifies the differences. This illustrates a well-known advantage of such current stress experiments, which highlights the weaknesses in the MOS structures, in the bulk oxide or at the interfaces. In the case presented here, the defects are localized in the bird's-beak region. This region has been denuded by a strong etch prior to gate oxidation. The oxide has grown in a non-planar region. This kind of defects does not affect the breakdown voltage because oxide thickness remains uniform, but alters intrinsic part of the Q_{bd} distribution. This is certainly due to the field enhanced injection in the regions with rough interfaces.

3.3. Comparison between V_{bd} and Q_{bd} measurements in the case of 'extrinsic' samples

The histogram representations (Fig. 5) show for very poor quality MOS capacitors, the statistic of breakdown for both measurements. The area of the capacitors tested is 0.006 cm^2 ; the oxide thickness is 12 nm .

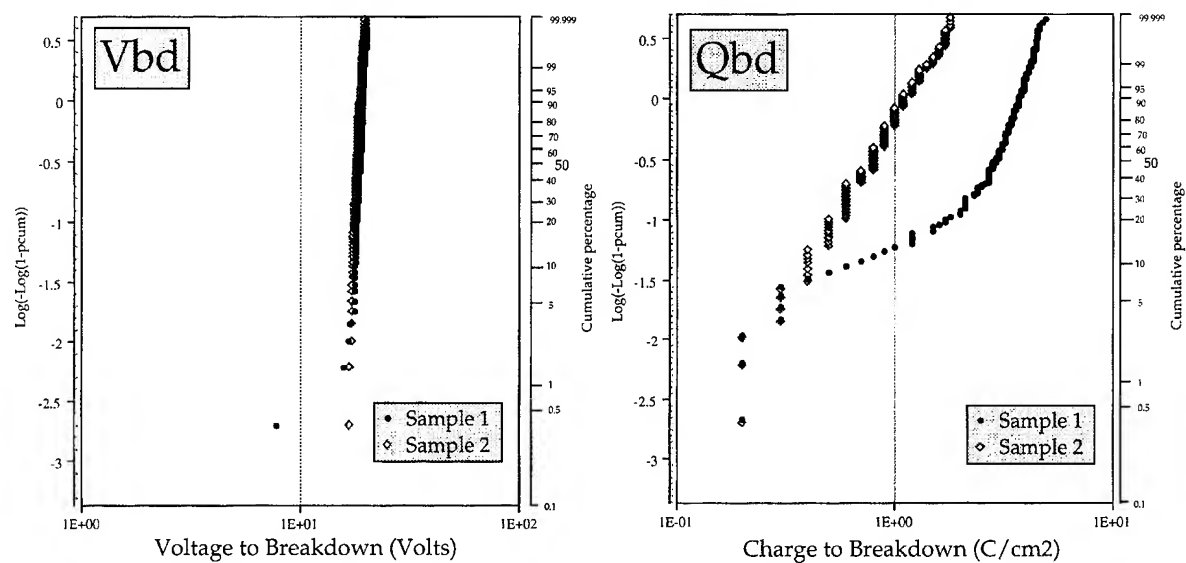


Fig. 4. Comparison between both measurements, in the case of 'intrinsic' samples.

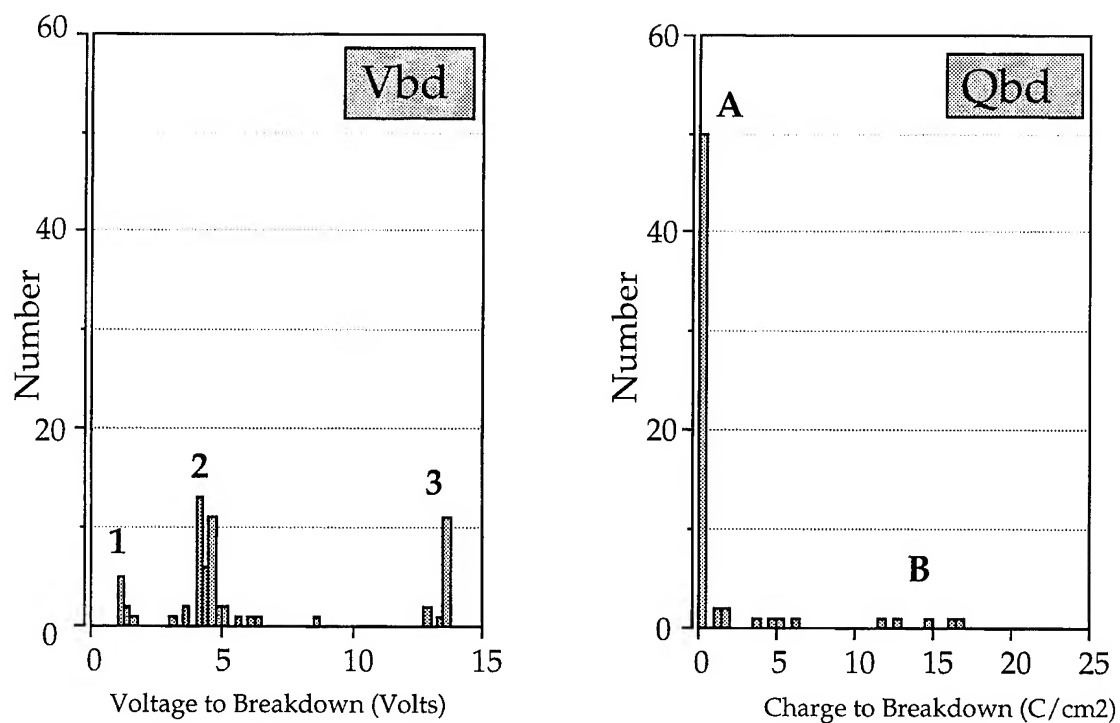


Fig. 5. Comparison between both measurements, in the case of 'extrinsic' samples.

In this case, we observe a large population of extrinsic defects. We can clearly distinguish three groups of failures in the V_{bd} histogram: Group 1 corresponds to the as-born defects (near zero breakdown voltage), Group 2 to the early failures (breakdown occurs for $E_{bd} < 4$ MV/cm) and the third to intrinsic breakdown ($E_{bd} \approx 10$ MV/cm).

Examination of Fig. 5 (right), the results of Q_{bd} experiments provide very little information. Most of the capacitors (Group A) have broken down at very low fluences ($\approx 70\%$ at $Q_{inj} < 0.1$ C/cm²). We remark that this percentage corresponds exactly to the sum of the Groups 1 and 2 in the V_{bd} histogram.

In such a situation, where devices are of poor quality, the current stress experiment is too severe to distinguish as-born and early defects. From this result, we can also conclude that all immediate failures in Q_{bd} experiment correspond to the total events which occur before 7 MV/cm in the V_{bd} one.

In the case for poor-quality samples, the number of events in the intrinsic region (Group B) is too low to give valuable information. The magnifying effect of the Q_{bd} measurement, in this case, causes a loss of sensitivity.

4. Conclusions

We have shown that the percentage of as-born defects measured by current stress corresponds mainly to the percentage of failure events in the field range from zero and 7 MV/cm as measured by V_{bd} . Slight differences between good quality oxides

cannot be highlighted by V_{bd} experiment, especially in the field region around 10 MV/cm (intrinsic breakdown).

The only advantage of V_{bd} experiment has been found for poor-quality samples. V_{bd} experiment should then preferably be used, for newer unstabilized technologies.

On the other hand, current stress experiments should preferably be used to evaluate the time-dependent breakdown of stabilized technologies. In this case, we have shown that our Q_{bd} method combining a very short current ramping followed by a constant current stress presents the advantages of a good sensitivity, together to determinate as-born and early fails but also to describe the intrinsic distribution.

The authors wish to thank MATRA MHS Nantes France for their financial support. They also thank Dr R.A.B. Devine for helpful discussions and his critical reading of the manuscript.

References

- [1] J. Lee, I. Chen and C. Hu, IEEE Trans. Electron. Dev. 35 (1988) 2268.
- [2] P. Solomon, J. Vac. Sci. Technol. 14 (1977) 1122.
- [3] H. Abe, F. Kiyosumi, K. Yosshioka and M. Ino, IEDM Technol. Dig. (1985) 372.
- [4] J.F. Verwey and D.R. Wolters, INFOS (1985) 125.
- [5] E. Harari, J. Appl. Phys. 49 (1978) 2478.
- [6] J.J. Van der Schoot and D.R. Wolters, INFOS (1983) 270.
- [7] P.P. Apte, T. Kubota and K.C. Saraswat, J. Electrochem. Soc. 140 (1993)



ELSEVIER

Journal of Non-Crystalline Solids 187 (1995) 195–198

JOURNAL OF
NON-CRYSTALLINE SOLIDS

Leakage current reduction due to hot carrier effects in n-channel polycrystalline silicon thin film transistors

G. Tallarida^a, A. Pecora^a, G. Fortunato^{a,*}, F. Plais^b, P. Legagneux^b, T. Kretz^b, D. Pribat^b

^a Istituto di Elettronica dello Stato Solido, Consiglio Nazionale delle Ricerche, via Cineto Romano, 00156 Rome, Italy

^b Thomson-CSF, LCR, 91404 Orsay cédex, France

Abstract

As is well known, the application of gate-voltage stresses in conjunction with high source-drain voltages, V_{ds} , modifies the electrical characteristics of polycrystalline silicon thin film transistors. In particular negative gate-voltage stresses on n-channel devices usually reduce both the leakage current and the transconductance. In this paper a complete analysis of hot carrier effects induced by different gate-bias stresses at high V_{ds} is presented and discussed in terms of trap and interface state creation. It is shown that in certain stress regimes the leakage current can be reduced without the accompanying transconductance degradation.

1. Introduction

Hot carriers phenomena are likely to occur in polycrystalline silicon (polysilicon) thin film transistors (TFTs), employed in driving circuits where supply voltages can be relatively high. It is therefore important to investigate the hot carrier effects in order to determine the long-term reliability of polysilicon TFTs. Indeed, the application of prolonged bias stress in n-channel TFTs, operated at high V_{ds} and different V_g , can greatly affect the transconductance G_m as well as the off-current [1]. It has already been shown that these effects can be related to hot hole injection in the dielectric, due to the presence of a high electric field in the region

near the drain junction. On the other hand it is well known that hot holes injection in c-Si n-channel MOSFETs causes the creation of trap centres in the oxide and interface states. [2].

In this paper we report an interesting effect induced by prolonged negative bias stress. In particular the leakage current can be reduced by up to two orders of magnitude, without any appreciable change of the 'on' characteristics. Furthermore, a complete analysis of the hot carrier effects induced by different gate-bias stresses at high V_{ds} is presented.

2. Device fabrication

The polysilicon TFTs used in the experiments have been fabricated according to a classical procedure, using a four mask sequence (active layer,

* Corresponding author. Tel: +39-6 415 221. Telefax: +39-6 4152 2220. E-mail: guglielmo@iess.rm.cnr.it.

gate conductor, contact opening, aluminium source and drain metallisation). The doping of the source and drain regions was performed by self-aligned ion implantation of phosphorous.

Special attention has been devoted to obtaining a high quality active layer and gate oxide. For this purpose, the amorphous precursor was deposited by LPCVD in an ultraclean reactor (ultrahigh vacuum reactor atmosphere) equipped with point-of-use gas purifiers [3]. This has allowed us to control impurity incorporation into the deposited films to around ppm levels (C and O concentrations as determined by SIMS are below 10^{17} cm^{-3}), particularly when disilane (Si_2H_6) is used as the source gas at a deposition pressure of about 1 Torr [3]. Moreover, the use of Si_2H_6 has also allowed us to obtain very large grain sizes (up to $3 \mu\text{m}$ for film thickness below 100 nm) after solid phase crystallisation at typically 580°C [4].

The gate dielectric (SiO_2) was deposited by distributed electron cyclotron resonance plasma enhanced chemical vapour deposition (DECR-PECVD) at floating temperature and without biasing the substrate. In such conditions, we were able to obtain resistivity values above $10^{16} \Omega \text{ cm}$, critical fields around 5 MV cm^{-1} and an interface trap density at mid-gap of $3 \times 10^{10} \text{ cm}^{-2} \text{ eV}^{-1}$ on (100) Si substrates [5].

With the above combination of clean polysilicon and DECR oxide, we obtain field effect mobility values of $70 \text{ cm}^2 \text{ V}^{-1} \text{ s}^{-1}$ without a post-hydrogenation treatment and with a maximum processing temperature of 580°C [6]. The leakage current of the as-fabricated non-hydrogenated devices is still high, but as will be shown below, it can be drastically reduced by simple electrical stresses, without appreciable alteration of the on-current.

3. Results and discussion

In Fig. 1 the transfer characteristics, I_d – V_g , are shown for different V_{ds} , before and after bias stressing for 12 h at $V_g = -15 \text{ V}$ and $V_{ds} = 20 \text{ V}$. As can be seen the main effect is a considerable reduction in the off-current, more evident at $V_{ds} = 10 \text{ V}$. The off-current reduction is better evidenced in Fig. 2 where the drain current I_{ds} is plotted as

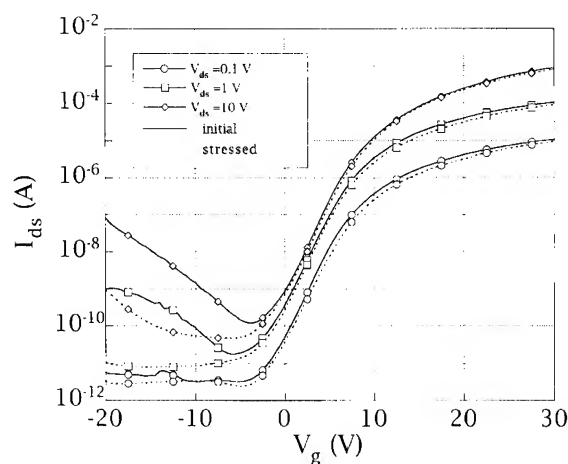


Fig. 1. Drain current I_{ds} as a function of gate voltage V_g , for different source-drain voltages V_{ds} ($V_{ds} = 0.1 \text{ V}$ (\circ); $V_{ds} = 1 \text{ V}$ (\square); $V_{ds} = 10 \text{ V}$ (\diamond)) measured before (continuous line) and after (dashed line) bias stressing for 12 h at $V_{ds} = 20 \text{ V}$ and $V_g = -15 \text{ V}$. The channel width is $W = 20 \mu\text{m}$, the channel length is $L = 5 \mu\text{m}$. Lines are drawn as a guide for the eye.

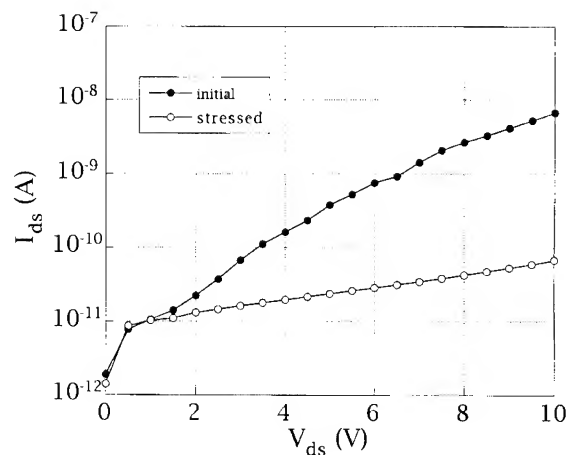


Fig. 2. Drain current I_{ds} versus source-drain voltage V_{ds} , measured at fixed gate voltage $V_g = 12 \text{ V}$ (off-state) before (\bullet) and after (\circ) bias stressing for 12 h at $V_g = -15 \text{ V}$ and $V_{ds} = 20 \text{ V}$. Lines are drawn as a guide for the eye.

a function of V_{ds} for fixed $V_g = -12 \text{ V}$ (off-state). As can be observed a reduction of about two orders of magnitude can be achieved. As is well known, the off-current in polysilicon TFTs at high V_{ds} depends

on field enhanced generation mechanisms. Therefore the off-current reduction has to be related to a reduction in the local electric field. This may be due to the presence of positive charges at the oxide/semiconductor interface that partially screen the negative charges on the gate electrode. The build-up of positive charges in the gate oxide can arise from hot-hole injection in the region near the drain where, due to the presence of high electric fields, carriers may gain enough energy to be injected into the oxide. In some respects, the presence of positive injected charge produces the same situation as the one occurring in field induced drain (FID) structures, which are used in order to reduce the leakage current [8].

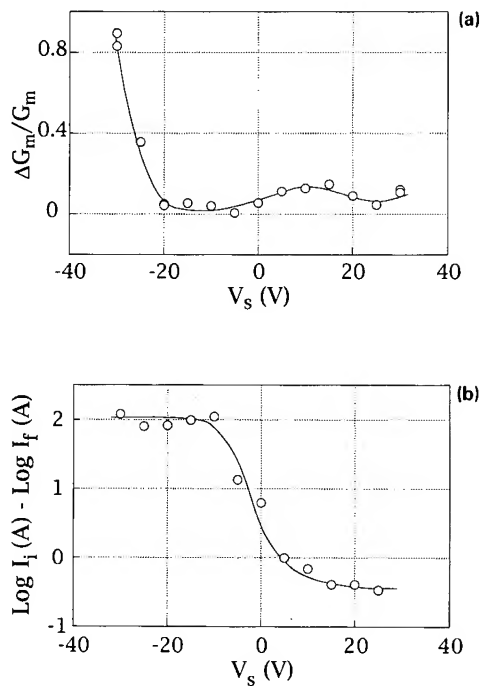


Fig. 3 (a) Relative transconductance variation, $\Delta G_m/G_m$, versus stressing gate bias V_s , after stressing for 12 h at fixed source-drain voltage $V_{ds} = 20$ V (each point is relative to a different sample). Lines are drawn as a guide for the eye. (b) Variation of $(\log I_i - \log I_f)$ versus stressing gate bias V_s , where I_i and I_f are the off-current measured at $V_g = -12$ V and $V_{ds} = 10$ V, before and after bias stressing for 12 h at $V_{ds} = 20$ V, respectively (each point is relative to a different sample).

In Figs. 3(a) and (b) the relative variation of the transconductance $\Delta G_m/G_m$ (where $\Delta G_m = G_m - G_r$, with G_m and G_r the before and after stress transconductance, respectively) and the variation of the leakage current $\Delta I_{off} = (\log I_i - \log I_f)$ (where I_i and I_f are the off-currents measured at $V_g = -12$ V and $V_{ds} = 10$ V before and after stress respectively), after stressing for 12 h at $V_{ds} = 20$ V, are shown as a function of stressing gate bias V_s . From the data in Fig. 3(a) three regions can be distinguished.

(1) $V_s > 0$ V. In this case the transconductance variations resemble those observed in n-channel c-Si MOSFETs. The degradation increases with V_s with a maximum at $V_s = V_{ds}/2$ and can be related to the generation of acceptor-like interface states [9]. Furthermore, as V_s increases in this region, the off-current increases too, due to electron injection near the drain junction. A negative interface charge, indeed, increases the local electric field, leading to an increase of the off-current.

(2) $-20 \text{ V} < V_s < 0$ V. In this region the off-current is significantly reduced due to hot-hole injection, as already discussed. This off-current reduction is accompanied by only a very small G_m degradation. This suggests that hot-hole injection mainly causes, in this bias regime, the formation of oxide hole traps that are charged positively during the bias stress [7]. It is important to note that for $-20 \text{ V} < V_s < -10$ V the off-current after stress can be reduced by up to two orders of magnitude without any appreciable degradation in G_m ($< 5\%$).

(3) $V_s < -20$ V. At these stresses, V_s , a dramatic degradation in G_m occurs, along with off-current reduction. The onset of G_m degradation coincides with the increase in the gate leakage current, as shown in Fig. 4, where the gate leakage current is measured as a function of V_g for fixed $V_{ds} = 20$ V. The gate leakage current is likely to be due to electrons injected by the Fowler–Nordheim mechanism from the polysilicon gate into the oxide. Therefore the transconductance degradation could be explained in terms of interface state generation caused by electron–hole recombination at the insulator/semiconductor interface, as proposed by Lai [10]. In particular we suggest that Si–O strained or weak bonds at the insulator/semiconductor

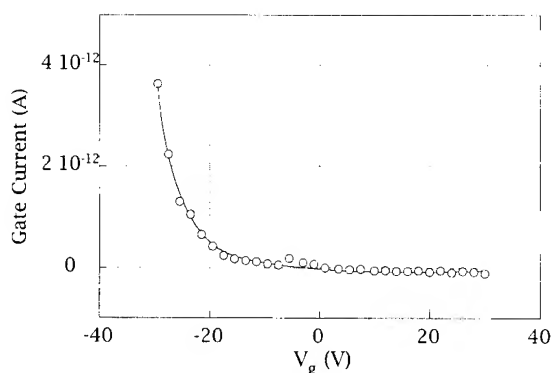


Fig. 4. Gate leakage current as a function of gate voltage V_g , measured at fixed $V_{ds} = 20$ V. Lines are drawn as a guide for the eye.

interface can be broken by the energy released by the electron-hole recombination process. The oxygen atom may move to a lower strain position. As a consequence, a neutral oxide trap, that can be positively charged during the negative bias stress, and a singly occupied silicon dangling bond, acting as an acceptor-like state, are formed at the insulator/semiconductor interface.

4. Conclusions

In this work we have shown that hot-hole injection in polysilicon TFTs produces two effects: off-current reduction and transconductance degradation, with the two effects not necessarily occurring concomitantly. Off-current reduction has to be related to the formation of oxide traps that are charged positively, while the G_m degradation is thought to be due to the formation of oxide traps and acceptor-like interface states. The formation of interface states strongly depends on the simultaneous presence at the interface of holes and electrons. The latter may reach the interface after injection

from the polysilicon gate, as suggested by the increase in the gate leakage current. On the other hand it is worth pointing out that, in the stressing gate voltage range between $-20 \text{ V} < V_g < -10 \text{ V}$, it is possible to induce a large reduction in the off-current, without any appreciable degradation in transconductance, since in this bias regime the injection mainly causes the formation of oxide interface traps that are charged positively during the stress. Due to the marginal transconductance reduction, this effect could be effectively used in order to reduce the leakage current of these devices and make them attractive as pixel switches in active matrix liquid displays.

References

- [1] G. Fortunato, A. Pecora, G. Tallarida, L. Mariucci, C. Reita and P. Migliorato, *IEEE Trans. Electron Dev.* 41(1994) p. 340.
- [2] K.R. Hofmann, C. Werner, W. Weber and G. Dorda, *IEEE Trans. Electron Dev.* ED-32 (1985) 691.
- [3] D. Pribat, F. Plais, P. Legagneux, T. Kretz, R. Stroth, O. Huet, C. Walaine and M. Magis, *Rev. Techn. Thomson-CSF* 26 (1994) 73.
- [4] T. Kretz, R. Stroth, P. Legagneux, O. Huet, M. Magis and D. Pribat, in: *Polycrystalline Semiconductor III – Physics and Technology, Solid State Phenomena*, Vol. 37&36, ed. H.P. Strunk, J.H. Werner, B. Fortin and O. Bannaud (Scitec, Switzerland, 1994) p. 311.
- [5] N. Jiang, M.C. Huong, B. Agius, T. Kretz, F. Plais, D. Pribat, T. Carriere and M. Puech, *Jpn. J. Appl. Phys.* 31 (1992) L1404.
- [6] F. Plais, P. Legagneux, T. Kretz, R. Stroth, O. Huet and D. Pribat, in: *Flat Panel Display Materials*, ed. J.J. Batey, P. Bocko, A. Chiang and P. Holloway, *Mater. Res. Soc. Proc.*, Vol. 345, San Francisco, CA (1994), in press.
- [7] W. Weber, *IEEE Trans. Electron Dev.* 35 (1988) 1476.
- [8] K. Tanaka, K. Nakazawa, S. Suyama and K. Kato, in: *Ext. Abstract of 22nd Conf. on Solid State Devices and Materials*, Sendai (1990) pp. 1011–1014.
- [9] A. Schwerin, W. Hansch and W. Weber, *IEEE Trans. Electron Dev.* 34 (1987) 2493.
- [10] S.K. Lai, *Appl. Phys. Lett.* 39 (1981) 58.



ELSEVIER

Journal of Non-Crystalline Solids 187 (1995) 199–205

JOURNAL OF
NON-CRYSTALLINE SOLIDS

Section 7. Si/SiO₂ interface, characterization and electrical properties

Enhanced MOS 1/f noise due to near-interfacial oxygen deficiency

D.M. Fleetwood^{a,*}, W.L. Warren^a, M.R. Shaneyfelt^a, R.A.B. Devine^b, John H. Scofield^c

^a Sandia National Laboratories, Albuquerque, NM 87185-1083, USA

^b France Telecom/CNET, BP 98, 38243 Meylan, France

^c Physics Department, Oberlin College, Oberlin, OH 44074, USA

Abstract

The 1/f noise and radiation response of MOS transistors have been compared. A strong correlation is found between the pre- and post-irradiation noise of the transistors and their threshold-voltage shifts due to radiation-induced oxide-trap charge. It is inferred that the noise is caused by a subset of the oxide traps, which is referred to as 'border traps'. These defects are near-interfacial oxide traps which can communicate with the Si on the timescales of the measurements, and have been mistaken for interface traps in some previous work on 1/f noise and/or radiation effects on MOS devices. Comparisons of electron-paramagnetic-resonance and radiation-effects studies offer compelling evidence that radiation-induced oxide-trap charge is associated with oxygen-deficient centers (oxygen vacancies and vacancy complexes) near the Si/SiO₂ interface. It is concluded that these same defects also enhance the 1/f noise of MOS transistors, which should help to resolve the long-standing debate on the origin of MOS noise. Independent estimates of radiation-induced border-trap charge densities using a dual-transistor technique that combines threshold-voltage and charge-pumping measurements agree well with 1/f noise estimates.

1. Introduction

1/f fluctuations are a common feature of glassy electronic systems [1–5]. Perhaps the most studied of these is the MOS transistor, where the conduction properties are determined to a large extent by the quality of the amorphous, thin-film SiO₂ layer used to passivate the Si channel surface and to insulate the gate from the channel. Defects in the oxide and at the Si/SiO₂ interface can play a crucial role in determining MOS quality, performance,

reliability, and/or radiation hardness [6,7]. After many years of controversy in which alternate explanations were also explored (e.g., carrier-phonon scattering [8,9] and quantum fluctuations [9–11]), it now seems clear that much, if not all, of the 1/f noise typically observed in MOS transistors is caused by channel carrier-number and/or mobility fluctuations associated with similar defects [12–15]. That MOS devices historically have shown larger levels of low-frequency excess (1/f) noise than some other types of electronic devices (e.g., JFETs) has been attributed to the amorphous gate insulator and its associated traps. Uncertainty in the type and location (oxide versus interface) of the specific defects that cause the noise has made it

* Corresponding author. Tel: +1-505 844 1825 Telefax: +1-505 844 2991. E-mail: dmfleet@smtplink.mdl.sandia.gov.

difficult to optimize MOS processing to reduce low-frequency noise levels. This has limited the semiconductor industry's ability to design MOS devices or circuits for low-noise applications at frequencies below ~ 1 –100 kHz.

In this paper, work will be briefly reviewed that, over the last six years, has compared the low-frequency $1/f$ noise of MOS transistors manufactured with commercial-like and radiation-hardened gate oxides. It is found that techniques that reduce the amount of bulk-oxide-trap and/or 'border-trap' [16] charge in irradiated MOS transistors can also proportionally reduce the magnitude of the $1/f$ noise of both unirradiated and irradiated devices. MOSFETs built in a radiation-hardened process can show $1/f$ noise levels (before irradiation) up to a factor of 10 or more lower than standard commercial MOS transistors of comparable dimensions [17,18]. After irradiation, this difference can become even greater. Our quietest MOS transistors are beginning to approach the low noise levels of JFETs [18,19]. We have also found that $1/f$ noise measurements appear very promising as candidates for providing the first non-destructive test for the radiation hardness of MOS devices [20], which is potentially of great significance to many space, military, nuclear reactor, and high-energy particle accelerator applications. Due to manuscript length

limitations, only a portion of the principal results will be presented here; the reader is directed to Refs. [16–18, 20–35] for additional details.

2. Comparison of noise and radiation response

The first set of experiments we discuss was performed to see whether there is a correlation between the $1/f$ noise of unirradiated MOS transistors and the radiation-induced buildup of oxide- and/or interface-trap charge in these devices. Fig. 1 shows the key result. Here we plot the room-temperature normalized noise-power, K , as a function of MOS transistor threshold-voltage shifts due to radiation-induced oxide-trap charge, ΔV_{ot} , for MOS transistors fabricated in the same lot but with different gate oxidation and post-oxidation annealing steps [17,21]. Most notably, processes D–E of Fig. 1 received a high-temperature, 30 min N_2 post-oxidation anneal that processes A–C did not receive, as discussed in detail in Refs. [17,18,21]. Here

$$K \equiv S_v f (V_g - V_{th})^2 V_d^{-2} \quad (1)$$

is the noise magnitude expressed such a way that the drain- and gate-voltage dependencies are normalized out [15,20,32]. S_v is the excess drain-

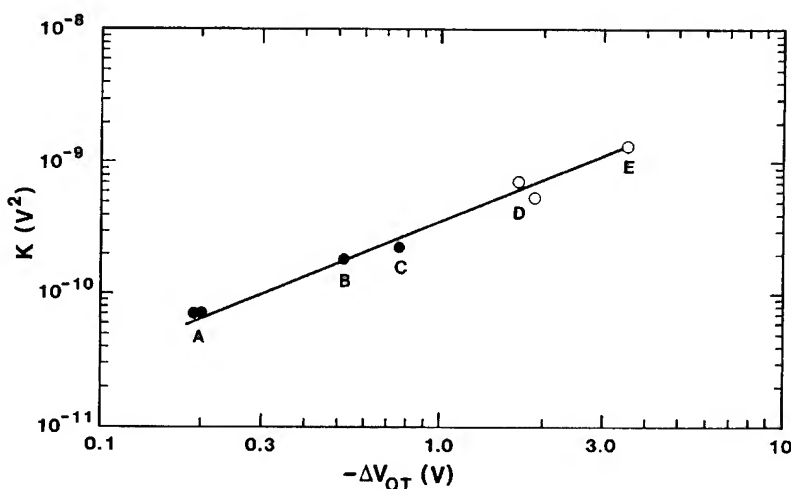


Fig. 1. Normalized noise magnitude of unirradiated MOS transistors as a function of radiation-induced threshold-voltage shifts due to oxide-trap charge following 100 krad (SiO_2) irradiation with Co-60 gamma rays at an electric field of ~ 3 MV/cm. (After Ref. [17].)

voltage noise-power spectral density (where the zero-current background noise of the device and system have been subtracted out [21]), V_g and V_d are the gate and drain voltages applied during

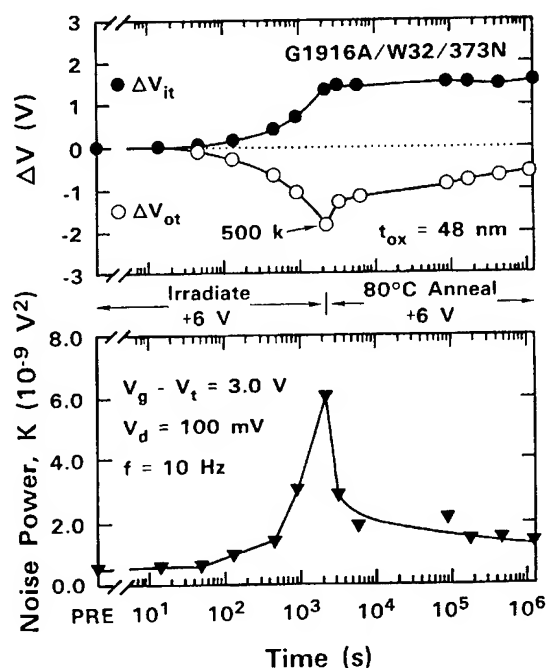


Fig. 2. Threshold-voltage shifts due to oxide-trap and interface-trap charge (top) and normalized noise power (bottom) as a function of irradiation and anneal time for nMOS transistors with moderately hard 48 nm gate oxides. Irradiations were performed at room temperature; anneals were performed at 80°C. All measurements were performed at room temperature. (After Ref. [22].)

the noise measurements, V_{th} is the transistor threshold-voltage, and f is the frequency. A clear correlation is demonstrated in Fig. 1 between the pre-irradiation $1/f$ noise and the post-irradiation oxide-trap charge. No such correlation is observed with the threshold-voltage shift due to interface-trap charge, ΔV_{it} [17,18,21]. The results of Fig. 1 suggest that (1) processes that reduce radiation-induced oxide-trap charge also reduce the noise of unirradiated transistors [17,18,33], and (2) $1/f$ noise measurements made before irradiation often can predict oxide charge trapping after irradiation [17,20,21,33]. Heretofore, a non-destructive electrical method to predict ΔV_{ot} was not available [21,33].

Fig. 2 shows the results of a second study, in which the buildup and annealing of $1/f$ noise through an irradiation and annealing sequence is compared to radiation-induced oxide- and interface-trap charge [22,23]. No attempt was made to separate out border-trap effects at this point. During irradiation, both ΔV_{ot} and ΔV_{it} , as well as the noise, increase in magnitude. So, from the left-hand side of Fig. 2 or most other similar studies of irradiated or similarly (e.g., hot-carrier) stressed devices, it is difficult merely from 'stress versus duration' data to tell what type of defect is responsible for the observed noise. When the transistors are subjected to a high-temperature annealing sequence, however, the magnitudes of the oxide-trap charge and the noise both decrease significantly, while the interface-trap charge remains constant. Moreover, in Fig. 3 it is shown that the noise goes

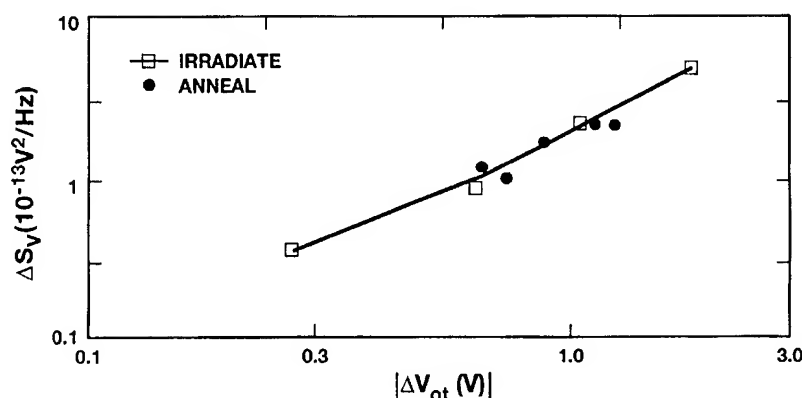


Fig. 3. Drain-voltage noise-power spectral density as a function of ΔV_{ot} for the irradiation and annealing sequence of Fig. 2. (After Ref. [22].)

up as the magnitude of ΔV_{ot} increases during irradiation, and comes down the same curve as the magnitude of ΔV_{ot} decreases during annealing. Thus, Figs. 1–3 strongly suggest that the noise of unirradiated or irradiated devices is more closely associated with oxide traps than interface traps.

3. Defects in thin-film SiO_2

Fig. 4 schematically illustrates the two principal defects that have been identified in electron-paramagnetic-resonance studies of amorphous, thermally grown, thin-film SiO_2 . Fig. 4(a) shows the classic E'_γ center, which is a hole trapped at an oxygen vacancy [26–28,31,36]; and Fig. 4(b) shows the E'_δ center, a defect only recently observed in thermal SiO_2 , which has been ascribed to a Si interstitial/oxygen vacancy complex [26–28,31,37]. The most important point to note here is that excess Si and/or oxygen deficiency in the SiO_2 is associated with each center, emphasizing the crucial role of oxygen vacancies in MOS hole-injection or radiation response [26,31].

In recent work, a model has been developed to predict the density of oxygen vacancies in Si/ SiO_2 /Si structures [26–28,31] subjected to the kinds of high-temperature anneals commonly performed after the gate oxidation step in MOS transistor processing [17,34]. These anneals are known to strongly affect MOS radiation response and $1/f$ noise [17,20]. The model presumes that oxygen vacancies are created by O diffusing out of the oxide and into the Si substrate or polycrystalline Si (as O interstitials) [26,31]. The driving force for this process is simply the chemical potential difference of the O in the SiO_2 and Si substrate. A semi-quantitative estimate of O vacancy profiles in the oxide, obtained by applying Fick's law of diffusion to a model Si/ SiO_2 boundary system [26,31], is shown in Fig. 5 for non-oxidizing post-gate anneals from 800 to 1000°C. With increasing anneal temperature, more oxygen vacancies are formed deeper in the oxide. Integrating the O vacancy profiles in Fig. 5, and calculating equivalent threshold-voltage shifts due to charged-oxygen vacancies (assuming that during irradiation or hole injection each O vacancy captures a single hole), one can assess the

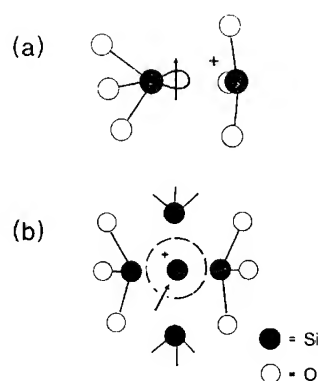


Fig. 4. Schematic illustrations of two oxygen-deficient centers observed during electron-paramagnetic-resonance studies of amorphous thin-film Si/ SiO_2 structures: (a) E'_γ and (b) E'_δ . (After Refs. [26, 31].)

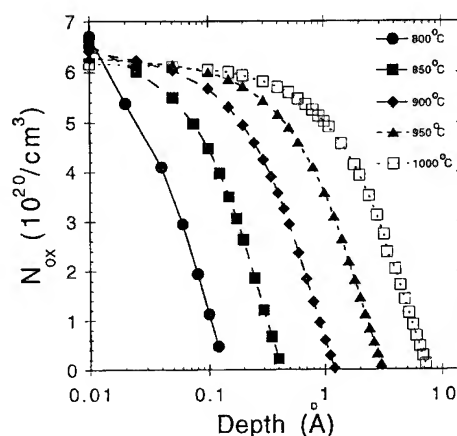


Fig. 5. Oxygen vacancy profiles in the oxide near the Si/ SiO_2 interface predicted using a simple diffusion model for 30 min, high-temperature post-oxidation anneals of Si/ SiO_2 /Si structures in an inert ambient. Depth = 0 is the Si/ SiO_2 interface. (After Ref. [31].)

impact of oxygen deficiency on, for example, MOS radiation response. This is shown in Fig. 6, where the model results are compared to experimental data on irradiated MOS capacitors from Ref. [34]. That the model overpredicts the observed shifts is not surprising, given (1) its approximate nature and (2) that not every trap in the oxide will capture a hole after 1 Mrad irradiation (well below saturation of charge trapping in these oxides). Nevertheless, the agreement between the effect of the post-oxidation anneals on the density of vacancies and the

density of radiation-induced trapped-oxide charge indicated by Fig. 6 is quite dramatic, and strongly suggests that oxygen deficiency leads to enhanced radiation-induced-hole trapping. Because similar enhancement of $1/f$ noise is also caused by such annealing treatments (Refs. [17,18,21] and Fig. 1), we conclude that increasing the density of oxygen vacancies in the SiO_2 increases MOS $1/f$ noise.

That simple oxygen vacancies or vacancy complexes may not be the complete story is suggested

by Fig. 7, in which it is shown that increasing the amount of hydrogen (present during high-temperature anneals) in the MOS processing sequence can also increase radiation-induced oxide- and interface-trap charge [35]. It would certainly be interesting to perform a similar study on MOS transistors in which the effects of hydrogen on MOS noise could also be assessed.

4. Border-trap model

Because of the timescales involved in typical $1/f$ noise measurements (generally ~ 0.1 Hz to 100 kHz or so), not all of the oxide traps can fluctuate in occupancy during the measurement interval and thereby contribute to the noise. Instead, only those oxide traps close enough to the Fermi level in energy and near enough spatially to the Si channel can do so. On the other hand, the timescales for interface traps to communicate with the Si evidently are too fast for them to contribute significantly to the $1/f$ noise [22–24], except perhaps in unusual circumstances [38]. Thus, it seems that much, if not all, of the typical low-frequency $1/f$ noise observed in MOS transistors is due to ‘border traps’ defined as near-interfacial oxide traps that exchange charge with the Si [16,24,30,33]. A schematic illustration of this is given in Fig. 8.

Recently a method has been developed to independently estimate MOS bulk-oxide, interface, and border-trap densities [29,30]. The ‘dual-transistor border-trap’ (DTBT) method takes advantage of

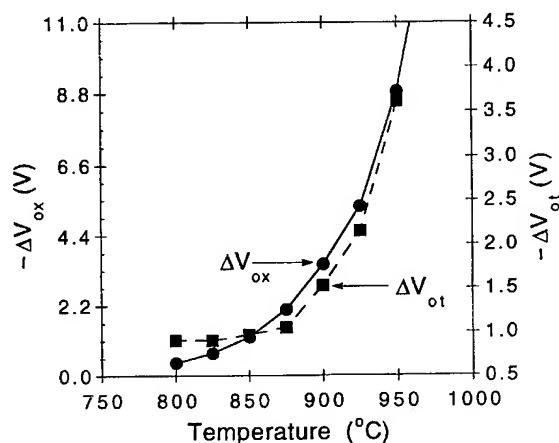


Fig. 6. Measured ΔV_{ot} (squares, right-hand scale) and predicted shift, ΔV_{ox} (circles, left-hand scale), due to oxygen vacancies using the model of Fig. 5 for MOS capacitors exposed to 30 min post-oxidation anneals at varying temperature. The data are for 1 Mrad(SiO_2) X-ray irradiations of capacitors with 45 nm oxides at ~ 2 MV/cm from Ref. [34], and the model predictions are from Ref. [31].

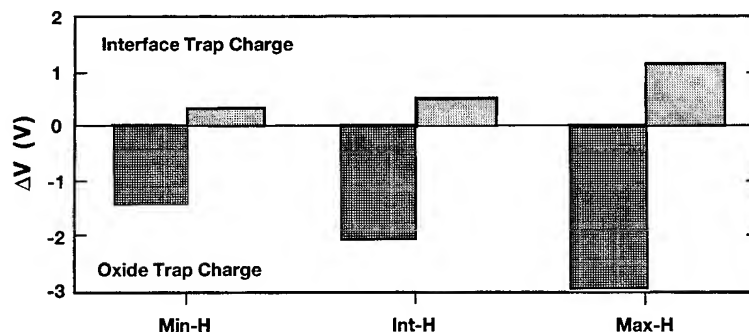


Fig. 7. Threshold-voltage shifts due to interface- and oxide-trap charge for MOS capacitors with 100 nm oxides processed with varying amounts of hydrogen, irradiated to 100 krad(SiO_2) at ~ 1 MV/cm with 10 keV X-rays. (After Ref. [35].)

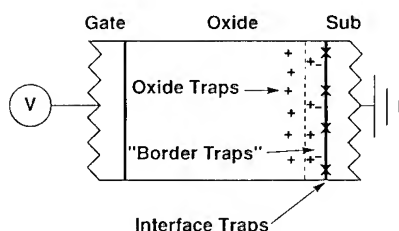


Fig. 8. Schematic illustration of oxide, interface, and border traps in MOS devices. 'Border traps' are a newly defined subclass of defects, and refer to near-interfacial oxide traps that can communicate with the underlying Si on sufficiently rapid time-scales that they can sometimes be mistaken for interface traps. (After Refs. [16,24].)

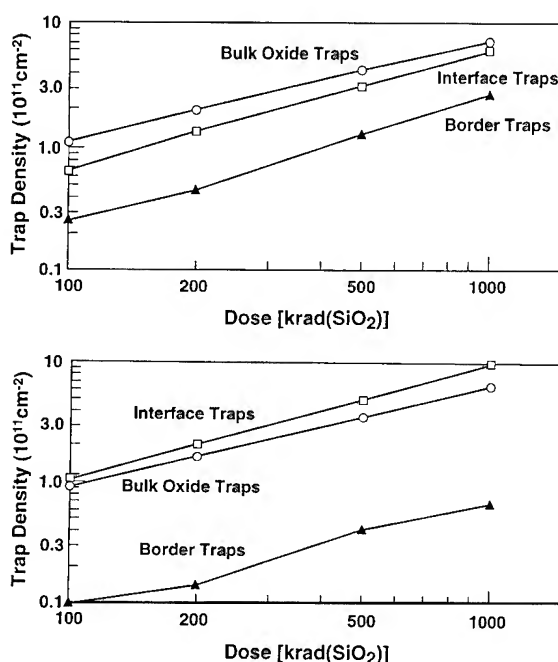


Fig. 9. Bulk-oxide, interface, and border-trap densities as a function of dose for nMOS transistors on the same chip with hardened 24 nm oxides irradiated with 10 keV X-rays at ~ 2 MV/cm: (a) channel length = $1.2 \mu\text{m}$, width = $50 \mu\text{m}$; (b) channel length = $50 \mu\text{m}$, width = $50 \mu\text{m}$. (After Refs. [29,30].)

the different timescales of conventional (low-frequency) threshold-voltage and (high-frequency) charge-pumping measurements on n- and p-channel MOS transistors to estimate the three types of charge densities. For details, see Refs. [29,30]. Fig. 9 illustrates an example of applying the DTBT method. Note that the density of border traps in the

$1.2 \mu\text{m} \times 50 \mu\text{m}$ transistor (Fig. 9(a)) is more than twice the density in the $50 \mu\text{m} \times 50 \mu\text{m}$ transistor (Fig. 9b) on the same chip [25,29]. Simple number-fluctuation-model estimates of border-trap densities based on the noise measurements for the two devices are similar to DTBT estimates of border-trap densities in each case (agreement within better than a factor of two [29]), and similar trends are observed in noise and border-trap density scaling (more noise and greater border-trap density in the shorter-gate-length transistor [29]), reinforcing the utility of the border-trap model. More details are provided in Refs. [25,29,30,33].

5. Conclusions

The $1/f$ noise of irradiated and unirradiated MOS transistors correlates strongly with oxide-trap charge, but not usually with interface-trap charge. Much, if not all, of MOS $1/f$ noise in the devices we have studied is caused by near-interfacial oxide traps that exchange charge with the Si, i.e., border traps. Independent estimates of border-trap densities agree well with $1/f$ noise estimates. Comparisons among radiation, hole-injection, and electron-paramagnetic-resonance studies of MOS structures suggest a key role for O vacancies in the SiO_2 in the formation of oxide and border traps. The correlation between $1/f$ noise and radiation response demonstrated here and in the supporting literature [17,18,20–25,33] suggests that oxygen deficiency near the Si/ SiO_2 interface also plays a key role in determining MOS $1/f$ noise, although a (possibly supporting) role for hydrogen cannot be excluded. We believe these results should help to resolve the long-standing controversy about the origin(s) of $1/f$ noise in MOS transistors.

The authors thank T.L. Meisenheimer, J.R. Schwank, P.S. Winokur, D. Mathiot, B. Aspar, and M.B. Weissman for stimulating discussions; and N. Borland, T.P. Doerr, P. Klimecky, M. Trawick, L.C. Riewe, and R.A. Reber Jr. for experimental assistance. The portion of this work performed at Sandia National Laboratories and at Oberlin College was supported by the US Department of Energy through contract No. DE-AC04-94AL85000.

References

- [1] M.B. Weissman, Rev. Mod. Phys. 65 (1993) 829.
- [2] K.S. Ralls and R.A. Buhrman, Phys. Rev. B44 (1991) 5800.
- [3] M.B. Weissman, Rev. Mod. Phys. 60 (1988) 537.
- [4] Sh.M. Kogan, Sov. Phys. Usp. 28 (1985) 170 [Usp. Fiz. Nauk 145 (1985) 285].
- [5] K.L. Ngai, Phys. Rev. B22 (1980) 2066.
- [6] E.H. Nicollian and J.R. Brews, MOS (Metal Oxide Semiconductor) Physics and Technology (Wiley, New York, 1982).
- [7] T.P. Ma and P.V. Dressendorfer, Ionizing Radiation Effects in MOS Devices and Circuits (Wiley, New York, 1989).
- [8] For example, F.N. Hooge, T.G.M. Kleinpenning and L.K.J. Vandamme, Rep. Prog. Phys. 44 (1981) 479.
- [9] A. van der Ziel, Adv. Electron. Electron Phys. 49 (1979) 225.
- [10] P.H. Handel, Phys. Rev. A22 (1980) 745.
- [11] C.M. van Vliet, Solid State Electron. 34 (1991) 1.
- [12] A.L. McWhorter, in: Semiconductor Surface Physics (Univ. of Pennsylvania, Philadelphia, 1957) p. 207.
- [13] C.T. Sah and F.H. Hielscher, Phys. Rev. Lett. 17 (1966) 956.
- [14] C. Surya and T.Y. Hsiang, Phys. Rev. B33 (1986) 4898.
- [15] J.J. Simonne, G. Blasquez and G. Barbottin, in: Instabilities in Silicon Devices: Silicon Passivation and Related Instabilities, Vol. 2 (Elsevier, Amsterdam, 1989) p. 639.
- [16] D.M. Fleetwood, IEEE Trans. Nucl. Sci. 39 (1992) 269.
- [17] D.M. Fleetwood and J.H. Scofield, Phys. Rev. Lett. 64 (1990) 579.
- [18] D.M. Fleetwood, T.L. Meisenheimer and J.H. Scofield, in: Noise in Physical Systems and $1/f$ Noise, ed. P.H. Handel and A.L. Chung (AIP Conference Proceedings No. 285, 1993) p. 339.
- [19] W. Buttler, H. Vogt, G. Lutz, P.F. Manfredi and V. Speziali, IEEE Trans. Nucl. Sci. 38 (1991) 69.
- [20] J.H. Scofield and D.M. Fleetwood, IEEE Trans. Nucl. Sci. 38 (1991) 1567.
- [21] J.H. Scofield, T.P. Doerr and D.M. Fleetwood, IEEE Trans. Nucl. Sci. 36 (1989) 1946.
- [22] T.L. Meisenheimer and D.M. Fleetwood, IEEE Trans. Nucl. Sci. 37 (1990) 1696.
- [23] T.L. Meisenheimer, D.M. Fleetwood, M.R. Shaneyfelt and L.C. Riewe, IEEE Trans. Nucl. Sci. 38 (1991) 1297.
- [24] D.M. Fleetwood, P.S. Winokur, R.A. Reber Jr., T.L. Meisenheimer, J.R. Schwank, M.R. Shaneyfelt and L.C. Riewe, J. Appl. Phys. 73 (1993) 5058.
- [25] M.R. Shaneyfelt, D.M. Fleetwood, P.S. Winokur, J.R. Schwank and T.L. Meisenheimer, IEEE Trans. Nucl. Sci. 40 (1993) 1678.
- [26] R.A.B. Devine, D. Mathiot, W.L. Warren, D.M. Fleetwood and B. Aspar, Appl. Phys. Lett. 63 (1993) 2926.
- [27] R.A.B. Devine, W.L. Warren, M.R. Shaneyfelt, D.M. Fleetwood and B. Aspar, Nucl. Instr. and Meth. B 84 (1994) 254.
- [28] R.A.B. Devine, D. Mathiot, W.L. Warren and D.M. Fleetwood, Mater. Res. Soc. Symp. Proc. 318 (1994).
- [29] D.M. Fleetwood, M.R. Shaneyfelt and J.R. Schwank, Appl. Phys. Lett. 64 (1994) 1965.
- [30] D.M. Fleetwood, M.R. Shaneyfelt, W.L. Warren, J.R. Schwank, T.L. Meisenheimer and P.S. Winokur, Microelectronics Reliability 35 (1995) 403.
- [31] W.L. Warren, D.M. Fleetwood, M.R. Shaneyfelt, P.S. Winokur, R.A.B. Devine, D. Mathiot, I.H. Wilson and J.B. Xu, Mater. Res. Soc. Symp. Proc. 338 (1994) 3; W.L. Warren, D.M. Fleetwood, M.R. Shaneyfelt, J.R. Schwank, P.S. Winokur, R.A.B. Devine and D. Mathiot, Appl. Phys. Lett. 64 (1994) 3452.
- [32] J.H. Scofield, N. Borland and D.M. Fleetwood, IEEE Trans. Electron Dev. 41 (1994) 1946.
- [33] D.M. Fleetwood, T.L. Meisenheimer and J.H. Scofield, IEEE Trans. Electron Dev. 41 (1994) 1953.
- [34] J.R. Schwank and D.M. Fleetwood, Appl. Phys. Lett. 53 (1988) 770.
- [35] J.R. Schwank, D.M. Fleetwood, P.S. Winokur, P.V. Dressendorfer, D.C. Turpin and D.T. Sanders, IEEE Trans. Nucl. Sci. 34 (1987) 1152.
- [36] P.M. Lenahan and P.V. Dressendorfer, J. Appl. Phys. 55 (1984) 3495.
- [37] K. Vanheusden and A. Stesmans, J. Appl. Phys. 74 (1993) 275.
- [38] M.H. Tsai and T.P. Ma, IEEE Trans. Electron Dev. 14 (1993) 256; IEEE Trans. Nucl. Sci. 39 (1992) 2178.



ELSEVIER

Journal of Non-Crystalline Solids 187 (1995) 206–210

JOURNAL OF
NON-CRYSTALLINE SOLIDS

The microscopic nature of donor-type Si–SiO₂ interface states

K.G. Druijf*, J.M.M. de Nijs, E. v.d. Drift, V.V. Afanas'ev, E.H.A. Granneman, P. Balk

Delft Institute of Microelectronics and Submicrotechnology, (DIMES), Delft University of Technology, PO Box 5053, 2600 GB Delft, The Netherlands

Abstract

Donor-type interface states, generated by vacuum ultraviolet irradiation have been studied. They anneal at room temperature but only when in a neutral state. This anneal is accompanied by the release of atomic hydrogen. It is proposed that the states are formed by H loosely bonded to sites in the SiO₂ network at or near the interface. Anneal would take place by removal of H. Capturing a hole would strengthen the bond between H and the network site.

1. Introduction

The microscopic nature of the electrical states at the Si–SiO₂ interface has been a matter of considerable interest for many years. It has become clear that upon electrical stressing [1], irradiation [2] or exposure to atomic hydrogen [3] not only trivalent silicon defects (P_b centres) but also centres of a different nature are being generated reaching densities as large as 10¹³ cm^{−2}. The involvement of H in the generation of the latter type of centres has been clearly demonstrated [2–4].

In a preceding paper [5] we have shown that non-P_b like centres can be produced by vacuum ultraviolet (VUV) irradiation; these centres are donor-type and anneal at room temperature. In the present study we will show that these donor centres anneal only when in a neutral state and that the anneal is accompanied by the release of H. Based

on these observations we will propose a microscopic model for the donor states.

2. Experimental

In the present study we have used 35 and 31 nm oxides on 100 Ω cm p- and n-type Si(100) substrates, respectively; n- and p-type samples were used to study the interface state density above and below mid-gap. The oxides were grown in a double walled furnace in pure O₂ at 1000°C followed by a 1 h anneal in N₂ at the same temperature. MOS capacitors were defined by resistive evaporation of an optically transparent (10 nm) aluminium gate through a shadow mask. The samples did not receive further anneals. Capacitance–voltage (CV) measurements showed that the as-prepared MOS system contains 1 × 10¹¹ cm^{−2} eV^{−1} interface states at mid-gap. By generation of 1.5 × 10¹⁶ cm^{−2} electron hole pairs in the oxide using a VUV Kr lamp (*hν* = 10 eV) at +3 V gate bias, interface states and trapped holes were produced.

* Corresponding author. Tel: +31-15 783 868. Telefax: +31-15 622 163.

Subsequently the trapped holes were neutralised by photo injection of $2 \times 10^{13} \text{ cm}^{-2}$ electrons at 0 V bias using a ultraviolet (UV) Hg lamp ($h\nu < 6 \text{ eV}$). After hole neutralisation no bulk oxide charge is left; the only charges in the Si-SiO₂ system are those in the interface states (concentration $\approx 10^{13} \text{ cm}^{-2}$). All our experiments were performed at room temperature.

3. Results

First we studied the bias dependence of the anneal of the donor states by monitoring the change of the HF CV curves with time while keeping the gate at various biases between the measurements. Figs. 1 and 2 show the change of the CV curves with time for an n- and a p-type sample, respectively, while keeping the gate biased at 0 V. At this condition all interface states are neutral. For comparison also the curves recorded prior to VUV irradiation are shown. Notice that the stretch-out extends towards negative biases indicating that the states are donor-type [5]. The stretch-out in Fig. 1 decreases with time due to the anneal of the states above mid-gap. The curves in Fig. 2 show a decreasing stretch-out due the anneal of the centres below mid-gap and horizontal shift due the anneal of the states above mid-gap. Thus, all donor states, above and below mid-gap anneal when they are neutral.

Figs. 3 and 4 show the CV curves for an n- and a p-type sample, respectively, with the gate biased at -7 V between the measurements; in this case the states above mid-gap are positively charged whereas those below mid-gap are neutral. In Fig. 3 we see no major change of the stretch-out of the CV curves with time. Thus the positively charged states above mid-gap are conserved. Fig. 4 shows a decreasing stretch-out with time, indicating that the states below mid-gap, being neutral, do anneal. Fig. 5 shows the CV curves for a p-type sample with the gate biased at -15 V between the measurements; all donor states are charged positively in this case. Apart from a minor shift during the first minutes no change of the slope or a shift in the CV curves is observed; neither the states above nor those below mid-gap anneal at this bias voltage.

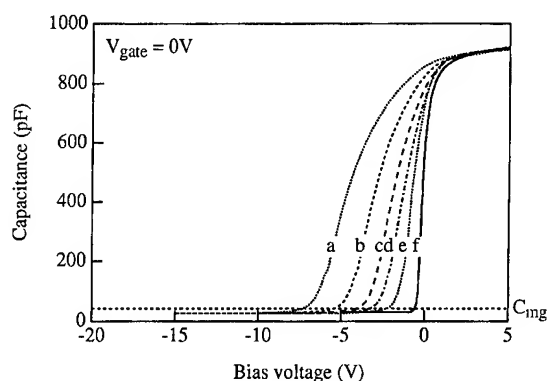


Fig. 1. HF CV curves for a n-type sample while biased 0 V in between the measurements. Curves after 3.5 (a), 10 (b), 30 (c), 98 (d), 1122 (e) minutes waiting at room temperature and the pre-irradiation curve (f) are given. The mid-gap capacitance is indicated by the dashed line.

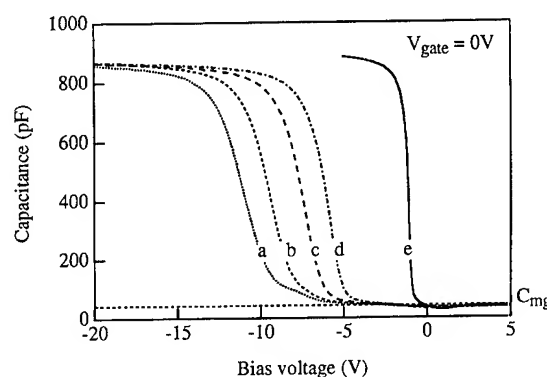


Fig. 2. HF CV curves for a p-type sample while biased 0 V in between the measurements. Curves after 4.3 (a), 10 (b), 74 (c), and 1114 (d) minutes waiting at room temperature and the pre-irradiation curve (e) are given. The mid-gap capacitance is indicated by the dashed line.

The above results clearly demonstrate that donor states generated by VUV irradiation anneal when neutral and do not anneal when charged positively.

Because it is well known that H can be involved in the generation of interface states, we decided to monitor the appearance of mobile H during the anneal. This was done by determining deactivation of boron in the substrate from the inversion capacitance of the HF CV curves [6, 7]. To stabilise the structure at conditions where no H is released,

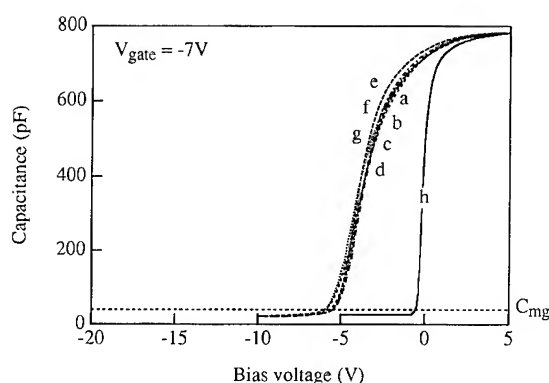


Fig. 3. HF CV curves for a n-type sample while biased -7 V in between the measurements. Curves after 2.8 (a), 5.8 (b), 10.8 (c), 21 (d), 53 (e), 203 (f), 503 (g) minutes waiting at room temperature and the pre-irradiation curve (h) are given. The mid-gap capacitance is indicated by the dashed line.

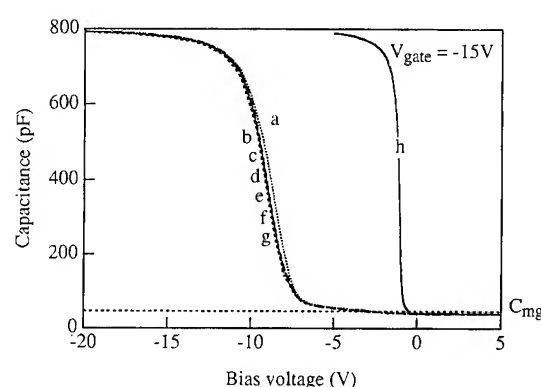


Fig. 5. HF CV curves for a p-type sample while biased -15 V in between the measurements. Curves after 3.2 (a), 6.2 (b), 11.2 (c), 21.2 (d), 53.2 (e), 203.2 (f), 502.2 (g) minutes waiting at room temperature and the pre-irradiation curve (h) are given. The mid-gap capacitance is indicated by the dashed line.

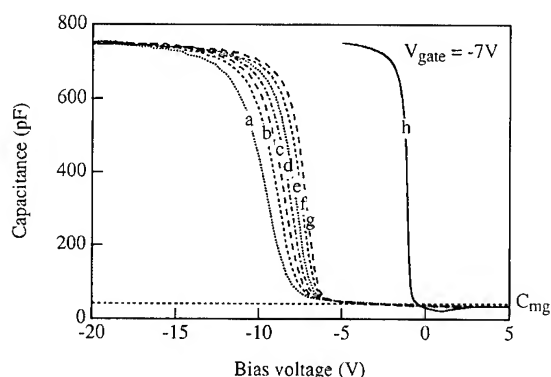


Fig. 4. HF CV curves for a p-type sample while biased -7 V in between the measurements. Curves after 2.5 (a), 5.5 (b), 10.5 (c), 20.5 (d), 52.5 (e), 202.5 (f), 502.5 (g) minutes waiting at room temperature and the pre-irradiation curve (h) are given. The mid-gap capacitance is indicated by the dashed line.

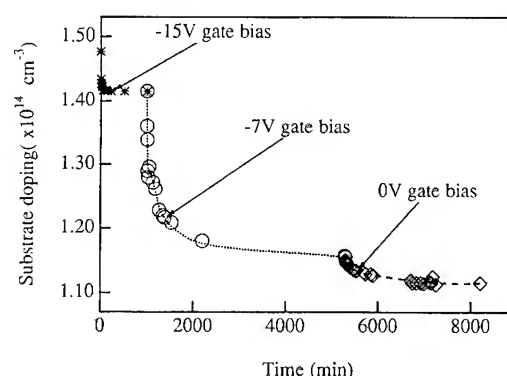


Fig. 6. Substrate doping level in the depletion layer versus time. The stars, circles and diamonds give the doping level for the case the gate was biased at -15 , -7 and 0 V, respectively. The lines are a guide to the eye.

we biased the gate at -15 V for 1000 min directly after the VUV and UV illuminations were completed. At -15 V interface state annealing is inhibited. Subsequently the gate bias was switched to -7 V, letting the states below mid-gap anneal. After 4000 min at -7 V the bias was switched to 0 V letting also the states above mid-gap anneal. The results, in Fig. 6, show the stable condition at -15 V, a reduction of the boron concentration in the depletion layer after biasing the gate at -7 V and an additional reduction upon switching the

bias to 0 V. Although the quantitative aspects of these results are not immediately clear, the data unambiguously show that room temperature annealing of the donor states is accompanied by the release of atomic H.

4. Discussion

A model for the donor interface states thus should account for the following observations: these

centres anneal already at room temperature, but only if they are neutral; simultaneous with the anneal H is being released; when positively charged the states are stable; the density of states may be quite large; one way of generating them is exposure of the Si–SiO₂ system to atomic H [3]. These features show that the presence of hydrogen is essential for the existence of the centre. In fact, the simplest explanation would be that the centre is the H atom itself, attached in some manner to a site near the Si–SiO₂ interface in the chemically saturated oxide network. Of these sites there are large numbers available. We have to postulate further that the bonding to the network is strong when the defect is charged positively, and weak when neutral. In contrast to the P_b centre, which is removed by the bonding of H, the donor centre is formed by the presence of H. For the attachment site for the H atom leading to the donor state one might consider the O atom of the Si–O–Si configuration, thus giving rise to an analogue of the hydronium ion: $\text{H}^+ + \text{H}_2\text{O} \rightarrow \text{H}_3\text{O}^+$. Neutral H atoms are able to escape and to wander from site to site. Annealing would take place by the formation of H₂ dimers or escape of H into the bulk of the oxide or into the Si.

The general availability of Si–O–Si sites throughout the oxide gives rise to the question if H atoms would not also bond to bulk sites similar to those at the interface. In the bulk the centres could not be charged by simply applying an electric field. However, a neutral H atom, probably set free from the SiO₂–Al interface, could upon interaction with a hole generated by the VUV irradiation become attached to a network site in the bulk of the oxide. Thus, neutral hydrogen would constitute a bulk hole trap and, consequently, the charged oxide would store hydrogen. Neutralisation of the positive charge would release this hydrogen which should result in the generation of additional interface states and the deactivation of boron. We performed an experiment similar to Lai [8], in which 10^{15} cm^{-2} holes were injected into the oxide. Upon neutralisation by electrons we observed generation of additional donor states, like Lai did, and deactivation of boron. We would like to mention the existence of a hole traps with small cross-section ($\sigma < 10^{-15} \text{ cm}^{-2}$) that has not been identified so

far [9]. In our view, this trap may be related to the atomic H that is bonded upon interaction with a hole at a network site in the bulk, as discussed above.

When neutralising the trapped holes by photo injection of electrons the H atoms would be less firmly bound at its site in the oxide. In fact, we claim that its bonding energy would be less than that in a corresponding site near the Si–SiO₂ interface, so that the neutral H atom could move around rather freely. The experiment of Fig. 6 supports this contention. When applying a –15 V bias to the gate after the VUV and UV exposure the positively charged bonding state near the interface constitutes the energy minimum for hydrogen. Thus it can be expected that all neutral H atoms present in the oxide would be collected at interfacial sites where, upon capture of a hole from the silicon, they would become strongly bonded. If the strength of the bonding of neutral H were the same in the bulk as at the interface, one would expect a time constant of 10 min to hours for the formation of additional donor states. Because such a generation was not observed, the time constant for hydrogen release from bulk sites must be smaller than the time required to perform the measurement ($< 1 \text{ min}$) and thus smaller than the time constant for release of H from the interfacial sites. This indicates weaker bonding in the bulk.

The conclusion that the bonding energy for neutral H in the bulk and at the interface differ is not too surprising. The strain in the interfacial region has been claimed to produce increased sensitivity for interface state generation due to electrical stressing or irradiation [10]. The attachment sites for H near the interface are similar but not identical. A redistribution of interface traps, as reported by Ma [11] is quite compatible with this idea. The redistribution would simply imply a rearrangement of H over the available sites to minimise the energy of the overall system.

5. Conclusion

By formulating the above suggestions the authors hope to contribute to the current discussion on the microscopic nature of interface states. It will be

important to have critical contributions from theorists. The present authors are in the process of obtaining additional supporting experimental evidence for the model for the donor states presented in this paper.

References

- [1] J.H. Stathis, *Microelectron. Eng.* 22 (1993) 191.
- [2] C.T. Sah, J.Y. Chen and J.J.T. Tzou, *J. Appl. Phys.* 53 (1982) 8886.
- [3] E. Cartier, J.H. Stathis and D.A. Buchanan, *Appl. Phys. Lett.* 63 (1993) 1510.
- [4] N.M. Johnson, D.K. Biegelsen, M.D. Moyer, V.R. Deline and C.A. Evans Jr., *Appl. Phys. Lett.* 38 (1981) 995.
- [5] K.G. Druif, J.M.M. de Nijs, E. v.d. Drift, E.H.A. Granneman and P. Balk, *Appl. Phys. Lett.* 65 (1994) 347.
- [6] C.T. Sah, J.Y. Chen and J.J.T. Tzou, *Appl. Phys. Lett.* 43 (1983) 204.
- [7] G.G. Deleo and W.B. Fowler, *Phys. Rev.* B31 (1985) 6861.
- [8] S.K. Lai, *J. Appl. Phys.* 53 (1983) 2540.
- [9] A.R. Stivers and C.T. Sah, *J. Appl. Phys.* 51 (1981) 6292.
- [10] K. Kasama, M. Tsukiji and K. Kobayashi, *IEEE Trans. Nucl. Sci.* NS-34 (1987) 1202.
- [11] T.P. Ma, *Semicond. Sci. Technol.* 4 (1989) 1061.



ELSEVIER

Journal of Non-Crystalline Solids 187 (1995) 211–215

JOURNAL OF
NON-CRYSTALLINE SOLIDS

Three-level charge pumping study of radiation-induced defects at Si–SiO₂ interface in submicrometer MOS transistors[☆]

Jean-Luc Autran^{a,*}, Bernard Balland^a, Daniel Babot^b

^aLaboratoire de Physique de la Matière, URA CNRS 358, bâtiment 502, Institut National des Sciences Appliquées de Lyon, 20 avenue Albert Einstein, 69621 Villeurbanne, France

^bEquipe Contrôle Non Destructif par Rayonnements Ionisants, bâtiment 303, Institut National des Sciences Appliquées de Lyon, 20 avenue Albert Einstein, 69621 Villeurbanne, France

Abstract

The charge pumping response of interface traps and near-interfacial oxide traps (border traps) induced by Co⁶⁰ gamma rays in submicrometer (0.5 μm channel length) metal-oxide-semiconductor transistors has been studied. Using an improved three-level charge pumping technique, the energy distribution of interface trap parameters (emission times, capture cross-sections and interface state density) has been determined after irradiation in both the upper and lower parts of the silicon band gap on *n*-channel devices. The influence of border traps on three-level charge pumping measurements is demonstrated for the first time. Good agreement has been found between standard charge pumping and three-level charge pumping characteristics in terms of 'breakpoint frequency' at which the charge recombined per cycle deviates from the fast interface state response. The distance of border traps from the interface has been estimated to be $\sim 15\text{--}20$ Å from a trap-to-trap tunneling model. In addition, a new technique is presented based on three-level charge pumping measurements to determine a border trap distribution in the silicon band gap.

1. Introduction

The increase of trapped charge in the oxide and the increase of interface state density, D_{it} , are the most important phenomena produced by radiation exposure in the Si/SiO₂ system. But ionizing radiation can also induce a complete change in the nature of the electrically active defects at the interface in the oxide layer in terms of energy distri-

bution of D_{it} or in terms of trapping–detrapping properties [1,2]. Recently, it has been reported by Paulsen et al. [3] that the standard charge pumping technique can provide an interesting way to separate the contribution of the near-interface oxide traps (called border traps too [4,5]) that exchange charge with the semiconductor and the Si/SiO₂ interface traps (fast states). In this work, we have used both standard charge pumping (CP) [6] and 3-level charge pumping (3CP) [7–10] techniques on irradiated submicrometer metal-oxide-semiconductor field effect transistors (MOSFETs) in order to determine the energy distributions of interface trap parameters (emission times, capture cross-

[☆]This work is partially supported by IBM Microelectronics, IC Manufacturing Plant of Corbeil-Essonnes, France.

* Corresponding author. Tel: +33 72 43 87 33. Telefax: +33 72 43 85 31. E-mail: autran@insa.insa-lyon.fr.

sections, D_{it}) and to examine the charge pumping response of interface and border traps. We also discuss a new method, based on the three-level charge pumping technique, for the determination of a D_{it} distribution related to the fastest border traps measureable above the interface-trap background in the silicon band gap.

2. Experimental procedure

The n -channel interdigital MOSFETs used in this study have been fabricated at IBM Microelectronics (Corbeil-Essonnes) using a 0.5 μm CMOS technology. The source and the drain form a single comb-shaped junction with the substrate that interpenetrates the polysilicon gate comb. As a consequence, there is a large gate area (14000 μm^2) in spite of a short effective channel length (0.5 μm). Charge-voltage (Q - V) and charge pumping measurements can be made directly on the same devices.

The samples were irradiated using the INSA Co⁶⁰ gamma-ray source with a dose rate of 59 krad (SiO₂) per hour. For convenience, the MOSFETs were kept unbiased (floating) during irradiation. There was a delay of about 50 h at room temperature between the end of the exposure and the post-irradiation characterization. This delay was chosen to reduce the possibility that the post-irradiation interface trap buildup might influence our results.

In the 3CP method introduced by Saks and Ancona [7,8], a three-level waveform, as shown schematically in Fig. 1 (inset) is applied to the gate of the MOSFET under test to select a time window and an energy window in the silicon band gap for studying the electrical response of the traps in emission or capture regimes. Recently, a new 3CP procedure, used in this study and based on the use of a high performance arbitrary function generator, has been proposed [9,10]. 3CP and Q - V measurements involve a LeCroy 9101 generator, a Keithley 617 electrometer and an IBM computer. The experimental relation between the gate voltage, V_G , and the surface potential, Φ_s , is needed to calculate the energy distribution of interface-trap parameters. The method used in this study to calculate

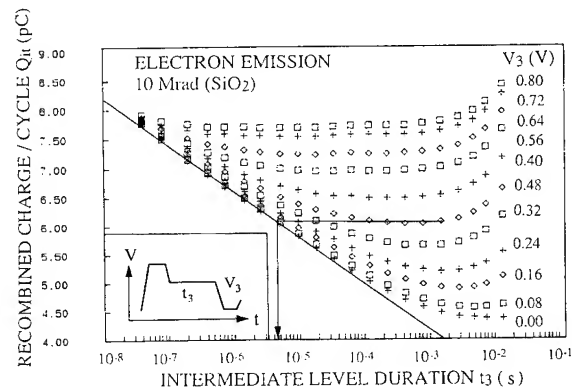


Fig. 1. Recombined charge per cycle Q_{it} as a function of third-level parameters t_3 and V_3 in electron emission for a 10 Mrad irradiated MOSFET. The emission times of fast interface states are extracted from these data by a graphic construction for each value of V_3 . Inset: Three-level waveform used in 3CP experiment. Duration t_3 and voltage V_3 refer to the intermediate level.

the $\Phi_s(V_G)$ curve consists in resolving Poisson's equation with the appropriate (post-irradiation) doping profile and then calculating the theoretical capacitance-voltage (C - V) curve by the method introduced by Panagaphi [11,12]. An excellent agreement is found between the theoretical curve and experimental C - V data obtained from static Q - V measurements made on the gate-substrate capacitor (source-drain and substrate are grounded [13]). This agreement ensures a good accuracy for the energy trap positions. Thus, problems relating to potential errors in inversion regimes can be eliminated [10]. The complete procedure and various experimental results have been detailed elsewhere [10] and a recent discussion of this problem has been made by Nicollian [1].

3. Results

Fig. 1 shows the variations of the recombined charge per cycle Q_{it} pumped into the substrate with the third level parameters (duration t_3 and voltage level V_3) for a 10 Mrad irradiated device in electron emission regime. Generally, a saturation of Q_{it} has been observed for long t_3 : this feature corresponds to an equilibrium state (constant interface trapped charge) since all traps above the Fermi level (fixed

by V_3) have emitted their electron [7]. In Fig. 1, one can see that Q_{it} remains non-constant for most values of V_3 after the beginning of the saturation regime and abnormally increases for t_3 above ~ 1 ms. We attribute this increase to radiation-induced traps located in the interfacial region that exchange charges with the semiconductor, i.e. border traps [4,5]. This assumption has also been recently reported by Paulsen et al. within the framework of a CP experiment [3]. For irradiated devices or ultrathin tunnel oxide non-volatile memories, the authors have observed an increase of Q_{it} when the frequency of the gate square pulses tends towards small values. As shown in Fig. 2, a similar experiment has been performed on our 10 Mrad irradiated devices in order to compare CP and 3CP results. A 'breakpoint frequency' is observed between 300 and 600 Hz; this value can be interpreted as the inverse of the time constant of the charge exchange mechanism between the border traps and the semiconductor. According to 3CP data of Fig. 1, a good agreement is found between the two techniques. Emission times of border traps can be estimated in the decade between 1 and 10 ms for V_3 values between 0.8 and 0.24 V; they are above 10 ms for V_3 values less than 0.16 V. Different models of border traps (and/or 'slow states') have been developed in the literature [13]. They

generally consider border traps as defects which can trap charges by a tunneling mechanism directly from the silicon or indirectly via fast interface traps. We have used the model proposed by Roy [3,14] for the estimation of the tunneling distance d of the traps from the Si/SiO₂ interface. With an average value of $D_{it} \approx 7 \times 10^{11} \text{ eV}^{-1} \text{ cm}^{-2}$, we estimate d to be between 15 and 20 Å for a 10 Mrad irradiated device. A similar result is obtained in the case of a 1 Mrad dose exposure.

Before examining how to estimate a border trap distribution with 3CP, we now investigate by 3CP the change in fast interface state properties after irradiation. From $Q_{it}(t_3, V_3)$ curves, the energy distribution of emission times t_e can be determined in the upper part of the band gap for electron traps and in the lower part of the band gap for hole traps [7,8]. Using the Shockley–Read–Hall formalism [13], it is then possible to calculate the corresponding capture cross-section distribution. In Fig. 3, $t_e(E)$ and $\sigma(E)$ spectra are plotted for virgin and 10 Mrad irradiated devices. Fig. 3(a) shows that irradiation induces a non-uniform increase of the emission times in the silicon band gap. For electron traps, this increase is approximately one decade; a slope of $\sim q/kT$ ($\approx 38 \text{ eV}^{-1}$ at 300 K) is observed before and after irradiation. Thus, corresponding capture cross-sections displayed in Fig. 3(b) are

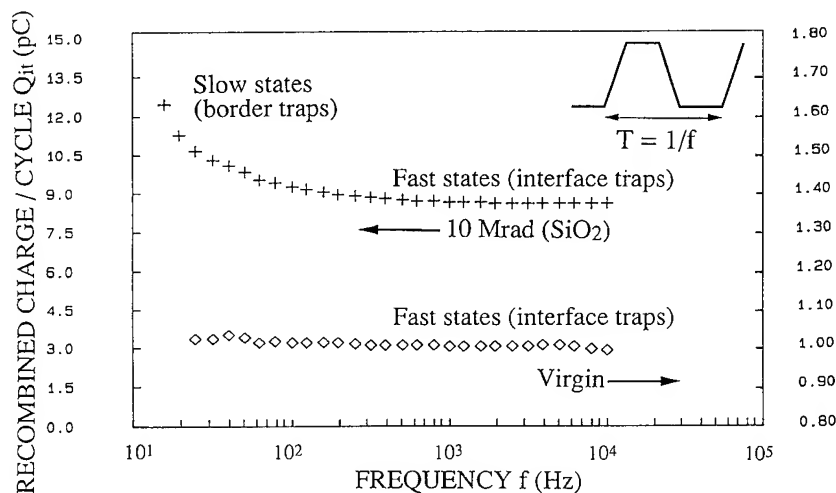


Fig. 2. Recombined charge per cycle Q_{it} versus the frequency f of the pulses for a non-irradiated device and for a 10 Mrad irradiated device.

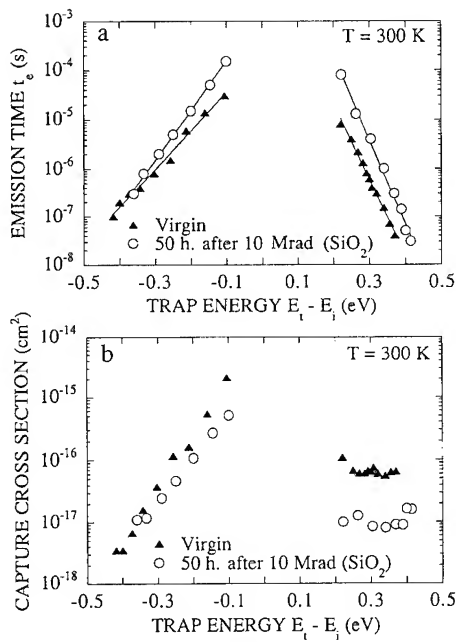


Fig. 3. Energy distribution of electron (above midgap) and hole (below midgap) emission times (a) and capture cross-sections (b) in the silicon band gap for a non-irradiated MOSFET (triangles) and for a MOSFET irradiated to 10 Mrad and annealed for 50 h at room temperature (open circles).

weakly dependent on energy and significantly decrease (about one decade) for irradiated devices with respect to virgin devices. This evolution is consistent with experimental observations in conductance technique [15,16]. In the case of hole traps, the changes in t_e and σ are not constant with respect to the trap energy level. The fact that capture cross-sections seem to be energy dependent before (and after) irradiation is perhaps due to the fabrication process that induces specific defects in the interfacial region. These defects may have an electrical behavior different from those of intrinsic interface defects [17], but this difference is presently unclear. Fig. 4 shows $D_{it}(E)$ spectra obtained from $Q_{it}(V_3)$ characteristics in emission (equilibrium) regime for various radiation exposure doses (the duration of $t_3 = 6$ ms determines the emission rate of the technique [17]). The curves exhibit two 'humps' of D_{it} at approximately $\sim E_v + 0.35$ eV and $\sim E_v + 0.75$ eV. These local increases of density in the band gap are very well correlated with

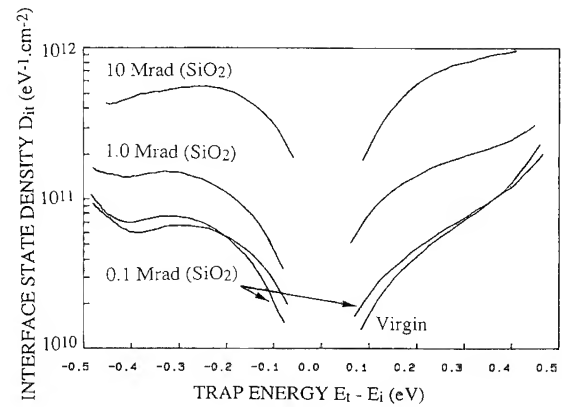


Fig. 4. Energy distributions of interface state density in silicon band gap obtained for transistors irradiated to different doses and annealed for 50 h at room temperature; $t_3 = 6$ ms.

the dose of irradiation and have been observed by many authors [2]. But this classical approach of 3CP measurement does not allow us to distinguish fast interface trap density from border trap density in the band gap.

To evaluate the contribution of these two categories of traps to the charge pumping response in emission regime, as shown in Fig. 1, we have performed two consecutive acquisitions of $Q_{it}(V_3)$ curves with two different values of t_3 . The first value (1.2 ms) was chosen to involve the greater part of fast states during the charge pumping cycle (see Fig. 1), whereas the second value 40 ms allows a part of border traps (the fastest traps that can communicate during this delay with the silicon) to participate in the recombination process. Subtracting the two curves and expressing the derivative of this result with respect to the surface potential and solving for D_{it} , we obtain a border trap distribution in the silicon band gap, similar to the fast state distribution, which refers to a given emission window. Fig. 5 shows such a border trap distribution estimated with this new method for an irradiated device. Two peaks of density that correspond preferentially to border traps clearly appear in the band gap: one above midgap ($\sim E_v + 0.74$ eV), the other below midgap ($\sim E_v + 0.36$ eV). Similar energy positions of D_{it} peaks induced by irradiation have been often reported by other authors using various techniques [2,18]; but, in this

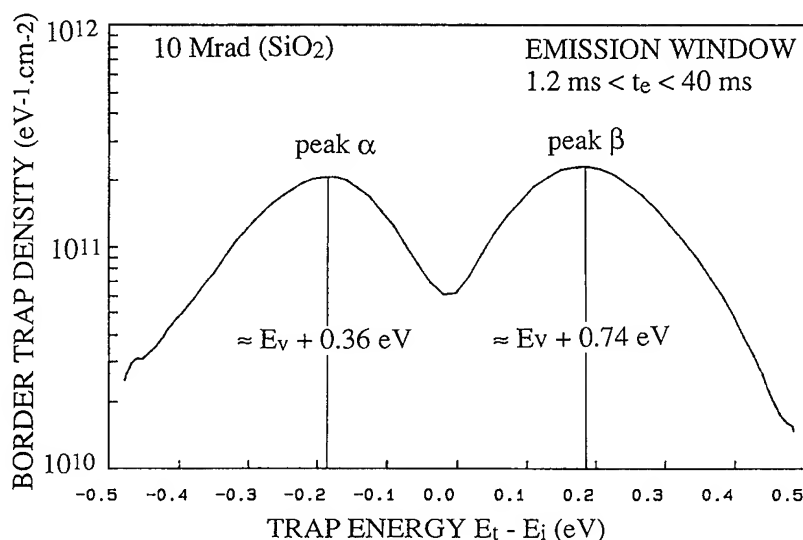


Fig. 5. Energy distribution of border trap density for emission times between 1.2 and 40 ms. This curve is calculated from the difference of two 3CP measurements, for two distinct values (1.2 and 40 ms) of the intermediate level in emission regime.

case, we can unambiguously say that these peaks are due to border traps instead of fast interface traps, in view of the emission window using in this method.

4. Conclusion

To our knowledge, this is the first 3-level charge pumping study carried out on irradiated devices, in spite of the fact that this technique can provide various information about interface traps concerning most of the band gap on a single device. We have observed the electrical behavior of interface traps and border traps by this technique and by standard charge pumping analysis in submicrometer *n*-channel MOSFETs, irradiated or not. For fast interface traps, a strong evolution of capture cross-sections has been observed after irradiation; the change of σ appears to be a function of energy trap level in the silicon band gap. For border traps, we have developed a modified 3CP method that provides the way to estimate quantitatively a trap distribution in the silicon band gap. An additional study is planned to investigate border traps in more detail with this new approach of charge pumping.

References

- [1] E.H. Nicollian, *J. Electron. Mater.* 21 (1992) 721.
- [2] T.P. Ma, *Microelectron. Eng.* 22 (1993) 197, and references therein.
- [3] R.E. Paulsen, R.R. Siergiej, M.L. French and M.H. White, *IEEE Electron Device Lett.* 13 (1992) 627.
- [4] D.M. Fleetwood, *IEEE Trans. Nucl. Sci.* NS-39 (1992) 269.
- [5] D.M. Fleetwood, P.S. Winokur, R.A. Reber, T.L. Meisenheimer, J.R. Schwank, M.R. Shaneyfelt and L.C. Riewe, *J. Appl. Phys.* 73 (1993) 5058, and references therein.
- [6] G. Groeseneken, H.E. Macs, N. Beltran and R.F. De Keersmaecker, *IEEE Trans. Electron Devices* 31 (1984) 42.
- [7] N.S. Saks and M.G. Ancona, *IEEE Trans. Electron Devices* 37 (1990) 1057.
- [8] M.G. Ancona and N.S. Saks, *J. Appl. Phys.* 71 (1992) 4415.
- [9] J.L. Autran and B. Balland, *Rev. Sci. Instrum.* 65 (1994) 2141.
- [10] J.L. Autran, B. Balland and L.M. Gaborieau, *IBM J. Res. Develop.* (1995) to be published.
- [11] R.F. Pierret and G. Panigrahi, *J. Appl. Phys.* 41 (1970) 2260.
- [12] G. Panigrahi, *Electron. Lett.* 9 (1973) 43.
- [13] B. Balland, *Instabilities in Silicon Devices*, ed. G. Barbotin and A. Vapaille (Elsevier, Amsterdam, 1989) ch. 10.
- [14] A. Roy, PhD dissertation, Lehigh University (1989).
- [15] W. Chen and T.P. Ma, *J. Appl. Phys.* 70 (1991) 860.
- [16] W. Chen, A. Balasinski and T.P. Ma, *IEEE Trans. Nucl. Sci.* 39 (1992) 2152.
- [17] J.L. Autran, F. Seigneur, C. Plossu and B. Balland, *J. Appl. Phys.* 74 (1993) 3932.
- [18] P.J. McWhorter, D.M. Fleetwood, R.A. Pastorek and G.T. Zimmerman, *IEEE Trans. Nucl. Sci.* 36 (1989) 1792.



ELSEVIER

Journal of Non-Crystalline Solids 187 (1995) 216–220

JOURNAL OF
NON-CRYSTALLINE SOLIDS

The no-thermal activation of the defect generation mechanism in a MOS structure

A. El-Hdiy^{a,*}, G. Salace^a, A. Meinertzhagen^b, M. Jourdain^b, C. Petit^{a,b}, A. Aassime^a

^aLaboratoire d'Analyse des Solides Surfaces et Interfaces (LASSI) and

^bLaboratoire d'Application de la Microélectronique (LAM), Université de Reims, BP 347, 51062 Reims cédex, France

Abstract

The oxide positive charge and the interface-state formation caused by a negative gate bias in a polycrystalline silicon gate-oxide-semiconductor capacitor versus injecting temperature in the range of 77–400 K is studied. It is found that the generation of both interface-states and oxide charge is temperature independent which indicates that the motion of each mobile species (as the hydrogen-related species) must be excluded. The formation of interface-states is linked to the break of Si–Si or Si–O distorted bonds at the Si/SiO₂ interface, and the generation of the oxide positive charge to the electron-emission from pre-existing or created neutral traps.

1. Introduction

On the topic of the defect generation in MOS structures, the oxide positive charge creation and the interface-state formation have been usually explained on the basis of two principal models: the hole process which consists in the hole creation and their possible conversion to interface-states [1–4]. The second called the hydrogen model consists in the hydrogen release in the bulk of the oxide and its migration to the Si/SiO₂ interface generating interface-states by depassivating Si–H bonds [5–7]. This second model was confirmed by SIMS experiments [5] and also by the thermal activation study of the defect creation in which the diffusion coefficient of the hydrogen in the gate oxide was reached

[8]. This study gives some further insight on these mechanisms.

2. Experimental procedure

2.1. Sample description

MOS capacitors used in this work were fabricated on a $\langle 100 \rangle$ silicon substrate doped with boron to $1.7 \times 10^{17} \text{ cm}^{-3}$ and thermally oxidized to 11 nm for thickness at 900°C for 5 min in O₂ + N₂(33%) gas, and then for 7 min in O₂ + N₂(30%) + HCl(3%) gas at the same temperature. Afterwards, samples were cooled for 30 min in N₂ gas to room temperature. They were submitted to boron implantation through the gate oxide to $3.5 \times 10^{12} \text{ cm}^{-2}$ under 40 keV to adjust the transistor threshold voltage (transistors and capacitors were fabricated in the same wafer). In the

* Corresponding author: Tel: +33 26 05 33 27. Telefax: +33 26 05 32 50. E-mail: lasssi@univ-reims.fr.

end, samples were annealed in a $H_2 + N_2$ gas at 450°C for 30 min. The gate area for the capacitors is $4 \times 10^{-4} \text{ cm}^2$.

2.2. Electrical measurements

Electrical damages were caused by high electric field stress at different temperatures in the range of 77–400 K. Electrons were injected into MOS capacitors under negative constant voltage, measured and integrated by a HP4140B picoammeter to give charge densities, N_{inj} , and energetic interface-state distributions were measured by the superimposition of high- and low-frequency capacitance voltage at room temperature [9].

3. Results

3.1. Interface-state generation

Fig. 1 shows the energy spectrum of the interface-states. This energetic distribution is approximately flat in the range of about 0.6 eV around the mid-gap. For each stress, the interface state density was taken at the mid-gap energy and represented according to the injected electron density. Fig. 2 shows the evolution of interface-state density with electron density for three high electric fields (11, 11.5 and 12 MV/cm). These kinetics do not follow the well-known exponential law but rather a combination of this first-order mechanism with a linear regime. Creation cross-section values have been obtained from a complete analysis [10].

3.2. Positive charge creation

Usually, Fowler–Nordheim stress creates both oxide positive and negative charge. The positive charge appears in the beginning of the stress and the negative one appears afterwards [11]. Fig. 3 shows the evolution of mid-gap voltage, V_{mg} , following the injection and Fig. 4 gives the evolution of current measured during the stress at a constant voltage. Both these evolutions show that there is an increase of the oxide positive charge at the beginning of the stress and, for a critical injection value (10^{19} cm^{-2}), a decrease of this net oxide

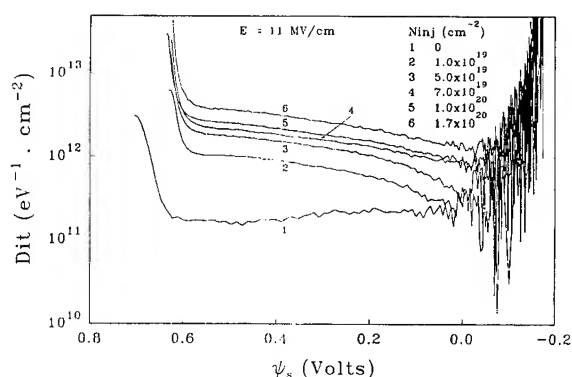


Fig. 1. Energetic distributions of interface-states in the silicon band gap for some electron densities injected in a MOS capacitor under 11 MV/cm at room temperature.

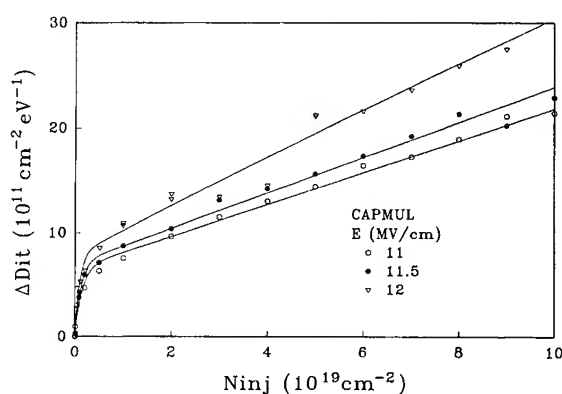


Fig. 2. Mid-gap interface-state density versus injected electron density at room temperature for some high electric fields.

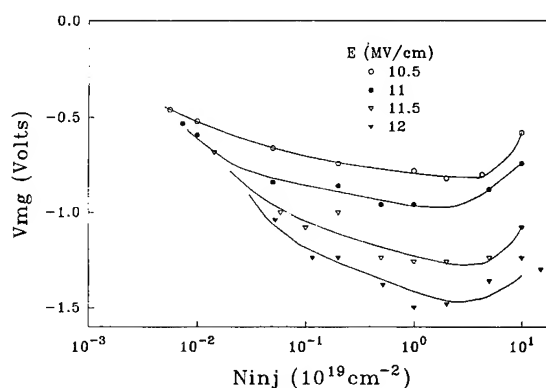


Fig. 3. Mid-gap voltage, V_{mg} , versus injected charge density, N_{inj} .

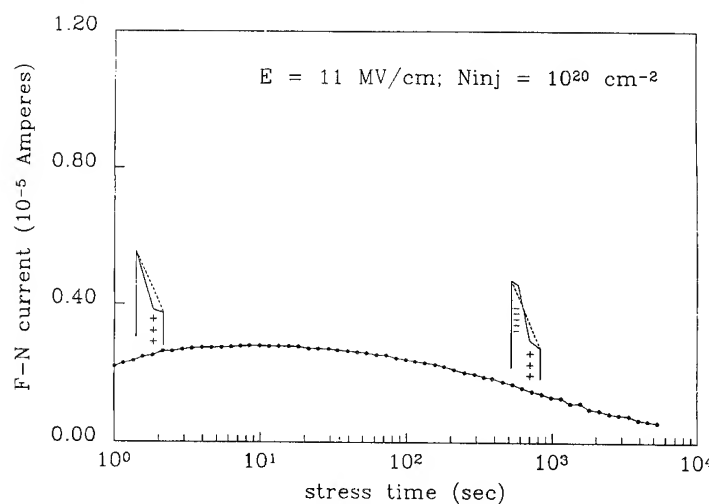
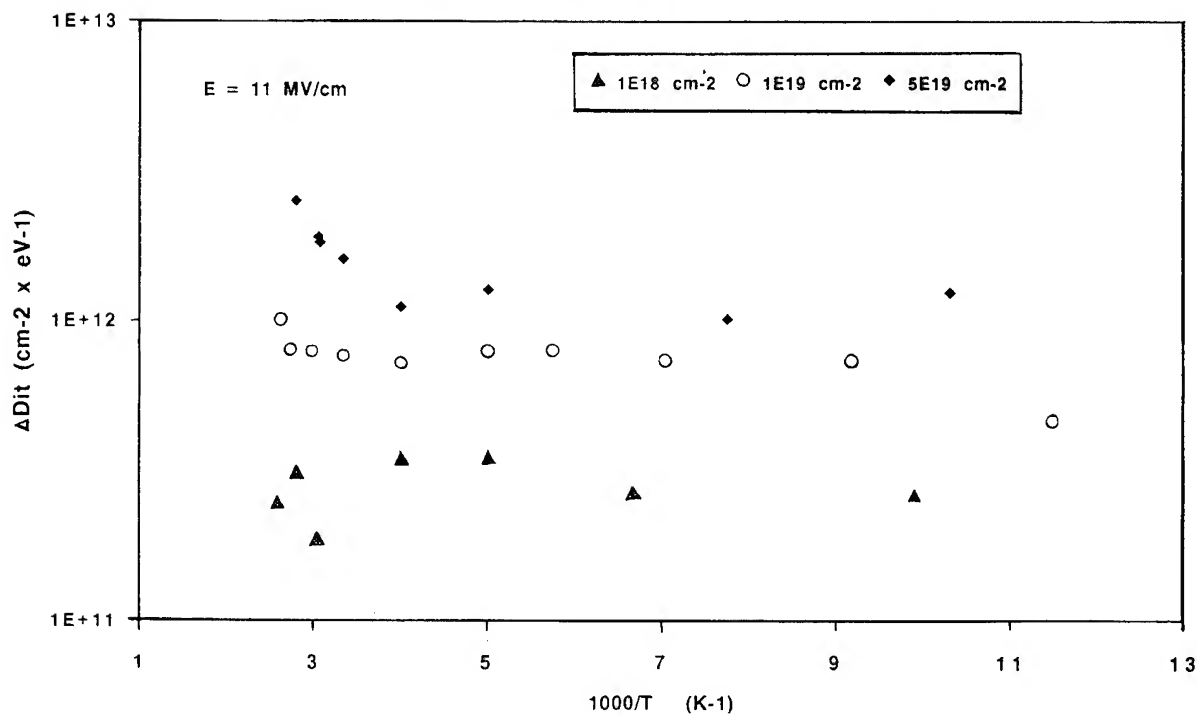


Fig. 4. Tunneling current versus stress time.

Fig. 5. Mid-gap interface-state density versus $1000/T$ (where T is the injecting temperature).

positive charge. This decrease is due to the creation and filling of neutral traps in the gate oxide by electrons during high field stress. It is remarkable to note that the injected charge density of 10^{19} cm^{-2} corresponding to the turnaround point in the

V_{mg} versus N_{inj} characteristics corresponds also to the dominance of the linear regime in the ΔD_{it} versus N_{inj} . Some authors have suggested that the production of trapped electron centers was required for subsequent production of interface-

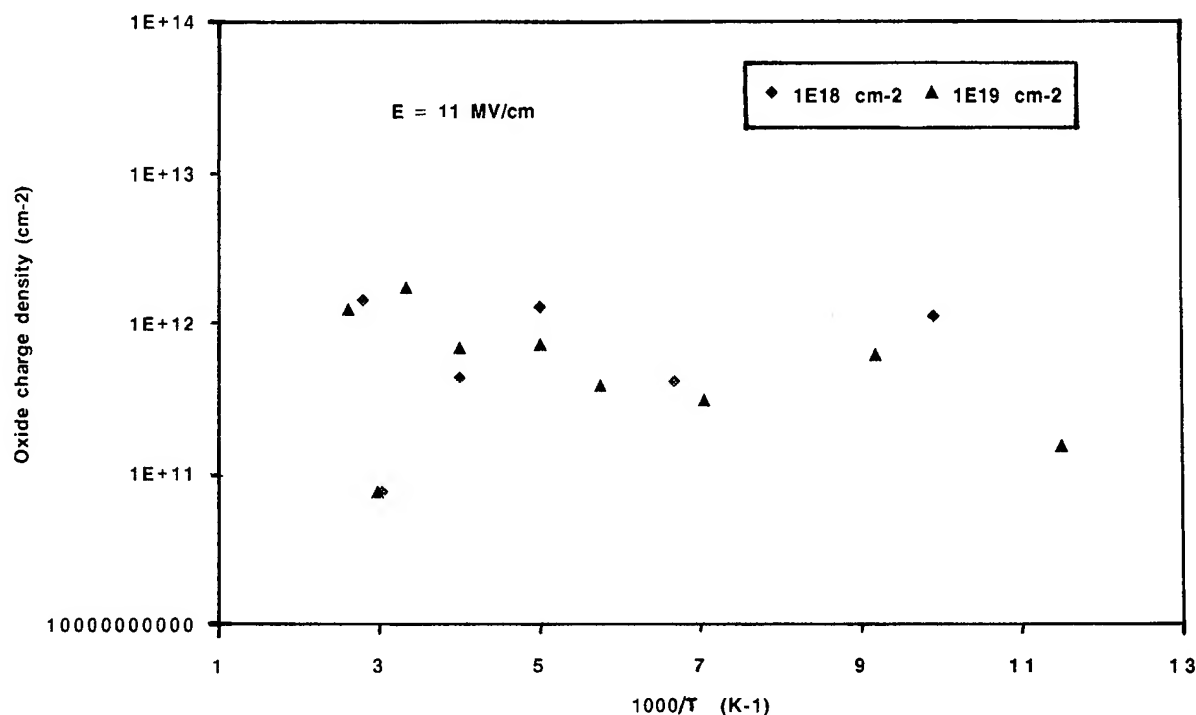


Fig. 6. Net oxide positive charge density versus $1000/T$ (where T is the injecting temperature).

states [12]. Our results indicate that the presence of negative charge is a direct or indirect precursor of appearance of the linear regime.

4. Discussion

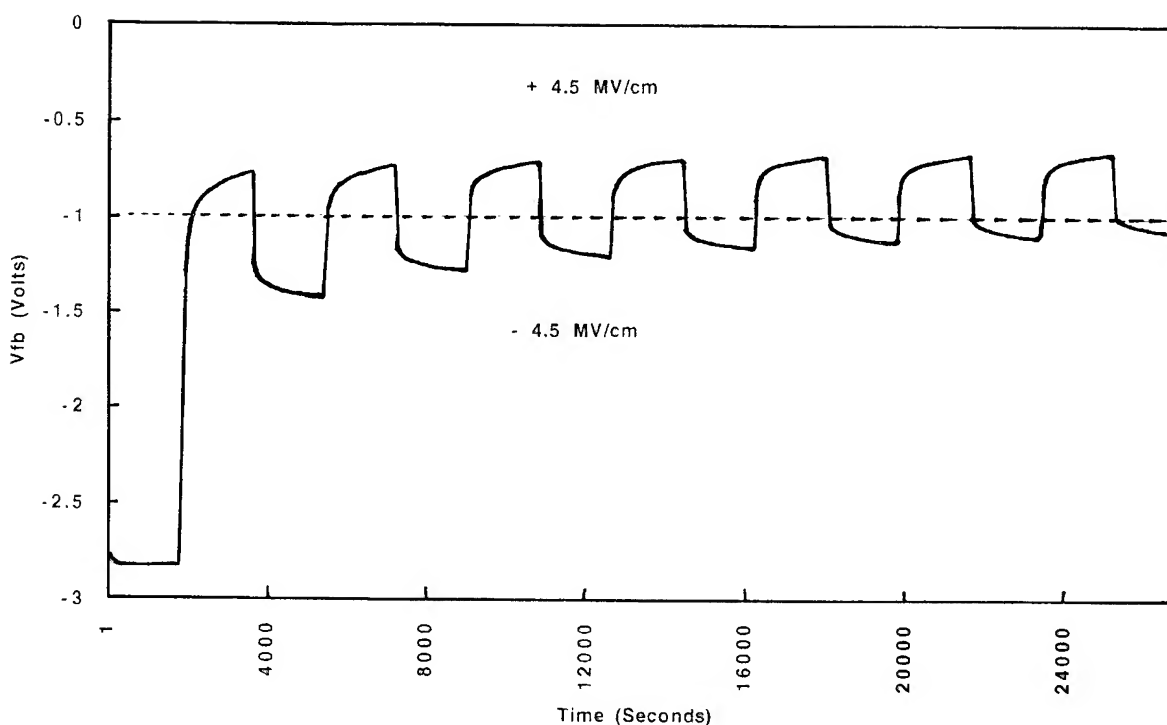
Fig. 5 shows the influence of the stress temperature on the interface-state generation for 11 MV/cm and for three injection values (10^{18} , 10^{19} and $5 \times 10^{19} \text{ cm}^{-2}$). Some authors have found that the interface-state density depends on the injecting temperature [8,13], but in this study it is obvious there is no thermal activation in temperature range from 77 to 400 K. For higher injecting temperatures, a weak increase occurs; however, if we assume that the stress temperature dependence of mid-gap interface-state density obeys an Arrhenius law [8,13], the activation energy calculated from Fig. 5 is about 5 meV. This energy is much lower than thermal energy ($k_B T/q$). This excludes the contribution of mobile species in the creation of inter-

face-states which is linked to the rupture of Si–Si and Si–O distorted bonds at the Si/SiO₂ interface.

As far as the net oxide positive charge is concerned, Fig. 6 shows no evidence for temperature playing an important role in the thermal activation of the generation mechanism. Some authors have suggested that the interaction of hydrogen with trapped holes induces the appearance of anomalous positive charge centers (APCs) in the bulk of the oxide [14]. In this work, created APCs represent more or less 30% of the generated positive charge (Fig. 7). This confirms our prior no thermal activation results and excludes the presence of mobile species in the bulk of the oxide. The generated positive charge is due to electron-emission from pre-existing or created neutral traps [15].

5. Conclusion

The no thermal activation of defect generation in MOS capacitors studied here allows us to exclude

Fig. 7. APC's variation under ± 4.5 MV/cm.

mobile species in the creation of oxide and interface defects. The responsible mechanisms of the oxide positive charge and interface-state generation are suggested to be electron-emission from neutral traps in the bulk of the oxide and the break of Si–Si and Si–O distorted bonds at the Si/SiO₂ interface, respectively.

References

- [1] G. Hu and W.C. Johnson, *Appl. Phys. Lett.* 36 (1980) 590.
- [2] S.K. Lai, *J. Appl. Phys.* 54 (1983) 2540.
- [3] S.J. Wang, J.M. Sung and S.A. Lyon, *Appl. Phys. Lett.* 52 (1988) 1431.
- [4] P.U. Kenkare and S.A. Lyon, *Appl. Phys. Lett.* 55 (1989) 2328.
- [5] R. Gale, F.J. Feigl, C.W. Magee and D.R. Young, *J. Appl. Phys.* 54 (1983) 6938.
- [6] D.J. DiMaria and J.W. Stasiak, *J. Appl. Phys.* 65 (1989) 2342.
- [7] D.A. Buchanan and D.J. DiMaria, *J. Appl. Phys.* 67 (1990) 7439.
- [8] D. Vuillaume, A. Mir, R. Bouchakour, M. Jourdain, A. El-Hdiy and G. Salace, *J. Appl. Phys.* 73 (1993) 277.
- [9] R. Castagné and A. Vapaille, *Surf. Sci.* 28 (1979) 557.
- [10] A. El-Hdiy, G. Salace, C. Petit, M. Jourdain and D. Vuillaume, *J. Appl. Phys.* 74 (1993) 1124.
- [11] P. Fazan, M. Dutoit, C. Martin and M. Ilegems, *Solid State Electron.* 30 (1987) 829.
- [12] F.J. Feigl, D.R. Young, D.J. DiMaria, S.K. Lai and J. Calise, *J. Appl. Phys.* 52 (1981) 5665.
- [13] M. Sakashita, S. Zaima and Y. Yasuda, *J. Appl. Phys.* 67 (1990) 6903.
- [14] Y. Roh, L. Trombetta and J. Stathis, *Microelectron. Eng.* 22 (1993) 227.
- [15] S.E. Thompson and T. Nishida, *J. Appl. Phys.* 72 (1992) 4683.



ELSEVIER

Journal of Non-Crystalline Solids 187 (1995) 221–226

JOURNAL OF
NON-CRYSTALLINE SOLIDS

A study comparing measurements of roughness of silicon and SiO₂ surfaces and interfaces using scanning probe microscopy and neutron reflectivity

A. Crossley^{a,*}, C. J. Sofield^a, J. P. Goff^b, A. C. I. Lake^b, M. T. Hutchings^a, A. Menelle^c

^aAEA Technology, 447 Harwell Laboratory, Harwell, Oxon OX11 0RA, UK

^bUniversity of Oxford, Department of Physics, Clarendon Laboratory, Parks Road, Oxford OX1 3PU, UK

^cLaboratoire Leon Brillouin, CE Saclay, 91191 Gif sur Yvette, France

Abstract

Ultrahigh vacuum scanning tunnelling microscopy (UHV-STM) and air/liquid atomic force microscopy (AFM) have been used to evaluate the roughness of silicon surfaces after they have been subjected to pre-gate oxide cleaning. The pre-gate oxide cleaning procedure has involved the removal of the 'native oxide' with solutions of buffered HF (BHF) and dilute HF (DHF). The DHF treatment of Si{100} surfaces has been found by UHV-STM to give the smoothest surfaces for pre-gate oxidation in accord with HREELS and IR studies. A comparison of roughness measurement by UHV-STM relative to air/liquid AFM is given to elucidate the relative merits of those techniques which have different spatial resolution. The MOS gate oxide performance is correlated with pre-gate oxide silicon surface roughness. Data published on the Si/SiO₂ interface roughness following growth of the gate oxide are inconsistent. A comparative study of interface roughness, determined with the gate oxide present, by neutron reflectivity experiments, and after removal of the gate oxide with DHF, by scanning probe measurements (SPM) is reported. Since the MOS performance may also depend on the SiO₂/contact interface roughness, roughness measurements of the SiO₂ gate oxide surface obtained using neutron reflectivity are also reported.

1. Introduction

The current drive to smaller MOS gate structures and thinner gate oxides in VLSI CMOS devices gives rise to the need for atomic scale control of the silicon/silicon oxide interface. Thus, there is a clear requirement for roughness measurements

with atomic resolution. The intrinsic roughness of the silicon surface prior to gate oxide growth is determined by factors such as the method of silicon wafer production and pre-gate oxide cleaning procedures. Rough silicon surfaces are known to degrade CMOS device yield and reliability [1–3]. For example, a single atomic step on a Si(100) surface is about 7% of the thickness of a 4 nm thick gate oxide and thus may give rise to a significant field enhancement, even for uniform oxide coverage. Scanning probe microscopies [4,5], particularly the

*Corresponding author. Tel: +44-235 433 108. Telefax: +44-235 433 029. E-mail: crossley@acat.co.uk.

scanning tunnelling microscope (STM) and the atomic force microscope (AFM) offer the required vertical resolution and, in the former case, the required spatial resolution.

Clearly, it is desirable to make measurements over the dimensions of a whole silicon wafer surface if issues of variability and device yield are to be addressed. However, current scanning probe methods are too time consuming to cover the atomic length scale over a whole wafer. Abe et al. [6] have found good agreement in average roughness measurements between laser scanning light scattering (LSLS), scanning optical microscopy (SOM), AFM and STM methods despite the very different roughness length scales samples.

In order to understand the relation between silicon surface roughness and gate oxide integrity it would be useful to know whether or not the oxidation process changes the surface roughness at the growing oxide/silicon interface and also how smooth the oxide surface is on which the electrical contact is deposited in an MOS structure. The neutron reflectivity technique is capable of probing the SiO_2 thickness and density, and the Si/SiO_2 interface roughness. However, it is limited to oxides greater than 20 nm. This limit is set primarily by the source intensity.

In order to apply scanning probe microscopy to assess the Si/SiO_2 interface roughness the oxide must first be removed by etching with HF solution

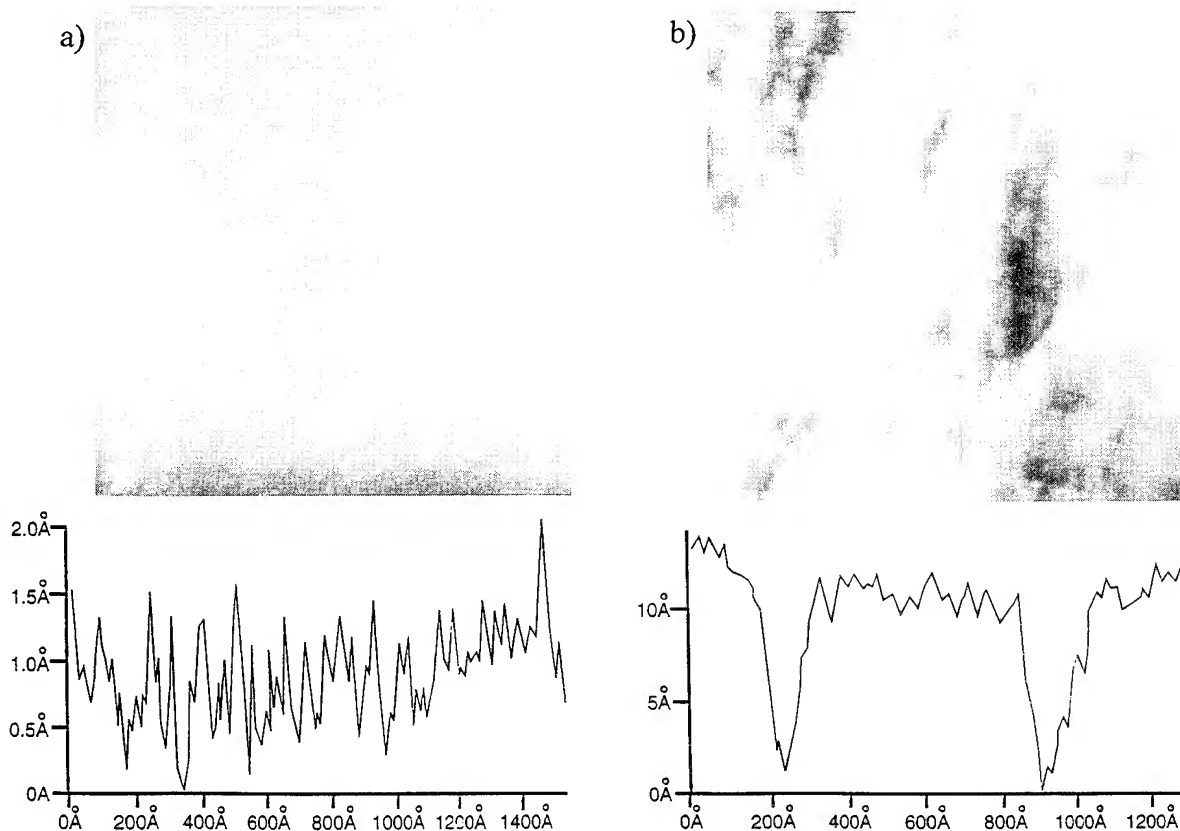


Fig. 1. STM images $0.1 \mu\text{m} \times 0.1 \mu\text{m}$, taken from (a) $\text{Si}(111)$ wafer dipped in 7:1 BHF followed by a 5 min DI water rinse and (b) $\text{Si}(100)$ wafer dipped in 7:1 BHF followed by a 5 min DI water rinse. (Samples bias +2.0 V, tunnelling current 2 nA.) Line scans taken diagonally across the images are also shown.

until the wafer is hydrophobic, and then the surface profile measured. Great care has to be exercised in the control of the HF solution strength, purity and subsequent water rinsing to avoid confounding effects from silicon surface etching [7]. HF etching and AFM/STM measurements of roughness are relatively fast to make. However, data on the Si/SiO₂ interface roughness following growth of the gate oxide are inconsistent [8–10].

This paper reports measurements of silicon surface roughness before and after oxidation by SPM, and preliminary Si/SiO₂ surface and interfacial roughness by neutron reflectivity.

2. Experimental procedures

The silicon wafers were supplied by Wacker-Chemitronic GmbH. Two Si(100) 3" wafers (1.5–2.5 Ω cm) and one Si(111) 3" wafer (6–9 Ω cm) were used for the neutron reflectivity experiments. Wafers were prepared in a class 100 clean room. Prior to oxide growth the wafers were dipped in HF of different pH until hydrophobic, then rinsed in DI water. One (100) wafer was dipped in 7:1 buffered HF (BHF) and the other in 10:1 dilute HF (DHF). The (111) wafer was dipped in BHF. The SiO₂ was grown in oxygen at 900 °C for 70 min. The oxide thickness, measured by ellipsometry, was found to be: Si(100)/BHF, 232 Å; Si(100)/DHF, 214 Å and; Si(111)/BHF, 357 Å. For the SPM experiments small pieces (~ 1 cm \times 1 cm) were cut from 4" wafers ((100) and (111)) of hyperpure silicon. The wafers were examined before and after dipping in BHF and DHF.

The neutron reflectivity measurements were performed using the white beam time-of-flight neutron reflectometer, EROS, at Saclay. Scanning tunnelling microscopy experiments were performed in UHV using an Omicron STM. Samples were introduced into the UHV chamber, via a load lock pumped with a turbomolecular pump. Samples were examined 'as inserted' and after degassing ($T \sim 200$ °C) overnight. This procedure generally gave better images. Sample bias voltages of 2–3 V, tunnelling current ~ 2 nA were typically used. An

East Coast Scientific instrument was used for the AFM studies. Measurements were taken in contact mode in liquid (2-butoxyethanol).

3. Results

Fig. 1 shows STM images and line scans obtained from Si(111) and Si(100) wafers dipped in BHF then DI water rinsed. Table 1 lists AFM RMS roughness measurements calculated from Si(100) and Si(111) 'as received' and after dipping in HF. Table 1 also lists the roughness measurements for the Si/SiO₂ interface from the samples used in the neutron experiments, after removal of the thermally grown oxide with dilute HF. Corresponding atomic force microscopy images from these samples and from Si(100) 'as received' are shown in Fig. 2. Fig. 3 shows the neutron reflectivity profiles obtained from silicon wafers with 200–300 Å of thermally grown SiO₂.

Table 1
AFM roughness measurements for Si(100) and Si(111) wafers 'as received' and after HF dipping followed by DI rinsing

Sample	Treatment	Scan size (μ m)	RMS (Å)
Si(100)	"as received"	1.0	0.77
		0.6	0.79
Si(100)	BHF/DI	4.0	1.28
		1.0	1.17
Si(100)	DHF/DI	0.6	1.18
		4.0	1.49
Si(100)		1.0	1.18
		0.6	1.06
Si(111)	"as received"	1.0	1.42
		0.6	1.22
Si(100) ^a	BHF/DI	1.0	1.8
		0.6	1.7
Si(100) ^a	DHF/DI	4.0	2.76
		1.0	1.99 \pm 0.01
Si(100) ^a		0.6	1.5 \pm 0.09
		1.0	1.79
Si(111) ^a	BHF/DI	1.0	1.79
		0.6	1.26 \pm 0.22

^a Si samples used in the neutron reflectivity experiment, after removal of the thermally grown oxide with dilute HF.

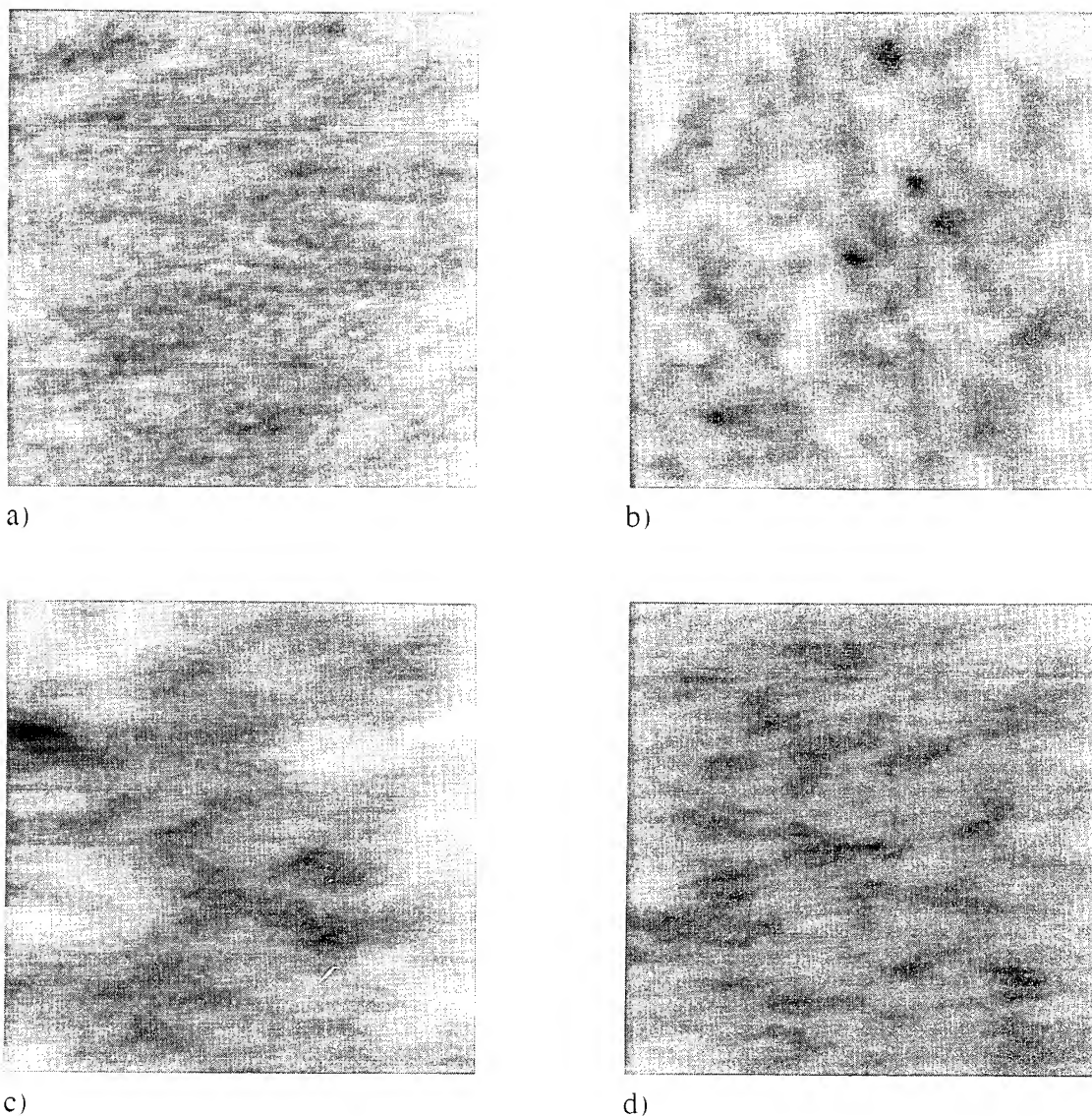


Fig. 2. AFM images, $0.6 \times 0.6 \mu\text{m}$, taken in 2-butoxy-ethanol from (a) Si(100) 'as received', RMS 0.79 \AA ; (b) Si(100) dipped in 7:1 BHF prior to thermal oxidation, oxide removed with 10:1 DHF, RMS 1.7 \AA ; (c) Si(100) dipped in 10:1 DHF prior to thermal oxidation, oxide removed with 10:1 DHF, RMS 1.42 \AA ; and (d) Si(111) dipped in 7:1 BHF prior to thermal oxidation, oxide removed with 10:1 DHF, RMS 1.28 \AA .

4. Discussion

The Si(111) wafer was extremely flat over the 2000 \AA maximum STM scan length. This is in agreement with previous observations of BHF smoothing Si(111) surfaces and roughening

Si(100) [7,11] and is attributed to preferential etching of Si(111) by HF solutions of higher pH. Atomic resolution on H-terminated Si(111) has been observed by other authors [12,13] but was not observed in the present study. Etch pits, 1 nm deep, 10 nm wide were observed on the Si(100) wafer

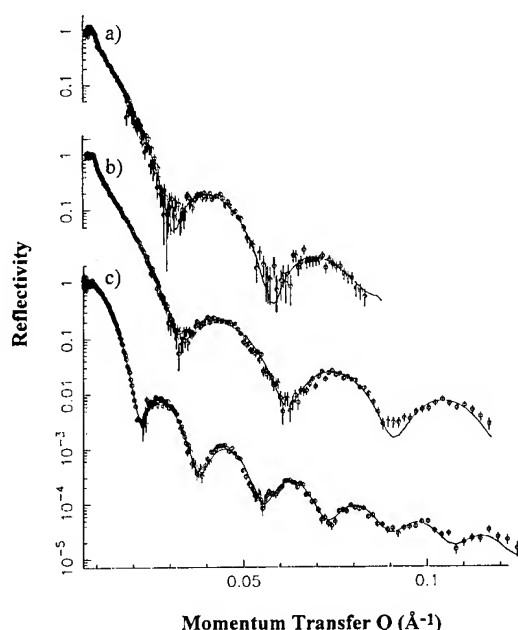


Fig. 3. Neutron reflectivity profiles for silicon samples with 200–300 Å gate oxide, after various pre-gate oxide treatments: (a) Si[100] dipped in BHF; (b) Si[100] dipped in DHF; and (c) Si[111] dipped in BHF.

dipped in BHF. It is doubtful that such small features could be detected by AFM.

The roughness parameter is dependent on the length scale of the scan. On the smallest scale measured ($0.6 \times 0.6 \mu\text{m}$) the RMS roughness is greatest, as expected, for Si(100) dipped in BHF. This remains the case after removal for the thermally grown oxide. The Si(100) surface, after removal of the 'native oxide' was also rougher than the 'as received' wafer. It is impossible to compare directly the wafers used in the neutron experiments with those examined 'as received' since these came from different batches. Further studies are in progress using epitaxially grown silicon wafers.

Rocking curves for Si(111)/BHF and Si(100)/DHF showed that these samples used in the neutron reflectivity experiments were macroscopically flat, within instrumental resolution. However, broadening of the rocking curve for the Si(100)/BHF showed large-scale surface undulations, i.e., on a scale large compared to the coherence length of the neutron ($\sim 10 \mu\text{m}$). To a first

approximation these can be modelled as a deterioration in angular resolution.

The reflectivity profiles (Fig. 3) clearly show the interference fringes from the SiO_2 layer. When the scattered wave is small compared to the incident wave, the interference effects can be described in terms of a refractive index n given by

$$n = 1 - \frac{\lambda^2}{2\pi} Nb, \quad (1)$$

where N is the atomic number density, b is the bound coherent neutron scattering length and λ is the wavelength of the neutron. The form of the neutron reflectivity as a function of wave vector transfer Q perpendicular to the surface is determined by the refractive index profile normal to the surface. This may be related by Eq. (1) to the layer thickness, densities and roughness at the interfaces. A preliminary analysis indicates that the layer density is consistent with amorphous SiO_2 , and the overall layer thicknesses are 224, 205 and 356 Å for Si(100)/BHF, Si(100)/DHF and Si(111)/BHF respectively, in good agreement with the ellipsometry measurements. The Gaussian interfacial roughnesses are all small ($< 4 \text{ Å}$). The oxide surface of the Si(100)/BHF sample was found to be the roughest ($\sim 12 \text{ Å}$). Initial analysis of the data from Si(111)/BHF gave a higher interfacial roughness than the other two samples. This was a surprising result in view of the SPM data. However, it is possible that the deviation from a perfectly sharp interface suggested by the fit to the data may be due to the presence of an intermediate layer. A full analysis of the data, investigating the possibility of intermediate layers is underway and will be reported in elsewhere.

5. Conclusions

Our results are in general agreement with previous published studies utilising other characterisation techniques. We conclude from our results the following.

Removing the native oxide with BHF leaves a roughened Si(100) surface and a smoother Si(111) surface. There is also evidence for some increased roughness after dipping Si(100) in DHF.

Evidence suggests that a rough silicon surface leads to a rough oxide surface.

AFM measurements of roughness are fast to make but the lateral resolution might not be good enough to pick out individual atomic scale defects which might be responsible for break down of gate oxides. STM offers the best overall lateral resolution but images are degraded on Si wafer samples without further in vacuo treatment. In general, the scan area is too small to be truly representative of a wafer surface.

Using SPM to study buried Si/SiO₂ interfaces the SiO₂ must first be removed using HF. Great care has to be exercised in the control of the HF solution strength, purity and subsequent water rinsing to avoid confounding effects from Si surface etching.

Neutron reflectivity has slightly poorer resolution than SPM for simple roughness measurements, though the fact that this technique can probe the buried interface makes it worth pursuing. The major benefit of the neutron reflectivity technique is the potential characterisation of the oxide layer, near the interface. This is becoming increasingly important as gate oxides decrease in thickness.

This work was funded by AEA Technology Corporate Research Programme and the CEC under the ESPRIT Basic Research Action 6108 (ASSIST). The authors thank Dr Dieter Gräf at Wacker Chemitronic for supplying some of the silicon wafers used in this study. They also thank Dr A. M. Stoneham for helpful discussions.

References

- [1] M. Heyns, C. Hasenack, R. De Keersmaecker and R. Falster, in: *Proc. 1st Int. Symp. on Cleaning Technology in Semiconductor Device Manufacturing*, Fall ECS (1989), ed. J. Ruzyllo and R. E. Novak, PV 90–9 (Electrochemical Society, Pennington, NJ, 1990) p. 293.
- [2] M. Miyashita, T. Tusga, K. Makiyara and T. Ohmi, *J. Electrochem. Soc.* 139 (1992) 2133.
- [3] C.J. Sofield, M.P. Murrell, S. Sugden, M. Heyns, S. Verhaverbeke, M.E. Welland, B. Golan and J. Barnes, in: *Proc. Spring Meeting MRS*, San Francisco, CA, 1992.
- [4] G. Binnig and H. Rohrer, *IBM J. Res. Develop.* 30 (1986) 355.
- [5] M. Komiyama, M. Kirino and H. Kurokawa, *Jpn. J. Appl. Phys.* 32 (1993) 2934.
- [6] T. Abe, E. F. Steigmeier, W. Hagleitner and A. J. Pidduck, *Jpn. J. Appl. Phys.* 31 (1992) 721.
- [7] S. Verhaverbeke, H. Bender, M. Meuris, P. W. Mertens, H. F. Schmidt and M. M. Heyns, in: *Proc. Spring Meeting MRS*, San Francisco, CA, 1993.
- [8] K. Nakamura, K. Ohmi, K. Yamamoto, K. Makiyara and T. Ohmi, in: *Extended Abstracts, Int. Conf. on Solid State Devices and Materials*, Chiba, Japan (1993).
- [9] Y. Homma, M. Suzuki and N. Yabumoto, *J. Vac. Sci. Technol.* A10 (1992) 2055.
- [10] V. Nayar, R. Jackson, A. J. Pidduck and C. Pickering, in: *Phys. Chem. of SiO₂ and Si–SiO₂ Int.* 2, ed. Helms and Deal (Plenum, New York, 1993).
- [11] D. Graf, S. Bauer-Mayer and A. Schnedd, *J. Vac. Sci. Technol.* A11 (1993) 4.
- [12] G.S. Higashi, R.S. Becker, Y.J. Chabal and A.J. Becker, *Appl. Phys. Lett.* 58 (1991) 1656.
- [13] H.E. Hessel, A. Feltz, M. Reiter, U. Memmert and R.J. Behm, *Chem. Phys. Lett.* 186 (1991) 275.



ELSEVIER

Journal of Non-Crystalline Solids 187 (1995) 227–231

JOURNAL OF
NON-CRYSTALLINE SOLIDS

Characterization of ion-implanted silicon-insulator interfaces by reflected optical second harmonic generation

I.V. Kravetsky*, L.L. Kulyuk, A.V. Micu, V.I. Tsytsanu, I.S. Vieru

Institute of Applied Physics, Academic str. 5, Kishinau 277028, Moldova

Abstract

Optical second harmonic generation has been applied for the study of the ion-implanted $\text{SiO}_2/\text{Si}(111)$ interface and $\text{Si}(111)$ surfaces. Experimental results of real-time measurements of the second harmonic generation signal during thermal oxide etching are presented and analyzed taking into consideration various contributions to the non-linear-optical response from oxide/silicon interface such as the silicon substrate, the static electric field, the inhomogeneous deformation and the crystalline oxide interlayer. The symmetry properties of the thermal oxide/ $\text{Si}(111)$ interface have also been studied by measuring the rotational dependences of the second harmonic generation signal before and after oxide etching. It is shown that second harmonic rotational anisotropy and intensity strongly depend on the disordering of the interface and surface induced by ion implantation.

1. Introduction

The insulator/silicon interface structure is of great interest from both fundamental and technological point of view and has therefore stimulated theoretical and experimental research [1–3]. On the other hand, the increased use of ion implantation in electronic device fabrication has increased interest in diagnostic techniques capable of probing both the implanted ion depth distribution and the structural changes produced by the implantation on silicon surfaces and interfaces. Optical techniques are particularly attractive here, since they

are non-destructive and contactless. At the same time, these techniques can be used to make real-time measurements with high spatial resolution. Optical second harmonic generation (SHG), in particular, has been identified as a versatile and sensitive probe for surfaces and interfaces [4–6]. This laser-based method has the advantage of being applicable to any object accessible by laser beam and can be used for the control of the technological processes in liquids and at the relatively high gas pressure conditions (conventional surface sensitive techniques are not appropriate for this purpose). This method is especially useful in the case of materials with inversion symmetry (e.g., Si and Ge) because the SHG process is electric dipole forbidden within the bulk of the centrosymmetric media, but allowed in the near-surface region where the inversion symmetry is broken [7]. The SHG

* Corresponding author. Tel: +373-2 739 513. Telefax: +373-2 738 149. E-mail: igor@icm.moldova.su.

method is very suitable for the study of the surface and interface symmetry as well as for the study of changes in these symmetries which occur at phase transformations and at any surface modifying process [8–10].

In this paper we report the experimental results obtained by probing ion-implanted thermal oxide/silicon interface structure as well as the silicon surfaces by the SHG method.

2. Experimental procedure

In our experiments, the Si(111) and SiO₂/Si(111) samples implanted with BF₂⁺ and As⁺ ions with energy of 130 keV and doses of 10¹³–10¹⁵ cm^{−2} were studied. The thermal oxide thickness was ≈ 100 nm. Thermal annealing of the investigated samples was carried out in an ultrahigh vacuum chamber at a base pressure of ≈ 10^{−10} Torr at the temperature of ≈ 600°C. For the SHG experiments, a Q-switched YAG: Nd³⁺ (neodymium-doped yttrium aluminum garnet) laser operating at λ_ω = 1064 nm and producing 15 nm pulses at a 5 Hz repetition rate was used. The s-polarized (i.e., polarized perpendicularly to the plane of incidence) laser radiation was incident at an angle of ≈ 45° onto the sample surface. The power density (≈ 50 MW cm^{−2}) was well below that of the threshold of any laser-induced damages in the surface. The reflected SHG signal at λ_{2ω} = 532 nm was detected by a photomultiplier and a standard boxcar-integrator technique after being isolated by appropriate spectral filtering.

The symmetry properties of the ion-implanted SiO₂/Si(111) interface (before and after oxide etching) and Si(111) surfaces (before and after thermal annealing) were probed by measuring the SHG intensity while the samples were rotated about their normal at a constant rate. The rotation angle φ was defined as the angle between the plane of incidence and the projection of the crystallographic axis [100] on the (111) plane.

The study of SiO₂/Si(111) interface structure which is based on the in situ control of the slow chemical etching process of oxide layer by the SHG method was carried out. The sample located in an optical cell was treated with the solution

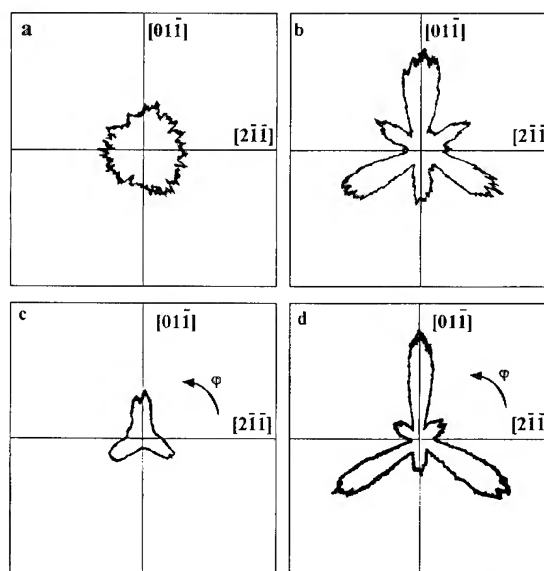


Fig. 1. p-polarized SH intensity from Si(111) implanted with BF₂⁺ (a, b) and As⁺ (c, d) ions with an energy of 130 keV and dose of 10¹⁵ cm^{−2} before (a, c) and after (b, d) thermal annealing, respectively, as a function of the sample rotation angle φ.

(H₂O + NH₄F + HF) at room temperature and was simultaneously subjected to pump radiation at 45° incidence. The etching rate varied from 10 to 1 nm min^{−1} depending on the reagent concentration. The experimental conditions excluded photochemical etching [11].

3. Results

Fig. 1 shows p-polarized (i.e., polarized in parallel to the plane of incidence) SH intensity from Si(111) implanted with BF₂⁺ and As⁺ ions with a dose of 10¹⁵ cm^{−2} before (Figs. 1(a) and (c)) and after (Figs. 1(b) and (d)) thermal annealing, respectively, as a function of the sample rotation angle φ in the polar coordinate system. It should be noted that in the case of the initial Si(111) surface (assumed C_{3v} symmetry), the I_{2ω}(φ) dependence is well approximated by (A + B cos 3φ)² for p-polarized SHG light, where the isotropic contribution A (it does not depend on the angle φ) is much less than the anisotropic contribution B to the SHG and, therefore, shows six equally spaced peaks [12].

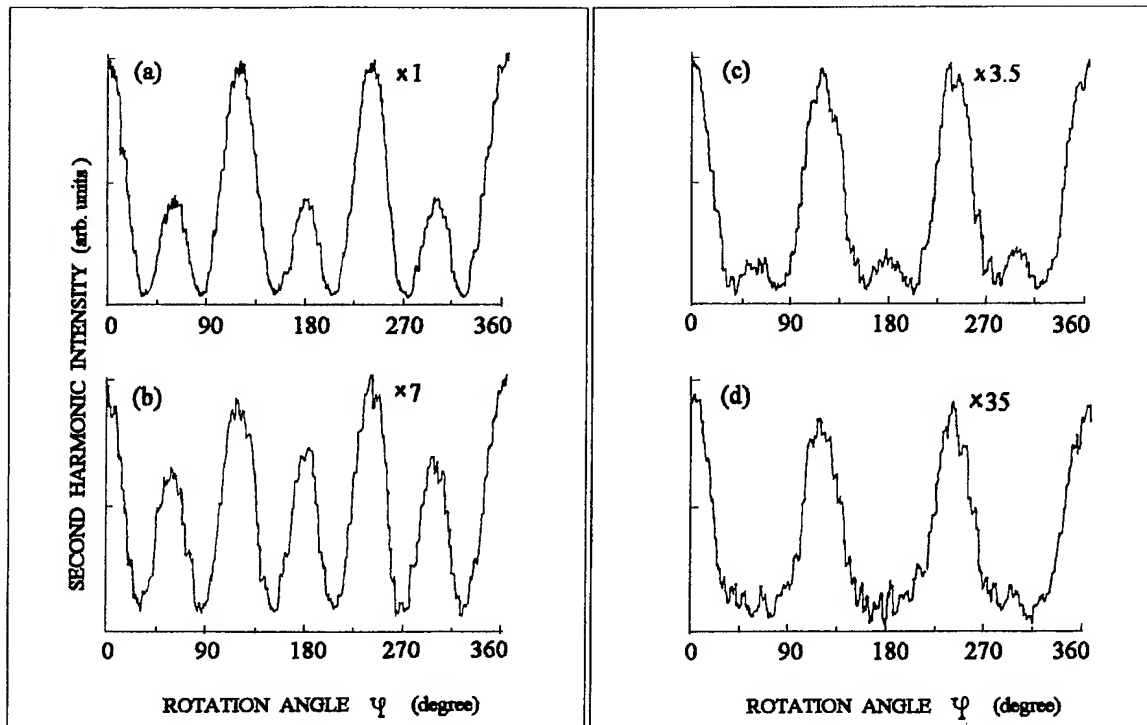


Fig. 2. p-polarized SH intensity from $\text{SiO}_2/\text{Si}(111)$ samples implanted with BF_2^+ with an energy of 130 keV: with a dose of 10^{14} cm^{-2} before (a) and after (b) thermal oxide etching, with a dose of 10^{15} cm^{-2} before (c) and after (d) thermal oxide etching as a function of the sample rotation angle φ . The initial oxide thickness is $\approx 100 \text{ nm}$.

Fig. 2 shows p-polarized SH intensity from $\text{SiO}_2/\text{Si}(111)$ samples implanted with BF_2^+ with a dose of 10^{14} cm^{-2} before (Fig. 2(a)) and after (Fig. 2(b)) oxide etching as well as with a dose of 10^{15} cm^{-2} before (Fig. 2(c)) and after (Fig. 2(d)) oxide etching, respectively, as a function of the sample rotation angle φ .

To probe the $\text{SiO}_2/\text{Si}(111)$ interface structure the real-time measurements of the second harmonic generation signal during thermal oxide etching were carried out. The intensity of the reflected pump radiation at $\lambda_w = 1064 \text{ nm}$ did not change during the oxide etching, which proves the uniformity of the etching process and absence of considerable interference effects in the oxide film. The etching rate was $V = (6 \pm 1) \text{ nm min}^{-1}$. Assuming that the etching process is linear [13], we transformed $I_{2\omega}(t)$ to $I_{2\omega}(d_{\text{OX}})$, where oxide thickness $d_{\text{OX}} = d_{\text{in}} - Vt$ (where d_{in} is initial thermal oxide

thickness, t is the etching time). Fig. 3 shows the p-polarized SH intensity reflected from $\text{SiO}_2/\text{Si}(111)$ samples implanted with BF_2^+ with doses of $D = 10^{14} \text{ cm}^{-2}$ (curve 1) and $D = 10^{15} \text{ cm}^{-2}$ (curve 2) as a function of the oxide thickness.

4. Discussion

It is seen that the $I_{2\omega}(\varphi)$ dependences change considerably: the threefold (111) symmetry is clearly broken (see Figs. 1(a) and (c)), but after thermal annealing the symmetry is reconstructed (Figs. 1(b) and (d)). It is also seen (comparing Fig. 1(a) with Fig. 1(c)) that implantation of BF_2^+ changes the $\text{Si}(111)$ symmetry more than the implantation of As^+ ions. For s-s polarization geometry (s-polarized SHG signal is registered) only a weak isotropic signal was detected from both

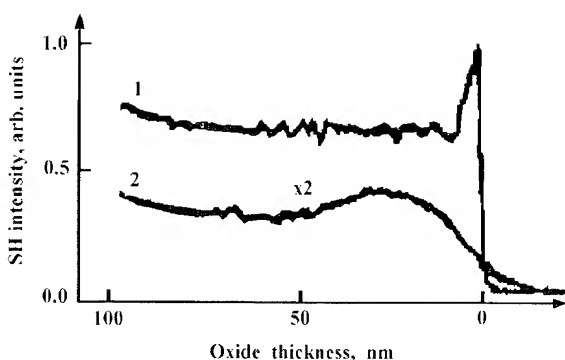


Fig. 3. Variation of the SH intensity reflected from $\text{SiO}_2/\text{Si}(111)$ samples implanted with BF_2^+ with an energy of 130 keV and doses of $D = 10^{14} \text{ cm}^{-2}$ (curve 1) and $D = 10^{15} \text{ cm}^{-2}$ (curve 2) during thermal oxide etching. The initial oxide thickness is $\approx 100 \text{ nm}$.

BF_2^+ and As^+ implanted $\text{Si}(111)$ samples, but after thermal annealing the symmetry properties of $\text{Si}(111)$ were reconstructed and corresponded to initial not implanted $\text{Si}(111)$ symmetry. The s-polarized SHG intensity was proportional to $\sin^2(3\varphi)$ and thus showed six equivalent maxima that were equally spaced [9, 12].

The results obtained (see Fig. 2) show a strong effect of the ion implantation on the redistribution of the peak amplitudes (compare Fig. 2(a) with Fig. 2(c)). It was observed that the increasing of the implantation dose leads to the increasing of the SHG isotropic contribution which is connected with the increase of the interface disordering induced by ion implantation.

Examining the $I_{2\omega}(d_{\text{OX}})$ dependences in Fig. 3, we suppose that the slight drop at the beginning of both curves 1 and 2 is connected with the decrease in the thermoelastic strain contribution to the SHG [2] as well as in the contribution of the static electric field which takes place in the oxide/silicon interface [14, 15]. It is known that maximum thermoelastic strain concentration ($\sim 10 \text{ kbar}$) is on the SiO_2/Si interface [2]. Therefore, when the oxide layer is becoming very thin, the thermoelastic strain breaks off it, which induces the creation of the microcrystal oxide islands. Such island-shaped crystalline regions, in their turn, can cause an increase in the reflected SH signal [16] (see the peak in

curve 1). The abrupt decrease of the SH intensity (curve 1) at the end of the etching process shows that the non-linear response is mainly determined by the thin transition oxide layer of $\approx 5 \text{ nm}$ thickness as well as that the $\text{SiO}_2/\text{Si}(111)$ interface is sharp within an atomic dimension [1, 17, 18]. The silicon substrate contribution to the nonlinear response of the BF_2^+ implanted $\text{SiO}_2/\text{Si}(111)$ interface is $\approx 15\%$ of the total value.

The different behavior of the SH intensity in the case of $\text{SiO}_2/\text{Si}(111)$ sample implanted with $D = 10^{15} \text{ cm}^{-2}$ (curve 2) suggests that the dose of 10^{15} cm^{-2} is enough to destroy the interface sharpness and to relax the thermoelastic strains on the interface. So the monotonic decrease of SH intensity at the end of the etching process is observed (curve 2). In this case, non-linear optical response is mainly determined by the oxide layer of $\approx 25 \text{ nm}$ thickness and the silicon substrate contribution to the non-linear response of the ion-implanted $\text{SiO}_2/\text{Si}(111)$ interface does not exceed 10% of the total value.

5. Conclusions

The in situ control of the selective etching of the thermal oxide made it possible to discover the qualitative difference between the non-linear-optical responses from $\text{SiO}_2/\text{Si}(111)$ interfaces implanted with BF_2^+ in doses of 10^{14} cm^{-2} and 10^{15} cm^{-2} . In both cases the non-linear optical response is mainly determined by the transition oxide layer ($\approx 5 \text{ nm}$ and $\approx 25 \text{ nm}$) which is adjacent to silicon substrate. The high contribution of this layer to the SHG can be explained by the existence of a space-charge region [14, 15] and a crystalline oxide interlayer with non-centrosymmetric structures [1, 17] situated between a thick amorphous oxide layer and the silicon substrate. It is shown that SHG method is sensitive and suitable for the characterization of ion-implanted silicon surfaces and thermal oxide/silicon interface structures. The correlation between isotropic and anisotropic contributions to the SHG could be used as quantitative criteria for the surface and interface disordering induced by ion implantation or other factors.

References

- [1] A. Ourmazd, P.H. Fuoss, J. Bevk and J.F. Morar, *Appl. Surf. Sci.* 41&42 (1989) 365.
- [2] S.V. Govorcov, V.I. Emel'yanov, N.I. Koroteev, G.I. Petrov, I.L. Shumay and V.V. Yakovlev, *J. Opt. Soc. Am. B6* (1989) 1117.
- [3] B. Schubert, P. Avouris and R. Hoffmann, *J. Chem. Phys.* 98 (1993) 7593.
- [4] J.F. McGilp, *J. Phys.: Condens. Matter* 2 (1990) 7985.
- [5] G. Lupke, D.J. Bottomley and H.M. van Driel, *Phys. Rev. B47* (1993) 10 389.
- [6] T.F. Heinz, M.M.T. Loy and W.A. Thompson, *J. Vac. Sci. Technol. B3* (1985) 1467.
- [7] Y.R. Shen, *The Principles of Nonlinear Optics* (Wiley, New York, 1984).
- [8] T.F. Heinz, M.M.T. Loy and W.A. Thompson, *Phys. Rev. Lett.* 54 (1985) 63.
- [9] C.W. van Hasselt, M.A. Verheijen and Th. Rasing, *Phys. Rev. B42* (1990) 9263.
- [10] G.G. Malliaras, H.A. Wierenga and Th. Rasing, *Surf. Sci.* 287&288 (1993) 703.
- [11] S. Affrossman, R.T. Bailey, F.R. Cramer, F.R. Cruickchank, J.M.R. Macallister and J. Alderman, *Appl. Phys. A49* (1989) 533.
- [12] J.A. Litwin, J.E. Sipe and H.M. van Driel, *Phys. Rev. B31* (1985) 5543.
- [13] Y. Hayafuji and K. Kajiwara, *J. Electrochem. Soc.* 129 (1982) 2102.
- [14] C.H. Lee, R.K. Chang and N. Bloembergen, *Phys. Rev. Lett.* 18 (1967) 167.
- [15] N.F. Mott, *Adv. Phys.* 26 (1977) 363.
- [16] C.K. Chen, A.B.R. Castro and Y.R. Shen, *Phys. Rev. Lett.* 46 (1981) 145.
- [17] A. Ourmazd, D.W. Taylor, J.A. Rentschler and J. Bevk, *Phys. Rev. Lett.* 59 (1987) 213.
- [18] O.L. Krivanek and J.H. Mazur, *Appl. Phys. Lett.* 37 (1980) 392.



ELSEVIER

Journal of Non-Crystalline Solids 187 (1995) 232–243

JOURNAL OF
NON-CRYSTALLINE SOLIDS

Section 8. Hydrogen in MOS structures and oxides

Dissociation of H_2 at silicon dangling orbitals in a-SiO₂: a quantum mechanical treatment of nuclear motion

Arthur H. Edwards*

Department of Electrical Engineering, University of North Carolina at Charlotte, Charlotte, NC 28223, USA

Abstract

The current experimental understanding of the interactions between hydrogen and defects in the MOS system, plus the theoretical progress to date toward explaining these observations are reviewed. One of the outstanding theoretical problems is the dissociation of hydrogen molecules in SiO₂. A simple but fully quantum mechanical treatment of the dissociation of hydrogen molecules at silicon dangling orbitals in SiO₂ is presented. It is found that inclusion of quantum mechanical effects in the treatment of nuclear motion is fundamentally important to understanding the dissociation process. In the model calculations, it is estimated that the activation energy is 0.16 eV, in very good agreement with the experimental results of Li et al.

1. Introduction

Over the past twenty years it has become obvious that hydrogen plays several complex roles in the behavior of silicon-based metal-oxide-semiconductor (MOS) devices. In the mid 1970s Balk found that if an MOS capacitor or a field-effect transistor was subjected to a 400°C anneal in forming gas (90% N₂, 10% H₂), there was a dramatic decrease in the density of interface traps [1]. This discovery was probably the reason for the success of the MOS process. Within the last 10–15 years, however, several groups have identified degradation processes

that *rely* on the presence of hydrogen [2–5]. All of the models for these processes involve the transport of a hydrogenic species to the Si–SiO₂ interface, where it causes an increase in the number of interface states. Initially the models were mostly speculative and, at best, relied on indirect evidence for their validity. Only recently have both experimental and theoretical studies started to give a detailed understanding of hydrogen chemistry in SiO₂, Si, and at the Si–SiO₂ interface. This understanding is, of course, crucial for deciding the appropriate use of hydrogen in the fabrication of MOS devices.

In this paper, we review the experimental and theoretical understanding of the interaction between both atomic and molecular hydrogen and defects in the MOS system. We also present our

* Corresponding author. Tel: +1-704 547 4392. Telefax: +1-704 547 2352. E-mail: edwards@mosaic.ucc.edu

recent theoretical results for hydrogen reactions, including a fully quantum mechanical model for H_2 dissociation at a defect in $a\text{-SiO}_2$, the E'_c center. The inclusion of quantum mechanical treatment of the nuclear motion is essential for understanding this, and probably any other, H_2 dissociation reaction. The balance of the paper is organized as follows. In Section 2, we present the current understanding of hydrogen interactions with defects in $a\text{-SiO}_2$. In Section 3, we present our theoretical results and compare them to experiment. We present a brief discussion of our results in Section 4, and conclude in Section 5.

2. Experimental and theoretical background

In this section we present a fairly focused review of experimental results and theoretical calculations pertaining to interactions of hydrogen with defects in the MOS system. We review the earliest literature that showed the beneficial effects of hydrogen. We also include experimental results that are relevant to one of the two models for device degradation. The first model (model I), originally proposed by McLean [5], and later revisited by Griscom and co-workers [6,7], addresses the long-term buildup

of interface states in irradiated MOS devices that was first observed by Winokur and Boesch [8]. The second model (model II) was developed by DiMaria and co-workers over many years to address a large set of data on hot-electron degradation in MOS devices. We discuss each model in turn.

2.1. Model I

In the late 1970s Winokur and co-workers performed a series of time-resolved, irradiation experiments wherein, after a very short burst of high energy irradiation, the growth of interface states was monitored over several decades in time under a variety of biasing conditions [8]. The results are shown in Fig. 1. Note that there is a very strong bias dependence; devices that were held under positive bias throughout the experiment showed the largest final interface state density, while devices held under negative bias after the irradiation showed only a small increase that occurred over a short time interval. Furthermore, in devices that underwent switched bias procedures, the data indicates that the buildup of interface states was halted during the negative bias intervals, and resumed during the positive bias intervals. However, the final value of interface-state density decreased

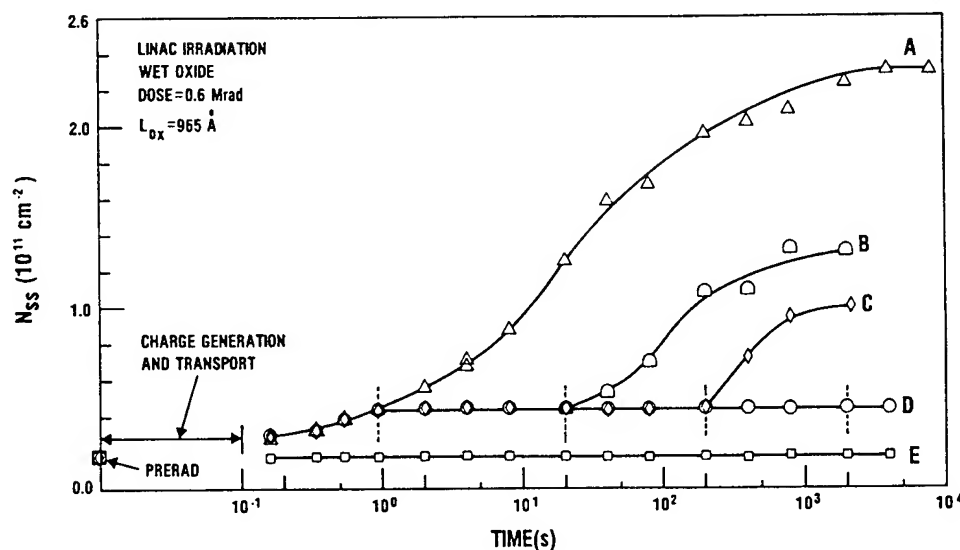


Fig. 1. Density of interface states at mid-gap as a function of time after a $7 \mu\text{s}$ LINAC irradiation. From Ref. [5].

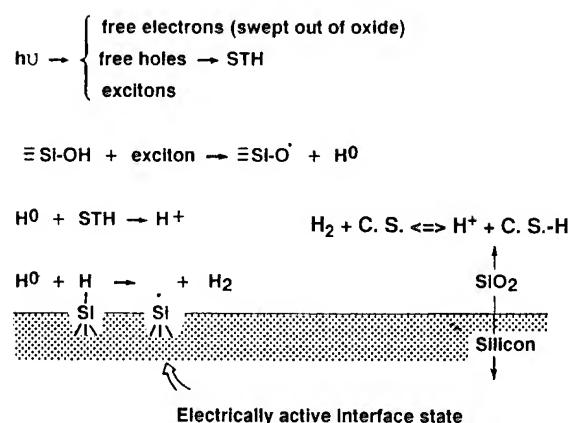


Fig. 2. Model proposed originally by McLean [5], and later revised by Griscom [7] to explain the bias-dependent, long-term buildup of interface states shown in Fig. 1. From Ref. [7].

monotonically with the increase of the duration of the negative bias intervals. In Fig. 2, we present a schematic representation of model I, as articulated by McLean and modified by Griscom. The two processes that are fundamental to this model are (1) the creation of a positively charged hydrogenic species, which we shall call a proton, that migrates toward the Si–SiO₂ interface under the influence of a positive gate bias, and toward the metal gate under the influence of a negative bias, and (2) an interaction between this proton and the interface through which a trivalent silicon atom that is initially passivated by a hydrogen atom becomes depassivated. Griscom suggested the reaction shown in Fig. 2. Note the central role hydrogen plays in this model. We should mention that when McLean originally proposed this model it was highly speculative. While Hofstein had given some experimental evidence for the existence of protons in SiO₂, Raider and Flitsch subsequently showed that his results were suspect [9]. Furthermore, the connection between Hofstein's results and radiation effects was tenuous. Finally, the interaction of hydrogen at the interface was only hypothetical.

2.2. Model II

Over the last twenty years, DiMaria and co-workers have studied the effects of carrier injection

on device reliability. While many other groups have contributed to our understanding of these phenomena, the DiMaria group has used the most complete set of tools, including electrical measurements (*C–V* and *I–V*), ESR, Nuclear reaction analysis and very careful Monte Carlo simulations. We will discuss only their results on electron injection. They have shown, and others have confirmed, that significant device degradation occurs only if the field in the oxide is larger than 1.5 MV/cm. Monte Carlo simulations indicate that this field strength is the approximate threshold for electron heating. For fields larger than 1.5 MV/cm, electrons can gain and maintain significant kinetic energy (several eV above the conduction band edge). In the model proposed to explain this phenomenon, the heated electrons deposit their energy at the anode. If their excess kinetic energy is greater than ~2.3 eV, they will liberate a neutral hydrogenic species that can migrate to the cathode where it creates interface states. For a more complete description of this work see Refs. [2,10].

In both of these models, a hydrogenic species is assumed to traverse the oxide and to create interface states. Thus, our experimental review will be limited to results that pertain to these two conjectures. Interestingly enough, the same mechanisms that lead to interface state passivation are part of the physics of depassivation.

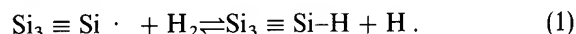
2.2.1. Hydrogen interactions at the Si–SiO₂ interface

As noted in the introduction, Balk was the first to observe that an annealing step at ~560°C (post-metallization anneal, or PMA), designed to form an ohmic contact between aluminum and silicon, reduced the number of so-called fast-states dramatically [1]. We should point out that what Balk and others referred to as fast-states are now called simply interface states. We will use the terms interchangeably. This anneal occurs after the deposition of the aluminum on top of the SiO₂ gate dielectric. Balk surmised that water reacted with the aluminum, forming a mobile hydrogenic species that migrated to the Si–SiO₂ interface, where it reacted with the fast states. Deal and co-workers also contributed to the empirical understanding of this phenomenon [11]. They fabricated Al–Si₃N₄–SiO₂–Si structures, where the SiO₂ was grown

thermally, and the Si_3N_4 was deposited using SiCl_4 and NH_3 , or SiH_4 and NH_3 in a chemical vapor deposition reactor. The carrier gas was either H_2 or N_2 . Structures fabricated using N_2 as a carrier gas that received a PMA did not exhibit the reduction in fast-states observed by Balk, while those fabricated using H_2 as a carrier gas showed a significant, though smaller reduction. It is well known that Si_3N_4 is an excellent diffusion barrier. Thus, one would expect a Si_3N_4 layer to inhibit motion of H to the Si– SiO_2 interface. In the same paper, Deal and co-workers reported further experiments involving three-layer dielectric stacks that lent strong support to this interpretation, and hence to Balk's model. We should point out, however, that the model for this phenomenon was merely speculative. The nature of the fast-states was unknown, and it was not clear whether H or H_2 was the diffusing hydrogenic species. Do Thanh and Balk revisited this problem using H and H_2 sources and a variety of annealing regimens [12]. They found that the efficiency of passivation was a function of temperature. Lower temperature annealing steps ($\sim 200^\circ\text{C}$) gave less efficient passivation than higher temperature ($\sim 400^\circ\text{C}$) steps. This had, in fact, been observed by Razouk and Deal much earlier. However, Do Thanh and Balk found that the degree of passivation depended on the *last* anneal temperature. If they gave a sample a 400°C anneal for one hour, followed by a 200°C anneal for one hour, the number of interface states would *increase* during the second anneal. They also found that the source of hydrogen (atomic or molecular) had little effect on the final degree of passivation; it only effected the kinetics. Anneals in atomic hydrogen reached their steady-state value much more rapidly.

All of the studies discussed so far relied on electrical measurements. While these methods have remarkable sensitivity, they give little information about the reactions responsible for changes in fast-state densities. The most useful technique applied to this system for obtaining microscopic information has been electron spin resonance (ESR). Through ESR, Poindexter et al. were the first to surmise and, later, Brower was the first to demonstrate without ambiguity, that trivalent silicon atoms give rise to fast-states [13,14]. Later, Brower

and co-workers gave the first clear evidence about the chemical reactions that lead to passivation of interface states. Working over fairly large ranges in temperature and H partial pressure, Brower and Myers deduced that the passivation reaction follows the form



Here, the \equiv symbol indicates that the silicon is bonded to three equivalent silicon atoms, and the \cdot symbol indicates an unpaired electron. Brower obtained a 1.66 eV activation energy for the reaction in Eq. (1). In other experiments, Brower and Myers determined that the Si–H binding energy at a P_b center was about 2.46 eV. Assuming that the binding energy of H_2 is changed little in SiO_2 , then the reverse reaction (Eq. (1) going right to left) should occur without activation.

The $\langle 111 \rangle$ interface appears to be understood relatively well experimentally. While there are interesting features of P_b centers that are unresolved [15], the nature of the defect is not in question. This is true in part because several theoretical studies have led to qualitatively identical conclusions. Edwards [16] and Cook and White [17,18] studied the P_b center in the $\langle 111 \rangle$ interface. Their calculated ^{29}Si principal hyperfine values agreed very well with those reported by Brower. Furthermore, both groups predicted a superhyperfine interaction that was subsequently confirmed by Brower [19] and by Carlos [20]. This agreement is significant because the methods used by Edwards and by Cook and White were significantly different. While both used a molecular orbital framework applied to similar clusters of atoms, Edwards used a semiempirical Hamiltonian, while Cook and White used local density theory. Using the same semiempirical Hamiltonian, Edwards has studied the interaction of hydrogen with dangling orbital defects at the $\langle 111 \rangle$ Si– SiO_2 interface [21]. Using semiempirical methods, he predicted a 1.3 eV activation energy for Eq. (1) and an Si–H binding energy of 2.7 eV. Furthermore, the potential surfaces were in complete agreement with Brower's surmise that the depassivation reaction should have a negligible activation energy.

The nature of interface states, and of their interactions with hydrogen, are more poorly understood

on the $\langle 100 \rangle$ interface. On this interface there are two distinct, spin active defects, labeled P_{b1} and P_{b0} , that give rise to fast states. P_{b0} has ESR parameters nearly identical to the P_b center on the $\langle 111 \rangle$ interface. The P_{b1} defect is significantly different, however, so that it is not clear whether the kinetics observed on the $\langle 111 \rangle$ interface should be identical to those on the $\langle 100 \rangle$ interface. Recently, Cartier et al. have performed experiments similar to Do Thanh and Balk's, but using ESR, instead of electrical measurements, to monitor changes in the density of interface states on both $\langle 111 \rangle$ and $\langle 100 \rangle$ interfaces [22]. Their results were as surprising as they were enlightening. On both interfaces, the direction in which Eq. (1) was driven depended on the preceding treatment, in qualitative agreement with Do Thanh and Balk. On the $\langle 111 \rangle$ interface, their results are also in agreement with Brower's results; if initially there are many P_b centers (i.e. after a vacuum anneal) then exposure to atomic hydrogen will passivate most of them, and the ESR intensity will decrease. On the other hand, if there is a relatively high initial level of hydrogen passivation (as for an as-grown sample), then a *room temperature* anneal will actually lead to depassivation because of the 1.66 eV activation energy measured by Brower. The $\langle 100 \rangle$ results were more complex and harder to understand. The P_{b0} and P_{b1} defects exhibited strikingly different behavior from each other, and the P_{b0} defect on the $\langle 100 \rangle$ interface behaved differently from the P_b center on the $\langle 111 \rangle$ interface. We would expect that both signals would decrease on vacuum-annealed samples and increase on as-grown samples exposed to atomic hydrogen. However, on vacuum-annealed $\langle 100 \rangle$ interfaces, the P_{b1} signal decreased much more readily than the P_{b0} signal, while on as-grown interfaces, the P_{b0} increased much more readily than the P_{b1} signal (see Fig. 2, Ref. [23]). A careful discussion of these results would require a larger digression than is warranted for our purposes. Furthermore, because there are no detailed microscopic models for P_{b0} and P_{b1} that agree with all experimental results, theorists are unable to contribute to our understanding of this very interesting set of results. We note, however, that despite the surprising behavior of each defect, taken together, they behave as

would be expected; the total number of defects increases on an as-grown interface and decreases on a vacuum-annealed interface upon exposure to atomic hydrogen. Thus, while the depassivation may not follow the simple physics of Eq. (1), Stathis and Cartier have demonstrated that it will occur [23].

2.2.2. Hydrogen interactions in the oxide

Several recent experiments have confirmed and broadened the McLean model for long-term buildup of interface states by altering the amount of hydrogen present in the oxide, and by replacing hydrogen with deuterium. These experiments have been reviewed recently in Ref. [24], so we will only outline the results. Saks and co-workers have performed several studies to address whether the bias dependence of McLean's data was due to a positively charged, hydrogenic species moving through the oxide. In one experiment, MOS devices were irradiated and held under a positive bias while the temperature was varied between 77 K and room temperature [25]. At temperatures below ~ 130 K, there was no appreciable buildup of interface states, while above this temperature, they obtained data similar to that of Winokur. This result was important because it correlated strongly with the low temperature ESR studies of Brower et al. [26], wherein they observed large quantities of atomic hydrogen (identified through its ^1H hyperfine interaction) below 130 K, and almost none above, indicating that above 130 K, the neutral hydrogen atoms become mobile and either recombine to form H_2 or combine with self-trapped holes to become protons. In another experiment the same group measured $C-V$ shifts as a function of time for MOS capacitors that have been irradiated and subsequently held under positive bias [27]. They observed a small but measurable negative shift in the $C-V$ curves with time, indicating that a positive species was traversing the oxide. Finally, they saturated two sets of identical MOS capacitors with H_2 and with D_2 and performed irradiation experiments similar to those in Ref. [8] [3]. If hydrogen transport is part of the process that leads to long-term buildup of interface states, one would expect an isotope effect; interface states

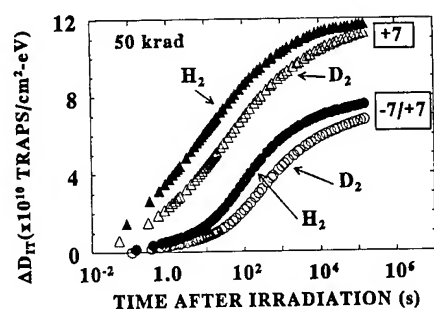


Fig. 3. Density of interface states for irradiated MOS capacitors that have been exposed to H_2 and to D_2 . Boxed numbers are values of the oxide electric field (in MV/cm) during post-irradiation anneal. $-7/+7$ refers to a switched-bias experiment. Figure from Ref. [3].

should build up more slowly in the D_2 samples than in the H_2 samples. The results, shown in Fig. 3, are even more dramatic than would be predicted from classical diffusion. If one assumes that the diffusing species is essentially uncoupled from the system, and if one ignores the effects of randomness inherent in an amorphous system, the classical diffusion rate should be proportional to $m^{-0.5}$. Flynn and Stoneham [28] and Kagan and Klinger [29] have considered various quantum mechanical modifications to the theory. In the temperature range of the Saks–Rendell experiment, the diffusion coefficient is predicted to be proportional to either m^{-1} or $m^{-0.5}$. The isotope dependence observed by Saks and Rendell was between 1.8 and 3.2 times as large as that predicted by $m^{-0.5}$ dependence. The discrepancy can be explained by a dispersive transport model appropriate to amorphous materials [3]. It could be argued that the concentration of hydrogen is much larger than would be found in commercial devices, and so the conclusions may not be generally applicable. However, the time dependence is identical to that of the Winokur results, when the difference in oxide field is taken into account. Thus, for irradiated devices, these results give the clearest possible indication that the McLean–Griscom model is correct.

Other groups have also performed experiments that illuminate the crucial importance of hydrogen. Stahlbush and coworkers have performed several sets of experiments in which forming gas was

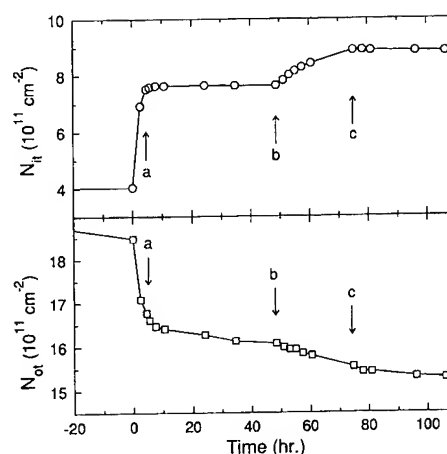
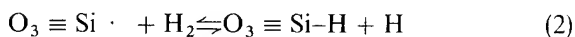


Fig. 4. The effect of the ambient upon the number of interface states, N_{it} , and upon the number of trapped positive charges, N_{ot} , in a 5- μ -long irradiated MOSFET with its gate at +5 V. Hydrogen (10/90% H_2/N_2) is introduced at 0 and 48 h and nitrogen is introduced at 4 and 76 h. Arrows a, b, and c point to the ambient changes at 4, 48, and 76 h, respectively. The MOSFET is irradiated to 1 Mrad(SiO_2) 65 h before hydrogen is first introduced. From Ref. [4].

introduced into MOS field effect transistors held under several different biasing conditions after X-irradiation [4,30,31]. In Fig. 4, we show some of the most dramatic data obtained during these experiments. The devices from which these data were obtained were held under positive bias during and after irradiation and held in a nitrogen atmosphere for 65 h prior to any hydrogen exposure, to exhaust the rapid self-annealing. After this nitrogen exposure, the devices were exposed to forming gas (10% H_2) at $t = 0$ and at the time b. At times a and c, the hydrogen was removed. Note that during oxygen exposure there is a dramatic increase in interface state density concomitant with a similar decrease in oxide positive charge. This effect is highly dependent on the sign of the gate bias; for negative gate voltages the oxide positive charge decreases at roughly the same rate, but the interface states increase much more slowly. To explain these observations, Stahlbush et al. modified the McLean model to include a reaction in which molecular hydrogen was dissociated at a pre-existing, positively charged defect [31]. As shown in Fig. 2, it was assumed that this reaction would lead to the creation of a proton.

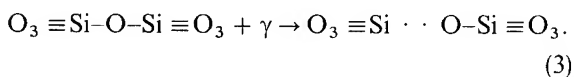
As part of this set of studies, Edwards performed a set of semiempirical molecular orbital calculations on two model defects for the dissociation site; the E'_γ center and a proposed defect, the strained-bond oxygen-related hole trap. Based on estimations of energies of reaction and of activation, Edwards predicted that the E'_γ center was an unlikely candidate for the H_2 dissociation site.

It is interesting that, while semiempirical calculations led to conclusions to the contrary, there is a relatively large experimental literature indicating that the reaction



occurs rapidly at room temperature [32–34]. This reaction has been inferred from observations at room temperature of a decrease in intensity of the E'_γ ESR signal as a function of time after the introduction of forming gas. Vikhrev was the first to report such an observation in thermally grown SiO_2 that had been bombarded with boron ions [32]. Li et al. have also studied thermal oxides and have obtained an activation energy of 0.3 eV [33]. Finally, Conley and Lenahan [34] have added to the literature by studying the same reaction in novel oxides, as well as in thermal oxides. They were the first and the only group to report a concomitant decrease in the E'_γ intensity and increase in the intensity of the 74 Gauss doublet, which has been identified as an E'_γ center with one of the nearest-neighbor oxygen atoms replaced by a hydrogen atom.

While the results of the room-temperature hydrogen annealing experiments suggest that the E'_γ dissociates hydrogen molecules readily, they are not conclusive. During γ -irradiation experiments, several groups have observed a simultaneous increase in non-bridging oxygen (NBO) centers and E'_γ centers [35,36]. They have speculated that this observation arises from homolytic bond scission,



This model raises the possibility that hydrogen molecules could dissociate on the NBO to form an OH group. The remaining neutral hydrogen could then passivate the dangling orbital on the silicon

atom. The plausibility of this suggestion combined with the previous semiempirical results, made obvious the need for further theoretical study.

3. Calculations

To model Eq. (2), we calculated the energy of reaction and the energy of activation using two methods: the semiclassical approximation in which these energies are identified with the extrema on an adiabatic potential surface (I), and a model wherein a series of adiabatic potential surfaces were incorporated into a Shroedinger equation for nuclear motion (II). In both (I) and (II) we used Gaussian 92 [37], an ab initio molecular orbital package to calculate total energies and to locate equilibrium geometries under a variety of constraints. We applied this package to two clusters shown in Fig. 5. The small cluster was used to explore the effects of basis size and of the inclusion of electron correlation effects, and to consider several different reaction paths. The large cluster was a more realistic model of the E' center as the positions of the neighboring atoms are appropriate to α -quartz. We should point out that Gaussian 92 has features for finding the correct transition state, and hence the correct activation energy, within the semiclassical approximation, assuming we know the conformations of the products and reactants in Eq. (2). However, in our case both of these are asymptotic conformations; they correspond to either the H_2 molecule or the H atom being far from the reaction site. This attribute renders the transition state software unusable. The calculations for methods (I) and (II) will be discussed in turn.

3.1. Semiclassical estimation of reaction and activation energies (I)

The details of these calculations are given elsewhere [24]. We chose as the reaction coordinate the distance between the center of mass of the H_2 molecule and the equilibrium position of the Si-H bond ($Si-H^q$). This is shown in Fig. 6. At each value of R_{cm} , we allow the H-H bond length to relax. As the molecule approaches, we find that the H-H stretching mode softens until there is no

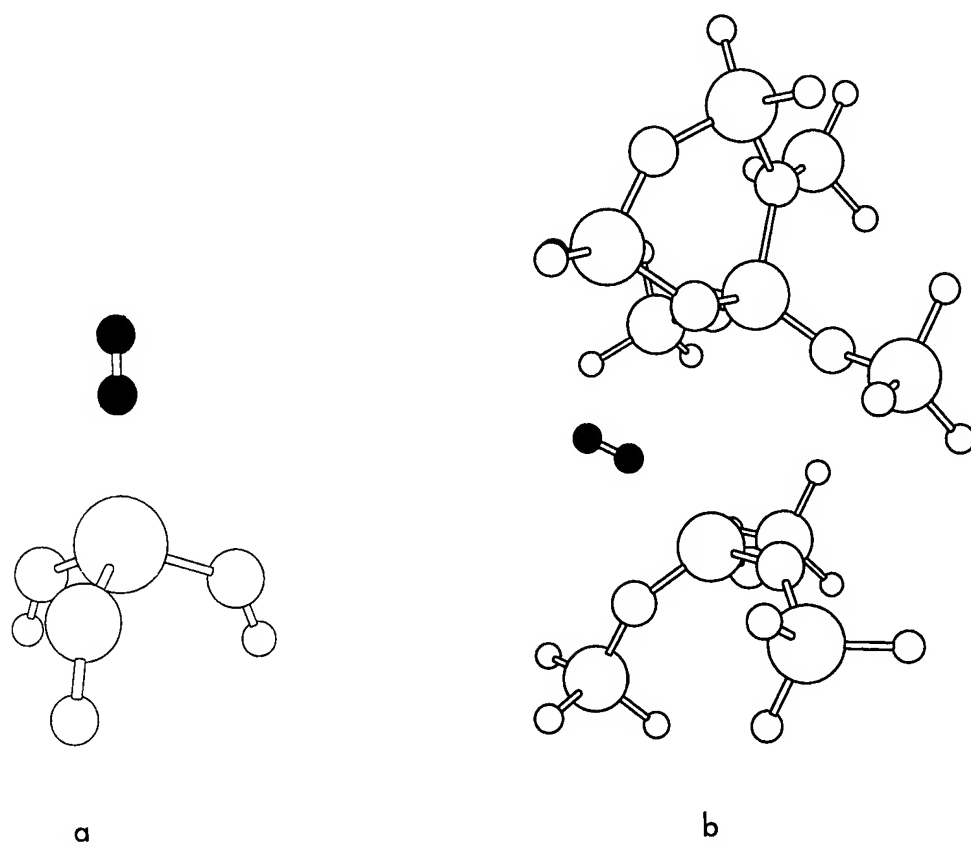


Fig. 5. Clusters used for this study. (a) Small cluster used for basis set and correlation studies, and for the model calculations for quantum mechanical motion of H₂. (b) Cluster used to represent the E'_1 center in α -quartz. The latter cluster is only used for semiclassical calculations.

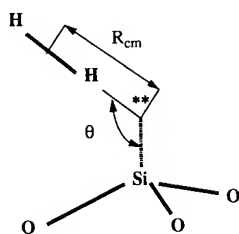


Fig. 6. Schematic representation of reaction coordinate for cluster shown in Fig. 1(a). R_{cm} is the reaction coordinate.

longer a local minimum corresponding to the H–H bond. We define the activation energy as the difference in total energy between $R_{cm} = 9 \text{ \AA}$ (\sim the same as ∞) and the smallest value of R_{cm} for which there is an attractive interaction between the two hydrogen atoms that comprise the hydrogen molecule.

The energy of reaction is defined according to Eq. (2) with either the center of mass of the H₂ molecule, or the H atom 9 \AA away from Si–H^{eq}. As reported in Ref. [24], we found that the 3–21G* basis was adequate, and that inclusion of perturbative configuration interaction was unnecessary to obtain the correct qualitative picture. Using the unrestricted Hartree–Fock approximation and the 3–21G* basis, we estimate that the activation energy is 0.58 eV , and that the reaction energy is -0.42 eV . Introduction of a very large basis set, and inclusion of second-order perturbative CI changes the activation energy to 0.7 eV and the reaction energy to 0.004 eV . While these results differ quantitatively, the qualitative interpretation is identical; the reaction reduces to a catastrophic H₂ mode-softening. Furthermore, the activation

energy for all calculation is at least twice as large as the experimental value.

Because of the level of computational effort required in the large cluster calculations, we restricted ourselves to the semiclassical calculation. The method of calculation was identical to that used for the smaller cluster except that θ was allowed to vary along the reaction path. The resulting estimate for the activation energy was 0.72 eV. As discussed elsewhere [24], the difference between the small and large cluster result probably reflects the finite size of the oxygen vacancy. We note, however, that the mechanism for dissociation is the same for the larger cluster and the distance at which the H_2 dissociates is very close to that predicted by the small cluster. Because of this qualitative and, in large measure, quantitative agreement between calculations performed on large and small clusters, we believe the results discussed in the next section would apply directly to the large cluster calculation.

3.2. Quantum mechanical treatment of the H_2 motion (II)

To appreciate the possible importance of quantum mechanical effects, it is instructive to plot the adiabatic potential for dissociation at several points along the adiabatic reaction path, i.e., for several values of R_{cm} . We show three of these in Fig. 7. The potential is drawn as a function of the relative motion of the two hydrogen atoms. We see that this is a double well system; one corresponding to an H-H bond and the other corresponding to an Si-H bond. As the center of mass of the H_2 molecule moves closer to the silicon atom, the H_2 well becomes ever more shallow until it vanishes. The point at which it vanishes corresponds to the transition state (and activation energy) calculated in Section 3.1. However, we can look at the problem differently if we ask the following question: what is the activation energy for H_2 dissociation if R_{cm} is fixed? In the

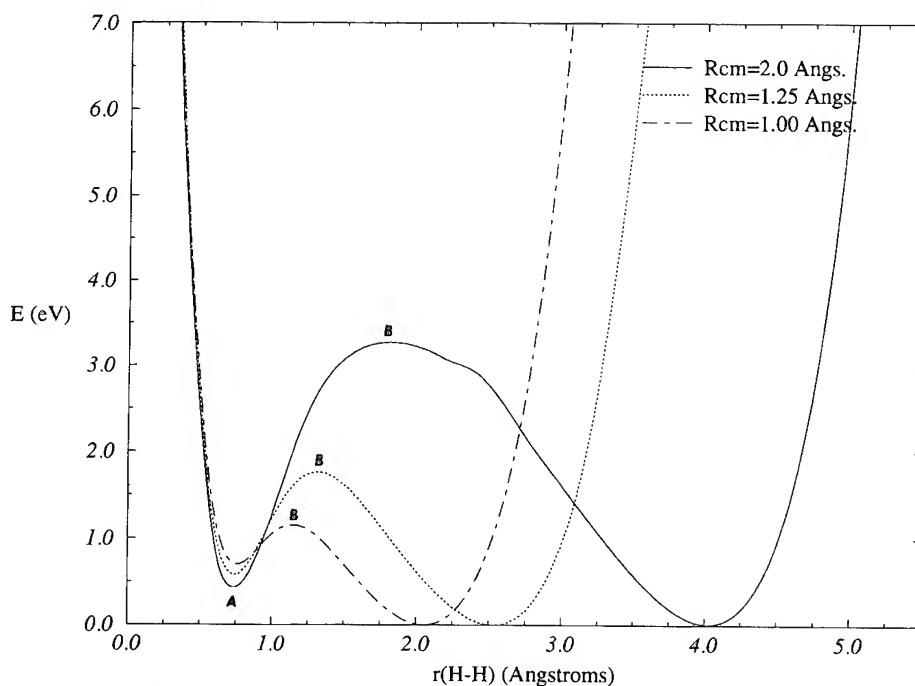


Fig. 7. Three adiabatic potentials for H_2 dissociation. R_{cm} has the same meaning as in Fig. 6.

adiabatic approximation, it would be the difference between points *A* and *B* in Fig. 7. An entirely different picture emerges if we actually solve the Schroedinger's equation using R_{H-H} as the spatial coordinate and $\mu = m_H/2$ for the reduced mass. To solve the one-dimensional Schroedinger equation we used finite element analysis. We used linear shape functions on a grid of 160 elements of equal length. We did not obtain values for the potential at each point using Gaussian 92. Rather we obtained ~ 20 – 30 points and used a cubic spline interpolation to obtain values at the rest of the mesh points. In Fig. 8 we show the results of this analysis for the three potentials shown in Fig. 7. The energy level for each of the displayed states is the zero of wave function amplitude. To interpret these results we make the following assumptions: (1) the system starts in the H_2 well (the minimum on the left in Figs. 7 and 8), (2) to make a transition to the Si–H well there must be either significant differential overlap between two states associated primarily with each well, or a state with significant amplitude in each well, and (3) the activation energy is just the difference in the eigenvalues for the two states. In our picture, the hydrogen molecule approaches the dangling silicon orbital slowly compared to the vibrational motion, so that it senses the entire potential surface. The states shown in Fig. 8 are, then, slowly varying functions of time. To make a transition between two of these states there must be an operator that connects them, i.e., a perturbation absent in our nuclear Hamiltonian. Any vibration of the network, of the silicon atom, for instance, could admix the states.

With this model in hand, we consider the results in Fig. 8. When $R_{cm} = 2.0 \text{ \AA}$ (Fig. 8(a)), the adiabatic approximation holds reasonably well. The first state with appreciable amplitude in both wells is within 0.1 eV of the semiclassical barrier, while the ground state of the H–H well is $\sim 0.35 \text{ eV}$ above the semiclassical minimum. While the quantum mechanical prediction of E_A is 0.4 eV below the adiabatic estimate, the relative error is small because the barrier is so large. When $R_{cm} = 1.25 \text{ \AA}$, we see that quantum effects are substantial; E_A (adiabatic) = 1.2 eV, while E_A (q.m.) = 0.63 eV. This dramatic reduction arises from a reduction in the height and width of the barrier

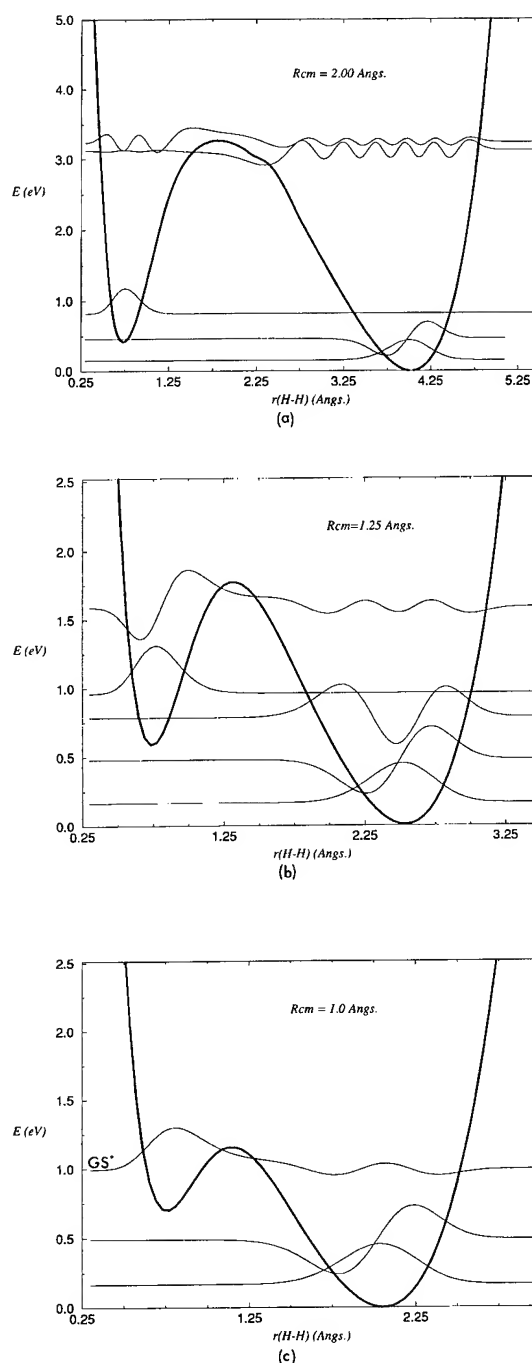


Fig. 8. Wave functions displayed at their respective energy levels for the three potential functions shown in Fig. 7. (a) $R_{cm} = 2.0 \text{ \AA}$. (b) $R_{cm} = 1.25 \text{ \AA}$. (c) $R_{cm} = 1.00 \text{ \AA}$. The difference between GS^* and the ground vibronic state for $R_{cm} = 9.0 \text{ \AA}$ is our estimate of the activation energy.

between the two wells. Note that this is approximately the same activation energy as was predicted as given in Section 2, while the physics is remarkably different. However, the most dramatic quantum effects are seen at $R_{\text{cm}} = 1.0 \text{ \AA}$ (Fig. 8(c)). Note that there is no ground state wave function localized in the H–H well. Because the zero point energy is so large, the wave function tunnels readily through the barrier between the two wells. Thus, at this value of R_{cm} , we would say that the hydrogen molecule would dissociate spontaneously. The activation energy, then, is not the excitation energy between two quantum states of one of the double well systems. Rather, we estimate an upper bound as the difference in total energy between the state marked GS* in Fig. 8(c) and the ground state of the H–H well at $R_{\text{cm}} = 9.0 \text{ \AA}$. We obtain $E_A = 0.16 \text{ eV}$.

4. Discussion

This simple extension to the adiabatic theory of activation energies has yielded what appears to be fresh insight into the physics of H_2 dissociation at silicon dangling orbitals. We should note, however, that the importance of quantum mechanical effects in H_2 dissociation has been recognized for a very long time. Several groups have studied H_2 dissociation on metal surfaces by solving the time-dependent Schrodinger equation [38–40]. It is clear from these studies that the most obvious shortcoming of our present calculation is the absence of time dependence. We are unable to estimate tunneling or dissociation rates using the present theory. We note that in the case of a symmetric double well system, one can obtain a tunneling frequency from the energy difference between ground state (even, or bonding state) and the first excited (odd or antibonding state). Appropriate sums of these states lead to wave functions localized in each of the wells. Thus in the time-dependent picture, the system will oscillate between the two wells at the frequency $\omega = \Delta E_{\text{g-c}}/\hbar$. However, in our case there are two complicating factors. First, the wells are not symmetric. Sussmann showed that even a small asymmetry leads to almost complete localization in one well [41] so that if we prepare the system in one well, it will stay there. The second complication is

that in our case the tunneling event involves vibrationally excited states. Without knowledge of the admixture coefficients of the states of the isolated wells, we have no chance of developing a simple time-dependent picture. Thus the results presented here must be considered somewhat preliminary. We have not attempted to estimate a tunneling rate, and we have not explored even the two-dimensional potential surface (in R_{cm} and $r_{\text{H-H}}$) completely. However, we believe these one-dimensional results exhibit the essential physics. The cost in total energy to reduce R_{cm} to 1.0 \AA , and, thus, to alter the potential surface so that the lowest state in the H_2 well has large amplitude in both wells is very small—much smaller than the energy required to surmount the adiabatic barrier. It is clear from this study that the zero-point energy of the H_2 molecule has the largest effect on the activation energy. This is due in part not only to the shape of the H–H well, but also to μ_{eff} . That is to say that while the curvature of the well effects the positions of the energy levels, μ_{eff} is half of the hydrogen atom mass, thus amplifying the quantum effects. Recall that for a simple harmonic oscillator, the energy eigenvalue is proportional to $(\mu_{\text{eff}})^{-0.5}$. We might expect, then, that D_2 would dissociate more slowly than H_2 . However, our calculations indicate that the changes would be slight; at $R_{\text{Si-Si}} = 1.0 \text{ \AA}$, the wave function is not confined to one well so that the simple harmonic oscillator result is invalid. Thus, one could argue that H_2 is so reactive in SiO_2 because it is so light. Its small mass causes the ground-state energy level to be high enough in the well that it is very sensitive to barrier lowering. This observation should apply not only to dissociation at E' centers, but to other defects as well. We would expect, for instance, that hydrogen would dissociate at NBO centers very readily through the same tunneling process.

5. Conclusions

In this paper we have reviewed some of the important effects in the MOS system that rely on the presence of hydrogen. We have seen that the mechanisms that lead to passivation of interface states at one temperature lead to depassivation at different temperatures. We have also presented our

recent results on dissociation of H_2 molecules at dangling silicon orbitals in α - SiO_2 . Through simple model calculations we have demonstrated that inclusion of quantum effects is requisite to understand this reaction. Our simple model predicts an activation energy of 0.16 eV. This is well below the activation energy observed by Li et al. Because the activation energy for diffusion that has been measured by Shelby is roughly 0.38 eV [42] our calculation supports the view, originally proposed by Mrstik [43] that the H_2 dissociation reaction is limited by diffusion. Finally, because the small activation energy is due mostly to properties of the hydrogen molecule, we would expect to see similarly high dissociation probabilities at other defects in the MOS system.

The author acknowledges gratefully several important conversations with Professor W.B. Fowler, Professor A.M. Stoneham, and Dr D. Babic. Funding through ONR Grand No. N00014-92-J-2001 is gratefully acknowledged. Computation were made possible by a generous grant of computer time from the North Carolina Supercomputing Center.

References

- [1] P. Balk, Extended Abs., Electronics Div.; Electrochem. Soc. 14 (1965) 237.
- [2] D.J. DiMaria and J.W. Stasiak, J. Appl. Phys. 65 (1989) 2342.
- [3] N.S. Saks and R.W. Rendell, IEEE Trans. Nucl. Sci. NS-39 (1992) 2220.
- [4] R.E. Stahlbush, A.H. Edwards, D.L. Griscom and B.J. Mrstik, J. Appl. Phys. 73 (1993) 658.
- [5] F.B. McLean, IEEE Trans. Nuc. Sci. NS-27 (1980) 1651.
- [6] D.L. Griscom, D.B. Brown and N.S. Saks, in: The Physics and Chemistry of SiO_2 and the Si- SiO_2 Interface, ed. C.R. Helms and B.E. Deal (Plenum, New York, 1988) p. 287.
- [7] D.L. Griscom, J. Electron. Mater. 21 (1992) 763.
- [8] P.S. Winokur and H.E. Boesch, IEEE Trans. Nucl. Sci. NS-27 (1980) 1647.
- [9] S. Hofstein, IEEE Trans. Electron Devices ED-14 (1967) 749; S.I. Raider and R. Flitsch, J. Electrochem. Soc. 118 (1971) 1011.
- [10] D.J. DiMaria, E. Cartier and D. Arnold, J. Appl. Phys. 73 (1993) 3367.
- [11] B.E. Deal, E.L. Mackenna and P.L. Castro, J. Electrochem. Soc. 116 (1969) 997.
- [12] L. Do Thanh and P. Balk, J. Electrochem. Soc. 135 (1988) 1797.
- [13] E.H. Poindexter, E.R. Ahlstrom and P.J. Caplan, in: The Physics of SiO_2 and its Interfaces, ed. S.T. Pantelides (Pergamon, New York, 1978) p. 227.
- [14] K.L. Brower, Appl. Phys. Lett. 43 (1983) 1111.
- [15] Recently Stesmans and Stathis have studied independently the ^{17}O hyperfine associated with the P_b center. They have found that the defect is always associated with one oxygen atom. Stesmans has found that there are two other oxygen atoms interacting less strongly. See A. Stesmans and K. Vanheusden, Phys. Rev. B44 (1991) 11353. and J.R. Stathis, S. Rigo and I. Trimaille, Mater. Sci. Forum. 83–87 (1992) 1421.
- [16] A.H. Edwards, Phys. Rev. B36 (1987) 9638.
- [17] M. Cook and C.T. White, Phys. Rev. Lett. 59 (1987) 1741.
- [18] M. Cook and C.T. White, Semiconductor Sci. Tech. 4 (1990) 1012.
- [19] K.L. Brower, Phys. Rev. B38 (1988) 9657.
- [20] W.E. Carlos, Appl. Phys. Lett. 50 (1987) 1450.
- [21] A.H. Edwards, Phys. Rev. B44 (1991) 1832.
- [22] E. Cartier, J.H. Stathis and D.A. Buchanan, Appl. Phys. Lett. 63 (1993) 1510.
- [23] J.H. Stathis and E. Cartier, Phys. Rev. Lett. 72 (1994) 2745.
- [24] A.H. Edwards, J.A. Pickard and R.E. Stahlbush, J. Non-Cryst. Solids 179 (1994) 148.
- [25] N.S. Saks, R.B. Klein and D.L. Griscom, IEEE Trans. Nucl. Sci. 35 (1988) 1234.
- [26] K.L. Brower, P.M. Lenahan and P.V. Dressendorfer, Appl. Phys. Lett. 41 (1982) 251.
- [27] N.S. Saks and D.B. Brown, IEEE Trans. Nucl. Sci. NS-37 (1990) 1.
- [28] C.P. Flynn and A.M. Stoneham, Phys. Rev. B10 (1970) 3966.
- [29] Y. Kagan and M.I. Klinger, J. Phys. C7 (1974) 2791.
- [30] R.E. Stahlbush, B.J. Mrstik and R.K. Lawrence, IEEE Trans. Nucl. Sci. NS-37 (1990) 1641.
- [31] R.E. Stahlbush, R.K. Lawrence and W. Richards, IEEE Trans. Nucl. Sci. NS-36 (1989) 1998.
- [32] B.I. Vikhrev, N.N. Gerasimenko and G.P. Lebedev, Mikroelektronika 6 (1977) 71.
- [33] Z. Li, S.J. Fonash, E.H. Poindexter, M. Harmatz, F. Rong and W.R. Buchwald, J. Non-Cryst. Solids 126 (1990) 173.
- [34] J.F. Conley and P.M. Lenahan, Appl. Phys. Lett. 62 (1993) 40.
- [35] H. Imai, K. Arai, J. Isoya, H. Hosono, Y. Abe and H. Imagawa, Phys. Rev. B48 (1993) 3116.
- [36] R.A.B. Devine and J. Arndt, Phys. Rev. B39 (1989) 5132.
- [37] A.M.J. Frisch, G.W. Trucks, M. Head-Gordon, P.M.W. Gill, M.W. Wong, J.B. Foresman, B.G. Johnson, H.B. Schlegel, M.A. Robb, E.S. Replogle, R. Gomperts, J.L. Andres, K. Raghavachari, J.S. Binkley, C. Gonzalez, R.L. Martin, D.J. Fox, D.J. Defrees, J. Baker, J.J.P. Stewart and J.A. Pople, Gaussian 92 (Gaussian, Pittsburgh, PA, 1992).
- [38] D. Halstead and S. Holloway, J. Chem. Phys. 93 (1990) 2859.
- [39] B. Jackson and H. Metiu, J. Chem. Phys. 86 (1987) 1026.
- [40] C. Engdahl and U. Nielsen, J. Chem. Phys. 98 (1993) 4223.
- [41] J.A. Sussmann, Phys. Kondens. Mater. 2 (1964) 146.
- [42] J.E. Shelby, J. Appl. Phys. 48 (1977) 3387.
- [43] B.J. Mrstik, J. Electron. Mater. 20 (1991) 627.



ELSEVIER

Journal of Non-Crystalline Solids 187 (1995) 244–247

JOURNAL OF
NON-CRYSTALLINE SOLIDS

Atomic hydrogen-induced degradation of thin SiO₂ gate oxides

E. Cartier*, D.A. Buchanan, J.H. Stathis, D.J. DiMaria

IBM Research Division, Thomas J. Watson Research Center, Yorktown Heights, NY 10598, USA

Abstract

The generation of interface states at the Si/SiO₂-interface caused by atomic hydrogen, H⁰, from a remote hydrogen plasma has been studied. It is found that H⁰ produces large numbers of interface-states, irrespective of the oxide thickness and the substrate orientation. The interface-state density is found to increase linearly with the H⁰-dose over a wide range. The rate at which the interface-states are created appears to be thermally activated with an activation energy of ≈ 200 meV. The rate increases with decreasing oxide thickness, indicating that the generation may be limited in part by the H⁰ diffusion to the interface. The Si (1 1 1) interface is found to degrade faster than the Si (1 0 0) interface.

1. Introduction

The interfacial properties of electronic devices are typically optimized by annealing in forming gas (nitrogen/hydrogen mixture) above 400°C. This procedure leads to the passivation of process-induced, electrically active defects at the Si/SiO₂ interface by hydrogen. Ironically, the hydrogen incorporated during this optimization process (and during device fabrication) seems to be partially responsible for the degradation of such optimized devices during their subsequent operation: hydrogenic species are known to be released by hot-electrons, and it has been shown that simultaneously with its release a rapid degradation of the interface does occur [1,2]. To optimize and predict device reliability, it is therefore crucial to understand the hydrogen chemistry at device operation

temperature and to identify the chemical reactions (involving hydrogenic species) that largely reverse the improvement gained in hydrogen anneals at higher temperatures.

To highlight the connection of the remote hydrogen plasma experiments reported in this paper with the degradation of electronic devices, let us consider the high-field degradation of a metal-oxide-semiconductor (MOS) capacitor during homogeneous electron injection by Fowler–Nordheim (FN) tunnelling under positive gate bias. Naively, one might expect that hot-electron induced damage would be restricted exclusively to the oxide/metal (poly-Si) interface because the electron distribution is only gradually heated by the oxide field after tunnelling through the substrate/SiO₂ interfacial region [3]. This is not the case. Considerable degradation is also observed near the Si substrate even though hot electrons are completely absent at this interface [4–7]. Many researchers have proposed that this damage may be caused by released hydrogenic species which subsequently diffuse from the

* Corresponding author. Tel: +1-914 945 2832. Telefax: +1-914 945 2141. E-mail: cartier@Watson.ibm.com.

gate to the substrate to produce interface states by reacting chemically with certain precursor sites. Such precursor sites can be defects previously passivated in forming gas anneals.

Extending hydrogen plasma studies by DoThanh and Balk [8], we have demonstrated that neutral, atomic hydrogen, H^0 , is a prime candidate for the hydrogenic species causing interface degradation after hot-electron induced release at room temperature [9]. Using electron spin resonance [9,10], we also succeeded to identify the P_bH -defect, which is the hydrogen-passivated silicon dangling bond or P_b -defect, as one specific precursor site with which H^0 does react at room temperature to produce an interface-state via the reaction,

$$P_bH + H^0 \rightarrow P_b + H_2. \quad (1)$$

We also showed that this P_bH -precursor accounts for only a small fraction of the total number of precursor sites that are transformed into interface-states by H^0 from a remote plasma. The microscopic structure of the majority of precursor sites thus remains to be identified.

To further study the consequences of hydrogen release by hot electrons at device operation temperatures, we systematically measured the interface-state generation caused by H^0 from a remote plasma source. Since H^0 from the remote plasma penetrates into and diffuses through the oxide before it causes damage in the interfacial region, these experiments provide a test for part of the previously described degradation concept and the damage caused by H^0 can be isolated from other degradation mechanisms also occurring under high-field stress [11].

2. Experimental procedure

To obtain uniform exposures, gate-free samples were subjected to H^0 in a specially designed remote plasma system that prevents all effects due to energetic particles and UV radiation [12]. (We were unable to detect any changes in the interface properties of large area MOS capacitors even after heavy exposures. The diffusion of H^0 through poly-Si (Al) gates and its lateral in-diffusion along the gate oxide is strongly suppressed. We can prove

that this happens because H^0 is rapidly scavenged at the device perimeter. The damaged area remains too small to be detected in large area structures.) The H^0 -concentration in the remote plasma was monitored at the sample position via a silver-coated thermocouple. The temperature increase due to the H^0 surface-recombination on silver yields a quantitative measure for the H^0 -concentration and provides accurate control over the H^0 -dose.

Exposed, gate-free samples were electrically characterized by the high/low frequency capacitance–voltage method using a mercury probe, or by depositing thin aluminum gates after exposure [12]. The increase of the interface-state density at mid-gap, $\Delta D_{it} = D_{it} - D_{it}^0$, was used as a quantitative measure for the interface degradation. D_{it}^0 is the value measured prior to H^0 exposure.

3. Experimental results and discussion

Typical experimental results of the interface-state buildup during remote H^0 exposure at 23°C are shown in Fig. 1. As can be seen, D_{it} increases linearly with the H^0 -dose and there is no indication that D_{it} saturates at values below $10^{13} \text{ eV}^{-1} \text{ cm}^{-2}$. Therefore, the interface-state generation rate, R_{it} , as defined in Fig. 1, can be used to fully characterize the interface degradation. (At temperatures above 60°C we observe that D_{it} does saturate at values below $10^{13} \text{ eV}^{-1} \text{ cm}^{-2}$. In these cases, the generation rate was extracted from D_{it} -values well below saturation.) As can be seen from Fig. 1, the (111)-interface degrades roughly 2.5 times faster than the (100)-interface. This difference appears to be the same over the whole oxide thickness range studied here (see Fig. 2). It might therefore reflect an ‘intrinsic’ interface property, possibly a higher precursor site density at the (111) interfaces.

In Fig. 2, the interface-state generation rate is shown as a function of oxide thickness, t_{ox} , for Si (111) and Si (100) substrates. In addition to the dependence of R_{it} on the substrate orientation, a rather weak t_{ox} -dependence is also observed. R_{it} decreases as $t_{ox}^{-1/2}$. Qualitatively, such a decrease can be explained by diffusion–reaction models similar to those used to quantify oxide growth. For

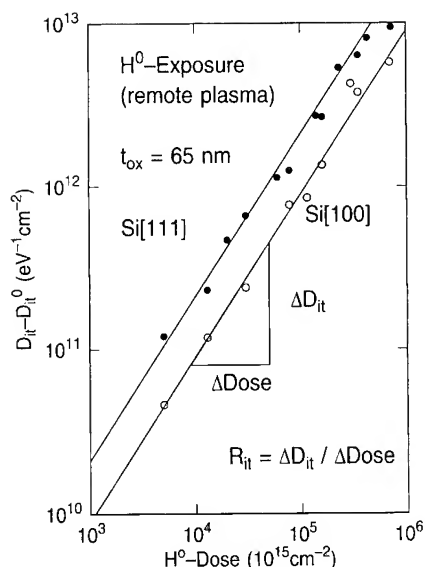


Fig. 1. Interface-state buildup at mid-gap as a function of atomic hydrogen, H^0 , dose measured in a remote hydrogen plasma at room temperature. Samples with 65 nm thick oxides grown on Si (111) and Si (100) substrates are compared. The interface-state density increases linearly with the hydrogen dose such that the degradation can be quantified by an interface state generation rate, R_{it} , as defined in the figure.

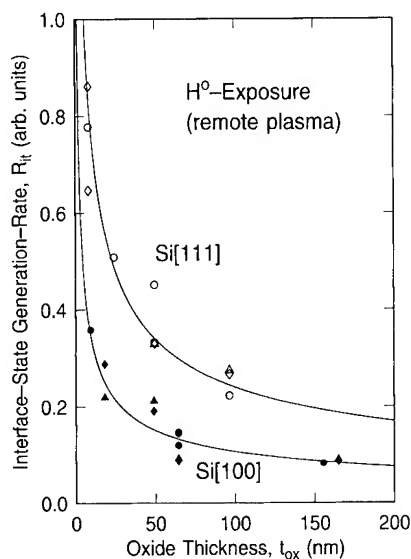


Fig. 2. Thickness dependence of the interface-state generation rate in a remote hydrogen plasma as a function of oxide thickness, measured at room temperature. Data for Si (111) and Si (100) substrate are compared. The rates were obtained from dose dependent measurements as illustrated in Fig. 1. The lines represent $t_{ox}^{-1/2}$ dependence.

diffusion-limited interface-state generation, one would expect a t_{ox}^{-1} -dependence, while reaction-limited generation should be independent of t_{ox} . Attempts have been made to use reaction/diffusion models to explain the interface degradation under high-field stress [13]. A detailed interpretation of the data in Fig. 2 is difficult at present. As mentioned above, many different chemical reactions – some of them still unknown – contribute to the interface-state generation and a model based on one single interface reaction is not expected to apply. In fact, we know that electrically active sites produced by H^0 can also be removed by it. For example, a silicon dangling bond produced via reaction (1) at 23°C can also be repassivated by H^0 at the same temperature by the reaction



as recently demonstrated by electron spin resonance [14].

By varying the H^0 -partial pressure in the plasma, we found that molecular recombination via



is probably not the main cause for the decrease of the generation rate with increasing oxide thickness. Only for H^0 -partial pressures much higher than those used in this study, we were able to observe a clear dependence of R_{it} on this pressure.

Finally, the measured temperature dependence of R_{it} is shown in Fig. 3. As can be seen, interface-state generation appears to be thermally activated with an apparent activation energy of approximately 200 meV. This number is comparable to the activation energy for H^0 -diffusion at low temperatures, suggesting that a phenomenological diffusion/reaction scheme as outlined above might be useful to parameterize interface-state generation by H^0 .

4. Conclusions

All these results prove that the release of atomic H^0 by hot-electrons during device operation would inevitably lead to severe interface degradation at typical device operation temperatures, irrespective of the gate oxide thickness and substrate orientation.

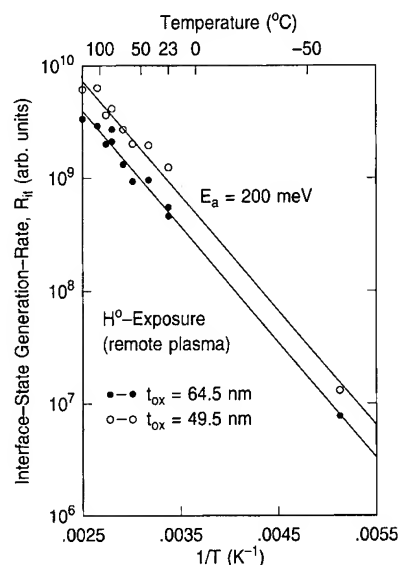


Fig. 3. Temperature dependence of the interface-state generation rate measured in a remote hydrogen plasma. The generation appears to be thermally activated with an activation energy, E_a , of about 200 meV.

Since hydrogen-release is known to be caused by hot electrons with energies as low as 2 eV, one may speculate that hydrogen-release/-diffusion/-chemistry is the dominant degradation mechanism in very thin oxides where electrons are not heated to energies large enough to produce holes in the oxide. [11,15].

If all this correct, it can be expected that the reliability of electronic devices – at least for the stress condition discussed in the introduction – can be enhanced simply by preventing the diffusion of atomic hydrogen to the Si/SiO₂-interface. In a recent study, we were able to prove that reoxidized-nitrided oxides – which are known to reduce the

interface state generation – have exactly this property: The nitrogen incorporated in these films drastically suppresses the flux of atomic hydrogen to the underlying interface, explaining its superiority as compared to thermal oxide [7,16].

References

- [1] F.J. Feigl, R. Gale, H. Chew, C.W. Magee and D.R. Young, Nucl. Instr. and Meth. B1 (1984) 348.
- [2] D.A. Buchanan, A.D. Marwick, D.J. DiMaria and L. Dori, in: The Physics and Chemistry of SiO₂ and the Si-SiO₂ Interface, ed. C.R. Helms and B.E. Deal (Plenum, New York, 1993) p. 481.
- [3] M.V. Fischetti, D.J. DiMaria, S.D. Brorson, T.N. Theis and J.R. Kirtley, Phys. Rev. B31 (1985) 8124.
- [4] D.J. DiMaria and J.W. Stasiak, J. Appl. Phys. 65 (1989) 2342.
- [5] D.A. Buchanan and D.J. DiMaria, J. Appl. Phys. 67 (1990) 7439.
- [6] D.J. DiMaria, in: Insulating Films on Semiconductors, ed. W. Eccleston and M. Uren (Adam Hilger, Bristol, 1991) p. 65.
- [7] D.J. DiMaria and J.H. Stathis, J. Appl. Phys. 70 (1991) 1500.
- [8] L. DoThanh and P. Balk, J. Electrochem. Soc. 135 (1988) 1798.
- [9] E. Cartier and D.J. DiMaria, Microelectron. Eng. 22 (1993) 207.
- [10] J.H. Stathis and D.J. DiMaria, Appl. Phys. Lett. 61 (1992) 2887.
- [11] D. Arnold, E. Cartier and D.J. DiMaria, Phys. Rev. B49 (1994) 10278.
- [12] E. Cartier, J.H. Stathis and D.A. Buchanan, Appl. Phys. Lett. 63 (1993) 1510.
- [13] D. Vuillaume, A. Mir, R. Bouchakour and M. Jordain, J. Appl. Phys. 73 (1993) 277.
- [14] J.H. Stathis and E. Cartier, Phys. Rev. Lett. 72 (1994) 2745.
- [15] D.J. DiMaria, E. Cartier and D. Arnold, J. Appl. Phys. 73 (1993) 3367.
- [16] E. Cartier, D.A. Buchanan and G.J. Dunn, Appl. Phys. Lett. 64 (1994) 901.



ELSEVIER

Journal of Non-Crystalline Solids 187 (1995) 248–252

JOURNAL OF
NON-CRYSTALLINE SOLIDS

The role of hydrogen in the action of fluorine in Si/SiO₂ structures

V.V. Afanas'ev, J.M.M. de Nijs*, P. Balk

Delft Institute of Microelectronics and Submicrotechnology (DIMES), Delft University of Technology, PO Box 5053, NL-2600 GB Delft, The Netherlands

Abstract

The effect of hydrogen exposure and subsequent annealing of F-implanted oxides on the generation of donor-type Si/SiO₂ interface states was studied. F appears to reduce the amount of H in the oxide, which otherwise is instrumental in producing these hydrogen-related states. This elimination of hydrogen is of catalytic nature; formation of the mobile species HF is suggested. Confinement of these F species by the gate is essential to prevent their escape from the oxide.

1. Introduction

Incorporation of F in Si/SiO₂ structures has been shown to improve substantially their MOS properties [1]. Particularly, the generation of the Si/SiO₂ interface states during electrical stress or irradiation was found to be strongly reduced [1–4]. We have previously demonstrated that the beneficial effect of fluorination requires activation by hydrogen [5]. Here we will show that fluorination specially affects the generation of fast donor states related to the presence of atomic H at the Si/SiO₂ interface [6], suggesting a removal of hydrogen by the fluorine dopant. The results indicate that mobile F species are formed that eliminate H in a catalytic manner.

2. Experimental

In the present study we have used F-implanted ($E = 15$ keV, $D = 1 \times 10^8$ – 2×10^{15} cm⁻²) dry oxides (66 nm) grown at 1000°C on p-Si(100) substrates. Samples implanted with noble gas (Ar, $E = 30$ keV, $D = D_F/2$) ions were also studied for comparison. To remove the implantation damage the samples were annealed in N₂ at 1000°C. Metal-oxide-semiconductor (MOS) capacitors were completed by evaporating semitransparent (18 nm) Al electrodes through a shadow mask. Finally, the structures received a standard 30 min post-metallization forming gas anneal (FGA; FG: N₂ + 10% H₂) at 400°C.

Interface states were produced by irradiation of MOS structures by vacuum-ultraviolet (VUV) photons ($h\nu = 10$ eV) at incident flux of 10^{15} cm⁻² s⁻¹ with the metal biased positively (+7 V). The injection was periodically interrupted and the shift of the high-frequency (HF) $C-V$ curve measured. After the VUV injection, 10^{14} electrons cm⁻² were

* Corresponding author. Tel: +31-15 787 200. Telefax: +31-15 622 163. E-mail: denijs@dimes.tudelft.nl.

photoinjected from the Si substrate using ultra-violet (UV) light, thus neutralizing the holes trapped in the oxide layer. Next, the generated interface states were studied by the HF-quasi-static (QS) $C-V$ technique. Additionally, the active boron concentration in the Si substrate was determined from the inversion part of the HF $C-V$ curve in order to monitor the hydrogen release during VUV irradiation. The hydrogen liberated in the MOS system has been shown to deactivate the boron dopant [7], which phenomenon was used in our study.

3. Results

In Fig. 1 the changes of midgap voltage during the hole–electron injection cycle are shown for F-free and F-implanted samples. The fluorine implanted specimen (F + Al + FGA) exhibits a much smaller density of positive charge after hole injection than the control sample. The neutralization of trapped holes by electron injection removes only part of positive charge; the remaining part cannot be neutralized. This latter fraction is related to donor interface states generated by hydrogen at the Si/SiO₂ interface [8–10].

The energy distributions of the generated interface states are presented in Fig. 2(a). These data

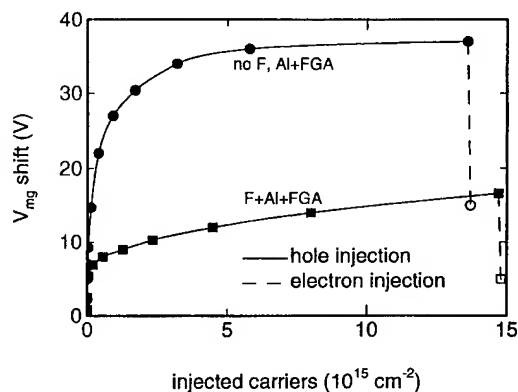


Fig. 1. Changes of mid-gap voltage during successive illumination of positively biased MOS capacitors with VUV and UV photons. Implantation of F (10^{14} cm^{-2}) and subsequent anneal and metallization sequence are indicated for each curve.

indicate a considerable suppression of the generation process in the fluorinated sample. As shown, a subsequent 5 min anneal at 150°C removes a substantial fraction of the interface states [6]. This effect is particularly large in the case of the control sample, where the fraction of annealed defects amounts to over 10^{12} cm^{-2} . The HF $C-V$ curves (Fig. 2(b)) exhibit shifts to less negative voltages; we conclude that exclusively donor interface states are removed. Implantation of fluorine preferentially affects generation of these donor states.

The efficiency of defect generation, given by the density of the generated interface states normalized with respect to that in a non-implanted sample, is

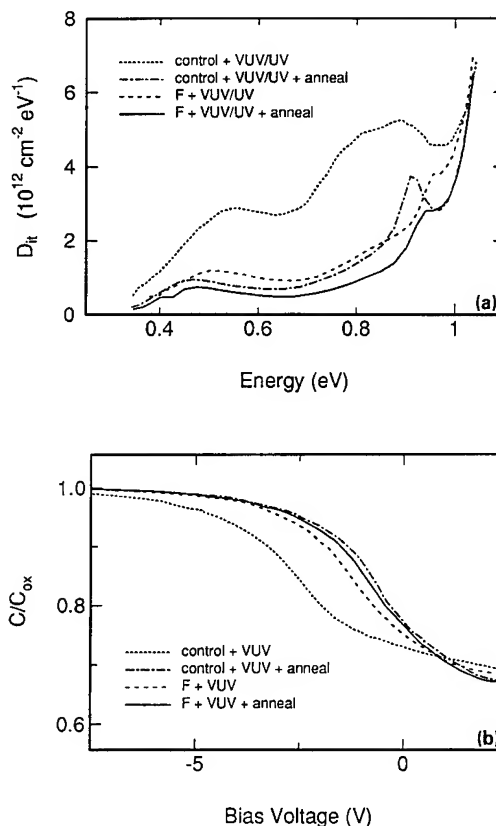


Fig. 2. Energy distributions of generated Si/SiO₂ interface states (a) and corresponding changes of HF $C-V$ curves (b) after successive 5 s VUV + 10 s UV irradiation of non-implanted and F-implanted (10^{13} cm^{-2}) MOS capacitors. The capacitors had received FGA after Al evaporation. Curves after 5 min anneal at 150°C are also shown.

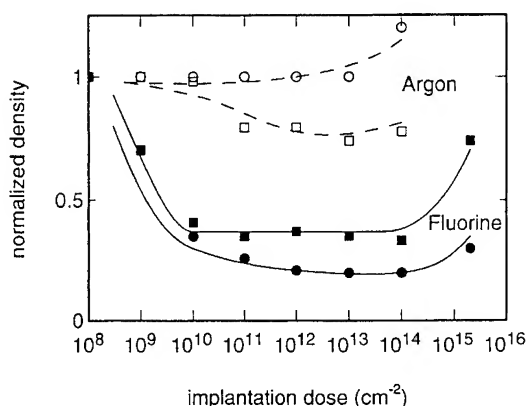


Fig. 3. Normalized densities of VUV generated interface states (circles) and deactivated boron in Si substrate (squares) in F- (closed symbols) and Ar-implanted (open symbols) sample versus implantation dose. Lines represent guide for the eye.

plotted in Fig. 3 against implantation dose. A negligible effect is obtained in the case of Ar implantation, but a significant reduction is observed in the F case, indicating that this reduction is not caused by implantation damage. Thus, F appears to affect the chemistry of the process. Moreover, it saturates when as few as 10^{10} F atoms per cm² are introduced into the oxide, preventing the generation of 1 to 2×10^{12} interface states per cm². This suggests that the F action has a catalytic character.

The normalized densities of B acceptors in the Si deactivated during VUV exposure are also plotted in Fig. 3. The suppression of the deactivation process over a wide range of F doses is evident; it correlates with the suppression of interface states generation.

So far we presented data on the action of F in samples subjected to FGA after Al evaporation. For comparison we next show results on Si/SiO₂ structures exposed to hydrogen before Al evaporation using isochronal (30 min) annealing in FG (FGA) at temperatures from 200 to 400°C. This FGA was done both for samples with bare oxide and samples protected by a thin (18 nm) Al blanket layer. The same anneals were performed in pure N₂ for comparison. After the annealing the blanket Al was etched off and semitransparent gates were evaporated through a mask, followed by 400°C post-metallization FGA. After this anneal VUV and UV injection took place. When FGA is done

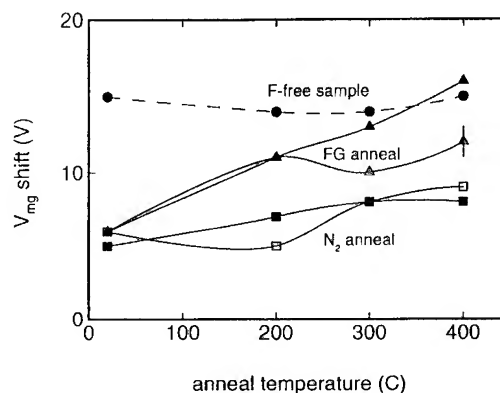
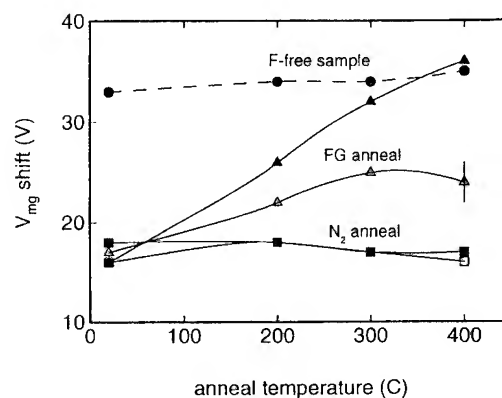


Fig. 4. Shifts of the midgap voltage after injection of 10^{17} holes cm⁻² (a) and neutralization of trapped positive charge by electron injection (b) in F-implanted (10^{14} cm⁻²) MOS capacitors. Specimens were annealed in FG (triangles) or N₂ (squares) at different temperatures with (open symbols) or without (closed symbols) Al blanket. After the anneal the Al blanket was removed and samples were metallized again followed by 400°C FGA. Results for a F-free control samples (anneal of bare oxide, circles) are also shown. Lines represent guide for the eye.

without metal overlayer, the beneficial effect of the F disappears despite subsequent metallization and the 'activating' final FGA.

The midgap voltage shift after injection of 10^{17} holes cm⁻² and its component remaining after neutralization of trapped holes (related to donor interface states) are presented in Figs. 4(a) and (b), respectively, for the specimens annealed at different temperatures before Al gate evaporation and the final FGA. A FGA of the bare oxide leads to

increased suppression of the beneficial action of F for increasing annealing temperatures; after a 400°C anneal the sample behaves similar to the non-implanted one. The presence of the Al blanket layer during FGA apparently prevents such a 'recovery' suggesting that H and F form a mobile species and that the removal of these species from the oxide is prevented. When the anneal is performed in pure nitrogen, the loss in the fluorination efficiency appears to be minimal.

4. Discussion

Irradiation produces two types of interface traps: amphoteric Si dangling bond defects (ESR-active P_b centers) and hydrogen related donor states (ESR-inactive) [6]. In the samples used in the present study we deal mainly with donor states, as indicated by the behaviour of the samples exposed to VUV for 10^5 s; the interface state density determined from $C-V$ measurements reaches 10^{13} cm^{-2} , but no significant P_b signal was detected (detection limit of $6 \times 10^{11} \text{ cm}^{-2}$).

Elsewhere we show that the generation of the donor states appears to be a result of the interaction of atomic H, liberated during charge injection or irradiation (radiolytic hydrogen), with the SiO_2 network at the interface [6]. Recent experiments on interface state generation by exposure to atomic H [11] support this model. Consequently, it appears reasonable to explain the suppression of the generation of donor states in fluorinated samples from a reduced availability of atomic H in the MOS system. Indeed, monitoring of the amount of released H from B deactivation supports this idea and presents additional evidence for the involvement of H in the production of these interface traps (note the correlation in Fig. 3). Thus, the action of F includes elimination of hydrogen that otherwise will be released during charge injection.

After the 1000°C post-implantation anneal some F remains in the oxide. This is possible only if it is firmly bonded, which prevents diffusion out of the oxide. Of the two possible configurations, Si–F and Si–O–F, only the former is stable at 1000°C, which suggests that F is present in this form. When H is introduced in the oxide by FGA, fluorine is liber-

ated from this bonded state. We propose that the mobile species HF are formed. The observed reduction in F-implanted oxides of the amount of radiolytic hydrogen, produced from its precursor in the network by irradiation, apparently takes place by the interaction of this precursor with HF and produces a more stable form of hydrogen. Because per F atom a large number of radiolytic hydrogen precursors can be rendered harmless, it is likely that HF is being recycled in this process. At the present time a more detailed discussion of the process is superfluous, because neither the nature of the precursor nor that of the final hydrogen species is known.

If FGA is performed on bare oxides, the mobile fluorine species will escape to the ambient and the beneficial effect is lost. Apparently, a diffusion barrier is needed to confine the F species to the oxide during the anneal in a H containing ambient. Our results suggest that even a thin Al blanket suffices to prevent such out-diffusion. This result also explains the lack of improvement of the electrical properties of poly-Si gated structures when F is implanted in the SiO_2 prior to poly-Si deposition [12]. Apparently, the dopant is lost at the initial stages of poly-Si growth when the oxide is exposed to the silane containing ambient at 600°C. The beneficial action is observed only if F is implanted into the poly-Si layer after deposition. During the high-temperature anneal the F will diffuse into the oxide which acts as a sink.

5. Conclusions

The presented results suggest a double role of hydrogen in the fluorine effect. H appears necessary to initiate the action of F by liberating it from the Si–F bonded configuration, forming a mobile species. On the other hand, hydrogen itself is instrumental in the generation of interfacial donor states upon carrier injection or irradiation. To obtain a reduced generation of the interface states requires a reduction of the amount of radiolytic hydrogen in the oxide. This apparently is realised by the F action. To obtain the desired beneficial effect care should be taken to prevent the escape of F from the oxide.

The authors thank T. Zijlstra, A. Apon and S. Bootsma for assistance in the preparation of the samples. The ESR measurements by Dr A. Stesmans (KU Leuven, Belgium) are gratefully acknowledged. One of the authors (V.A.) is indebted to DIMES, TU Delft for financial support.

References

- [1] T.P. Ma, *J. Vac. Sci. Technol. A* 10 (1992) 712.
- [2] E.F. da Silva, Y. Nishioka and T.P. Ma, *IEEE Trans. Nucl. Sci.* NS-34 (1987) 1190.
- [3] K. McWilliams, L. Halle and T. Zietlow, *IEEE Electron. Dev. Lett.* EDL-11 (1990) 3.
- [4] V.V. Afanas'ev, M. Depas, J.M.M. de Nijs and P. Balk, *Microelectron. Eng.* 22 (1993) 93.
- [5] V.V. Afanas'ev, J.M.M. de Nijs and P. Balk, *Appl. Phys. Lett.* 63 (1993) 2949.
- [6] K.G. Druif, J.M.M. de Nijs, E. v.d. Drift, V.V. Afanas'ev, E.H.A. Granneman and P. Balk, these Proceedings, p. 206.
- [7] C.T. Sah, J.Y.-C. Sun and J.J.-T. Tzou, *Appl. Phys. Lett.* 43 (1983) 204.
- [8] F.J. Feigl, D.R. Young, D.J. DiMaria, S. Lai and J. Calise, *J. Appl. Phys.* 52 (1981) 5665.
- [9] S.K. Lai and D.R. Young, *J. Appl. Phys.* 52 (1981) 6231.
- [10] C.T. Sah, J.Y.-C. Sun and J.J.-T. Tzou, *J. Appl. Phys.* 54 (1983) 2547.
- [11] E. Cartier, J.M. Stathis and D.A. Buchanan, *Appl. Phys. Lett.* 63 (1993) 1510.
- [12] V.V. Afanas'ev, J.M.M. de Nijs and P. Balk, in: *Proc. ESSDERC'93*, ed. J. Borel, P.-Gentil, J. Noblanc, A. Nouailhat and M. Verdone (Editions Frontiers, Grenoble, 1993) p. 415.



ELSEVIER

Journal of Non-Crystalline Solids 187 (1995) 253–256

JOURNAL OF
NON-CRYSTALLINE SOLIDS

Hydrogen-annealing induced positive charge in buried oxides: correspondence between ESR and $C-V$ results

K. Vanheusden^a, A. Stesmans^{a,*}, V. V. Afanas'ev^{b,1}

^a Department of Physics, Katholieke Universiteit Leuven, 3001 Leuven, Belgium

^b Delft Institute of Microelectronics and Submicrotechnology (DIMES), Delft University of Technology, 2600 GB Delft, Netherlands

Abstract

The positive charge, introduced into the buried oxide (BOX) layer of separation by implanted oxygen (SIMOX) material by annealing in hydrogen in the temperature range 450–700°C, has been measured by a novel charge sensing technique based on electron spin resonance (ESR). Standard capacitance–voltage ($C-V$) analysis has been used as a crucial test for this ESR method, yielding excellent agreement between the areal BOX-charge densities as obtained by the two techniques. Photoinjection of charges and optical excitation experiments have been performed subsequent to the hydrogen charging treatment to obtain additional information on location and stability of the hydrogen-induced positive centers. The charge injection experiments revealed that these centers are very stable (even electron injection does not affect them despite their Coulombic attractive potential). Generally, the charge injection and optical excitation data, together with the results from both ESR and $C-V$ etchback experiments, show that the BOX charge is located very near the two Si/BOX interfaces (within a layer of ≤ 20 nm).

1. Introduction

Separation by implantation of oxygen (SIMOX) is one of the leading techniques for producing silicon-on-insulator (SOI) material. However, a number of irradiation and charge injection experiments have demonstrated that the buried oxide (BOX) contains large concentrations of deep charge traps [1, 2]. Also, the enhanced sensitivity of the BOX to

defect generation [3–5] and to treatments involving hydrogen [3, 6] has demonstrated its inferior quality as compared to standard thermal SiO_2 . In recent work it was shown that simple annealing in hydrogen in the temperature range 450–700°C introduces positive charge in the BOX [7]. This positive charge was detected by electron spin resonance (ESR). Although no *direct* ESR signal associated with the positive charge centers was observed, both the charge sign and density of the centers were determined through their band bending effect which activates a shallow O-related donor residing in the interfacial Si regions near the BOX. This could be done because the detected shallow donor areal spin density (up to

* Corresponding author. Tel: +32-16 327 179. Telefax: +32-16 327 987. E-mail: andre.stesmans@fys.kuleuven.ac.be.

¹ Permanent address: Institute of Physics, St. Petersburg University, St. Petersburg 198904, Russian Federation.

$\sim 5 \times 10^{12} \text{ cm}^{-2}$) was observed to match the areal density of positive BOX charge.

In the present study this new charge sensing technique was combined with standard capacitance–voltage ($C-V$) analysis, both as a crucial test for the ESR method and to characterize further the hydrogen-induced hole centers. Both the ESR and the $C-V$ method were combined with etchback experiments, yielding BOX-charge depth profiles. In addition, charge injection experiments were performed subsequent to the hydrogen charging treatment to obtain additional information on location and stability of the charge centers.

2. Experimental procedures

State-of-the-art SIMOX samples were formed by single (SI) or multiple (MI) implantation of an n-type (001) Si substrate maintained at 600°C with 200 keV O^+ ions to a final dose of ~ 1.8 and $\sim 2.25 \times 10^{18} \text{ cm}^{-2}$ and annealing at 1325°C in $\text{Ar} + 1\% \text{ O}_2$ for 5 h, yielding a BOX layer of ~ 400 and $\sim 490 \text{ nm}$, respectively, and a crystalline top Si layer of $\sim 200 \text{ nm}$. The samples were etched in 50% KOH solution at 43°C to remove the top Si layer.

The hydrogen charging anneals were performed in H_2 (99.9999% pure; 1.1 atm) for 20 min in the range $223\text{--}1050^\circ\text{C}$, as described elsewhere [7]. As explained above, the positive BOX charge was sensed indirectly, by ESR detection of shallow-donor spins residing in the Si near the BOX/Si interfaces, using a K-band ($\sim 20.2 \text{ GHz}$) absorption spectrometer. The areal density of repopulated (spin-active) shallow donors in the samples was determined at 4.3 K relative to a Si:P powder intensity standard of $[\text{P}] = 1.7 \times 10^{18} \text{ cm}^{-3}$ which was always identically attached to the samples. This was done by comparing both signal intensities and taking into account the Curie–Weiss temperatures of both spin systems, as outlined elsewhere [8]. The absolute accuracy reached on the areal spin density is estimated at $\sim 20\%$, while the relative accuracy in comparing an ESR signal of one sample over various treatments may be better than 6%.

For the photoinjection of charges and optical excitation of defects MOS capacitors were fabricated on the various SIMOX substrates. This was

achieved by deposition of semitransparent Al or Au gate electrodes on top of the exposed BOX layers followed by UV or VUV illumination under the desired gate bias. High-frequency $C-V$ measurements were performed at 1 MHz using similar MOS structures. In order to obtain BOX charge depth profiles, both the $C-V$ and the ESR charge sensing methods were carried out in combination with etchback experiments. The BOX layers were thinned in HF solution and the thickness was monitored by ellipsometry and by stylus profilometry.

3. Experimental results

Fig. 1 shows the remaining areal ESR-active donor density relative to the initial value versus the remaining layer thickness as obtained from etchback experiments on SI samples positively charged by a hydrogen anneal. As the detected areal donor density matches the areal density of positive charge units in the BOX, the derivative of this plot directly yields the BOX charge depth profile.

In Fig. 2 the $C-V$ curve shift is plotted versus the remaining BOX thickness. This etchback experiment was performed on MI samples that were

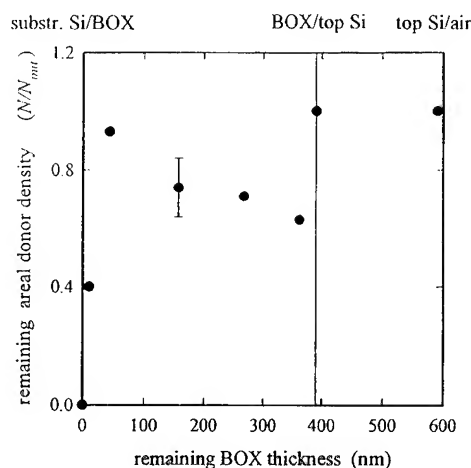


Fig. 1. Remaining areal donor density relative to the initial value as a function of remaining buried oxide layer thickness as obtained from etchback experiments on single implanted SIMOX that was positively charged by hydrogen annealing.

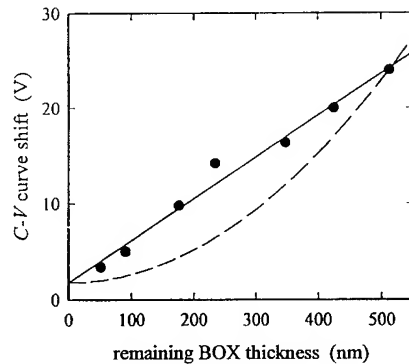


Fig. 2. $C-V$ curve shift versus remaining BOX thickness as obtained from etchback experiments on triple implanted SIMOX that was positively charged by annealing in H_2 at 520°C . The dashed and the full curve show the expected $C-V$ shift versus BOX thickness behavior for a uniform positive charge distribution in the BOX and for one located at the substrate interface, respectively.

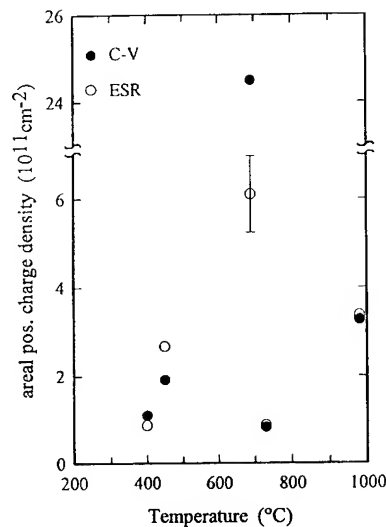


Fig. 3. Areal positive BOX charge measured by the $C-V$ and ESR methods on a set of single implanted SIMOX samples annealed in H_2 at different temperatures (yielding different BOX charge contents).

positively charged by annealing in H_2 . The data clearly exhibit a linear dependence on remaining BOX thickness which is expected from $C-V$ theory only if the positive charge is located right at the substrate Si/BOX interface. For comparison, the

dashed parabolic curve shows the expected $C-V$ shift versus BOX thickness behavior if one would assume a uniform positive charge distribution for the BOX.

Fig. 3 shows the areal positive BOX charge as obtained by both the $C-V$ and ESR method on a set of SI samples annealed in H_2 at different temperatures (yielding different BOX charge contents).

4. Discussion

As can be seen from Fig. 1, all the positive BOX charge is located very close to the two BOX/Si interfaces (≤ 20 nm layers). The slope exhibited by the datapoints in the bulk of the BOX is tentatively associated with the presence of negative charge. The $C-V$ etchback data presented in Fig. 2 confirm the result from the ESR depth profile, i.e., the hydrogen-induced BOX charge is located near the interfaces.

Having ascertained the location of the positive charges in the BOX, the areal positive BOX-charge densities can be calculated straightforwardly from the measured $C-V$ curve shift values. These values can then be compared to the values obtained by the ESR method, allowing an absolute test of this novel charge sensing technique. As the ESR method does not require any metal gate contacts, it follows from simple semiconductor device theory that the areal positive BOX-charge density equals the detected areal density of spin active donor centers. This means that each positive charge unit in the BOX must be compensated by an electron trapped at a donor site, yielding a paramagnetic center. The data in Fig. 3 show good agreement between the BOX charge as obtained by ESR and $C-V$, except for the $T = 690^\circ\text{C}$ point. In the latter case, the ESR value is far too low. This, however, can easily be explained as the charge sensing donor probe saturates at a given value [8], i.e., at the onset of strong accumulation (inversion).

Optical excitation of defects by UV irradiation under negative gate bias (-1 MV/cm) was observed to introduce positive charge into the BOX with an areal density of $\sim 5 \times 10^{11}\text{cm}^{-2}$ (saturation level). This effect was observed in a control sample (standard BOX) as well as in BOX that

received a 900°C H₂ anneal inducing positive BOX charge ($\sim 1.3 \times 10^{12} \text{ cm}^{-2}$). UV irradiation under zero bias again neutralized the UV-induced charge in both samples but did not affect the H₂-annealing-induced charge. As the saturation level of the positive charge density introduced in this manner is bias field dependent [9], this means that the hydrogen charging treatment has little effect on the electric field near the substrate Si/BOX interface, which is again confirmed by the observed perfect charge compensation upon UV irradiation under zero bias. This is only possible if the charge is located very near to the substrate Si/BOX interface. This result confirms the etchback data.

Photoinjection of electrons was achieved by VUV irradiation under negative gate bias (-1 MV/cm). Surprisingly, both BOX layers (standard and H₂ annealed) trap about the same amount of electrons, i.e., saturation occurs at $\sim 1.2 \times 10^{12} \text{ cm}^{-2}$. So, the initial (H₂-annealing induced) charge difference is not affected. This means that the hydrogen-induced positive charge centers are very stable: not only do they survive storage for months, but they even remain stable under electron injection. Apparently, electrons cannot be trapped by these centers despite of their Coulombic attractive potential. This situation only seems possible if the centers are located near the Si/BOX interface (i.e., if the first electron level in the Coulomb potential well lies above the Si conduction band edge). This result again confirms the UV and the etchback data.

5. Conclusions

As a main result, good agreement has been observed between the BOX-charge densities determined by $C-V$ analysis and the density values determined by a novel charge sensing technique based on ESR. From a technical point of view, it

validates the outlined ESR method as an adequate tool for BOX charge sensing, providing accurate data without the complications of metal gate electrodes and contacts.

The charge injection and optical excitation experiments show that the hydrogen-induced charge centers are very stable: they survive storage for months and even electron injection does not affect these centers despite their Coulombic attractive potential. This feature, and the results from both ESR and $C-V$ etchback experiments, yielding BOX charge depth profiles, demonstrate that this charge is located mainly very near the two Si/BOX interfaces (in a layer of $\leq 20 \text{ nm}$). This is likely related to the assumed presence of Si clusters in these regions [9].

Support to this work by the Belgian National Fund for Scientific Research is gratefully acknowledged.

References

- [1] J. F. Conley, P. M. Lenahan and P. Roitman, IEEE Trans. Nucl. Sci. NS-38 (1991) 1247.
- [2] W. L. Warren, D. M. Fleetwood, M. R. Shaneyfelt, J. R. Schwank, P. S. Winokur and R. A. B. Devine, Appl. Phys. Lett. 62 (1993) 3330.
- [3] M. Zvanut, R. Stahlbush, W. Carlos, H. Hughes, R. Lawrence, R. Hevey and G. Brown, IEEE Trans. Nucl. Sci. 38 (1991) 1253.
- [4] R. A. B. Devine, J. L. Leray and J. Margail, Appl. Phys. Lett. 59 (1991) 2275.
- [5] K. Vanheusden and A. Stesmans, J. Appl. Phys. 74 (1993) 275.
- [6] S. M. Myers, Mater. Res. Soc. Symp. Proc 107 (1988) 105; S. M. Myers, G. A. Brown, A. G. Revesz and H. L. Hughes, J. Appl. Phys. 73 (1993) 2196.
- [7] K. Vanheusden and A. Stesmans, Microelectron. Eng. 22 (1993) 371; Appl. Phys. Lett. 64 (1994).
- [8] K. Vanheusden and A. Stesmans, J. Appl. Phys. 73 (1993) 876.
- [9] S. I. Fedoseenko, V. K. Adamchuk and V. V. Afanas'ev, Microelectron. Eng. 22 (1993) 367.



ELSEVIER

Journal of Non-Crystalline Solids 187 (1995) 257–263

JOURNAL OF
NON-CRYSTALLINE SOLIDS

Chemical reactions of hydrogenous species in the Si/SiO₂ system

Edward H. Poindexter*

Army Research Laboratory, Fort Monmouth, NJ 07703, USA

Abstract

Recent studies involving hydrogen and its compounds in the Si/SiO₂ system are examined as a basis for a comprehensive model of hydrogen physical chemistry in the system. A model will require resolution of contradictions among experimental findings on passivation of P_b centers, radiation damage mechanisms, diffusion, and physisorption and chemisorption in the SiO₂ lattice. New findings on bias-temperature instability suggest approaches which may resolve some key problems.

1. Introduction

Hydrogen has figured heavily in semiconductor technology for many years, and is crucial in metal-oxide-silicon (MOS) integrated circuits (IC). It is essential as passivant for interface traps, and was applied early for this. As IC devices advanced, problems surfaced; various instabilities seemed vaguely connected with hydrogen. Despite this suspicion, and despite the vast investment in IC, systematic research on physical chemistry of hydrogen in the Si/SiO₂ system has never been done. The knowledge gleaned has been fragmentary. By now, however, these disconnected fragments have willy-nilly built to a substantial mass. In this paper, we will examine selected findings and interpretations. We will include our own recent results, which correct one major deficiency in the mass, and we will attempt to fuse some disparate findings into the

beginnings of a general model for hydrogen in the Si/SiO₂ system.

2. Experimental and theoretical approach

The reader should consult the references for approaches used in the cited studies. We are presenting only a few of our own unpublished findings; the major effort here is to scrutinize and reinterpret published works. Our bias-temperature and annealing studies were largely done with aid of electron spin resonance (ESR), along with simple capacitance–voltage techniques. Better electrical techniques were used by our colleagues elsewhere.

3. Observed results

3.1. Atomic hydrogen

The behavior of purported atomic hydrogen in Si/SiO₂ is ambiguous and paradoxical. Atomic H is

* Corresponding author. Tel: +1908 544 4233. Telefax: +1908 544 4306. E-mail: epindex@ftmon.arl.mil.

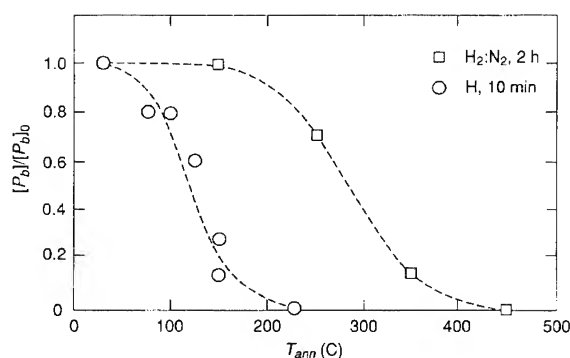


Fig. 1. Passivation of P_b centers by molecular H_2 , and rf-plasma-generated atomic H. Adapted from Refs. [3] and [4].

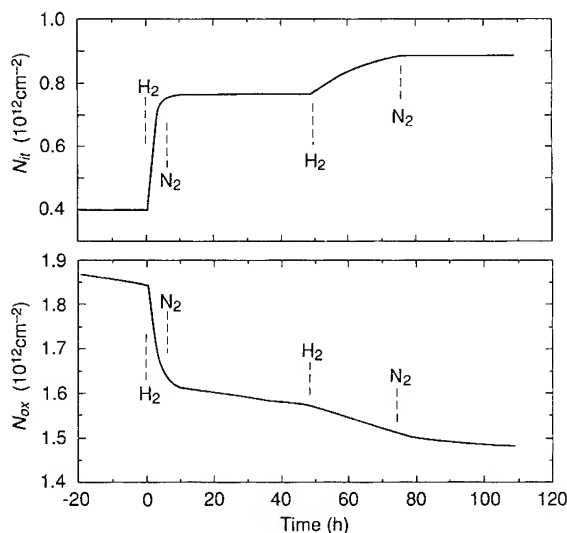


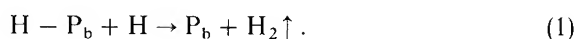
Fig. 2. Concerted evolution of oxide charges N_{ox} and interface traps N_{it} . Radiation, -65 h; gas introduced as marked. After Ref. [8].

easily detected at low temperature by ESR in either thermal film [1] or vitreous silica [2] after irradiation. The ESR disappears above 100 K, indicating a great decrease in $[H]$. Nevertheless, the existence of atomic H in thermal SiO_2 at 300 K and above is suggested by the much easier passivation of P_b centers ($\cdot Si \equiv Si_3$) or interface traps N_{it} as compared to the effect of molecular H_2 . The atomic H was produced either by rf plasma or by reaction of SiO_2 surface silanols (hydroxyls) with an alumi-

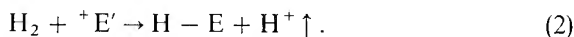
num metallization above 600 K. Simple experiments using both atomic H and molecular H_2 are shown in Fig. 1 [3,4]. A great difference in anneal temperature between H and H_2 is seen. Measurements from the latter and some better studies show activation energy, E_a , 0.3–0.6 eV for passivation by atomic H [5], compared to 2.6 eV for molecular H_2 [6]. The contradictions regarding atomic H above 100 K might be resolved by another H-bearing entity.

3.2. Radiation-generated interface traps

Generation of N_{it} by attack of radiolytic hydrogen has been proposed several times [7,8], in accord with



Some appealing experiments have supported this idea or variants thereof. Among them, the temporal growth and decline of positive oxide charges N_{ox} , correlated with the subsequent growth of N_{it} [8], Fig. 2, supports a two-stage process. The first is the cracking of radiolytic H_2 by E' damage centers ($O_3 \equiv Si \cdots \cdots Si \equiv O_3$) near the Si/SiO_2 interface:



Molecular orbital calculations predict that this would be an easy reaction [9]; widely unheralded experiments have shown that molecular H_2 passivates E' centers at room temperature, Fig. 3 [10]. Later experiments confirmed the ease of the reaction [11,12], and showed E_a to be very low, only about 0.3 eV [11], Fig. 3. The protons are then driven to the interface by the positive bias, where they are neutralized upon picking up an electron from the Si surface. Interface traps N_{it} are then proposed to be generated by the reaction of Eq. (1).

3.3. Passivation and depassivation of P_b centers

3.3.1. Reduced-passivant ambients

Depassivation of P_b centers has been studied in two ways. In the first, a previously hydrogen-passivated sample is exposed to vacuum, nitrogen, or air [6]. In the second, depassivation is (perhaps surprisingly) observed in a nominally hydrogenous

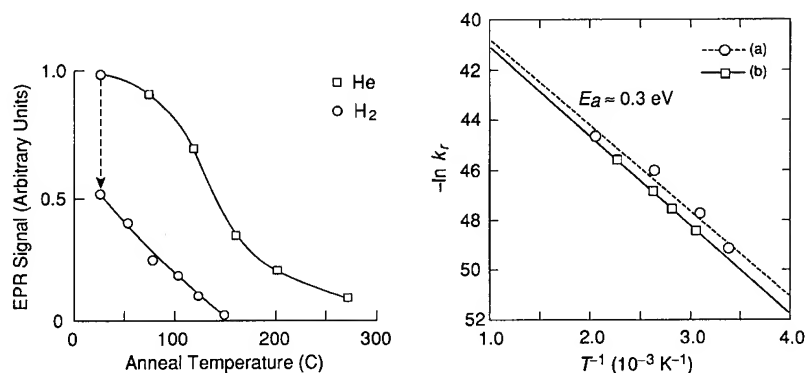


Fig. 3. Reaction of H₂ with E' centers. (a) Boron implant. (b) Electron irradiation. After Refs. [7] and [11].

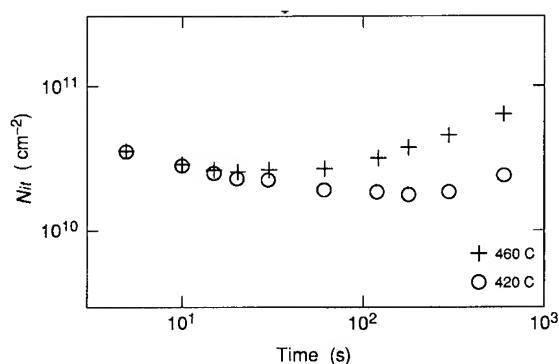


Fig. 4. Passivation/depassivation of interface traps with atomic H from Al/silanol reaction in (111) wafer. After Ref. [5].

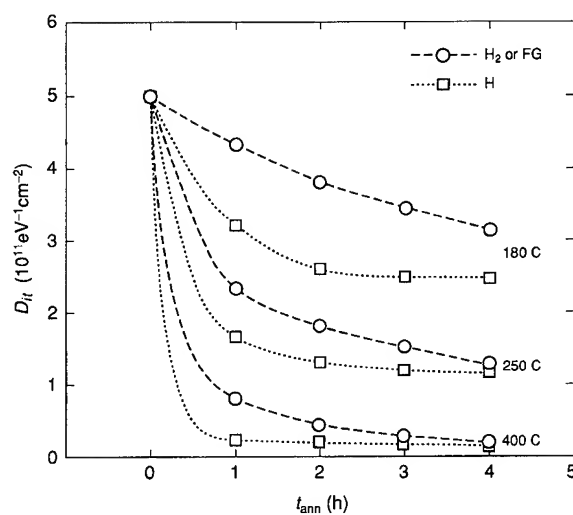


Fig. 5. Interface-trap passivation by molecular H₂ or rf-plasma atomic H; $D_{it} = N_{it}/(1.1 \text{ eV})$. Adapted from Ref. [13].

atmosphere immediately following passivation with a limited supply of passivant, as in a metallized sample with the only source of H being the silanols [5]. In these cases, $[P_b]$ or N_{it} increases as temperature is raised above the original passivating range, or as the passivation anneal is prolonged at the original temperature. An example of the latter is shown in Fig. 4. The kinetics were well developed in both cited studies. The possibility that atomic H might act as depassivant in a reaction like that of Eq. (2) was considered; and while this mechanism was judged plausible, it was found not in accord with the kinetics. Simple dissociation of passivated P_b centers was found to be strongly preferred in the cases at hand [5,6].

3.3.2. Unlimited passivant

Passivation with unlimited supply of H or H₂ offers a still better demonstration of the inconsistency of rad-damage and annealing results. In a Si/SiO₂ samples annealed with a constant supply of passivant, either H₂ or (plasma-generated) H ultimately approached the same N_{it} , characteristic of the anneal temperature [13], Fig. 5. The only difference was that atomic H acted much faster. Higher temperature anneal effected a greater reduction in N_{it} , and a sample previously annealed at a higher

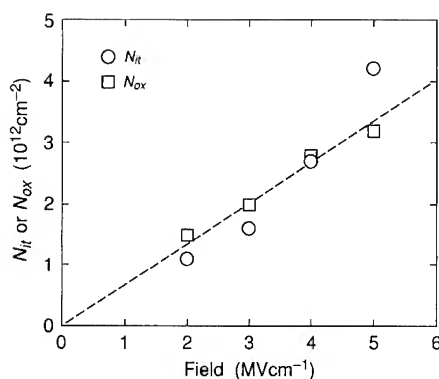


Fig. 6. Dependence of negative-bias-temperature instability on electric field. After Ref. [15].

temperature would depassivate at a lower temperature, asymptotically reaching the N_{it} characteristic of the same temperature. These results counter-indicate any forward and reverse reaction equilibrium incorporating Eq. (1), since the same equilibrium condition (revealed in N_{it}) could not occur for the widely differing $[H]$ and $[H_2]$ imposed by the contrasting ambients.

3.4. Negative-bias-temperature instability

The anomalies among experimental results suggest the need for one or more additional hydrogenous species which buffer the system. The negative-bias-temperature instability (NBTI) has recently been the basis for a suggestion of one new species, viz., H_3O^+ [14]. This species, often called the hydronium ion, has been only rarely invoked in Si/SiO₂ studies, though its stature in the physical chemistry of liquids, gases, and solids has grown steadily in the past 40 years. In the NBTI, N_{it} and Q_{ox} ($= N_{ox} \times \text{electronic charge}$) are produced by heating with concurrent application of a negative electric field [15], Fig. 6. The effect is stronger in wet oxides than dry, but no systematic study of the role of water was undertaken until fairly recently. In this newest study, it was found that the induced $N_{it} = N_{ox}$, and that both were linearly dependent on field. Moreover, the detailed effect of oxide hydrogen content was quite unexpected.

Samples prepared with graded $[H]$ were stressed with either field (to 10 MV cm^{-1}) or heat (to 700 K)

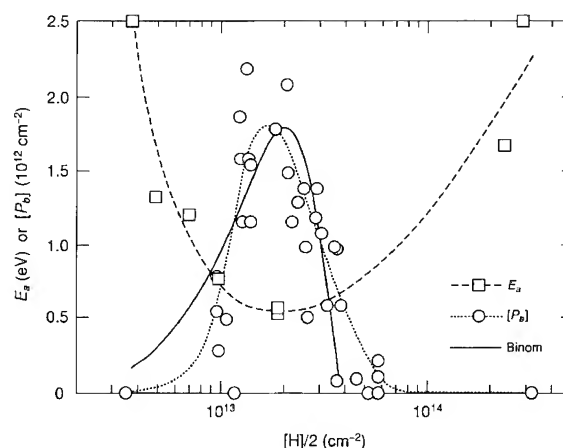
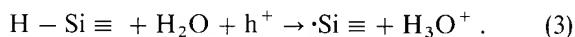


Fig. 7. Generation of $[P_b]$ by electric field at 300 K; E_a for thermal generation without field; $[P_b]$ predicted for binomial distribution of H₂O molecules in SiO₂ pores

applied independently. The surprising results are shown in Fig. 7 [14]. The NBTI does not increase steadily with hydrogen content; it is maximized at a value of about 10^{13} cm^{-2} . The activation energy E_a for depassivation is very low at this value of $[H]$. Reactions which show a minimum in E_a at some intermediate condition are known in electrochemistry, and a recent model for a general case of minimum E_a is termed the Marcus effect [16]. Consideration of these model mechanisms, and many reaction studies over the years, led to the proposal of the NBTI reaction



The hole is h^+ . The binding energy of a proton to H₂O is very high, at least 8 eV, depending on the amount of water in the vicinity and other factors. The higher end of the range is stronger than any other chemical bond in the Si/SiO₂ system. Hydronium is clearly a species to be reckoned with.

The binding energy has been calculated by molecular orbitals and measured by electrochemical cycles, and is found to range from 8 eV for H_3O^+ to 13 eV for $H_3O^+ \cdot 4H_2O$ [17]. In accord with Marcus, it was suggested that E_a goes through its minimum with 2 H₂O molecules. If one assumes that SiO₂ is a matrix with pores that can hold 4 H₂O molecules, and starts to fill them randomly, then

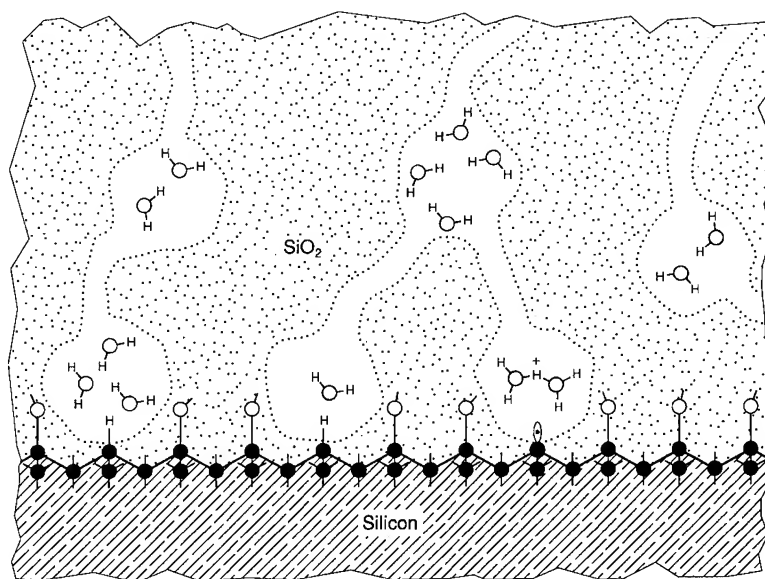
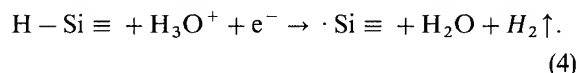


Fig. 8. Occupancy of pores in SiO_2 by H_2O molecules and preferential depassivation of P_b centers by optimum number of H_2O .

the number of pores with two molecules is maximized when their aggregate capacity is half full. The distribution predicted by binomial or Poisson statistics is shown in Fig. 7 and the pore-filling argument for the NBTI is shown in Fig. 8.

The postulated presence of H_3O^+ opens possibilities for new reaction mechanisms which might unify some of the discordant results above and explain other phenomena, as well. For one example, hydrogen-related generation of interface traps might proceed by a converse of Eq. (3):



The slow generation of N_{it} after a radiation event has been found to depend on the electric field [18], but the relationship is complicated and unsettled. Electric fields in the MV cm^{-1} range would have drastic effects on $[\text{e}^-]$ or $[\text{h}^+]$ at the interface, and thereby on reaction rates. The reaction of Eq. (4) could comprise the second stage of the E'-model, but without the discrete neutralization of protons at the Si interface.

In a second example, the seemingly unavoidable positive oxide charge after thermal oxidation has

never been identified with any particular defect moiety by ESR. Perhaps it is H_3O^+ , existing in a buffered double-layer equilibrium near the negatively-charged Si surface. Finally, some of the depassivation kinetics in nominally very dry oxides should perhaps be reconsidered if there is a chance that H_2O may have been formed along the way. It has been found that even ultradry oxides have considerable $[\text{H species}]$ near the Si interface [19].

3.5. Silanol disposition and water diffusion in SiO_2

It has been determined that H_2O is readily transported through thermal oxides at about 350 K [19], much faster than the diffusion constants from vitreous silica predict [20]. Yet neither the NBTI nor the much-studied bulk oxide electron trapping [19] is abetted by this low-temperature water infusion. The higher temperature required, > 400 K, could mean that physisorbed and chemisorbed H_2O must be specifically included in any model for hydrogen reactions [21]. These species are shown in Fig. 9. Chemisorbed water is easily produced in any SiO_2 -growth process in a wet environment. The chemisorbed H_2O constitute paired silanols. They desorb above 700 K, but their resorption in

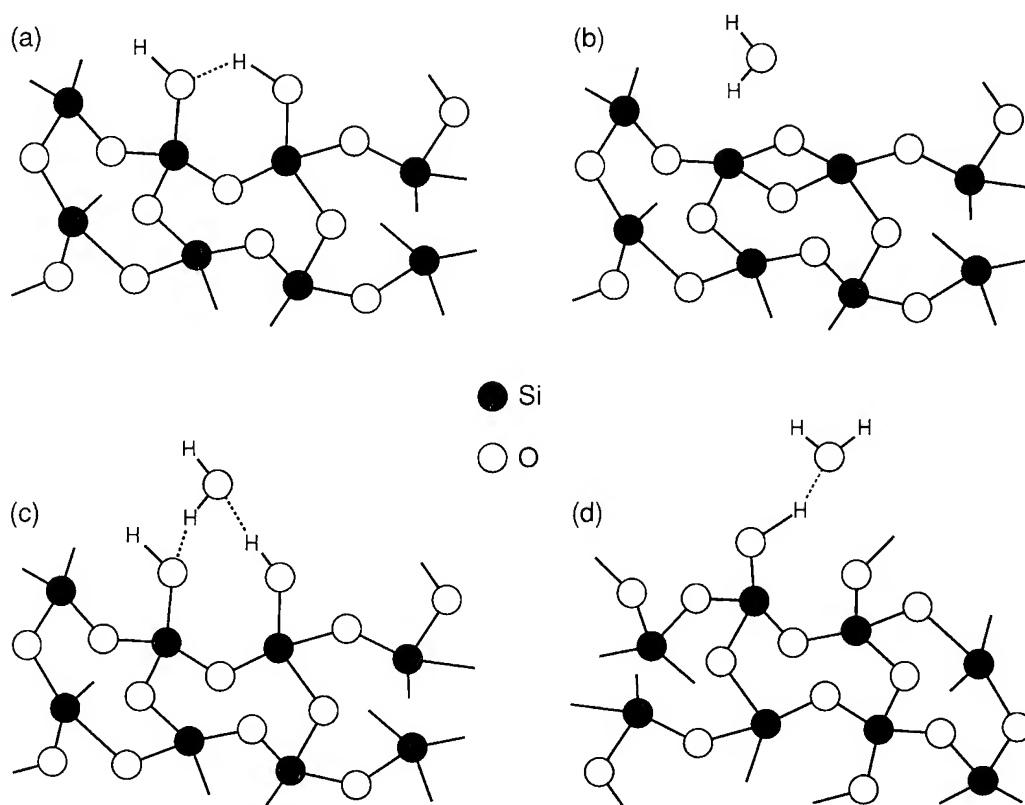


Fig. 9. Disposition of H_2O in amorphous SiO_2 . (a) H-bonded vicinal silanols, comprising chemisorbed H_2O . (b) H_2O molecule thermally ejected from silanol pair, with condensation of dehydrated site to form a siloxane linkage, $=\text{Si}-\text{O}_2-\text{Si}=$. (c) H_2O H-bonded to vicinal silanols, comprising first-layer physisorbed H_2O . (d) H_2O H-bonded to isolated silanol.

already-grown SiO_2 has not been well defined; it is not a simple process occurring when temperature is lowered. Another complexity is physisorbed water, attached to the silanols. The first layer of physisorbed water is dislodged with E_a only about 0.5 eV. The second layer binds much more strongly, indicating some molecular reorganization. With the strongest bond of all, a proton would no doubt attack all forms of adsorbed H_2O .

The solubility of H_2O in vitreous SiO_2 is proportional to the square root of $[\text{H}_2\text{O}]$ in the ambient [20], Fig. 10, meaning that two species are present in the SiO_2 . Their identity is a mystery; OH^- and H_3O^+ is one possibility. Diffusion of charged species would be subject to much drag, and so the fast ingress at 360 K probably implicates a porous structure. In a water-laden matrix, protons might be transported by tunneling between adjacent H_2O

molecules, which is pertinent to the proton diffusion proposed as part of rad-damage N_{it} generation.

4. Concluding remarks

We can draw only partial conclusions in the areas of study examined here. Depassivation findings appear to rule against radiation-damage mechanisms which postulate attack by atomic H on passivated P_b centers. The seeming disappearance of atomic H above 100 K, coupled with its continued passivating power, suggests the presence of an unsuspected hydrogenous entity. The newly developed working hypothesis for the NBTI introduces H_3O^+ in perhaps the most complex chemical argument yet applied to the Si/ SiO_2 system. The

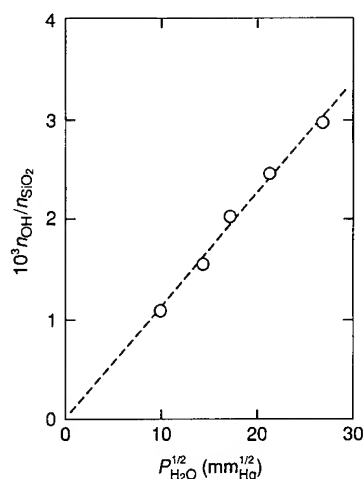


Fig. 10. Solubility of H_2O in vitreous SiO_2 . Number of molecular moieties is n ; P is partial pressure After Ref. [20].

very high affinity of H_2O for the odd proton mandates that H_3O^+ be considered in modeling of H-related phenomena near the Si/SiO₂ interface – a region which is always hydrogen – and probably silanol-rich. The existence of two exponentially dependent reaction rate factors (carrier concentration and Arrhenius activation) may explain the wide divergence in experimental results and interpretations. Hopefully, the proposed model for the NBTI, derived from broad-range control of [H species] in the samples, will inspire a similar approach to radiation effects and depassivation.

References

- [1] K.L. Brower, P.M. Lenahan and P.V. Dressendorfer, Appl. Phys. Lett. 41 (1982) 251.
- [2] D.L. Griscom, Nucl. Instr. Meth. B46 (1990) 12.
- [3] N.M. Johnson, D.K. Biegelsen and M.D. Moyer, J. Vac. Sci. Technol. 19 (1981) 390.
- [4] P.J. Caplan and N.M. Johnson, unpublished results.
- [5] M.L. Reed and J.D. Plummer, J. Appl. Phys. 63 (1988) 5776.
- [6] K.L. Brower, Phys. Rev. B42 (1990) 3444.
- [7] N.S. Saks and D.B. Brown, IEEE Trans. Nucl. Sci. 36 (1989) 1848.
- [8] R.E. Stahlbush, A.H. Edwards, D.L. Griscom and B. J. Mrstik, J. Appl. Phys. 73 (1993) 658.
- [9] A.H. Edwards, unpublished results.
- [10] B.I. Vikhrev, N.N. Gerasimenko and G.P. Lebedev, Mikroelektronika 6 (1977) 71.
- [11] Z. Li, S.J. Fonash, E.H. Poindexter, M. Harmatz, F. Rong and W.R. Buchwald, J. Non-Cryst. Solids 126 (1990) 173.
- [12] J.F. Conley and P.M. Lenahan, Appl. Phys. Lett. 62 (1993) 40.
- [13] L. DoThanh and P. Balk, J. Electrochem. Soc. 135 (1988) 135.
- [14] G.J. Gerardi, E.H. Poindexter, M. Harmatz, W.L. Warren, E.H. Nicollian and A.H. Edwards, J. Electrochem. Soc. 138 (1991) 3765.
- [15] C.E. Blat, E.H. Nicollian and E.H. Poindexter, J. Appl. Phys. 69 (1991) 1712.
- [16] R.A. Marcus, Discuss. Faraday Soc. 29 (1960) 21.
- [17] B.E. Conway, Ionic Hydration in Chemistry and Biophysics (Elsevier, Amsterdam, 1981) pp. 394–404.
- [18] M.R. Shaneyfelt, J.R. Schwank, D.M. Fleetwood, P.S. Winokur, K.L. Hughes and F.W. Sexton, IEEE Trans. Nucl. Sci. NS-37 (1990) 1632.
- [19] R. Gale, H. Chew, F.J. Feigl and C.W. Magee, in: The Physics and Chemistry of SiO₂ and the Si/SiO₂ Interface, ed. C. R. Helms and B. E. Deal (Plenum, New York, 1988) p. 177.
- [20] A.J. Moulson and J.P. Roberts, Trans. Br. Ceram. Soc. 59 (1960) 1208.
- [21] R.K. Iler, The Chemistry of Silica (Wiley, New York, 1979) pp. 622–648.



ELSEVIER

Journal of Non-Crystalline Solids 187 (1995) 264–269

JOURNAL OF
NON-CRYSTALLINE SOLIDS

Measurement and analysis of hydrogen depth profiles in MOS-structures by using the ^{15}N nuclear reaction method

J. Krauser*, F. Wulf, D. Bräunig

Hahn-Meitner-Institut Berlin GmbH, Dept. AT, Glienicker Strasse 100, 14109 Berlin, Germany

Abstract

The application of the $^1\text{H}(^{15}\text{N}, \alpha\gamma)^{12}\text{C}$ nuclear reaction analysis method promises to become the preferred measurement tool for hydrogen depth profiling in solids. A depth resolution of approximately 5 nm in the near surface region and a sensitivity < 50 ppma makes it the best choice for the analysis of thin films such as the metal–oxide–silicon system in semiconductor research. The experimental setup for depth profiling at the authors' laboratory, which was recently improved, is presented and its main features are highlighted. The recorded measurement data need to undergo a deconvolution procedure which is solved by the use of a computer program. Hydrogen depth profiles of aluminum and poly-Si gate metal–oxide–silicon capacitors are presented to show the usefulness of this deconvolution. Applying physically justifiable parameters, a deeper insight at the important interface region is possible.

1. Introduction

It is widely accepted that hydrogen plays one of the key roles in MOS-device degradation. Over the last few years different attempts have been made to determine the exact degradation mechanism. Different models exist describing the time, bias and temperature dependent build-up of interface states and oxide charges [1–3]. Many of them deal with hydrogen and some even propose its location and distribution [4]. Recent measurements at our laboratory also show that there is a direct correlation between hydrogen content and device degradation [5,6]. Different analysis techniques are capable of

detecting the total hydrogen content in solids. Secondary ion mass spectroscopy (SIMS) has been used to show the accumulation of hydrogen at the SiO_2/Si interface after electron injection from the silicon [7]. Nevertheless, the results of this method on detecting light elements like hydrogen are thought to be influenced by different limiting factors (e.g. charging effects and sputtering environment contamination). Elastic-recoil detection analysis (ERDA) in reflection [8] and transmission [9] geometry has also been applied during the last few years. Hydrogen depth profiling using the $^1\text{H}(^{15}\text{N}, \alpha\gamma)^{12}\text{C}$ nuclear reaction analysis (NRA) method is more and more becoming the preferred measurement tool in hydrogen research, since it was first introduced by Lanford et al. [10]. This is due to its good sensitivity and the excellent depth resolution [11,12]. Nevertheless, as the measured yield is

* Corresponding author. Tel: +49-30 8062 2372. Telefax: +49-30 8062 2931. E-mail: dah@dcon1.hmi.de.

a convolution of the excitation function and the initial hydrogen distribution, deconvolution is necessary. This is specially valid for thin multilayer structures like the MOS-system. A computer program was developed at the HMI to perform the deconvolution [13]. The purpose of this paper is to show how the analysis is performed and to demonstrate its usefulness by a number of examples of hydrogen depth profiles in MOS-structures. In the following section the advanced experimental setup for ^{15}N profiling at our laboratory is described.

2. Experimental setup

The experimental setup for ^{15}N depth profiling at our laboratory was described previously by Briere et al. [14]. Recently there have been changes to increase performance and accuracy of the measurements. Fig. 1 shows the schematic view of the setup as it is used now. The $^{15}\text{N}^{2+}$ ion beam is obtained from a new electron-cyclotron-resonance (ECR) ion source for highly charged ions developed at the HMI and ion currents greater than $10\ \mu\text{A}$ are now possible. First measurements with $^{15}\text{N}^{4+}$ ion beams have been made to further increase detection sensitivity [15]. To avoid local sample heating, measurement currents in our experiments are typically between 300 and 600 nA. The beam can be scanned electro-magnetically in

horizontal and vertical directions. A vacuum better than $4 \times 10^{-6}\ \text{Pa}$ is provided by the use of two turbomolecular pumps and two large cold traps to reduce the buildup of hydrocarbons at the sample surface during measurement to a minimum. Up to six samples of maximum $4\ \text{cm}^2$ in size are mounted on a sample holder that is movable in all three spatial directions. The vertical translation is performed by a computer-controlled step motor. The temperature of the sample holder is controlled in the range from 80 to 500 K and does not deviate more than 2 K in the region below room temperature and 4 K at elevated temperatures during depth profiling. Measurements presented in the following sections were generally performed at 80 K. To enable direct measurement of the target current, the manipulator unit is completely isolated from the beam line. Suppression of secondary electrons rejected from the sample surface is attained by a magnetic suppression plate. This ensures exact determination of the target current, which is integrated electrically up to the desired charge per data point. Charge collection per data point varies between 10 and $200\ \mu\text{C}$, depending on hydrogen content of the sample and required accuracy. The 4.43 MeV gamma rays of the nuclear reaction are detected by a $3'' \times 3''$ bismuth germanate scintillation detector (BGO) placed 2 cm behind the samples and at an angle of 0 degrees to the beam. Measurements have shown that this angle position

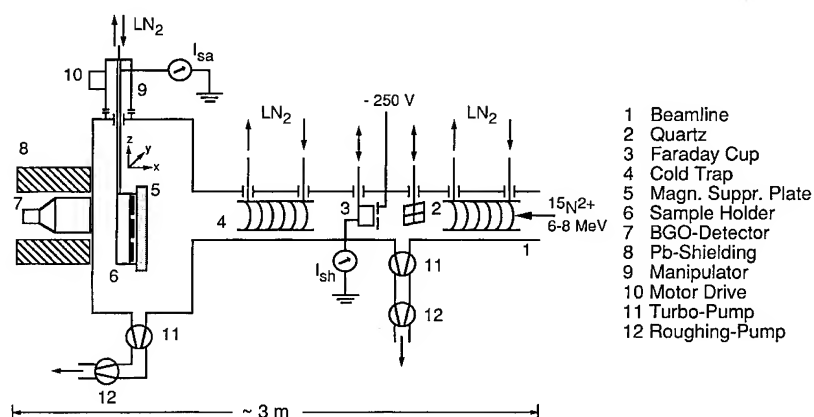


Fig. 1. Schematic drawing of the ^{15}N experimental setup at the HMI.

provides the highest counting rates. The detector is shielded by lead bricks to reduce the background counting rate which is in the range of 0.03 counts/s. Calibration of the system is performed by using an ion-implanted SiO₂ sample as a standard. The absolute overall accuracy of the measurement is better than 15% where statistical errors dominate (up to 10%).

3. Theory of depth profiling and data processing

3.1. Theory

The principle of the ¹⁵N method has been given by a number of authors [16,17]. It is not the intention of this paper to review the theory of depth profiling using ion beam techniques in an all-embracing way. An excellent discussion of this theory is given by Maurel et al. [18]. Nevertheless, it will be useful for the following description of the computer analysis to outline the basic formulae. Using narrow resonance technique and considering a flat target with uniform composition and containing the nuclei of interest (e.g. hydrogen) in a depth dependent concentration $H(x)$, the measured gamma ray yield is given by

$$Y(E_0) = \int_0^\infty H(x) \Phi \left(E_0 - x \frac{dE}{dx}, x \right) dx. \quad (1)$$

E_0 is the energy of the ions n_0 penetrating the target and $\Phi(E, x)$ is the probability for an incoming particle to be converted into a detected event. The upper infinite limit of the integral points out the value above which $H(x)$ has reached a value where no counts produced by the nuclear reaction are detected. Later in the program it will be replaced by the thickness d of the hydrogen bearing film. $\Phi(E, x)$ is the result of a folding product (*) of several Gaussian and a Lorentzian function:

$$\Phi(E, x) = n_0 \zeta \Delta \Omega h(E_0) * L(E) * D(E, \sigma) * g(E, x), \quad (2)$$

where n_0 is the number of ¹⁵N-ions hitting the target, ζ is the detector efficiency, and $\Delta \Omega$ is the detector solid angle.

In Eq. (2), $h(E_0)$ denotes the energy distribution in the ion beam (Gaussian) and $L(E) * D(E, \sigma)$ is the

reaction cross-section near the resonance energy (6.41 MeV), a folding product of a Lorentzian ($\Gamma = 1.8$ keV FWHM) [19] and a Gaussian shaped function. The latter contributes to the Doppler broadening effect ($\sigma_D = 12$ keV FWHM) [19]. The factor $g(E, x)$ is the probability that an ion will lose energy E while penetrating the thickness x (Gaussian). E_0 is the initial beam energy and σ the standard deviation of the energy distribution. After folding the Gaussian and Lorentzian parts one gets the following expression for $\Phi(E, x)$:

$$\Phi(E, x) = \frac{1}{\sqrt{2\pi}\sigma(x)} \int_{-\infty}^{+\infty} \exp \left[-\frac{t^2}{2\sigma^2(x)} \right] \times \frac{\alpha^2}{(E-t)^2 + \alpha^2} dt, \quad (3)$$

with t as a dummy variable and $\alpha = \Gamma/2$ (Lorentzian parameter). For this integral a solution can be found and $\Phi(E, x)$ finally writes as

$$\Phi(E, x) = \frac{\alpha\sqrt{\pi}}{\sqrt{2}\sigma(x)} \operatorname{Re} \omega \left(\frac{E}{\sqrt{2}\sigma(x)} + i \frac{\alpha}{\sqrt{2}\sigma(x)} \right). \quad (4)$$

The standard deviation of the energy distribution $\sigma(x)$ is given by

$$\sigma(x) = \sqrt{Qx + \sigma_0^2}. \quad (5)$$

Here Q is the straggling cross-section and σ_0^2 denotes all contributions that do not depend on the sample thickness. From this, it is clear that the accuracy of the hydrogen profiles determined is highly dependent on the accuracy of energy loss (dE/dx) and energy straggling of the ion beam. The values of dE/dx and Q for the different materials presented in the following examples were taken from the work of Briere [20]. Independent film thickness measurements show that this data results in excellent fits. The product $\zeta \Delta \Omega$ in Eq. (2) can be determined by the use of a calibration standard with known hydrogen content (e.g. H implanted SiO₂ sample).

3.2. Data processing

The deconvolution of the measured hydrogen profile is performed by folding $\Phi(E, x)$ with a model

hydrogen distribution $H(x)$ until a best fit to the data is achieved. Therefore, the deconvolution program has to solve Eq. (1) in the following limits:

$$Y(E) = \int_{-3\sigma(1)}^{3\sigma(n)+d} H(x) \Phi(E, x) dx. \quad (6)$$

The additional 3σ values of the integration borders have been chosen to get a smooth course in the graphic output of the calculation. $H(x)$ is described as a composition of half Gaussian functions at the interfaces and linear regions in the bulk of the structure. These two functional forms are well suited and common descriptions for interfacial pile-up and steady state diffusion, respectively. By changing interactively the functional parameters (see Fig. 2) of this model $H(x)$ profile, we successively approximate a best fit to the measured data points. With every approximation a plot of the error distribution is updated, thus the user is informed about the remaining difference between data points and calculated curve. All other parameters needed (e.g. stopping power dE/dx , straggling data Q) are stored in a parameter list and accessible for modifications in the main menu of the program. Fig. 2 shows the description of the functional parameters of one peak position (the number of peaks is only limited by storage capacity). Dividing the curve in two half Gaussians, makes it possible to refer to asymmetrical profiles which can occur when the hydrogen content changes very rapidly at an interfacial site. Three different intervals characterize a peak position:

$$\text{left curve part} = h_0 \exp \left[-\frac{(x - x(n))^2}{2\sigma_{\text{left}}^2(n)} \right],$$

$$\text{right curve part} = h_0 \exp \left[-\frac{(x - x(n))^2}{2\sigma_{\text{right}}^2(n)} \right],$$

$$\text{straight line} = h_1(n) + h_2(n)(x - x(n)).$$

The integration of Eq. (6) over the individual parts of the model function is performed by a routine of the IMSL MATH/LIBRARY. The program is written in standard FORTRAN and implemented on a Convex C240 computer. Depending on the required accuracy of the approximation and capacity of our computer network, calculations last a few seconds up to 1 minute.

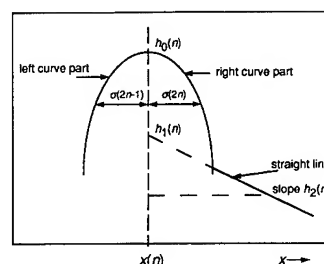


Fig. 2. Description of the functional parameters for the model $H(x)$ curve at peak position $x(n)$.

4. Discussion and examples

4.1. Al gate samples

In a recent study of degradation behaviour, we investigated samples of Al gate MOS capacitors with different annealing history [6]. The MOS capacitors were fabricated on n-type $\langle 100 \rangle$ Si wafers by dry oxidation at 950°C leading to an oxide thickness of 95 nm (determined by ellipsometric measurement). Aluminum contacts with 1.5 cm diameter for ^{15}N profiling and small dots (1 mm) for $C(V)$ measurements were formed using e-gun evaporation (80–100 nm). Fig. 3 shows the measured and fitted hydrogen depth profiles of two MOS capacitors. Sample Al1 received both, post oxidation anneal (POA) at 900°C , 30 min, in nitrogen and post metallization anneal (PMA) at 450°C , 30 min, in nitrogen. Sample Al2 only received PMA following oxidation. The measured profiles show significant differences in hydrogen content in the bulk SiO_2 as well as at the interfaces of the MOS system. Readers may refer to Ref. [6], where the influence of post oxidation treatment is reported in detail. The model $H(x)$ distributions for the fits are shown in Fig. 4. Now the program has transformed the energy loss scale to a depth scale by using the appropriate stopping powers for the different layers. These, as well as all other parameters needed for the fits in these and the next examples are presented in Table 1. The height of the surface peak depends mainly on vacuum conditions and is found to reach values up to $6 \times 10^{15} \text{ cm}^{-2}$. It is interesting to note that it is not possible to get a good fit at the Al/ SiO_2 interface by using the same small

sigma values like for the surface peak and the peak at the SiO₂/Si interface. For both samples the spatial H distribution has to be enlarged, for sample Al2 up to 16 nm. Large spatial distributions

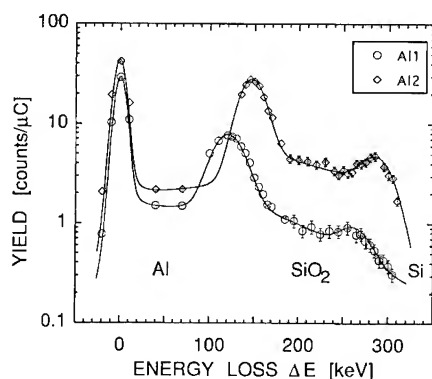


Fig. 3. Measured and fitted hydrogen depth profiles of Al gate MOS capacitors treated with different POA and PMA steps. Lines are the result of the fitting procedure.

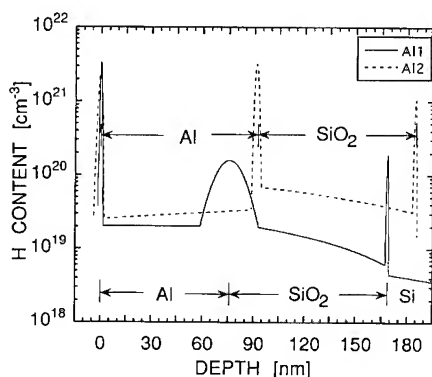


Fig. 4. Model hydrogen profiles $H(x)$ to achieve the fits in Fig. 3.

Table 1

Fitting parameters for the examples presented in Figs. 3 and 5.

Sample	Peak position $x(n)$ (nm)	Peak width $\sigma(2n-1)$; $\sigma(2n)$ (nm)	Peak height $h_0(n)$	Straight line, slope $h_1(n)$, $h_2(n)$	stopping power (keV/nm)	Straggling Q (10^5 eV ² /nm)
Al1	0/75.5/168.5	0.5; 0.5/8; 8/0.5; 0.3	240/11/13.5	1.45/1.63/0.32 0/ - 0.013/ - 0.003	1.6/1.54/1.43	1.62/1.18/1.52
Al2	0/91.5/186	1.3; 0.7/1; 1/0.7; 0.5	180/228/75	3.3/8.1/1 0.01/ - 0.04/-0.1	1.6/1.54/1.43	1.62/1.18/1.52
950°C	0/99/200.5	0.5; 0.5/0.5; 0.5/0.5; 0.5	290/8/8.3	1/0.55/0.4 - 0.0048/0/0	1.43/1.54/1.43	1.52/1.18/1.52
800°C	0/88/187	0.5; 0.5/0.5; 0.5/0.5; 0.5	363/8/14.5	0.69/0.34/0.15 - 0.0045/0/0	1.43/1.54/1.43	1.52/1.18/1.52

of H segregated at an Al/Si interface of approx. 13 nm have also been reported by Liu et al. [21]. The interfacial hydrogen contents are found by integrating $H(x)$ over the region of interest (done by the program). For the Al gate examples of Fig. 4 these values are $2 \times 10^{13} \text{ cm}^{-2}$ (Al1) and $9 \times 10^{13} \text{ cm}^{-2}$ (Al2) at the SiO₂/Si as well as $3 \times 10^{14} \text{ cm}^{-2}$ and $8 \times 10^{14} \text{ cm}^{-2}$ at the Al/SiO₂ interface, respectively.

4.2. Poly-Si gate samples

The measured and fitted hydrogen depth profiles for two poly-Si gate MOS capacitors are shown in Fig. 5. Their fitting parameters are listed in Table 1. The most striking difference to the Al gate samples is that there is no significant peak in hydrogen concentration found at the gate/SiO₂

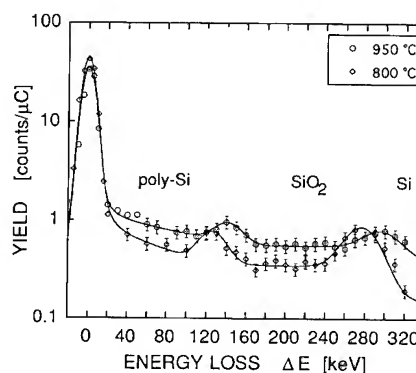


Fig. 5. Measured and fitted hydrogen depth profiles of poly-Si gate MOS capacitors treated with different POA temperatures after thermal oxidation.

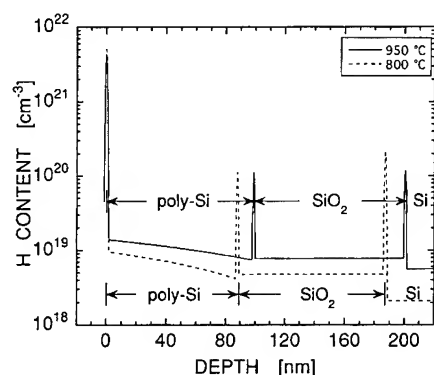


Fig. 6. Model hydrogen profiles $H(x)$ to achieve the fits in Fig. 5.

interface. Hydrogen content within the bulk oxide is generally decreased and does not show a negative gradient in concentration towards the SiO_2/Si interface. The average hydrogen concentration in the bulk SiO_2 is determined to $4.7 \times 10^{18} \text{ cm}^{-3}$ (800°C) and $7.7 \times 10^{18} \text{ cm}^{-3}$ (950°C) with an overall error of 15%, indicated by the error bars. The composed model $H(x)$ distributions for the poly-Si samples are shown in Fig. 6. The interfacial hydrogen contents are again determined from these curves with values of $2.2 \times 10^{13} \text{ cm}^{-2}$ (950°C) and $2.5 \times 10^{13} \text{ cm}^{-2}$ (800°C) at the SiO_2/Si and 1.4×10^{13} and $1.3 \times 10^{13} \text{ cm}^{-2}$ at the poly/ SiO_2 interface, respectively.

5. Conclusions

An advanced experimental setup is available to perform accurate hydrogen depth profiling in thin films. The measured depth profiles have to undergo a deconvolution procedure where the depth resolution of the method is folded with a model hydrogen distribution composed under the assumption of physically useful parameters. Thus the true hydrogen distribution as well as the interfacial hydrogen content can be extracted from the measured data, providing a deeper insight at the important interface regions. Hydrogen depth profiles in MOS

structures with Al and poly-Si gates have been presented to show the usefulness of the deconvolution.

The authors would like to thank Dr R. Schmidt, Dr M.A. Briere, H. Tillner, A. Deeg, A. Burmester, T. Kowsky and Dr J. Grzanna for their work in developing the computer code.

References

- [1] F.B. McLean, IEEE Trans. Nucl. Sci. NS-27 (1980) 1651.
- [2] D.L. Griscom, J. Appl. Phys. 58 (1985) 2524.
- [3] S.K. Lai, J. Appl. Phys. 54 (1983) 2540.
- [4] D.B. Brown and N.S. Saks, IEEE Trans. Nucl. Sci. 39 (1992) 2236.
- [5] M.A. Briere, R. Radke and D. Bräunig, in: Proc. ESA Electronic Comp. Conf., ESTEK, Noordwijk, Netherlands (1990) p. 293.
- [6] J. Krauser, F. Wulf, M.A. Briere, J. Steiger and D. Bräunig, Microelectron. Eng. 22 (1993) 65.
- [7] R. Gale, F.J. Feigl, C.W. Magee and D.R. Young, J. Appl. Phys. 54 (1983) 6938.
- [8] A. Turos and O. Meyer, Nucl. Instr. and Meth. B4 (1984) 92.
- [9] J. Tirira, P. Trocellier and J.P. Frontier, Nucl. Instr. and Meth. B45 (1990) 147.
- [10] W.A. Lanford, H.P. Trautvetter, J.F. Ziegler and J. Keller, Nucl. Instr. and Meth. 149 (1) (1976) 566.
- [11] A.D. Marwick and D.R. Young, J. Appl. Phys. 63 (1988) 2291.
- [12] K.M. Horn and P.M. Lanford, Nucl. Instr. and Meth. B45 (1990) 256.
- [13] J. Krauser and T. Kowsky, HMI Report # HMI-B 514 (1994).
- [14] M.A. Briere, F. Wulf and D. Bräunig, Nucl. Instr. and Meth. B45 (1990) 45.
- [15] W. Rudolph, C. Bauer, P. Gippner, D. Grambole, C. Heiser, F. Herrmann and H.-J. Thomas, J. Rad. Nucl. Chem. 83(1) (1984) 99.
- [16] M.A. Briere and D. Bräunig, IEEE Trans. Nucl. Sci. 37 (1990) 1658.
- [17] G. Amsel and B. Maurel, Nucl. Instr. and Meth. 218 (1983) 183.
- [18] B. Maurel, G. Amsel and J.P. Nadai, Nucl. Instr. and Meth. 197 (1982) 1.
- [19] M. Zinke-Allmang, S. Kalbitzer and M. Weiser, Z. Phys. A325 (1986) 183.
- [20] M.A. Briere, PhD dissertation, TU Berlin (1992).
- [21] J.C. Liu, A.D. Marwick and F.K. LeGoues, Phys. Rev. B44 (1991) 1861.



ELSEVIER

Journal of Non-Crystalline Solids 187 (1995) 270–272

JOURNAL OF
NON-CRYSTALLINE SOLIDS

Electrical properties of hydrogen-rich Si/SiO₂ structures

P. Danesh, A. Szekeres*

Institute of Solid State Physics, Bulgarian Academy of Sciences, Tzarigradsko Chaussee 72, 1784 Sofia, Bulgaria

Abstract

The electrical properties of Si/SiO₂ interfaces grown by oxidation of a-Si:H films are studied using quasistatic and high frequency capacitance–voltage measurements. The results obtained point out that the presence of hydrogen in the ambient and in the oxidizing film leads to an increase in the density of the interface states. This effect is suggested to be similar to postoxidation hydrogenation.

1. Introduction

The effect of hydrogen on the properties of the Si/SiO₂ interface has been widely and intensively studied [1–10]. In the oxide, hydrogen reacts with dangling bonds back bonded to three oxygen atoms (E' centers). At the interface, hydrogen passivates dangling bonds of silicon back bonded to three silicon atoms (P_b centers). Usually, hydrogen is introduced into the structures at relatively low temperatures (< 500°C) after the formation of the Si/SiO₂ interface and reacts with the already existing strained bonds and point defects. In this work we study the effect of hydrogen on the electrical properties of the Si/SiO₂ interface, as hydrogenation proceeds simultaneously with oxide growth. The Si/SiO₂ interface can receive a great deal of hydrogen through oxidation in wet oxygen or in steam. However, in this case the extremely high oxidation rate resulting in a low quality interface

might obscure the effect of the simultaneous high-temperature hydrogenation. Therefore, we have oxidized hydrogenated amorphous silicon (a-Si:H) in dry oxygen, assuming that the hydrogen involved in the oxidation process is either from the ambient, to which it has outdiffused, or is from the rest of the film.

2. Experimental

a-Si:H films were grown by the plasma-enhanced chemical vapour deposition technique under conventional conditions (13.56 MHz, 270°C, 133 Pa, 48 mW/cm²) and contained about 10% hydrogen. N-type silicon wafers with (1 1 1) orientation and resistivity of 6–9 Ω cm were used as substrates. The film thickness of 30–40 nm was chosen to ensure subsequent complete oxidation of the a-Si:H and penetration of the Si/SiO₂ interface into the crystalline silicon. This approach was chosen in order to avoid the effect of the different structural matching between the oxide and crystallized a-Si:H films, which have microcrystalline

*Corresponding author. Tel: Telefax: +359-2 757 032.
E-mail: physic@bgeam (iftt).

structure [11]. The oxide thickness was in the range of 50–60 nm. The oxidation was carried out at 1060°C in dry oxygen with less than 3 ppm H₂O content. No subsequent high temperature annealing was performed in order to keep the maximum amount of hydrogen in the Si/SiO₂ structures. Aluminium dot electrodes were deposited by thermal evaporation. After metallization, MOS structures were annealed in nitrogen at 400°C for 30 min. The properties of MOS structures prepared from a-Si:H films (denoted as Si_A samples) were compared with those from crystalline silicon. There were two kinds of reference samples. The first set, called hereafter Si_C samples, was prepared by oxidation of bare substrates in the same run with the a-Si:H covered ones. The other set, referred to as etalon samples, Si_E, was obtained by oxidation of silicon wafers under the same conditions, but in separate runs.

The electrical properties of MOS structures were evaluated by employing high-frequency (1 MHz) and quasistatic capacitance–voltage (C–V) measurements. The oxide charge, Q_{mg} , and the effective charge, Q_{eff} , were calculated from the midgap and flatband voltages, respectively. The interface states were characterized by their density at the midgap, $D_{\text{it}}^{\text{mg}}$, and the quantity, N_{it} , which was obtained by integration of the density distribution between the midgap and the Fermi level of silicon.

3. Results and discussion

Fig. 1 demonstrates the distribution of the interface states for a representative series of samples Si_A, Si_C, Si_E. As is seen, the curves have rather similar shapes, but are shifted with respect to each other. The same trend is evident in Table 1, which summarizes all the data determined from the C–V measurements. The values presented are averaged over more than 10 wafers.

The values of N_{it} and $D_{\text{it}}^{\text{mg}}$ are much greater in the Si_A samples than in the etalon ones. Furthermore, the Si_C samples also differ from the etalons. In this case, N_{it} and $D_{\text{it}}^{\text{mg}}$ are greater than in the Si_E samples, but lower than in the Si_A ones. It is reasonable to suggest that the increased density of interface states in both Si_A and Si_C samples have a common origin and this origin is the increased content of

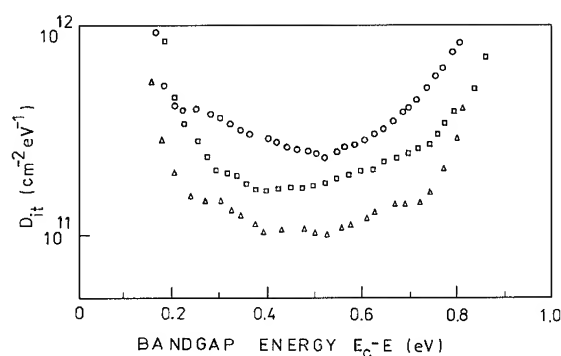


Fig. 1. Distribution of the density of interface states for Si_A (○), Si_C (□) and Si_E (△) samples.

Table 1
Electrical properties of the Si/SiO₂ interface for Si_A, Si_C and Si_E samples

	Si _A	Si _C	Si _E
Q_{eff} (cm ⁻²)	8.6×10^{11}	6.4×10^{11}	6.7×10^{11}
Q_{mg} (cm ⁻²)	9.0×10^{11}	6.6×10^{11}	6.3×10^{11}
N_{it} (cm ⁻²)	8.0×10^{10}	5.4×10^{10}	4.3×10^{10}
$D_{\text{it}}^{\text{mg}}$ (eV ⁻¹ cm ⁻²)	2.5×10^{11}	2.1×10^{11}	1.8×10^{11}

hydrogen. Actually, some of the hydrogen which outdiffused from the a-Si:H films should penetrate into the oxidizing samples. Concerning the Si_A samples, the hydrogen remaining in the film should also be taken into account. Thus, one can consider Si_A and Si_C samples as hydrogen-rich compared to the etalon ones. Moreover, Si_A samples should contain more hydrogen than Si_C samples.

It has been shown that the passivation and the depassivation processes occur simultaneously, but the former is more favourable and dominates at all temperatures leading to a concentration of the P_{b} centers much less than half of their 'intrinsic' value [3,4]. On the other hand, it is established that exposure of the Si/SiO₂ interface to atomic hydrogen at room temperature produces P_{b} centers [4] and increases the density of the interface states [5]. Also annealing in molecular hydrogen at high temperatures (500°C, 900°C) creates interface states in the midgap of silicon [6]. Thus, the depassivation becomes apparent when the structures are post-preparation hydrogenated. The results in Fig. 1 and Table 1 indicate that the increased content

of hydrogen in the oxidizing ambient has the same effect as the post-preparation hydrogenation, as the depassivation reactions are intensified and have a greater contribution in establishing the number of the interface states (P_b centers).

Once it is assumed that both Si_A and Si_C samples are hydrogen-rich, it is expected that if hydrogen affects the positive oxide charge, it would cause similar changes in the values of Q_{eff} and Q_{mg} . But unlike the Si_A samples, where an essential increase in the Q_{eff} and Q_{mg} is observed (Table 1) Si_C samples have values of oxide charges as low as in the etalons.

In thermal oxides E' centers are the dominant deep hole traps [7]. Recent EPR studies have shown that hydrogen reacts with E' centers [8,9]. Under some conditions these reactions lead to structural changes at the E' center and creation of different hydrogen coupled complexes. Both positively charged and neutral paramagnetic hydrogen coupled defects have been reported [8,9]. It has been suggested that the reactions between hydrogen and E' centers proceed depending on the oxide structure [10]. Therefore, there might be two alternative explanations for the observed discrepancy in the oxide charges – (i) during oxide growth hydrogen reacts with E' centers in different ways creating neutral hydrogen coupled defects in Si_C samples and positively charged ones in Si_A samples; (ii) there is no difference in the behaviour of hydrogen and the significantly higher values of Q_{eff} and Q_{mg} in Si_A samples are entirely due to the more defective structure of the oxide grown from a-Si:H.

4. Conclusion

The study of the electrical properties of MOS structures prepared from a-Si:H films has shown that

they are hydrogen-rich irrespective of the outdiffusion of hydrogen during the high temperature oxidation. Moreover, the oxidation of crystalline silicon in the same run with a-Si:H covered wafers provides hydrogen-rich MOS structures, as well. The results obtained point out that the introduction of additional hydrogen during the oxidation has the same effect, as the post-oxidation hydrogenation and results in an increase in the density of the interface states.

This work was supported by the National Foundation of Scientific Research under Contract No. F-95 with the Bulgarian Ministry of Science and Education.

References

- [1] Y.C. Cheng, *Progr. Surf. Sci.* 8 (1977) 181.
- [2] S. Alexandrova and A. Szekeres, *Phys. Status Solidi (a)* 96 (1986) 363.
- [3] A. Stesmans and G. Van Gorp, *Appl. Phys. Lett.* 57 (1990) 663.
- [4] E. Cartier, J.H. Stathis and D.A. Buchanan, *Appl. Phys. Lett.* 63 (1993) 1510.
- [5] L. DoThanh and P. Balk, *J. Electrochem. Soc.* 135 (1988) 1797.
- [6] H. Fukuda, M. Yasuda and T. Iwabuchi, *J. Appl. Phys.* 72 (1992) 1906.
- [7] P.M. Lenahan and P.V. Dressendorfer, *J. Appl. Phys.* 55 (1984) 3495.
- [8] J.F. Conley and P.M. Lenahan, *Appl. Phys. Lett.* 62 (1993) 40.
- [9] W.L. Warren, J.R. Schwank, M.R. Shaneyfelt, D.M. Fleetwood and P.S. Winokur, *Appl. Phys. Lett.* 62 (1993) 1661.
- [10] M.E. Zvanut, R.E. Stahlbush and W.E. Carlos, *Appl. Phys. Lett.* 60 (1992) 2989.
- [11] P. Danesh, I. Savatinova and A. Szekeres, *SPIE* 1983 (1993) 1078.



ELSEVIER

Journal of Non-Crystalline Solids 187 (1995) 273–277

JOURNAL OF
NON-CRYSTALLINE SOLIDS

Surface potential dependence of interface state passivation in metal-tunnel oxide–silicon diodes

M.O. Andersson*, A. Lundgren, P. Lundgren

Department of Solid State Electronics, Chalmers University of Technology, S-412 96 Göteborg, Sweden

Abstract

Interface state passivation during dc biased post metallization annealing at $\sim 350^\circ\text{C}$ was studied in very thin oxide, $\sim 31 \text{ \AA}$, aluminum-tunnel oxide- $\langle 111 \rangle$ p-type silicon structures. Capacitance–voltage and tunnel current–voltage measurements were used after the anneals to monitor the passivation of interface states. It was found that the passivation process of interface states in the as-manufactured devices is directly dependent on the surface potential but not on the average oxide electric field or the tunnel current. A negative gate voltage increases the passivation rate, whereas a positive gate voltage decreases it as compared to unbiased annealing. The interface states resemble P_b centres, which are dangling bonds on trivalently bonded Si atoms at the interface. The present observations are found to agree well with theoretical calculations by Edwards (1991) on the surface potential dependence of the passivation of P_b centers by H_2 . It is possible to find an optimum time and voltage for annealing, roughly 1000 s and -1.2 V in our case, for simultaneously minimizing the dc tunnel current, flatband voltage shifts and the density of fast interface states in these diodes.

1. Introduction

The electrical, physical and chemical properties of thin dielectrics based on silicon dioxide is a key research field for the successful manufacture of future ultra-small electronic devices and circuits in silicon. A good as-grown oxide–silicon interface can be made to show an extremely low defect density through the use of various anneal schemes [1]. Some reasons for the continuing interest in the Si/SiO₂ interface from industrial and applied scientific viewpoints are that thermal treatments at temperatures above 500°C [2], electrical stress or

electromagnetic radiation can increase the defect density to high levels.

We have previously investigated several aspects of the electrical behavior of very thin oxides in metal-tunnel oxide–silicon (MTOS) diodes. These aspects include random two-level fluctuations [3], electron trapping and noise in as-grown oxides [4,5] charging effects caused by electrical stress [6–8] and, most recently, post-metallization annealing (PMA) of fast interface states [9] and relaxation of stress-induced charges [5,10].

The present experimental work shows how PMA under an applied dc bias can provide new information on the passivation mechanics of fast interface states by relating their rate of passivation to the charge state. The effects of biased PMA were predicted by Edwards [11] for the P_b center [12] in

* Corresponding author. Tel: +46-31 772 1878. Telefax: +46-31 772 3622. E-mail: mats@ic.chalmers.se.

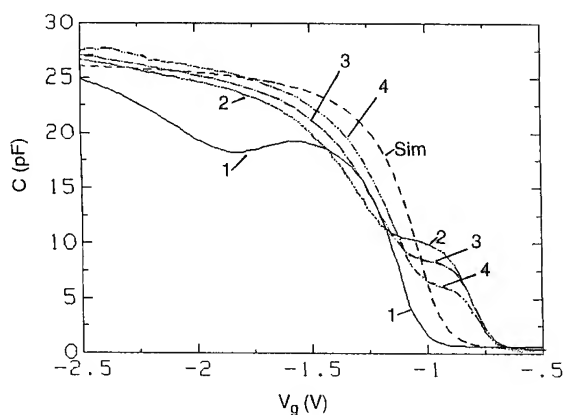


Fig. 1. Capacitance–voltage curves measured at 300 K for a device subjected to unbiased PMAs at 350°C. Curve 1: fresh device; 2: after 1000 s; 3: after 3000 s; 4: after 10 000 s. The curve marked 'Sim' is a theoretically generated curve assuming no defect charges.

a paper concerning the hydrogen passivation reactions at the $\langle 111 \rangle$ Si–SiO₂ interface. The results on the interface state density, D_{it} , in our devices are in qualitative accordance with his results. Finally we give an empirically obtained recipe for simultaneously minimizing the dc tunnel current density, J , the density of fast interface states, D_{it} , and the initial negative flatband voltage shift in these diodes under a biased PMA.

2. Experimental

The devices were made from $\langle 111 \rangle$ oriented, p-type silicon wafers from Wacker Chemitronic GmbH with a substrate resistivity of about 10 Ω cm. Active areas were formed in a field oxide by photolithography and wet etching in buffered oxide etch. After RCA cleaning the tunnel oxide was allowed to grow at 750°C in dry oxygen to a thickness of about 30 Å. On top of this oxide, immediately after oxidation, a 5000 Å thick aluminium layer was evaporated from a heated crucible. The devices were not subjected to an initial PMA. Results from experiments on samples from the same batch have been published previously [5,9].

The biased annealing was performed in a horizontal, tubular quartz furnace with a gas flow of

2 l min⁻¹ H₂/Ar through the furnace. For some experiments, N₂ was used instead with no appreciable difference noted. The sample holder, mounted onto a 1 m long, 2-hole rod of Al₂O₃, was made of aluminum with a tip of molybdenum. The gate voltage V_g was assigned values between +0.9 and –2.0 V to allow for a variation of the surface potential at the silicon–oxide interface during the PMA. Capacitance–voltage (C – V) curves at a signal frequency of 10 kHz and a temperature of 300 K were taken at regular intervals during a PMA series. Current–voltage (I – V) measurements were performed following some C – V measurements. A typical set of C – V curves from a fresh MTOS structure and after unbiased PMAs is shown in Fig. 1. We have shown [5,9] previously that the fast interface states in these devices can contribute directly to the capacitance at 10 kHz. In the present case, an easy and straightforward way to obtain the D_{it} distribution is therefore to compare the measured C – V curve to a simulated curve generated without considering interface states. This is in close analogy with the well-known quasistatic-theoretical C – V method [1], which cannot be used here as the quasistatic measurement is hardly possible to implement on these tunnel devices. The valid region of this method spans roughly the lower half of the band gap in the p-type case for tunnel oxides with thickness less than ~ 40 Å. In Fig. 2, the D_{it} distributions obtained from the C – V curves in Fig. 1 after unbiased PMAs at 350°C for 0, 1000, 3000 and 10 000 s are shown. In the following data reduction, the D_{it} values used are the peak values obtained from such plots at the energy level $E - E_{vs} = 0.25$ eV above the silicon valence band. The oxide thickness was determined [13] to be ~ 31 Å from the value of the oxide capacitance.

We have previously found [5] that if we integrate the charge from the extracted D_{it} distribution in the lower half of the band gap, assuming either donor or acceptor states, and include the voltage contribution when synthesizing a C – V curve, it is still not possible to match the measured curve for any combination of donors and acceptors. Instead, we observe that an additional negative voltage shift ΔV (≈ -0.4 V initially) remains in the measured curve. During the course of a PMA, it was shown [9] that the magnitude of this shift decreases

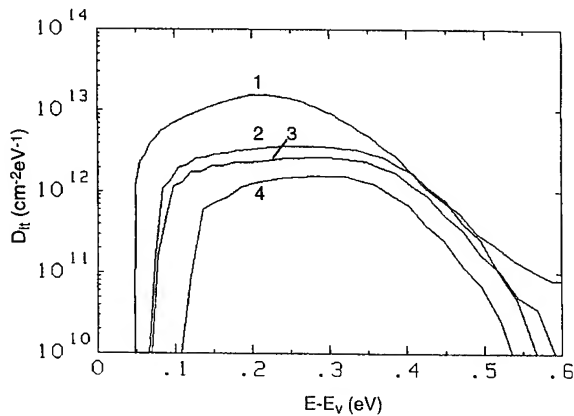


Fig. 2. Extracted interface state densities versus energy above the valence band edge with the anneal time as a parameter. The data correspond to the $C-V$ curves in Fig. 1 for the case of unbiased PMA, $V_g = 0$ V. Curve 1: fresh device; 2: after 1000 s; 3: after 3000 s; 4: after 10000 s.

gradually with very similar dynamics to the peak D_{it} when plotted on a normalized scale. Here, we briefly address the issue of the dependence of ΔV on bias during PMA. A more thorough description of the experiments is presented elsewhere [14].

3. Results

Comparing the biased PMA to the unbiased case at 0 V, in the simplest qualitative description, the peak D_{it} decreased more quickly if a negative bias was applied and more slowly if the bias was positive instead, as shown in Fig. 3. In this figure, D_{it} at the

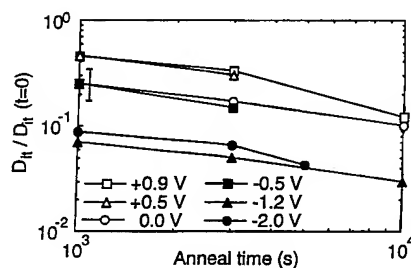


Fig. 3. The time evolution of the density of interface states for biased PMA with the gate voltage as a parameter. The data in each curve are normalized to the initial value of D_{it} for the fresh device.

Table 1

General trends in the time evolution of the density of interface states, D_{it} , the absolute value of the voltage shift, $|\Delta V|$, and the tunnel current density, J , for different gate voltages during biased PMA.

PMA V_g (V)	D_{it}		$ \Delta V $		J	
	Time Short	Long	Time Short	Long	Time Short	Long
-2.0	↓	↘	↓	↗	No	data
-1.2	↓	↘	↓	↘	↓	↗
± 0	↘	↘	↘	↘	↘	→
+0.9	↘	↘	↘	↗	↘	↗

An arrow pointing downwards refers to a decrement, the steeper the slope the stronger the decrease, and vice versa. The notations 'short' and 'long' refer very roughly to anneal times shorter or longer than about 1000 s.

energy level $E - E_{vs} \approx 0.25$ eV is plotted versus the anneal time with the applied bias as a parameter. The data are normalized to the initial peak value in each case, so the data on the ordinate commence at unity at $t = 0$ s. The spread in the data at a given bias from device to device, monitored on a total of six devices, was roughly a factor of two. This is indicated by the 'error bar' in the figure for the PMA at $V_g = 0$ V. The bias dependence of the passivation rate is most pronounced before 1000 s, a period which was difficult for us to monitor because of experimental limitations. However, the effect of the initial bias dependence sets its clear mark on the curves at longer times; the level continues to be lower or higher as compared to the unbiased case even if the slopes are approximately the same on this scale. At $V_g = +0.9$ V and at $V_g = -2.0$ V, saturation effects are observed as the curves coincide with the curves taken at $+0.5$ and -1.2 V, respectively, to within experimental uncertainty. An overview of the general trends in the time evolution of D_{it} , $|\Delta V|$ and J for different gate voltages during biased PMA is shown in Table 1.

4. Discussion

The interface states in the present diodes can safely be considered [14] to arise from defects

intrinsic to the oxides/silicon interface and not from, for instance, metallic penetration from the gate. We list below five arguments supporting that the relation between D_{it} in the present devices and P_b centers is very close. (1) The value of D_{it} at the peak maximum is about 5 times larger in these $\langle 111 \rangle$ oriented samples than in identically treated samples of $\langle 100 \rangle$ orientation, in coherence with previous reports [15]. (2) The interface states in the present devices respond to a PMA [9] at 250–350°C in qualitatively much the same way, although slower, as do P_b centers and interface states in thicker oxides [16]. (3) Using electron paramagnetic resonance (EPR), Poindexter et al. [15] found large concentrations of P_b centers in as-grown 50 Å oxides on $\langle 111 \rangle$ faces. The integrated defect density from D_{it} in our fresh samples is $3.4 \times 10^{12} \text{ cm}^{-2}$. This number does not exceed the maximum possible number of about 10^{13} cm^{-2} P_b centers on the $\langle 111 \rangle$ face [17]. (4) The energy positions of the maxima in the D_{it} distributions in Fig. 2 match well with EPR measurements for the P_b center $+ / 0$ transition level of $E - E_{vs} \approx 0.3 \text{ eV}$ and the corresponding D_{it} -peak at $E - E_{vs} \approx 0.26 \text{ eV}$ obtained from $C-V$ data [18]. (5) We have found [5] that when subjecting a fresh, unannealed device to low-voltage stress a reduction of positive charge in fast interface states occurs, i.e. these states in the lower half of the band gap are most probably donors, as is the P_b center.

Edwards [11] found that the activation energy for the reaction of direct passivation of P_b centers by molecular hydrogen, $H_2 + P_b \rightarrow H + HP_b$, is $E_{act} = 1.3 \text{ eV}$. This result was obtained for the neutral charge state of the defect. Edwards extended his study to predict that H_2 passivation of the negative charge state of P_b centers would have a much slower course than in the neutral defect case. It would be characterized by roughly twice the activation energy of the neutral case. This condition would be reached if $E_f - E_{vs} > 0.85 \text{ eV}$, where the P_b $0/ -$ transition occurs. It may also occur that an antibonding state of the P_b -H center becomes occupied under a strong positive bias, a situation which would enhance depassivation of the defect. On the other hand, for negative biases such that the $+ / 0$ transition level is above the Fermi level, the H_2 passivation can be enhanced as compared to the

unbiased case. Our results are qualitatively consistent with these predictions, also when considering the effects of the temperature and the interface charge variations on the surface potential during PMA [14].

There seems to be no direct dependence of the passivation rate on the oxide field per se. This can be inferred from the fact that the D_{it} curve in Fig. 3 for $V_g = -1.2 \text{ V}$ falls very close to the one for $V_g = -2.0 \text{ V}$ (as do the curves for $V_g = +0.5 \text{ V}$ and $V_g = +0.9 \text{ V}$ to each other). From simulations we find that the magnitudes of the initial average oxide fields in these respective cases differ roughly by a factor of two. The bias saturation effect seems to counter-indicate both the appearance of a charged passivation series as well as any dependence of the passivation on the surface concentration of mobile carriers. The current can also be ruled out as a controlling factor of the passivation; the current at 350°C was at least 10 times larger at -2 V than at -1.2 V . The surface potential is thus the strongest alternative as the controlling factor behind the voltage dependence.

5. Conclusions

It is concluded that in aluminum gate $\langle 111 \rangle$ p-type MTOS structures, the passivation rate of interface states for biased PMA increases with respect to the unbiased case when annealing is performed under the influence of a negative V_g , but it decreases if the bias is positive. The bias dependence agrees well with calculations by Edwards [11] for the case in which the passivation of P_b centers occurs directly by a reaction with molecular hydrogen. The present work also shows that the passivation processes is neither field- nor current-controlled. The beneficial effect of a negatively biased PMA makes it possible to find an optimum voltage, $V_g = -1.2 \text{ V}$ in our case, to simultaneously minimize J as well as ΔV and D_{it} in these diodes. The optimum duration of this treatment was found to be $\sim 1000 \text{ s}$ at 350°C.

This work was sponsored by a grant from Tekniskvetenskapliga Forskningsrådet (TFR). Thanks are due to Professor Olof Engström and Dr Kenneth R. Farmer for valuable discussions.

References

- [1] E.H. Nicollian and J.R. Brews, *MOS Physics and Technology* (Wiley, New York, 1982).
- [2] K.L. Brower, *Phys. Rev. B* 42 (1990) 3444.
- [3] M.O. Andersson, Z. Xiao, S. Norrman and O. Engström, *Phys. Rev. B* 41 (1990) 9836.
- [4] M.O. Andersson, K.R. Farmer and O. Engström, *J. Appl. Phys.* 71 (1992) 1846.
- [5] M.O. Andersson, P. Lundgren, O. Engström and K.R. Farmer, *Microelectron. Eng.* 22 (1993) 235.
- [6] K.R. Farmer, M.O. Andersson and O. Engström, *Appl. Phys. Lett.* 58 (1991) 2666.
- [7] K.R. Farmer, M.O. Andersson and O. Engström, *Appl. Phys. Lett.* 60 (1992) 730.
- [8] K.R. Farmer, P. Lundgren, M.O. Andersson and O. Engström, *Mater. Res. Soc. Symp. Proc.* 284 (1993) 229.
- [9] P. Lundgren, M.O. Andersson and K.R. Farmer, *J. Appl. Phys.* 74 (1993) 4780.
- [10] P. Lundgren, M.O. Andersson, K.R. Farmer and O. Engström, these Proceedings, p. 140.
- [11] A.H. Edwards, *Phys. Rev. B* 44 (1991) 1832.
- [12] Y. Nishi, *Jpn. J. Appl. Phys.* 10 (1971) 52.
- [13] B. Ricco, P. Olivo, T.N. Nguyen, T. Kuan and G. Ferriani, *IEEE Trans. Electron Dev.* ED-35 (1988) 432.
- [14] M.O. Andersson, A. Lundgren and P. Lundgren, *Phys. Rev. B* 50 (1994) 11666.
- [15] E.H. Poindexter, P.J. Caplan, B.E. Deal and R.R. Razouk, *J. Appl. Phys.* 52 (1981) 879.
- [16] N.M. Johnson, D.K. Biegelsen, M.D. Moyer, S.T. Chang, E.H. Poindexter and P.J. Caplan, *Appl. Phys. Lett.* 43 (1983) 563.
- [17] A. Stesmans and G. Van Gorp, *Appl. Phys. Lett.* 57 (1990) 2663.
- [18] E.H. Poindexter, G.J. Gerardi, M.-E. Rueckel, P.J. Caplan, N.M. Johnson and D.K. Biegelsen, *J. Appl. Phys.* 56 (1984) 2844.



ELSEVIER

Journal of Non-Crystalline Solids 187 (1995) 278–286

JOURNAL OF
NON-CRYSTALLINE SOLIDS

Section 9. Nitrides, structure and defects

Structural and bonding properties of amorphous silicon nitride films

S. Hasegawa*, T. Inokuma, Y. Kurata

Department of Electronics, Faculty of Technology, Kanazawa University, Kanazawa 920, Japan

Abstract

Amorphous Si nitride ($a\text{-SiN}_x\text{:H}$) films were deposited at 300°C by plasma-enhanced chemical vapor deposition. It is demonstrated that a charge-transfer model combined with a modified random-bonding model describes well the changes of the bonding properties as a function of x . The oscillator strength of the SiH absorption is determined, and shifts of the SiH peak and the core level spectra are systematically explained. As three or more N atoms are bonded to a Si atom, it is suggested that NH bonds are favorably formed in the films, and that the Urbach tail slope increases through enhanced bond distortion. The stress and buffered HF etch rate for films with a near-stoichiometric composition were also investigated as functions of rf power and hydrogen dilution ratio.

1. Introduction

Amorphous $\text{SiN}_x\text{:H}$ ($a\text{-SiN}_x\text{:H}$) films deposited by plasma-enhanced chemical vapor deposition (PECVD) have attracted increased interest with respect to wide applications in silicon-device technology, such as a gate insulator in thin-film transistors (TFTs) and as passivation layers. The PECVD $a\text{-SiN}_x\text{:H}$ films can be formed at deposition temperature T_d as low as 300°C, but they contain a large amount of hydrogen, forming SiH and NH bonds. Also, incorporated N atoms are bonded to three Si atoms for a relatively low N content, x , range, and

for the present films N atoms with two Si and one H nearest neighbors occur at higher x [1]. Furthermore, the formation of Si and N dangling bonds which act as charge-trap states strongly depends on the constraints imposed by the bonding network [2–6]. Thus, since the bonding structures affect the device performance in a complex way, an understanding of the structural and bonding properties is necessary. In the present work, the structural and bonding properties for PECVD $a\text{-SiN}_x\text{:H}$ films are investigated by means of X-ray-induced photoelectron spectroscopy (XPS), infrared (IR) vibrational absorption, and electron spin resonance (ESR). Applicability of a charge-transfer model (CTM) combined with a modified random-bonding (MRB) model to the analyses of these bonding properties are examined. Results of the stress measurements

* Corresponding author. Tel: +81 762 344 881. Telefax: +81 762 344 900.

and the buffered HF etch rate are also examined in connection with these bonding properties.

2. Experimental

The samples were deposited on single crystal Si and fused quartz substrates at 300°C, by rf glow-discharge decomposition of a $\text{SiH}_4\text{--NH}_3\text{--H}_2$ mixture. The gas volume ratios of both $[\text{NH}_3]/[\text{SiH}_4]$ ($= R_N$) and $[\text{H}_2]/[\text{SiH}_4]$ ($= R_H$) were varied from 0 to 30. The rf power supplied to the glow discharge was varied between 0 and 30 W, and the gas pressure was fixed at 0.3 Torr. The N content x in SiN_x varied from 0 to 1.6, and was measured by means of electron probe microanalysis (EPMA). The x values were also estimated from the intensities of N 1s and Si 2p XPS spectra.

3. Models

3.1. Modified random-bonding (MRB) model

According to the random bonding model (RBM) first put forward by Philipp [7], a- SiN_x films can be represented as a statistically controlled mixture of five $\text{Si}(\text{Si}_{4-n}\text{N}_n)$ bonding configurations, occurring with a probability $f_n(x')$ ($n = 0, \dots, 4$) for generating each configuration for a given x' . The n in $f_n(x')$ defines the number of N atoms bonded to a Si atom, and the parameter x' is the atomic ratio $[\text{N}]/[\text{Si}]$ expected in the absence of H atoms. In a- $\text{SiN}_x\text{:H}$ films including hydrogen, the SiH bonds

will be introduced by replacing one Si nearest neighbor at the Si site in $\text{Si}(\text{Si}_{4-n}\text{N}_n)$ by a H atom, and the Si–NH bonds are formed in an analogous manner. Using the MRB model, the identification of local bonding units in a- $\text{SiN}_x\text{:H}$ films can then be performed by fitting the calculated density of SiH and NH bonds to the observed ones, as shown in Section 4.2. The results are summarized in Table 1. In Table 1, the bonding units denote minimum clusters displaying a ‘basic’ configuration. This means that the bonding structure around a Si atom has the neighbors represented by the basic configuration for a given n value, under an assumption that the film is composed of a single type of a bonding unit corresponding to this configuration. On the basis of the MRB model, the bonding properties of the a- $\text{SiN}_x\text{:H}$ films can then be derived from the characteristics of the individual bonding units shown in Table 1 [1,8,9].

3.2. Charge-transfer model (CTM)

In the MRB model, it has been assumed that the observed property will show a statistical average over the different n values based on the properties expected for a uniform film composed of the bonding units for a given n value as described in Section 3.1. In practice the presence of different types of bonding units surrounding a given bonding unit will affect the characteristics of that bonding unit. For measurements of the averaged properties, however, these effects will be reduced through the statistical averaging process. For films composed of a single type of bonding unit, the charge-neutrality

Table 1

Modified random-bonding model for a- $\text{SiN}_x\text{:H}$. $f_n(x')$ is a generation probability, in which p is 0.75. The bonding unit denotes a minimum cluster originating in the basic configuration. $A_p(n)$ is the occupying probability of the bonding units with hydrogen, in the film

n	$f_n(x')$	SiN_x		$\text{SiN}_x\text{:H}$		$A_p(n)$
		Basic configuration	Bonding unit	Basic configuration	Bonding unit	
0	$(1 - px')^4$	$\text{Si}(\text{Si}_4)$	Si	$\text{H--Si}(\text{Si}_3)$	SiH	0.08
1	$4(px')(1 - px')^3$	$\text{Si}(\text{Si}_3\text{N})$	Si_3N	$\text{H--Si}(\text{Si}_2\text{N})$	$(\text{SiH})_3\text{N}$	0.28
2	$6(px')^2(1 - px')^2$	$\text{Si}(\text{Si}_2\text{N}_2)$	Si_2N_2	$\text{H--Si}(\text{SiN}_2)$	$(\text{SiH})_2\text{N}_2$	0.25
3	$4(px')^3(1 - px')$	$\text{Si}(\text{SiN}_3)$	SiN	$\text{HN--Si}(\text{SiN}_2)$	$\text{Si}_6\text{N}_4(\text{NH})_3$	1.0
4	$(px')^4$	$\text{Si}(\text{N}_4)$	Si_3N_4	$(\text{HN})_2\text{--Si}(\text{N}_2)$	$\text{Si}_3\text{N}_2(\text{NH})_3$	1.0

Table 2

Partial charge $\delta_M(n)$ ($M = \text{Si, N, and H}$) in each bonding unit shown in Table 1. The values of $\delta_{\text{NA}}(n)$ and $\delta_{\text{NB}}(n)$ denote the partial charge on a N atom in $\text{N}(\text{Si}_3)$ and Si-NH-Si bonds, respectively

n	SiN_x			$\text{SiN}_x\text{:H}$				
	Bonding unit	$\delta_{\text{Si}}(n)$	$\delta_{\text{N}}(n)$	Bonding unit	$\delta_{\text{Si}}(n)$	$\delta_{\text{NA}}(n)$	$\delta_{\text{NB}}(n)$	$\delta_{\text{H}}(n)$
0	Si	0		SiH	0.096			− 0.096
1	Si_3N	0.099	− 0.296	$(\text{SiH})_3\text{N}$	0.142	− 0.262		− 0.055
2	Si_3N_2	0.163	− 0.245	$(\text{SiH})_3\text{N}_2$	0.178	− 0.233		− 0.022
3	SiN	0.209	− 0.209	$\text{Si}_6\text{N}_4(\text{NH})_3$	0.199	− 0.216	− 0.061	− 0.048
4	Si_3N_4	0.243	− 0.182	$\text{Si}_3\text{N}_2(\text{NH})_3$	0.222	− 0.198	− 0.050	− 0.040
3				$(\text{SiH})\text{N}$	0.207	− 0.210		+ 0.004

conditions apply within that bonding unit. Using Sanderson's bonding model [10], the partial charge δ_M on the constituent M ($= \text{Si, N, or H}$) atom in the bonding unit $(\text{Si}_k\text{N}_m\text{H}_n)$ can be estimated by

$$\delta_M = (S_{\text{BU}} - S_M)/(2.08 S_M^{1/2}), \quad (1)$$

where

$$S_{\text{BU}} = (S_{\text{Si}}^k S_{\text{N}}^m S_{\text{H}}^n)^{1/(k+m+n)}. \quad (2)$$

Here, S_{Si} , S_{N} , and S_{H} , respectively, are the electronegativities of Si, N, and H atoms as defined by Sanderson [10]: $S_{\text{Si}} = 2.84$, $S_{\text{N}} = 4.49$, and $S_{\text{H}} = 3.55$. The value of S_{BU} is the effective electronegativity of the bonding unit. The charge neutrality implies $k\delta_{\text{Si}} + m\delta_{\text{N}} + n\delta_{\text{H}} = 0$. Moreover, additional effective-charge on an M atom is given by $4\delta_M$ [8]. Details of this estimation procedure for δ_M have been presented in previous papers [8, 9], and the resulting estimated values of δ_M are summarized in Table 2. In this table, the results for a $\text{H-Si}(\text{N}_3)$ bonding configuration (the corresponding bonding unit is $(\text{SiH})\text{N}$) are also shown for comparison.

4. Results

4.1. Shifts of XPS spectra

The net effect of charge transfer among the constituent atoms in a-SiN_x can be correlated with the chemical shifts of the Si 2p core level spectra. This shifts relative to that for crystalline Si is dominated by changes of the partial charge on Si atoms in

a-SiN_x . Using the MRB and CTM models (Tables 1 and 2), the averaged partial charge $\delta_{\text{Si}}(x)$ on a Si atom can be estimated by

$$\delta_{\text{Si}}(x) = \frac{\sum_{n=0}^4 \delta_{\text{Si}}(n) f_n(x)}{\sum_{n=0}^4 f_n(x)}. \quad (3)$$

From conditions of the charge neutrality in the film, $\delta_{\text{N}}(x)$ on a N atom is given by $-\delta_{\text{Si}}(x)/x$. The presence of incorporated H atoms will in principle affect the value of $\delta_M(x)$. However, as shown in Section 4.2., the H density is below 20 at.% for the films having values of x smaller than 0.5, while for higher values of x (or a larger n value) the difference between the $\delta_M(x)$ values for bonding configurations with and without H atoms is rather small as shown in Table 2.

The observed Si 2p XPS spectra exhibit an asymmetric line shape which depends on values of x . This asymmetric shape is because the film is composed of various bonding units in which the number of N atoms bonded to the Si atom in their respective bonding units is different from each other. The effective peak binding energies [$E_{\text{B}}(\text{Si } 2\text{p})$], defined as the center of gravity of the spectra, can then be correlated with the value of $\delta_{\text{Si}}(x)$ in Eq. (3) which corresponds to the partial charge value on a Si atom with the averaged number of N atom neighbors for a given value of x , based on the MRB model. Fig. 1 shows $E_{\text{B}}(\text{Si } 2\text{p})$ as a function of $\delta_{\text{Si}}(x)$ for a-SiN_x films in the published works [8]. The results for stoichiometric compounds, SiC , Si_3N_4 , and SiO_2 , are also shown for comparison. With the

exception of the results for a-SiN_x films with a near-stoichiometric composition, the $E_B(\text{Si } 2p)$ values for all kinds of samples are found to fit well to an expected straight line with the relation of

$$E_B(\text{Si } 2p) = 10.2 \delta_{\text{Si}}(x) + 99.3. \quad (4)$$

A relationship similar to Eq. (4) has been presented by Lucovsky [11]. The values of $E_B(\text{N } 1s)$ have also been found to vary as a linear function of $\delta_{\text{N}}(x)$ [8]. In Fig. 1, the deviation of the data for a-SiN_x from the straight line is probably due to a charging effect during the XPS measurement; this can be a serious problem for thicker a-SiN_x films with a high x .

4.2. Intensity of SiH absorption from IR measurements

The density $[\text{SiH}]$ of SiH bonds is estimated from the intensity I_{SiH} of SiH stretching absorption, as $[\text{SiH}] = A_{\text{SiH}} I_{\text{SiH}}$, where A_{SiH} is given by [12]

$$A_{\text{SiH}} = cn_r \mu \omega / (2\pi^2 e^{*2}) \\ = 1.989 \times 10^{15} n_r \omega / e^{*2} \quad (\text{cm}^{-2}). \quad (5)$$

A_{SiH} is a proportionality coefficient, c the speed of light, n_r the refractive index, μ the reduced mass, and e^* the effective charge of the Si–H dipole. Units of ω and e^* are cm^{-1} and the electron charge, respectively.

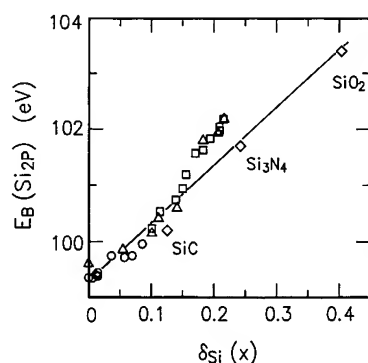


Fig. 1. Effective peak binding energy $E_B(\text{Si } 2p)$ as a function of the averaged partial charge $\delta_{\text{Si}}(x)$ for a-SiN_x films in the published works (see Ref. [8]). The experimental data for SiC, Si₃N₄, and SiO₂ are also shown. The line is drawn as a guide for the eye.

In a previous paper [9], it has been suggested that the e^* value in Eq. (5) can be estimated from the partial charges on the Si and H atoms as in $e^* = 2(\delta_{\text{Si}} - \delta_{\text{H}})$. From the experimental values of ω for monohydride in a-SiN_x [13] and the calculated e^* values, we estimate $\omega/e^{*2} = (1.35 \pm 0.01) \times 10^4$. We then obtain the following expression for A_{SiH} .

$$A_{\text{SiH}} = 2.68 \times 10^{19} n_r \quad (\text{cm}^{-2}). \quad (6)$$

For a-Si:H films with $n_r = 3.5$, we obtain a value for $A_{\text{SiH}}(2000 \text{ cm}^{-1}) = 9.4 \times 10^{19} \text{ cm}^{-2}$, which is in excellent agreement with the experimental value $(9.0 \times 10^{19} \text{ cm}^{-2})$ [14].

The profiles of the SiH absorption can be decomposed into two Gaussian components at around 2000 and 2100–2200 cm^{-1} [15]. For a-Si:H films without nitrogen, only 2000 cm^{-1} band is observed. Furthermore, since a signal from dihydride groups, SiH₂, was not found for x less than 0.4, through a simulation analysis [15], the presence of dihydride was ignored for the absorption analyses in the present work. Fig. 2(a) shows the ratio

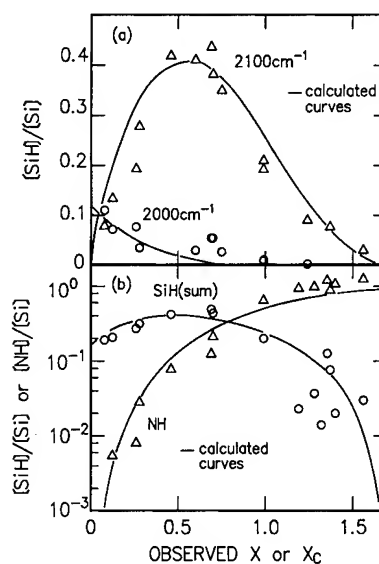


Fig. 2. (a) Ratios $[\text{SiH}]/[\text{Si}]$ for the 2000 (circles) and 2100–2200 cm^{-1} (triangles) bands; and (b) the ratio $[\text{SiH}]/[\text{Si}]$ (circles) for the sum of both bands in (a) and the ratio $[\text{NH}]/[\text{Si}]$ (triangles), as a function of the observed x . The solid curves as a function of x_c are calculated using the MRB model.

[SiH]/[Si] of the density of SiH bonds to that of Si atoms for the 2000 and 2100–2200 cm^{-1} bands, as a function of x . Fig. 2(b) shows the density ratio for the sum of both SiH bands and the [NH]/[Si] ratio. On the basis of the MRB model, the [SiH]/[Si] and [NH]/[Si] ratios can be calculated as a function of x' [1], using $f_n(x')$ for each bonding unit shown in Table 1, as given by

$$\begin{aligned} [\text{SiH}]/[\text{Si}] = & A_p(0)x_0(\text{SiH})f_0(x') \\ & + \sum_{n=1}^2 A_p(n) x_n(\text{SiH}) f_n(x'), \end{aligned} \quad (7)$$

$$[\text{NH}]/[\text{Si}] = \sum_{n=3}^4 A_p(n) x_n(\text{NH}) f_n(x'). \quad (8)$$

Here $A_p(n)$ values are the occupying probabilities of the bonding units with hydrogen (see Table 1). $x_n(\text{SiH})$ and $x_n(\text{NH})$ are the [SiH]/[Si] and [NH]/[Si] ratios within the bonding unit, respectively. In Si nitride films including NH bonds, we note that the expected ratio [N]/[Si] ($=x_c$) is different from the value of x' used as a parameter in $f_n(x')$. The expected ratio x_c can be estimated as a function of x' , using the $f_n(x')$ and $A_p(n)$ values and the atomic ratio [N]/[Si] within the particular bonding unit [1]. The observed [SiH]/[Si] and [NH]/[Si] ratios can then be compared with the calculated ones by converting those to a function of x_c . The results are represented by the solid curves in Fig. 2, and the values of $A_p(n)$, determined through the fitting, are shown in Table 1. Excellent agreement between the calculated curve and the experimental results is found, providing the applicability of the MRB model to determination of the bonding structure.

4.3. Frequency of SiH absorption

For the SiH stretching absorption, it has been found that a scaling law exists between the frequency ν_{SiH} and interatomic distance d_{SiH} of Si–H bonds, as given by [16,17]

$$\nu_{\text{SiH}}(d_{\text{SiH}})^3 = 7074 \quad (=C_0). \quad (9)$$

Units of ν_{SiH} and d_{SiH} are cm^{-1} and Å, respectively. Lucovsky [17] has found that the SiH frequency for various compounds is proportional to the value

of the electronegativity sum (ENS) of the constituent atomic species bonded to the SiH. This is because the ENS value reflects changes in the partial charges of the atomic constituents. This model, however, does not include the condition of charge neutrality in the bonding systems under consideration. Furthermore, the SiH, SiH₂, and SiH₃ peaks as a function of the ENS values are represented by different formulas [17], and are independent of each other.

In a previous paper [9], using Sanderson's model [10], estimates of d_{SiH} were made by summing the covalent radii of Si and H atoms, which are calculated as a linear function of δ_{Si} and δ_{H} , respectively. However, the increased number of unknown parameters for determining d_{SiH} limited any systematic analyses of the SiH vibrational properties for the various Si substituents. Furthermore, since the partial charge is delocalized, the d_{SiH} value may be dominated by the additional charge, $\delta_{\text{Si}} + \delta_{\text{H}}$ ($=\delta_+$), on the SiH bond rather than the partial charge on individual atoms. In this case, an increase in positive charge on the SiH bond should lead to a reduction in d_{SiH} . The d_{SiH} value may therefore be better approximated by

$$d_{\text{SiH}} = d_0 - k_s \delta_+. \quad (10)$$

The relationship given by Eq. (10) is similar to the result that d_{SiH} values are proportional to the ENS values [18]. Substituting Eq. (10) for d_{SiH} in Eq. (9), Eq. (11) can be approximated provided that the value of d_0 is sufficiently larger than $k_s \delta_+$, as

$$\ln \nu_{\text{SiH}} = \ln C_0 - 3 \ln d_0 + (3k_s/d_0) \delta_+. \quad (11)$$

Fig. 3(a) shows the observed values of ν_{SiH} [16,17] as a function of δ_+ for various substituted silane molecules [$\text{H-Si}(\text{H}_{3-n}\text{M}_n)$, ($\text{M} = \text{H}, \text{Br}, \text{Cl}, \text{or F}$)]. Further, Fig. 3(b) shows ν_{SiH} as a function of δ_+ for $\text{H-Si}(\text{Si}_{3-n}\text{M}_n)$ ($\text{M} = \text{H}, \text{N or O}$) bonding configurations in different solid compounds. The data in this figure were cited from the results in Refs. [13,16,17]. The values of δ_{Si} and δ_{H} were calculated for the corresponding bonding units in which the charge-neutrality conditions can be satisfied (see Sections 3.1. and 3.2.). The relation of Eq. (11) would also be applicable to the analyses of ν_{SiH} as a function of x for a-SiN_x:H films, using the averaged values of δ_+ (n) for each bonding unit in

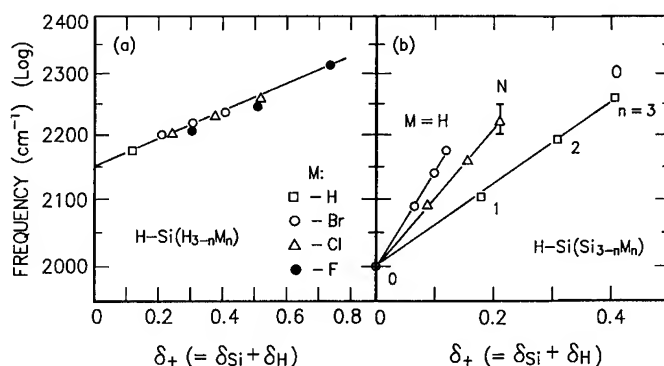


Fig. 3. (a) ν_{SiH} for various substituted silane molecules [$\text{H-Si}(\text{H}_{3-n}\text{M}_n)$, ($\text{M} = \text{H}, \text{Br}, \text{Cl}, \text{or F}$)], and (b) for $\text{H-Si}(\text{Si}_{3-n}\text{M}_n)$ ($\text{M} = \text{H}, \text{N}$ or O) bonding configurations in SiH-related solid compounds, as a function of $\delta_{\text{Si}} + \delta_{\text{H}} (= \delta_+)$ estimated using Eq. (1). The lines are drawn as a guide for the eye.

Table 1, as follows:

$$\delta_+(x') = \frac{\sum_{n=0}^3 \delta_+(n) A_p(n) f_n(x')}{\sum_{n=0}^3 A_p(n) f_n(x')}. \quad (12)$$

The $\delta_+(x')$ values must further be converted into $\delta_+(x_c)$, using the relation between x' and x_c as described in Section 4.2. Fig. 4 shows ν_{SiH} as a function of $\delta_+(x_c)$ for $\text{a-SiN}_x\text{:H}$ films. The line in the figure is the same as that for $\text{H-Si}(\text{Si}_{3-n}\text{N}_n)$ shown in Fig. 3(b). Thus, the dependence of ν_{SiH} vs. x can be interpreted in terms of a change in δ_+ .

4.4. Urbach tail

In a-Si films, the optical absorption in the range of the absorption coefficient α smaller than 10^4 cm^{-1} exhibits the characteristic Urbach form, corresponding to transition from exponential valence-band tail to conduction-band states. The shape of the tail distribution may be approximated by

$$N_{\text{T}}(E) = N_{\text{w}0} \exp[-(E - E_{\text{w}0})/E_0]. \quad (13)$$

Here, the zero of energy is defined at the valence-band mobility edge, and the tail states start at $E_{\text{w}0}$. $N_{\text{w}0}$ is the density of the states at $E_{\text{w}0}$. Fig. 5 shows the slope E_0 of the Urbach tail and the density N_s of Si dangling bonds (Si DB) as a function of x for $\text{a-SiN}_x\text{:H}$ films. The tail states should be related to bond distortion which is caused by bond-length

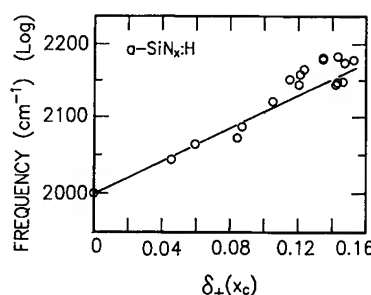


Fig. 4. ν_{SiH} as a function of $\delta_+(x_c)$ for $\text{a-SiN}_x\text{:H}$ films. The line in the figure is the same as that for the $\text{H-Si}(\text{Si}_{3-n}\text{N}_n)$ configuration shown in Fig. 3(b).

and bond-angle fluctuations. In addition, they may also be associated with the band-gap fluctuations due to compositional and/or structural inhomogeneity [19]. Smith and Wagner [20] and Stutzmann [21] assumed that the tail states consist of Si-Si weak bonds, and suggested that the weak bonds closer to midgap will convert into Si DBs. In a previous paper [2], we also showed that changes of the E_0 and the band gap in $\text{a-SiN}_x\text{:H}$ films describe well the dependence of N_s on x . Moreover, we recently found that an increase in the density of trivalent Si atoms having three Si back bonds (D center) as a function of x in $\text{a-SiO}_x\text{:H}$ films corresponds well with the increased E_0 values [22].

Although origins of the tail states is unclear as stated above, the bond distortion should act to increase both E_0 and Si DB density in the same

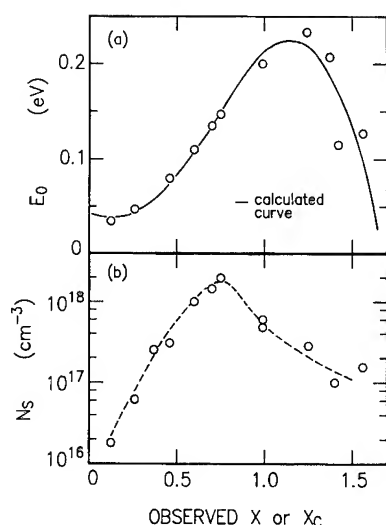


Fig. 5. (a) Slope E_0 of the Urbach tail and (b) the ESR spin density N_s as a function of x for a-SiN_x:H films. In (a), the solid curve as a function of x_c is calculated using the MRB model. The broken curve in (b) is drawn as a guide for the eye.

way. Since the flexibility of bonding will be reduced as a coordination number averaged over all constituent atoms in films increases, it is expected that the presence of Si–Si bonds in films, compared with SiN, SiH, and NH bonds, will enhance the bond distortion. Accordingly, if a specific part of Si–Si bonds is connected with the bond distortion, its density, N_U , can be estimated using the MRB model as [2]

$$N_U/N_{Si} = \sum_{n=0}^3 [1 - A_p(n)] \gamma'(n) [(4-n)/2] f_n(x') + \sum_{n=0}^2 A_p(n) \gamma(n) [(3-n)/2] f_n(x') + A_p(3) \gamma(3) (1/2) f_3(x'). \quad (14)$$

Here $\gamma'(n)$ and $\gamma(n)$ are the ratios of N_U to the total density of Si–Si bonds in each bonding unit, and N_{Si} is the density of Si atoms in the film. The values of $A_p(n)$ are determined from the results of IR measurements (Section 4.2. and Table 1). If N_U is proportional to the total density over the Urbach tail, through the bond distortion as stated above, the N_U value can be linked to E_0 by integrating $N_T(E)$ in Eq. (13) over E higher than E_{w0} , as $E_0 N_{w0} = A_U N_U$. A_U is a proportionality coefficient.

The values of E_0 can then be estimated from Eq. (14), by selecting the proper $A_U \gamma'(n)$ and $A_U \gamma(n)$ values. The result of the fitting is shown by the solid curve in Fig. 5(a). Through the fitting, we found $A_U \gamma(3) = 2.1 \times 10^{-2}$, and 4×10^{-4} for the other $A_U \gamma'(n)$ and $A_U \gamma(n)$, within an error of 10%. We also assumed the value of $N_{w0} = 10^{21} \text{ cm}^{-3}$.

4.5. Stress

As x increases, the experimentally determined stress changes from compressive to tensile stress [23]. The tensile stress in the high x range increases with x , and then saturates it for x larger than 1.2. In a previous work [23], it has been shown that the tensile stress measured over the range of x above 1.0 is caused by intrinsic stress rather than stress due to thermal expansion mismatch. This intrinsic stress may be caused by reconstruction of the network at the growth surface during film deposition [23,24]. The increased intrinsic stress with increasing x may be related to an increase in E_0 through favored bond distortion as described in Section. 4.4. Moreover, the high density of NH bonds for high x shown in Fig. 2(b) may be incorporated for relaxing the stress.

In nitride films having x greater than 1.2, the bonding properties do not appreciably change by varying the supplied rf power values. The stress values and buffered HF (BHF) etch rate, however, strongly depends on the rf power. The stress was also strongly dependent on the H dilution ratio R_H in the feed gas [24]. Fig. 6 shows the stress as a function of rf power for films with R_H values of 0 and 30. The positive values denote tensile stress. These films have values of x greater than 1.2, except for an rf power of 5 W. Under conditions of $R_H = 0$, the tensile stress values are independent of rf power. On the other hand, for films with $R_H = 30$, the stress changes to weak compressive stress with increasing rf power. For application of these films to device technology, conditions of weak compressive stress rather than tensile stress are desirable in order to avoid the occurrence of cracks. For both samples shown in Fig. 6, the BHF etch rates monotonically decrease with increasing rf power [24]. As seen in Fig. 6, such a decrease in the etch rate is independent of changes in the stress. These results

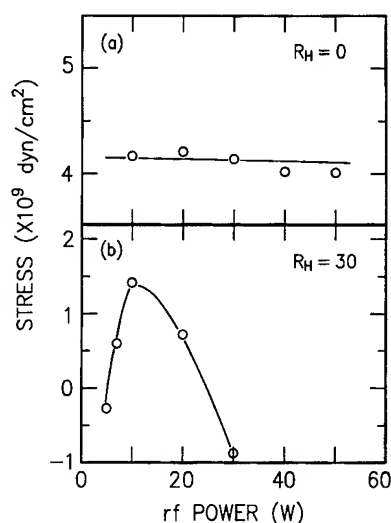


Fig. 6. Stress as a function of rf power for films with R_H values of 0 and 30. The positive values denote tensile stress. These films have values of x greater than 1.2, except for rf power of 5 W. The lines are drawn as a guide for the eye.

suggest that Si nitride films having lower stress and lower BHF etch rate can be obtained by increasing both rf power and R_H values.

5. Discussion

As shown in Fig. 1, a difference in the Si 2p core levels for films having different x values can be interpreted in terms of the CTM combined with the MRB model. Based on the values of $\delta_{Si}(n)$ in Table 2, the results shown in Fig. 1 predicts that the spacing of the Si 2p lines arising from each of five components ($n = 0-4$; see Table 1) decreases with increasing n . Note that n is the number of N neighbors bonded to a given Si atom. The dependence of the SiH and NH bond density as a function of x can also be explained using the MRB model as shown in Fig. 2. From the values of $A_p(n)$ (see Table 1), determined through the fitting, it is found that Si–NH–Si bonds are formed instead of $N(Si_3)$ bonds when three or more N atoms are bonded to a Si atom. The favored formation of these NH bonds can be correlated with an increase in the film stress [23]. Furthermore, for the bonding configurations shown in Table 1, a maximum value ex-

pected for x is predicted to be 1.67, which is consistent with the typical values of the saturated composition for PECVD a-SiN_x:H films, where values of $x = 1.6-1.7$ are reported by some research groups [1,3,6,25].

As seen in Fig. 3(a), the v_{SiH} values for SiH_{*n*} groups ($n = 1-3$) are found to fit an expected straight-line relation given by $\ln v_{SiH} = 7.673 + 0.1006\delta_+$. From Eq. (11) the values of d_0 and k_s are then estimated to be $d_0 = 1.488 \text{ \AA}$ and $k_s = 0.050$. We find that the value of d_0 , predicted for $\delta_+ = 0$, is in excellent agreement with the value ($= 1.49 \text{ \AA}$) [10] of the interatomic distance of SiH bonds for nonpolar conditions. Further, a linear relationship between v_{SiH} and δ_+ for solid compounds is also found as seen in Fig. 3(b). However, the k_s values depend on the electronegativity values of the Si substituents, in contrast with that for substituted silanes shown in Fig. 3(a). Furthermore, the value of d_0 is found to increase from 1.488 \AA for the silanes to 1.524 \AA for the solids. This increase indicates that the Si and H atoms in the solids under $\delta_+ = 0$ conditions are polarized; i.e. which implies $\delta_{Si} = -\delta_H \neq 0$ (see Table 2). On the other hand, the condition for $\delta_+ = 0$ in the silanes should imply $\delta_{Si} = -\delta_H = 0$, although it is an unreal condition as seen in Eq. (1). Moreover, we note that the atomic radius of a constituent atom in solid compounds in general is larger than that of the atom in gaseous materials as the atom in both phases has the same amount of partial charge [10].

As described in Section 4.4., if a specific part of Si–Si bonds is connected with formation of the Urbach tail states, the large value of $\gamma(3)$ in Eq. (14) suggests that the bond distortion, due to the presence of the Si–Si bonds, is favored as three N atoms are bonded to a Si atom. This is the same rule as that applied for incorporation of NH bonds as stated above.

6. Conclusion

The structural and bonding properties for PECVD a-SiN_x:H films were investigated by means of XPS, IR, and ESR. These properties as a function of x were examined using the CTM combined with the MRB model. This model was

applicable to analyses of the properties of various Si-related materials. For a-SiN_x:H films, it was suggested that incorporation of NH bonds is favored and that the Urbach tail slope increases through enhanced bond distortion, as three or more N atoms are bonded to a Si atom. The stress and BHF etch rate for films with a near-stoichiometric composition were also investigated as functions of rf power and R_H . It was suggested that Si nitride films having lower stress and lower BHF etch rate can be obtained by increasing both rf power and R_H values.

The authors are indebted to Professor T. Shimizu for stimulating discussion, and also to Mr L. He for his help with the experiments. This work has been partially supported by Grant-In-Aid for Scientific Research from the Ministry of Education, Research and Culture, the Japanese Government.

References

- [1] S. Hasegawa, M. Matsuda and Y. Kurata, Appl. Phys. Lett. 57 (1990) 2211.
- [2] S. Hasegawa, M. Matsuda and Y. Kurata, Appl. Phys. Lett. 58 (1991) 741.
- [3] J. Kanicki, W.L. Warren, C.H. Seager, M.S. Crowder and P.M. Lenahan, J. Non-Cryst. Solids 137&138 (1991) 291.
- [4] W.L. Warren, J. Kanicki, F.C. Rong and E.H. Poindexter, J. Electrochem. Soc. 139 (1992) 880.
- [5] J. Robertson, Mater. Res. Soc. Symp. Proc. 284 (1992) 65.
- [6] W.L. Warren, J. Kanicki, J. Robertson and E.H. Poindexter, Mater. Res. Soc. Symp. Proc. 284 (1992) 101.
- [7] H.R. Philipp, J. Non-Cryst. Solids 8-10 (1972) 627.
- [8] S. Hasegawa, L. He, T. Inokuma and Y. Kurata, Phys. Rev. B46 (1992) 12478.
- [9] S. Hasegawa, L. He, Y. Amano and Y. Inokuma, Phys. Rev. B48 (1993) 5315.
- [10] R.T. Sanderson, Chemical Bonds and Bond Energy, 2nd Ed. (Academic Press, New York, 1976) p. 77.
- [11] G. Lucovsky, J. Phys. (Paris) 42 (1981) C4-741.
- [12] M. Cardona, Phys. Status Solidi B118 (1983) 463.
- [13] A. Chayahara, M. Ueda, T. Hamasaki and Y. Osaka, Jpn. J. Appl. Phys. 24 (1985) 19.
- [14] A.A. Langford, M.L. Fleet, B.P. Nelson, W.A. Lanford and N. Maley, Phys. Rev. B45 (1992) 13367.
- [15] S. Hasegawa, M. Matuura, H. Anbutsu and Y. Kurata, Philos. Mag. B56 (1987) 633.
- [16] A.L. Smith and N.C. Angelotti, Spectrochim. Acta 15 (1959) 412.
- [17] G. Lucovsky, Solid State Commun. 29 (1979) 571.
- [18] G. Lucovsky, AIP Conf. Proc. 73 (1981) 100.
- [19] H. Fritzsche and Y. Nakayama, Philos. Mag. B69 (1994) 359.
- [20] Z.E. Smith and S. Wagner, Phys. Rev. Lett. 59 (1987) 688.
- [21] M. Stutzmann, Philos. Mag. B60 (1989) 531.
- [22] T. Inokuma, L. He, Y. Kurata and S. Hasegawa, unpublished.
- [23] S. Hasegawa, Y. Amano, T. Inokuma and Y. Kurata, J. Appl. Phys. 72 (1992) 5676.
- [24] S. Hasegawa, Y. Amano, T. Inokuma and Y. Kurata, J. Appl. Phys. 75 (1994) 1493.
- [25] I. Umezu and K. Maeda, Jpn. J. Appl. Phys. 30 (1991) 2547.



ELSEVIER

Journal of Non-Crystalline Solids 187 (1995) 287–290

JOURNAL OF
NON-CRYSTALLINE SOLIDS

A comparative study on structural and electronic properties of PECVD a-SiO_x with a-SiN_x

Keiji Maeda*, Naomichi Sakamoto, Ikurou Umezu

Department of Materials Science and Technology, Science University of Tokyo, Noda, Chiba 278, Japan

Abstract

Structural and electronic properties of plasma-enhanced chemical vapor deposition (PECVD) a-SiO_x thin films were investigated and compared with those of PECVD a-SiN_x thin films. The hydrogen content of a-SiO_x is much smaller than that of a-SiN_x in a composition range of large x values. Discontinuous chemical shifts with x were found in the IR absorption peak of the Si–H stretching mode and also in the XPS spectral peak of the Si 2p core level. These chemical shifts were continuous in a-SiN_x. The results indicate that the random bonding model, which is applicable to a-SiN_x, is not strictly applicable to a-SiO_x. The network formation by PECVD is supply-controlled in a-SiN_x but somewhat reaction-controlled in a-SiO_x.

1. Introduction

Amorphous Si thin film transistor (TFT) is now being developed for driving large liquid crystal displays. While thermally oxidized Si is used as a gate insulator in metal-oxide-semiconductor (MOS) field-effect transistor (FET) of crystalline Si, a-SiN_x deposited by plasma-enhanced chemical vapor deposition (PECVD) is used in a-Si TFT. Preparation conditions for PECVD a-SiO_x and a-SiN_x are similar, both of which can be successively prepared with a-Si:H. The reason for the above choice is that the interface condition of a-SiN_x/a-Si:H performs better than that of

a-SiO_x/a-Si:H. The electronic properties of the materials depend on preparation methods. Since we previously studied the atomic structure and electronic properties of a-SiN_x deposited by PECVD [1], we study PECVD a-SiO_x now to find differences between them.

Structural and bonding properties of PECVD a-SiO_x have been investigated by several workers by IR absorption and X-ray photoelectron spectroscopy (XPS) [2–4]. Their conclusions on the variation of these properties with composition x can be roughly divided into two groups. One is that the variation is smooth and continuous with x [2, 3], and the other is not [4]. To describe atomic microstructure in such materials, the random bonding model (RBM) has been used, which assumes no preference for atomic species in making bonds. Therefore, the above conclusions can be

* Corresponding author. Tel: +81-471 24 1501. Telefax: +81-471 23 9362.

divided according to the applicability of RBM. Since RBM was found to be applicable to a-SiN_x [1], attention was paid to its applicability to a-SiO_x in this investigation.

In this work, a-SiO_x thin films of various composition x were prepared and investigated by XPS and IR and optical absorption. These results were compared with those of a-SiN_x to deduce the cause of differences between them. Experimental results on a-SiN_x described in this paper were given in Ref. [1].

2. Experimental procedure

Thin films of a-SiO_x were deposited by PECVD in the same apparatus as for a-SiN_x. Preparation conditions were: raw reacting gases SiH₄, N₂O and H₂, a substrate temperature of 250°C, gas pressure in the reactor at 0.5 Torr and a rf power density of 0.08 W/cm². The gas flow ratio $R = [\text{N}_2\text{O}]/[\text{SiH}_4]$ was varied from 0 to 80. Several kinds of substrate were used depending on purpose: fused silica glass for optical absorption, undoped FZ Si wafer for IR absorption and NiCr-evaporated Corning 7059 glass for XPS.

A surface oxide layer was removed by Ar ion etching just before the XPS measurements. The composition x was determined by comparing the integrated spectral intensity of the Si 2p core-level with the O 1s core-level using a stoichiometric SiO₂ glass as a calibration standard. The peak shift in XPS due to charging up of the sample was corrected by the peak energy of Ar 2p, which was incorporated by the Ar ion etching.

3. Experimental results

The composition x of the films deposited from the plasma of the gas flow ratio R is shown in Fig. 1, where x is nearly proportional to $\log R$ and approaches 2, the stoichiometric value, at a very large value of R . These films contain N atoms which come from the N₂O gas. Fig. 1 also shows N atom concentration $y = [\text{N}]/[\text{Si}]$ in the film expressed as a-SiO_xN_y, which increases with

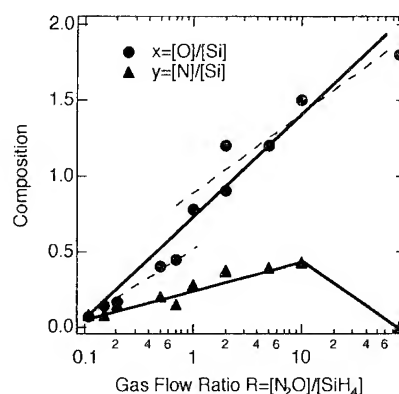


Fig. 1. Gas flow ratio $R = [\text{N}_2\text{O}]/[\text{SiH}_4]$ and composition $x = [\text{O}]/[\text{Si}]$ and $y = [\text{N}]/[\text{Si}]$ in a-SiO_xN_y. Lines are drawn as guides for the eye.

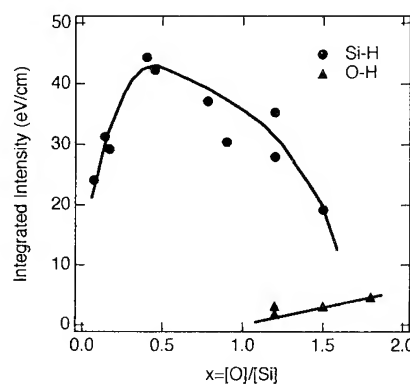


Fig. 2. Integrated IR absorption intensities of Si-H and O-H stretching mode against composition x . Lines are drawn as guides for the eye.

R being equal to about $x/3$ for $x < 1.5$, and then decreases. Since the N concentration is not important compared with O in the present material, N is not mentioned in other sections of this paper. Although scattering of the data is large in Fig. 1 it seems possible to consider that there is discontinuity in the composition from $x = 0.5$ to 0.8 for about $R = 1$.

IR absorption of the Si-H stretching mode indicates that the H concentration increases with x up to about $x = 0.5$, then decreases and cannot be detected for $x > 1.5$ as shown in Fig. 2. The intensity of the O-H stretching mode at 3460 cm^{-1}

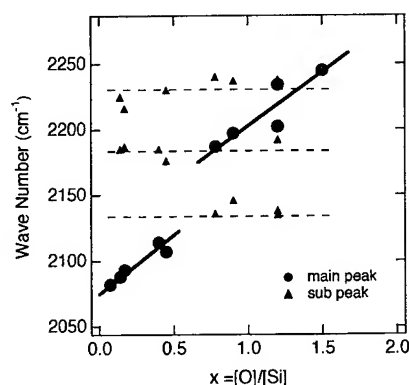


Fig. 3. Shift in the main peak of Si-H stretching mode in IR absorption spectrum against composition x . Lines are drawn as guides for the eye.

can be detected for $x > 1.1$ and increases with x . However, the O-H intensity is weaker than the Si-H intensity even for the largest O-H intensity in our sample of $x = 1.8$.

While several small peaks were resolved at fixed frequencies in the absorption spectrum of the Si-H stretching mode, the frequency of the main peak shifts with composition x , reflecting a change in the averaged electronegativities of atoms bonded to the Si atom [3]. This shift in the main peak has discontinuity in the range $x = 0.5$ – 1.0 as shown in Fig. 3, indicating a discontinuous change in x in the probability of O atoms bonded to the Si atoms as the nearest neighbors.

In the XPS, the chemical shift of the Si 2p core-level spectra is observed with increasing x . The spectrum becomes broad and double peaked in the range $x = 0.5$ – 1.0 , and the chemical shift is discontinuous in this range. This result also implies a discontinuous change with x in the probability of O atoms bonded to the Si atom.

By the optical absorption measurement, it becomes clear that the optical band gap E_0 increases gradually from $x = 0$ to about 3.2 eV at $x = 1.3$, and then increases rapidly to 9 eV at $x = 2.0$. The value of the \sqrt{B} coefficient in the Tauc plot decreases linearly with x from $850 \text{ (eV cm)}^{-1/2}$ at $x = 0$ to $250 \text{ (eV cm)}^{-1/2}$ at $x = 1.5$, and then increases rapidly.

4. Discussion

In comparison with the results on a-SiN_x, the following points are noted to be discussed in the experimental results on a-SiO_x.

In a-SiN_x, x becomes 1.7 for large values of $R = [\text{NH}_3]/[\text{SiH}_4]$, larger than the stoichiometric value 4/3, because of the large NH concentration in the film to release stress and to decrease the defect density in the network. In a-SiO_x, the largest x value obtained is nearly equal to but less than 2.0 for the stoichiometric composition. The maximum OH concentration in a-SiO_{1.8} is smaller than the maximum NH concentration in a-SiN_{1.7} by an order of magnitude. This result indicates that the atomic network of a-SiO_x has less stress due to a small coordination number of O atoms than that of a-SiN_x.

In the analysis of the chemical shift in XPS of a-SiN_x, the shift is linear with x and extends to $x = 1.7$. There was no preference for atoms in bond making. RBM applies quite well to a-SiN_x. In the present case of a-SiO_x, discontinuity with composition was observed in the chemical shift of XPS peak as well as in the IR absorption frequency in nearly the same composition range.

Deconvolution of the observed XPS spectra was made by assuming a presence of five kinds of Si-centered tetrahedrons, Si-(Si_{4-n}O_n) where $n = 0$ – 4 . The peak shift and the change in the spectral shape result from a variation in the distribution of these tetrahedrons. XPS spectra of a-Si:H and fused quartz were measured to obtain the binding energy and the spectral width (FWHM) of Si 2p core-level of the extreme compositions: 99.3 and 1.3 eV for a-Si:H and 103.5 and 2.0 eV for SiO₂, respectively. The remaining spectra were assumed to be equally spaced with increased width proportional to n . The observed spectra were reproduced quite well by a superposition of the component spectra. The relative concentration of each tetrahedron obtained in this way is shown in Fig. 4. When Fig. 4 is compared with the symmetric distribution of n and $4 - n$ components based on RBM [3], it is clearly shown that the contribution of the $n = 3$ Si-(SiO₃) component is larger, but those of the $n = 1$ Si-(Si₃O) and $n = 2$ Si-(Si₂O₂) components are smaller than the model distribution.

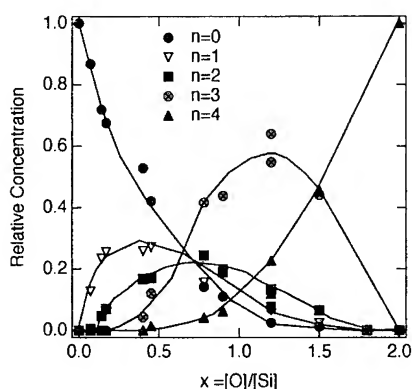


Fig. 4. Relative contribution of five Si-centered tetrahedrons $\text{Si}-(\text{Si}_{4-n}\text{O}_n)$ obtained by XPS against composition x . Lines are drawn as guides for the eye.

The chemical shift in the Si-H stretching mode is also explained by a presence of four kinds of Si tetrahedrons with one SiH bond $\text{SiH}-(\text{Si}_{3-n}\text{O}_n)$ where $n = 0-3$. The discontinuity in the chemical shift shown in Fig. 3 can be shown to correspond to a small ratio of presence in the $\text{SiH}-(\text{Si}_2\text{O})$ and $\text{SiH}-(\text{SiO}_2)$ tetrahedrons as expected based on the relation between frequency shift and electronegativity. There was no such discontinuity in the shift in the Si-H stretching mode in a-SiN_x with composition.

The above results in XPS and IR absorption indicate that the RBM does not strictly hold in a-SiO_x. The applicability of RBM implies that there is no preferable atomic configuration in a-SiN_x. In other words, the network formation in a-SiN_x is supply-controlled. On the other hand, there is some preference for atomic configuration in a-SiO_x. The network formation in a-SiO_x is somewhat reaction-controlled. This difference in the preference of atomic configuration seems to be related to the difference in bond energy discussed below.

The optical properties, i.e., the dependence of E_0 and B coefficient on x , of a-SiO_x are qualitatively the same as those of a-SiN_x. They are explained by the following model. The band gap

between the conduction band and the valence band, both derived from the Si-Si bond at $x = 0$, increases with x . For large x values, the Si-O bond or the Si-N bond forms the conduction band, and the O lone pair or the N lone pair forms the valence band, in a-SiO_x or a-SiN_x, respectively. Since the energy gaps of SiO₂ and Si₃N₄ are 9 and 5.3 eV, respectively, the Si-O bond is much stronger than the Si-N bond. This comparison is consistent with the IR absorption frequency of the symmetric stretching mode of 980 cm^{-1} for the Si-O bond compared with 450 cm^{-1} for the Si-N bond.

Although further studies are necessary, it is generally considered that the interface between the two extreme compositions, i.e., the insulator and a-Si:H, is likely to be defect-free when structures of intermediate composition take place with equal probability under supply-controlled conditions.

5. Conclusion

From this comparative study of PECVD a-SiO_x with a-SiN_x for various composition x , the following differences between them are found. Judging from its small H content and strong bond energy, a-SiO_x is more stable than a-SiN_x for large x values. However, the distribution of Si suboxide tetrahedron structures with one or two O atoms is smaller than that expected by RBM, which is applicable to a-SiN_x. This result may be a cause of defect formation at the interface between a-SiO_x and a-Si:H.

References

- [1] K. Maeda and I. Umezū, J. Appl. Phys. 70 (1991) 2745.
- [2] D.V. Tsu, G. Lucovsky and B.N. Davidson, Phys. Rev. B40 (1989) 1795.
- [3] S. Hasegawa, L. He, T. Inokuma and Y. Kurata, Phys. Rev. B46 (1992) 12478.
- [4] G. Shimaoka, Y. Suzuki and Y. Hatanaka, Appl. Surf. Sci. 33 & 34 (1988) 784.



ELSEVIER

Journal of Non-Crystalline Solids 187 (1995) 291–296

JOURNAL OF
NON-CRYSTALLINE SOLIDS

The effect of hydrogen and temperature on the optical gaps of silicon nitride and comparative stoichiometry studies on SiN thin films

J. Petalas^a, S. Logothetidis^{a,*}, S. Bouladakis^a, A. Markwitz^b

^aDepartment of Physics, Aristotle University of Thessaloniki, GR 54 006 Thessaloniki, Greece

^bInstitut für Kernphysik der J.W. Goethe-Universität, D-6000 Frankfurt am Main 90, Germany

Abstract

The optical properties of a variety of silicon nitride films prepared by different techniques are investigated with conventional and synchrotron radiation spectroscopic ellipsometry. The existence of hydrogen in near-stoichiometric SiN films is found to cause a red-shift of the fundamental and mean optical gaps, thought to be due to the existence of Si–H bonds. Temperature-dependent measurements up to 700 K reveal a recession of the fundamental gap and an increase of the mean optical gap with temperature. Analysis of the experimental spectra with the microscopic tetrahedron model indicates the superiority of the chemical vapour deposition growth technique in terms of film quality and homogeneity. Finally, a new method is used for the determination of the [N]/[Si] concentration ratio from tetrahedron model analysis and the results compare well to those from Rutherford backscattering spectroscopy and nuclear reaction analysis.

1. Introduction

The development of several low-cost physical and chemical deposition techniques for silicon nitride (hereafter denoted 'SiN') films enables the use of SiN films in electronic devices, such as thin-film transistors and multilayer structures in conjunction with the well-studied α -Si(H) and SiO_x. The effect of hydrogen on the dielectric and electrical properties of SiN is more complicated in comparison to α -Si:H, since hydrogen can be bonded directly either to Si or N atoms and thus affect the val-

ence-band density of states in a complex manner. Furthermore, the dependence of the dielectric properties of SiN films on temperature allows for predictions on the materials performance in possible optoelectronic applications. Therefore, in this work we present experimental evidence on the dependence of the fundamental and mean optical gaps of hydrogenated SiN on the hydrogen concentration and study the variation of the optical properties of SiN with temperature, on which there exist up to now no data in the literature. Finally, a new method based on a modified tetrahedron model analysis is used to estimate the stoichiometry of SiN films and the results are compared to corresponding ones from Rutherford backscattering spectroscopy (RBS) and nuclear reaction analysis (NRA).

*Corresponding author. Tel: +30-31 998 174. Telefax: +30-31 246 484.

2. Experimental procedure

The SiN films studied were prepared by various deposition techniques, namely chemical vapour deposition (CVD), physical vapour deposition (PVD), direct nitridation (DN), plasma-enhanced CVD (PECVD), sputtering (SP) and photo-CVD (Ph-CVD). The samples had different nitrogen concentrations, thicknesses ranging between 500 and 6000 Å, and several of them contained a significant amount of hydrogen. Details on their preparation and characterization can be found elsewhere [1].

The experimental probe we applied in order to study the optical properties of these films was spectroscopic ellipsometry (SE), a non-destructive optical technique that measures directly the real and imaginary parts of the complex dielectric function $\epsilon(\omega)$ ($= \epsilon_1(\omega) + i\epsilon_2(\omega)$). Analysis of the SE spectra of amorphous materials can yield the film thickness, the composition and the location of the major optical gaps. Measurements were taken in the energy regions 1.5–6.3 eV and 4.5–10 eV using conventional (Xe lamp) and synchrotron radiation (SR) light sources. The respective measurements were performed at the University of Thessaloniki and the Synchrotron Radiation Laboratory BESSY in Berlin. The SR ellipsometric measurements were taken under high-vacuum conditions ($P < 10^{-8}$ Torr), whereas temperature-dependent measurements were performed between 80 and 700 K.

3. Results

3.1. The effect of hydrogen and temperature on the optical gaps

In order to examine the effect of hydrogen on the fundamental gap of silicon nitride we studied Si- and N-rich SiN films. Firstly we performed annealing experiments at 500°C for 30 min on Si-rich films. Typical results are shown in Fig. 1 for the case of two PVD SiN films in the as-grown and after-annealing states. The lower-energy parts of the $\epsilon_2(\omega)$ spectra are dominated by interference fringes, which are due to the multiple reflection of light at the film/substrate interface and diminish in the region of the fundamental gap due to the rise of

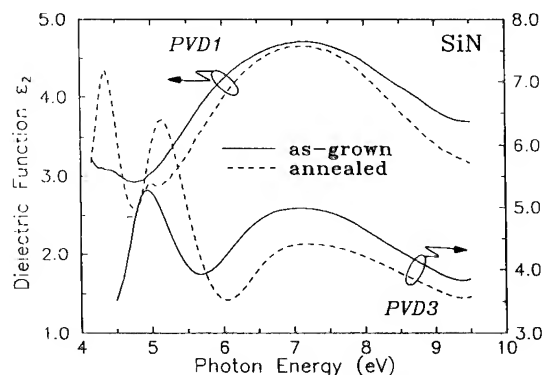


Fig. 1. Spectra of the imaginary part $\epsilon_2(\omega)$ of the dielectric function of two Si-rich SiN films in the as-grown and after-annealing states (solid and dashed lines, respectively).

film absorption. It is evident from Fig. 1 that the fringes are blue-shifted with annealing, which implies that a significant increase of the fundamental gap took place.

In order to isolate the effect of hydrogen on the gaps, we selected films close to stoichiometric Si_3N_4 (i.e. with concentration ratios $[\text{N}]/[\text{Si}]$ between 1.25 and 1.3), as determined by combined measurements of RBS and NRA, and determined the so-called Tauc gap, E_T [2], from the SE spectra. The results on the dependence of E_T on hydrogen are shown in Fig. 2 (open circles) and each point corresponds to one film. The data on the hydrogen concentration are deduced by elastic recoil detection analysis (ERDA) measurements, performed at the University of Frankfurt. The Tauc gap is found from Fig. 2 to decrease with increasing hydrogen content and therefore a subsequent hydrogen effusion, i.e. caused by annealing experiments, is expected to increase its value. A similar trend is observed for the mean optical gap of SiN, a measure of which is the energy position of the peak of $\epsilon_2(\omega)$ (denoted $\epsilon_{2\text{max}}$). In Fig. 2 we present the dependence of $\epsilon_{2\text{max}}$ on the hydrogen content for the films having $[\text{N}]/[\text{Si}]$ between 1.25 and 1.3 (solid circles). The solid line represents the fit to the data considering a linear model and a red-shift of the gap with increasing hydrogen content is observed.

For the determination of the temperature dependence of the fundamental absorption of SiN films the so-called E_{03} gap was considered. This

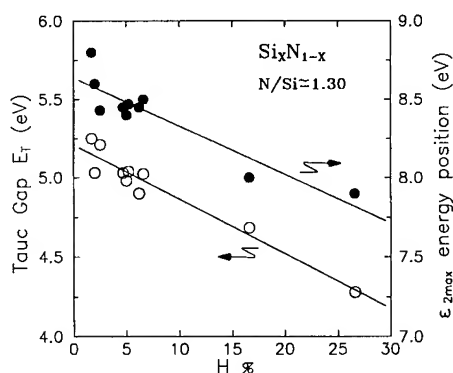


Fig. 2. Tauc gap and energy position of $\epsilon_{2\max}$ versus hydrogen concentration for SiN films having concentration ratio $[N]/[Si]$ around 1.30 (open and solid circles, respectively). Lines are drawn as guides for the eye.

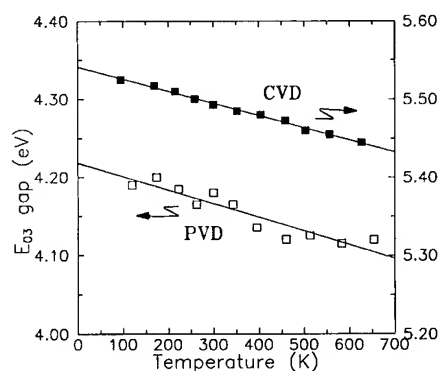


Fig. 3. Temperature dependence of the energy position of the E_{03} gap for two SiN films. The lines are drawn as guides for the eye.

gap corresponds to the photon energy at which the absorption coefficient rises to 10^3 cm^{-1} . The shift of E_{03} with temperature for one PVD ($[N]/[Si] = 1.0$, $[H] = 7\%$) and one CVD ($[N]/[Si] = 1.3$, $[H] = 2\%$) is presented in Fig. 3 and a red-shift of the gap is verified for both cases. In the case of the mean optical gap, three methods have been applied: (i) estimation of the $\epsilon_{2\max}$ energy position directly from the experimental spectra, (ii) fitting of the imaginary part of the dielectric function with the theoretical model proposed by Campi and Coriasso [3] and (iii) fitting of both parts of the dielectric function with the theoretical dispersion relations proposed by Forouhi and Bloomer [4]. In

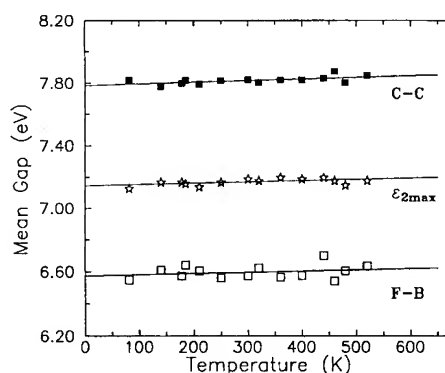


Fig. 4. The mean optical gap of a PVD SiN film (estimated by three models) versus temperature.

Fig. 4 we present typical results on the temperature dependence of one PVD SiN film, from which a slight blue-shift is observed.

3.2. Comparative stoichiometry studies with the tetrahedron model

Significant information on the quality and stoichiometry of silicon nitride films may be obtained via the tetrahedron model analysis of the dielectric function spectra [5, 6]. The model considers SiN to be comprised of Si-centered tetrahedra of the form $\text{Si-Si}_{4-v}\text{N}_v$ (designated hereafter as T_v). The dielectric response of these individual tetrahedra is known and therefore the experimental dielectric function spectra of the various films may be analyzed in terms of these tetrahedra with a Bruggeman effective-medium theory. In such a way one may estimate the volume fractions of the existing tetrahedra in each case. The results are presented in Table 1 for various SiN films. The void volume fraction (u_{voids}) listed in the table represents the effect of voids and other deficiencies on the dielectric function.

An extension of this analysis has been proposed [6] in order to deduce the nitrogen-to-silicon ratio ($[N]/[Si]$) from the tetrahedron volume fractions. The basic concept is to consider the material as a sum of distinct (i.e. non-intersecting and overlapping) Si-centered tetrahedra, bonded to each other (and thus constituting a solid) via the atoms situated at their four tetrahedron corners. In this

Table 1

Results of tetrahedron model analysis of the dielectric function of several SiN thin films prepared by various techniques; the estimated $[N]/[Si]$ ratios are also listed, along with the corresponding results from RBS/NRA

Sample	Tetrahedron volume fractions (%)				Void fraction (%)	$[N]/[Si]$	
	T_1	T_2	T_3	T_4		TM	RBS/NRA
PVD1	6.6	32.5		60.9	28.3	0.84	1.0
PVD2	11.6	23.6		64.8	31.0	0.85	1.0
PVD3	4.2	35.2		60.6	29.5	0.85	1.0
PVD4	1.2	39.8		59.0	32.7	0.86	1.0
CVD1			18.7	81.3	16.2	1.21	1.3
CVD2		1.4	24.2	74.4	21.1	1.16	1.3
CVD3		0.5	25.1	74.4	21.2	1.16	1.3
CVD4		4.0	19.8	76.2	19.7	1.15	1.27
DN1		10.9		89.1	27.2	1.18	1.2
DN2		6.0		94.0	31.4	1.25	1.29
SP1	1.0	16.4		82.6	37.3	1.10	1.3
SP2		11.3		88.7	12.0	1.18	1.17
SP3		12.4		87.6	17.2	1.16	1.27

manner one can count the number of Si and N atoms that belong to a certain $Si-Si_{4-r}N_r$ tetrahedron and thus deduce the $[N]/[Si]$ ratio from the volume fractions T_i . The results are presented in the seventh column of Table 1.

4. Discussion

The increase of the fundamental gap of Si-rich SiN films after annealing (refer to Fig. 1) may be interpreted in terms of the existence of Si-H bonds, since annealing at temperatures above 350°C is known to cause breaking of Si-H bonds and subsequent hydrogen effusion from the material. Thus, the observed blue-shift of the gap may be due to the dissolving of Si-H bonds and their replacement by Si-N ones, while the N-H bonds, known to be stable up to 800°C, remain unaffected. This result is in agreement with the red-shift of the Tauc gap with increasing hydrogen observed for films having $[N]/[Si]$ close to 1.3 (refer to Fig. 2), which can also be attributed to the existence of Si-H bonds: these bonds lie rather close to the valence band (VB) top and therefore their presence is expected to raise the VB top and thus decrease the fundamental gap,

since the conduction band minimum is reported to be insensitive to the presence of hydrogen. On the other hand, N-H bonds lie deeper in the VB and hence are expected to have negligible effect on the VB top. This fundamental gap shift is opposite to what is reported for α -Si:H [7], where the gap is blue-shifted with increasing hydrogen. This dependence may be explained by considering that the incorporation of hydrogen in α -Si:H substitutes Si-Si bonds that determine the VB top with Si-H ones that lie ≈ 7 eV lower and thus cause the VB top to recede.

In order to verify the existence of Si-H bonds we performed additional Raman spectroscopy measurements on the SiN films using an Ar laser (5145 Å) in the energy regions 1800–2400 cm^{-1} and 3000–3600 cm^{-1} , where silicon-hydrogen and nitrogen-hydrogen stretching vibrational modes are occurring. Although the samples having hydrogen lower than 5% did not yield detailed information, apparently due to their low H content, the two SiN films that have the highest hydrogen content (PECVD and PhCVD, with $[H] = 16\%$ and 26% , respectively) gave pronounced structures. The corresponding Raman spectra of these films are shown in Fig. 5. The peak around 2100 cm^{-1} corresponds

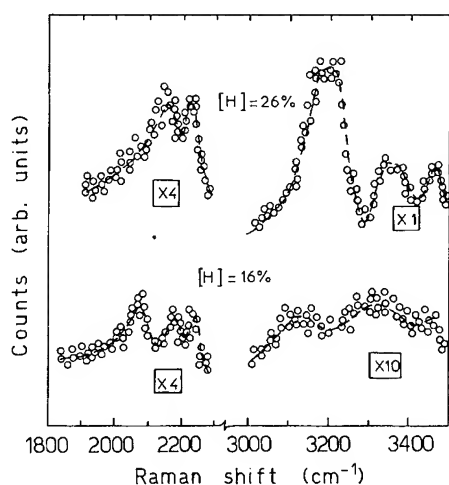


Fig. 5. Raman spectra in the regions 1800–2300 cm^{-1} and 3000–3600 cm^{-1} of the PECVD and PhCVD SiN films, reported to have hydrogen concentrations 16% and 26%, respectively. The lines are drawn as guides for the eye.

to the Si–H stretching mode, whereas these around 2180 and 2240 cm^{-1} to stretching modes of more complex units [8]. On the other hand, the peaks around 3300 and 3450 cm^{-1} are identified with the N–H and N–H₂ stretching modes. Thus from Fig. 5 the existence of N–H as well as Si–H bonds in these films is established.

The E_{03} gap of SiN films was found to decrease with temperature (refer to Fig. 3). The temperature coefficients for the PVD and CVD films shown in the figure are estimated to be 1.75(22) and 1.55(39) $\times 10^{-4}$ eV/K, respectively, where the numbers in parentheses indicate the 95% confidence limits. Larger coefficients are found for α -Si and α -Si:H (about 2×10^{-4} eV/K) and this must be associated with the existence of nitrogen, since it is generally observed that the more insulating a material the smaller the temperature shift of its fundamental gap. In the case of the mean optical gap one can note that an ascending trend is established by all models used, in contrast to what is observed for α -Si. Model (i) seems to provide the most consistent data that have the smallest dispersion. The average temperature coefficient is estimated to be $0.83(37) \times 10^{-4}$ eV/K.

From the types and volume fractions of the existing tetrahedra in SiN films one can deduce qualitatively

conclusions concerning the film quality. From Table 1 it can be seen that only the CVD films exhibit tetrahedra T_2 , T_3 and T_4 together. Furthermore, the volume fractions of these tetrahedra follow the relation $u_2 \ll u_3 \ll u_4$, which is predicted by the literature, in all cases but one. These results, along with the relatively low void volume fraction, are indicative of gradual nitridation, i.e. homogeneous dispersion of the Si–Si and Si–N bonds within the respective films, and high film quality. The DN, SP and PVD films exhibit low homogeneity, i.e. non-negligible distinct phases, and in most cases high void fraction, which is related to the quality. Thus, this study proposes that the CVD technique produces films of superior quality and homogeneity. Furthermore, the values of the $[\text{N}]/[\text{Si}]$ ratio estimated by the tetrahedron model are in agreement within 15% with the corresponding RBS/NRA estimations (refer to columns 7 and 8 of Table 1), which is acceptable since the error limit of the RBS/NRA technique is 5–10%.

5. Conclusions

The fundamental and mean optical gaps of SiN:H films close to stoichiometric were found to red-shift with increasing hydrogen in the films, a trend attributed to the existence of Si–H bonds and verified by additional Raman spectroscopy measurements. Temperature dependence measurements showed a red shift of the fundamental gap, lower than that observed in α -Si(H). On the other hand, analysis of the dielectric function with the tetrahedron model allows for qualitative comparative studies between SiN prepared by different techniques and revealed the superiority of the CVD technique in terms of film quality and homogeneity. Estimation of the $[\text{N}]/[\text{Si}]$ ratio with this model is in good agreement with the corresponding results from RBS/NRA analysis.

References

- [1] E.C. Paloura, J. Lagowski and H.C. Gatos, J. Appl. Phys. 69 (1991) 3995; A. Markwitz, H. Baumann, E.F. Krimmel, M. Rose, K. Bethge, P. Misaclides and S. Logothetidis,

- Vacuum 44 (1992) 397; E.C. Paloura, A. Knop, K. Holdack, U. Doebler and S. Logothetidis, *J. Appl. Phys.* 73 (1993) 2995.
- [2] S. Logothetidis, J. Petalas, A. Markwitz and R.L. Johnson, *J. Appl. Phys.* 73 (1993) 8514.
- [3] D. Campi and C. Coriasso, *J. Appl. Phys.* 64 (1988) 4128.
- [4] A.R. Forouhi and J. Bloomer, *Phys. Rev. B* 34 (1986) 7018.
- [5] Z. Yin and F.W. Smith, *Phys. Rev. B* 42 (1990) 3658.
- [6] J. Petalas and S. Logothetidis, *Phys. Rev. B* 50 (1994) 11801.
- [7] G.F. Feng, M. Katiyar, J.R. Abelson and N. Maley, *Phys. Rev. B* 45 (1992) 9103.
- [8] S. Hasegawa, L. He, Y. Amano and T. Inokuma, *Phys. Rev. B* 48 (1993) 5315.



Nature of the Si and N dangling bonds in silicon nitride

J. Robertson^{a,*}, W.L. Warren^b, J. Kanicki^c

^a Department of Engineering, University of Cambridge, Cambridge CB2 1PZ, UK

^b Sandia National Laboratories, Albuquerque, NM 87185-1349, USA

^c Department of EECS, University of Michigan, Ann Arbor, MI 48109-2108, USA

Abstract

Si and nitrogen dangling bond defects in amorphous silicon nitride $a\text{-SiN}_x\text{:H}$ are most stable in their charged, diamagnetic states. Excitation to their paramagnetic states is found to occur by both charge conversion of Si defects or N defects or by charge transfer between Si and N defects. The stability of charged defects is modelled in terms of potential fluctuations whose magnitude exceeds their positive correlation energy.

1. Introduction

Amorphous hydrogenated silicon nitride ($a\text{-SiN}_x\text{:H}$) is widely used as the gate dielectric in thin film transistors and as the charge storage medium in non-volatile memories. These applications require an understanding of the nature of the charge trapping centers in $a\text{-SiN}_x\text{:H}$. The defects expected in a random network of mainly Si–N bonds are the Si and N broken (dangling) bonds (DB) [1]. These defects have been extensively characterized, as reviewed recently [2–5]. The Si dangling bond backbonded to three N atoms, denoted the K center, is the dominant trapping center in silicon nitride. It forms a state near the middle of the band gap (Fig. 1). The N dangling bond is observed in stoichiometric ($x \approx \frac{4}{3}$) and N-rich $a\text{-SiN}_x\text{:H}$ and gives rise to a state just above the valence band

edge E_v . Each center is amphoteric, with three charge states, +, 0 and –, and is neutral when single occupied.

2. Results

The energy level diagram (Fig. 1) suggests that if both K and N centers are present, then *charge transfer* between defects will create K^+ and N^- centers,



leaving some K^0 or N^0 centers, depending on whether K or N centers are in overall excess. If so, ultraviolet (UV) illumination should reverse this reaction,



and re-form the neutral, paramagnetic centers which would be seen by electron spin resonance (ESR). In practice, only K^0 centers are seen in

*Corresponding author. Tel: +44-1223 332 689. Telefax: +44-1223 332 662. E-mail: jr@eng.cam.ac.uk.

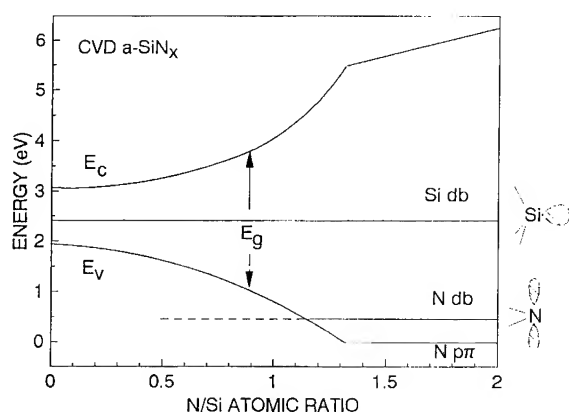


Fig. 1. Band diagram for a-SiN_x showing the K center at mid-gap and the N center just above E_v.

as-deposited a-SiN_x:H. Room temperature UV illumination creates many more K⁰ centers but no N⁰ centers, contrary to Eq. (2) and Fig. 1. The kinetics suggest that K⁰ creation occurs by *charge conversion*,



of existing charged, diamagnetic defects. N⁰ centers are created in N-rich nitride by annealing to over 500°C followed by UV illumination [2, 6]. This treatment creates *only* N⁰ centers, presumably with the UV step causing charge conversion of diamagnetic precursors,



which is again contrary to Eq. (2).

This problem was resolved by UV illuminating as-deposited N-rich nitrides at low temperatures, 110 K, which is found to create both K⁰ and N⁰ centers, with K⁰ in excess [7]. This shows that N-rich nitride contains precursors of both K⁰ and N⁰ centers and that the centers are created by a combination of reactions (2) and (3). This result validates the original band diagram of Fig. 1. The N⁰ centers formed at 110 K are less stable than those formed by the anneal/illumination treatment, decaying below room temperature, which is why they were not seen previously. This suggests that annealing sharpens the valence band tail, effectively deepening the N DB level and stabilizing it against decay by hole emission.

3. Discussion

We now consider the nature of the individual centers. Reaction (3) indicates that the K defect is more stable in its charged, diamagnetic states. Indeed, charge injection can convert K⁺ directly to K⁻ centers, and back, without forming the intervening K⁰ state [8]. This behavior is generally taken as evidence that the defect level possesses a negative effective correlation energy, *U*. This means that there is an effective attraction between electrons in the defect level so it prefers to be in its empty (K⁺) or fully occupied (K⁻) state. A negative *U* also causes the K⁻ level to lie below the K⁺ level in the gap. Kanicki et al. [3] recently estimated *U* ≈ -0.9 eV for the K center, while Chen et al. [9] studied whether a range of K centers exist with both positive and negative *U* values.

A negative *U* arises, in general, from a strong electron-lattice coupling or rebonding at one of the charged centers. However, the bonding mechanism causing the negative *U* in silicon nitride is unclear. A negative *U* arises in group VI elements like a-Se by overcoordination of the positive defect [10]. This mechanism requires the existence of non-bonding valence electrons such as the pπ states of Se, which form an extra bond to the empty DB orbital. A negative *U* also needs a low coordination, floppy network as in a-Se which can relax during rebonding. A more limited form of negative *U* occurs in group V elements like a-As, where the valence s electrons are non-bonding. Group IV elements like Si have no non-bonding electrons, so a-Si has a positive *U*.

N is a group V element, so silicon nitride could also be negative *U*, in principle (although its mean coordination of 3.4 inhibits easy relaxation). Due to N's unusual planar geometry, the non-bonding electrons are the N pπ states. However, Robertson [5] argued that the steric hindrance which makes N planar also inhibits the bond-forming ability of the N pπ orbital. A negative *U* is therefore unlikely, unless steric hindrance is relieved when N bonds to hydrogen, as in =NH or -NH₂ groups. Hydrogen also helps by lowering the network coordination [11]. These factors conflict with the increasing stability of charged K centers observed in nitride deposited at higher temperatures (Fig. 2), whose

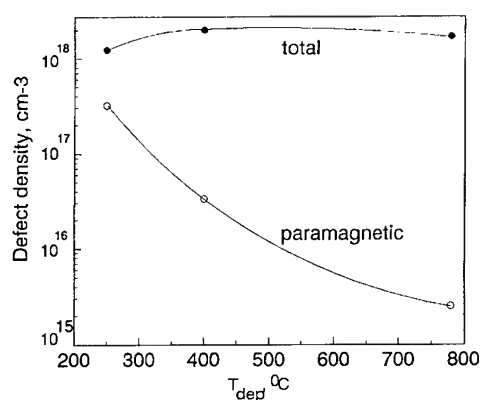


Fig. 2. Variation of light-induced and dark K^0 density as a function of deposition temperature, for near-stoichiometric nitride. Lines are drawn as guides for the eye.

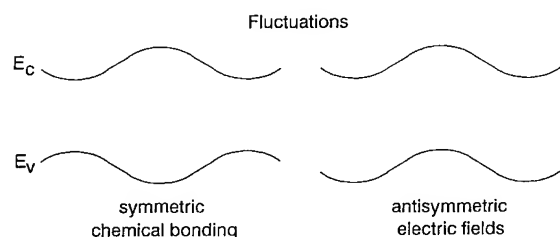


Fig. 3. Symmetric and antisymmetric fluctuations.

hydrogen content declines rapidly. Indeed, a key test of any model is to account for the very low fraction of K^0 centers in stoichiometric, chemical vapor deposited (CVD) nitride ($T_d = 800^\circ\text{C}$) [12] whose hydrogen content is low ($< 3\%$).

The photocreation of N^0 centers by Eq. (4) implies that N centers are also more stable in their charged, diamagnetic states. Thus, in this model both K and N centers need a negative U . There are two problems with a negative U N center. First, the N^+ would need to bond to a bulk N site and form an N–N bond. This bond is quite unstable, and is not found in the bulk (see however Ref. [13]). Second, the closeness of the N DB levels to E_v (Fig. 1) precludes the energy span needed for configuration coordinate shifts at a negative U center.

An alternative model is that charged defects arise from the effect of potential fluctuations on defects of positive U . Charged defects predominate if the

fluctuation amplitude V exceeds $|U|$ [14]. Fritzsche and Nakayama [15] suggested that the persistent photoconductivity and photoinduced changes in the Urbach tail of a-SiN_x:H arose from potential fluctuations.

There are two types of fluctuations in semiconductors (Fig. 3): symmetric fluctuations due to 'compositional' variations between bonding types with different local band gaps (e.g. Si–Si and Si–N bonds) and antisymmetric fluctuations due to Coulombic fields. Compositional fluctuations are generally short range ($< 10 \text{ \AA}$) and in principle need not arise in stoichiometric CVD silicon nitride. We focus on potential fluctuations. These could arise from random orientations of polar bonds or a random distribution of trapped charges. The main effect is from polar bonds; the effect of, say, $n = 5 \times 10^{18} \text{ cm}^{-3}$ charged defects is

$$V \approx n^{1/3} / 4\pi\epsilon_0\epsilon,$$

or only about 0.02 eV for a-SiN_x:H. Ley et al. [16] observed that the weakly polar Si–H bonds produce random potentials in a-Si:H of order 0.3 eV. The effect is likely to be much larger in a-SiN_x:H because Si–N bonds are more polar and the permittivity is lower. The Si–N bond is 50% ionic, giving site charges of $\text{Si}_3^{2+}\text{N}_4^{1.5-}$ [5]; for comparison the Si–O bond is 60% ionic giving $\text{Si}^{2.4+}\text{O}_2^{1.2-}$. The deconvolved core spectra of a-SiN_x:H are consistent with FWHM random potentials of perhaps 0.6 eV [17]. The random potentials are quenched into a-SiN_x:H during deposition. Similar effects could occur in deposited a-SiO_x:H.

The effect of a random potential on a set of initially degenerate defect levels is shown in Fig. 4(a). Defect energy levels vary according to the local potential. States lying $-U/2$ below the defect Fermi level E_F become filled and negatively charged, while those lying $U/2$ above E_F will be empty and positive. Charged defects predominate if the fluctuation amplitude V exceeds U . The D^- levels now lie below D^+ levels. The potential fluctuations on the K and N centers are equal in this model. Band gap UV illumination will excite carriers which trap and neutralize at charged centers, Fig. 4(b). Changes in defect occupancy alter the potentials by only $\approx 0.02 \text{ eV}$, much less

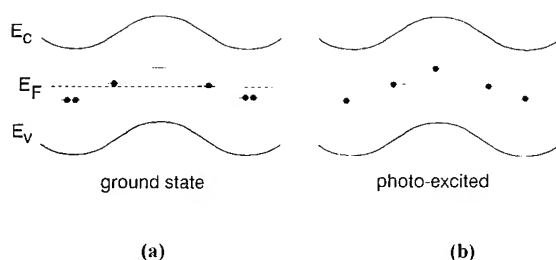


Fig. 4. (a) Defect occupancies in the presence of symmetric fluctuations. (b) Defects neutralized affect photoexcitation.

than the background fluctuations, so defect charges will decay back to their original states. This accounts for the observed light-induced ESR.

The potential fluctuation model differs from the defect pool model, the favored model of dangling bonds in a-Si:H [18]. In the defect pool model, defects are created from a large pool of possible defects of different energy levels. Defects of all three charge states are formed and charged defects slightly outnumber neutral defects for the model parameters presently used for a-Si:H [19]. The models are similar in that a random potential can place the $D^{+/0}$ level above the $D^{0/-}$ level for a positive U center [14, 18]. The models differ in that the number of defects is fixed in the fluctuation model but variable in the defect pool model.

4. Conclusions

In conclusion, the stability of K centers and N centers in their charged, diamagnetic states can be attributed to the effects of static charge fluctuations, and photoexcitation of K^0 and N^0 states has been found to occur by both charge conversion of each center and charge transfer between centers.

The portion of this work performed at SNL was supported by US DOE under contract DE-AC04-94AL85000.

References

- [1] J. Robertson and M. J. Powell, Appl. Phys. Lett. 44 (1984) 415.
- [2] W.L. Warren, J. Kanicki, F.C. Rong and E.H. Poindexter, J. Electrochem. Soc. 139 (1992) 880.
- [3] J. Kanicki and W.L. Warren, J. Non-Cryst. Solids 164 (1993) 1055.
- [4] J. Robertson, Matter. Res. Soc. Symp. Proc. 284 (1993) 65.
- [5] J. Robertson, Philos. Mag. B63 (1991) 47.
- [6] W.L. Warren, J. Kanicki, J. Robertson and E.H. Poindexter, Mater. Res. Soc. Symp. Proc. 284 (1993) 101.
- [7] W.L. Warren, J. Robertson and J. Kanicki, Appl. Phys. Lett. 63 (1993) 2685.
- [8] W.L. Warren, J. Kanicki, J. Robertson, E.H. Poindexter and P.J. McWhorter, J. Appl. Phys. 74 (1993) 4034.
- [9] D. Chen, J.M. Viner, P.C. Taylor and J. Kanicki, Phys. Rev. B49 (1994) 14320.
- [10] M. Kastner, D. Adler and H. Fritzsche, Phys. Rev. Lett. 37 (1976) 1504.
- [11] T. Shimizu, M. Kumeda, A. Morimoto and H. Yokomichi, J. Non-Cryst. Solids 77 (1985) 377.
- [12] S. Fujita and A. Sasaki, J. Electrochem. Soc. 132 (1985) 398.
- [13] H. Yan, M. Kumeda, N. Ishii and T. Shimizu, Jpn. J. Appl. Phys. 32 (1993) 876.
- [14] H.M. Branz and M. Silver, Phys. Rev. B42 (1990) 7420; Mater. Res. Soc. Symp. Proc. 192(1990) 261.
- [15] H. Fritzsche and Y. Nakayama, Philos. Mag. B69 (1994) 354.
- [16] L. Ley, J. Reichart and R.L. Johnson, Phys. Rev. Lett. 49 (1982) 1664.
- [17] R. Karcher, L. Ley and R.L. Johnson, Phys. B30 (1984) 1896.
- [18] K. Winer, Phys. Rev. Lett. 63 (1989) 1487.
- [19] S.C. Deane and M.J. Powell, Phys. Rev. Lett. (1993) 1654.



ELSEVIER

Journal of Non-Crystalline Solids 187 (1995) 301–307

JOURNAL OF
NON-CRYSTALLINE SOLIDS

Morphology of LPCVD Si_3N_4 films after high temperature treatment and HF etching

G. Beshkov*, V. Lazarova, D.B. Dimitrov

Institute of Solid State Physics, Bulgarian Academy of Sciences, Tzarigradsko Chaussee 72, Sofia 1784, Bulgaria

Abstract

The influence of high temperature treatments in a nitrogen ambient at temperatures 1000 and 1100°C and in water vapor at 900, 1000, and 1100°C for 270 and 720 min on the structure, on the morphology and on the electrical properties of LPCVD Si_3N_4 layers has been investigated. The Si_3N_4 layers have been deposited by the LPCVD technique using the composition $\text{SiH}_2\text{Cl}_2\text{--NH}_3$. The presence of a crystalline phase of $\alpha\text{-Si}_3\text{N}_4$ has been established after 270 min annealing at 1000°C in water ambient. A sharp change of the surface morphology of the layers has been observed after wet etching in 40% HF for 10 s.

1. Introduction

Si_3N_4 layers are often used in modern micro-electronic devices and integrated circuits. During the technological fabrication of the devices the Si_3N_4 layers are subjected to high temperature treatments. These high temperature treatments change the morphology, the structure and the electrophysical properties of the layers. The detailed analysis of the effect of high temperature treatments on LPCVD Si_3N_4 layers is important from the application point of view as well as for the establishment of the physico-chemical properties of the layers. In some recent investigations it has been reported that vacuum annealing at 900–950°C still retains the amorphous structure of the layers but

annealing at 1000°C and above leads to the formation of α and β modified Si_3N_4 [1]. The alkaline impurities (Li, Na, K) do not enhance the process of crystallization. It is also established that annealing in an oxygen ambient does not enhance the crystallization, but if the concentration of oxygen in the carrier gas (N_2) is of the order of 5 ppm the deposited layer has larger grains in comparison to the case of 1 ppm oxygen concentration [2]. In the case of SiN silicon-rich layer deposition a crystalline phase is observed at the beginning of the deposition process [3].

In this work we report morphological investigations of Si_3N_4 layers obtained by the LPCVD technique annealed at high temperatures in N_2 and in H_2O vapor. All layers are etched in 40% HF for 10 s. The grain size distribution of the layers is analyzed before and after high temperature annealing. It is established that crystalline inclusions with a typical size of 300 nm are observed

* Corresponding author. Telefax: +359-2 757 032.
dbdim@bgcict.bitnet.

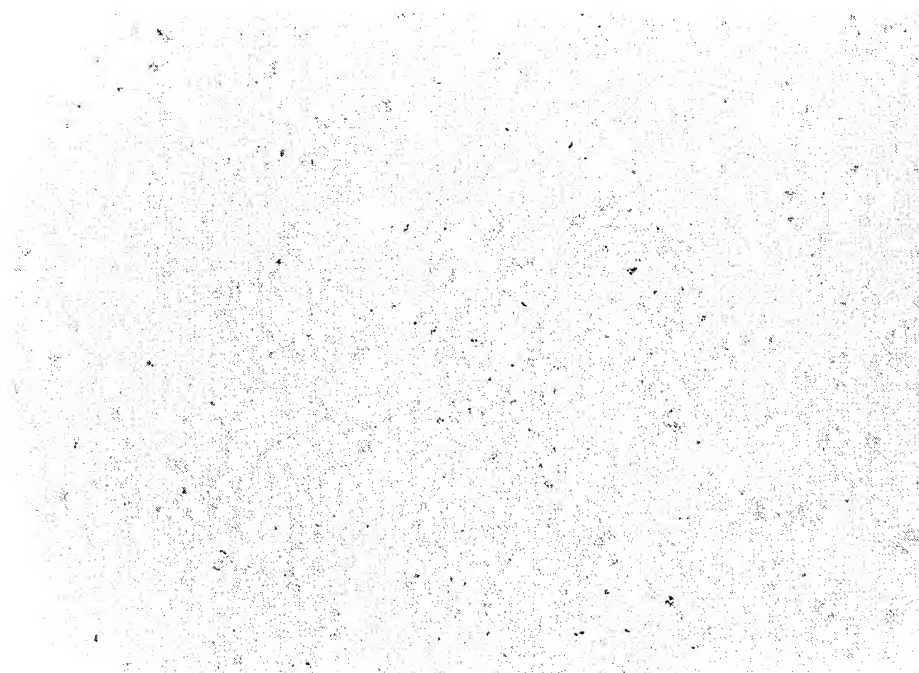


Fig. 1. Morphology of an as-deposited LPCVD Si₃N₄ layer (magnification $\times 50\,000$).

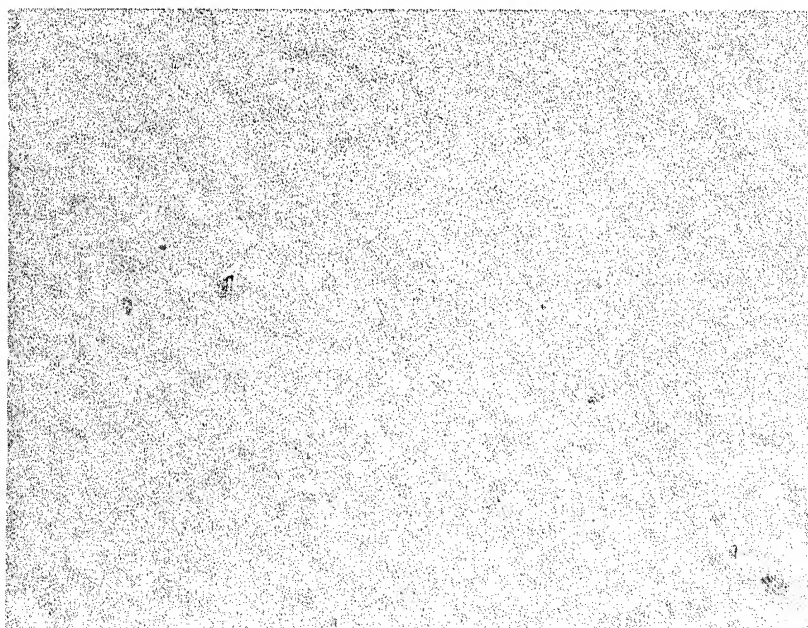


Fig. 2. Morphology of an LPCVD Si₃N₄ layer annealed for 270 min in N₂ at 1000°C (magnification $\times 50\,000$).

after wet etching of the layers annealed in an oxygen ambient.

2. Experimental procedure

For the experiments n-type silicon wafers (100) oriented, 4–6 Ω cm, have been used. The wafers were cleaned in deionized water. Prior to this cleaning, the native silicon oxide was removed by 1 min treatment in HF:H₂O (1:10) solution.

Si₃N₄ deposition has been performed in an industrial type LPCVD reactor at a temperature $T_{\text{dep}} = 780^\circ\text{C}$, in a gas mixture of SiH₂Cl₂ and NH₃ (1:3). The working pressure in the reactor chamber was 550 mTorr, the deposition rate 70 Å/min, and the thickness of the layers 3000 Å.

After deposition the samples were separated in two batches. The first batch was annealed in a nitrogen ambient at 1000°C, 270 min; 1100°C, 270 min; 1100°C, 720 min. The second batch was treated in a water vapor ambient under the following conditions: 900°C, 720 min; 1000°C, 720 min; 1100°C, 270 min. The wafers were investigated by TEM (Hitachi-HU11A) with a resolution of 7 Å and a beam energy of 75 keV. The morphology was studied by C-sampling. The thickness of the carbon layer was 15 Å. The electrical characteristics of the layers were determined by the high frequency 1 MHz C–V technique.

3. Results

The morphology of the Si₃N₄ layer after the deposition is shown in Fig. 1. It may be seen that the as-deposited layer is homogeneous, having clusters with a density of $280 \times 10^8 \text{ cm}^{-2}$. The cluster size is in the range 20–30 nm.

An electron micrograph of the Si₃N₄ layer annealed in nitrogen at 1000°C for 270 min is shown in Fig. 2. The roughness of the surface is larger in comparison to that of the as-deposited layers and to that of the samples annealed at 1100°C. The pits have a depth of 70–80 nm. An electron micrograph of Si₃N₄ layers annealed at 1100°C in N₂ is shown in Fig. 3.

The surface morphology of the layers annealed in a water vapor ambient changes considerably for all annealing temperatures. The roughness is significantly larger, the depth of the pits being of the order of 10–100 nm. A typical electron micrograph of a sample annealed at 1100°C for 270 min is shown in Fig. 4. Fig. 5 presents the electron micrograph of the N₂ 1000°C annealed sample.

The morphology of the samples etched in 40% HF for 10 s is presented in Figs. 6 and 7. In both micrographs the presence of crystalline inclusions with size 200–290 nm may be clearly seen.

4. Discussion

The presence of cluster inclusions with size 20–30 nm and density $280 \times 10^8 \text{ cm}^{-2}$ observed in the as-deposited samples is most likely due to the microscopic local fluctuation of the active gas near the substrate determined by some morphological inhomogeneities at the substrate surface. The presence of surface roughness determines chemically active centers at which the deposition rate changes.

The homogenization of the surface after 1100°C N₂ annealing for 270 and 720 min shows that this process depends mainly on the annealing temperature. The roughening of the surface after water vapor annealing is due to the oxidation of the Si₃N₄ surface. The oxidation is faster for the agglomerated regions which have larger surface.

All layers show amorphous structure before and after annealing. The layers annealed in H₂O show the presence of crystalline inclusions. The observation of crystalline inclusions after HF etching is possible because of the slower etching rate of the crystal phase. The 10 s etching of the layers in 40% HF has effect only on the amorphous phase of the layers. The presence of a crystal phase in the etched layers is also confirmed by the electronographic analysis. A good correlation between the available data about the inter-plane distances and electronographic lines (Figs. 6 and 7) may be established.

In addition to the morphological investigations, the C–V curves of LPCVD Si₃N₄ layers were measured. The measurements show that before

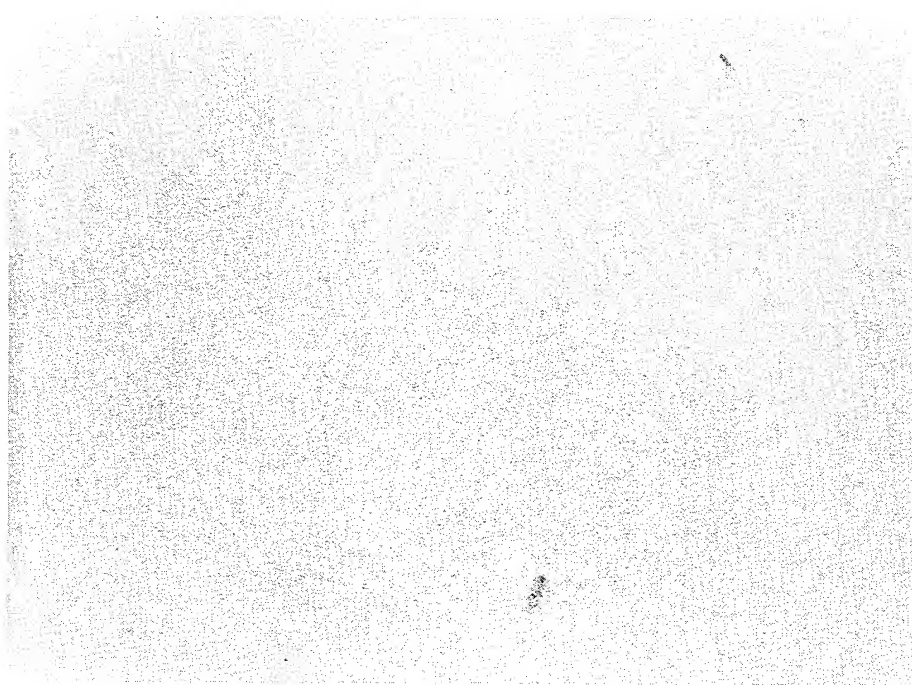


Fig. 3. Morphology of an LPCVD Si_3N_4 layer annealed for 720 min in N_2 at 1100 °C (magnification $\times 50\,000$).



Fig. 4. Morphology of an LPCVD Si_3N_4 layer annealed for 270 min in H_2O at 1100 °C (magnification $\times 50\,000$).

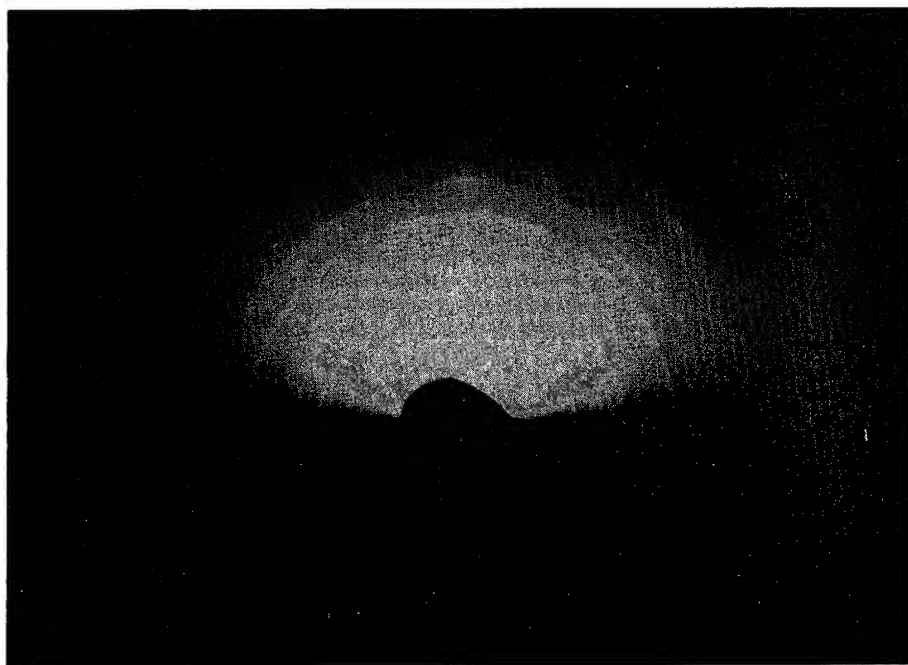


Fig. 5. Electronograph picture of an S_3N_4 layer annealed for 270 min in N_2 at $1000^\circ C$.

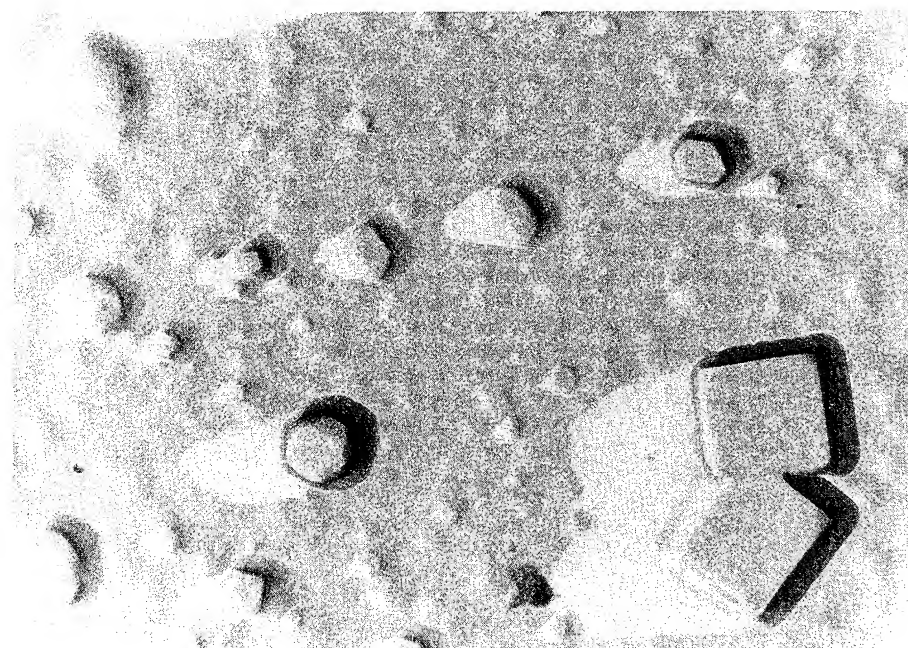


Fig. 6. Morphology of an LPCVD Si_3N_4 layer annealed for 270 min in H_2O at $900^\circ C$ and etched in 40% HF for 10 s (magnification $\times 50\,000$).



Fig. 7. Morphology of an LPCVD Si_3N_4 layer annealed for 270 min in H_2O at 1000 °C and etched in 40% HF for 10 s (magnification $\times 50000$).

annealing the properties of LPCVD layers are comparable to those of thermal CVD layers [4,5]. The relative dielectric constant of the layers may be calculated from the capacitance of the metal- Si_3N_4 n-silicon structure, measured under accumulation condition. The thicknesses of the deposited layers are known from ellipsometric measurements. The relative dielectric constant is of the order of 4.5 for as-deposited samples and increases after high temperature annealing at 1100°C to 5.5. 900°C annealing has almost no effect on the dielectric constant. The electrical charges distributed in the metal-LPCVD Si_3N_4 n-silicon structures may be analyzed from the shape of the $C-V$ curves. The flat band voltage shift (ΔV_{FB}) toward negative values along the voltage axis shows the presence of positive charges. ΔV_{FB} of as-deposited LPCVD SiN_x layers is of the order of 7 V, which is equivalent to the presence of $2.41 \times 10^{11} \text{ cm}^{-2}$ positive charges in the structure. ΔV_{FB} depends on the annealing ambient and on the annealing temperature. Up to 1000°C the annealing in an

H_2O ambient leads to a slight decrease of ΔV_{FB} . Obviously this decrease is due to the increase of the negatively charged bulk and surface traps, because it is accompanied with a decrease of the $C-V$ curves slope. A slight increase of the leakage current is also a feature of the water vapor annealed wafers. An increase of the water vapor annealing temperature to 1100°C leads to a sharp drop of the leakage current and an increase of the ΔV_{FB} to 16.6 V. The effect is due to the penetration of water molecules to the Si- SiO_2 interface and to subsequent oxidation of the silicon substrate.

Nitrogen annealing has a different effect on the electrical properties of metal- Si_3N_4 n-silicon structures. The observed decrease of the slope of the $C-V$ curves shows that the density of negatively charged traps decreases. This is not accompanied with the annealing of the positive charges – the measured ΔV_{FB} , which is the net result of the sum of positive and negative charges, continuously increases from –9 V for unannealed samples to –11 V for the ones annealed at 1100°C. The

leakage currents for the N_2 high temperature annealed samples are far less than the leakage currents of the water vapor annealed samples.

5. Conclusion

The high temperature annealing of LPCVD Si_3N_4 layers in an N_2 ambient leads to a homogenization of the layers, to a reduction of the leakage currents, and to an increase of the dielectric constant of the layers. The high temperature annealing in water vapor ambient changes considerably the surface of the layers in comparison to the as-deposited layers, giving as a result a rougher surface and higher leakage currents. The presence of αSi_3N_4 crystalline inclusions was observed after $1100^\circ C$ annealing in H_2O ambient.

This work has been supported by the Bulgarian Ministry of Science and Education under contract $\Phi 326$ and $\Phi 73$.

References

- [1] L.N. Aleksandrov and F.L. Edelman, *Electron. Ind.* 30 (1979) 28.
- [2] G. Beshkov, L. Popova and V. Georgiev, in: *Proc. Int. Conf. on Defect Control in Semiconductors*, ed. K. Sumino (Elsevier, Amsterdam, 1990) p. 1162.
- [3] E. Irene, N. Chou, D. Dong and E. Tierney, *J. Electrochem. Soc.* (1980) 2518.
- [4] M. Yoshimoto, K. Takubo, T. Saito, T. Ohtsuki, M. Komoda and H. Matsunami, *IEICE Trans. Electronics* E75-C (1992) 1019.
- [5] J. Kanicki and D. Jousse, *IEEE Electron. Device Lett.* 10 (1989) 277.



ELSEVIER

Journal of Non-Crystalline Solids 187 (1995) 308–312

JOURNAL OF
NON-CRYSTALLINE SOLIDS

Hydrogen content of amorphous PECVD $\text{SiN}_x\text{:H}$ films by infrared spectroscopy and hydrogen forward scattering results

Giuliana Morello*

Centro Studi E Laboratori Telecomunicazioni S.p.A., Via Reiss Romoli, 274, 10148 Turin, Italy

Abstract

In the present work, a comparison between infrared spectroscopy (IR) and hydrogen forward scattering (HFS) results is presented. The hydrogen content has been calculated in terms of number of atoms/cm³ using the Lanford and Rand absorption cross-section values, and as absolute atomic percentage. The total atomic density value has been evaluated from density measurements (relative error less than 4%) obtained by weighing the sample before and after the deposition. The relative error of the H content is less than 15% for IR measurements (calculated through the propagation law) and about 10% for HFS results. These two techniques have been found to be in good agreement within experimental errors. A second finding is that deposition temperature strongly influences the total H content while no significant dependence with rf power density and NH_3/SiH_4 ratio has been observed. The NH_3/SiH_4 ratio is strictly related to [Si–H] and [N–H] bond concentrations.

1. Introduction

Amorphous hydrogenated silicon nitride ($\text{a-SiN}_x\text{:H}$) films deposited by plasma-enhanced chemical vapour deposition (PECVD) are used for several applications in electronic and optoelectronic device technology (interlayer insulation, device passivation, mechanical protection) [1–9].

For these applications $\text{SiN}_x\text{:H}$ films must fulfill stringent requirements such as high dielectric strength, excellent adhesion and absence of ‘holes’ or ‘bubbles’. These and other characteristics are strongly influenced by the hydrogen (H) content.

Several techniques can be used to measure the H content, such as nuclear reaction analysis, infrared (IR) spectroscopy and hydrogen forward scattering (HFS). Each of these presents some advantages and some critical aspects.

In particular, IR spectroscopy is widely available and easy to use but requires a careful spectra interpretation in order to obtain reliable quantitative results.

In 1978 Lanford and Rand [10] published for the first time a method to obtain quantitative H analysis in $\text{a-SiN}_x\text{:H}$ films using this technique. They showed that the total density of H bonds can be calculated by the equation

$$H(\text{bonds/cm}^2) = 1.4 \frac{\text{Area}_{\text{N-H}}}{\sigma_{\text{N-H}}} + \frac{\text{Area}_{\text{Si-H}}}{\sigma_{\text{Si-H}}},$$

* Corresponding author. Tel: +39-11 228 5229. Telefax: +39-11 228 5695. E-mail: morello@eiclus.cselt.stet.it.

where $\text{Area}_{\text{N-H}}$, $\text{Area}_{\text{Si-H}}$ are the areas of the N-H and Si-H stretching-mode absorption peaks and $\sigma_{\text{N-H}}$, $\sigma_{\text{Si-H}}$ are the absorption cross-sections, respectively. The 1.4 factor and the cross-section values were obtained from a calibration with nuclear reaction analysis.

Since then, many authors calculated the H content using the following expression:

$$H(\text{bonds/cm}^2) = K_{\text{N-H}} \int \left(\frac{\alpha(\omega)}{\omega} \right)_{\text{N-H}} d\omega + K_{\text{Si-H}} \int \left(\frac{\alpha(\omega)}{\omega} \right)_{\text{Si-H}} d\omega,$$

where ω is the wave number of the peak centre and $K_{\text{N-H}}$ and $K_{\text{Si-H}}$ are proportionality factors. For these constants, several couples of values have been reported up to now [11–17].

These facts suggest that an accurate calibration should be performed for each specific deposition equipment in order to obtain reliable quantitative measurements of the amount of H using IR spectroscopy.

In this work we adopted IR and HFS techniques: the former for the reasons mentioned above, the latter because of its quantitative analysis capability.

The IR spectra have been interpreted using the Lanford and Rand method.

2. Experimental procedures

a-SiN_x:H films have been deposited in a 13.56 MHz PECVD Vacutec 1523 equipment using SiH₄ and NH₃ pure gases.

The chamber has been cleaned after each deposition with a plasma of CF₄ and O₂ at room temperature (chamber pressure $p = 500$ mTorr, rf power density $P = 0.600$ W/cm², CF₄ flow: 43 sccm, O₂ flow: 10 sccm).

An a-SiN_x:H layer of about 1000 Å has been pre-deposited before each run in order to have the same initial conditions before each deposition (deposition temperature $T = 350^\circ\text{C}$, $p = 300$ mTorr, $P = 0.16$ W/cm², SiH₄ flow: 10 sccm, NH₃ flow: 90 sccm).

Seven samples have been deposited on (100) Si substrates under the deposition conditions shown in Table 1. Thickness values represent the mean of at least 10 measurements obtained on different sample points with a profilometer (Tencor α -step 200). Specimens 1 and 7 have been properly treated in order to force the H amount to extreme concentration values (annealing for 1 h at 700°C under vacuum and $T = 150^\circ\text{C}$, respectively). Different pieces of each sample have been analyzed by IR spectroscopy (IR spectrophotometer Perkin Elmer 683) and Hydrogen forward scattering (HFS)/Rutherford back scattering (RBS) (Evans and Associates Labs) in order to measure the H content and the Si and N percentages.

Film density (ρ) has been evaluated by weighing the sample before and after the deposition. We made sure to remove the a-SiN_x:H deposited on the edges and under the substrate by masking accurately the sample surface with wax and etching it briefly in 49% hydrofluoric acid (HF). Using this technique, density measurements with a relative error less than 4% (calculated through the error propagation law [21]) have been obtained.

Table 1
Deposition conditions for the samples used to perform the comparison between IR and HFS/RBS results

Sample	Thickness (Å)	Deposition temperature (°C)	Annealing temperature (°C)	NH ₃ /SiH ₄ flow ratio	Total flow (sccm)	Pressure (mTorr)	RF power density (W/cm ²)
1	2475	350	700	4	100	300	0.12
2	3021	350	No annealing	2	100	300	0.12
3	2475	350	No annealing	4	100	300	0.12
4	2803	350	No annealing	19	100	300	0.12
5	2375	350	No annealing	9	100	300	0.16
6	3297	350	No annealing	5	100	300	0.12
7	2767	150	No annealing	9	100	300	0.16

A second set of samples, different from the one described in Table 1, have been deposited keeping constant p (300 mTorr), T (350°C) and the total flow (100 sccm) and varying P and the NH_3/SiH_4 ratio (R) from 0.04 to 0.2 W/cm^2 and from 2 to 19, respectively.

3. Results and discussion

The hydrogen content has been calculated in terms of number of atoms/ cm^3 ($[\text{H}]$) using the Lanford and Rand absorption cross-section values, and as absolute atomic percentage ($[\text{H}\%]$). The total atomic density value ($[\text{at}]$) necessary for determining $[\text{H}\%]$ has been measured by RBS or calculated from the film density (ρ) and the $[\text{Si}]/[\text{N}]$ ratio (k) according to the following equations:

$$[\text{at}] = [\text{H}] + [\text{Si}] + [\text{N}];$$

Assuming that all N atoms are bonded to Si we have

$$[\text{N}] = [\text{SiN}] \text{ and so } [\text{Si}] = k[\text{SiN}];$$

the film density ρ is given by

$$\rho = \frac{[\text{SiN}]\text{SiN} + [\text{H}]\text{H}}{N_0}.$$

In each molecule of SiN there is one atom of N and k of Si, so the molecular weight of SiN is

$$\text{SiN} = k\text{Si} + \text{N}.$$

Here, SiN, Si, N, H are the molecular or atomic weights of the species. Symbols between square brackets indicate the molecular and atomic densities. N_0 is the Avogadro's number. The parameter k has been measured by RBS and $[\text{H}]$ by IR.

Fig. 1 shows the $[\text{at}]$ values obtained by these two methods. The two sets of data are in agreement within the experimental errors (less than 15% for both techniques).

The comparison between $[\text{H}\%]$ measured by HFS/RBS and IR spectroscopy is shown in Fig. 2. IR $[\text{H}\%]$ has been determined using the $[\text{at}]$ value obtained from ρ and k parameters.

The relative error of the H content is less than 15% for IR measurements (calculated with the propagation law) and about 10% for HFS results. The results are in good agreement within the experimental errors.

From Fig. 2 data we can also see that the temperature strongly influences the total H content: sample 1 (deposited at $T = 350^\circ\text{C}$ and subsequently annealed at 700°C under vacuum for 1 h) has the lowest H percentage (about 15%). Sample 7 ($T = 150^\circ\text{C}$) contains about 40% of H. Sample 5, directly comparable to sample 7, except the deposition temperature, has an H percentage value of 26%. All the other samples ($T = 350^\circ\text{C}$) present

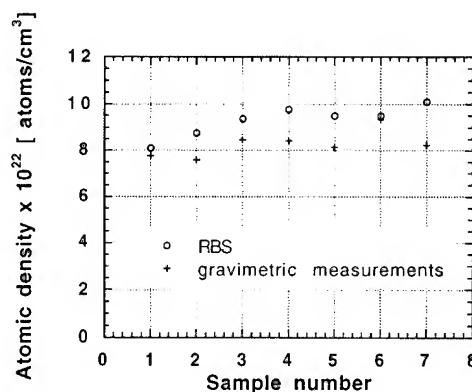


Fig. 1. Comparison between total atomic density values obtained from RBS analysis and film density measurements.

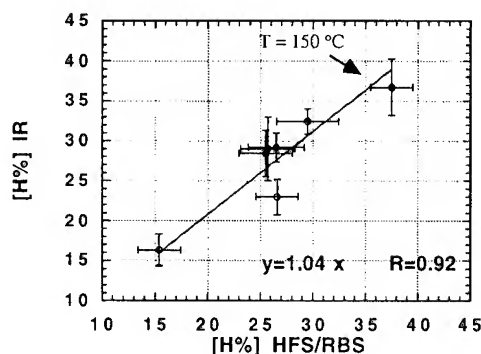


Fig. 2. Absolute H percentage in $\text{SiN}_x\text{:H}$ films evaluated by IR and HFS techniques. $\text{SiN}_x\text{:H}$ films have been deposited using deposition conditions of Table 1. Sample 1 has been annealed at 700°C for 60 min. T was 350°C where not otherwise specified.

a small variation of $[H\%]$ (from 25 to 30%), even though R and P have been varied from 2 to 19 and from 0.12 to 0.16, respectively.

In order to examine these aspects thoroughly, H content has been measured on the second set of samples using IR spectroscopy only. Figs. 3 and 4 show the total amount of H and the percentage of H atoms bound to Si or N versus the NH_3/SiH_4 flows ratio and the RF power density.

These data confirm that no significant dependence of the total H content with RF power density and NH_3/SiH_4 ratio exists.

In the range explored, the $[Si-H]$ and $[N-H]$ bond concentrations are not influenced by rf power density value.

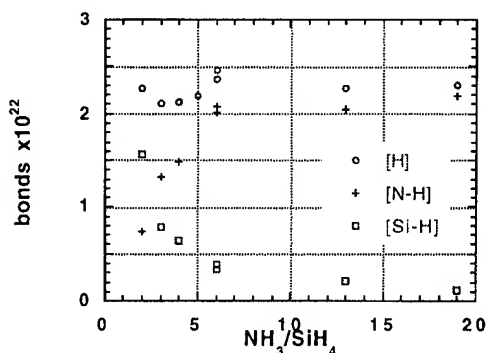


Fig. 3. $[H]$, $[N-H]$ and $[Si-H]$ bonds versus NH_3/SiH_4 ratio. Deposition conditions: $p = 300$ mTorr, $T = 350^\circ C$, rf power density = 0.12 W/cm^2 , total flow = 100 sccm .

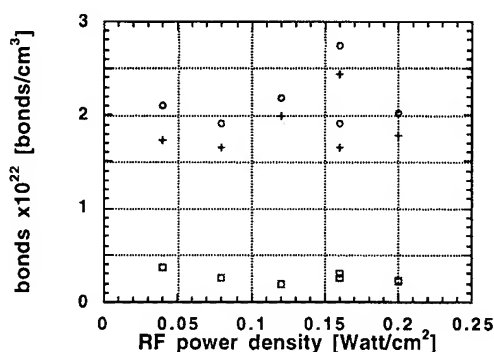


Fig. 4. $[H]$, $[N-H]$ and $[Si-H]$ bonds versus rf power density. Deposition conditions: $p = 300$ mTorr, $T = 350^\circ C$, $NH_3/SiH_4 = 9$, total flow = 100 sccm .

On the other hand, the $[Si-H]$ and $[N-H]$ bond concentrations are strictly related to NH_3/SiH_4 ratio: higher the SiH_4 concentration, higher the probability that the H is incorporated bonded to Si atoms as a consequence of the partial dissociation of the SiH_4 molecule.

These results agree with those reported in the literature [10,18–20].

4. Conclusions

Hydrogen content of $a-SiN_x:H$ films deposited by PECVD has been measured by means of IR and HFS/RBS analysis. The results obtained with these two techniques are in good agreement within the experimental errors (less than 15% and 10% for IR and HFS/RBS results, respectively).

Based on this agreement, H content has been measured on other samples using IR spectroscopy only.

The main finding is that deposition temperature strongly influences the total H content while a significant dependence on rf power density and NH_3/SiH_4 ratio has not been observed.

$[N-H]$ and $[Si-H]$ bond concentrations are directly and inversely proportional to NH_3/SiH_4 ratio, respectively.

The author would like to thank C. Papuzza and P. Pastorino (CSELT) for helpful comments and the useful discussions.

References

- [1] J.T. Milek, ed., Handbook of Electronic Materials, Vol. 3, Silicon Nitride for Microelectronic Applications, Part I: Preparation and Properties (Plenum, New York, 1971).
- [2] J.T. Milek, ed., Handbook of Electronic Materials, Vol. 6, Silicon Nitride for Microelectronic Applications, Part II: Application and Devices (Plenum, New York, 1972).
- [3] A. Hashimoto, M. Kobayashi, T. Kamijoh, H. Tanako and M. Sakuta, J. Electrochem. Soc. 133 (1986) 1464.
- [4] C.J. Dell'Oca and M.L. Barry, Solid State Electron. 15 (1972) 659.
- [5] P.M. Petroff, G.A. Rozgony and T.T. Sheng, J. Electrochem. Soc. 123 (1976) 565.
- [6] M.J. Helix, K.V. Vaidyanathan, B.G. Streetman, H.B. Dietrich and P.K. Chatterjee, Thin Solid Films 55 (1978) 143.

- [7] E.Y. Chang, G.T. Cibuzar, T.K. Yard and K.P. Pande, *Mater. Res. Soc. Symp. Proc.* 126 (1988) 271.
- [8] A. Piccirillo and A.L. Gobbi, *J. Electrochem. Soc.* 137 (1990) 3910.
- [9] R. Audino, F. Cannistraci, G. Morello and P. Valenti, *these Proceedings*, p. 477.
- [10] W.A. Lanford and M.J. Rand, *J. Appl. Phys.* 49 (1978) 2473.
- [11] S. Hasegawa, L. He, Y. Amano and T. Inokuma, *Phys. Rev. B* 48 (1993) 5315.
- [12] J. Campmany, E. Bertan, J.L. Andujar, A. Canillas, J.M. Lopez-Villegas and J.R. Morante, *Mater. Res. Soc. Symp. Proc.* 258 (1992) 643.
- [13] B. Reynes, C. Ance, J.P. Stoquert and J.C. Bruyere, *Thin Solid Films* 203 (1991) 87.
- [14] E. Bustarret, M. Bensouda, M.C. Habrard, J.C. Bruyere, S. Poulin and S.C. Gujrathi, *Phys. Rev. B* 38 (12) (1988) 38.
- [15] A.C. Adams, *Solid State Technol.* 26 (4) (1983) 135.
- [16] V.J. Kapoor, R.S. Bailey and H.J. Stein, *J. Vac. Sci. Technol. A* 1 (1983).
- [17] T. Makino, *J. Electrochem. Soc.* 130 (1983) 450.
- [18] W.A.P. Classen, H.A.J.Th. v.d. Pol, A.H. Goemans and A.E.T. Kuiper, *J. Electrochem. Soc.* 133 (1986) 1458.
- [19] H. Watanabe, K. Kato and S.I. Imagi, *Thin Solid Films* 136 (1986) 77.
- [20] H. Dun, P. Pan, F.R. White and R.W. Douse, *J. Electrochem. Soc.* 128 (1981) 1555.
- [21] J.R. Taylor, *An Introduction to Error Analysis* (Mill Valley (US) University Science Books, 1982).



ELSEVIER

Journal of Non-Crystalline Solids 187 (1995) 313–318

JOURNAL OF
NON-CRYSTALLINE SOLIDS

Bias stress studies of a-SiN:H/a-Si:H MIS structures from quasistatic capacitance measurements

J. Reynaud, J.P. Kleider, D. Mencaraglia*

Laboratoire de Génie Electrique de Paris (LGEP, URA 127 CNRS), Ecole Supérieure d'Electricité, Universités de Paris VI et Paris XI, Plateau de Moulon, 91192 Gif-sur-Yvette cedex, France

Abstract

Quasistatic capacitance measurements are used to study the effect of thermal bias annealing where small gate bias stresses ranging from -5 V to $+6$ V are applied at 200°C for 15 min on top nitride amorphous silicon–silicon nitride MIS structures. After negative gate bias stresses, the $C(V_G)$ curves (capacitance versus gate bias) are found to be slightly shifted towards negative voltages and their shape is altered. The minimum of the $C(V_G)$ curves increases with the stress amplitude indicating the creation of defects in the probed energy range. After positive gate bias stresses, $C(V_G)$ curves are shifted towards positive voltages without showing any significant shape changes. This indicates either that negative charges have been injected into the insulator, or that negatively charged defects have been created in the a-Si:H layer (or at the a-Si:H/nitride interface) outside the probed energy range (0.15–0.65 eV below the conduction band edge). The results can be qualitatively described by changes in the defect distribution in agreement with what is expected in the framework of the defect pool model.

1. Introduction

Hydrogenated amorphous silicon is an important material for commercial applications in large-area electronics, in particular in active matrix liquid-crystal displays. In these displays, the active element, usually a thin-film transistor (TFT), is submitted to relatively high gate biases (low duty cycle pulsed) and strong illumination during operation. This can cause threshold voltage instabilities, which have been actively studied in the last few years. Two mechanisms can account for the

threshold voltage shifts observed after gate bias stresses: charge trapping in the gate insulator and creation/removal of localized states in the gap of the semiconductor [1–4]. The gate bias stress induced metastabilities have been generally studied through electrical characterization of the TFTs, and only little work has made use of the capacitance of MIS structures. In this paper, we show that quasistatic capacitance measurements on MIS structures can also be very helpful in the study of stress induced metastabilities. Since the predominance of charge trapping seems to be agreed at high gate bias stresses, we focus on the effect of low gate bias stresses, for which the results reported in the literature are still a matter of controversy.

* Corresponding author. Tel: +33-1 69 85 16 44. Telefax: +33-1 69 41 83 18. E-mail: mencaraglia@lgep.supelec.fr.

2. Experimental procedure

The MIS structures used in our study were fabricated in the top gate configuration at CNET [5]. Three layers of 4 nm thick n^+ doped a-Si:H, 1 μm thick intrinsic a-Si:H and 100 nm thick silicon nitride were successively deposited at a substrate temperature of 180°C by plasma enhanced chemical vapor deposition (PECVD) on a glass substrate covered with ITO. Finally, aluminum was deposited and patterned to form the gate electrode. The area of the MIS capacitance is $S = 7.85 \times 10^{-3} \text{ cm}^2$.

These structures were submitted to thermal bias annealing treatments. Low gate bias stresses ranging from $V_G = -5 \text{ V}$ to $+6 \text{ V}$ were applied to these structures at 200°C for a duration of 15 min. These gate biases correspond to a maximum induced charge density Q ($Q = V_G C_i / qS$, C_i being the insulator capacitance and q the absolute value of the electronic charge) equal to $2 \times 10^{12} \text{ cm}^{-2}$. The high bias annealing temperature was chosen to facilitate the reequilibration of the defects in a-Si:H. The structures were then cooled down rapidly (about 1°C/s) to 0°C, with the gate bias stress still applied. Then the quasistatic capacitance C was recorded as a function of the bias V_G at 80°C. This temperature was found high enough to obtain a true quasistatic curve in a reasonable measurement time and low enough to avoid partial annealing effects. We also limited the bias range in order to avoid charge injection effects which could be produced during recording, and to limit the leakage currents at very low levels ($< 0.05 \text{ pA}$). After each bias-stress and $C(V_G)$ recording sequence, the MIS structures were annealed at 200°C for 20 min under zero bias. We checked that the bias-stressed MIS structure recovered the unstressed $C(V_G)$ curves after such a zero bias annealing. Additional conductance measurements as a function of temperature and gate bias were performed, in the annealed state, on top gate TFTs processed in the same way as the MIS devices [5]. The deduced activation energy is an estimate of the position of the Fermi level relative to the conduction band edge at the interface, which helped us in the determination of the energy range probed in the quasistatic capacitance

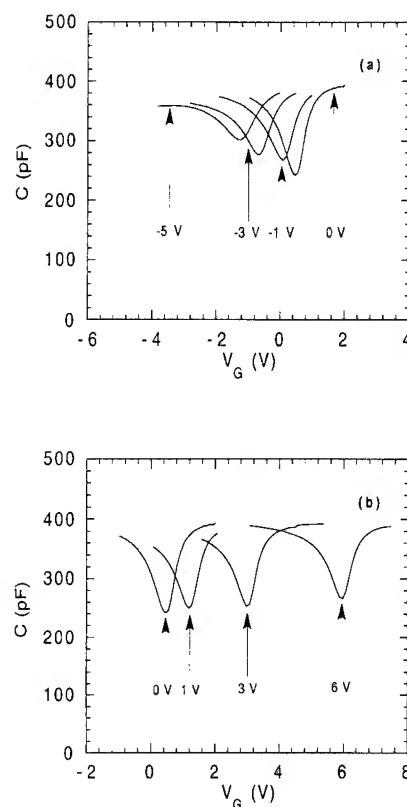


Fig. 1. Quasistatic capacitance C versus gate voltage V_G after negative and positive bias stress annealing, (a) and (b) respectively. The curves are labelled according to the gate bias stress value.

measurements, as presented in the following section.

3. Results

Figs. 1(a) and (b) shows the quasistatic capacitance of the MIS structures obtained after negative and positive thermal bias annealing (200°C), respectively. Positive bias stresses shift the quasistatic $C(V_G)$ curve towards higher voltages, the shift amplitude being approximately equal to the bias stress. The shape of the curves is not modified and the minimum of the capacitance is practically always the same except after the 6 V stress where the minimum of the capacitance slightly increases (from 240 pF to 260 pF). Negative bias stresses shift

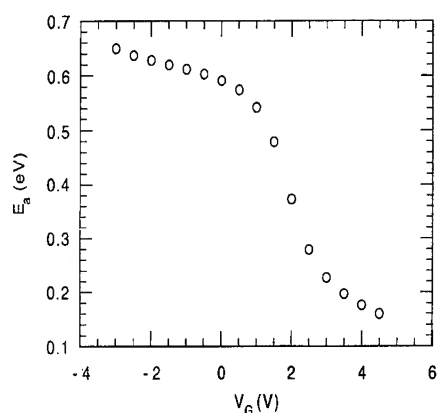


Fig. 2. Experimentally derived activation energy E_a of the conductance of TFTs as a function of the gate voltage V_G .

the quasistatic $C(V_G)$ curve towards lower voltages, the shift amplitude being approximately 20% of the negative bias stress. Moreover, the shape of the curves is modified and the minimum of the capacitance increases with the absolute value of the voltage stress.

To estimate the energy range swept by the Fermi level in our $C(V_G)$ measurements, we have used the results of the conductance measurements performed on TFTs at different temperatures and gate biases. An Arrhenius plot of this conductance exhibits a gate bias dependent activation energy shown in Fig. 2. The obtained curve indicates that the activation energy varies from 0.15 eV to 0.65 eV for gate bias voltages varying from 5 V to -3 V. Since this S-shaped curve varies slowly for gate biases above 4 V (accumulation regime) and below 0 V (depletion regime), we can consider that the range which spans from 0.15 to 0.65 eV from E_C is a good estimation of the energy range of the density of states probed with the quasistatic capacitance technique when the MIS device is also biased from the accumulation to the depletion regime. These results are in good agreement with the amplitude of the probed energy range (0.5 eV) calculated from the $C(V_G)$ curves of the MIS devices in the annealed state through Berglund's formula [6], integrating the quantity $(1 - C(V_G)/C_i)$ (C_i being the insulator capacitance)

over the voltage range swept during the quasistatic capacitance measurement.

4. Discussion

We have shown in a previous paper that the same kind of theoretical $C(V_G)$ curves can be obtained in an amorphous semiconductor by attributing the contribution of localized states either to the interface or to the bulk [7]. The purpose of the present paper is not to try to distinguish between interface and bulk state effects but rather to analyze which mechanism (charge trapping in the gate insulator or creation/removal of localized states in the gap of the semiconductor) can account for our thermal bias stress experimental results. Therefore, in the following, we present the results of a numerical simulation which takes into account homogeneous bulk density of states (DOS) without any additional surface states, but it should be kept in mind that our final conclusions concerning the creation/removal of states in the semiconductor bandgap could also apply to interface states. The homogeneous bulk DOS considered here is made of two exponential band tails and a Gaussian distribution of deep defects. For the sake of simplicity, all the states are considered as monovalent and their occupancy is calculated from Fermi–Dirac statistics. Moreover, the assumption is made that the semiconductor layer is thick enough so that intrinsic bulk characteristics (e.g. bulk Fermi level position, no band bending) are reached far from the insulator interface. We have shown previously that this is a reasonable assumption for MIS devices with 1 μm thick a-Si:H layers [7].

Fig. 3(a) shows two examples of the DOS used to calculate the $C(V_G)$ curves of Fig. 3(b). These two DOS only differ by the value of the full width at half maximum (FWHM) of the deep defects Gaussian distribution. Case i) represents an almost energy independent distribution of these defects whereas case ii) shows a more pronounced variation with energy (FWHM ≈ 0.35 eV). We can see in Fig. 3(b) that outside the strong accumulation and inversion regimes, the quasistatic $C(V_G)$ curves are directly related to the deep defect DOS shape and density:

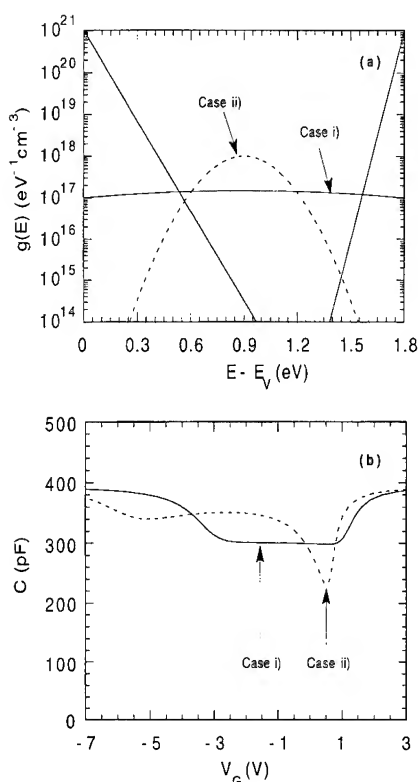


Fig. 3. (a) Models of the density of states $g(E)$ in the a-Si:H and (b) corresponding calculated quasistatic capacitance versus gate voltage V_G . In case (i) the deep defect distribution is nearly constant, while in case (ii) it consists of a Gaussian distribution centered at 0.9 eV above the valence band edge E_v with a FWHM equal to 0.35 eV. In our simulation, the relative dielectric constants of the silicon nitride and a-Si:H layers were taken equal to 6 and 12, respectively.

a nearly constant DOS is associated to a plateau in the $C(V_G)$ curve extending over a large range of gate biases, whereas sharper variations in the $C(V_G)$ curve are associated to more pronounced variations with energy of the DOS. Moreover, the lower the DOS minimum, the lower the minimum of the quasistatic capacitance [7]. Comparing Fig. 1 with Fig. 3(b), we deduce that a DOS distribution of deep defects exhibiting rather rapid variations with energy (case (ii)) of Fig. 3(a) is more representative of our experimental $C(V_G)$ curves.

Turning now to the origin of the bias stress induced shifts of the $C(V_G)$ curves on our samples,

we remind that the electrostatic potential difference $\Psi_s(0)$ between the bulk of the semiconductor and the nitride/a-Si:H interface is related to the gate bias V_G through

$$\Psi_s(0) = (\Phi_M - \Phi_S) - V_G - \frac{\tilde{Q}_i}{C_i} - \frac{Q_s}{C_i},$$

$(\Phi_M - \Phi_S)$ being the metal gate-amorphous silicon work function difference, \tilde{Q}_i the first momentum of the volume density of nitride trapped charge, and Q_s the charge stored in the semiconductor. This relation shows that a $C(V_G)$ curve shift may be produced by the modification of two kinds of charges: the charge in the insulator and the charge in the semiconductor. However, it is worth pointing out that \tilde{Q}_i does not depend on $\Psi_s(0)$ during the $C(V_G)$ measurement, while Q_s does. Therefore, on the one hand, if \tilde{Q}_i changes during the thermal bias annealing treatment, this will only induce a rigid shift in the $C(V_G)$ curve along the V_G axis. On the other hand, a modification of Q_s during the thermal bias annealing, associated to a modification of the DOS, can induce a shift in the $C(V_G)$ curve, but it will also induce a change in the shape of this curve if the DOS has changed in the energy range probed by the capacitance measurements.

The above discussion of the origin of the shifts observed in the $C(V_G)$ curves, whether they are coupled to a change in the shape of the curve or not, leads us to the following interpretation of our thermal bias annealing experiments. For negative bias stresses, due to the change of the $C(V_G)$ curve shape, there is clearly a modification in the DOS of a-Si:H. This consists mainly in an increase of positively charged defects located between 0.4 and 0.65 eV below the conduction band edge, E_c , as estimated from Berglund's formula [6]. For positive bias stresses, our results can be interpreted either as the injection of electrons from the a-Si:H into the nitride, or as the creation in the a-Si:H layer of negatively charged defects which are not probed by our $C(V_G)$, and should therefore be located below 0.65 eV from E_c .

Most of the bias-stress results reported in the literature concern the more common bottom nitride configuration. Gelatos and Kanicki observed the same kind of shifts in the high frequency $C(V_G)$

curves of metal/insulator/a-Si:H/n-type crystalline silicon structures [1]. From additional photo-capacitance measurements, they concluded that, for negative bias stresses, the shift towards negative biases was due only to charge injection into the nitride, while for positive bias stresses, the shift towards positive biases was due both to charge injection into the nitride and to defect creation in a-Si:H with a predominant contribution of charge injection. Their conclusions can explain our results for the positive bias stresses, but for the negative bias stresses, there is strong evidence from our experiments that the DOS has changed. Thermal bias annealing experiments have also been interpreted in terms of changes in the defect distribution for both low positive and low negative biases by Powell and co-workers, on the basis of the defect pool model [3,4]. According to this model, it is expected that a positive thermal bias stress should increase the density of negatively charged dangling bonds. These states are mainly located below midgap. Thus, they will mainly produce a rigid shift in our $C(V_G)$ curve which probes the states above 0.65 eV from E_C , and can therefore account for our results. For negative bias stresses, we expect both a decrease of the density of dangling bonds below midgap and an increase of the density of dangling bonds above midgap. Again, this could qualitatively account for our results. Indeed, these changes result in a net positive charge variation which can explain the observed shift while the DOS changes above midgap can explain the observed modification in the shape of the $C(V_G)$ curve.

In summary, the main trends of our experimental thermal bias annealing results obtained on MIS devices for both negative and positive gate stress biases are consistent with the defect-pool model. However, a more careful observation of the shape evolution of the $C(V_G)$ curves after a negative stress reveals some discrepancy. Indeed, when the device is negatively stressed, the Fermi level moves towards the valence band edge and as predicted by the defect-pool model, removal and creation of states occur simultaneously below and above midgap, respectively. Then, there should exist a bias stress value for which the corresponding defect-pool DOS had to approach that of good quality

intrinsic a-Si:H, that is a rather flat distribution of deep gap states at a level around $10^{16} \text{ cm}^{-3} \text{ eV}^{-1}$ looking like that defined by case i) of Fig. 3(a) (see also Fig. 6 of Ref. [8]). In such a case, the corresponding $C(V_G)$ curve shown in Fig. 3(b) is expected. This is not experimentally observed: even after a bias stress of -5 V , the experimental $C(V_G)$ curve of Fig. 1 still exhibits very sharp variations which cannot be accounted for by the flat DOS expected in the framework of the defect pool. To check if this is a real discrepancy, a more quantitative analysis is required, taking into account the spatial variation of the DOS across the sample induced by the varying Fermi level position relative to E_C , due to band bending during the bias stress at high temperature [8].

5. Conclusions

Thermal bias annealing treatments of top nitride hydrogenated amorphous silicon MIS structures have been analysed through quasistatic capacitance measurements. For low positive bias stresses, we mainly observe a rigid shift of the $C(V_G)$ curves towards higher voltages. For low negative bias stresses, we observe both a slight shift of the curves towards lower voltages and a change in the shape of the $C(V_G)$ curves. Though the injection of electrons from the a-Si:H into the nitride cannot be ruled out for positive bias stresses, the results can be explained by the creation of negatively charged dangling bonds. For negative bias stresses, our experiments provide strong evidence for the modification of the DOS in a range of energy estimated between 0.4 and 0.65 eV below the conduction band edge. These results can be *qualitatively* described in the framework of the defect pool model. However, the check of this model and of its parameters requires a more quantitative analysis which should also include the non-homogeneous DOS distribution induced by the bias stress at high temperature.

The authors thank J. Richard and A. Rolland at CNET Lannion for providing the MIS and TFT structures. This work was partially supported by CNET under contract no. 93 8B 077.

References

- [1] A.V. Gelatos and J. Kanicki, Appl. Phys. Lett. 57 (1990) 1197.
- [2] F.R. Libsch and J. Kanicki, Appl. Phys. Lett. 62 (1992) 1286.
- [3] M.J. Powell, S.C. Deane and W.I. Milne, Appl. Phys. Lett. 60 (1992) 207.
- [4] M.J. Powell, C. van Berkel, A.R. Franklin, S.C. Deane and W.I. Milne, Phys. Rev. B45 (1992) 4160.
- [5] M. Bonnel, B. Vinouze, J. Richard, F. Morin, P. Weisse, M. Le Contellec and F. Maurice, in: Eurodisplay 87, Proc. Seventh Int. Display Research Conf., p. 180. Society for Information Display, Playa del Rey, CA (1987).
- [6] C.N. Berglund, IEEE Trans. Electron. Devices ED-13 (1966) 701.
- [7] A. Rolland, J. Richard, J.P. Kleider and D. Mencaraglia, J. Electrochem. Soc. 140 (1993) 3679.
- [8] S.C. Deane and M.J. Powell, J. Appl. Phys. (1993) 6655.



ELSEVIER

Journal of Non-Crystalline Solids 187 (1995) 319–323

JOURNAL OF
NON-CRYSTALLINE SOLIDS

Selective thermal – as opposed to non-selective plasma – nitridation of Si–Ge related materials examined by in situ photoemission techniques

D. Aubel, M. Diani, L. Kubler*, J.L. Bischoff, D. Bolmont

Laboratoire de Physique et de Spectroscopie Electronique, URA CNRS 1435, Faculté des Sciences, Université de Haute Alsace, 68093 Mulhouse cédex, France

Abstract

NH_3 thermal and N_2 plasma reactivity with $\text{Si}(001)$, $\text{Ge}(001)$, $\text{Si}_{1-x}\text{Ge}_x(001)$ surfaces has been studied by means of in situ X-ray photoelectron spectroscopy (XPS) in a temperature domain ($T \sim 600^\circ\text{C}$) compatible with the MBE growth of Ge–Si-based heterostructures. $\text{Si}(001)$ surfaces present a strong initial thermal reactivity against NH_3 , contrary to $\text{Ge}(001)$ which is totally inert. The selectivity against thermal nitridation, which may be anticipated for thermodynamical reasons, has been verified by nitrogen uptake measurements of N 1s core level intensities as a function of NH_3 exposure, both for $\text{Si}(001)$ and $\text{Ge}(001)$ surfaces. As a consequence of this strong reactivity difference, an exclusive Si_3N_4 formation and Ge phase separation result from nitridation attempts of $\text{Si}_{1-x}\text{Ge}_x$ alloys. Thus, an important finding is the indispensable utilization of plasma-assisted nitridation methods in order to achieve low-temperature Ge nitridation, either on clean $\text{Ge}(001)$ surfaces or simultaneously with Si on SiGe alloys. In this paper, the first results relevant to Ge and SiGe alloy nitridation by irradiation of these surfaces by electron cyclotron resonance (ECR) nitrogen (N_2) plasmas are presented. These alloys are thermally unstable as nitridation transfer from Ge to Si occurs after annealing, in accordance with thermally favored Si nitridation. In addition, Ge_3N_4 (Si_3N_4) thick layers were grown using ECR N_2 plasma treatment associated with a concomitant Ge (Si) atom-supply on the substrate, performed by Ge evaporation (SiH_4 reacting gas).

1. Introduction

In comparison with the huge number of reports devoted to the comprehension of clean silicon nitridation, germanium nitridation has been only scarcely investigated. The main part of the avail-

able works is restricted to the fundamental interaction of some nitriding molecules such as NH_3 , NO or NO_2 with Ge surfaces in the near room temperature (RT) or low-temperature range [1–5], pointing out the non-dissociative character of the adsorption of these molecules on clean Ge surfaces in these conditions. Nevertheless, the recent interest in Si- and Ge-based devices and their promising electronic applications implies a future control of dielectric materials on Si and Ge compounds and

*Corresponding author. Tel: +33 89 59 63 59. Telefax: +33 89 59 63 54.

that in a temperature range compatible with Si/Ge heterostructure fabrication (room temperature = $RT < T < 600^\circ\text{C}$).

In the present work, after a brief reminder of the present status of knowledge of thermal nitridation of silicon by ammonia (NH_3), we show in Section 3.1. that the previously observed non-interacting regime of NH_3 with $\text{Ge}(001)$ can be extended in the high-temperature range, in complete opposition to the $\text{Si}(001)$ behavior. This negative result concerning Ge thermal nitridation is then confirmed when an epitaxial $\text{Si}_{1-x}\text{Ge}_x$ (also abbreviated SiGe) alloy grown on $\text{Si}(001)$ by MBE is tentatively nitrided. It results in a selective Si nitridation with Ge remaining in its elemental form. These very different thermal reactivities between Si and Ge imply the necessary use of plasma enhanced nitridation methods in order to obtain simultaneous Si and Ge nitridation in SiGe alloys. Vancauwenberghe and co-workers [6, 7] have previously addressed the problem of ion beam oxidation and nitridation of SiGe, using O_2^+ and N_2^+ ion implantation to form oxides and nitrides, respectively. We present here in Section 3.2. the first results relevant to Ge and SiGe alloy nitridation by irradiation of these surfaces by electron cyclotron resonance (ECR) nitrogen (N_2) plasmas. To date, ECR-plasma nitridation has been reported with Si [8] but not with Ge. The problem of the thermal stability of the alloy nitride is also addressed.

2. Experiment

All the experiments were carried out in situ in a two chamber ultrahigh vacuum (UHV) system operating at base pressures in the low 10^{-10} range and consisting of an analysis chamber equipped with low energy electron diffraction (LEED), X-ray photoelectron spectroscopy (XPS) and ultraviolet photoelectron spectroscopy (UPS) techniques and a sample treatment chamber. The XPS spectra are obtained using Mg K_α radiation (1253.6 eV). The preparation chamber includes all fittings for in situ sample cleaning, heating, gas exposures, layer deposition and control. The thermal nitridation, on routinely, in situ, cleaned substrates were obtained by heating the crystal to the desired temperature,

followed by backfilling the chamber with NH_3 at a given pressure and exposure for various lengths of time. The exposures are expressed in langmuir (L) ($1\text{L} = 10^{-6}$ Torr). Separate or concomitant Si and Ge evaporations, calibrated by a quartz crystal monitor, are obtained by means of an electron gun and a Knudsen cell, respectively. Prior to the $\text{Si}_{1-x}\text{Ge}_x$ growths at 400°C (obtained by codeposition of Si and Ge), a Si buffer layer of about 500 Å was systematically deposited at 600°C on the preceding cleaned surface improving the quality of the starting surface as checked by relevant increases of the UPS surface state intensity and of the LEED spot brightness.

The ECR plasma used for low-temperature plasma assisted nitridation is generated by a UHV compatible, commercial, 250 W, 2.45 GHz microwave source with electromagnets producing a 875 G magnetic field. As process gas, 99.9995% pure nitrogen (N_2) is used, its flow rate being regulated by a variable leak valve and keeping the chamber pressure typically around 10^{-4} mbar with the 5001/s pumping speed.

3. Results

3.1. Thermal nitridation with NH_3

3.1.1. Clean Ge and Si substrates

In this section we first compare the well-differentiated thermal interactions of NH_3 molecules with $\text{Si}(001)$ and $\text{Ge}(001)$ surfaces. To date, low-temperature adsorption studies have been conducted by Chen and Ranke [3] which have shown that only NH_3 molecular physisorption may occur on Ge below 200 K. Cohen et al. [9] have given recently an upper limit for the initial sticking coefficient S_0 for the molecular NH_3 adsorption on $\text{Ge}(001)$ ($S_0 < 10^{-4}$) at 173 K. The present study extends the lack of dissociative interaction of NH_3 to the high temperatures (up to 600°C). Indeed we failed to produce any nitrided layer on $\text{Ge}(001)$ either at RT or at 600°C for NH_3 exposures up to 10^4 L within our surface nitrogen N 1s detection limit which is lower than 0.1 monolayer-equivalent (ML) – 1 ML corresponds to 6.8×10^{14} atoms/cm²

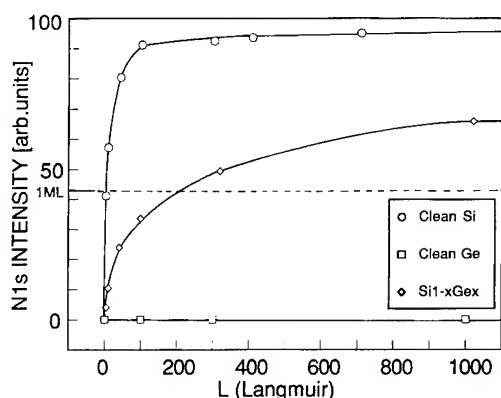


Fig. 1. Evolution of the N 1s intensities as a function of 600°C NH₃ exposure in the initial thermal nitridation stage of different surfaces: ○, clean Si(001); □, clean Ge(001); ◇, 200 Å Si_{0.7}Ge_{0.3} alloyed layer epitaxiated at 400°C on Si(001). Lines are drawn as guides for the eye.

on the Si(001) surface (Fig. 1). This behavior is in deep contrast with the consistent picture provided by many extensive studies [10–14] (and references quoted therein) concerning the NH₃/Si(001) system where the RT NH₃ adsorption results in partial dissociation producing NH₂ and H species which passivate the surface dimer dangling bonds.

A binding energy inspection has made possible the discrimination between this NH₂ feature (398.6 eV) [13] and the non-dissociated NH₃ contribution on the one hand (400.1 eV) [10, 12] and the atomic nitrogen signature near 398.0 eV, on the other hand. The latter value, which depends slightly on coverage and T_s [13], can be obtained either by annealing above 600°C the adlayer adsorbed at RT or by direct adsorption at these T_s . With the purpose of thermal nitridation of Si and Ge compounds in mind, we want to focus only on the latter adsorption scheme which is the sole allowing the start of true thermal nitridation of Si. As expected, Fig. 1 indicates a very reactive Si(001) surface with an initial fast nitridation stage followed by a saturating one at high exposures denoting the low diffusion of the reacting species through the formed nitride, in agreement with previous reports. In the low exposure domain corresponding to low coverages ($Q_N \leq 1$ ML), the following linear relationship, previously detailed [13], can be used to convert the N 1s intensity I_N in atomic nitrogen coverage

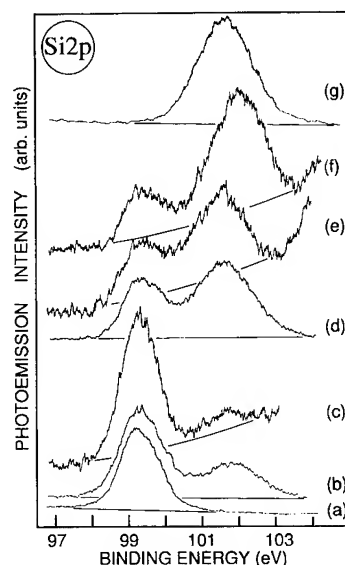


Fig. 2. Si 2p core level peaks taken from different surfaces: (a) clean Si(001); (b) clean Si(001) exposed at 600°C to 10^4 L NH₃; (c) clean Si_{1-x}Ge_x(001) exposed to 100 L NH₃ at 600°C; (d) clean Si(001) treated by ECR N₂ plasma at RT; (e) Si_{1-x}Ge_x(001) processed by a N₂ ECR plasma at RT, plasma power = 80 W, $P_{N_2} = 10^{-4}$ mb, process time = 1 min; (f) sample condition as in (d) but annealed at 800°C for 1 min; (g) deposited Si₃N₄ layer by N₂ ECR plasma associated with SiH₄ gas arrival at RT.

($Q_N = 0.16 \times 10^{14} I_N \text{ cm}^{-2}$ where I_N is the nitrogen intensity expressed in the normalized scale of Fig. 1). A rough estimate of about 6.5×10^{14} atoms/cm² (near 1 ML = 6.8×10^{14} atoms/cm²) is deduced for 4 L or a 2.0×10^{15} molecules/cm²s exposure. These values lead to a rather high sticking mean value $S_0 = 0.33$ averaged on these first 4 L for the Si silicon surface to be compared to the extremely low upper value relevant to Ge ($< 3 \times 10^{-6}$). This nitridation selectivity between Si and Ge, essentially discussed here in the light of N 1s uptake changes, is confirmed and also illustrated by a significant Si 2p component, chemically shifted towards the high binding energy side after NH₃ treatment (Fig. 2(b)) and caused by the Si–N bonds versus the absence of any corresponding Ge 3d shift (Fig. 3(b)).

3.1.2. SiGe

A 200 Å thick Si_{1-x}Ge_x layer, with $x \sim 0.3$, is epitaxiated, at 400°C by MBE co-evaporation on the

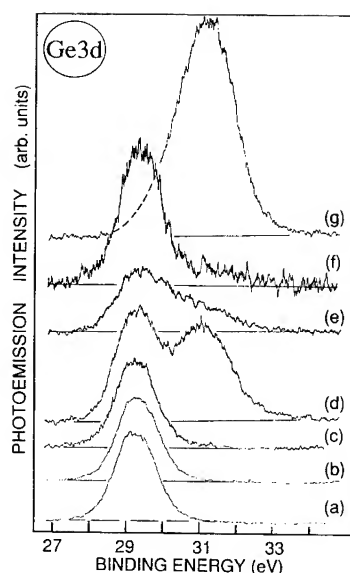


Fig. 3. Ge 3d core levels corresponding to the Si 2p peaks in Fig. 3, the same letters referring to the same treatments: (a) clean Ge(001), (b) clean Ge exposed to NH_3 , etc. Spectrum (3f) corresponds to a deposited Ge_3N_4 layer obtained by the N_2 ECR plasma treatment at RT associated with Ge evaporation from a Knudsen cell.

Si(001) substrate. The epitaxial character of the SiGe layer has been ascertained by different techniques whose results are presented elsewhere [15].

Immediately after the growth by coevaporation, such an SiGe layer is submitted, in situ, to NH_3 exposure at 600°C . As expected, the resulting nitrogen adsorption curve (Fig. 1) lies in between the zero-adsorption curve of pure Ge and the maximum one relevant to silicon. The examination of the Si 2p and Ge 3d peaks shows, similarly to the clean substrates, that only Si is nitrided (Fig. 2(c)), Ge remaining in its elemental form (Fig. 3(c)) in the alloy. Moreover, only one N1s core level component is detected presenting a binding energy near 398.0 eV corresponding to nitrogen in the nitride environment ($\text{N} \equiv \text{Si}_3$) as previously determined [13]. As a consequence, the elaboration of a SiGe nitrided layer, as a reaction-product by thermal interaction of NH_3 , both with Si and Ge is not possible. These results could have been anticipated thermodynamically, considering the strong differences between silicon and germanium nitride formation enthalpies (–177 kcal/mol and –15 kcal/

mol, respectively) [16] and Si–N and Ge–N bond strengths (105 and 65 kcal/mol, respectively) too detrimental to Si–N breaking and Ge–N formation. Moreover, we notice from the initial slope of the nitrogen uptake curve, that the initial sticking $S_0 = 0.03$, determined as before for pure Si and also averaged on the first 4 L, is now at least ten times lower, whereas the mean Ge contents in the layer ($x \sim 0.3$) would only contribute to lower the density of the reacting Si surface atoms by 30%. We explain this unexpected low sticking value by a Ge concentration gradient near the surface which is in favour of a Ge enrichment of the alloy overlayers and limits the Si reactivity. The fact that Ge could never be thermally nitrided with NH_3 necessitates the use of a plasma assisted method to realize simultaneous Si and Ge nitridation which will be the topic of the following section.

3.2. ECR N_2 plasma assisted nitridation

The ECR plasma source may be used in two ways, the one for surface nitridation of clean Si(001), Ge(001) or $\text{Si}_{1-x}\text{Ge}_x$ surfaces by surface exposure with the N_2 ECR plasma without any Si or Ge deposit, the other for similar plasma treatments associated with Si or Ge deposits which result in the growth of thicker Si or Ge nitride layers. In a previous report [8], we have detailed the saturating Si_3N_4 nitride growth by Si-surface ECR treatment. Depending on the exposure time, the operating N_2 pressure and the substrate temperature, Si_3N_4 thicknesses ranging from 10 to 20 Å have been obtained with a near-stoichiometric composition. In Fig. 2, selected Si 2p spectra are given comparing thermal nitridation of Si (Fig. 2(b)) and $\text{Si}_{1-x}\text{Ge}_x$ (Fig. 2(c)) alloy with RT N_2 plasma nitridation of $\text{Si}_{1-x}\text{Ge}_x$ (Fig. 2(d)). In the former cases, the nitrogen N 1s component is located at a binding energy near 398.0 eV representative of nitrogen threefold-bound to Si. In Fig. 3 we display some corresponding Ge 3d spectra when a Ge(001) substrate is similarly processed. The lack of any thermal nitridation of Ge is evidenced in Fig. 3(b). Nevertheless, similarly to silicon [8], the plasma treatments now result in efficient surface nitridation, both for the Ge substrate (Fig. 3(d)) and SiGe alloy (Fig. 3(e)). The N 1s

binding energy in the Ge nitride is very close to the corresponding value in Si nitride (398 eV) as $\text{Ge}_3 \equiv \text{N}$ and $\text{Si}_3 \equiv \text{N}$ bond contributions could not be resolved when these two forms coexist in SiGe. The Ge 3d binding energy shift in the nitrated component is reduced (2.0 eV) as compared to the 2.5 eV for Si 2p in agreement with the lower electronegativity difference of Ge and N with regard to Si and N. The growth of these Ge nitride layers, resulting from the plasma irradiation which is typically a non-thermal equilibrium process, may be explained by the ion bombardment effects (10–20 eV) forcing, already at RT, nitrogen atoms in the substrate. Contrarily to the thermal interaction of SiGe alloys with NH_3 leading to the nitridation of the sole Si part, Ge and Si could be nitrated simultaneously by N_2 plasma irradiation but nevertheless with a more pronounced inclination to form Si_3N_4 (Figs. 2(e) and 3(e)), as expected when thermodynamic arguments are considered. Indeed, relatively to the respective Ge and Si contents, the nitrated Ge 3d part is lower than the Si 2p one. The Ge 3d shifted component is rather smooth and non-resolved, implying a probable presence of many subnitrides and formation of intermediate SiGeN_x compounds where Ge is not systematically fourfold-bonded with nitrogen but forms mixed environments with Si and nitrogen ($\text{Ge}(\text{Si}_{4-x}\text{N}_x)$). Clearly favored Si nitridation, with rejection of the nitrogen from Ge to Si, is observed when the RT plasma processed SiGe alloy is subsequently annealed (Figs. 2(f) and 3(f)). The silicon nitride component of the Si 2p level increases with annealing temperature to the detriment of the vanishing Ge 3d shifted contribution. The N 1s line also becomes narrower. This behavior is thoroughly similar to the previously observed oxidation scheme of SiGe alloys [17] for which formation of SiO_2 is also thermodynamically favored with respect to GeO_2 . Nevertheless, in the latter case, GeO suboxides can already be formed thermally, whereas it is not possible to form the nitrated counterpart. In order to overcome the problem of too limited nitride thicknesses when the ECR plasma is only used for surface irradiation, Si and Ge must be supplied at the growing surface during the ECR plasma process by appropriate sources. Thus, we were able to grow thick Si and Ge nitride layers, asserted by the

disappearance of the substrate contribution in Figs. 2(g) and 3(g). A Ge evaporation source and a SiH_4 gas-supply have been used, respectively, in order to elaborate these Ge_3N_4 and Si_3N_4 layers.

4. Conclusion

To summarize, this report emphasizes the strict thermal nitridation selectivity between Ge and Si, caused by the NH_3 failure to nitride Ge and implying the indispensable use of plasma assisted methods in order to achieve simultaneous Ge and Si low-temperature nitridation of Si and Ge materials. This point is checked using an UHV-compatible ECR N_2 plasma source.

References

- [1] W. Ranke, X.H. Chen and E. Schröder-Bergen, *Vacuum* 41 (1990) 656.
- [2] A.G. Entringer, R. Shinar and H.R. Shanks, *Surf. Sci.* 234 (1990) 221.
- [3] X.H. Chen and W. Ranke, *Surf. Sci.* 262 (1992) 294.
- [4] X.H. Chen and W. Ranke, *Surf. Sci.* 264 (1992) 292.
- [5] W. Ranke, *J. Electron Spectroscopy Related Phenomena* 61 (1993) 231.
- [6] O. Vancauwenberghe, O.C. Hellman, N. Herbots and W.J. Tan, *Appl. Phys. Lett.* 59 (1991) 2031.
- [7] O.C. Hellmann, N. Herbots, O. Vancauwenberghe, R.J. Culbertson and W.J. Croft, *J. Vac. Sci. Technol. A* 10 (1992) 1631.
- [8] D. Bolmont, J.L. Bischoff, F. Lutz and L. Kubler, *Surf. Sci.* 269&270 (1992) 924.
- [9] S.M. Cohen, Y.L. Yang, E. Rouchouze, T. Jin and M.P. D'Evelyn, *J. Vac. Technol. A* 10 (1992) 2166.
- [10] E.K. Hlil, L. Kubler, J.L. Bischoff and D. Bolmont, *Phys. Rev. B* 35 (1987) 5913.
- [11] M.J. Dresser, P.A. Taylor, R.M. Wallace, W.J. Choyke and J.T. Yates, *Surf. Sci.* 218 (1989) 75.
- [12] J.L. Bischoff, F. Lutz, D. Bolmont and L. Kubler, *Surf. Sci. Lett.* 248 (1991) L240.
- [13] L. Kubler, F. Lutz, J.L. Bischoff and D. Bolmont, *Phys. Rev. B* 38 (1988) 13113.
- [14] G. Dufour, F. Rochet, H. Roulet and F. Sirotti, *Surf. Sci.* 304 (1994) 33.
- [15] D. Aubel, M. Diani, M. Stoehr, J.L. Bischoff, L. Kubler, D. Bolmont, B. Fraisse, R. Fourcade and D. Muller, *J. Phys. III (Paris)* 4 (1994) 733.
- [16] R.C. Weast, ed., *Handbook of Chemistry and Physics* (CRC, Boca Raton, FL, 1984).
- [17] K. Prabhakaran, T. Nishioka, K. Sumitomo, Y. Kobayashi and T. Ogino, *Appl. Phys. Lett.* 62 (1993) 864.



ELSEVIER

Journal of Non-Crystalline Solids 187 (1995) 324–328

JOURNAL OF
NON-CRYSTALLINE SOLIDS

Section 10. Silicon nitride, deposition

Influence of gas residence time on the deposition of nitrogen-rich amorphous silicon nitride

D.T. Murley^{a,*}, R.A.G. Gibson^a, B. Dunnett^a, A. Goodyear^b, I.D. French^b^a Amorphous Materials Group, A.P.E.M.E., University of Dundee, Dundee, Scotland DD1 4HN, UK^b Philips Research Laboratories, Cross Oak Lane, Redhill, Surrey RH1 5HA, UK

Abstract

The importance of gas phase reactions in plasmas containing ammonia and silane used to deposit amorphous silicon nitride was first demonstrated by Smith et al. in 1990 [J. Electrochem. Soc. 37 (1990) 614]. These workers concluded that, at high NH_3/SiH_4 ratios ($R = 25$) and rf power densities ($> 60 \text{ mW cm}^{-2}$), it was possible to fully aminate all of the available silane in the plasma to produce tri- and tetra-aminosilanes as the dominant plasma species. Nitride films grown from such an aminosilane plasma regime were nitrogen-rich and contained no measurable Si–H bonding (by FT-IR). In this work, optical emission spectroscopy (OES) and as-deposited film bonding data have been used to establish deposition conditions consistent with such an aminosilane plasma regime. The gas residence time, τ , was then varied by altering the total gas flow to the reactor while keeping pressure, NH_3/SiH_4 ratio, rf power and substrate temperatures constant. A gradual shift from an aminosilane to a silane dominated plasma, as the residence time is decreased, was observed (via OES of the SiH $A^2\Delta$ emission at 414.2 nm). In addition, at low τ , the re-appearance of Si–H bonding in the as-grown films indicates a significant decrease in the degree of amination of the available silane in the plasma, consistent with the OES results. Conversely, it is shown that full amination of the silane is possible even with a lower NH_3/SiH_4 ratio and rf power density than those used by Smith et al. [J. Electrochem. Soc. 37 (1990) 614], provided the residence time is sufficiently long.

1. Introduction

Amorphous silicon nitride thin films have been used extensively in the semiconductor industry for over two decades, an application of particular recent importance being as the gate insulator in amorphous silicon thin film transistors [1]. The

scientific study of this material prepared from mixed NH_3 and SiH_4 plasmas (PECVD) was first reported in 1977 [2], but it was only recently that a study of the plasma chemistry was undertaken by Smith and co-workers at Xerox [3]. They found that suitable manipulation of applied rf power and SiH_4 flow rate allowed operation in a regime where aminosilanes ($\text{Si}[\text{NH}_2]_{3,4}$) were the dominant plasma species. Nitride films grown from such a regime had no measurable Si–H bonding and exhibited superior dielectric properties when compared with ‘standard’ Si–H containing films [4]. A subsequent spectroscopic study of emission lines

* Corresponding author. Present address: Department of Electronic and Electrical Engineering, University of Surrey, Guildford, Surrey GU2 5XH, UK. Tel: +44-1483 300 800, ext. 2289. Telefax: +44-1483 34 139. E-mail: d.murley@ee.surrey.ac.uk.

in NH_3/SiH_4 plasmas led Hicks and Gibson [5] to conclude that their findings were best explained by a model similar to Smith's aminosilane formation model.

However, comparison of the results of Smith et al. [3] with the findings of Hicks and Gibson [5] reveals significant differences in the 'recipes' given for an aminosilane plasma regime. For example, Smith claimed a minimum power density of 60 mW cm^{-2} was needed with an NH_3/SiH_4 ratio of 25, whereas Hicks' work implied aminosilane formation was complete at an NH_3/SiH_4 ratio of 12 with a power density of only 20 mW cm^{-2} .

In this work we have identified the gas residence time, τ , as a possible cause of these differences since we estimate a $\tau \leq 1 \text{ s}$ for the Xerox work while in Hicks' experiments $\tau \geq 4.4 \text{ s}$. The gas residence time is a function of pressure, gas flow rate and reactor volume [6], hence knowledge and control of this variable should allow PECVD processes to be scaled more readily between different sized reactors.

2. Experiment

Details of the reactor and OES equipment were as reported previously [5]. Deposition details were as follows, $\text{NH}_3/\text{SiH}_4 = 12$, pressure 0.25 torr, rf power density 20 mW cm^{-2} and substrate temperature 330°C . The residence time, τ , was varied from 0.6 to 4.5 s by changing the total gas flow fed to the reactor from 62 to 8 sccm. Optical emissions from the plasma were collected as a function of wavelength. The SiH^* (414.2 nm) and NH_2^* (570.7 nm) emission intensities in particular were monitored as the residence time was altered.

Films were deposited on glass/Cr substrates for thickness determination via Dektak etch profiling and on high resistivity c-Si wafers (polished on both sides) to allow infra-red characterisation. These latter measurements were recorded on an ATI-Unicam Galaxy 7000 series spectrometer over the wave number range $400\text{--}4000 \text{ cm}^{-1}$.

3. Results

The optical emission in the wavelength range 400–430 nm from pure silane and pure ammonia

plasmas are shown in Figs. 1(a) and (b) respectively. The $\text{SiH A}^2\Delta$ emission band consists of several peaks, the most intense of which occurs at 414.2 nm. The emission from a pure NH_3 plasma is quite different, with five peaks from the N_2 second positive system dominating the spectrum. Fig. 1(c) shows the NH_2 emission at 570.7 nm which was also monitored in this work.

Fig. 2 shows the emission from mixed NH_3/SiH_4 plasmas for various gas residence times, τ . Comparison with Figs. 1(a) and (b) clearly reveals a smooth change from a SiH_4 dominated plasma at short τ to an NH_3 like plasma at the longest τ , with both SiH^* and N_2^* emission lines visible when $\tau = 1.5 \text{ s}$.

The variation of the SiH^* and NH_2^* intensities (integrated peak areas) for different residence times are presented in Fig. 3(a). The emission from SiH^* decreases with a well defined $1/\tau$ dependence up to $\tau = 3 \text{ s}$. However, at longer residence times the emission was not detected (see Fig. 2, $\tau = 3.5 \text{ s}$). The behaviour of the NH_2 radical emission at

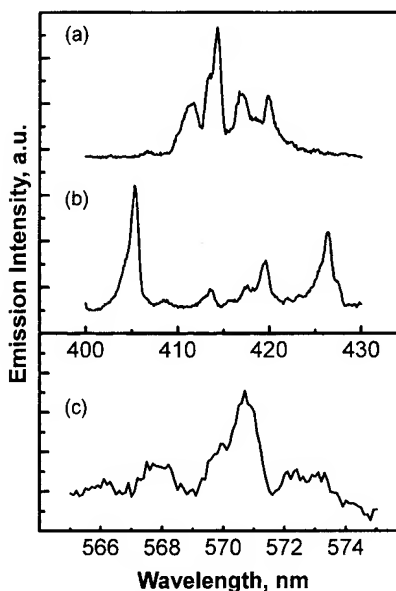


Fig. 1. Optical emissions from NH_3/SiH_4 plasmas. (a) $\text{SiH A}^2\Delta$ emission at 414.2 nm from a pure silane plasma. (b) Emissions from a pure ammonia plasma over wavelength range 400–430 nm. (c) NH_2 emission at 570.7 nm from a mixed NH_3/SiH_4 ($R = 12$) plasma.

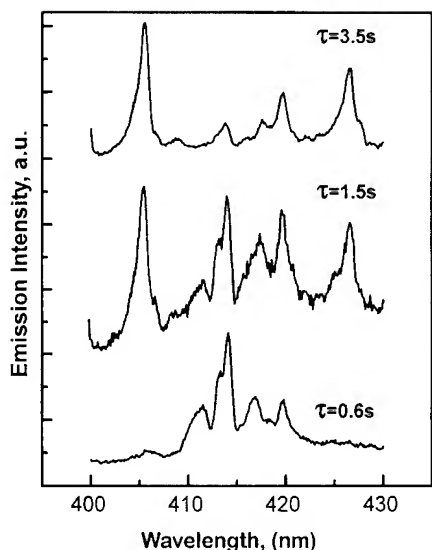


Fig. 2. Optical emissions from mixed NH_3/SiH_4 plasmas as a function of gas residence time. Note the change from a silane-like to an ammonia-like plasma as τ is increased.

570.7 nm was markedly different. The intensity at first rises as τ increases from 0.6 s to about 2 s. In the region $2\text{ s} < \tau < 3\text{ s}$ the intensity remains roughly constant before decreasing rapidly as τ is further increased beyond 3 s.

In Fig. 3(b) we present the NH_2^* emission intensity from a pure NH_3 plasma as a function of residence time. The emission increases steadily as τ is increased, in contrast to the behaviour found when silane is added (Fig. 3(a)). These results will be discussed in the next section.

Fig. 4 shows the infra-red spectra obtained from a- $\text{SiN}_x\text{:H}$ films prepared from the above plasmas. The influence of the gas residence time on the film hydrogen bonding is clearly visible. The N–H stretching vibration at 3350 cm^{-1} was found in all films while the Si–H vibration around 2175 cm^{-1} [7,8] was only found in films where $\tau < 3\text{ s}$. The ratio of hydrogen bonded to silicon to that of hydrogen bonded to nitrogen (Si–H/N–H) was calculated using the method of Lanford and Rand [9] and is plotted as a function of τ in Fig. 5. The Si–H concentration falls exponentially as τ increases up to about 3 s, beyond which only Si–N, N–H and H–N–H bonding configurations were observed, i.e. the bonding configurations in the films were

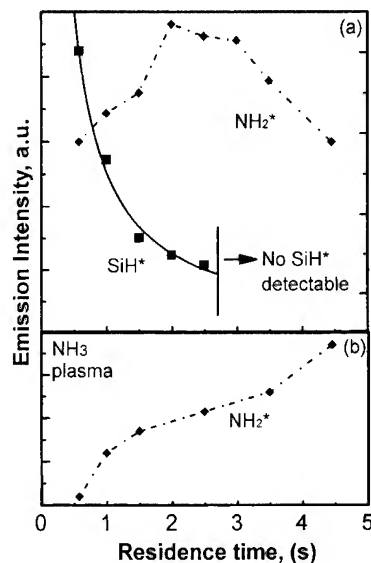


Fig. 3. Integrated emission intensities as a function of gas residence time. (a) SiH^* and NH_2^* from mixed NH_3/SiH_4 plasmas. (b) NH_2^* emission from pure NH_3 plasma. Lines are drawn as a guide to the eye except for the SiH^* data, which shows a fitted $1/\tau$ power regression line.

indicative of an ‘aminosilane like’ growth regime [3,5] for gas residence times greater than 3 s.

In summary, for residence times greater than 3 s, no SiH^* was detected in the plasma and no Si–H bonding was detected in the as-deposited nitride films. The NH_2^* emission rose, levelled and fell as τ increased.

4. Discussion

In order to interpret these results the mechanisms for SiH_n , NH_2 and aminosilane formation will be reviewed. The reactivity of NH_2 with SiH_4 is believed to be very low (see Kushner [10] and references therein) and so it seems reasonable to assume that any aminosilane formation occurs via $\text{NH}_2 + \text{SiH}_n$ ($n = 0$ to 3) reactions [5]. Therefore the silane and the ammonia must first dissociate in order to provide the precursors for aminosilane formation.

The SiH^* emission has been shown to be proportional to the SiH_4 molecular concentration [11,12] which varies inversely with the gas residence time in

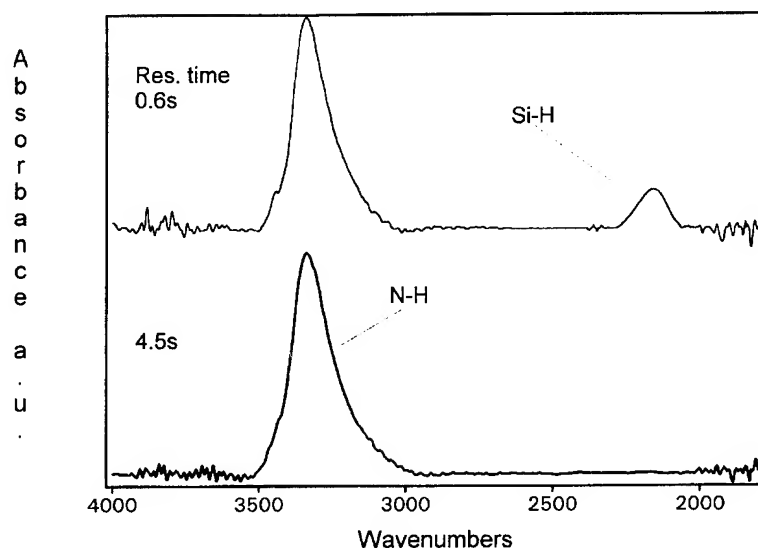


Fig. 4. Comparison of hydrogen bonding in a-SiN_x:H films grown from plasmas with $\tau \sim 0.6$ s and 4.5 s. Note the lack of Si-H bonding in the lower trace ($\tau = 4.5$ s), indicative of growth from an aminosilane plasma regime.

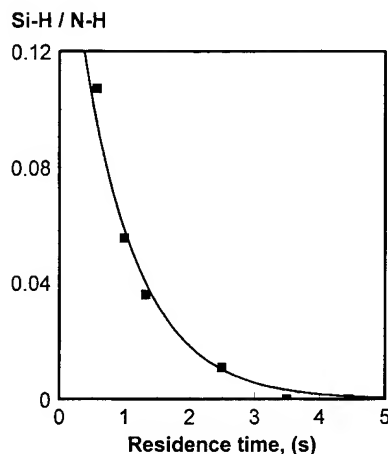


Fig. 5. Calculated Si-H/N-H bonding ratio for nitride films grown from plasmas with varying τ . The line drawn is an exponential fit to the data. Note the absence of Si-H bonding for $\tau > 3$ s.

these experiments. Therefore, the $1/\tau$ dependence found for $0.6 \text{ s} < \tau < 2.5 \text{ s}$ (Fig. 3(a)) can be explained as a result of SiH₄ depletion via electron impact dissociative excitation [11,12] and H abstraction [10]. Over the same τ interval, the NH₂^{*} emission, which mostly arises from electron impact excitation of NH₂, increases and then roughly

levels out, i.e. the NH₂ concentration increases and then remains constant. Gas phase reactions between the NH₂-SiH_n radicals start to become significant around $\tau = 2.5$ s, reducing the NH₂ concentration and thereby quenching the excited state. For $\tau > 3$ s, there are now enough NH₂ radicals available to fully aminate all of the available SiH_n in the reactor, and enough time for these reactions (producing tri- and tetra-aminosilane molecules) to occur. Hence the NH₂ emission is further quenched, an aminosilane plasma regime is established and films grown contain no Si-H bonding.

It is interesting to note that Kushner [10] has suggested that the rate limiting step in aminosilane formation is producing sufficient quantities of NH₂. The production of NH₂ from NH₃ releases H which can then in turn abstract H from SiH₄ leaving SiH₃. Reactions between NH₂ and SiH_n then liberate more H atoms which can produce more SiH_n radicals for amination, *provided the amino groups are available*. The results reported here are consistent with Kushner's suggestions. The longer an NH₃ molecule is resident in the plasma the more likely it is to dissociate, producing an NH₂. Therefore longer residence times produce higher densities of NH₂ radicals (Fig. 3(b)), allowing an aminosilane dominated plasma to be established.

These results also explain the differences between the findings of the Xerox group [3] and Hicks' reported work [5]. Hicks achieved an aminosilane plasma regime with low rf power and NH_3/SiH_4 ratio but a long residence time (4.5 s). Smith used a short residence time (~ 1 s) but compensated for this by increasing the rf power and using higher NH_3/SiH_4 ratios, thereby achieving the excess NH_2 concentration needed for full amination in the short time available for deposition.

By controlling the residence time we have produced Si–H free nitride on reactors varying in volume from 0.5 to 11 l with NH_3/SiH_4 ratios in the range 8–15 and power densities varying in 20–50 mW cm^{-2} . This knowledge has also suggested a hydrogen dilution study of the aminosilane plasma regime, the results of which will be published shortly.

5. Conclusions

The gas residence time has a direct effect on the NH_2 concentration in an NH_3/SiH_4 glow discharge, which in turn controls the extent to which any silane radicals are aminated. Hence operation in an aminosilane dominated plasma regime is pos-

sible at lower NH_3/SiH_4 ratio and rf power than those first reported [3], provided the gas residence time is sufficiently large.

One of the authors (D.T.M.) gratefully acknowledges the financial support of the E.P. S.R.C. (PhD CASE award number 91316321) and Philips Research Laboratories, Redhill, England.

References

- [1] P.G. LeComber, *J. Non-Cryst. Solids*, 115 (1) (1989).
- [2] D. Anderson and W.E. Spear, *Philos. Mag.* 35 (1) (1977).
- [3] D. Smith, A. Alimonda, C. Chen, S. Ready and B. Wacker, *J. Electrochem. Soc.* 37 (1990) 614.
- [4] D. Smith, A. Alimonda, C. Chen and H. Tuan, *J. Electron. Mater.* 19 (1) (1990) 19.
- [5] S. Hicks and R. Gibson, *J. Plas. Chem. Plas. Proc.* 11 (1991) 455.
- [6] B. Chapman, ed., *Glow Discharge Processes* (Wiley, New York, 1980).
- [7] Y. Masaki, R. Gibson and P. G. LeComber, *J. Appl. Phys.* 73 (1993) 10.
- [8] G. Lucovsky, *Solid State. Commun.* 29 (1979) 571.
- [9] W. Lanford and M. Rand, *J. Appl. Phys.* 49 (1978) 4.
- [10] M. Kushner, *J. Appl. Phys.* 71 (1992) 4173.
- [11] F. Kampas and R. Griffith, *J. Appl. Phys.* 52 (1981) 1285.
- [12] J. Perrin and E. Delafosse, *J. Phys. D13* (1980) 759.



ELSEVIER

Journal of Non-Crystalline Solids 187 (1995) 329–333

JOURNAL OF
NON-CRYSTALLINE SOLIDS

Influence of the deposition parameters on the bonding and optical properties of SiN_x ECR films

S. Garcia^{a,*}, J.M. Martin^a, I. Martil^a, M. Fernandez^b, E. Iborra^{*c}, G. Gonzalez-Diaz^a^a Departamento de Electricidad y Electronica, Facultad de Fisicas, Universidad Complutense, 28040 Madrid, Spain^b Instituto de Ciencia de Materiales, CSIC, Calle Serrano 144, 28006, Madrid, Spain^c Departamento de Tecnologia Electronica, ETSIT, UPM, 28040, Madrid, Spain

Abstract

SiN_x films are deposited at room temperature using an electron cyclotron resonance plasma system for different N_2/SiH_4 gases flow ratios (1.6–9) and microwave powers (50–200 W). The optical and bonding properties of the films and their N/Si ratio are studied as a function of the deposition parameters. Two operation modes of the ECR source, that we call mode A and mode B, resulting in films with similar properties are found. In fact, the films deposited at low powers (50–100 W) and high N_2/SiH_4 ratios (7.5–9) (mode A) have similar characteristics to those deposited at high powers (150–200 W) and low N_2/SiH_4 ratios (1.6–3). Near stoichiometric SiN_x films are obtained in both modes, at 50 W and N_2/SiH_4 ratio = 9 or at 150 W and N_2/SiH_4 ratio = 1.6. A threshold in the microwave power (150 W) for the effective formation of the SiN_x films is found. The two operation modes and the threshold are explained as a function of the strong dependence of the ion current density on the microwave power.

1. Introduction

Amorphous SiN_x films deposited by plasma methods are widely used as passivating layers, diffusion barriers, gate insulators in MISFET devices, etc. [1]. The SiN_x films obtained by these methods contain a large amount of hydrogen, and the irradiation damage produced by the energetic ions leads to the degradation of the integrated circuits performance.

In the last years, the electron cyclotron resonance (ECR) plasma method has been

extensively used to deposit SiN_x films. Films with low hydrogen content (below 15%) can be obtained at low substrate temperatures (room temperatures – 250°C) due to the high ionization efficiency of this plasma method [2]. Moreover, the substrate position (out of the plasma source) and the low energy of the ions (about 40 eV) prevent the irradiation damage of the growing film.

The large number of variables that the ECR-CVD technique offers (microwave power, magnetic field configuration, pressure, gases flow ratio, and even, the design of the plasma source), and the strong dependence of the plasma characteristics on these parameters [3,4] make necessary detailed studies devoted to the relation between deposition parameters and the properties

* Corresponding author. Tel: +34-1 394 4435. Telefax: +34-1 394 5196. E-mail: silvia@eucmvx.sim.ucm.es.

of the films obtained. In this paper, the influence of microwave power and gases flow ratio on the SiN_x properties is analyzed, and the equivalence between both parameters to change the film properties is deduced. Due to this equivalence, two operation modes of the ECR source resulting in films with stoichiometric properties are found. When the films are deposited in conditions out of these modes, the films are silicon or nitrogen rich, depending on the parameters used.

2. Experimental

The distributed ECR system employed is an Astex Compact-ECR source, that use N_2 , introduced at the top of the plasma source, and pure SiH_4 , introduced into the deposition chamber, as reactive gases. The substrate holder is floating and not intentionally heated. The films are deposited at constant pressure (0.6 mTorr) and flow rate (10.5 sccm), nitrogen plus silane, using different microwave powers (50–200 W) and N_2/SiH_4 gas flow ratios, R (1.6–9).

Transmittance and reflectance of the films are measured in the ultraviolet-visible-near infrared (UV-VIS-NIR) spectral range (200–2500 nm) to determine the refractive index (n) and the optical band gap, E_g . This characterization is performed on SiN_x films deposited on quartz substrates using a Perkin Elmer Lambda9 spectrophotometer. The refractive index and the absorption coefficient, α , are calculated from the rigorous expressions for the transmittance and reflectance [5], and E_g is deduced adjusting the absorption coefficient to the Tauc plot. The refractive index results presented in this work are the n values at 633 nm. Infrared absorption spectra of the SiN_x films, deposited on silicon substrates, are measured to investigate their bonding configuration, using a FTIR spectrometer (Nicolet 5PC FTIR) operating in the mid-infrared region (400–4000 cm^{-1}). The vibration modes that appear in the spectra are the conventional for SiN_x films, the N–H (3340 cm^{-1}), Si–H (2160 cm^{-1}) and Si–N (830 cm^{-1}) stretching modes.

Silicon substrates are also used for the compositional analysis of the films determined by Auger electron spectroscopy (AES). These analysis

are carried out in a JEOL system (JAMP-SIO) using an electron probe of 0.1 mm diameter at 5 kV. The samples are bombarded with 2 kV Ar^+ ions rastered across a surface area of 4 mm^2 in order to obtain results corresponding to the bulk region.

3. Results and discussion

The influence of both microwave power and R is shown in Fig. 1, where the variation of E_g as a function of the ratio R for different microwave powers is presented. E_g clearly increases with R (from 2.0 to 4.8 eV) for low microwave powers (50–100 W) whereas for higher microwave powers (150–200 W), E_g is less sensitive to R , with values between 3.7 and 5.2 eV. A similar behavior can be obtained as observed in Fig. 1 if the ratio R is exchanged by the microwave power [6]. That is, at low R (1.6–5), E_g strongly increases with the microwave power (from 2.0 to 5.2 eV) and, at high R (7.5–9), it scarcely increases from 3.8 to 5.1 eV. Moreover, if we see the variation ranges, we realize that they are similar at low powers or low R and, they are also similar for high powers or high R . From these results it can be concluded that microwave power and gases flow ratio affect the optical band gap in the same way.

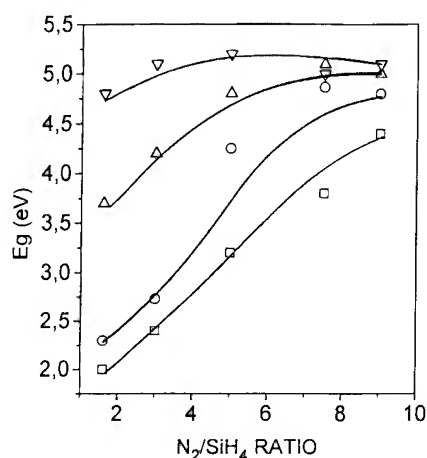


Fig. 1. E_g values as a function of the ratio R for different microwave powers: \square , 50 W; \circ , 100 W; Δ , 150 W; ∇ 200 W. Lines are drawn as guides for the eye.

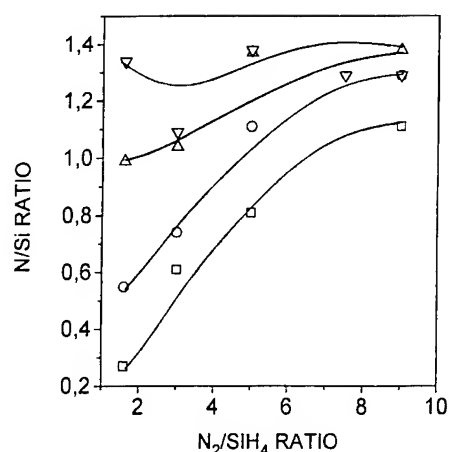


Fig. 2. N/Si ratio for films deposited at different microwave powers as a function of the N_2/SiH_4 ratio: \square , 50 W; \circ , 100 W; Δ , 150 W; ∇ , 200 W. Lines are drawn as guides for the eye.

To further confirm this equivalence between both parameters, Fig. 2 presents the N/Si ratio in the films as a function of R for different microwave powers. At low powers, the N/Si ratio increases with R (0.27–1.38), whereas the rise at high powers is small, between 1.11 and 1.38. Similar results are obtained when the microwave power and the ratio R are exchanged.

Due to this equivalence, the work conditions of the ECR source can be divided in four groups, resulting in films with different properties, as Table 1 shows. Two of these work conditions, the operation modes that we call mode A (50–100 W and $R = 7.5$ –9) and mode B (150–200 W and $R = 1.6$ –3), result in similar and, moreover, high quality SiN_x films; meanwhile the other two lead to

SiN_x films with properties far from the stoichiometric ones. In any case, the profiles of the Si–H and Si–N absorption peaks that appeared in the infrared spectra are Gaussian and not symmetric with respect to the maximum of the peak. Table 1 shows that the operation modes A and B are equivalent modes of the source resulting in films with similar properties, and that near stoichiometric SiN_x films ($n \sim 1.98$, $E_g \sim 4.7$ eV, N/Si ratio between 1.1 and 1.4, Si–H stretching mode around 2160 cm^{-1} and Si–N at 833 cm^{-1}) are obtained in both modes at specific combinations of power and ratio (50 W and $R = 9$, or 150 W and $R = 1.6$). Very different film properties are obtained when using deposition conditions out of the two operation modes. Silicon-rich films are obtained at low microwave powers and N_2/SiH_4 ratios; meanwhile higher powers and R result in nitrogen-rich or oxygen-contaminated films, probably due to the sputtering of the quartz liner located into the source. The study to determine the oxygen contamination or not is currently in progress as either the excess of nitrogen or the presence of oxygen result in films with roughly similar properties [7].

The variation of the film properties with the N_2/SiH_4 ratio is similar to that found in PCVD systems [8], where E_g and the N/Si ratio increase with the nitrogen flow, corresponding to a higher incorporation of nitrogen atoms into the silicon matrix. However, the strong variation of the SiN_x films properties with the power described above is only found in ECR deposition methods [2], being not so clear in other PCVD systems [9,10]. In these

Table 1
 SiN_x films grouped in different zones determined by the microwave power and the N_2/SiH_4 ratio

	n	E_g (eV)	[N]/[Si] ratio	Si–N position (cm^{-1})	Si–H position (cm^{-1})	FWHM Si–N (cm^{-1})	FWHM Si–H (cm^{-1})
Mode A ^a	1.80–1.93	3.8–4.9	1.11–1.29	825–841	2191	206	120–135
Mode A ^b	1.81–1.84	3.7–5.1	0.99–1.34	831–856	2176–2191	207	111–141
Si Rich ^c	2.21–2.71	2.0–2.7	0.27–0.74	818–825	2106–2137	220	156
N Rich or O Contam ^d	1.72–1.76	5.1	1.38	879–887	2214–2191	226	99

^aMode A, 50–100 W and $R = 7.5$ –9; ^bMode B, 150–200 W and $R = 1.6$ –3; ^cSi-rich films, 50–100 W and $R = 1.6$ –3; ^dN-rich films or O-contaminated, 150–200 W and $R = 7.5$ –9.

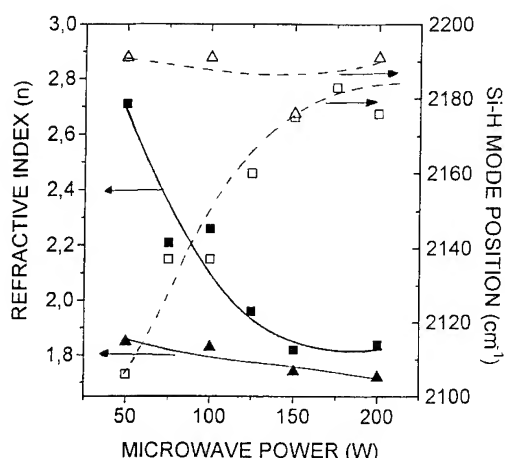


Fig. 3. Refractive index (solid symbols) and Si-H mode position (open symbols) for films deposited at $R = 1.6$ (squares) and $R = 7.5$ (triangles) as a function of the microwave power. Lines are drawn as guides for the eye.

systems, the N_2 (or NH_3) to SiH_4 gas flow ratio is used as the main parameter to change the film composition, whereas the results presented in this work seem to indicate that, in ECR systems, the microwave power can change the composition in a similar way. The very different influence that the power has in ECR-CVD methods respect to rf-plasma methods can be explained by the strong dependence of the ion current density of the plasma on the microwave power. Published results on ECR plasmas [3,4] indicate that the ion current density is constant at low microwave powers, sharply increasing when the power overcomes a value that depends on the design of the source [4] and on the gas flow rate supporting the plasma [3]. This sharp increase could explain the strong dependence of the film properties on the microwave power.

To confirm this, Fig. 3 presents the refractive index and the Si-H vibration mode position as a function of the microwave power for different R values. The figure shows that, for power values below 150 W, n and the Si-H mode position clearly depend on R , and near stoichiometric films are only obtained at high ratios R . Beyond 150 W, these properties are independent of this parameter and high quality SiN_x films are obtained at any R . These results indicate that there is a threshold in the power needed for the efficient formation of the

SiN_x films, related to the sharp increase of the ion current density. Not enough work (like optical diagnosis of the plasma) has been done yet to determine if the ions or the radicals are responsible for the film growth in ECR systems. The results about the film properties presented in this work together with the results published on the dependence of the ion current density of the plasma on the microwave power [3,4] seems to indicate that below a threshold value (150 W for the system used here) not enough ionized N species are presented in the plasma to react with the Si (or SiH_n , $n = 1, 2, 3$) species or to break the SiH_4 molecules, resulting in silicon rich films except if high ratios R are used for the depositions. Beyond 150 W, the number of ionized N species increases and reaches a saturation value [3], with N atoms reacting with the Si ones at any ratio. The threshold value depends on the characteristics of the deposition system that affect the ion current density, as the design of the source, the microwave mode used, the magnetic field profile and the gas flow rate used to sustain the plasma. This fact could explain the different behaviors found in the literature on SiN_x deposition by ECR. In fact, Popov et al. [11] obtain films with properties that, at 200 W, clearly vary with the ratio R , meanwhile the results obtained at the same power by Manabe and Mitsuyu [12] scarcely vary with R . This strong influence of the power on the plasma characteristics probably explain the differences with the rf-PCVD methods, where the power is matched to the plasma using inductive or capacitive coupling and not a resonant cavity, which results in different efficiency of the power absorption, better in ECR systems.

4. Conclusions

The relation between the deposition conditions and the SiN_x film properties obtained using an ECR-CVD system has been studied as a function of the microwave power and the N_2/SiH_4 gases flow ratio. Two operation modes of the plasma source (low powers together with high ratios or high powers together with low ratios), that reveal the equivalence between the microwave power and

the N_2/SiH_4 ratio to obtain films with similar properties have been found. A threshold in the power (150 W) to obtain SiN_x films with properties near the stoichiometric ones has been deduced. The two operation modes and the power threshold have been explained as a function of the strong dependence that the ion current density has on the microwave power. The threshold value depends on the different parameters that influence the plasma density, as the design of the source, gas flow rate, microwaves modes and magnetic field profile.

This work has been partially supported by the CAM and the Spanish Government (CICYT) through grants TIC 92-1214-E and TIC 93-0175.

References

- [1] S.K. Ghandhi, *VLSI Fabrication Principles*, 2nd Ed. (Wiley, New York, 1994) ch. 8.
- [2] T. Hirao, K. Setsune, M. Kitagawa, T. Kamada, K. Wasa, K. Tsukamoto and T. Izumi, *Jpn. J. Appl. Phys.* 27 (1988) 30.
- [3] E. Ghanbari, I. Trigor and T. Nguyen, *J. Vac. Sci. Technol.* A7 (1989) 918.
- [4] S. Samukawa, S. Mori and M. Sasami, *J. Vac. Sci. Technol.* A9 (1991) 85.
- [5] J.L. Hernandez-Rojas, M.L. Lucia, I. Martil, G. Gonzalez-Diaz, J. Santamaria and F. Sanchez Quesada, *Appl. Optics* 31 (1992) 1606.
- [6] S. Garcia, J.M. Martin, I. Martil and G. Gonzalez-Diaz, *Vacuum* 45 (1994) 1027.
- [7] J. Robertson, *Philos. Mag.* B69 (1994) 307.
- [8] A.D. Stewart and D.I. Jones, *Philos. Mag.* B57 (1988) 431.
- [9] D.V. Tsu and G. Lucovsky, *J. Vac. Sci. Technol.* A4 (1986) 481.
- [10] S. Hasegawa, M. Matsuda and Y. Kurata, *Appl. Phys. Lett.* 58 (1991) 741.
- [11] O.A. Popov, S.Y. Shapoval and M.D. Yoder, *J. Vac. Sci. Technol.* A10 (1992) 3055.
- [12] Y. Manabe and T. Mitsuyu, *J. Appl. Phys.* 66 (1989) 2475.



Room-temperature deposition of SiN_x using ECR-PECVD for III/V semiconductor microelectronics in lift-off technique

A. Wiersch^a, C. Heedt^a, S. Schneiders^a, R. Tilders^a, F. Buchali^b, W. Kuebart^b, W. Prost^{a,*},
F.J. Tegude^a

^a Solid State Electronics Department, Sonderforschungsbereich 254, Gerhard-Mercator-University,

Kommandantenstr. 60, 47057 Duisburg, Germany,

^b Alcatel SEL, Stuttgart, Germany

Abstract

Room-temperature deposition of silicon-nitride on InP-substrates for electronic applications is reported. A plasma enhanced chemical vapour deposition apparatus equipped with an electron cyclotron resonance source was used. Molecular nitrogen and silane diluted in helium are chosen as precursors. The dielectric films are defined by means of optical lithography and lift-off technique. C - f measurements reveal a dielectric constant of about 9 and a dissipation factor $\tan \delta = 3 \times 10^{-1}$ ($f = 10$ kHz) while the breakdown field is 2 MV/cm ($I = 250 \mu\text{A}/\text{mm}^2$). A strong improvement of the dissipation factor by more than one order of magnitude under both electrical and thermal stress, respectively, has been observed which could not be related to a variation of Si-H or N-H bonds measured by Fourier transformed infrared spectroscopy. The influence of silicon-nitride deposition on the electrical properties of an InAlAs/InGaAs heterostructure field-effect transistor is investigated. The most significant change is found as an improvement of gate leakage current by 90% while other dc- and rf-properties remain unchanged.

1. Introduction

Silicon nitride (SiN_x) deposited by means of plasma-enhanced (PE) chemical vapour deposition (CVD) is widely used in III/V-microelectronics. Deposited at a substrate temperature of 250–400°C with silane (SiH_4) and ammonia (NH_3) as precursors, it exhibits excellent dielectric properties such as low conductivity, high breakdown field strength,

E_D , and low dissipation factor, $\tan \delta$. In microelectronics fabrication, the lift-off technique based on photo-resist structures provides reliable, damage-free high resolution processing. However all films to be processed by lift-off technique have to be deposited at a substrate temperature below 120°C. For the deposition of SiN_x at these low temperatures, electron cyclotron resonance PECVD with N_2 as nitrogen source is favourable [1]. This way the disadvantage of high hydrogen content in the films using NH_3 and a low deposition rate is avoided [3] because of the extremely high electron energy. In addition, the very dense electron cyclotron

* Corresponding author. Tel: +49-203 379 2989. Telefax: +49-203 379 3400.

resonance (ECR) plasma can be spatially separated from the sample allowing a high flow of ionized particles with a low kinetic energy to the sample ($I = 5 \text{ mA/cm}^2$, $E = 20\text{--}30 \text{ eV}$ [2]). This technique has been adopted for III/V microelectronics. Room-temperature ECR PECVD films exhibit excellent I–V characteristics [4] and the process has proven capability for passivation of InP based devices [5] and surfaces with SiO_x [6]. In this work, we present process optimization of room-temperature deposited ECR-PECVD SiN_x which can be successfully processed by lift-off technique. It is shown that this material has a dielectric quality comparable to material deposited at higher temperatures ($T \geq 250^\circ\text{C}$) and that it can be used for metal–insulator–metal (MIM) capacitors. In addition, ECR PECVD deposited SiN_x is well suited for a damage-free deposition on InAlAs/InGaAs/InP heterostructure field-effect transistor as shown by improved dc- and unchanged rf-performance.

2. Experimental procedure

For deposition of the silicon nitride layers, a PlasmaLab System 90 ECR-PECVD from Oxford Instruments has been used. No heating was applied to the system throughout this study. A detailed setup of the system is shown in Fig. 1. Molecular nitrogen (N_2) and silane (SiH_4) diluted in helium (5%/95%) are used. The magnetic field of the ECR region is provided by two electro magnets using a current of 180 and 120 A for the top and the bottom magnet, respectively. The vacuum system consists of a roots/rotary combination and a turbo-molecular pump providing a base pressure better than $1 \times 10^{-7} \text{ mbar}$. Pressure during process is controlled with the use of a baratron and a pressure controller (APC) in the range of 1 up to 100 mTorr. The process pressure studied is 5–10 mTorr. MIM capacitors have been fabricated with optical lithography. The capacitance has been measured using a Hewlett Packard 4275 A Multi-Frequency LCR

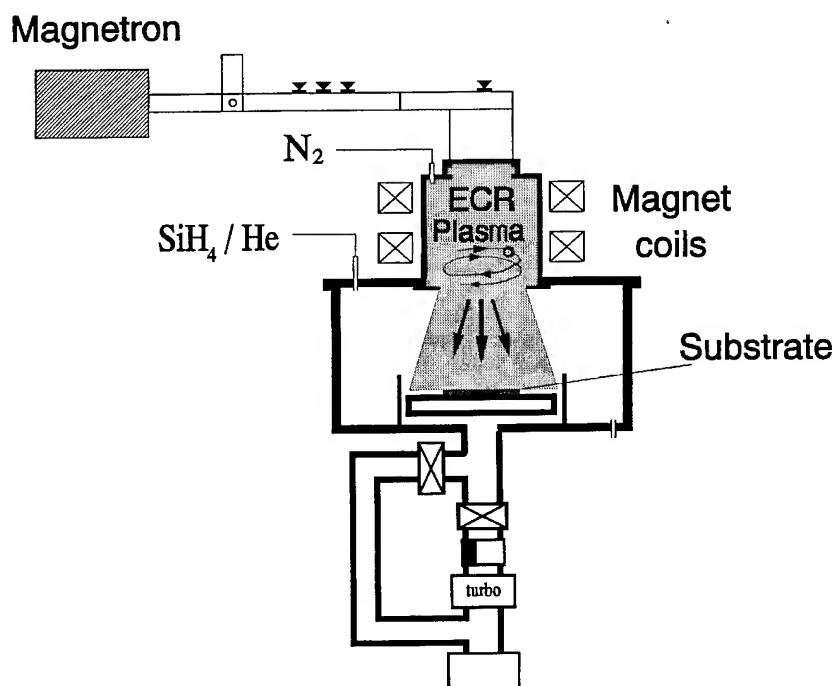


Fig. 1. Schematic description of the ECR-PECVD system for SiN_x deposition at room temperature.

bridge in the parallel equivalent circuit mode for the complex resistance. With the measured capacitance and conductance the relative dielectric constant, ϵ_r , and the dielectric dissipation factor, $\tan \delta$, have been deduced. The bond characteristic of the SiN_x was deduced by absorption measurements in the infrared wavelength range using a Biorad FTIR. Peaks in the absorption characteristic can be correlated with bonds in the layer, while the substrate was subtracted.

3. Results and discussion

In the first step, the applicability of the ECR-PECVD deposited SiN_x layer for lift-off has been evaluated. A photo resist structure with a negative undercut has been prepared using an image reversal resist. This resist lip (cf. Fig. 2) is known to be very sensitive to enhanced temperatures. After deposition of 200 nm SiN_x , no damage can be detected. The variation of process parameters has been checked over a wide range and resist damage oc-

curs only at very high power levels of more than 450 W. Despite the widely isotropic deposition, a reliable lift-off process can be obtained in boiling acetone without any mechanical aid. However this process becomes critical if very small areas of resist are covered within large areas where the SiN_x layer is directly deposited on the substrate.

The composition of the SiN_x layers can be estimated from the refractive index, n [7]. In Fig. 3 the dependence of the refractive index deduced from ellipsometry measurements is given as a function of the gas flow ratio silane to nitrogen. A SiH_4/N_2 ratio close to unity corresponds to $n \approx 2$, indicating normally stoichiometric Si_3N_4 . However we found that a ratio SiH_4/N_2 of 0.2–0.4 ($n \approx 1.7$) is recommended for improved dielectric properties attributed to reduced hydrogen incorporation.

Metal-insulator-metal capacitors with an area of $2 \times 10^{-4} \text{ cm}^2$ have been produced using the lift-off technique for patterning the silicon nitride films. I–V measurements of all devices revealed a breakdown field strength above 1 MV/cm and a standard value of 2 MV/cm. The dielectric properties were

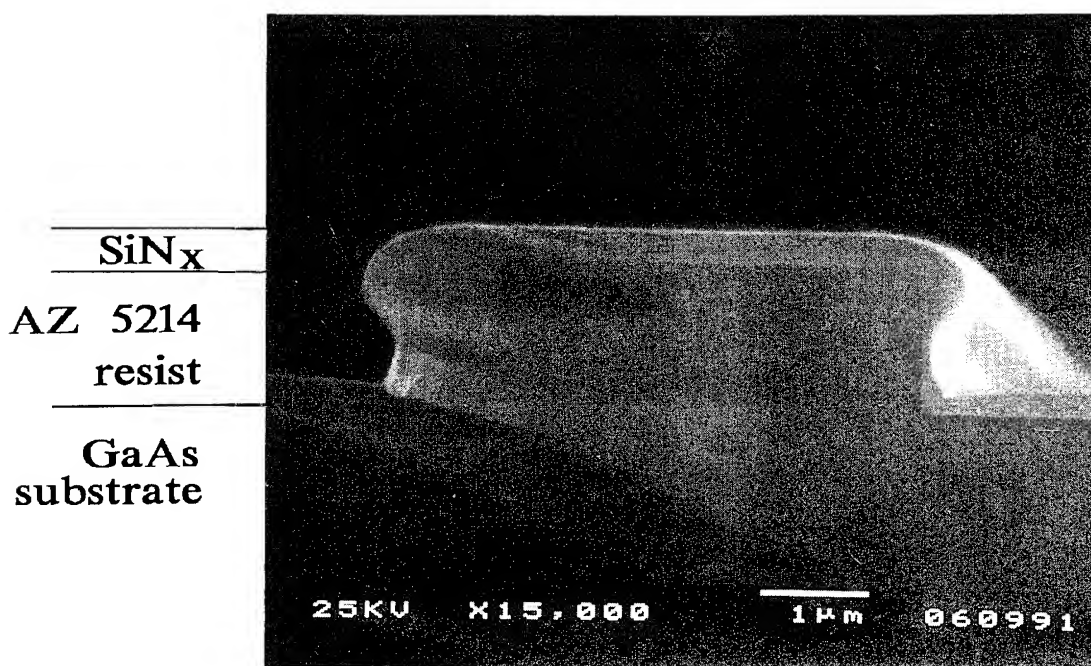


Fig. 2. SEM picture of a photo resist edge with undercut after deposition of 200 nm SiN_x at a thermocouple temperature of 40°C. ($\text{SiH}_4/\text{N}_2 = 0.4$, $p = 6 \text{ mTorr}$, $P = 250 \text{ W}$.)

analyzed by means of C - f measurements without any dc bias. For the investigated deposition conditions, the silane to nitrogen ratio has been varied from 0.2 to 0.9 resulting in dielectric constants between $\epsilon_r \approx 7$ (nitrogen rich) to $\epsilon_r \approx 12.5$ (silicon rich). A low dielectric dissipation factor is obtained for high nitrogen flow only. Silicon-rich samples, however, exhibit a high dissipation, $\tan \delta$. Both electrical and temperature stress was studied with respect to the dissipation factor. In Fig. 4 the dissipation factor is plotted as a function of frequency for an unstressed device (first measurement, curve (a)). At 10 kHz, $\tan \delta$ was measured to 1.3×10^{-1} while at 1 MHz the dissipation factor drops down to 4.1×10^{-2} . The second measurement revealed a drastic reduction of $\tan \delta$ at low frequencies which is in agreement with the observation of Jeon et al. who found a strongly reduced leakage current in the second I-V measurement at low DC bias [4]. It is worth noting that in our case no dc bias has been applied and the ac voltage is below 100 mV in all cases. A thermal annealing of MIM test structures was carried out at 200°C for 2.5 h using the same wafer as for curve (a) and the result is shown in curve (b) of Fig. 4. Even electrically unstressed devices exhibit a strong reduction of the dissipation factor comparable to the data obtained by electrical stress. The quality of room-temperature-deposited silicon nitride layers and the influence of thermal stress was further studied by FTIR measurements. Results of our analysis are shown in Fig. 5 where the absorbance of the different layers are

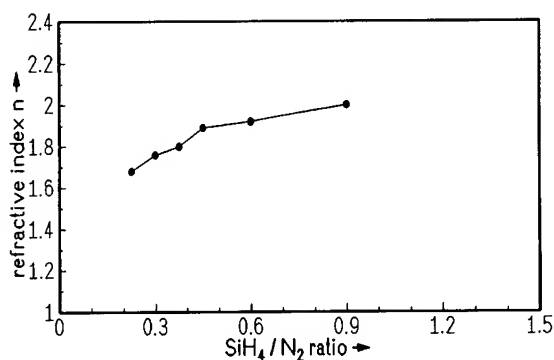


Fig. 3. The refractive index of RT deposited SiN_x as a function of silane to nitrogen ratio flow (SiH_4/N_2).

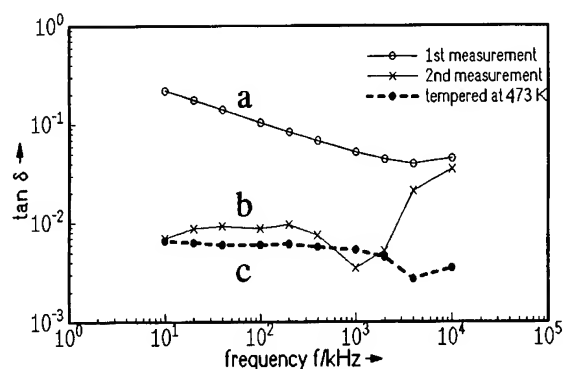


Fig. 4. Stress investigation of the dielectric dissipation factor, $\tan \delta$ as a function of frequency for differently stressed MIM capacitors fabricated with room-temperature-deposited SiN_x ($\text{SiH}_4/\text{N}_2 = 0.4$, dc bias = 0V): (a) without stress, first measurement; (b) second measurement of the same device; (c) first measurement of a device stressed at 200°C for 2.5 h under nitrogen ambient.

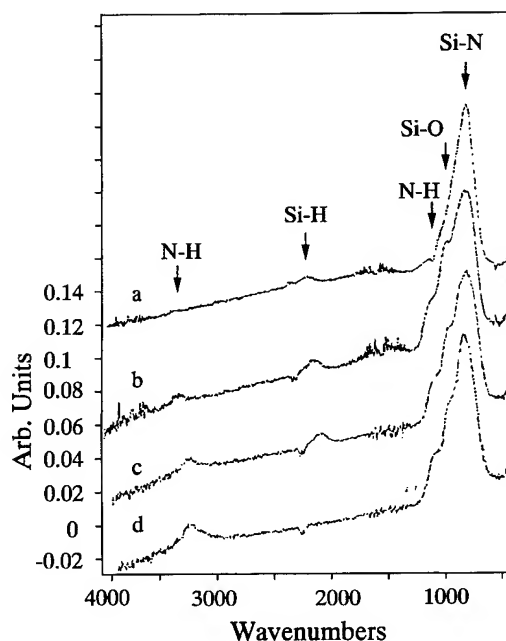


Fig. 5. Infrared absorption spectra of different SiN_x layers deposited on boron doped Si-wafers. The absorption of the substrate is subtracted. (a) Reference sample deposited by means of a standard PECVD system at a substrate temperature of 250°C. (b) Low nitrogen content ($\text{SiH}_4/\text{N}_2 = 0.2$, $n = 1.7$) RT deposited SiN_x . (c) Same sample shown in (b) but post annealed at 250°C in nitrogen ambient for 30 min. (d) High nitrogen content ($\text{SiH}_4/\text{N}_2 = 0.9$, $n = 2.0$) RT deposited SiN_x .

plotted as a function of the wave number. For comparison, a layer deposited at 250°C in a standard PECVD system with parallel plate electrode configuration without ECR was measured (curve (a) in Fig. 5). According to the analysis in Refs. [8–11], absorbance peaks are correlated with specific bonds in the material. All samples exhibit the main absorbance peak due to Si–N bonds. Samples deposited at room temperature show a weak peak or shoulder at the high wave number side of the main Si–N peak. This feature is attributed to a Si–O_x bond. Oxygen may originate from residual water in the system because no additional heating is applied to the sample prior to deposition and no load-lock is used. The second shoulder is correlated with a N–H bond and is somewhat higher than in the case of a higher deposition rate. The influence of deposition conditions can be associated to the occurrence of the Si–H bonds at a wave number of about 2200, only. In the nitrogen-rich sample (curve (a) in Fig. 5) with a silane to nitrogen ratio of about 0.2, this peak is absent, while in a silane-rich-deposited layer (curve (b) in Fig. 5) with a silane to nitrogen ratio of about 0.9, this peak can easily be seen. Even after thermal stress ($T = 250^\circ\text{C}$, 30 min) the Si–H bond related peak is not changed (curve (c)). Finally an increased N–H-bond-related peak at a wave number of about 3300 can be seen for the nitrogen rich deposited layer (curve (d)). In summary, changing the deposition conditions from silane rich (b, c) to nitrogen rich (d) clearly results in a decreased Si–H bond related peak towards an

enhanced N–H bond related peak. The Si–H-bond-related peak cannot be reduced by thermal stress in the investigated range but by means of a higher nitrogen flow. In addition, we have observed that the deposition rate does not increase with higher nitrogen flow. Hence we can assume that nitrogen replaces hydrogen in the layer.

Finally the influence of room temperature-deposited SiN_x on the electrical performance of InAlAs/InGaAs/InP heterostructure field effect transistors (HFET) grown by MBE has been investigated. This material system is of major interest for future high frequency and opto-electronic applications. A 300 nm passivation layer has been deposited using nitrogen rich conditions ($\text{SiH}_4/\text{N}_2 = 0.4$, $p = 10$ mTorr, $P = 185$ W) on top of fully processed transistors. The thermocouple temperature never exceeded 25°C. The bond pads of the devices were covered with photo resist which was removed after deposition using the lift-off technique. MBE growth and device fabrication procedure is described elsewhere [12]. Table 1 shows the results of the statistical dc characterization on 25 devices across a quarter of a two inch wafer prior to and after deposition of the SiN_x layer. With respect to the threshold voltage, V_T , output conductance, g_d , and drain current, I_D , no degradation was observed. A reduction of the maximum output conductance of 6.3% was found. The strongest improvement has been achieved for the gate-leakage current of the transistors in agreement with [5]. A reduction from $I_G = 28$ $\mu\text{A}/\text{mm}$ prior to SiN_x

Table 1

Dc-parameter deviations of 25 InGaAs/InAlAs HFETs before and after room-temperature deposition of 300 nm SiN_x passivation layer

InGaAs/InAlAs HFET $L_g = 1$ μm , $W_g = 50$ μm (25 devices)	Prior to passivation	After deposition of 300 nm SiN _x	Deviation (%)
Threshold voltage V_T (mS/mm) : $V_{DS} = 2.5$ V	−0.667	−0.657	+1.5
Transconductance $g_{m,\text{max}}$ (mS/mm) :	355	333	−6.3
Drain current, I_D (mA/mm) : $V_{GS} = 0$ V, $V_{DS} = 2.5$ V	151	146	−3.3
Output conductance, g_d (mS/mm) : $V_{GS} = 0$ V, $V_{DS} = 2.5$ V	10.2	0.2	0
Gate current, I_G ($\mu\text{A}/\text{mm}$) : $V_{GS} = 0$ V, $V_{DS} = 2.5$ V	−29.5	2.54	−91

deposition down to $I_G = 2.54 \mu\text{A}/\text{mm}$ after SiN_x deposition can be observed. Following the explanation from Trew and Mishra [13], the silicon nitride layer could provide a sufficiently high trap concentration at the gate edge to accommodate injected electrons from the gate contact. This leads to a reduced electric field and thereby reduced gate-leakage current. The SiN_x deposition shows no impact on the RF performance. Devices with a gate length of about $1 \mu\text{m}$ exhibit a transit frequency (current gain $h_{21} = 1$) of $f_T \approx 40 \text{ GHz}$ and a maximum frequency of oscillation (unilateral gain $GU = 1$) $f_{\text{max}} \approx 115 \text{ GHz}$ before and after deposition.

4. Conclusion

SiN_x deposited by ECR-PECVD at room-temperature is shown to be suitable for lift-off processing. The layers exhibit quality comparable to silicon nitride deposited at enhanced temperatures. We have found that nitrogen rich deposition conditions resulting in non-stoichiometric SiN_x with a refractive index of 1.7 are highly recommended for a low dissipation factor and reduced hydrogen incorporation in the material. Both thermal and electric stress, respectively, improves the dissipation factor of room temperature ECR-PECVD deposited silicon nitride. Finally the deposition of SiN_x on InAlAs/InGaAs/InP HFET does degrades

neither dc nor rf performance but improves the gate leakage current.

References

- [1] S. Matsuo and I. Kiachi, in: Proc. Symp. on Very-Large-Scale Integration Science and Technology (Electrochemical Society, Punington, NJ, 1982).
- [2] S. Matsuo, in: Handbook of Thin-Film Deposition Processes and Techniques, ed. K. Schuegraf (Noyes, Park Ridge, NJ, 1988) ch. 5.
- [3] H. Dun, P. Pan, F.R. White and R.W. Douse, J. Electrochem. Soc. 128 (1981) 1555.
- [4] Y.C. Jeon, H.Y. Lee and S.K. Joo, J. Appl. Phys. 75 (1991) 979.
- [5] D.J. Newson, A.J. Murrell, R.C. Grimwood and I.D. Henning, Electron. Lett. 29 (1993) 472.
- [6] Y.Z. Hu, M. Li, Y. Wang, E.A. Irene, M. Rowe and H.C. Casey, Appl. Phys. Lett. 63 (1993) 1113.
- [7] W.A.P. Claasen, W.G.J.N. Valkenburg, M.F.C. Willemsen, and W.M. c.d. Wiggert, J. Electrochem. Soc. 130 (1983) 2419.
- [8] S.E. Hicks and R.A.G. Gibson, Plasma Chem. Plasma Proc. 11 (1991) 455.
- [9] M. Boudreau, M. Boumerzoug, R.V. Kruselecky, P. Mascher, P.E. Jessop and D.A. Thompson, Can. J. Phys. 70 (1992) 1404.
- [10] P.G. Pai, S.S. Chao and Y. Takagi, J. Vac. Sci. Technol. A4 (1986) 689.
- [11] A.S. Harrus and E.P. van de Ven, Semicond. Int. (May 1990) 124.
- [12] C. Heedt, P. Gottwald, F. Buchali, W. Prost, H. Künzel, F.J. Tegude, presented at 4th InP and Related Materials Conference, Apr. 1992, Newport, RI, IEEE Catalog # 92CH3104-7, WD 4, p. 238.
- [13] R. Trew and U.K. Mishra, IEEE Electron Dev. Lett. 12 (1991) 524.



ELSEVIER

Journal of Non-Crystalline Solids 187 (1995) 340–346

JOURNAL OF
NON-CRYSTALLINE SOLIDS

Control of bonded-hydrogen in plasma-deposited silicon nitrides: Combined plasma-assisted deposition and rapid thermal annealing for the formation of device-quality nitride layers for applications in multilayer dielectrics

Z. Lu, S.S. He, Y. Ma, G. Lucovsky*

Departments of Physics, Materials Science and Engineering, and Electrical and Computer Engineering, North Carolina State University, Raleigh, NC, 27695-8202, USA

Abstract

This paper discusses silicon nitride layers for applications in silicon device technologies, and in particular deposited nitride films for gate multi-layer dielectrics for (i) amorphous and microcrystalline silicon (a-Si and μ c-Si, respectively) thin film transistors (TFTs), and (ii) crystalline silicon (c-Si) MOS capacitors and field effect transistors (FETs). A low temperature (300°C) remote plasma-enhanced chemical-vapor deposition process was used to form the silicon nitride films. A materials issue impacting on the targeted applications is the stability of bonded-hydrogen atoms in Si–H and SiN–H bonding groups at the respective TFT and FET processing temperatures.

1. Introduction

One of the important material constituents of thin film transistor (TFT) and field effect transistor (FET) devices is the gate dielectric. Thermally grown silicon dioxide (SiO₂) has been the standard for crystalline silicon FETs, whereas deposited silicon oxides and nitrides have been used in a-Si and μ c-Si TFTs. The use of thermally grown SiO₂ in c-Si FETs derives from device-quality electrical properties that are at least part a consequence of the high temperature (~ 850 – 1000°C) oxidation

process. These include (i) a high breakdown strength ($> 10 \text{ MV cm}^{-1}$), (ii) a low density of fixed and mobile charge in the oxide layer ($\leq 10^{11} \text{ cm}^{-2}$), and (iii) a low density of defects at Si–SiO₂ interface ($\sim 10^{10} \text{ cm}^{-2} \text{ eV}^{-1}$ at mid-gap). As dielectric thicknesses shrink below 10 nm to remain in step with the lateral sub-micron dimensions ($\sim 0.25 \mu\text{m}$ and less) required for ULSI circuits, the time-temperature budgets available for gate oxide formation place severe limitations on processing windows for thermal and rapid thermal oxidation (RTO). In addition, the eventual requirement for ultra-thin oxides ~ 3 – 5 nm thick makes it difficult to find processing conditions that will prevent dopant-atom transport from poly-Si gate electrodes to the FET channel regions. These factors

* Corresponding author. Tel: +1-919 515 3301, Telefax: +1-919 515 7331.

have stimulated research in (i) alternative low temperature processing techniques with reduced thermal budgets, and (ii) alternative materials for gate dielectrics which offer a more effective barrier to dopant-atom diffusion than SiO_2 .

Our research efforts which initially focused on deposited oxides have now been extended to include nitride materials with improved diffusion barrier properties. These include homogeneous silicon oxynitride alloys [1], as well as composite dielectrics with oxide (O) and nitride (N) layers as in ONO structures [2]. This development of low temperature/low thermal budget processing for the N-containing materials has evolved from a two-step 300°C process used for Si– SiO_2 structures [3]. In this approach, Si– SiO_2 interface formation, and oxide deposition are controlled separately in a process that includes (i) a pre-deposition plasma-assisted oxidation, followed by (ii) a remote plasma-enhanced chemical-vapor deposition (RPECVD) oxide deposition. The same type of two-step approach to interface formation by a plasma-assisted oxidation, and deposition by RPECVD has been applied to gate dielectrics with oxynitrides [1], and ONO sandwich structures [2]. A post-deposition rapid thermal anneal (RTA) for 30 s at 900°C was required to promote device-quality electrical properties when the N-containing dielectrics were used in MOS devices. However, TFTs with state of the art electrical performance were routinely fabricated using the same nitride and oxide films without the need for the high temperature RTA [4,5]. These differences in processing requirements derive from materials issues unique to the nitrides and oxynitrides that distinguish their bonding properties, and electrical performance from deposited oxides. The special features are (i) increases in the defect state density at the Si-dielectric interface that derive from N-atom migration to that interface, and (ii) increases in the fixed charge and trap state densities within the bulk dielectrics that are associated with intrinsic bonding defects involving the N-atoms. The focus of this paper is on multilayer dielectrics comprised of O and N layers, and we address the issue of why different combinations of plasma and rapid thermal processing are needed for the TFT, and the MOS/FET applications. However, although the

primary focus is on nitrides in ONO structures, similar considerations also apply to the oxynitride alloys [1].

2. Deposition and characterization of nitride films

Nitride films were deposited by an RPECVD process described in detail elsewhere [2,6]. Films were deposited at 300°C , initially on substrates for characterizations: (i) c-Si for (a) on-line Auger electron spectroscopy (AES), and (b) off-line infra-red (IR) absorption; and (ii) fused silica for optical absorption. Source gases for the deposition were silane (SiH_4) and ammonia (NH_3). Performance of nitrides as gate dielectrics was found to vary significantly with the flow ratio (R) of NH_3 to SiH_4 [1,6], which in turn had a strong influence on the local bonding.

Figs. 1(a) and (b) summarize the results of AES and IR studies, respectively, for depositions in which NH_3 and SiH_4 were injected downstream from a He plasma [2]. Similar results have also been obtained when the NH_3 is injected upstream and subjected to direct plasma excitation; however the flow ratios that mark demarcation points for the different local bonding arrangements are shifted. Returning to Figs. 1(a) and (b), as R is increased there are systematic changes (i) in the Si_{LVV} feature of the AES spectra indicative of a transition from a dominance of Si–Si bonding (~ 91 eV) to Si–N bonding (~ 83 eV); and (ii) in the IR spectra indicative of a transition from a dominance of Si–H to SiN–H bonding. The flow ratio at which these changes occur is about the same for both of these changes. The use of nitride films in composite dielectrics for TFTs and FETs must meet two material constraints: R must be (i) sufficiently high so there is no AES detectable Si–Si bonding, and (ii) not so high that the SiN–H concentration becomes too large. For downstream deposited nitrides this range is $\sim 7 < R < \sim 10$ [2,4–6]. Note that for this range of R there is IR absorption in both Si–H and SiN–H modes, but the absorption in the SiN–H modes dominates. In previous studies, we did not explain the observation that even though similar ratios of R were used to optimize electrical properties of c-Si-MOS devices with ONO dielectrics and

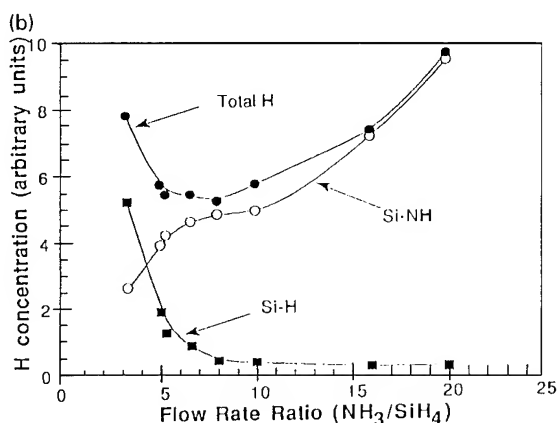
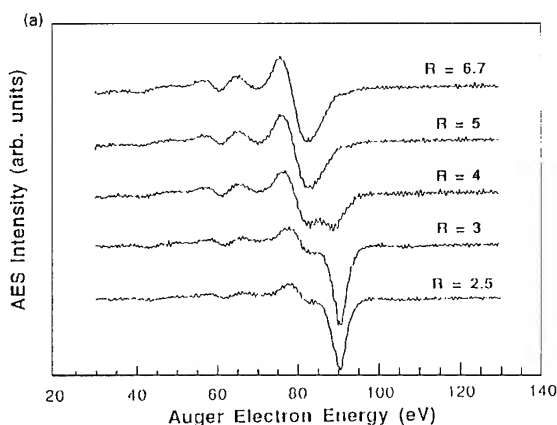


Fig. 1. (a) AES spectra in the $\text{Si}_{L,VV}$ region as a function of the flow ratio (R) of HN_3 to SiH_4 ; (b) reduced IR data for total bonded-H, Si-H and SiN-H as a function of R . Lines are drawn as guides for the eye.

TFTs with ON structures, the c-Si devices required an RTA step at 900°C [1,2] whereas the as-deposited TFT devices at 300°C did not [3–5]. The results presented below identify the origin of this significant difference in device processing requirements.

Studies of IR absorption, ($A(\text{Si-H})$ and $A(\text{SiN-H})$), as a function of post-deposition isochronal (30s) RTAs indicate that the bonded-H concentrations in the Si-H and SiN-H configurations are each reduced as the temperature is increased (see Fig. 2). There are at most relatively small

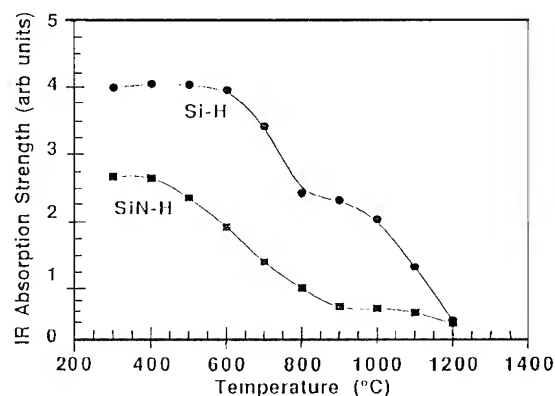


Fig. 2. Hydrogen evolution as a function of temperature for $R = 2$ sample. Lines are drawn as guides for the eye.

changes in $A(\text{Si-H})$ and $A(\text{Si-NH})$ for temperatures below about 400°C , whereas there are significant and similar decreases in both $A(\text{Si-H})$ and $A(\text{SiN-H})$ in the temperature range between $\sim 450^\circ\text{C}$ and 1000°C . The Si-H and N-H bond energies are very different, ~ 3.35 eV and 4.05 eV, respectively, and also sufficient large, so that (i) significant H-evolution at that temperatures as low as 500°C ($kT \sim 0.07$ eV) is at first surprising, and in addition (ii) similar release rates of H from both Si-H and SiN-H are not anticipated. This low temperature release of H is similar to what has been reported for H-evolution for hydrogenated amorphous Si where the microscopic basis has not as yet been unambiguously determined.

3. Device properties

3.1. Thin film transistors

Studies of (i) the effective channel mobility, and (ii) the threshold voltage of bottom gate a-Si TFTs as a function of R indicate that TFT performance is optimized for $R \sim 10$. This is at a flow ratio at which Si-Si bonds cannot be detected by AES, and where absorption in Si-H and Si-NH bonds is detected, but where the Si-NH is stronger than the Si-H [4]. The TFT devices were fabricated using a process that included: (i) sequential RPECVD depositions of SiO_2 , Si_3N_4 :H, a-Si:H, and n^+ a-Si (or n^+ $\mu\text{c-Si}$)

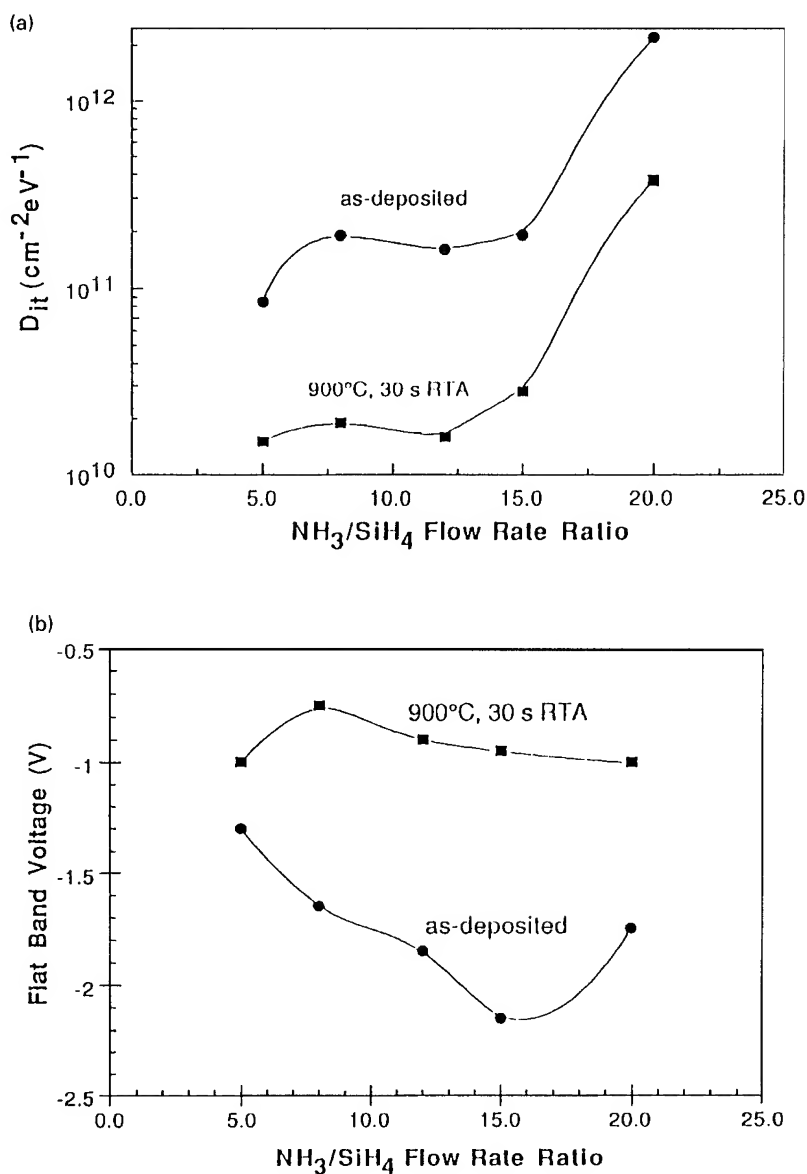


Fig. 3. Electrical test data on MOS capacitors as a function of R for as-deposited (300°C, and 400°C) PMA, and RTA ONO sandwiches: (a) D_{it} , and (b) V_{fb} . Lines are drawn as guides for the eye.

onto a glass substrate with pre-deposited W-gate electrodes; (ii) deposition of Al onto the n^+ regions and for the source and drain contacts; (iii) selective etching to define the TFT geometry; and (iv) formation of a thin Si oxynitride passivation layer over the exposed back of the channel [4]. Note that: (i)

all processing steps were done at temperatures $\leq 300^\circ\text{C}$; (ii) the back channel passivation step was essential to maximize the drive current, and thereby yield effective channel mobilities of $\sim 1.5 \text{ cm}^2 \text{ V}^{-1} \text{ s}^{-1}$ [4]; and (iii) the threshold voltage was reduced to values between 1 and 2 V by

substituting $n^+ \mu\text{-Si}$ for $n^+ \text{a-Si}$ source and drain contacts. The properties of the a-Si:H TFTs are at, or above the current manufacturing state of the art. Further increases in the drive current and channel mobility to $\sim 6.5 \text{ cm}^2 \text{ V}^{-1} \text{ s}^{-1}$ have been achieved by using B-compensated $\mu\text{-Si}$ [5], but as with poly-Si TFTs, at the expense of a reduced $I_{\text{on}}/I_{\text{off}}$ ratio.

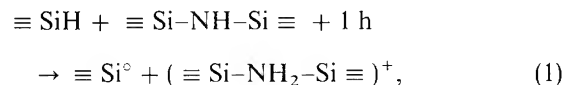
3.2. MOS capacitors

Figs. 3(a) and (b), respectively, display flatband voltage (V_{fb}) and interface trap (D_{it}) data for MIS capacitors with ONO dielectrics (all layers $\sim 5 \text{ nm}$ thick). The as-deposited values are higher than for MOS capacitors with deposited oxide dielectrics even though both types of devices have been subjected to the same processing temperatures: 300°C for the oxidation and deposition steps, and 400°C for the post metallization anneals (PMA). However, after a 900°C , 30 s anneal in Ar with a partial pressure of O_2 sufficient to prevent formation of SiO at the Si-SiO_2 interface, (i) the values of D_{it} approach those of devices with oxide dielectrics, whilst (ii) the values of Q_{f} are still about a factor of 2–3 higher. The best electrical performance after the RTAs is for values of R of ~ 8 – 10 , essentially the same as for optimized performance in the a-Si TFTs.

4. Discussion

The differences in the processing requirements for optimized electrical performance are explained by combining the temperature dependent IR absorption in Fig. 2 with the device results. This assumes that release of bonded-H at temperatures between 400 and 800°C results in defect generation via the creation of both Si and N-atom dangling bond defects, and that these defects are annealed at higher temperatures $\sim 900^\circ\text{C}$. In this model, the achievement of optimized performance in the TFTs with processing temperatures no higher than about 300°C derives from the IR results which indicate that 300°C is well below the threshold for detectable H-atom release. In contrast, the MOS structures with Al electrodes require a PMA at

~ 400 – 450°C , a temperature range in which there is measurable release of H-atoms from both the Si-H and SiN-H sites. The fact that IR absorptions for both groups decrease together suggests the release of this H is a cooperative phenomena. Fig. 4 indicates a bonding model that shows how this defect generation/annealing process can proceed. Fig. 4(a) indicates a portion of the nitride film that contains near-neighbor Si-H and SiN-H groups prior to thermally generated H-release. The proximity of these groups is consistent with constraints imposed by network topology. For Fig. 4(b), the temperature has been raised sufficiently (e.g., to 500 – 800°C) to promote H-atom release from both sites creating two dangling bonds [7], and a H_2 molecule that evolves out of the material. For Fig. 4(c), the temperature has been raised further (e.g., to 900°C) to a regime where atomic relaxations occur and the near-neighbor dangling bonds combine to produce an Si-N bond. This aspect of the 900°C RTA then eliminates defects induced by H-evolution during the PMA step. Other studies we have performed indicate that it is likely that there is a precursor state to the cooperative release, and this is shown in Fig. 4(d), where an intimate valence alternation pair is created via the trapping of a hole, following a mechanism that has been proposed for the Staebler–Wronski effect in a-Si , N:H alloys prepared from NH_3 [8]. The model in Ref. [8] is based on the fact that near-neighbor Si-H and SiN-H groups are linked through the H-bonding interaction as shown in Fig. 4(d). Trapping of a thermally or optically generated hole at this center will produce a metastable defect pair as shown in Fig. 4(e), and as represented by the reaction equation presented below:



where $\equiv \text{Si}^\bullet$ denotes a Si-atom dangling bond. In a-Si , N:H this reaction can be reversed by trapping of a thermally generated electron during a low temperature anneal at 175 – 200°C ; the activation energy for this process is ~ 0.85 – 0.9 eV consistent with a mid-gap Fermi level position in the light-soaked a-Si:H . In contrast, for the hydrogenated silicon nitride films, heating the material to

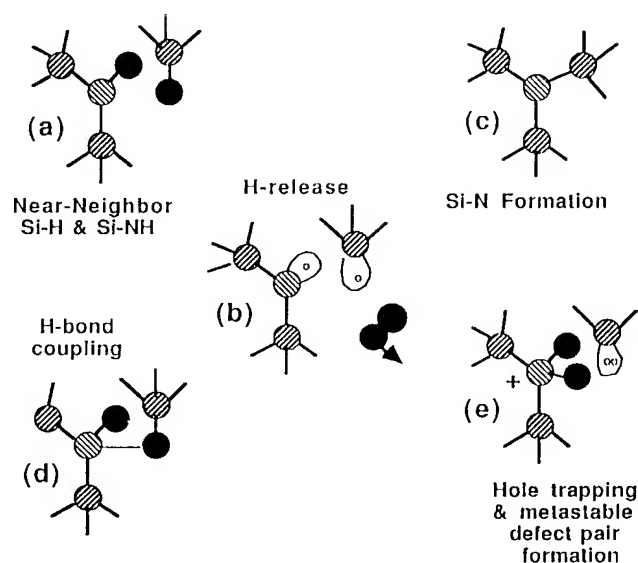
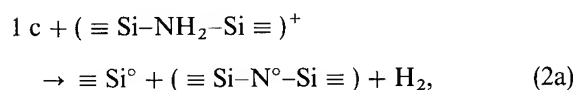
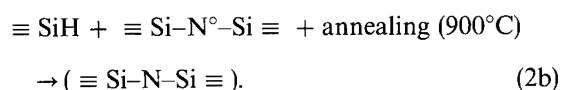


Fig. 4. Changes in local bonding arrangements for H_2 evolution from near-neighbor Si-H and SiN-H groups in hydrogenated silicon nitride films.

temperatures in excess of 400°C is sufficient to release H_2 molecules, where the release process may also involve trapping of a thermally generated electron at the $(\equiv \text{Si}-\text{NH}_2-\text{Si} \equiv)^+$ center, followed by creation and evolution of H_2 . A mechanism whereby hole trapping initiates the formation of a metastable center, and trapping of an electron plays a role in the release of bonded-H would then account for the energetic balance necessary for the H-evolution process to proceed. Eqs. (2a) and (2b) indicate the final two steps of the proposed process:



and



Studies of nitride films prepared from deuterated ammonia (ND_3) are currently underway. Nitride films prepared from ND_3 and SiH_4 contain only

SiN-D groups, but both Si-H and Si-D groups, so that evolution of HD species from films prepared in this way would reinforce the proposed model.

5. Conclusions

Device quality, deposited silicon nitride films can be prepared by low-temperature/low thermal budget plasma assisted processing. This research has identified several processing constraints that impact on film quality, and are different for different applications. Films deposited at 300°C by RPECVD contain bonded hydrogen in both Si-H and SiN-H groups, and depending on the source gas ratio, R , of NH_3 to SiH_4 , may also contain Si-Si bonding. In order to minimize defects, it is necessary to minimize Si-Si bonding; this requires values of R greater than about 7. In addition, it is necessary to minimize the total bonded hydrogen concentration; this restricts R to being less than about 10. Films deposited at 300°C can be employed in device structures, provided that post-deposition processing does not exceed the deposition

temperature. This has been demonstrated in TFT devices with amorphous and microcrystalline channel regions. If post-deposition temperatures exceed the deposition temperature of 300°C, as for example in PMA steps used in MOS devices, then hydrogen is released from the Si–H and SiN–H groups of the nitride. If the post-deposition processing is restricted to temperatures below 900°C, then this evolution of hydrogen results in defect generation in the bulk of the nitride film, and at nitrated Si–SiO₂ interfaces. On the other hand, if a relatively low thermal budget RTA is employed, e.g., 900°C for 30 s, then Si–N bonds can reform after release of hydrogen, and defect densities comparable to those of thermal oxides can be obtained both in the bulk nitride films, and at the nitrated Si–SiO₂ interfaces. Experimental results on hydrogen evolution from the nitride films suggests that the H-release, and bond-healing mechanisms involve near-neighbor bonded-H groups, which are coupled together via hydrogen-bond interactions.

This work is in part supported by ONR, the NSF and SEMATECH.

References

- [1] Yi Ma and G. Lucovsky, *J. Vac. Sci. Technol.* B12 (1994) 2504.
- [2] Yi Ma, T. Yasuda, S. Habermehl and G. Lucovsky, *J. Vac. Sci. Technol.* B11 (1993) 1533.
- [3] T. Yasuda, Yi Ma, S. Habermehl and G. Lucovsky, *Appl. Phys. Lett.* 60 (1992) 434.
- [4] S.S. He, D.J. Stephens, R.W. Raymaker and G. Lucovsky, *Mater. Res. Soc. Symp. Proc.* 284 (1993) 413.
- [5] G. Lucovsky, S.S. He, M.J. Williams and D.J. Stephens, *Microelectron. Eng.* 25 (1994) 329.
- [6] G. Lucovsky, Y. Ma, S.S. He, T. Yasuda, D.J. Stephens and S. Habermehl, *Mater. Res. Soc. Symp. Proc.* 284 (1993) 34.
- [7] J. Robertson, *Philos. Mag.* B63 (1991) 47.
- [8] G. Lucovsky, M.J. Williams, S.M. Cho, Z. Jing and J.L. Whitten, *Mater. Res. Soc. Spring MRS* 1994, in press.



ELSEVIER

Journal of Non-Crystalline Solids 187 (1995) 347–352

JOURNAL OF
NON-CRYSTALLINE SOLIDS

Plasma-enhanced silicon nitride deposition for thin film transistor applications

L.J. Quinn*, S.J.N. Mitchell, B.M. Armstrong, H.S. Gamble

Northern Ireland Semiconductor Research Centre, Department of Electrical and Electronic Engineering, The Queen's University of Belfast, Ashby Building, Stranmillis Road, Belfast, BT9 5AH, UK

Abstract

The characteristics of silicon nitride films deposited in a multiprocess reactor have been investigated to determine the most suitable layers for dielectric and passivation applications. Process parameters such as rf power, temperature and gas flow ratios have been varied to control the stoichiometry of the films, and associated parameters such as refractive index, BHF etch rate, relative permittivity and breakdown field. Using these results, silicon nitride films with favourable characteristics have been deposited and used successfully in thin film transistors.

1. Introduction

Plasma-enhanced silicon nitride (SiNH) layers have a number of important applications in the semiconductor industry. They are used extensively for the passivation of devices, i.e., protection of completed devices from a hostile environment, and as a dielectric in non-volatile memory elements in MNOS devices or high efficiency inversion layer solar cells [1–4]. Excellent step coverage, good adhesion to underlying layers and a diffusion barrier to water vapour and sodium ions, make SiNH ideal for encapsulating devices after the final metalisation layer. It also gives particle and scratch protection to devices during mounting operations. For the production of thin film transistors (TFTs)

on glass, SiNH can be used for two purposes. Glass plates provide a low cost substrate on which TFTs may be fabricated for LCD panels [5]. However, glass contains many alkali impurities detrimental to device performance. SiNH can be deposited over the glass substrate to prevent diffusion of the impurities into the active layers. In addition it has been shown that good quality SiNH can be deposited and used as a reliable gate dielectric in a TFT [6]. This paper will include the characterisation of SiNH layers deposited in a multiprocessing environment and their application to TFTs.

2. Experimental details

Deposition experiments were performed in a custom-built multiprocess reactor which has been described previously [7]. Silicon substrates ([100] 2–5 Ω cm, n-type) were given a $\text{H}_2\text{O}_2/\text{H}_2\text{SO}_4$ chemical

* Corresponding author. Tel: +44-232 245 133. Telefax: +44-232 667 023. E-mail: l.quinn@ee.qub.ac.uk.

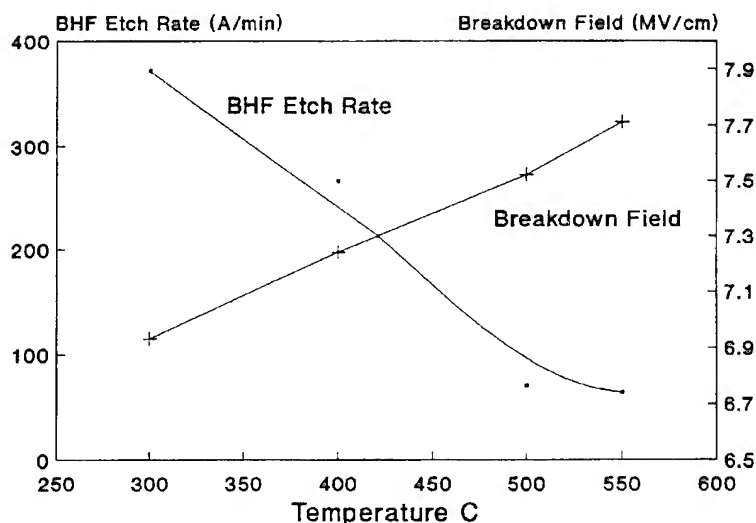


Fig. 1. Breakdown field and BHF etch rate versus temperature at a rf power of 100 W and NH_3/SiH_4 ratio of 8:1. The lines are drawn as guides for the eye.

clean, 10:1 HF dip, DI rinse and spin dry before loading into the reactor. SiNH was deposited by ionising silane (diluted in nitrogen) and ammonia in a glow discharge created by an inductively coupled antenna. The maximum rf power was 1 kW, at a frequency of 13.56 MHz. The process conditions investigated were reactive gas flow ratio (NH_3/SiH_4 varied 8:1–2:1), temperature (range 300–550°C), and rf power (100–200 W). In each experiment a SiNH layer of approximately 1000 Å was deposited. For each process condition, deposition rate, BHF (7%) etch rate and refractive index were measured. In addition MNS capacitors were fabricated and used to obtain further information about the layers, namely the relative permittivity and the breakdown field.

3. Results and discussion

It is widely known that the hydrogen content in a SiNH layer increases dramatically when deposited at temperatures below 300°C [8]. This temperature has traditionally been used to deposit SiNH for passivation applications where the layer does not experience further high temperature processing. It has been shown that hydrogen which leaves the

SiNH layer during subsequent high temperature processing can be detrimental to device performance [9]. Fig. 1 shows the breakdown voltage and BHF etch rate of SiNH layers deposited in the temperature range 300–550°C. The reduction in BHF etch rate indicates a decreased oxygen content and higher density. The hydrogen content is also lower in films deposited at higher temperatures. It is also favourable to work at these relatively high temperatures for SiNH deposition since this minimises time between SiNH deposition and polysilicon gate deposition for in situ sequential processing in TFT fabrication. The benefits of the multiprocess are that the SiNH layer is never exposed to atmosphere and interface contamination is minimised. For these reasons all subsequent SiNH depositions were performed at 550°C. The dependence of refractive index and BHF etch rate on the active gas flow ratio at different rf powers is given in Figs. 2 and 3. For an increase in rf power the refractive index decreases, this can be interpreted as a reduction in the Si/N ratio in the film. As the NH_3/SiH_4 ratio is decreased the films become increasingly silicon rich which results in a higher refractive index. This is correlated with a lower BHF etch rate. SiNH films with a higher silicon content are more suited to passivation

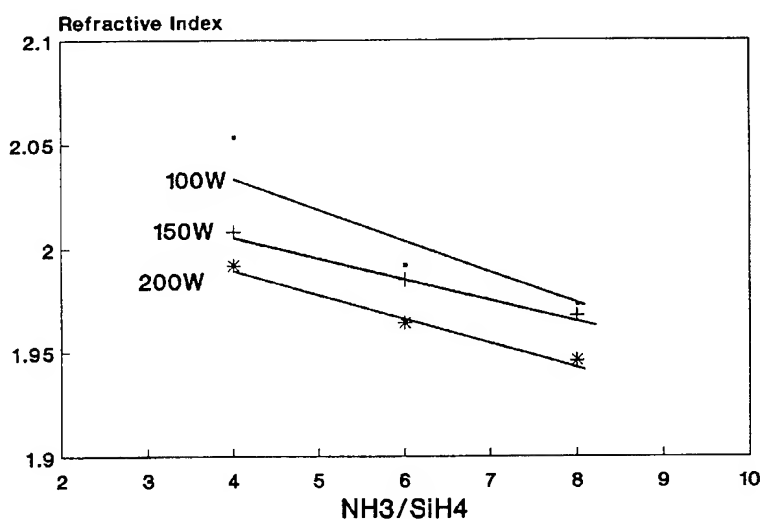


Fig. 2. Refractive index versus gas flow ratio at three levels of rf power and a temperature of 550°C. The lines are drawn as guides for the eye.

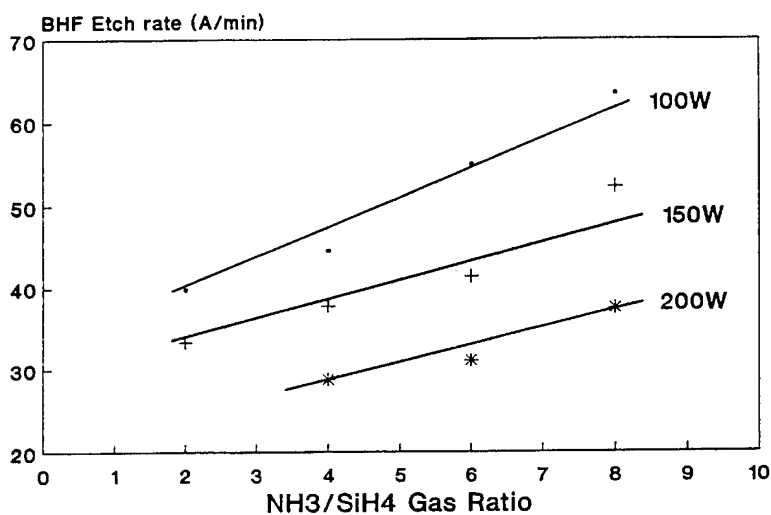


Fig. 3. BHF etch rate versus gas flow ratio at three levels of rf power and a temperature of 550°C. The lines are drawn as guides for the eye.

applications since these layers have a high density but have a relatively low breakdown field.

Mean electron energy or electron temperature in the plasma is much higher than the substrate temperature so it may be concluded that the electron impact dissociation rate is nearly independent of the substrate temperature. In fact the plasma

enhanced deposition rate was found to have a low thermal activation energy of 0.01 eV.

From Figs. 4 and 5 it can be seen that the SiNH deposition rate depends only slightly on gas phase composition and total pressure. Slight changes in the deposition rate for different gas compositions can be explained by the small variations in the

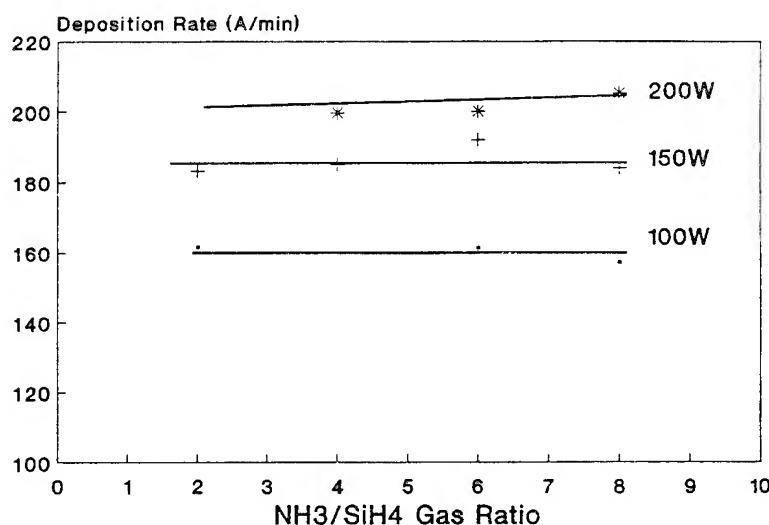


Fig. 4. Deposition rate versus NH₃/SiH₄ gas flow ratio at a temperature of 550°C. The lines are drawn as guides for the eye.

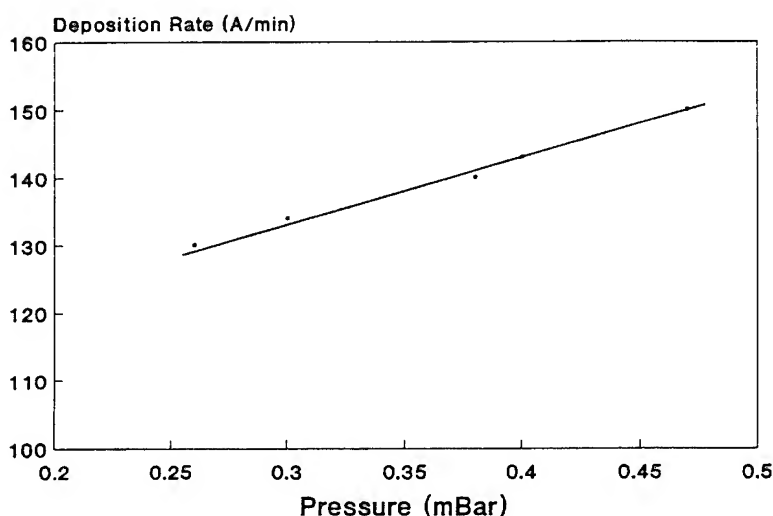


Fig. 5. Deposition rate versus pressure at a rf power of 100 W and temperature of 550°C. The line is drawn as a guide for the eye.

cross-section for ionisation and dissociation for the different gases since mean electron energy is also dependent on composition. Pressure has little effect on the deposition rate since at lower pressures the mean electron energy is higher but ionisation and dissociation are proportional to total pressure [10]. The relative permittivity, ϵ_r , is also dependent on the process conditions and results indicate that

ϵ_r increases as the NH₃/SiH₄ gas flow ratio increases, which suggests a reduction in the Si/N ratio giving a nitrogen rich film. The breakdown field follows a similar pattern with the most insulating layer, i.e., highest breakdown field, corresponding to the highest NH₃/SiH₄ ratio. These results were obtained from measurements on MNS capacitors.

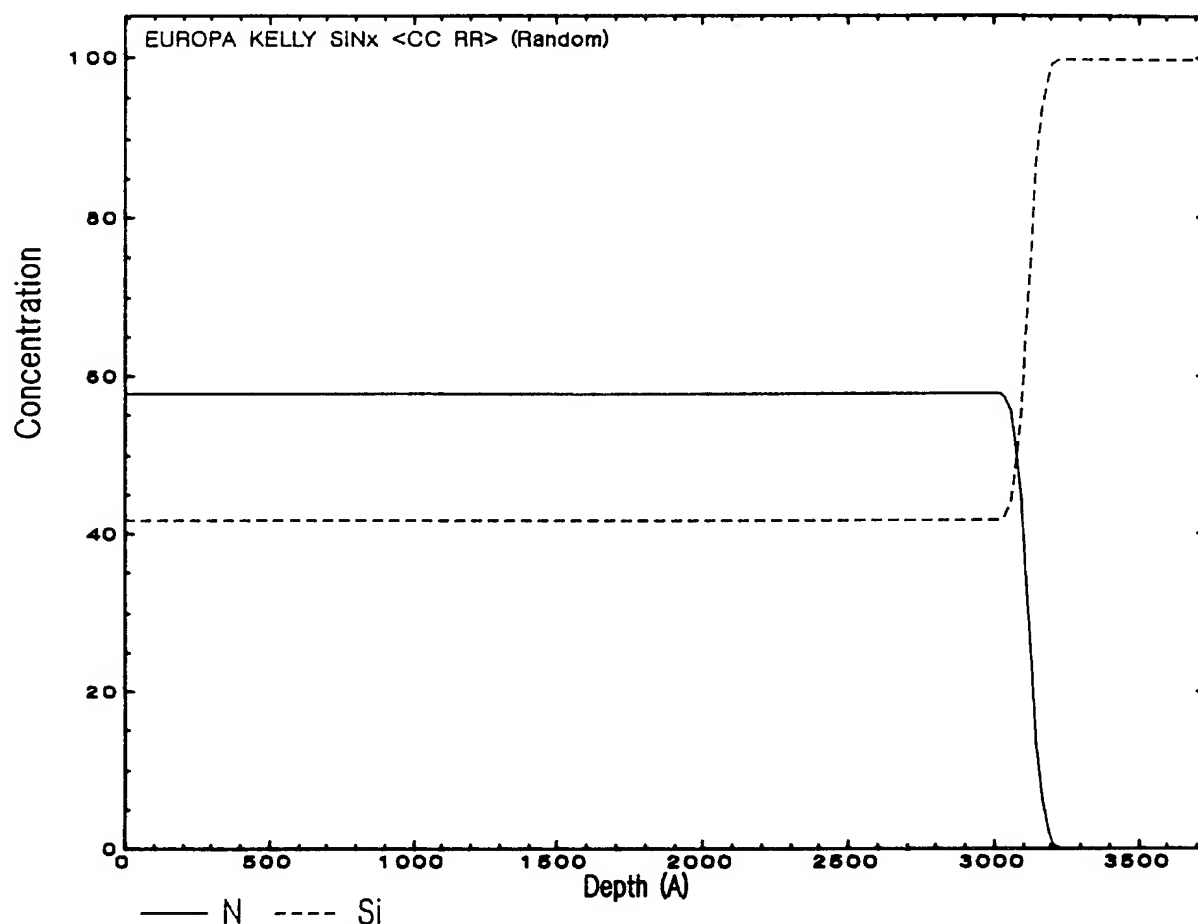


Fig. 6. RBS depth profile of optimised SiNH sample.

4. Process conditions and RBS/SIMS analysis of the SiNH layer

From the data above it was possible to select deposition parameters to deposit SiNH as a dielectric and a passivation layer. A passivation layer requires a dense film to prevent the diffusion of impurities. As a gate insulator the film should also have a minimal H and O content, low pinhole density and a high breakdown field. A SiNH layer with the above properties can be deposited using the following conditions, NH_3/SiH_4 ratio of 8:1, rf power 150 W and a substrate temperature of 550°C. This process has a deposition rate of 185 Å/min, and the SiNH film has a relative permit-

tivity of 6.75 and a breakdown field of 7.7 MV/cm. RBS and SIMS analysis of the layers were carried out to verify the initial experimental work. The RBS spectra were acquired at backscattering angles of 160° and 111° with a primary He^{2+} ion beam operating at 2.275 MeV. The results for a 3100 Å thick SiNH sample deposited on a silicon ([100] n-type) substrate are shown in Fig. 6. The layer has a Si/N ratio of 0.73 and there are 2.43×10^{18} atoms/cm² present in the samples giving a density of 2.7 g/cm³. No variations in the Si or N concentrations were detected with respect to depth in the film and no impurities were detected. The detection limit for C and O was approximately 5 at.% while for atoms heavier than P the detection

limit was 0.05 at.% or less. Hydrogen cannot be detected by RBS so to complete the analysis a SIMS profile of a TFT type structure was obtained. From this it was calculated that the layer contains 11% of atomic hydrogen.

5. TFT fabrication

Using the above process conditions for the SiNH layer, TFTs were fabricated by the procedure reported previously [11]. The SiNH films were deposited in a multiprocess procedure, such that the gate dielectric layer was never directly exposed to atmosphere. The characteristics of these devices were significantly better than those fabricated with a high temperature thermal gate oxide. The improvements in the characteristics will be discussed elsewhere [12]. Devices fabricated yielded a mobility of $30 \text{ cm}^2/\text{Vs}$, threshold voltages of 2.7 V, $I_{\infty}(V_g = 10) / I_{\text{off}}(V_g = 0)$ of 10^4 and the sub-threshold slope at $V_g = 5 \text{ V}$ was 2 V/decade.

6. Conclusions

PECVD deposition of SiNH was investigated in the temperature range of 300–550°C. The deposition process was optimised and incorporated in a multiple in situ layer deposition schedule for the

production of TFTs. For this application considerable advantages are gained by depositing the films at temperatures above 300°C, where the H content is reduced and dielectric properties are improved. Experimental work showed that a slightly nitrogen rich film yields the best characteristics for use as a dielectric. No impurities were detected in the layers from RBS analysis and SIMS results showed that the layers had a H content of less than 11%. TFTs fabricated using these layers have given excellent results with high mobilities and low threshold voltages.

References

- [1] V. Dharmadhikari, *Thin Solid Films* 153 (1987) 459.
- [2] R. Schomer and R. Hezel, *IEEE Trans. Electron Dev.* ED-28 (1981) 1466.
- [3] A.K. Sinha, *J. Electrochem. Soc.* 125 (1978) 601.
- [4] H.A. Mar and J.G. Simmons, *IEEE Trans. Electron Dev.* ED-24 (1977) S40.
- [5] A. Mumumura, *IEEE Trans. Electron Dev.* ED-36. (2) (1989) 351.
- [6] I. Kobayashi, *Jpn. J. Appl. Phys.* 31 (1992) 336.
- [7] L.J. Quinn, *EMRS Symposium D*, Paper D-I.4, Spring 1993.
- [8] H. Dun, *J. Electrochem. Soc.* 128 (1981) 1555.
- [9] W.A. Land and M.J. Rand, *J. Appl. Phys.* 49 (1978) 2473.
- [10] W.A.P. Claassen, *J. Electrochem. Soc.* 132 (1985) 893.
- [11] L.J. Quinn, *Proc. IEEE Melecon 2* (1994) 599.
- [12] L.J. Quinn, in: *Proc. ESSDERC'94*, Vol. 24, ed. C. Hill and P. Ashburn (Editions Frontières, Gif-sur-Yvette, 1994) p. 581.



ELSEVIER

Journal of Non-Crystalline Solids 187 (1995) 353–360

JOURNAL OF
NON-CRYSTALLINE SOLIDS

Deposition of amorphous silicon nitride thin films by CO₂ laser-induced chemical vapour deposition

J. Serra, T. Szörényi¹, D. Fernández, P. González, E. García, J. Pou, B. León*,
M. Pérez-Amor

Departamento Física Aplicada, Universidad de Vigo, Lagoas-Marcosende 9, 36280 Vigo, Spain

Abstract

Hydrogenated amorphous silicon nitride films have been prepared by laser-induced chemical vapour deposition from NH₃–SiH₄–Ar gas mixtures, heated by the gas-phase absorption of CO₂ laser radiation. Samples have been characterized by ellipsometry ($\lambda = 632$ nm) and Fourier transform infrared spectroscopy to determine refractive index, thickness and bond composition. With regard to the power density effect, there is a non-linear dependence of the reaction process leading to film growth, opposite to what has been found for the SiO₂ deposition from silane and nitrous oxide using the same experimental set-up. Starting from certain conditions, by only increasing the laser power from 24 to 30 W a dramatic change in growth rate is obtained from 10 to 200 Å/min. Moreover by holding constant all other processing parameters and increasing the total pressure the deposition rate could be further enhanced, the upper limit being when the formation of powdery deposits began. The study of the dependence of growth rate on total gas pressure for a NH₃/SiH₄ = 20 gas flow rate ratio has demonstrated that the peak gas temperature controls the deposition rate, revealing that the process is driven by gas phase reactions. A strong influence of the NH₃/SiH₄ gas flow ratio on the film properties has been observed. An increment of this ratio produces a drop in the refractive index, indicating that the film incorporates more nitrogen. This behaviour is corroborated by infrared spectra. The Si–N stretching peak shifts from 844 to 835 cm^{–1} and a diminution of the full width at half-maximum is observed. These changes are probably related to the incorporation of bonded hydrogen.

1. Introduction

Silicon nitride films on silicon or silicon dioxide are commonly used in semiconductor technology, as gate dielectric, diffusion mask, and for passivation [1]. A major use constitutes the manufacturing

of integrated circuits as a barrier layer to encapsulate the final circuits. It has been found that nitride films have the capability of retaining for a long time current carriers of both signs: electrons and holes. Based on this phenomenon, non-volatile memory devices have been produced. The requirement of a thin silicon nitride film (≈ 400 Å) with reproducible electrical properties has precluded the usage of plasma chemical vapour deposition (CVD), and therefore thermal CVD is an alternative choice [2]. Both plasma and thermal CVD silicon nitride films

* Corresponding author. Tel: 34-86 812 216. Telefax: + 34-86 812 201.

¹ Permanent address: Research Group on Laser Physics H-6720, Szeged, Dóm Tér 9, Hungary.

used in circuit manufacturing contain measurable amounts of incorporated hydrogen. The amount depends on the deposition process parameters and post treatment of the films. The incorporation of hydrogen into these films actually benefits their electrical properties by reducing defects associated with uncoordinated silicon bonds [3]. The laser-induced CVD method reported here not only retains the advantage of low (and controllable) substrate temperatures associated with plasma CVD methods, but should more closely approximate thermal activation of the precursor reaction gases.

The use of a CO₂ laser-induced CVD technique to deposit films of silicon nitride from SiH₄ and

NH₃ mixtures is reported here. With these gases as precursors the 10.6 μm line of the CW-CO₂ laser is resonantly absorbed by the SiH₄ and NH₃ molecules [4]. Energy redistribution by intermolecular collisions leads to gas heating, which controls the gas-phase reaction [5]. An exhaustive study has been carried out on the role of the power density and the total pressure on deposition and growth rate. These results were compared to those obtained with SiO₂ deposited from SiH₄ + N₂O mixtures [6,7] using the same experimental set-up, showing the contribution of NH₃ in the gas heating. Moreover the influence of the NH₃/SiH₄ gas flow rate ratio on the film refractive index and bond composition has been investigated.

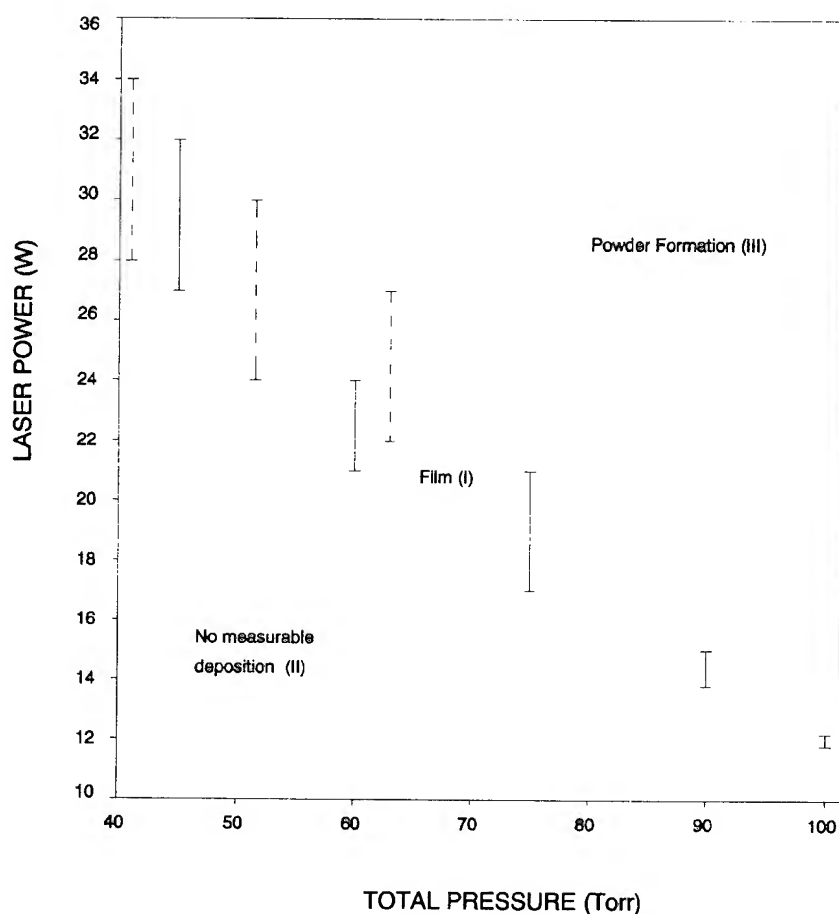


Fig. 1. Influence of the laser power density and the total pressure on film deposition, for two flow rate ratios (—) NH₃/SiH₄ = 8, (---) NH₃/SiH₄ = 20.

2. Experimental details

The experimental set-up consists of a CO₂ laser beam tuned at 10.6 μm passing through a reaction chamber filled with the reactive gases [7], SiH₄ and NH₃. Substrates are Si(100) wafers placed on a temperature-controlled heater, positioned parallel to the laser beam. The chamber is placed on an elevating stage that allows adjustment of the distance between the beam axis and the substrate surface with an accuracy of ± 0.1 mm.

The beam is focussed by a KCl lens with a focal length of 500 mm, which yields a beam of 2 mm diameter with a focal depth of 14 cm. At this is the same length as the deposition zone in the chamber, the focused beam can be considered cylindrical in the deposition zone. The power transmitted by the gas mixture was monitored at the exit window. After an initial period of irradiation, the transmitted power reaches a stationary value, which allows one to calculate the absorption coefficient of the gas mixture for each set of the experimental conditions.

Gas flow rates were monitored by electronic mass flow controllers. The gas pressure was measured by a capacitance manometer. In addition to the reactive gases, an Ar stream was used to purge the inlet window to prevent the formation of deposits on its inner surface, which could decrease the power coming into the chamber. The reactive gases entered into the reaction zone through pinholes distributed uniformly along a tube situated perpendicular to the beam pathway. The reaction zone of the chamber was separated from the window zones by baffles, which stabilize the reactive flow in the reaction area. Operation without baffles leads to lower deposition rates as well as to powder formation on the windows. All experiments reported here were performed at a substrate temperature of 300°C. The films were characterized by ellipsometry ($\lambda = 632.8$ nm) and Fourier transform infrared (FTIR) spectroscopy.

For the deposition of silicon-nitride films, electronic grade SiH₄ and NH₃ (as the reactant gases) and 99.995% pure Ar were used. The NH₃/SiH₄ mass flow ratios were 8 and 20. The laser power

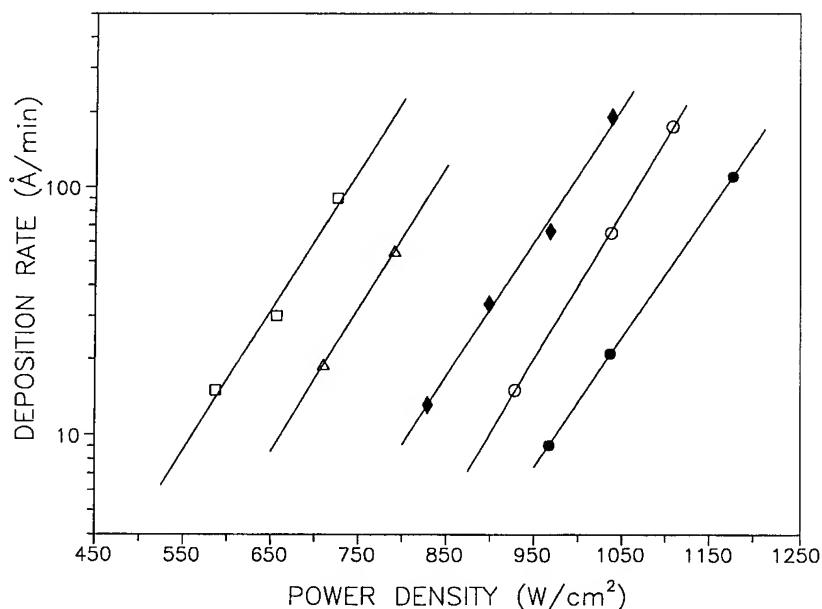


Fig. 2. Dependence of deposition rate on the power density for two flow rate ratios. (1) NH₃/SiH₄ = 8: ○, 45 Torr; △, 60 Torr; □, 75 Torr. (2) NH₃/SiH₄ = 20: ●, 41 Torr; ◆, 50 Torr. Lines are drawn as guides for the eye.

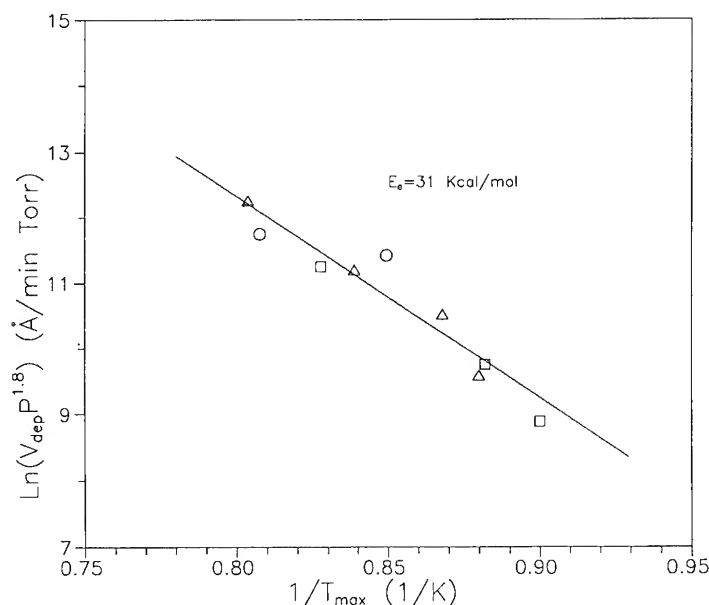


Fig. 3. Arrhenius plot of the growth rate as a function of the reciprocal calculated peak gas temperature for films made at $\text{NH}_3/\text{SiH}_4 = 20$. \square , 41 Torr; Δ , 50 Torr; \circ , 63 Torr; $T_s = 300^\circ\text{C}$. The data are fitted to the function $\ln(V_{\text{dep}} P^{1.8}) = A + B/T$.

and the total pressure were varied in the range of 12–34 W and 40–106 Torr, respectively.

3. Results and discussion

The experimental parameters which influence the growth rate and the chemical composition of silicon nitride are the laser power, the total pressure, the substrate temperature, and the reaction gas composition. Each of these parameters may alter the fundamental physical and chemical processes occurring in the CVD reactor in a complex way. A single experimental variable can change several of the film properties, and many variables appear interrelated. We present a generalized picture of how the main CVD experimental variables influence several of the measured film properties.

Previous studies of the reaction kinetics in the system have revealed that this laser-induced chemical vapour deposition (LCVD) process is a thermally activated process [8]. The growth rate of nitride films should be controlled by the thermal dissociation and reaction of SiH_4 and NH_3 ; thus, it

should be exponentially dependent on the peak gas temperature, T_g . The peak gas temperature can be calculated from a steady-state energy balance between the energy absorbed by the gas and the energy lost by thermal conduction [5,8,9].

3.1. Influence of power density and total pressure on film deposition

To investigate the domain of nitride film deposition, experimental series varying the total pressure and power density were performed for two NH_3/SiH_4 flow rate ratios, while keeping constant the substrate temperature and the geometrical parameters. Fig. 1 shows the influence of laser power intensity and total pressure on deposition of film. Three zones have been identified: (I) film deposition, (II) no measurable deposition and (III) formation of powder or powdery film. The behaviour is similar for the two series. A study of the power absorbed by the gas mixture shows both lower and upper limits for obtaining no measurable deposition and powder formation, respectively. These values are independent of the total pressure

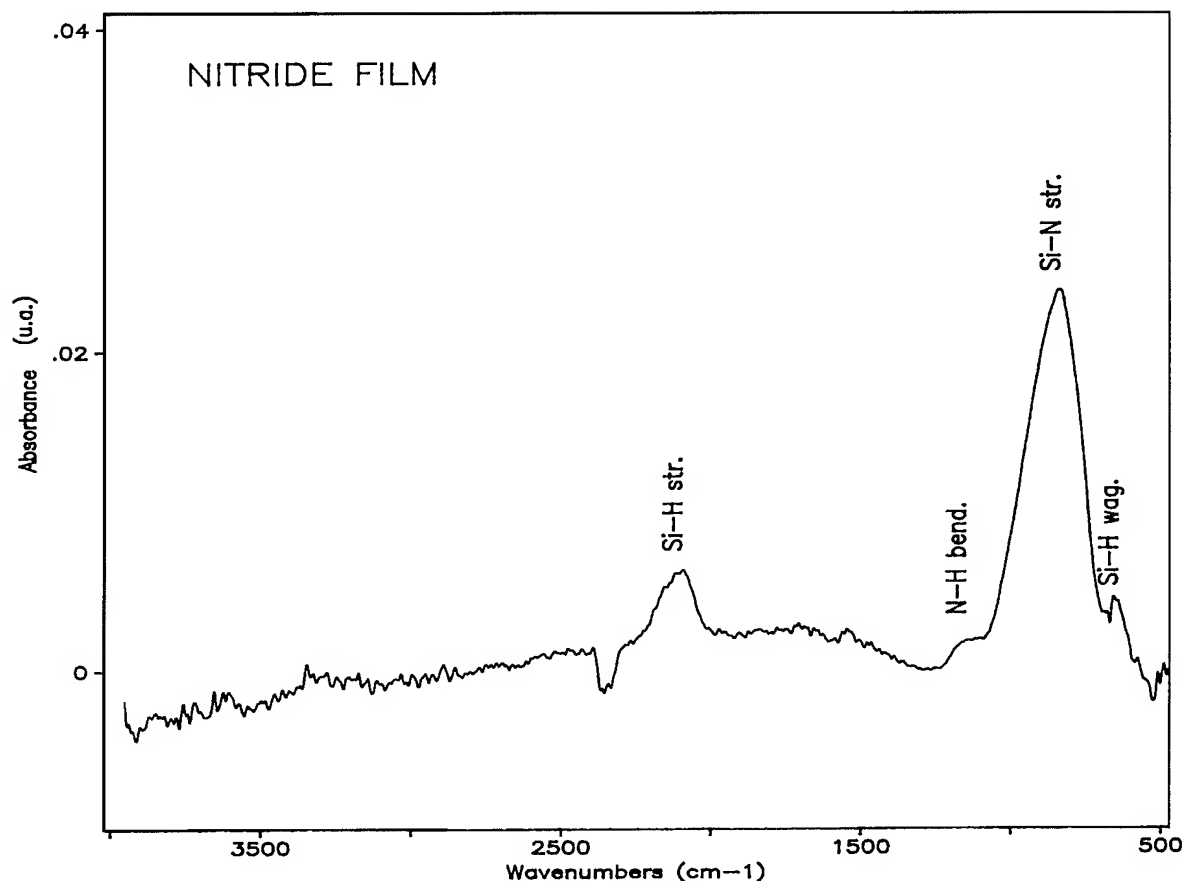


Fig. 4. IR spectra of a nitride film deposited at total pressure of 42 Torr, 32 W power intensity and $\text{NH}_3/\text{SiH}_4 = 20$.

and the laser power density. This result indicates that the nitride deposition film by CO_2 laser-induced CVD is controlled by the gas temperature.

In the domain of film formation growth rates from 10 to 200 Å/min were obtained. Fig. 2 shows the dependence of the growth rate on the laser power density. In this range the growth rate is an exponential function of the power density. Since for the different series performed at various total pressure values and flow rate ratios the same exponential coefficient proportional to the laser power density is obtained, it can be concluded that the chemical dynamics remains the same within this range of experimental conditions. However, this

result differs from the linear variation of deposition rate with power density that has been obtained by our group [6] for SiO_2 films ($\text{SiH}_4 + \text{N}_2\text{O} + \text{Ar}$ mixture) with the same experimental set-up. This difference of behaviour could arise from the fact that in the $\text{SiH}_4 + \text{NH}_3 + \text{Ar}$ mixture both silane and ammonia absorb. In fact, the coupled energy in this process becomes larger as the gas is heated to higher temperatures for higher power densities, indicating that either or both the thermal excited precursor molecules and their fragments contribute significantly this increase.

The chemical reaction leading to the film growth depends on both the gas temperature and the reactant concentration. By applying the temperature

Table 1
Film properties for samples deposited at two NH_3/SiH_4 gas flow ratios

Sample	Pressure (Torr)	Flow ratio NH_3/SiH_4	FWHM (cm^{-1})	Peak position Si-N (cm^{-1})	n
m28	40	8	215	845	2.9
m36	40	20	175	832	2.7

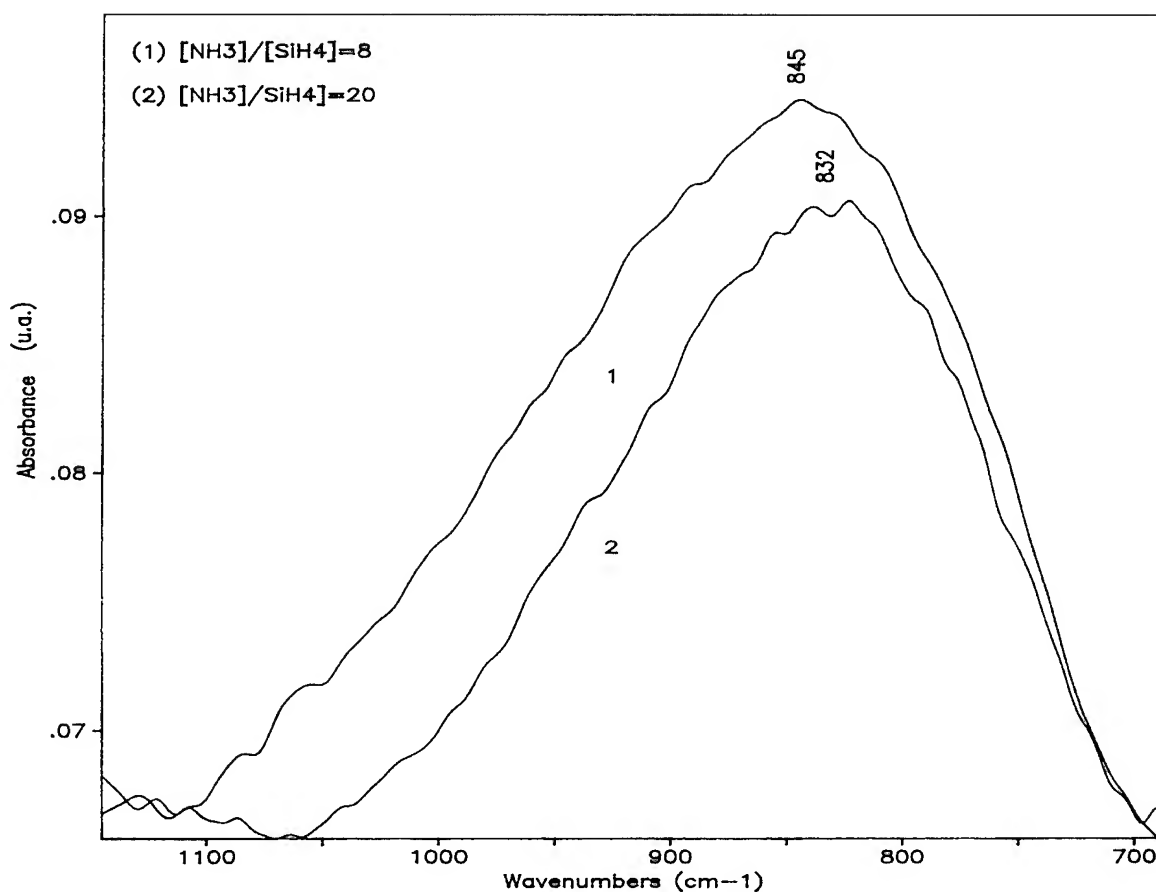


Fig. 5. Si-N stretching band of nitride films deposited at $P_T = 40$ Torr and $T_S = 300^\circ\text{C}$.

calculation model developed in Ref. [8], the stationary peak gas temperature was determined for each experiment related to the produced films. Fig. 3 shows a pressure-independent Arrhenius plot for samples deposited at several pressures and

power density. All points overlap approximately on a line of best fit, from which an apparent activation energy of $E_a = 31$ kcal/mol has been calculated [5,8]. This result demonstrates that the peak gas temperature controls the film growth rate.

Moreover, it indicates that the reaction is kinetically limited in the gas phase (at least under our specific experimental conditions).

3.2. Dependence of refractive index and chemical bonding on the $[\text{NH}_3]/[\text{SiH}_4]$ flow ratio

The refractive index is a commonly measured property of LCVD silicon nitride films. The values for refractive index have many variations depending on the deposition techniques, deposition and geometrical parameters. The NH_3/SiH_4 flow ratio is a very important parameter in the LCVD of Si_3N_4 as well as in other techniques. High values of the refractive index are caused by silicon-rich films such as those formed with high silicon to ammonia or silane to nitrogen ratios [2]. Too low values of the refractive index may indicate oxygen impurities. In our case, taking into account that the reactor base vacuum pressure was 10^{-5} Torr, oxygen contamination may be precluded.

The chemical bonding in the deposited Si_3N_4 thin films has been studied. Fig. 4 shows the IR-absorption spectra of films grown in these experiments having characteristics similar to those produced by other techniques [10,11]. Following features may be identified: (1) a Si–N stretching vibration near 835 cm^{-1} , (2) a Si–H stretching vibration at 2100 cm^{-1} , (3) a the N–H bending vibration near 1150 cm^{-1} , and (4) a Si–H wagging vibration at 640 cm^{-1} . There is no evidence for any absorption associated with N–H stretching vibration, which would occur between $3000\text{--}3500\text{ cm}^{-1}$. The Si–N bond concentration cannot be accurately quantified from the FTIR spectrum since the peak around $800\text{--}900\text{ cm}^{-1}$ represents the contributions of two peaks due to both Si–N stretching and Si–H bending modes. Moreover, no contribution from Si–O was observed, corroborating that the layers are nitrides and not oxynitrides.

The influence of the NH_3/SiH_4 ratio on the refractive index and structure has been investigated, by ellipsometry and FTIR spectroscopy analysis. The refractive index shows a strong dependence on the flow ratio, and the behaviour is similar for the two series (Table 1). The refractive index decreases when the NH_3/SiH_4 flow ratio increases, indicating a change in the film properties.

This behaviour is corroborated by IR-spectroscopy measurements.

The Si–N stretching band of our samples for $\text{NH}_3/\text{SiH}_4 = 8, 20$ at constant pressure is shown in Fig. 5. The curves show a small shift towards lower frequencies in the peak position of the Si–N stretching mode and a diminution of the full width at half maximum (FWHM) with increasing flow ratio. These changes are probably related to the amount of bonded hydrogen. The frequency changes of the Si–N bond vibration are related to the modifications in the nearest-neighbour environment of both the Si and N atoms [10,11]. Having N–H bonds within the film, the Si–N stretching vibration will tend to decrease to 835 cm^{-1} when incorporating more N, it means less H.

The high value of refractive index and the strong presence of the Si–H stretching mode and specially the appearance of the Si–H wagging vibration at 640 cm^{-1} , a peak not usually reported in silicon nitride, but common in a-Si:H films, could indicate that the films may be nitrogen-poor and hydrogen-rich. Rutherford backscattering spectrometry (RBS) and elastic recoil detection analysis (ERDA) stoichiometric measurements are being performed presently to confirm this hypothesis.

4. Conclusions

A systematic study has been performed on the CO_2 LCVD of nitride films in a parallel configuration. The dependence of the deposition rate of the Si_3N_4 films on power density and total pressure in LCVD has been studied. The growth rate is an exponential function of the laser power density. All series show the same exponential coefficient independent of the total pressure and the NH_3/SiH_4 flow rate ratio. Using a very simple temperature calculation model, differential experimental series have been brought to agreement on a single pressure-independent Arrhenius plot, demonstrating that the growth mechanism is thermally driven in the gas phase. Infrared transmission spectra of these films show the characteristic absorption bands of Si–N, Si–H and N–H. RBS and ERDA stoichiometric measurements will confirm to what extent the films are poor in nitrogen and the degree of hydrogenation.

References

- [1] V.I. Belyi, L.L. Vasilyeva, A.S. Ginovker, V.A. Gritsenko, S.M. Repinsky, S.P. Sinitsa, T.P. Smirnova and F.L. Edelman, eds., *Silicon Nitride in Electronics*. (Elsevier, Amsterdam, 1988) ch. 1, p.1.
- [2] A.C. Adams, in: *Silicon Nitride and Other Insulator Films*, ed. J. Mort and F. Jansen (CRC, Boca Raton, FL, 1988) ch. 5, p. 129.
- [3] A.C. Adams, *Solid State Technol.* 26 (1983) 135.
- [4] W.R. Cannon, S.C. Danforth, J.H. Flint, J.S. Haggerty and R.A. Marra, *J. Am. Ceram. Soc.* 65 (1982) 324.
- [5] M. Meunier, J.H. Flint, J.S. Haggerty and D. Adler, *J. Appl. Phys.* 62 (1987) 2812.
- [6] D. Fernández, PhD Physics, University of Santiago (1992).
- [7] D. Fernández, P. González, J. Pou, E. García, B. León and M. Pérez-Amor, *Thin Solid Films* 220 (1992) 100.
- [8] D. Fernández, C. Garrido, P. González, J. Pou, E. García, J. Serra, B. León and M. Pérez-Amor, *J. Vac. Sci. Technol. A* 12 (1994) 1.
- [9] E.T.S. Pan, J.H. Flint, D. Adler and J.S. Haggerty, *J. Appl. Phys.* 61 (1987) 4535.
- [10] G. Lucovsky and D.V. Tsu, *J. Vac. Sci. Technol. A* 5 (1987) 2231.
- [11] R.C. Budhani, S. Prakash, H.J. Doerr and R.F. Bunshah, *J. Vac. Sci. Technol. A* 5 (1987) 1644.



ELSEVIER

Journal of Non-Crystalline Solids 187 (1995) 361–364

JOURNAL OF
NON-CRYSTALLINE SOLIDS

Section 11. ONO and nitrated oxides

Structural and electrical properties of thin SiO₂ layers grown by RTP in a mixture of N₂O and O₂

A.J. Bauer*, E.P. Burte

*Fraunhofer-Institut für Integrierte Schaltungen, Bereich Bauelementechnologie, Schottkystrasse 12, D-91058 Erlangen, Germany***Abstract**

Ultrathin (< 10 nm) dielectric films for application in metal-oxide-semiconductor devices have been fabricated in an O₂:N₂O atmosphere using rapid thermal processing. It is shown that with increasing N₂O content in the mixtures of N₂O and O₂, the oxide thickness decreases and the interfacial nitrogen concentration increases. Therefore, the nitrogen concentration at the Si/SiO₂ interface, responsible for improved electrical characteristics, is adjustable by the O₂:N₂O ratio. High charge-to-breakdown (Q_{BD}) values comparable to oxides processed in pure N₂O atmosphere are obtained for electron injection from the Si substrate. For electron injection from the gate, the Q_{BD} values are considerably higher. For an O₂:N₂O ratio of 3:1 the highest Q_{BD} values have been obtained together with a very homogeneous Q_{BD} distribution across the wafer.

1. Introduction

In the near future, the development of highly reliable, very thin SiO₂ films will be of crucial importance for the manufacture of sub-0.25 μ m metal-oxide-semiconductor field-effect transistors (MOSFETs). The oxide thickness will decrease from 9 nm for 0.35 μ m to 6.5 nm for 0.25 μ m ULSI devices due to device design rules [1]. Using rapid thermal processing (RTP) oxynitride grown in a pure N₂O atmosphere on silicon substrates has recently drawn attention to its candidature as a gate dielectric for deep submicron MOSFET devices. It exhibits high charge-to-breakdown Q_{BD} values [2,3] and high hot carrier integrity [4].

However, thickness and electrical inhomogeneities across the wafer of the dielectric films grown in pure N₂O atmosphere are reported [5] and the self-limiting growth of oxynitrides resulting in prolonged processing times increases the thermal budget.

In this paper we report on structural and electrical properties of dielectric films processed in mixtures of N₂O and O₂ by RTP as proposed by [6] and compare them with oxides grown in pure O₂ and N₂O atmospheres. This process has a lower thermal budget due to the enhanced oxidation rate and exhibits a better film thickness homogeneity compared to an oxynitridation process in pure N₂O atmosphere. Furthermore, this method provides excellent control of nitrogen peak concentration at the SiO₂/Si interface, which is an important parameter determining MOSFET characteristics [7]. By varying the N₂O:O₂ ratio in the gas

* Corresponding author. Tel: +49-9131 761 308. Telefax: +49-9131 761 390. E-mail: a.bauer@iis-b.fhg.de.

mixture improved Q_{BD} distributions across the wafer and higher Q_{BD} values for electron injection from the substrate compared to oxynitride films oxidized in pure N_2O atmosphere could be obtained.

2. Experimental procedure

The SiO_2 and SiO_xN_y films were grown on 4–6 Ω cm, p-type (100) Si wafers after a standard wet cleaning procedure by applying the following oxidation and nitridation process steps: (a) oxidation in dry oxygen, (b) oxidation in dry nitrous oxide and (c) oxidation in a mixture of oxygen and nitrous oxide with $O_2:N_2O$ ratios of 1:3, 1:1 and 3:1. The oxidation temperature was 1120°C and the flow rate of the gases during the oxidation was set to 2 slm. After growth of the dielectric, a 500 nm thick polysilicon layer was deposited by low-pressure chemical vapor deposition (LPCVD) at 620°C. The layer was doped with phosphorus at 950°C. The gates of area $A = 0.02$ nm² of MOS capacitors were defined by photolithography and wet etching.

The nitrogen depth profiles were determined by secondary ion mass spectroscopy (SIMS) using Cs^+ bombardment at an energy of 5 keV and CsN^+ ion detection. The electrical properties of these dielectric films were evaluated by high-frequency (1 MHz) $C-V$, quasi-static $C-V$ and $I-V$ measurements. The reliability of the dielectric films was evaluated from time-dependent dielectric-breakdown (TDDB) characteristics. The TDDB measurements were performed at negative and positive gate bias on 53 capacitors by applying a constant current density of $j = \pm 200$ mA/cm². The increase or decrease of the gate voltage observed during the TDDB measurements is related to the buildup of negative or positive charge in the oxide.

3. Results

The average oxide thickness obtained was 8.0 ± 0.5 nm for all the various oxides. The homogeneity of the oxide thickness attained from standard deviation calculations was best with a value of $\sigma = 0.1$ nm for the O_2 -oxide and worst ($\sigma = 0.6$ nm)

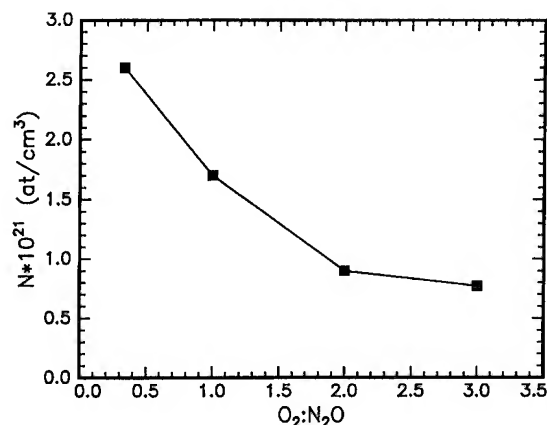


Fig. 1. Nitrogen peak concentration N of the dielectric films as a function of the $O_2:N_2O$ ratio. The oxidation temperature was 1120°C and the total gas flow was 2 slm (standard liter/minute).

for the N_2O -oxide. The standard deviation values of the $O_2:N_2O$ -oxides were between the above values in such a way that the value of the $O_2:N_2O$ -oxide with the highest $O_2:N_2O$ ratio was near the value of the O_2 -oxide and increased with increasing N_2O content in the oxidizing atmosphere.

Fig. 1 shows the nitrogen peak concentration N of the various oxynitride films as a function of the $O_2:N_2O$ ratio during oxidation. The nitrogen concentration increases with increasing N_2O content in the oxidizing atmosphere.

For all oxides investigated, the density of interfacial traps was as low as $D_{IT} \approx 1.5 \times 10^{10}$ eV⁻¹ cm⁻², while the density of fixed interface charges was lower than 0.5×10^{11} cm⁻². Fig. 2 shows the dependence of the charge-to-breakdown $Q_{BD}(63\%)$ values (63% cumulative failure) under constant current stress on the N_2O content for both gate polarities. The injection current density was $j = \pm 200$ mA/cm². If the N_2O content in the oxidizing atmosphere is equal to or lower than 50%, then the $Q_{BD}(63\%)$ values are higher than the values of the O_2 - and N_2O -oxides for substrate and gate injection. The $Q_{BD}(63\%)$ values for negative gate polarity are about three times lower than for positive polarity.

In Fig. 3 the Weibull plots of the Q_{BD} values of Fig. 2 are presented. A homogeneous Q_{BD} distribution (for positive and negative gate

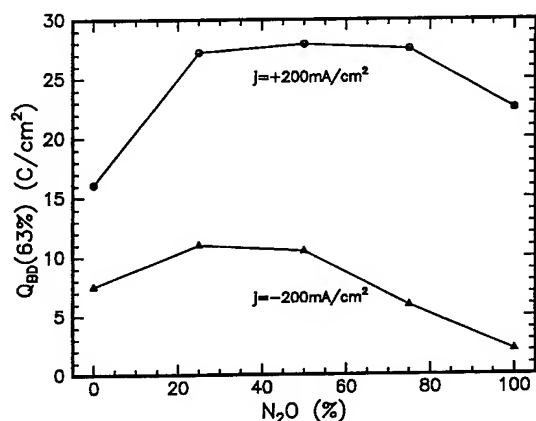


Fig. 2. Dependence of the $Q_{BD}(63\%)$ values on the N_2O content of the oxidizing atmosphere after a constant current injection with a current density of $j = \pm 200 \text{ mA/cm}^2$ for both gate polarities.

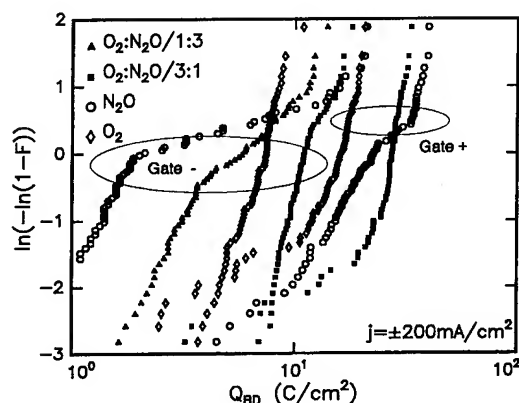


Fig. 3. Weibull plots of charge-to-breakdown in MOS capacitors (area: 0.02 mm^2) with different gate dielectrics under both gate polarities.

polarity) across the wafer can be seen only for the O_2 -oxides and the $O_2:N_2O$ -oxides which were oxidized in an $O_2:N_2O$ atmosphere with an $O_2:N_2O$ ratio higher than one. On the other hand, the N_2O -oxide exhibits above all a broad Q_{BD} distribution for electron injection from the gate. The Weibull plots for the $O_2:N_2O$ ratio of 1:1 are similar to those of the $O_2:N_2O$ ratio of 3:1 and are therefore not shown in Fig. 3.

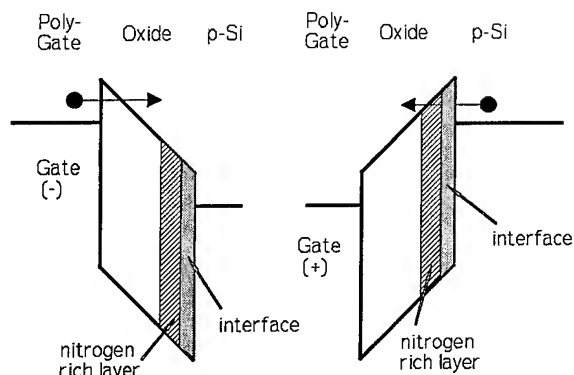


Fig. 4. Schematic energy-band diagram with a nitrogen-rich layer at the SiO_2/Si interface showing electron injection from poly gate and Si substrate.

4. Discussion

It is well known that an optimized RTP N_2O oxidation process can result in high $Q_{BD}(63\%)$ values [8,9]. This is attributed to nitrogen incorporation into the SiO_2/Si interface which strengthens the interface against hot carrier damage. Our results show, too, that nitrogen is incorporated in the bulk of the dielectric film near the SiO_2/Si interface (see Fig. 4) after a N_2O oxidation at high temperatures ($1050^\circ\text{C} < T < 1150^\circ\text{C}$). This nitrogen-rich layer may be responsible for the Q_{BD} degradation under negative gate polarity. In this case, the electrons are tunneling from the polysilicon gate into the conduction band of the dielectric film. Here, the electrons are accelerated on account of the applied electric field. From there, they gain sufficient energy to generate traps in the nitrogen-rich layer near the anode by breaking Si-N or O-N bonds, the binding energy of which is lower than the Si-O bond [10]. Hence, if there is a nitrogen-rich layer in the dielectric film near the interface to silicon, more traps than in nitrogen-free oxides are generated resulting in lower $Q_{BD}(63\%)$ values.

But, if the electrons are injected from the Si substrate, they are tunneling through the nitrogen-rich interfacial layer (Fig. 4) and have not yet gained sufficient energy to break N bonds. So, less traps responsible for dielectric breakdown are generated at the anode. Only the beneficial influence of the nitrogen incorporated in the interface becomes

evident. By that, the broad Q_{BD} distribution of the N_2O -oxide for negative gate polarity can be explained. Oxidation processes in pure N_2O atmosphere show, preferentially in the center of the wafer, a high nitrogen peak concentration at the SiO_2/Si interface and a low one at the outer area of the wafer. Consequently, high Q_{BD} values will be seen, where least nitrogen is incorporated in the bulk of the dielectric film.

An oxynitridation process, in which the nitrogen incorporation into the dielectric film can be controlled and where no nitrogen is incorporated in the bulk oxide, e.g. an oxidation in a mixture of O_2 and N_2O , shows more homogeneous Q_{BD} distributions with higher Q_{BD} (63%) values than a N_2O -oxide, therefore.

5. Conclusions

In summary, excellent control of the nitrogen peak concentration at the SiO_2/Si interface by a rapid thermal oxynitride process using mixtures of oxygen and nitrous oxide was established. This process provides lower thermal budget, better Q_{BD} uniformity, and higher Q_{BD} (63%) values than a process which uses RTP temperature alone to

control the nitrogen concentration. The broad Q_{BD} distribution and the low Q_{BD} values of the N_2O -oxides for electron injection from the gate can be explained by a model which includes a nitrogen-rich layer at the SiO_2/Si interface.

References

- [1] E.L. Hall, in: Proc. 1st Int. Rapid Thermal Processing Conf., RTP 93, ed. R.B. Fair and B. Lojek, Scottsdale, Arizona, 8–10 September (1993) p. 22.
- [2] H. Hwang, W. Ting, D.L. Kwong and J. Lee, IEDM Tech. Dig. (1990) 421.
- [3] W. Ting, G.Q. Lo, J. Ahn, T.Y. Chu and D.L. Kwong, IEEE Electron. Dev. Lett. 12 (1991) 416.
- [4] H. Hwang, W. Ting, D.L. Kwong and J. Lee, IEEE Electron. Dev. Lett. 12 (1991) 495.
- [5] T.Y. Chu, W.T. Ting, J. Ahn and D.L. Kwong, J. Electrochem. Soc. 138 (1991) L13.
- [6] Y. Okada, Ph.J. Tobin and R.I. Hegde, Appl. Phys. Lett. 61 (1992) 3163.
- [7] J. Nulman, in: Reduced Thermal Processing for ULSI, ed. R.A. Levy (Plenum, New York, 1991) p. 1.
- [8] P. Lange, H. Bernt, E. Hartmannsgruber and F. Naumann, J. Electrochem. Soc. 141 (1994) 259.
- [9] W. Ting, G.Q. Lo, J. Ahn, T.Y. Chu and D.L. Kwong, IEEE Electron. Dev. Lett. 12 (1991) 416.
- [10] R.C. Weast, M.J. Astle and W.H. Beyer, eds., CRC Handbook of Chemistry and Physics, 67th Ed. (CRC, Boca Raton, FL, 1985) pp. F174–F179.



ELSEVIER

Journal of Non-Crystalline Solids 187 (1995) 365–368

JOURNAL OF
NON-CRYSTALLINE SOLIDS

Damage induced by carrier injection in 8 nm thick oxides and nitrided oxides

A. Bravaix^a, D. Vuillaume^{a,*}, V. Thirion^b, D. Dorval^b, A. Straboni^b

^a *Institut d'Electronique et de Microelectronique du Nord (IEMN), UMR 9929, CNRS, Institut Supérieur d'Electronique du Nord (ISEN), 41 Boulevard Vauban, 59046 Lille cédex, France*

^b *France Télécom, Centre National d'Etude des Télécommunications, Chemin du vieux chêne, 38243 Meylan cédex, France*

Abstract

Charge trapping and interface trap creation phenomena observed in 8 nm thick thermally grown oxides and oxides nitrided by low pressure ammonia plasma are reported. These phenomena are observed for samples subjected to uniform high-field current injection. It is demonstrated that trap creation is limited to the generation of interface states. No electron trapping and no positive charge generation are observed for injected fluences ranging from 10^{-6} – 10^2 C/cm² at oxide fields in the range 8–11 MV/cm. Quite similar trap creation rates and kinetics are observed in both samples, which demonstrates the good reliability performance of the nitrided oxide. Results are discussed in terms of impact ionization and trap creation by hydrogen-related species models.

1. Introduction

In 0.5 and 0.35 μ m CMOS technologies with dual n⁺ and p⁺ polycrystalline silicon gates, an alternative gate insulator to silicon dioxide (SiO₂) with a good blocking barrier against boron diffusion is obtained by nitrided oxides (NOX) and reoxidized-nitrided oxides (RONOX). However, the use of ammonia (NH₃) was recognized to increase the charge trapping in these films due to the incorporation of nitrogen and water [1]. Thus care must be taken in optimizing such technologies in

order to reduce this drawback. A reoxidation (O₂ annealing) of the nitrided oxide has shown promising trends towards reducing charge trapping and interface defect creation [2]. In this study, we demonstrate that lightly nitrided oxides made by low pressure plasma nitridation in ammonia [3] allow us to obtain 8 nm thick gate dielectrics with reliability performance similar to pure thermal oxides of the same thickness. Damage created under high field injection (Fowler–Nordheim) is limited to interface state creation. No electron trapping and no positive charge formation are observed for oxide fields larger than 8 MV/cm. This absence of charge trapping is explained by field-enhanced detrapping of electrons at these large fields and low probability for hole creation (and then to the formation of trapped holes) by impact ionization.

* Corresponding author. Tel: +33 20 30 62 20. Telefax: +33 20 54 56 66. E-mail: vuillaume@isen.fr.

2. Experimental procedure, sample description

The devices were made with a 0.35 μm CMOS technology, with dual n^+ and p^+ polycrystalline silicon gate materials. Gate oxides (8 nm thick) were made by thermal oxidation at 925°C in dry O_2 , followed by a postmetallization annealing at 925°C for 30 min. Without nitridation, these oxides serve as reference samples (called OX, in the following). Nitrided oxides (called NOX) have been fabricated using low pressure (70 μbar) plasma nitridation in pure ammonia at 950°C for 40 min [3]. This procedure leads to a lightly nitrided Si–SiO₂ interface as revealed by Auger electron spectroscopy [4]. Trapping and trap creation phenomena were observed at room temperature (295 K) in p-channel MOSFETs (channel length $L = 1 \mu\text{m}$, channel width $W = 100 \mu\text{m}$) when subjected to uniform high-field electron injection from the substrate (Fowler–Nordheim injection at constant positive gate voltages). Average oxide fields were in the range 8–11 MV/cm with typical injected current densities in the range 10^{-6} – 10^{-3} A/cm^2 . Charge trapping and interface state creation were measured by the charge pumping (CP) technique. Positive charge trapping is detected by CP when measuring the charge pumping current as a function of the high level of the gate voltage ($I_{\text{CP}} - V_{\text{high}}$) while the low level gate voltage is kept constant [5]. Trapping is clearly observed by following the voltage shift of the peak of the derivative curve $dI_{\text{CP}}/dV_{\text{high}}$ versus V_{high} . Negative charge trapping is detected by measuring the charge pumping current as a function of the low level of the gate voltage ($I_{\text{CP}} - V_{\text{low}}$ and $dI_{\text{CP}}/dV_{\text{low}} - V_{\text{low}}$) while V_{high} is kept constant [5]. We have also injected electrons at lower oxide fields using localized hot-carrier injection at low negative V_G and high negative V_D (in this study, $V_G = -1.25 \text{ V}$ and $V_D = -7 \text{ V}$). Damage was also measured by the shifts of the MOSFET parameters (threshold voltage V_T , transconductance g_m and drain current I_D).

3. Results

Fowler–Nordheim (FN) plots show that both OX and NOX have the same potential barrier

height at the interface with silicon. During the injections, the current densities stay constant for both samples, except at higher fields (11 MV/cm) for which a slight decrease has been observed. This effectively corresponds to slight electron trapping at this field as further revealed by CP analysis. For these high field FN injections we have observed that the oxide field F_{ox} must be higher than a threshold oxide field F_{th} of 8–9 MV/cm to induce a significant degradation in both OX and NOX samples. This value is roughly the same for the two processes.

Fig. 1 shows typical CP curves (I_{CP} and $dI_{\text{CP}}/dV_{\text{high}} - V_{\text{high}}$) recorded on NOX samples during FN injection at 11 MV/cm and for injected fluences from 10^{-3} to 10 C/cm^2 . Interface state creation is clearly shown, while no positive charge is generated. This is evidenced by the fact that the peak in the derivative curve ($dI_{\text{CP}}/dV_{\text{high}}$) is not shifted towards negative voltages. Similar results are obtained in both OX and NOX samples for FN oxide fields in the range 8–11 MV/cm. Fig. 2 compares the interface state generation in OX and NOX samples. The same rates of trap creation are observed in both cases. For injected fluences Q_{inj} lower than a critical amount of about 10^{-3} – 10^{-2} C/cm^2 , the trap creation is very low (less than $10^{10} \text{ cm}^{-2} \text{ eV}^{-1}$). To first order, the

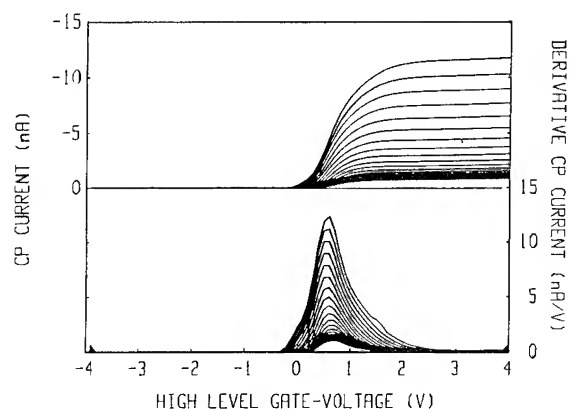


Fig. 1 Charge pumping measurements (top: I_{CP} versus V_{high} , bottom: $dI_{\text{CP}}/dV_{\text{high}}$ versus V_{high}) for NOX samples stressed by FN injection at 10 MV/cm from 0 C/cm^2 to a fluence of 10 C/cm^2 using a logarithmic incremental step. CP measurements at $f = 100 \text{ kHz}$, $V_{\text{low}} = -4 \text{ V}$.

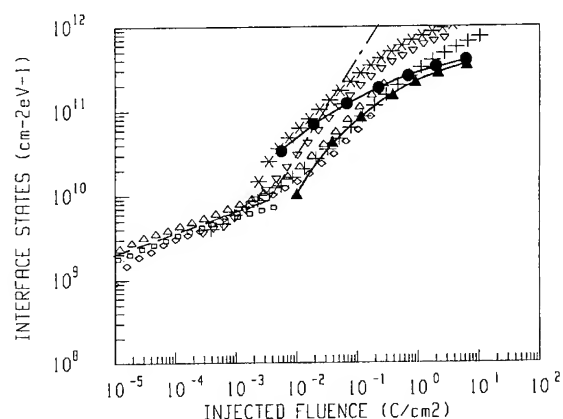


Fig. 2 Created interface states versus injected fluences for various oxide fields. OX samples at 9 MV/cm (□), 10 MV/cm (Δ) and 11 MV/cm (▽). NOX samples at 9 MV/cm (◇), 10 MV/cm (+) and 11 MV/cm (*). Dashed line corresponds to kinetics following a power law $\Delta N_{it} = A Q_{inj}^n$ with $n \approx 0.25$, and dot-dashed line corresponds to $n \approx 0.77$. The solid lines are data from Refs. [7, 9, 11]: 9.3 nm thick oxides stressed by FN injections at 9 MV/cm (▲) and 11 MV/cm (●).

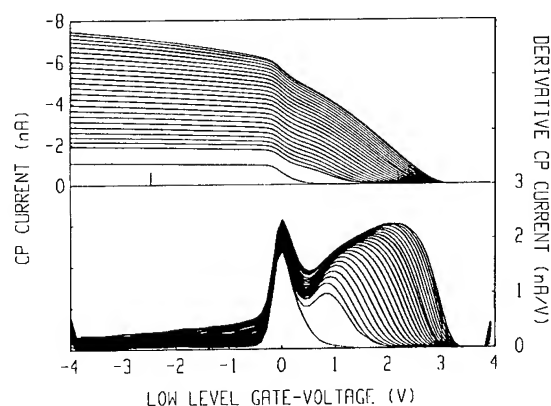


Fig. 3 Charge pumping measurements (top: I_{CP} versus V_{low} , bottom: dI_{CP}/dV_{low} versus V_{low}) for NOX samples stressed by localized hot electron injections ($V_D = -7$ V, $V_G = -1.25$ V) from a stress time of $0-4 \times 10^4$ s, using a logarithmic incremental step. CP measurements at $f = 100$ kHz, $V_{high} = 4$ V.

dashed line in Fig. 2 shows that interface state generation follows a power law, $\Delta N_{it} = A Q_{inj}^n$, with $n \approx 0.25$. For injected fluences larger than 10^{-2} C/cm², a larger trap creation is observed (Fig. 2), which always obeys a power law with an exponent $n \approx 0.77$ (dot-dashed lines), before the

beginning of saturation for injected fluences larger than 1 C/cm².

We have also injected electrons into the oxide at lower fields using localized hot-carrier injection at $V_D = -7$ V and $V_G = -1.25$ V. In this case, the oxide field, in the part of the device where injection takes place, is about 7 MV/cm, i.e. lower than the threshold for FN degradation. Under this injection condition, electron trapping is observed in both OX and NOX devices in addition to interface state creation, as revealed by the CP measurements (Fig. 3). The increasing electron trapping (as a function of the stress time) is measured by the increasing shift of the right hand side peak in the derivative of the CP current $dI_{CP}/dV_{low}-V_{low}$ towards positive voltages. Electron trapping kinetics are similar for both devices.

4. Discussion

These results show that the reliability of the oxides is similar to that of thermal oxides in terms of interface state creation by FN injection and in terms of electron trapping. This shows that a light nitridation using low pressure pure ammonia plasma is not detrimental for the reliability of the interface, while it is efficient to act as a good barrier against boron diffusion (p^+ gate) [6]. Basic mechanisms for interface degradation have been extensively discussed in the literature [7,8]. They are: (i) hole creation and trapping, and subsequent interface state creation, due to impact ionization (II), and (ii) trap creation (TC) by the release of hydrogen-related species by hot-electrons with energy higher than ≈ 2 eV, their diffusion and accumulation at the interface where they create defects. The weak interface state creation and the absence of a positive charge formation (Figs. 1 and 2) for Q_{inj} lower than $10^{-3} - 10^{-2}$ C/cm² are fully consistent with the low probability for II to occur in such 8 nm thick insulating layers [7,9]. At higher injected fluences, trap creation by hydrogen-related species is the dominant mechanism in oxide films thicker than about 20 nm [7–10], and it is the main mechanism in thinner oxide [7]. This mechanism explains the observed increase in interface state densities in our samples. For comparison purpose,

solid lines in Fig. 2 are the data measured by DiMaria and co-workers [7,9,11] (referred to subsequently as IBM) on 9.3 nm thick thermal oxide at 9 and 11 MV/cm. Similar trap creation rates are observed. In both series of devices (OX, NOX and IBM), the creation rates $\Delta N_{it}/Q_{inj}$ typically range between 10^{-8} and 10^{-7} created state per injected electron. These values are expected for polycrystalline silicon gate technologies with reduced hydrogen contamination in the gate insulators. The absence of significant electron trapping after FN stresses at high field (> 8 MV/cm), while electron trapping has been readily observed in the same OX and NOX devices for electron injection at lower fields, can be accounted for by a detrapping of these electrons at fields exceeding 8 MV/cm. Typical evidence of this detrapping effect is shown in Fig. 4. Before the detrapping experiments, an electron injection is performed at $V_D = -6$ V and $V_G = -1.2$ V for 25 s in NOX devices. After the injection, ΔV_T is +6 mV, indicating net electron trapping. Detrapping is performed by applying a positive gate voltage while drain, source and substrate are grounded. With a detrapping oxide field of 4 and 6 MV/cm, only a small number of the trapped electrons is detrapped. After detrapping of electrons at 8 MV/cm, ΔV_T is negative due to the dominant effect of donor-like interface states alone [12]. This effect (and its threshold field at about

8 MV/cm) is similar to the experiments reported by DiMaria and Stathis on thicker (52 nm) NOX and RONOX films [13]. A possible mechanism to explain this discharge phenomenon would be trap ionization.

5. Conclusions

This study demonstrates that 8 nm thick lightly nitrided oxides obtained using low pressure ammonia plasmas do not show enhanced degradation under high field Fowler–Nordheim injection when compared to pure thermal oxides. Degradation is limited to a substantial interface state creation at injected fluences larger than 10^{-2} C/cm². No electron trapping, nor positive charge formation is evidenced in these thin nitrided oxides. These results are mainly explained by (i) a low probability for impact ionization to occur, (ii) a field-assisted detrapping of electrons at fields larger than 8 MV/cm and (iii) an interface state creation by hydrogen-related species diffusion.

A.B.R. and D.V.U. acknowledge financial support from CNET under contract no. 923B043.

References

- [1] S.K. Lai, D.W. Dong and A. Hartstein, *J. Electrochem. Soc.* 129 (1982) 2042.
- [2] T. Hori, *Microelectron. Eng.* 22 (1993) 245.
- [3] B. Piot, A. Straboni, B. Vuillermoz, K. Barla, M. Berenguer and J.F. Portailier, in: *Proc. ESSDERC'89*, ed. A. Heuberger, H. Ryssel and P. Lange (Springer, Berlin, 1989) p. 366.
- [4] K. Barla, R. Pantel, B. Vuillermoz, A. Straboni and Y. Caratini, *J. Appl. Phys.* 68 (1990) 3635.
- [5] W. Chen, A. Balasinski and T.P. Ma, *IEEE Trans. Electron Dev.* 40 (1993) 187.
- [6] B. Piot, PhD thesis, Grenoble (1991) unpublished.
- [7] D.J. DiMaria, E. Cartier and D. Arnold, *J. Appl. Phys.* 73 (1993) 3367 and references therein.
- [8] A. Mir and D. Vuillaume, *Appl. Phys. Lett.* 62 (1993) 1125, and references therein.
- [9] D.J. DiMaria, D. Arnold and E. Cartier, *Appl. Phys. Lett.* 61 (1992) 2329.
- [10] D. Vuillaume, *Appl. Phys. Lett.* 59 (1991) 3118.
- [11] D.J. DiMaria, private communication.
- [12] A. Bravaix, D. Vuillaume, V. Thirion, A. Straboni and M. Haond, in: *Proc. ESSDERC'94*, ed. C. Hill and P. Ashburn (Edition Frontières, Gif-sur-Yvette, 1994) p. 317.
- [13] D.J. DiMaria and J. Stathis, *J. Appl. Phys.* 70 (1991) 1500.

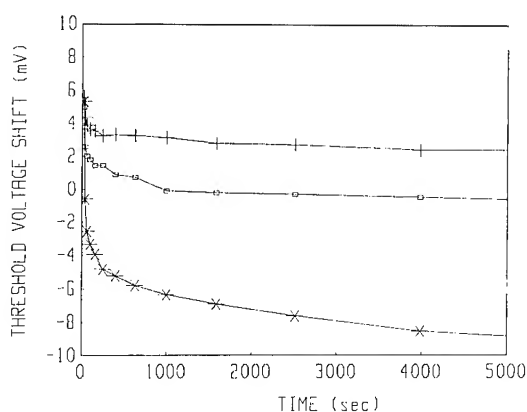


Fig. 4 Detrapping experiments: threshold voltage shift versus detrapping time for various detrapping oxide fields: +, 4 MV/cm; □, 6 MV/cm; *, 8 MV/cm. Lines are drawn as guides for the eye.



ELSEVIER

Journal of Non-Crystalline Solids 187 (1995) 369–373

JOURNAL OF
NON-CRYSTALLINE SOLIDS

Characterization of thin nitrided oxide layers using high spatial resolution transmission electron energy loss spectrometry

C. Bernardi^{a,b,*}, C. d'Anterrockes^b

^a Philips Electron Optics, 22, av. Descartes, BP 45, 94454 Limeil Brevannes cédex, France

^b France Telecom-CNET, 28 Chemin du Vieux Chêne, BP 98, F38243 Meylan cédex, France

Abstract

Nitrided gate oxide layers have been characterized using electron energy loss spectroscopy coupled with a field emission gun electron microscope. It is demonstrated that quantitative analysis of nitrogen is possible with a high analytical spatial resolution of the order of 1 nm. A profile of the nitrogen distribution from the Si/(nitrided oxide) interface to the surface has been obtained.

1. Introduction

Characterization methods that address both sequential materials processing and device performance issues at the nanometer scale are of fundamental interest. Future 0.35 and 0.25 μm metal-oxide-semiconductor field effect transistor technologies require reductions of the lateral and consequently the vertical dimensions of devices. In particular the introduction of thin gate oxides with thicknesses below 10 nm has required new developments which necessitates nitrided gate oxides. Such layers are very attractive because of their excellent barrier properties to various contaminants and dopants and for their good resistance under electrical stress. The electrical properties as well as the chemical structure vary strongly with the nitrogen distribution which depends upon the technological

process. However, more fundamental properties such as the interface states and chemical bonding near the SiO_2/Si interface cannot be fully explained on the basis of electrical measurements alone. It is therefore of crucial importance to be able to characterize such layers, and more particularly to quantify nitrogen incorporation with a high spatial resolution. For this purpose we are currently investigating the potential of parallel electron energy loss spectroscopy (PEELS), in which one studies the energy distribution of 'fast' electrons after interaction with a sample. Inelastic scattering of the incident beam caused by the inner shell electrons of atoms produces edges in the energy loss spectrum corresponding to the core loss edges, characteristic for the material present in the beam. It is therefore possible to obtain detailed chemical, structural and electronic data from the irradiated volume. The spatial resolution of this technique is directly linked to the excitation volume, which is determined by the probe size. A field emission gun transmission electron microscope (FEG-TEM), besides being

* Corresponding author. Tel: +33 76 76 42 20. Telefax: +33 76 76 43 79. E-mail: cecile.bernardi@cns.cnet.fr.

a high resolution tool, is capable of generating very small electron probes (< 1 nm) so that, when equipped with a PEELS spectrometer, it becomes a powerful instrument to measure these atomic profiles. Furthermore, EELS is the only technique capable of analyzing light elements at the nanometer level with the required speed. There have been few reports on nitrided oxide characterization making use of this technique [1]. In this paper the first qualitative results obtained on a thin nitrided oxide layer are presented.

2. Experimental details

2.1. Samples

The specimen analysed for this study was a 16 nm thick full wafer (measured using high resolution electron microscopy) silicon dioxide layer thermally grown in dry O_2 at atmospheric pressure and $925^\circ C$ on a silicon (100) substrate. The oxide was then nitrided by rapid thermal nitridation (RTN) at $1150^\circ C$ for 60 s under an atmospheric pressure of ammonia. The sample was studied in cross-section close to the $[011]$ zone axis. Specimen preparation for TEM observation and PEELS analysis was as follows: first the wafer was sliced into rectangular strips (2×3 mm²), then two strips were bounded together by their oxidized surfaces. Subsequently, the specimen was mechanically ground and finally argon ion milled. The final thickness of the specimen is typically ≈ 30 nm. A cross-sectional high resolution view is shown in Fig. 1. As can be observed, the film is relatively regular and the Si/(nitrided oxide) interface atomically flat.

2.2. Equipment and experimental conditions

The first experiment was performed on a Philips CM200 SuperTWIN FEG microscope operating at 200 kV. The measured probe size was 0.7 nm FWHM (full width at half maximum) and 1.5 nm FWTM (full width at tenth maximum) (measured with a slow scan CCD camera) and the corresponding beam current and convergence half-angle were respectively 90 pA and 7 mrad. The second profile was acquired on a Philips CM20 FEG TWIN operated at 160 kV. The estimated probe size was 1 nm

and the beam current and convergence half-angle were respectively below 50 pA and 5 mrad. Both microscopes were operated in the nanoprobe mode with the extraction voltage of the Schottky emitter set at 4.5 kV and a 30 μm condenser aperture. The parallel electron energy loss spectrometer is a Gatan model 666. In order to maximize the acceptance half angle, without compromising too much the energy resolution, spectrum acquisition was done using the 3 mm spectrometer aperture combined with the shortest camera length. Under these conditions the acceptance half angles were 15.2 and 10.4 mrad, respectively, for the CM 200 and CM 20. The PEELS energy resolution, according to experimental conditions, is about 1.5 eV measured with an energy dispersion of 0.5 eV/channel. Quantitative EELS nanoanalysis was obtained with the ELP/2.1 Gatan software. All PEELS spectra are acquired in diffraction mode and in specimen areas thin enough so as to meet the single scattering criterion which stipulates that the first plasmon to zero loss intensity ratio must be less than 0.2 [3]. The exact focus of the beam was checked in the shadow image of the transmitted beam. A liquid nitrogen cooled specimen holder was used to minimize specimen contamination build up and local specimen heating. Auger electron profiling was performed on the same sample using a Riber MP 2000 microp profiler. The experiment was carried out using a 3 keV, 5 μA electron beam and for the sputtering a 2.5 keV, 10 nA argon ion beam was used.

3. Results and discussion

3.1. Quantitative analysis

The layer composition was determined quantitatively using the core loss edges of oxygen and nitrogen. Fig. 2 shows typical spectra obtained at the interface Si/(nitrided oxide) and in the middle of the nitrided oxide. The K-shell ionization energies of oxygen and nitrogen are at 532 eV and 401 eV, respectively. The nitrogen to oxygen atomic concentration ratio is given by

$$N_N/N_O = [I_N(\Delta, \beta) \times \sigma_O(\Delta, \beta)] / [I_O(\Delta, \beta) \times \sigma_N(\Delta, \beta)], \quad (1)$$

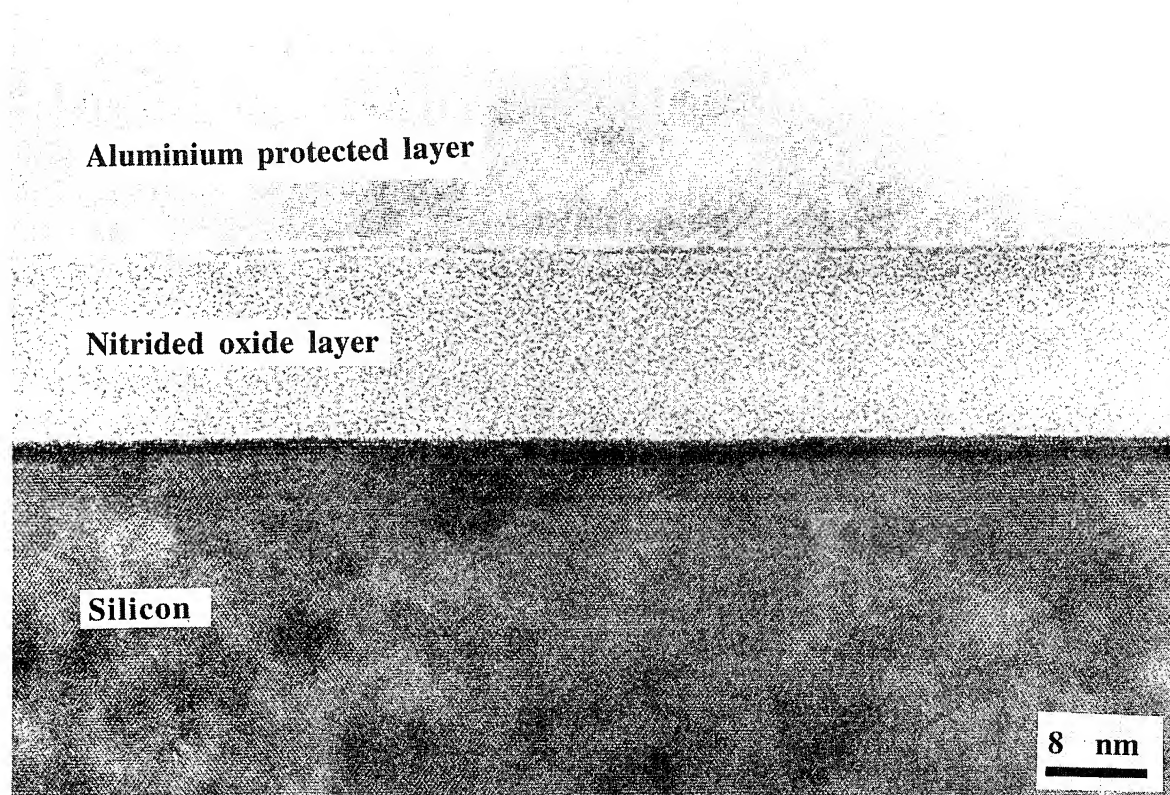


Fig. 1. Cross-sectional high resolution electron microscopy image of the 16 nm nitride oxide film on the Si (0 1 1) surface viewed along the [0 1 1] axis. As one can see, the film is relatively regular and the Si/(nitrided oxide) interface atomically flat.

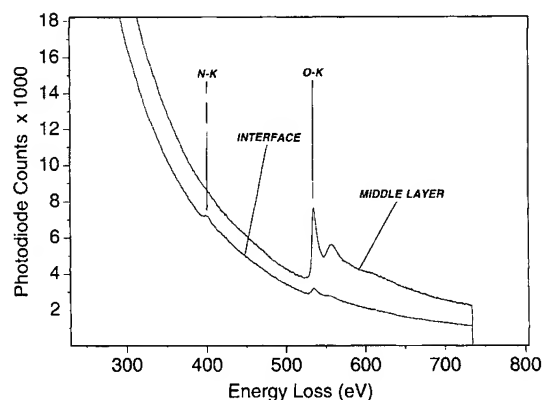


Fig. 2. Typical PEELS spectrum obtained (with the CM 200) at the interface Si/(nitrided oxide) and in the middle of the nitrided oxide.

where $I_x(\Delta, \beta)$ is the edge integral extracted directly from the acquired spectrum after removal of the background using the power law fitting. $\sigma_x(\Delta, \beta)$ is the partial cross-section, calculated analytically with the Sigma K program [2], which is based on a hydrogenic model and the partial cross-section for the K shell. Δ, β are, respectively, the energy window for the integration and the spectrometer acceptance angle. The accuracy of such a determination is a function of many different parameters. It is important to note that an EELS quantitation does not yield a unique result, because the size of the energy window Δ can be chosen arbitrarily during the data reduction process. However, for spectra where plural scattering is not severe (first plasmon to zero loss intensity ratio

< 0.2) and where the energy window is larger than 50 eV, the final results are independent of the choice of Δ within about 5% [3]. With this proviso the accuracy of the quantitation is governed by three factors: the statistical quality of the spectrum, the accuracy of the cross section model, and the specimen and electron-optical parameters. In the literature, the accuracy is estimated to be about 10%.

3.2. Profiles

The first nitrogen profile was generated by manually shifting the beam in regular steps across the oxide layer. This procedure, although sufficiently accurate for this example, has been replaced for the second profile by an automatic beam shift procedure using the microscope's remote control facility. This will enhance both resolution and reproducibility of the steps and will be indispensable for thinner oxides. The absolute distance scale of the profiles is established via the structural composition of the material, since oxygen is a perfect trigger to determine the exact extent of the oxide layer. The two PEELS profiles yield similar quantitative results (Fig. 3) which proves the reproducibility of the experiment. There are no significant differences between 160 and 200 kV, except that at 200 kV the signal to noise ratio is improved and consequently the sensitivity and accuracy of the experiment [4]. 200 kV is also to be preferred because the mean free path of the electrons is larger and this will improve the 'transparency' of the sample, reducing multiple scattering. Finally the step size of the automatic beam shift procedure can be further reduced by a factor five, this will enable thinner gate oxides to be analysed with a satisfactory spatial resolution.

3.3. Auger-PEELS comparison

Auger profiling was performed by sequential sputtering and analysis, process which may be troublesome if atom recoil and diffusion occurs. Furthermore, the Auger signal is a sum of different depth contributions due to the fact that the escape depth of the Auger electron is finite. This induces an effective modification of the concentration profile. Consequently the PEELS results are compared

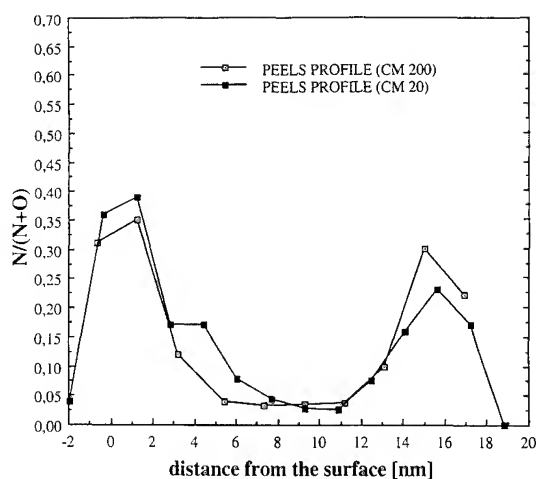


Fig. 3. Comparison between the PEELS profiles obtained with the CM 200 and CM 20 microscopes. Lines are drawn as guides for the eye.

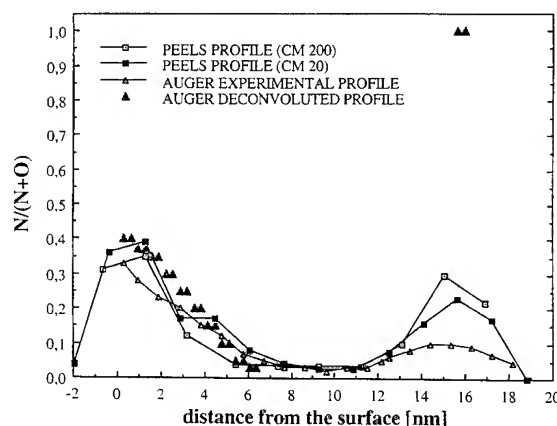


Fig. 4. Comparison between PEELS and Auger experimental profiles and the corresponding deconvoluted Auger profile. Lines are drawn as guides for the eye.

with a depth sputtered Auger profile which has been adjusted using a sequential sputtering model allowing a more realistic nitrogen distribution to be determined [5].

Comparison between the PEELS profiles and the experimental and deconvoluted Auger profiles (Fig. 4) clearly shows that the quantitative results near the surface obtained are very similar. Concerning the interface, experimental nitrogen profiles appear broader by both techniques than they

actually are. The probe used in the PEELS experiment has a finite size so that averaging effects will broaden the profile to some extent in a similar way one observes in Auger profile. In the case of the PEELS, deconvolution of the probe size requires further evaluation. However PEELS yields a more precise characterization of the interface because it does not suffer from the of uncertainties generated by the Auger deconvolution process. In particular, the Auger electron escape depth is much larger than the PEELS beam diameter so that the profiling errors induced in Auger analysis should be more significant.

4. Conclusion

This work has demonstrated that quantitative nitrogen profiles can be acquired on a 16 nm thick RTN nitrated oxide using EELS. The previously observed nitrogen segregation at the surface and at the interface has been confirmed with a spatial resolution in order of 1 nm. Improvement of the experimental conditions such as reduction of the step size of the automatic beam shift procedure and

the use of smaller probes (0.6 nm) will enable thinner gate oxides to be analyzed with an adequate spatial resolution.

The authors wish to thank Philips Electron Optics France for their financial support. The experiment with the CM200 FEG microscope was performed at the Philips Electron Optics Applications laboratory (Eindhoven). They particularly acknowledge Dr E. Van Cappellen for his active contribution to the experiment and the helpful discussions. They also thank Professor R.A.B. Devine and Professor J.L. Buevoz for their assistance and critical reading of the manuscript.

References

- [1] H. Fukuda, M. Yasuda, T. Iwabuchi and S. Ohno, *Appl. Surf. Sci.* 60&61 (1992) 359.
- [2] R.F. Egerton, *Electron Energy Loss Spectroscopy in the Electron Microscope* (Plenum, New York, 1986).
- [3] D.C. Joy and D.M. Maher, *J. Microsc.* 124 (1981) 37.
- [4] D.C. Joy and D.M. Maher, *Ultramicroscopy* 5 (1980) 333.
- [5] K. Barla, D. Nicolas, R. Pantel, B. Villermoz, A. Straboni and Y. Caratini, *J. Appl. Phys.* 68 (1990) 3635.



ELSEVIER

Journal of Non-Crystalline Solids 187 (1995) 374–379

JOURNAL OF
NON-CRYSTALLINE SOLIDS

A comparison of Si–SiO₂ interface trap properties in thin-film transistors with thermal and plasma nitrided oxides

Jean-Luc Autran^{a,*}, Carole Plossu^a, Frédéric Seigneur^a, Bernard Balland^a,
Alain Straboni^b

^a *Laboratoire de Physique de la Matière, URA CNRS 358, bâtiment 502, Institut National des Sciences Appliquées de Lyon, 20 avenue Albert Einstein, 69621 Villeurbanne cédex, France*

^b *Centre National d'Etudes des Télécommunications, 28 chemin du Vieux Chêne, BP 98, 38243 Meylan cédex, France*

Abstract

In this work, electrical properties of the Si–SiO₂ interface have been investigated in terms of interface-trap parameters (emission time, capture cross-section, state density) by standard and three-level charge pumping techniques in n-channel thin-film (8 nm) metal-oxide-semiconductor field-effect transistors. Some of the devices have been nitrided in an ammonia plasma reactor and reoxidized in oxygen. For nitrided devices, a significant decrease of interface state density, D_{it} , has been observed as compared with pure oxide devices. This reduction clearly corresponds to both an uniform decrease of D_{it} over the silicon band gap and a decrease of a D_{it} peak in the upper part of the band gap. The evolution of capture cross-sections has been also monitored and found to significantly vary for electron traps. This substantial change in electron interface-trap properties could be at the origin of the augmentation of the high field transconductance observed for these n-channel devices after such a nitridation process.

1. Introduction

Nitridation of thermally grown SiO₂ thin films has been extensively investigated in recent years and shown to improve several critical properties of the dielectric as compared to pure oxide [1–6]. Many studies have concluded that the incorporation of nitrogen at the Si/SiO₂ interface leads to modification of the electronic properties of the traps in the oxide bulk [7,8] and in the interfacial

region and is responsible for variation of electron and hole mobilities [9,10] in the channel. In the case of a low pressure plasma nitridation process in NH₃, a change in D_{it} has been previously reported [11–13] and it has been found that this nitridation process induces an increase of the electron mobility in the case of n-channel devices without significant attenuation of the hole mobility for p-channel devices [14]. In this work, we present a detailed comparison of the electrical properties of interface traps investigated by three-level charge pumping [15] and by standard charge pumping analysis [16] in micrometer n-channel metal-oxide semiconductor field-effect transistors (MOSFETs) with pure and

* Corresponding author. Tel: +33 72 43 87 33. Telefax: +33 72 43 85 31. E-mail: autran@insa.insa-lyon.fr.

plasma nitrided gate oxides. High and low field transconductances have been also investigated and found to vary in excellent agreement with the change in interface-trap properties induced by nitridation.

2. Experimental procedure

2.1. Device fabrication

The devices were fabricated at CNET/CNS (Meylan) using a 0.35 μm CMOS technology with low pressure plasma enhanced nitridation in an ammonia plasma URANOS reactor [17]. The ammonia plasma (70 μbar pressure) is generated using a 600 W external capacitive coupling of a 13.56 MHz generator. Measurements were performed on n-channel MOSFETs with a lightly doped drain (LDD) and a channel length of 1 μm . The gate area (100 μm^2) was chosen to perform both capacitance and charge pumping measurements on the same devices. Two categories of devices were studied; category PO refers to pure thermal gate oxide which was grown at 925°C in dry oxygen at atmospheric pressure. Category NO refers to the same oxide which was nitrided in the ammonia plasma for 15 min at 950°C and re-oxidized in oxygen at 950°C for 10 min.

2.2. Techniques

In three-level charge pumping (3CP) [15,18–21], a three-level pulse is applied to the MOSFET gate. The intermediate level is used to select interface traps which are involved at each charge pumping cycle; the charge pumping current is measured at the substrate by an electrometer. By varying, respectively, the duration t_3 and the voltage V_3 of the intermediate level (see the inset of Fig. 3), it is possible to select independently an emission time window and an energy window in the silicon band gap for studying the electrical response of the traps in emission or capture regimes. The 3CP instrumentation and the new acquisition procedure used in this work have been proposed recently and detailed elsewhere [20,21]. Briefly, it is based on the use of a high performance arbitrary function generator

and a Keithley 617 electrometer driven by a computer. The main characteristics of this 3CP station are: time resolution 5 ns; voltage step 12 mV; current sensitivity 0.1 fA. In order to calculate the energy distribution of interface-trap parameters and because emission times and D_{it} are sensitive functions of interface-trap energy position, one must carefully determine the experimental relationship between the gate voltage V_G and the surface potential Φ_s . A preliminary capacitance–voltage (C – V) study is then directly made on the MOSFET under test. C – V data are extracted from a static charge–voltage measurement performed on the gate–substrate capacitor with the source and the drain shorted to the substrate [22]. Berglund's method is used to evaluate the $\Phi_s(V_G)$ relationship from the experimental C – V curve so obtained [23]. A detailed description of this method and of the measurement setup is made in Ref. [21].

3. Results and discussion

The variations of the charge pumping current I_{cp} with the low level V_{gl} of a square-wave signal applied to the gate are shown in Fig. 1 for both pure and nitrided oxide. As is well known [15], the shape of the maximum of the $I_{cp}(V_{gl})$ curve reflects the variation of D_{it} along the MOSFET channel. Fig. 1 shows that the maximum (I_{cp} plateau) of the characteristics is directly affected by the nitridation which induces a uniform decrease of I_{cp} in the case of NO devices as compared to PO devices: this decrease corresponds to a uniform reduction of D_{it} for NO devices. As can be seen in the figure, a positive shift of the rising edge of the curve labeled 'nitrided oxide' is observed with respect to the curve 'pure oxide'. This shift is certainly due to a creation of negative charge in the oxide after nitridation and not to the fact that interface traps are non-uniformly distributed along the channel of the devices. Fig. 2 shows the variation of the recombined charge per cycle $Q_{it} = I_{cp}/f$ (f is the frequency of the gate signal) with the intermediate duration t_3 as measured for various intermediate levels V_3 (NO devices). As shown in Fig. 2, emission times of the traps can be extracted from $Q_{it}(V_3, t_3)$

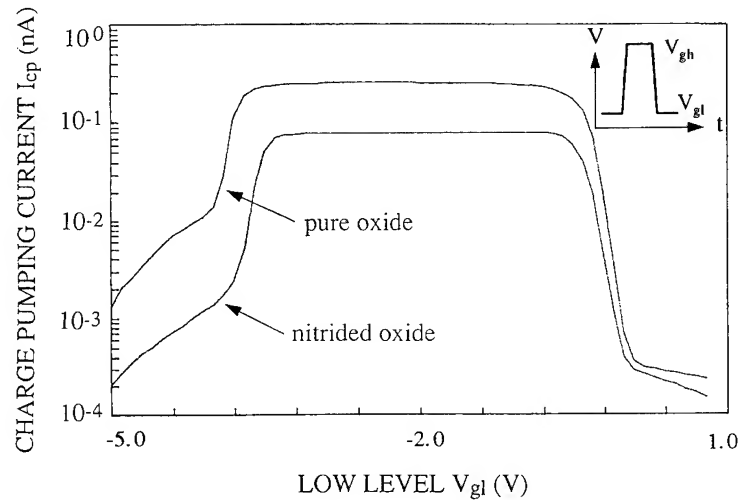


Fig. 1. Charge pumping current I_{cp} as a function of the low level V_{gl} of the gate pulse for devices with a pure gate oxide and a nitrided gate oxide.

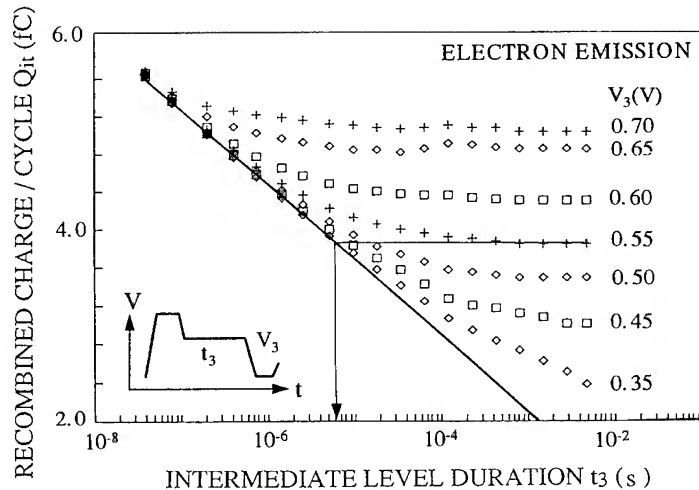


Fig. 2. Recombined charge per cycle Q_{it} as a function of gate pulse third level parameters t_3 and V_3 in the electron emission regime for NO devices. Inset: Schematic of the gate voltage waveform used in the 3CP experiment.

data by a graphic construction for each value of V_3 and also for the corresponding energy trap level in the silicon band gap [14]. The energy dependence of electron and hole emission times is displayed in Fig. 3(a) for both PO and NO devices. Note the difference of slope between the two distributions for electron traps in the upper part of the band gap: about 38 V^{-1} for NO structures and

24 V^{-1} for PO structures (38 V^{-1} for holes traps in the lower part of the band gap for both categories of devices). From the Shockley–Read–Hall (SRH) formalism [23] used for the calculation of the capture cross-sections σ , a slope of q/kT (38 V^{-1} at $T = 300 \text{ K}$) corresponds to cross-sections independent of the trap level energy [15]. Fig. 3(b) shows that hole-trap cross-sections are

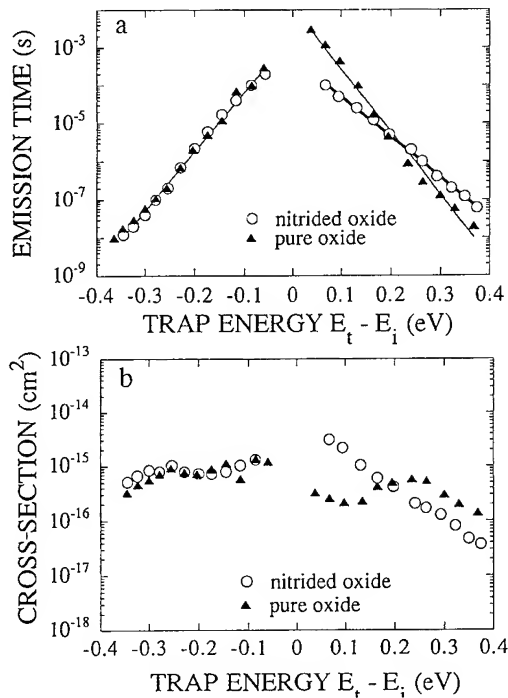


Fig. 3. Energy distributions of electron and hole emission times (a) capture cross-sections (b) in the silicon band gap for devices with pure gate oxide and nitrided gate oxide. (Lines are guides to the eye only.)

approximately the same for NO and PO devices and vary weakly with energy (mean value about $8 \times 10^{-16} \text{ cm}^2$). On the other hand, $\sigma(E)$ distributions are very different for electron traps: the variation of σ with E is weak ($4 \pm 2 \times 10^{-16} \text{ cm}^2$) for PO samples, whereas it is large and exponential (over two decades) for NO samples. By standard charge pumping [16], the geometric mean value of capture cross-sections $\langle \sigma \rangle$ extracted from $Q_{it}(f)$ characteristics for triangular pulses is found equal to $\langle \sigma \rangle = 5 \times 10^{-16} \text{ cm}^2$ for category PO and to $\langle \sigma \rangle = 8 \times 10^{-16} \text{ cm}^2$ for category NO. Note that these values are in reasonable agreement with 3CP data. The change in $\sigma(E)$ distributions may be interpreted as a modification of the nature of electron traps at the Si/SiO₂ interface induced by the nitridation process. Another result in favour of this assumption is given by the energy distributions $D_{it}(E)$ displayed in Fig. 4. These curves have been calculated from $Q_{it}(V_3)$ data for a fixed intermediate level duration $t_3 = 6 \text{ ms}$, which ensures an emission rate of 167 s^{-1} [19]. As can be seen, there is a major difference in the two D_{it} profiles for NO samples as compared to PO samples. Nitridation seems to induce an uniform decrease of D_{it} but also a decrease of a D_{it} peak located at about $E_t + 0.2 \text{ eV}$, as shown by the comparison between

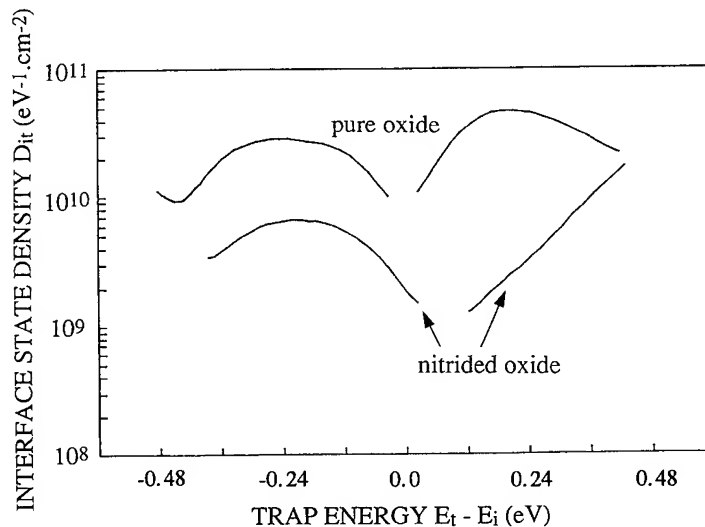


Fig. 4. Energy distributions of the interface state density D_{it} in the silicon band gap for devices with pure gate oxide and nitrided gate oxide ($t_3 = 6 \text{ ms}$).

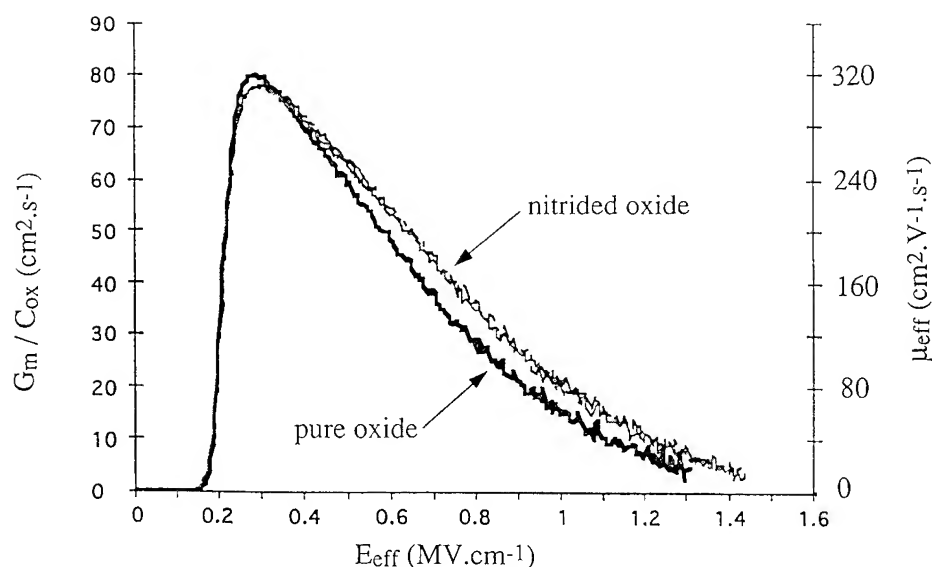


Fig. 5. Variations of the normalized transconductance G_m/C_{ox} with the perpendicular electric field as obtained on pure oxide and nitrided oxide devices ($V_d = 50$ mV).

curves labeled 'nitrided oxide' and 'pure oxide'. Note also the extremely low D_{it} mean levels for both categories of devices: about $3 \times 10^{10} \text{ eV}^{-1} \text{ cm}^{-2}$ for PO devices and $6 \times 10^9 \text{ eV}^{-1} \text{ cm}^{-2}$ for NO devices. The evolution of $D_{it}(E)$ spectra could correspond to a change in the nature of interface electron traps in the upper part of the band gap. This change may be induced by the diffusion of nitrogen species at the interface during the nitridation process [6,8]. Fig. 5 shows the variation of the normalized transconductance G_m/C_{ox} (measured at a drain voltage $V_d = 50$ mV) with the perpendicular electric field E_{eff} in the channel. As shown in this figure, the maximum transconductance is very comparable for both categories of devices: the channel mobility at low electric field is preserved after nitridation which is in favour of an excellent quality of the interface, previously observed by charge pumping. For high electric fields, an increase (about 20%) of the transconductance and so of the channel electron mobility is clearly observed for NO structures as compared to PO structures. This increase of mobility may be related to the decrease of D_{it} in the band gap, especially for electron traps. To our knowledge in the case of n-channel devices, this is the first time

that an improvement in electron transport properties has been correlated with a reduction of the electron interface-trap density after nitridation [12].

4. Conclusion

In summary, the effect of plasma nitridation of thin oxides on electrical properties of the Si/SiO₂ interface has been studied in the case of n-channel MOSFETs by standard and three-level charge pumping. Owing to the great sensitivity of these techniques and to the advantage of the 3CP method in addressing a large part of the band gap on a single device, a significant improvement of the interface state density has been found after nitridation which is more pronounced for electron traps than for holes traps. The evolution of emission trap properties observed in this case may be interpreted as a change in the nature of interface defects induced by nitridation. These results, correlated with the evolution of the transconductance, show that nitridation in an ammonia plasma leads to a decrease of D_{it} in the silicon band gap, which could explain the increase of electron mobility in n-channel devices observed after such treatment.

References

- [1] T. Ito, T. Nakamura and H. Ishikawa, *IEEE Trans. Electron. Devices* ED-29 (1982) 498.
- [2] S.K. Lai, J. Lee and V.K. Dham, *IEDM Proc.* (IEEE, New York, 1983) 190.
- [3] F.L. Terry, R.J. Aucoin, M.L. Naiman and S.D. Senturia, *IEEE Electron Device Lett.* EDL-4 (1983) 191.
- [4] T. Hori, H. Iwasaki, Y. Naito and W.E. Bailey, *IEEE Trans. Electron Devices* ED-34 (1987) 2238.
- [5] G.J. Gunn, R. Jayaraman, W. Yang and C.G. Sodini, *Appl. Phys. Lett.* 52 (1988) 1713.
- [6] P. Debenest, K. Barla, A. Straboni and B. Vuillermoz, *Appl. Surf. Sci.* 36 (1989) 196.
- [7] B. Balland, A. Glachant, J.C. Bureau and C. Plossu, *Thin Solid Films* 190 (1990) 103.
- [8] C. Plossu, F. Seigneur, B. Balland, B. Piot and A. Straboni, *Mater. Res. Soc. Symp. Proc.* 284 (1992) 325.
- [9] T. Hori, Y. Naito, H. Iwasaki and H. Esaki, *IEEE Trans. Electron. Device Lett.* EDL-7 (1986) 669.
- [10] T. Hori and H. Iwasaki, *IEEE Electron Device Lett.* EDL-9 (1988) 168.
- [11] B. Piot, PhD thesis, Joseph Fourier University, Grenoble (1991).
- [12] A. Emrani, G. Ghibaudo, F. Balestra, B. Piot, V. Thirion and A. Straboni, *J. Appl. Phys.* 73 (1993) 5241.
- [13] V. Thirion, PhD thesis, Joseph Fourier University, Grenoble (1994).
- [14] B. Piot, A. Straboni, B. Vuillermoz, K. Barla, M. Berenguer and J.F. Portailier, in: *ESSDERC Proc.*, ed. A. Heuberger, H. Ryssel and P. Lange (Springer, Berlin, 1989) p. 366.
- [15] N.S. Saks and M.G. Ancona, *IEEE Electron Device Lett.* 11 (1990) 339.
- [16] G. Groeseneken, H.E. Maes, N. Beltran, and R.F. De Keersmaecker, *IEEE Trans. Electron Devices* 31 (1984) 42.
- [17] M. Berenguer, A. Straboni and B. Vuillermoz, European patent EP0142450 (1984).
- [18] N.S. Saks and M.G. Ancona, *J. Appl. Phys.* 71 (1992) 4415.
- [19] J.L. Autran, F. Seigneur, C. Plossu and B. Balland, *J. Appl. Phys.* 74 (1993) 3932.
- [20] J.L. Autran and B. Balland, *Rev. Sci. Instrum.* 65 (1994) 2141.
- [21] J.L. Autran, PhD thesis, Institut National des Sciences Appliquées, Lyon (1994).
- [22] N.S. Saks, *J. Appl. Phys.* 74 (1993) 3303.
- [23] E. Klausmann, W.R. Fahmer and D. Brauning, in: *Instabilities in Silicon Devices*, ed. G. Borbottin and A. Vapaille (Elsevier, Amsterdam, 1989) ch. 12.



ELSEVIER

Journal of Non-Crystalline Solids 187 (1995) 380–384

JOURNAL OF
NON-CRYSTALLINE SOLIDS

Structural and optical properties of nitrided silicon oxide layers rapid thermally grown in a pure N_2O ambient

E. Hartmannsgruber^{a,*}, U. Rossow^b, A. Hoyer^a, P. Lange^a

^a *Fraunhofer-Institut für Siliziumtechnologie, Dillenburger Str. 53, 14199 Berlin, Germany*

^b *Institut für Festkörperphysik der TU Berlin, Sekr. PN6-1, Hardenbergstr. 36, 10623 Berlin, Germany*

Abstract

Thin nitrided silicon oxide layers with thicknesses in the 3–12 nm range were grown in a rapid thermal processor in a pure N_2O ambient. These layers were investigated by X-ray photoelectron spectroscopy, spectroscopic ellipsometry and wet etching experiments and compared with oxides grown in a O_2 ambient. Information about the distribution and binding properties of nitrogen in the oxide and its interfacial properties are provided. The nitrogen concentration peaks at the interface and decreases towards the oxide bulk to an extent of approximately 5 nm for a film thickness of 9 nm. Compared with O_2 grown oxides, the nitrided oxides show an enhanced saturation of Si-dangling bonds by nitrogen and a reduction of the suboxide regime. These facts may explain the up to now reported improved electrical performance of metal oxide semiconductor devices using N_2O grown oxides as the gate dielectric.

1. Introduction

Thin nitrided silicon oxide layers rapid thermally grown in a N_2O ambient either directly on silicon or on a pregrown SiO_2 film on silicon have attracted much attention recently. Their application as gate dielectrics in the complementary metal oxide semiconductor (CMOS) technology promise a better performance of ultra-large-scale integrated (ULSI) devices when gate oxide thicknesses below 10 nm are required. Compared with conventional oxides the N_2O grown dielectrics profit from the benefits of nitrogen incorporation into SiO_2 such

as an increase of the dielectric strength and an enhanced resistance against hot carrier stress as well as impurity penetration [1–4] without suffering from the problems related to hydrogen incorporation occurring from NH_3 thermal nitridation [5].

Nevertheless, up to now the mechanisms of nitrogen incorporation into N_2O grown oxides have not been completely understood and therefore also the physical properties of these dielectrics have to be examined. Of significant interest is the structure of the Si/SiO_xN_y interfacial region, which is assumed to be particularly responsible for the resulting electrical properties of MOS devices. Most work which has been done in this field was focussed on concentration depth profiling of the incorporated nitrogen as obtained from secondary ion mass spectroscopy (SIMS) [2,4,6], Auger electron

* Corresponding author. Tel: +49-30 8299 8431. Telefax: +49-30 8299 8199.

spectroscopy (AES) [1,7], elastic recoil detection (ERD) [7], and X-ray photoelectron spectroscopy (XPS) [8]. Results showed that the nitrogen is mainly located at the Si/SiO_xN_y interface with a concentration of a few at.%, which decreases towards the oxide bulk. The structural arrangement in the bulk of N₂O grown and conventionally grown oxides was found to be almost identical by Fourier transform infrared (FTIR) spectroscopy [9]. Chemical analysis of XPS [8] and FTIR [9] spectra showed the formation of SiN bonds to be much more likely than that of NO bonds.

The goal of this work is the presentation of new results concerning the incorporation of nitrogen at the interface and in the bulk of the oxide. The distribution of nitrogen was obtained from XPS and wet chemical etch rate measurements. Results from spectroscopic ellipsometry (SE) in the visible and UV spectral region will be discussed with respect to the extent and structure of the interfacial transition region of N₂O grown as compared to O₂ grown oxides. For these investigations we prepared N₂O oxide samples with a relative high nitrogen content by directly oxidizing silicon substrates in a pure N₂O ambient in a RTP reactor. For comparison, non-nitrided oxides were grown in a pure O₂ ambient in the same reactor.

2. Experimental procedure

The RTP system (AST 100) is equipped with 21 tungsten halogen lamps for both sides illumination of single wafers with a 100 mm diameter lying inside a cold-wall quartz reactor. This arrangement is surrounded by a highly reflective gold-plated process chamber. The temperature is monitored by a pyrometer with a sensitivity maximum at 2.7 μm . An additional silicon reflection ring is placed around the wafer to enhance the temperature uniformity across the wafer. More details of the RTP equipment have been given in Ref. [9]. The silicon substrates used were n-type, phosphorous-doped with a resistivity of 1–3 Ωcm and $\langle 100 \rangle$ orientation. They were transferred from the storage box to the reactor without any precleaning procedure to avoid surface roughening which might result from

native oxide etching. Thin layers with thicknesses in the 2–12 nm range were grown either in a pure N₂O ambient (RTON) or, for comparison, in a pure O₂ ambient (RTO) at 1150°C. The gas flow was parallel to the wafer surface with a rate adjusted to 5 l/min in both cases.

A single wavelength ellipsometer (SWE) equipped with a He–Ne laser (632.8 nm) was used to determine the layer thicknesses directly after growth and the wet chemical etch rates of RTON and RTO samples in a highly diluted (about 1 : 100) HF:H₂O solution. The refractive index used was fixed to a value of 1.475 assuming a SiO₂ bulk layer, which is thinner than 20 nm [10]. In addition, a spectroscopic ellipsometer with rotating analyzer was used in the spectral range 1.8–5.5 eV. In this case the raw data were converted into an effective dielectric function $\langle \epsilon \rangle$ [11,12] which describes the effective response of the oxide layer and the silicon substrate. For the interpretation of the measured $\langle \epsilon \rangle$ modelling is necessary. For a single layer on a substrate a so-called three-phase model is appropriate [12]. In this model the three phases are vacuum, layer and substrate, assuming no interfacial layer. An effective dielectric function can be calculated with the well-known dielectric function of silicon [11] and that of the layer as well as the layer thickness as input. As a layer dielectric function that of SiO₂ [13] was used for the non-nitrided as well as the nitrided oxides. This serves as a good approximation since the nitrogen content in the RTON samples is small (lower than 5 at.%, see below) and the optical gaps of an amorphous SiO_xN_y compound are in the UV above 5.5 eV. Deviations between the measured and calculated effective dielectric function must be correlated for the interfacial or layer properties and can be compared between RTON and RTO samples.

XPS spectra were recorded using a commercially available XPS system (VG ESCALAB) using Al K α radiation (1486.6 eV) and a hemispherical photoelectron energy analyser. From the Si 2p, N 1s and O 1s core level peaks the binding energy and the concentration of these elements were derived. For concentration depth profiling argon ion sputtering was used.

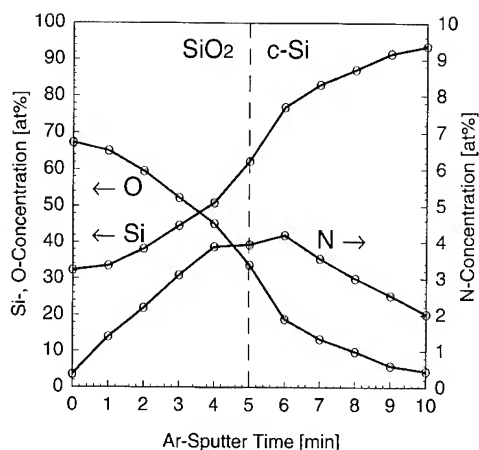


Fig. 1. XPS depth profile of an N_2O oxide layer with 10 nm thickness with the concentrations in at.% of silicon, oxygen, and nitrogen. The Si/SiO_xN_y interface is indicated by the dashed line. The solid lines are drawn as guides for the eye.

3. Results and discussion

3.1. XPS measurements

A great deal of spectroscopic data for N_2O oxides addressing the concentration of nitrogen at the interface, bulk and surface has been published. However, recently a discrepancy in the atomic percentage of interfacial nitrogen was reported [6]. For the purposes of comparison, we would like to discuss very briefly the XPS results that we obtained on our samples. From the depth profiles for a RTON sample of 10 nm thickness a nitrogen concentration of about 4 at.% at the interface was determined with decreasing concentration towards the bulk of the oxide (Fig. 1). This result corresponds well to that reported in Ref. [8]. According to the suggestions made therein for an evaluation of the measured binding energies we obtained 295.0 eV for the Si 2p (oxide) and N 1s peak separation and 429.4 eV for the Si 2p (oxide) and O 1s peak separation indicating that the nitrogen is solely bonded to silicon and not to oxygen. Depth profiling of the binding energies was not performed since argon ion sputtering induces damage of the chemical environment. The depth resolution of XPS for concentration profiling is restricted to

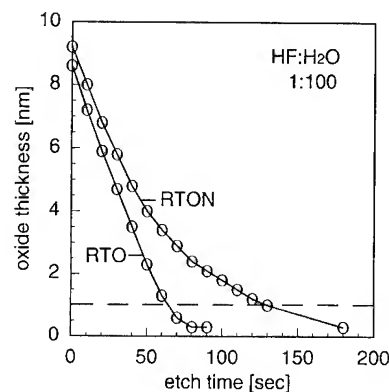


Fig. 2. Oxide thickness as a function of etching time in highly diluted HF. The dashed line indicates the region where the measurement is effected by the growth of native oxide. The solid lines are drawn as guides for the eye.

3–4 nm due to the escape depth of the photoelectrons and sidewall effects of the sputtered crater.

3.2. Wet etch experiments

A more exact estimate of the extent of the nitrogen containing region is provided by the measurement of the wet chemical etch rate of the layer. This method is based on the fact that SiO_2 can easily be removed by HF while the etch rate for Si_3N_4 is rather low. Therefore, regions with a higher nitrogen content etch slower in HF than those with a lower nitrogen concentration [14]. Fig. 2 shows the measured film thickness over the etching time in highly diluted HF for a RTON and, for comparison, for a RTO sample of nearly the same original thickness. In contrast to the constant etch rate of the RTO sample we observed for the RTON sample a more or less continuous etch rate reduction. The onset of this effect is observable roughly 5 nm above the interface. Below this thickness a decrease of the slope of the curve takes place indicating an increasing amount of incorporated nitrogen. However, a quantification of the nitrogen content from this measurement appears difficult, because nitrogen-induced network relaxation effects can also contribute to the etch rate reduction. Nevertheless, it becomes clear that this method is very

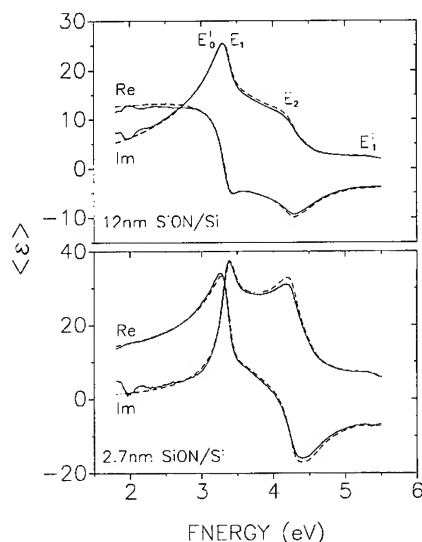


Fig. 3. Energy dependence of the effective dielectric function $\langle \epsilon \rangle$ for a 12 and a 2.7 nm layer of N_2O grown oxide. The dashed lines indicate the calculated spectra.

effective to estimate the spatial extent of the nitrogen containing region.

3.3. SE measurements

Finally, information about the electronic properties of the interface can be provided by applying spectroscopic ellipsometry as a non-destructive method. In Fig. 3 the energy dependence of the effective dielectric function $\langle \epsilon \rangle$ for a 12 and a 2.7 nm thick layer is displayed. The dashed lines represent the simulated spectra. The fundamental transitions are also indicated. The three-phase model fits very well the experimental spectra of both samples, although some deviations appear, which increase with decreasing layer thickness. This effect was also reported for conventionally grown SiO_2 films [15] where the observed deviations were attributed to interfacial properties, which are of course more effective with decreasing layer thickness. To estimate any differences in this regard between nitrided and non-nitrided oxides a series of both oxide types with thicknesses below 10 nm was measured. For all measured samples modelling was performed and these data were

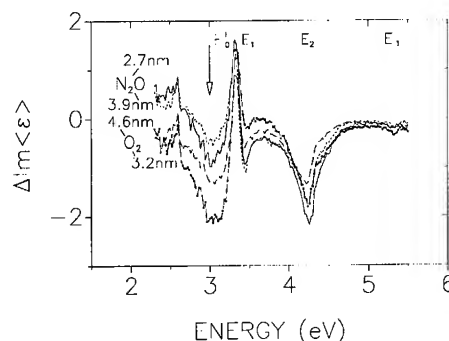


Fig. 4. Difference spectra of the imaginary part of the effective dielectric function $\Delta \text{Im} \langle \epsilon \rangle$ as a function of energy for N_2O grown oxides (2.7 nm solid line, 3.9 nm dashed line) and O_2 grown oxides (3.2 nm dotted dashed line and 4.6 nm dashed line).

subtracted from the experimental ones. Fig. 4 shows the difference in the imaginary part of the effective dielectric function $\Delta \text{Im} \langle \epsilon \rangle$ as a function of energy for two N_2O and two O_2 grown oxides. In this figure three distinct features are observable, at the E_2 -gap, at the E'_0 , E_1 -gap, and in the region around 3 eV. The two first-named features are of the same order of magnitude for all samples and can therefore not be related to the incorporated nitrogen in the RTON samples. A deviation at the E_2 -gap can be attributed to the surface roughness of silicon at the interface to the oxide [16] and a deviation at the E'_0 , E_1 -gap may be caused by a change of the silicon bulk properties.

By contrast, the peak located around 3 eV observed in Fig. 4 shows a strong dependence on the layer thickness and on the type of growth process. Since the only difference between RTON and RTO samples is the nitrogen appearance in the former this feature must be effected by the incorporated nitrogen. The smallest deviations at 3 eV in Fig. 4 are appearing for the nitrided samples. Since a good fit for RTON was obtained with the properties of SiO_2 and no consideration of nitrogen, it is most likely that no nitrogen-related transitions can contribute significantly to the spectrum. This assumption is also supported by the fact that the optical gap of an amorphous Si_3N_4 layer is in the UV region above 5.5 eV. If there is a deviation at 3 eV occurring, the question for the nature of these

transitions appears. It has been reported [17–19] that the saturation of Si-dangling bonds by arsenic and hydrogen leads to a bulk termination of silicon. This means that the silicon states at the surface resemble much more those in the silicon bulk than in the case of a clean surface. Consequently, the dielectric function of a clean surface differs from that where the dangling bonds are saturated. We are convinced that a similar effect occurs for the system under investigation. The nitrogen at the interface is saturating Si-dangling bonds and leads to a bulk termination of silicon. The remaining small deviations between fit and experimental data are due to the remaining non-saturated Si-dangling bonds. In turn, the larger deviations appearing for the RTO samples are reflecting an increased number of dangling bonds.

If the interfacial region, which contains the dangling bonds, is viewed as a transition region, which contains also Si_xO_y suboxides, additional arguments for the explanation above can be provided. SiO , one species of the possible Si_xO_y suboxides has a band gap around 3 eV, thus optical transitions at this energy may contribute to this spectrum. From the magnitude of deviations in the spectra, it can be concluded that in the case of nitrated oxides this suboxide containing interlayer is reduced.

4. Conclusion

From the results reported we conclude that the extent of the interfacial transition regime, which is mainly caused by interface roughness, is very similar for N_2O and O_2 grown oxides. A pronounced Si-dangling bond saturation by nitrogen occurs and the region in which suboxides are formed, however, appears significantly smaller for the N_2O oxides. These findings may contribute to the explanation of the improved electrical performance of N_2O oxides as compared to O_2 oxides. Beyond this, an effective method has been presented to

locate the distribution of nitrogen within the oxide layer by wet chemical etching in highly diluted HF. Furthermore, XPS data were presented which correlate well with the results reported earlier by other research groups.

Part of this work was funded by the CEC Esprit Basic Research action no. 6878 'EASI' and by the JESSI BT1B/ESPRIT 7236 project 'ADEQUAT'.

References

- [1] H. Hwang, W. Ting, D.L. Kwong and J. Lee, IEEE IEDM Tech. Dig. (1990) 421.
- [2] A. Uchiyama, H. Fukuda, T. Hayashi, T. Iwabuchi and S. Ohno, IEEE IEDM Tech. Dig. (1990) 425.
- [3] H. Fukuda, T. Arakawa and S. Ohno, IEEE Trans. Electron Dev. 39 (1992) 127.
- [4] Y. Okada, P.J. Tobin, R.I. Hedge, J. Liao and P. Rushbrook, Appl. Phys. Lett. 61 (1992) 3163.
- [5] T. Hori, T. Yasui and S. Akamatsu, IEEE Trans. Electron Dev. 39 (1992) 134.
- [6] Y. Okada, P.J. Tobin, P. Rushbrook and W.L. DeHart, IEEE Trans. Electron Dev. 41 (1994) 191.
- [7] A.E.T. Kuiper, H.G. Pomp, P.M. Asveld, W. Arnold Bik and F.H.P.M. Habraken, Appl. Phys. Lett. 61 (1992) 1031.
- [8] E.C. Carr and R.A. Buhrman, Appl. Phys. Lett. 63 (1993) 54.
- [9] P. Lange, H. Bernt, E. Hartmannsgruber and F. Naumann, J. Electrochem. Soc. 141 (1994) 259.
- [10] A. Kalnitsky, S.P. Tay, J.P. Ellul, S. Chongsawangvirod, J.W. Andrews and E.A. Irene, J. Electrochem. Soc. 137 (1990) 234.
- [11] D.E. Aspnes and A.A. Studna, Phys. Rev. B27 (1983) 985.
- [12] R.M.A. Azzam, N.M. Bashara, Ellipsometry and Polarized Light (North-Holland, Amsterdam, 1977).
- [13] E.D. Palik, ed., Handbook of Optical Constants of Solids (Academic Press, New York, 1985).
- [14] M.M. Moslehi and K.C. Saraswat, IEEE Trans. Electron Dev. ED-32 (1985) 106.
- [15] E.A. Irene, Thin Solid Films 233 (1993) 96.
- [16] U. Rossow, PhD thesis, TU Berlin (1993).
- [17] U. Rossow, U. Frotscher, W. Richter and D.R.T. Zahn, Surf. Sci. 287&288 (1993) 718.
- [18] M.K. Kelly, S. Zollner and M. Cardona, Surf. Sci. 285 (1993) 282.
- [19] A.B. Müller, U. Rossow, U. Resch and W. Richter, Thin Solid Films 233 (1993) 19.



ELSEVIER

Journal of Non-Crystalline Solids 187 (1995) 385–394

JOURNAL OF
NON-CRYSTALLINE SOLIDS

Section 12. Silicon oxynitride and other dielectrics

Structural identification of point defects in amorphous silicon oxynitrides

Y. Cros*, J. Krautwurm¹*Laboratoire d'Etudes des Propriétés Electroniques des Solides, Associé à l'Université J. Fourier, CNRS, 166X, 25 avenue des Martyrs, 38042 Grenoble cedex, France*

Abstract

The nature and the behaviour of point defects in amorphous hydrogenated silicon oxynitrides $\text{SiO}_x\text{N}_y\text{H}_z$ are reviewed and compared to that in plasma-enhanced chemical vapour deposition silicon dioxide and silicon nitrides. These defects are studied by electron spin resonance measurements after the ESR signal amplitude saturation by VUV illumination. The influences of the chemical composition (atomic ratio $\text{O}/\text{O} + \text{N}$ in the $\text{SiO}_x\text{N}_y\text{H}_z$) and of the hydrogen density on the type and density of defects are investigated. This is achieved by working on usual silicon oxynitrides containing high hydrogen densities (HHD) and on a new family of materials, the low hydrogen densities (LHD) silicon oxynitrides. Two defects are found in LHD silicon oxynitrides, the silicon dangling bond (Si_{db}) and a new type of nitrogen related defect, the N_x defect. By contrast, three defects are found in the usual HHD silicon oxynitrides, the Si_{db} , the nitrogen dangling bond (N_b) and the N_x defect. The N_x defect is described by an axially symmetrical paramagnetic centre with $g_{\parallel} = 2.0030$, $g_{\perp} = 2.0017$, $A_{\text{iso}} = 18.9$ G and $A_{\text{aniso}} = 9.7$ G. Compared to the situation observed in the silicon nitride where the nitrogen defects are only observed after rough treatments, the nitrogen defects are easily detected in the silicon oxynitrides.

1. Introduction

Amorphous silicon nitrides, silicon oxides and silicon oxynitrides films, prepared by plasma deposition, have a large variety of applications in very large scale integrated (VLSI) technology, especially in those cases where a low process temperature is a prerequisite.

We prepared and undertook a detailed investigation of a limited number of silicon oxynitrides with various ratios of oxygen atomic density on the sum of oxygen and nitrogen atomic densities $[\text{O}/(\text{O} + \text{N})]$. The usual silicon oxynitrides $\text{SiO}_x\text{N}_y\text{H}_z$ containing high hydrogen densities (HHD films) were first studied [1,2] and, in order to evaluate the effect of the hydrogen content, a new family of $\text{SiO}_x\text{N}_y\text{H}_z$ containing low hydrogen densities (LHD films) [3] was prepared. The ellipsometry, the high energy ion beam methods and the infrared absorption spectrometry provided a macroscopic description of the layers such as the composition, the thickness and the type of hydrogen bonds in the

* Corresponding author. Tel: +33 76 88 74 52. Telefax: +33 76 88 79 88. E-mail: cros@lepes.polycnrs-gre.fr.

¹ Present address. Institute of Physics, Czech Academy of Sciences, Cukrovarnická 10, 162 53 Prague 6, Czech Republic.

layer [1–5]. The optical gap variation with the composition were found from 5.6 eV to 8.9 eV for $O/(O + N)$ increasing from 0.04 to 0.95 [6,7].

For the amorphous silicon dioxide, it has been established since 1964 that the radiation damage of metal-thermal SiO_2 -semiconductor devices involves two major aspects: the creation of interface states at the Si– SiO_2 interface and the capture of holes in deep traps near Si– SiO_2 interface. Moreover, it was shown, through a sequence of ultraviolet illuminations, electron spin resonance measurements and capacitance versus voltage measurements in metal-thermal SiO_2 -semiconductor, that the E' center was a deep hole trap, positively charged and working as a reversible defect [8]. By contrast, the neutral E' center, unpaired electron on the silicon back-bonded to three oxygen, was observed in plasma-enhanced chemical vapour deposition (PECVD) SiO_2 [9].

For the amorphous silicon nitride $Si_3N_4:H$, the direct experimental evidence of linkage between a specific structural defect and a deep trapping center was brought by the observation of a strong correlation between changes in the density of the paramagnetic silicon dangling bond centers and changes in the space charge density of films subjected alternatively to illumination and both positive and negative charge injection [10,11]. An excellent review for the paramagnetic point defects in amorphous silicon dioxide and amorphous silicon nitride thin films was published in 1992 [12]. Relying on these results, it is likely that the point defects studies, which can be performed by electron spin resonance (ESR) techniques, are the key for the understanding of the electrical properties of the amorphous insulating silicon oxynitrides with a band gap between that of silicon nitride and oxide.

For the defect studies, the ESR signal of the as-deposited layers were, as a preliminary, measured (DESR signal). Thereafter, the thin films were illuminated by photons with energy higher than the band gap of the silicon oxynitride and the ESR signal, photo-enhanced and saturated in time, was then recorded (LESR signal). The present study only reports the LESR results of the LHD and HHD silicon oxynitrides. The absorption derivative LESR signal is calculated involving isotropic

and axially symmetric dangling bonds, the latter with a nuclear spin of 1 for the ^{14}N atom. The fit with the experimental signals can be obtained with a ESR derivative signal computation involving only two point defects for the new LHD $SiO_xN_yH_z$ and three point defects for the usual HHD $SiO_xN_yH_z$.

2. Experimental procedure

The layers were grown into a plasma process and using respectively SiH_4 , N_2O , NH_3 for the usual silicon oxynitrides HHD $SiO_xN_yH_z$ [1] and SiH_4 , N_2O , N_2 and He for the new LHD $SiO_xN_yH_z$ [3]. The samples were deposited on very pure $15 \times 4 \times 0.5$ mm fused silica (tetrasil with 1000 ppm OH) and on single intrinsic c-Si crystal, at $380^\circ C$, in a PECVD process. The gas pressure was fixed at 1 Torr, the plasma rf was 25 kHz and the supplied power amounted to $0.095 W/cm^2$.

With gas volume ratios $(N_2O + NH_3)/SiH_4$ fixed at 50 and $N_2O/(NH_3 + N_2O)$ varied between 0 to 1, the first set of HHD $SiO_xN_yH_z$ was obtained with the $O/(O + N)$ composition from 0.04 to 0.95. With gas volume ratios $(N_2O + N_2)/SiH_4$ fixed at 24.2, the helium dilution $(He)/SiH_4$ fixed at 50 and $N_2O/(N_2 + N_2O)$ varied between 0 to 1, the second set of LHD $SiO_xN_yH_z$ was deposited with the $O/(O + N)$ composition from 0.04 to 0.85.

The elemental composition of the HHD layers was determined using the high energy ion beam techniques Rutherford backscattering spectrometry (RBS) and elastic recoil detection (ERD) [4,5]. This procedure resulted in the contents of all relevant elements Si, O, N and H atoms per cm^3 in the oxynitride films. The infrared transmission spectroscopy measurements were performed on samples deposited on doubly polished intrinsic c-silicon. These results were used to obtain the experimental curve of the maximum peak position of the main Si–O–Si–N collective mode located between 850 and $1060 cm^{-1}$ versus the $O/(O + N)$ composition [1]. This curve was afterwards used to obtain the $O/(O + N)$ ratio from the peak position for the LHD silicon oxynitrides [3].

The spectra were analyzed in the region of the absorption features, and subsequent numerical

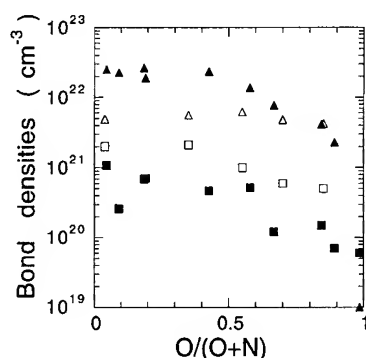


Fig. 1. Bond densities measured from infrared transmission spectroscopy versus the $O/(O+N)$ composition in the silicon oxynitrides with high (HHD) and low (LHD) hydrogen densities. \blacktriangle , \blacksquare , N–H and S–H, respectively; for HHD; \triangle , \square , N–H and Si–H, respectively, for LHD.

integration of the peaks of N–H, Si–H and O–H stretching mode located respectively around 3300, 2200 and 3660 cm^{-1} was performed. From the spectra, the bond density per cm^3 was calculated using the relation $(X-H) = A_{XH} I_{XH}$, where A_{XH} and I_{XH} are respectively the calibration factor (cm^{-2}) and the total integrated and normalized area (cm^{-1}) of the X–H absorption band. The calibration factors of N–H and Si–H found in previous works where fixed respectively at 2×10^{20} and $8 \times 10^{19} \text{cm}^{-2}$ [1].

The ESR experiments were performed at LEPES-Grenoble with a Bruker ESP300 X band spectrometer (9.4 GHz) and at Department Natuurkunde – Leuven with a home-made K band (20.4 GHz) spectrometer.

The layer was illuminated for 8 h, at room temperature and under vacuum, with a 150 W deuterium lamp emitting a large photon spectrum between 2 and 10.5 eV with an intense peak at 10.2 eV. It is known that the ESR signal of the usual HHD silicon nitride [13,14] or oxynitrides [15] is increased and finally saturated after an illumination by photons with energy of the order of the band gap. The LESR saturated signal can be subsequently lowered by a light-induced annealing (photobleaching with sub-band gap photons) [16] or by an appropriate thermal annealing [17], but at room temperature it takes one month or more for the LESR saturated signal to fall down to its initial low DESR level.

The X band signals were accumulated at 40 or 20 K, with a magnetic field modulation of 100 kHz and of 0.3–3 Gauss amplitude, at microwave powers from 10 μW to 10 mW. The saturation properties with the microwave power of the different ESR lines detected in the signal were studied and correction factors were used to calculate the spin densities. The absolute defect concentrations were calculated using double integration of the derivative absorption signals and comparison with a calibrated low pitch standard.

The K band measurements were carried out at 4.3 K, with a magnetic field modulation of 86 kHz and of 0.4 Gauss amplitude, at microwave powers from 1 nW to 1 μW .

3. Results

The (N–H) and (Si–H) bond densities variations versus the $O/(O+N)$ composition for the silicon oxynitrides are indicated in Fig. 1. For the LHD set compared with the HHD silicon oxynitrides, we observe:

- (i) a strong lowering of (N–H) for $O/(O+N)$ ratios between 0 and 0.6;
- (ii) a much more limited decrease for $O/(O+N) > 0.6$;
- (iii) a little increase of (Si–H) for all the compositions.

The ratio of hydrogen atomic density over the $\text{Si} + \text{O} + \text{N} + \text{H}$ total atomic number/ cm^3 is about 25% in the nitrogen rich silicon oxynitrides ($O/(O+N) < 0.5$) HHD layers grown with NH_3 ; it is lowered below 10% in the nitrogen rich silicon oxynitrides LHD layers grown with N_2 and He. For the oxygen-rich silicon oxynitrides ($O/(O+N) > 0.5$), the H density lowering between the two sets is limited. We must notice that the commonly mentioned silicon oxynitride in the literature are the HHD layers and that this paper presents the first systematic study for silicon oxynitrides with a low amount of hydrogen.

The LESR saturated signals of the LHD and HHD films are presented in Fig. 2. It appears very clearly that, for each LHD or HHD set, the signal is relatively simple for $O/(O+N)$ below 0.3 and that it becomes more complex for an increasing oxygen

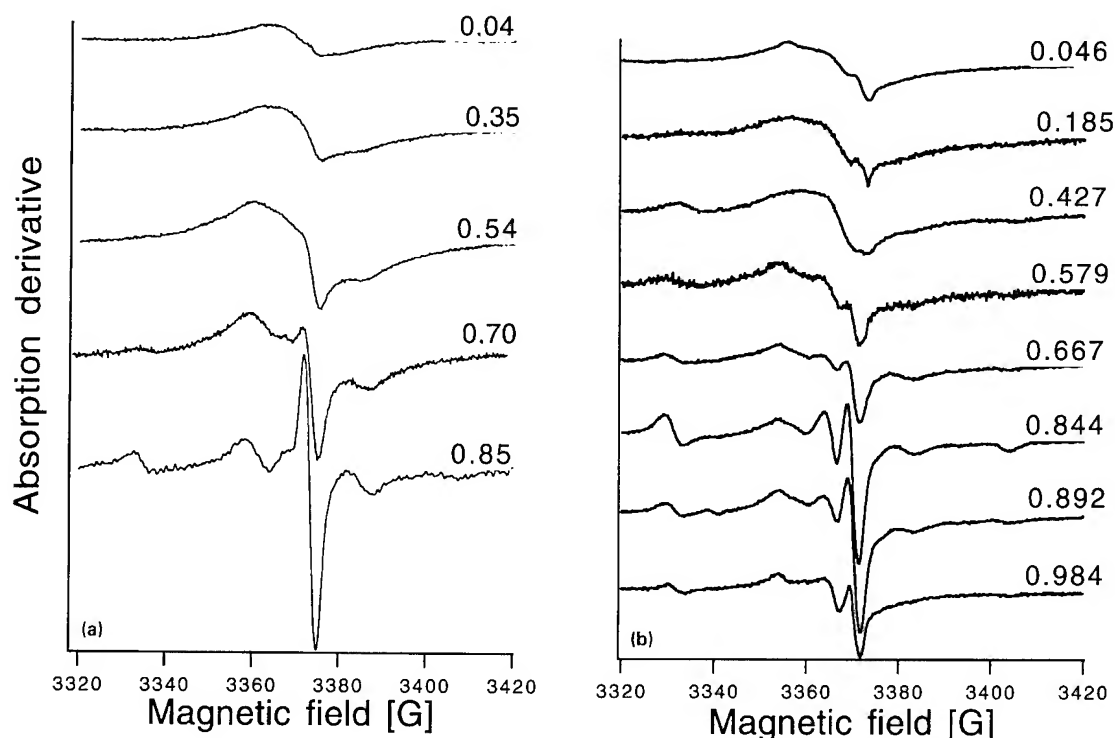


Fig. 2. The saturated X band LESR signal measured at 40K after VUV illumination of the silicon oxynitrides with low (a) and high (b) hydrogen density deposited on very pure silica. Experiments are performed with a Bruker ESR 300 Spectrometer.

content in the film. It can also be noticed that with an equivalent $O/(O + N)$ ratio, the LESR signal is more complex in the LHD than in the HHD materials.

Typical saturated X (20 K) and K band (4.3 K) LESR spectra, observed on a $SiO_xN_yH_z$ LHD films with $O/(O + N) = 0.85$ deposited on c-Si and tetrasil, respectively, are shown in Fig. 3. The superposed spectra are normalized by shifting the K band spectrum and the central-line zero crossing field corresponds to $g = 2.0010 \pm 0.0002$. The spectra are quite similar, both showing one intense central line at $g = 2.0010$ amid two smaller satellites of nearly the same intensity separated by 24.5 G, and with small structures, respectively A, B and C. The spectral X band features B and C, with 75.6 G separation, are better resolved on Fig. 4 for the same layer grown on tetrasil while the line C is not observable in K band (Fig. 3).

4. Computer simulation

Most of the defects found in the silicon alloys are dangling bonds, amphoteric in nature, with three available charge states for each structural point defect, neutral and paramagnetic with one electron on the orbital, positively/negatively charged and diamagnetic for zero/two electrons with antiparallel spins on the orbital. The electron spin resonance measurements only detects to the paramagnetic states. The ESR experiments measure the absorption of microwave power at a fixed frequency ν as a function of an applied magnetic field, H . The ESR spectrum may be approached in terms of a spin Hamiltonian [18]:

$$\mathcal{H} = \beta \hbar g S + I \vec{A} \cdot \vec{S}, \quad (1)$$

where the first term is the electronic Zeeman interaction (β is the Bohr magneton) and the second

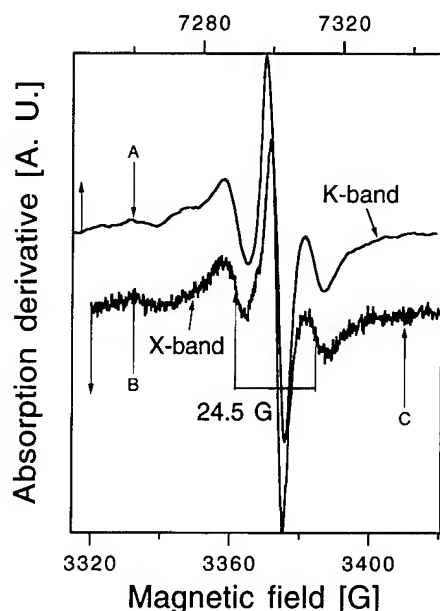


Fig. 3. X and K band LESR saturated signal of LHD with $O/(O + N) = 0.85$. Bottom: X band (20 K) of sample deposited on c-Si. Top: K band (4.3 K) of the same layer deposited on tetrasil. The K band line is shifted in order to superpose the central line zero crossing corresponding to $g = 2.0010 \pm 0.0002$.

represents the hyperfine interaction between the electron of spin S and the nucleus of spin I . In the silicon-based amorphous insulators where $S = 1/2$ is the general case, the quadratic order in S is neglected. \vec{g} and \vec{A} are the coupling dyadics for the Zeeman and hyperfine terms respectively and are assumed to be independently diagonalizable with a negligible error. In the silicon oxynitrides, among the nuclei with $I = 1$, only ^{14}N (99.6% abundant) is a reasonable candidate compared with ^2H (only 0.01 abundant). The orbitals in amorphous materials, thought to be isolated and randomly oriented, are conveniently described with an axial symmetry. We shall assume that the nitrogen defect center shows this axial symmetry. Then, in this case and with collinear principal axes for \vec{g} and \vec{A} matrices, we can write, in first order perturbation theory, the resonance relationship

$$H = \frac{h\nu}{\beta g} - \frac{K}{\beta g} m_1, \quad (2)$$

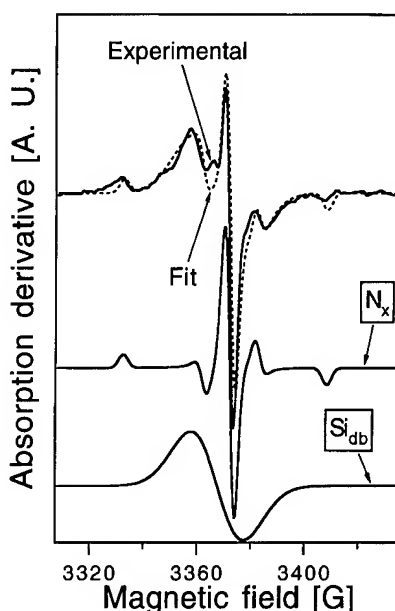


Fig. 4. The computed X band ESR derivative signal (---) compared with the LESR saturated X band signal of LHD with $O/(O + N) = 0.85$ deposited on tetrasil and measured at 20 K (—). A good fitting is obtained by the sum of a silicon dangling bond with simple isotropic ESR signature ($g = 2.0047$ and $\Delta H_{pp} = 19.7$ G) and of a new nitrogen-related defect, the N_x center characterised by hyperfine values $g_{\parallel} = 2.0030$, $g_{\perp} = 2.0017$, $A_{\parallel}/g_{\parallel}\beta = 8.2$ G, $A_{\perp}/g_{\perp}\beta = 9.2$ G and a broadening factor $f_c = 3.5$ G.

where

$$g = (g_{\parallel}^2 \cos^2 \theta + g_{\perp}^2 \sin^2 \theta)^{1/2} \quad (3)$$

$$K = (1/g) (A_{\parallel}^2 g_{\parallel}^2 \cos^2 \theta + A_{\perp}^2 g_{\perp}^2 \sin^2 \theta)^{1/2}, \quad (4)$$

where $h\nu$ is the applied microwave photon energy, m_1 is the nuclear spin magnetic quantum number, θ is the angle between the magnetic field direction and the symmetry axis, and g_{\parallel} , g_{\perp} , A_{\parallel} and A_{\perp} are the principal values of the \vec{g} and \vec{A} dyadics, respectively. For a nuclear spin $I = 1$, the hyperfine splitting leads to hyperfine spectral lines corresponding to m_1 values $-1, 0, +1$.

In powdered and amorphous materials, averaging of the resonance condition over all angles results in a mathematically absorption envelope called a 'powder pattern'. The principal components of the \vec{g} and \vec{A} tensors can be roughly

estimated from the experimental powder spectrum and these initial estimates can be used for spectrum simulation. The best fit is then researched between the experimental curve, first derivative of microwave absorption versus magnetic field on one side and the calculation of the theoretical powder pattern from the resonance condition, convoluted with Lorentzian and/or Gaussian broadening functions (called the broadening factor f_c) and differentiated with respect to magnetic field on the other side. This results in a measurement of the principal axis components g_{\parallel} , g_{\perp} , A_{\parallel} and A_{\perp} of \vec{g} and \vec{A} as well as a determination of the spin I of the nucleus of the hyperfine interaction. On this basis, the magnetic nucleus can usually be identified and the degree to which the orbital ψ_0 of the unpaired spin occupies atomic orbitals of this nucleus can be estimated from the magnitude of the A -tensor components. With a ground state wave function

$$\psi_0 = \alpha|2s\rangle + \alpha|2p\rangle + \sum_i \delta_i |k_i\rangle \quad (5)$$

where $|2s\rangle$ and $|2p\rangle$ are orbitals centered on the magnetic nitrogen nucleus and $|k_i\rangle$ are the remaining orbitals in which the unpaired spin can be found. Then

$$\alpha^2 = \frac{A_{\text{iso}}}{A_{2s}} = (1/3 A_{2s}) (A_{\parallel} + 2A_{\perp}), \quad (6)$$

$$\beta^2 = \frac{A_{\text{aniso}}}{A_{2p}} = (1/3 A_{2p}) (A_{\parallel} - 2A_{\perp}) \quad (7)$$

and

$$\alpha^2 + \beta^2 + \sum_i \delta_i^2 = 1, \quad (8)$$

where A_{iso} , A_{aniso} are the isotropic (2s type) and anisotropic (2p type) hyperfine tensor components, respectively, for the ^{14}N atom and A_{2s} and A_{2p} are the 2s-state and 2p-state coupling constants, respectively, for the free atom [19]. α^2 and β^2 give the localization percentage on 2s and 2p orbitals and are of fundamental interest to characterise the point defect.

5. Discussion

5.1. The LESR spectrum of LHD silicon oxynitrides near silicon nitride

Fig. 2(a) ($\text{O}/(\text{O} + \text{N}) = 0.04$), shows the ESR spectrum observed after VUV soaking in as-deposited silicon oxynitride with a composition very close to that of silicon nitride. It presents a very simple line with $g = 2.0030$ and a line width (widening factor, f_c) of 13 G. In N-rich PECVD silicon nitrides films with high hydrogen density, the K center is photo-enhanced by UV light [11,20,21]. The K center is an unpaired electron on a silicon bonded to three nitrogen atoms in configuration $^{\circ}\text{SiN}_3$. The ESR signature corresponds to a \vec{g} tensor with a small anisotropy, with a central line zero crossing at $g = 2.0030$ and a line width of 13 G (Table 1). Our LESR signal is

Table 1

The g values and line widths of the silicon dangling bond used for computation of the experimental spectra of the LHD silicon oxynitrides. The N_x center ESR components for the fitting are $g_{\parallel} = 2.0030 \pm 0.0005$, $g_{\perp} = 2.0017 \pm 0.0007$, $A_{\parallel}/g_{\parallel}\beta = 38.2 \pm 0.2$ G, $A_{\perp}/g_{\perp}\beta = 9.2 \pm 0.02$ G and a broadening factor $f_c = 3.5 \pm 0.3$ G

O/(O + N) composition	Si_{db} g value	ΔH_{pp} (G) linewidth	Si_{db} ($\times 10^{18} \text{ cm}^{-3}$) LESR	N_x zero crossing	N_x (cm^{-3}) LESR
0.04	2.0030	13	1.0		
0.35	2.0033	15.5	2.2	2.0011	8.9×10^{16}
0.55	2.0033	17.5	7.2	2.0012	1.8×10^{17}
0.70	2.0042	18.5	4.1	2.0013	5.7×10^{17}
0.85	2.0044	20	2.7	2.0013	8.7×10^{17}

The table indicates the computed central line zero crossing of the N_x center. The densities of the two defects are calculated using double integration of the separated computed signals and by comparison with a calibrated weak pitch standard measured in the same experimental conditions.

obviously the K center. It is an indication that the point defect in LHD silicon nitrides are the same as that in HHD silicon nitrides.

5.2. The LESR spectrum of LHD silicon oxynitrides with $O/(O + N) > 0.2$

In Fig. 2(a), it is obvious that the LESR spectra of the layers with $O/(O + N)$ above 0.4 become more complex and that they cannot be computed with only an Si_{ab} isotropic center. The sample with $O/(O + N) = 0.85$ in Fig. 2(a) shows clearly a spectrum with six features, a central line with g zero crossing at 2.0012 with two pairs of satellites of 24.5 and 75.6 G separations and a small feature at $g = 2.0032$. We notice that it is quite different from the spectrum of Fig. 2(c) reported in HHD oxygen-rich PECVD silicon oxynitride with equivalent composition and attributed to an over-coordinated nitrogen, ONC [15]. The ONC is a four coordinated nitrogen with, at 110 K, a central line zero crossing $g = 2.0036$ and a pair with 36 G separation. Its ESR characteristics are $g_{\parallel} = 2.0043$, $g_{\perp} = 2.0023$, $A_{iso} = 18.6$ G, and $A_{aniso} = 2.8$ G, which means that the nitrogen portion of the unpaired electron at the nitrogen center is only 20% localized [22]. We must also mention that, in N-rich PECVD HHD silicon nitrides, the nitrogen bridging N_b center was created by UV soaking after high temperature annealing [11,20,21]. The N_b center is an unpaired electron on an under-coordinated nitrogen bridging atom bonded with two silicon atoms in configuration $^{\circ}NSi_2$. Its ESR components are $g_{\parallel} = 2.0035$, $g_{\perp} = 2.0078$, $A_{iso} = 11$ G, and $A_{aniso} = 12.5$ G which indicate that the unpaired spin is strongly localized (74%) on the 2p-orbital of the nitrogen atom [20]. These values were confirmed by the computation of X band spectra of HHD silicon nitrides films prepared at a high deposition rate with ^{14}N and ^{15}N isotopes, annealed at 600°C and submitted to UV light [23,24].

A computer simulation based respectively on a sum of an Si_{ab} center with the ONC or on a sum of an Si_{ab} center with the N_b center using the hyperfine components mentioned above failed to reproduce the six feature spectrum of the 0.85 sample in Fig. 2(a). This spectrum was also very different from the N-pair center identified recently

in as-deposited HHD silicon nitride prepared at a high deposition rate [24]. The N-pair defect, in $Si-^{\circ}N-N-Si_2$ configuration, presents a microscopic structure similar to that of the peroxy radical defect $^{\circ}O-O-Si$ [25]. It is described as a pure p-type unpaired spin strongly localized on two inequivalent nitrogen atoms bonded to each other. It shows a very complex ESR spectrum with eight features, among which two pairs with 92 G and 42 G separations are well marked. It was correctly computed involving only one center with $g_{\parallel} = 2.0038$, $g_{\perp} = 2.0055$ and two inequivalent (1) and (2) nitrogen atoms with hyperfine tensor parameters, respectively $A_{iso}(1) = 10.20$ G, and $A_{aniso}(1) = 10.10$ G and $A_{iso}(2) = 5.29$ G, $A_{aniso}(2) = 5.27$ G.

Eventually, our LHD oxygen-rich silicon oxynitrides, which are new materials with a low hydrogen content are likely to involve a new type of point defect.

It is clear from relation (2) that the Zeeman term is a function of the micro wave frequency, while the hyperfine splitting is not. The lineshape of the spectra in X-band and K band frequencies of Fig. 3 are quite similar; the little changes detected come probably from a small g -tensor anisotropy. The 24.5 G pair and the small structures B and A appears at the same magnetic field values. In the case of different defects, the change of frequency from X to K band would have induced significant relative shifts between some spectra features. We can only conclude that these spectra are related to a unique defect center, probably related to the nitrogen atoms.

Fig. 4 shows the X band LESR experimental spectrum (full line) of a LHD $SiO_xN_yH_z$ 0.85 film grown on tetrasil, where signal averaging was used to improve the signal to noise ratio. The spectra of Figs. 4, 2(a) and 3 come from layers with the same composition but deposited on different substrates located at various position in the PECVD reactor. Five or six different spectral features are resolved. One of them, a small signal at magnetic field value near of 3365 G ($g = 2.0032$), has a relative change of amplitude from one sample to another (Fig. 2(a) compared with Fig. 4) or is not observed (Fig. 3). We assign it to a carbon defect resulting from a contamination during the sample preparation; this signal was observed in amorphous silicon

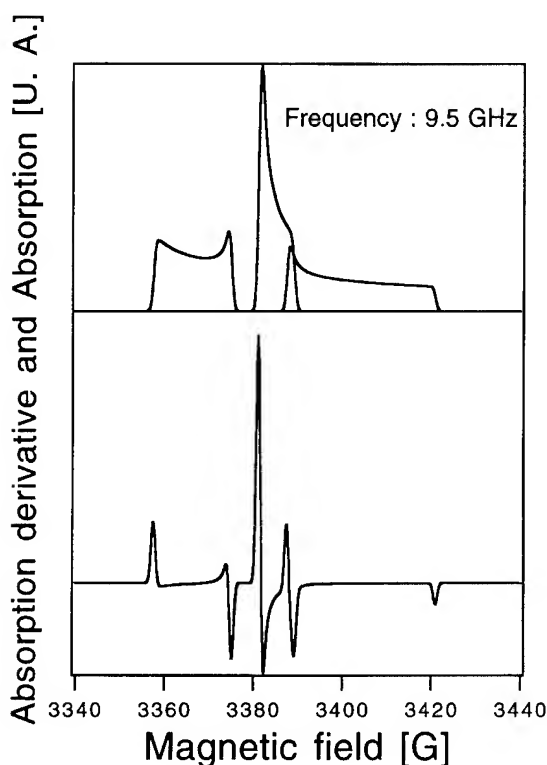


Fig. 5. The X-band computed absorption and absorption derivative of an axially symmetric nitroxide signal with $g_{\parallel} = 2.0025$, $g_{\perp} = 2.0075$, $A_{\parallel}/g_{\parallel}\beta = 32$ G, $A_{\perp}/g_{\perp}\beta = 6$ G and a small widening factor.

carbide ($g = 2.0034$) [26] and reported in HHD silicon nitride [24].

The powder pattern for a spin $I = 1$ nucleus may present contrasted shapes depending on the g -tensor and hyperfine tensor anisotropies [21]. For instance, the X-band absorption and absorption derivative ESR spectra computed with the values $g_{\parallel} = 2.00327$, $g_{\perp} = 2.0075$, $A_{\parallel}/g_{\parallel}\beta = 32$ G, $A_{\perp}/g_{\perp}\beta = 6$ G and with a very small broadening factor are shown in Fig. 5. The ESR parameters are those of a nitroxide radical. Nitroxides are stable free radicals which serve as probes called spin labels and which attach themselves to active sites in proteins or other molecules [27]. Motional effects on nitroxide spectra, in the slow tumbling region and in the case of the rigid limit, induce spectra which are very similar to those of the oxygen rich LHD silicon oxynitrides [28].

The remaining five spectral features of the 0.85 LHD silicon oxynitride, the central line and the two pairs with 24.5 and 75.6 G separations, suggest that the spectrum is much reminiscent of the powder pattern composed of three spectral lines of a center exhibiting large hyperfine tensor anisotropy. This observation underlies the computer simulation of the spectrum. The dashed line in Fig. 4 represents the result obtained by adding the powder spectra—depicted separately on the bottom part in Fig. 4—of two ESR point defects. The first is the Si_{db} defect in silicon oxynitrides, a Gaussian signal characterized by an isotropic $g = 2.0047$ and a peak-to-peak $\Delta H_{\text{pp}} = 19.7$ G. The second, labeled the N_{x} center, is a hyperfine spectrum characterized by axially symmetric \vec{g} and \vec{A} matrices, of principal values $g_{\parallel} = 2.0030$, $g_{\perp} = 2.0017$, $A_{\parallel}/g_{\parallel}\beta = 38.2$ G, $A_{\perp}/g_{\perp}\beta = 9.2$ G and a broadening factor $f_c = 3.5$ G. With the relations (6) and (7), we calculate $A_{\text{iso}} = 18.9$ G, $A_{\text{aniso}} = 9.7$ G, a dangling bond 2s character at 3% and its 2p character at 57%, giving a total localization on the nitrogen atom of 60%. This total localization value is intermediate between that of ONC (20%) and that of N_{b} center (76%).

The fitting of Fig. 4 reproduces the experimental spectrum accurately. We conclude that the LHD oxygen-rich silicon oxynitrides present only two types of point defect, the Si_{db} and what we called the N_{x} center. This type of decomposition was also satisfactory for the 0.70, 0.54 and 0.35 samples of the Fig. 2(a). The ESR components used for the Si_{db} centers are indicated in Table 1. We observe that the Si_{db} g value increases to 2.0042 for $\text{O}/(\text{O} + \text{N}) > 0.55$, while ΔH_{pp} increases for increasing $\text{O}/\text{O} + \text{N}$; this type of evolution of g and ΔH_{pp} values was already found in HHD silicon oxynitrides [2]. The ESR components (g_{\parallel} , g_{\perp} , A_{\parallel} and A_{\perp}) of the N_{x} center extracted from the fittings remain nearly the same as those found for the 0.85 sample as it is indicated by the little variation of the central line zero crossing.

Based on the similarity of the ESR spectra [28], we think, as a hypothesis which need strongly to be confirmed, that this N_{x} center could be the signature of $^{\circ}\text{N}-\text{O}$ centers in the LHD silicon oxynitrides. Finally, Fig. 6 indicates the variation of the two point-defect densities as a function of the

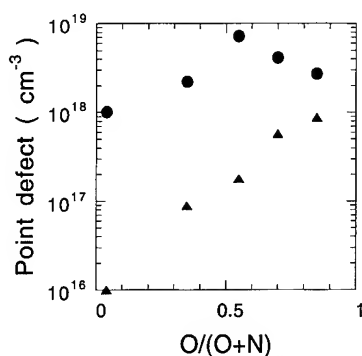


Fig. 6. The point defect densities as a function of the O/(O + N) composition in the silicon oxynitrides with low density of hydrogen (LHD). The silicon dangling bond (●) is observed for all the compositions and the nitrogen N_x center (▲) only detected for O/(O + N) > 0.30. The sensitivity limit is $10^{16}/\text{cm}^3$.

O/(O + N) composition. The Si_{db} centers are dominant (above 10^{18}cm^{-3}) for all compositions, a maximum of density is observed at O/(O + N) = 0.55. The N_x center is not detectable in LHD silicon nitride (below the sensitivity limit of 10^{16}cm^{-3}), it is very clearly present at 0.35 and its density increases versus the O/(O + N) composition. For 0.85 sample, the Si_{db} density is only four times higher than the N_x one.

5.3. The LESR spectrum of HHD silicon oxynitrides

Fig. 7 represents the LESR saturated X band experimental signal of HHD silicon oxynitrides with O/(O + N) = 0.84 deposited on tetrasil and measured at 20 K (full line). The best fit (dashed line in Fig. 7) is obtained with the sum of an Si_{db} ($g = 2.0029$ and $\Delta H_{\text{pp}} = 16$ G), a nitrogen N_x center ($g_{\parallel} = 2.0022$, $g_{\perp} = 2.0007$, $A_{\parallel}/g_{\parallel}\beta = 37.5$ G, $A_{\perp}/g_{\perp}\beta = 9.2$ G and $f_e = 3$ G), a nitrogen bridging N_b center ($g_{\parallel} = 2.0033$, $g_{\perp} = 2.0109$, $A_{\parallel}/g_{\parallel}\beta = 38$ G, $A_{\perp}/g_{\perp}\beta = 1.5$ G and $f_e = 4$ G) and a signal generated by the carbon contamination on the substrate ($g = 2.0036$, $f_e = 3.2$ G). This fitting reproduces the position in magnetic field of the main features of the complicated LESR spectrum, but the amplitudes are not well reproduced. The hyperfine anisotropy of the extracted N_b center corresponds to $A_{\text{iso}} = 13.5$ G and $A_{\text{aniso}} = 12$ G. We notice that the

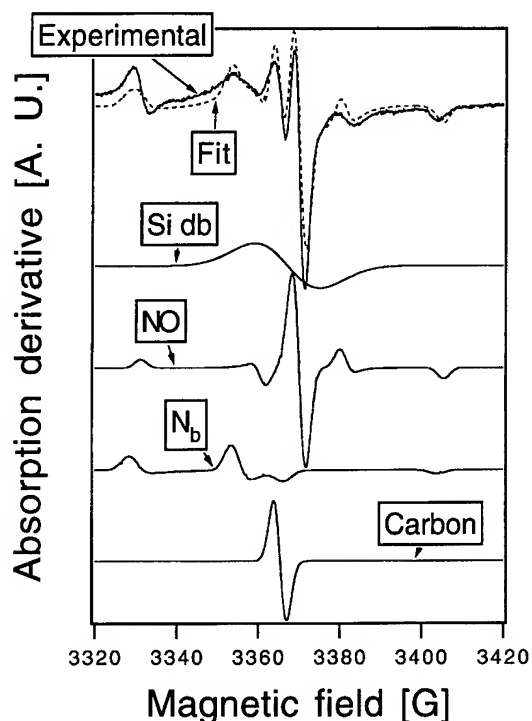


Fig. 7. The computed X band ESR derivative signal (---) compared with the LESR saturated X band signal of HHD with O/(O + N) = 0.84 deposited on tetrasil and measured at 20 K (—). The best fitting is obtained with a Silicon dangling bond (Si_{db}), a nitrogen N_x center (N_x), a nitrogen bridging center (N_b) and a signal generated by the carbon present on the substrate.

values of $g_{\perp} = 2.0109$ and $A_{\text{iso}} = 13.5$ G differ from the 2.0078 and 13.5 G currently accepted in HHD silicon nitride for the N_b center [20]. Our computation based on axially symmetric defects needs to be extended to anisotropic defects in order to obtain a more satisfactory fitting and to be able to obtain the relative density of each defect as a function of the composition. Right now, we just can observe that, by contrast with previous work on HHD silicon oxynitrides where we proposed four types of defects [2], only three different point defects are now found in HHD silicon oxynitrides.

6. Conclusion

The new LHD silicon oxynitrides are found to contain, in addition to the silicon dangling bonds

a special type of defect, the N_x center, related to the nitrogen atom which was not mentioned yet in the silicon based amorphous insulating thin films. It would possibly correspond to the nitroxide radical $^{\circ}\text{NO}$ known as a spin labelling radical. By contrast with the situation observed in the HHD silicon nitride where the N_b defect is only observed after rough treatment, the N_x defects are detected in the silicon oxynitrides without any annealing process. With silicon oxynitrides becoming more and more oxygen-rich/nitrogen-poor, the density of this point defect increases. In other words, the ratio of N_x density/N atomic density increases sharply. It is an indication that the nitrogen atoms undergo growing difficulties to incorporate as a normal trivalent atom bonded to silicon or hydrogen atoms in the amorphous network dominated by SiO_4 local tetrahedra. The more complex situation occurring in HHD silicon oxynitrides corresponds to the presence of three point defect types, the Si_{ab} , the N_x and the N_b centers. A quantitative evolution of the density of these defects with the composition cannot be achieved yet.

The authors are indebted to Professor A. Stesmans, Department Natuurkunde, Universiteit Leuven, for the K band ESR measurements and for stimulating discussions.

References

- [1] S. Viscaino, PhD thesis, Université J. Fourier, Grenoble I (1992).
- [2] S. Viscaino, Y. Cros and B. Ruf, *Mater. Res. Soc. Symp. Proc.* 284 (1993) 339.
- [3] J. Krautwurm, PhD thesis, Université J. Fourier, Grenoble I (1994).
- [4] W.M. Arnold Bik, C.T.A.M. de Laat and F.H.P.M. Habraken, *Nucl. Instrum. and Meth. B* 64 (1992) 832.
- [5] W. Arnold Bik, PhD thesis, Utrecht University (1992).
- [6] C. Ance, F. de Chelle, J.P. Ferraton, G. Lévêque, P. Ordejon and F. Yndurain, *Appl. Phys. Lett.* 60 (1992) 1399.
- [7] P. Ordejon, PhD thesis, Universidad Autonoma de Madrid (1993).
- [8] H.S. Witham and P.M. Lenahan, *Appl. Phys. Lett.* 51 (1987) 1007.
- [9] W.L. Warren, P.M. Lenahan and B. Robinson, *Appl. Surf. Sci.* 39 (1989) 406.
- [10] D.T. Krick, P.M. Lenahan and J. Kanicki, *J. Appl. Phys.* 64 (1988) 3558.
- [11] D.T. Krick, P.M. Lenahan and J. Kanicki, *Phys. Rev. B* 38 (1988) 8226.
- [12] W.L. Warren, E.H. Poindexter, M. Offenberger and W. Müller-Warmuth, *J. Electrochem. Soc.* 139 (1992) 872.
- [13] D.T. Krick, P.M. Lenahan and J. Kanicki, *Appl. Phys. Lett.* 51 (1987) 608.
- [14] D. Jousse and J. Kanicki, *Appl. Phys. Lett.* 55 (1989) 1112.
- [15] J.T. Young, G.T. Kraus, P.M. Lenahan and D.T. Krick, *J. Appl. Phys.* 70 (1991) 4969.
- [16] M.S. Crowder, E.D. Tober and J. Kanicki, *Appl. Phys. Lett.* 57 (1990) 1995.
- [17] E.D. Tober, J. Kanicki and M.S. Crowder, *Appl. Phys. Lett.* 59 (1991) 1723.
- [18] G.E. Pake and T.L. Estle *The Physical Principle of Electron Paramagnetic Resonance* (Benjamin, Boston, MA, 1971) p. 131.
- [19] C.M. Hurd and P. Coodin, *J. Phys. Chem. Solids* 28 (1967) 523.
- [20] W.L. Warren, P.M. Lenahan and S.E. Curry, *Phys. Rev. Lett.* 65 (1990) 207.
- [21] W.L. Warren, F.C. Rong, E.H. Poindexter, G.J. Gerardi and J. Kanicki, *J. Appl. Phys.* 70 (1991) 346.
- [22] T.E. Tsai, D.L. Griscom and E.J. Friebele, *Phys. Rev. B* 38 (1988) 2140.
- [23] M. Kumeda, N. Awaki, H. Yan, A. Morimoto and T. Shimizu, *J. Non-Cryst. Solids* 137&138 (1991) 887.
- [24] H. Yan, M. Kumeda, N. Ishii and T. Shimizu, *Jpn. J. Appl. Phys.* 32 (1993) 876.
- [25] E.J. Friebele, D.L. Griscom, M. Stapelbrock and R.A. Weeks, *Phys. Rev. Lett.* 42 (1979) 1346.
- [26] G.W. Wagner, B.K. Na and M.A. Vannice, *J. Phys. Chem.* 93 (1989) 5061.
- [27] C.P. Poole, *Electron Spin Resonance. A comprehensive Treatise on Experimental Techniques* (Wiley, New York, 1983) p. 539.
- [28] L.J. Berliner, *Spin Labelling. Theory and Applications* (Academic Press, New York, 1976) p. 98.



ELSEVIER

Journal of Non-Crystalline Solids 187 (1995) 395–402

JOURNAL OF
NON-CRYSTALLINE SOLIDS

Silicon oxynitride study by the tetrahedron model and by spectroscopic ellipsometry

A. Sassella^{a,*}, P. Lucarno^a, A. Borghesi^b, F. Corni^b, S. Rojas^c, L. Zanotti^c

^a *Dipartimento di Fisica 'A. Volta' dell'Università, Via Bassi 6, I-27100 Pavia, Italy*

^b *Dipartimento di Fisica dell'Università, Via Campi 213 a, I-41100 Modena, Italy*

^c *SGS-Thomson Microelectronics, Via Olivetti 2, I-20041 Agrate B. (MI), Italy*

Abstract

Silicon oxynitride samples deposited by plasma-enhanced chemical vapour deposition are characterized by different techniques to obtain their stoichiometry and density. From these data and applying the tetrahedron model, the optical functions in the range from 0.23 to 0.90 μm are calculated and compared with the results of spectroscopic ellipsometry.

1. Introduction

Silicon oxynitride (SiO_xN_y) films are currently used in microelectronics technology mainly as final passivation layers for non-volatile memory cells. Further, silicon oxynitrides are also considered interesting materials in optoelectronics due to the possibility of continuously varying their optical functions by adjusting deposition parameters. It is known that these materials show a significant presence of hydrogen in their structure since they are usually deposited by plasma-enhanced chemical vapour deposition technique. The effect of hydrogen on the optical properties of these compounds has not yet been clearly understood; also interpretation of experimental data is often controversial. The knowledge of the influence of material

stoichiometry and hydrogen content on the optical properties is, then, needed to better understand the physical characteristics of the material and to optimize its technological applications.

The tetrahedron model, recently extended to cover hydrogen-rich silicon oxynitrides, allows a direct calculation of the optical properties from the experimental density and stoichiometry of the material, thus enabling a comparison between calculated and experimental data.

In this paper, the results of a wide characterization carried out on hydrogen-rich silicon oxynitride samples with different stoichiometry by means of Rutherford back scattering (RBS), nuclear reaction analysis (NRA), elastic recoil detection (ERD) analysis, infrared (IR) spectroscopy and density measurements are reported. On this basis, the tetrahedron model has been successfully applied and the calculated optical functions compared with experimental data derived from spectroscopic ellipsometry measurements. From such a comparison,

* Corresponding author. Tel: +39-382 507 457. Telefax: +39-382 507 563. E-mail: sassella@pavia.infn.it.

Table 1

Experimental stoichiometry, density and [Si–H]/[N–H] ratio for the test sample and for samples 1 and 2 ($\text{SiO}_x\text{N}_y\text{H}_z$).

	<i>x</i>	<i>y</i>	<i>z</i>	[Si–H]/[N–H]	<i>d</i> (g/cm ³)
Test sample	0.50	0.85	0.48	0.006	2.33
Sample 1	1.82	0.13	0.14	0.067	2.18
Sample 2	1.16	0.46	0.26	0.009	2.25

an indication of the sensitivity of the tetrahedron model on stoichiometry and density together with information on the properties of the hydrogen-rich silicon oxynitride samples are obtained.

2. Experimental

Silicon oxynitride films about 0.25 μm thick were deposited at 400°C using a single wafer cluster deposition plasma-enhanced chemical vapour deposition system. P-type CZ silicon wafers (100) oriented with 16–24 Ωcm resistivity were used as substrates for the deposition of different films. Deposition conditions are reported in detail elsewhere [1]. Different stoichiometries were obtained by varying the $[\text{N}_2\text{O}]/([\text{SiH}_4] + [\text{NH}_3] + [\text{N}_2])$ ratio of the fluxes of the reactants. The wafers, 150 mm in diameter and 675 μm in thickness, were back lapped to avoid light scattering during IR transmission measurements.

The relative concentrations of silicon, oxygen, nitrogen, and hydrogen in the films were measured combining different nuclear techniques using a 2.4 MeV accelerator. The hydrogen content and the in-depth distribution were evaluated by ERD analysis. Oxygen and nitrogen content, integrated over the entire thickness of the film, was measured by NRA using the reactions $^{16}\text{O}(\text{d}, \text{p}_0)^{17}\text{O}$ and $^{14}\text{N}(\text{d}, \text{p}_5)^{15}\text{N}$ with a 625 keV D^+ beam. The silicon atoms concentration and the in-depth distribution were measured by RBS. All these techniques, providing the atomic concentration per square centimetre, allow to determine the composition of the films with an error estimated of 10% in the formula units. Whether and in which measure hydrogen is directly bonded to silicon atoms or forms NH and OH groups in the films is determined by means of IR absorption measurements. The [Si–H]/[N–H]

ratio is obtained by evaluating the areas of the absorption peaks relative to N–H (3400 cm^{-1}) and Si–H (2250 cm^{-1}) vibrational modes [2]. The band areas are converted into bond densities on the basis of the conversion factors proposed by Lanford and Rand [3] for Si_3N_4 . Indeed it has been shown that using such factors the agreement between IR and NRA results on bond concentration is very good even for oxygen-rich compounds [4]. Absorption bands caused by the presence of OH bonds were not revealed in the spectra; this indicates that OH bond concentration in the films is less than 0.1% in weight.

The density of the films was evaluated by weight and volume measurements. The uncertainty on density results is estimated to be $\pm 5\%$ of the measured values.

A complete series of seven samples with stoichiometry ranging from SiO_2 to Si_3N_4 were deposited and characterized with respect to stoichiometry and density. Among these, two samples with different composition were investigated in detail. The measured stoichiometry and density of each of the investigated samples is reported in Table 1 together with the [Si–H]/[N–H] ratio.

Ellipsometric functions $\tan \psi$ and $\cos \Delta$ were measured in the spectral range from 0.23 to 0.9 μm using a spectroscopic ellipsometer (SOPRA ES4G) with tracking analyzer. The slit width was 150 μm (resolution better than 2 Å) and each datum was taken by averaging the signal for some minutes to improve the signal to noise ratio. The angle of incidence during the measurements was evaluated to be 75.06°.

3. Results and discussion

Silicon oxides, nitrides and oxynitrides are known to possess a characteristic short-range order

whose basic units are tetrahedra with a central silicon atom and oxygen or nitrogen atoms at the vertices. On the basis of such a microscopic structure, the so-called tetrahedron model has been developed [5] to calculate the complex dielectric function of silicon oxides (SiO_x) and nitrides (SiN_x) taking into account the material stoichiometry. Substoichiometric silicon oxides and nitrides can be described considering also Si atoms as possible vertex atoms. In this way the Si/O and Si/N ratio in the compound can be different from $\frac{1}{2}$ and $\frac{3}{4}$, respectively. A dielectric function is then associated to each tetrahedron, which is supposed to compose the material, by scaling the dielectric function of an adequate reference material. Scaling is performed using two factors evaluated for each tetrahedral structure on the basis of its characteristic bonds. Given the four vertex atoms, properties such as the bond length in the tetrahedron, the tetrahedron volume, and the energy gap are derived by averaging the corresponding properties of known materials where all bonds are the same. The dielectric functions of the tetrahedra are then combined together according to Bruggeman effective medium approximation (EMA) and taking into account the volume fraction that each tetrahedral species occupies in the material (related to the stoichiometry index x).

Recently, the tetrahedron model has been extended [6] to include hydrogen-rich silicon oxynitrides ($\text{SiO}_x\text{N}_y\text{H}_z$); in this model the material is supposed to be composed by the tetrahedra typical for SiO_x and for SiN_x , by mixed structures with the contemporary presence of oxygen and nitrogen vertex atoms and also by tetrahedra with hydrogen atoms and NH groups at the vertices. In particular, if we indicate a Si-centered tetrahedron with four atoms A at the four vertices as Si-A_4 , the following tetrahedra are considered for oxynitrides: $\text{Si-Si}_{4-v}\text{N}_v$, $\text{Si-Si}_{4-v}\text{O}_v$, $\text{Si-O}_{4-v}\text{N}_v$, $\text{Si-N}_{4-v}(\text{NH})_v$, $\text{Si-O}_{4-v}(\text{NH})_v$, $\text{Si-HO}(\text{NH})_2$, $\text{Si-HO}_2(\text{NH})$, $\text{Si-HN}(\text{NH})_2$, $\text{Si-HN}_2(\text{NH})$, $\text{Si-SiO}(\text{NH})_2$, $\text{Si-SiO}_2(\text{NH})$, $\text{Si-Si}(\text{NH})_3$, $\text{Si-SiN}(\text{NH})_2$, $\text{Si-SiN}_2(\text{NH})$. It is worth noting that in principle also OH groups should be included as vertex species and thus also tetrahedra containing OH should be considered. Since OH absorption bands have not been detected in the IR spectra, the presence of tetrahedra with OH as vertex groups is

here neglected, supposing that their contribution is very small.

In the tetrahedron model every bond is supposed to be saturated, i.e. there are no dangling bonds in the material. It is also supposed that the material is homogeneous on a microscopic scale, thus excluding phase separation. This last assumption is supported by IR results: a phase separation in the material would imply the presence of absorption bands relative to each phase, while only one band at a wave number intermediate between those of SiO_2 and Si_3N_4 was detected. As will be shown, the effect of micro voids and density variations in the material can heavily affect the optical properties of oxynitrides films. The samples must therefore be characterized not only according to stoichiometry, but also to density. It is possible to quantify the effect of voids in the material by comparing the experimental density d_e of a sample with its theoretical density d_t as calculated according to the sample stoichiometry. Indicating the fraction of volume occupied by void as v , the following relation holds:

$$v = 1 - \frac{d_e}{d_t} \quad (1)$$

Once v is defined, the volume fractions relative to all N tetrahedra under consideration and v itself must be renormalized in such a way to have $v + \sum v_i = 1$. In this manner void is considered as a constituent of the material and its effect can be included in the EMA evaluation after associating to the volume fraction v the void dielectric function $1 + i0$.

The effects of density variations within experimental uncertainty on the dielectric function of a test sample of stoichiometry $\text{SiO}_{0.5}\text{N}_{0.85}\text{H}_{0.48}$ is shown in Fig. 1. The solid curves are the real and imaginary parts of the complex refractive index $\tilde{n} = n + ik$ calculated considering the experimentally determined density value of 2.33 g/cm^3 , while the dashed lines represent n and k for density variations of $\pm 5\%$ on the experimental value. Such modifications produce variations of as much as 4% in the n and k optical functions calculated by the tetrahedron model. Of course, variations occur in such a way to increase n and k as the material becomes more dense. The sensitivity of the model requires the samples to be well characterized with respect to density.

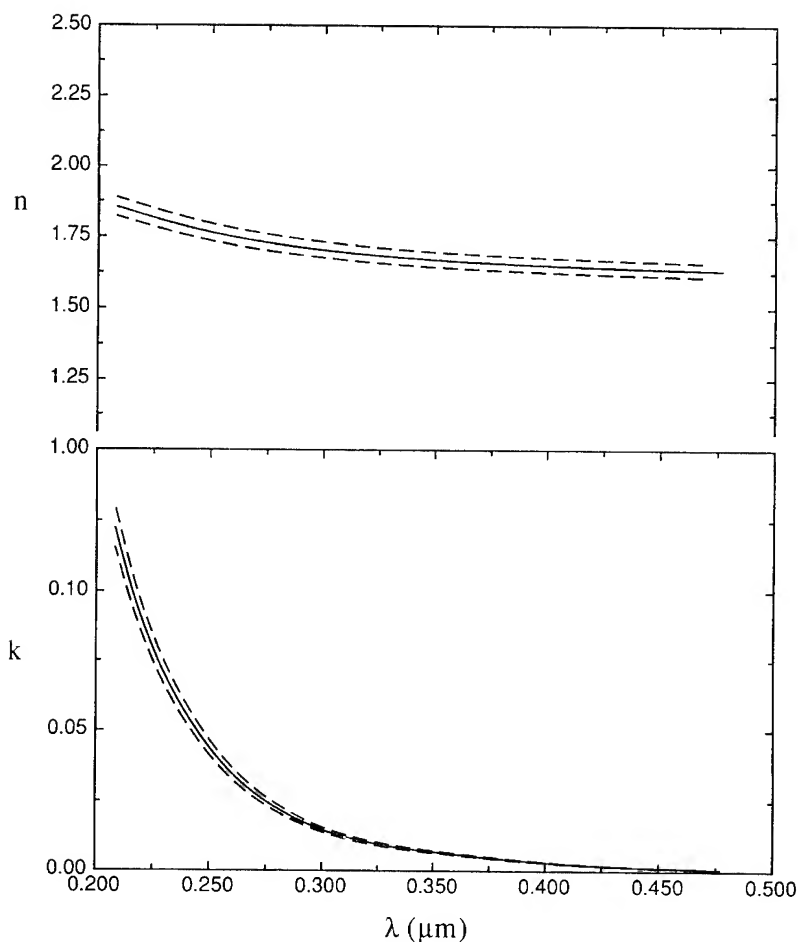


Fig. 1. Real and imaginary parts of the complex refractive index of the test sample (—) calculated considering Table 1 data and varying the density values by 5% (----).

Then the model sensitivity on stoichiometry variations for a fixed density of the sample has been tested. The results for a test sample are shown in Fig. 2, where the solid lines represent n and k functions calculated for the experimental stoichiometry (see Table 1) and the dashed lines those evaluated considering stoichiometry variations comparable with the experimental uncertainty. Variations of $\pm 10\%$ on the stoichiometry indexes for oxygen (x) and nitrogen (y) produce variations of about 15% in the calculated n optical function. It is worth noting that when a real material is simulated with the tetrahedron model, as in this case, the effects of

the experimental uncertainty on both the density value and the stoichiometry indexes have to be considered; this leads in some cases to an appreciable range of variation of the model results.

Spectroscopic ellipsometry is, in general, a powerful non-destructive technique for evaluating optical functions. The influence of the analytical models used to calculate n and k from ellipsometric functions $\tan \psi$ and $\cos \Delta$ is often very strong. The results of direct inversion of ellipsometric equations are often not accurate due to the presence in the experimental spectra of points in which $\tan \psi = 0$ and $\cos \Delta = -1$. In these points several pairs of

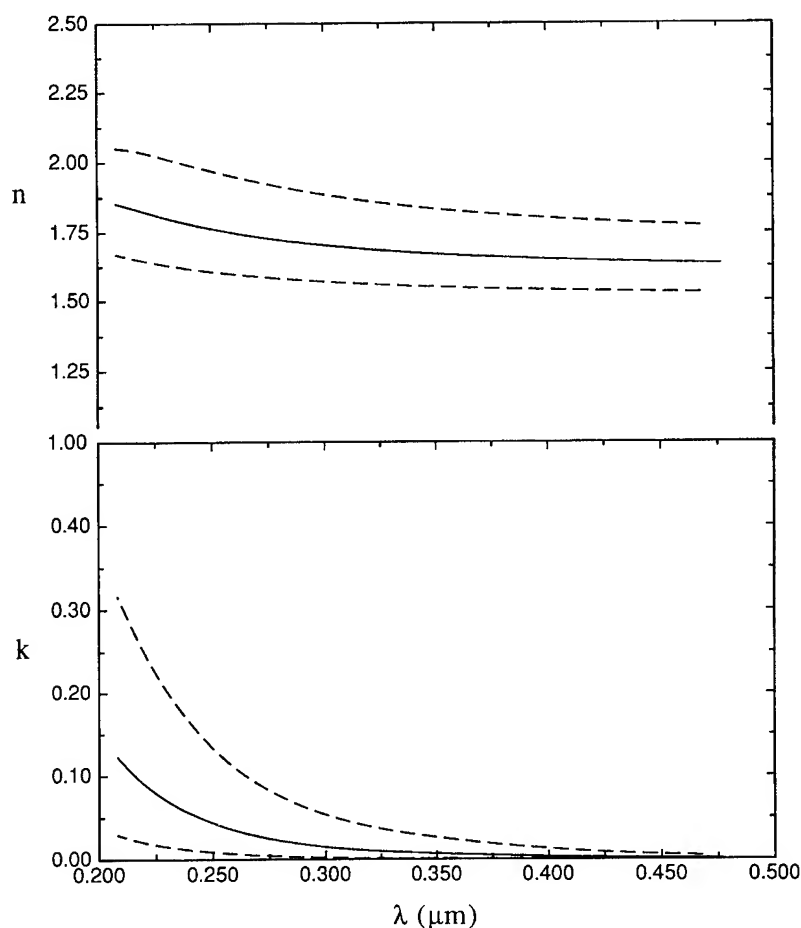


Fig. 2. Real and imaginary parts of the complex refractive index of the test sample (—) calculated considering Table 1 data and varying the stoichiometry indices x and y by 10% (----).

n and T values can solve ellipsometric equations making the accuracy of the derived parameters very poor [1, 7]. The data analysis was then performed following two methods. The first one consists of fitting the experimental spectra starting from the Sellmeier dispersion formulae:

$$n^2 = 1 + \frac{A}{1 + B^2/\lambda^2}, \quad k = \frac{C}{nD\lambda + E/\lambda + 1/\lambda^3}, \quad (2)$$

where A , B , C , D and E are the free parameters of the fit. This analytical model was chosen because it is one of the most accurate for dielectric material in

the visible range. Thickness values T for the oxynitrides films were evaluated setting also T as a free parameter. The second analysis of ellipsometric functions $\tan \psi$ and $\cos \Delta$ was based on the Bruggeman EMA [8]. A geometrical model constituted by different layers made of physical mixtures of two different phases on a single crystalline silicon substrate was assumed. The first layer is supposed to be composed of SiO_2 and Si_3N_4 and the second one of amorphous silicon and Si_3N_4 . SiO_2 and a-Si concentrations together with film thickness T are taken as free parameters for the fit of experimental $\tan \psi$ and $\cos \Delta$. The two-layer model based on

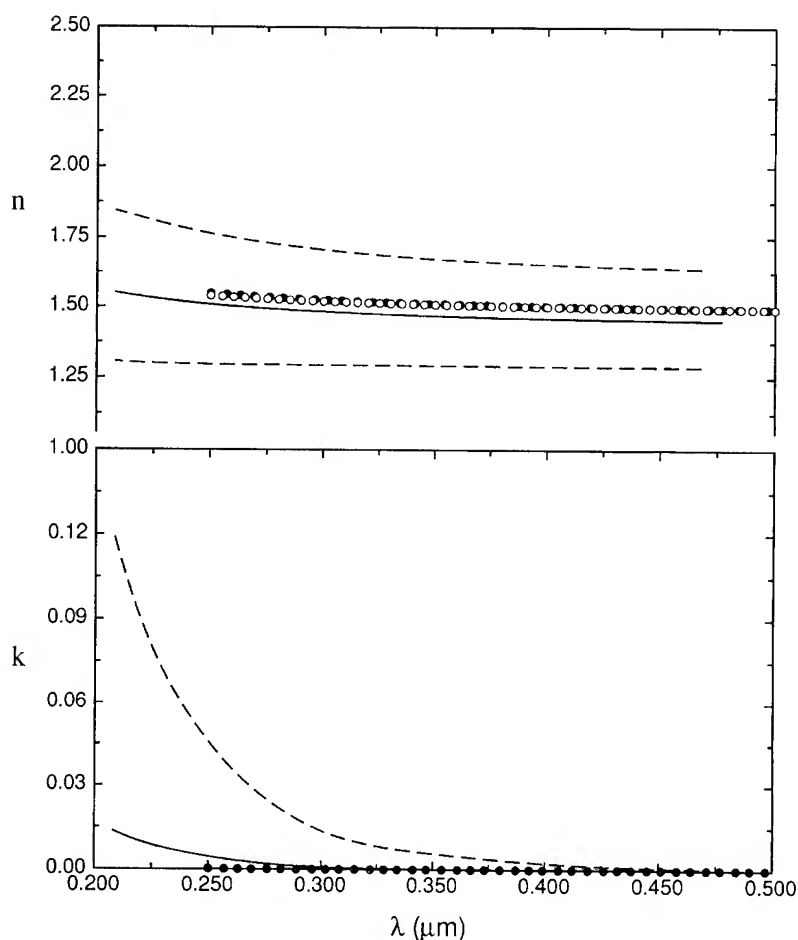


Fig. 3. Real and imaginary parts of the complex refractive index of sample 1 (—) calculated considering Table 1 data and varying both density by 5% and stoichiometry indices x and y by 10% (---). Ellipsometric data are reported for comparison as evaluated using Sellmeier analytical model (○) and Bruggeman EMA (●).

Bruggeman EMA permits a significant improvement in the least square deviation of the fit with respect to the other two models. Bruggeman EMA has been applied here only to reach a best fit with experimental ellipsometric data and then derive n and k . It should be stressed that in this case it is not a good physical model for oxynitrides films since it assumes two distinct phases, i.e. SiO_2 and Si_3N_4 , as composing the films. Nonetheless, the obtained n and k spectra are reliable, since they come from a good fit of the experimental data.

A comparison between ellipsometric experimental data and calculated optical functions for

samples with the stoichiometry and the density reported in Table 1 is shown in Figs. 3 and 4. The areas between the dashed lines correspond to the region in which the optical functions calculated with the tetrahedron model can vary due to the experimental uncertainty of $\pm 10\%$ in the stoichiometry and of $\pm 5\%$ in density value. Experimental data have been obtained from ellipsometric functions by Sellmeier and Bruggeman EMA fitting models (n) and only from Bruggeman EMA (k). In the case of Sellmeier analytical fitting the k spectra are not significant owing to their very low values and to the presence of some discontinui-

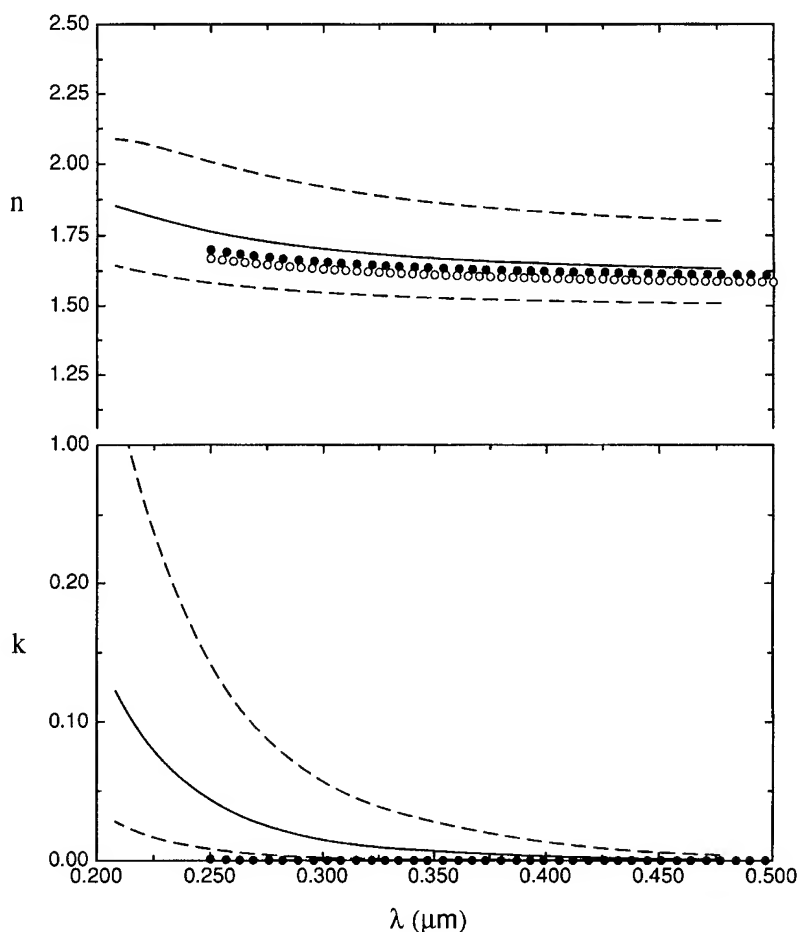


Fig. 4. Real and imaginary parts of the complex refractive index of sample 2 (—) calculated considering Table 1 data and varying both density by 5% and stoichiometry indices x and y by 10% (---). Ellipsometric data are reported for comparison as evaluated using Sellmeier analytical model (○) and Bruggeman EMA (●).

ties. Considering the n spectra in Figs. 3 and 4, we note a good agreement between theory and experiment for both samples over the entire spectral region. The agreement is slightly worse in the short wavelength region, in particular for sample 2. This can be ascribed to the fact that the tetrahedron model neglects the possible presence of dangling bonds. It is known that in PECVD oxynitride films the Si dangling bonds density can be of the order of 10^{19} cm^{-3} ; despite this low density, bonds could have a certain influence on the calculated optical spectra. In fact if the stoichiometry indices are such that some Si bonds remain unsaturated, Si-Si

bonds are introduced in the model (through tetrahedra with Si vertex atoms), affecting the short wavelength part of the spectra. In this case experimental spectra show lower n and k values with respect to those calculated using the model. Unfortunately, the dangling bonds cannot be included in the model, since this would require to associate them a dielectric function, which is not straightforward.

As for the k spectra, the agreement is poor. Also in this case the Si-Si bonds strongly influence the model results at short wavelengths. Moreover, for such low k values ellipsometry reliability is known to be poor.

4. Conclusions

The tetrahedron model is here used to calculate the optical functions of hydrogen-rich silicon oxynitrides also including the effects of microvoids and density variations in the material. The sensitivity of the tetrahedron model on both density and stoichiometry variations was analyzed. It was found that the experimental uncertainties on density and stoichiometry values could lead sometimes to an appreciable range of variations of the model results. Finally, a comparison between calculated and experimental optical functions for the hydrogen-rich oxynitrides samples of different stoichiometry and density has been carried out finding a satisfactory agreement between theory and experiment.

References

- [1] A. Borghesi, E. Bellandi, G. Guizzetti, A. Sassella, S. Rojas and L. Zanotti, *Appl. Phys.* A56 (1993) 147.
- [2] A. Sassella, A. Borghesi, R. Rojas and L. Zanotti, in: *Proc. 9th Int. Conf. on Fourier Transform Spectroscopy*, ed. J.E. Bertie and H. Wieser, *Proc. SPIE* 2089 (1993) 398.
- [3] W.A. Lanford and M.J. Rand, *J. Appl. Phys.* 49 (1978) 2473.
- [4] S. Rojas, L. Zanotti, A. Borghesi, A. Sassella and G. U. Pignatelli, *J. Vac. Sci. Technol.* B11 (1993) 2081.
- [5] D.E. Aspnes and J.B. Theeten, *J. Appl. Phys.* 50 (1979) 4928.
- [6] A. Sassella, *Phys. Rev.* B48 (1993) 14208.
- [7] A. Borghesi, A. Sassella and S. Rojas, *Thin Solid Films* 233 (1993) 227.
- [8] D.A.G. Bruggeman, *Ann. Phys. (Leipzig)* 24 (1935) 636.



ELSEVIER

Journal of Non-Crystalline Solids 187 (1995) 403–408

JOURNAL OF
NON-CRYSTALLINE SOLIDS

Effect of process parameters on the properties of electron cyclotron resonance plasma deposited silicon-oxynitride

Pavel V. Bulkin, Pieter L. Swart*, Beatrys M. Lacquet

Sensors Sources and Signal Processing Research Group, Materials Laboratory, Rand Afrikaans University, P.O. Box 524, Auckland Park 2006, South Africa

Abstract

Silicon-oxynitride layers were deposited by electron cyclotron resonance plasma enhanced chemical vapour deposition onto silicon and glass substrates. Working pressure ranged from 0.8 to 4 mTorr. Thin films of SiO_xN_y with different composition were obtained by a change of gas flow ratio under computer control. The optical properties of thin SiO_xN_y films grown from O_2/Ar , N_2 and SiH_4/Ar gas mixtures were determined by optical transmission spectroscopy and Fourier transform infrared spectroscopy. Growth rate was in the range 2–10 nm/min, while refractive index changed from 2.6 to 1.48 with a corresponding change in $\text{O}_2/(\text{N}_2 + \text{O}_2)$ from 0.01 to 0.318 at constant total flow and constant silane flow. The influence of gas flow ratio and substrate bias on refractive index, growth rate and on chemical composition of grown layers was also studied.

1. Introduction

New generations of electronic and optical devices place new demands on current fabrication technology. These include a further reduction in deposition temperature and stringent control of the energy of particles bombarding the wafer surface to prevent radiation damage of sensitive structures [1].

Silicon nitride and silicon-oxynitride films have found many applications in integrated circuits and devices as dielectrics, diffusion barriers, as well as for isolation and passivation of semiconductor

structures [2]. It is also a very attractive material for optical thin films since refractive index can be varied according to needs over an extremely broad range without the problems associated with matching materials with different chemical and mechanical properties [3–5]. Common methods to produce silicon nitride and oxynitride thin layers are 13.56 MHz PECVD, afterglow CVD or thermal CVD techniques [6].

One of the candidates to replace standard 13.56 MHz plasma deposition of thin films is a hybrid 2.45 GHz electron cyclotron resonance plasma enhanced chemical vapour deposition (ECR-PECVD) technology [7–9]. In this arrangement microwave excitation creates a low energy, low pressure, high density plasma, while 13.56 MHz bias allows for precise control of the energy of

* Corresponding author. Tel: +27-11 489 2351. Telefax: +27-11 489 2344. E-mail: pls@ing1.rau.ac.za.

charged particles striking the substrate surface and therefore control over the stress in the films.

2. Experiment

2.1. Deposition system

The vacuum system consists of a pumping station, main chamber, compact ECR source and gas distribution system. It is schematically represented in Fig. 1. A Leybold-Heraeus 360 CSV turbomolecular pump together with a TRIVAC D30A rough pump were used to provide sufficient pumping speed and base pressure of less than 10^{-7} Torr in the chamber. A pneumatic gate valve was installed on the pumping port. A bypass line (not shown) allows loading of samples in the chamber while the turbomolecular pump is running.

The stainless steel high vacuum chamber was equipped with two CF63 and several KF40 flanges to allow flexible installation of the ECR source, electrical and gas feedthroughs, a quadrupole mass spectrometer and vacuum gauges. Convectron gauges were used to monitor pressure during deposition and a cold cathode Penning gauge and

mass spectrometer were employed for base pressure monitoring. The typical pumpdown time from atmosphere to 2×10^{-7} Torr was 30 min. A substrate holder, made from aluminium and Teflon and with rf/dc biasing capabilities, holds the sample in a vertical position at variable distance from the source, and at any chosen angle to the direction of the plasma stream. A compact ECR plasma source was installed on the chamber in a horizontal position and equipped with an additional Tesla coil for extraction of ions. Since the ECR source was described elsewhere [10] it will not be described here in detail.

Several gas channels were used to deliver the gases into the chamber. One line was dedicated to deliver N_2 and 9% O_2 in Ar, and a separate line for 30% SiH_4 in Ar. The first line was used to feed the ECR source, while the second one introduced silane through a gas distribution ring placed close to the substrate holder. The correct position of the gas ring relative to the substrate was found to be very important for satisfactory uniformity and growth rate. The third gas channel is dedicated for backfilling of the system with nitrogen. Filters were put in every gas line to ensure absence of particles in the gas stream. Two Aalborg Instruments

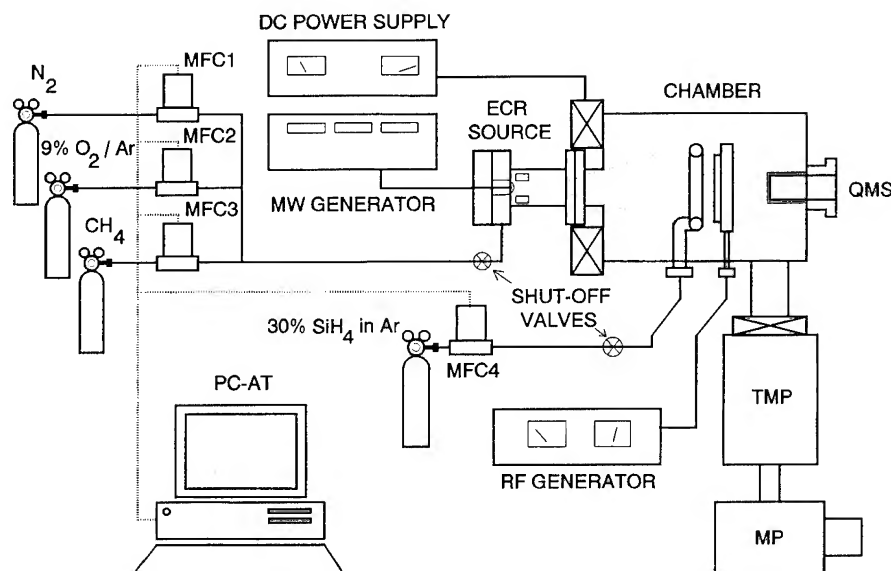


Fig. 1. Schematic representation of the computer controlled ECR deposition system.

AFC-2600 mass flow controllers (MFC) with normally closed control valves and a flow rate up to 100 sccm, and two Tylan 2900 MFCs with a maximum flow rate of 50 sccm provide smooth changes of gas flows. Valves, mass flow controllers, filters and gas inlets were equipped with VCR type fittings for maximal leak tightness. All tubing was chemically polished inside to ensure minimum outgassing capacity.

Microwave energy was supplied to the source via a flexible coaxial line from the 2.45 GHz magnetron generator. The manually controlled generator provides 5–800 W microwave power to the quarter-wave antenna isolated from vacuum by a cap made of alumina ceramic, which is cooled with pressurized nitrogen. A regulated 13.56 MHz radio frequency (rf) generator with a power amplifier was used to bias the substrate in order to control the energy of ions arriving onto the substrate. Self-bias was monitored during deposition.

A personal computer is the key device in the control system for the deposition machine. Two PCL-718 multi-function data acquisition cards [11] which were attached to the computer carried out the control of the gas flows, providing a predetermined set of flow rates. Each card is used in a differential unipolar analog input configuration and employs an industrial standard 12-bit successive approximation converter (HI-674A) to convert analog inputs. The maximum A/D sampling rate is 60 kHz which is more than enough during control of the MFCs. Each card also has two 12-bit monolithic D/A output channels with an output range of 0 to +5 V for driving the MFC up to full flow rate.

2.2. Deposition and characterization

During deposition the conditions were as follows: 100 W microwave power; base pressure less than 10^{-6} Torr; working pressure of about 2 mTorr; gas flow rates set from 3 to 13 sccm; total flow rate was kept constant at 21 sccm; 10 W rf-bias power. Deposition was carried out onto $\langle 100 \rangle$ p-type silicon substrates. For FTIR transmission measurements, 3 in high resistivity double-side polished silicon wafers were cut into four. One sample from each wafer was used as reference in

FTIR measurements. The other three quarter pieces of each wafer were used as carriers for deposition of layers of different composition, but with the same thickness of 150 nm. Before deposition all silicon substrates were cleaned with the standard RCA cleaning procedure.

Deposited films were studied with a Rudolf Research Auto-EL ellipsometer at a single wavelength of 632.8 nm for estimation of growth rate and refractive indices of the films. A UV-VIS-NIR spectrophotometer Hitachi model U-3400 was used for transmission measurements. The values of optical band gap were calculated from these transmission spectra [12]. Infrared transmission measurements were performed in the 2.5–25 μm wavelength range using a Perkin-Elmer 1600 FTIR spectrophotometer.

3. Results and discussion

Data of growth rate versus gas flow ratio are shown in Fig. 2. The growth rate increased with increasing $\text{O}_2/(\text{N}_2 + \text{O}_2)$ ratio. Simultaneously, the refractive index, measured at a wavelength of 632.8 nm, decreased, because of the substitution of Si–N bonds with Si–O bonds, and oxidation of excessive silicon in the layers.

For infrared transmission measurements seven samples of SiO_xN_y with different $\text{O}_2/(\text{O}_2 + \text{N}_2)$ flow ratio were used. Thin films of pure SiO_2 and Si_3N_4 were grown for reference. Gas mixtures of 4 sccm 30% SiH_4 in Ar with 16 sccm 9% O_2 in Ar, and 4 sccm 30% SiH_4 in Ar with 16 sccm N_2 were used, respectively. The results of FTIR measurements are presented in Fig. 3. A clear tendency can be observed in the change of optical absorption peak positions. With an increase in $\text{O}_2/(\text{O}_2 + \text{N}_2)$ ratio the main peak of the Si–N stretching mode in Si_3N_4 at 830 cm^{-1} is smoothly shifting towards 1040 cm^{-1} , which is the Si–O stretching mode in SiO_2 . One should notice that transition from mostly silicon nitride to mostly silicon dioxide takes place between 0.027 and 0.049 gas flow ratios. The corresponding change in refractive index can be seen in Fig. 2. Also, there are hardly any Si–H or N–H bonds at wave numbers 2160 cm^{-1} and 3330 cm^{-1} , respectively. The exception is the

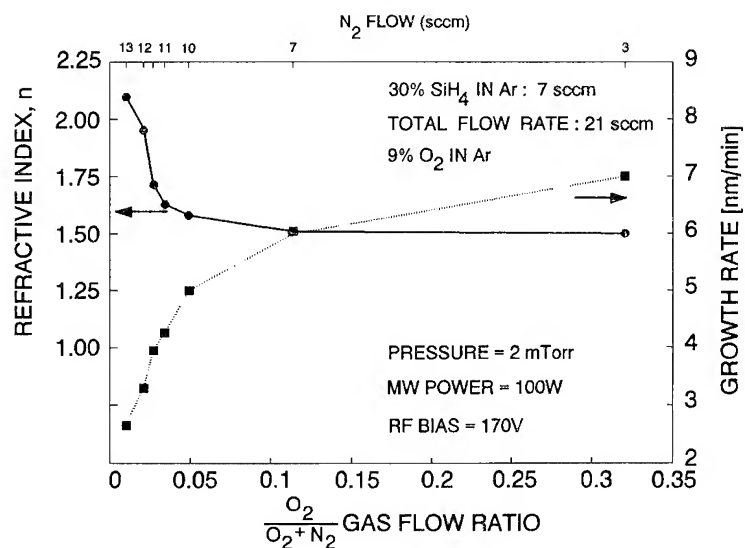


Fig. 2. Dependence of refractive index and growth rate of SiO_xN_y on $\text{O}_2/(\text{N}_2 + \text{O}_2)$ flow ratio at a constant 7 sccm flow of SiH_4 . Lines are drawn as guides for the eye.

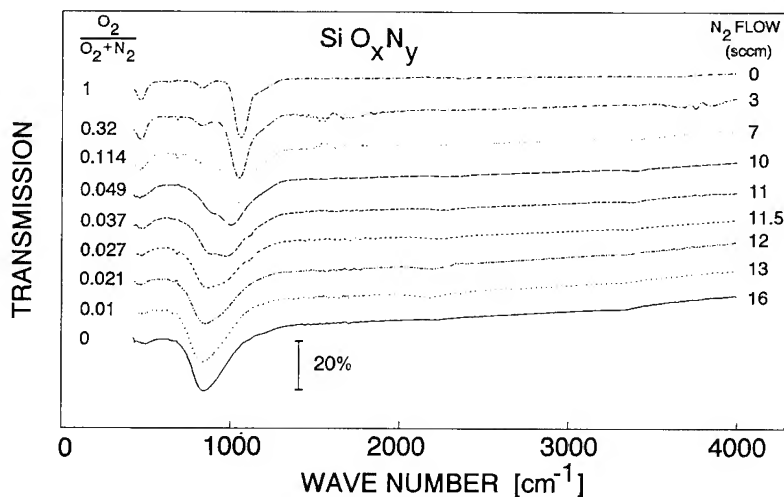


Fig. 3. FTIR transmission spectra of SiO_xN_y films (all layers are of approximately equal thickness, 150 nm).

samples grown at 0.01 and 0.021 gas flow ratios, for which the small number of Si–H bonds is attributed to excessive silicon in the layers [13].

In Fig. 4 the dependence of growth rate and refractive index at 632.8 nm on self-bias is shown for a flow ratio $\text{O}_2/(\text{O}_2 + \text{N}_2) = 0.114$. Growth rate

increased linearly from 1.5 to 8.8 nm/min, while the refractive index increased only slightly from 1.522 to 1.552, most probably because of some densification resulting from an increase of ion bombardment following the increase in self-bias from 50 to 250 V.

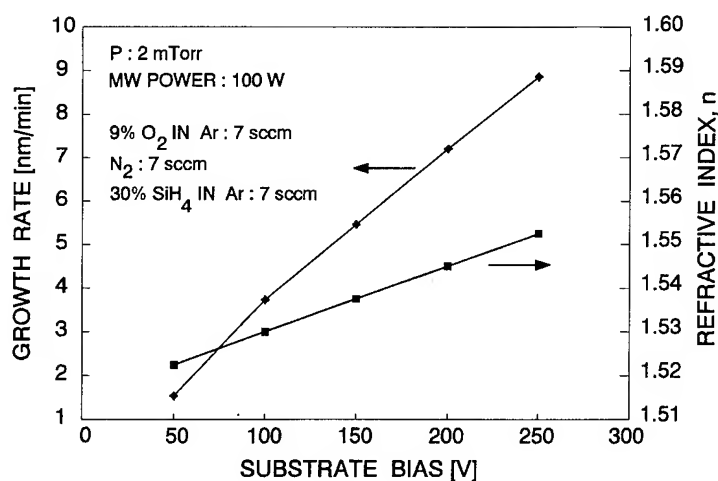


Fig. 4. Dependence of refractive index of SiO_xN_y at 632.8 nm and growth rate of SiO_xN_y on self-bias of the substrate. Lines are drawn as guides for the eye.

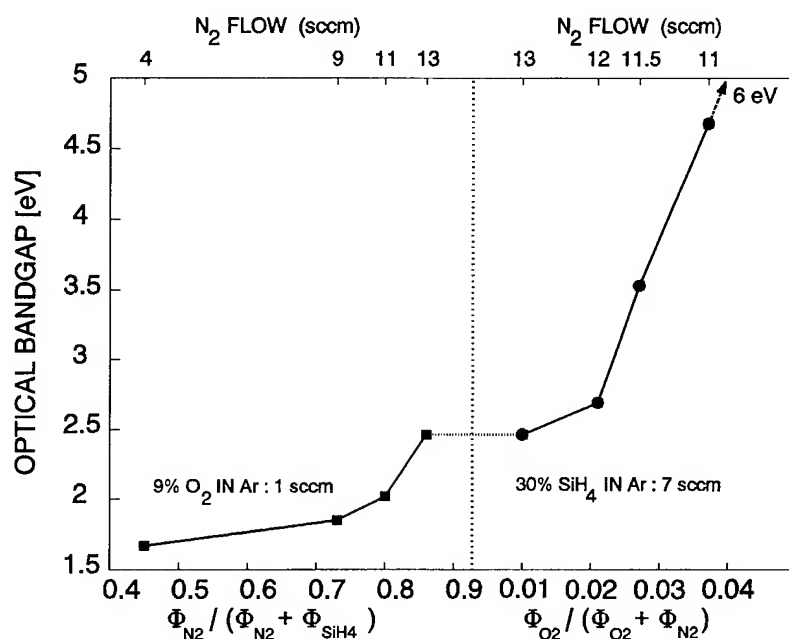


Fig. 5. Optical band gap E_g versus gas flow ratio for SiO_xN_y . Lines are drawn as guides for the eye.

The values of optical band gap are represented in Fig. 5. It increases from 1.7 to more than 6 eV (not shown in the graph) with an increase in the proportion of nitrogen and oxygen in the gas composition, corresponding to an increase in

nitrogen and oxygen content in the film (decrease in refractive index). This indicates the transition from silicon to silicon-rich oxynitride and further to silicon dioxide in the chemical composition of the film.

4. Conclusions

ECR-PECVD of silicon-oxynitride layers was investigated for different gas flow ratios and substrate bias. It was found that increased self-bias resulted in a large increase of growth rate, while the refractive index changed only slightly. The gas flow ratio determined refractive index over a broad range as a result of changes in chemical composition. FTIR measurements showed a smooth transition between silicon dioxide and silicon nitride.

The authors would like to thank Mr Anatoli Scherbakov of Sensors Sources and Signal Processing Research Group, RAU, who provided specialized software for digitizing graphical information. Ms Erna Burger of SABAX (Pty) Ltd. is thanked for use of their FTIR spectrophotometer, and Mr Berto Monard and Francois Denner of the Division of Production Technology of the CSIR for use of their UV-VIS-NIR spectrophotometer.

References

- [1] S.T. Picraux, E. Chason and T.M. Mayer, *Mater. Res. Soc. Bull.* 17 (1992) 52.
- [2] S.V. Nguyen, *J. Electron. Mater.* 16 (1987) 275.
- [3] P.V. Bulkin, P.L. Swart, B.M. Lacquet and F.J. Burger, *S. Afr. J. Phys.* 16 (1993) 33.
- [4] P.V. Bulkin, P.L. Swart and B.M. Lacquet, *Thin Solid Films* 241 (1994) 247.
- [5] P.V. Bulkin, P.L. Swart and B.M. Lacquet, *Opt. Eng.* 33 (1994) 2894.
- [6] R.S. Rosler, *Solid State Technol.* 34 (1991) 67.
- [7] B. Gorowitz, R.H. Wilson and T.B. Gorczyca, *Solid State Technol.* 30 (1987) 97.
- [8] J. Asmussen, *J. Vac. Sci. Technol.* A7 (1989) 883.
- [9] S. Matsuo and M. Kiuchi, *Jpn. J. Appl. Phys.* 22 (1983) L210.
- [10] S.Yu. Shapoval, P.V. Bulkin, A.A. Chumakov, S.A. Khudobin, I.A. Maximov and G.M. Mikhailov, *Vacuum* 43 (1992) 195.
- [11] Model PCL-718, User's Manual, Advantech Co., Ltd., Taiwan (1988).
- [12] R. Swanepoel, *J. Phys.* E16 (1983) 1214.
- [13] D. Schalch, A. Scharmann and R. Wolfrat, *Thin Solid Films* 124 (1985) 301.



ELSEVIER

Journal of Non-Crystalline Solids 187 (1995) 409–414

JOURNAL OF
NON-CRYSTALLINE SOLIDS

Electrical properties of Au/Bn/InP MIS diodes

O. Baehr^a, M. Barrada^a, A. Bath^{a,*}, B. Lepley^a, P. Thévenin^a, J. Schoonman^b

^a LICM/CLOES-Supélec, University of Metz, 2 rue E. Belin, 57078 Metz, France

^b Laboratory for Inorganic Chemistry, Delft University of Technology, Julianalaan 136, 2628 BL Delft, The Netherlands

Abstract

Capacitance–voltage characteristics of metal–insulator–semiconductor structures of boron nitride on InP have been investigated. The measurements show an overall good capacitance modulation. In accumulation, the frequency dependence of the capacitance of these diodes is consistently attributed to tunneling-related trapping. Bias–temperature–stress (BTS) measurements are used to evaluate the density and sign of the ions which are mobile at 400 K. BTS measurements at 300 K show effects mainly attributed to electron injection from the InP into traps located in the insulator near the interface.

1. Introduction

Indium phosphide (InP) metal–insulator–semiconductor (MIS) field-effect transistors (MISFETs) present potential applications in high frequency digital circuits, microwave power amplifiers and monolithic optoelectronic devices. Thus many efforts were directed at the development of a high quality InP MIS technology. Plasma enhanced chemical vapor deposition (PECVD) processes are known to allow deposition of dielectric films at low temperatures, avoiding thermal damage to the semiconductor substrates.

In the present work, MIS structures based on boron nitride (BN) films have been characterized by capacitance–voltage measurements, at different

frequencies and different temperatures for bias–temperature–stress (BTS) measurements.

2. Experimental procedure

Boron nitride thin films were deposited on InP, by a PECVD technique, using the reaction of borane-dimethylamine (BDMA) and ammonia [1]. The InP substrates were located downstream the plasma region in order to minimize surface damage. Before introduction into the reactor, the samples were chemically etched in HCl. The deposition was then performed by applying an rf plasma power of 50 W for 2 h, with a substrate temperature fixed at 320°C. The BDMA is heated up to 45°C and hydrogen is used as the carrier gas to transport its vapor into the reaction chamber. The samples were annealed at 400°C for 30 min in nitrogen. To study the electrical properties, Au/BN/InP MIS structures were prepared.

* Corresponding author. Tel: +33 87 75 96 09. Telefax: +33 87 75 96 01. E-mail: bath@esemetz.es-metz.fr.

3. Results and discussion

The resistivity of the insulating layers, deduced from current–voltage measurements, was found in the 10^{11} – 10^{12} Ω cm range. From the capacitance–voltage characteristic measured at 1 MHz, the distribution of the interface states density was deduced following the lines of the Terman method. A minimum value of 3×10^{11} cm^{-2} eV^{-1} was found. In the following we first present our results on the frequency dispersion of the C – V curves and then the hysteresis effects which have been studied by BTS measurements.

3.1. Anomalous frequency dispersion in accumulation

Fig. 1 shows the C – V curves measured at various frequencies for a given sample A. In accumulation, the capacitance of this structure decreases by about 11% when the frequency increases from 1 kHz to 1 MHz. A similar frequency dispersion has been observed in many InP MIS diodes [2–8] and various mechanisms have been proposed [2,4,8–12], including the frequency dispersion of the permittivity of the insulator, the presence of a parasitic series impedance, of high leakage currents in the insulator layer, and the existence of

a high-density distribution of states at the interface or in the insulator.

The frequency dependence of the permittivity of the insulator has been ruled out by the study of a metal–insulator–metal structure.

An alternative explanation which has also been ruled out is the presence of a parasitic series impedance. Indeed, in the studied frequency range, the series resistance, 25 Ω , evaluated for the structure A only induced 0.25% in the frequency dispersion, which is very weak compared with the experimental value. Thus the parasitic series impedance has an insignificant effect on the measured accumulation capacitance.

The observed variations cannot also be attributed to a high leakage current in the BN layer, as we shall see now. In the accumulation regime, the semiconductor capacitance, C_{sc} , is much higher than the insulator capacitance, C_i . If we only consider the effect of the conductance of the insulator, G_i , the measured capacitance is approximately given by

$$C_m = C_i \left[1 + \frac{G_i^2}{C_{sc} C_i \omega^2} \right]. \quad (1)$$

The experimental C_m versus $1/\omega^2$ curve, for $V_g = +3$ V, exhibits a non-linear behavior which implies that the high leakage current in the BN

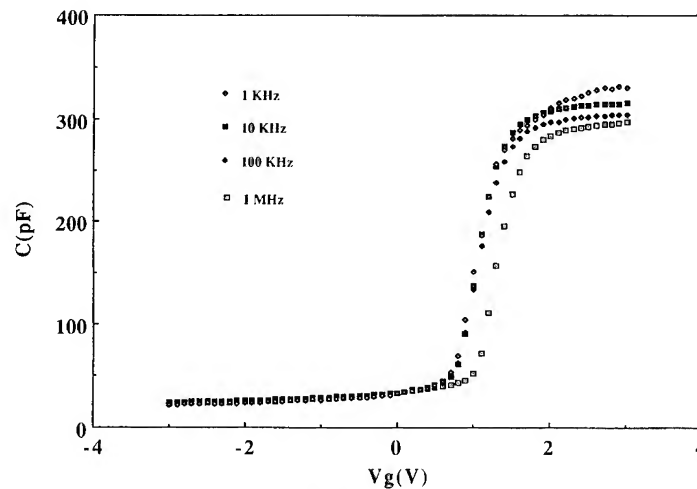


Fig. 1. C – V curves at different frequencies (1 kHz to 1 MHz) of a BN–InP MIS structure (sample A).

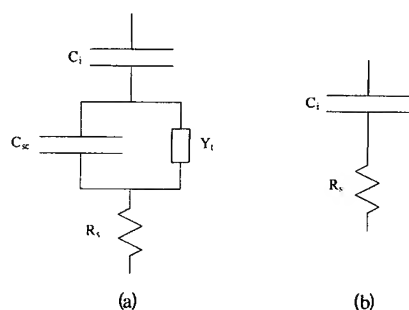


Fig. 2. Conventional circuit diagrams [13] of the insulator-semiconductor interface in (a) depletion and (b) accumulation.

layer cannot be the main origin of the observed frequency dispersion.

The fourth hypothesis to explain this phenomenon is the existence of interface states. The conventional circuit diagram [13] is shown in Fig. 2(a) where the trap admittance, Y_t , is a parallel combination of the trap capacitance, C_t , and the trap conductance, G_t . The frequency response of the trap can be described by Lehocvec's [14] expression:

$$C_t = \frac{C_{it}}{\omega\tau} \tan^{-1}(\omega\tau), \quad (2)$$

where C_{it} is the interface trap capacitance and τ the trap response time. In accumulation, the impedance of C_{sc} is negligible, Y_t is nearly short-circuited leading to the simplified circuit shown in Fig. 2(b). According to this circuit model no frequency dispersion is expected in accumulation [11].

Mui et al. [11] have proposed a new circuit model to explain this phenomenon. The insulator is assumed to be perfect apart from the fact that it contains a spatial distribution of traps, located near the semiconductor/insulator interface, whose energy distribution is arbitrary. They assumed that the traps which respond to the applied ac signal are close in energy to the conduction band edge of the semiconductor. Consequently the capture of tunneling electrons by these traps can be direct, without the need of a two-step process, Shockley-Read-Hall (SRH) mechanism followed by tunneling, as in the model of Heiman and Warfield [15].

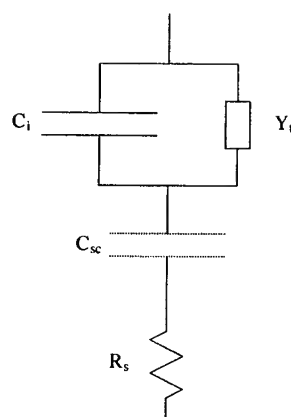


Fig. 3. Circuit model which describes the tunneling-related trapping in accumulation [11].

They showed that with direct capture of tunneling electrons by interface traps, the appropriate circuit model is modified as reported in Fig. 3. In this model the large value of C_{sc} no longer short-circuits the trap admittance. According to their derivation, the interface trap capacitance is frequency dependent, and also includes some other physical parameters such as the density, N_t of tunneling-related traps, the response time, τ , of the traps, the electron tunnel wave vector, k_0 and the thickness, δ , of the trapping layer. The measured capacitance versus frequency, in accumulation at $V_g = 3$ V, is reported in Fig. 4. By matching the calculated capacitive frequency dispersion to measured data, the following values were obtained:

$$N_t \cong 2 \times 10^{18} \text{ eV}^{-1} \text{ cm}^{-3}, \quad \delta \cong 12 \text{ \AA},$$

$$k_0 \cong 0.8 \times 10^8 \text{ cm}^{-1}, \quad \tau \cong 2 \times 10^{-6} \text{ s}.$$

These values seem physically consistent and nearly comparable to those reported by Mui et al. [11]. The observed behavior can be explained by the fact that, as the frequency measurement decreases, more traps can respond, and a consequence the measured capacitance increases as the frequency decreases. Thus tunneling-related trapping becomes important in accumulation, and may be responsible for the observed capacitance dispersion.

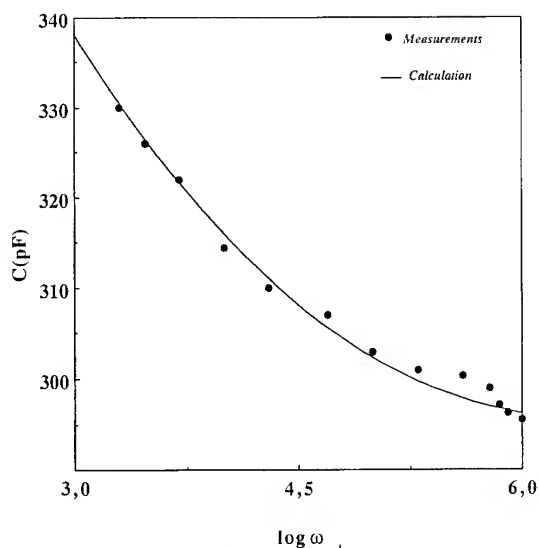


Fig. 4. Comparison of measured capacitance (dots), and calculated capacitance of sample A (solid line) from Eq. (15b) of Ref. [11].

3.2. Hysteresis

3.2.1. Hysteresis effects and trapped carriers

The hysteresis may have several physical origins [10,15–17]. Among these mechanisms, there can be

trapping of the electrons at the semiconductor surface by traps located in the insulator adjacent to the semiconductor. This problem has been considered by Heiman and Warfield [15]. We have performed two types of experiments to check this model for our structures.

In the first experiment the C – V characteristics at various frequencies have been measured. A systematic dispersion of flat-band voltages with frequency has been observed. A typical result for a sample B of the flat-band voltage, V_{FB} , versus frequency is given in Fig. 5. Such a result, $V_{FB} \propto \log \omega$, is consistent with the model of Heiman and Warfield which assumes, for the trap states, an exponential distribution of time constants with depth in the insulator.

In the second experiment, the MIS structure was subjected to BTS cycles [18,19]. The results are shown in Fig. 6. All these C – V measurements at 1 MHz have been performed at 77 K. Curve 1 was obtained without bias stress. For curve 2, before the measurements, the MIS structure was biased for 3 min at 300 K, under $V_g = 5$ V, and subsequently cooled to 77 K with the bias still applied. This procedure was repeated for 15 min (curve 3), and for 15 min under a negative bias of -5 V (curve 4). We note that for curves 2 and 3, the shift is toward

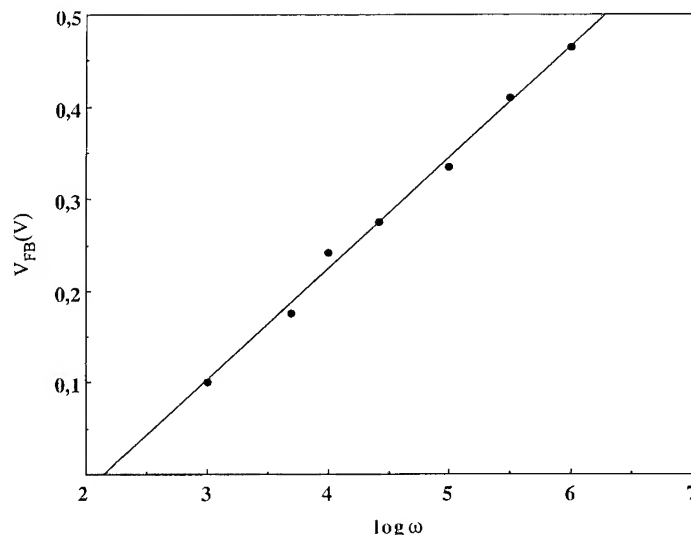


Fig. 5. Flat-band voltage shifts of a MIS structure (sample B) versus frequency. The line is drawn as a guide for the eye.

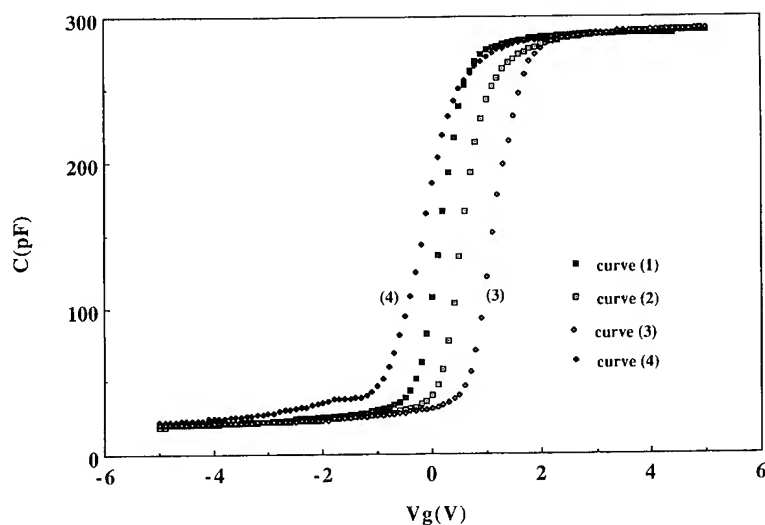


Fig. 6. Effect of BTS measurements: sample B with bias stress starting at 300 K. Curve 1, unstressed; curve 2, after positive BTS for 3 min; curve 3, after positive BTS for 15 min; curve 4, after negative BTS for 15 min.

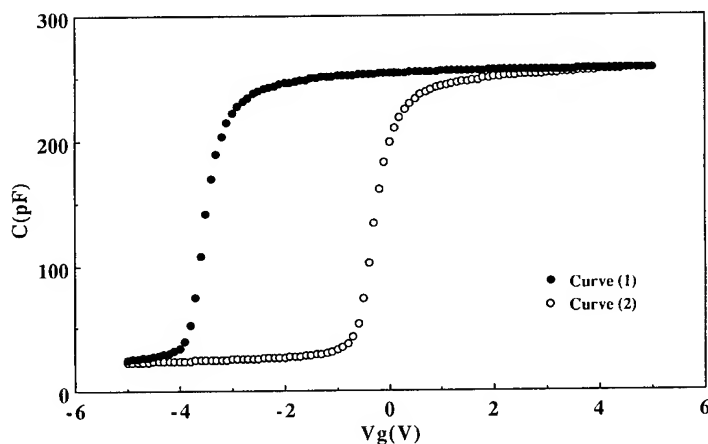


Fig. 7. Effect of BTS measurements: sample B with bias stress starting at 400 K. Curve 1, positive BTS for 15 min, curve 2, negative BTS for 15 min.

positive gate bias, which is consistent with a trapped insulator charge or interface states, lying deep in the gap, becoming more negative when the stress time increases at $V_g = 5$ V, whereas for a negative bias stress, the opposite effect is observed.

3.2.2. Ion drift

The movement of mobile ions is enhanced by elevated temperatures and an applied electric

field strong enough to cause the mobile ions to drift. A typical set of results (left going curves) for the sample B is shown in Fig. 7. In this figure the MIS structure was warmed up to 400 K with a gate bias $V_g = 5$ V. The situation was maintained for 15 min, and then the C - V curve 1 was measured after the MIS structure had been cooled to 77 K. This procedure was repeated with a negative gate bias $V_g = -5$ V (curve 2).

These experiments show that the C – V curve is translated along the voltage axis in a direction consistent with positive ion motion in the insulator. When the positive bias is applied the resulting electric field pushes the positively charged mobile ions toward the insulator/semiconductor interface. Therefore, the MIS C – V plot shifts to the left (curve 1) in proportion to the number of ions involved and the distance they have drifted. To obtain the mobile ion concentration at 400 K, we have performed a second bias–temperature measurement with a stress bias opposite to the first one, in order for the ions to drift to the other side of the insulator. The mobile ion concentration N_i is determined at 400 K by the shift ΔV_{FB} between the two curves [4]:

$$N_i = \frac{C_i}{qS} \Delta V_{FB},$$

where C_i is the insulator capacitance, q is the electronic charge and S is the area of the gate electrode. For sample B, a value of $N_i \cong 8 \times 10^{11} \text{ cm}^{-2}$ has been found which is very representative of most of our samples.

4. Conclusions

In summary, MIS structures formed by PECVD of BN on InP exhibit charge injection instability, hysteresis effects and anomalous frequency dispersion. The frequency dispersion of the C – V curves in accumulation has been attributed mainly to tunneling of electrons into trap states located within a very thin layer of thickness δ in the insulator, and which are very close in energy to the conduction band. The BTS experiments at 400K show that the

behavior of the C – V curves (1 MHz) is dominated by the presence of mobile ions, whereas at 300 K the measurements are consistent with a model of electron trapping in the insulator.

References

- [1] A. Bath, O. Baehr, M. Barrada, B. Lepley, P.J. van der Put and J. Schoonman, *Thin Solid Films* 241 (1994) 278.
- [2] T. Kobayashi and Y. Shinoda, *J. Appl. Phys.* 53 (1982) 3339.
- [3] Y.H. Jeong, S. Takagi, F. Arai and T. Sugano, *J. Appl. Phys.* 62 (1987) 2370.
- [4] P. Klopfenstein, G. Bastide and M. Rouzeyre, *J. Appl. Phys.* 63 (1988) 150.
- [5] P. Viktorovitch, *J. Electrochem. Soc.* 136 (1989) 1431.
- [6] P. Dimitriou, G. Post and A. Scavennec, *J. Phys. (Paris)* 50 (1989) 675.
- [7] A. Bath, P.J. van der Put, J.G.M. Becht, J. Schoonman and B. Lepley, *J. Appl. Phys.* 70 (1991) 4366.
- [8] Y. Shacham-Diamand, N. Moriya and G. Bahir, *Appl. Phys. Lett.* 58 (1991) 1314.
- [9] T. Sawada and H. Hasegawa, *Thin Solid Films* 56 (1979) 183.
- [10] T.Y. Chou and M.S. Lin, *J. Appl. Phys.* 59 (1986) 3778.
- [11] D.S.L. Mui, J. Reed, D. Biswas and H. Morkoç, *J. Appl. Phys.* 72 (1992) 553.
- [12] D.S.L. Mui, Z. Wang and H. Morkoç, *Thin Solid Films* 231 (1993) 107.
- [13] E.H. Nicollian and J.R. Brews, *MOS (Metal Oxide Semiconductor) Physics and Technology* (Wiley, New York, 1982).
- [14] K. Lehovec, *Appl. Phys. Lett.* 8 (1966) 48.
- [15] F.P. Heiman and G. Warfield, *IEEE Trans. Electron Devices* ED 12 (1965) 167.
- [16] L. He, H. Hasegawa, T. Sawada and H. Ohno, *J. Appl. Phys.* 63 (1988) 2120.
- [17] J.G. Simmons and L.S. Wei, *Solid State Electron.* 16 (1973) 53.
- [18] A. Etchells and C.W. Fisher, *J. Appl. Phys.* 47 (1976) 4605.
- [19] E.H. Snow, A.S. Grove, B.E. Deal and C.T. Sah, *J. Appl. Phys.* 36 (1963) 1664.



ELSEVIER

Journal of Non-Crystalline Solids 187 (1995) 415–419

JOURNAL OF
NON-CRYSTALLINE SOLIDS

Surface plasmon-induced luminescence: a probe to study electrical aging and dielectric breakdown in polymer-like thin films

A. Foulani^a, C. Laurent^{a,*}, P. Canet^b

^a Laboratoire de Genie Electrique, CNRS URA 304, Université Paul Sabatier, 118 route de Narbonne, 31062 Toulouse cédex, France

^b Laboratoire d' Electronique et de Physico-Chimie des Couches Minces, Université Aix, Marseille, France

Abstract

Electroluminescence was observed in sandwich structures composed of a thick layer of plasma-deposited hydrogenated carbon and two metallic electrodes. Luminescence experiments combined with transport analysis show that the light comes from the radiative decay of electrode surface plasmons excited by hot electrons produced in the films. The precise nature of the dielectric is unimportant since the emission process involves the electrode parameters. The optical response is governed by the nature and thickness of the positively biased electrode: (i) when a thick electrode is used, the only excited surface plasmon mode is located at the dielectric–electrode interface which acts as a probe for the low energy end of the electron energy distribution function; (ii) when a semi-transparent electrode is used, electrons with an energy of a few eV can cross the metallic layer. These hot carriers are able to excite a surface plasmon mode located at the outer interface. Depending on the temperature and metal thickness, hot carriers of different kinetic energies can excite this surface plasmon mode. The interface acts as a probe for the high energy end of the electron energy distribution function. Detection of luminescence due to electrode surface plasmon decay gives access to carrier energy which is the main aging and breakdown controlling factor of the dielectric layer.

1. Introduction

The understanding of electrical degradation (aging) and dielectric breakdown of thin insulating films is an important task. Numerous investigations have been devoted to the study of inorganic layer like SiO₂ since the reliability of MOS devices is affected by the degradation of the insulator [1].

The problem is also important for organic materials [2]. Factors of electronic origin are the result of the interaction of excess non-thermalized carriers with the dielectric material, which in turn can induce both thermal and higher energy chemical reactions [3]. Hot electrons have already been identified as a decisive factor in ultimate breakdown [4]. Although they have been mentioned to lead to aging, there is still little direct experimental evidence for this phenomenon. Because the electronic properties of insulators in general, and of polymeric insulators in particular, are only poorly

* Corresponding author. Tel: +33 61 55 82 41. Telefax: +33 61 55 64 52. E-mail: laurent@lget.ups-tlse.fr.

understood, it is difficult to approach the electron energy distribution in the dielectric. The present paper deals with high-field effects leading to aging in amorphous hydrogenated carbon thin films (a-C:H) prepared from gas phase polymerization. Electroluminescence due to the radiative decay of the electrode surface plasmon appears to be a promising tool to investigate degradation of the insulating layer since it is a probe sensitive to the existence of carriers with kinetic energies of a few eV.

2. Experimental details

The samples consist of a three-layer sandwich coating $4 \times 6 \text{ mm}^2$. The bottom electrode, on glass, was either a 2000 Å thick layer of transparent and conductive indium–tin–oxide (ITO) made by radio-frequency sputtering, or a 300 Å thick semi-transparent evaporated layer of aluminum. The organic layers were prepared from plasma polymerization of methane or propane at low pressure (a few mTorr) in a diode system. The third layer was a resistively evaporated Al electrode. The experimental configuration is shown in Fig. 1. The electrode on glass was positively biased relative to the Al top electrode. Light was detected through the glass substrate in a direction normal to the sample surface. A conventional photon counting technique was used to detect electroluminescence in the visible region (quasi-flat response of the detection system from 300 to 800 nm).

The (a-C:H) layers prepared by gas phase polymerization have different composition and electrical properties depending on the monomer and deposition conditions. Using methane as a monomer and a voltage excitation frequency of 20 kHz, we get (a-C:H) films containing a variable amount of graphite carbon mainly controlled by the power density of the discharge [5]. The low field electrical resistivity of the films is from 10^{+10} to $10^{+14} \Omega \text{ cm}$ as a function of its composition. Using propane and a 13.56 MHz frequency discharge, we end up with a film composed of dense hydrocarbon with a very small proportion of graphite-carbon-like structure, with a low field resistivity of $\approx 10^{+15} \Omega \text{ cm}$ [6]. (a-C:H) thin films are deposited on the ITO elec-

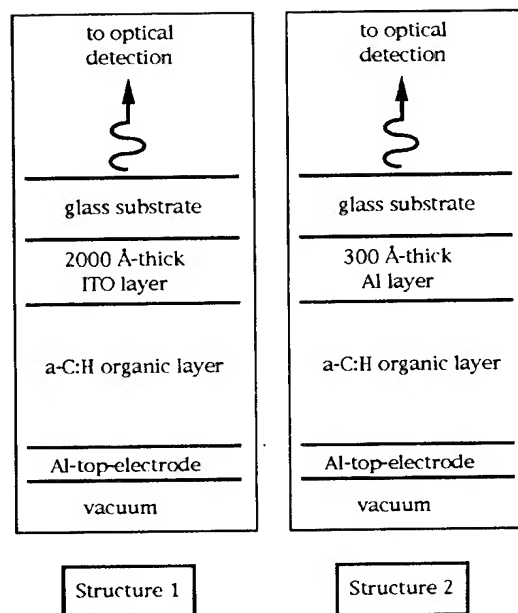


Fig. 1. Observation configuration. The relative thickness of each layer is not considered in the diagram. The amorphous hydrogenated carbon (a-C:H) layer is prepared by glow discharge polymerization of propane or methane.

trode. Surface chemical reactions due to oxygen reduction of ITO by hydrogen atoms present in the gas phase occur in the early phase of film growth. It leads to the formation of a $\approx 30 \text{ Å}$ thick (In–Sn) enriched layer at the ITO surface as shown by secondary ion mass spectroscopy analysis [7]. This thin metallic layer changes the optical surface properties of the ITO electrode.

3. Combined electroluminescence and transport analysis

Electroluminescence can be excited in the metal–insulator–metal (MIM) structures by application of dc, ac, and pulsed voltages [8]. A careful analysis of charge transport in the plasma polymerization layers has shown that the current is space charge limited. Depending on the electrical properties of the layer, the trap filled limit voltage, V_{TFL} can be smeared out. But in every case, the light emission onset corresponds to a change of

the transport process denoted by an increase of the conductivity.

In order to identify the emission process, we have tested two polymer-like layers with very different electrical properties. The first type of film has a low field resistivity of $\approx 10^{+15} \Omega \text{ cm}$ and is composed of dense hydrocarbon with a very small proportion of graphitic-carbon-like structure. The second type of thin film is composed of graphitic islands – roughly 100 Å in extension – dispersed in a more insulating matrix. The low field resistivity is around $10^{+12} \Omega \text{ cm}$. Two different electrode arrangements were used. (i) In one case, the two kinds of matrix were grown on the ITO transparent electrode and a thick Al top electrode was subsequently deposited. Light was detected through the ITO layer and the glass substrate. (ii) In the other case, they were grown on a thick Al electrode and a semi-transparent gold layer was deposited on top of the structures. Light was detected through the gold layer. The external quantum luminescence efficiency of each structure was roughly estimated by dividing the number of photons detected in a direction normal to the surface of the device by the number of electrons flowing through the insulating film. The interesting point is that it only depends on the electrode arrangement and not on the dielectric matrix. If a matrix contribution to the emitted light cannot be ruled out, it must be very weak. Further

experiments [5] have shown that electroluminescence efficiency is controlled by the characteristics of the electrodes, i.e. the nature and thickness of the metallic layer and its surface roughness. A very strong analogy exists between our observations and the emission from what has been called electron-injector structures [9]. In the latter case, luminescence arises from radiative decay of plasmons excited by the hot electron current component on the positively biased electrode, with a strong dependence of the emission efficiency on the nature of the metal electrode. In the following section, we demonstrate that this emission process can qualitatively account for the experimental behavior reported so far.

4. Emission process

Two surface plasmon (SP) modes were of interest in our experimental configuration (see Fig. 1): one was located at the glass–electrode interface, the other at the electrode–dielectric interface. Both were able to radiate, if excited, through the residual roughness of the interface. The relative excitation and radiative decay efficiencies of these two SP modes determine their relative contribution to the final radiative output of the MIM structure. Radiative coupling between SP and photons in the

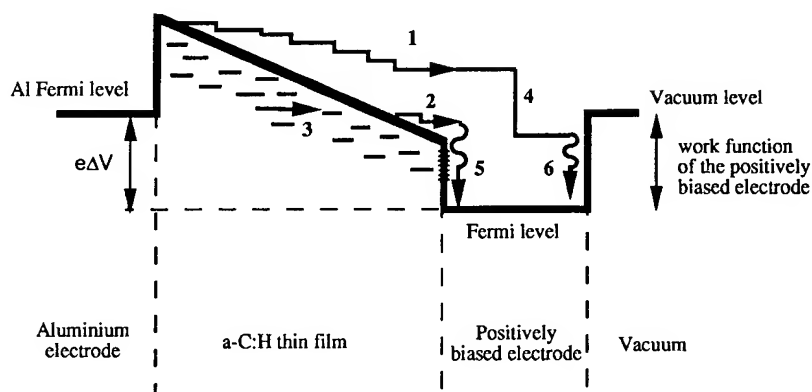


Fig. 2. Inferred processes leading to light emission in the MIM structures. Process 1: hot electron scattering in the conduction band of (a-C:H) thin film; process 2: electrons at the conduction band edge with lower kinetic energies; process 3: conduction involving localized states in the forbidden gap; process 4: scattering of hot electrons injected into the metal; process 5: surface plasmons to photons conversion at the inner interface; process 6: surface plasmons to photons conversion at the outer interface.

visible range is straightforward in the case of aluminum since the theoretical limiting wavelength of surface plasmon excitation is around 1200 Å for this metal [10]. Due to the optical properties of ITO (the real part of the dielectric constant is positive in the visible), SP cannot radiate into the visible part of the spectrum [11]. The formation of a thin (In–Sn) layer with metallic properties at the ITO surface in the early phase of film growth accounts for a shift of the limiting wavelength of SP to the visible region. The temperature dependence of the light efficiency was studied for both structures (same dielectric layer) in the temperature range between -185°C and 0°C . It stays constant for structure 1 through the whole temperature range whereas it sharply decreased for structure 2 from about -80°C up to room temperature. From this behavior, it is possible to evaluate the contribution of each SP mode to the radiative output of the structure along the following lines.

The electron energy distribution at the interface between the insulator and the positively biased electrode is certainly not monochromatic. The existence of traps in the dielectric and the scattering process in the conduction band of the insulator lead to a broad distribution from about the conduction band minimum minus the Fermi level of the metal, $(E_c - E_f)$ up to a few eV. The hot conduction electrons injected into the metal at the insulator–electrode interface (process 1, Fig. 2) can excite the outer SP mode of the metallic electrode (process 6, Fig. 2) if it is sufficiently thin to prevent a complete relaxation of the electron distribution in the bulk of the metal (process 4, Fig. 2). In structure 1, the ITO electrode was 2000 Å thick, which appears too thick to allow electrons to reach the outer surface taking into account the typical value of the ballistic mean free path of hot electrons in metals. Moreover, coupling between SP and visible photons would have not been possible at this interface due to the optical properties of ITO as previously reported. In structure 2, however, the Al thickness is comparable to the electron mean free path. Electron–photon scattering is temperature dependent due to freezing of the metal phonons. A decreasing temperature increases the light efficiency by allowing more electrons to reach the out metal surface. This was indeed observed. It appears therefore that

the light from structure 1 was just due to the radiative decay of SP at the inner ITO–dielectric interface (process 5, Fig. 2). In structure 2, it was dominated by SP modes localized at the outer Al–glass interface (process 6, Fig. 2).

The low energy tail of the electron energy distribution provides conditions for SP generation at the inner interface of the positively biased electrode whereas electrons of higher energies are injected into the metal. If we consider that they are relaxed after a few scattering processes, most of the electrons are lost in the bulk ITO. On the contrary, they can excite SP at the outer surface of the thin Al electrode. If this picture is correct, the inner interface of the positively biased electrode must be a probe for the low energy tail of the electron energy distribution whereas the outer metal surface must probe the high energy tail.

A study of the current dependence of the spectra confirms this view. For structure 1, the light spectrum does not change with the current or the temperature. This is consistent with a picture involving coupling between SP and the low energy tail of the electron energy distribution at the dielectric–ITO interface. Generation of plasmons is only due to electrons with virtually no kinetic energies, i.e. those electrons located at the bottom of the conduction band with energy $\approx (E_c - E_f)$. Electrons

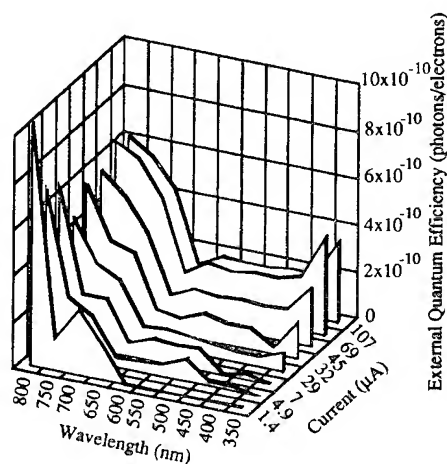


Fig. 3. Temperature dependence of the emission spectra for structure 2 (current is 5 μA).

with higher energies enter the metal and relax in the bulk ITO by phonon emission. The spectrum dependence on current for structure 2 is shown in Fig. 3. The shift towards the blue region with an increasing current can reasonably be attributed to a contribution of electrons with higher energies to the excitation of SP. Similarly, we observed a blue shift of the emission spectrum with decreasing temperature (under constant excitation current).

5. Conclusion

Light emission from metal–insulator–metal structures composed of a thick organic layer and two metallic electrodes is reported. The space-charge limited conduction current provides excitation conditions of surface plasmons at the positively biased electrode surface above the trapped limit voltage. Coupling to the radiation field occurs through the surface roughness. Surface plasmons can only be created on one surface of a thick collecting electrode. It behaves like a probe for the low energy tail of the electron energy distribution function. When a semi-transparent electrode is used, both surfaces can contribute to the light output. The relative contribution of the two surface plasmon modes can be investigated by studying the

temperature dependence of the light efficiency and of the spectral shape. The outer surface of the metallic electrode is a probe for electrons with higher energies. This can be of great interest for the understanding of dielectric breakdown and electrical aging of the insulating layer.

References

- [1] D.J. DiMaria, T.N. Theis, J.R. Kirtley, F.L. Pesanto and D.W. Dong, *J. Appl. Phys.* 57 (1985) 1214.
- [2] L. Sanche, *IEEE Trans. Elect. Insul.* 28 (1993) 789.
- [3] E. Cartier and P. Pfluger, *IEEE Trans. Elect. Insul.* 22 (1987) 123.
- [4] M. Sparks, D.L. Mills, R. Warren, T. Hostein, A.A. Maradudin, L.J. Sham, E. Loh Jr. and D.F. King, *Phys. Rev. B* 24 (1981) 3519.
- [5] P. Canet, C. Laurent, J. Akinnifesi and B. Despax, *J. Appl. Phys.* 73 (1993) 384.
- [6] L.F. Floutard, J. Akinnifesi, E. Cambril and B. Despax, *J. Appl. Phys.* 70 (1991) 798.
- [7] P. Canet and C. Laurent, *J. Appl. Phys.* 75 (1994)
- [8] P. Canet, C. Laurent, J. Akinnifesi and B. Despax, *J. Appl. Phys.* 72 (1992) 2423.
- [9] J.R. Kirtley, T.N. Theis, J.C. Tsang and D.J. DiMaria, *Phys. Rev. B* 27 (1983) 4601.
- [10] A. Daude, A. Savary and S. Robin, *J. Opt. Soc. Am.* 62 (1972) 1.
- [11] H. Köstlin, R. Jost and W. Lems, *Phys. Status Solidi A* 29 (1975) 87.



ELSEVIER

Journal of Non-Crystalline Solids 187 (1995) 420–424

JOURNAL OF
NON-CRYSTALLINE SOLIDS

Structure rearrangement and electrochromic properties of amorphous tungsten trioxide films

Irina V. Shiyanovskaya*

Institute of Physics, Ukrainian Academy of Science, Pr. Nauki 46, 252028 Kiev, Ukraine

Abstract

The correlation between the electrochromic properties and the structure rearrangements of amorphous WO_3 films induced by the storage in aqueous electrolyte used in electrochromic cells has been established. Water penetration into the amorphous WO_3 framework from electrolyte and formation of crystalline hydrates $\text{WO}_3 \cdot n(\text{H}_2\text{O})$ lead to the decrease of electrochromic efficiency in the visible spectral range due to the strong red shift of electrochromic absorption band of formed hydrates. The different electron transfer energy responsible for coloration of $\text{WO}_3 \cdot 2(\text{H}_2\text{O})$ and $\text{WO}_3 \cdot \frac{1}{3}(\text{H}_2\text{O})$ is caused by various degrees of ordering of these hydrates.

1. Introduction

Amorphous tungsten trioxide (a-WO_3) films have been the subject of many experimental and theoretical studies due to their possible application in electrochromic (EC) devices such as passive high contrast displays with wide view angles, light modulators, 'smart' windows, etc. [1,2]. In spite of numerous investigations of WO_3 films, such displays are not commercially available yet. The main problem lays in short device lifetime due to the fast film degradation.

It is now well known that EC coloration of WO_3 films owes to a double injection of electrons and protons (or cations). The coloration is reached by polarizing WO_3 film in an electrolytic medium. Reverse polarization causes the bleaching to the original colorless state.

Several models of EC coloration have been proposed up to date. Deb [3] was the first one to suggest the formation of F centers in reduced tungsten trioxide: oxygen vacancies with a trapped electron. Model of intervalence charge transfer of Faughnan et al. [4] supposes that the injected electron is trapped at a W^{6+} site adjacent to a proton thus forming a W^{5+} color center. Light absorption occurs due to charge transfer between two neighboring tungsten sites $\text{W}^{5+} \rightarrow \text{W}^{6+}$. Injected protons compensate for the negative charge of injected electrons. Schriener et al. [5] have suggested that injected electrons are localized on W^{6+} sites perturbing the surrounding lattice and forming small polarons. The underlying physics of this model is similar to the last one. Dautremont-Smith et al. [6] have explained the light absorption by conduction electron interband transitions and by transitions between the cation band and the WO_3 conduction band. The models of intervalence charge transfer and small polaron are the most widely accepted.

The EC properties of a-WO_3 films are considerably affected by the deposition methods. Numerous

* Corresponding author. Tel: + 380-44 265 9831. Telefax: + 380-44 265 4463. E-mail: kinr@sovam.com.

studies [7–14] have confirmed that water content in the films plays an important role in EC coloration. The states of water in the WO_3 film may be classified into three groups: physisorbed water, chemisorbed water, known as Bronsted acid site, and hydrated water having a crystal structure [7]. The a- WO_3 films stored in high humidity air were studied in [7–9]. The water absorbed from atmosphere (approximately 0.3 water molecule per WO_3 unit) results in fast cathodic and anodic reactions. On the other hand, absorbed water reacts gradually with WO_3 by hydroxylation and/or hydrolysis. A hydroxylated film has a negative shift in the potential of the cathodic reaction [8]. Then hydroxylated film loses the EC coloration density at the same applied voltage as before. The change of electrochromic efficiency of WO_3 films depends on the charge-transfer process in the film which in its turn depends on water states.

By contrast with extensive studies understanding the relationship between the EC properties and the water state in the WO_3 films, little is known about the property changes of WO_3 films, induced by the WO_3 /electrolyte interface [12,14–16]. Aqueous solution of H_2SO_4 is an electrolyte that is widely used in EC cells and in which the fast coloration due to high proton mobility was observed.

It is now known [12] that chemical stability of a- WO_3 in aqueous electrolytes is far from perfect and EC properties are gradually lost during the storage in electrolyte owing to the dissolution and physical erosion. But very fast loss of electrochromic efficiency in electrolyte (50 h) and slow dissolution rate (4 nm/day) testifies that additional degradation mechanisms have to exist. In our previous works [15,16] we have found that the storage in sulfuric acid electrolyte results in a- WO_3 transformation into tungsten trioxide crystalline hydrates $\text{WO}_3 \cdot n(\text{H}_2\text{O})$.

In this paper, we study the correlation between EC properties and structure changes in a- WO_3 induced by the existence of film/electrolyte interface.

2. Experimental procedures

Amorphous WO_3 films about 0.5 μm thick were deposited by thermal evaporation from a tantalum

boat in vacuum of 0.1 Pa on glass coated with SnO_2 layer with different deposition rates of 0.5 and 5 nm/s. The film thickness was determined by quartz microbalance during deposition. The substrate temperature was 100–120°C. Deposited films were confirmed to be amorphous by electron diffraction.

To study the influence of electrolytic medium, the evaporated films were stored in 1% H_2SO_4 for 50 h at room temperature. As we have shown earlier [15,16] initial a- WO_3 films are transformed into tungsten trioxide crystalline hydrates $\text{WO}_3 \cdot n(\text{H}_2\text{O})$ during storage in electrolyte for this time. The water molecules penetrate into the film forming hydrated water in crystalline hydrate $\text{WO}_3 \cdot 2(\text{H}_2\text{O})$ and $\text{WO}_3 \cdot \frac{1}{3}(\text{H}_2\text{O})$. The type of crystalline hydrates depends on the deposition rate, which in turn determines pore sizes in initial films. We have obtained $\text{WO}_3 \cdot 2(\text{H}_2\text{O})$ from a- WO_3 films deposited with slow rate (0.5 nm/s) and $\text{WO}_3 \cdot \frac{1}{3}(\text{H}_2\text{O})$ – with fast rate (5 nm/s).

Cyclic voltammetry measurements were carried out in the three-electrode electrochemical cell with 1% H_2SO_4 electrolyte. The working electrode was a- WO_3 film on conducting substrate. A Pt plate was used as the counter electrode. The reference electrode was a saturated calomel electrode (SCE). Potential scan rate was 30 mV/s. A voltage ± 1 V was applied between the SnO_2 and the counter electrodes.

Optical data have been obtained by automatic spectrometer KSVU-12 in the range of 200–1300 nm in electrochemical cell for colored and bleached films.

3. Results

Cyclic voltammograms of as-deposited a- WO_3 films (solid curve 1) and stored films of $\text{WO}_3 \cdot \frac{1}{3}(\text{H}_2\text{O})$ (dashed curve 2) and $\text{WO}_3 \cdot 2(\text{H}_2\text{O})$ (solid curve 3) are shown in Fig. 1. The cathodic current is associated with the coloration process and the anodic one is associated with bleaching process. Fig. 1 shows that for crystallized films, cathodic and anodic currents decrease. Coloration and bleaching become slower. The peak potentials

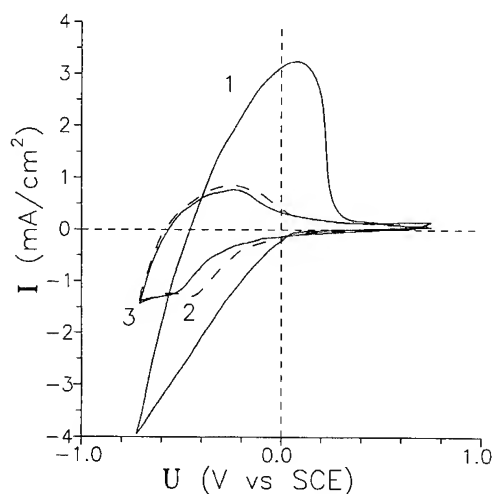


Fig. 1. Cyclic voltammograms at 30 mV/s scan rate in 1% H₂SO₄ electrolyte of a-WO₃ films (solid curve 1) and films transformed with storage in electrolyte during 50 h: WO₃·2(H₂O) (dashed curve 2) and WO₃·1/3(H₂O) (solid curve 3).

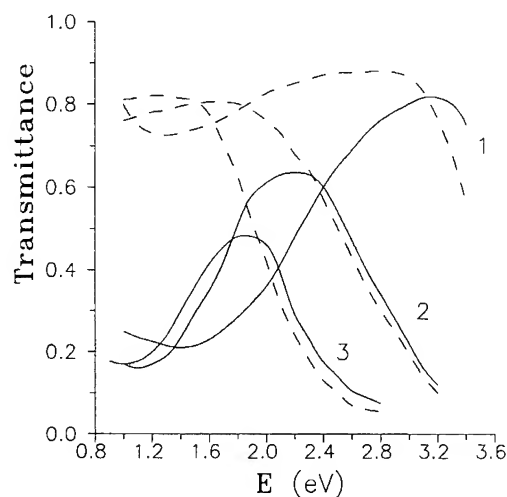


Fig. 2. Optical transmission spectra of electrochemical colored and bleached a-WO₃ film (curves 1) and crystalline hydrates WO₃·1/3(H₂O) (curves 2) and WO₃·2(H₂O) (curves 3). The dashed and solid curves represent the bleached and colored states, respectively.

of anodic and cathodic current are strongly shifted to the negative side.

Fig. 2 shows the optical transmission spectra of as-deposited a-WO₃ films (curves 1) and crystalline

hydrate films WO₃·1/3(H₂O) (curves 2) and WO₃·2(H₂O) (curves 3) in colored and bleached states. The dashed and solid curves represent the bleached and colored states, respectively. The red shift of the absorption band in colored state has been observed for crystalline hydrates in comparison with a-WO₃ films. The absorption band maximum in the spectrum of WO₃·1/3(H₂O) is located at 1.1 eV, in spectrum of WO₃·2(H₂O) – at 1.0 eV and for a-WO₃ – at 1.3–1.4 eV.

4. Discussion

Cyclic voltammograms (Fig. 1) show that both the anodic and cathodic reactions become slower with formation of crystalline hydrates. Since the crystalline structure is more dense than the amorphous, the crystallization may hamper the proton diffusion.

As shown by optical data (Fig. 2), the crystalline hydrates are EC materials but the absorption bands induced by EC coloration are strongly shifted to the red spectral range. The absorption band maxima are peaked in near infrared range. The EC efficiency (a ratio of induced optical density to the injected charge) or the crystalline hydrates is about 80 cm²/C at maximum of induced absorption band. Thus, the crystalline hydrates can be used as EC materials for application in near infrared range taking into consideration their high stability in electrolytes.

The decrease in EC efficiency of a-WO₃ in visible spectral range with the storage in electrolyte is caused by strong red shift of induced absorption band of the crystalline hydrates.

The different red shift of absorption maxima for WO₃·2(H₂O) and WO₃·1/3(H₂O) can be explained in terms of small polaron model.

It is known that EC absorption band arises owing to the intervalence charge transfer between W⁵⁺ and W⁶⁺ sites. The electron transfer energy depends on the film structure, local surrounding of W⁵⁺ optical centers and lattice disorder. The different red shift of EC band for hydrates WO₃·2(H₂O) and WO₃·1/3(H₂O) seems to be due to unequal electron transition energy in these hydrates.

The structure of crystalline hydrates $\text{WO}_3 \cdot 2(\text{H}_2\text{O})$ is formed by identical tungsten–oxygen octahedra. These octahedra contain a coordinated water molecule and an opposite terminal oxygen ion $\text{W} = \text{O}$. The octahedra share a corner with each of four neighboring octahedra within the layer (in a-b octahedron plane). The second water molecule forms hydrogen bond between layers [17].

There are two types of tungsten–oxygen octahedron in the crystalline hydrates $\text{WO}_3 \cdot \frac{1}{3}(\text{H}_2\text{O})$. The first ones are the same as in the $\text{WO}_3 \cdot 2(\text{H}_2\text{O})$ and the second ones are WO_6 octahedra which share six oxygen atoms [18]. The existence of two kinds of tungsten–oxygen octahedra brings about the unequal static deformation energy of W^{6+} sites in the crystalline hydrates $\text{WO}_3 \cdot \frac{1}{3}(\text{H}_2\text{O})$.

The energy of electron transfer liable for coloration consists of two terms. The first one is determined by energy lowering of electrons trapped at W^{5+} sites because of the lattice polarization and the formation of small polarons. The second one is attributed to different initial potential energy of electrons localized at non-equivalent W^{6+} sites with different local surroundings. The greater the disorder the greater the second term. Therefore, the electron transfer energy in disordered a- WO_3 film is maximal (1.3–1.4 eV). Crystallization results in equivalence of W^{6+} sites and lowering of electron transfer energy (1.0 eV for $\text{WO}_3 \cdot 2(\text{H}_2\text{O})$ and 1.1 eV for $\text{WO}_3 \cdot \frac{1}{3}(\text{H}_2\text{O})$).

The different red shift of the EC absorption band of the crystalline hydrates $\text{WO}_3 \cdot 2(\text{H}_2\text{O})$ and $\text{WO}_3 \cdot \frac{1}{3}(\text{H}_2\text{O})$ is due to the existence of the tungsten–oxygen octahedra of one kind in $\text{WO}_3 \cdot 2(\text{H}_2\text{O})$ and of two kinds in $\text{WO}_3 \cdot \frac{1}{3}(\text{H}_2\text{O})$. The energy equivalence of W^{5+} sites in $\text{WO}_3 \cdot 2(\text{H}_2\text{O})$ results in that the electron transfer energy is determined only by lattice polarization, that is by a polaron term. In case of $\text{WO}_3 \cdot \frac{1}{3}(\text{H}_2\text{O})$ the existence of two kinds of tungsten–oxygen octahedron gives an additional term in transfer energy due to unequal energy of static deformation of W^{6+} sites belonging to tungsten–oxygen octahedra of different kinds.

For display applications the crystallization of a- WO_3 films is an undesirable phenomenon. The amorphous nature of the film is necessary for a high coloration efficiency in visible range. To prevent crystallization the protect layer deposition was

used. In the same vacuum cycle, WO_3 films are covered by SiO_x thin film (20–30 nm). Such SiO_x film does not change the coloration efficiency and entirely prevents the crystallization of a- WO_3 during the time up to six months of storage in electrolyte.

5. Conclusions

The a- WO_3 film/aqueous electrolyte interface causes the transformation of initial amorphous structure to the crystalline state. Water molecules penetrate into amorphous WO_3 framework and form crystalline hydrates $\text{WO}_3 \cdot n(\text{H}_2\text{O})$. The decrease in EC efficiency of a- WO_3 in the visible spectral range with storage in electrolyte is due to red shift of induced absorption band of the crystalline hydrates. The different electron transfer energy liable for coloration of $\text{WO}_3 \cdot 2(\text{H}_2\text{O})$ and $\text{WO}_3 \cdot \frac{1}{3}(\text{H}_2\text{O})$ films is caused by various degrees of ordering of these hydrates. Taking into account high stability in electrolytes, and high EC efficiency of the crystalline hydrates, they can be used for applications in near IR range. The coloration and bleaching reactions in hydrates are reduced due to a dense structure which hampers proton diffusion.

The author is grateful to Dr V.I. Styopkin for many helpful discussions and Mr V.B. Nechitayilo for expert technical assistance.

References

- [1] S.K. Deb, Sol. Ener. Mater. Sol. Cell 25 (1992) 327.
- [2] C.G. Granquist, Thin Solid Films 193&194 (1990) 730.
- [3] S.K. Deb, Philos. Mag. 27 (1973) 801.
- [4] B.W. Faughnan, P.S. Crandall and P.M. Heyman, RCA Rev. 36 (1975) 177.
- [5] O.F. Schriener, V. Wittwer, B. Baur and G. Brandt, J. Electrochem. Soc. 124 (1977) 749.
- [6] W.C. Dautremont-Smith, M. Green and K.S. Kang, Electrochim. Acta 22 (1971) 751.
- [7] N. Yoshike, M. Ayusawa and S. Kondo, J. Electrochem. Soc. 131 (1984) 2600.
- [8] N. Yoshike and S. Kondo, J. Electrochem. Soc. 130 (1983) 2283.
- [9] N. Yoshike and S. Kondo, J. Electrochem. Soc. 131 (1984) 809.

- [10] T. Arnoldussen, *J. Electrochem. Soc.* 128 (1981) 117.
- [11] B. Reichman and A.J. Bard, *J. Electrochem. Soc.* 126 (1979) 583.
- [12] J.P. Randin, *J. Electron. Mater.* 7 (1978) 47.
- [13] R. Hudritch, *Electron. Lett.* 11 (1975) 142.
- [14] S.-S. Sun and P.H. Holloway, *J. Vac. Sci. Technol. A* 1 (1983) 529.
- [15] T.A. Gavrilko, V.I. Stepkin and I.V. Shivanovskaya, *J. Molec. Struct.* 218 (1990) 411.
- [16] I.V. Shivanovskaya, T.A. Gavrilko and E.V. Gabrusenoks, *J. Molec. Struct.* 293 (1993) 295.
- [17] M.S. Daniel, B. Desbat, J.C. Lasseques, B. Gerand and M. Figlarz, *J. Solid State Chem.* 67 (1987) 235.
- [18] B. Gerand, G. Nowogrocki and M. Figlarz, *J. Solid State Chem.* 38 (1981) 312.



ELSEVIER

Journal of Non-Crystalline Solids 187 (1995) 425–429

JOURNAL OF
NON-CRYSTALLINE SOLIDS

Section 13. High ϵ materials and ferroelectrics

Low pressure chemical vapour deposition of tantalum pentoxide thin layers

E.P. Burte*, N. Rausch

Fraunhofer-Institut für Integrierte Schaltungen, Bereich Bauelementetechnologie, Schottkystr. 10, D-91058 Erlangen, Germany

Abstract

Tantalum pentoxide thin films were grown by a low pressure chemical vapour deposition process using a metal-organic tantalum precursor material. After characterizing the deposition process, the stoichiometry, structure and electrical properties of the tantalum oxide thin films were investigated before and after annealing in oxygen and nitrogen at various temperatures. At annealing temperatures higher than 700°C, the as-deposited amorphous film becomes polycrystalline. Refractive index, dielectric permittivity and leakage current behaviour are improved by this phase transition.

1. Introduction

On account of their high permittivity of about $\epsilon = 25$ [1], tantalum pentoxide films have attracted much interest due to their potential applications as dielectric films for storage capacitors of memory cells and gate insulators in field effect transistors for future ultra large scale integrated circuits beyond the 64 Mbit device generation. Further, ion sensitive field effect transistors with a tantalum pentoxide gate dielectric layer have proven to be superior to those with silicon oxide and nitride thin films [2].

In this paper, we deal with low pressure (LP) metal-organic chemical vapour deposition (MOCVD) of tantalum pentoxide (Ta_2O_5) carried out in a newly developed hotwall-type vertical

reactor, and with the structural, optical and electrical properties of these films.

2. Experimental

Tantalum pentoxide (Ta_2O_5) films were deposited on wet chemically cleaned n-doped, 100 oriented, 3" silicon wafers in a low pressure vertical hot wall reactor using tantalum ethylate ($\text{Ta}(\text{OC}_2\text{H}_5)_5$) as the metal-organic (MO) precursor material of 99.99% purity. Oxygen was added to the process gas atmosphere in order to minimize oxygen deficiency in the Ta_2O_5 films. Further details and a schematic cross-section of the used MOLPCVD equipment have been published elsewhere [3].

After deposition, annealing treatments were performed in nitrogen and oxygen at temperatures ranging from 500 to 900°C. Stoichiometric and

*Corresponding author. Tel: +49-9131 761 310. Telefax: +49-9131 761 390.

structural data on the layers were obtained by ellipsometry, secondary-neutral mass spectroscopy (SNMS), X-ray photoelectron spectroscopy (XPS), Rutherford backscattering spectroscopy (RBS), X-ray diffraction (XRD) and high resolution transmission electron spectroscopy (HRTEM).

For electrical characterization, MIS capacitors were fabricated. High frequency capacitance–voltage ($C-V$) and current–voltage ($I-V$) measurements were carried out in order to determine the permittivity and the insulating properties of the films, respectively.

3. Results

3.1. The deposition process

Deposition rate and homogeneity across the wafer were monitored, as a function of temperature, pressure, oxygen flow and tantalum ethylate flow. For an optimized tantalum oxide deposition process, the following parameters were determined: deposition temperature 400–425°C; deposition pressure 33–60 Pa; tantalum ethylate flow 200–600 mg/h; oxygen flow 100–200 sccm. Deposition rates between 2.8 and 6.1 nm/min were obtained with a homogeneity across the wafer better than 4.3%. Depletion of the process gas across the boat could be compensated by adjusting a positive temperature gradient across the deposition zone, which is about zero at a deposition temperature of $T = 375^\circ\text{C}$ and increases up to 5 K/cm at $T = 500^\circ\text{C}$. The activation energy of the deposition process was determined to be $E_A = 0.8$ eV in the temperature range between 375 and 500°C.

3.2. Composition and structure

The stoichiometry of the tantalum oxide films was investigated by SNMS and XPS analyses. Fig. 1 shows a SNMS depth profile of the masses Ta (181), O (16) and Si (28) of a layer of thickness 75 nm. As can be seen from the figure, the layer composition is homogeneous across the depth with an abrupt interface corresponding to the bulk silicon. The atomic ratio of Ta to O was determined to be 2:5 for both the as-deposited and the annealed

samples. XPS combined with sputtering by an Ar beam of 3 keV confirmed the SNMS results.

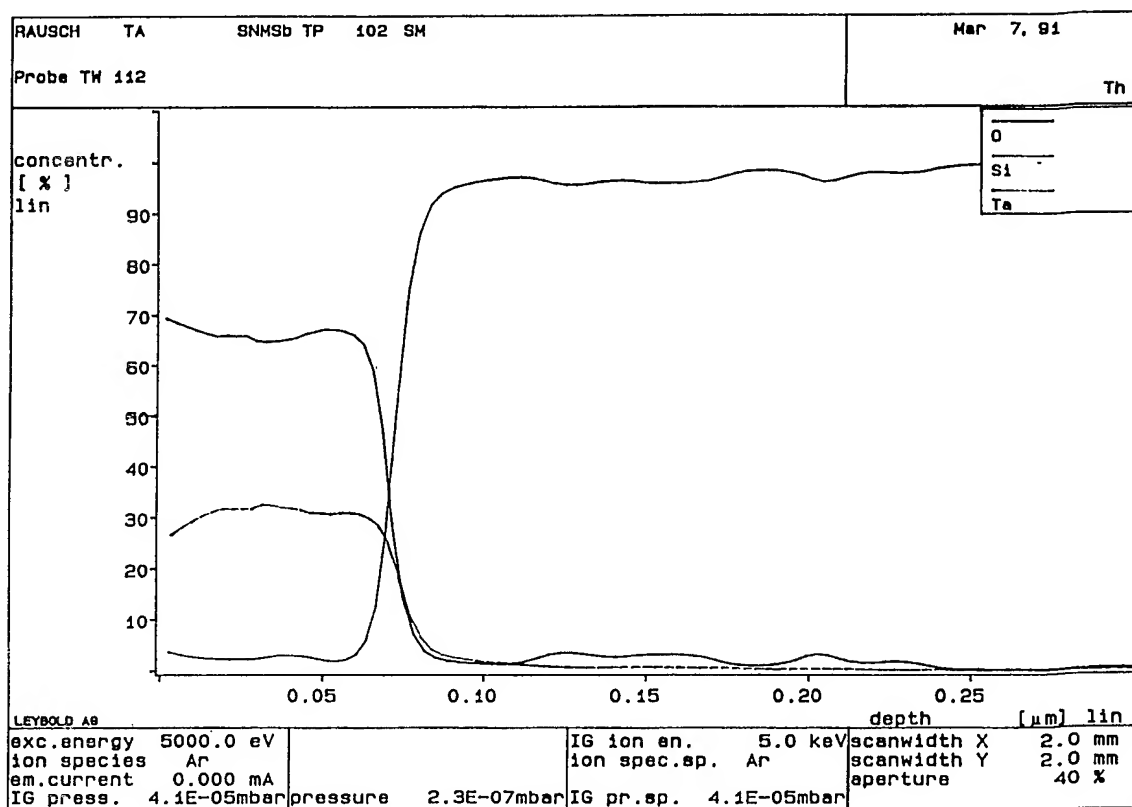
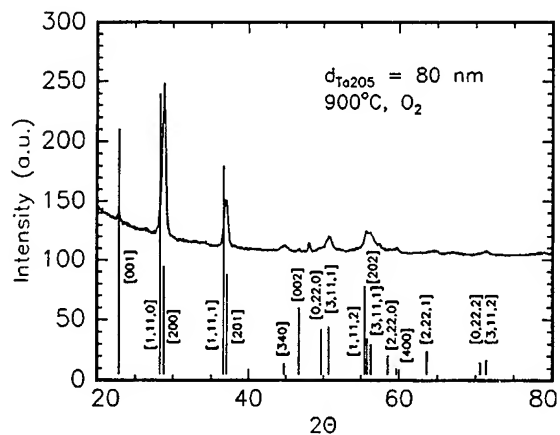
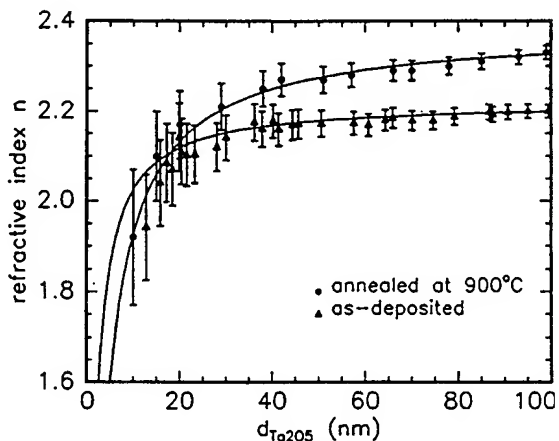
Due to the metalorganic precursor material (tantalum ethylate), carbon and hydrogen atoms were incorporated into the Ta_2O_5 film. The contents of amorphous and polycrystalline (annealed at 900°C in oxygen) tantalum oxide films were determined by secondary ion mass spectroscopy (SIMS). The concentration of carbon and hydrogen were ascertained to be 1.9 and 0.7 at.%, respectively, for the as-deposited film and 1.7 and 1.2%, respectively, for the annealed sample. The carbon content of our films was almost unchanged by annealing in contradiction to the results reported by Shinriki and Nakata [4] who observed a decrease by an order of magnitude. The change in the hydrogen content is within the limit of accuracy of the applied measurement method.

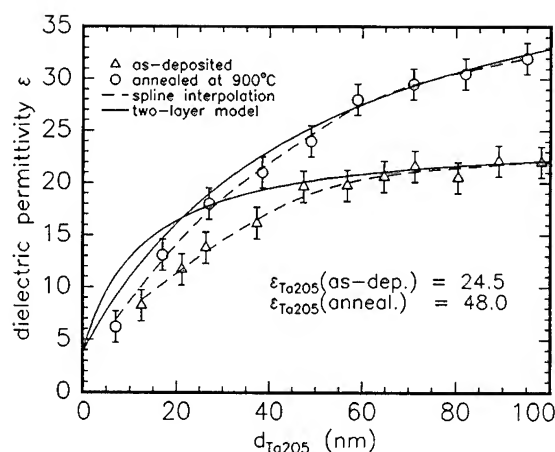
The crystal structure of the as-grown films and the films annealed in oxygen for 30 min at temperatures ranging from 500 to 900°C was investigated by XRD ($\text{Cu K}\alpha$, $\lambda = 0.15406$ nm).

While the as-grown samples and those annealed at 500, 600 and 700°C showed no peaks in the XRD pattern related to the presence or formation of a crystalline phase, the samples annealed at 800 and 900°C exhibited a polycrystalline structure. The temperature of the phase transition, therefore, is between 700 and 800°C. Fig. 2 shows the X-ray intensity vs. the diffraction angle 2θ of the sample annealed at 900°C. Included in the figure are the peaks of polycrystalline bulk material of the low temperature crystalline phase $\beta\text{-Ta}_2\text{O}_5$ [5]. From the comparison with the reference spectrum, it can be seen that the measured spectrum is identical with the exception of certain peaks in crystal directions, such as $[1,11,0]$, $[1,11,1]$ and $[0,22,0]$.

3.3. Optical properties

Fig. 3 shows the refractive index, n_{eff} , versus the ellipsometrically determined thickness, d , of a thin as-grown film and a film annealed at 900°C. Annealing at 900°C in oxygen increases the thickness of the thin silicon oxide layer below the Ta_2O_5 film from 1.5 nm for the as-grown film up to 4 nm. The thickness dependence of the refractive index, therefore, is due to this stack of the dielectric films SiO_2

Fig. 1. SNMS depth profile of the Ta_2O_5 film.Fig. 2. X-ray diffraction pattern of a polycrystalline Ta_2O_5 film.
 $T_{\text{anneal}} = 900^\circ\text{C}$.Fig. 3. Thickness dependence of refractive index, n .

Fig. 4. Thickness dependence of dielectric constant, ϵ .

and Ta_2O_5 . The solid lines included in the figure are theoretical calculations of the refractive index of the layer stack using the formula

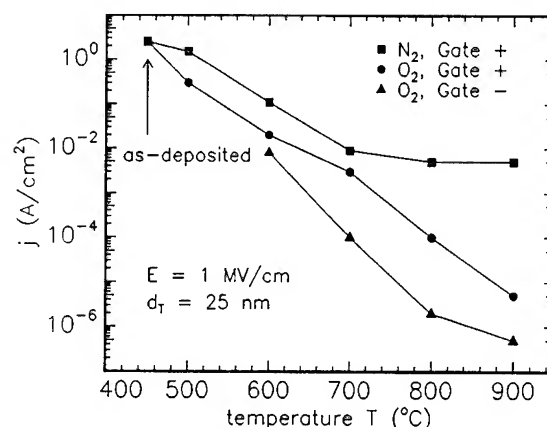
$$\frac{n^2 - 1}{n^2 + 1} = \frac{d_S}{d_S + d_T} \frac{n_S^2 - 1}{n_S^2 + 1} + \frac{d_T}{d_S + d_T} \frac{n_T^2 - 1}{n_T^2 + 1},$$

where n is refractive index, d is film thickness, and S and T indicate silicon oxide and tantalum oxide, respectively.

For the as-grown and annealed tantalum oxide films, values of the refraction index of $n_T = 2.22$ and $n_T = 2.38$, respectively, were used. The optical band gap, E_g , of the tantalum oxide films was investigated by absorption spectroscopy. For the amorphous films $E_g = 4.4$ eV, while for annealed polycrystalline films a value of $E_g = 4.2$ eV was determined.

3.4. Electrical properties

By using the capacitance value in accumulation of 1 MHz capacitance/voltage measurements, the permittivity of the films was determined. Fig. 4 shows the thickness dependence of the dielectric permittivity, ϵ , before and after the annealing treatment in oxygen ambient. For film thickness values exceeding 60 nm, the experimental ϵ values are very well fitted by a two-layer model assuming a serial connection of two capacitors with the dielectrics

Fig. 5. Leakage current density, j , vs. annealing temperature.

SiO_2 and Ta_2O_5 [6] because a thin SiO_2 layer grows at the interface. Although the intrinsic permittivity of polycrystalline Ta_2O_5 films was reported to be about $\epsilon = 25$ [7], values up to $\epsilon = 32$ were measured.

The density of the leakage current of as-grown Ta_2O_5 films is rather high by comparison with silicon oxide. In order to reduce it, a post-deposition annealing step is necessary. Fig. 5 shows the leakage current density at an applied field of 1 MV/cm vs. the temperature for films of thickness 25 nm annealed in oxygen and nitrogen ambient. As can be seen in the figure, annealing in oxygen is superior to that in nitrogen.

4. Discussion

As the deposition process temperature ranges between 375 and 500°C, the process is well suited to ultra large scale integrated devices due to its very low thermal budget. The reference XRD pattern of the low temperature phase crystalline $\beta\text{-Ta}_2\text{O}_5$ coincides with the measured spectrum of the annealed films with the exception of certain peaks.

This effect derives from the textured polycrystalline film with an orthorhombic structure. The longest axis of the unit cell is preferentially oriented perpendicular to the surface. Since in this direction,

the material is easier to polarize, higher values of the permittivity are possible compared with the random oriented case. In deviation from values of the intrinsic dielectric constant of $\epsilon = 25$ published in the literature [7], ϵ -values up to 32 were measured. This effect is due to the texture of the anisotropic crystal structure – as outlined above – which grows out of the amorphous Ta_2O_5 film at annealing temperatures $> 700^\circ\text{C}$. Post deposition annealing in oxygen is superior to that in nitrogen. This is due to three phenomena reducing the leakage current level: (i) the completing of oxygen vacancies in the Ta_2O_5 network, (ii) the densification and crystallization of the structure, and (iii) the growth of a thin interfacial SiO_2 layer between the silicon substrate and the Ta_2O_5 film. Topic (ii) is also valid for nitrogen annealing. Leakage current values below $10\text{--}5\text{ A/cm}^2$ can be achieved allowing the application of the films to electronic devices.

5. Conclusions

In this paper we have studied the low pressure chemical vapour deposition process of high

dielectric constant tantalum oxide thin films using a metal organic precursor material. The as-grown films revealed to be amorphous of stoichiometric composition Ta_2O_5 . Annealing at temperatures beyond 700°C results in textured polycrystalline Ta_2O_5 films with a orthorhombic structure. A thin interfacial silicon oxide layer is lying beneath the tantalum oxide films influencing refractive index and dielectric permittivity of the dielectric film. Annealing in oxygen lowers the leakage current by several orders of magnitude.

References

- [1] H. Shinriki et al., *IEEE Trans. Electron Dev.* ED-37, (1990) 1939.
- [2] W. Göpel, J. Hesse and J.N. Zenel, eds., *Sensors*, Vol. 2 (VCH, Weisheim, 1991).
- [3] E.P. Burte and N. Rausch, in: *Proc. INFOS '91 Conf.*, Liverpool, Apr. 1991, ed. W. Eccleston and M. Urrer (Adam Hilger, Bristol) p. 199.
- [4] H. Shinriki and M. Nakata, *IEEE Trans. Electron Dev. Lett.* EDL-38, (1991) 455.
- [5] R.S. Roth, J.L. Waring and H.S. Parker, *J. Solid State Chem.* 2 (1970) 445.
- [6] N. Rausch and E.P. Burte, *Microelectron. J.* 24, (1993) 421.
- [7] M. Saito et al., *IEDM Tech. Dig.* (1986) 680.



ELSEVIER

Journal of Non-Crystalline Solids 187 (1995) 430–434

JOURNAL OF
NON-CRYSTALLINE SOLIDS

Investigation of the film growth of a new titanium precursor for MOCVD

F.-R. Lang^a, E.C. Plappert^a, K.-H. Dahmen^{a,*}, R. Hauert^b, P. Nebiker^c, M. Döbeli^c

^a *Laboratorium für Anorganische Chemie, ETH Zentrum, Universitätsstrasse 6, 8092 Zürich, Switzerland*

^b *EMPA, Überlandstr.129, 8600 Dübendorf, Switzerland*

^c *PSI, Labor für Ionenstrahlphysik, Würenlingen Switzerland*

Abstract

Thin TiO₂ films were grown with a new solid titanium pyrazolylborate precursor by thermal metal organic chemical vapour deposition (MOCVD) in a temperature range of 300–800°C. Previous differential thermal analysis/thermogravimetric measurements have shown that this precursor is suitable for reduced pressure MOCVD systems. The amorphous character of the films deposited on quartz, sapphire, and Si [1 0 0] substrates was proven by X-ray diffraction. Oxygen and ammonia were used as reaction gases.

1. Introduction

TiO₂-films have found numerous applications such as antireflection coatings, sensors and photo catalysts [1,2]. This is due, in part, to the high refractive index, high dielectric constant and excellent transmittance in the visible and near-IR spectra range [3].

The most common chemical vapour deposition (CVD) techniques for TiO₂-film deposition employ either titanium tetrachloride (TiCl₄) [4,5] or titanium alkoxides (Ti(OR)₄) [6–10].

We report here the thermoanalysis of a new solid titanium pyrazolylborate MOCVD precursor HB(pz)₃Ti(OⁱPr)₃ (sketched formula, Scheme 1) and the film growth of amorphous TiO₂ on several

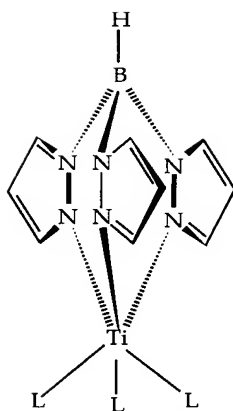
substrates. The film growth behaviour at various process conditions was carefully investigated.

2. Experimental procedure

All films were prepared from the precursor HB(pz)₃Ti(OⁱPr)₃, where HB(pz)₃ and OⁱPr denote the trispyrazolylborate and isopropoxide ligands, respectively. The synthesis of this complex, as well as those of the methyl derivatives, will be published elsewhere [11]. The thermal analysis (DTA/TGA) of HB(pz)₃Ti(OⁱPr)₃ was measured on a Mettler TA-2000C Thermoanalyzer. The evaporation rates were determined by weight loss experiments in the MOCVD apparatus as described in [12].

Thin amorphous films of TiO₂ were grown on quartz, sapphire, and Si[100] substrates in a horizontal quartz reactor described elsewhere [12] at low pressure conditions of 20–30 mbar. The substrates were located on a graphite susceptor heated

*Corresponding author: Present address: Department of Chemistry and MARTECH, The Florida State University, Tallahassee, FL, 32306–3006, USA. Tel: +1-304 944 4074. E-mail: dahmen@chen.fsu.edu.



Scheme 1. Sketched formula for the solid titanium pyrazolylborate MOCVD precursor $\text{HB}(\text{pz})_3\text{Ti}(\text{O}^i\text{Pr})_3$.

by infrared lamps. The growth of the film was investigated at various substrate temperatures from 300 to 800°C. The precursor was evaporated in a ceramic boat which was brought into the system. In all experiments, helium was used as the carrier gas to transport the precursor vapour to the substrate with a flow rate of 66 sccm. Reaction gases such as the oxygen and ammonia were introduced in the reaction chamber with a flowrate of 108 sccm.

The transparent films were analyzed with UV/VIS (Uvikon 820). All other films were investigated by X-ray diffraction (XRD) (Phillips PW1710), profilometry (Tencor alpha-step 200), ellipsometry (Plasmos SD2300), Rutherford backscattering spectroscopy (RBS), Auger electron spectroscopy (AES) (Perkin-Elmer PHI 4300 SAM) and X-ray photoelectron spectroscopy (XPS) (Perkin-Elmer PHI 5400 ESCA). Details will be published elsewhere.

3. Results

In order to test the use of the volatile $\text{HB}(\text{pz})_3\text{Ti}(\text{O}^i\text{Pr})_3$ as a MOCVD precursor, thermal analysis was carried out in argon with a heating rate of 10 K/min. The results of the thermogravimetric analysis (TGA) (Fig. 1) show that, at normal pressure, the weight loss of the precursor starts at 150°C. From differential thermal analysis, an endothermic peak at 118°C could be identified as the melting

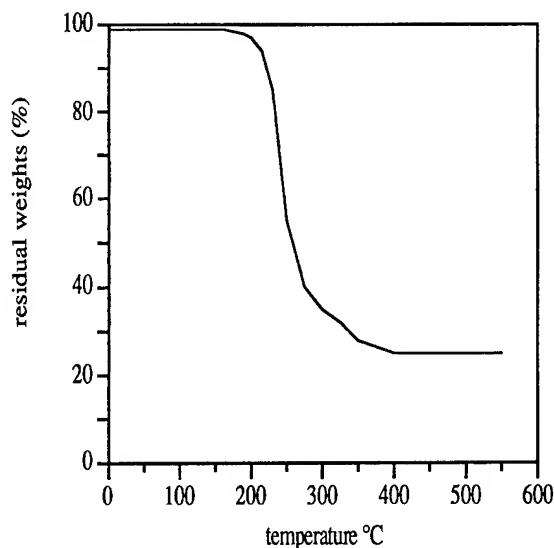


Fig. 1. Thermal analysis of $\text{HB}(\text{pz})_3\text{Ti}(\text{O}^i\text{Pr})_3$ by TGA.

point of the precursor. The experimental result of the evaporation rate of the precursor as a function of the evaporation temperature is shown as an Arrhenius plot in Fig. 2(b). The heat of evaporation was calculated from the slope of this straight line with $\Delta H_{\text{evap}} = 85.0 \pm 3 \text{ kJ/mol}$.

The film deposition was carried out under various physical conditions and some of the experimental results were plotted as graphs.

Fig. 2(a) shows an Arrhenius plot of the film growth as a function of the evaporation temperature at 450°C substrate temperature. From the slope of this line, a pseudoactivation energy of $\Delta E_a = 80.3 \text{ kJ/mol}$ was calculated. The dependence of the growth rate on substrate temperature was carried out for various evaporation temperatures of the precursor and for various evaporation rates of the precursor. The results of the first are shown as an Arrhenius plot in Fig. 3(a), while the latter is given in Fig. 3(b). Both results will be discussed in more detail.

Changes in physical properties such as the amorphous/crystalline state, the refractive index and the band gap as a function of the substrate temperature were also correlated. These results can be summarized as follows.

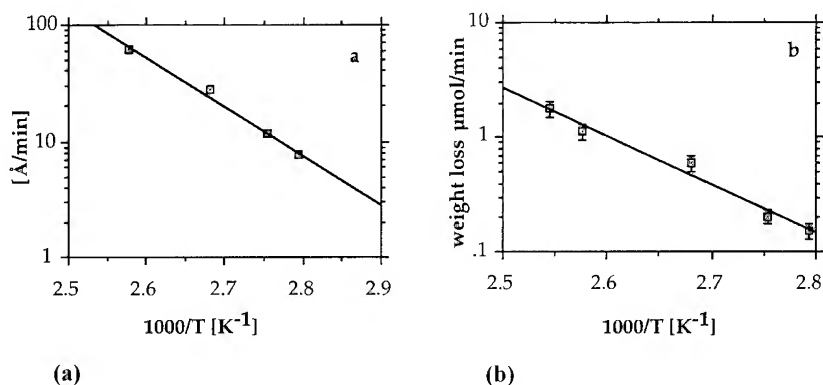


Fig. 2. Experimental data. (a) Growth rate of TiO_2 as a function of the evaporation temperature at a substrate temperature of 450°C . (b) Evaporation rate of the precursor (weight loss) as a function of the evaporation temperature. Lines are drawn as guides for the eye.

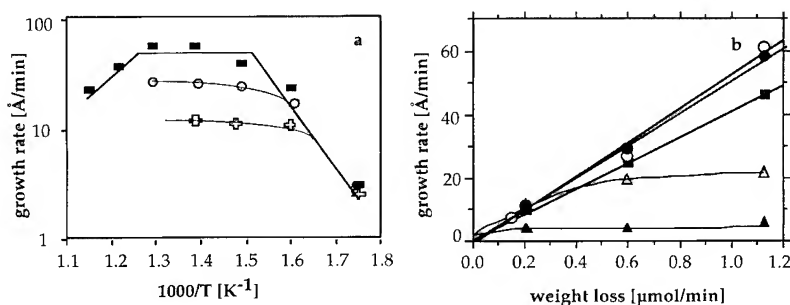


Fig. 3. Experimental data. (a) Arrhenius plot for film growth rate as a function of substrate temperature for various evaporation temperatures: \square , 90°C ; \circ , 105°C ; \blacksquare , 115°C . (b) Growth rate as a function of evaporation rate of the precursor (weight loss) for various substrate temperatures: \blacktriangle , 300°C ; \triangle , 350°C ; \blacksquare , 400°C ; \circ , 450°C ; \bullet , 500°C .

The thickness and refractive index of the films on $\text{Si}[100]$ and sapphire were determined by ellipsometry at 632.8 nm . The refractive index is dependent on the substrate temperature and changes from $n = 1.9$, at 300°C , to a maximum of $n = 2.05$ at 400°C but decreases thereafter to 1.8 at 500°C . The thickness of the films and the average roughness were determined by profilometry and found to have a value of 10 Å for most of the films. Depending on the growth conditions, thicknesses up to 1500 Å were measured for the deposition times over 30 min .

The UV/VIS spectra of the films grown on sapphire, at different temperatures are shown in Fig. 4. A band gap for all films of $3.63 \pm 0.11\text{ eV}$ was derived from the onset of the slopes at 342 nm .

The amorphous character of the films was proven by XRD. No crystalline phase could be determined up to temperatures of 800°C on any of the substrates. Even after annealing in air at 1000°C for 12 h , the probes showed no crystalline phase.

4. Discussion

The data of Figs. 1(a) and 2(b) demonstrate that the compound $\text{HB}(\text{pz})_3\text{Ti}(\text{O}i\text{Pr})_3$ is sufficiently volatile to carry out MOCVD experiments.

The growth rate of the film (Fig. 2(a)) as well as the evaporation rate of the precursor (Fig. 2(b)) as a function of the evaporation temperature had Arrhenius plots of approximately the same slopes.

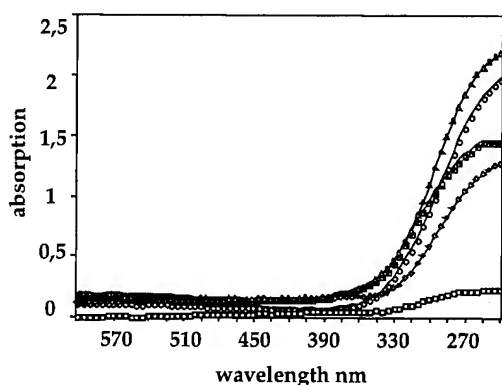


Fig. 4. UV/VIS spectra of TiO_2 films at different substrate temperatures: \square —, 300°C; \diamond —, 350°C; \circ —, 400°C; \triangle —, 450°C; \square —, 500°C.

Therefore the values for the pseudo-activation energy and heat of evaporation are about the same indicating that the evaporation of the precursor is the rate limiting step in the growth of the films at $T_{\text{sub}} = 450^\circ\text{C}$.

Fig. 3(a) shows the growth rate dependence on the substrate temperature at different evaporation temperatures. Two growth regions can be distinguished, i.e., the kinetically controlled ($T_{\text{sub}} = 370^\circ\text{C}$) and the mass flow controlled region, where, for each evaporation rate, one finds a constant film growth. An average activation energy, E_a , of 116 ± 4 kJ/mol, can be deduced from the slopes in the kinetic part. This value can not be correlated directly with either any bond cleavage (Ti–N (464 kJ/mol), Ti–O (661.9 ± 15.5 kJ/mol) [13]), or to

the lowest bond (B–N) dissociation energy (389 ± 21 kJ/mol) of the pyrazolylborate ligand itself. The relatively low values for the assigned bond energies, E_a , can be explained by the contribution of the mass transport, (e.g., mass flow) to the decomposition kinetics [14]. Thus, for the MOCVD of Y_2O_3 from $\text{Y}(\text{thd})_3$, $E_{a(\text{exp})}$ and $E_{a(\text{corr})}$ of 114 and 320 kJ/mol, respectively, were reported [15].

Fig. 3(b) shows the growth rates measured for a series of different substrate temperatures and weight losses of the precursors $\text{HB}(\text{pz})_3\text{Ti}(\text{O}^i\text{Pr})_3$. In the kinetically controlled regime of the low temperature range between 300 and 370°C , the reaction order of deposition changes with decreasing mass flow of the precursor from first order to zero order. This indicates that, within this temperature window, the reaction is strongly surface-dependent and causes fast saturation of the adsorption sites that are necessary for the growth. In the mass flow controlled regime from 400 to 500°C , straight lines result over the entire range. The slope of these lines, in a logarithmic scale, is around 1 (e.g., 0.9 for $T_{\text{sub}} = 400^\circ\text{C}$) and implies that the deposition reaction is almost first order under these conditions. Therefore, the growth rate is strongly dependent on the partial pressure of the precursor and supports the suggestion that the evaporation rate is the rate limiting step in the high temperature range. The films obtained were all amorphous, even at high temperatures. This was proven by XRD as well as by determination of the band gap. The value of 3.63 ± 0.11 eV is in the range of those values found in the literature for amorphous TiO_2 .

Table 1

AES, XPS and RBS measurements of film composition (in at.%) deposited on Si[1 0 0] at substrate temperatures of 350°C (kinetically controlled region) and 450°C (mass flow controlled region)

	$T_{\text{sub}} = 350^\circ\text{C}$		$T_{\text{sub}} = 450^\circ\text{C}$		$T_{\text{sub}} = 500^\circ\text{C}$
	AES	XPS	AES	XPS	RBS
titanium	28%	28%	27%	$32 \pm 3\%$	$31 \pm 1.55\%$
oxygen	56%	$60 \pm 6\%$	66%	$62 \pm 6\%$	$69 \pm 3.45\%$
carbon	$4 \pm 3\%$	$2 \pm 1\%$	$2 \pm 2\%$	$2 \pm 1\%$	n.a.
boron	$9.2 \pm 3\%$	$9.1 \pm 1\%$	$6.7 \pm 2\%$	$39 \pm 1\%$	n.a.
nitrogen	n.a.	1.2 ± 0.2	n.a.	0.8 ± 0.2	n.a.

Instrumental error for the measurements are: for RBS 5%, for AES 30% and for XPS 10%; n.a. = not analyzed.

[7–9,16]. Also, the refractive index ($n = 2.05$) is in the usual range of amorphous TiO_2 ($n = 2.35$ for anatase and 2.65 for rutile) [4,6]. The fact that the films remain in the amorphous state even at elevated temperatures indicates that, during the decomposition of the precursor, boron might be incorporated and react with oxygen to form B_2O_3 . AES and XPS depth profile measurements of two samples confirm that the films homogeneously contain boron from the precursor ligand. Therefore, due to this small boron contamination, amorphous boron glasses or some mixed $\text{Ti}_x\text{O}_y\text{B}_z$ phases may be formed that inhibit the crystallization of the deposited titanium oxide layers even at high temperature and post-annealing in air.

The use of boron-free precursors such as $\text{Ti}(\text{O}^i\text{Pr})_4$ leads, under these experimental conditions, to polycrystalline films on Si. All techniques, AES, XPS and RBS, showed a high oxygen (Table I) content and confirm the formation of B_2O_3 in the TiO_2 films.

It appears that higher deposition temperatures also lead to the formation of deposits with negligibly small carbon and nitrogen contents as well as a lower boron content.

The dependence on the oxygen flow and other reactants such as alcohol is currently under investigation and will be published elsewhere [11]. Preliminary results suggest that the elimination of the boron content results in polycrystalline TiO_2 films. Further, preliminary experiments with ammonia as a reaction gas show that it is possible to grow films on sapphire, at 600°C Over a period of 30 min, a 940 Å thick oxygen deficient film was grown having the composition $\text{TiO}_{0.5}\text{N}_{0.3}$ (measured by RBS) and a band gap of 2.88 eV. This suggests that it is also possible to grow oxonitride films with this precursor.

5. Conclusions

Amorphous titanium oxide films were prepared by MOCVD in a temperature range of 300–800°C on quartz, sapphire and Si[100], using a new titanium precursor $\text{HB}(\text{pz})_3\text{Ti}(\text{O}^i\text{Pr})_3$. We found a boron content up to 9%. Obviously, this conta-

mination is responsible for the amorphous film growth. We determined an average heat of evaporation, ΔH_{evap} , for this precursor as 82.7 ± 5 kJ/mol. An average activation energy, E_a , of 116 ± 4 kJ/mol for the film deposition was found under the conditions used. Under ammonia, oxygen deficient Ti–O–N films were obtained.

This research was supported by 'Kredite und Forschung' of the ETH Zürich. The authors would like to express their thanks to Dr Marek Mackjewski for DTA/TG measurements.

References

- [1] J. Augustynski, Aspects of Photo-Electrochemical and Surface Behaviour of Titanium(IV) Oxide (Springer, Berlin, 1988).
- [2] M. Fleischer and H. Meixner, *Sensors Actuators B4* (1991) 437.
- [3] I.H.K. Pulker, *Appl. Opt.* 18 (1979) 1969.
- [4] K.S. Yeung and J.W. Lam, *Thin Solid Films* 109 (1983) 169.
- [5] E. Fredriksson and J.O. Carlsson, *J. Vac. Sci. Technol. A4* (1986) 2706.
- [6] M. Yokozawa and H. Iwaseh, *Jpn. J. Appl. Phys.* 7 (1968) 96.
- [7] N. Rausch and E. Burte, *J. Electrochem. Soc.* 140 (1) (1993) 143.
- [8] E.T. Fitzgibbons, H.J. Sladek and W.H. Hartwig, *J. Electrochem. Soc.* 119 (6) (1972) 735.
- [9] H. Minoura, M. Nasu and Y. Takahashi, *Ber. Bunsenges. Phys. Chem.* 89 (1985) 1064.
- [10] K.L. Siefering and G.L. Griffin, *J. Electrochem Soc.* 137 (1990) 1206.
- [11] (a) E.C. Plappert F.-R. Lang and K.-H. Dahmen, manuscript in preparation. (b) E.C. Plappert, thesis, ETH-Zürich (1995).
- [12] M. Becht, T. Gerfin and K.-H. Dahmen, *Chem. Mater.* 5 (1993) 137.
- [13] R.C. Weast and M.J. Asle, eds., *Handbook of Chemistry and Physics*, 62nd Ed. (CRC, Boca Raton FL, 1982) p. F-188.
- [14] M.L. Hitchman, in: *Progress in Crystal Growth and Characterisation*, ed. B.T. Pamplin (Pergamon, Oxford, 1981) p. 249.
- [15] M.L. Hitchmann und S.H. Shamlan, personal communication; lecture at the 9th European Conf. on Chemical Vapour Deposition, Tampere, Finland, 1993.
- [16] M. Radecka, G. Zakrzewska, H. Cztemastek, and T. Stapinski, *Appl. Surf. Sci.* 65&66 (1993) 227.



ELSEVIER

Journal of Non-Crystalline Solids 187 (1995) 435–442

JOURNAL OF
NON-CRYSTALLINE SOLIDS

Low temperature deposition of gallium phosphate amorphous dielectric thin films by aerosol CVD

F. Tourtin*, S. Daviero¹, A. Ibanez², A. Haidoux, C. Avinens, E. Philippot

Laboratoire de Physicochimie des Matériaux Solides, UM II, URA D0407, Place E. Bataillon, F-34095 Montpellier cédex 5, France

Abstract

Gallium phosphate thin films on silicon substrates have been made from gallium acetylacetonate and tributylphosphate precursors in solution by an aerosol chemical vapor deposition named 'pyrosol'. Thin films produced are amorphous and a large range of chemical compositions with the experimental conditions can be observed. The X-ray absorption measurement results show that in these thin film structures there are Ga atoms in both tetrahedral and octahedral sites. Their electrical (resistivity) and dielectric (permittivity) characteristics are different to those of the crystallized gallium phosphate.

1. Introduction

Our laboratory takes a particular interest in the family of materials $M^{III}X^VO_4$ where $M = Al, Ga$ or Fe and $X = P$ or As , which displays extensive structural similarities with α -quartz SiO_2 . Thus, we set about developing the crystal growth and the characterization of the quartz-like materials such as the α -gallium orthophosphate ($GaPO_4$), and berlinite ($AlPO_4$) having piezoelectric properties similar or greater than those of α -quartz SiO_2 [1,2] and high

dielectric properties [3,4]. Thus we decided to deposit them as insulating thin films on III–V semiconductor substrates. In the case of silicon, oxidation at the surface of the material can be controlled precisely so as to produce an insulating thin film of silica. Further, the silicon semiconductor passivation technique by oxidation, which produces MOS, MIS or MISFET devices, is not transposable to III–V semiconductors. Thus, we set about developing the fabrication of gallium phosphate thin films on the corresponding III–V semiconductor using the 'pyrosol' method. In our previous work, [5] aluminium phosphate films were deposited on a silicon substrate. Now, we are working on the fabrication of gallium phosphate on silicon substrates. These deposits were characterized by means of infrared spectroscopy, X-ray diffraction, electron-probe microanalysis, scanning electron microscopy and secondary ion mass spectroscopy (SIMS).

* Corresponding author. Tel: +33 67 14 33 19. Telefax: +33 67 14 42 90. E-mail: philip@lpms.univ-montp2.fr.

¹Present address: Laboratoire de Cristallographie et Physicochimie du Solide, BP 108, F-59652 Villeneuve d'Ascq cédex, France

²Present address: Laboratoire de Cristallographie du Solide, BP 166, F-38042 Grenoble cédex 9, France

In particular, we studied the physical properties: the dielectric constant and conductivity measurements on gallium phosphate thin films. Indeed, dielectric properties of massive crystallized material GaPO_4 have been studied: the values of dielectric constants ($\epsilon'_{11}^T = 6.2$ and $\epsilon'_{33}^T = 6.6$ at 20°C and 50 kHz , [3]) as well as the influence of temperature, frequency and impurities have been investigated. Permittivity is found to be nearly constant below room temperature, whereas it becomes temperature-frequency-impurities dependent above room temperature [3].

In order to complete this study, we set out to characterize thin films of gallium phosphate by X-ray absorption spectroscopy at the gallium K-edge [6]. The experimental results on the aluminium phosphate at both aluminium and phosphorus K-edges were already developed [7].

This study aimed to gain a better understanding of aluminium and gallium phosphate thin film

structure and the nature of the defects so as then to be in a position to enhance their dielectric properties [8].

2. Experimental procedure

Thin films of aluminium and gallium phosphate were deposited on doped silicon substrates by the 'pyrosol' process. This method is based on thermolysis of an aerosol produced from a solution containing the organometallic precursors. This solution is pulverized on the surface of the liquid by an ultrasonic source. The resultant mist is propelled by a vector gas (air or nitrogen) towards the heated ($T^\circ\text{C}$) silicon substrate. On contact, the solvent is vaporized and the precursors are cracked, inducing the formation of thin homogeneous layers. Fig. 1 schematizes a classic 'pyrosol' installation used for this study. By this process, materials

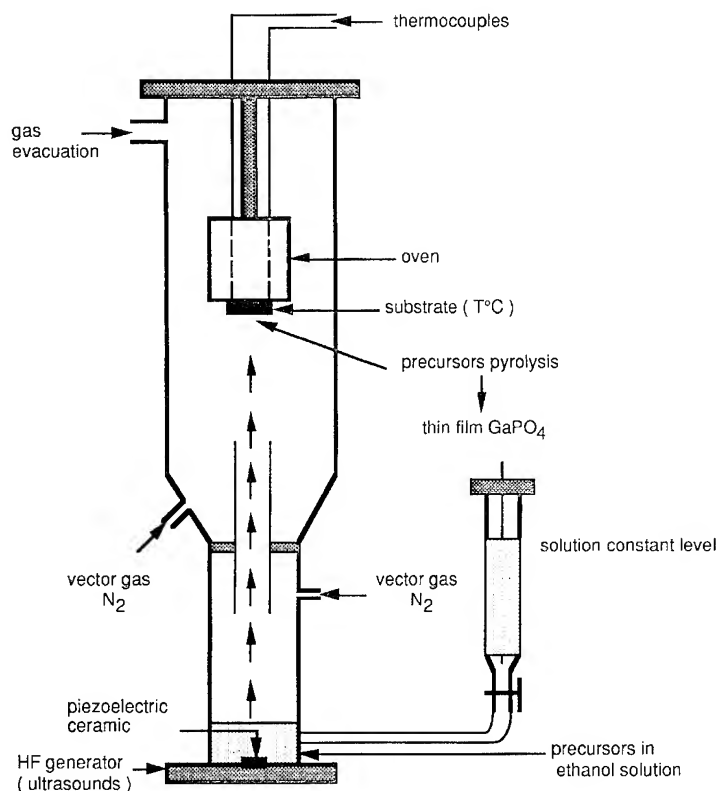


Fig. 1. Pyrosol reactor.

Table 1

Gallium phosphate thin films composition and oxygen excess in connection with temperatures and initial compositions for several ratios GaAA/TBP

<i>T</i> (°C)	25/75		33/66		50/50	
	Ga/P (at.%)	O _{th} /O _{exp}	Ga/P (at.%)	O _{th} /O _{exp}	Ga/P (at.%)	O _{th} /O _{exp}
370			0.76	0.99		
360	1.99	0.85	0.89	0.94		
350	2.73	0.76			2.19	0.84
340						
330					3.17	0.85
320			3.11	0.83		
310						
300	3.26	0.82	3.91	0.83	4.17	0.85
280			4.89	0.82		
250			7.52	0.90		

not available by chemical vapor deposition (CVD) techniques (no gaseous precursors) can be obtained. But the precursor dissolution allows the precursors to react at lower temperatures (lower than 500°C), and modifies the layer concentration by varying the initial solution composition. Precursors are chosen so as to simulate pyrolysis inducing the formation of gallium phosphate. On the other hand, they need a common solvent. Therefore, the precursors selected to form deposits of gallium phosphate were tributyl-phosphate (TBP) and gallium acetylacetonate (GaAA) dissolved in ethanol. By varying the composition of this initial solution and the temperature of the substrate (*T*°C) we obtained films of varying compositions. These compositions are expressed by the ratio Ga/P of the atomic percentages of gallium and phosphorus as determined by electron probe microanalysis. Moreover, oxygen excess as compared to stoichiometric GaPO₄ is expressed by the ratio O_{th}/O_{exp}, where O_{exp} is the atomic percentage of oxygen as measured by the microprobe and O_{th} is calculated on the basis of the Ga and P contents (atomic percentage) measured by the electron probe and expressed in the form of two oxides, Ga₂O₃ and P₂O₅, given that in this calculation 2GaPO₄ corresponds to Ga₂O₃ + P₂O₅ thus giving O_{th} = $\frac{5}{2}$ [P] + $\frac{3}{2}$ [Ga]. The optimum layer growth conditions are obtained for a vibration frequency of 774–775 kHz and an

equal flow rate for the two gas intakes $\approx 250 \text{ l h}^{-1}$. Table 1 shows the results obtained. From our results, we can observe a decrease of gallium concentration when the substrate temperature increases. We observe a strong evolution over a small temperature range ($\Delta T \approx 10^\circ\text{C}$). So, during the deposition, it is necessary to have a good temperature control system. We obtain homogeneous and adhered thin films for substrate temperature between 200 and 400°C. We suspect that there is a competition between two reactions: the first corresponds to a reaction between the two precursors, tributylphosphate and gallium acetylacetonate, resulting in the formation of (O–Ga–O–P)_{*n*} chains, and the second is due to the cracking of the GaAA precursor alone, resulting in the formation of (O–Ga–O–Ga)_{*n*} chains characteristic of the gallium oxide (Ga₂O₃).

3. Thin film characterizations

When thin films have an excess of phosphorus, the film surface state is granular. The grain dimension decreases when the ratio Ga/P increases to achieve a smooth surface for Ga/P > 3. The cross-section of the deposit observed by scanning electron microscopy (SEM) shows a columnar structure. Their thickness varies between 0.3 and 0.6 μm depending upon the deposit times and the substrate

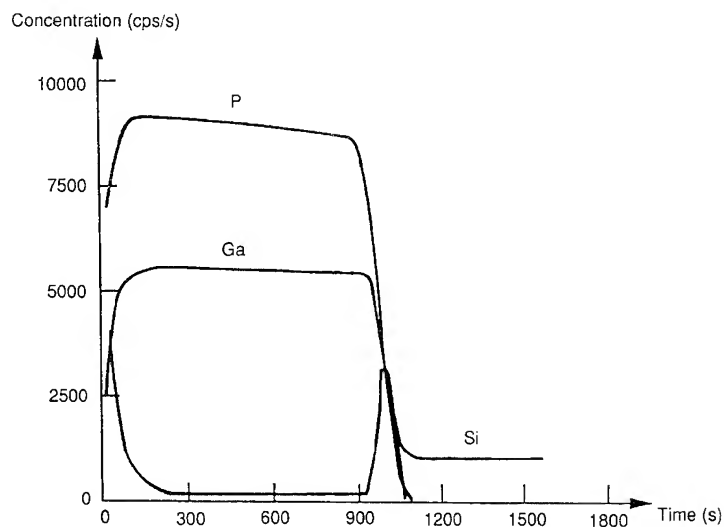


Fig. 2. Ga and P depth concentration profile for a Ga/P ratio thin film = 0.76.

temperature. The deposition rate is about 0.08–0.09 μm per hour. In infrared thin film spectra, we observe absorption bands characteristic of GaO_4 and PO_4 groups. The large absorption bands are characteristic of an amorphous material. The most Ga-enriched film absorption band is broad at low frequency and confirms the presence of gallium oxide (Ga_2O_3), like the aluminium phosphate thin films [5]. By X-ray diffraction, in any case, aluminium or gallium phosphate thin films spectra present a large diffusion ring characteristic of an amorphous state [5]. Fig. 2 shows both a homogeneous concentration profile of phosphorus and gallium, involving a regular thin film growth which was also homogeneous. The peak corresponding to a time of 1000 s indicates the presence of a silicon oxide at the gallium phosphate–silicon interface.

4. Thin films physical properties

4.1. X-ray absorption spectroscopy (XAS)

We have completed a qualitative structural study made by X-ray absorption near edge structures (XANES) spectroscopy on aluminium phosphate thin films [6] (Al and P K-edges) by the characterization of the local range order of Ga atoms in

gallium phosphate films. We recorded XANES and EXAFS (extended X-ray absorption fine structure) Ga K-edge (10 367 eV) spectra for thin films of various compositions and for several crystalline (c) compounds: c- GaPO_4 (quartz-like structure, where Ga atoms are in tetrahedral sites GaO_4 [9]), β - Ga_2O_3 (Ga are located in both tetrahedral and octahedral sites [10]) and c- GaOOH (Ga exhibits octahedral sites [11]). All these spectra were obtained from the XAS 4 station of the DCI storage ring at LURE (Orsay), using the electron conversion method [12].

The main XANES results are shown in Fig. 3(a) and (b). For thin film enriched in phosphorus ($\text{Ga/P} < 1$, Fig 3(a)), the spectra are a linear combination of the reference spectra of c- GaPO_4 and c- GaOOH as for that of β - Ga_2O_3 . When the film composition approaches GaPO_4 stoichiometry ($\text{Ga/P} = 0.83$, Fig 3(a)), the XANES spectrum becomes closer to that of c- GaPO_4 . For deposits enriched in gallium ($\text{Ga/P} > 1$, Fig 3(b)), the spectra are very similar to that of c- GaOOH . In addition, annealing (950°C in air) for thin films enriched in phosphorus leads to XANES spectra more similar to that of c- GaPO_4 . This annealing effect is weaker for gallium enriched deposits which still present intermediate features between c- GaPO_4 and c- GaOOH spectra.

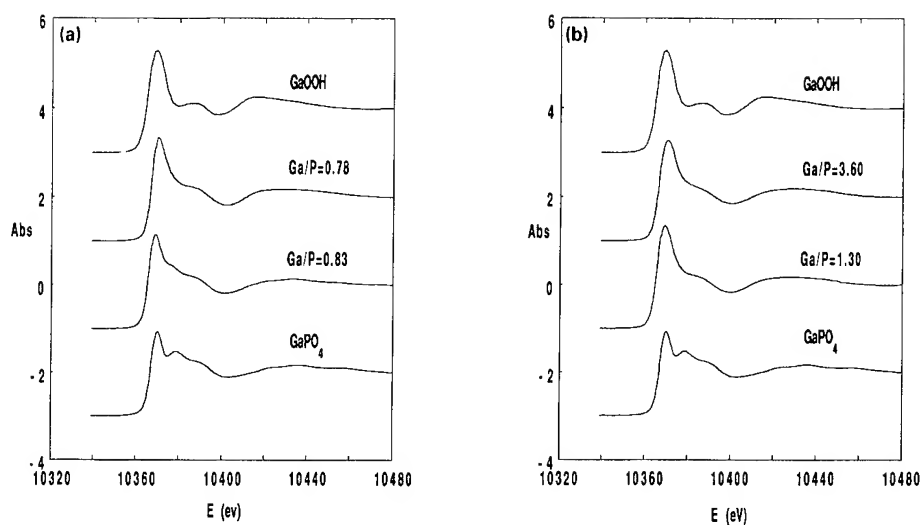


Fig. 3. Normalized XANES spectra for thin films (a) Ga/P = 0.83, 0.78 and (b) Ga/P = 1.30, 3.60, by comparison with the crystallized references GaPO_4 and GaOOH .

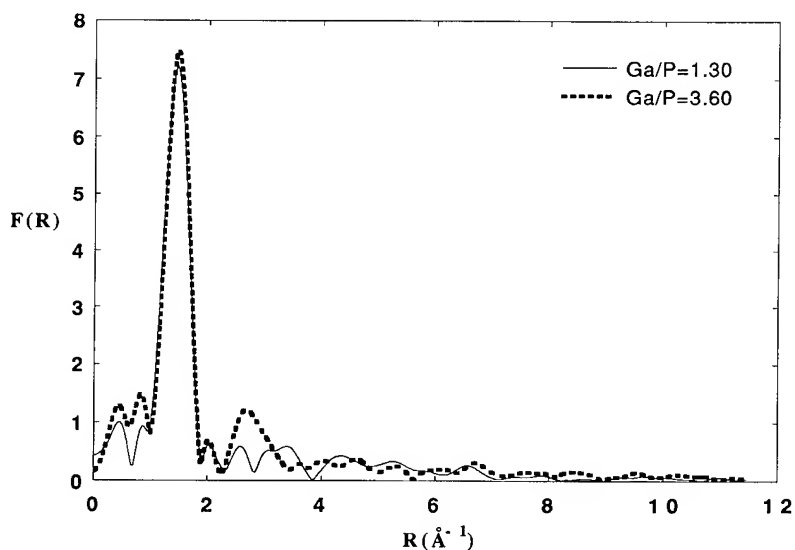


Fig. 4. FT-moduli of EXAFS spectra for Ga-enriched thin films.

These qualitative structural results have been confirmed by a Ga K-edge EXAFS analysis. Only the first coordination shell of gallium with oxygen atoms was made evident by the Fourier transform (FT) moduli of the normalized EXAFS oscillations (Fig 4). Nevertheless, for high Ga contents, a second peak around 2.5 \AA appears. A mean square

fitting procedure of the Fourier filtered signal has been performed, using the standard EXAFS oscillations expression and experimental backscattered phases and amplitudes ($c\text{-GaPO}_4$), in order to obtain the Ga structural parameters. In P-enriched thin films, Ga is both tetrahedrally and octahedrally surrounded by oxygen with an average

coordination number $N \approx 5$ and an average bond length $R \approx 1.84 \text{ \AA}$ (Ga–O) which is intermediate between tetrahedral (1.81 \AA) and octahedral ($1.88\text{--}1.90 \text{ \AA}$) environments. For Ga enriched deposits, the Ga atoms are located essentially in octahedral sites ($N \approx 6$, $R \approx 1.89 \text{ \AA}$ and the Debye Waller factor $\sigma \approx 0.08 \text{ \AA}$). We did not simulate the second coordination shell registered in this case (Fig. 4) very well, but the backscattered amplitudes extracted from the second peak of the FT modulus around 2.5 \AA characterize the gallium atoms resulting from $[\text{O-Ga-O-Ga}]_n$ chains. The annealing effect was also confirmed by EXAFS. We registered in this case a simultaneous decrease of the structural parameters referred to the corresponding values obtained for the raw thin films. For $\text{Ga/P} < 2$ compositions, Ga atoms are mainly in tetrahedral sites ($N \approx 4\text{--}4.4$, $R \approx 1.81\text{--}1.82 \text{ \AA}$ and $\sigma \approx 0.03 \text{ \AA}$), which agrees with the recrystallisation under the cristobalite form of GaPO_4 made evident by X-ray diffraction, while for high Ga contents, the Ga octahedral surroundings remain predominant ($N \approx 5.5$, $R \approx 1.84 \text{ \AA}$ and $\sigma \approx 0.08 \text{ \AA}$).

4.2. Dielectric properties

Conductivity measurements have been carried out on a small part of a layer on the doped silicon substrate (resistivity: $R = 1.7 \times 10^{-4} \Omega \text{ m}$, doped

type n with Sb). The layer surface is metallized with gold sputtering deposition (2000 \AA) and the electrodes are copper wires. For each sample, we carried out electrical measurements over a frequency range of 100 Hz to 1 MHz and a temperature range of $250\text{--}350^\circ \text{K}$. The signal measured by an impedance analyzer HP 92A which gives capacitance C (F) and conductance G (S or Ω^{-1}) as a function of frequency. For three samples ($\text{Ga/P} = 3.01$, $O_{\text{th}}/O_{\text{exp}} = 0.75$; $\text{Ga/P} = 0.76$, $O_{\text{th}}/O_{\text{exp}} = 0.99$ and $\text{Ga/P} = 0.89$, $O_{\text{th}}/O_{\text{exp}} = 0.94$) we plotted the values of $\log(\text{cond.}) = f(\log(\text{freq.}))$ variation (Fig. 5) at room temperature. The obtained values are higher ($\sigma = 10^{-7}\text{--}10^{-8} (\Omega \text{ m})^{-1}$) than expected, as for the material ($\sigma > 10^{-14} (\Omega \text{ m})^{-1}$) [13]. We observe a strong increase of the conductivity with frequency. At room temperature, the conductivity increases with the gallium concentration and with the oxygen excess ($O_{\text{th}}/O_{\text{exp}} < 1$). In Fig. 6, we have plotted the values of $\log(\text{cond.}) = f(\log(\text{freq.}))$ variation for sample $\text{Ga/P} = 3.01$, $O_{\text{th}}/O_{\text{exp}} = 0.75$ at several temperatures. We observe a weak conductivity evolution with temperature and an important one with the frequency. An accurate determination of C_i (insulator capacity) requires biasing the surface by the applied potential such as $C_{\text{SC}} + C_{\text{SS}} \gg C_i$ where C_{SC} and C_{SS} are, respectively, the semiconductor space charge and the interfacial surface state charge. The measured capacity is then equal to C_i .

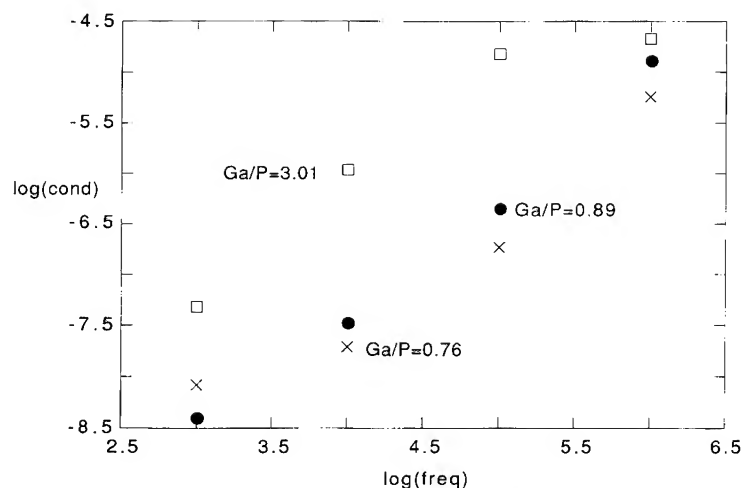


Fig. 5. Experimental $\log(\text{cond.}) = f(\log(\text{freq.}))$ curve at room temperature for several thin films.

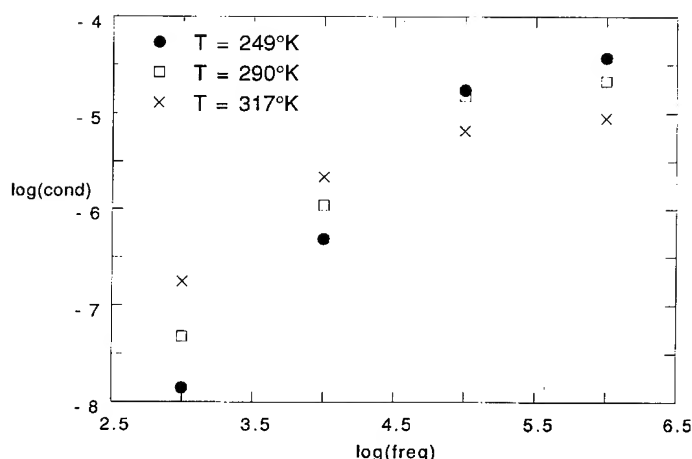


Fig. 6. Experimental $\log(\text{cond.}) = f(\log(\text{freq.}))$ curve at several temperatures for $\text{Ga/P} = 3.01$ and $\text{O}_{\text{th}}/\text{O}_{\text{exp}} = 0.76$ thin films.

The relative permittivity ϵ' was calculated from the expression $C_i = \epsilon_0 \epsilon' S/d$ where ϵ_0 is the vacuum permittivity, S the layer surface and d the layer thickness. We have attempted some layer relative permittivity constant measurements on various gallium and phosphorus compositions. The layer relative permittivities found are much smaller ($\epsilon' \approx 3$ at room temperature and $\text{freq.} = 10^5 \text{ Hz}$) than GaPO_4 crystal constant measurements, $\epsilon'_{11} = 6.2$ and $\epsilon'_{33} = 6.6$ (room temperature and $\text{freq.} = 50 \text{ kHz}$), which do not vary with frequency [3]. The diminution of the dielectric constant at lower frequency, compared with the case of GaPO_4 crystal, is expected to be a direct result of the changes in the gallium oxide environment. However, the SIMS curve (Fig. 2) shows that the silicon signal is enhanced at the interface and thus indicates the presence of silicon oxide sandwiches between gallium phosphate and silicon substrate. The insulator capacity (C_i) measurement is then modified. The variation of conductivity under alternating current with frequency is probably the result of carrier hopping or tunneling between impurity sites and dangling bond in gallium phosphate band gap.

5. Conclusions

In this study, we defined the experimental deposition conditions of gallium phosphate thin films on

silicon substrate by the pyrosol process. We obtained homogeneous and stable thin films without cracks. We observed a large composition range versus the substrate temperature and the initial solution containing the precursors. Whatever the temperature deposition was, thin layers were amorphous and could be recrystallized in GaPO_4 cristobalite form by annealing.

The structural results lead us to believe that in these thin films, two types of chain coexist $[\text{O-Ga-O-P}]_n$ and $[\text{O-Ga-O-Ga}]_n$, with Ga atoms in both tetrahedral and octahedral sites. We can therefore assume that the structure of these thin films comprise two types of aggregate:

(i) the first one, based on the structure of cristobalite GaPO_4 recrystallizing in this form when heated;

(ii) the second one, based on the structure of amorphous gallium oxide (Ga_2O_3), would become largely predominant in gallium-rich deposits and would not recrystallize at 950°C .

This study has produced interesting results concerning the first gallium coordination sphere, but, our goal would be to investigate the medium surrounding of gallium atoms in order to explain the competition between the two reactions involving the gallium oxide or the gallium phosphate formation.

The conductivity measurement results mean that our gallium phosphate thin films have a high resistivity but less than the bulk material one. The first

dielectric characterizations show weak dielectric constants in comparison with GaPO_4 crystal. At the moment, our results are not conclusive. Further, studies will be undertaken in order to thoroughly explore the dielectric measurements (dielectric constant and dielectric loss) for several gallium, phosphorus and oxygen concentration thin films. In these studies, we would like to develop properties of MIS devices by standard $C-V$ and $I-V$ methods.

References

- [1] E. Philippot, A. Ibanez, A. Goiffon, M. Cochez, A. Zarka, B. Capelle, J. Schwartzel and J. Détaint, *J. Cryst. Growth* 130 (1993) 195.
- [2] E. Philippot, A. Goiffon and M. Maurin, *J. Cryst. Growth* 104 (1990) 713.
- [3] J.D. Foulon, J.C. Giuntini and E. Philippot, *Eur. J. Solid State Inorg. Chem.* 31 (1994) 245.
- [4] H. Ribes, J.C. Giuntini, A. Goiffon and E. Philippot, *Eur. J. Solid State Inorg. Chem.* 25 (1988) 201.
- [5] S. Daviero, C. Avinens, A. Ibanez, C. Cambié, M. Maurin and E. Philippot, *Le Vide, les Couches Minces* 250 (1990) 23.
- [6] F. Tourtin, A. Ibanez, A. Haidoux and E. Philippot, *Thin Solid Films* (1995) in press.
- [7] S. Daviero, A. Ibanez, C. Avinens, A.M. Flank and E. Philippot, *Thin Solid Films* 226 (1993) 207.
- [8] S. Daviero, C. Avinens, A. Ibanez, J.C. Giuntini and E. Philippot, *J. Non-Cryst. Solids* 146 (1992) 279.
- [9] A. Goiffon, J.C. Jumas, M. Maurin and E. Philippot, *J. Solid State Chem.* 61 (1986) 384.
- [10] M.F. Pye, J.J. Birtilland and P.G. Dickens, *Acta Crystallogr.* B33 (1977) 3224.
- [11] S. Geller, *J. Chem. Phys.* 33 (1960) 676.
- [12] G. Tourillon, E. Dartyge, A. Fontaine, M. Lemonier and F. Bartol, *Phys. Rev. Lett.* A121 (1987) 251.
- [13] P. Krempel, J. Stadler, W. Wallnöfer, W. Ellmeyer and R. Selic, in: *Proc. 5th European Frequency and Time Forum, Besancon* (1991) p. 143.



ELSEVIER

Journal of Non-Crystalline Solids 187 (1995) 443–447

JOURNAL OF
NON-CRYSTALLINE SOLIDS

Fabrication, characterization and electro-optic performances of proton-implanted waveguides in LiNbO_3

A. Boudrioua^a, P. Moretti^b, J.C. Loulergue^{a,*}

^a *Laboratoire Matériaux Optiques à propriétés spécifiques, Centre Lorrain d'Optique et Electronique des Solides, Université de Metz et Ecole Supérieure d'Electricité, Technopôle Metz 2000, 2 rue Edouard Belin, 57078 Metz cedex 3, France*

^b *Département de Physique des Matériaux, URA no. 172, Université Claude Bernard, Lyon I, 43, Bd, du 11 November 1918, F68622 Villeurbanne, France*

Abstract

Planar optical waveguides were built up by proton implantation (ion of H^+) in single crystal of lithium niobate. The waveguide properties are investigated by a prism coupling technique (M-lines spectroscopy). The reconstructed refractive index variation profile obtained with the inverse WKB method, is compared with the ion concentration profile as determined by TRIM simulation program. The electro-optic coefficient, r_{13} , has been measured through the change in coupling angle of the modes excitation under an applied electric field.

1. Introduction

Among the potential optical materials for integrated optics, lithium niobate (LiNbO_3) has been subject to extensive development [1]. The LiNbO_3 crystal growth process is well developed and large single crystal of excellent optical quality are presently commercially available [2]. Planar and stripes waveguides have been produced in this material using techniques such as thermal titanium indiffusion, proton exchange [3–5] or more recently, by mean of ion implantation He^+ [6], and H^+ [7].

Light ion (He^+ , H^+) implantation is a powerful and very attractive method for waveguide fabrication

since it can be potentially applied to any crystalline materials, pure or doped and whatever their composition. A proper dielectric waveguide is a planar structure with refractive index greater than the surrounding materials. There are discrete guided modes which propagate without divergence. By proton implantation in LiNbO_3 , the ordinary and the extraordinary refractive indices are decreased where the ions are deposited producing an optical barrier [7].

The electro-optical performance of these ion implantation-produced waveguides may not be identical to that of the bulk material, since the fabrication process produces damage in the crystal lattice of the material [8].

In this contribution, we describe the experiments to produce planar waveguide without post annealing procedure in LiNbO_3 crystal by H^+

* Corresponding author. Tel: +33 87 75 96 08. Telefax: +33 87 75 96 01. E-mail: boudrioua@esemetz.esemetz.fr.

implantation, and we give the refractive index variation profile obtained by M-lines spectroscopy. The results of the EO effect are reported showing that the coefficient, r_{13} , is only reduced by less than 10% for applied dc voltage as compared to the crystals bulk value.

2. Waveguide fabrication, optical and electro-optic properties

We use commercially available y-cut LiNbO_3 plates [2] typically with dimensions of $20 \times 10 \times 1$ mm. The samples were mounted onto a special temperature controlled stage in the beam line of a 2 MeV Van De Graaf accelerator. The largest face was irradiated with 600 keV protons (H^+) at a fluence of $5 \times 10^{16} \text{ ions cm}^{-2}$. The sample temperature was carefully kept close to 300 K to prevent thermal beam effects which may frustrate the barrier formation (see Fig. 1). Moreover, the beam was scanned over an area of 10 cm^2 to guarantee homogeneous irradiation at low flux ($= 0.1 \text{ A cm}^{-2}$) to minimize the charge effects on the irradiated surface. Charging effects disturb the initial ferroelectric state of the crystal.

The prism coupling technique (M-lines spectroscopy) [9] was used to investigate the optical waveguide properties (see Fig. 2). The incident (He–Ne) laser beam, polarized TE, was fed into the waveguide using a rutile (TiO_2) prism. A power meter and a beam splitter were used to monitor the

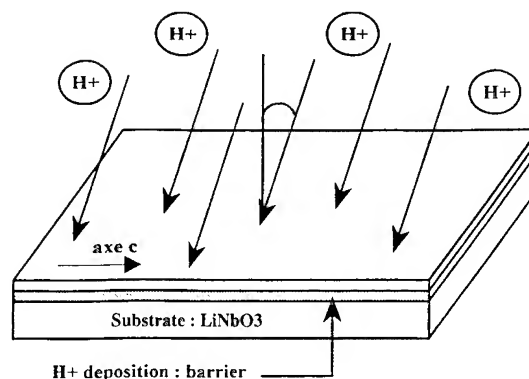


Fig. 1. Formation of a planar waveguide in LiNbO_3 by 600 keV H^+ ion implantation along the crystallographic a axis; the dose is $5 \times 10^{16} \text{ ion/cm}^2$.

ingoing laser power as well as the power reflected by the base of the coupling prism.

The coupler is mounted onto a goniometer stage which can be turned with constant speed by a feedback controlled dc motor.

The electro-optic (EO) effect was investigated using the modification of the resonance excitation of M-lines. This new method consists of detecting the change of the coupling angles of M-lines when an electric field is applied. A direct voltage was applied to the sample using two deposited electrodes on the waveguide surface. The output dark lines spectroscopy comprised a series of dips which were shifted angularly. By measuring the angle shift of the modes, we determine the variation of the refractive index, Δn_0 .

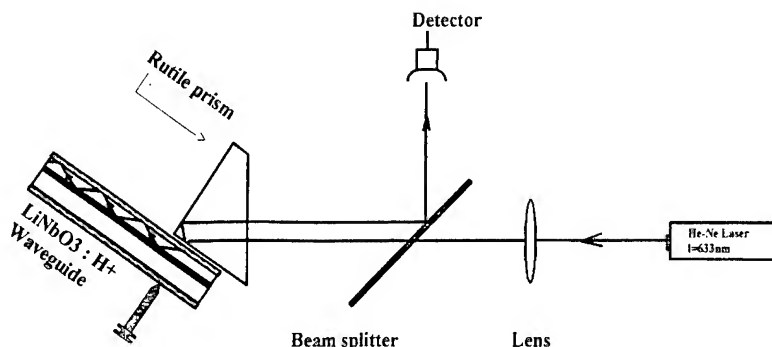


Fig. 2. The prism coupling setup to obtain the modes profile and the EO coefficient, r_{13} .

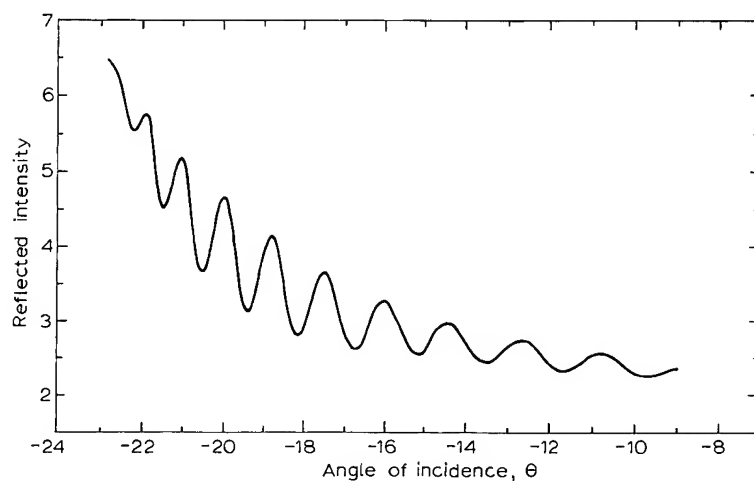


Fig. 3. Typical reflected intensity as a function of incidence angle, θ , obtained by the prism coupling method. In that example, propagation is parallel to the c axis (n_o excitation). The TE modes are related to the dips in the spectra.

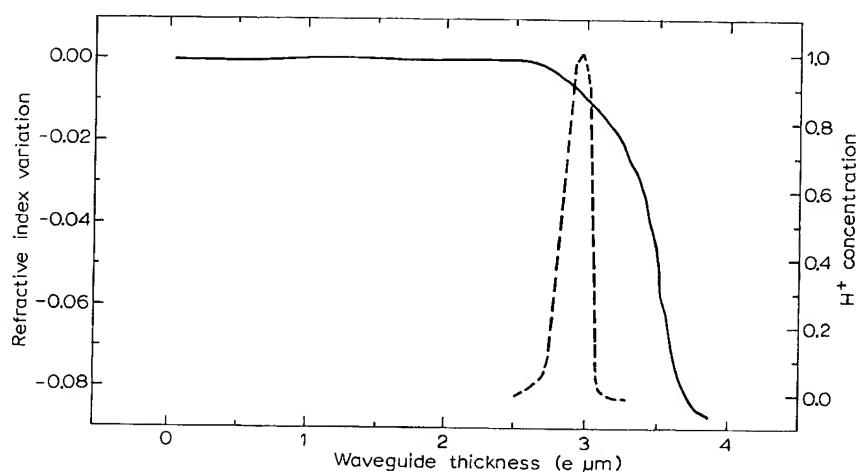


Fig. 4. Refractive index change, n_o (left scale and solid line), and calculated proton concentration, c (right scale and dashed line), versus depth for LiNbO₃ energy 600 keV, dose 5×10^{16} ions/cm².

3. Results

The modes profile is obtained by measuring the reflected intensity versus the angle of incidence (see Fig. 3). The reflectivity dips at given coupling angles indicate the excitation of guided modes. Their effective indices are used to reconstruct the refractive index profile, utilizing an inverse

WKB method [10]. The depth profile of implanted ions was calculated using the TRIM code program [11].

Both the reconstructed refractive index variation profile and the TRIM results of protons deposition are presented in Fig. 4.

The variation of the reflected intensity, ΔR , of M-lines, for different amplitude of the voltage, was

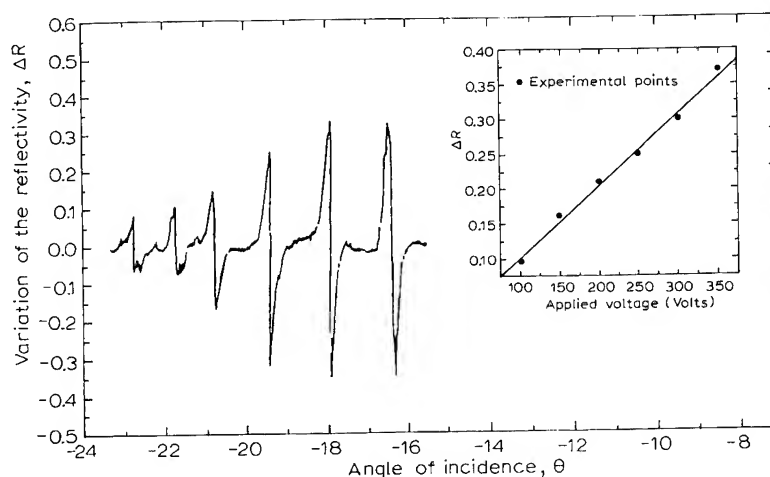


Fig. 5. Typical differential reflectivity, ΔR , measured for $V = 350$ V. Inset: ΔR versus the applied voltages.

investigated versus the angle of incidence, θ . A linear dependence of ΔR as a function of the applied voltage was observed (see Fig. 5).

When the electrical field, E , is applied, the refractive index variation induced in the direction of the electric field of a TE polarized wave is given by

$$dn_{TE} = \frac{1}{2} n_0^3 r_{13} E.$$

In order to describe completely the device, it is necessary to know the effective electric field applied to the sample. We have

$$E = V/t,$$

where v and t are, respectively, the applied voltage and the gap between the two electrodes. Then, we find for an as implanted sample

$$r_{13} = 9 \text{ pm V}^{-1} \pm 1 \text{ pm V}^{-1}.$$

4. Discussion

As we see in Fig. 3, massive losses of higher order modes due to tunneling are indicated by their increased linewidth [12].

The profile reconstruction scheme (see Fig. 4) returns particularly reliable values for the surface value and the barrier position. However, the deep decrease of the refractive index is found rather

below. This behaviour is not observed for He^+ implanted waveguides [7] and could be due to less accurate parameters used in the TRIM program for H^+ implantation simulation.

From our electro-optic measurements, we deduce that the value of the EO coefficient r_{13} is only reduced by 10%, in H^+ implanted waveguides, from that of the bulk material ($r_{13} = 11 \text{ pm V}^{-1}$) [13]).

Moreover, the EO effect, as it has been suggested [8,14], should be reduced in ions implanted waveguides, owing to the damaging nature of the particle-substrate interaction. Particularly, the energy part transferred to the target atoms by inelastic processes, which are preponderant at high energy, may produce complex defects in the waveguiding layer for H^+ implanted waveguide.

Our results demonstrate that H^+ implantation is a very attractive method for waveguide elaboration. Also, it must be emphasized that the sample has not been annealed prior to our electro-optic measurements.

5. Conclusions

We have demonstrated that optical modes can be excited in LiNbO_3 proton implanted waveguide

with no annealing procedure. Therefore, light ion implantation offers the possibility of producing waveguides in photorefractive materials such as ABO_3 ferroelectrics where other methods using thermal processes must be avoided.

Moreover, the intrinsic electro-optic properties of these H^+ implantation-produced waveguides are rather well preserved.

References

- [1] See, for example, numerous related papers in: P. Gunter and J.P. Huignard, eds., *Photorefractive Materials and their Applications II* (Springer, Berlin, 1989).
- [2] Cristal Tec, Grenoble, France.
- [3] M.N. Armenise, *IEEE Proc.* 135, (2) part j (1988) p. 85 and references therein.
- [4] Masuda, M. Mitsunaga, K. Murakami and J. Koyama, *Laser Rev.* 5 (2) (9–16 Sept. 1977) 152.
- [5] J.L. Jackel, C.E. Rice and J.J. Veselka, *Appl. Phys. Lett* 41 (1982) 607.
- [6] P.D. Townsend, *Cryst. Latt. Def. Amorph. Mater.* 18 (1989) 377.
- [7] P. Moretti, P. Thevenard, K. Wirl and P. Hertel, *Mater. Res. Symp. Proc.* 244 (1992) 323.
- [8] G.L. Destefanis, J.P. Gaillard, E.L. Ligeon, S. Valette, B.W. Farmery, P.D. Townsend and A. Perez, *J. Appl. Phys.* 50 (1979) 7898.
- [9] R. Ulrich and R. Torge, *Appl. Opt.* 12 (1973) 2901.
- [10] P. Hertel and H.P. Menzler, *Appl. Phys.* B44 (1987) 75.
- [11] J.F. Ziegler, J.P. Biersack and U. Littmark, *The Stopping and Ranges of Ions in Solids* (Pergamon, New York 1988).
- [12] F.P. Strohkendl, P. Gunter, Ch. Buchal and R. Irmscher, *J. Appl. Phys.* 69 (1991) 84–4.
- [13] P. Gunter, ed., *Electro-optic and Photorefractive Materials* (Springer, Berlin 1987).
- [14] G.T. Reed and B.L. Weiss, *Electron. Lett.* 23 (1987) 424.



ELSEVIER

Journal of Non-Crystalline Solids 187 (1995) 448–452

JOURNAL OF
NON-CRYSTALLINE SOLIDS

Photo-assisted switching and trapping in BaTiO_3 and $\text{Pb}(\text{Zr}, \text{Ti})\text{O}_3$ ferroelectrics

W.L. Warren*, D. Dimos

Sandia National Laboratories, Albuquerque, NM 87185-1349, USA

Abstract

The effects of optical illumination and charge creation have been investigated in $(\text{Pb}, \text{La})(\text{Zr}, \text{Ti})\text{O}_3$ (PLZT) and BaTiO_3 ferroelectric materials. Intrinsic photo-induced switching and charge trapping are observed in both perovskite materials. The trapping manifests itself by pinning domain walls, thereby suppressing the amount of switchable polarization. The photoferroelectric effects are found to be reproducible, reversible, and stable in both PLZT and BaTiO_3 . These results reinforce the idea that electronic charge trapping centers can lock certain domain configurations.

1. Introduction

Lead lanthanum zirconate titanate (PLZT) materials have shown great potential for use in optical storage applications [1–5]. PLZT materials are promising materials for optical memories since they are photo-sensitive and have large electrooptic coefficients. The non-volatile images stored in PLZT are induced by an ultra-violet (UV) light/applied bias combination [1–5]. This combination leads to the creation, and subsequent trapping, of charge carriers. Upon trapping, a space charge field is created that can change the polarization state of the ferroelectric. Since birefringence is polarization dependent, the optical images are revealed by modulating the transmitted, or reflected, light intensity.

Birefringence and domain formation can be strongly affected by optically illuminating materials

such as BaTiO_3 , SrTiO_3 , and LiNbO_3 [6–8]. In this study, we explore another optically-induced phenomenon in BaTiO_3 and PLZT; we examine the nature of optically-induced hysteresis suppression in these ferroelectric materials.

2. Experimental

The BaTiO_3 single crystals used in this study were fabricated by the Remeika [9] flux method. The polycrystalline PLZT hot pressed ceramic samples were obtained from a commercial supplier [10]. Both samples were nominally 0.025 cm thick. The PLZT composition was $\text{Pb}_{0.93}\text{La}_{0.07}(\text{Zr}_{0.65}\text{Ti}_{0.35})\text{O}_3$. Semi-transparent indium tin oxide (ITO) electrodes were sputter deposited on the plates for electrical contact. Polarization–voltage (P – V) measurements were made with a Radiant Technologies tester. A 100 W Hg arc lamp (Oriel) was used to optically illuminate

* Corresponding author. Tel: +1-505 272 7628. Telefax: +1-505 272 7304. E-mail: wwarren@somnet.sandia.gov.

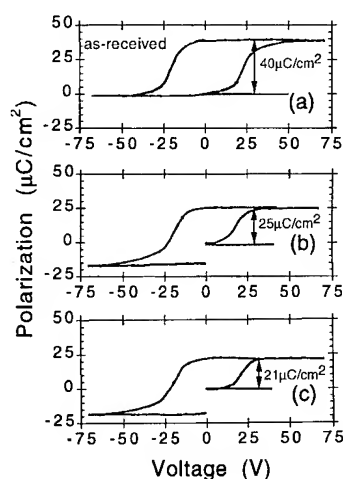


Fig. 1. Hysteresis measurements of BaTiO₃ crystals subjected to various conditions: (a) initial, (b) +10 V dc bias for 2 min and (c) a +10 V/UV combination for 2 min. The UV/bias treatment leads to photo-assisted switching.

the samples at 300 K under various applied biases.

3. Photo-assisted switching in BaTiO₃

The information storage process can be based on the ability to reduce the switching voltage for domain reorientation using light. This photo-assisted switching is manifested if a bias/light combination changes the polarization state of the ferroelectric to a greater extent than an applied bias (less than the saturation voltage) by itself. Fig. 1 illustrates the P - V measurements on BaTiO₃ crystals for various bias and illumination conditions. Fig. 1(a) is for the initial BaTiO₃ sample showing that roughly 40 $\mu\text{C}/\text{cm}^2$ of charge is switched when ramping the capacitor from 0 to 70 V. If a +10 V bias is applied for 2 min (Fig. 1(b)), only 25 $\mu\text{C}/\text{cm}^2$ charge is switched by ramping from 0 to 70 V. (The +10 V bias was applied after first poling the crystal to negative remanent polarization $\{-P_r\}$.) The positive bias alone caused 15 $\mu\text{C}/\text{cm}^2$ of charge to be switched ($40 - 25 \mu\text{C}/\text{cm}^2$). Fig. 1(c) shows that a +10 V/UV combination further enhances the domain switching process from the $-P_r$ state since ramping from 0 to 70 V now switches 21 $\mu\text{C}/\text{cm}^2$ of

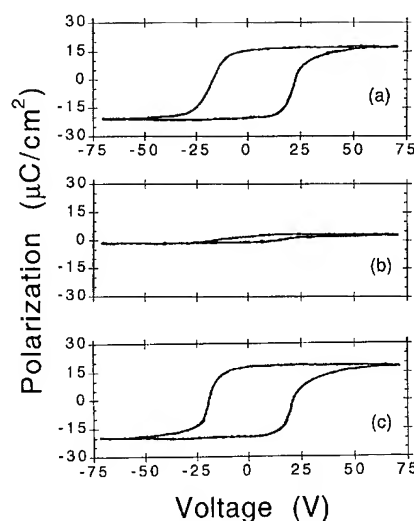


Fig. 2. P - V measurements of BaTiO₃ crystal plates subjected various charge injection treatments: (a) initial, (b) -6 V/UV combination (electron injection), and (c) subsequent +25 V/UV combination (hole injection).

charge; 19 $\mu\text{C}/\text{cm}^2$ of charge was switched by this bias/UV scenario. This indicates that light does indeed enhance domain switching in these BaTiO₃ crystals.

4. Photo-induced trapping

The P - V measurements on BaTiO₃ crystals exposed to different bias/UV combinations are illustrated in Fig. 2. Fig. 2(a) shows the initial hysteresis loop of the BaTiO₃ crystal. The hysteresis loop shown in Fig. 2(b) was taken after first poling the BaTiO₃ crystal to the $+P_r$ and then subjecting the capacitor to a -6 V/UV combination. (The illuminated electrode was biased negatively with respect to the grounded bottom electrode.) This bias/UV treatment has clearly suppressed the amount of switchable polarization. This suppressed state is described as optically written. The optically written state can also be achieved by a positive bias/UV treatment (the positive bias is applied after poling the capacitor to $-P_r$). In either case, we find that the amount the switchable polarization is suppressed strongly depends on the bias voltage

during illumination [4, 11]. The effect is maximized by partially switching the domains with a bias below the coercive voltage (the voltage when the polarization is = 0). (The photo-induced switching vs. suppression phenomena are discussed below.) The optically written state can also be erased by illuminating the samples with UV light while applying the opposite *saturating* bias (a bias corresponding to the saturation voltage) to which the sample was originally written, or by illuminating the samples with bandgap light while cycling around the hysteresis loop. Fig. 2(c) illustrates the particular case in which the BaTiO₃ crystal was erased by a + 25 V/UV combination.

Comparable photo-induced hysteresis effects are also observed in PLZT materials as illustrated in Fig. 3. The only difference is that the photo-induced suppression observed in Fig. 3(b) was induced by a - 75 V/UV combination and that optical erasure was achieved by a + 350 V/UV combination (Fig. 3(c)). The photo-induced PLZT hysteresis effects have been observed by a number of other investigators [1–6], we simply use BaTiO₃ to show that similar photo-induced effects are observed in two different ferroelectric materials.

Following optical writing, a thermal anneal can rejuvenate the switchable polarization in both ferroelectric materials. The isochronal anneals were performed in air for 15 min. Complete restoration of P_r occurs when the anneal temperature

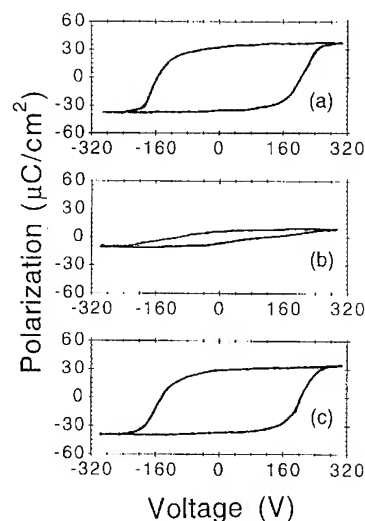


Fig. 3. P - V measurements of poly-crystalline PLZT ceramic plates subjected various charge injection scenarios: (a) initial, (b) - 75 V/UV combination (electron injection), and (c) subsequent + 350 V/UV combination (hole injection).

exceeds the Curie temperature in both the BaTiO₃ ($\approx 120^\circ\text{C}$) and PLZT ($\approx 180^\circ\text{C}$) samples.

Fig. 4 shows that the BaTiO₃ crystal can be repeatedly written and erased using a suitable bias/UV approach. As mentioned earlier, and illustrated in Fig. 4, the samples can be optically written with either a positive bias/UV or negative bias/UV

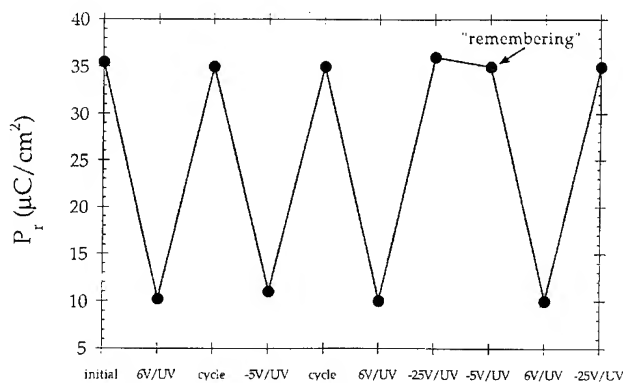


Fig. 4. Repetitive writing and erasing of the BaTiO₃ crystal using various bias/UV combinations. The line is drawn as a guide for the eye.

combination. Fig. 4 also illustrates one anomaly with respect to the optical writing phenomenon in BaTiO_3 . If the crystal is erased with the opposite saturating bias with which it was written (rather than cycling around the hysteresis loop while illuminating), then subsequent writing can only occur with a bias of the same sign as the original writing bias. For example, during the sixth charge injection sequence, when the capacitor was written with a +6 V/UV treatment, and subsequently erased by a -25 V/UV treatment, then it can only be subsequently written with a positive bias/UV process. A negative (-5 V) bias/UV combination is no longer able to optically write the BaTiO_3 crystal. It appears that the sample 'remembers' how it was written and erased even though erasure appears to restore the hysteresis loop back to its initial state. This remembering peculiarity was exploited in Fig. 1. To observe the photo-assisted domain switching without accompanying polarization suppression, the sample was first written with a -6 V/UV combination and then erased with a +50 V/UV combination. Hence, when the sample was subsequently subjected to a +10 V/UV combination to observe the photo-assisted switching, no polarization suppression occurred. This anomalous effect is not observed in PLZT materials (not shown). Nonetheless, these results demonstrate that the photoferroelectric hysteresis effects are reversible; the ferroelectric capacitors can be repeatedly written and erased using a suitable bias/UV approach.

5. Discussion

For an account of these photo-induced changes we consider the interaction between the photo-generated carriers and the differing domain configurations [3,4]. Domain boundaries that have a polarization discontinuity, i.e., 90° boundaries, or perhaps head-to-head configurations are reasonable trapping sites for the photo-generated carriers. The domain can no longer switch since the trapped charge inhibits its motion, thereby, reducing the amount of switchable polarization. The suppressed polarization is restored to its initial state if the

trapped carriers recombine with carriers of the opposite sign. There appears to be a link between the domain pinning effect in these BaTiO_3 crystals and isolated Fe^{3+} centers [11]. We found that changes in the switchable polarization by the bias/UV combination are also accompanied by changes in the isolated Fe^{3+} density via carrier trapping at this site. The nature of the electronic traps responsible for the domain pinning in the PLZT ceramics are still undetermined [3,4].

It has been known for some time that PLZT is a suitable medium for optical storage. Two material requirements for an optical storage medium are that the (1) light can create a change in the material and (2) that this change can be optically detected. We have shown that the light in combination with a bias can substantially affect the polarization state of the ferroelectric. Light can be used to monitor the change in the polarization state via birefringence; therefore, it appears as though BaTiO_3 should satisfy both criterion.

6. Conclusions

We have demonstrated large intrinsic photo-induced hysteresis effects in BaTiO_3 crystals by a combined bias/UV combination. These photoferroelectric effects have now been observed in two ferroelectric materials (BaTiO_3 and PLZT). Last, these results re-inforce the notion that charge trapping centers can suppress the switchable polarization by locking certain domain configurations.

The authors would like to thank G.E. Pike, B.A. Tuttle, and R.W. Schwartz for many useful discussions. They are also indebted to Joe Kubas for excellent technical support. This work was supported by the US Department of Energy under contract DE-AC04-94AL85000.

References

- [1] C.E. Land and P.S. Peercy, *Ferroelectrics* 22 (1978) 677.

- [2] C.H. Haertling, *Ferroelectrics* 75 (1987) 25.
- [3] D. Dimos, W.L. Warren and B.A. Tuttle, *Mater. Res. Soc. Symp. Proc.* 310 (1993) 87.
- [4] D. Dimos, W.L. Warren, M.B. Sinclair, B.A. Tuttle and R.W. Schwartz, *J. Appl. Phys.* 76 (1994) 4305.
- [5] C.E. Land, *Ceramic Trans.* 11 (1990) 343.
- [6] E. Possenriede, P. Jacobs and O.F. Schirmer, *J. Phys.: Condens. Matter* 4 (1992) 4719.
- [7] H. Kurz, E. Fratzig, W. Keune, H. Engelmann, U. Gonser, B. Dischler and A. Rauber, *Appl. Phys.* 12 (1977) 355.
- [8] V.M. Fridken, *Photoferroelectrics* (Springer, Berlin, 1979).
- [9] J.P. Remeika, *J. Am. Chem. Soc.* 76 (1954) 940.
- [10] Ceramics Division, Motorola Inc., Albuquerque NM 87113, USA.
- [11] W.L. Warren and D. Dimos, *Appl. Phys. Lett.* 64 (1994) 866.



ELSEVIER

Journal of Non-Crystalline Solids 187 (1995) 453–456

JOURNAL OF
NON-CRYSTALLINE SOLIDS

Optical properties of sol–gel derived ferroelectric films

M. Bertolotti^{a,*}, S. Mura^a, E. Pennella^a, F. Senesi^a, C. Sibilis^a, A. Montenero^b,
G. Gnappi^b, S. Pigi^b

^aDipartimento di Energetica, Università di Roma 'La Sapienza', and GNEQP of CNR, INFN, Via Scarpa 16, 00161 Rome, Italy

^bDipartimento di Chimica Generale ed Inorganica, Università di Parma, Viale delle Scienze, 43100 Parma, Italy

Abstract

Optical characterization of thin films of PbO–TiO₂ and PbO–ZrO₂, prepared via the sol–gel route, is presented. Linear optical properties of the thin films have been studied by spectral analysis in the range of visible and near infrared. A non-linear thermal characterization through z-scan technique is presented.

1. Introduction

Chemical derived (sol–gel) thin films are receiving increasing attention because of their electrical and optical properties. Among such films, ferroelectric ceramics appear to offer particular promises for device applications [1]. To date major emphasis has been focused on PbO–TiO₂ and PbO–ZrO₂ systems [1], where a comparison between sputtered and sol–gel derived lead zirconate titanate films shows that the latter films have generally superior ferroelectrical (FE) properties.

In the present paper optical properties of thin films prepared in the system PbO–TiO₂ and PbO–ZrO₂ via the sol–gel route are presented.

Lead acetate, titanium isopropoxide and zirconium *n*-propoxide were used as precursor compounds: molar ratios PbO–TiO₂ and PbO–ZrO₂ were chosen equal to 1:1. Films were deposited from the sol on glass substrates by the dipping method. Thermal treatments were performed at 100, 200 and 300°C to start the film densification and formation of microcrystallites.

Linear optical properties of the prepared thin films have been studied by a spectral analysis in the visible and near IR ranges.

2. Optical spectral analysis

The optical transmission has been studied experimentally using a spectrometer in the visible and near IR range from 300 to 1100 nm.

To compare theory and experiments, we have applied a suitable expression of the spectral transmissivity through a three-layer system [2],

*Corresponding author. Tel: +39-6 4991 6542. Telefax: +39-6 4424 0183. E-mail: bertol88@itcaspur.caspur.it.

$$T = \left(n_3 \frac{\tau_{12}^2 \tau_{23}^2 e^{-2k_2 \eta}}{1 + \rho_{12}^2 \rho_{23}^2 e^{-4k_2 \eta} + 2\rho_{12} \rho_{23} e^{-2k_2 \eta} \cos(\phi_{23} + \pi + \phi_{12} + 2n_2 \eta)} \right)^2 \quad (1)$$

where 1 labels the air region, 2 labels the glass layer, and 3 labels the substrate, $\rho_{ij}^2 = ((n_i - n_j)^2 + k_j^2) / ((n_i + n_j)^2 + k_j^2)$, n_j is the real part of the refractive index of the material, k_j is the extinction coefficient which is proportional to the absorption coefficient, $\tan \phi_{ij} = 2k_j n_i / (n_j^2 + k_j^2 - n_i^2)$, $\tau_{ij}^2 = 4n_i^2 / ((n_j + n_i)^2 + k_j^2)$, and η is the film thickness.

To Eq. (1), to fit theory and experiment, we have included a spectral absorption dispersion, mainly associated with the titania component of the glass. The optical transmission spectrum for the zirconate films is shown in Fig. 1. We observe that the thermal treatment of the samples influences the optical transmission: a large number of oscillations is present for the sample treated at 300°C. The number of oscillations in the spectrum is related to interference in the film. From the fit between theory and experiment we obtain the values of refractive index and sample thickness shown in Table 1.

The spectral transmission of titanate films is shown in Fig. 2. We observe that the thermal treat-

ment induces only a small shift in the position of the maximum transmission value. The data from the fit are shown in Table 2, where the absorption coefficient is assumed to behave as

$$k(\lambda) = k_0 \left[\frac{\lambda - \lambda_0}{\lambda} \right].$$

In conclusion, we observe that the thermal treatment influences the spectral properties of films producing an increase of the refractive index.

Table 1
Extinction coefficient, k , refractive index, n , and film thickness, η , for zirconate films

	k	n	η (μm)
PZ1 (100°C)	0	1.85	0.345
PZ2 (200°C)	0	2.1	0.325
PZ3 (300°C)	0.01	2	0.270

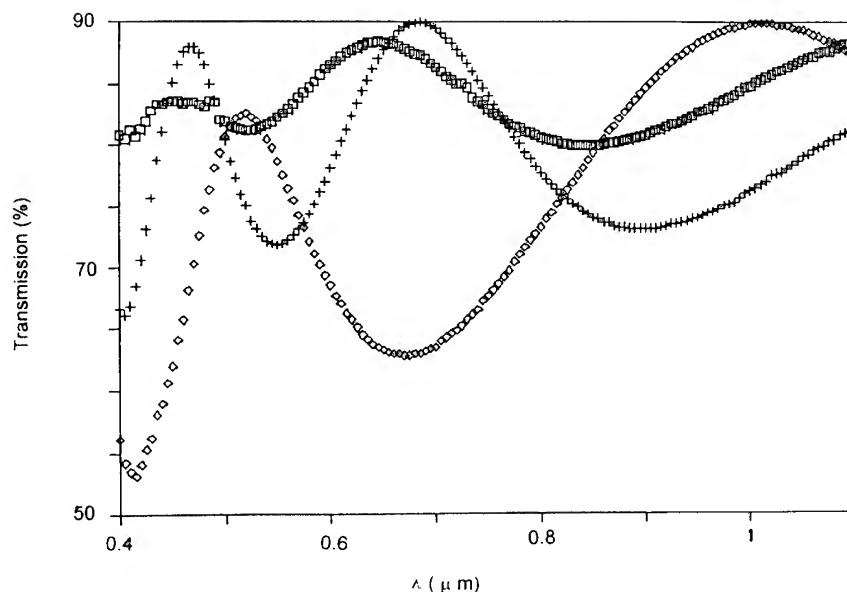


Fig. 1. Optical transmission spectrum of zirconia films: \square , PZ1; $+$, PZ2; \diamond , PZ3.

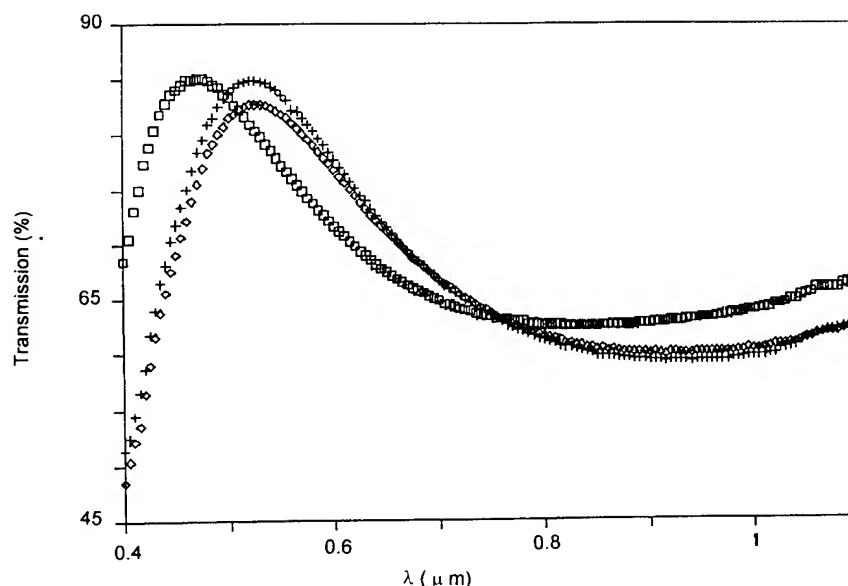


Fig. 2. Optical transmission spectrum of titania films: \square , PT1; $+$, PT2; \diamond , PT3.

Table 2

Extinction coefficient, k_0 , refractive index, n , and film thickness, η , for titanate films

	k_0	n	η (μm)
PT1 (100°C)	0.01	1.85	0.280
PT2 (200°C)	0.01	2	0.270
PT3 (300°C)	0.01	2	0.270

3. Thermal non-linear behaviour

The thermal non-linear behaviour of the refractive index of the samples examined has been evaluated through the z -scan technique. This technique is based on the principle of spatial beam distortion [3]: using a single laser beam in a tight focus geometry, the transmittance through the non-linear medium in the 'far field' is measured, as a function of the sample position z , with respect to the focal plane of the lens. The measurement can be understood assuming the material with its non-linear refractive index change acts as a variable focus lens. A negative self-lens prior to focus will tend to collimate the beam, causing a beam narrowing

at the aperture, which results in an increase in the measured transmittance. With the sample on the $+z$ side of the focus, the negative lens effect tends to increase diffraction, and the aperture transmittance is reduced. For still larger $+z$ the irradiance is reduced and the transmittance recovers the original linear value. The approximate null at $z=0$ is analogous to placing a thin lens at the focus that results in a minimal far-field pattern change. A positive non-linearity results in the opposite effects: lowered transmittance for the sample in the negative z and enhanced transmittance at positive z (see Ref. [3]). This technique is able to give information not only on the sign of the non-linearity but also on its magnitude.

For a cubic or a thermal non-linearity we have

$$n = n_0 + \Delta n = n_0 + n_2 |I|^2 = n_0 + (dn/dT_c) \Delta T_c, \quad (3)$$

where n_0 is the linear refractive index, I the light intensity and T_c the temperature. When we consider a Gaussian beam travelling in the $+z$ direction we can evaluate the non-linear phase of the

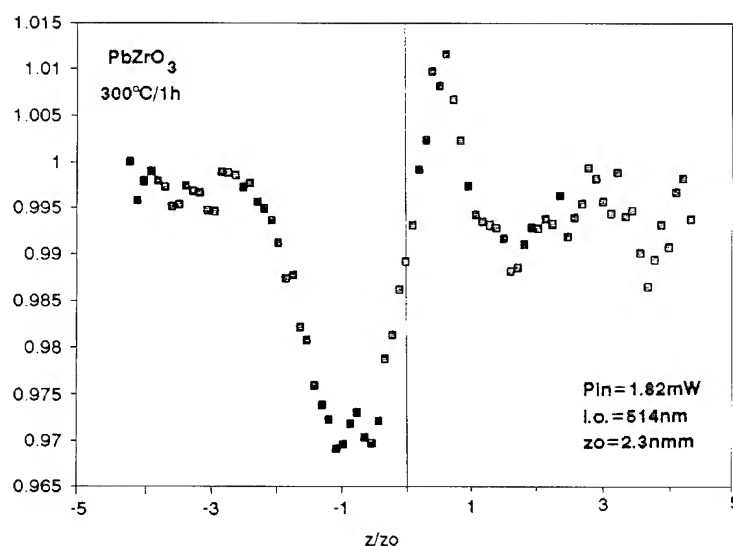


Fig. 3. z-scan transmission test for PZ3 film.

electric field of the laser beam as

$$\Delta\Phi = 2\frac{\pi}{\lambda} \Delta n \frac{[1 - \exp(-\alpha\eta)]}{\alpha}, \quad (4)$$

where α is the sample linear absorption and η its thickness. The transmittance difference between peak and valley is proportional to the phase change:

$$\Delta T \approx \Delta\Phi,$$

and by the help of this equation the non-linear refractive index can be derived within an experimental error of 3%.

The z-scan measurements, by using a c.w. Ar source at 514 nm, on our samples provided good results only for the PZ3 sample (see Fig. 3), where we found a refractive index change $\Delta n = 2.5 \times 10^{-2}$, corresponding to $n_2 = 1.17 \times 10^{-4} \text{ cm}^2/\text{W}$. These values have been obtained by using $\eta = 345 \text{ nm}$ and $I = 2.2 \times 10^2 \text{ W/cm}^2$.

4. Conclusions

Optical transmission properties of PbO-TiO_2 and PbO-ZrO_2 films have been studied, obtaining the refractive index value and thickness of films, which received a different thermal treatment. Also a preliminary non-linear refractive index, of thermal origin, has been estimated, but only for the PZ3 sample.

References

- [1] D.R. Uhlmann, G. Teowee, J. Boulton, S. Motakef and S.C. Lee, *J. Non-Cryst. Solids* 147&148 (1992) 409.
- [2] M. Born and E. Wolf, *Principles of Optics* (Pergamon, New York, 1975).
- [3] M. Sheik-Bahae, A.A. Said, Tai-Huei Wei, D.J. Hagan and E.W. Van Stryland, *IEEE J. Quant. El QE* 26 (1990) 760.



ELSEVIER

Journal of Non-Crystalline Solids 187 (1995) 457-472

JOURNAL OF
NON-CRYSTALLINE SOLIDS

Section 14. Optical applications

Chemical interaction in ion-implanted amorphous SiO_2 and application to formation and modification of nanosize colloid particles

Hideo Hosono*

*Research Laboratory of Engineering Materials, Tokyo Institute of Technology, Nagatsuta, Midori-ku, Yokohama 227, Japan
and Institute for Molecular Science, Myodaiji, Okazaki 444, Japan*

Abstract

Ion-solid chemistry approached from structural defects produced by implantation is summarized for implanted amorphous SiO_2 (a- SiO_2). The primary factor controlling the chemical interaction of implanted ions with substrate structure is the electronegative nature of implants. Implants with electropositive nature (M) pull oxygens out from the silica network structure to form M-O bonds, leaving Si-Si bonds at concentrations comparable to those of the implant, whereas implants (A) with electronegative nature react chemically with Si atoms to form Si-A bonds, forming O_2 molecules and peroxy radicals. Implants with weak chemical reactivity occur in a neutral state such as diatomic molecules and elementary colloids. The importance of Si-Si bonds as an active intermediate in dual implantation is stressed illustrating the formation of Si-N bonds. The effectiveness of ion implantation as a tool to fabricate nanosize colloids embedded in glass is demonstrated and a criterion of colloid formation in a- SiO_2 by implantation established. The morphology and optical absorptions of Cu colloid particles have been found to be modified by subsequent implantation of F ions, and the mechanism is considered on the basis of ion-solid chemistry. Formation of and nature of nanosize colloids of a-phosphorus and a novel approach to synthesize Ge nanocrystals are briefly described.

1. Introduction

Ion implantation is a processing technique to significantly modify surfaces and near-surface properties of materials. Implantation in amorphous materials has been mainly used to modify optical properties such as refractive index [1]. Various

phenomena specific to implants such as the formation of compounds between implants and constituents of substrates and colloid formation of implants are known as chemical effects. Understanding and utilization of these phenomena are keys to effective modification of amorphous materials and preparation of novel photonic glasses. For example, the increment of refractive index of SiO_2 glasses implanted with N ions is greater by several times than that with other ions. This is explained as due to formation of high index clusters or phases such as

* Corresponding author. Tel: +81-45 924 5359. Telfax: +81-45 922 5169. E-mail: hhosono@nc.titech.ac.jp

SiON and Si₃N₄ besides densification effects which commonly occur in implanted with SiO₂ glasses [2]. To elucidate these chemical effects is, therefore, indispensable for a comprehensive understanding of ion-beam interactions with solids and conclusions obtained should be a fundamental basis of ion-beam modification of amorphous materials as well as creation of new photonic glasses. Various types of structural defects are produced in glasses along their trajectories as a consequence of the interaction of ion beams with amorphous materials. We have examined structural defects produced by implantation and approached ion-solid chemistry in implanted amorphous SiO₂ on the basis of the results obtained.

In recent years nanometer-sized metals and semiconductors embedded in dielectrics such as glass have attracted much attention because of a fundamental interest in low-dimensional properties of the electronic states and novel application as photonic switching devices based on large third-order optical susceptibility. Synthesis of these nanocomposites by means of ion implantation has now been demonstrated [3] and a criterion [4] to predict the colloid formation in SiO₂ glasses has been proposed. A variety of nanosized colloid particles including materials chemically active in ambient atmosphere such as amorphous red phosphorus [5] can be fabricated by ion implantation without post thermal annealing. Implantation is a process which fits well with technologies for microelectronics such as fine patterning and carrier doping into semiconductors. It is, therefore, considered that ion implantation is a very promising technique to synthesize these nanocomposite materials for photonic applications.

The reasons why amorphous SiO₂ (a-SiO₂) was chosen as a substrate are as follows. (1) It has a simple, stoichiometry and the fewest impurities. (2) Point defects are simple due to the strong localization of electrons. Knowledge about diamagnetic defects as well as paramagnetic defects in a-SiO₂ has accumulated over the past three decades [6]. (3) a-SiO₂ has a less dense-packed structure composed of building units of SiO₄ tetrahedra, hence it is possible to identify and quantify molecular species, which are expected to be created during implantation as an interstitial defect by using a vacuum extraction technique at elevated temperatures. (4)

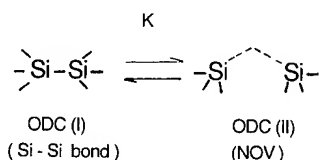
In terms of applications a-SiO₂ is a key material in MOS-type semiconductor devices and optical parts for excimer lithography.

In this paper I summarize ion-solid chemistry approached from structural defects in implanted a-SiO₂ and show some examples of the formation and modification of nanosize colloid particles by implantation.

2. Outline of experimental procedures

Substrates used were SiO₂ glasses (OH contents: $4 \times 10^{19} \text{ cm}^{-3}$) prepared by hydrolysis of SiCl₄ with an O₂-H₂ flame. 'Wet' silica is very favorable because some 'dry' silica glasses exhibit an intense absorption band peaking at 7.6 eV [7], which obscures the effects we are looking for, even in the as-delivered state. Substrates (1 cm × 1 cm × 0.1 mm thick) were implanted at room temperature with Li⁺, B⁺, C⁺, N⁺, O⁺, F⁺, Si⁺, P⁺, Ti⁺, Cr⁺ and Cu⁺. Fluence ranges from 0.5×10^{16} to $5 \times 10^{17} \text{ cm}^{-2}$, and acceleration voltage and dose rate were 160 kV and $\sim 2.5 \mu\text{A/cm}^2$, respectively, unless otherwise noted.

Vacuum ultraviolet (VUV) UV absorption spectra were measured for substrates before and after implantation. Electron paramagnetic resonance (EPR) spectra were measured at 300 and 77 K in the X-band. Fourier-transform infrared attenuated total reflection spectroscopy (FTIR/ATR) was used to examine changes in surface structures with implantation [8]. Gas species desorbed from implanted substrates upon heating were analyzed with a thermal-gas analyzing instrument (Ushio, Tokyo, Japan) [9], which consists of a high vacuum system, a quadrupole mass filter and an electric furnace. Transmission electron microscopy (TEM) observation was made on thinned specimens, applying an acceleration voltage of 300 kV. Detailed sample preparation procedures for cross-sectional observation were described in Ref. [10]. Ion-thinning technique could not be used for preparation of P-implanted specimens because phosphorus colloids were easily evaporated away during the ion-thinning process. In this case, observation was made on the edges of thin leaves peeled by scratching the implanted surface with a diamond pencil.

Fig. 1. Two types of neutral oxygen vacancy in a-SiO₂.

3. Two types of oxygen-deficient defects in a-SiO₂

Since oxygen-deficient type defects provide a novel clue to understand ion-solid chemistry in implanted SiO₂, their models and properties are briefly described. Arnold [11] proposed a model of a neutral oxygen vacancy (NOV) coordinated by two Si atoms, suggesting that the NOV gives an absorption band centered at 5 eV. O'Reilly and Robertson [12] calculated the energy of two types of oxygen-deficient defects, ODC(I) and (II) as shown in Fig. 1. The separations between two Si atoms in ODC(I) and (II) are close to that of Si₂H₆ molecule and Si-O-Si bond in silica, respectively. According to their calculations, ODC(I) and ODC(II) give optical bands near 7.5 and 5 eV, respectively. Since these ODCs may be regarded as relaxed and unrelaxed oxygen vacancies, ODC(I) and ODC(II) are called a Si-Si bond and a neutral oxygen vacancy (NOV), respectively, hereafter.

Experimental evidence for these two ODC models were obtained by Imai et al. [13]. They showed selective bleaching of 5 eV band in oxygen-deficient SiO₂ glasses which exhibit absorption bands at 7.6 and 5 eV in the as-delivered state, with KrF laser light (5 eV). Hosono et al. [14] proposed direct

evidence for the Si-Si bond model of the 7.6 eV band using a reaction of H₂ gas with Si-Si bonds in oxygen-deficient type SiO₂ glasses, i.e., they found a decrease in the intensity of the 7.6 eV band (Fig. 2(a)) and an appearance of Si-H bonds (2260 cm⁻¹) (Fig. 2(b)) upon heating samples in H₂ gas. Although the magnitude of the decrease in the intensity of the 7.6 eV band does not change

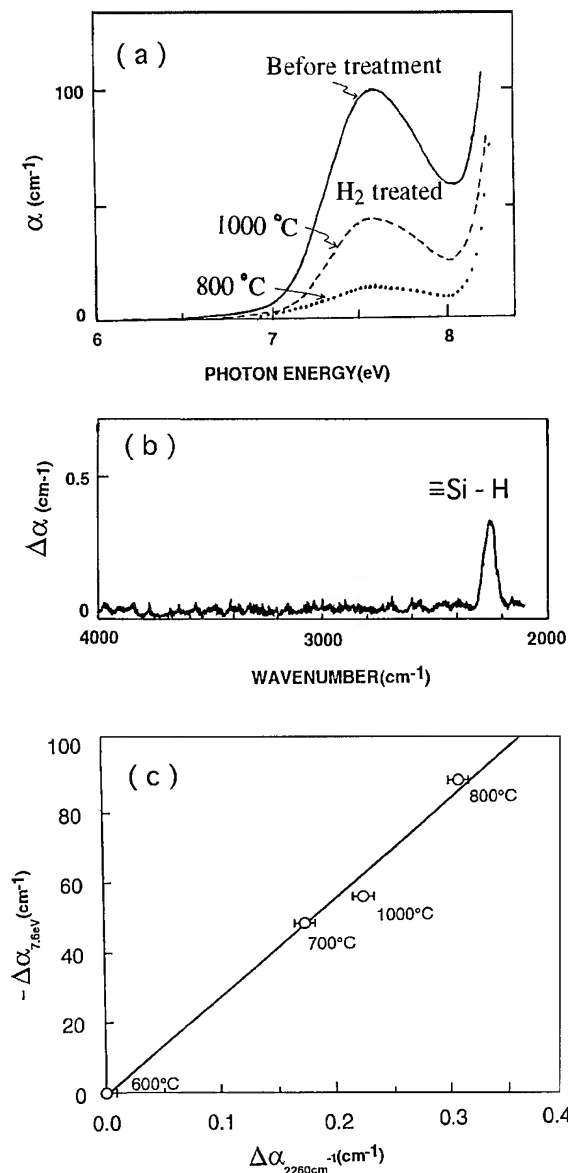


Fig. 2. Experimental evidence for the Si-Si bond model of the 7.6 eV band in a-SiO₂. (a) Changes in the VUV spectra of oxygen-deficient type SiO₂ glass with heat treatment in H₂ atmosphere. —, before treatment; ----, H₂-treated at 1000°C for 1 h; ····, H₂ treated at 800°C for 1 h. (b) Effectively induced infrared absorption spectrum which was obtained by subtracting the spectrum before treatment from that after H₂-treatment. A band centered at 2260 cm⁻¹ is due to the bond stretching mode of ≡Si-H. (c) Correlation between the decrease in the absorption coefficient ($\alpha_{7.6 \text{ eV}}$) of the 7.6 eV band and the increase in the absorption coefficient ($\alpha_{2260 \text{ cm}^{-1}}$) of the 2260 cm⁻¹. The temperature of H₂ treatment is indicated near the data points.

monotonically with temperature, a close correlation is seen between the decrease in the 7.6 eV band and an increase in the Si-H band (Fig. 2(c)) at each temperature. These results can be explained by the following reaction:



The absorption cross-section evaluated was $7.3 \times 10^{-17} \text{ cm}^2$ using the slope of Fig. 2(c) and a value of $35 \text{ l mol}^{-1} \text{ cm}^{-1}$ for the molar extinction coefficient of the Si-H band was. This value is close to that ($6 \times 10^{17} \text{ cm}^{-2}$) of the 7.56 eV band of a Si_2H_6 molecule containing a Si-Si bond, which in turn substantiates the validity of the model.

The Si-Si bond configuration is more stable than the oxygen vacancy configuration. These two types of configurations are considered to be in an equilibrium state and the enthalpy difference evaluated by an experiment is $\sim 1 \text{ eV}$ [13]. In bulk a-SiO₂ (fictive temperature is $\sim 1300 \text{ K}$) the equilibrium constant K is of the order of 10^{-3} [13].

4. Chemical interaction of implanted ions with the substrate structure

Various types of structural defects are created by implantation. What is the predominant factor controlling this defect formation? Dose ranges we will focus on here are over 10^{15} cm^{-2} . In such a dose range cascades of each ion heavily overlap with each other as shown by an experiment by Devine and Golanski [15]. Let us consider energy deposition. Fig. 3 shows an example of paramagnetic defects produced by implantation of Cr ions. Depth concentrations of PORs ($\text{Si-O-O} \cdot$ or O_2^-) [16] and E'-type centers ($\cdot \text{Si} = \text{Si}_n\text{O}_{3-n}$, where n is 1 and/or 2) [17,18] appear to be complementary with each other. The concentrations of both centers are not monotonic. The highest concentration of PORs is in the range of the peak of the distribution of the implanted ions. It has been demonstrated that the POR is created in a-SiO₂ by dense electronic excitation via self-trapped excitons [19,20]. Thus, if energy deposition is the major factor, it is expected that the depth concentration of POR is close to the profile of electronic energy deposition as shown in Fig. 3 (upper left). However, the observed profile is

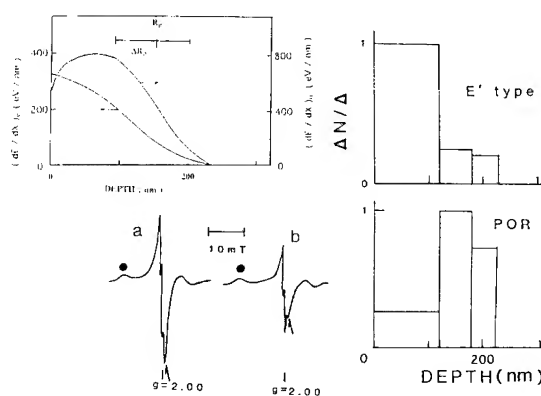


Fig. 3. Energy depositions (upper left) calculated with a TRIM code and depth concentrations (right) of E'-type center associated with a Si-Si bond and peroxy radical (POR). Sample: a-SiO₂ implanted with Cr⁺ to $0.5 \times 10^{16} \text{ cm}^{-2}$ at 160 keV. Examples of changes in EPR spectra with etching (lower left). Spectrometer sensitivity is kept unchanged. a, before; b, after 4 min etching with 5% HF. A closed circle and an arrow indicate characteristic resonance fields of POR and E'-type signals, respectively.

opposite to the expectation. It is, therefore, suggested that energy deposition is not the predominant factor in the defect formation in a-SiO₂ by implantation of non-rare gas ions.

4.1. Predominant defects produced by implantation

Fig. 4 (left) shows an example of VUV absorptions induced by implantation. An absorption band is seen at around 7.6 eV and its intensity strongly depends on implants. Intensities of F- and O-implanted specimens are smaller by an order of magnitude than those samples implanted with other ions. It is known that two defects with entirely different nature give an absorption band peaking at $\sim 7.6 \text{ eV}$ in amorphous SiO₂: (a) peroxy radical (POR) [16], which is paramagnetic, and an oxygen-surplus-type defect, (b) Si-Si bond [14], which is diamagnetic, and an oxygen-deficient-type defect. Since molar extinction coefficients of the POR ($5 \times 10^4 \text{ l mol}^{-1} \text{ cm}^{-1}$) and the Si-Si bond (2×10^4) were already reported and concentrations of the POR can be evaluated separately by EPR spectra measured at low temperatures, it may be possible to calculate the contribution of PORs and Si-Si

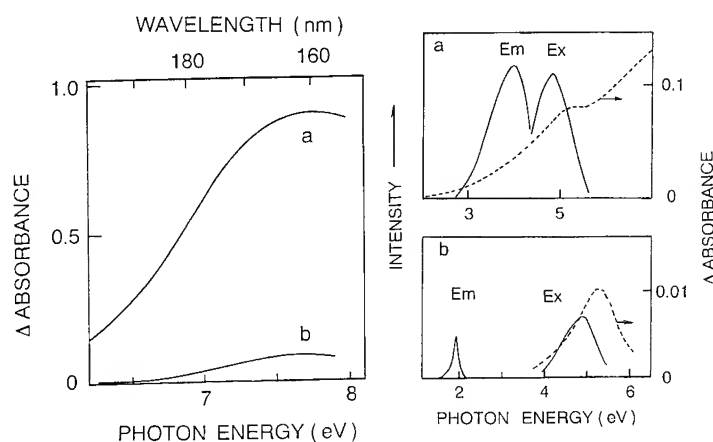


Fig. 4. Implantation-induced VUV (left) and UV (right) absorptions. Photoluminescence spectra were also shown along with induced UV absorption. Ex: excitation, Em: emission. Sample a: P^{+} ; b: F^{+} -implanted $a\text{-SiO}_2$. Acceleration voltage: 160 kV; fluence: $3 \times 10^{16} \text{ cm}^{-2}$.

bonds to the intensities of the 7.6 eV band. Concentrations of PORs in F- and O-implanted specimens were larger by several orders of magnitude than those in other ion-implanted specimens. Peak intensities of the 7.6 eV band calculated from the concentrations of PORs in these samples implanted with F and O ions are comparable to observed intensities, but are, at most, 3% in the samples implanted with other ions. Concentrations of Si-Si bonds calculated from intensities of PORs by subtracting the concentration of PORs are quite large and are comparable to those of implanted ions in the latter. Fig. 4 (right) shows a comparison of photoluminescence spectra of B- and F-implanted specimens. It is evident that although UV absorption bands (with different intensities) at around 5 eV are seen in both specimens, there is a distinct difference between photoluminescence spectra of these two specimens, i.e., the peak of photoemission bands from the B- and F-implanted appears at 4.3 and 1.9 eV, respectively. The 4.3 eV emission was commonly observed for all the specimens except for the F- and O-implanted specimens but the 1.9 eV luminescence band was seen only for the F- and O-implanted specimens. This difference indicates that the defect responsible for the absorption near 5 eV in the F- and O-implanted specimen differs from that in the others. The 4.3 eV and the 1.9 eV emission bands upon excitation with 5 eV light are

known to be attributed to a neutral oxygen vacancy (NOV) coordinated with two silicon atoms and an O_3 molecule, respectively [6]. Since the NOV is an oxygen-deficient-type defect and an ozone molecule is an oxygen-surplus-type defect, the results of these photoluminescence are consistent with the above conclusions. Fig. 5 shows changes in 5 eV band in P^{+} and Si^{+} -implanted substrates with illumination of 5 eV light. The 5 eV bands in both substrates are bleached in a similar manner. This property agrees with that of the NOV.

Thermal gas desorption measurements of implanted substrates provide novel information about predominant defects in F-implanted substrates. They revealed that although F_2 molecules were not desorbed, release of O_2 molecules was seen in the temperature range of 150–600°C. No perceptible release of O_2 molecules were observed for substrates implanted with other ions except with oxygen ions. Here we make the following assumptions to obtain quantitative relations between produced defects and implants: (i) fluorine and oxygen atoms occur nominally as -1 and -2 charge states, respectively, and, thereby, an oxygen atom in the substrate structure is replaced by two implanted fluorine atoms due to the requirement of electroneutrality. This assumption is justified because the formation of Si-F bonds is confirmed by

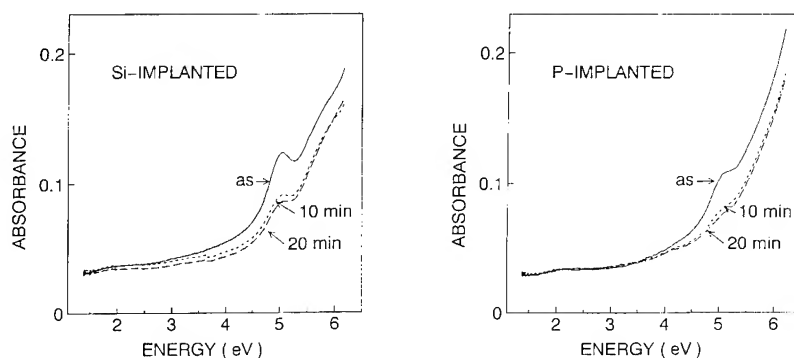


Fig. 5. Bleaching of implantation-induced UV absorptions with 5 eV light from a Hg discharge lamp. Dose: $3 \times 10^{16} \text{ cm}^{-2}$.

FTIR/ATR spectra [8,21]; (ii) a POR is created by reaction of a recoil oxygen atom with the silica network structure. Table 1 summarizes concentration ratios of predominant induced-defects relative to implants. The type of predominant defects is classified into three groups, (I) Li, B, C, Si, P, Ti, Cr (II) O, F (III) N. Fig. 6 shows an example of dose dependence of various types of defects produced in a Cr-implanted substrate. It is evident that the dominant defect is a Si-Si bond and its concentration is comparable to those of implanted ions at each dose. The concentration ratio of the NOV's to Si-Si bonds is ~ 0.1 . This ratio is larger by about 2 orders of magnitude than that (10^{-3}) reported for bulk a-SiO₂ with oxygen deficiency [13], suggesting that an extremely high temperature state is realized in implanted substrates. In N-implanted specimens concentrations of Si-Si bonds or O₂ + POR are much less than those of implants. Although NO₂ molecules, which are produced by the reaction of implanted N atoms with O atoms in the lattice, are observed by EPR [22], their concentrations are only 1% of implanted N atoms. Therefore, we consider from the data of XPS [23] and thermal-gas-analysis [24] that a major fraction of nitrogens occur as N₂ molecules without forming chemical bonds with constituents of substrates and the remaining fraction occur in the form of silicon oxynitrides. An indication of formation of N₂ molecules as the major product is also seen in a trapezoidal shape of depth profile of implanted N ions [23(b)]. Table 1 summarizes concentrations of predominant defects and implanted ions.

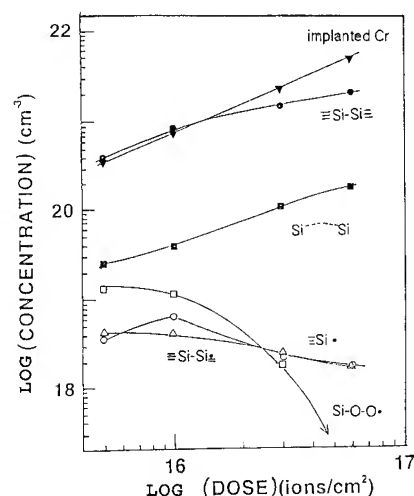


Fig. 6. Implantation-induced structural defects in a-SiO₂ as a function of fluence of Cr⁺. Acceleration voltage: 160 kV.

4.2. Ion-solid chemistry

Although no correlation between energy deposition and the above three groups was noted [24,25], we found a close correlation between electronegativities (EN) of the relevant implants and the above three groups (see Table 1). Implants with $EN < 2.5$ and > 3.5 may be classified into groups I and II, respectively. This finding indicates that the electronegative nature of implants determines the type of predominant defects created by implantation. Electropositive implants (M) such as B ions

Table 1
Concentration ratios of major structural defects produced by implantation relative to implants

Implants (electronegativity)	Li (1.0)	B (2.0)	C (2.6)	N (3.0)	O (3.5)	F (4.0)	Si (1.8)	P (2.1)	Ti	Cr
$\frac{[\text{Si-Si}]^a}{[\text{Implant}]}$	0.65	0.83	0.7	~ 0.1	< 0.05	< 0.05	1.6	1.4	1.0	0.6
$\frac{n[\text{O}_2] + n/2 [\text{POR}]^b}{[\text{Implant}]}$	d				0.49	0.48				
					$(0.46 + 0.03)^c$	$(0.38 + 0.03)^c$				

^a Brackets denote concentration.

^b POR and O₂ are assumed to be created from one and two oxygens recoiled from substrates of a-SiO₂. Two F ions form two Si-F bonds, recoiling an oxygen. Thus, *n* is taken to be 4 for F and 2 for O.

^c The former and the latter values denote ratios of O₂ and POR to implants, respectively.

^d Since the release of O₂ gases was not detected at a temperature $< 500^\circ\text{C}$. It is not possible to obtain an exact ratio. The crude value of this ratio is $\sim 10^{-4}$ neglecting [O²].

react chemically with oxygen atoms in the substrate structure to form M-O bonds, leaving Si-Si bonds at concentrations comparable to those of implants. On the other hand, electronegative implants (A) such as F ions knock oxygens out from the network structure to form Si-A bonds and the recoiled oxygens combine with each other to form O₂ molecules or react with the network structures to form PORs. When the chemical interaction of implants with the silica substrates is weak, a major fraction of implants occurs in a neutral state such as elementary colloids and molecules without forming chemical bonds with silicons or oxygens in the substrate structure [26]. Consequently, concentrations of Si-Si bonds or the total concentrations of O₂ molecules and PORs are much lower than those of implants. Nitrogen is an example of this category.

5. Si-Si bonds as active intermediate

The formation of Si-N bonds is important in optical and electrical applications. Since the major fraction of implanted N ions occur as N₂ molecules in N-implanted SiO₂, implanted N's are easily desorbed upon heating. Dual implantation of Si (not limited to Si as will be stated later) and N ions results in efficient Si-N bond formation as shown in XPS data of Fig. 7(a). As a consequence, the stability of implanted nitrogens is much improved as

shown in Fig. 7(b). The mechanism of this coimplantation effect is considered from a viewpoint of structural defects. Fig. 8 summarizes concentrations of Si-Si bonds created by implantation of relevant ions. Concentrations of Si-Si bonds are comparable to those of implanted ions in Si or P-implanted substrates, whereas the concentration ratio of Si-Si bonds to implanted ions is ~ 0.1 in N-implanted substrates. The Si-Si bond concentrations in the coimplanted substrates are $\sim 45\%$ of the sum of the concentrations in either implanted one. Taking into consideration a mismatch (according the calculations with the TRIM code, the overlap area is $\sim 70-80\%$) of the distribution width of implanted Si or P ions and N ions, it is concluded that the Si-Si bonds are converted efficiently into Si-N bonds through reactions with implanted N ions. High reactivity of Si-Si bonds will be related with that of Si metals with N ions. Silicon-silicon bonds are produced as the dominant defects in a-SiO₂ implanted with ions with electropositive nature and their concentrations are comparable to those of the implanted ions. Therefore, Si-Si bonds are not just 'defects' but may be rather regarded as a main product. Although few studies have been carried out on dual implantation into a-SiO₂ so far, we expect dual implantation will offer novel possibilities to fabricate new materials which cannot be made, or are difficult to obtain, by other conventional techniques.

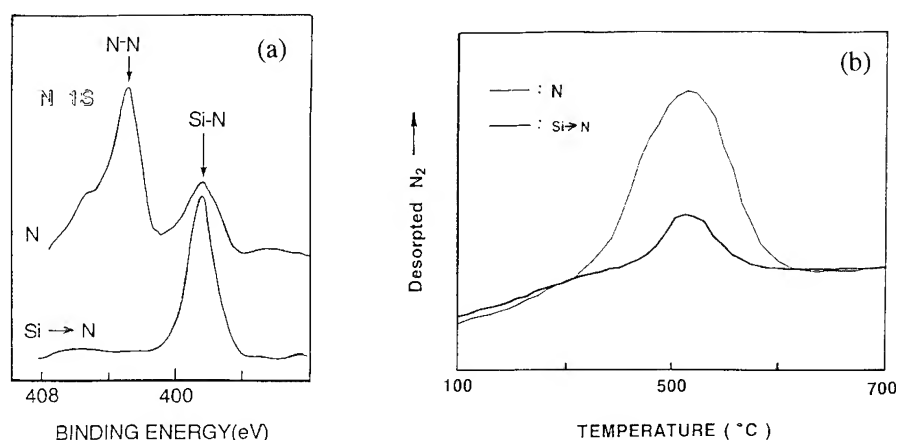


Fig. 7. (a) N 1s X-ray photoelectron (XPS) spectra of N- and Si + N implanted a-SiO₂. (b) Thermal desorption spectra of N₂ molecules from N and Si + N implanted a-SiO₂. Heating rate: 5 K/min.

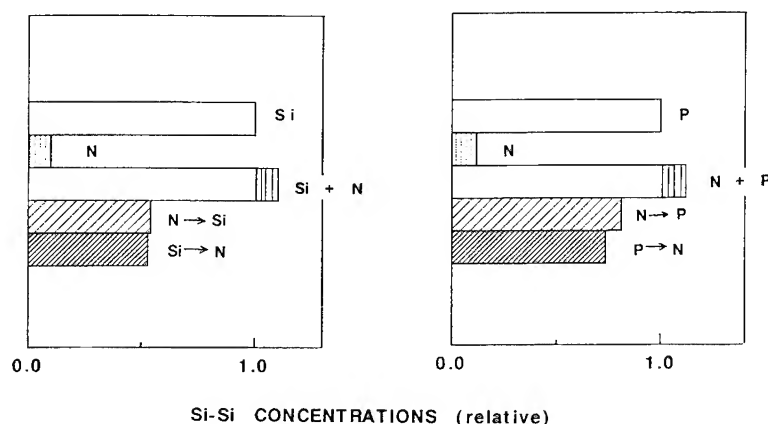


Fig. 8. Comparison of Si-Si bond concentrations in (left) Si-, N-, N → Si, and Si + N or (right) P-, N-, N → P, and P + N implanted a-SiO₂. The third datum from the top is a hypothetical value (simple sum of the concentrations in the substrates either implanted with Si (or P or N)). Acceleration voltage: 160 kV for Si⁺ and P⁺, 90 kV (chosen so as to meet the peak depth with Si⁺ and P⁺) for N⁺. Fluence: $3 \times 10^{16} \text{ cm}^{-2}$.

6. Formation and modification of nanosize colloids

Ion implantation has several advantages over other techniques for modification of surface and near-surface properties of glasses. It is a low temperature process, provides a precise control of profile and concentrations of desired ions, allows the preparation of chemical states which cannot be realized by conventional glass-melting techniques, and may stabilize chemically unstable states under an ambient atmosphere because implants exist not

on surfaces but on the buried layers of glasses. Nanoscale semiconductor and metal colloids embedded in a dielectric such as a glass exhibit large third-order optical susceptibility and picosecond response time arising from quantum confinement effects. These properties are anticipated to be applicable to photonic devices such as a switch in optical computing. Therefore, the fabrication of nanocomposites composed of these colloids and glass is a subject of current interest. Ion implantation is, undoubtedly, a favorable method to

fabricate these composites because of its advantages described above. In this section, I describe a simple criterion for colloid formation and formation and modification of nanosize Cu and other colloids by implantation.

6.1. Criterion for colloid formation by implantation

When chemical interaction of implanted ions with substrate structures is weak, a major fraction of implanted ions do not react chemically with the oxygens. Consequently, the major fraction of implants occur as elementary states such as homomolecules, clusters and colloids. It is, therefore, evident from the ion-solid chemistry in Section 4.2. that a weak chemical interaction with oxygens is required for implants to form their elementary colloids. In the criterion for the colloid formation from implants a widely available physical quantity is needed as a measure of this chemical interaction instead of the concentration ratio of Si–Si bonds relative to implants. I proposed [4] the free energy of oxide formation as this quantity because this data has been compiled for most elements and is easily available now. Implant ions (M) and silicon ions are in mutual competition to attract oxygens in the substrate structure. Colloid formation will occur when the affinity of M to the oxygen is smaller than that of Si^{4+} . It is, therefore, considered that the colloid formation occurs when the standard free energy of formation of oxides of an implant, $\Delta G_f(\text{M}_x\text{O}_2)$, is greater than that of SiO_2 , $\Delta G_f(\text{SiO}_2)$. Since ΔG_f is a function of temperature, a temperature is needed to be specified to compare $\Delta G_f(\text{M}_x\text{O}_2)$ with $\Delta G_f(\text{SiO}_2)$. It will be reasonable to choose the fictive temperature T_f of implanted glass layers as this specified temperature. Energetic incoming ions dissipate their energies in a very short time in the substrates. It is, therefore, expected that an extremely high temperature state is created in the implanted layers. We made an estimation of the T_f of implanted layers of SiO_2 glasses by two different ways, i.e. the first [17] is to use information about two types of oxygen-deficient type point defects (see Section 2) produced implantation, and the second [8] is based on information about lattice vibrations of the silica network. These two ways based on quite different basis

gave a similar T_f , ~ 3000 K, which is almost independent on doses and types of implants. These values were determined by extrapolating the relations (which had been measured in the temperature range up to ~ 1800 K) between T_f and T_f -dependent quantities to the values obtained for implanted specimens. They are similar to the T_f , which was estimated by the same procedures using T_f -dependent Raman bands, in neutron-bombarded SiO_2 glass [27]. It was suggested that realization of such an extremely high T_f is associated with the 'thermal spike' model of particle irradiation damage. Local heating due to energy generated in the collision of energetic ions with the substrate melts a microscopic volume around the sites of the primary knocked-on atoms and their extremely small volumes are rapidly quenched. An extremely high fictive temperature in the implanted layers creates an extremely high fraction of reduced states of implants [28] because redox equilibrium shifts to the reduced side with increasing temperature for multivalence ions. From the above discussion we propose the following criterion: *When the standard free energy of formation of the oxides of the implant M, $\Delta G_f(\text{M}_x\text{O}_2)$, is greater than that of SiO_2 , $\Delta G_f(\text{SiO}_2)$ at ~ 3000 K, estimated by extrapolating the known temperature dependence of ΔG_f , then colloid formation of implants occurs in SiO_2 glass.* Fig. 9 shows $\Delta G_f(\text{M}_x\text{O}_2)$ of relevant oxides as a function of temperature (this type of figure is called Ellingham diagram). Colloid formation in a- SiO_2 by implantation was observed for Au, Cu, Sb, Ge, P and Fe, and the formation of diatomic molecules was observed for N. All of these implants agree with the prediction from the criterion ($\Delta G_f(\text{M}_x\text{O}_2) > \Delta G_f(\text{SiO}_2)$). Although the fraction of Ti^{3+} ions in implanted silica is extremely high (10–40% of the total Ti) compared with that (1% >) in conventionally prepared glasses, no formation of titanium colloids was observed [28]. This result is consistent with prediction ($\Delta G_f(\text{TiO}_2, \text{Ti}_2\text{O}_3) < \Delta G_f(\text{SiO}_2)$).

6.2. Formation of and modification of Cu colloids

As an example of nanosize metal colloids, the formation of Cu colloids and modification of the

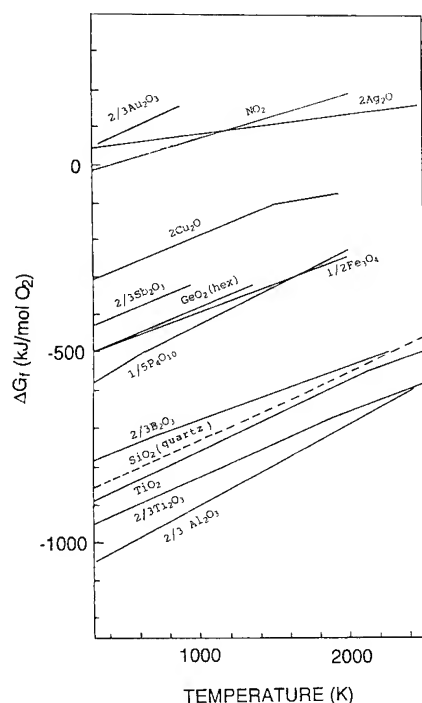


Fig. 9. Standard free energy of formation of oxides as a function of temperature.

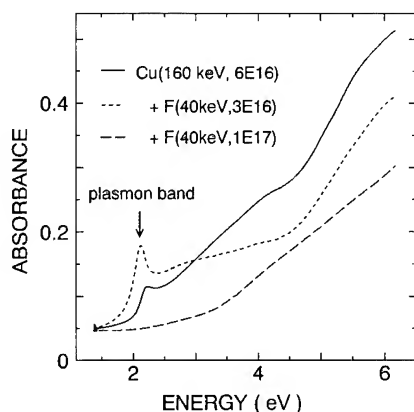


Fig. 10. Effects of sequential implantation of F ions on the optical absorption spectra of Cu-implanted SiO_2 . Note changes of Cu plasmon band with fluence of F ions.

colloids by sequential implantation of F ions is described. Fig. 10 shows optical absorption spectra of substrates implanted with Cu^+ to a fluence of $6 \times 10^{16} \text{ cm}^{-2}$ and dually implanted with Cu^+

Implanted silica glass

Cu; 160 keV, $6 \times 10^{16} \text{ cm}^{-2}$, F; 40 keV

Cu Cu → F
[F] = 3×10^{16} 1×10^{17}

Fig. 11. Photo of Cu- and Cu → F implanted a- SiO_2 .

(160 keV, $6 \times 10^{16} \text{ cm}^{-2}$) and subsequently F (40 keV¹, 3×10^{16} and $1 \times 10^{17} \text{ cm}^{-2}$). A sharp absorption band peaking at 2.2 eV, which is attributed to the surface plasmon peak of copper colloids, is seen in the Cu-implanted substrate, the position of the plasmon band shifts to lower energy and the intensity is increased in the substrate subsequently implanted with F ions at a dose of $3 \times 10^{16} \text{ cm}^{-2}$, and the plasmon band appears to disappear in the substrate implanted with $1 \times 10^{17} \text{ cm}^{-2}$ F ions. Fig. 11 shows the photo of the above three substrates. When F ions were implanted into already Cu-implanted substrates, the color of the sample changed from yellowish red to reddish violet for a dose of $3 \times 10^{16} \text{ cm}^{-2}$ and to almost colorless for $1 \times 10^{17} \text{ cm}^{-2}$. Depth distributions of Cu in each of the substrate are bimodal in shape. Fig. 12 shows the cross-sectional TEM photos of the above three substrates. In the Cu-implanted substrate, particles are observed in the range from the implanted surface to the depth $> 200 \text{ nm}$ and the particle diameters are almost constant at a given depth, but vary in the range 2–8 nm with depth. It was found that the distribution of Cu colloid diameters has a shape that is close to that of the implanted Cu concentrations [10]. Two changes were seen in the morphology of these colloid particles after F-implantation. First,

¹ This acceleration voltage was chosen so as to match the peak of the distribution of F with that of Cu.

particles with nonspherical shape became prominent. Second, the particle size increased. These changes may be explained by coalescence of small colloidal particles [29]. These particles in substrates implanted with Cu and Cu + F ($3 \times 10^{16} \text{ cm}^{-2}$) were

identified as Cu from selected area electron diffraction (SAED) patterns. Changes in the position and intensity of Cu plasmon band agree well with those expected from the Maxwell–Garnett theory [30] incorporating size corrections. On the other hand,

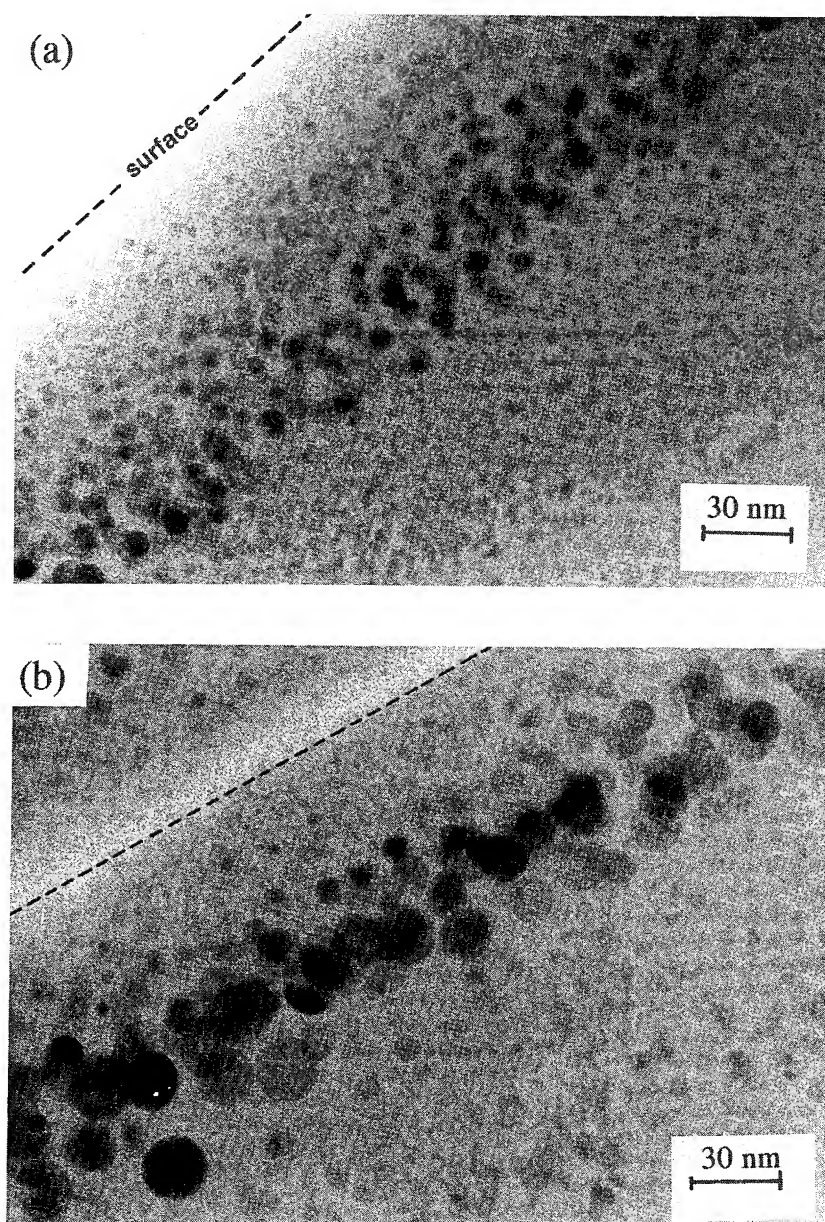


Fig. 12. Cross-sectional TEM photograph of substrates implanted with Cu or Cu \rightarrow F ions. (a) Cu⁺ (160 keV, $6 \times 10^{16} \text{ cm}^{-2}$), (b) Cu⁺ (160 keV, $6 \times 10^{16} \text{ cm}^{-2}$) \rightarrow F (40 keV, $3 \times 10^{16} \text{ cm}^{-2}$), and (c) Cu⁺ (160 keV, $6 \times 10^{16} \text{ cm}^{-2}$) \rightarrow F (40 keV, $1 \times 10^{17} \text{ cm}^{-2}$). Selected area electron diffraction pattern indexed as arising from Cu and Cu₂O is also shown for sample (c).

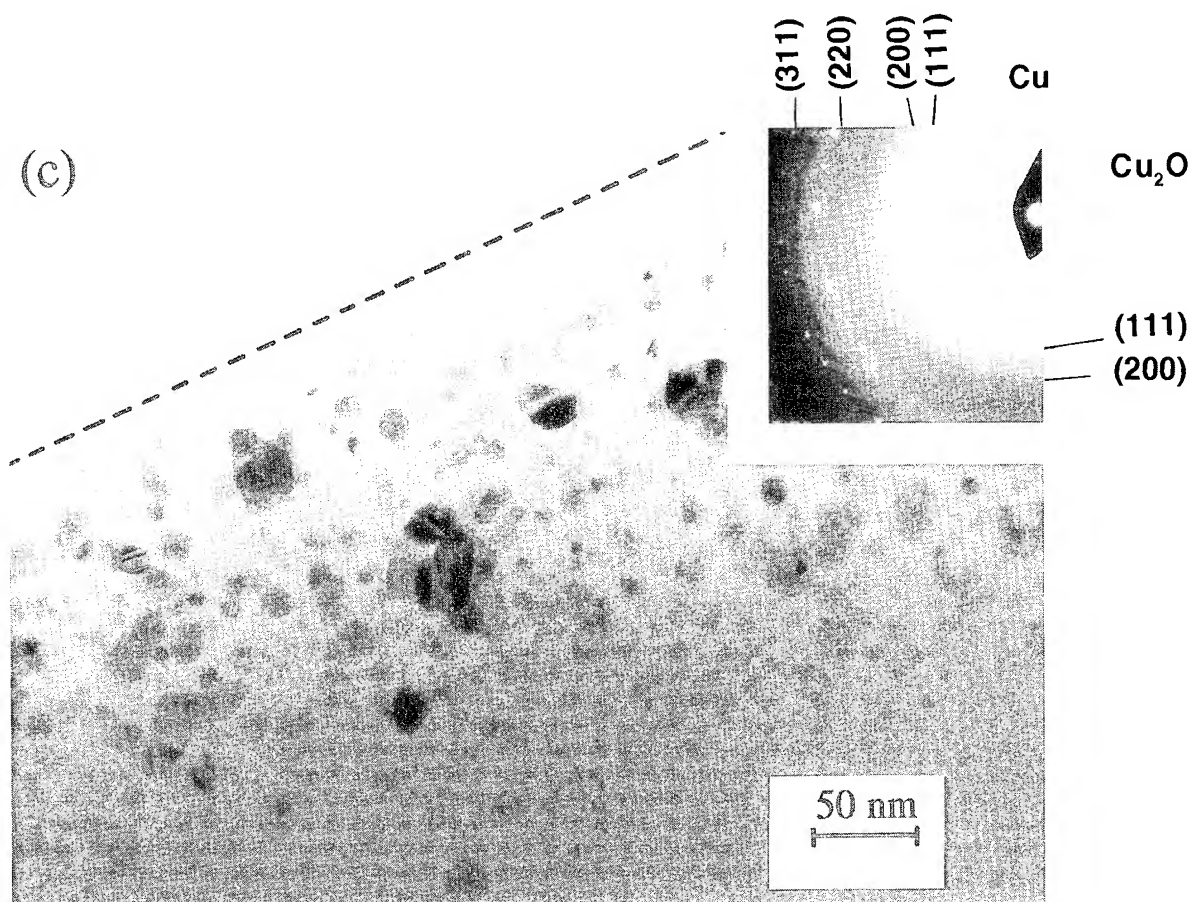


Fig. 12 (Continued)

the SAED patterns of colloid particles in the decolored substrate (F ; $1 \times 10^{17} \text{ cm}^{-2}$) may be indexed as arising from Cu and Cu_2O . Formation of Cu_2O may be explained by ion-solid chemistry summarized in Section 4.2. Implanted F ions form Si-F bonds (demonstrated by FTIR/ATR), recoiling O atoms from Si-O-Si bonds. Resulting recoiled oxygens having high kinetic energy react with Cu colloid particles to form dual structured colloid particles made up of Cu_2O (shell) and Cu (core). This assumption is supported by thermal-gas-analysis as shown in Fig. 13. Desorption of O_2 molecules is observed for both substrates implanted with $F(1 \times 10^{17} \text{ cm}^{-2})$ ions and $\text{Cu} \rightarrow \text{F}$ ions. However, a distinct difference in the desorption behavior and the amount of desorbed O_2 is observed between these samples. A single peak is

seen at $\sim 250^\circ\text{C}$ for the F-implanted substrate, whereas a continuous desorption up to $> 700^\circ\text{C}$ is followed by a peak at $\sim 250^\circ\text{C}$ for the co-implanted substrate. The ratio of the amount of O_2 desorbed from the coimplanted substrate relative to the F-implanted substrate is ~ 0.4 in the temperature range up to $\sim 300^\circ\text{C}$ or ~ 0.8 for up to $\sim 700^\circ\text{C}$. A decrease in the desorbed amount of O_2 up to $\sim 300^\circ\text{C}$ in the coimplanted substrate is considered to be a consequence of oxidation of the Cu colloids, i.e. formation of Cu_2O . Restoration of the plasma band at 2.2 eV is observed for the decolored substrate after once heating to $\sim 450^\circ\text{C}$ as shown in inset of the figure. Cu_2O is thermodynamically unstable at high temperatures, dissociating into Cu and O_2 . Continuous desorption of O_2 molecules is attributed to the dissociation of Cu_2O colloids. We

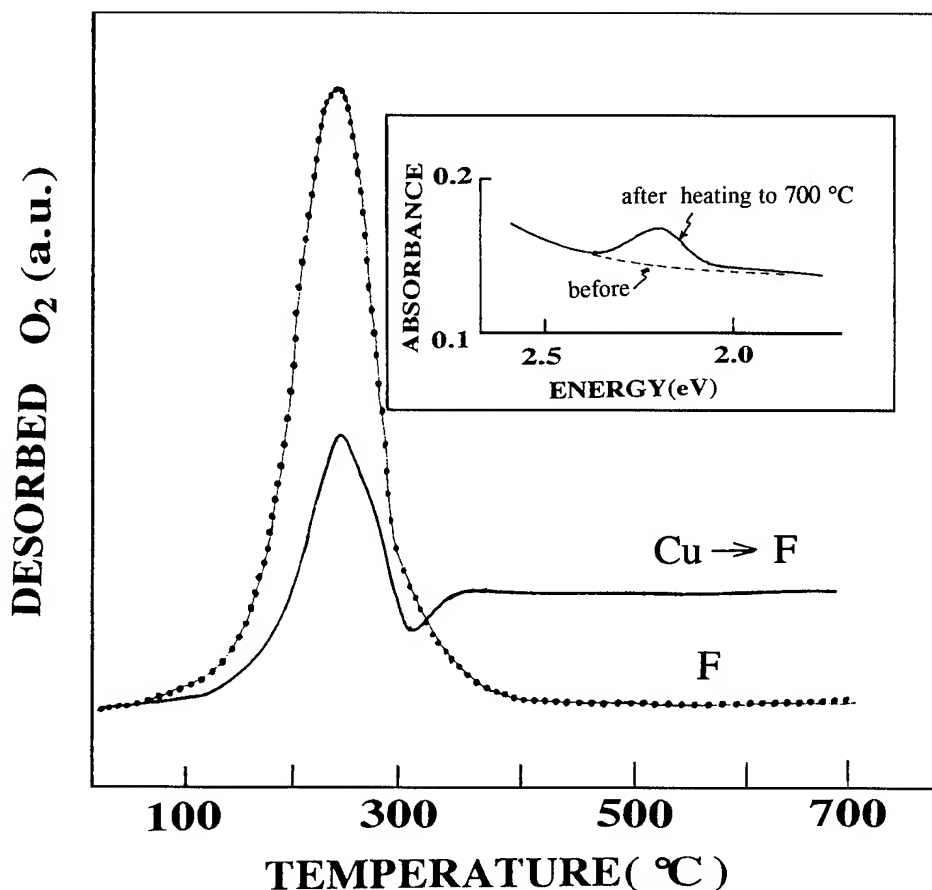


Fig. 13. Thermal desorption spectra of O_2 molecules from implanted substrates. Heating rate: 5 K/min. -----, F (40 keV, $1 \times 10^{17} \text{ cm}^{-2}$); —, Cu^+ (160 keV, $6 \times 10^{16} \text{ cm}^{-2}$) \rightarrow F (40 keV, $1 \times 10^{17} \text{ cm}^{-2}$). Inset shows the optical absorption spectra of a coimplanted substrate before and after heating to 700°C. Note that the 2.2 eV band, which is missing in the substrate before heating, is distinctly observed.

consider that nanosize colloid particles in this decolored substrate have a composite structure made up of Cu (core) and Cu_2O (shell). Optical absorption spectra of colloidal copper particles in dielectrics is well reproduced by the Maxwell-Garnett theory [30,31] incorporating size correction of imaginary part of the dielectric function. According to the calculation, intensities of the absorption due to Cu colloid particles are sharply decreased when the particle diameter decreases to below $\sim 5 \text{ nm}$ [31]. Although the apparent particle size of colloids increases due to implantation of Cu followed by F, we consider that the diameter of the Cu core in the resulting dual colloid particles is decreased to a size

smaller than $\sim 5 \text{ nm}$. Further efforts including observation of cross-section of composite colloids are in progress.

6.3. Other colloids

6.3.1. Amorphous P colloids

Fig. 14 shows TEM and SEM (reflection electron image) photographs of substrates implanted with P^+ ions to a dose of $5 \times 10^{17} \text{ cm}^{-2}$ at 180 keV. Nanometer-size colloid particles are noted in the as-implanted substrates [5]. The SAED patterns show the resulting P colloids to be amorphous. When the as-implanted substrate is once heated to

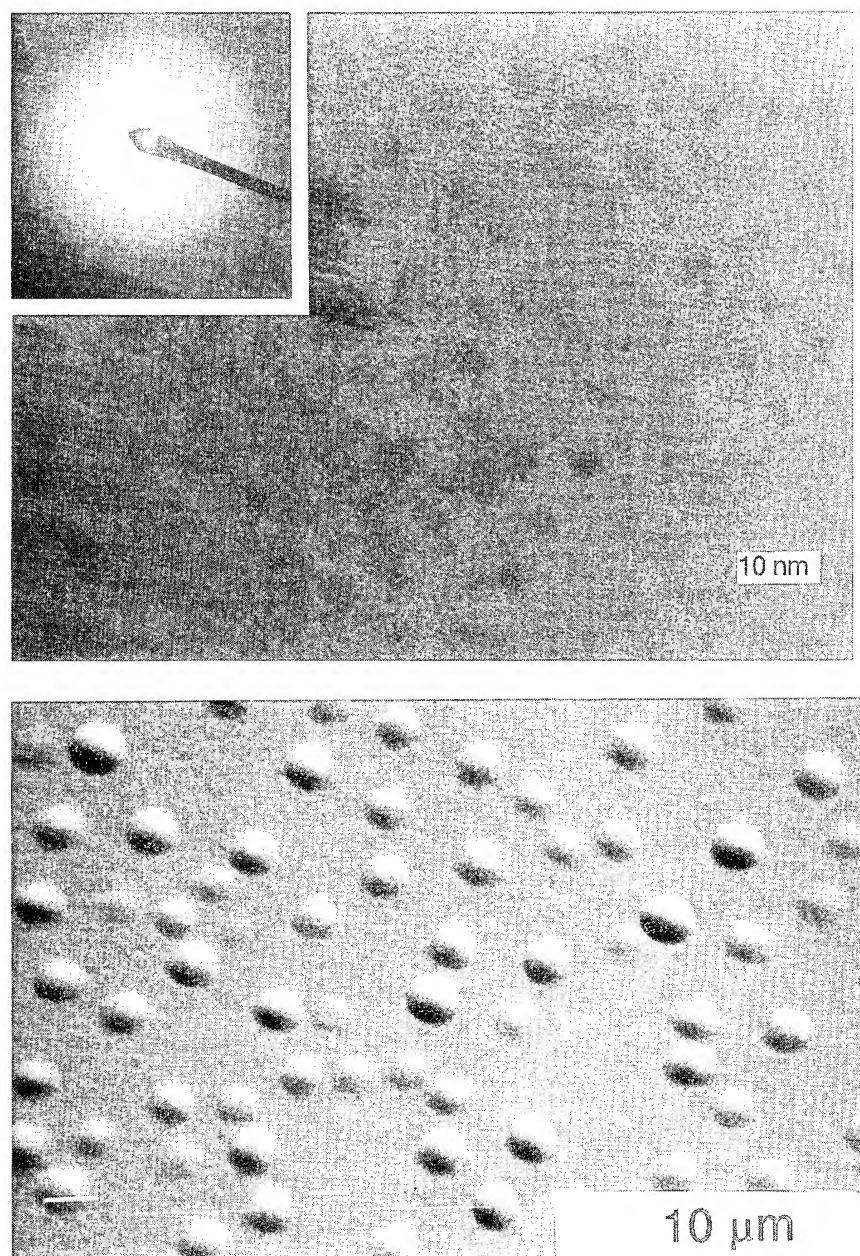


Fig. 14. Photo of a-SiO₂ implanted with P⁺ ions to a dose of $5 \times 10^{17} \text{ cm}^{-2}$ at 180 keV. (Top) TEM photo of as-implanted substrate. (Bottom) SEM photo of substrate after once heating to $\sim 600^\circ\text{C}$ and being cooled to room temperature. Note the difference in scale of the two photos.

$\sim 600^\circ\text{C}$, the colloid diameter viewed from the implantation surface grows from 3–4 nm to $\sim 2 \mu\text{m}$. Since no significant changes were seen in the width of P in the RBS spectra, the shape of resulting

colloids is considered to be not spherical but disk-like. Then, the band gap shifted to a lower energy side by $\sim 0.3 \text{ eV}$ and almost agreed with that ($\sim 2.1 \text{ eV}$ [32]) of bulk amorphous red

phosphorus. The optical band gap of nano-sized clusters of semiconductors is larger than that of the bulk because of quantum confinement effects. Therefore, we conclude that the observed red shift of the absorption edge is due to the decrease in the optical band gap of amorphous red phosphorus, which originated from approach of the particle size to bulks. This is the first example showing quantum size effect on the band gap in amorphous semiconductors, to our knowledge. Large third-order nonlinear susceptibility was also obtained for the as-implanted substrates [33].

Amorphous red phosphorus is a moderately unstable material. At normal temperatures and humidities, it reacts slowly with water vapor and oxygen in air to form phosphine and mixture of the oxyacids of phosphorus. Furthermore, band gap illumination drastically enhances these degradation reactions [34]. Since implantation forms nanometer-sized a-P colloids in buried layers of the SiO_2 substrate (resulting colloids are separated from atmosphere by SiO_2 layers which are densified by implantation), no degradation was perceived after implanted specimens were allowed to be placed in ambient atmosphere for 4 yr (up to date).

6.3.2. Ge nanocrystals by proton implantation

All nanosized colloid particles in glass formed by implantation have been synthesized by the implantation of the ions composing the colloids, to our knowledge. Recently, there has been a novel approach to fabricate nanosized Ge colloid particles in germania-silica glasses utilizing the chemical reaction of implanted protons with constituents in the substrate [35]. From thermodynamic arguments, whether the elementary state is formed or not is determined by the magnitude of free energy changes (ΔG_f) in the formation of an oxide of an ion, as described in Section 6.1. ΔG_f of GeO_2 is much smaller than that of SiO_2 , hence it is considered that GeO_2 is much easily reduced to elementary colloids compared with SiO_2 . This is consistent with the experimental result that Si colloids are not formed but Ge colloids are produced in germanosilica glasses implanted with H^+ . Microcrystalline (μc)-Ge particles embedded in a-silica are usually fabricated by co-sputtering of Ge and SiO_2 . Particles of Ge are amorphous in as-

sputtered samples in this case. Post annealing at temperatures $> 700^\circ\text{C}$ is needed to convert them into the crystalline phase [36]. However, Ge particles created in H-implanted $\text{SiO}_2:\text{GeO}_2$ glasses are not amorphous but crystalline in the as-implanted state. Implantation of protons into multi-component glasses will provide a novel route to synthesize nanocomposite materials.

7. Concluding remarks

Types and concentrations of structural defects produced by implantation into a-silica are primarily controlled by the nature of implants. Si-Si bonds and O_2 molecules + PORs are the predominant defects produced by implantation of implants with electropositive nature and electronegative nature, respectively. Concentrations of these defects are comparable to those of implants. Therefore, these species are not just 'defects' and may be rather regarded as 'a main product', hence they will provide novel possibilities to realize new materials as exemplified in the formation of Si-N bonds by coimplantation. Recently, novel photonic properties based on responses of structural defects [37] to photons have been reported, photo-induced refractive index changes (Hill gratings [38]) in $\text{SiO}_2:\text{GeO}_2$ glasses, i.e., second-harmonic generation [39] from germanosilica fibers, and phototropy in reduced calcium aluminate glasses [40]. I believe that ion-implantation is an appropriate tool to facilitate 'defect engineering' in amorphous materials because the control of type and depth concentrations is possible on the basis of knowledge of ion-solid chemistry accumulated so far. As for nanosize colloid formation, synthesis of dual-structured colloids [41] appears to be a challenge for dual implantation. According to the calculations of Haus et al. [42], enhancement of nonlinear optical susceptibilities is expected for heterostructure nanoparticles. Consequently, the establishment of fundamentals of dual implantation such as the effect of the implantation sequence will be an important subject.

Historically, a great success of ion implantation in materials science is in the generation of electrical carriers in silicon [43]. I believe that control of

electrical conductivities in wide gap insulating amorphous materials by carrier generation by implantation is a current and worth challenging problem. Recently, we have reported that a transparent electroconducting amorphous oxide [44] and fast proton conducting oxide glasses [45] have been created by ion implantation. Consideration about chemical interaction of implanted ions with substrate structures offers a fundamental means to proceed in material design with these materials.

The author is grateful to Professor Robert A. Weeks of Vanderbilt University (Nashville, Tennessee, USA) for his stimulating discussion and guidance at the initial stage of this work. The present work was supported in part by a grant-in-aid scientific research from the Japanese Ministry of Education, Science and Culture.

References

- [1] G.W. Arnold, *Rad. Eff.* 65 (1982) 17; P. Mazzoldi and G. Arnold, *Ion Beam Modification of Insulators* (Elsevier, Amsterdam, 1987); P.D. Townsend, *Rep. Prog. Phys.* 50 (1987) 501; R.A. Weeks, in: *Glasses and Amorphous Materials*, ed. J. Zarzycki (VCH, Weinheim, 1971).
- [2] R.A.B. Devine, *J. Non-Cryst. Solids* 152 (1993) 50.
- [3] R.F. Haglund Jr., L. Yang, K. Becker, R.H. Magruder, J.E. Wittig and R.A. Zuhr, *Opt. Lett.* 18 (1993) 373.
- [4] H. Hosono, *Jpn., J. Appl. Phys.* 32 (1993) 3892.
- [5] H. Hosono, Y. Suzuki, Y. Abe, K. Oyoshi and S. Tanaka, *J. Non-Cryst. Solids* 142 (1992) 287.
- [6] D.L. Griscom, *J. Ceram. Soc. Jpn.* 99 (1991) 923.
- [7] I.P. Kaminow, B.G. Bagley and C.G. Olson, *Appl. Phys. Lett.* 32 (1978) 98.
- [8] H. Hosono, *J. Appl. Phys.* 69 (1991) 807.
- [9] Y. Morimoto, T. Igarashi, H. Sugawara and S. Nasu, *J. Non-Cryst. Solids* 139 (1992) 35.
- [10] H. Hosono, H. Fukushima, R.A. Weeks and R.A. Zuhr, *J. Non-Cryst. Solids* 143 (1992) 157.
- [11] G. Arnold, *IEEE Trans. Nucl. Sci.* NS-20 (1978) 220.
- [12] E.P. O'Reilly and J. Robertson, *Phys. Rev.* B27 (1983) 3780.
- [13] H. Imai, K. Arai, H. Imagawa, H. Hosono and Y. Abe, *Phys. Rev.* B38 (1988) 12 772, B44 (1991) 4812.
- [14] H. Hosono, Y. Abe, H. Imagawa, H. Imai and K. Arai, *Phys. Rev.* B44 (1991) 12043.
- [15] R.A.B. Devine and A. Golanski, *J. Appl. Phys.* 54 (1983) 3833.
- [16] M. Stapelbroek, D.L. Griscom, E.J. Friebele and G.H. Sigel Jr., *J. Non-Cryst. Solids* 32 (1979) 313.
- [17] H. Hosono and R.A. Weeks, *Phys. Rev.* B40 (1989) 10 543.
- [18] H. Hosono, H. Kawazoe, K. Oyoshi and S. Tanaka, *J. Non-Cryst. Solids* 179 (1994) 70.
- [19] K. Tanimura, T. Tanaka and N. Itoh, *Phys. Rev. Lett.* 51 (1983) 423.
- [20] T.E. Tsai and D.L. Griscom, *Phys. Rev. Lett.* 67 (1991) 2517.
- [21] H. Hosono and H. Imagawa, *Nucl. Instr. and Meth.* B91 (1994) 510.
- [22] H. Hosono, Y. Abe, K. Oyoshi and S. Tanaka, *Phys. Rev.* B43 (1991) 11 966.
- [23] A. Corneta, P. Mazzoldi, A. Boscolo-Bischoletto, F. Cascavale, R. Buttoncello, G. Grarozzi, I. Spagno and G. Battaglin, *J. Non-Cryst. Solids* 125 (1990) 293; K. Oyoshi, T. Tagami and S. Tanaka, *J. Appl. Phys.* 68 (1990) 3653; G. Arnold, *J. Non-Cryst. Solids* 120 (1990) 234.
- [24] H. Hosono, *Nucl. Instr. and Meth.* B65 (1992) 375.
- [25] H. Hosono and N. Matsunami, *Phys. Rev.* B48 (1993) 13 469.
- [26] H. Hosono, R.A. Weeks, H. Imagawa and R.A. Zuhr, *J. Non-Cryst. Solids* 120 (1990) 250.
- [27] J.C. Mikkelsen Jr. and F.L. Galeener, *J. Non-Cryst. Solids* 37 (1980) 71.
- [28] G. Whichard, H. Hosono, R.A. Weeks, R.A. Zuhr and R.A. Magruder, *J. Appl. Phys.* 67 (1990) 7526.
- [29] H. Hosono, Y. Abe and N. Matsunami, *Appl. Phys. Lett.* 60 (1992) 2613.
- [30] R. Rupp, *J. Appl. Phys.* 59 (1986) 1355.
- [31] D.G. Galimov, A.M. Gubaidullina and A.I. Neich, *Fiz. Khim. Stekla.* 13 (1987) 50.
- [32] K. Kawashima, H. Hosono and Y. Abe, *J. Non-Cryst. Solids* 95&96 (1987) 741.
- [33] H. Hosono, Y. Abe, Y.L. Lee, T. Tokizaki and A. Nakamura, *Appl. Phys. Lett.* 61 (1992) 2747.
- [34] K. Kawashima, H. Hosono and Y. Abe, *Appl. Phys. Lett.* 57 (1990) 1595.
- [35] H. Hosono, N. Matsunami, H. Kudo and T. Ohtsuka, *Appl. Phys. Lett.* 65 (1994) 1632.
- [36] R. Hayashi, M. Yamamoto, K. Tsunemoto, K. Kohno, Y. Osaka and H. Nasu, *Jpn. J. Appl. Phys.* 29 (1990) 756.
- [37] H. Hosono, Y. Abe, D.L. Kinser, R.A. Weeks and H. Kawazoe, *Phys. Rev.* B46 (1992) 11445.
- [38] K.O. Hill, Y. Fujii, D.C. Johnson and B.S. Kawasaki, *Appl. Phys. Lett.* 32 (1978) 647; G. Meltz, W.W. Morey and W.H. Glenn, *Opt. Lett.* 14 (1989) 823.
- [39] U. Osterberg and W. Margulis, *Opt. Lett.* 11 (1986) 516.
- [40] H. Hosono, N. Asada and Y. Abe, *J. Appl. Phys.* 67 (1990) 2840; H. Hosono, K. Yamazaki and Y. Abe, *J. Am. Ceram. Soc.* 70 (1987) 872.
- [41] H. Hosono, *Phys. Rev. Lett.* 74 (1995) 110.
- [42] J.W. Haus, H.S. Zhou, S. Takami, M. Hirasawa, I. Honma and H. Komiyama, *J. Appl. Phys.* 73 (1993) 1.
- [43] W. Shockley, US patent no. 2,787,564 (1957).
- [44] H. Hosono, N. Kikuchi, N. Ueda and H. Kawazoe, submitted to *Philos. Mag. Lett.*
- [45] H. Hosono, N. Ueda, H. Kawazoe and N. Matsunami, *J. Non-Cryst. Solids* 182 (1995) 109.



ELSEVIER

Journal of Non-Crystalline Solids 187 (1995) 473–476

JOURNAL OF
NON-CRYSTALLINE SOLIDS

Light-assisted deposition of silicon-based dielectrics for optical interconnection in optoelectronics

Abdeljalil Sayah*, Yves. I. Nissim

France Telecom/CNET/PAB, Laboratoire de Bagneux 196, Avenue H. Ravera, BP 107, 92225 Bagneux cédex, France

Abstract

The structural quality of rapid thermal chemical vapour deposited dielectric films have been utilized to fabricate optical waveguides at 1.5 μm . The guides composed of SiO_xN_y guiding layer sandwiched between two SiO_2 layers. A precise model has been utilized to define the indexes of refraction and thicknesses of the different layers. Special care has been made in the fabrication process to define the entrance and exit facets of the guide. A resulting loss of 1.5 dB/cm has been measured in this structure. This result is among the lowest losses reported on as-deposited dielectric guides.

1. Introduction

Silicon nitride and silicon oxynitride thin films exhibit useful and often excellent combinations of electrical, optical, chemical and mechanical properties, and therefore there has been a growing interest in the deposition of these films for micro and optoelectronic applications. Silicon oxynitride films, which can be described as a solid solution between silicon nitride and silicon oxide, have attracted special attention because the film composition can be precisely controlled with the deposition conditions and therefore it is possible to monitor its main physical and chemical properties over a wide range. As a result, it is often possible to achieve a combi-

nation of material characteristics which are impossible to obtain either with pure silicon nitride or silicon dioxide.

Silicon nitride and silicon oxynitride are desirable as waveguide materials since both have high index of refraction with respect to silicon dioxide. If the residual hydrogen-bond content in this guiding layers is low, it can be expected that the resulting guides display low losses. Low loss SiON dielectric waveguide have been produced on Si substrates with different growth techniques: PECVD [1–3], thermal nitridation [4], CVD [5], LPCVD [6] or ion implantation [7]. The purpose of this paper is to present results obtained on a dielectric optical waveguide fabricated on silicon when rapid thermal chemical vapour deposition (RTCVD) is used, and eventually address the problem of guide fabrication technology on optoelectronics materials such as InP and InP-based materials.

* Corresponding author. Tel: +33-1 42 53 75 85 Telefax: +33-1 42 53 49 30.

2. Experimental

2.1. Rapid thermal chemical vapour deposition

Rapid thermal chemical vapour deposition is a combination of rapid thermal processing (RTP) and chemical vapour deposition (CVD). It utilizes rapid temperature cycling as a switch to turn on and off thermally driven gas surface reactions. The wafer can be brought to 750°C in less than 5 s and can cool down to below deposition temperature in less than 2 s. The use of highly controllable temperature changes to control the deposition offers with RTCVD the ability to reproducibly grow precisely controlled thin layers with very low defect densities, while minimizing thermal exposure. Our RTCVD system is a single horizontal reactor consisting of quartz chamber, the wafer is supported on a susceptor by four quartz pins and is heated from below with a bank of nitrogen cooled tungsten halogen lamps. The chamber is made of high quality fused quartz and is highly transparent in the spectral range of the lamps, allowing the chamber to remain cool relative to the wafer and thereby recover the advantages of a cold-wall system. A set of UV lamps are mounted above the reactor allowing UV-CVD films to be deposited. A more detailed and complete description of the system can be found in Ref. [8].

2.2. Waveguide fabrication and characterization

SiO_xN_y films were deposited by RTCVD at 750°C from the reactive gases SiH_4 , NH_3 , N_2O diluted in a carrier gas N_2 with a total pressure of 50 T. Composition control of the SiO_xN_y films was obtained with the N_2O flow rate alone, all the other CVD parameters being constant. The index of refraction of the film was controlled via the N_2O flow rate as can be seen from Fig. 1. A continuous variation of the index of refraction from 1.45 (index of refraction of SiO_2) to 2.1 (index of refraction of Si_3N_4) was obtained as measured by ellipsometry at 6328 Å [8]. It has been also verified that N_2O flow rate is directly connected to the stoichiometry of the SiO_xN_y films, a more detailed description of the deposition parameters and material properties can be found in Ref. [9].

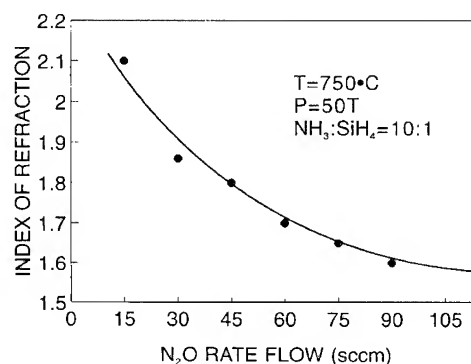


Fig. 1. Variation of the refractive index of SiO_xN_y films as a function of the N_2O flow rate.

Light can be guided in a high refractive index material sandwiched between two low refractive index materials. The size of the guide, the index of refraction and the thickness of each layer have been calculated for monomode propagation at 1.5 μm using a program developed at the CNET Bagneux called ALCOR [10]. The waveguide design resulting from this model is a SiO_xN_y film between two SiO_2 films with the following characteristics: a first cladding layer made of a thick SiO_2 film obtained by thermal oxidation of a Si substrate. The SiO_2 thickness is 2 μm and the refractive index has a value of 1.46. This oxide layer is used to optically decouple the waveguide from the underlying Si substrate. The guiding layer is then formed with RTCVD SiO_xN_y . The thickness of this SiO_xN_y layer is 0.6 μm and the refractive index is 1.72. Finally, the processed wafer is covered with a RTCVD SiO_2 layer with a thickness of 1 μm and a refractive index of 1.46.

To permit the lateral confinement of the guided modes, only the SiO_2 overlayer is etched to the lateral size of the guide down to the SiO_xN_y guiding layer. The etching of this overlayer results in a large change in the effective index (N_{eff}) of the guided mode. This change saturates as soon as the overlayer thickness becomes greater than the penetration depth of the evanescent field of the guided mode. This can be observed by computing the effective index of refraction change between the guided region with a SiO_2 overlayer and the region where the overlayer has been removed. This calculation is illustrated in Fig. 2 and as can be seen an

overlayer of $1\text{ }\mu\text{m}$ in our calculated structure is acceptable. Since the etching process can be monitored by in situ reflectometry, it is possible to stop the SiO_2 etching right at the interface with the SiO_xN_y layer. Consequently, the control of the effective index change (N_{eff}) is very accurate.

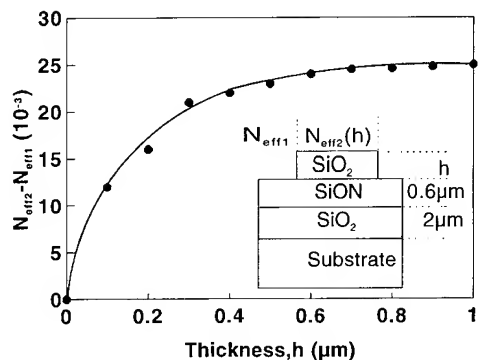


Fig. 2. Effective refractive index change in the guiding layer as function of the thickness of the SiO_2 top layer.

2.3. Waveguide facets fabrication

In addition to the propagation losses in the waveguides, the insertion losses caused by a rough entrance and exit facet have an essential influence on the total loss of the device. There are several techniques for mirror like facet fabrication, including chemical or plasma etching. A mask for lithography is defined with thickness and composition that will allow its removal without affecting the underlying waveguide. The most desirable mask has straight sidewalls and is highly resistive to the guide etchants. Metals are useful for ion etching but their polycrystalline nature degrades sidewall definition. Photoresists provide good structural definition but are affected by the ion etching heating process. Good results have been obtained using a trilayer resist consisting of a thick photoresist planarizing layer, a intermediate UV-CVD SiO_2 layer grown at 100°C and a thin photoresist imaging layer. This trilayer is presented for the first time here for semiconductor technology applications. The unique feature of this structure is obtained by the ability to deposit a SiO_2

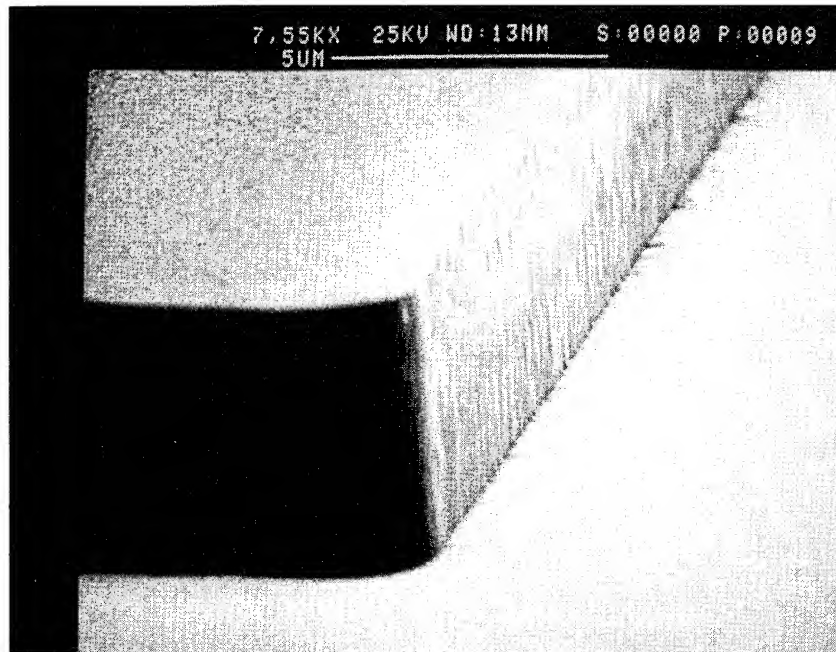


Fig. 3. SEM micrograph of the facet of the waveguide after RIE.

layer on resist surface at 100°C without major resist hardening. This film deposited by UVCVD utilizes Kr flash lamps described elsewhere [11]. After the photolithography patterning of the top photoresist, the image was transferred to the underlying layers using reactive ion etching (RIE). The gases used to etch the thin oxide and the thick photoresist were CHF_3/SF_6 and O_2 , respectively.

The patterned image from the trilayer photoresist was transferred to the planar waveguide, using RIE to form the end facets of the waveguide. The gases used for this purpose were CHF_3/SF_6 . The result is shown in the scanning electron micrograph of Fig. 3. The resulting peak to peak roughness of the facet measure on this micrograph is about 700 Å. This result is completely acceptable for a 1.5 µm propagation light.

3. Propagation loss measurements and discussion

The propagation losses on the fabricated waveguide were obtained by varying the sample length using the cut-back method and carefully measuring the output intensities of the TE_0 mode. The light from an He–Ne laser operating at 1.5 µm wavelength was coupled into and out of the waveguide by means of microscope objectives and the intensities of the transmitted light were measured by a photodiode. To avoid changes of the input and the output coupling efficiency during the measurements, waveguides with different length were prepared during the same process and at the

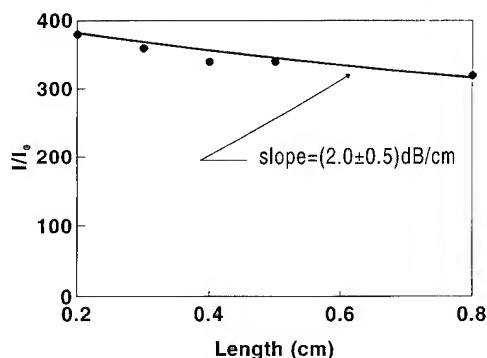


Fig. 4. Variation of the normalized transmitted intensity at 1.5 µm as a function of the length of the waveguide.

same time so as to obtain waveguides with the same facet quality. The result of this measurement is shown in Fig. 4. It indicates that propagation losses of the RTCVD SiO_xN_y waveguides are of the order of (2 ± 0.5) dB/cm. This result obtained on an as-deposited SiO_xN_y guide is among the best results on an as-deposited structures. In silicon technology an annealing step at 1000°C for 1 h brings the measured losses down to 0.2 dB/cm [12], but this annealing step is not acceptable on an optoelectronic material.

4. Conclusion

SiO_xN_y film deposited by RTCVD has been shown to be an excellent propagation medium for passive waveguide operated at 1.5 µm wavelength. Optical propagation loss for the fundamental TE_0 mode at 1.5 µm wavelength have been measured using the cut back method. Without annealing the loss is (2 ± 0.5) dB/cm. Progress is being made to transfer this technology to InP-based substrates, the mechanical stress induced by this multilayer structure being the most difficult problem to overcome.

The authors would like to thank G. Hervé-Gruyer for introducing us to ALCOR. This work would not have been performed without the technical assistance of C. Meriadec.

References

- [1] D.K.W. Lam, Appl. Opt. 23 (1984) 2744.
- [2] K. Kaper, C. Wagner and P.P. Deinel, IEEE Photon. Technol. Lett. 3 (1991).
- [3] D.E. Bossi, J.M. Hommer and J.M. Shaw, Appl. Opt. 26 (1987) 609.
- [4] D.E. Zelmon, J.J. Boyd and H.E. Jackson, Appl. Phys. Lett. 47 (1985) 353.
- [5] M.J. Rand and R.D. Standely, Appl. Opt. 11 (1972) 2482.
- [6] W. Gleine and J. Muller, Appl. Opt. 31 (1992) 2036.
- [7] I.K. Naik, Appl. Phys. Lett. 43 (1983) 519.
- [8] F. Leblond, doctoral thesis, Université de Paris VII (1992).
- [9] Y.I. Nissim, J.L. Regolini, D. Bensahel and C. Licoppe, Electron. Lett. 24 (1988) 488.
- [10] BPM-CNET (ALCOR) Software developed and distributed by France Telecom/CNET.
- [11] J. Flicstein, Y.I. Nissim, C. Licoppe and Y. Vittel, France Telecom/CNET Patent number 9103964, 1991.
- [12] Massimo del Giudice, Franco Bruno, Tito Cicinelli and Marco Valli, Appl. Opt. 29 (1990) 3489.



ELSEVIER

Journal of Non-Crystalline Solids 187 (1995) 477–483

JOURNAL OF
NON-CRYSTALLINE SOLIDS

PECVD a-SiN_x:H films for dielectric insulation in buried ridge structure Fabry–Perot and distributed feedback laser devices

R. Audino, F. Cannistraci, G. Morello*, P. Valenti

CSELT – Centro Studi e Laboratori Telecomunicazioni S.p.A., Via Reiss Romoli, 274, 10148 Turin, Italy

Abstract

In this work, use of plasma-enhanced chemical vapour deposition of amorphous hydrogenated silicon nitride (PECVD a-SiN:H) films (deposited utilizing SiH₄ and NH₃) as insulators for the realization of buried ridge structure (BRS) Fabry–Perot and distributed feed back (DFB) optoelectronic laser devices is focussed upon. To this aim, on the one hand a-SiN_x:H films are required to have a high dielectric strength and, on the other hand, the sequence semiconductor/dielectric/metallization must, as a whole, show a good resistance to thermal and mechanical treatments occurring during the device processing. Values for these properties are strictly related to the dielectric characteristic quality. Optimizing the deposition conditions, a-SiN_x:H films with Si/N ratio = 0.75, hydrogen percentage ≈ 25%, refractive index = 1.92 (at 632 nm), optical gap = 4.8 eV and film density of ≈ 2.5 g/cm³ have been obtained. This material shows a dielectric strength of ≈ 10⁷ V/cm, resistivity of ≈ 5 × 10¹⁴ Ω cm and a good spatial uniformity and time stability of the dielectric properties. The mechanical adhesion has been checked by using special tests performed on actual laser devices. No significant detachments of the TiPtAu/a-SiN:H sequence have been observed with either p-side down or p-side up mounting configuration. BRS Fabry–Perot and DFB lasers devices with state-of-art optical and electrical characteristics have been manufactured.

1. Introduction

Amorphous hydrogenated silicon nitride films deposited by plasma-enhanced chemical vapour deposition (PECVD a-SiN_x:H) are used for several applications in the electronic and optoelectronic devices technology (interlayer insulation, device passivation, mechanical protection) [1–8].

In this work we are particularly interested in the dielectric insulation performance for the realization of buried ridge structure (BRS) Fabry–Perot and

distributed feed back (DFB) optoelectronic laser devices based on the III–V semiconductor system (Fig. 1). To this aim, some critical aspects exist. In order to minimize the threshold current, a-SiN_x:H films are requested to have high dielectric strength and resistivity. In addition, the adhesion between dielectric/semiconductor and metallization/dielectric layers must be very good. Finally, the InP/a-SiN_x:H/TiPtAu sequence must show a good resistance to the thermal and mechanical treatments occurring during the device processing such as diffusion and ohmicization for the ohmic contact realization, chip cleaving, p-side down or up chip mounting, wedge or ball-bolding soldering.

* Corresponding author. Tel: +39-11 228 5229. Telefax: +39-11 228 5695. morello@eiclus.cselst.stet.it.

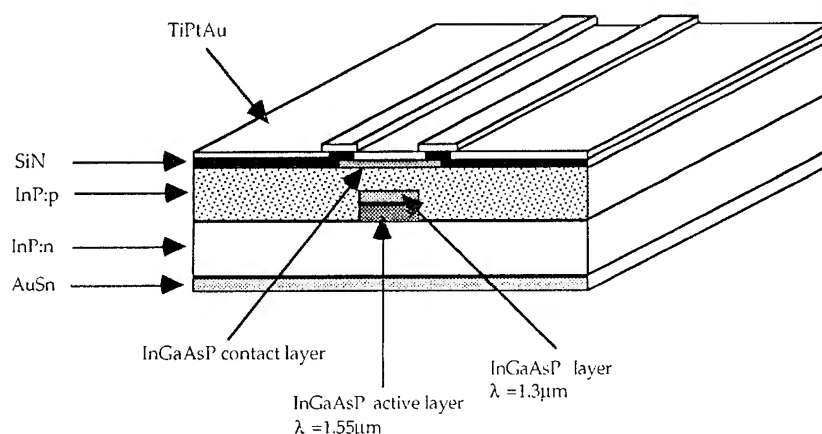


Fig. 1. Sketch (not to scale) of a BRS Fabry-Perot laser structure. Approximate layer thicknesses are as follows: AuSn 0.3 μm , InP:n substrate 100 μm , InP:p 1.5 μm , InGaAsP ($\lambda = 1.55 \mu\text{m}$) 0.3 μm , InGaAsP ($\lambda = 1.33 \mu\text{m}$) 0.1 μm , SiN 0.25 μm , TiPtAu 0.4 μm .

While the electrical characteristics of PECVD a-SiN_x:H films have been widely studied [9-17], no literature exists to our knowledge about the evaluation of the latter properties.

2. Experimental procedures

A-SiN_x:H films have been deposited in a 13.56 MHz PECVD Vacutec 1523 equipment by using SiH₄ and NH₃ pure gases.

The chamber has been cleaned after each deposition with a plasma of CF₄ and O₂ at room temperature (chamber pressure $p = 500$ mTorr, rf power density $P = 0.600$ W/cm², CF₄ flow: 43 sccm, O₂ flow: 10 sccm).

An a-SiN_x:H layer of about 1000 Å has been pre-deposited before each run (deposition temperature $T = 350^\circ\text{C}$, $p = 300$ mTorr, $P = 0.16$ W/cm², SiH₄ flow: 10 sccm, NH₃ flow: 90 sccm). Several samples have been deposited varying the NH₃/SiH₄ gas flow ratio (R) from 2 to 19 and P from 0.04 to 0.2 W/cm². Total flow, F , p and T have been kept constant to 100 sccm, 300 mTorr and 350°C, respectively.

The electrical characteristics of SiN_x:H films have been tested by dielectric strength, E_D , and resistivity measurements on Si/Al/SiN:H/Al structures. We assumed the dielectric strength value as

the electric field corresponding to a current of 10^{-7} A on a contact with a diameter of 550 μm . Each structure has 195 contacts. The E_D values reported in the following represent the mean value of about 100 measurements executed on as many as different contacts. The standard deviation has been used as an estimate of experimental errors. The presence of porosity has been evaluated by counting 'holes' and 'bubbles' on SiN_x:H/InP samples which have been evidenced by means of selective etching (Br: CH₃COOH = 1:100 for 10') before and after the thermal treatment (diffusion: $T = 450^\circ\text{C}$ for 16' in sealed ampoule with ZnAs₂ and Zn₃P₂ sources). Si/N and optical gap (E_g) values have been calculated from absorbance spectra obtained on a-SiN_x:H/quartz structures (Varian Cary 2300) using the absorption edge and the Tauc plot methods, respectively [18,19]. IR analysis has been used to measure the hydrogen (H) content in SiN:H/Si samples [20] (Perkin-Elmer 683 spectrophotometer). Refractive index and thickness have been evaluated by ellipsometry at 632, 1303 and 1535 nm (Plasmos SD 2300). Thickness has been also determined using a profilometer (Tencor α -step 200). Film density (ρ) has been evaluated by weighing the sample before and after the deposition. We made sure to remove the a-SiN_x:H deposited on the edges and under the substrate by masking accurately the sample surface

with wax and etching it briefly in 49% hydrofluoric acid (HF). Using this technique, density measurements affected by a relative error less than 4% (calculated with the propagation law) have been obtained.

Special tests have been used to evaluate qualitatively the adhesion between dielectric/semiconductor and metallization/dielectric layers. A significant number of BRS Fabry–Perot and DFB laser devices (chip dimensions: 300 min \times 400 μ m) have been soldered with In in the p-side up configuration and observed using scanning electron microscopy (SEM) in order to reveal eventual detachments of the TiPtAu or TiPtAu/a-SiN_x:H layers caused by the chip cleaving. A second set of devices have been soldered in the p-side down configuration and subsequently abruptly removed using tweezers. The

removed chip and the mark left on the submount have been analyzed by SEM and energy dispersive spectroscopy (EDS) to evaluate the quality of the dielectric/semiconductor and metallization/dielectric adhesion.

3. Results and discussion

Before checking the electrical performances, we investigated the deposition conditions in order to obtain a-SiN_x:H films with good physical and structural properties. Particular care has been taken to maximize the density and to minimize the presence of pores and 'bubbles' that can be caused by the eventual H release occurring during the sample heating.

Table 1
PECVD a-SiN_x:H film porosity before and after the diffusion treatment versus rf power density value.

rf power density (W/cm ²)	a-SiN _x :H pore density before diffusion (number/cm ²)	a-SiN _x :H pore density after diffusion (number/cm ²)	a-SiN _x :H 'bubble' density before diffusion (number/cm ²)	a-SiN _x :H 'bubble' density after diffusion (number/cm ²)
0.04	0	40	0	30
0.08	0	12	0	70
0.12	0	0	0	0
0.16	0	0	0	3
0.2	0	80	0	30

Table 2
PECVD a-SiN_x:H film porosity before and after the diffusion treatment versus NH₃/SiH₄ gas flow ratio

NH ₃ /SiH ₄ gas flow ratio	a-SiN _x :H pore density before diffusion (number/cm ²)	a-SiN _x :H pore density after diffusion (number/cm ²)	a-SiN _x :H 'bubble' density before diffusion (number/cm ²)	a-SiN _x :H 'bubble' density after diffusion (number/cm ²)
2	0	0	0	Region with many 'bubbles'
3	0	NA	2	NA
4	0	23	0	0
5	0	3	0	0
6	0	0	0	0
7	0	0	0	0
9	0	0	0	0
13	0	10	0	0
19	0	50	0	0

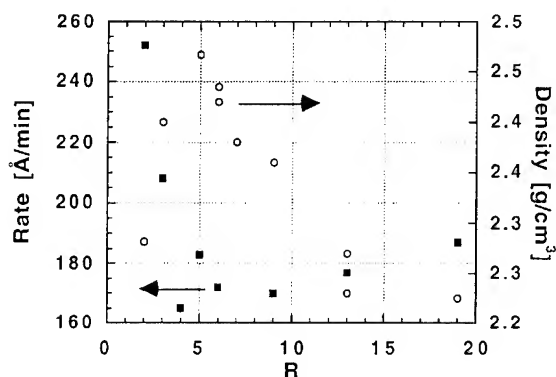


Fig. 2. Dependence of the deposition rate and film density on the NH_3/SiH_4 gas-flow ratio. rf power density, chamber pressure, deposition temperature and total flow have been kept constant to 0.12 mW/cm^2 , 300 mTorr , 350°C and 100 sccm , respectively.

Porosity before and after the diffusion treatment has been measured on samples deposited at varying P and R as mentioned above (P : $0.04\text{--}0.2 \text{ W/cm}^2$, $R = 9$, $p = 300 \text{ mTorr}$, $T = 350^\circ\text{C}$, $F = 100 \text{ sccm}$ and R : $2\text{--}19$, $P = 0.12 \text{ W/cm}^2$, $p = 300 \text{ mTorr}$, $T = 350^\circ\text{C}$, $F = 100 \text{ sccm}$). Pores and 'bubbles'

are practically absent for rf power density of 0.12 W/cm^2 and for R of $5\text{--}9$ (see Tables 1 and 2).

Fig. 2 shows ρ and the deposition rate values versus R . The desired condition is for $R = 5$ where the density and deposition rate reach their maximum and minimum values, respectively. Furthermore, samples deposited using $R = 5$, $p = 0.12 \text{ W/cm}^2$, $p = 300 \text{ mTorr}$, $T = 350^\circ\text{C}$ and $F = 100 \text{ sccm}$ present desirable compositional and optical properties such as an Si/N ratio $= 0.75$, $E_0 = 4.8 \text{ eV}$ and $n = 1.92$ at 632 nm . A hydrogen percentage of about 25% has further been measured. This fact may explain why the n value is less than 2 [21,22].

Electrical measurements performed on samples deposited using the optimized deposition conditions, yielded a dielectric strength of $9 \pm 1 \text{ MV/cm}$ (sample thickness: $\approx 3300 \text{ \AA}$) and a resistivity of $\approx 5 \times 10^{14} \Omega \text{ cm}$. The current dependence versus the electric field applied, E , can be explained by the Poole–Frenkel effect for high E values [23]. Measurements repeated on the same contact up to 20 times during a period of 3 months did not evidence degradation of the dielectric properties (Fig. 3). To our knowledge, these are state-of-art characteristics [9–17,24,25].

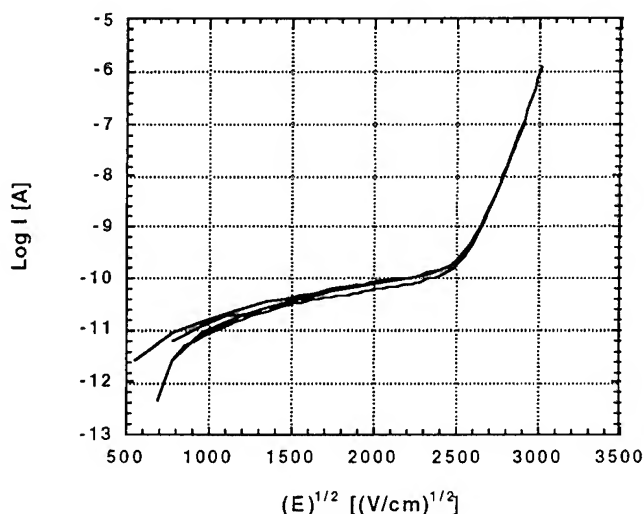


Fig. 3. $\text{Log } I$ versus applied electric field measurements taken at different times during a period of three months on the same contacts of an $\text{Al/a-SiN}_x\text{:H/Al}$ structure. Dielectric deposition conditions: $R = 5$, $P = 0.12 \text{ mW/cm}^2$, $p = 300 \text{ mTorr}$, $T = 350^\circ\text{C}$, $F = 100 \text{ sccm}$. No degradation of the dielectric properties can be observed. At high electric fields, the curves are in agreement with the Poole–Frenkel effect.

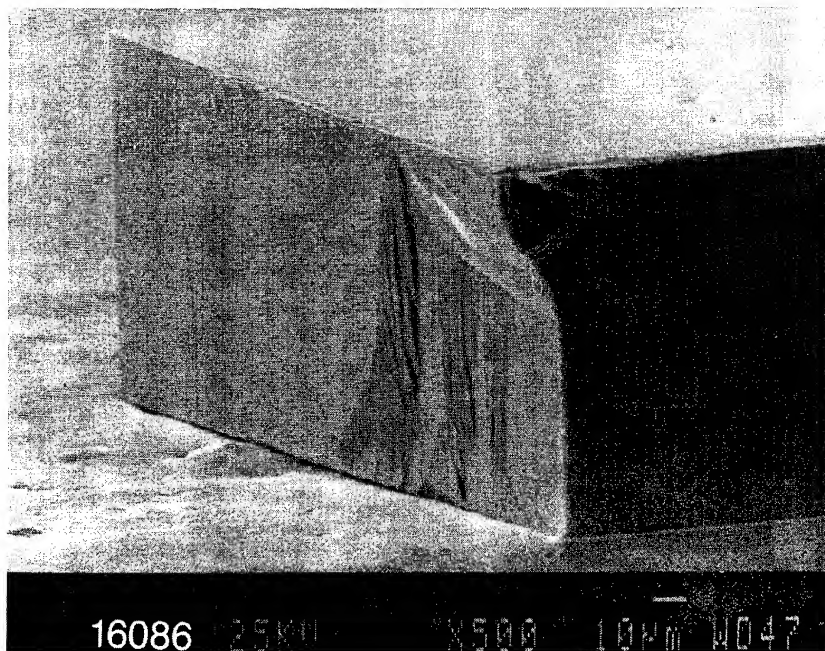


Fig. 4. Typical picture of a $300\ \mu\text{m} \times 400\ \mu\text{m}$ BRS Fabry-Perot laser device soldered in the p-side up configuration. Chip cleaving did not cause any detachments of the dielectric/metallization layer neither near the edges.

Samples deposited varying the rf power density in the aforementioned range or with different R present satisfactory breakdown field and resistivity values of $4\text{--}5\ \text{MV/cm}$ and $10^{14}\text{--}10^{16}\ \Omega$, respectively. In some cases, the reproducibility and the spatial uniformity were lower and some of the contacts broke down while repeating the measurement. We are not able to give a complete and rigorous explanation of the existence of these undesirable effects with the elements presently available.

The a-SiN_x: H film resistance to the mechanical treatments occurring during the device fabrication of BRS Fabry-Perot and DFB lasers, have been tested on actual devices from different processes by means of the techniques described above. Fig. 4 is a typical picture of a $300\ \mu\text{m} \times 400\ \mu\text{m}$ BRS Fabry-Perot laser device soldered in the p-side up configuration. No detachment of the dielectric/metallization layer can be observed. Figs. 5 and 6 show a soldered chip side and its chip mark left on the submount after the abrupt removal. In Fig. 5 dark grey spots (indicated by arrows) can be ob-

served. In these regions, the a-SiN_x: H/TiPtAu came off leaving the chip InP surface uncovered as checked by EDS analysis. Correspondingly fragments of the dielectric/metallization sequence on the chip mark (Fig. 6) are present. In all the devices examined, the detachments observed are absent or confined in small areas along the edges, where the stress is enhanced. The test executed has been thought to simulate conditions much more brutal than the actual situations. A behaviour like that here reported has thus to be considered absolutely satisfactory.

BRS Fabry-Perot and DFB lasers obtained present state-of-art electrical and optical characteristics [26].

4. Conclusions

Optimizing the deposition condition, PECVD a-SiN_x: H films with absence of porosity, film density

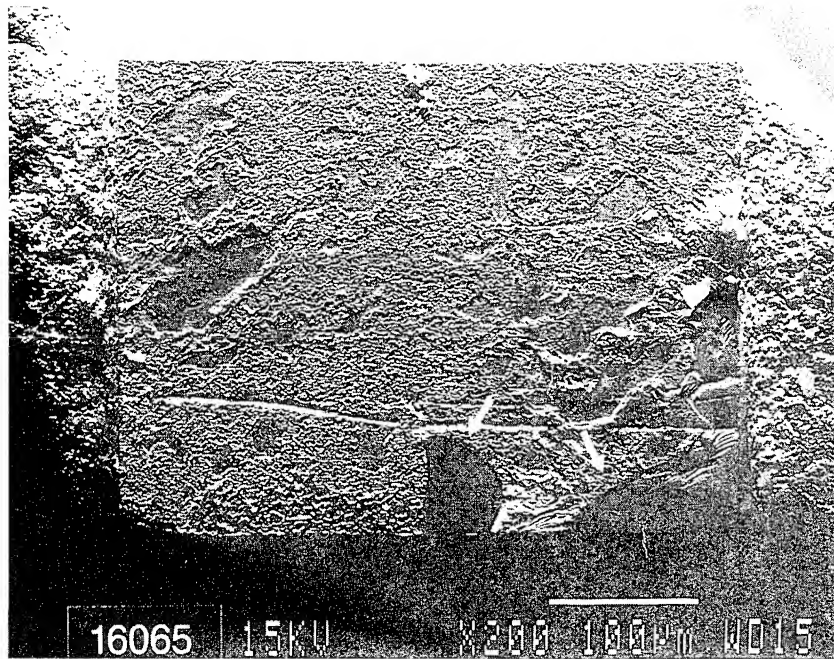


Fig. 5. Picture of the soldered side of a BRS Fabry-Perot laser device after its abrupt removal from the submount. In the dark grey spots indicated by the arrows the a-SiN_x:H/TiPtAu was lifted off leaving the InP surface uncovered.

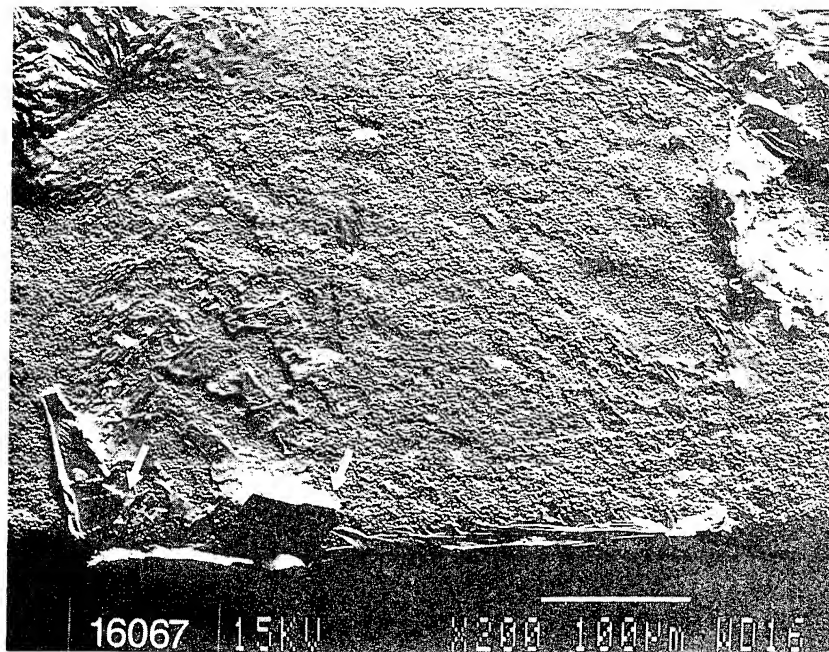


Fig. 6. Picture of the mark left on the submount by the chip shown in Fig. 5. Fragments of the dielectric/metallization hole can be observed in correspondence of the dark grey regions indicated in Fig. 5.

of $\approx 2.5 \text{ g/cm}^3$, Si/N ratio = 0.75, hydrogen percentage of 25%, refractive index = 1.92 (632 nm), optical gap = 5.2 eV have been obtained.

This material shows a dielectric strength of $\approx 10^7 \text{ V/cm}$, a resistivity of $\approx 5 \times 10^{14} \Omega \text{ cm}$ and a good spatial uniformity and time stability of the dielectric properties. Log I versus E curves are in agreement with the Poole-Frenkel effect.

The resistance to the thermal and mechanical treatments occurring during device processing has been checked on actual laser devices. The good results from these tests confirm that the PECVD a-SiN_x: H films obtained can be satisfactorily used in the BRS Fabry-Perot and DFB optoelectronic laser fabrication.

Devices with state-of-art optical and electrical characteristics have been fabricated.

The authors would like to acknowledge the CSELT Optoelectronic Technologies Department for co-operation and, in particular, L. Busso, D. Re, G. Gastaldi and G. Meneghini for the technological support and assistance in computer programming, C. Coriasso and R. De Franceschi for the absorbance measurements and the SEM analysis, G. Magnetti, C. Papuzza, A. Piccirillo, F. Taiariol and S. Tamagno for useful discussions.

References

- [1] J.T. Miley, ed., Handbook of Electronic Materials, Vol. 3, Silicon Nitride for Microelectronic Applications, Part I: Preparation and Properties (Plenum, New York, 1971).
- [2] J.T. Miley, ed., Handbook of Electronic Materials, Vol. 6, Silicon Nitride for Microelectronic Applications, Part II: Application and Devices (Plenum, New York, 1972).
- [3] A. Hashimoto, M. Kobayashi, T. Kamijoh, H. Tanako and M. Sakuta, J. Electrochem. Soc. 133 (7) (1986) 1464.
- [4] C.J. Dell'Oca and M.L. Barry, Solid State Electron. 15 (1972) 659.
- [5] P.M. Petroff, G.A. Rozgony and T.T. Sheng, J. Electrochem. Soc. 123 (1976) 565.
- [6] M.J. Helix, K.V. Vaidyanathan, B.G. Streetman, H.B. Dietrich and P.K. Chatterjee, Thin Solid Films 55 (1978) 143.
- [7] E.Y. Chang, G.T. Cibuzar, T.K. Yard and K.P. Pande, Mater. Res. Soc. Symp. Proc. 126, p. 271.
- [8] A. Piccirillo and A.L. Gobbi, J. Electrochem. Soc. 137 (1990) 3910.
- [9] J.M. Lopez-Villegas, B. Garrido, M.S. Benrakkad, J. Samitier, A. Canillas and J.R. Morante, Mater. Res. Soc. Symp. 258 (1992) 655.
- [10] X. Zhang, G. Shi, A. Yang and D. Shao, Thin Solid Films 215 (1992) 134.
- [11] J.W. Osenbach, W.R. Knolle and A. Elia, J. Electrochem. Soc. 136 (1989) 3409.
- [12] M. Maeda and Y. Arita, J. Appl. Phys. 53 (1982) 6852.
- [13] G. Ripoché, Ph. Decor, C. Blanjot, B. Bourdon, P. Salsac and E. Duda, IEEE Electron. Dev. Lett. 6 (1985) 631.
- [14] W.S. Lau, S.J. Fonash and J. Kanicki, J. Appl. Phys. 66 (1989) 2765.
- [15] J. Robertson, Mater. Res. Soc. Symp. Proc. 284 (1993) 65.
- [16] J.H. Souk, G.N. Parsons and J. Baley, Mater. Res. Soc. Symp. Proc. 219 (1991) 787.
- [17] M.A. Khaliq, Q.A. Shams, W.D. Brown and H.A. Naseem, J. Electr. Mater. 17 (1988) 355.
- [18] M.J. Rand and D.R. Wonsiler, J. Electrochem. Soc. 125 (1) (1978) 99.
- [19] J. Tauc, Amorphous and Liquid Semiconductor (Plenum, London, 1974).
- [20] G. Morello, these Proceedings, p. 308.
- [21] H. Watanabe, K. Katoh and S.I. Imagi, Thin Solid Films 136 (1986) 77.
- [22] W.A.P. Claassen, W.G.J.N. Valkenburg, F.H.P.M. Habraken and Y. Tamminga, J. Electrochem. Soc. 130 (1983) 2419.
- [23] S. Sze, Physics of Semiconductor Devices, 2nd Ed. (Wiley Interscience, New York, 1981).
- [24] K. Maeda, I. Umezu, J. Non-Cryst. Solids 137&138 (1991) 883.
- [25] S. Hasegawa, M. Matsuda and Y. Kurata, Appl. Phys. Lett. 58 (1991) 741.
- [26] D. Bertone, L. Boschis, G. Fornuto, L. Gastaldi, M. Madella, M. Meliga and A. Stano, to be published in ESSDERC 1994 Proceedings.



ELSEVIER

Journal of Non-Crystalline Solids 187 (1995) 484–488

JOURNAL OF
NON-CRYSTALLINE SOLIDS

Properties and applications of electron cyclotron plasma deposited SiO_xN_y films with graded refractive index profiles

Pavel V. Bulkin, Pieter L. Swart*, Beatrys M. Lacquet

Sensors Sources and Signal Processing Research Group, Materials Laboratory, Rand Afrikaans University, PO Box 524, Auckland Park 2006, South Africa

Abstract

In the experiments in the present study, electron cyclotron resonance plasma enhanced chemical vapour deposition was used for the deposition of SiO_xN_y films from O_2/Ar , N_2 and SiH_4/Ar mixtures. Optical properties of the films were studied by means of transmission spectroscopy in the wavelength range 200–2600 nm. Refractive indices ranged between 1.5 and 3.5 (measured at 632.8 nm) for different film compositions. The extinction coefficient showed a strong blue shift with decrease of silane content in the gas mixture. Optical interference filters with continuously varying refractive index profiles were designed, and manufactured by our computer controlled electron cyclotron resonance system. Designs which take into account dispersion of refractive index, and absorption in the constituent SiO_xN_y material, differ only significantly from designs in which it is neglected at wavelengths shorter than 700 nm.

1. Introduction

Optical coatings with gradient refractive index profiles, rugate filters in particular, attracted considerable interest in recent years [1–5]. The flexible optical properties of these filters, the possibility to form multiple reflecting bands and their high laser damage threshold, are very attractive for various applications [6]. Contrary to the highly developed design procedures available, fabrication technologies are far from ideal at the moment.

Electron cyclotron resonance plasma enhanced chemical vapour deposition (ECR-PECVD) is a modern and effective tool for the fabrication of

structures having complicated refractive index profiles [7–9]. Among the materials that can be used for visible and near-infrared filters is SiO_xN_y , where x and y are varied according to a chosen design. The optical properties of this material can be adjusted by control of the process variables. A prototype rugate filter with reflection higher than 80%, made by computer control of SiH_4 and N_2 flows, was reported by us [8] earlier. However, filters based on SiN_x have a relatively high achievable lowest refractive index, which is equal to the refractive index of Si_3N_4 , and a corresponding reflectance in the transparent region of more than 15%. SiO_xN_y , on the other hand, could have refractive index as low as that of SiO_2 , yielding a much larger range of refractive indices and a reduced reflection of 5–8% outside the stopband.

* Corresponding author. Tel: +27-11 489 2351. Telefax: +27-11 489 2344. E-mail: pls@ing1.rau.ac.za.

This paper discusses the wavelength dependencies of refractive index and extinction coefficient of these SiO_xN_y layers as a function of gas flow ratios. This information is then used in the design and manufacture of an optical rugate interference filter based on gradient index SiO_xN_y . The parameters of the manufactured filter and the design values are compared.

2. Deposition and characterization

Deposition of thin films was carried out by computer controlled ECR-PECVD in the high vacuum system described previously [7–8]. During deposition conditions were as follows: 100 W microwave power; base pressure less than 10^{-6} Torr; working pressure of about 2 mTorr; gas flow rates set from 3 to 16 sccm with a total constant flow rate of 21 sccm; and 10 W rf-bias power. Corning 7059 glass and quartz substrates were degreased in isopropanol in an ultrasonic bath and rinsed in deionised water prior to deposition. Individual layers were grown to a thickness of approximately 1 μm .

Bare substrates and substrates with SiO_xN_y films deposited onto it were studied by optical transmission spectroscopy on a Hitachi model U-3400 spectrophotometer in the 200–2600 nm wavelength range at room temperature. In the case of a coated substrate, the beam was incident from the SiO_xN_y layer. Refractive index versus wavelength, $n(\lambda)$, calculated from transmission spectra was extrapolated to the wavelength region where the interference fringes disappear. The extinction coefficient, $k(\lambda)$, was also calculated [10].

3. Material properties

The 'process trajectory' is shown in Fig. 1. Points on this graph correspond to the values of O_2/SiH_4 and N_2/SiH_4 flow ratios for which layers were grown. Specific points have been chosen to satisfy the need for a large excursion of refractive index for optical interference filter design. The real and imaginary parts of refractive indices, n and k , as obtained from the measurements, are depicted in Figs. 2 and 3, respectively, as a function of

wavelength for different gas compositions. An increase of the silane content in the gas mixture leads to an increase in refractive index over the wavelength range of interest. All layers are transparent in the 900–2600 nm region. However, there is a notable shift of the absorption edge towards shorter wavelengths with increase in nitrogen and oxygen content in the layer. At the extremes of the trajectory defined in Fig. 1, materials can be regarded as oxygen-doped silicon (point 1), silicon rich silicon oxynitride (point 4) and stoichiometric silicon dioxide (point 10). Smooth transition from one material to another is provided by the existence of a continuous series of solid solutions in the Si–O–N system.

4. Application of inhomogeneous SiO_xN_y for optical coatings

Availability of extensive data on the optical properties of the SiO_xN_y films makes the design of rugate filters possible which takes into account absorption in layers and dispersion of refractive index. Absorption in the layers, which starts to play a substantial role only at wavelengths shorter than 700 nm helps to completely suppress the reflection peak at double the frequency of the reflection band of the rugate filter. Fig. 4 presents three-dimensional graphs of n and k as functions of depth and

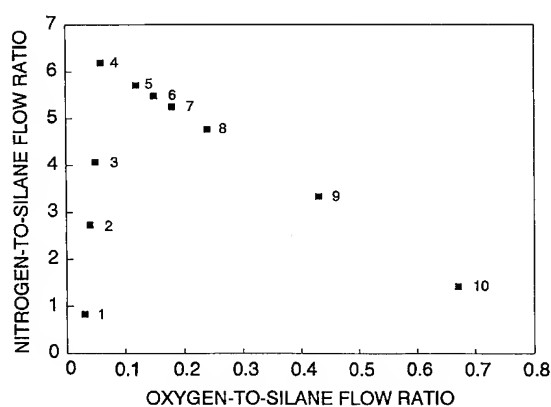


Fig. 1. Process trajectory for set of experiments.

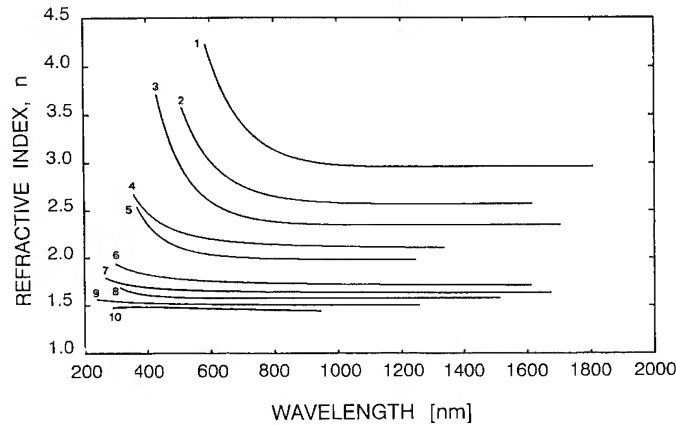


Fig. 2. Wavelength dependence of refractive index, n , of SiO_xN_y (numbers on the curves refer to the corresponding numbers on the process trajectory).

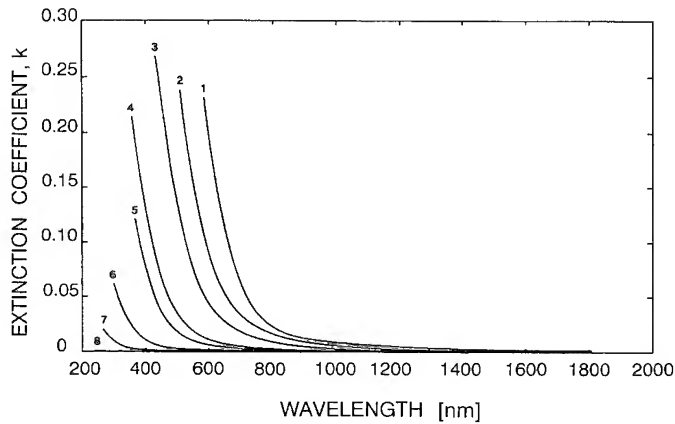


Fig. 3. Wavelength dependence of extinction coefficient, k , of SiO_xN_y (numbers on the curves refer to the corresponding numbers on the process trajectory).

wavelength for a rugate optical filter. This single-band rugate filter was designed for maximum reflectance at a wavelength of 680 nm. For a total layer thickness of $2.11 \mu\text{m}$ the theoretical reflectance in the band was 97.6%. The refractive index profile comprised of a sinusoid of the appropriate period modulated by a Kaiser window for the entire length of the coating, superimposed on a rugated quintic transitional matching layer from air to filter and from filter to substrate [4,11]. The average refractive index in the filter proper was chosen to be 2.0, and the maximum peak-to-valley excursion of refractive index equalled 1.0, while the

adjustable parameter of the Kaiser window was set at 4.25 [12].

For experimental verification of the technique SiO_xN_y rugate structures were grown on Corning 7059 glass substrates. Temporal changes of the gas flows needed during the growth of the filter described above is shown in Fig. 5. Fig. 6 shows the reflectance spectra of an as-grown single-band filter with correction for non-ideality of the reference aluminium mirror employed in the spectrophotometer. The corresponding simulated spectrum is shown by a dashed line. The maximum in the reflectance band of the grown filter occurs at

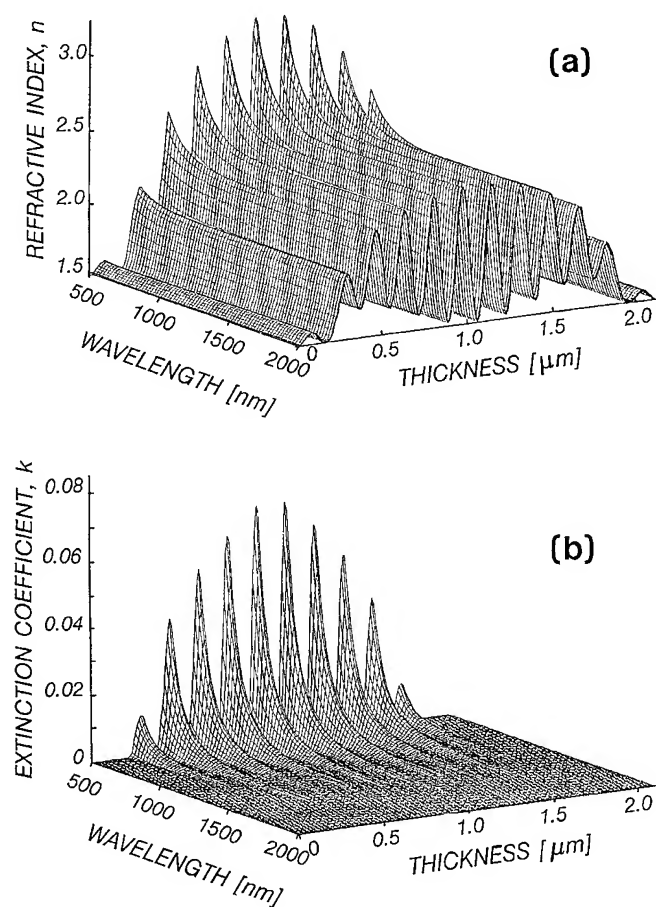


Fig. 4. A three-dimensional representation of the complex refractive index of the rugate filter as a function of wavelength and depth: (a) refractive index; (b) extinction coefficient.

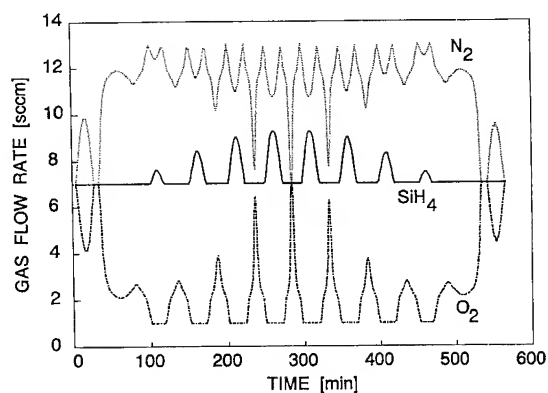


Fig. 5. Temporal gas flows maintained during deposition of rugate filter.

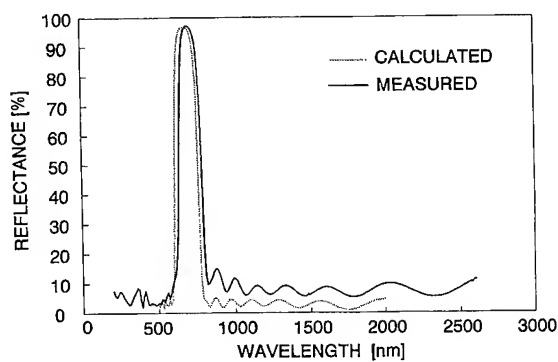


Fig. 6. Calculated and measured reflectance of rugate filter on a glass substrate.

700 nm and its height equals the design value. The wavelength shift is about a 3% deviation from the designed value of 680 nm. This discrepancy is attributed to fluctuations in the self-bias of the substrate, which was not under closed-loop control. The experimental value for bandwidth (FWHM) is as expected equal to 150 nm. Sidelobes outside the stopband of about 10% are considerably higher than expected. This is attributed to the reflectance from the backside of the glass substrate.

5. Conclusions

The data presented here show that the optical properties of amorphous SiO_xN_y films strongly depend on the chemical composition. Chemical composition can be conveniently controlled by the gas composition during deposition. Parameters affecting these optical properties can be controlled reproducibly in order to obtain complicated refractive index profiles. This is especially important for optical coatings manufacturing. We demonstrated that ECR-PECVD can be used successfully for the fabrication of rugate optical filters with pre-programmed graded refractive index profiles by controlling the N_2/SiH_4 and O_2/SiH_4 gas flow ratios.

The authors would like to thank Ms. Erna Burger of SABAX (Pty) Ltd. for use of their FTIR spectrophotometer, and Messrs. Berto Monard and Francois Denner of the Division of Production Technology of the CSIR for use of their UV-VIS-NIR spectrophotometer.

References

- [1] E.P. Donovan, D. Van Vechten, A.D.F. Kahn, C.A. Carosella and G.K. Hubler, *Appl. Opt.* 28 (1989) 2940.
- [2] A.G. Greenham, B.A. Nichols, R.M. Wood, N. Nourshargh and K.L. Lewis, *Opt. Eng.* 32 (1993) 1018.
- [3] W.J. Gunning, R.L. Hall, F.J. Woodberry, W.H. Southwell and N.S. Gluck, *Appl. Opt.* 28 (1989) 2945.
- [4] W.H. Southwell, *Appl. Opt.* 28 (1989) 5091.
- [5] P.G. Verly, J.A. Dobrowolski, W.J. Wild and R.L. Burton, *Appl. Opt.* 28 (1989) 2864.
- [6] H.A. Macleod, *Laser Focus World* 28 (1992) 111.
- [7] P.V. Bulkin, P.L. Swart, B.M. Lacquet and F.J. Burger, *S. Afr. J. Phys.* 16 (1993) 33.
- [8] P.V. Bulkin, P.L. Swart and B.M. Lacquet, *Thin Solid Films* 241 (1994) 247.
- [9] P.V. Bulkin, P.L. Swart and B.M. Lacquet, *Opt. Eng.* 33 (1994) 2894.
- [10] R. Swanepoel, *J. Phys.* E16 (1983) 1214.
- [11] Southwell and R.L. Hall, *Appl. Opt.* 28 (1989) 2949.
- [12] A.V. Oppenheim and R.W. Schaffer, *Discrete-Time Signal Processing* (Prentice-Hall, London, 1989) p. 444.



ELSEVIER

Journal of Non-Crystalline Solids 187 (1995) 489–493

JOURNAL OF
NON-CRYSTALLINE SOLIDS

Light-modulated carrier injection across the interface between transparent conducting oxide (n^+ - SnO_2) and semi-insulating amorphous silicon-carbide

R. Vincenzoni^{a,*}, M.C. Rossi^a, G. Leo^a, F. Galluzzi^b

^a *Department of Electronic Engineering, III University of Rome, Via Eudossiana, 18, 00184 Rome, Italy*

^b *Faculty of Engineering, University of Messina, Messina, Italy*

Abstract

Device-quality amorphous silicon-carbon alloys have been grown by PECVD. Using these materials, $n\text{-SnO}_2/\text{a-SiC:H/Al}$ structures have been fabricated which exhibit promising optoelectronic properties. Since the transport properties of the $n\text{-SnO}_2/\text{a-SiC:H}$ interfacial region are strongly dependent on the applied bias, these devices exhibit both voltage-dependent gain and voltage-tunable spectral response.

1. Introduction

The availability of processes able to grow device-quality amorphous silicon-carbon films with high carbon content [1,3] opens the way to a wider application of these semi-insulating materials in optoelectronic devices, such as photodetectors, photovoltaic cells and light-emitting diodes [4]. One of the simplest device configurations is represented by Schottky-type junctions between a-SiC:H and transparent conductive oxide (SnO_2 , ITO), which, however, have been reported to exhibit new effects such as photocurrent multiplication and current photomodulation [5,6]. In order to gain a deeper insight into the behaviour of these structures, we investigated carrier injection

across the $n^+\text{-SnO}_2/\text{a-SiC:H}$ interface, under illumination.

2. Experimental

Undoped $1\text{ }\mu\text{m}$ -thick $\text{a-Si}_{1-x}\text{C}_x\text{:H}$ thin films with $x = 0.2\text{--}0.5$, having optical gaps between 2.0 and 2.2 eV, were deposited on $n^+\text{-SnO}_2$ -coated glass substrates by rf glow-discharge decomposition of H_2 -diluted methane-silane mixtures. The growth pressure and the radio-frequency power were 1 Torr and 0.3 W/cm^2 , respectively, while the substrate temperature varied from 230 to 300°C . Structural and optical properties of these materials were reported in Ref. [3]. After the growth, contacts were made to a-SiC:H films with Al layers deposited by vacuum evaporation. Electronic properties of $n^+\text{-SnO}_2/\text{a-SiC:H/Al}$ devices were investigated by current-voltage measurements, carried out in dark conditions and under white and monochromatic

* Corresponding author. Tel: +39-6 4458 5462. Telefax: +39-6 474 2647.

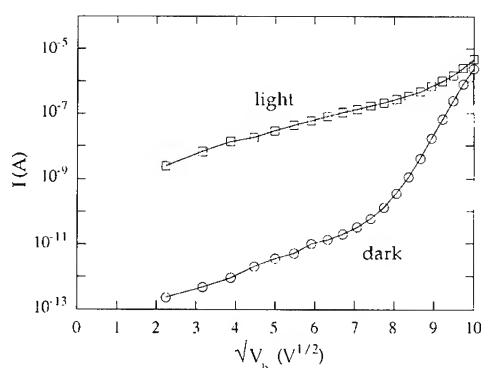


Fig. 1. Current-voltage characteristics in dark conditions and under white light illumination (100 mW/cm²).

illumination. The spectral response of the devices was investigated with standard equipment [7].

3. Results and discussion

In Fig. 1 a semilog plot of the current versus $\sqrt{V_b}$ in dark conditions and under white light illumination (100 mW/cm²) is shown for the sample with a carbon fraction x of about 0.5 (amorphous silicon-carbide). It has been shown [8] that the two-slope behaviour of the dark characteristic corresponds to Schottky injection at lower fields and Frenkel-Poole emission at higher fields. In the former case the electron current across the n^+ -SnO₂/a-SiC:H interface is given by [9]

$$I_D = I_0 \exp(-\Phi_D/kT), \quad (1)$$

with

$$\Phi_D = \Phi_0 - \alpha\sqrt{V_b}. \quad (2)$$

Here Φ_D is the total Schottky barrier height in the dark, Φ_0 is the zero-field barrier height, α is the field-induced barrier-lowering coefficient, k is the Boltzmann constant, T is the absolute temperature and I_0 is a pre-exponential factor. Under illumination, Schottky injection from SnO₂ to a-SiC:H is made easier by a large interface barrier decrease, and the corresponding current can be expressed by the equation

$$I_L = I_D \exp\left(\frac{\Delta\Phi_L}{kT}\right), \quad (3)$$

where $\Delta\Phi_L$ is the light-induced barrier lowering. Such lowering can be attributed [10] to excess holes photogenerated in the a-SiC:H layer and accumulated at the valence band discontinuity between the SnO₂ ($E_g = 3.5$ eV) and a-SiC:H ($E_g = 2.0$ -2.2 eV). According to this model, we have

$$\Delta\Phi_L = kT \ln\left(1 + \frac{\Delta p_{\text{int}}}{p_0}\right), \quad (4)$$

where Δp_{int} and p_0 are the excess and the equilibrium hole densities at the interface, respectively. Δp_{int} can be related to the current photogenerated in the a-SiC:H layer, I_{ph} , by the equation

$$\Delta p_{\text{int}} = \frac{I_{\text{ph}}}{q\mu_p E_{\text{int}}}, \quad (5)$$

where q is the electronic charge, μ_p is the hole mobility and E_{int} is the electric field at the interface.

The corresponding spectral quantum yield, defined as

$$Y = \frac{I_L - I_D}{qF_\lambda} \quad (6)$$

(where F_λ is the photon flux at the wavelength λ) can therefore be written

$$Y = C_0 Y_{\text{int}} \exp(\alpha\sqrt{V_b}/kT), \quad (7)$$

where $C_0 = (I_0/q\mu_p p_0 E_{\text{int}}) \exp(-\Phi_0/kT)$ is a dimensionless factor and $Y_{\text{int}} = I_{\text{ph}}/qF_\lambda$ is the internal photocurrent quantum yield of the a-SiC:H layer.

The experimental field-dependence of the total quantum yield is shown in Fig. 2 for an amorphous silicon-carbide sample ($x = 0.5$) at $\lambda = 450$ nm, while the experimental spectral dependence is shown in Fig. 3 for the same sample at two voltages. The data clearly confirm the exponential dependence on $\sqrt{V_b}$ given by Eq. (7), suggesting a weaker voltage-dependence of the internal quantum yield. On the other hand, Y_{int} completely determines the wavelength dependence of the total quantum yield.

In order to explain the observed spectral response at high electric fields we assume that excess holes are photogenerated within the a-SiC:H layer

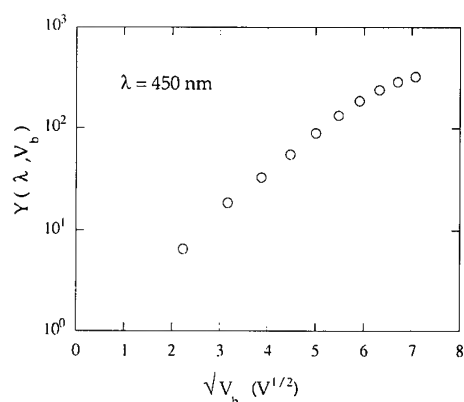


Fig. 2. Photocurrent yield $Y(\lambda, V_b)$ as a function of the applied voltage V_b . Illumination at $\lambda = 450$ nm.

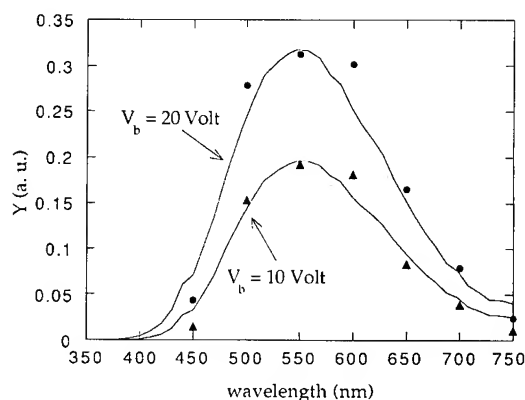


Fig. 3. Photocurrent yield $Y(\lambda, V_b)$ as a function of the wavelength λ for different applied voltages. Dots represent experimental values, continuous lines represent fits obtained from Eq. (10).

at a rate

$$G(\lambda, z) = \alpha(\lambda) \exp[-\alpha(\lambda)z], \quad (8)$$

where α is the absorption coefficient, and collected at the front interface with a probability

$$P_c(z) = \exp[-(z - z_f)/L], \quad (9)$$

where L is the effective collection length and z_f is the depth of a characteristic *dead layer* close to the $\text{SnO}_2/\text{a-SiC}$ interface. The reasons for introducing such a dead layer will be briefly explained in the following.

Owing to the low values of mobility-lifetime products in silicon-carbon alloys ($\mu\tau \approx 10^{-10} \text{ cm}^2 \text{ V}^{-1}$), diffusion lengths are negligible (≈ 10 nm) [3]. So that carrier collection is dominated by drift and L is essentially identical to the drift length, which at $V_b \approx 10$ V can be estimated around $0.1 \mu\text{m}$.

In the region close to the interface, where the accumulation of positive charges occurs, the effective field strength dramatically decreases, thereby leading to a layer in which photogenerated carriers are practically not collected. Moreover, during the growth, several chemical reactions occur between SnO_2 and the reducing species present in the plasma [11], leading to the formation of a very defective interface region (containing metal-Sn, SiO_x , etc.), with a high recombination rate. All these effects contribute to the formation of the dead layer introduced in our simple model through the thickness z_f .

The existence of a dead layer is experimentally confirmed by the very low values of photocurrent quantum yield at wavelengths below 450 nm. As the applied voltage is increased, the photocurrent yield increases, due to better carrier collection. At the same time, the peak wavelength remains almost constant.

Under these assumptions the internal photocurrent quantum yield of the a-SiC: H layer can be written as [12]

$$Y_{\text{int}}(\lambda) = \int_{z_f}^d G(\lambda, z) P(z) dz = \frac{\alpha}{A} \exp(z_f/L) \times \{\exp(-Az_f) - \exp(-Ad)\}, \quad (10)$$

with $A = \alpha + 1/L$ and d thickness of the amorphous layer. Starting from this expression, the experimental data shown in Fig. 3 can be fitted assuming a dead layer of thickness $z_f = 0.3 \mu\text{m}$, a collection length slightly increasing with the applied voltage V_b and experimental values for $\alpha(\lambda)$ [3]. It is noteworthy that the optical filtering effect of the SnO_2 layer (with $E_g = 3.5$ eV) occurs at wavelengths lower than 350 nm.

In order to improve the spectral response in the blue region of the spectrum, samples with a lower carbon content ($x = 0.2$) have been examined, whose experimental quantum yield is shown in

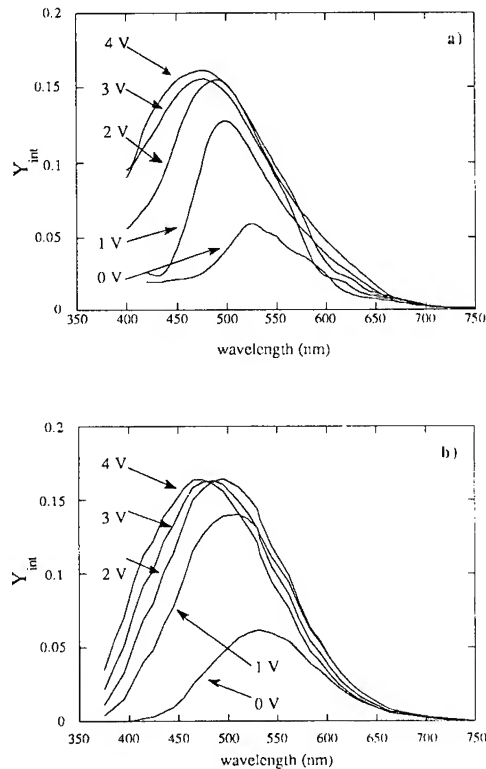


Fig. 4. (a) Experimental values of the internal photocurrent quantum yield for several different applied voltages; V_b , (b) calculated responses obtained from Eq. (10).

Fig. 4(a) for different applied voltages. The increase of V_b leads not only to an increase of the curve but yields a shift of the peak towards smaller wavelengths. This behaviour can be well described by assuming a progressively thinner dead layer, due to a stronger confinement of accumulated excess holes by the applied electric field. Similar behaviour was not observed in samples with higher carbon content (Fig. 3). This is tentatively attributed to the pinning of the dead layer edge by the higher defect density of carbon-rich alloys. Fig. 4(b) shows internal quantum yields, calculated according to Eq. (10), assuming values of the dead layer thickness from 0.3 to 0.8 μm . The simulated spectral responses describe fairly well the experimental data. The bias dependence of the dead layer thickness is shown in Fig. 5. In the range 1–4 V such

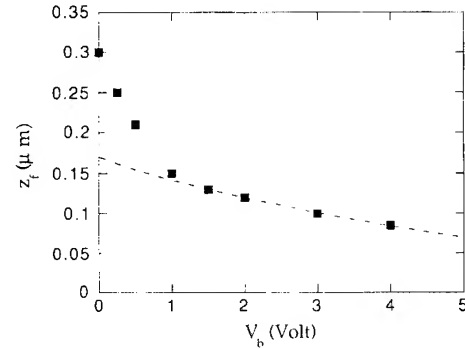


Fig. 5. Dead layer thickness z_f as a function of the applied voltage the dotted line represents a theoretical fit, as described in the text.

a dependence is well represented by the equation

$$z_f = d - W_0 \sqrt{1 + \frac{V_b}{V_{bi}}}, \quad (11)$$

where $(d - W_0)$ is the dead layer at zero field, V_{bi} is the built-in voltage and the second term represents the voltage-induced widening of the depleted region [9]. Its behaviour is shown as a function of V_b by the dashed line in Fig. 5.

4. Conclusions

Device-quality amorphous silicon-carbon alloys have been grown by PECVD using large hydrogen dilution (90%) and high deposition temperature (300°C). In view of their application as optoelectronic materials, double Schottky barrier structures n^+ - $\text{SnO}_2/\text{a-SiC:H}/\text{Al}$ have been fabricated and investigated. As shown from current-voltage measurements under monochromatic illumination, the dominant transport mechanism is electron injection from TCO to a-SiC:H but the interfacial barrier height is controlled by the accumulation of holes photogenerated in the amorphous layer. Their presence is also responsible for a 'dead' front region which limits the blue spectral response. In less defective materials the width of such a region is controlled by the applied bias. These interfacial effects allow us to obtain devices with voltage-dependent gain and voltage-tunable spectral response.

References

- [1] A. Matsuda, T. Yamaoka, S. Wolff, M. Koyama, Y. Imanishi, H. Kataoka, H. Matura and K. Tanaka, *J. Appl. Phys.* 60 (1986) 4025.
- [2] S.H. Baker, W.E. Spear and R.A.G. Gibson, *Philos. Mag.* B62 (1990) 213.
- [3] G. De Cesare, F. Galluzzi, G. Guattari, G. Leo, R. Vincenzoni and E. Bemporad, *Diam. Mater.* 2, (1993) 773.
- [4] Y. Hamakawa, in: M.M. Rahman, C.Y.-W. Yang, G.L. Harris, eds., *Amorphous and Crystalline Silicon Carbide and Related Materials II* (Springer, Berlin, 1989) p. 164.
- [5] M. Hiramoto, K. Yoshimura, Y. Nakayama, S. Akita, T. Kawamura and M. Yokoyama, *Appl. Phys. Lett.* 59 (1991) 1992.
- [6] M. Hiramoto, K. Yoshimura and M. Yokoyama, *Appl. Phys. Lett.* 60 (1992) 1102.
- [7] M.S. Bennet and R.R. Arya, *Solar Cells* 18 (1986) 289.
- [8] R. Vincenzoni, G. Masini, G. Leo, G. Guattari and F. Galluzzi, *Mater. Res. Soc. Symp. Proc.* 297 (1993) 525.
- [9] S. Sze, *Physics of Semiconductor Devices*, 2nd Ed. (Wiley Interscience, New York, 1981) chs. 5 and 7.
- [10] R. Vincenzoni, G. Masini, G. Leo and F. Galluzzi, *Solid State Electron.* 37 (1994) 1937.
- [11] G. Grillo, G. Conte, D. Della Sala and F. Galluzzi, *IEEE Trans. Electron. Dev.* 36 (1989) 2829.
- [12] R.H. Bube, *Photoelectronic Properties of Semiconductors* (Cambridge University, Cambridge, 1992) p. 252.



ELSEVIER

Journal of Non-Crystalline Solids 187 (1995) 494–497

JOURNAL OF
NON-CRYSTALLINE SOLIDS

Thermo-optic mode extinction modulation in polymeric waveguide structures

F.R. Akkari*, K.H. Cazzini, W. Blau

Department of Physics, Trinity College, Dublin 2, Ireland

Abstract

Thermo-optic mode extinction modulation was demonstrated in polymeric waveguide structures. A strip heater was used to control mode extinction via the thermo-optic effect. Mode extinction occurs due to the counteracting effect which arises from a polymeric waveguide with a negative thermo-optic coefficient and a glass substrate with a positive coefficient. Complete mode extinction was achieved at a low driving voltage (1.6 V). Several devices were fabricated and tested using sine and square wave ac voltages up to 40 kHz. Switch ON and OFF times in the millisecond range were obtained. All devices were made of commercially available clear polyurethane varnish on BK-7 glass substrates.

1. Introduction

In optoelectronics guided optical beams may be switched, deflected or modulated by electro-, acousto-, magneto- or thermo-optic effects. While the first three effects have received much attention in the past, thermo-optic effects were only considered recently on glass or polymeric thin film structures [1–4]. Thermally induced refractive index variation is provided by an electrically driven strip heater deposited on the interaction region of these devices. It is well known that polymers possess negative temperature coefficients while some glasses possess a positive coefficient [5,6]. When a polymer is spun on a glass substrate a counteracting

effect arises which can be utilized to design and fabricate a thermo-optic mode extinction modulator (TOMEM) [7]. Essentially, a thermo-optic mode extinction modulator is a weakly guiding waveguide section to which a strip heater is added to control the guidance by means of the thermo-optic effect. Complete mode extinction occurs when the waveguide is brought to cut-off via thermally induced refractive index changes in both the guiding polymer thin film and the glass substrate. Among the common polymers in use in integrated optics polyurethane has the highest thermo-optic coefficient (dn/dT). It was chosen for this investigation to yield low driving voltages. Its thermo-optic coefficient was measured to be $-5.3 \times 10^{-4} \text{ K}^{-1}$. The refractive index of polyurethane was 1.522. A BK-7 glass substrate with a refractive index of 1.515 was used to reduce the change in refractive index required to produce complete mode extinction. A

* Corresponding author. Tel: +353-1 608 2404. Telefax: +353-1 671 1759. kcazzini@vax1.tcd.ie.

metallic stripe heater driven by a stabilized power supply was used to induce temperature changes in the weakly guiding section. Although thermo-optic devices have slow speeds of operation, they can be useful in applications where high speed is not required. In this paper, we describe the fabrication and experimental demonstration of a thermo-optic mode extinction modulator.

2. Experimental details

The thermo-optic mode extinction modulator was fabricated using commercially available clear varnish polyurethane thin film. It was spin coated on a BK-7 glass substrate. It has a thickness of $3.4\text{ }\mu\text{m}$ and a refractive index of 1.522 determined by M-line technique. A PMMA buffer layer was spun on this layer and finally a strip heater was sputtered on top. The PMMA protective layer has a thickness of $0.3\text{ }\mu\text{m}$ and a refractive index of 1.488. The strip heater was cold sputtered through a mechanical mask, 10 mm long and 1 mm wide. The refractive index of the BK-7 glass substrate is 1.515. Several devices were fabricated and tested at different strip heater total resistances. Conventional prism coupling was used to couple light (HeNe $\lambda = 0.6328\text{ }\mu\text{m}$) in and out of the polyurethane weakly guiding single mode and thin film waveguide. The out coupled light was focused on a photodetector connected to a storage oscilloscope. The modulator was tested while exciting the transverse electric (TE) guided mode only. Electrical control of the guided mode extinction by a dc voltage applied across the strip heater terminals. The dissipated electrical power in the strip heater was used to change the temperature of the thin film. The guided beam was coupled such that it propagated normal to the strip heater length.

3. Results

A TE polarized He–Ne laser light was coupled in and out the polymeric thin film waveguide. Electrical control of the guided mode extinction by a dc voltage applied across a $15\text{ }\Omega$ strip heater is depicted in Fig. 1, where complete mode

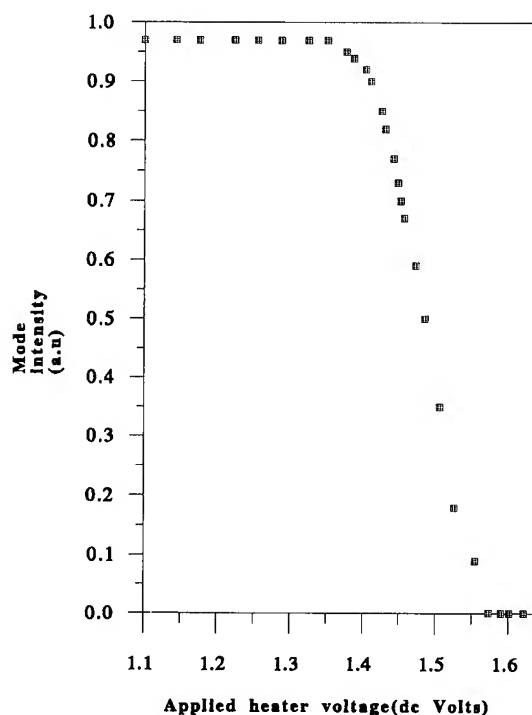


Fig. 1. Variation of guided mode intensity with applied dc voltage with a strip heater of $15\text{ }\Omega$ total resistance.

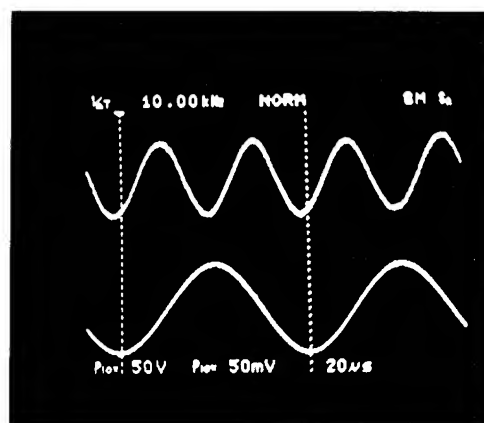
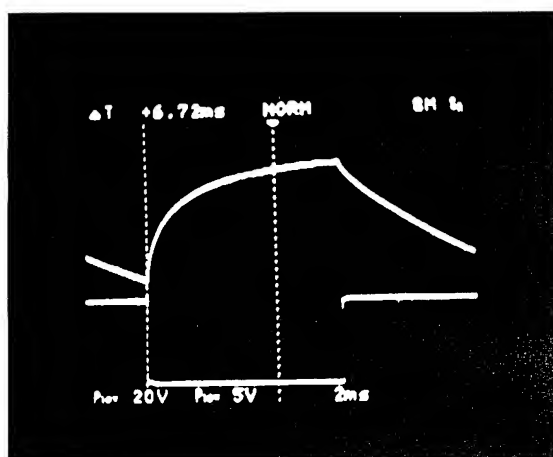
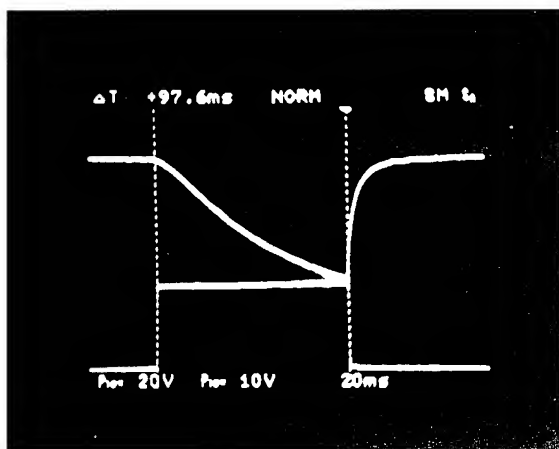


Fig. 2. Modulator response (upper trace) to a sine-wave 7 V peak to peak (lower trace) with a strip heater of $270\text{ }\Omega$ total resistance.

extinction is evident at $\sim 1.6\text{ V}$. When the strip heater was driven with a pure sine wave the modulated amplitude had twice the frequency of the applied signal because the thermo-optic mode



(a)



(b)

Fig. 3. Modulator square wave response: (a) upper trace switch OFF response; (b) upper trace switch ON response.

extinction effect is related to the dissipated power rather than the applied voltage. In Fig. 2 we present the modulator response to sine wave at a frequency of 10 kHz and peak to peak voltage of 7 V applied across a 270 Ω strip heater. Although no attempt was made to optimize this modulator we were able to measure its response up to 40 kHz. To measure the switching response the modulator was driven with a square wave (Fig. 3) where it can be seen that the switching from extinction cut-off state to total trans-

mission state is ~ 6.7 ms, and is determined by the strip heater geometry and heat sinking. The switching from total transmission state to cut-off state is slow and determined by the thin film thermal properties.

4. Discussion

In principle a mode extinction modulator consists of a weakly guiding waveguide section, where changes can be introduced in the guiding thin film refractive index to achieve modulation of the guided optical beam intensity. This can be achieved thermo-optically in polymers using polyurethane on a BK-7 glass substrate. The refractive index changes in both the polymer thin film and the substrate can be induced by temperature changes. The temperature can be controlled by a strip heater deposited on top of the polymer thin film. The choice of a polymer having a high negative thermo-optic coefficient together with a substrate namely BK-7 having a close refractive index to that of the polymer and a positive thermo-optic coefficient resulted in a modulator requiring a low driving voltage to achieve complete (100%) mode extinction. As can be seen in Fig. 1 complete mode extinction happened at ~ 1.6 V across a 15 Ω heater. This corresponds to about 170 mW of dissipated power across the heater length, and only 40 mW are needed across the interaction region. The temperature is dependent on the dissipated power rather than the applied voltage. When a sine-wave signal is applied across the heater the guided beam is modulated at twice its frequency, as can be seen in Fig. 2.

Using a square wave the modulator was tested up to 40 kHz in an on-off mode. No attempt was made to optimize the response speed in this investigation. It can be seen that the switching response from total transmission state to cut-off was very slow. It was determined by the thin film thermal properties. The response time for the switching from cut-off state to total transmission was ~ 6.7 ms. It was determined by the heater geometry and heat sinking. Thermo-optic devices in general have a low speed disadvantage, but they can be very low-cost useful components in applications where high speed is not required. They can be useful for temperature, pressure and gas flow sensing applications.

5. Conclusions

In conclusion, we have demonstrated thermo-optic mode extinction modulation in polymeric waveguide structure using polyurethane thin film on a BK-7 glass substrate at low driving voltages. The required driving power to achieve complete (100%) mode extinction is about 40 mW. The speed of operation is limited to milliseconds range as is the case for most thermo-optic devices.

References

- [1] M. Haruna and J. Koyama, *Appl. Opt.* 21 (1982) 3461.
- [2] M.B.J. Diemeer, J.J. Brons and E.S. Trommel, *J. Lightwave Technol.* 7 (1989) 449.
- [3] R.A. Mayer, K.H. Jung, W.D. Lee, D. Kwong and J.C. Campbell, *Opt. Lett.* 17 (1992) 1812.
- [4] C.C. Lee and T.J. Su, *Appl. Opt.* 33 (1994) 7016.
- [5] J.M. Cariou, J. Dugas, L. Martin and P. Michel, *Appl. Opt.* 25 (1986) 334.
- [6] J.M. Jewell, *J. Non-Cryst Solids* 146 (1992) 145.
- [7] P.R. Ashley and W.S.C. Chang, *IEEE J. Quantum Electron.* QE-22 (1986) 920.



Author index

- Aassime, A., see El-Hdiy, A. 187 (1995) 216
- Afanas'ev, V.V., J.M.M. de Nijs and P. Balk, The role of hydrogen in the action of fluorine in Si/SiO₂ structures 187 (1995) 248
- Afanas'ev, V.V., see Drujff, K.G. 187 (1995) 206
- Afanas'ev, V.V., see Vanheusden, K. 187 (1995) 253
- Akai, M., see Shimizu-Iwayama, T. 187 (1995) 112
- Akkari, F.R., K.H. Cazzini and W. Blau, Thermo-optic mode extinction modulation in polymeric waveguide structures 187 (1995) 494
- Alhallani, B., see Suchaneck, G. 187 (1995) 86
- Andersson, M.O., A. Lundgren and P. Lundgren, Surface potential dependence of interface state passivation in metal-tunnel oxide-silicon diodes 187 (1995) 273
- Andersson, M.O., see Lundgren, P. 187 (1995) 140
- Armstrong, B.M., see Quinn, L.J. 187 (1995) 347
- Atanassova, E., see Paskaleva, A. 187 (1995) 35
- Aubel, D., M. Diani, L. Kubler, J.L. Bischoff and D. Bolmont, Selective thermal – as opposed to non-selective plasma – nitridation of Si-Ge related materials examined by in situ photoemission techniques 187 (1995) 319
- Audino, R., F. Cannistraci, G. Morello and P. Valenti, PECVD a-SiN_x:H films for dielectric insulation in buried ridge structure Fabry-Perot and distributed feedback laser devices 187 (1995) 477
- Autran, J.-L., B. Balland and D. Babot, Three-level charge pumping study of radiation-induced defects at Si-SiO₂ interface in sub-micrometer MOS transistors 187 (1995) 211
- Autran, J.-L., C. Plossu, F. Seigneur, B. Balland and A. Straboni, A comparison of Si-SiO₂ interface trap properties in thin-film transistors with thermal and plasma nitrided oxides 187 (1995) 374
- Avinens, C., see Tourtin, F. 187 (1995) 435
- Babot, D., see Autran, J.-L. 187 (1995) 211
- Baehr, O., M. Barrada, A. Bath, B. Lepley, P. Thévenin and J. Schoonman, Electrical properties of Au/Bn/InP MIS diodes 187 (1995) 409
- Balk, P., Dielectrics in microelectronics – problems and perspectives 187 (1995) 1
- Balk, P., see Afanas'ev, V.V. 187 (1995) 248
- Balk, P., see Drujff, K.G. 187 (1995) 206
- Balland, B., see Autran, J.-L. 187 (1995) 211
- Balland, B., see Autran, J.-L. 187 (1995) 374
- Barrada, M., see Baehr, O. 187 (1995) 409
- Bath, A., see Baehr, O. 187 (1995) 409
- Bauer, A.J. and E.P. Burte, Structural and electrical properties of thin SiO₂ layers grown by RTP in a mixture of N₂O and O₂ 187 (1995) 361
- Bernardi, C. and C. d'Anterrosches, Characterization of thin nitrided oxide layers using high spatial resolution transmission electron energy loss spectrometry 187 (1995) 369
- Bertolotti, M., S. Mura, E. Pennella, F. Senesi, C. Sibilia, A. Montenero, G. Gnappi and S. Pigoni, Optical properties of sol-gel derived ferroelectric films 187 (1995) 453
- Beshkov, G., V. Lazarova and D.B. Dimitrov, Morphology of LPCVD Si₃N₄ films after high temperature treatment and HF etching 187 (1995) 301
- Beshkov, G., see Paskaleva, A. 187 (1995) 35
- Bischoff, J.L., see Aubel, D. 187 (1995) 319
- Blau, W., see Akkari, F.R. 187 (1995) 494
- Boivin, P., see Ciantar, E. 187 (1995) 144
- Bolmont, D., see Aubel, D. 187 (1995) 319
- Borghesi, A., see Sassella, A. 187 (1995) 395
- Bota, S., see Garrido, B. 187 (1995) 101
- Bouchakour, R., see Limbourg, I. 187 (1995) 160
- Boudrioua, A., P. Moretti and J.C. Loulergue, Fabrication, characterization and electro-optic performances of proton-implanted waveguides in LiNbO₃ 187 (1995) 443
- Boulliard, J.C., see Poncey, C. 187 (1995) 40
- Boultadakis, S., see Petalas, J. 187 (1995) 291
- Bourée, J.E., see Etemadi, R. 187 (1995) 70
- Bräunig, D., see Krauser, J. 187 (1995) 264
- Bravaix, A., D. Vuillaume, V. Thirion, D. Dorval and A. Straboni, Damage induced by carrier injection in 8 nm thick oxides and nitrided oxides 187 (1995) 365
- Brenot, R., see Etemadi, R. 187 (1995) 70
- Brevet-Philibert, O., see Monin, J. 187 (1995) 129

- Brière, O., P. Cottin and A. Straboni, Comparison of rapid ramp voltage and tunnelling injection stress experiments for the characterization of thin MOS gate oxides 187 (1995) 190
- Buchali, F., see Wiersch, A. 187 (1995) 334
- Buchanan, D.A., see Cartier, E. 187 (1995) 244
- Bulkin, P.V., P.L. Swart and B.M. Lacquet, Effect of process parameters on the properties of electron cyclotron resonance plasma deposited silicon-oxynitride 187 (1995) 403
- Bulkin, P.V., P.L. Swart and B.M. Lacquet, Properties and applications of electron cyclotron plasma deposited SiO_xN_y films with graded refractive index profiles 187 (1995) 484
- Burle, M., see Ciantar, E. 187 (1995) 144
- Burte, E.P. and N. Rausch, Low pressure chemical vapour deposition of tantalum pentoxide thin layers 187 (1995) 425
- Burte, E.P., see Bauer, A.J. 187 (1995) 361
- Canet, P., see Foulani, A. 187 (1995) 415
- Cannistraci, F., see Audino, R. 187 (1995) 477
- Cartier, E., D.A. Buchanan, J.H. Stathis and D.J. DiMaria, Atomic hydrogen-induced degradation of thin SiO_2 gate oxides 187 (1995) 244
- Cazzini, K.H., see Akkari, F.R. 187 (1995) 494
- Charlot, J.J., see Limbourg, I. 187 (1995) 160
- Cho, K.-I., see Park, H.-H. 187 (1995) 149
- Ciantar, E., P. Boivin, M. Burle, C. Niel, J.M. Moragues, B. Sagnes, R. Jerisian and J. Oualid, Influence of FN electron injections in dry and dry/wet/dry gate oxides: relation with failure 187 (1995) 144
- Ciantar, E., see Moragues, J.M. 187 (1995) 156
- Cimalla, V., see Zöllner, J.-P. 187 (1995) 23
- Corni, F., see Sassella, A. 187 (1995) 395
- Cottin, P., see Brière, O. 187 (1995) 190
- Cros, Y. and J. Krautwurm, Structural identification of point defects in amorphous silicon oxynitrides 187 (1995) 385
- Crossley, A., C.J. Sofield, J.P. Goff, A.C.I. Lake, M.T. Hutchings and A. Menelle, A study comparing measurements of roughness of silicon and SiO_2 surfaces and interfaces using scanning probe microscopy and neutron reflectivity 187 (1995) 221
- Dahmen, K.-H., see Lang, F.-R. 187 (1995) 430
- Danesh, P. and A. Szekeres, Electrical properties of hydrogen-rich Si/SiO_2 structures 187 (1995) 270
- Danesh, P., see Szekeres, A. 187 (1995) 45
- d'Anterrosches, C., see Bernardi, C. 187 (1995) 369
- da Silva, M.F., see Parada, E.G. 187 (1995) 75
- Daviero, S., see Tourtin, F. 187 (1995) 435
- de Nijs, J.M.M., see Afanas'ev, V.V. 187 (1995) 248
- de Nijs, J.M.M., see Druijf, K.G. 187 (1995) 206
- Devine, R.A.B., see Fleetwood, D.M. 187 (1995) 199
- Devine, R.A.B., see Martinet, C. 187 (1995) 96
- Diani, M., see Aubel, D. 187 (1995) 319
- DiMaria, D.J., see Cartier, E. 187 (1995) 244
- DiMaria, D.J., see Roh, Y. 187 (1995) 165
- Dimitrov, D.B., see Beshkov, G. 187 (1995) 301
- Dimos, D., see Warren, W.L. 187 (1995) 448
- Döbeli, M., see Lang, F.-R. 187 (1995) 430
- Dolique, A. and A.H. Reader, Low-temperature voltage enhanced UV-assisted oxidation of silicon 187 (1995) 29
- Domínguez, C., see Garrido, B. 187 (1995) 101
- Dorval, D., see Bravaix, A. 187 (1995) 365
- Drévilion, B., see Etemadi, R. 187 (1995) 70
- Druijf, K.G., J.M.M. de Nijs, E. v.d. Drift, V.V. Afanas'ev, E.H.A. Granneman and P. Balk, The microscopic nature of donor-type $\text{Si}-\text{SiO}_2$ interface states 187 (1995) 206
- Dufour, G., see Poncy, C. 187 (1995) 40
- Dunnett, B., see Murley, D.T. 187 (1995) 324
- Edwards, A.H., Dissociation of H_2 at silicon dangling orbitals in a- SiO_2 : a quantum mechanical treatment of nuclear motion 187 (1995) 232
- El-Hdiy, A., G. Salace, A. Meinertzhagen, M. Jourdain, C. Petit and A. Aassime, The no-thermal activation of the defect generation mechanism in a MOS structure 187 (1995) 216
- El-Hdiy, A., see Meinertzhagen, A. 187 (1995) 181
- Elrharbi, S. and M. Jourdain, Influence of the oxide charge build-up during Fowler-Nordheim stress on the current-voltage characteristics of metal-oxide-semiconductor capacitors 187 (1995) 175
- Engström, O., see Lundgren, P. 187 (1995) 140
- Etemadi, R., C. Godet, M. Kildemo, J.E. Bourée, R. Brenot and B. Drévilion, Dual-mode radio frequency/microwave plasma deposition of amorphous silicon oxide thin films 187 (1995) 70
- Farmer, K.R., see Lundgren, P. 187 (1995) 140
- Fernández, D., see Serra, J. 187 (1995) 353
- Fernandez, M., see Garcia, S. 187 (1995) 329
- Fleetwood, D.M., W.L. Warren, M.R. Shaneyfelt, R.A.B. Devine and J.H. Scofield, Enhanced MOS $1/f$ noise due to near-interfacial oxygen deficiency 187 (1995) 199
- Flietner, H., see Lisovskii, I.P. 187 (1995) 91
- Fortunato, G., see Tallarida, G. 187 (1995) 195
- Foulani, A., C. Laurent and P. Canet, Surface plasmon-induced luminescence: a probe to study electrical aging and dielectric breakdown in polymer-like thin films 187 (1995) 415
- French, I.D., see Murley, D.T. 187 (1995) 324
- Frolov, S.I., see Lisovskii, I.P. 187 (1995) 91
- Fujita, K., see Shimizu-Iwayama, T. 187 (1995) 112

- Fussel, W., see Lisovskii, I.P. 187 (1995) 91
- Galluzzi, F., see Vincenzoni, R. 187 (1995) 489
- Gamble, H.S., see Quinn, L.J. 187 (1995) 347
- García, E., see Serra, J. 187 (1995) 353
- Garcia, S., J.M. Martin, I. Martil, M. Fernandez, E. Iborra and G. Gonzalez-Diaz, Influence of the deposition parameters on the bonding and optical properties of SiN_x ECR films 187 (1995) 329
- Garrido, B., J. Samitier, S. Bota, C. Domínguez, J. Montserrat and J.R. Morante, Structural damage and defects created in SiO₂ films by Ar ion implantation 187 (1995) 101
- Gasser, W., see Morishita, S. 187 (1995) 66
- Gaunau, M., see Nédélec, S. 187 (1995) 106
- Gibson, R.A.G., see Murley, D.T. 187 (1995) 324
- Gnappi, G., see Bertolotti, M. 187 (1995) 453
- Godet, C., see Etemadi, R. 187 (1995) 70
- Goff, J.P., see Crossley, A. 187 (1995) 221
- Gonon, P., see Paillet, P. 187 (1995) 170
- Gonzalez-Diaz, G., see Garcia, S. 187 (1995) 329
- González, P., see Parada, E.G. 187 (1995) 75
- González, P., see Serra, J. 187 (1995) 353
- Goodyear, A., see Murley, D.T. 187 (1995) 324
- Granneman, E.H.A., see Druif, K.G. 187 (1995) 206
- Haddad, N.F., see Henley, W.B. 187 (1995) 134
- Haidoux, A., see Tourtin, F. 187 (1995) 435
- Hardy, L., see Limbourg, I. 187 (1995) 160
- Hartmannsgruber, E., U. Rossow, A. Hoyer and P. Lange, Structural and optical properties of nitrided silicon oxide layers rapidly thermally grown in a pure N₂O ambient 187 (1995) 380
- Hasegawa, S., T. Inokuma and Y. Kurata, Structural and bonding properties of amorphous silicon nitride films 187 (1995) 278
- Hattangady, S.V., see Lucovsky, G. 187 (1995) 60
- Hauert, R., see Lang, F.-R. 187 (1995) 430
- He, S.S., see Lu, Z. 187 (1995) 340
- Heedt, C., see Wiersch, A. 187 (1995) 334
- Henley, W.B., L. Jastrzebski and N.F. Haddad, Effects of iron contamination in silicon on thin oxide breakdown and reliability characteristics 187 (1995) 134
- Homma, T., Fluorinated interlayer dielectric films in ULSI multilevel interconnections 187 (1995) 49
- Hosono, H., Chemical interaction in ion-implanted amorphous SiO₂ and application to formation and modification of nanosize colloid particles 187 (1995) 457
- Hoyer, A., see Hartmannsgruber, E. 187 (1995) 380
- Hutchings, M.T., see Crossley, A. 187 (1995) 221
- Ibanez, A., see Tourtin, F. 187 (1995) 435
- Iborra, E., see Garcia, S. 187 (1995) 329
- Inokuma, T., see Hasegawa, S. 187 (1995) 278
- Jastrzebski, L., see Henley, W.B. 187 (1995) 134
- Jerisian, R., see Ciantar, E. 187 (1995) 144
- Jerisian, R., see Moragues, J.M. 187 (1995) 156
- Jourdain, M., see El-Hdiy, A. 187 (1995) 216
- Jourdain, M., see Elrharbi, S. 187 (1995) 175
- Jourdain, M., see Limbourg, I. 187 (1995) 160
- Jourdain, M., see Meinertzhagen, A. 187 (1995) 181
- Kanicki, J., see Robertson, J. 187 (1995) 297
- Keubart, W., see Wiersch, A. 187 (1995) 334
- Kildemo, M., see Etemadi, R. 187 (1995) 70
- Kim, K.-S., see Park, H.-H. 187 (1995) 149
- Kleider, J.P., see Reynaud, J. 187 (1995) 313
- Krauser, J., F. Wulf and D. Bräunig, Measurement and analysis of hydrogen depth profiles in MOS-structures by using the ¹⁵N nuclear reaction method 187 (1995) 264
- Krautwurm, J., see Cros, Y. 187 (1995) 385
- Kravetsky, I.V., L.L. Kulyuk, A.V. Micu, V.I. Tsytsanu and I.S. Vieru, Characterization of ion-implanted silicon-insulator interfaces by reflected optical second harmonic generation 187 (1995) 227
- Kretz, T., see Tallarida, G. 187 (1995) 195
- Kubler, L., see Aubel, D. 187 (1995) 319
- Kulyuk, L.L., see Kravetsky, I.V. 187 (1995) 227
- Kurata, Y., see Hasegawa, S. 187 (1995) 278
- Lacquet, B.M., see Bulkin, P.V. 187 (1995) 403
- Lacquet, B.M., see Bulkin, P.V. 187 (1995) 484
- Lake, A.C.I., see Crossley, A. 187 (1995) 221
- Lang, F.-R., E.C. Plappert, K.-H. Dahmen, R. Hauert, P. Nebiker and M. Döbeli, Investigation of the film growth of a new titanium precursor for MOCVD 187 (1995) 430
- Lange, P., see Hartmannsgruber, E. 187 (1995) 380
- Laurent, C., see Foulani, A. 187 (1995) 415
- Lazarova, V., see Beshkov, G. 187 (1995) 301
- Lee, J.-L., see Park, H.-H. 187 (1995) 149
- Lee, J.-S., see Park, H.-H. 187 (1995) 149
- Lee, Y.-H., see Park, H.-H. 187 (1995) 149
- Legagneux, P., see Tallarida, G. 187 (1995) 195
- Leo, G., see Vincenzoni, R. 187 (1995) 489
- León, B., see Parada, E.G. 187 (1995) 75
- León, B., see Serra, J. 187 (1995) 353
- Lepley, B., see Baehr, O. 187 (1995) 409
- Leray, J.-L., Buried oxides: where we have been and where we are going 187 (1995) 10
- Leray, J.-L., see Paillet, P. 187 (1995) 170
- Limbourg, I., L. Hardy, M. Jourdain, R. Bouchakour and J.J. Charlot, Modeling and simulation of homogeneous degradation for N-channel MOSFETS 187 (1995) 160
- Lin, S.-S., see Yeh, C.-F. 187 (1995) 81
- Liotard, J.L., see Moragues, J.M. 187 (1995) 156

- Lisovskii, I.P., G.P. Romanova and E.G. Schmidt, Field mechanism of defect generation at Si-SiO₂ interface under hot electron injection 187 (1995) 186
- Lisovskii, I.P., V.G. Litovchenko, V.B. Lozinskii, S.I. Frolov, H. Flietner, W. Fussel and E.G. Schmidt, IR study of short-range and local order in SiO₂ and SiO_x films 187 (1995) 91
- Litovchenko, V.G., see Lisovskii, I.P. 187 (1995) 91
- Logothetidis, S., see Petalas, J. 187 (1995) 291
- Loulergue, J.C., see Boudrioua, A. 187 (1995) 443
- Lozinskii, V.B., see Lisovskii, I.P. 187 (1995) 91
- Lu, Z., S.S. He, Y. Ma and G. Lucovsky, Control of bonded-hydrogen in plasma-deposited silicon nitrides: Combined plasma-assisted deposition and rapid thermal annealing for the formation of device-quality nitride layers for applications in multilayer dielectrics 187 (1995) 340
- Lucarno, P., see Sassella, A. 187 (1995) 395
- Lucovsky, G., V. Misra, S.V. Hattangady, T. Yasuda and J.J. Wortman, Deposition of ultra-thin oxide dielectrics for MOSFETs by a combination of low-temperature plasma-assisted oxidation, and intermediate and high-temperature rapid thermal processing 187 (1995) 60
- Lucovsky, G., see Lu, Z. 187 (1995) 340
- Lundgren, A., see Andersson, M.O. 187 (1995) 273
- Lundgren, P., M.O. Andersson, K.R. Farmer and O. Engström, Instability of charged defects in electrically stressed metal-tunnel oxide-silicon diodes 187 (1995) 140
- Lundgren, P., see Andersson, M.O. 187 (1995) 273
- Ma, Y., see Lu, Z. 187 (1995) 340
- Maeda, K., N. Sakamoto and I. Umezu, A comparative study on structural and electronic properties of PECVD a-SiO_x with a-SiN_x 187 (1995) 287
- Markwitz, A., see Petalas, J. 187 (1995) 291
- Martil, I., see Garcia, S. 187 (1995) 329
- Martin, J.M., see Garcia, S. 187 (1995) 329
- Martinet, C. and R.A.B. Devine, Comparison of experimental and calculated TO and LO oxygen vibrational modes in thin SiO₂ films 187 (1995) 96
- Martini, M., F. Meinardi, E. Rosetta, G. Spinolo and A. Vedda, Wavelength resolved thermally stimulated luminescence of SiO₂ films 187 (1995) 124
- Mathiot, D., see Nédélec, S. 187 (1995) 106
- Matsumura, M., see Morishita, S. 187 (1995) 66
- Meinardi, F., see Martini, M. 187 (1995) 124
- Meinertzhagen, A., G. Yard, C. Petit, M. Jourdain, A. El-Hdiy, G. Salace and G. Reimbold, Comparison of the generated oxide charge by injection of electrons for both polarities 187 (1995) 181
- Meinertzhagen, A., see El-Hdiy, A. 187 (1995) 216
- Mencaraglia, D., see Reynaud, J. 187 (1995) 313
- Menelle, A., see Crossley, A. 187 (1995) 221
- Merenda, P., see Moragues, J.M. 187 (1995) 156
- Micu, A.V., see Kravetsky, I.V. 187 (1995) 227
- Misra, V., see Lucovsky, G. 187 (1995) 60
- Mitchell, S.J.N., see Quinn, L.J. 187 (1995) 347
- Monin, J., H. Sahsa and O. Brevet-Philibert, A novel ellipsometric set up for high precision thin films measurements 187 (1995) 129
- Montenero, A., see Bertolotti, M. 187 (1995) 453
- Montserrat, J., see Garrido, B. 187 (1995) 101
- Moragues, J.M., B. Sagnes, R. Jerisian, J. Oualid, E. Ciantar, J.L. Liotard and P. Merenda, Influence of WSi₂ polysilicide gate process on integrity and reliability of gate and tunnel oxides 187 (1995) 156
- Moragues, J.M., see Ciantar, E. 187 (1995) 144
- Morante, J.R., see Garrido, B. 187 (1995) 101
- Morello, G., Hydrogen content of amorphous PECVD SiN_x:H films by infrared spectroscopy and hydrogen forward scattering results 187 (1995) 308
- Morello, G., see Audino, R. 187 (1995) 477
- Moretti, P., see Boudrioua, A. 187 (1995) 443
- Morishita, S., W. Gasser, K. Usami and M. Matsumura, New substances for atomic-layer deposition of silicon dioxide 187 (1995) 66
- Mura, S., see Bertolotti, M. 187 (1995) 453
- Murley, D.T., R.A.G. Gibson, B. Dunnett, A. Goodyear and I.D. French, Influence of gas residence time on the deposition of nitrogen-rich amorphous silicon nitride 187 (1995) 324
- Nahm, S., see Park, H.-H. 187 (1995) 149
- Nakao, S., see Shimizu-Iwayama, T. 187 (1995) 112
- Nebiker, P., see Lang, F.-R. 187 (1995) 430
- Nédélec, S., D. Mathiot, M. Gauneau and A. Straboni, Boron diffusion in SiO₂ based dielectric thin layers 187 (1995) 106
- Niel, C., see Ciantar, E. 187 (1995) 144
- Nissim, Y.I., see Sayah, A. 187 (1995) 473
- Oualid, J., see Ciantar, E. 187 (1995) 144
- Oualid, J., see Moragues, J.M. 187 (1995) 156
- Paillet, P., P. Gonon, C. Schwebel and J.-L. Leray, Comparison of X-ray-induced electron and hole trapping in various materials (YSZ, SIMOX, thermal SiO₂) 187 (1995) 170
- Panaccione, G., see Poncey, C. 187 (1995) 40
- Parada, E.G., P. González, J. Serra, B. León, M. Pérez-Amor, M.F. da Silva, H. Wolters and J.C. Soares, Hydrogen incorporation in silicon oxide films deposited by ArF laser-induced chemical vapor deposition 187 (1995) 75
- Park, H.-H., S. Nahm, K.-S. Suh, J.-L. Lee, K.-I. Cho, K.-S. Kim, S.-C. Park, J.-S. Lee and Y.-H. Lee, Investigation on the interfacial reaction of SiO₂/Ti_{0.1}W_{0.9} system 187 (1995) 149

- Park, S.-C., see Park, H.-H. 187 (1995) 149
- Paskaleva, A., E. Atanassova and G. Beshkov, Rapid thermal annealing of SiO₂ for VLSI applications 187 (1995) 35
- Pecora, A., see Tallarida, G. 187 (1995) 195
- Pennella, E., see Bertolotti, M. 187 (1995) 453
- Pérez-Amor, M., see Parada, E.G. 187 (1995) 75
- Pérez-Amor, M., see Serra, J. 187 (1995) 353
- Petalas, J., S. Logothetidis, S. Bouladakis and A. Markwitz, The effect of hydrogen and temperature on the optical gaps of silicon nitride and comparative stoichiometry studies on SiN thin films 187 (1995) 291
- Petit, C., see El-Hdiy, A. 187 (1995) 216
- Petit, C., see Meinertzhagen, A. 187 (1995) 181
- Pezoldt, J., see Zöllner, J.-P. 187 (1995) 23
- Philippot, E., see Tourtin, F. 187 (1995) 435
- Pigoni, S., see Bertolotti, M. 187 (1995) 453
- Plais, F., see Tallarida, G. 187 (1995) 195
- Plappert, E.C., see Lang, F.-R. 187 (1995) 430
- Plossu, C., see Autran, J.-L. 187 (1995) 374
- Poindexter, E.H., Chemical reactions of hydrogenous species in the Si/SiO₂ system 187 (1995) 257
- Poncey, C., F. Rochet, G. Dufour, H. Roulet, W.N. Rodrigues, M. Sauvage-Simkin, J.C. Boulliard, F. Sirotti and G. Panaccione, A synchrotron Si2p and As3d core level study of the As-terminated Si(0 0 1) surface oxidation 187 (1995) 40
- Pou, J., see Serra, J. 187 (1995) 353
- Pribat, D., see Tallarida, G. 187 (1995) 195
- Prost, W., see Wiersch, A. 187 (1995) 334
- Quinn, L.J., S.J.N. Mitchell, B.M. Armstrong and H.S. Gamble, Plasma-enhanced silicon nitride deposition for thin film transistor applications 187 (1995) 347
- Rausch, N., see Burte, E.P. 187 (1995) 425
- Reader, A.H., see Dolique, A. 187 (1995) 29
- Reimbold, G., see Meinertzhagen, A. 187 (1995) 181
- Reynaud, J., J.P. Kleider and D. Mencaraglia, Bias stress studies of a-SiN:H/a-Si:H MIS structures from quasistatic capacitance measurements 187 (1995) 313
- Robertson, J., W.L. Warren and J. Kanicki, Nature of the Si and N dangling bonds in silicon nitride 187 (1995) 297
- Rochet, F., see Poncey, C. 187 (1995) 40
- Rodrigues, W.N., see Poncey, C. 187 (1995) 40
- Roh, Y., L. Trombetta and D.J. DiMaria, Interface traps induced by hole trapping in metal-oxide semiconductor devices 187 (1995) 165
- Rojas, S., see Sassella, A. 187 (1995) 395
- Romanova, G.P., see Lisovskii, I.P. 187 (1995) 186
- Rosetta, E., see Martini, M. 187 (1995) 124
- Rossi, M.C., see Vincenzoni, R. 187 (1995) 489
- Rossow, U., see Hartmannsgruber, E. 187 (1995) 380
- Roulet, H., see Poncey, C. 187 (1995) 40
- Sagnes, B., see Ciantar, E. 187 (1995) 144
- Sagnes, B., see Moragues, J.M. 187 (1995) 156
- Sahsah, H., see Monin, J. 187 (1995) 129
- Saitoh, K., see Shimizu-Iwayama, T. 187 (1995) 112
- Sakamoto, N., see Maeda, K. 187 (1995) 287
- Salace, G., see El-Hdiy, A. 187 (1995) 216
- Salace, G., see Meinertzhagen, A. 187 (1995) 181
- Samitier, J., see Garrido, B. 187 (1995) 101
- Sassella, A., P. Lucarno, A. Borghesi, F. Corni, S. Rojas and L. Zanotti, Silicon oxynitride study by the tetrahedron model and by spectroscopic ellipsometry 187 (1995) 395
- Sauvage-Simkin, M., see Poncey, C. 187 (1995) 40
- Sayah, A. and Y.I. Nissim, Light-assisted deposition of silicon-based dielectrics for optical interconnection in optoelectronics 187 (1995) 473
- Schade, K., see Suchaneck, G. 187 (1995) 86
- Scheerlinck, F., see Stesmans, A. 187 (1995) 119
- Schmidt, E.G., see Lisovskii, I.P. 187 (1995) 186
- Schmidt, E.G., see Lisovskii, I.P. 187 (1995) 91
- Schneiders, S., see Wiersch, A. 187 (1995) 334
- Schoonman, J., see Baehr, O. 187 (1995) 409
- Schwebel, C., see Paillet, P. 187 (1995) 170
- Scofield, J.H., see Fleetwood, D.M. 187 (1995) 199
- Seigneur, F., see Autran, J.-L. 187 (1995) 374
- Senesi, F., see Bertolotti, M. 187 (1995) 453
- Serra, J., T. Szörényi, D. Fernández, P. González, E. García, J. Pou, B. León and M. Pérez-Amor, Deposition of amorphous silicon nitride thin films by CO₂ laser-induced chemical vapour deposition 187 (1995) 353
- Serra, J., see Parada, E.G. 187 (1995) 75
- Shaneyfelt, M.R., see Fleetwood, D.M. 187 (1995) 199
- Shimizu-Iwayama, T., K. Fujita, M. Akai, S. Nakao and K. Saitoh, Formation of visible photoluminescence bands in Si⁺-implanted silica glasses and thermal oxide films on crystalline Si 187 (1995) 112
- Shiyanovskaya, I.V., Structure rearrangement and electrochromic properties of amorphous tungsten trioxide films 187 (1995) 420
- Sibilia, C., see Bertolotti, M. 187 (1995) 453
- Sirotti, F., see Poncey, C. 187 (1995) 40
- Soares, J.C., see Parada, E.G. 187 (1995) 75
- Sofield, C.J., see Crossley, A. 187 (1995) 221
- Spinolo, G., see Martini, M. 187 (1995) 124
- Stathis, J.H., see Cartier, E. 187 (1995) 244
- Steinke, O., see Suchaneck, G. 187 (1995) 86
- Stesmans, A. and F. Scheerlinck, Parameters controlling the generation of natural intrinsic EX defects in thermal SiO₂ on Si 187 (1995) 119
- Stesmans, A., see Vanheusden, K. 187 (1995) 253
- Straboni, A., see Autran, J.-L. 187 (1995) 374

- Straboni, A., see Bravaix, A. 187 (1995) 365
 Straboni, A., see Brière, O. 187 (1995) 190
 Straboni, A., see Nédélec, S. 187 (1995) 106
 Suchaneck, G., O. Steinke, B. Alhallani and K. Schade, Oxygen-rich phase segregation in PECVD a-SiO_x:H semi-insulators 187 (1995) 86
 Suh, K.-S., see Park, H.-H. 187 (1995) 149
 Swart, P.L., see Bulkin, P.V. 187 (1995) 403
 Swart, P.L., see Bulkin, P.V. 187 (1995) 484
 Szekeres, A. and P. Danesh, Oxidation of amorphous and crystalline silicon 187 (1995) 45
 Szekeres, A., see Danesh, P. 187 (1995) 270
 Szörényi, T., see Serra, J. 187 (1995) 353
- Tallarida, G., A. Pecora, G. Fortunato, F. Plais, P. Legagneux, T. Kretz and D. Pribat, Leakage current reduction due to hot carrier effects in n-channel polycrystalline silicon thin film transistors 187 (1995) 195
 Tegude, F.J., see Wiersch, A. 187 (1995) 334
 Thévenin, P., see Baehr, O. 187 (1995) 409
 Thirion, V., see Bravaix, A. 187 (1995) 365
 Tilders, R., see Wiersch, A. 187 (1995) 334
 Tourtin, F., S. Daviero, A. Ibanez, A. Haidoux, C. Avinens and E. Philippot, Low temperature deposition of gallium phosphate amorphous dielectric thin films by aerosol CVD 187 (1995) 435
 Trombetta, L., see Roh, Y. 187 (1995) 165
 Tsytsanu, V.I., see Kravetsky, I.V. 187 (1995) 227
- Umezu, I., see Maeda, K. 187 (1995) 287
 Usami, K., see Morishita, S. 187 (1995) 66
- Valenti, P., see Audino, R. 187 (1995) 477
 Vanheusden, K., A. Stesmans and V.V. Afanas'ev, Hydrogen-annealing induced positive charge in buried oxides: correspondence between ESR and C-V results 187 (1995) 253
- v.d. Drift, E., see Drujff, K.G. 187 (1995) 206
 Vedda, A., see Martini, M. 187 (1995) 124
 Vieru, I.S., see Kravetsky, I.V. 187 (1995) 227
 Vincenzoni, R., M.C. Rossi, G. Leo and F. Galluzzi, Light-modulated carrier injection across the interface between transparent conducting oxide (n⁺-SnO₂) and semi-insulating amorphous silicon-carbide 187 (1995) 489
 Vuillaume, D., see Bravaix, A. 187 (1995) 365
- Warren, W.L. and D. Dimos, Photo-assisted switching and trapping in BaTiO₃ and Pb(Zr, Ti)O₃ ferroelectrics 187 (1995) 448
 Warren, W.L., see Fleetwood, D.M. 187 (1995) 199
 Warren, W.L., see Robertson, J. 187 (1995) 297
 Wiersch, A., C. Heedt, S. Schneiders, R. Tilders, F. Buchali, W. Keubart, W. Prost and F.J. Tegude, Room-temperature deposition of SiN_x using ECR-PECVD for III/V semiconductor microelectronics in lift-off technique 187 (1995) 334
 Wolters, H., see Parada, E.G. 187 (1995) 75
 Wortman, J.J., see Lucovsky, G. 187 (1995) 60
 Wulf, F., see Krauser, J. 187 (1995) 264
- Yard, G., see Meinertzhagen, A. 187 (1995) 181
 Yasuda, T., see Lucovsky, G. 187 (1995) 60
 Yeh, C.-F. and S.-S. Lin, Effects of plasma treatment on the properties of room-temperature liquid-phase deposited (LPD) oxide films 187 (1995) 81
- Zanotti, L., see Sassella, A. 187 (1995) 395
 Zöllner, J.-P., V. Cimalla and J. Pezoldt, RTP – temperature monitoring by means of oxidation 187 (1995) 23



ELSEVIER

Journal of Non-Crystalline Solids 187 (1995) 505-510

JOURNAL OF
NON-CRYSTALLINE SOLIDS

Subject index

Amorphous Semiconductors

- Capacitance Methods, Electrical Properties, Silicon Nitride 187 (1995) 313
Growth Kinetics, Oxidation Reduction, Silicon Dioxide 187 (1995) 45

Annealing Effects

- Defects, Electrical Properties, Silicon Dioxide 187 (1995) 35

Barium Titanate

- Photoinduced Effects, Polarization 187 (1995) 448

Bonding

- Deposition Techniques, Refractive Index, Silicon Nitride 187 (1995) 329
Electron Spin Resonance, Infra-red Absorption, Photo-emission, Silicon Nitride 187 (1995) 278
Ellipsometry, Modelling, Oxynitride Glasses 187 (1995) 395
Hydrogen Effects, Optical Properties, Silicon Nitride 187 (1995) 291
Infra-red Absorption, Modelling, Silicon Dioxide 187 (1995) 91
Infra-red Absorption, Processing Variables, Silicon Dioxide 187 (1995) 96
Optical Fibers, Oxynitride Glasses, Structure 187 (1995) 380

Boron

- Diffusion, Modelling, Silicon Dioxide 187 (1995) 106
Electrical Properties, III-V semiconductors, Plasma Deposition 187 (1995) 409
Infra-red Absorption, Modelling, Silicon Nitride 187 (1995) 340

Capacitance Methods

- Amorphous Semiconductors, Electrical Properties, Silicon Nitride 187 (1995) 313
Electrical Properties, Hydrogen Effects, Silicon Dioxide 187 (1995) 270

Chemical Modification

- Defects, Hydrogen Effects, Silicon Dioxide 187 (1995) 248

Crystallization

- Silicon Nitride 187 (1995) 301

Dangling Bonds

- Electron Spin Resonance, Electronic Structure, Photoinduced Effects, Silicon Nitride 187 (1995) 297
Electron Spin Resonance, Ion Implantation, Luminescence, Silicon Dioxide 187 (1995) 112
Hydrogen Effects, Silicon Dioxide 187 (1995) 232

Defects

- Annealing Effects, Electrical Properties, Silicon Dioxide 187 (1995) 35
Chemical Modification, Hydrogen Effects, Silicon Dioxide 187 (1995) 248
Electrical Properties, Electron Spin Resonance, Radiation Effects, Silicon Dioxide 187 (1995) 199
Electrical Properties, High Field Effects, Injection of Carriers, Silicon Dioxide 187 (1995) 175
Electrical Properties, Injection of Carriers, Silicon Dioxide 187 (1995) 140
Electrical Properties, Injection of Carriers, Silicon Dioxide 187 (1995) 181
Electrical Properties, Interfaces, Silicon Dioxide 187 (1995) 206
Electrical Properties, Interfaces, Silicon Dioxide 187 (1995) 273
Electrical Properties, Radiation Effects, Silicon Dioxide 187 (1995) 170
Electron Spin Resonance, Hydrogen Effects, Silicon Dioxide 187 (1995) 253
Electron Spin Resonance, Nitridation, Oxynitride Glasses 187 (1995) 385
High Field Effects, Interfaces, Silicon Dioxide 187 (1995) 186
Hydrogen Effects, Interfaces, Silicon Dioxide 187 (1995) 216
Hydrogen Effects, Interfaces, Silicon Dioxide 187 (1995) 244
Hydrogen Effects, Interfaces, Silicon Dioxide 187 (1995) 257
Infra-red Absorption, Ion Implantation, Silicon Dioxide 187 (1995) 101
Injection of Carriers, Interfaces, Silicon Dioxide 187 (1995) 165
Injection of Carriers, Modelling, Silicon Dioxide 187 (1995) 160
Interfaces, Radiation Effects, Silicon Dioxide 187 (1995) 211
Luminescence, Radiation Effects, Silicon Dioxide 187 (1995) 124
Nitridation 187 (1995) 374

Deposition Techniques

- Bonding, Refractive Index, Silicon Nitride 187 (1995) 329
- Devices, Infra-red Absorption, Silicon Dioxide 187 (1995) 49
- Devices, Silicon Dioxide 187 (1995) 60
- Dielectric Properties, Electrical Properties, Refractive Index 187 (1995) 425
- Electric Properties, Liquids, Silicon Dioxide 187 (1995) 81
- Electrical Properties, III-V semiconductors, Silicon Nitride 187 (1995) 334
- Electrical Properties, Plasma Deposition, Refractive Index, Silicon Nitride 187 (1995) 347
- Ellipsometry, Growth Kinetics, Silicon Dioxide 187 (1995) 70
- Field Effect, Ion Implantation, Raman Spectra, Silicon Dioxide 187 (1995) 10
- Gallium Phosphide, Structure 187 (1995) 435
- Hydrogen Effects, Infra-red Absorption, Silicon Dioxide 187 (1995) 75
- Infra-red Absorption, Refractive Index, Silicon Nitride 187 (1995) 353
- Infra-red Absorption, Silicon Dioxide 187 (1995) 66
- Kinetics, Oxidation Reduction, Silicon Dioxide 187 (1995) 29
- Oxynitride Glasses, Refractive Index 187 (1995) 484
- Photo-deposition, Thin Films 187 (1995) 473

Devices

- Deposition Techniques, Infra-red Absorption, Silicon Dioxide 187 (1995) 49
- Deposition Techniques, Silicon Dioxide 187 (1995) 60
- Electrical Properties, Interfaces, Silicon Dioxide 187 (1995) 1
- Field Effect, Silicon Dioxide 187 (1995) 195
- High Field Effects, Injection of Carriers, Silicon Dioxide 187 (1995) 156

Dielectric Properties

- Deposition Techniques, Electrical Properties, Refractive Index 187 (1995) 425
- Luminescence, Polymers 187 (1995) 415
- Optical Properties, Sol-Gel Method 187 (1995) 453

Diffusion

- Boron, Modelling, Silicon Dioxide 187 (1995) 106

Electric Properties

- Deposition Techniques, Liquids, Silicon Dioxide 187 (1995) 81

Electrical Properties

- Amorphous Semiconductors, Capacitance Methods, Silicon Nitride 187 (1995) 313
- Annealing Effects, Defects, Silicon Dioxide 187 (1995) 35
- Boron, III-V semiconductors, Plasma Deposition 187 (1995) 409
- Capacitance Methods, Hydrogen Effects, Silicon Dioxide 187 (1995) 270
- Defects, Electron Spin Resonance, Radiation Effects, Silicon Dioxide 187 (1995) 199

Defects, High Field Effects, Injection of Carriers, Silicon Dioxide 187 (1995) 175

- Defects, Injection of Carriers, Silicon Dioxide 187 (1995) 140
- Defects, Injection of Carriers, Silicon Dioxide 187 (1995) 181
- Defects, Interfaces, Silicon Dioxide 187 (1995) 206
- Defects, Interfaces, Silicon Dioxide 187 (1995) 273
- Defects, Radiation Effects, Silicon Dioxide 187 (1995) 170
- Deposition Techniques, Dielectric Properties, Refractive Index 187 (1995) 425
- Deposition Techniques, III-V semiconductors, Silicon Nitride 187 (1995) 334
- Deposition Techniques, Plasma Deposition, Refractive Index, Silicon Nitride 187 (1995) 347
- Devices, Interfaces, Silicon Dioxide 187 (1995) 1
- Fabrication, Nitridation, Silicon Dioxide 187 (1995) 361
- Glasses Containing Transition Metal Ions, Oxides 187 (1995) 134
- High Field Effects, Injection of Carriers, Silicon Dioxide 187 (1995) 144
- Infra-red Absorption, Oxynitride Glasses, Plasma Deposition, Processing Variables 187 (1995) 403
- Nitridation, Silicon Dioxide 187 (1995) 365

Electrochemical Properties

- Hydrodynamics, Structure 187 (1995) 420

Electron Microscopy

- Nitrogen, Oxynitride Glasses 187 (1995) 369

Electron Spin Resonance

- Bonding, Infra-red Absorption, Photo-emission, Silicon Nitride 187 (1995) 278
- Dangling Bonds, Electronic Structure, Photoinduced Effects, Silicon Nitride 187 (1995) 297
- Dangling Bonds, Ion Implantation, Luminescence, Silicon Dioxide 187 (1995) 112
- Defects, Electrical Properties, Radiation Effects, Silicon Dioxide 187 (1995) 199
- Defects, Hydrogen Effects, Silicon Dioxide 187 (1995) 253
- Defects, Nitridation, Oxynitride Glasses 187 (1995) 385
- Ion Implantation, Optical Properties, Silicon Dioxide 187 (1995) 457
- Processing Variables, Silicon Dioxide 187 (1995) 119

Electronic Structure

- Dangling Bonds, Electron Spin Resonance, Photoinduced Effects, Silicon Nitride 187 (1995) 297
- Silicon Dioxide, Silicon Nitride, Structure 187 (1995) 287

Ellipsometry

- Bonding, Modelling, Oxynitride Glasses 187 (1995) 395
- Deposition Techniques, Growth Kinetics, Silicon Dioxide 187 (1995) 70
- Optical Properties, Silicon Dioxide 187 (1995) 129
- Oxides, Processing Variables, Thin Films 187 (1995) 23

Fabrication

- Electrical Properties, Nitridation, Silicon Dioxide 187 (1995) 361
 Lithium Niobate, Optical Properties 187 (1995) 443

Field Effect

- Deposition Techniques, Ion Implantation, Raman Spectra, Silicon Dioxide 187 (1995) 10
 Devices, Silicon Dioxide 187 (1995) 195

Gallium Phosphide

- Deposition Techniques, Structure 187 (1995) 435

Germanium

- Photo-emission, Silicon Alloys, Silicon Nitride 187 (1995) 319

Glasses Containing Transition Metal Ions

- Electrical Properties, Oxides 187 (1995) 134
 Thin Films, Vapour Phase Deposition 187 (1995) 430

Growth Kinetics

- Amorphous Semiconductors, Oxidation Reduction, Silicon Dioxide 187 (1995) 45
 Deposition Techniques, Ellipsometry, Silicon Dioxide 187 (1995) 70

High Field Effects

- Defects, Electrical Properties, Injection of Carriers, Silicon Dioxide 187 (1995) 175
 Defects, Interfaces, Silicon Dioxide 187 (1995) 186
 Devices, Injection of Carriers, Silicon Dioxide 187 (1995) 156
 Electrical Properties, Injection of Carriers, Silicon Dioxide 187 (1995) 144
 Injection of Carriers, Silicon Dioxide 187 (1995) 190

Hydrodynamics

- Electrochemical Properties, Structure 187 (1995) 420

Hydrogen Effects

- Bonding, Optical Properties, Silicon Nitride 187 (1995) 291
 Capacitance Methods, Electrical Properties, Silicon Dioxide 187 (1995) 270
 Chemical Modification, Defects, Silicon Dioxide 187 (1995) 248
 Dangling Bonds, Silicon Dioxide 187 (1995) 232
 Defects, Electron Spin Resonance, Silicon Dioxide 187 (1995) 253
 Defects, Interfaces, Silicon Dioxide 187 (1995) 216
 Defects, Interfaces, Silicon Dioxide 187 (1995) 244
 Defects, Interfaces, Silicon Dioxide 187 (1995) 257
 Deposition Techniques, Infra-red Absorption, Silicon Dioxide 187 (1995) 75
 Interfaces, Silicon Dioxide 187 (1995) 264

Hydrogenation

- Infra-red Absorption, Processing Variables, Silicon Nitride 187 (1995) 308

III-V semiconductors

- Boron, Electrical Properties, Plasma Deposition Deposition Techniques, Electrical Properties, Silicon Nitride 187 (1995) 409
 187 (1995) 334

Infra-red Absorption

- Bonding, Electron Spin Resonance, Photo-emission, Silicon Nitride 187 (1995) 278
 Bonding, Modelling, Silicon Dioxide 187 (1995) 91
 Bonding, Processing Variables, Silicon Dioxide 187 (1995) 96
 Boron, Modelling, Silicon Nitride 187 (1995) 340
 Defects, Ion Implantation, Silicon Dioxide 187 (1995) 101
 Deposition Techniques, Devices, Silicon Dioxide 187 (1995) 49
 Deposition Techniques, Hydrogen Effects, Silicon Dioxide 187 (1995) 75
 Deposition Techniques, Refractive Index, Silicon Nitride 187 (1995) 353
 Deposition Techniques, Silicon Dioxide 187 (1995) 66
 Electrical Properties, Oxynitride Glasses, Plasma Deposition, Processing Variables 187 (1995) 403
 Hydrogenation, Processing Variables, Silicon Nitride 187 (1995) 308
 Photoconductivity, Plasma Deposition, Silicon Dioxide 187 (1995) 86
 Silicon Nitride, Structure 187 (1995) 324

Injection of Carriers

- Defects, Electrical Properties, High Field Effects, Silicon Dioxide 187 (1995) 175
 Defects, Electrical Properties, Silicon Dioxide 187 (1995) 140
 Defects, Electrical Properties, Silicon Dioxide 187 (1995) 181
 Defects, Interfaces, Silicon Dioxide 187 (1995) 165
 Defects, Modelling, Silicon Dioxide 187 (1995) 160
 Devices, High Field Effects, Silicon Dioxide 187 (1995) 156
 Electrical Properties, High Field Effects, Silicon Dioxide 187 (1995) 144
 High Field Effects, Silicon Dioxide 187 (1995) 190
 Interfaces, Optical Properties, Silicon Alloys 187 (1995) 489

Interfaces

- Defects, Electrical Properties, Silicon Dioxide 187 (1995) 206
 Defects, Electrical Properties, Silicon Dioxide 187 (1995) 273
 Defects, High Field Effects, Silicon Dioxide 187 (1995) 186
 Defects, Hydrogen Effects, Silicon Dioxide 187 (1995) 216
 Defects, Hydrogen Effects, Silicon Dioxide 187 (1995) 244
 Defects, Hydrogen Effects, Silicon Dioxide 187 (1995) 257
 Defects, Injection of Carriers, Silicon Dioxide 187 (1995) 165
 Defects, Radiation Effects, Silicon Dioxide 187 (1995) 211
 Devices, Electrical Properties, Silicon Dioxide 187 (1995) 1
 Hydrogen Effects, Silicon Dioxide 187 (1995) 264
 Injection of Carriers, Optical Properties, Silicon Alloys 187 (1995) 489
 Silicon Dioxide, Structure, Surface Properties 187 (1995) 149

Ion Implantation

- Dangling Bonds, Electron Spin Resonance, Luminescence, Silicon Dioxide 187 (1995) 112

- Defects, Infra-red Absorption, Silicon Dioxide 187 (1995) 101
 Deposition Techniques, Field Effect, Raman Spectra, Silicon Dioxide 187 (1995) 10
 Electron Spin Resonance, Optical Properties, Silicon Dioxide 187 (1995) 457
 Optical Properties, Silicon Dioxide 187 (1995) 227
- Kinetics**
 Deposition Techniques, Oxidation Reduction, Silicon Dioxide 187 (1995) 29
- Liquids**
 Deposition Techniques, Electric Properties, Silicon Dioxide 187 (1995) 81
- Lithium Niobate**
 Fabrication, Optical Properties 187 (1995) 443
- Luminescence**
 Dangling Bonds, Electron Spin Resonance, Ion Implantation, Silicon Dioxide 187 (1995) 112
 Defects, Radiation Effects, Silicon Dioxide 187 (1995) 124
 Dielectric Properties, Polymers 187 (1995) 415
- Modelling**
 Bonding, Ellipsometry, Oxynitride Glasses 187 (1995) 395
 Bonding, Infra-red Absorption, Silicon Dioxide 187 (1995) 91
 Boron, Diffusion, Silicon Dioxide 187 (1995) 106
 Boron, Infra-red Absorption, Silicon Nitride 187 (1995) 340
 Defects, Injection of Carriers, Silicon Dioxide 187 (1995) 160
- Nitridation**
 Defects, Electron Spin Resonance, Oxynitride Glasses 187 (1995) 385
 Defects 187 (1995) 374
 Electrical Properties, Fabrication, Silicon Dioxide 187 (1995) 361
 Electrical Properties, Silicon Dioxide 187 (1995) 365
- Nitrogen**
 Electron Microscopy, Oxynitride Glasses 187 (1995) 369
- Optical Fibers**
 Bonding, Oxynitride Glasses, Structure 187 (1995) 380
- Optical Properties**
 Bonding, Hydrogen Effects, Silicon Nitride 187 (1995) 291
 Dielectric Properties, Sol-Gel Method 187 (1995) 453
 Electron Spin Resonance, Ion Implantation, Silicon Dioxide 187 (1995) 457
 Ellipsometry, Silicon Dioxide 187 (1995) 129
 Fabrication, Lithium Niobate 187 (1995) 443
 Injection of Carriers, Interfaces, Silicon Alloys 187 (1995) 489
 Ion Implantation, Silicon Dioxide 187 (1995) 227
 Optical Waveguide, Orientational Glasses, Silicon Nitride 187 (1995) 477
 Optical Waveguide, Polymers 187 (1995) 494
- Optical Waveguide**
 Optical Properties, Orientational Glasses, Silicon Nitride 187 (1995) 477
 Optical Properties, Polymers 187 (1995) 494
- Orientational Glasses**
 Optical Properties, Optical Waveguide, Silicon Nitride 187 (1995) 477
- Oxidation Reduction**
 Amorphous Semiconductors, Growth Kinetics, Silicon Dioxide 187 (1995) 45
 Deposition Techniques, Kinetics, Silicon Dioxide 187 (1995) 29
- Oxides**
 Electrical Properties, Glasses Containing Transition Metal Ions 187 (1995) 134
 Ellipsometry, Processing Variables, Thin Films 187 (1995) 23
- Oxynitride Glasses**
 Bonding, Ellipsometry, Modelling 187 (1995) 395
 Bonding, Optical Fibers, Structure 187 (1995) 380
 Defects, Electron Spin Resonance, Nitridation 187 (1995) 385
 Deposition Techniques, Refractive Index 187 (1995) 484
 Electrical Properties, Infra-red Absorption, Plasma Deposition, Processing Variables 187 (1995) 403
 Electron Microscopy, Nitrogen 187 (1995) 369
- Photoconductivity**
 Infra-red Absorption, Plasma Deposition, Silicon Dioxide 187 (1995) 86
- Photo-deposition**
 Deposition Techniques, Thin Films 187 (1995) 473
- Photo-emission**
 Bonding, Electron Spin Resonance, Infra-red Absorption, Silicon Nitride 187 (1995) 278
 Germanium, Silicon Alloys, Silicon Nitride 187 (1995) 319
 Silicon, Surface Analysis 187 (1995) 40
- Photoinduced Effects**
 Barium Titanate, Polarization 187 (1995) 448
 Dangling Bonds, Electron Spin Resonance, Electronic Structure, Silicon Nitride 187 (1995) 297
- Plasma Deposition**
 Boron, Electrical Properties, III-V semiconductors 187 (1995) 409
 Deposition Techniques, Electrical Properties, Refractive Index, Silicon Nitride 187 (1995) 347
 Electrical Properties, Infra-red Absorption, Oxynitride Glasses, Processing Variables 187 (1995) 403
 Infra-red Absorption, Photoconductivity, Silicon Dioxide 187 (1995) 86

- Polarization**
Barium Titanate, Photoinduced Effects 187 (1995) 448
- Polymers**
Dielectric Properties, Luminescence 187 (1995) 415
Optical Properties, Optical Waveguide 187 (1995) 494
- Processing Variables**
Bonding, Infra-red Absorption, Silicon Dioxide 187 (1995) 96
Electrical Properties, Infra-red Absorption, Oxynitride Glasses, Plasma Deposition 187 (1995) 403
Electron Spin Resonance, Silicon Dioxide 187 (1995) 119
Ellipsometry, Oxides, Thin Films 187 (1995) 23
Hydrogenation, Infra-red Absorption, Silicon Nitride 187 (1995) 308
- Radiation Effects**
Defects, Electrical Properties, Electron Spin Resonance, Silicon Dioxide 187 (1995) 199
Defects, Electrical Properties, Silicon Dioxide 187 (1995) 170
Defects, Interfaces, Silicon Dioxide 187 (1995) 211
Defects, Luminescence, Silicon Dioxide 187 (1995) 124
- Raman Spectra**
Deposition Techniques, Field Effect, Ion Implantation, Silicon Dioxide 187 (1995) 10
- Refractive Index**
Bonding, Deposition Techniques, Silicon Nitride 187 (1995) 329
Deposition Techniques, Dielectric Properties, Electrical Properties 187 (1995) 425
Deposition Techniques, Electrical Properties, Plasma Deposition, Silicon Nitride 187 (1995) 347
Deposition Techniques, Infra-red Absorption, Silicon Nitride 187 (1995) 353
Deposition Techniques, Oxynitride Glasses 187 (1995) 484
- Silica**
Silicon, Surface Properties 187 (1995) 221
- Silicon**
Photo-emission, Surface Analysis 187 (1995) 40
Silica, Surface Properties 187 (1995) 221
- Silicon Alloys**
Germanium, Photo-emission, Silicon Nitride 187 (1995) 319
Injection of Carriers, Interfaces, Optical Properties 187 (1995) 489
- Silicon Dioxide**
Amorphous Semiconductors, Growth Kinetics, Oxidation Reduction 187 (1995) 45
Annealing Effects, Defects, Electrical Properties 187 (1995) 35
Bonding, Infra-red Absorption, Modelling 187 (1995) 91
Bonding, Infra-red Absorption, Processing Variables 187 (1995) 96
Boron, Diffusion, Modelling 187 (1995) 106
Capacitance Methods, Electrical Properties, Hydrogen Effects 187 (1995) 270
Chemical Modification, Defects, Hydrogen Effects 187 (1995) 248
Dangling Bonds, Electron Spin Resonance, Ion Implantation, Luminescence 187 (1995) 112
Dangling Bonds, Hydrogen Effects 187 (1995) 232
Defects, Electrical Properties, Electron Spin Resonance, Radiation Effects 187 (1995) 199
Defects, Electrical Properties, High Field Effects, Injection of Carriers 187 (1995) 175
Defects, Electrical Properties, Injection of Carriers 187 (1995) 140
Defects, Electrical Properties, Injection of Carriers 187 (1995) 181
Defects, Electrical Properties, Interfaces 187 (1995) 206
Defects, Electrical Properties, Interfaces 187 (1995) 273
Defects, Electrical Properties, Radiation Effects 187 (1995) 170
Defects, Electron Spin Resonance, Hydrogen Effects 187 (1995) 253
Defects, High Field Effects, Interfaces 187 (1995) 186
Defects, Hydrogen Effects, Interfaces 187 (1995) 216
Defects, Hydrogen Effects, Interfaces 187 (1995) 244
Defects, Hydrogen Effects, Interfaces 187 (1995) 257
Defects, Infra-red Absorption, Ion Implantation 187 (1995) 101
Defects, Injection of Carriers, Interfaces 187 (1995) 165
Defects, Injection of Carriers, Modelling 187 (1995) 160
Defects, Interfaces, Radiation Effects 187 (1995) 211
Defects, Luminescence, Radiation Effects 187 (1995) 124
Deposition Techniques, Devices, Infra-red Absorption 187 (1995) 49
Deposition Techniques, Devices 187 (1995) 60
Deposition Techniques, Electric Properties, Liquids 187 (1995) 81
Deposition Techniques, Ellipsometry, Growth Kinetics 187 (1995) 70
Deposition Techniques, Field Effect, Ion Implantation, Raman Spectra 187 (1995) 10
Deposition Techniques, Hydrogen Effects, Infra-red Absorption 187 (1995) 75
Deposition Techniques, Infra-red Absorption 187 (1995) 66
Deposition Techniques, Kinetics, Oxidation Reduction 187 (1995) 29
Devices, Electrical Properties, Interfaces 187 (1995) 1
Devices, Field Effect 187 (1995) 195
Devices, High Field Effects, Injection of Carriers 187 (1995) 156
Electrical Properties, Fabrication, Nitridation 187 (1995) 361
Electrical Properties, High Field Effects, Injection of Carriers 187 (1995) 144
Electrical Properties, Nitridation 187 (1995) 365
Electron Spin Resonance, Ion Implantation, Optical Properties 187 (1995) 457
Electron Spin Resonance, Processing Variables 187 (1995) 119
Electronic Structure, Silicon Nitride, Structure 187 (1995) 287
Ellipsometry, Optical Properties 187 (1995) 129

- | | | | |
|---|----------------|---|----------------|
| High Field Effects, Injection of Carriers | 187 (1995) 190 | Optical Properties, Optical Waveguide, Orientational Glasses | 187 (1995) 477 |
| Hydrogen Effects, Interfaces | 187 (1995) 264 | | |
| Infra-red Absorption, Photoconductivity, Plasma Deposition | 187 (1995) 86 | Sol-Gel Method | |
| Interfaces, Structure, Surface Properties | 187 (1995) 149 | Dielectric Properties, Optical Properties | 187 (1995) 453 |
| Ion Implantation, Optical Properties | 187 (1995) 227 | | |
| Silicon Nitride | | Structure | |
| Amorphous Semiconductors, Capacitance Methods, Electrical Properties | 187 (1995) 313 | Bonding, Optical Fibers, Oxynitride Glasses | 187 (1995) 380 |
| Bonding, Deposition Techniques, Refractive Index | 187 (1995) 329 | Deposition Techniques, Gallium Phosphide | 187 (1995) 435 |
| Bonding, Electron Spin Resonance, Infra-red Absorption, Photo-emission | 187 (1995) 278 | Electrochemical Properties, Hydrodynamics | 187 (1995) 420 |
| Bonding, Hydrogen Effects, Optical Properties | 187 (1995) 291 | Electronic Structure, Silicon Dioxide, Silicon Nitride | 187 (1995) 287 |
| Boron, Infra-red Absorption, Modelling | 187 (1995) 340 | Infra-red Absorption, Silicon Nitride | 187 (1995) 324 |
| Crystallization | 187 (1995) 301 | Interfaces, Silicon Dioxide, Surface Properties | 187 (1995) 149 |
| Dangling Bonds, Electron Spin Resonance, Electronic Structure, Photoinduced Effects | 187 (1995) 297 | Surface Analysis | |
| Deposition Techniques, Electrical Properties, III-V semiconductors | 187 (1995) 334 | Photo-emission, Silicon | 187 (1995) 40 |
| Deposition Techniques, Electrical Properties, Plasma Deposition, Refractive Index | 187 (1995) 347 | Surface Properties | |
| Deposition Techniques, Infra-red Absorption, Refractive Index | 187 (1995) 353 | Interfaces, Silicon Dioxide, Structure | 187 (1995) 149 |
| Electronic Structure, Silicon Dioxide, Structure | 187 (1995) 287 | Silica, Silicon | 187 (1995) 221 |
| Germanium, Photo-emission, Silicon Alloys | 187 (1995) 319 | Thin Films | |
| Hydrogenation, Infra-red Absorption, Processing Variables | 187 (1995) 308 | Deposition Techniques, Photo-deposition | 187 (1995) 473 |
| Infra-red Absorption, Structure | 187 (1995) 324 | Ellipsometry, Oxides, Processing Variables | 187 (1995) 23 |
| | | Glasses Containing Transition Metal Ions, Vapour Phase Deposition | 187 (1995) 430 |
| | | Vapour Phase Deposition | |
| | | Glasses Containing Transition Metal Ions, Thin Films | 187 (1995) 430 |